CODEN: JASMAN

The Journal of the Acoustical Society of America

ISSN: 0001-4966

Vol. 113, No. 6 June 2003

(Continued)

THE JOURNAL OF THE ACOUSTICAL SOCIETY OF AMERICA VOL. 113, NO. 6, JUNE 2003

CONTENTS—*Continued from preceding page*

(Continued)

THE JOURNAL OF THE ACOUSTICAL SOCIETY OF AMERICA VOL. 113, NO. 6, JUNE 2003

CONTENTS—*Continued from preceding page*

(Continued)

THE JOURNAL OF THE ACOUSTICAL SOCIETY OF AMERICA VOL. 113, NO. 6, JUNE 2003

CONTENTS—*Continued from preceding page*

ACOUSTICAL NEWS—USA

Elaine Moran
Acoustical Society of America, Suite 1NO1, 2 Huntington Quadrangle, Melville, NY 11747-4502

Editor's Note: *Readers of this Journal are encouraged to submit news items on awards, appointments, and other activities about themselves or their colleagues. Deadline dates for news items and notices are 2 months prior to publication.*

Reviewers of Manuscripts, 2002

Each year the *Journal* endeavors to publish a list of all the persons who reviewed manuscripts during the preceding year. Such a list is a compendium of names supplied by the Associate Editors. Because our peer review system depends strongly on the continuing anonymity of the reviewers, the *Journal* publishes these names in alphabetical order without identification of the associate editors who provided the names and without identification of the papers they reviewed. The primary reason for the publication of the list is to express the *Journal's* gratitude to its reviewers. Reviewing a paper is often a very time consuming and demanding task, and the anonymity requirement yields no professional recognition to those who generously provide their time to help the Associate Editors decide which papers should be published and to give constructive criticisms to the authors. The *Journal* is justifiably proud of this list, which includes a goodly proportion of all the researchers and eminent authorities in acoustics and related fields. In a compendium of this length, omissions and errors are inevitable. If anyone notices such, please send the corrections and missing names via e-mail or regular mail to either Elaine Moran (asa@aip.org) or Allan Pierce (adp@bu.edu).

Abawai, Ahmad
Abbas, Paul J.
Abdalla, Caroline
Abraham, Doug
Abrahamson, Arthur A.
Achenbach, Jan D.
Adachi, Seiji
Adams, Scott G.
Adler, Laszlo
Ahmad, Faiz
Ahuja, K.
Aifantis, E. C.
Ainslie, Michael
Akay, Adnan
Akeroyd, Michael A.
Albert, Donald
Alexander, Duncan
Alipour, Fariborz
Allen, Jont
Altes, Richard
Amabili, Marco
Antohe, B. V.
Aranov, B. A.
Arenas, Jorge
Arnold, Walter
Arnott, W. Patrick
Astley, H. Jeremy
Atchley, A. A.
Attalla, N.
Attenborough, Keith
Au, Whitlow W. L.
Audoin, Bertrand
Augspurger, George
Augusztinovicz, Fulop
Auriault, Jean-Louis
Avan, Paul
Bacon, Sid P.
Badiey, Mohsen
Baer, Thomas
Baggeroer, Arthur
Bai, Mingsan
Bailey, Michael D.
Baillet, Helene
Bakhaus, Scott
Balizer, E.
Ballato, Arthur
Barbone, Paul E.
Barger, James E.
Barney, Anna
Barron, Michael
Bartram, J. F.
Bass, Henry
Bates, S. M.
Battle, David
Baum, Shari R.
Beard, P.
Bech, Soren
Beckman, Mary
Beddor, Patrice S.
Begault, Durand
Behrman, Alison
Bell, Allan E.
Benes, Ewald
Benjamin, Kim C.
Bentler, Ruth
Beranek, Leo L.
Berge, Patricia
Berger, Elliott
Berman, A.
Berndt, Tobias
Berry, Alain
Berry, David A.
Berryman, James
Berthelot, Y. H.
Bertrand, Michael
Bertsch, M.
Besing, Joan M.
Besson, Mireille
Bishop, Garner
Blackstock, David T.
Blomgren, Peter
Blonigen, F.
Bloothooft, Gerrit
Blue, Joseph E.
Boersma, Paul
Boettcher, Flint
Boisvert, Jeffrey
Boonman, Arjan
Booth, Kay
Boothroyd, Arthur
Bosmans, Ivan L.
Botteldooren, Dick
Boutillon, Xavier
Bowles, Ann
Bradley, Charles E.
Bradley, David
Bradley, John S.
Bradlow, Ann
Brandstätt, Peter
Brant, Larry J.
Brayman, Andrew
Breazeale, Mack
Breebaart, D. Jeroen
Brennan, Michael
Brenner, Michael
Bright, C. B.
Broad, David J.
Bronkhorst, Adelbert W.
Brooke, Gary
Brown, Charles
Brown, D.
Brown, David
Brown, Michael
Bruce, Ian C.
Brujan, Emil-Alexandru
Brungart, Douglas S.
Bucaro, Joseph A.
Buchanan, George
Buck, Karl
Buckingham, Michael J.
Buder, Eugene H.
Buell, Thomas N.
Burdisso, Ricardo
Burkhardt, John
Burkhkard, Mahlon D.
Burnett, David
Burnett, Theresa A.
Burns, Edward M.
Burov, V. A.
Burroughs, Courtney B.
Busch-Vishniac, Ilene
Buss, Emily
Butler, J. L.
Buus, Søren
Byrd, Dani
Cable, Peter
Campbell, Murray
Candy, James V.
Cantrell, John H.
Carder, Donald A.
Carey, William M.
Carlyon, Robert P.
Carrell, Thomas
Carroll, Gerald
Carstensen, Edwin
Cato, Doug
Cawley, Peter
Cazals, Yves
Cazzolato, Ben
Chaigne, Antoine
Chailkian, Tigran
Chalikia, Magdalene
Chambers, David
Chambers, James M.
Chambers, James P.
Champlin, Craig
Chan, Philemon
Chandiramani, Khushi L.
Chapman, C. John
Chapman, David M. F.
Chapman, Ross
Chatterjee, Monita
Cheeke, Jdn
Cheeke, David
Chen, P. T.
Chen, X.
Cheney, Margaret
Cheng, Alexander H. D.
Cheng, Arthur
Cheng, C. H.
Cheng, Jun
Cherukuri, Harischandra P.
Cheyne, Stanley A.
Chial, Michael R.
Chimenti, Dale
Chien, Ting
Ching, Teresa
Chiu, Ching-Sang
Choi, Sunghoon
Cholewiak, Roger
Chondros, Thomas G.
Chotiros, Nicholas
Choy, Y. S.
Christensen-Dalsgaard, Jakob
Christie, Douglas
Chu, Dezang
Chu, Wing T.
Church, Charles
Ciocca, Valter
Clark, Christopher
Clark, J. A.
Clark, Rob
Clark, William W.
Clarkson, Marsha
Clay, Clarence S.
Clermont, Frantz
Cleveland, Robin C.
Coakley, W. Terence
Cohen, Leon
Colburn, H. Steven
Cole, Bernard
Collins, Leslie
Collins, Michael
Colonius, Tim
Colosi, John A.
Colousi, A.
Colton, Raymond H.
Connine, Cynthia
Conoir, Jean Marc
Cook, Perry

 0001-4966/2003/113(6)/2947/6/$19.00

Coombs, Sheryl
Cooper, Nigel
Cornuelle, Bruce
Corsaro, Robert
Cottingham, James
Coulevrat, Francois
Cowan, Brenda
Cowin, S.
Cox, Robyn
Cranford, Ted
Crystal, Thomas H.
Culling, John F.
Cummins, Fred
Cummings, William C.
Cunefare, Kenneth C.
Cuomo, F. W.
Cuschieri, Joseph
Dabelsteen, Torben
Dahl, Peter H.
Daigle, Gilles
Darve, Eric
Darvennes, Corinne
Darwin, Christopher J.
Dassios, George
Datta, Subhendu
Dau, Torsten
Davis, Anthony J. M.
Dean, Cleon
de Boer, Egbert
de Cheveigne, Alain
De Donato, Stefano R.
Degertekin, Levent
de Hoop, A.
de Hoop, Martin
de Jong, Kenneth J.
de Krom, Guus
Delgutte, B.
de Lima, Washington
Demany, Laurent
Demer, David
Dent, Micheal
Depollier, Claude
Deutsch, Diana
de Vries, D.
Dhar, Sumit
Diaz, Jose
Dickey, Joseph
Diehl, Randy L.
Dillon, Harvey
Dimitriadis, Emilios
Divenyi, Pierre
Doherty, Karen
Dokumaci, E.
Dolan, David
Donaldson, Gail
Dong, S. B.
Donskoy, Dimitri
Dooling, Robert
Dorman, Michael
Dosso, Stan
Doucet, John
Dowling, David
Downing, Micah
Dragonette, Louis
D'Spain, Gerald
Du, Gonghuan
Dual, J.
Dubno, Judy
Duda, Timothy
Dunn-Rankin, Derek
Dunn, Martin L.
Duraiswami, Ramani
Durlach, Nathaniel I.
Durocher, Jean-Noel
Dye, Raymond
Dyer, Ira
Dzieciuch, Matthew
Eckoldt, D.
Eddington, Donald K.
Edds-Walton, P.
Edelmann, Geoffrey
Edwards, Brent
Eggermont, Jos
Ehrmet, Helmut
Eilers, Rebecca
Eisenberger, Moshe
Ekholdt, D.
Elder, S. A.
Elishakoff, Isaac
Elko, G. W.
Elliott, Stephen
Elmore, Paul
Embleton, Tony F. W.
Embrechts, J. J.
Enflo, Bengt O.
Engstrand, Olle
Erbe, Christine
Erdreich, John
Erickson, Mary L.
Essert, Robert
Evans, Gary
Evans, Richard B.
Evans, William
Eversman, Walter
Every, A. G.
Fabre, Benoit
Fahey, Paul
Fahnline, John B.
Fahy, Francis
Fastl, Hugo
Faulkner, Andrew
Fawcett, John A.
Fay, Richard
Feeney, Patrick
Fegant, Oliver
Fei, Dong
Feit, David
Feke, Donald
Feleppa, Ernest
Fenton, Brock
Ferassat, Feri
Ferber-Viart, Chantal
Ferla, Carlo
Festen, Joost
Feth, Lawrence
Feuillaude, Chris
Fields, James
Finch, R. D.
Fink, M.
Finneran, James
Fischer, Julia
Fishman, Lou
Fitch, W. Tecumseh
Fitting, D. W.
Fitzgibbons, Peter
Flanagan, James
Flannery, Colin
Flatau, Allison
Flege, James E.
Fletcher, Neville H.
Florentine, Mary
Floyd, Robert
Foote, Kenneth
Forbes, Barbara
Ford, John
Forssen, Jens
Fourakis, Marios
Fowler, Carol A.
Fowlkes, Jeffrey B.
Fox, Robert
Fox, Warren
Frampton, Kenneth
Frankel, Steven H.
Frankenthal, S.
Franzoni, Linda
Fredberg, Jeffrey
Frederiksen, Erling
Freeman, Dennis
Freund, R.
Freyman, Richard L.
Fricke, F.
Frisk, George
Frizzell, Leon
Fromme, Paul
Fryba, Ladislav
Fu, Quan
Fucci, Donald
Fuchs, Helmut V.
Furusawa, Masahiko
Fuzessery, Nick
Gabrielson, Thomas
Gade, Anders
Galland, Marie-Annick
Gallasch, Eugene
Gallen, Eric
Gammell, Paul M.
Garces, Milton A.
Garrelick, Joel
Garrett, Steven
Gascon, Francisco
Gaumond, Charles
Gaunaurd, Guillermo
Gauss, Roger
Gautier, Jean
Gedon, David
Geers, Thomas L.
Gentner, Tim
Gerratt, Bruce R.
Gerstein, Ed
Gerstoft, Peter
Gibbs, Gary
Gibian, Gary
Gick, Bryan
Gilbert, Joel
Gilbert, Kenneth
Gilmore, Richard Grant
Ginsberg, Jerry
Glattke, Ted
Gobl, Christer
Godin, Oleg
Goldstein, Julius
Gonzalez, Iciar
Goode, Richard
Goodman, Ralph R.
Goold, John C.
Gordon-Salant, Sandra
Gorga, Michael P.
Gottleib, H.
Gracewski, Sheryl
Grantham, D. Wesley
Gratton, Michael Anne
Green, W. A.
Greenberg, Steven
Greene, Charles
Greene, Corriegh
Greenlaw, Charles
Gridin, Dmitir
Griesenger, David
Griffiths, T. D.
Griffond, Jerome
Grigoriu, Mircea D.
Grimault, Nicholas
Grondel, Sebastian
Grose, John
Grosh, Karl
Grove, Deborah
Guettler, Knut
Guillot, F.
Guinan, John
Gumerov, Nail A.
Gummer, Anthony
Gurevich, Boris
Gusev, Vitalyi
Gutfinger, Chaim
Ha, Sung Kyu
Haak, Hein
Haber, Robert B.
Haberman, Robert C.
Haddrow, James B.
Hafter, Ervin
Haines, Mary
Hald, Jorgen
Hall, Donald
Hall, Joseph L.
Hall, Joseph W.
Hallaj, Ibrahim
Hambric, Steven
Hamilton, Mark F.
Hammerton, Paul
Hanagud, Sathya
Handel, Steven
Hansen, Uwe J.
Hanyga, Andrzej
Harland, Andy
Harris, Francis P.
Harris, G. R.
Harris, John G.
Hartmann, William M.
Hasegawa-Johnson, Mark
Hatfield, Julie
Hattis, Dale
Havelock, D. I.
Hawks, John
Hayek, Mike
Hayek, Sabih I.
Hayward, Gordon
Heaney, K.
Hedbergm, Claes
Heffner, Rickeye
Heffner, Todd
Heffner, Henry
Heinz, M.
Heinz, Michael G.
Hellman, Rhona
Henrich, Nathalie
Henyey, Frank
Herdic, Peter C.
Hermand, Jean-Pierre
Herstein, Louis
Hertrich, Ingo
Herzel, Hanspeter
Hestholm, Stig
Heutschi, Kurt
Heyliger, Paul R.

Hickey, Craig
Hickling, Robert
Hilgenfeldt, Sacsha
Hillenbrand, James M.
Hiller, Robert
Hirschberg, Avraham
Hirsekorn, Sigrun
Hixson, Elmer
Hodgkiss, William S.
Hodgson, Murray
Hoit, Jeanette
Holger, Jens
Holland, Charles
Holland, Christy
Holland, Keith
Hollenberg, Lloyd
Holliday, D. Vance
Hom, C. L.
Homm, Andreas
Homm, Anton
Hoole, Philip
Hoppgood, Dr.
Horonjeff, Richard
Horoshenkov, Kirill
Hossock, John A.
Hosten, Bernard
Houde, John F.
Houde, Robert
Houston, Brian H.
Houtsma, Adrian
Howarth, Thomas R.
Howe, Bruce
Howe, Michael S.
Howell, Peter
Huang, Lixi
Huang, Viaojun
Humes, Larry
Hunsaker, Don, II
Hurley, Donna
Hursky, Paul
Hutchins, David
Hwang, Wei-Sheng
Igusa, Takeru
Ih, Jeong-Guon
Imai, Akihisa
Impagliazzo, John
Ingham, Roger J.
Insana, Michael
Iordache, Dan
Irino, Toshio
Iskarous, Khalil
Ison, James
Iverson, Paul
Jackson, Darrell R.
Jackson, Michel T. T.
Jacobs, Laurence
Jacobsen, Finn
Janssen, Thomas
Janssens, Marcel
Jansson, Eric
Jarzynski, Jacek
Javel, Eric
Jayachandran, Vijay
Jensen, Finn
Jesteadt, Walt
Jiang, Jack
Johnson, D. L.
Johnson, David
Johnson, Mary E.
Johnson, Marty E.
Jones, Dennis
Jones, Jeffery A.
Jongman, Allard
Kaernbach, Christian
Kahana, Yuvi
Kaimya, N.
Kalveram, Karl T.
Kamakura, Tomoo
Kang, Jian
Kaplunov, Julius
Kapodistrias, George
Kargl, Steven
Karnell, Michael P.
Karpov, Sergi
Kashino, Makio
Kastak, David
Kates, James
Katsnelson, Boris
Katz, Brian F.
Katz, R.
Katz, Richard A.
Keefe, Douglas H.
Keidel, James
Keltie, Richard
Kempster, Gail B.
Kendall, N.
Keolian, Robert
Keppens, Veerle
Kergomard, Jean
Kerry, Geoff
Ketten, Darlene
Ketterling, Jeffrey
Kidd, Gary R.
Kidd, Gerald
Kiefte, Michael
Kihlman, Tor
Kim, J.
Kirby, Ray
Kirk, Karen
Kirkeby, Ole
Kitahara, Michihiro
Klauson, Aleksander
Kluender, Keith
Klump, George
Knobles, David
Kob, Malte
Koc, S.
Koehnke, Janet
Koelsch, Stefan
Koenig, Laura L.
Koessel, Manfred
Kohlrausch, Armin
Kollmeier, Birger
Konrad-Martin, Dawn
Kopec, John W.
Korman, Murray
Kovitz, Paul
Koziak, Richard
Krakow, Rena
Krane, Michael H.
Kreiman, Jody
Kremkau, Fred
Krishnamurthy, Ashok
Krishnan, Ananthanarayan
Krishnaswamy, S.
Krokstad, Asbjorn
Kroll, Judith
Kryiakakis, Chris
Kuhl, Patricia K.
Kujawa, Sharon
Kundu, Tribikram
Kuperman, William A.
Kuttruff, K.
Kuzmenko, A.
Kwon, Bom Jun
Lacerda, Francisco
Lafluer, L. Dwynn
Lagakos, N.
Lam, K. Y.
Lam, L. W.
Lam, Yiu
Lane, Harlan
Lane, Steve
Langendijk, Erno
Langley, Robin S.
Laoulache, Raymond N.
Larsen, Ole
Lauchle, Gerald C.
Laugier, Pascal
Laura, Particio A.
Lauriks, Walter
Lavenex, Pamela Banta
Lavery, Andone
Lawrie, J. M.
Lee, Ding
Lee, Jang Moo
Lee, Joon
Lee, Wei
Lees, Sidney
Legendre, Dominique
Lehr, Andre
Leissa, Arthur W.
Lentz, Jennifer
LePage, Kevin
Lercher, Peter
Lermusiaux, Pierre
Letcher, S. V.
Letowski, Thomas
Levinson, Steven
Lewin, Peter
Lhemery, Alain
Liberman, M. C.
Liebler, Marko
Liew, K. M.
Lightfoot, Jay
Liljencrants, Johan
Lilly, Jerry
Lim, Raymond
Lin, K.
Lindevald, I. M.
Lipkins, Bart
Liss, Julie M.
Liszka, Ludwik
Litovsky, Ruth
Liu, Chang
Liu, Qing-Huo
Liu, Yijun
Lizzi, Frederic
Ljunggren, Sten
Lobkis, Oleg
Lock, James
Logan, John
Logan, Kenneth J.
Loizou, Philipos
Long, Glenis R.
Long, Lyle
Lorenzi, Christian
Lotto, Andrew J.
Lowe, Michael
Lu, I-Tau
Lucero, Jorge L.
Ludlow, Christy L.
Ludvigsen, Carl
Lutfi, Robert A.
Luz, George A.
Lynch, James F.
Macaulay, Gavin
Mace, B.
Madden, John
Magen, Harriet
Maidanik, Gideon
Makris, Nicholas
Mangiante, Gerard
Mann, David
Mann, J. A., III
Manning, Jerome
Manohar, C. S.
Mansy, H. A.
Marks, Lawrence E.
Marsh, Alan H.
Marston, Philip L.
Martin, Glenn
Martin, Paul
Mashie, James J.
Maslov, Konstantin
Masson, Patrice
Mast, T. Douglas
Masters, Mitch
Masters, William
Matsuo, Ikuo
Matthies, Melanie
Matula, Thomas
Mauermann, Manfred
Mayer, W. G.
Maynard, J. D., Jr.
McCall, Katherine R.
McCammon, Diana
McClements, Julian D.
McCormack, David
McCowan, Brenda
McCoy, John J.
McDaniel, J. Gregory
McDermott, Hugh
McEachern, James
McFadden, Dennis
McGowan, Richard S.
McKay, Colette S.
McNab, Alistair
McQueen, James
Mehl, James B.
Mellert, Volker
Meloni, Tommaso
Mendel, Jerry
Menge, Christopher W.
Menounou, Penelope
Mercer, James
Mettin, Robert
Meyer, Jens
Michaelis, Dirk
Michalopoulou, Eliza
Micheyl, Christophe
Miedema, Henk M. E.
Migliori, Albert
Miles, Ronald
Miller, Douglas
Miller, James G.
Miller, Morton
Miller, Patrick
Mills, D. M.
Mills, David
Mills, John H.
Minachi, Ali
Moeser, Michael
Moffett, Mark B.

Mohl, Bert
Moldover, Michael
Moody, David
Moore, Brian C. J.
Moore, Christopher A.
Moore, David
Moore, Patrick
Moorhouse, Andrew
Moran, Brian
Morillas, J. M. B.
Morimoto, Masayuki
Moros, E. G.
Moss, Cynthia
Mourpopulos, John
Mozurkewich, G.
Muehleisen, Ralph
Mueller, Rolf
Muesch, Hannes
Mullennix, John
Munhall, Kevin G.
Munjal, Manohar Lal
Munro, Murray
Murphy, John C.
Murray, Todd
Myrberg, Arthur
Nachbin, Andre
Naghshineh, Koorosh
Nagy, Peter B.
Nakagawa, Seigi
Naugolnykh, Konstantin
Nazarov, V. E.
Nearey, Terrance
Nederveen, Cornelis
Nedzelnitsky, Victor
Neeley, Stephen
Neise, Wolfgang
Neff, Donna
Nelson, David A.
Nelson, Philip
Nemeth, Erwin
Neubauer, Juergen
Neuman, Arlene
Newman, Rochelle S.
Nicholson, Patrick
Nielsen, Peter
Nightingale, Trevor
Nittrouer, Susan
Nizami, Lance
Noble, William
Nolle, A. W.
Nooteboom, Sieb
Norris, Andrew
Notwotny, Helmuth
Novarini, Jorge
Nusbaum, Howard
Nuttall, Alfred
Nyborg, Wesley L.
Nye, Patrick W.
Oakley, Clyde
Oba, Roger
Oden, Gregg
Odom, Robert
Oelze, Michael
Ogren, Mikael
Ohala, John
Ohde, Ralph N.
Oldham, David
Olivieri, Marc
Olson, Elizabeth
Onsay, Tanner
Ophir, Jonathan
Orr, Marshall
Orris, Greg
Osetrov, A.
Ostrovsky, Lev
Ostry, David J.
Oxenham, Andrew
Ozer, Bulent
Padilla, Frederic
Palmer, David
Palombit, Ryne
Pan, Jie
Pandey, P. C.
Panetta, Paul
Panneton, Raymond
Papadakis, John
Papanicolaou, George
Parkins, John W.
Parncutt, Richard
Parrott, Tony
Paul, Hari
Pavic, Goran
Peake, William T.
Pearson, Antony
Pearsons, Karl S.
Peat, Keith
Pelorson, Xavier
Penel, Amandine
Percin, Gokham
Petculescu, Andi
Peters, Robert
Petersson, B.
Pfingst, Bryan
Phillips, Dennis
Phillmore, Leslie
Photiadis, Douglas
Picaut, Judicael
Picheny, Michael
Piercy, J. E.
Pierucci, Mauro
Pilakowski, Bogdan
Pinsky, Peter
Piquette, Jean C.
Pitermann, Michel
Pitts, Todd A.
Plack, Christopher
Plotkin, Kenneth
Pompino-Marschall, Bernd
Pompoli, Roberto
Ponton, Curtis
Popovics, John S.
Popp, K.
Popper, Arthur
Porter, Michael B.
Potel, Catherine
Potter, John
Premat, Eric
Pressnitzer, Daniel
Preston, Al
Pride, Stephen R.
Prosperetti, Andrea
Psencik, Ivan
Puria, Sunil
Pyle, Robert
Qiu, Xiaojun
Qu, Jianmin
Rabinkin, D. V.
Radcliffe, Clark
Rafaely, Boaz
Ragot, Richard
Raju, P. K.
Rakerd, Brad
Rankovic, Christine
Rasmussen, Gunnar
Raspet, Richard
Ratner, Nan Bernstein
Ravicz, Michael E.
Rawlins, Tony
Ray, Laura
Recio, Alberto
Redekop, David
Reeves, Jon
Reico, Alberto
Reid, John M.
Remington, Paul J.
Rew-Gottfried, Terry
Rhode, William S.
Rice, H. J.
Richards, Virginia
Richardson, Bernard
Richardson, Michael
Ricker, Denny
Ridgway, Sam
Ring, Martin D.
Robinson, Harold C.
Rodet, Xavier
Rodgers, Oliver
Rogers, James
Rogers, Peter H.
Rokhlin, Stan
Rolt, K. D.
Romeu, Jordi
Rose, G.
Rose, Joseph
Rosen, Stuart
Rosenblum, Larry
Roskowski, John J.
Rossing, Thomas
Roumeliotis, John A.
Roux, P.
Roy, Ronald A.
Royston, Thomas J.
Rubenstein, Jay
Rudolphi, Thomas J.
Rumerman, Melvyn
Ruzzene, Massimo
Rvachew, Susan
Sabina, Federico J.
Sakagami, Kimihiro
Salomons, Erik M.
Salvi, Richard
Salzburger, Hans Jurgen
Sammelmann, Gary
San Andres, Luis
Santos-Sacchi, Jose
Sapienza, Christine H.
Sapozhniko, Oleg
Sarkissian, Angie
Sawusch, James R.
Scaife, Rónán
Scandrett, Clyde
Scavone, Gary P.
Scharf, Bert
Scheifele, Peter
Schellenberg, Glenn
Scherer, Ronald C.
Schilt, Carl
Schluach, Robert
Schmidt, A. M.
Schmidt, Henrik
Schmiedt, Richard
Schmitt, Denis
Schneider, Bruce
Schneider, John
Schoentgen, Jean
Schomer, Paul D.
Schreiner, Christoph
Schroeder, Manfred
Schuhmacher, Andreas
Schulte-Fortkamp, Brigitte
Schumacher, Robert T.
Schusterman, Ronald
Scott, Waymond
Sek, Alexander
Selamet, Ahmet
Sessler, Gerhard, M.
Sethares, William
Seybert, Andrew
Shackleton, Trevor
Shadle, Christine
Shamma, Shihab A.
Shankar, P.
Shannon, Robert V.
Sharp, Stephen
Sheft, Stanley
Shepard, W. Steve
Shera, Christopher A.
Sherman, Charles
Shields, F. Douglas
Shinn-Cunningham, Barbara G.
Shore, Susan
Shorter, Phil
Shung, K. Kirk
Sibul, Leon
Siderius, Martin
Siegel, Jon
Siegmann, William L.
Sigrist, M.
Silcox, Richard J.
Silvia, Manuel T.
Simmen, Jeff
Simmons, James
Sinclair, A. N.
Sinder, Daniel J.
Singh, R.
Singh, Rajendra
Sinkus, Ralph
Skelton, Elizabeth, A.
Skinner, Margo
Slaton, Willian
Smith, Barton
Smith, John
Smith, Kevin
Smits, Roel
Smoorenburg, Guido
Smurzynski, Jacek
Snell, Karen B.
So, Jin-Hyun
Soegijanto, B.
Soize, C.
Solé, Maria-Josep
Solna, Knut
Solodov, Igor
Sommerfeldt, Scott
Sorkin, Robert
Sostaric, Joe
Sousa Lima, Renata
Souza, Luiz
Spahr, Webb
Sparrow, Victor W.
Spicer, James B.
Spies, Martin
Spiesberger, John
Spitzer, Matt

Spoor, Philip S.
Stafford, Kate
Stanton, Tim
Stellmack, Mark
Stelmachowicz, Pat
Stepanishen, Peter R.
Stephen, Ralph
Stephenson, Uwe
Stergiopoulos, Stergios
Stinson, M. R.
Stoel-Gammon, Carol
Stoker, R.
Stone, Maureen
Stone, Michael
Story, Brad H.
Stotts, Stephen A.
Strange, Winifred
Strasberg, Murray
Streltsov, Vladimir
Strickland, Elizabeth
Strik, Helmer
Strong, William J.
Sugimoto, Nobumasa
Sullivan, Brenda
Sullivan, E. J.
Summerfield, Quentin
Summers, Van
Sun, Jian-Qiao
Supin, A.
Surprenant, Aimee
Sussman, Elyse
Sussman, Joan E.
Suter, Alice
Sutherland, Louis C.
Suthers, Roderick
Sutin, Alexander M.
Svensson, Peter
Swallowe, Gerry
Swanson, David
Swift, Gregory
Szabo, Thomas
Tabain, Marija
Taber, Larry
Takagi, Naoyuki
Takagi, Kenshiro
Takahashi, Daiji
Takeuchi, T.
Talmdadge, Carrick
Tan, Hong Z.
Tang, J.
Tang, S. K.
Tarnow, Viggo
Taylor, Larry
Telschow, Kenneth
Temkin, S.
Ternstrom, Sten
Tew, Richard
Thode, Aaron
Thompson, Bruce
Thompson, D. J.
Thompson, David
Thompson, Lonny
Thompson, S. C.
Thomson, David
Thorsos, Eric
Thwaites, Suzanne
Tindle, Chris
Ting, Robert
Titterton, Paul J., Jr.
Titze, Ingo
Todd, Neil
Toksoz, M. N.
Tolstoy, A.
Toole, Floyd
Tougaard, Jakob
Towers, David
Tracey, Brian
Trahey, Gregg
Trainor, Laurel
Traunmiller, Hartmut
Tressler, J. F.
Turgut, Altan
Turner, Christopher W.
Turner, Joseph
Tyler, Richard S.
Uchanski, Rosalie
Ueha, Sadayuki
Umnova, Olga
Ungar, Eric E.
Unger, Evan
Vakakis, Alexander F.
Valle, Christine
Van Buren, A. L.
Van Den Abeele, Koen
van den Honert, Christopher
van der Heijden, Marcel
van de Par, Steven
Van Dijk, Pim
Vanhille, Christian
van Hoesel, Richard
Van Parjis, Sofie
Van Tassel, Dianne
van Wieringen, Astrid
Vaudrey, Michael A.
Vedit, Martin
Verdolini, Katherine
Vignola, Joe
Vilkman, Erkki
Vipperman, Jeffrey
Vollmann, Jacqueline
von Estorff, Otto
Vorlaender, Michael
Voronovich, Alex
Vos, Joos
Voss, Susan
Waag, Robert C.
Wahlberg, Magnus
Wakeland, Ray
Walden, Brian
Walerian, Elzbieta
Wall, David
Wallace, David
Wang, L.
Wang, Lily
Wang, X.
Wapenaar, C. P. A.
Warren, Richard
Watkins, William
Watson, Charles S.
Wauer, Joerg
Waxler, Roger
Wear, Keit
Weaver, R. L.
Weisenberger, Janet M.
Weismer, Gary G.
Werner, Lynne
Wesler, Eric
Wessel, David
Wester, Eric
Westwood, Evan K.
Wettergren, Thomas
Wible, Brad
Wightman, Frederic L.
Wilen, Larry A.
Williams, David
Williams, Earl G.
Williams, Kevin
Williamson, R.
Willott, James
Wilson, Blake
Wilson, D. Keith
Wilson, O. B.
Wilson, P.
Wilson, Preston S.
Wirgin, Armand
Wodicka, George R.
Wojtcik, Magda
Wolfe, J.
Wolfson, Michael
Wong, G. S. K.
Woodhouse, James
Worcester, Peter C.
Wouters, Jan
Wright, Beverly
Wu, J.
Wu, Junru
Wu, Kuangcheng
Wu, Ping
Wu, Ru-Shan
Wu, Sean
Xi, Zhichen
Xu, Yi
Yamamoto, Tok
Yang, T. C.
Yasui, H.
Yoshikawa, Shigeru
Yost, William A.
Yost, William T.
Yuan, Jing
Kim, Kwang Yul
Zagzebski, J. A.
Zahorian, Stephen A.
Zahorik, Pavel
Zaitsev, V. Yu.
Zattore, Robert J.
Zeegers, Jos
Zeng, Fan-Gang
Zeroug, S.
Zhong, Pei
Ziegler, Wolfram
Zimmer, Karin
Zinszner, Bernard
Zirkelback, Nicole
Zuckerwar, Allan J.
Zurk, L.

USA Meetings Calendar

Listed below is a summary of meetings related to acoustics to be held in the U.S. in the near future. The month/year notation refers to the issue in which a complete meeting announcement appeared.

2003

23–25 June	NOISE-CON 2003, Cleveland, OH [INCE Business Office, Iowa State Univ., 212 Marston Hall, Ames, IA 50011-2153; Fax: 515-294-3528; E-mail: ibo@ince.org].
27–30 July	1st Conference on Acoustic Communication by Animals, University of Maryland, College Park, MD [Acoustical Society of America, Suite 1 NO1, 2 Huntington Quadrangle, Melville, NY 11747-4502; Tel.: 516-576-2360; Fax: 516-576-2377; E-mail: asa@aip.org; WWW: http://asa.aip.org/communication.html].
5–8 Oct.	IEEE International Ultrasonics Symposium, Honolulu, HI [W. D. O'Brien, Jr., Bioacoustics Research Lab., Univ. of Illinois, Urbana, IL 61801-2991; Fax: 217-244-0105; WWW: www.ieee-uffc.org].
10–14 Nov.	146th Meeting of the Acoustical Society of America, Austin, TX [Acoustical Society of America, Suite 1NO1, 2 Huntington Quadrangle, Melville, NY 11747-4502; Tel.: 516-576-2360; Fax: 516-576-2377; E-mail: asa@aip.org; WWW: asa.aip.org]. Deadline for receipt of Abstracts: 2 July 2003.

2004

24–28 May	75th Anniversary Meeting (147th Meeting) of the Acoustical Society of America, New York, NY [Acoustical Society of America, Suite 1NO1, 2 Huntington Quadrangle, Melville, NY 11747-4502; Tel.: 516-576-2360; Fax: 516-576-2377; E-mail: asa@aip.org; WWW: asa.aip.org].
3–7 Aug.	8th International Conference of Music Perception and Cognition, Evanston, IL [School of Music, Northwestern Univ., Evanston, IL 60201; WWW: www.icmpc.org/conferences.html].
15–19 Nov.	148th Meeting of the Acoustical Society of America, San Diego, CA [Acoustical Society of America, Suite 1NO1, 2 Huntington Quadrangle, Melville, NY 11747-4502; Tel.: 516-576-2360; Fax: 516-576-2377; E-mail: asa@aip.org; WWW: asa.aip.org].

Cumulative Indexes to the *Journal of the Acoustical Society of America*

Ordering information: Orders must be paid by check or money order in U.S. funds drawn on a U.S. bank or by Mastercard, Visa, or American Express credit cards. Send orders to Circulation and Fulfillment Division, American Institute of Physics, Suite 1NO1, 2 Huntington Quadrangle, Melville, NY 11747-4502; Tel.: 516-576-2270. Non-U.S. orders add $11 per index.

Some indexes are out of print as noted below.

Volumes 1–10, 1929–1938: JASA and Contemporary Literature, 1937–1939. Classified by subject and indexed by author. Pp. 131. Price: ASA members $5; Nonmembers $10.

Volumes 11–20, 1939–1948: JASA, Contemporary Literature, and Patents. Classified by subject and indexed by author and inventor. Pp. 395. Out of Print. **Volumes 21–30, 1949–1958:** JASA, Contemporary Literature, and Patents. Classified by subject and indexed by author and inventor. Pp. 952. Price: ASA members $20; Nonmembers $75.

Volumes 31–35, 1959–1963: JASA, Contemporary Literature, and Patents. Classified by subject and indexed by author and inventor. Pp. 1140. Price: ASA members $20; Nonmembers $90.

Volumes 36–44, 1964–1968: JASA and Patents. Classified by subject and indexed by author and inventor. Pp. 485. Out of Print.

Volumes 36–44, 1964–1968: Contemporary Literature. Classified by subject and indexed by author. Pp. 1060. Out of Print.

Volumes 45–54, 1969–1973: JASA and Patents. Classified by subject and indexed by author and inventor. Pp. 540. Price: $20 (paperbound); ASA members $25 (clothbound); Nonmembers $60 (clothbound).

Volumes 55–64, 1974–1978: JASA and Patents. Classified by subject and indexed by author and inventor. Pp. 816. Price: $20 (paperbound); ASA members $25 (clothbound); Nonmembers $60 (clothbound).

Volumes 65–74, 1979–1983: JASA and Patents. Classified by subject and indexed by author and inventor. Pp. 624. Price: ASA members $25 (paperbound); Nonmembers $75 (clothbound).

Volumes 75–84, 1984–1988: JASA and Patents. Classified by subject and indexed by author and inventor. Pp. 625. Price: ASA members $30 (paperbound); Nonmembers $80 (clothbound).

Volumes 85–94, 1989–1993: JASA and Patents. Classified by subject and indexed by author and inventor. Pp. 736. Price: ASA members $30 (paperbound); Nonmembers $80 (clothbound).

Volumes 95–104, 1994–1998: JASA and Patents. Classified by subject and indexed by author and inventor. Pp. 632. Price: ASA members $40 (paperbound); Nonmembers $90 (clothbound).

ACOUSTICAL NEWS—INTERNATIONAL

Walter G. Mayer
Physics Department, Georgetown University, Washington, DC 20057

A new regional acoustics association founded in Europe

During the second congress of the Slovenian Acoustical Society, held in September 2002, representatives of the Austrian and Croatian Acoustical Societies initiated the founding of a regional association which is now known as the Alps-Adria Acoustics Association (AAAA). This new association will be supported by acousticians in about 18 regions of seven countries: Austria, Croatia, Germany (Bavaria), several regions of Hungary and Italy, and also Slovenia and Switzerland (Ticino).

The first president of AAAA is Mirko Čudina of the University of Ljubljana, representing Slovenia. According to the by-laws of the Alps-Adria Acoustics Association the president, elected for a two-year term, will organize the next congress. The first congress of the new association will be held in Portorož, Slovenia, in September 2003.

International Meetings Calendar

Below are announcements of meetings and conferences to be held abroad. Entries preceded by an * are new or updated listings.

June 2003

5–6 *__Spring Meeting of the Swiss Acoustical Society__, Geneva, Switzerland. (SGA-SSA, c/o Akustik, Suva, P.O. Box 4358, 6002 Luzern, Switzerland; Fax: +41 419 62 13; Web: www.sga-ssa.ch)

8–13 **XVIII International Evoked Response Audiometry Study Group Symposium**, Puerto de la Cruz, Tenerife, Spain. (Web: www.ierasg-2003.org)

16–18 **Acoustics 2003—Modeling & Experimental Measurements**, Cadiz, Spain. (Fax: +44 238 029 2853; Web: www.wessex.ac.uk/conference/2003/acoustics/index.html)

29–3 **8th Conference on Noise as a Public Health Problem**, Amsterdam-Rotterdam, The Netherlands. (Fax: +31 24 360 1159; Web: www.icben2003.nl)

30–3 **Ultrasonics International (UI'03)**, Granada, Spain. (Fax: +44 1295 253 334; Web: www.ui03.com)

July 2003

7–11 **10th International Congress on Sound and Vibration**, Stockholm, Sweden. (Fax: +46 88 661 9125; Web: www.congex.com/icsv10)

14–16 **8th International Conference on Recent Advances in Structural Dynamics**, Southampton, UK. (Web: www.isvr.soton.ac.uk/sd2003)

August 2003

6–9 **Stockholm Music Acoustics Conference 2003 (SMAC03)**, Stockholm, Sweden. (Web: www.speech.kth.se/music/smac03)

25–27 **Inter-Noise 2003**, Jeju Island, Korea. (Fax: +82 42 869 8220; Web: www.internoise2003)

25–29 **XIII Session of the Russian Acoustical Society**, Moscow, Russia. (Fax: +7 095 126 0100; Web: www.akin.ru)

September 2003

1–2 *__First Congress of the Alps-Adria Acoustics Association (AAAA)__, Portorož, Slovenia. (Jurij Prezelj, Mechanical Engineering, University of Ljubljana, Aškerčeva 6, 1000 Ljubljana, Slovenia; Fax: +386 1 251 8567; Web: www.fs.uni-lj.si/sda)

1–4 **Eurospeech 2003**, Geneva, Switzerland. (Web: www.symporg.ch/eurospeech2003)

7–10 **World Congress on Ultrasonics**, Paris, France. (Fax: +33 1 46 33 56 73; Web: www.sfa.asso.fr/wcu2003)

16–19 **Autumn Meeting of the Acoustical Society of Japan**, Nagoya, Japan. (Fax: +81 3 5256 1022; Web: wwwsoc.nii.ac.jp/asj/index-e.html)

18–19 **Surface Acoustics 2003**, Salford University, Manchester, UK. (Web: www.ioa.org.uk/salford2003)

23–25 **2nd International Symposium on Fan Noise**, Senlis, France. (Fax: +33 4 72 44 49 99; Web: www.fannoise2003.org)

October 2003

15–17 **34th Spanish Congress on Acoustics**, Bilbao, Spain. (Fax: +34 91 411 7651; Web: www.ia.csic.es/sea/index.html)

15–17 **Acoustics Week in Canada**, Edmonton, AB, Canada. (Fax: +1 780 414 6376; Web: caa-aca.ca/edmonton-2003.html)

30–31 *__Autumn Meeting of the Swiss Acoustical Society__, Basel, Switzerland. (SGA-SSA, c/o Akustik, Suva, P.O. Box 4358, 6002 Luzern, Switzerland; Fax: +41 419 62 13; Web: www.sga-ssa.ch)

November 2003

5–6 *__Institute of Acoustics (UK) Autumn Conference__, Oxford, UK. (Institute of Acoustics, 77A St. Peter's Street, St. Albans, Herdfordshire AL1 3BN, UK; Fax: +44 1727 850553; Web: www.ioa.org.uk)

7–9 *__Reproduced Sound__, Oxford, UK. (Institute of Acoustics, 77A St Peter's Street, St. Albans, Herdfordshire AL1 3BN, UK; Fax: +44 1727 850553; Web: www.ioa.org.uk)

December 2003

10–12 **3rd International Workshop on Models and Analysis of Vocal Emissions for Biomedical Applications**, Firenze, Italy. (Fax: +39 55 479 6767; Web: www.maveba.org)

March 2004

17–19 **Spring Meeting of the Acoustical Society of Japan**, Atsugi, Japan. (Fax: +81 3 5256 1022; Web: wwwsoc.nii.ac.jp/asj/index-e.html)

22–25 *__Joint Congress of the French and German Acoustical Societies (SFA-DEGA)__, Strasbourg, France. (Fax: +33 1 48 88 90 60; Web: www.sfa.asso.fr/cfa-daga2004)

31–3 **International Symposium on Musical Acoustics (ISMA2004)**, Nara, Japan. (Fax: +81 77 495 2647; Web: www2.crl.go.jp/jt/a132/isma2004)

April 2004

5–9 **18th International Congress on Acoustics (ICA2004)**, Kyoto, Japan. (Fax: +81 66 879 8025; Web: www.ica2004.or.jp)

11–13 **International Symposium on Room Acoustics (ICA2004 Satellite Meeting)**, Hyogo, Japan. (Fax: +81 78 803 6043; Web: rad04.iis.u-tokyo.ac.jp)

 0001-4966/2003/113(6)/2953/2/$19.00

May 2004

17–21 *__International Conference on Acoustics, Speech, and Signal Processing (ICASSP 2004)__, Montréal, Canada. (Web: www.icassp2004.com)

June 2004

8–10 __Joint Baltic-Nordic Acoustical Meeting__, Mariehamn, Åland, Finland. (Fax: +358 09 460 224; e-mail: asf@acoustics.hut.fi)

July 2004

5–8 __7th European Conference on Underwater Acoustics (ECUA 2004)__, Delft, The Netherlands. (Fax: +31 70 322 9901; Web: www.ecua2004.tno.nl)

11–16 __12th International Symposium on Acoustic Remote Sensing (ISARS)__, Cambridge, UK. (Fax: +44 161 295 3815; Web: www.isars.org.uk)

August 2004

23–27 __2004 IEEE International Ultrasonics, Ferroelectrics, and Frequency Control 50th Anniversary Conference__, Montréal, Canada. (Fax: +1 978 927 4099; Web: www.ieee-uffc.org/index2-asp)

22–25 __Inter-noise 2004__, Prague, Czech Republic. (Web: www.internoise2004.cz)

September 2004

13–17 __4th Iberoamerican Congress on Acoustics, 4th Iberian Congress on Acoustics, 35th Spanish Congress on Acoustics__, Guimarães, Portugal. (Fax: +351 21 844 3028; Web: www.spacustica.pt/novidades.htm)

November 2004

4–5 *__Autumn Meeting of the Swiss Acoustical Society__, Rapperswil, Switzerland. (SGA-SSA, c/o Akustik, Suva, P.O. Box 4358, 6002 Luzern, Switzerland; Fax: +41 419 62 13; Web: www.sga-ssa.ch)

August 2005

7–10 __Inter-Noise__, Rio de Janeiro, Brazil. (Details to be annouced later)

28–2 __Forum Acusticum Budapest 2005__, Budapest, Hungary. (Details to be announced later)

Preliminary Announcement 2008

June/July __Joint Meeting of European Acoustical Association (EAA), Acoustical Society of America (ASA), and Acoustical Society of France (SFA)__, Paris, France. (Details to be announced later)

REVIEWS OF ACOUSTICAL PATENTS

Lloyd Rice
11222 Flatiron Drive, Lafayette, Colorado 80026

The purpose of these acoustical patent reviews is to provide enough information for a Journal reader to decide whether to seek more information from the patent itself. Any opinions expressed here are those of reviewers as individuals and are not legal opinions. Printed copies of United States Patents may be ordered at $3.00 each from the Commissioner of Patents and Trademarks, Washington, DC 20231. Patents are available via the Internet at http://www.uspto.gov.

Reviewers for this issue:

GEORGE L. AUGSPURGER, *Perception, Incorporated, Box 39536, Los Angeles, California 90039*
MARK KAHRS, *Department of Electrical Engineering, University of Pittsburgh, Pittsburgh, Pennsylvania 15261*
DAVID PREVES, *Starkey Laboratories, 6600 Washington Ave. S., Eden Prairie, Minnesota 55344*
DANIEL R. RAICHEL, *2727 Moore Lane, Fort Collins, Colorado 80526*
CARL J. ROSENBERG, *Acentech, Incorporated, 33 Moulton Street, Cambridge, Massachusetts 02138*
KEVIN P. SHEPHERD, *Mail Stop 463, NASA Langley Research Center, Hampton, Virginia 23681*
WILLIAM THOMPSON, JR., *Pennsylvania State University, University Park, Pennsylvania 16802*
ERIC E. UNGAR, *Acentech, Incorporated, 33 Moulton Street, Cambridge, Massachusetts 02138*
ROBERT C. WAAG, *Department of Electrical and Computer Engineering, Univ. of Rochester, Rochester, New York 14627*

6,471,111

43.10.Pr METHOD AND APPARATUS FOR ACOUSTIC PRESSURE ASSISTED WAVE SOLDERING

Allen D. Hertz, Boca Raton, Florida *et al.*
29 October 2002 (Class 228/111.5); filed 20 January 1999

In circuit board assembly, component connectors are inserted into a printed circuit board, soldering flux is added, and the assembly is heated to activate the flux. The underside of the board (with the protruding connectors) is then subjected to a bath of molten solder, which fuses to the exposed metal surfaces. In an arrangement according to the present patent, an airborne acoustic pressure wave is applied to the solder bath and to the circuit board, with the intent of improving the penetration of solder into small openings and removing excess solder from areas where it is not wanted.—EEU

6,487,915

43.20.Ye METHOD FOR CHARACTERIZING RESIDUAL STRESS IN METALS

Loren A. Jacobson *et al.*, assignors to the United States of America as represented by the Secretary of the Navy
3 December 2002 (Class 73/801); filed 28 September 2001

This method consists of drilling a least one hole to a preselected depth in a metal workpiece and mounting one or more acoustical sensors on the metal workpiece. The sensors are connected to an electronic detecting/recording device and a liquid metal (e.g., mercury) capable of penetrating the metal workpiece is placed at the bottom of the hole(s). A recording is made over a period of time, usually within about 2 h, of the magnitude and number of noise events which occur as the liquid metal penetrates the workpiece structure. The magnitude and number of noise events may then be correlated to the internal stresses in the region of the hole bottoms in the workpiece. The method cannot be considered to be completely nondestructive.—DRR

6,490,226

43.28.Tc ULTRASONIC SONAR AND METHOD USING TRANSMISSION FREQUENCY DIFFERENT FROM REVERBERATION FREQUENCY

Nobuyuki Iwasaki *et al.*, assignors to Nippon Soken, Incorporated
3 December 2002 (Class 367/97); filed in Japan 4 February 2000

In an obstacle avoidance sonar, such as those mounted in automobile bumpers, the source transducer is excited at a frequency different from the resonance frequency of that transducer. Hence any echo signal can, by simple digital signal processing techniques, be separated from the ring-down or reverberation signal generated by the source transducer.—WT

6,498,767

43.30.Wi CRUISE MISSILE DEPLOYED SONAR BUOY

Paul J. Carreiro, assignor to the United States of America as represented by the Secretary of the Navy
24 December 2002 (Class 367/4); filed 11 April 2001

It is proposed to mount, and subsequently deploy, a number of sonar buoys from a cruise missile.—WT

6,481,268

43.35.Bf PARTICLE MEASUREMENT BY ACOUSTIC SPECKLE

Malcolm J. W. Povey *et al.*, assignors to Baker Hughes, Incorporated
19 November 2002 (Class 73/61.75); filed 12 October 1999

Small particles in a static fluid move randomly with Brownian motion. The particles scatter some of the acoustic energy that impinges on them from a single-frequency ultrasound source of a certain wavelength. Some of the particles assemble stochastically in a common plane for a brief period, resulting in a coherent ''speckle'' signal at a sensing transducer. Using the technique described in this patent, the size, concentration, and size distribution of particles in a fluid are determined from acoustic speckle signals. The apparatus consists of a focused ultrasonic transducer, a sensor, and a computer.—EEU

 0001-4966/2003/113(6)/2955/17/$19.00

6,491,685

43.35.Sx LASER AND ACOUSTIC LENS FOR LITHOTRIPSY

Steven R. Visuri *et al.*, assignors to The Regents of the University of California
10 December 2002 (Class 606/2.5); filed 1 March 2000

In endoscopic lithotripsy a small tube is inserted into a patient's body in order to break up gallstones or kidney stones. In the device described in this patent the tip of an optical fiber is placed in contact with one of these stones and light from a laser is fed into the other end of the fiber. The tip of the optical fiber encapsulates a layer of exogenous absorbing dye, which produces a stress wave via thermoelastic expansion when it is subjected to an intense light pulse of short duration. The end of the tip is configured into an acoustic lens that focuses the stress wave.—EEU

6,482,649

43.35.Yb ACOUSTIC CONSUMPTION MONITOR

Carl A. Gogol, Jr. *et al.*, assignors to Leybold, Inficon, Incorporated
19 November 2002 (Class 436/34); filed 23 September 1999

As with most industrial process patents the invention is described clearly and in considerable detail. To accurately monitor chemical vapor deposition *in situ*, acoustic cells are used to determine gas compositions at the inlet and outlet sides of the reactor. Each cell contains a driving transducer and a receiving microphone. These transducers are coupled to external circuitry that can identify a resonant frequency resulting from the specific gases and their composition ratios. From this information, the composition of the binary gas mixture can be calculated.—GLA

6,494,222

43.35.Yb ULTRASONIC CLEANING APPARATUS FOR AN ENDOSCOPE

Naotake Mitsumori and Joji Watanabe, assignors to Fuji Photo Optical Company, Limited
17 December 2002 (Class 134/184); filed in Japan 28 October 1999

This ultrasonic cleaning apparatus is a fairly conventional device adapted and sized to cleansing of endoscopes.—DRR

6,487,324

43.35.Zc STEPPED ACOUSTIC IMPEDANCE-MATCHING TRANSFORMER FOR VERY NARROW CHANNEL ACOUSTIC TRAVELING WAVE LENS WAVEGUIDE

Robert M. Montgomery *et al.*, assignors to Harris Corporation
26 November 2002 (Class 385/7); filed 29 June 2001

In an acoustic traveling-wave lens device a laser's beam is focused onto an acousto-optic beam deflector to which a rf input signal is applied. The resulting modulated beam is focused onto a traveling-wave cell and from there transmitted to an image-collecting medium, such as photographic film. Traveling waves are induced in the aforementioned cell by means of a transducer mounted at its end. This transducer is coupled to the cell via an impedance-matching transformer consisting of a metal block, whose cross-sectional area is tapered in accordance with the difference between the acoustic impedance of the block and that of the elements to which it is connected.—EEU

6,483,924

43.38.Ar ACOUSTIC ELEMENTS AND METHOD FOR SOUND PROCESSING

Kari Kirjavainen, assignor to Panphonics Oy
19 November 2002 (Class 381/191); filed in Finland 26 February 1996

One reason that electret condenser microphones can be produced cheaply is that the prepolarized diaphragm is allowed to rest directly on the backplate (stator). Because the surface of the backplate is irregular a multiplicity of back cavities is formed, each covered by its own mini diaphragm. The same configuration could be used as a sound generator having limited dynamic range and restricted frequency response. But suppose the backplate were porous. And suppose the diaphragm were sandwiched between front and rear backplates. Such an ''acoustic element'' could serve equally well as a sensor or actuator. A stack of actuators and sensors might be designed as the key element of an active noise control system. The patent suggests additional applications but the basic invention is described in little more detail than the preceding sentences.—GLA

6,485,205

43.38.Fx MEDIA WEIGHT SENSOR USING AN ACOUSTIC RESONATOR

Phillip R. Luque, assignor to Hewlett-Packard Company
26 November 2002 (Class 400/56); filed 19 December 2000

The purpose of this device is to sense the weight (or density) of paper in a printer. The sensor includes a transducer consisting of a metal disk and a piezoelectric element shaped to form a Helmholtz resonator cavity. It is mounted in a printer in such a manner that paper (i.e., the media) moves across the top of the Helmholtz resonator where an opening is located. Paper weight is discerned by measuring the change in the resonant frequency of the piezoelectric element with and without the media. Heavier weight results in a lower resonator frequency. Since a difference measurement is entailed, the assertion is made that the device will be insensitive to factors such as wear and temperature.—DRR

6,498,769

43.38.Fx METHOD AND APPARATUS FOR A NON-OIL-FILLED TOWED ARRAY WITH A NOVEL HYDROPHONE DESIGN AND UNIFORM BUOYANCY TECHNIQUE

Richard Pearce, assignor to Input/Output, Incorporated
24 December 2002 (Class 367/188); filed 4 August 2000

One element of a towed line array is illustrated. A diaphragm sleeve with eight slightly concave faces **11** separated by eight longitudinal ridges **10** is slipped over a similar shaped back plane structure **12** sized so that there is interference fit between the ridges **10** and **13** of the two parts. Air voids are created between the two sets of faces of different concavity. A sheet of PVDF with gaps in its electrode pattern corresponding to the positions of ridges **10** is wrapped around and bonded to the diaphragm sleeve creating a circumferential set of eight bender transducers. The electrical cable passes through the central portion of back plane structure **12** and

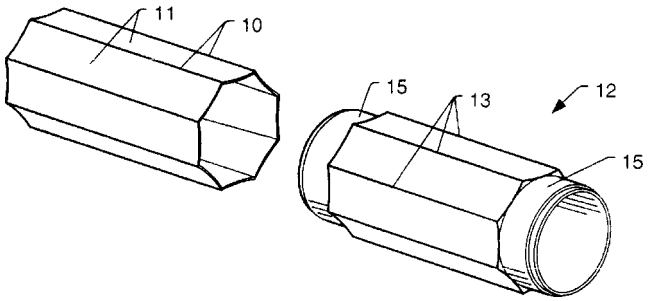

connection to the numerous bender elements is accomplished. A number of these hydrophone elements are mechanically connected together with suitable spacer elements to form a portion of the line array. A sleeve of suitable acoustic window material is slipped over the PVDF film and any air voids on the front face of the PVDF are filled with suitable potting material. These spacers between hydrophone elements can have their buoyancy adjusted by a reaction molding process involving a polyurethane material and hollow microspheres to accomplish uniform buoyancy along the length of the line array.—WT

6,469,732

43.38.Hz ACOUSTIC SOURCE LOCATION USING A MICROPHONE ARRAY

Pi Sheng Chang *et al.*, assignors to VTEL Corporation
22 October 2002 (Class 348/14.08); filed 6 November 1998

Small, inexpensive, video teleconference systems have become as indispensable as office copiers. They allow several work groups at different locations to conveniently meet face to face as often as needed. When a group consists of more than two people then the TV camera should automatically focus on the person speaking. Since audio pickup may involve only one or two microphones, a separate talker identification system must be used. This patent describes such a system intended to overcome deficiencies in prior art. ''The present invention provides accurate location of a speaking participant of a video conference using as few as four microphones in a 3-dimensional configuration.'' Those involved in this field will find the patent informative.—GLA

6,473,514

43.38.Hz HIGH DIRECTIVITY MICROPHONE ARRAY

Martin Reed Bodley *et al.*, assignors to GN Netcom, Incorporated
29 October 2002 (Class 381/355); filed 5 January 2000

A portable, foldable microphone line array is intended for use with computers or cellular phones. Like certain commercial loudspeaker systems, a visual indicator is included which can only be seen when the user is in the zone of optimum voice pickup.—GLA

6,467,103

43.38.Ja SOUND TRANSMISSION SYSTEM AND ILLUMINATION SYSTEM FOR A TUB, SPA, POOL, BATH OR SHOWER

W. John Gardenier and Anthony Brennan, assignors to Saratoga Spa & Bath Company, Incorporated
22 October 2002 (Class 4/541.1); filed 12 April 2001

This deluxe spa is said to be easy to fabricate and ship. It includes built-in waterproof loudspeakers **20**. Alternatively, loudspeakers and coupling chambers can be located in cavities below the contoured floor. In the latter case, waveguides conduct sound energy to appropriate locations.—GLA

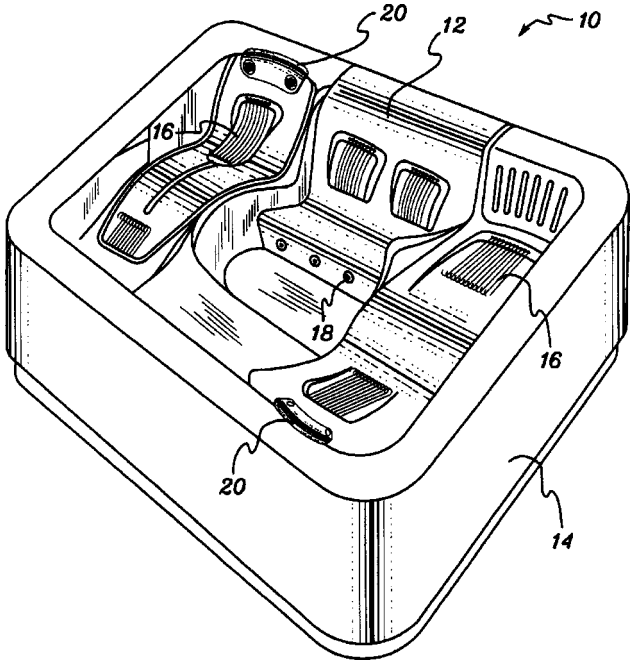

6,470,088

43.38.Ja VENTED LOUDSPEAKER ENCLOSURE WITH LIMITED DRIVER RADIATION

Wayne M. Schott, assignor to Koninklijke Philips Electronics, N.V.
22 October 2002 (Class 381/347); filed 27 December 2000

What is shown in the illustration and described in the patent claims is straightforward: loudspeaker **18** is mounted in a conventional vented box **10** to which is added ''highly restrictive acoustic foam'' **20**. Unfortunately, the method of operation described in the patent is based on a combination of

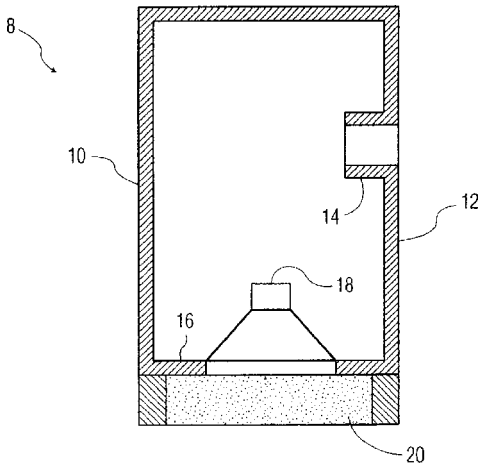

wishful thinking and faulty analog circuit analysis. The absorptive foam is assumed to attenuate front radiation all the way down to 10 Hz or so with no effect on cone movement. In the real world a large stuffed pipe at least 15 feet long would be required to approach this goal.—GLA

6,478,108

43.38.Ja SPEAKER BOX

Klaus Linhard and Gerhard Schaller, assignors to DaimlerChrysler AG

12 November 2002 (Class 181/141); filed in Germany 16 August 1999

Small, directional, low-frequency loudspeaker systems are currently in vogue. Such a system is most easily designed as a first-order gradient acoustic source using two loudspeakers. However, single-loudspeaker designs are equally feasible and commercial examples go back at least 30 years. This

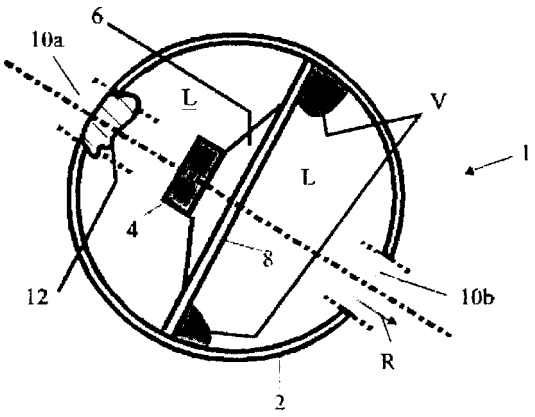

patent describes a two-chamber variant. Sound from the front chamber emerges through one or more openings **10b**. The rear chamber is similar except that openings **10a** are damped to provide the phase shift required for a given directional pattern. This geometry lends itself to inclusion in automobile head rests.—GLA

6,478,109

43.38.Ja LAMINATED COMPOSITE PANEL-FORM LOUDSPEAKER

Tai-Yan Kam, Hsin Chu, Taiwan, Province of China

12 November 2002 (Class 181/177); filed 5 July 2000

A bending-wave, panel-form loudspeaker is described that utilizes a sophisticated, laminated diaphragm incorporating peripheral stiffening and damping. The patent is clearly written and informative.—GLA

6,480,614

43.38.Ja PLANAR ACOUSTIC TRANSDUCER

Sakuzo Denda and Toshiiku Miyazaki, assignors to FPS, Incorporated

12 November 2002 (Class 381/423); filed in Japan 9 July 1997

One form of electrodynamic planar loudspeaker employs a lightweight diaphgram suspended in close proximity to an array of bar magnets. A flat conductive coil bonded to the diaphragm takes the form of an elongated spiral or series of spirals. The patent argues that a gridlike array of magnets and coils can make more efficient use of available magnetic flux.—GLA

6,469,974

43.38.Md RECORD PLAYER

Hisao Kaneko, assignor to Vestax Corporation

22 October 2002 (Class 369/127); filed in Japan 14 January 1999

In the dark ages before television or tape recorders, radio programs were recorded on 33 $\frac{1}{3}$ rpm disks for delayed playback. Playback turnables were fitted with felt surfaces to facilitate reverse rotation cueing and subse-

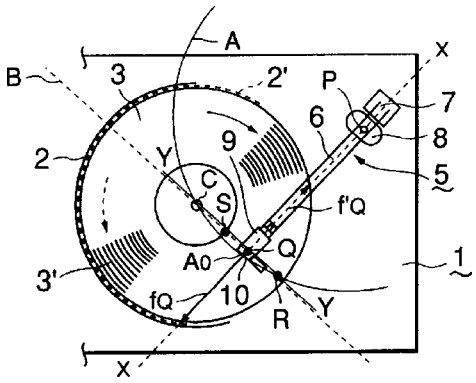

quent slip-starting. Western Electric tone arms were long and straight to minimize skating forces. Vestax Corporation has rediscovered this technology and somehow managed to patent it.—GLA

6,473,375

43.38.Md METHOD FOR RECORDING DATA ON A RECORDING MEDIUM AND FOR DELETING A SILENT PORTION OF THE RECORDED DATA

Junichi Aramaki, Shinagawa-ku, Tokyo, Japan

29 October 2002 (Class 369/47.13); filed in Japan 8 October 1993

One way to compress speech or audio data is the detection of silent periods. The patent proposes using the separate control block in a CD to signal the presence of silence. Silence is defined as a signal being less than 80 dB for 20 s.—MK

6,490,241

43.38.Ne SOUND CARRIER FOR A SOUND ILLUSTRATED BOOK

Viturin Doering, Moosburg, Germany

3 December 2002 (Class 369/282); filed in Germany 20 August 1999

Inverting the design of a record player of ancient yore, the inventor

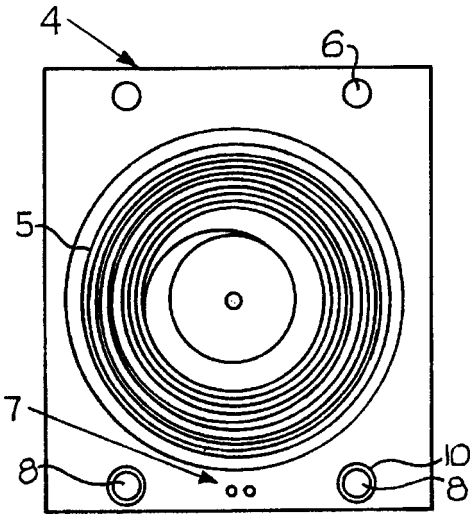

advocates a fixed spiral track and a movable pickup for application in illustrated books. The player/readout is not discussed or illustrated.—MK

6,473,625

43.38.Si EARPIECE ACOUSTICS

David Williams and John Mercer, assignors to Nokia Mobile Phones Limited
29 October 2002 (Class 455/550); filed in the United Kingdom 31 December 1997

This interesting earpiece design is intended for use in small wireless telephones. Sound energy from loudspeaker **6** drives output port **4** and a side

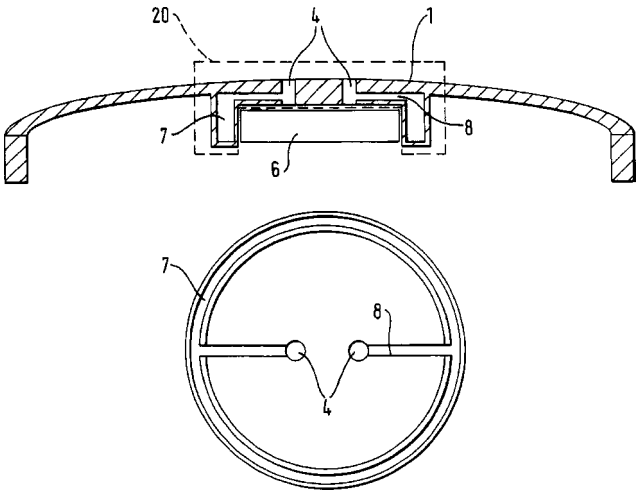

branch Helmholtz resonator **7**, **8**. The arrangement is said to provide several advantages over prior art, including leak-tolerant performance and resistance to dirt and damage.—GLA

6,470,087

43.38.Vk DEVICE FOR REPRODUCING MULTI-CHANNEL AUDIO BY USING TWO SPEAKERS AND METHOD THEREFOR

Jung-Kwon Heo and Young-Nam Oh, assignors to Samsung Electronics Company, Limited
22 October 2002 (Class 381/17); filed in the Republic of Korea 8 October 1996

A digitized audio bitstream is decoded into the standard 5.1 surround sound format. The five resulting channels are then run through a ''directivity preserving'' processor, which uses head-related transfer functions to yield a total of nine signals. These are then matrixed down to two, driving left and right loudspeakers. The 33 patent claims are written in polished legalese, allowing broad interpretation of basic terms.—GLA

6,477,255

43.38.Vk AUDIO SYSTEM

Minoru Yoshida *et al.*, assignors to Pioneer Electronic Corporation
5 November 2002 (Class 381/86); filed in Japan 5 August 1998

Amplifiers **14**, **15** and loudspeakers **10**, **11** are normal components of an automotive stereo installation. Everything else is a sophisticated sound field control system designed to counteract low-frequency standing waves in

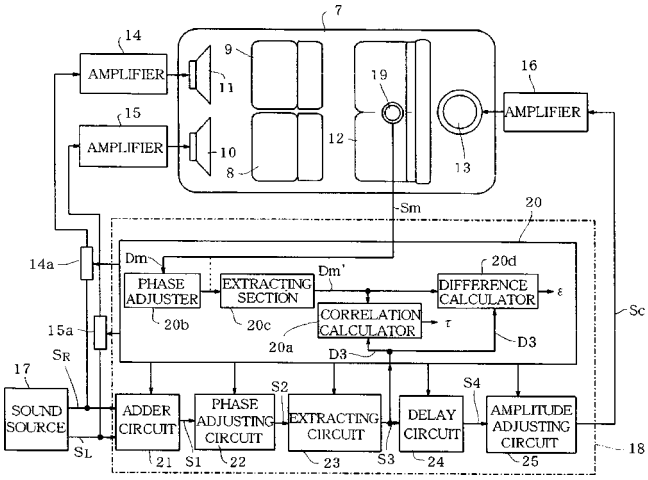

the passenger compartment. As shown, the system uses a signal from microphone **19** to dynamically analyze and adjust sound field correction. A simpler variant simply stores the information relating to a particular vehicle.—GLA

6,462,308

43.40.Cw UTILIZING ALTERED VIBRATION RESPONSES OF WORKPIECES, SUCH AS GAS TURBINE ENGINE BLADES

David F. Lahrman and Allan H. Clauer, assignors to LSP Technologies, Incorporated
8 October 2002 (Class 219/121.85); filed 23 November 1999

Laser shock peening is applied at the location of nodal lines on a gas turbine engine blade to modify its natural vibration frequencies. Methods are described which determine the natural frequency both before and after peening. This technique may be used to ''tune'' the structure. It may also be used to quantify the extent of laser peening applied to the structure for the pur-

pose of improving its fatigue life. Examples of the process applied to steel, aluminum, and titanium are given.—KPS

6,470,903

43.40.Le ENHANCED AND REMOTE METER READING WITH VIBRATION ACTUATED VALVE

Mark Reyman, Mount Vernon, New York
29 October 2002 (Class 137/1); filed 1 October 1999

This system for shutting off gas flows in pipes in the event of a rupture due to an earthquake consists in essence of a flow control device, a vibration sensor, a gas flow meter, and a microprocessor. The microprocessor prompts the control device to shut off the gas flow if (1) the vibration sensor detects a vibration that exceeds a predetermined threshold value and (2) the flow meter detects an increase in the gas flow rate.—EEU

6,457,553

43.50.Gf LOW COST MUFFLER

Gary D. Goplen and Kory J. Schuhmacher, assignors to Nelson Industries, Incorporated
1 October 2002 (Class 181/272); filed 4 August 2000

A clever, low-cost muffler design consists of three components joined at their periphery. The two shells and internal baffle form three chambers

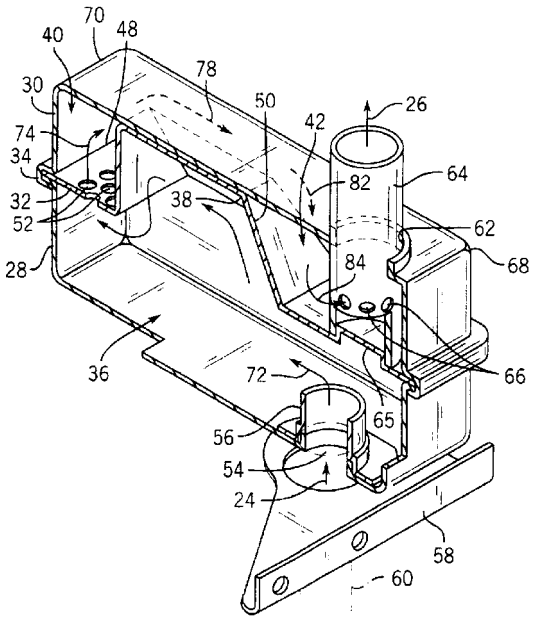

and multiple sound-attenuating tubed passages.—KPS

6,457,555

43.50.Gf SOUND MUFFLING MATERIAL AND METHOD OF MAKING THEREOF

Stephen James Saughnessy, assignor to Acousta-Fil Limited
1 October 2002 (Class 181/294); filed 10 July 2000

A sound-absorbing material for use in an exhaust muffler consists of fibers retained in a compressed form by a material having a low softening temperature. After installation in the muffler, hot exhaust gases soften the sacrificial material, thus allowing the compressed fibers to expand and fill the cavity.—KPS

6,467,571

43.50.Gf SOUND ABSORBING MATERIAL, MUFFLER USING THE SOUND ABSORBING MATERIAL, AND METHOD FOR FORMING SOUND ABSORBING LAYER THEREOF

Yukihiro Nakagawa, assignor to Nakagawa Sangyo Company, Limited; Toyota Jidosha Kabushiki Kaisha
22 October 2002 (Class 181/252); filed 11 December 2000

It is proposed that basalt fibers be used in place of fiberglass in exhaust mufflers. This material is said to have superior resistance to both acids and alkalines present in exhaust gas flows. Methods for manufacturing the fibers and installing them in a muffler are given.—KPS

6,467,572

43.50.Gf MUFFLER

Jefferson Liu, Shuiching, Peitun, Taichung, Taiwan, Province of China
22 October 2002 (Class 181/272); filed 15 August 2000

A muffler consists of perforated baffles and a series of throats **121**, **122**, **123**. The exhaust gases first pass through the largest of these **121** and

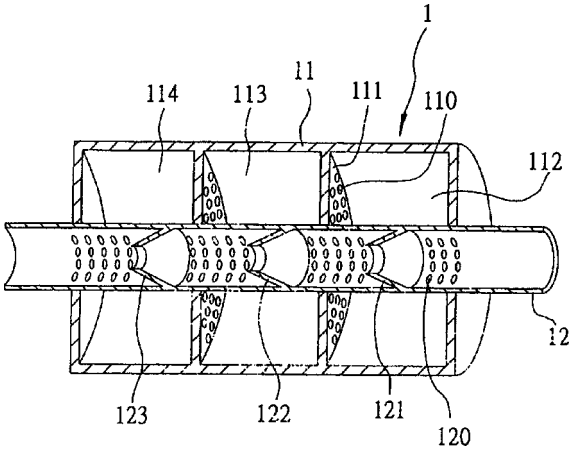

then to the smaller ones **122**, **123**. Backpressure generated by this arrangement is designed to minimize the power loss due to the early opening of the engine exhaust valve in the expansion stroke.—KPS

6,488,472

43.50.Gf AXIAL FAN, CENTRIFUGAL FAN, AND ELECTRONIC EQUIPMENT EMPLOYING ONE OF THESE FANS

Atsushi Miyazawa, assignor to Seiko Epson Corporation
3 December 2002 (Class 416/144); filed in Japan 28 January 2000

An attempt is made here to minimize noise in centrifugal and axial fans, which are generally used for cooling electronic equipment. The technique proposed is to reconfigure the blades such that they differ in cross-sectional areas, pitch, and angles of attack.—DRR

6,492,816

43.50.Gf ACOUSTIC LINER FOR MRI GRADIENT COILS

Peter John Feenan, Oxfordshire, the United Kingdom
10 December 2002 (Class 324/318); filed in the United Kingdom 7 October 1999

This is an acoustic liner for use with a magnetic field gradient coil in a magnetic resonance imaging system. The liner consists of a compressible acoustic sheet adapted to be fitted to the gradient coil in such a manner that the inner surface of the sheet is movable relative to the gradient coil and relative to an acoustically and electrically conducting path (preferably in the form of a flexible thin coating). The setup is arranged so that current pulses can be synchronously applied to the gradient coil and to the acoustically conducting path, thus generating a Lorentz force on the acoustically conducting path and also on the gradient coils. This will cause the acoustically conducting path to move and compress (or expand) the compressible acoustic sheet. If the current pulse's phase and amplitude are chosen to cause the inner skin to move an equal and opposite amount to the original gradient inner surface, then the net movement of the surface of the sheet of the compressible material will be zero and no sound would be generated.—DRR

6,486,678

43.50.Jh METHOD FOR NON-DESTRUCTIVE ANALYSIS OF ELECTRICAL POWER SYSTEM EQUIPMENT

Paul Spears, assignor to Paul Spears
26 November 2002 (Class 324/555); filed 28 November 2000

This method of monitoring electrical power systems does not seem to be a particularly novel one. It would work by detecting and evaluating acoustical output of individual components of the system for aberrations in these acoustical signals that would indicate mechanical malfunction or substandard performance.—DRR

6,493,689

43.50.Ki NEURAL NET CONTROLLER FOR NOISE AND VIBRATION REDUCTION

Antonios N. Kotoulas *et al.*, assignors to General Dynamics Advanced Technology Systems, Incorporated
10 December 2002 (Class 706/23); filed 29 December 2000

This is a form of active noise/vibration control involving two neural networks, one to model the complex, nonlinear output of multicomponent plant machinery and the other to act upon the modeling and provide control to modify and affect the vibration and noise characteristics of the plant.—DRR

6,471,157

43.50.Nm DEVICE AND METHOD FOR REDUCING AIRCRAFT NOISE

Craig L. Streett and John C. Lin, assignors to the United States of America as represented by the Administrator of the National Aeronautics and Space Administration
29 October 2002 (Class 244/1 N); filed 22 March 2000

Noise generated by airflow over an airfoil such as the flap on an aircraft wing may be caused by vortices rolling up and over the edge of the airfoil. It is proposed that devices placed along the edge (chordwise) will

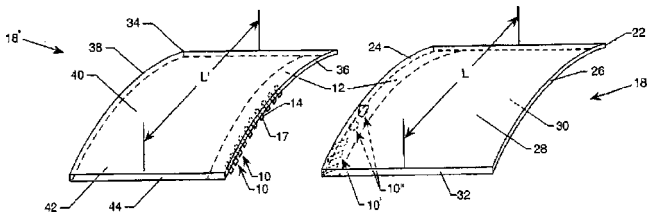

serve to thicken the shear layer, resulting in a reduction of the radiated noise. Extensive details are given concerning methods to achieve the thickening of the shear layer, including shapes and dimensions of candidate tabs and cavities.—KPS

6,487,822

43.55.Ev CEILING ELEMENT FOR A COMPOSITE CEILING

Jörg Haack, Wesseling and Andreas Gradinger, Kürten, both of Germany
3 December 2002 (Class 52/144); filed in Germany 12 June 1998

This patent relates to the way a sound insulation layer such as an open-pore foam would be attached with adhesive to the webs of an open metal ceiling, thus keeping the apertures of the metal ceiling free of adhesive.—CJR

6,494,008

43.55.Ev DUAL SECTION SOUND WALL PANEL AND METHOD OF MANUFACTURE

Alec C. Bloem and William J. Neely, assignors to L. B. Foster Company
17 December 2002 (Class 52/405.1); filed 8 August 2001

This sound wall for use as a highway noise barrier is comprised of two half walls that are then raised and joined together. In this manner, the wall can be poured on a flat surface, the outer surface can be carefully controlled so it looks pretty, and the two halves become as one when raised and bolted or attached together. This also means that if one side of the wall is damaged, just that side can be replaced without having to replace the entire wall.—CJR

6,483,926

43.55.Ti FLOOR IMPACT NOISE SUPPRESSOR IN A MULTI-STORIED BUILDING

Yasuhiro Yamashita and Hiroaki Hiraguri, assignors to Taisei Electronic Industries Company, Limited; Yasihiro Yamashita
19 November 2002 (Class 381/762); filed in Japan 3 August 1995

The patent is for an active noise cancellation system to reduce floor impact noise generated from an upper story to a lower story, as in a multistory residential building. The device uses a reference sensor, signal processing, and loudspeaker in the floor cavity.—CJR

6,488,558

43.58.Wc VEHICLE NOISEMAKER

Tommy E. Scrivner, Omaha, Nebraska
3 December 2002 (Class 446/267); filed 6 November 2001

Will the inventive mind never cease? What could be more useful than a flatulent vehicle? Use a gas storage bladder together with a membrane in addition to a display board (flatulence isn't sufficient to convey your opinion) and you too can tell the driver following you new expressions of grati-

tude. Curiously, the inventor did not propose using the car exhaust as source of the gas.—MK

6,496,115

43.60.Bf SYSTEM AND METHOD FOR ANALYZING BABY CRIES

Kaoru Arakawa, assignor to Meiji University Legal Person
17 December 2002 (Class 340/573.1); filed in Japan 22 March 2001

Parents learn to be good judges of baby cries. In this invention, parents are replaced with the FFT and heuristics. The system identifies hungry, painful, and sleepy cries. The heuristics depend on periodicity (via the cepstrum) and spectrum evolution over time. If it works, nurses and babysitters will rejoice.—MK

6,476,308

43.60.Lq METHOD AND APPARATUS FOR CLASSIFYING A MUSICAL PIECE CONTAINING PLURAL NOTES

Tong Zhang, assignor to Hewlett-Packard Company
5 November 2002 (Class 84/616); filed 17 August 2001

To classify a musical piece, the following steps are proposed: (1) detect note onsets via rectification and filtering, (2) detect harmonic partials, (3) compute spectral features like brightness, (4) normalize to even the spectrum, (5) classify notes using a neural network, and, finally, (6) classify the piece of music.—MK

6,490,359

43.60.Lq METHOD AND APPARATUS FOR USING VISUAL IMAGES TO MIX SOUND

David A. Gibson, Palo Alto, California
3 December 2002 (Class 381/119); filed 17 June 1998

This apparatus is a system for mixing audio signals, whereby the audio signals are transformed into visual images and the visual images are displayed on a video monitor as part of a three-dimensional volume of space. The characteristics of the visual images, e.g., shape, size, spatial locations,

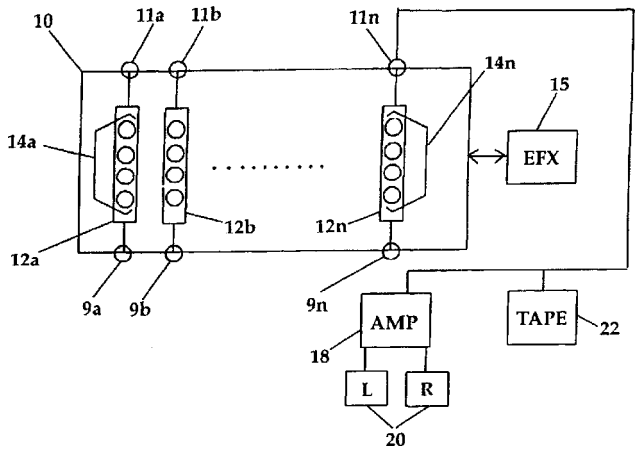

color, density, and texture, are correlated to selected audio characteristics, viz. frequency, amplitude, and time, such that manipulation of the visual characteristics causes a correlated response in the audio characteristics and vice versa.—DRR

6,493,426

43.60.Lq RELAY FOR PERSONAL INTERPRETER

Robert M. Engelke *et al.*, assignors to Ultratec, Incorporated
10 December 2002 (Class 379/52); filed 14 February 2001

This relay system, intended to facilitate the translation of information and communication between deaf and hearing persons, includes a call assistant who revoices the words of the hearing person. The words spoken by the call assistant are recognized by a speech recognition computer program which has been trained to the voice pattern of the call assistant, such that the words are promptly translated into text and formatted into high-speed communication protocol. That high-speed communication message is then trans-

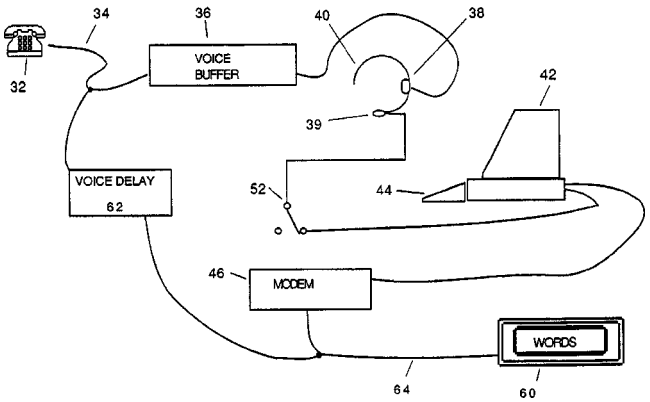

mitted electronically promptly by telephone into a visual display accessible to deaf persons. To this reviewer, this system, if it works properly, could readily replace the current TTY mode of communication in which the sender does manual typing and, moreover, could be adapted to translate from one language into another. It is also apparent that the techniques of word recognition to be converted into text that are used to supplement certain word-processing computer programs are being applied here.—DRR

6,493,687

43.60.Lq APPARATUS AND METHOD FOR DETECTING GLASS BREAK

Ji Wu and William S. DiPoala, assignors to Detection Systems, Incorporated
10 December 2002 (Class 706/15); filed 18 December 1999

In a building with many windows, it is infeasible to place piezoelectric transducers on each window as an intruder alarm. So, the inventors describe a fairly simple neural-network-based classifier that identifies the sound of broken glass.—MK

6,470,214

43.66.Ts METHOD AND DEVICE FOR IMPLEMENTING THE RADIO FREQUENCY HEARING EFFECT

James P. O'Loughlin and Diana L. Loree, assignors to the United States of America as represented by the Secretary of the Air Force
22 October 2002 (Class 607/56); filed 13 December 1996

Suppressed carrier amplitude modulation is used to encode speech for use in a ''radio frequency hearing system.'' Preprocessing before modulating includes low-pass filtering, adding a bias level, and taking a root of the predistorted waveform. The demodulated output is said to be intelligible via

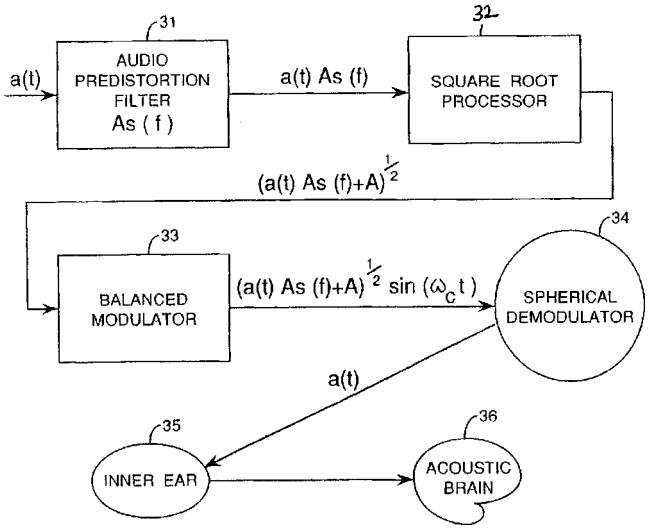

a ''rf hearing effect'' if either single sideband suppressed carrier or double sideband suppressed carrier AM encoding is employed. The rf hearing model is based on demodulating the rf signal via thermal energy absorbed by the listener's head, resulting mechanical movement, and hence an acoustic signal.—DAP

6,493,454

43.66.Ts HEARING AID

Teck Enn Loi and Matthew James Hall, assignors to NHAS National Hearing Aids Systems
10 December 2002 (Class 381/328); filed in Australia 24 November 1997

A semi-modular hearing aid is composed of a custom ear shell over which two plates sit. The outer periphery of the bottom plate, which has an opening, is attached via adhesive to the outer periphery of the shell over the opening in the shell. The outer periphery of the top plate is removably

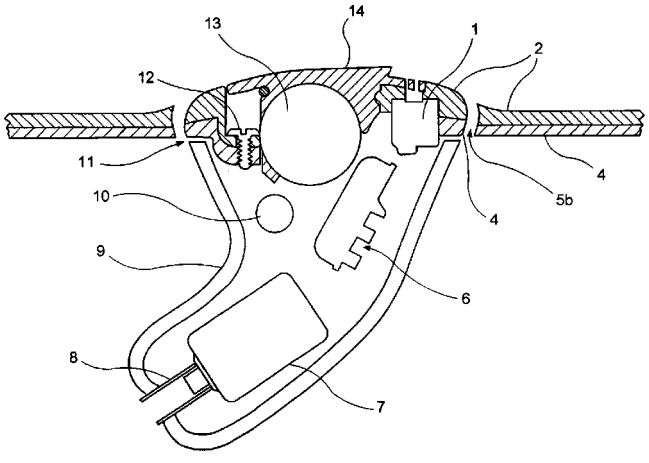

attached via screws to the bottom plate. Electrical components, such as the battery, microphone, volume control, and memory select switch, are mounted on the top plate and extend into the shell through the hole in the bottom plate. The assembly is said to facilitate easier repair because the bottom plate is not removed from the earshell to access the components.—DAP

6,496,587

43.66.Ts HEARING AID

Josef Mueller, assignor to Phonak AG
17 December 2002 (Class 381/330); filed with the World Intellectual Property Organization 9 February 2000

A rotatable horn **2** protects the acoustic input and output apertures of a behind-the-ear hearing aid from contamination in daily use. The acoustic input aperture is covered by a wedge-shaped, open-pore detachable lid **3**.

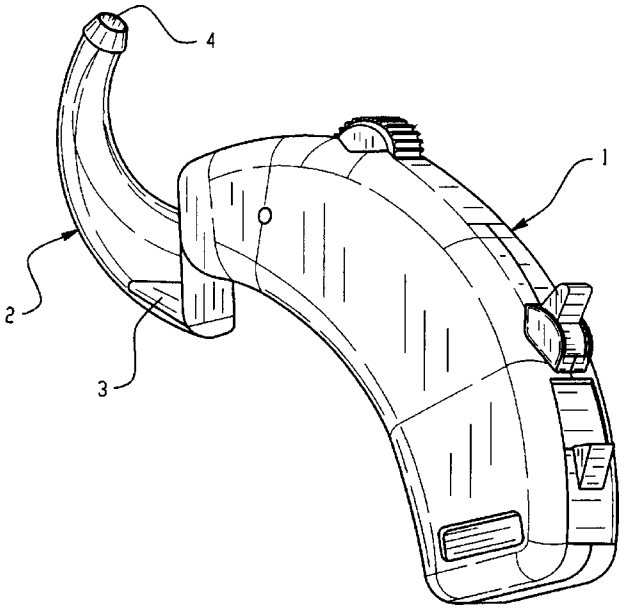

During servicing, the horn, which is connected to the hearing aid case, is rotated to release a soiled lid from a recess to permit exchanging it for a fresh lid.—DAP

6,498,455

43.66.Ts WIRELESS BATTERY CHARGING SYSTEM FOR EXISTING HEARING AIDS USING A DYNAMIC BATTERY AND A CHARGING PROCESSOR UNIT

Uwe Zink and Gary Skuro, assignors to Gary Skuro
24 December 2002 (Class 320/108); filed 22 February 2002

A rechargeable battery system consists of an inductor formed by winding a coil of wire around the battery housing. Batteries are recharged via

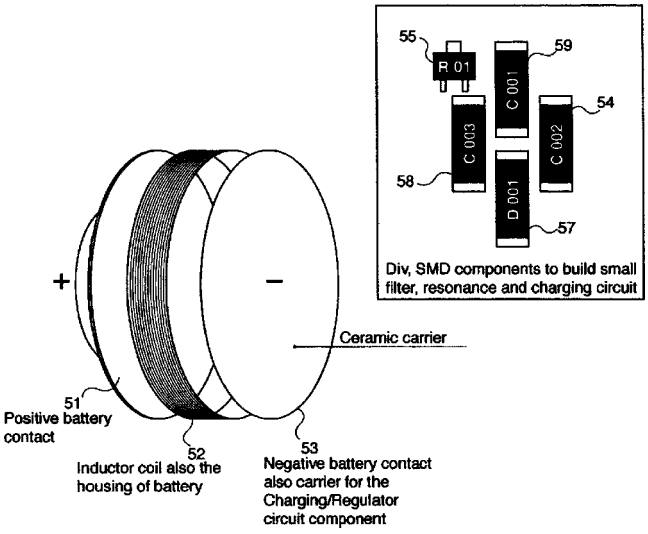

induction means in existing hearing aids without redesign and without removing the batteries from the hearing aids. A combined rechargeable battery and inductive charging circuit are housed within a standard hearing aid battery enclosure. The charging circuitry includes a tuned resonant circuit, consisting of a coil having about the same diameter as the battery, a surface mount capacitor, and a regulated charging integrated circuit. In one embodiment, a rotatable induction coil produces optimal recharging current for the battery.—DAP

6,498,858

43.66.Ts FEEDBACK CANCELLATION IMPROVEMENTS

James Mitchell Kates, assignor to GN ReSound A/S
24 December 2002 (Class 381/318); filed 21 December 2000

Adaptive cancellation of acoustic feedback in hearing aid fittings is achieved with two cascaded adaptive filters and a short bulk delay. Using a white noise probe signal when the hearing aid is initially turned on in the ear of wearer, the first filter adapts quickly to model the steady-state portions of the acoustic feedback path. In daily use of the hearing aid, the coefficients of the first filter remain frozen and the second filter adapts to the acoustic feedback model rapidly if the hearing aid becomes oscillatory. The second filter also adapts more slowly without a probe signal to changes in the feedback path caused, for example, by chewing, sneezing, or using a telephone handset.—DAP

6,496,585

43.66.Yw ADAPTIVE APPARATUS AND METHOD FOR TESTING AUDITORY SENSITIVITY

Robert H. Margolis, Arden Hills, Minnesota
17 December 2002 (Class 381/60); filed 27 January 2000

An adaptive method is described for developing automatically a diagnostic audiogram in which test ear and test frequencies are selected automatically. Advantages over routine manual clinical methodology are said to include greater accuracy, reporting test–retest reliability, and standardizing the number of test stimuli as well as the rules for the use of contralateral masking noise. The examiner is alerted for hearing thresholds that may be inaccurate due to inappropriate masking or subject inconsistency.—DAP

6,487,535

43.72.Gy MULTI-CHANNEL AUDIO ENCODER

Stephen Malcolm Smyth *et al.*, assignors to Digital Theater Systems, Incorporated
26 November 2002 (Class 704/500); filed 4 November 1998

A multi-channel audio coder is described that is said to have better than CD quality at high bit rates, improved quality at low bit rates, reduced playback latency, simplified error detection, and future expandability to higher sampling rates. High-frequency encoding is performed independently of the baseband signal. Each audio channel is windowed into a sequence of

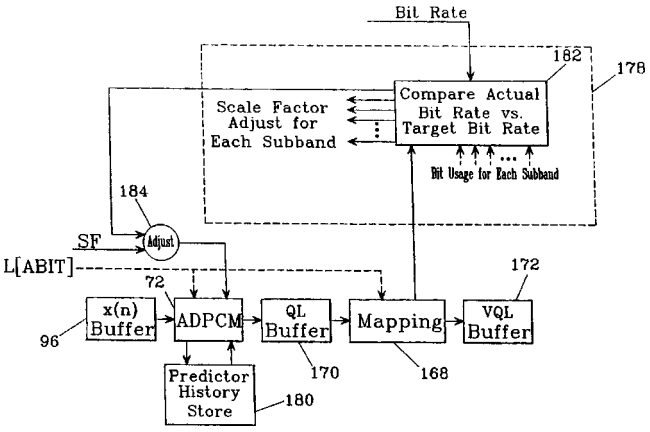

frames and each baseband signal is divided into a number of subbands. An ADPCM coder encodes lower frequency subbands. Each subband includes at least one subframe, each of which is analyzed to estimate the predicted gain of the ADPCM coder. The amount of RAM required at the decoder to buffer incoming data is said to be relatively low.—DAP

6,489,546

43.75.Kk MUSICAL INSTRUMENT AND METHOD OF MAKING SAME

Raymond Enhoffer *et al.*, assignors to Latin Percussion, Incorporated
3 December 2002 (Class 84/406); filed 17 January 2001

The existing cowbell percussion instrument has two halves welded together. The inventors claim that not only do the welds break under repeated usage, but the welds are deleterious to the sound quality. So, form a single fan-shaped piece of metal, fold five times, and you have a single seam. The results are said to last longer and (of course) sound better.—MK

6,495,748

43.75.Tv SYSTEM FOR ELECTRONICALLY EMULATING MUSICAL INSTRUMENT

Chung-Tsan Wang *et al.*, assignors to Behavior Tech Computer Corporation
17 December 2002 (Class 84/658); filed 10 July 2001

This vacuous patent describes how a synthetic/plastic instrument (such as a guitar with resistive sensors) could be made to sound like an acoustic model. No details are given and the extensive prior art is not studied, contemplated, or referenced.—MK

6,486,387

43.75.Wx FINGERING INFORMATION ANALYZER, ELECTRONIC MUSICAL INSTRUMENT INCLUDING FINGERING INFORMATION ANALYSIS AND METHOD THEREFORE

Hiroshi Munekawa *et al.*, assignors to Yamaha Corporation
26 November 2002 (Class 84/477 R); filed in Japan 23 March 1994

Allocation of a fixed resource is always problematic. In this case, the resource is fingers. The algorithm presented allocates fingers (and hands) in a piano score. The algorithm presented is *ad hoc* and probably works up to a point.—MK

6,485,434

43.80.Qf APPARATUS FOR ACOUSTIC PERCUSSION OF A BODY

Doron Kahana *et al.*, all of Chicago, Illinois
26 November 2002 (Class 600/552); filed 3 July 2000

The device appears to be a modern way of ''thumping'' a patient in order to assess the state of internal organs and structures, air fluid levels, and air–fluid–solid transitions. To execute the acoustic percussion of a human or animal body, the apparatus includes an oscillator circuit for generating electrical signals for exciting a loudspeaker and producing sound waves. A waveform shaping circuit modifies the electrical signals. These are amplified to the desired level and fed to the loudspeaker. Two potentiometers provide control of the waveform and the loudspeaker volume.—DRR

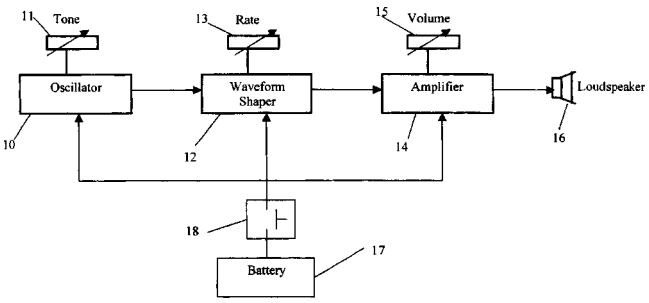

6,486,588

43.80.Qf ACOUSTIC BIOSENSOR FOR MONITORING PHYSIOLOGICAL CONDITIONS IN A BODY IMPLANTATION SITE

Eyal Doron and Avi Penner, assignors to Remon Medical Technologies Limited
26 November 2002 (Class 310/322); filed 1 June 2001

This acoustic biosensor is intended for implantation at a site within the body, such as an abdominal aortic aneurysm. The biosensor consists of a sensor element for measuring a physiological condition at the implantation site and for generating an information signal denoting the physiological condition. The biosensor also includes a piezoelectric transducer element for converting an externally generated acoustic interrogation signal into electrical energy to activate the sensor and means for modulating the interrogation signal, e.g., by the use of a switching element to alternate the mechanical impedance of the transducer element in order to transmit the information signal out of the body.—DRR

6,488,625

43.80.Qf MEDICAL DIAGNOSTIC ULTRASOUND SYSTEM AND METHOD

Kevin S. Randall and Andrew J. Wood, assignors to Ecton, Incorporated
3 December 2002 (Class 600/437); filed 14 September 1999

This system and its methodology are rather far from being unique, as inventions go. The ultrasound diagnostic system is designed to be portable to the degree that one person can tote the device along on his/her medical rounds. A principal feature of this design is that the circuitry of the ultrasound system is distributed among several boards, which are interconnected directly with one another without the use of a backplane or motherboard.—DRR

6,488,626

43.80.Qf ULTRASONIC SENSING BY INDUCED TISSUE MOTION

Frederic L. Lizzi and Sheikh Kaisar Alam, assignors to Riverside Research Institute
3 December 2002 (Class 600/437); filed 6 April 2000

The idea of this method, a relatively recent concept (1990), is to measure mechanical properties of tissues by inducing mechanical vibrations and measuring ultrasonic echoes from within the tissues during the periods of vibration. Radiation pulses from a high-energy therapeutic sound system are used to stimulate tissue motion by radiation press.—DRR

6,489,706

43.80.Qf MEDICAL DIAGNOSTIC ULTRASOUND TRANSDUCER AND METHOD OF MANUFACTURE

John W. Sliwa, Jr. *et al.*, assignors to Acuson Corporation
3 December 2002 (Class 310/334); filed 13 November 1998

A number of piezoelectric bodies in the form of billets, slices, or monocrystals are combined to form a larger piezoelectric body. For example, a 2×16 cm footprint piezoelectric body can be assembled from eight 2×2 cm sections. It is proposed that since laterally small piezoelectric bodies cost less per unit area, a large piezoelectric body may be constructed at a lesser cost by merging a number of small panels.—DRR

6,490,470

43.80.Qf THERMOACOUSTIC TISSUE SCANNER

Robert A. Kruger, assignor to Optosonics, Incorporated
3 December 2002 (Class 600/407); filed 19 June 2001

In this device, imaging of biological tissue is based on photo-acoustic techniques to detect differential absorption of electromagnetic waves in differing tissue types. The system includes an electromagnetic radiation source for irradiating targeted tissue to stimulate a thermoacoustic response, a coupling medium for acoustically coupling the response to an acoustic sensor array, and the acoustic array itself. The array consists of sensors mounted on a rotatable surface. The electromagnetic radiation source consists of a number of sources arranged about the tissue and producing a synchronized electromagnetic radiation in varying polarizations or phases.—DRR

6,490,474

43.80.Qf SYSTEM AND METHOD FOR ELECTRODE LOCALIZATION USING ULTRASOUND

N. Parker Willis *et al.*, assignors to Cardiac Pathways Corporation
3 December 2002 (Class 600/424); filed 1 August 1997

This is a system and method for tracking the positions of devices implanted within the human body. The device uses one or more ultrasound reference catheters to establish a fixed three-dimensional coordinate system within a patient's heart, using the principles of triangulation. The coordinate system can be graphically represented on a video monitor to assist a clinician in guiding other medical devices, which also carry ultrasound transducers, through the body to locations where they are needed to execute clinical procedures. One embodiment uses the system in the heart to help the physician guide mapping catheters for measuring electrical activity and ablation catheters for ablating selected regions of cardiac tissue.—DRR

6,491,633

43.80.Qf MEDICAL DIAGNOSTIC ULTRASOUND SYSTEM AND METHOD FOR CONTRAST AGENT IMAGE BEAMFORMATION

Sriram Krishnan and Lewis J. Thomas, assignors to Acuson Corporation
10 December 2002 (Class 600/447); filed 10 March 2000

The patent presents a method and system for contrast agent beam formation. The acoustic energy of transmit beams is spread laterally to lessen its intensity, thereby reducing contrast agent destruction. As an ex

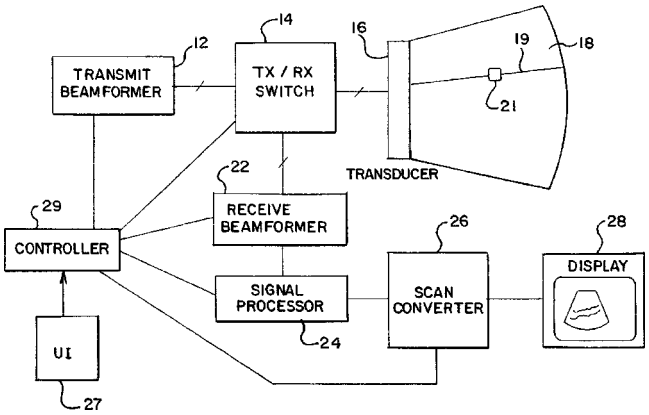

ample, a smaller aperture is provided for contrast agent imaging than for a default imaging mode. As another example, an apodization profile with a low amplitude for edge elements for contrast imaging is used as the basis for comparison with edge elements for the default imaging mode.—DRR

6,491,635

43.80.Qf DIGITAL ULTRASONIC DENSITOMETER

Richard B. Mazess *et al.*, assignors to Lunar Corporation
10 December 2002 (Class 600/449); filed 28 April 2000

This device constitutes an ultrasonic densitometer for *in vivo* measurement of the human *os calcis*. It includes an ultrasonic signal generator for producing a broadband electrical pulse at ultrasonic frequencies and an ultrasonic transducer connected to the signal generator for producing a corresponding acoustic signal transmitted along a transmission axis. A second transducer receives the transmitted acoustic signals and relays them to an A/D converter. This is followed by a microprocessor that initiates the pulse transmission and numerically analyzes the digitized acoustic return signal, distorted by the imposition of the human heel between the two transducers, to measure the time of flight of the transmission of the ultrasonic pulse from

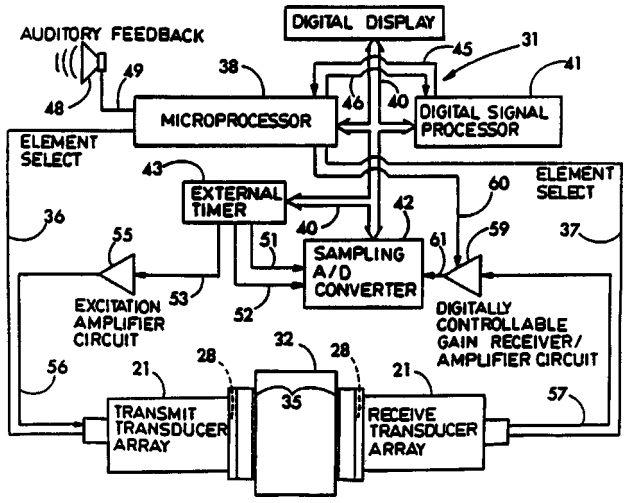

the emitting transducer to the receiving transducer. Increased accuracy of measurement of the speed of sound in bone *in vivo* is claimed.—DRR

6,491,637

43.80.Qf OPHTHALMOLOGICAL ULTRASONOGRAPHY SCANNING APPARATUS

Mark Leighton Foster *et al.*, assignors to Ultralink Ophthalmics Incorporated
10 December 2002 (Class 600/452); filed in Canada 6 January 2000

The human eye, particularly the cornea, presents special problems for optimal ultrasonographic B-scan imaging. The contour of the cornea can cause deviation in a transducer's focal point, producing less than optimal scanning (necessary for best resolution). One embodiment of this apparatus for ultrasound scanning of the eye includes a virtual center translocation mechanism that facilitates precise arcuate motion of an ultrasonic transducer to sustain the focal distance from the eye and to sustain normality of the ultrasound beam with respect to the surface of the eye. A radial adjust mechanism is also provided for altering the scanning radius to facilitate positioning of the transducer's focal point on selected surface areas of the eye. Centration optics are also included in order to enable alignment of the ultrasound transducer with the Purkinje (or another optical or geometric) axis of the eye.—DRR

6,491,641

43.80.Qf APPARATUS AND METHODS FOR ACOUSTIC RHINOMETRY

Steen Brabrand Rasmussen, assignor to Rhinometrics A/S
10 December 2002 (Class 600/529); filed in Denmark 27 July 1998

The patent subject relates to acoustically measuring lengths and cross sections in a patient's right and left nose cavities that are mutually separated by the nose separation (*septum nasi*), in the cavity behind the nose separation (*epipharynyx*), and in the throat (*neopharynx*). The device consists of an electro-acoustic sound emitter **25**, two transmission tubes **17**, **18** leading from the emitter into connecting pieces, means of attaching the tubes to one

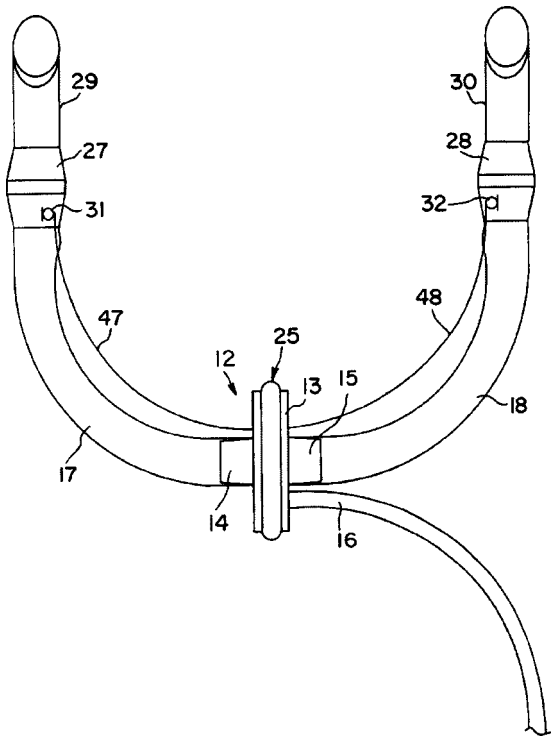

or both of the patient's nostrils, a proximal microphone located next to the emitter, and/or the microphones built into the connecting pieces, and a computer for generating electrical signals into the emitter and for sampling and analyzing the electrical signals from the microphone or microphones. Sound signals are emitted in two directions along separate transmission tubes. At the emitter, the two transmission tubes are located inline, providing symmetrical impedance and reflection conditions. The method for acoustically measuring the aforementioned cross sections is also described.—DRR

6,494,840

43.80.Qf PORTABLE ULTRASONIC PALPATION SYSTEM

Fuk Tat Mak and Yong Ping Zheng, assignors to The Hong Kong Polytechnic University
17 December 2002 (Class 600/446); filed 31 July 2000

The system relates to the use of indentation and ultrasound techniques to assess qualitatively the mechanical properties of soft tissues, particularly those covering a musculoskeletal system of a body. The portable device includes a hand-held palpation probe incorporating an ultrasonic transceiver connected in series with a load cell. During a test, the probe is placed on the tissue surface over a bony substratum. As the operator manually loads and unloads the probe on the tissue surface, an embedded microprocessor module continuously causes the ultrasound emitter to send pulses into the soft tissue. The ultrasound echo signal reflected from the bony interface is received and its flight time is used to compute the original thickness and the deformation of the soft tissue. The load cell, its driver and amplifier module, and the data collection modules continuously record the corresponding load applied to the tissue. The program then computes the Young's modulus of the soft tissue on the basis of the load-indentation response and a preset number of loading and unloading cycles.—DRR

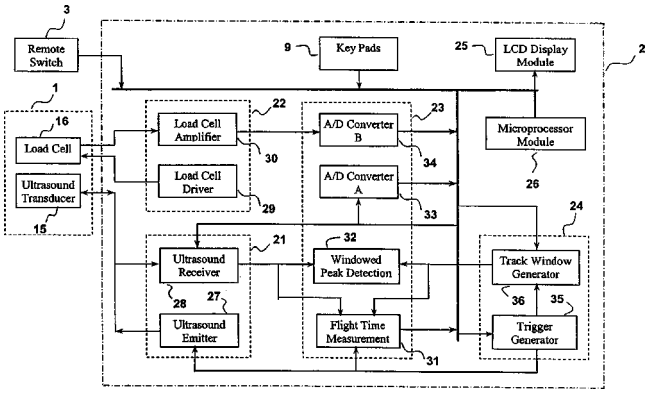

6,494,841

43.80.Qf MEDICAL DIAGNOSTIC ULTRASOUND SYSTEM USING CONTRAST PULSE SEQUENCE IMAGING

Lewis Jones Thomas *et al.*, assignors to Acuson Corporation
17 December 2002 (Class 600/447); filed 29 February 2000

This method of ultrasound medical diagnosis entails firing a sequence of pulses into a body and then receiving, beamforming, weighting, and summing the echo signals to suppress first-order echoes. The pulse sequence includes at least two pulses that differ in amplitude and phase. In one form, no two pulses of the sequence have the same amplitude with opposite phase. In the other form, only linear echoes are suppressed. The third form preserves the second- and third-order echoes, while suppressing the linear echoes. The method is claimed to increase specificity in contrast agents.—DRR

6,494,843

43.80.Qf TRANSESOPHAGEAL ULTRASOUND PROBE WITH EXPANDABLE SCANHEAD

Stephen Dodge Edwardsen and Jon Ronander, assignors to GE Medical Systems Global Technology Company, LLC
17 December 2002 (Class 600/463); filed 19 December 2000

The subject transesophageal probe includes an expandable scanhead for improving the positioning of an imaging element mounted on the scanhead. The scanhead is expanded (or contracted) by inflation (or deflation) or via a moving extensor located within the scanhead.—DRR

6,497,661

43.80.Qf PORTABLE ULTRASOUND DIAGNOSTIC DEVICE WITH AUTOMATIC DATA TRANSMISSION

George A. Brock-Fisher, assignor to Koninklijke Philips Electronics N.V.
24 December 2002 (Class 600/437); filed 31 July 2001

This is a fairly conventional portable ultrasonic diagnostic device with equipment for a telephonic connection to transmit diagnostic data collected by the device.—DRR

6,497,665

43.80.Qf SYSTEM AND METHOD FOR NON-LINEAR DETECTION OF ULTRASONIC CONTRAST AGENTS AT A FUNDAMENTAL FREQUENCY

Thomas J. Hunt *et al.*, assignors to Koninklijke Philips Electronics N.V.
24 December 2002 (Class 600/458); filed 14 July 2000

This is a system for real-time imaging of tissue perfused with a contrast agent. According to the patent document, an image with increased sensitivity to nonlinear responses can be achieved by detecting the ultrasound response at the fundamental frequency from tissue perfused with a contrast agent and excited by multiple excitation levels. The responses detected from the multiple levels can be gain-corrected in an amount corresponding to the difference in multiple excitation levels, and then mathemati-

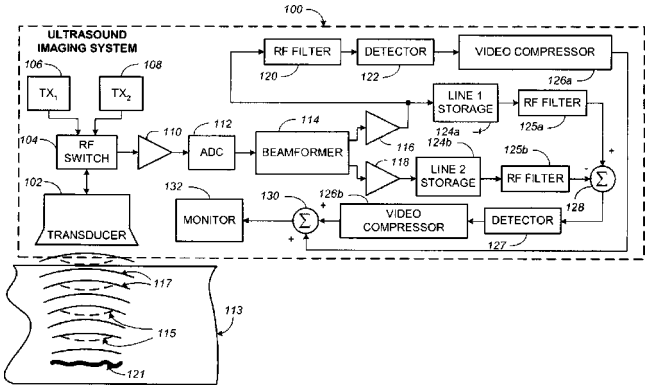

cally combined. This mathematical manipulation removes linear responses to the fundamental from the detected mode.—DRR

6,475,152

43.80.Sh BIOPSY NEEDLE GUIDE FOR ATTACHMENT TO AN ULTRASOUND TRANSDUCER

Walter Patrick Kelly, Jr. *et al.*, assignors to Koninklijke Philips Electronics N.V.
5 November 2002 (Class 600/461); filed 13 March 2000

This biopsy needle guide consists of two sections, an inner and an outer attachment block. The former contains a coupler to the ultrasound transducer and an engagement structure, while the latter unit contains a biopsy needle and another engagement structure. These two engagement structures mate and detach when desired, even when the inner attachment block is covered by a sterile film sheath.—DRR

6,487,447

43.80.Sh METHOD AND APPARATUS FOR IN-VIVO TRANSDERMAL AND/OR INTRADERMAL DELIVERY OF DRUGS BY SONOPORATION

Ludwig Weimann and Richard Childs, assignors to Ultra-Sonic Technologies, L.L.C.
26 November 2002 (Class 604/20); filed 17 October 2000

This method and apparatus are intended to deliver drugs transdermally or intra-transdermally by sonoporation. The apparatus includes a container featuring an end covered with a porous membrane and containing the drug solution and an ultrasound horn having a tip submerged in the drug solution. The horn sends an ultrasonic signal into the drug solution. The ultrasound radiation, which has a frequency range of 15 kHz to 1 MHz, is applied at an intensity for a period of time and at a distance from the skin area sufficiently strong so as to generate cavitation bubbles. The cavitation bubbles tend to collapse and transfer their energy into the skin area, thereby causing the formation of pores. The ultrasonic radiation intensity and distance from the skin area have the effect of generating ultrasonic jets that drive the drug solution through the porous membrane and the formed pores in the skin.—DRR

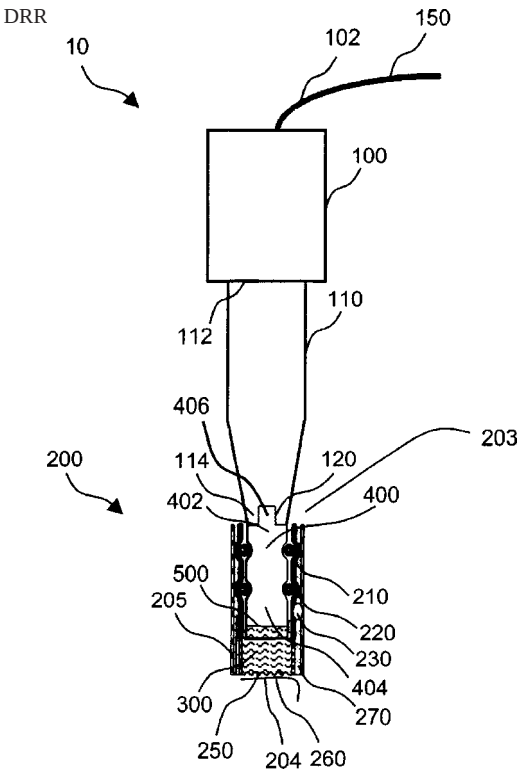

6,488,628

43.80.Sh METHOD FOR ULTRASONICALLY PROFILING THE DISTRIBUTION OF AN ADMINISTERED MEDICATION

Robert E. Reiss, assignor to SciMed Life Systems, Incorporated
3 December 2002 (Class 600/438); filed 31 July 2001

The widely used procedure of angioplasty as used to treat stenosis within a blood vessel is somewhat modified here to serve as a method for determining the extent of infiltration of a medication into the arterial wall. A balloon catheter infusion device containing the medication is positioned in the artery of the patient at the treatment site. Once it is properly positioned, the device injects the medication from inside the lumen into the artery wall. Such injections may occur at several points, in which case the device is

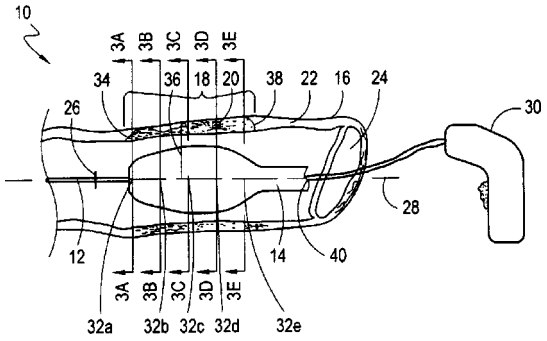

advanced to the most distal point and then gradually pulled back through the artery, while the medication is injected at several selected sites. A second catheter, containing an intravascular ultrasound device (IVUS), is advanced to the point of the most distal infusion, the ultrasound is activated, and it begins imaging the arterial wall at the start point. As the IVUS is gradually removed from the artery, images are generated to represent the extent of medication perfusion at each point of injection.—DRR

6,488,630

43.80.Sh ARRAYS OF QUASI-RANDOMLY DISTRIBUTED ULTRASOUND TRANSDUCERS

Jeffrey Warren Hand and Leonid Rafailovich Gavrilov, assignors to Imperial College Innovations Limited
3 December 2002 (Class 600/459); filed in the United Kingdom 19 February 1999

Optimizing an ultrasound transducer array for therapeutic procedures (such as tissue ablation and short duration high-intensity hyperthermia) constitutes a major problem in that such procedures should also be minimally invasive. This patent argues that optimal results may be obtained when the transducer elements are dispersed over the substrate surface in a quasi-

random distribution. If the elements' radiating area occupies between 40% and 70% of the total array area A, the operational frequency f of the ultrasound elements and the average diameter d of the elements are related according to the mathematical expression $d=(Ac)/f$, where c is the speed of the ultrasound signal.—DRR

6,488,639

43.80.Sh FREQUENCY ADJUSTMENT IN HIGH INTENSITY FOCUSED ULTRASOUND TREATMENT APPARATUS

Mathieu Ribault *et al.*, assignors to Technomed Medical Systems, S.A.; Institut National de La Santa et de La Recherche Medicale
3 December 2002 (Class 601/2); filed in France 13 May 1998

High-intensity focused ultrasound treatment involves heating tissue to elevated temperatures, typically greater than 45 °C. A number of problems arise in the use of this method, particularly differences in patient anatomy which require adjustments in focal length and wave frequency. An apparatus is proposed to provide adjustability of the focused ultrasound frequency according to the target attenuation, the thickness of the tissues traversed, the temperature evolution, or the lesion displacement during treatment. A number of embodiments are proposed, with hardly any details how to achieve the frequency adjustments.—DRR

6,490,469

43.80.Sh METHOD AND APPARATUS FOR DYNAMIC FOCUSING OF ULTRASOUND ENERGY

James V. Candy, assignor to The Regents of the University of California
3 December 2002 (Class 600/407); filed 14 March 2001

The purpose of this system is to noninvasively detect, separate, and destroy multiple masses (tumors, cysts, etc.). The system obtains time series measurement data to reconstruct inhomogeneous medium through the use of time-reversal focusing. Typical time reversal focusing techniques may involve focusing on the strongest scatterer and destroying it. Time reversal

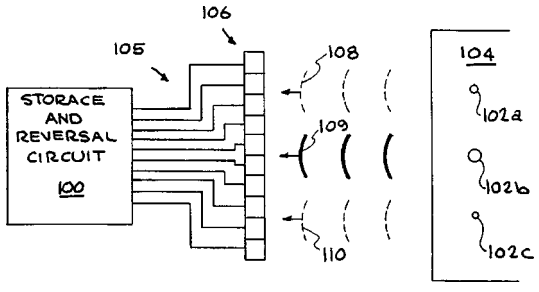

focusing is described as iteratively ''removing'' from the time series measurement data the aberrations created by an inhomogeneous medium illuminated by the propagating waves. This technique may be used iteratively and sequentially ''focus'' on a principal scatterer or flow dominating a pulse-echo response.—DRR

6,491,657

43.80.Sh ULTRASOUND ENHANCEMENT OF TRANSDERMAL TRANSPORT

Stephen Rowe *et al.*, assignors to Sontra Medical, Incorporated
10 December 2002 (Class 604/22); filed 21 May 2001

This is a device to channel and focus an ultrasound beam so that it is applied to a small area of the skin to enhance drug delivery and analyte collection. Two ultrasonic transducers with differing focal diameters are used to generate a combined signal. The ultrasound energy is applied through a vibrating element positioned just above, contacting, or extending into the skin. It is said that use of the element facilitates extraction of analyte and may enhance drug delivery.—DRR

6,494,891

43.80.Sh ULTRASONIC ANGIOPLASTY TRANSMISSION MEMBER

Wayne E. Cornish *et al.*, assignors to Advanced Cardiovascular Systems, Incorporated
17 December 2002 (Class 606/169); filed 30 December 1999

The ultrasonic angioplasty transmission wire described in the patent features regions of reduced cross-sectional diameter for increased flexibility of the wire and for compensating for degradation of longitudinal displacement due to acoustic losses along the wire. Constraining members are deployed at the reduced cross-sectional areas to prevent transverse vibrations at these points. The material contents of the transmission wire shaft are also specified.—DRR

6,497,715

43.80.Sh ULTRASONIC HAND PIECE AND ULTRASONIC HORN FOR USE WITH THE SAME

Yuichirou Satou, assignor to Miwatec Incorporated
24 December 2002 (Class 606/169); filed in Japan 7 November 2000

This device is an ultrasonic hand piece to be used with an ultrasonic horn for cutting bone in a living body operation. The hand piece contains an ultrasonic mechanism that outputs a longitudinal, a twisted, or a combined longitudinal and twisted ultrasonic vibration. A casing accommodates the ultrasonic mechanism and a horn is mounted on one end of the casing for cutting a bone or other hard tissue via the vibration transmitted from the ultrasonic mechanism. The horn consists of a main body portion and scalpel portion. It is claimed that the configuration of the hook-shaped scalpel portion and the application of the ultrasound cutting lessen the stress concentrations in the bone to prevent excess sting.—DRR

6,498,945

43.80.Sh SONODYNAMIC THERAPY USING AN ULTRASOUND SENSITIZER COMPOUND

Jan Alan Alfheim *et al.*, assignors to Amersham Health AS
24 December 2002 (Class 600/407); filed in the United Kingdom 19 May 1997

This type of therapy involves the use of ultrasound-susceptible modification agents, e.g., water-soluble polymers such as polyalkylene oxides and derivatives thereof, surfactants, oil-in-water emulsions, stabilized par-

ticles, and certain chromophonic groups such as sulfonated dyes, in treatment of humans or animals by sonodynamic therapy. A sensitizer agent is administrated to the body and the body is exposed to ultrasound to achieve a cythopathogenic effect at a selected site. The sensitizer agent, which should be a physiologically tolerable substance, enhances the cythopathogenic effect.—DRR

6,485,423

43.80.Vj CORRECTION OF PHASEFRONT ABERRATIONS AND PULSE REVERBERATIONS IN MEDICAL ULTRASOUND IMAGING

Bjorn A. J. Angelsen and Tonni F. Johansen, both of Trondheim, Norway
26 November 2002 (Class 600/458); filed 31 January 2001

Widely spaced point scatterers are introduced in the tissue being imaged. The point scatterers may be contrast agent bubbles in a dilute concentration. In the case of contrast agent bubbles, high-intensity transmitted pulse amplitudes are employed to destroy bubbles so point scatterers are dispersed. Alternately, a stochastic analysis of echo signals from dispersed scatterers is used.—RCW

6,485,424

43.80.Vj IMAGE FORMING METHOD AND APPARATUS, AND ULTRASONIC IMAGING APPARATUS

Yoichi Suzuki, assignor to GE Medical Systems Global Technology Company, LLC
26 November 2002 (Class 600/458); filed in Japan 22 March 2000

The variance of the Doppler shift of the signal from a moving harmonic producing contrast agent is used to adjust the signal strength of the image.—RCW

6,497,660

43.80.Vj ULTRASOUND IMAGING DEVICE

Richard F Dillman *et al.*, assignors to Koninklijke Philips Electronics N.V.
24 December 2002 (Class 600/437); filed 18 October 2000

This device has a bipolar signal generator, a transducer to emit an ultrasound wave in response to the generator, and a source to bias the bipolar voltage signal prior to applying it to the transducer so that the bias signal maintains the same polarity as the poling polarity of the transducer throughout the transmit cycle. This prevents depoling of the transducer that may occur if the transducer is repeatedly driven with a polarity opposite to the poling polarity.—RCW

6,488,629

43.80.Vj ULTRASOUND IMAGE ACQUISITION WITH SYNCHRONIZED REFERENCE IMAGE

Dagfinn Sætre *et al.*, assignors to GE Medical Systems Global Technology Company, LLC
3 December 2002 (Class 600/443); filed 31 July 2001

The viewing screen of an ultrasound scanner is divided into two parts. One part shows a reference image loop. The other part shows a live image loop. The reference image loop is retrieved from a frame memory based on the point in a stress test protocol. The speed of the reference image loop is set by software that uses the current heart rate.—RCW

6,491,631

43.80.Vj HARMONIC GOLAY-CODED EXCITATION WITH DIFFERENTIAL PULSING FOR DIAGNOSTIC ULTRASOUND IMAGING

Richard Yung Chiao and Theodore Lauer Rhyne, assignors to General Electric Company
10 December 2002 (Class 600/443); filed 11 January 2001

This excitation encodes the fundamental and second harmonic signal using quadrature phase shift signals implemented as quarter-cycle circular rotations or shifts of a base pulse. A different quadrature phase shift transmit code is used for each of four transmits. The coding and decoding suppresses the fundamental frequency and compresses the second harmonic.—RCW

6,491,632

43.80.Vj METHOD AND APPARATUS FOR PHOTOGRAMMETRIC ORIENTATION OF ULTRASOUND IMAGES

Geoffrey L. Taylor, Winnipeg, Manitoba, Canada
10 December 2002 (Class 600/443); filed 26 June 2001

A three-dimensional image is produced by using an ultrasonic transducer probe and a target plate attached to the probe. The probe is optically imaged during a sequence of ultrasound scans with different positioning of the scanning beam. Intersecting lines on the target plate are used to calculate image orientation.—RCW

6,491,634

43.80.Vj SUB-BEAMFORMING APPARATUS AND METHOD FOR A PORTABLE ULTRASOUND IMAGING SYSTEM

Steven C Leavitt *et al.*, assignors to Koninklijke Philips Electronics N.V.
10 December 2002 (Class 600/447); filed 13 October 2000

Subbeamforming is used in a portable ultrasonic imaging system. The circuitry may be included in the housing of the ultrasonic transducer to minimize the number of signals going between the probe assembly and the portable processor included in the imaging system. This also relieves the portable processor of some signal processing tasks.—RCW

6,494,839

43.80.Vj ULTRASONIC DIAGNOSTIC IMAGING SYSTEM TRANSMITTER FOR SUM AND DIFFERENCE FREQUENCY IMAGING

Michalakis Averkiou, assignor to Koninklijke Philips Electronics N.V.
17 December 2002 (Class 600/443); filed 6 August 2001

This system includes a transmitter that develops waveforms for two frequency bands of a transmit beam. The waveforms are combined and applied to the elements of a transducer array. A library of multi-frequency waveforms is maintained from which a desired waveform can be selected for transmit.—RCW

6,494,842

43.80.Vj ULTRASOUND RECEIVE BEAMFORMING APPARATUS USING MULTI STAGE DELAY DEVICES

Moo-Ho Bae, assignor to Medison Company, Limited
17 December 2002 (Class 600/447); filed in the Republic of Korea 10 June 2000

The structure of this apparatus produces data for multiple receive,

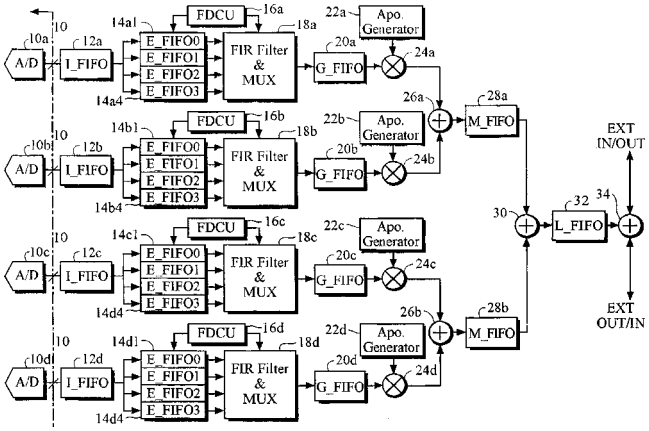

time-multiplexed scan lines with a reduced requirement for delay memory.—RCW

6,485,427

43.80.Vj COMPRESSIBILITY PROBE FOR MONITORING BLOOD VOLUME CHANGES

Jen-Shih Lee and Lian-Pin Lee, both of Charlottesville, Virginia
26 November 2002 (Class 600/468); filed 18 July 2001

Advantage is taken in this apparatus of the (approximately) linear relation between compressibility and density to measure these two parameters which are affected by infusion of saline and dialysate for the quantification of blood volume or microvascular pooling in patients. The device includes a combination of ultrasound transducers attached to the tubing in which blood is flowing. An indicator medium is injected into the bloodstream over one or more time points. Ultrasound waves are transmitted and monitored through the use of transducers and phase lock amplifiers to assess transmission time. Through the aforementioned relationship between density and compressibility, changes in blood density are computed from transmission time changes in order to yield blood density changes, blood volume, and microvascular pooling.—DRR

6,497,666

43.80.Vj MEDICAL ULTRASONIC CONTRAST AGENT IMAGING METHOD AND APPARATUS

Patrick J. Phillips and Ismayil M. Guracar, assignors to Acuson Corporation
24 December 2002 (Class 600/458); filed 25 October 2000

A set of two or more identical pulses are transmitted into tissue containing a contrast agent. A broadband filter passes the corresponding received signals at both the fundamental and at least one harmonic component of the echoes. A clutter filter then suppresses harmonic and fundamental responses from slowly moving and stationery tissue while passing contrast agent signals. This system includes other signal paths for producing conventional b-scan images as well as combined images that include components from a contrast-specific image as well as components from a b-scan image.—RCW

Recovering the Green's function from field-field correlations in an open scattering medium (L)

Arnaud Derode[a)]
Université Paris 7 and CNRS, LOA-ESPCI, 10 rue Vauquelin, 75005 France

Eric Larose
Université Joseph Fourier and CNRS, LGIT, BP 53, 38041 Grenoble, France

Mickael Tanter, Julien de Rosny, and Arnaud Tourin
Université Paris 7 and CNRS, LOA-ESPCI, 10 rue Vauquelin, 75005 France

Michel Campillo
Université Joseph Fourier and CNRS, LGIT, BP 53, 38041 Grenoble, France

Mathias Fink
Université Paris 7 and CNRS, LOA-ESPCI, 10 rue Vauquelin, 75005 France

(Received 10 October 2002; accepted for publication 24 February 2003)

The possibility of recovering the Green's function from the field-field correlations of coda waves in an open multiple scattering medium is investigated. The argument is based on fundamental symmetries of reciprocity, time-reversal invariance, and the Helmholtz–Kirchhoff theorem. A criterion is defined, indicating how sources should be placed inside an open medium in order to recover the Green's function between two passive receivers. The case of noise sources is also discussed. Numerical experiments of ultrasonic wave propagation in a multiple scattering medium are presented to support the argument. © *2003 Acoustical Society of America.*
[DOI: 10.1121/1.1570436]

PACS numbers: 43.20.−f [RLW]

Wave propagation in a multiple scattering or reverberating environment has been a subject of interest in a wide variety of domains ranging from solid state physics to optics or acoustics. Ultrasound is particularly interesting because it allows a direct measurement of the field fluctuations, both in amplitude and in phase. In connection with this, a remarkable work by Weaver and Lobkis[1–3] recently showed that the Green's function between two points could be recovered from the field-field correlation of a diffuse ultrasonic field. This amounts to doing ''ultrasonics without a source'' since they showed that thermal noise could be used instead of a direct pulse/echo measurement between the two points. The experiment was carried out in an aluminum block, and the theoretical analysis was based on discrete modal expansion of the field, with random modal amplitudes. Applications are promising: it would be possible to recover the Green's function of a complex medium just by correlating diffuse fields received on passive sensors (application to shallow water ocean acoustics, where the field is not diffuse but propagates in a wave guide, was also evoked[4]).

However, the basic assumption in the theoretical analysis is that the medium is closed and free of absorption. In a real medium, absorption will tend to cut out the longest scattering (or reverberating) paths, and discrete modes will not be resolved any more. Similar problems are expected if the medium is open rather than closed (actually, in an open medium, the fluctuation-dissipation theorem[3] establishes the result, as long as the field is diffuse in the thermal sense). The aim of this letter is to examine whether the Green's function can still be recovered from the correlations of an ultrasonic wave field in an open scattering medium, when a discrete expansion on orthogonal modes is no longer relevant and the field is not thermally diffuse.

To that end, we present 2-D numerical experiments of acoustic scattering on rigid inclusions randomly located either in a closed cavity or in a open medium. The wave equation is solved by a finite differences simulation (centered scheme); the boundary conditions is implemented following Collino's work.[5] Naturally, a finite difference scheme shows numerical dispersion. However, the essential point is that the fundamental symmetries of reciprocity and time reversal still hold in the numerical experiments.

To begin with, let us consider two receiving points A and B and a source C placed among a random collection of scatterers, as represented in Fig. 1. The scatterers are in water; only lossless acoustic waves are considered here. At the edges of the grid, the boundary conditions may be either perfectly reflecting (Dirichlet) as in a closed cavity or absorbing (open medium). The signal transmitted by C is a pulse with a center frequency 1 MHz and a Gaussian envelope ($\sigma = 0.7\ \mu$s).

We will note $h_{IJ}(t)$ as the impulse response between I and J, i.e., the wave field sensed in I when a Dirac $\delta(t)$ is sent by J. If $e(t)$ is the excitation function in C, then the wave field ϕ_A and ϕ_B received in A and B will be respectively $e(t) \otimes h_{AC}(t)$ and $e(t) \otimes h_{BC}(t)$, $\otimes$ representing convolution. The cross-correlation of the fields received in A and B is then

a)Electronic mail: arnaud.derode@espci.fr

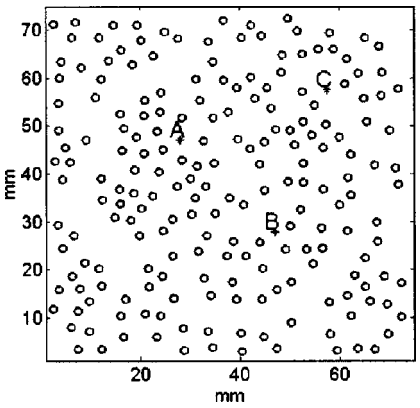

FIG. 1. Two hundred perfectly rigid scatterers (diameter 2.1 mm) are randomly distributed over a $7.5\times7.5\ \mathrm{cm}^2$ area. A point source is placed in *C*; *A* and *B* are receiving points. The boundary conditions may be perfectly reflecting (Dirichlet) as in a closed cavity or absorbing (open medium).

$$C_{AB}(t)=\int \phi_A(\theta)\phi_B(t+\theta)\,d\theta=h_{AC}(t)\otimes h_{BC}(-t)\otimes f(t)$$

with $f(t)=e(t)\otimes e(-t)$. $f(t)$ depends only on the excitation imposed at the source, whereas the information regarding the impulse response between *A* and *B* is hidden in $h_{AC}(t)\otimes h_{BC}(-t)$. Indeed, the impulse responses of a closed cavity satisfy a remarkable property, as shown by Carsten Draeger in 1999,[6] which he termed the "cavity equation:"

$$h_{AC}(t)\otimes h_{BC}(-t)=h_{AB}(t)\otimes h_{CC}(-t). \tag{1}$$

For this relation to hold, the cavity must be lossless and its eigenmodes not degenerate. Note that, in practice, the correlations cannot be performed over an infinite time interval (the ring time of a cavity is infinite if it is lossless); therefore the cavity equation can be compared to experimental results if the integration time ΔT is sufficiently large compared to $1/\Delta\omega$, with $\Delta\omega$ the characteristic distance between modes, so that the modes are resolved. $1/\Delta\omega$ is sometimes referred to as the Heisenberg time, or break time. Figure 2 illustrates the validity of the cavity equation; here the impulse responses have been recorded during an integration time of 80 ms (2×10^6 time steps), and the Heisenberg time is $\sim$5 ms. From Draeger's cavity equation, the correlation between the fields received in *A* and *B* is

$$C_{AB}(t)=h_{AB}(t)\otimes h_{CC}(-t)\otimes f(t).$$

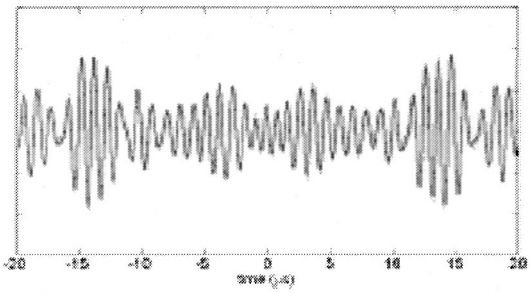

FIG. 2. Comparison between $C_{AB}(t)$ (thick continuous line) and $h_{AB}(t)\otimes h_{CC}(-t)\otimes f(t)$ (dotted line). The overall correlation coefficient between the two waveforms is 98.7%.

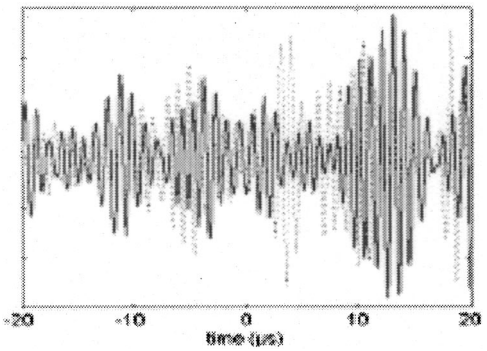

FIG. 3. Comparison between $C_{AB}(t)$ (thick continuous line) and $h_{AB}(t)\otimes h_{CC}(-t)\otimes f(t)$ (dotted line) in the open scattering medium. The impulse responses were recorded during 800 μs, until they became negligible. The overall correlation coefficient between the two waveforms is 0.48%.

Therefore, similarly to Weaver's results,[1–3] the direct Green's function h_{AB} *is* present in the correlations of the field within a closed cavity and can be recovered from C_{AB} provided that the h_{CC} term can be properly deconvolved, at least in the frequency domain limited by the spectrum of $f(t)$.

Is this valid in an open medium? We have conducted the same numerical experiment, with the same distribution of scatterers, but with absorbing instead of reflecting boundary conditions. As a result, the cavity equation is no longer valid and the correlation of the scattered field C_{AB} shows no resemblance whatsoever with the Green's function (the correlation coefficient function between wave forms represented on Fig. 3 is less than 0.5%).

However, a physical argument indicates that the Green's function can *still* be recovered from the correlations C_{AB}, even in an open medium, if several judiciously distributed sources are used instead of a single point *C*. To that end, we propose to analyze the experiment in terms of time-reversal symmetry. Indeed, there is a strong link between correlations of a diffuse field and time reversal.[7]

Because the scatterers do not move and there is no flow within the medium, the propagation is reciprocal, i.e., $h_{IJ}(t)=h_{JI}(t)$. When we cross-correlate the impulse responses received in *A* and *B*, the result $h_{AC}(t)\otimes h_{BC}(-t)$ is equal to $h_{CB}(-t)\otimes h_{AC}(t)$. Now, imagine that we do the following time-reversal experiment: *B* sends a pulse, *C* records the impulse response $h_{CB}(t)$, time reverses it and sends it back; the resulting wave field observed in *A* would then be $h_{CB}(-t)\otimes h_{AC}(t)$, which, because of reciprocity, is exactly the cross-correlation $h_{AC}(t)\otimes h_{BC}(-t)$ of the impulse responses received in *A* and *B* when *C* sends a pulse. We would like the direct Green's function h_{AB} to appear in the cross correlation. But in the most general case, $h_{CB}(-t)\otimes h_{AC}(t)$ has no reason to be equal to h_{AB}, as was shown in Fig. 3. Yet we can go beyond: imagine now that we use several points *C* to perform the time-reversal operation, and that we place them in such a way that they form a *perfect* time-reversal device, with no loss of information. Following the Helmholtz–Kirchhoff theorem, such would be the case if the sources *C* were continuously distributed on a surface surrounding the scattering medium. Then the time-reversal operation should be perfect. During the "forward" propagation, *B* sends a pulse that propagates everywhere in the medium

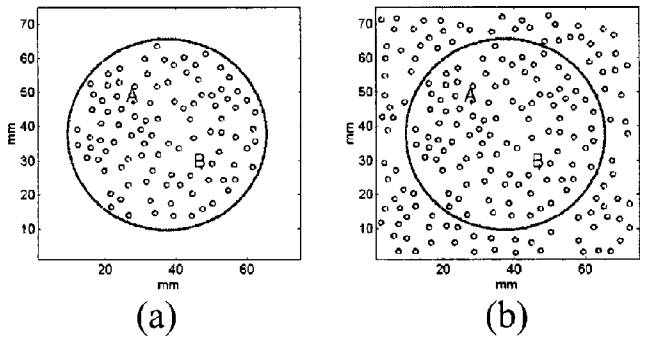

FIG. 4. A and B are receiving points. Two hundred fifty source points are placed regularly around a circle with radius 18.7 mm, 100 scatterers being inside the circle. They completely surround the medium (a), or only partially (b). The boundary conditions on the edges of the grid are absorbing (open medium), in both cases.

[including in A where the field received is $h_{BA}(t)$], it may be scattered many times and is eventually recorded on every point of the time-reversal device, with no loss. When the field is time reversed, since nothing of it has been lost, it should exactly go backward in time (and refocus on B at time $t=0$) everywhere in the medium, which implies that the field received in A after the time reversal is exactly $h_{BA}(-t)$, the time-reversed version of the direct Green's function. Then, once the wave has refocused on B (at time $t=0$), it does not stop since there is no "acoustic sink" in B:[8] the wave diverges again from B and gives rise, at times $t>0$, to $h_{BA}(t)$ in A.

Thus, if we use a collection of sources C arranged in such a way that they form a perfect time-reversal device, we should have

$$\sum_C h_{AC}(-t)\otimes h_{CB}(t)=h_{BA}(t)+h_{BA}(-t). \tag{2}$$

A more detailed analysis, taking into account the monopolar or dipolar nature of the source/receivers, is given by Didier Cassereau.[9] Equation (2) implies that the impulse response $h_{BA}(t)$ can still be recovered from the correlation of a diffuse field, even in an open medium, provided that the sources C are distributed judiciously, and all the correlation functions are summed over the source positions. Unlike the case of a closed medium, no additional deconvolution by h_{CC} is needed. From this time-reversal analogy, we deduce a condition for the Green's function to emerge from cross correlations in open media: the sources C must be placed so that they form a perfect time-reversal device.

We have checked this in the numerical experiments depicted in Fig. 4. The results are in excellent agreement with Eq. (2), as is shown in Fig. 5: the degree of correlation between waveforms is 97.4%. Of course, when the sources are not placed as a perfect mirror, as presented in Fig. 4(b), the results are less good (the degree of correlation between waveforms is 81.9%) because one part of the waves is not recorded by the time-reversal device due to the presence of scatterers outside the sources. Yet the main features of the Green's function can still be recognized, even at late times. If the number of sources is decreased, the reconstruction of the Green's function is less satisfactory, as shown in Fig. 6. With

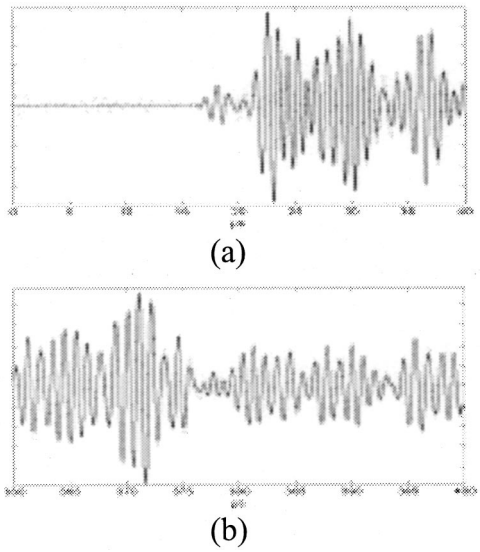

FIG. 5. Comparison between $\Sigma_C h_{AC}(t)\otimes h_{BC}(-t)\otimes f(t)$ (dotted line) and $h_{AB}(t)\otimes f(t)$ in the open scattering medium surrounded by 250 sources C as depicted in Fig. 4(a), at early times (a) and in the late coda, 360 μs later (b). The overall correlation coefficient between waveforms is 97.4%.

only 50 sources (instead of 250 previously) regularly spaced every $\sim 5\lambda/3$ all along a circle as in Fig. 4(a), the correlation coefficients between waveforms is 70%. However, if the 50 sources are gathered together in a 72° angular sector (pitch $\lambda/3$), it drops to 53%. Indeed, since the coherence length of a diffuse wave field is $\sim\lambda$, it is useless to place the sources closer.

So far, we have considered that the origin of the field measured in A and B was an active and coherent source transmitting a short pulse (or a collection of such sources). What if there are no such sources in the medium, but a diffuse continuous noise? The physical origin of this noise may be thermal vibrations.[3] In seismology, noise in the seismograms comes from a variety of different sources (traffic, sea waves, weather, human activity,...) continuously and (allegedly) randomly pumping energy into the earth and essentially exciting surface waves. In ocean acoustics, noise may originate from boats, surf, wind, animals, etc. By definition, the noise sources cannot be controlled. In the light of the discussion above, in order to recover the Green's function from the cross-correlation of the noise received in A and B, the most favorable situation would be that in which noise can be con-

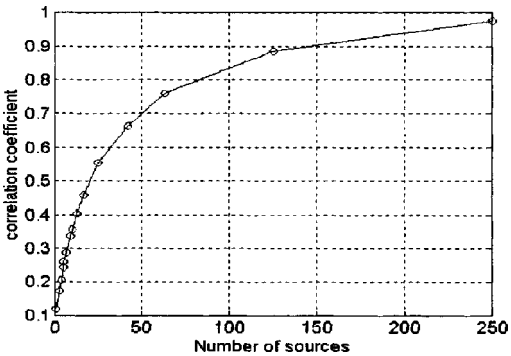

FIG. 6. Correlation coefficient between $\Sigma_C h_{AC}(t)\otimes h_{BC}(-t)\otimes f(t)$ and $h_{AB}(t)\otimes f(t)$ versus the number of sources employed.

sidered as coming from virtual point sources C randomly distributed everywhere in the medium and continuously generating uncorrelated white noises $n_C(t)$. In that case, the cross correlation between waveforms sensed in A and B would be

$$\sum_C \sum_{C'} h_{AC}(-t) \otimes n_C(-t) \otimes h_{C'B}(t) \otimes n_{C'}(t).$$

If the observation time ΔT is long enough compared to the correlation time of the noise, then $n_C(-t) \otimes n'_C(t)$ will converge to $\delta(t)\,\delta_{C,C'}$. Moreover, if the virtual noise sources C are distributed everywhere in the medium (in other words, if each degree of freedom is excited randomly and independently), then the C-points would necessarily constitute a perfect time-reversal device, so Eq. (2) should be verified again.

We have carried out a numerical experiment based on this idea. Two hundred forty sources were distributed at random inside the open scattering medium shown in Fig. 1, and 240 uncorrelated white noises, convolved by $e(t)$, were transmitted by these sources during 40 ms. The resulting wave forms are received in A and B. Their cross correlations $C_{AB}(t)$ is compared to the direct Green's function $h_{AB}(t) \otimes f(-t)$: the agreement is still very good (61% correlation coefficient) even at late times.

The emergence of the Green's function in the field-field correlations in a closed cavity with discrete modes is now well established.[1–3] In this letter, we have argued that recovering the Green's function was also possible in an open multiple scattering medium and we have proposed a criterion based on reciprocity, time-reversal symmetry, and the Helmholtz–Kirchhoff theorem: if sources are placed as if they were to form a perfect time-reversal device, then the Green's function can be recovered by summing the cross correlations. This has been validated by numerical experiments. The reduction of the number of sources was also discussed and the possibility of using noise sources was illustrated.

There is still much food for thought, particularly regarding the role of the scatterers in the reconstruction of the Green's function. The argument we developed here is valid for any medium (homogeneous, high-order multiple scattering, reverberant, ...) where reciprocity and invariance under time reversal hold. The field does not need to be thermally diffuse for the Green's function to emerge from the correlations, as long as there are enough well-positioned sources. Another approach is to consider the scatterers as secondary sources which are necessary to truly randomize the wave field emanating from a *single* original source. Correlating the late part of the coda would then permit us to reconstruct at least the early arrivals of the Green's function. Recent seismologic results support this idea.[10] The influence of absorption is also to be investigated.

ACKNOWLEDGMENTS

The authors wish to thank Ludovic Margerin and Anne Paul.

[1] R. L. Weaver and O. I. Lobkis, "On the emergence of the Green's function in the correlations of a diffuse field: pulse echo using thermal phonons," Ultrasonics **40**, 435–439 (2002).
[2] O. I. Lobkis and R. L. Weaver, "On the emergence of the Green's function in the correlations of a diffuse field," J. Acoust. Soc. Am. **110**, 3011–3017 (2001).
[3] R. L. Weaver and O. I. Lobkis, "Ultrasonics without a source: thermal fluctuation correlations at MHz frequencies," Phys. Rev. Lett. **87**(13), 134301–134304 (2001).
[4] P. Roux and M. Fink, "Green's function estimation using secondary sources in a shallow water environment," J. Acoust. Soc. Am. **113**, 1406–1411 (2003).
[5] F. Collino and P. Joly, "Absorbing boundary conditions for the finite element solution of 3D Maxwell's Equation," IEEE Trans. Magn. **14**(31), 1696–1701 (1995).
[6] C. Draeger and M. Fink, "One-channel time-reversal in chaotic cavities: theoretical limits," J. Acoust. Soc. Am. **105**, 611–617 (1999).
[7] A. Derode, A. Tourin, and M. Fink, "Random multiple scattering of ultrasound. II. Is time-reversal a self-averaging process?" Phys. Rev. E **64**(3), 036606–036618 (2001).
[8] J. de Rosny and M. Fink, "Overcoming the diffraction limit in wave physics using a time-reversal mirror and a novel acoustic sink," Phys. Rev. Lett. **89**(12), 124301–124304 (2002).
[9] D. Cassereau and M. Fink, "Time-reversal of ultrasonic fields-Part III: theory of the closed time-reversal cavity," IEEE Trans. Ultrason. Ferroelectr. Freq. Control **39**(5), 579–592 (1992).
[10] M. Campillo and A. Paul, "Long range correlations in the diffuse seismic coda," Science **299**, 547–549 (2003).

Response of strings to turbulence—Redux (L)

Richard H. Lyon[a)]
RH Lyon Corp, 691 Concord Avenue, Cambridge, Massachusetts 02138

(Received 9 October 2002; revised 28 February 2003; accepted 6 March 2003)

An unresolved issue in the author's Ph.D. thesis concerned the relation between turbulent flow speed and the maximum response of a string excited by the turbulence. The maximum response occurred at a flow speed significantly less than that predicted. This discrepancy was not resolved at the time, but can be resolved if one notes that the flow excitation is dispersive, with longer scale disturbances that flow faster than smaller scale disturbances. It is suggested that string response to turbulence may be a useful way to determine small-scale properties of a turbulent flow. © *2003 Acoustical Society of America.* [DOI: 10.1121/1.1572136]

PACS numbers: 43.28.Vd, 43.20.Tb [MSH]

This letter is concerned with an unresolved issue that occurred in the author's Ph.D. thesis and reported on in Ref. 1. A thin metal strip under tension was excited into vibration by turbulent flow along its length in a rectangular metal tube. The theory modeled the turbulence as a random and convected force field with a decaying correlation due to the continual decay and generation of turbulent ''eddies'' as the flow progressed.

The theory presented in Ref. 1 predicted that maximum vibration of each mode of the string would occur when the convection speed of the turbulence equals the wave speed of string vibrations. Generally, one would expect the convection speed to be slightly less than either the average or free stream flow speed because of boundary layer effects, so that maximum vibration should be observed when the average flow speed is somewhat greater than the string wave-speed. Unfortunately, in all the experiments, the maximum vibration occurred when the flow speed was *less* than the string wave-speed. Repeated checks of the flow calibration, string wave-speed, etc., failed to resolve the discrepancy.[2]

The response of a string $y(x,\omega)$ at frequency ω to a force $f(x,\omega)$ is governed by

$$c^2y''+\omega^2y=f/\rho, \tag{1}$$

where c is the string wave-speed and ρ is its lineal density. If we expand the displacement and force in wavenumber, we obtain

$$Y(k,\omega)=-F(k,\omega)/\rho(\omega^2-k^2c^2), \tag{2}$$

which is maximum when $c=\omega/k$, the phase velocity of the excitation.

In Ref. 1, the phase speed was equal to the convection velocity, since the random forces from the turbulence were assumed nondispersive. But it is known that turbulence pressures and velocities are dispersive. Larger scale fluctuations move faster than the smaller scale fluctuations that are created and decay in the slower boundary layer. The observed convection velocity of the turbulent forces represents the group velocity, which will differ from the phase velocity that controls the matching in both frequency and wavenumber.[3]

The general relation (one-dimensional) between the group velocity c_g and the phase velocity c_ϕ is

$$c_g=c_\phi+kdc_\phi/dk. \tag{3}$$

Therefore, if larger scale components or eddies (small k) travel faster than smaller components or eddies (large k), $dc_\phi/dk<0$, and therefore $c_\phi>c_g$. This means that matching of phase velocity with wave-speed $c_\phi=c$ will occur at a value of $c_g<c$, which was observed in Ref. 1.

The string wave-speed in Ref. 1 was 4400 cm/s, and the flow speed at which maximum response was observed was 3700 cm/s. In the experiment, therefore,

$$\frac{kdc_\phi/dk}{c_\phi}=\frac{d\ln c_\phi}{d\ln k}\approx -0.2, \quad \text{or} \quad c_\phi\propto k^{-1/5}. \tag{4}$$

Unfortunately, we do not have independent data for this dependence in the work of Ref. 1, but modern instrumentation and signal processing methods, including the use of micromachined strings or beams, might allow one to use string response to determine wavenumber/frequency dependences in turbulent flow.

a)Electronic mail: rhlyon@lyoncorp.com

[1] R. H. Lyon, ''Response of strings to random noise fields,'' J. Acoust. Soc. Am. **28**, 391–398 (1956) (available on Disc #1, JASA Archives on CD-ROM).

[2] As explained in Ref. 1, the ''string'' is a thin strip of steel (10 mils by 3/16 in., 44 cm long under tension, excited by airflow along its length in a 0.25×0.5 in. tube. Motion was observed by an optical arrangement that measured the string deflection.

[3] In a cross-correlation experiment, the output is that of a correlation detector where the reference is the signal from the upstream sensor. The time delay for the envelope of the output signal is determined by the signal or group delay of the system (in this case, the unknown dynamics of the turbulent flow). This delay is usually expressed in terms of a convection velocity by dividing the separation distance of the sensors by the time shift of the correlation peak.

Comment on "Multiple scattering in a reflecting cavity: Application to fish counting in a tank" [J. Acoust. Soc. Am. 109, 2587–2597 (2001)] (L)

Zhen Ye[a)]
Wave Phenomena Laboratory, Department of Physics, National Central University, Chung-li, Taiwan 32054

Dezhang Chu
Department of Applied Ocean Physics and Engineering, Woods Hole Oceanographic Institute, Woods Hole, Massachusetts 02543

(Received 30 October 2001; revised 5 September 2002; accepted 3 March 2003)

This paper presents a comment on the recent work on fish counting in a tank [J. Acoust. Soc. Am. **109**, 2587–2597 (2001)]. It is pointed out that there are ambiguities with the counting method. [DOI: 10.1121/1.1569938]

PACS numbers: 43.20.El, 43.30.Gv, 43.80.Ev [DLB]

In a recent paper,[1] de Rosny and Roux proposed a method for counting fish in a tank, an important issue for the fisheries community. As far as we know, this is the first published report on counting fish in a tank. We recognize that the fish information may have been detected by the method. In particular, the method tends to obtain reasonable fish number counts. However, in its present form of data analysis, we believe that some of the theoretical foundations for the approach are questionable. As a matter of fact, their approach was unable to provide reasonable scattering properties of fish. The reasons are elaborated below.

(1) The multiple scattering in a reflecting cavity. The basis for the fish counting method in Ref. 1 is described by Fig. 1 of Ref. 1. The analysis relies on the treatment of the multiple scattering picture in this figure. In the context, the authors argued that the effect of the reflecting boundaries of a tank can be regarded as mirrors, and thus acoustic scattering in such a system is regarded as a medium of scatterers and their images without the boundaries. The multiple reflections make the system equivalent to a system of infinite size.

The first ambiguity in the latter development is that effects from the images of the acoustic sources are not considered in Ref. 1. Although the images of the sources are shown in Fig. 1, possible effects from multiple source images are not discussed anywhere in Ref. 1. In addition, the reflection from the water surface is not taken into account either. The presence of the water surface also acts as a mirror, giving rise to interactions between the scatterers and their images due to this mirror. It is worth pointing out that the water surface acts as a pressure release plane, which has different effects from the presumably total-reflecting side boundaries of the tank.

The second ambiguity lies in the way the multiple scattering among the scatterers and the images in Fig. 1 is accounted for, a crucial problem in the analysis. In Ref. 1, the authors wrote down two formulas in Eqs. (1) and (2) for total and coherent intensity as a result of the multiple scattering; here we note that in Ref. 1 Eqs. (1) and (2) have been mistakenly regarded as the coherent intensity and incoherent intensity, respectively—the detailed information about the definitions of these quantities can be referred to Ref. 2. With reference to Ref. 2, it is easy to verify that both Eqs. (1) and (2) are actually the results of the multiple scattering when a wave propagates in a cloud of *completely independent* random scatterers (refer to, e.g., Chap. 14 in Ref. 2). In a system such as many scatterers in a reflecting cavity, the scatterers and their images are *not* independent scatterers. Thus Eqs. (1) and (2) are not applicable to the present case. There is a rich body of literature on acoustic scattering by bodies in the presence of boundaries (e.g., Refs. 3–6). Correlated scatterers can give rise to interference between multiply scattered waves that is absent in a group of independent scatterers. Take the simplest case of an object near a boundary as an example. The multiple scattering from a scatterer and its image differs from the scattering from two actual scatterers. This can be easily inferred from, for example, Ref. 6.

(2) The mathematical derivation. The results of Ref. 1 rely mainly on its Eq. (4). In writing down this equation, the authors made the assertion "Eq. (3) can be written [as Eq. (4)] by changing from a space variable to a time variable," then Eq. (4) is obtained. But no details were given. The derivation from Eq. (3) to Eq. (4) is mathematically unclear. Equation (3) denotes how a wave is attenuated after traveling a distance, but Eq. (4) represents the time evolution of backscattered or reflected signals. The former is a *forward* propagating process, while the latter is a combination of the forward process, via reflections, and the *backscattering* process. The link between the two is not obvious. In fact, the time evolution of backscattered signals has been detailed in Chap. 5 of Ref. 2. It is not evident how the time series of the ratio between the coherent and the total backscattered signals can be represented by a simple equation like Eq. (4).

(3) The experimental results. The method of Ref. 1 yields doubtful scattering properties of fish. The main goal of Ref. 1 is to obtain accurate total scattering cross section of fish. Two fish species are measured: zebra fish with length about 1 cm at 400 kHz and 35-cm-long striped bass at 12.8 kHz. Take the bass fish as the example. According to Ref. 1,

[a)]Electronic mail: zhen@phy.ncu.edu.tw

the total scattering cross section of the striped bass is $4\pi R^2$ with $R \sim 3.8$ cm, leading to $\sigma_s \sim 181\ \mathrm{cm}^2$. This value is much larger than what would be expected for a fish of 35 cm length. The reasons follow.

First, the total scattering cross section is a computable quantity. According to the optical theorem,[2] the total cross section can be calculated from the imaginary part of the forward scattering function of a scatterer,

$$\sigma_t = \sigma_s + \sigma_a = \frac{4\pi}{k}\,\mathrm{Im}[f(0)], \tag{1}$$

where $f(0)$ is the scattering function in the forward scattering direction, and σ_s and σ_a are the total scattering cross section and the absorption cross section, respectively; the absorption can be caused by such effects as thermal exchange or viscosity of the scatterer. For frequencies above the resonance of the fish swimbladder like the cases considered in Ref. 1, the absorption due to the swimbladder is negligible. Furthermore, the acoustic absorption due to fish bodies is also negligible. Therefore we have

$$\sigma_s \approx \sigma_t = \frac{4\pi}{k}\,\mathrm{Im}[f(0)]. \tag{2}$$

This applies to scattering by both fish swimbladders and fish bodies. The advances in modeling acoustic scattering by fish allow for reasonable estimates of fish scattering cross sections. Fish scattering models can be referred to, e.g., the textbook of Ref. 7. Indeed, the optical theorem has been applied to existing experimental measurements of various fish scattering cross sections, yielding encouraging agreements.[8] Applying the method in Ref. 8, we estimate that the total scattering cross section for a 35-cm-long fish at 12.8 kHz is at most around 30–40 cm^2, depending on the aspect ratio used in the modeling; we note that the dorsal and side aspects will not make much difference in the forward scattering. This is much smaller than the value obtained in Ref. 1. It is our experience that the scattering properties vary only slightly for different fish species with the same length.

Second, there exist experimental data on acoustic scattering on fish of similar length. For example, the previous experiment data on Saithe fish of 35.1-cm length yield a total scattering cross section around 30 cm^2,[9] in the same order as the theoretical value.[8] This experiment was carried out at a frequency higher than the 12.8 kHz used in Ref. 1. From the modeling, this would lead to a higher value in the total scattering cross section than that at 12.8 kHz. It is therefore reasonable to conclude that the total scattering cross section for a 35-cm-long fish at 12.8 kHz would be in the order of a few tens of square centimeters, which is considerably smaller than that obtained in Ref. 1.

(4) Finally, we would like to point out that although there are ambiguities in Ref. 1, the approach in the paper tends to get good fish number counts, a promising aspect of the method. This would indicate that though not rigorous, the method does capture some essence of the problem. It would be imperative to search for a sound and solid footing for the empirical approach of Ref. 1.

In conclusion, the method in Ref. 1 requires further development and elaboration in order to be more applicable to counting fish in an aquatic tank. Given the promising aspect of the paper, it is indeed worthwhile to do so.

ACKNOWLEDGMENTS

Dr. P.-G. Luan is thanked for bringing Ref. 1 to our attention. We thank Dr. Tim Stanton (WHOI) for useful correspondence. We appreciate that one of the referees pointed out that the formula of the target strength in Ref. 1 is only valid for the case of an omnidirectional scatterer. The work received support from the National Science Council through a grant to ZY.

[1] J. de Rosny and P. Roux, "Multiple scattering in a reflecting cavity: Application to fish counting in a tank," J. Acoust. Soc. Am. **109**, 2587–2597 (2001).
[2] A. Ishimaru, *Wave Propagation and Scattering in Random Media* (Academic, New York, 1978), Vols. I and II.
[3] J. C. Bertrand and J. W. Young, "Scattering between a cylinder and a plane," J. Acoust. Soc. Am. **60**, 1265–1269 (1976).
[4] G. C. Bishop and J. Smith, "Scattering from an elastic shell and a rough fluid-elastic interface," J. Acoust. Soc. Am. **101**, 767–788 (1997).
[5] J. A. Fawcett, W. L. J. Fox, and A. Maguer, "Modeling of scattering by objects on the seabed," J. Acoust. Soc. Am. **104**, 3296–3304 (1998).
[6] I. Tolstoy, "Superresonant systems of scatterers. I," J. Acoust. Soc. Am. **80**, 282–294 (1986).
[7] H. Medwin and C. S. Clay, *Acoustical Oceanography* (Academic, New York, 1997).
[8] Z. Ye, "On acoustic attenuation by swimblader fish," J. Acoust. Soc. Am. **100**, 669–672 (1996).
[9] K. G. Foote, "Analysis of empirical observations on the scattering of sound by encaged aggregations of fish," Fiskeridir. Skr., Ser. Havunders. **16**, 422–455 (1978).

Arctic field trials of source bearing estimation using ice-mounted geophones (L)

Stan E. Dosso[a)]
School of Earth and Ocean Sciences, University of Victoria, Victoria, British Columbia V8W 3P6, Canada

Michael Vinnins
Defence Research and Development Canada—Ottawa, Ottawa, Ontario K1A 0Z4, Canada

Garry J. Heard
Defence Research and Development Canada—Atlantic Dartmouth, Nova Scotia B2Y 3Z7, Canada

(Received 18 October 2002; accepted for publication 17 March 2003)

Results are presented from Arctic field trials carried out to estimate the bearing to acoustic sources in the water column using seismic particle motion measured at a tri-axial geophone mounted on the sea ice surface. Source bearings are estimated by applying polarization filters to suppress seismic waves with transverse particle motion and computing the incident power rotated into radial look angles from 0° to 360°; the inherent 180° ambiguity is resolved by requiring out-going (prograde) particle motion in the vertical-radial plane. An earlier study considered impulsive sources at ranges of 200–1000 m at a site characterized by mixed annual ice. The present work considers two studies of similar scale carried out at sites with uniformly smooth annual ice and rough, ridged annual ice, and a third study on multi-year ice involving sources at 2–50-km range. The results indicate good bearing estimation to long range with little dependence on ice type. [DOI: 10.1121/1.1572145]

PACS numbers: 43.30.Ma, 43.40.Dx [WLS]

I. INTRODUCTION

This letter considers the use of three-dimensional seismic particle motion measured at a tri-axial geophone on the surface of Arctic sea ice to estimate the bearing to an acoustic source in the water column. Sea ice is an anisotropic, polycrystalline solid which includes air pockets, precipitated salts, and liquid brine. On a larger scale, the ice pack is a conglomerate of first-year (annual) ice, multi-year ice floes, and pressure ridges. The upward-refracting ocean sound-velocity profile in the Arctic results in sound propagating to long ranges through repeated interactions at the rough underside of the ice, where it couples into several types of seismic waves producing complex particle motion. It is difficult to predict *a priori* the characteristics of seismo-acoustic waves in this environment, and, hence, the effectiveness of source-bearing estimation via particle-motion analysis must be studied by *in situ* field trials.

A rotational analysis to estimate source bearings using ice-mounted geophones was recently presented based on measuring ice seismic waves with particle motion oriented radially outward from the source.[1] For such waves, seismic recordings at two orthogonally mounted horizontal geophones can be combined geometrically to compute the wave power in horizontal look angles from 0° to 360°, with the angle of maximum power providing the optimal bearing estimate. The 180° ambiguity due to rotational symmetry is resolved by requiring out-going (prograde) particle motion in the vertical-radial plane. The analysis is enhanced by the application of polarization filters[1–3] to suppress seismic waves with transverse particle motion.

The rotational analysis in Ref. 1 was applied to data recorded for impulsive sources (imploding glass light bulbs[4]) at ranges of 200–1000 m and bearings of 0°–90°. The study site, located in the Lincoln Sea north of Ellesmere Island, Canada, was characterized by annual ice ~2 m thick, with several inclusions of multi-year ice blocks toward 90° bearing. The rotational analysis yielded bearing estimates with average errors of approximately 5°–10°.

Results from three new field trials are presented here. The first two consist of surveys of similar scale to that described above, and were carried out at sites characterized by uniformly smooth annual ice and by rough annual ice with a large pressure ridge separating sources from geophones. The third trial was carried out on thick multi-year ice and involved deploying SUS (signal, underwater sound) charge sources in the water column at ranges of 2–50 km. These new trials provide results for different ice types and, for one case much longer ranges than the original study.

II. FIELD TRIALS

Field trials were performed at three sites in the Lincoln Sea to investigate source-bearing estimation using ice-mounted geophones. In each case, a linear array of five geophones, spaced at 20-m intervals, was deployed on the ice surface, as shown in Fig. 1(a). The three sensors at the center of the array were tri-axial geophones, oriented as shown. The two outer sensors were vertical-component geophones. The geophones were positioned accurately using a laser surveying instrument and hand-deployed by removing the snow cover and freezing the sensor to the ice surface. In addition, a hydrophone was deployed through the ice to a depth of 20 m near the center of the array. The geophone and hydrophone signals were transmitted via over-ice cables to a

a)Electronic mail: sdosso@uvic.ca

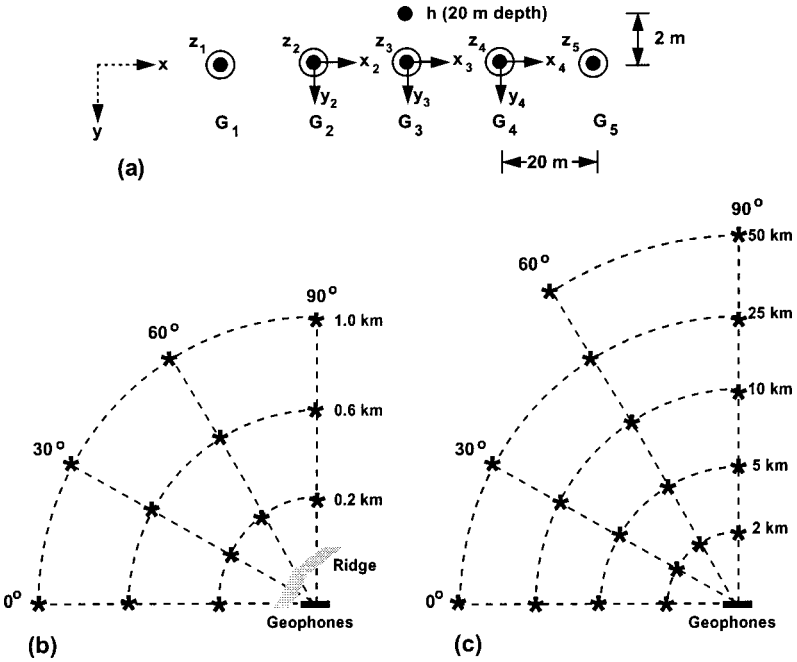

FIG. 1. Experiment geometry: (a) shows the sensor array with *G* indicating geophones (vertical and tri-axial) and *h* indicating the hydrophone; (b) shows light-bulb source locations for studies on annual ice (shaded region represents a pressure ridge present at the rough-ice site); and (c) shows the SUS-charge locations for the study on multi-year ice.

heated tent and recorded on a digital multichannel field seismograph at a sampling rate of 2000 Hz. However, since the instrument response of the geophones is unreliable for frequencies much greater than 200 Hz, all recordings considered here are low-pass filtered 0–200 Hz.

Two trial sites were located on annual ice, separated by approximately 3 km. The first site was characterized by smooth, flat ice, with a uniform thickness of 2 m. The water depth was 112 m at the geophone array, but decreased to only 18 m by a range of 1000-m endfire to the array. The second trial site was characterized by rough ice of variable thickness. At this site, the geophone array was located immediately adjacent to a pressure ridge that rose to a height ~2.5 m above the surrounding ice. Given a rule-of-thumb five-to-one ratio between ridge height and keel depth,[5] the ridge likely extended at least 10 m deeper than the surrounding ice. The water depth at the rough-ice site was approximately 160 m. At both annual-ice sites, impulsive sources were deployed at a depth of 50 m at ranges of 200, 600, and 1000 m along lines at 0°, 30°, 60°, and 90° bearing with respect to the array axis, as shown in Fig. 1(b). Note that at the rough-ice site the pressure ridge separated the geophones and sources. The sound sources at these sites consisted of imploding light bulbs.[1,4]

The third trial site was located on multi-year ice approximately 4.5 m thick. The sources consisted of 0.8-kg SUS charges which could be set for depths of either 18 or 180 m. Sources were deployed at nominal ranges of 2, 5, 10, and 25 km and bearings of 0°, 30°, 60°, and 90°. At these sites the water depth was less than 180 m, so the sources were deployed at 18-m depth. Additional source deployments were carried out at 50-km range and bearings of 60° and 90° where the water depth exceeded 180 m. At these sites sources were deployed at both 18- and 180-m depth. The source positions are shown in Fig. 1(c). Source deployments were carried via helicopter. For each source, the helicopter proceeded to a predetermined latitude and longitude, then searched the immediate vicinity for appropriate ice for landing and source deployment. The position of each source deployment was measured using GPS (global positioning system); from these positions accurate bearings for each source were calculated.

Several figures illustrating seismo-acoustic arrivals from light-bulb sources at ice-mounted geophones are given in Ref. 1. Figure 2 shows an example of the recordings at the multi-year ice site for a SUS-charge source at 0° bearing and 25-km range. Note that the transverse particle motion recorded at the *y*-component geophones is of comparable am-

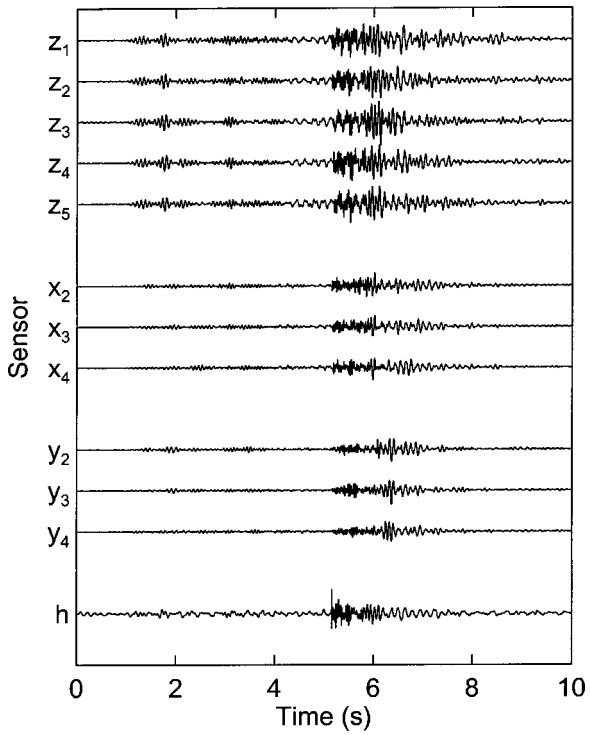

FIG. 2. Time series recorded at the multi-year ice test site for a SUS charge source at 0° bearing, 18-m depth, and 25-km range.

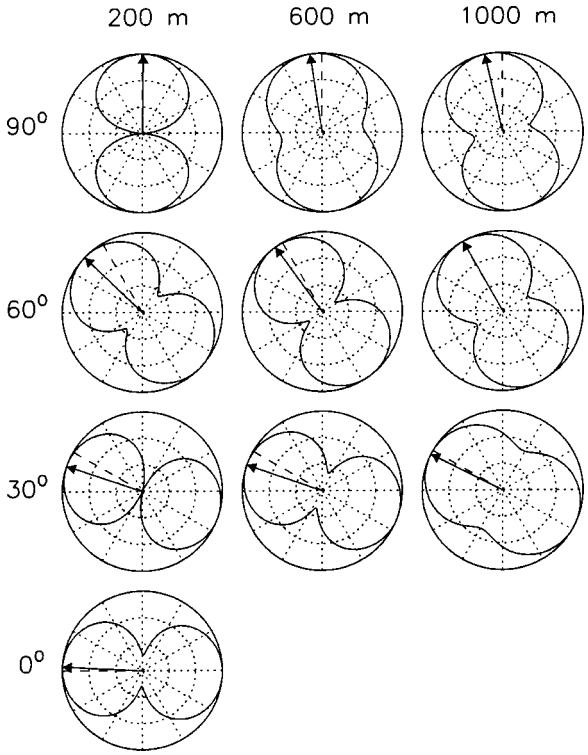

FIG. 3. Rotational power for light-bulb sources at the smooth-ice test site. Dotted circles indicate 5-dB increments; dashed lines indicate true source bearings, arrows indicate optimal bearing estimates. Shallow water at 0° bearing precluded 500- and 1000-m sources.

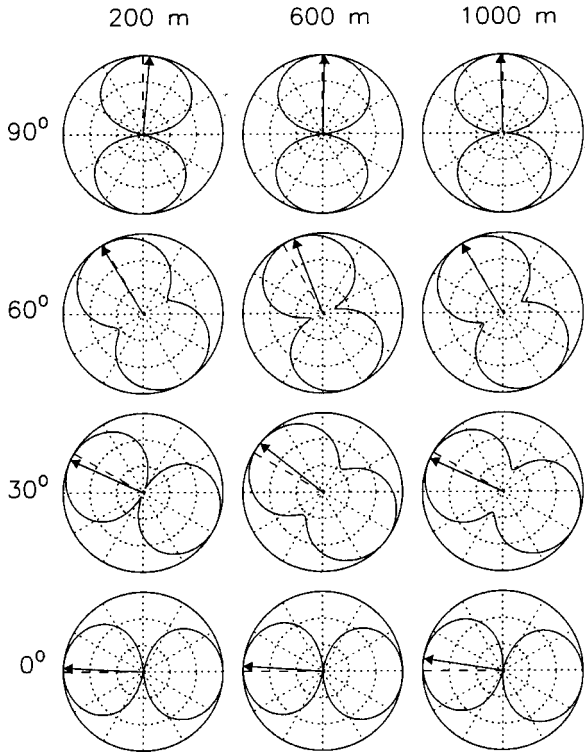

FIG. 4. Rotational power for light-bulb sources at the rough-ice test site.

plitude to the radial motion recorded at the *x*-component sensors, indicating strong coupling into S_H waves and/or scattering of P-S_V components.

III. RESULTS

Figure 3 shows examples of the rotational power[1] as a function of bearing angle for the smooth-ice trial site, with the optimal bearing estimates indicated by arrows. For brevity, the results shown are for the center geophone G_3 (Fig. 1); the results for geophones G_2 and G_4 are similar and are included in summarizing figures. Figure 3 shows that good estimates of the source bearing are obtained for all bearings and ranges. The maximum bearing error is approximately 16°, and most estimates are within 10° of the true bearing. The particle-motion power in the source direction is at least 7 dB greater than the power in the perpendicular direction (referred to as the discrimination level), and in several cases is $>$15 dB.

Figure 4 shows the bearing estimates for the rough-ice site, with good results obtained for all ranges and bearings. To compare the results for the two annual-ice sites, Fig. 5 shows the absolute value of the bearing errors for all geophones at both sites as a function of range and bearing. Overall, this figure shows that there does not appear to be a systematic difference between the results for the two sites. Considering all bearing estimates, the average error for the rough-ice site is slightly smaller than for the smooth-ice site ($5.2°\pm4°$ versus $7.2°\pm6°$), although the difference is not statistically significant. Hence, the variable ice and intervening pressure ridge at the rough-ice site does not appear to degrade the results. Figure 5(a) indicates that, with the exception of a few outliers, the errors do not vary substantially from bearing to bearing at either site, again suggesting that ice conditions between source and receiver is not a limiting factor. Finally, Fig. 5(b) shows that the bearing errors do not increase with range over 200–1000 m.

Figure 6 shows the bearing estimates at the multi-year ice site for SUS charge sources at 18-m depth and 2–25-km range (plots are corrected for small variations between actual and nominal source bearings). Consistently good bearing estimates are obtained, with a maximum error of 18°. Good bearing estimates were also obtained for sources at 50-km

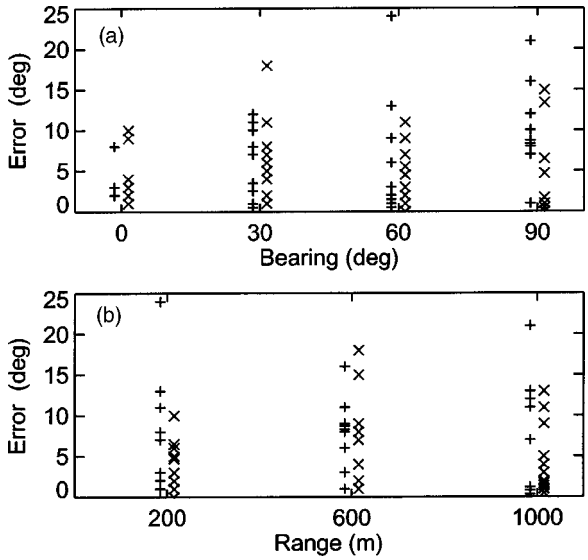

FIG. 5. Absolute errors in bearing estimates as a function of (a) bearing and (b) range for the smooth-ice and rough-ice test sites (+ and ×, respectively).

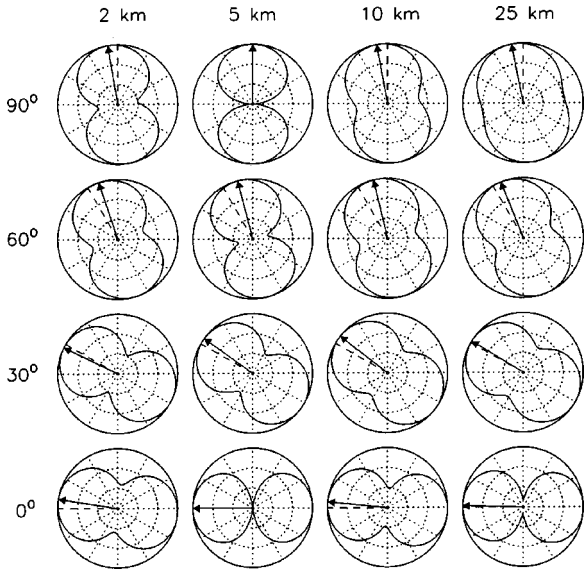

FIG. 6. Rotational power for SUS charge sources (18-m depth) at the multi-year ice test site.

range and depths of 18 and 180 m, as shown in Fig. 7 (bearings of 60° and 90°, see Fig. 1), with very similar results for the two source depths.

To compare all results, Fig. 8 shows the average bearing error and the average discrimination level as a function of range for light bulbs at ranges of 0.2–1 km on annual ice, and for SUS charges at ranges of 2–50 km on multi-year ice. The earlier results of trials on mixed annual ice reported in Ref. 1 are also included in these averages at ranges of 0.2–1 km. Figure 8 shows results obtained both with and without polarization filtering: It is clear that polarization filtering leads to substantial improvements in both bearing-estimation accuracy and discrimination level. Figure 8(a) shows that the accuracy of the source bearing estimates appear to be essentially independent of range from 0.2 to 1 km and from 2 to 50 km. The small increase in error (~3°) occurring between 1 and 2 km could be due to the different sources employed or the different ice types (the slight decrease in error with range from 2 to 50 km suggests it is not due to range). Figure 8(b) shows that the discrimination level generally decreases with range, with average values of 18 dB at 0.2-km range and 7 dB at 50-km range, and an abrupt decrease of 7 dB between 1- and 2-km range where source/ice types change.

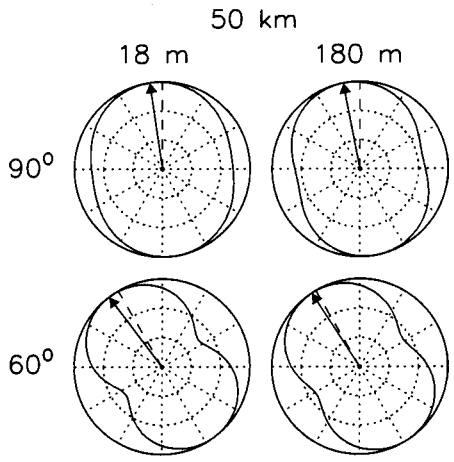

FIG. 7. Rotational power for SUS charge sources (18- and 180-m depth) at the multi-year ice test site.

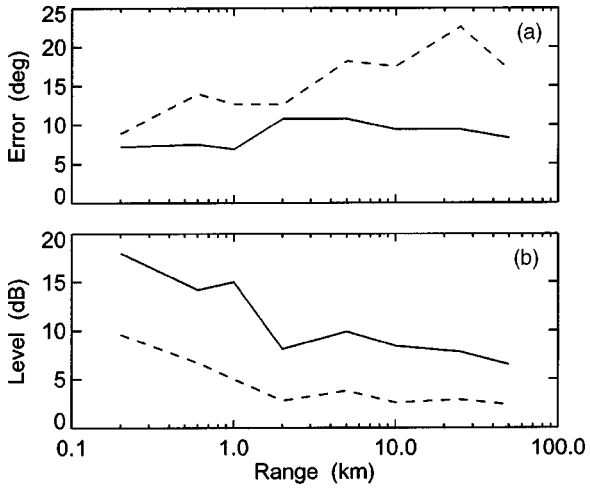

FIG. 8. Summary of results for all studies: (a) shows the average absolute error in the bearing estimate; (b) shows the average discrimination level. Solid lines indicate results obtained using seismic polarization filtering, dashed lines indicate results obtained without polarization filtering.

IV. CONCLUSIONS

The results of the Arctic field trials indicate consistently good ability to estimate source bearings for all ranges, ice types, sources types, and source depths considered. No significant differences in the bearing estimates were observed between the smooth and rough annual ice sites, despite the presence of a large pressure ridge running between sources and geophones at the rough-ice site. This is likely because the most important arrivals are due to water-borne acoustic waves incident on the ice below the geophone, and not due to seismic plate waves propagating along the ice.[1] Apparent biases (i.e., consistent errors) appear to occur for specific deployments and could be caused by ice conditions local to the geophones. Bearing errors increased slightly going from light-bulb sources and annual ice to SUS charges and multi-year ice, but otherwise appeared to be largely independent of range out to 50 km. The 180° bearing ambiguity was correctly resolved in all cases.

ACKNOWLEDGMENTS

We thank Ron Verrall, Richard Van Der Pryt, and Jim Perkins for their expertise in carrying out the field trials reported here.

[1] S. E. Dosso, G. J. Heard, and M. Vinnins, "Source bearing estimation in the Arctic using ice-mounted geophones," J. Acoust. Soc. Am. **112**, 2721–2734 (2002).
[2] J. E. White, "Motion product seismograms," Geophysics **29**, 288–298 (1964).
[3] Y. V. Dudko and H. Schmidt, "Near-field polarization processing of ice fracturing events," J. Acoust. Soc. Am. **102**, 3193 (1997).
[4] G. J. Heard, M. McDonald, N. R. Chapman, and L. Jaschke, "Underwater light bulb implosions: A useful acoustic source," in *Proc. Oceans97* (1997), Vol. 2, pp. 755–762.
[5] T. C. Yang and G. R. Giellis, "Experimental characterization of elastic waves in a floating ice sheet," J. Acoust. Soc. Am. **96**, 2993–3009 (1994).

Note on informational masking (L)

Nathaniel I. Durlach,[a] Christine R. Mason, Gerald Kidd, Jr., Tanya L. Arbogast, H. Steven Colburn, and Barbara G. Shinn-Cunningham
Hearing Research Center, Boston University, Boston, Massachusetts 02215

(Received 9 August 2002; revised 5 February 2003; accepted 24 February 2003)

Informational masking (IM) has a long history and is currently receiving considerable attention. Nevertheless, there is no clear and generally accepted picture of how IM should be defined, and once defined, explained. In this letter, consideration is given to the problems of defining IM and specifying research that is needed to better understand and model IM. © *2003 Acoustical Society of America.* [DOI: 10.1121/1.1570435]

PACS numbers: 43.66.Ba, 43.66.Dc, 43.66.Lj [MRL]

I. INTRODUCTION

This letter is intended to stimulate and broaden discussions about informational masking (e.g., Watson, 1987; Leek *et al.*, 1991; Neff *et al.*, 1993; Neff, 1995; Neff and Dethlefs, 1995; Oh and Lutfi, 1998, 2000; Lutfi *et al.*, 2003; Kidd *et al.*, 1998, 2002; Wright and Saberi, 1999; Richards *et al.*, 2002; Brungart *et al.*, 2001; Freyman *et al.*, 2001; Arbogast *et al.*, 2002). Although this term has been used in many ways, it is common to equate informational masking (IM) with nonenergetic masking, where energetic masking (EM) is defined as masking that results from competition between target and masker at the periphery of the auditory system, i.e., overlapping excitation patterns in the cochlea or auditory nerve (AN). Thus, EM is often equated with peripheral and IM with central masking. Also, because a primary function of peripheral processing is frequency analysis, most research in this area has focused on the frequency dimension. In a related definitional thread, IM has sometimes been defined as the elevation in threshold caused by stimulus uncertainty. Independent of the precise definition, and despite the association of IM with central attentional factors, IM is clearly distinguishable from general inattention to the overall experimental task (e.g., by differences in stimulus-response correlations).

Within the domain of nonenergetic masking, this note is confined to the detection of tonal targets in the presence of simultaneous multitone maskers. Nevertheless, it is hoped that it will prove useful when considering sequential masking, discrimination and recognition performance, or situations involving speech stimuli. [Some results of pioneering research on the effects of uncertainty that focuses on sequential masking for nonspeech stimuli are summarized in Watson (1987) and Espinoza-Varas and Watson (1989).]

IM is well illustrated by the case in which the target is a fixed-frequency tone and the masker is a ten-tone complex with the component frequencies selected randomly on each presentation, subject to the constraint that they all lie outside a protected region around the target tone (to minimize EM). In such a case, and for many listeners, the target threshold can exceed the average threshold obtained with the fixed exemplars of the random masker, or with a Gaussian noise masker having the same power, by as much as 40 dB. Apparently, under such conditions, these ''holistic'' listeners are severely distracted by the masker and find it difficult to perform well even though there is little masker energy in the frequency region of the target. Furthermore, the performance of these listeners cannot be easily improved by instructions, target cueing, or modest practice (Neff *et al.*, 1993). In contrast, the performance of these listeners can be greatly improved by altering the stimuli so that target-masker similarity is decreased, thereby reducing the tendency to confuse or group the target and masker (e.g., Kidd *et al.*, 1994; Neff, 1995; Oh and Lutfi, 2000; Durlach *et al.*, 2003). Also of importance, at the other end of the continuum, there exist ''analytic'' listeners who are highly resistant to spectral uncertainty (e.g., Neff and Dethlefs, 1995).

II. DEFINITIONAL ISSUES

Many factors drive the need for improved definitions, including (a) the lack of clarity in the notion of ''overlap'' or ''competition'' among peripheral channels; (b) the possibility of elevated masked thresholds being caused by uncertainty in dimensions other than frequency and/or by conditions other than stimulus uncertainty; and (c) the relativistic aspects of the distinction between peripheral and central (the meaning depending on one's physiological vintage point).

To help address such issues, for any location L in the ascending auditory pathway, we define PM(L)=peripheral masking at L=masked threshold for the ideal detector operating on the input at L; and CM(L)=central masking at L=masked threshold of human observer minus the quantity PM(L). In general, determination of PM(L) and CM(L) for a given experimental condition requires (a) constructing a statistical model of neural activity at L for that condition; (b) computing the performance of the ideal detector operating on this model activity, and (c) comparing the performance obtained with this ideal detector to that of human listeners under the same condition. EM(L) can then be identified with PM(L) and IM(L) can be regarded as a component of CM(L) that includes uncertainty effects.

Note that the word ''masking'' is used here to refer to a variety of different processes associated with threshold elevation [an issue discussed by Tanner (1958)]. Note also that the distinction between PM(L) and CM(L) is consistent with the approach introduced by Siebert and Colburn (e.g., Siebert, 1968; Colburn, 1973) for the special case L=auditory nerve (AN). For a variety of tasks, they determined how

[a]Electronic mail: durlach@mit.edu

 0001-4966/2003/113(6)/2984/4/$19.00

much information was lost in the transformation from acoustical stimulus to AN firing patterns and how much in the transformation from these firing patterns to the human psychophysical responses. With this approach, ''energetic masking'' (at L) is identical to ''peripheral masking'' (at L) and the notion of ''overlapping excitation patterns'' (at L) is replaced by the characterization ''masking that cannot be overcome even by the ideal detector'' (at L). Note finally that the extent to which CM(L)=IM(L) is left open.

Although this definitional structure is responsive to the problems cited above, it is not problem-free. For example, it does not specify which central limitations that lead to threshold elevation should be included under CM (an issue related to Tanner's problem). More relevant to our current concerns, it fails to specify which components of CM should be included in IM. In particular, should the effects of similarity as well as of uncertainty be included? In addition, the definitions are difficult to apply (even though they are in principle operational definitions). Application not only requires considering physiological as well as psychophysical data, but it becomes increasingly difficult as one proceeds up the auditory system because of increased system complexity. Furthermore, as evident even in the simple standard definition of masking (elevation in threshold due to the presence of the masker), there is considerable operational imprecision. For example, how much and what kinds of training should precede the threshold measurements? This issue becomes particularly crucial in the area of interest because of possible differential learning effects associated with PM and CM. Despite such problems, it is hoped that the above thoughts can prove useful in organizing various masking phenomena. In the remainder of this note, unless explicitly stated otherwise, it is assumed that L=AN.

III. NEEDED RESEARCH

A. Uncertainty and similarity

Two main factors controlling the magnitude of nonenergetic masking (i.e., CM) that have been considered (apart from listener identity) are stimulus uncertainty and target-masker similarity. However, further research is required to develop an adequate understanding of how these factors generate masking and how they interact.

Strictly speaking, stimulus uncertainty is neither necessary nor sufficient to produce nonenergetic masking. On the other hand, if the randomization occurs over a range that is small compared to the listener's resolution, the randomization will not elevate the listener's threshold. On the other hand, if a sequence of stimuli is sufficiently complex and rapidly varying to appear random to the listener even though it is technically deterministic, then the listener's threshold can be greatly elevated. Clearly, as far as uncertainty is concerned, what matters is the deviation between what the listener hears on a given trial and what the listener expects to hear on that trial. Further evidence that stimulus uncertainty does not necessarily produce large amounts of masking is evident in the results (a) for ''analytic'' listeners who are resistant to the effects of uncertainty (Neff and Dethlefs, 1995; Oxenham *et al.*, 2003) and (b) from experiments in which the effects of uncertainty are reduced by decreasing target-masker similarity (Kidd *et al.*, 1994; Neff, 1995; Oh and Lutfi, 2000; Durlach *et al.*, 2003). Additional indications that nonenergetic masking can occur without uncertainty are available in data on cross-frequency effects in binaural hearing (Bernstein and Trahiotis, 1993; Culling *et al.*, 2003). Illustrative data on the effects of different types or degrees of uncertainty can be found in Watson *et al.* (1976) and Lutfi (1992).

In the same vein, although target-masker similarity is an important factor in causing nonenergetic masking, there are unresolved problems here, too. One such problem resides in the notion that it is the target-masker similarity itself that counts. Because the task in these detection experiments is not to discriminate between the masker M and the target T but rather between M and M+T, what is really important here is not the similarity between M and T but between M and M+T. Although these two similarity factors are related, they are not interchangeable; there are many situations in which the addition of T to M leads to a change in the sound of the overall stimulus that is not well described by the notion that one ''hears out'' T. A second such problem concerns how best to quantify the similarity factor. Although the similarity–dissimilarity dimension is closely related to the grouping–segregating distinction considered in auditory scene analysis (Bregman, 1990), it is not obvious how best to quantify similarity.

Finally, once the definitions of uncertainty and similarity factors are clarified, there will still be the need to determine how best to combine them in an overall model of nonenergetic masking.

B. Nonfrequency domains, sites central to the auditory nerve

Consistent with the above definitions, it is appropriate to consider not only the case in which the peripheral channels are the frequency channels at the level of the AN, but also cases in which the location L of interest is higher up in the system and the relevant ''peripheral channels'' concern domains other than frequency. For example, it might be enlightening to consider the case in which the frequency domain is replaced by the spatial domain and to explore the extent to which masked thresholds are elevated when uncertainty is introduced into the spatial characteristics of the stimulus rather than the frequency characteristics. A possible experiment in this area would determine the increase in the masked threshold of a target noise source located at a fixed azimuth θ_T caused by randomizing the azimuth θ_M of an independent masking noise, where the random draw of θ_M is constrained by a protected angular region about θ_T to minimize the spatial-domain EM that would occur when target and masker overlap in some relatively peripheral azimuthal channel. Although some results suggest that uncertainty has only small effects in the spatial domain (Bernstein and Trahiotis, 1997), further research is needed to adequately explore this area. Obviously, one could consider similar experiments in other domains as well (e.g., amplitude modulation). In order to truly understand nonenergetic masking, it is important to determine the extent to which the various phenomena observed in the frequency domain occur in other domains. [For rel-

evant results of this type in sequential masking, see Watson and Kelly (1981)]. In the same spirit, it would be useful to compare results obtained in audition to those in vision (e.g., Turvey, 1973; Nakayama and Joseph, 1998; Cusack and Carlyon, 2000).

C. Psychometric functions, receiver operating characteristics, sequential effects

Most data on nonenergetic masking consists of thresholds measured using adaptive procedures. Relatively few data are available on psychometric functions, receiver operating characteristics (ROCs), or trial-to-trial sequential effects. Furthermore, initial examination of these elements (either by means of probe experiments or crude intuitive modeling) suggests that these elements may differ substantially in the different types of masking considered. For example, preliminary data from our lab (see also Wright and Saberi, 1999) indicate that psychometric functions from experiments like that outlined at the beginning of this note show important differences (in slope as well as lateral position) for the following three cases: (a) tests with a randomized masker, (b) tests with fixed exemplars of a randomized masker, and (c) tests with a randomized masker in which the results are sorted after the test to construct a psychometric function for each exemplar. It is expected that equally important differences will appear with ROCs and sequential effects. The results of such studies can provide important constraints on theoretical models of masking.

D. Individual differences

In the domain of nonenergetic masking studied to date (the frequency domain), intersubject differences are enormous. Whereas some listeners have their thresholds elevated by as much as 40 dB when masker uncertainty is introduced into a situation where target-masker similarity is high, other listeners appear insensitive to such uncertainty. Among the questions that arise here are (a) What are the sources of these intersubject differences? (b) How constant are they across conditions and domains? and (c) To what extent can they be reduced by training?

In the attempt to understand individual differences (e.g., Lutfi *et al.*, 2003), more data are needed in which the same subjects are tested in a wide variety of conditions concerned with the frequency domain as well as with other domains. In most previous studies, the subjects have varied between experiments. Also, in addition to continuing the search for new ways to characterize performance differences among subjects, more attention should be given to comparing methods already developed (involving critical bands, attentional bands, weighting constants, efficiency factors, etc.).

One special thrust to pursue concerns the Listener-Max-vs Listener-Min distinction (Durlach *et al.*, 2002; de Cheveigne and McAdams, 1995): Whereas Max is envisioned as an archetypal analytic listener who attempts to maximize the T/M ratio by maximizing T, Min is envisioned as an archetypal holistic listener who attempts to maximize the T/M ratio by minimizing M. In the frequency domain, Max constructs an acceptance filter focused on T without regard for M, whereas Min constructs a multiple notch-rejection filter matched to M without regard for T. In the spatial domain, Max points an acoustical searchlight at T, whereas Min points a set of nulls at the locations of the masker components. An interesting prediction that arises in connection with this distinction is the reversal in who does best when uncertainty shifts from M to T: when M is uncertain, Max should be best; when T is uncertain, Min should do best. Although previous data indicate that uncertainty in T is less disruptive than in M, no data are available to test this subject-reversal prediction. Research is also needed to explore the extent to which nonadditivity of masking (even when uncertainty is minimized) can be explained by special costs associated with the need for Min to create simultaneous multiple nulls.

A second thrust concerns the idea that, despite the focus on central processing in discussions of uncertainty effects, the observed intersubject differences may result from differences in peripheral processing (Carney, 2002; Lauter, 2002). For example, consider a random masker and suppose that two listeners, L1 and L2, have identical central processors but different peripheral representations of the ensemble of maskers. L1 and L2 might then reveal differences in susceptibility to uncertainty because (a) the same central processing is used to combat the uncertainty evident in two different peripheral representations of the masker ensemble or (b) two different central processing schemes are used, each of which is selected by the same central processor to optimize performance with the given peripheral representation. In either event, differences in peripheral processing would play a major role in causing the observed differences in susceptibility to uncertainty. Note also that, abstractly, the question of how susceptibility differs for L1 and L2 is essentially the same as the question of how susceptibility changes for either L1 or L2 when the ensemble of masking stimuli is changed. Note further that in order to pursue these issues, it would be useful not only to conduct relevant theoretical analyses (e.g., on the effects of different types of peripheral nonlinearities), but also to expand previous studies of the effects of sensorineural impairments (Doherty and Lutfi, 1999; Micheyl *et al.*, 2000; Kidd *et al.*, 2001). Of particular interest would be a comparison of monaural uncertainty effects between the two ears of subjects with unilateral impairments [similar to the work on grouping by Rose and Moore (1997)].

Finally, it is essential that further research be conducted on how much the very strong effects of uncertainty (or target-masker similarity) observed for some listeners can be reduced by training (and the extent to which generalization to other nonenergetic masking tasks occurs). Although such improvement in performance would appear less likely if the cause of the poor performance is peripheral rather than central, peripheral limitations would not be ruled out by such a finding. In any case, previous results on the difficulty of improving performance by target cueing, coaching, and limited training (e.g., Neff *et al.*, 1993) indicate that the training challenge is substantial.

In general, the fact that when target-masker similarity is high the effects of uncertainty are monstrous for some subjects and negligible for others implies that an understanding of individual differences in the effects of uncertainty, both pre- and posttraining, is essentially equivalent to understand-

ing the effects themselves. Without such understanding, creating an insightful theory of informational masking will not be possible.

In conclusion, it should be noted that a comprehensive theory of informational masking will need to address not only simultaneous masking (the focus of this letter), but also sequential masking. [Extensive research in this area that includes consideration of individual differences and training has been performed by Watson and colleagues (e.g., Watson *et al.*, 1976; Leek and Watson, 1984; Espinoza-Varas and Watson, 1986; Leek *et al.*, 1991; Surprenant and Watson, 2001; Watson and Kidd, 2002).]

ACKNOWLEDGMENTS

We are indebted to Dr. L. Bernstein, Dr. L. Carney, Dr. J. Culling, Dr. J. Lauter, Dr. M. Leek, Dr. R. Lutfi, Dr. V. Richards, and Dr. C. Watson for useful communications about the material in this note. Our work was supported by Grant Nos. DC00100 and DC04545 from NIH/NIDCD and F49620-01-1-0005 from AFOSR.

Arbogast, T. L., Mason, C. R., and Kidd, Jr., G. (**2002**). ''The effect of spatial separation on informational and energetic masking of speech,'' J. Acoust. Soc. Am. **112**, 2086–2098.

Bernstein, L. R., and Trahiotis, C. (**1993**). ''Spectral interference in a binaural detection task: effects of masker bandwidth and temporal fringe,'' J. Acoust. Soc. Am. **94**, 735–747.

Bernstein, L. R., and Trahiotis, C. (**1997**). ''The effects of randomizing values of interaural disparities on binaural detection and discrimination of interaural correlation,'' J. Acoust. Soc. Am. **102**, 1113–1120.

Bregman, A. S. (**1990**). *Auditory Scene Analysis: The Perceptual Organization of Sound* (MIT, Cambridge, MA).

Brungart, D. S., Simpson, B. D., Ericson, M. A., and Scott, K. R. (**2001**). ''Informational and energetic masking effects in the perception of multiple simultaneous talkers,'' J. Acoust. Soc. Am. **110**, 2527–2538.

Carney, L. H. (**2002**). Personal communication.

Colburn, H. S. (**1973**). ''Theory of binaural interaction based on auditory-nerve data. I. General strategy and preliminary results on interaural discrimination,'' J. Acoust. Soc. Am. **54**, 1458–1470.

Culling, J. F., Hodder, K. I., and Colburn, H. S. (**2003**). ''Interaural correlation discrimination with spectrally remote flanking noise: constraints for models of binaural interaction,'' J. Acoust. Soc. Am. (in review).

Cusack, R., and Carlyon, R. P. (**2000**). ''Auditory pop-out: Perceptual asymmetries in sequences of sounds,'' Br. J. Audiol. **34**, 112.

de Cheveigne, A., and McAdams, S. (**1995**). ''Identification of concurrent harmonic and inharmonic vowels: A test of the theory of harmonic cancellation and enhancement,'' J. Acoust. Soc. Am. **97**, 3736–3748.

Doherty, K. A., and Lutfi, R. A. (**1999**). ''Level discrimination of single tones in a multitone complex by normal-hearing and hearing-impaired listeners,'' J. Acoust. Soc. Am. **105**, 1831–1840.

Durlach, N. I., Kidd, Jr., G., Mason, C. R., Arbogast, T. L., Colburn, H. S., and Shinn-Cunningham, B. (**2002**). ''Informational masking: Toward improved understanding,'' J. Acoust. Soc. Am. **111**, 2337.

Durlach, N. I., Mason, C. R., Shinn-Cunningham, B. G., Arbogast, T. L., Colburn, H. S., and Kidd, Jr., G. (**2003**). ''Informational masking: Counteracting the effects of stimulus uncertainty by decreasing target-masker similarity'' (in press).

Espinoza-Varas, B., and Watson, C. S. (**1986**). ''Temporal discrimination for single components of nonspeech auditory patterns,'' J. Acoust. Soc. Am. **80**, 1685–1694.

Espinoza-Varas, B., and Watson, C. S. (**1989**). ''Perception of complex auditory patterns by humans,'' *The Comparative Psychology of Audition: Perceiving Complex Sounds*, edited by R. J. Dooling and S. H. Hulse (Erlbaum Associates, Hillsdale, NJ).

Freyman, R. L., Balakrishnan, U., and Helfer, K. S. (**2001**). ''Spatial release from informational masking in speech recognition,'' J. Acoust. Soc. Am. **109**, 2112–2122.

Kidd, Jr., G., Mason, C. R., and Arbogast, T. L. (**2002**). ''Similarity, uncertainty and masking in the identification of nonspeech auditory patterns,'' J. Acoust. Soc. Am. **111**, 1367–1376.

Kidd, Jr., G., Arbogast, T. L., Mason, C. R., and Walsh, M. (**2001**). ''Informational masking in listeners with sensorineural hearing loss,'' J. Assoc. Res. Oto. **3**, 107–119.

Kidd, Jr., G., Mason, C. R., Rohtla, T. L., and Deliwala, P. S. (**1998**). ''Release from masking due to spatial separation of sources in the identification of nonspeech auditory patterns,'' J. Acoust. Soc. Am. **104**, 422–431.

Kidd, Jr., G., Mason, C. R., Deliwala, P. S., Woods, W. S., and Colburn, H. S. (**1994**). ''Reducing informational masking by sound segregation,'' J. Acoust. Soc. Am. **95**, 3475–3480.

Lauter, J. (**2002**). Personal communication.

Leek, M., Brown, M. E., and Dorman, M. F. (**1991**). ''Informational masking and auditory attention,'' Percept. Psychophys. **50**, 205–214.

Leek, M., and Watson, C. S. (**1984**). ''Learning to detect auditory pattern components,'' J. Acoust. Soc. Am. **76**, 1037–1044.

Lutfi, R. A. (**1992**). ''Informational processing of complex sounds. III. Interference,'' J. Acoust. Soc. Am. **91**, 3391–3400.

Lutfi, R. A., Kistler, D. J., Oh, E. L., Wightman, F. L., and Callahan, M. R. (**2003**). ''One factor underlies individual differences in auditory informational masking within and across age groups,'' Percept. Psychophys. **65**, 396-406.

Micheyl, C., Arthaud, P., Reinhart, C., and Collet, L. (**2000**). ''Informational masking in normal-hearing and hearing-impaired listeners,'' Acta Otol. **120**, 242–246.

Nakayama, K., and Joseph, J. S. (**1998**). ''Attention, pattern recognition, and pop-out in visual search,'' in *The Attentive Brain*, edited by R. Parasuraman (MIT, Cambridge, MA).

Neff, D. L. (**1995**). ''Signal properties that reduce masking by simultaneous, random-frequency maskers,'' J. Acoust. Soc. Am. **98**, 1909–1920.

Neff, D. L., and Dethlefs, T. M. (**1995**). ''Individual differences in simultaneous masking with random-frequency, multicomponent maskers,'' J. Acoust. Soc. Am. **98**, 125–134.

Neff, D. L., Dethlefs, T. M., and Jesteadt, W. (**1993**). ''Informational masking for multicomponent maskers with spectral gaps,'' J. Acoust. Soc. Am. **94**, 3112–3126.

Oh, E. L., and Lutfi, R. A. (**1998**). ''Nonmonotonicity of informational masking,'' J. Acoust. Soc. Am. **104**, 3489–3499.

Oh, E. L., and Lutfi, R. A. (**2000**). ''Effect of masker harmonicity on informational masking,'' J. Acoust. Soc. Am. **108**, 706–709.

Oxenham, A. J., Fligor, B., Mason, C. R., and Kidd, Jr., G. (**2003**). ''Informational masking and musical ability'' (in review).

Richards, V. M., Tang, Z., and Kidd, Jr., G. (**2002**). ''Informational masking with small set sizes,'' J. Acoust. Soc. Am. **111**, 1359–1366.

Rose, M. M., and Moore, B. C. J. (**1997**). ''Perceptual grouping of tone sequences by normally hearing and hearing-impaired listeners,'' J. Acoust. Soc. Am. **102**, 1768–1778.

Siebert, W. M. (**1968**). ''Stimulus transformations in the peripheral auditory system,'' in *Recognizing Patterns*, edited by P. Kolers and M. Eden (MIT, Cambridge, MA).

Surprenant, A. M., and Watson, C. W. (**2001**). ''Individual differences in the processing of speech and nonspeech sounds in normal-hearing listeners,'' J. Acoust. Soc. Am. **110**, 2085–2095.

Tanner, W. P. (**1958**). ''What is masking?'' J. Acoust. Soc. Am. **30**, 919–921.

Turvey, M. T. (**1973**). ''On peripheral and central processes in vision: inferences from an information-processing analysis of masking with patterned stimuli,'' Psychol. Rev. **80**, 1–52.

Watson, C. S. (**1987**). ''Uncertainty, informational masking and the capacity of immediate auditory memory,'' in *Auditory Processing of Complex Sounds*, edited by W. A. Yost and C. S. Watson (Erlbaum, Hillsdale, NJ), pp. 267–277.

Watson, C. S., and Kelly, W. J. (**1981**). ''The role of stimulus uncertainty in the discriminability of auditory patterns,'' in *Auditory and Visual Pattern Recognition*, edited by D. J. Getty and J. H. Howard, Jr. (Erlbaum, Hillsdale, NJ), pp. 37–59.

Watson, C. S., and Kidd, G. (**2002**). ''On the lack of association between basic auditory abilities, speech processing, and other cognitive skills,'' Semin. Hear. **23**, 83–93.

Watson, C. S., Kelly, W. J., and Wroton, H. W. (**1976**). ''Factors in the discrimination of tonal patterns. II. Selective attention and learning under various levels of stimulus uncertainty,'' J. Acoust. Soc. Am. **60**, 1176–1186.

Wright, B. A., and Saberi, K. (**1999**). ''Strategies used to detect auditory signals in small sets of random maskers,'' J. Acoust. Soc. Am. **105**, 1765–1775.

Sound production in neonate sperm whales (L)

P. T. Madsen[a)]
The Whale Conservation Institute, Lincoln, Massachusetts and Department of Zoophysiology, University of Aarhus, 8000 Aarhus C, Denmark

D. A. Carder
Navy Marine Mammal Program, SSC SD, San Diego, California

W. W. L. Au and P. E. Nachtigall
Marine Mammal Research Program, Hawaii Institute of Marine Biology, Hawaii

B. Møhl
Deptartment of Zoophysiology, University of Aarhus, 8000 Aarhus C, Denmark

S. H. Ridgway
Navy Marine Mammal Program, SSC SD, San Diego, California

(Received 30 August 2002; revised 21 January 2003; accepted 14 March 2003)

Acoustic data from two sperm whale neonates (*Physeter macrocephalus*) in rehabilitation are presented and implications for sound production and function are discussed. The clicks of neonate sperm whale are very different from usual clicks of adult specimens in that neonate clicks are of low directionality [SL anomaly (0°–90°) <8 dB], long duration (2–12 ms), and low frequency (centroid frequency between 300 and 1700 Hz) with estimated SLs between 140 and 162 dB//1 μPa (rms). Such neonate clicks are unsuited for biosonar, but can potentially convey homing information between calves and submerged conspecifics in open ocean waters at ranges of some 2 km. Moreover, it is demonstrated that sperm whale clicks are produced at the anterior placed monkey lips, thereby substantiating a key point in the modified Norris and Harvey theory and supporting the unifying theory of sound production in odontocetes. © *2003 Acoustical Society of America.*
[DOI: 10.1121/1.1572137]

PACS numbers: 43.80.Ka, 43.80.Gx [FD]

I. INTRODUCTION

Norris and Harvey (1972) proposed that the sperm whale nasal complex, homologous with the sound producing nasal complex of smaller odontocetes (Cranford *et al.*, 1996), is a giant generator of clicks to be used for echolocation and communication. Array recordings have shown that sperm whales produce usual clicks with the highest source levels ever recorded in the animal kingdom (Møhl *et al.*, 2000, 2003) and show properties of high directionality (Møhl *et al.*, 2000, 2003; Thode *et al.*, 2002). Ridgway and Carder (2001) found that clicks are produced at the foremost part of the nasal complex, and deployment of sound recording tags has demonstrated that sperm whales produce at least two click types, usual clicks suited for biosonar, and coda clicks more suited for communication (Madsen *et al.*, 2002b). The latter study also revealed that sperm whales can maintain and regulate the acoustic output down to at least 700 m of depth, and that the clicks show properties similar to clicks from smaller odontocetes (Madsen *et al.*, 2002b). Acoustic experiments on recently expired sperm whales have shown that the spermaceti compartments of the nasal complex can transmit sound (Møhl, 2001), and that the spermaceti organ and the junk form an acoustic continuum (Møhl *et al.*, 2002).

Here we present acoustic data opportunistically collected from two neonate sperm whales in rehabilitation and discuss implications for sound production and function.

II. MATERIALS AND METHODS

A. Galveston calf

A neonate (umbilicus not healed), male sperm whale with a body length of 341 cm and a body weight of 546 kg was found stranded at Sabine Pass, Texas in September 1989 and moved to Sea-Arama Marine World for rehabilitation. Seven recording sessions were carried out in a 1-m deep, 3 $\times 10\ m^2$ concrete pool with a Racal Store7 instrumentation recorder with Ampex 797 tapes operated at varying tape speeds (17/8–60 ips). Two calibrated B&K 8103 hydrophones were connected to two B&K 2635 charge amplifiers, relaying the signals to the instrumentation recorder. Clicks were digitized with a PC-sound card (flat frequency response between 0.01 and 17 kHz) and analyzed with Cool Edit 2000 (*Syntrillium*), and custom designed routines in Matlab (*Mathworks 6.0*).

The rms sound pressures were obtained by integrating the square of the pressure over the interval between the −3-dB end points of the envelope of the signal and comparing it with calibration signals, recorded on the tapes. Source levels were estimated by back calculating (spherical spreading) from received sound pressure levels and from the distance between the whale and the hydrophones (noted on the tapes and documented by photographs). Durations of the clicks were defined as the time between the −10-dB points of the envelope of the signal.

[a)]Electronic mail: peter.teglberg@biology.au.dk

 0001-4966/2003/113(6)/2988/4/$19.00

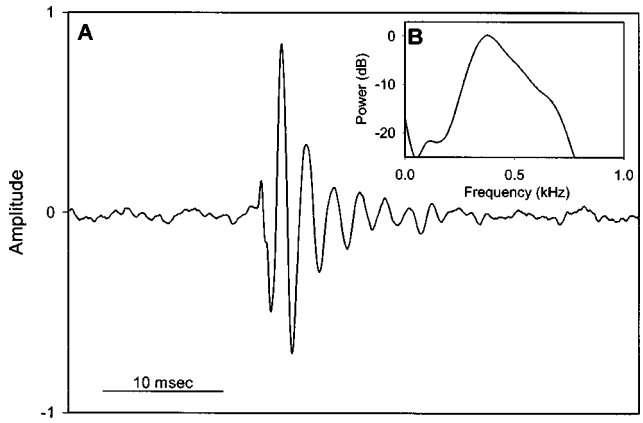

FIG. 1. (a) Waveform of a representative click from the Galveston neonate. SL of 160 dB//1 μPa rms. (b) Power spectrum of the click depicted in (a). Sample rate 48 kHz. FFT size 1024.

B. Kona calf

A neonate (umbilicus not healed), female sperm whale with a body length of 312 cm and an estimated weight of 400 kg was found stranded on the beach of Kona, Big Island, Hawaii on 14 August 2001. For rehabilitation, the animal was taken to a 1.2-m-deep, temporary pool (diameter of 6 m) at the Natural Energy Laboratory, Kona, Hawaii. The recording setup consisted of two calibrated B&K 8103 hydrophones connected to a custom built amplifier and a Sony TCD-D3 DAT recorder sampling at 48 kHz. During each recording session, the hydrophone placement was documented with a digital camera (courtesy of C. R. Kastak) and noted on the tapes. Time of arrival differences (TOADs) at the two hydrophones of the same click were determined by using cross-correlation routines written in Matlab (courtesy of M. Wahlberg). Post mortem, a dissection was conducted on the nasal complex, yielding data on the morphometrics of the structures involved in sound production and relative placement of the hydrophones.

III. RESULTS

A. Galveston calf

Preliminary results of acoustic recordings from this calf were presented in Ridgway and Carder (2001). Here a more detailed account is provided. A total of 253 clicks and 47 grunts were analyzed from seven recording sessions. The waveforms of the clicks have no apparent multipulse structure [Fig. 1(a)] and centroid frequencies between 300 and 1000 Hz [Fig. 1(b)] with −10 dB BW of 200–400 Hz (Table I). Duration of the clicks varied between 5 and 12 ms and may include some distortions due to the small tank size. Estimated click SLs (referred to 1 m from the anterior termination of the spermaceti organ) range from 150 to 162 dB//1 μPa rms. During one of the recording sessions, a hydrophone was suspended at one measured meter ahead of the animal and another hydrophone 1 m from the side of the animal, perpendicular to the eye as the calf was held in the water. Derived SLs were 4–8 dB higher when recorded with the hydrophone 1 m in front of the animal than when recorded lateral to the eye, thereby indicating a low, but present, directionality. Frequency content and duration of clicks recorded from these two aspects were alike. Grunts have messy waveforms with likely some distortions from pool walls and surface with durations of 50–150 ms and frequency emphasis around 500 Hz. Derived grunt SLs varied between 140 and 152 dB//1 μPa rms [also see grunt spectrograms published by Ridgway and Carder (2001)]. No consistent directionality effects pertaining to SL, frequency or duration were observed in the grunts.

B. Kona calf

A total of 58 clicks were recorded from this individual. Estimated SLs ranged from 150–161 dB//μPa rms. Estimated SLs from the two employed hydrophones differed by less than 6 dB, indicating a low directionality of the clicks. Frequency content and duration of the clicks were generally comparable to those of the Galveston calf (Table I). However, two clicks had a significantly different frequency content with peak frequencies around 8 kHz, but still no apparent multipulse structure. Four clicks contained two high frequency pulses (around 8 kHz), spaced 0.7 msec. No grunts were recorded from this individual.

34 of the 58 clicks were recorded from hydrophones, spaced 13 cm apart, held at the distal sac (hydrophone 1) and at the anterior part of the junk (hydrophone 2) (Fig. 2). A consistent TOAD was observed between the two hydrophones. The clicks recorded by the hydrophone placed at the anterior part of the junk were received with a delay of some 50 μs relative to the hydrophone placed at the distal sac. Based on this TOAD and knowledge of the speed of sound in the tissues, the sound source location can be restricted to a hyperboloid surface in the nasal complex (*ad modum* Diercks *et al.*, 1971). However, it may be too simplistic to assume a fixed sound speed in the various tissue types of the head for which reason two hyperboloid surfaces were generated, one for a sound speed of 1300 m/s and one for 1500 m/s to cover the relevant range of sound speeds in biological tissues. The hyperbolar interceptions between these hyperboloid surfaces and the sagital plane of the nasal complex are depicted in Fig. 2. It is seen that the hyperbolas are passing the location of the monkey lips. For further details on the morphology of this calf, see Møhl *et al.* (2002)

TABLE I. Characteristics of sound types from neonate sperm whales.

Sound type	SL (rms) (dB//1 μPa)	SL (pp) (dB//1 μPa)	Duration (ms)	Centroid frequency (Hz)	−10 dB BW (Hz)
Galveston Click	154–162	162–175	5–12	300–1000	200–350
Galveston Grunt	140–155	150–165	50–150	200–700	200–700
Kona Click	150–161	161–174	2–15	500–1700	200–450

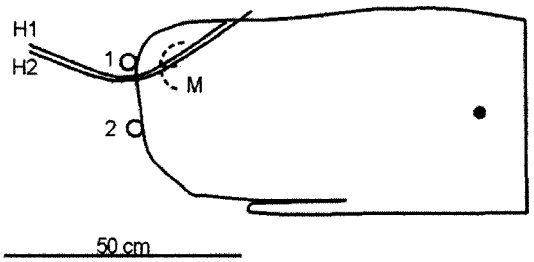

FIG. 2. Hydrophone placement (1,2) on the head of the Kona calf. H: Hyperbolas (1: sound speed of 1500 m/s, 2: sound speed of 1300 m/s) given by the interception between the sagital plane of the neonate head and the hyperboloid surfaces derived from the consistent TOAD between hydrophone 1 and 2. M: Monkey lips. Location of the monkey lips is based on a photo-documented dissection of the animal.

IV. DISCUSSION

The present data should be evaluated in the light of the opportunistic nature of recordings in temporary holding tanks not suited for acoustic investigations, and considering that the rehabilitating neonates most likely were not in good health. Despite this situation, the difference in recording gear and the different reverberation patterns in two different pool types, the recorded clicks from the two neonates are generally alike in having −10-dB bandwidths of 200 to 450 Hz, centroid frequencies around 500 Hz, SLs up to 162 dB//1 μPa rms, and durations of 2–15 ms (Table I). These source characteristics match the click properties of young sperm whale calves, reported by Watkins *et al.* (1988), and thus seem to be representative of the click repertoire of sperm whale neonates.

A few unusual higher frequency clicks from both calves, having pulses with frequency emphases at 8–16 kHz, did not fit the general picture. It is possible that these unusual higher frequency clicks are a beginning in the ontogeny of echolocation click that may be employed by the adult sperm whale (Møhl *et al.*, 2002). In the Kona calf, four clicks contained two such pulses with an interpulse interval (IPI) of 0.7 ms. It can be conjectured that the first pulse may represent the initial sound production event and the second pulse had traversed the spermaceti organ and junk of the nasal complex before entering the water. However, the lack of additional trailing pulses makes such a notion speculative. An IPI of 0.7 msec is intriguing, as it is comparable to an IPI of 0.8 ms found by projecting artificial pings into the nasal complex of the same, expired animal (Møhl *et al.*, 2002). In addition, an IPI of 0.7 ms is consistent with the two-way-travel time between the distal and the frontal air sac of the Kona neonate and the speed of sound in spermaceti oil (Møhl *et al.*, 2002). This finding is supportive of the view that the IPI of sperm whale usual clicks and coda clicks is given by the two-way-travel time of the spermaceti compartments (Norris and Harvey, 1972; Gordon, 1991), and that the spermaceti compartments are involved in sperm whale sound production. Due to the low-frequency nature and long duration of all other clicks produced, it is not possible to discuss the potential involvement of the spermaceti compartments in the production of these clicks.

Although the neonate clicks were generated in short trains, they do not show the repetitive, stereotyped click patterns found in codas produced by juvenile and adult sperm whales for communicative purposes (Watkins and Schevill, 1977; Weilgart and Whitehead, 1993). Older calves produce repetitive trains of two to five clicks that may be viewed as coda-precursors (Watkins *et al.*, 1988), but the random number of clicks and irregular click rate of these phonating neonates rather indicate that the number of clicks is likely not yet fully controlled. Watkins *et al.* (1988) argue that the long duration and low-frequency emphasis of most calf clicks make them unsuited for echolocation, and that they consistently resemble the properties of clicks from adult sperm whales. We do not share the latter view as adult sperm whale usual clicks have a multipulse structure totally dominated by a single p1 pulse of short duration with very high SL (Møhl *et al.*, 2000, 2003), high directionality (Møhl *et al.*, 2000, 2003; Thode *et al.*, 2002), and a frequency emphasis between 5 and 32 kHz (Watkins, 1980; Madsen *et al.*, 2002a), and are therefore not comparable to calf clicks (Table I).

The properties of the calf clicks are, as noted by Watkins *et al.* (1988) and in contrast to usual adult clicks, indeed not favorable for echolocation. Biosonar-signals should be of a shorter duration, higher frequency and more directional to allow for adequate temporal and spatial resolution in a noisy and cluttered environment (Au, 1993). While the apparent need for biosonar signals is very small in calves that are entirely nourished from suckling the first year of their lives (Rice, 1989), the need for communicative signals to maintain contact with babysitting adults seems more likely. Sperm whale calves remain at the surface while their mothers undertake feeding dives apparently too deep and too long for the calves to follow. This has led to development of asynchronous dive behavior and allomaternal care in the form of babysitting where calves at the surface are accompanied and often suckled by a number of different females (Gordon, 1987; Whitehead, 1996). Thus, sperm whale calves are unaccompanied at the surface for up to 31% of the time, and female sperm whales take turns in babysitting between feeding dives (Whitehead, 1996).

Considering the reduced mobility of neonate calves compared to their babysitters, it would seem advantageous if the calves produced homing signals to facilitate maternal localization. A maximized communicative space is achieved by using long duration, omni-directional signals of low frequency. Sperm whale calf clicks have such properties and we propose that these rudimentary clicks may play a communicative role in the allomaternal behavior of asynchronous dives and babysitting in sperm whales. The passive sonar equation can be used to assess the possible detection range of calf clicks by adult, babysitting whales. Assuming that a sperm whale neonate calf can be modeled as an omnidirectional source with a SL of 160 dB//1 μPa rms, and using a spectral noise density of 60 dB//1 μPa^2/Hz at 500 Hz (Urick, 1983), an auditory filter bandwidth corresponding to the centralized RMS-BW (Au, 1993) of a representative calf click (250 Hz) and a S/N of 10 dB for detection, it can be estimated that sperm whale calf clicks can be detected by conspecifics at a range of some 2 km [transmission loss$=$160 dB//1 μPa rms$-$(10 dB$+$60 dB// μPa^2/Hz$+$10 log(250 Hz))$=$66 dB, which corresponds to 2

km, assuming spherical spreading]. Such a range estimate may only be valid if the receiving whale is submerged in deep water away from the acoustic shadow zone.

The Galveston calf produced a large number of grunts, which are very different from clicks. This difference may relate to the structures involved in sound production as grunts appear to be produced near the frontal sac at the base of the skull [see Figs. 2–4 in Ridgway and Carder (2001)] and thus not at the monkey lips as is the case for clicks (see below). We have no clues as to the functional significance of grunts, but, considering that they generally have SLs some 10–15 dB lower than clicks, suggests that the potential communicative range would be reduced by a factor of 3–5.

Norris and Harvey (1972) surmised that the monkey lips, homologous with the phonic lips in delphinoids (Cranford *et al.*, 1996), are the sound source in sperm whales. That observation has gained support from palpative studies (Ellis, 1981) and palpative/stethoscope investigations (Ridgway and Carder, 2001), concluding that the sound source is located at the foremost part of the nasal complex of sperm whales, beneath the blowhole. From the consistent TOADs between the two hydrophones held at the anterior part of the nasal complex of the Kona calf, the location of the sound source could be restricted to a hyperboloid surface. When relating the hydrophone placement and the derived hyperboloid surfaces with the morphometrics of this calf (Fig. 2), it becomes evident that both hyperboloid surfaces are passing the location of the monkey lips. This finding is not only excluding a laryngeal sound source, but also demonstrating that the sound source for click generation in sperm whales is indeed the monkey lips. This demonstration substantiates a key point in the modified Norris and Harvey theory (Møhl, 2001), where the initial sound pulse of multipulsed usual clicks is to be generated at the monkey lips, before transmission through the acoustic continuum formed by the spermaceti organ and the junk.

With the vital sound source placed at the foremost part of the nasal complex, it would indeed be surprising if the primary use of the nasal complex of sperm whales is a ramming device in male-male interactions, as recently suggested by Carrier *et al.* (2002). Moreover, in their unifying theory of odontocete sound production, Cranford *et al.* (1996) proposed that clicks are produced in the same biomechanical way by homologous structures across the entire odontocete suborder. The present demonstration of sound production in the monkey lips is consistent with that notion.

ACKNOWLEDGMENTS

We thank a number of people for assistance during investigations and for valuable comments on the manuscript. Experiments were carried out under the authority of a permit afforded to S. H. Ridgway and all investigations were conducted in accordance with the conditions of that permit. The work on the Galveston calf was funded by ONR grants, issued to S. H. Ridgway and D. A. Carder by Dr. R. Gisiner. The Kona calf study was supported by the Edwin M. Pauley Foundation Summer Program of the Hawaii Institute of Marine Biology via a grant issued to P. E. Nachtigall. Additional support for equipment was available from ONR Grant No. N00014-98-1-0687 to P. E. Nachtigall and W. W. L. Au administered by Dr. R. Gisiner. Analysis was funded by the Danish National Research Foundation through Center for Sound Communication, USD.

Au, W. W. L. (**1993**). *The Sonar of Dolphins* (Springer Verlag, New York).
Carrier, D. R., Deban, S. M., and Otterstrom, J. (**2002**). ''The face that sank the *Essex*: potential function of the spermaceti organ in aggression,'' J. Exp. Biol. **205**, 1755–1763.
Cranford, T. W., Amundin, M., and Norris, K. S. (**1996**). ''Functional Morphology and Homology in the Odontocete Nasal Complex: Implications for Sound Generation,'' J. Morphol. **228**, 223–285.
Diercks, K. T., Trochta, R. T., Greenlaw, C. F., and Evans, W. E. (**1971**). ''Recording and analysis of dolphin echolocation signals,'' J. Acoust. Soc. Am. **49**, 1729–1732.
Ellis, R. (**1981**). ''The whale that visited New York,'' Bull. Am. Littoral. Soc. **13**, 5–12.
Gordon, J. C. (**1987**). ''The Behaviour and Ecology of Sperm Whales off Sri Lanka,'' Ph.D. thesis, Darwin College, Cambridge, UK.
Gordon, J. C. (**1991**). ''Evaluation of a method for determining the length of sperm whales (*Physeter catodon*) from their vocalizations,'' J. Zool. Lond. **224**, 301–314.
Madsen, P. T., Wahlberg, M., and Møhl, B. (**2002a**). ''Male sperm whale (*Physeter macrocephalus*) acoustics in a high latitude habitat: implications for echolocation and communication,'' Behav. Ecol. Sociobiol. **53**, 31–41.
Madsen, P. T., Payne, R., Kristiansen, N. U., Wahlberg, M., Kerr, I., and Møhl, B. (**2002b**). ''Sperm whale sound production studied with ultrasound-time-depth-recording tags,'' J. Exp. Biol. **205**(13), 1899–1906.
Møhl, B. (**2001**). ''Sound transmission in the nose of the sperm whale *Physeter catodon*. A post mortem study,'' J. Comp. Physiol. [A] **187**, 335–340.
Møhl, B., Wahlberg, M., Madsen, P. T., Heerford, A., and Lund, A. (**2003**). ''The monopulsed nature of sperm whale sonar clicks,'' J. Acoust. Soc. Am. (in press).
Møhl, B., Wahlberg, M., Madsen, P. T., Miller, L. A., and Surlykke, A. (**2000**). ''Sperm whale clicks: Directionality and source level revisited,'' J. Acoust. Soc. Am. **107**, 638–648.
Møhl, B., Madsen, P. T., Wahlberg, M., Au, W. W. L., Nachtigall, P., and Ridgway, S. (**2002**). ''Sound transmission in the spermaceti complex of a recently expired sperm whale calf,'' Acoust. Res. Lett. Online **4**(1), 19–24.
Norris, K. S., and Harvey, G. W. (**1972**). ''A Theory for the Function of the Spermaceti Organ of the Sperm Whale,'' NASA **SP-262**, 397–417.
Rice, D. W. (**1989**). ''Sperm Whale (*Physeter macrocephalus Linnaeus*, 1758),'' in *Handbook of Marine Mammals*, edited by S. H. Ridgway and R. Harrison (Academic, New York), Vol. 4.
Ridgway, S. H., and Carder, D. (**2001**). ''Assessing hearing and sound production in cetacean species not available for behavioral audiograms: experience with *Physeter, Kogia*, and *Eschrichtius*,'' Aquat. Mammals **27**, 267–276.
Thode, A., Mellinger, D. K., Stienessen, S., Martinez, A., and Mullin, K. (**2002**). ''Depth-dependent acoustic features of diving sperm whales (*Physeter macropcephalus*) in the Gulf of Mexico,'' J. Acoust. Soc. Am. **112**, 308–321.
Urick, R. J. (**1983**). *Principles of Underwater Sound*, 3rd ed. (McGraw–Hill, New York).
Watkins, W. A. (**1980**). ''Acoustics and the behavior of sperm whales,'' in *Animal Sonar Systems*, edited by R. Busnel and F. Fish (Plenum, New York), pp. 283–289.
Watkins, W. A., and Schevill, W. E. (**1977**). ''Sperm whale codas,'' J. Acoust. Soc. Am. **62**, 1485–1490.
Watkins, W. A., Moore, K. E., Clark, C. W., and Dahlheim, M. E. (**1988**). ''The sounds of sperm whale calves,'' in *Animal Sonar, Processes and Performance*, edited by P. E. Nachtigall and P. W. B. Moore (Plenum, New York), pp. 99–107.
Weilgart, L., and Whitehead, H. (**1993**). ''Coda communication by sperm whales (*Physeter macrocephalus*) off the Galápagos Islands,'' Can. J. Zool. **71**, 744–752.
Whitehead, H. (**1996**). ''Babysitting, dive synchrony, and indications of alloparental care in sperm whales,'' Behav. Ecol. Sociobiol. **38**, 237–244.

Scattering of elastic waves in damaged media

Liyong Yang and Joseph A. Turner[a)]
Department of Engineering Mechanics, W317.4 Nebraska Hall, University of Nebraska-Lincoln, Lincoln, Nebraska 68588-0526

(Received 31 May 2002; revised 17 February 2003; accepted 26 February 2003)

The scattering of elastic waves in a medium with damage from microcracking is discussed. The influence of damage from penny-shaped microcracks within a homogeneous medium is considered. The microcracks are assumed to be randomly oriented and uniformly distributed. Explicit expressions are derived for the attenuation of longitudinal and shear elastic waves in terms of the damage parameter and the effective elastic moduli of the medium. A generalized tensor-based approach is used such that the results are coordinate free. The derivation is based upon diagrammatic methods. The problem is formulated in terms of the Dyson equation, which is solved for the mean field response within the limits of the first-order smoothing approximation. The longitudinal and shear attenuations are discussed in terms of their frequency dependence and damage dependence. In particular, the attenuations are shown to scale linearly with the damage parameter. © *2003 Acoustical Society of America.* [DOI: 10.1121/1.1570444]

PACS numbers: 43.20.Bi, 43.20.Gp, 43.35.Cg [DEC]

I. INTRODUCTION

The scattering of elastic waves in complex media, particularly at ultrasonic frequencies, is of importance to nondestructive testing, materials characterization and other research areas. Information about the decay in the coherent field due to scattering attenuation may often be used to infer information about the microstructure of the material.[1] The incoherent field also contains microstructural information. Quantitative comparisons with experimental results require a well-developed model of the effects of the microstructure on the wave behavior. If the microstructure is modified, such as through the development of microcracks within the medium, this change in microstructure would manifest itself in the scattered wave fields as well. In the case of structural materials such as concrete, polycrystalline metals and most composites, these microcracks are typically induced by materials processing, manufacturing, aging and other in-service conditions. Changes in material response due to microcracking are typically inferred ultrasonically by the decrease in wave velocity or the increase in ultrasonic attenuation, both of which indicate a stiffness degradation or loss of strength of the material.[2] The limits of detecting these changes in wave behavior depend on the amount of increased scattering due to the system of microcracks. Studies of elastic wave attenuation in cracked materials are found in articles by Mal,[3,4] Piau,[5] Chatterjee *et al.*,[6] Zhang and Achenbach,[2] Zhang and Gross,[7] and Smyshlyaev and Willis,[8] for example. This previous research has primarily been focused on specific wave/crack interactions, rather than a more general description. More general, tensor-based, studies of elastic wave attenuation are mostly limited to polycrystalline media.[9–13]

In the present article, a generalized tensor-based approach is used to examine the attenuation of elastic waves in an isotropic, homogeneous medium with embedded microcracks. Here, the microcracks are assumed to be noninteracting, penny-shaped cracks that are randomly oriented. However, the coordinate-free approach allows for nonrandom ensembles of microcracks to be studied with relative ease. This topic is the subject of ongoing research by the authors. It is assumed that the constitutive behavior of the stiffness matrix or compliance matrix in the pristine state is sufficiently characterized at the local level by a linear elastic relation between the average stresses and average strains of the traditional form. In standard damage mechanics theory,[14,15] the continuum model is described by a macroscopic damage parameter attributed to the microcracks.

The effective elastic moduli of the medium that contains many penny-shaped cracks is first presented using techniques discussed by Nemat-Nasser and Hori[16] and Kachanov *et al.*[17] These techniques have been used to estimate the upper and lower bounds of the material properties with distributed damage. The general inequality was presented by Hashin and Shtrikman[18] using a variational approach. Similar ideas have been used to estimate the effective conductivity of such media.[19] The effective Lamé constants derived here are in agreement with previous analyses. Next, expressions for the moduli fluctuations are derived in terms of the single crack compliance. The fluctuations and corresponding covariance of the moduli are necessary for the attenuation derivation. This derivation is based upon the diagrammatic approach[12,20] in which the mean response is governed by the Dyson equation. The Dyson equation is then solved for the longitudinal and transverse attenuations within the limits of the first-order smoothing approximation (FOSA)[20] or Keller[21] approximation. The attenuations are shown to scale linearly with the damage parameter at low values. Finally, example numerical results are presented and discussed.

II. EFFECTIVE ELASTIC PROPERTIES OF A DAMAGED ELASTIC SOLID

Methods which make use of estimating the effective elastic properties of the statistically homogeneous elastic solids which contain a large number of microcracks are inves-

a)Author to whom correspondence should be addressed. Electronic mail: jaturner@unl.edu

 0001-4966/2003/113(6)/2992/9/$19.00

tigated by Nemat-Nasser and Hori,[16] Kachanov *et al.*,[17] and others. The first step in determining the effective properties of the damaged elastic solid involves consideration of a single penny-shaped crack, which is located within an infinite, homogeneous, isotropic and elastic continuum. In accordance with linear elastic fracture mechanics, the total, local and average stress $\overline{\boldsymbol{\sigma}}$ and strain $\overline{\boldsymbol{\gamma}}$ fields hold for superposition.[22] The average stress and strain are related by

$$\overline{\boldsymbol{\gamma}}=\overline{\mathbf{S}}\overline{\boldsymbol{\sigma}}, \quad \text{or} \quad \overline{\boldsymbol{\sigma}}=\overline{\mathbf{C}}\overline{\boldsymbol{\gamma}}, \tag{1}$$

where

$$\overline{\mathbf{S}}=\mathbf{S}+\mathbf{S}^*, \quad \overline{\mathbf{C}}=\mathbf{C}-\mathbf{C}^*. \tag{2}$$

In Eqs. (1) and (2), $\overline{\boldsymbol{\gamma}}=\langle\gamma(x)\rangle$ and $\overline{\boldsymbol{\sigma}}=\langle\sigma(x)\rangle$ are the ensemble average strain and average stress, respectively. Here $\overline{\mathbf{S}}$ and $\overline{\mathbf{C}}$ are the effective compliance and effective stiffness, respectively, of the elastic solid which contains the presence of the cracks. Here, $\mathbf{S}^*$ is defined as the effective compliance contributed by all cracks within the elastic solid and $\mathbf{C}^*$ is defined as the effective stiffness contributed by all cracks within the elastic solid. It should be noted that $(\mathbf{C}^*)^{-1} \neq \mathbf{S}^*$. The tensors $\mathbf{S}$ and $\mathbf{C}$ are the compliance and stiffness, respectively, of the pristine material.

The components of the effective compliance tensor $\mathbf{S}^*$ can be estimated from the contribution by the microcracks. The contributions are calculated by the complementary strain energy in terms of the path independent integral of fracture mechanics. The strain energy is expressed as

$$\psi^*=\int_0^a \frac{Q}{a}da, \tag{3}$$

where ψ^* is the Gibbs' energy and a is the crack radius. The factor Q in the integrand is written as the line integral of the J integral (energy release rate) along the crack perimeter L,

$$Q=\oint_L aJdL. \tag{4}$$

The energy release rate J is expressed in terms of the stress intensity factors K_m $(m=\mathrm{I,II,III})$ corresponding to the three fundamental crack modes as

$$J=\frac{1-\nu}{2\mu}(K_\mathrm{I}^2+K_\mathrm{II}^2)+\frac{1}{2\mu}K_\mathrm{III}^2, \tag{5}$$

where ν and μ are the Poisson's ratio and shear modulus, respectively, of the surrounding material. Thus, the final Gibbs' energy is derived in compact form as

$$\psi^*=\int_0^a\left[\oint \overline{M}_{mn}K_mK_ndL\right]da. \tag{6}$$

The tensor $\overline{\mathbf{M}}$ is given by

$$\overline{M}_{mn}=\frac{1}{2\mu}[(1-\nu)\delta_{mn}+\nu\delta_{m\mathrm{III}}\delta_{n\mathrm{III}}], \tag{7}$$

where δ_{mn} is the Kronecker delta, and the subscript n also represents the three fundamental cracks modes I, II, or III.

The components of the compliance tensor are related to the Gibbs' energy through $\tilde{S}^{(s)}_{ijkl}=\partial^2\psi^*/\partial\tilde{\sigma}_{ij}\partial\tilde{\sigma}_{kl}$ (in the local coordinate system, the notation $\sim$ is used). Thus, the compliance attributed to the presence of a single penny-shaped active crack in a representative volume V is then

$$\tilde{S}^{(s)}_{ijkl}=\frac{2}{V}\int_0^a\left[\oint \overline{M}_{mn}\frac{\partial K_m}{\partial\tilde{\sigma}_{ij}}\frac{\partial K_n}{\partial\tilde{\sigma}_{kl}}dL\right]da. \tag{8}$$

Substituting K_m into Eq. (8) and integrating gives the compact form[15]

$$\tilde{S}^{(s)}_{ijkl}=\frac{16}{3V}\frac{1-\tilde{\nu}}{2-\tilde{\nu}}\frac{1}{2\tilde{\mu}}a^3\{2\tilde{I}^{\,5}_{ijkl}-\tilde{\nu}\tilde{I}^{\,6}_{ijkl}\}. \tag{9}$$

In the global coordinate system, using a coordinate transformation and assuming the normal stress at the crack surface is tensile, the effective compliance attributable to a single, planar, penny-shaped crack of radius a is written in the simple form

$$S^{(s)}_{ijkl}=\frac{16}{3V}\frac{1-\nu}{2-\nu}\frac{1}{2\mu}a^3\{2I^5_{ijkl}-\nu I^6_{ijkl}\}. \tag{10}$$

The compliance of a single crack is dependent on the unit normal $\mathbf{n}$, which defines the crack orientation. This orientation is implicit in the tensors $\mathbf{I}^5,\mathbf{I}^6$. These tensors and other necessary basis tensors are given in terms of the unit normal vector $\mathbf{n}$ and Kronecker delta (δ) as[23]

$$\begin{aligned}
&I^1_{ijkl}=\tfrac{1}{2}(\delta_{ik}\delta_{jl}+\delta_{il}\delta_{jk}), \quad I^2_{ijkl}=\delta_{ij}\delta_{kl},\\
&I^3_{ijkl}=\delta_{ij}n_kn_l, \quad I^4_{ijkl}=n_in_j\delta_{kl}, \quad I^6_{ijkl}=n_in_jn_kn_l,\\
&I^5_{ijkl}=\tfrac{1}{4}(n_in_k\delta_{jl}+n_in_l\delta_{jk}+n_jn_k\delta_{il}+n_jn_l\delta_{ik}).
\end{aligned} \tag{11}$$

If it is assumed that the damaged medium is statistically homogeneous and statistically isotropic, the effective compliance attributable to a single crack is approximately the inverse of the effective stiffness. It is convenient to derive the attenuation in terms of the effective stiffness attributable to a penny-shaped crack. The compliance tensor of the pristine, undamaged elastic matrix is

$$S^0_{ijkl}=\frac{1}{2\mu}\left(I^1_{ijkl}-\frac{\nu}{1+\nu}I^2_{ijkl}\right). \tag{12}$$

Then the effective compliance expression for a simple crack in a matrix can be written

$$\hat{\mathbf{S}}=\mathbf{S}^{(s)}+\mathbf{S}^0=\frac{1}{2\mu}\sum_{i=1}^{6}e_i\mathbf{I}^i, \tag{13}$$

in which

$$\begin{aligned}
&e_1=1, \quad e_2=-\frac{\nu}{1-\nu}, \quad e_3=e_4=0,\\
&e_5=\frac{32}{3}\frac{1-\nu}{2-\nu}a^3, \quad e_6=-\frac{16}{3}\frac{\nu(1-\nu)}{2-\nu}a^3.
\end{aligned} \tag{14}$$

To calculate the stiffness tensor, the other irreducible tensor basis $\mathbf{J}$ $(J^i, i=1,2,\ldots 5,6)$ is used.[23] These basis tensors may be formed from the tensors $\mathbf{I}$ using a linear transformation. The effective compliance tensor expressed in terms of the $\mathbf{J}$ basis tensors is given by

$$\hat{\mathbf{S}}=\frac{1}{2\mu}\sum_{i=1}^{6} f_i\mathbf{J}^i, \tag{15}$$

where

$$\begin{aligned} f_1&=\frac{2-\nu}{2(1+\nu)}+\frac{8}{3}(1-\nu)a^3,\\ f_2&=\frac{\nu}{2(1+\nu)}+\frac{8}{3}(1-\nu)a^3,\\ f_3&=-\frac{3\nu}{2(1+\nu)},\quad f_4=-\frac{\nu}{2(1+\nu)},\\ f_5&=1+\frac{16}{3}\frac{1-\nu}{2-\nu}a^3,\quad f_6=1. \end{aligned} \tag{16}$$

The effective stiffness tensor may also be expanded in a similar way as

$$\hat{\mathbf{C}}=\hat{\mathbf{S}}^{-1}=2\mu\sum_{i=1}^{6} b_i\mathbf{J}^i, \tag{17}$$

where the scalar coefficients b_i are related to the scalar coefficients f_i,

$$\{b_1,b_2,b_3,b_4,b_5,b_6\}=\Delta\left\{f_1,-f_2,-f_3,-f_4,\frac{1}{f_5\Delta},\frac{1}{f_6\Delta}\right\}, \tag{18}$$

with

$$\Delta^{-1}=f_1^2-f_2^2-f_3^2+f_4^2. \tag{19}$$

If the penny-shaped crack volume is much smaller than the representative volume, the higher order terms in the coefficients may be neglected. This truncation is used to simplify the form of the derivation that follows and places some limits on the resulting attenuations. In this case, the corresponding coefficients are

$$\begin{aligned} b_1&=\frac{2-\nu}{2(1-2\nu)}+\frac{8}{3}\frac{(1-\nu)(-3\nu^2+2\nu-1)}{(1-2\nu)^2}a^3,\\ b_2&=-\frac{\nu}{2(1-2\nu)}-\frac{8}{3}\frac{(1-\nu)(-\nu^2-2\nu+1)}{(1-2\nu)^2}a^3,\\ b_3&=\frac{3\nu}{2(1-2\nu)}-\frac{8}{3}\frac{3\nu(1-\nu)^2}{(1-2\nu)^2}a^3,\\ b_4&=\frac{\nu}{2(1-2\nu)}-\frac{8}{3}\frac{\nu(1-\nu)^2}{(1-2\nu)^2}a^3,\\ b_5&=1-\frac{16}{3}\frac{1-\nu}{2-\nu}a^3,\quad b_6=1. \end{aligned} \tag{20}$$

Again the effective stiffness is represented in terms of the six fourth order tensors $\mathbf{I}$,

$$\hat{\mathbf{C}}=2\mu\sum_{i=1}^{6} c_i\mathbf{I}^i, \tag{21}$$

where the coefficients c_i are

$$\begin{aligned} c_1&=1,\quad c_2=\frac{\nu}{1-\nu}-\frac{16}{3}\frac{\nu^2(1-\nu)}{(1-2\nu)^2}a^3,\\ c_3&=c_4=-\frac{16}{3}\frac{\nu(1-\nu)}{1-2\nu}a^3, \end{aligned} \tag{22}$$

$$c_5=-\frac{32}{3}\frac{1-\nu}{2-\nu}a^3,\quad c_6=\frac{16}{3}\frac{\nu(1-\nu)}{2-\nu}a^3.$$

The single crack stiffness reduces the stiffness of the pristine, undamaged elastic matrix with stiffness $\mathbf{C}^0=2\mu(\mathbf{I}^1+[\nu/(1-\nu)]\mathbf{I}^2)$. Thus, the effective stiffness of the crack in a unit volume and matrix is

$$\mathbf{C}^{(s)}=\mathbf{C}^0-\hat{\mathbf{C}}=2\mu\sum_{i=1}^{6} d_i\mathbf{I}^i, \tag{23}$$

where the coefficients d_i are

$$\begin{aligned} d_1&=0,\quad d_2=\frac{16}{3}\frac{\nu^2(1-\nu)}{(1-2\nu)^2}a^3,\\ d_3&=d_4=\frac{16}{3}\frac{\nu(1-\nu)}{1-2\nu}a^3, \end{aligned} \tag{24}$$

$$d_5=\frac{32}{3}\frac{1-\nu}{2-\nu}a^3,\quad d_6=-\frac{16}{3}\frac{\nu(1-\nu)}{2-\nu}a^3.$$

To estimate the ensemble average properties, an infinitely extended, homogeneous, isotropic and elastic three-dimensional continuum is considered. The medium is assumed to contain a large number of microcracks which do not interact with each other. The effective compliance or stiffness may be determined by the superposition of the contributions of individual microcracks. In the case of a large number of microcracks, the summation can be replaced by an integration over a continuous distribution of crack sizes and orientations. The penny-shaped crack is characterized by its radius a and two Euler angles θ and φ that define the orientation of the unit normal $\mathbf{n}$. The specific distribution of the crack radii and orientations is expressed by the probability density function $W(a,\theta,\varphi)$. In some situations, the microcrack radii and orientations may be correlated. The density function is then replaced by the probability density function $P(a,\theta,\varphi)=P^{\theta\varphi}(\theta,\varphi)P^a(a|\theta,\varphi)$. Here, however, it is assumed that the microcrack radii and orientations are not correlated. In this case, the density function is expressed as

$$W(a,\theta,\varphi)=A(a)\zeta(\theta,\varphi). \tag{25}$$

The effective continuum properties per unit volume are expressed in terms of an ensemble average utilizing the density function in Eqs. (25) and (23) such that

$$C^*_{ijkl}=\frac{\varepsilon}{4\pi}\int_0^{2\pi}\int_{-\pi/2}^{\pi/2} C^{(s)}_{ijkl}\zeta(\theta,\varphi)d\theta\cos\varphi d\varphi. \tag{26}$$

In Eq. (26), the nondimensional microcrack density per unit volume is defined by

$$\varepsilon=N\langle a^3\rangle=\int_{a^-}^{a^+}A(a)a^3da, \tag{27}$$

where N is number of cracks per unit volume and the angular brackets represent the ensemble average. This damage factor was introduced by Walsh[24] for the case of an isotropic distribution of the penny-shaped microcracks. A more general

form of the damage factor in terms of elliptical microcracks is given by Budiansky and O'Connell,[25]

$$\varepsilon = \frac{2N}{\pi}\left\langle \frac{\Gamma^2}{P}\right\rangle, \tag{28}$$

where Γ and P are the crack surface area and the perimeter length, respectively.

The simplest model of the microcrack distribution is assumed when their orientations are random. In this case, the normal to the microcrack plane takes every direction with equal probability, such that the effective compliance or stiffness tensor attributable to the presence of microcracks is isotropic. In this case, the density function in Eq. (25) is given by

$$\zeta(\theta,\varphi)=1. \tag{29}$$

The effective stiffness attributable to the presence of N active microcracks per unit volume is then derived from Eq. (26),

$$C^*_{ijkl}=\frac{\varepsilon}{4\pi}\int_0^{2\pi}\int_{-\pi/2}^{\pi/2} C^{(s)}_{ijkl}(\theta,\varphi)\cos\varphi\, d\theta\, d\varphi, \tag{30}$$

where the $C^{(s)}_{ijkl}$ is expressed in Eq. (23). By integrating the expression in Eq. (30), the effective stiffness due to an isotropic distribution of penny shaped microcracks is derived as

$$C^*_{ijkl}=\frac{16}{45}\frac{1-\nu}{2-\nu}2\mu\varepsilon\left\{2(5-\nu)I^1_{ijkl} + \frac{\nu(\nu^2-16\nu+19)}{(1-2\nu)^2}I^2_{ijkl}\right\}. \tag{31}$$

In addition, the stiffness tensor of the homogeneous, isotropic and elastic solids in its pristine, undamaged state is

$$C^0_{ijkl}=\lambda I^2_{ijkl}+2\mu I^1_{ijkl}. \tag{32}$$

Here, the ensemble average stiffness is redefined such that the average fluctuations are zero. Such a procedure, while not necessary, is convenient for the calculation of material covariance and attenuation. The moduli are assumed to be spatially varying and of the form

$$\overline{C}_{ijkl}(\mathbf{x})=\overline{C}^0_{ijkl}+\delta\overline{C}_{ijkl}(\mathbf{x}), \tag{33}$$

where

$$\overline{C}^0_{ijkl}=C^0_{ijkl}-C^*_{ijkl}. \tag{34}$$

Thus, the moduli have the form of the average moduli

$$\overline{C}^0_{ijkl}=\langle\overline{C}_{ijkl}(\mathbf{x})\rangle=\overline{\lambda}I^2_{ijkl}+2\overline{\mu}I^1_{ijkl}, \tag{35}$$

plus the fluctuation about the mean $\delta\overline{C}_{ijkl}$. Hence, $\overline{C}_{ijkl}$ has the average value of $\overline{C}^0_{ijkl}$ and $\delta\overline{C}_{ijkl}$ represents the modulus fluctuation. The effective constants are

$$\overline{\mu}=\mu\left[1-\frac{32}{45}\frac{(1-\nu)(5-\nu)}{2-\nu}\varepsilon\right],$$
$$\overline{\lambda}=\lambda\left[1-\frac{16}{45}\frac{(1-\nu)(\nu^2-16\nu+19)}{(2-\nu)(1-2\nu)}\varepsilon\right]. \tag{36}$$

These results are identical with the results obtained by Krajcinovic,[15] Kachanov *et al.*,[26] Budiansky and O'Connell,[25] and Zimmerman.[27] The effective properties of the damaged material are shown by Eqs. (36) to be linearly related to the damage parameter ε. Thus, wave speed changes that are the result of damage will scale linearly with ε as well.

The fluctuations, which are defined here to have zero average, $\langle\delta\overline{C}\rangle=0$, are given by

$$\delta\overline{C}_{ijkl}(\mathbf{x})=C^*_{ijkl}-C^{(s)}_{ijkl}H(\mathbf{x}). \tag{37}$$

The function $H(\mathbf{x})$ is defined as

$$H(\mathbf{x})=\begin{cases}1 & \text{if } \mathbf{x}\in\mathbf{S},\\ 0 & \text{otherwise,}\end{cases} \tag{38}$$

where $\mathbf{S}$ is the spatial volume occupied by a crack.

III. ENSEMBLE AVERAGE RESPONSE

The propagation and scattering of elastic waves in heterogeneous media is presented in this section in terms of the Dyson equation. Such an approach has been discussed by Frisch[20] and used by others.[12,13] This section is primarily included for completeness. The equation of motion for the elastodynamic response of a linear, elastic solid to deformation is given in terms of the Green's dyadic by

$$\{-\delta_{jk}\rho(\mathbf{x})\partial_t^2+\partial x_i\overline{C}_{ijkl}(\mathbf{x})\partial x_l\}G_{k\alpha}(\mathbf{x},\mathbf{x}';t) = \delta_{j\alpha}\delta^3(\mathbf{x}-\mathbf{x}')\delta(t), \tag{39}$$

where $\delta^3(\mathbf{x}-\mathbf{x}')$ is the three-dimensional spatial Dirac delta function. The second order Green's dyadic, $G_{k\alpha}(\mathbf{x},\mathbf{x}';t)$, is defined as the displacement response at location $\mathbf{x}$ in the kth direction due to an unit impulsive force acting at position $\mathbf{x}'$ in the αth direction at time zero. The moduli are considered to vary spatially whereas the density is assumed uniform throughout with units chosen such that the density is unity $[\rho(\mathbf{x})=1]$. The effective fourth-rank stiffness tensor $\overline{C}_{ijkl}(\mathbf{x})$ is given in Eq. (33). It is assumed that the fluctuations are small, such that $\delta\overline{\mathbf{C}}\ll\overline{\mathbf{C}}^0$. The covariance of the moduli is characterized by an eighth rank tensor

$$\langle\delta C_{ijkl}(\mathbf{x})\,\delta C_{\alpha\beta\gamma\delta}(\mathbf{y})\rangle=\Xi^{\alpha\beta\gamma\delta}_{ijkl}\eta(|\mathbf{x}-\mathbf{y}|). \tag{40}$$

The spatial and tensorial parts of the covariance, η and Ξ, respectively, are assumed independent. Also, η is assumed to be a function of the magnitude of the difference between two vectors, $|\mathbf{x}-\mathbf{y}|$, rather than $\mathbf{x}$ and $\mathbf{y}$ separately. This assumption implies that the medium is statistically homogeneous and statistically isotropic.

The spatio-temporal Fourier transform pair for the function $f(\mathbf{x},t)$ and $\tilde{f}(\mathbf{p},\omega)$ is defined as

$$\tilde{f}(\mathbf{p},\omega)=\int_{-\infty}^{+\infty}\int_{-\infty}^{+\infty}f(\mathbf{x},t)e^{i\omega t}e^{-i\mathbf{x}\cdot\mathbf{p}}d^3x\,dt,$$
$$f(\mathbf{x},t)=\frac{1}{(2\pi)^4}\int_{-\infty}^{+\infty}\int_{-\infty}^{+\infty}\tilde{f}(\mathbf{p},\omega)e^{-i\omega t}e^{i\mathbf{x}\cdot\mathbf{p}}d^3p\,d\omega. \tag{41}$$

These definitions allow Eq. (39) to be temporally transformed in the following form:

$$\{\omega^2\delta_{jk}+\overline{C}^0_{ijkl}\partial_i\partial_l+\partial_i\delta\overline{C}_{ijkl}(\mathbf{x})\partial_l\}\mathbf{G}_{k\alpha}(\mathbf{x},\mathbf{x}';\omega)$$
$$=\delta_{j\alpha}\delta^3(\mathbf{x}-\mathbf{x}'). \tag{42}$$

The mean response is governed by the Dyson equation[12,20]

$$\langle G_{i\alpha}(\mathbf{x},\mathbf{x}')\rangle = G^0_{i\alpha}(\mathbf{x},\mathbf{x}')+\int\int G^0_{i\beta}(\mathbf{x},\mathbf{y})M_{\beta j}(\mathbf{y},\mathbf{z})\times\langle G_{j\alpha}(\mathbf{z},\mathbf{x}')\rangle d^3y d^3z. \tag{43}$$

The notation $G^0_{i\alpha}(\mathbf{x},\mathbf{x}')$ is the bare Green's dyadic defined as the ensemble average response of the medium (without fluctuations), namely, the solution to Eq. (42) when $\delta\overline{C}_{ijkl}(\mathbf{x})=0$. The second order tensor $\mathbf{M}$ is the mass (self-energy) operator. Equation (43) is easily solved in the Fourier transform domain under the assumption of statistical homogeneity. The spatial Fourier transform pair for $\mathbf{G}^0$ is first defined as

$$G^0_{i\alpha}(\mathbf{p})\delta^3(\mathbf{p}-\mathbf{q})=\frac{1}{(2\pi)^3}\int\int G^0_{i\alpha}(\mathbf{x},\mathbf{x}')\times e^{-i\mathbf{p}\cdot\mathbf{x}}e^{i\mathbf{q}\cdot\mathbf{x}'}d^3x d^3x',$$
$$G^0_{i\alpha}(\mathbf{x},\mathbf{x}')=\frac{1}{(2\pi)^3}\int\int G^0_{i\alpha}(\mathbf{p})\delta^3(\mathbf{p}-\mathbf{q})\times e^{i\mathbf{p}\cdot\mathbf{x}}e^{-i\mathbf{q}\cdot\mathbf{x}'}d^3p d^3q. \tag{44}$$

The bare Green's dyadic, $\mathbf{G}^0$, is the solution of Eq. (42) with the modulus fluctuation equal to zero. Hence,

$$\mathbf{G}^0(\mathbf{p})=\hat{\mathbf{p}}\hat{\mathbf{p}}g^0_L(p)+(\mathbf{I}-\hat{\mathbf{p}}\hat{\mathbf{p}})g^0_T(p), \tag{45}$$

for propagation in the $\hat{\mathbf{p}}$ direction. The bare longitudinal wave $g^0_L(p)$ and transverse wave $g^0_T(p)$ propagators are denoted

$$g^0_L(p)=[\omega^2-p^2c_L^2]^{-1},$$
$$g^0_T(p)=[\omega^2-p^2c_T^2]^{-1}, \tag{46}$$

where the c_L and c_T are the average longitudinal and transverse wave speeds, respectively. The Fourier transforms which define $\langle\mathbf{G}(\mathbf{p})\rangle$ and $\tilde{\mathbf{M}}(\mathbf{p})$ are given by expressions similar to those defining $\mathbf{G}^0(\mathbf{p})$. The assumption of statistical homogeneity ensures that they are functions of a single wave vector in Fourier space. The Dyson equation is then transformed and solved to give

$$\langle\mathbf{G}(\mathbf{p})\rangle=[\mathbf{G}^0(\mathbf{p})^{-1}-\tilde{\mathbf{M}}(\mathbf{p})]^{-1}. \tag{47}$$

Here $\tilde{\mathbf{M}}(\mathbf{p})$ is the spatial transform of the self-energy. The self-energy, in turn, can be written as an expansion in powers of material property fluctuations. An approximation of $\mathbf{M}$ is made to first order using the first term in such an expansion.[20,21] To this level of approximation, $\mathbf{M}$ is expressed as[12]

$$M_{\beta j}(\mathbf{y},\mathbf{z})\approx\left\langle\frac{\partial}{\partial y_\alpha}\delta\overline{C}_{\alpha\beta\gamma\delta}(\mathbf{y})\frac{\partial}{\partial y_\delta}\mathbf{G}^0_{\gamma k}(\mathbf{y},\mathbf{z})\frac{\partial}{\partial z_i}\delta\overline{C}_{ijkl}(\mathbf{z})\frac{\partial}{\partial z_l}\right\rangle. \tag{48}$$

The approximation is valid if the fluctuations are not too large. The spatial Fourier transform defined in Eq. (44) allows the transform of the self-energy to be written as a convolution

$$\tilde{M}_{\beta j}(\mathbf{p})=\int d^3s\,G^0_{\gamma k}(\mathbf{s})p_\alpha p_l s_\delta s_i\Xi^{\alpha\beta\gamma\delta}_{ijkl}\tilde{\eta}(\mathbf{p}-\mathbf{s}). \tag{49}$$

The spatial transform of the self-energy and the mean Green's dyadic have the same form as the bare Green's dyadic. Hence, one may write

$$\tilde{\mathbf{M}}(\mathbf{p})=\hat{\mathbf{p}}\hat{\mathbf{p}}m_L(p)+(\mathbf{I}-\hat{\mathbf{p}}\hat{\mathbf{p}})m_T(p),$$
$$\langle\tilde{\mathbf{G}}(\mathbf{p})\rangle=\hat{\mathbf{p}}\hat{\mathbf{p}}g_L(p)+(\mathbf{I}-\hat{\mathbf{p}}\hat{\mathbf{p}})g_T(p), \tag{50}$$

where

$$m_L(\mathbf{p})=-\int d^3s\;\underset{\hat{\mathbf{p}}\hat{\mathbf{p}}\hat{\mathbf{p}}\cdots}{\hat{\mathbf{p}}\hat{\mathbf{p}}\hat{\mathbf{s}}\cdots}\Xi\vdots\{\hat{\mathbf{s}}\hat{\mathbf{s}}g^0_L(\mathbf{s})+(\mathbf{I}-\hat{\mathbf{s}}\hat{\mathbf{s}})g^0_T(\mathbf{s})\}\tilde{\eta}(\mathbf{p}-\mathbf{s}),$$
$$m_T(\mathbf{p})=-\frac{1}{2}\int d^3s(\mathbf{I}-\hat{\mathbf{p}}\hat{\mathbf{p}})\;\underset{\hat{\mathbf{p}}\hat{\mathbf{p}}\cdots}{\hat{\mathbf{p}}\hat{\mathbf{s}}\cdots}\Xi\vdots\{\hat{\mathbf{s}}\hat{\mathbf{s}}g^0_L(\mathbf{s})+(\mathbf{I}-\hat{\mathbf{s}}\hat{\mathbf{s}})g^0_T(\mathbf{s})\}\tilde{\eta}(\mathbf{p}-\mathbf{s}) \tag{51}$$

and

$$g_L(p)=[\omega^2-p^2c_L^2+m_L(p)]^{-1},$$
$$g_T(p)=[\omega^2-p^2c_T^2+m_T(p)]^{-1}. \tag{52}$$

These are the expressions for the mean response. They define the phase velocity and the attenuation of longitudinal and transverse wave types. The inverse Fourier transform of $\langle\mathbf{G}(\mathbf{p})\rangle$ in Eq. (50) is dominated by the poles near $|p|=\omega/c_\beta$ with $\beta=L$ or T. Thus, the effective wave vectors, $\mathbf{p}$, are the solution to the required conditions

$$\omega^2-p^2c_L^2+m_L(p)=0 \tag{53}$$

and

$$\omega^2-p^2c_T^2+m_T(p)=0. \tag{54}$$

The real and imaginary parts of $\mathbf{p}$ give the phase velocity and attenuation, respectively. Equations (53) and (54) are usually solved numerically using root finding techniques. The solution for the attenuation can be calculated by making use of an approximation valid below the high frequency geometric optics limit. In this case, the solutions, $\mathbf{p}$, are approximated as equal to the bare solution. Such an approximation, $m(\mathbf{p})\approx m(\omega\hat{\mathbf{p}}/c_\beta)$ is sometimes called a Born approximation. In essence, the phase velocity is supposed to remain unchanged by the heterogeneities. Under this approximation the imaginary part can be evaluated from Eqs. (53) and (54). The attenuations, which are the imaginary part for each wave type, are calculated as

$$\alpha_\beta(\hat{\mathbf{p}})=-\frac{1}{2\omega c_\beta}\operatorname{Im}m_\beta\left(\frac{\omega}{c_\beta}\hat{\mathbf{p}}\right). \tag{55}$$

The imaginary parts of m_β (where $\beta=L$ or T) are determined from Eqs. (51) such that the attenuations are given by

$$\alpha_L(\hat{\mathbf{p}})=\frac{\pi}{4\omega c_L}\int \begin{matrix}\hat{\mathbf{p}}\hat{\mathbf{p}}\hat{\mathbf{s}}\hat{\mathbf{s}}\cdots\\ \hat{\mathbf{p}}\hat{\mathbf{p}}\hat{\mathbf{s}}\hat{\mathbf{s}}\cdots\end{matrix}\Xi\,\tilde{\eta}\left(\hat{\mathbf{p}}\frac{\omega}{c_L}-\hat{\mathbf{s}}\frac{\omega}{c_L}\right)\frac{\omega^5}{c_L^7}d^2\hat{\mathbf{s}}$$
$$+\frac{\pi}{4\omega c_T}\int \begin{matrix}\hat{\mathbf{p}}\hat{\mathbf{p}}\hat{\mathbf{s}}\\ \hat{\mathbf{p}}\hat{\mathbf{p}}\hat{\mathbf{s}}\end{matrix}(\mathbf{I}-\begin{matrix}\hat{\mathbf{s}}\\ \hat{\mathbf{s}}\end{matrix})\cdots\Xi\,\tilde{\eta}\left(\hat{\mathbf{p}}\frac{\omega}{c_L}-\hat{\mathbf{s}}\frac{\omega}{c_T}\right)\frac{\omega^5}{c_T^5c_L^2}d^2\hat{\mathbf{s}}$$

and

$$\alpha_T(\hat{\mathbf{p}})=\frac{\pi}{8\omega c_L}\int (\mathbf{I}-\begin{matrix}\hat{\mathbf{p}}\\ \hat{\mathbf{p}}\end{matrix})\begin{matrix}\hat{\mathbf{p}}\hat{\mathbf{s}}\hat{\mathbf{s}}\cdots\\ \hat{\mathbf{p}}\hat{\mathbf{s}}\hat{\mathbf{s}}\cdots\end{matrix}\Xi\,\tilde{\eta}\left(\hat{\mathbf{p}}\frac{\omega}{c_T}-\hat{\mathbf{s}}\frac{\omega}{c_L}\right)\frac{\omega^5}{c_L^5c_T^2}d^2\hat{\mathbf{s}}$$
$$+\frac{\pi}{8\omega c_T}\int (\mathbf{I}-\begin{matrix}\hat{\mathbf{p}}\\ \hat{\mathbf{p}}\end{matrix})\begin{matrix}\hat{\mathbf{p}}\hat{\mathbf{s}}\\ \hat{\mathbf{p}}\hat{\mathbf{s}}\end{matrix}(\mathbf{I}-\begin{matrix}\hat{\mathbf{s}}\\ \hat{\mathbf{s}}\end{matrix})\cdots\Xi$$
$$\times\tilde{\eta}\left(\hat{\mathbf{p}}\frac{\omega}{c_T}-\hat{\mathbf{s}}\frac{\omega}{c_T}\right)\frac{\omega^5}{c_T^7}d^2\hat{\mathbf{s}},$$

where the integrals are over the unit sphere $\hat{\mathbf{s}}$. Three additional functions are defined as

$$\eta_{LL}(\theta_{ps})=\tilde{\eta}\left(\hat{\mathbf{p}}\frac{\omega}{c_L}-\hat{\mathbf{s}}\frac{\omega}{c_L}\right),$$
$$\eta_{TT}(\theta_{ps})=\tilde{\eta}\left(\hat{\mathbf{p}}\frac{\omega}{c_T}-\hat{\mathbf{s}}\frac{\omega}{c_T}\right),\tag{56}$$
$$\eta_{LT}(\theta_{ps})=\eta_{TL}(\theta_{ps})=\tilde{\eta}\left(\hat{\mathbf{p}}\frac{\omega}{c_L}-\hat{\mathbf{s}}\frac{\omega}{c_T}\right),$$

where the direction $\hat{\mathbf{p}}$ defines the propagation direction, $\hat{\mathbf{s}}$ defines the scattered direction, and θ_{ps} is the angle between these directions (i.e., $\cos\theta_{ps}=\hat{\mathbf{p}}\cdot\hat{\mathbf{s}}$).

IV. ATTENUATIONS AND COVARIANCE

To derive the attenuations, the relevant inner products on the covariance of the effective moduli fluctuations are required. The covariance of the moduli fluctuations is represented by an eighth-rank tensor which is given in Eq. (40). The inner product is given explicitly by

$$\Xi\begin{matrix}\hat{\mathbf{u}}\hat{\mathbf{p}}\hat{\mathbf{s}}\hat{\mathbf{v}}\\ \hat{\mathbf{u}}\hat{\mathbf{p}}\hat{\mathbf{s}}\hat{\mathbf{v}}\end{matrix}\cdots=\Xi_{ijkl}^{\alpha\beta\gamma\delta}\hat{u}_\beta\hat{u}_k\hat{p}_\alpha\hat{p}_l\hat{s}_i\hat{s}_\delta\hat{v}_\gamma\hat{v}_j.\tag{57}$$

The covariance here is given in terms of an average over all crack orientations. Thus, the crack normal $\mathbf{n}$ may vary over all possible directions. In this case, the following identities are needed:

$$\begin{aligned}&\langle n_in_j\rangle=\tfrac{1}{3}\delta_{ij},\\ &\langle n_in_jn_kn_l\rangle=\tfrac{1}{15}(\delta_{ij}\delta_{kl}+\delta_{ik}\delta_{jl}+\delta_{il}\delta_{jk}),\\ &\langle n_in_jn_kn_ln_\alpha n_\beta\rangle=\tfrac{1}{105}(\delta_{ij}\delta_{kl}\delta_{\alpha\beta}+\text{all permutations}\\ &\qquad\qquad -15\text{ terms in all}),\\ &\langle n_in_jn_kn_ln_\alpha n_\beta n_\gamma n_\delta\rangle=\tfrac{1}{945}(\delta_{ij}\delta_{kl}\delta_{\alpha\beta}\delta_{\gamma\delta}\\ &\qquad\qquad +\text{all permutations}\\ &\qquad\qquad -105\text{ terms in all}),\end{aligned}\tag{58}$$

where the brackets, $\langle\ \rangle$, denote the ensemble average. All averages of odd numbers of $\mathbf{n}$'s are zero. The average of the tensorial part of the covariance over all orientations of crack normal is defined by

$$\Xi_{ijkl}^{\alpha\beta\gamma\delta}=\frac{1}{4\pi}\int_0^{2\pi}\int_{-\pi/2}^{\pi/2}\overline{C}_{ijkl}^{(s)}\overline{C}_{\alpha\beta\gamma\delta}^{(s)}\cos\varphi\,d\varphi\,d\theta.\tag{59}$$

Here, we use the relation $\langle H(\mathbf{x})H(\mathbf{y})\rangle=\varepsilon\Pr(r|0)$, where $\Pr(r|0)=(1-\varepsilon)\eta(r)+\varepsilon$ is defined as the conditional probability.[28] The notation r is used to denote the magnitude of the difference between two vectors, $\mathbf{x}$ and $\mathbf{y}$. Here, the second order terms are neglected under the assumption that the damage density is small. Thus, $\langle\delta C_{ijkl}(\mathbf{x})\delta C_{\alpha\beta\gamma\delta}(\mathbf{y})\rangle=\varepsilon\,\eta(r)\Xi_{ijkl}^{\alpha\beta\gamma\delta}$. It is noted that

$$\overline{\mathbf{C}}^{(s)}=2\mu\sum_{i=1}^{6}\overline{d}_i\mathbf{I}^i,\tag{60}$$

with

$$\begin{aligned}&\overline{d}_1=0,\quad \overline{d}_2=\frac{16}{3}\frac{\nu^2(1-\nu)}{(1-2\nu)^2},\quad \overline{d}_5=\frac{32}{3}\frac{1-\nu}{2-\nu},\\ &\overline{d}_3=\overline{d}_4=\frac{16}{3}\frac{\nu(1-\nu)}{1-2\nu},\quad \overline{d}_6=-\frac{16}{3}\frac{\nu(1-\nu)}{2-\nu}.\end{aligned}\tag{61}$$

Using the identities in Eqs. (58), the general form of Ξ is given in terms of Kronecker deltas. The expressions for the attenuations, in turn, involve certain inner products of Ξ with incoming and outgoing wave vectors. In terms of the angle between $\hat{\mathbf{p}}$ and $\hat{\mathbf{s}}$, these necessary inner products reduce to

$$\begin{aligned}\Xi\begin{matrix}\hat{\mathbf{p}}\hat{\mathbf{p}}\hat{\mathbf{s}}\hat{\mathbf{s}}\\ \hat{\mathbf{p}}\hat{\mathbf{p}}\hat{\mathbf{s}}\hat{\mathbf{s}}\end{matrix}\cdots&=[T_1+4T_4+4T_7]+[4T_2+4T_4\\ &\quad+32T_5+16T_6+16T_7]\cos^2\theta_{ps}\\ &\quad+[4T_3+16T_6+4T_7]\cos^4\theta_{ps},\\ \Xi\begin{matrix}\hat{\mathbf{p}}\hat{\mathbf{p}}\hat{\mathbf{s}}\hat{\mathbf{s}}_2\\ \hat{\mathbf{p}}\hat{\mathbf{p}}\hat{\mathbf{s}}\hat{\mathbf{s}}_2\end{matrix}\cdots&=\Xi\begin{matrix}\hat{\mathbf{p}}_2\hat{\mathbf{p}}\hat{\mathbf{s}}\hat{\mathbf{s}}\\ \hat{\mathbf{p}}_2\hat{\mathbf{p}}\hat{\mathbf{s}}\hat{\mathbf{s}}\end{matrix}\cdots\\ &=[T_4+2T_7]+[4T_5+4T_6+4T_7]\cos^2\theta_{ps},\\ \Xi\begin{matrix}\hat{\mathbf{p}}\hat{\mathbf{p}}\hat{\mathbf{s}}\hat{\mathbf{s}}_3\\ \hat{\mathbf{p}}\hat{\mathbf{p}}\hat{\mathbf{s}}\hat{\mathbf{s}}_3\end{matrix}\cdots&=\Xi\begin{matrix}\hat{\mathbf{p}}_3\hat{\mathbf{p}}\hat{\mathbf{s}}\hat{\mathbf{s}}\\ \hat{\mathbf{p}}_3\hat{\mathbf{p}}\hat{\mathbf{s}}\hat{\mathbf{s}}\end{matrix}\cdots\\ &=[T_4+4T_5+4T_6+6T_7]\\ &\quad+[4T_3+16T_6+4T_7]\cos^2\theta_{ps}\\ &\quad-[4T_3+16T_6+4T_7]\cos^4\theta_{ps},\\ \Xi\begin{matrix}\hat{\mathbf{p}}_2\hat{\mathbf{p}}\hat{\mathbf{s}}\hat{\mathbf{s}}_2\\ \hat{\mathbf{p}}_2\hat{\mathbf{p}}\hat{\mathbf{s}}\hat{\mathbf{s}}_2\end{matrix}\cdots&=[T_6+2T_7]+[T_3+3T_6+2T_7]\cos^2\theta_{ps},\\ \Xi\begin{matrix}\hat{\mathbf{p}}_3\hat{\mathbf{p}}\hat{\mathbf{s}}\hat{\mathbf{s}}_3\\ \hat{\mathbf{p}}_3\hat{\mathbf{p}}\hat{\mathbf{s}}\hat{\mathbf{s}}_3\end{matrix}\cdots&=[T_3+4T_6+4T_7]\\ &\quad+[-4T_3-16T_6-4T_7]\cos^2\theta_{ps}\\ &\quad+[4T_3+16T_6+4T_7]\cos^4\theta_{ps},\\ \Xi\begin{matrix}\hat{\mathbf{p}}_2\hat{\mathbf{p}}\hat{\mathbf{s}}\hat{\mathbf{s}}_3\\ \hat{\mathbf{p}}_2\hat{\mathbf{p}}\hat{\mathbf{s}}\hat{\mathbf{s}}_3\end{matrix}\cdots&=\Xi\begin{matrix}\hat{\mathbf{p}}_3\hat{\mathbf{p}}\hat{\mathbf{s}}\hat{\mathbf{s}}_2\\ \hat{\mathbf{p}}_3\hat{\mathbf{p}}\hat{\mathbf{s}}\hat{\mathbf{s}}_2\end{matrix}\cdots=[T_6+2T_7],\end{aligned}\tag{62}$$

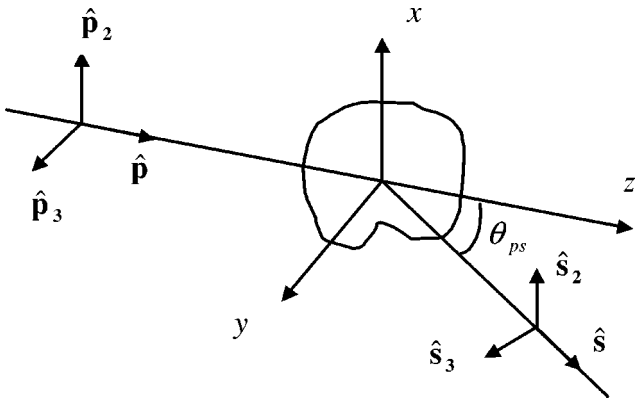

FIG. 1. Geometry for scattering in the local coordinate system.

$$\Xi^{\cdots\hat{\mathbf{p}}_2\hat{\mathbf{p}}\hat{\mathbf{s}}\hat{\mathbf{s}}_2}_{\cdots\hat{\mathbf{p}}_3\hat{\mathbf{p}}\hat{\mathbf{s}}\hat{\mathbf{s}}_3} = \Xi^{\cdots\hat{\mathbf{p}}_3\hat{\mathbf{p}}\hat{\mathbf{s}}\hat{\mathbf{s}}_3}_{\cdots\hat{\mathbf{p}}_2\hat{\mathbf{p}}\hat{\mathbf{s}}\hat{\mathbf{s}}_2}$$
$$= [-T_3 - 2T_6]\cos\theta_{ps} + [2T_3 + 4T_6]\cos^3\theta_{ps},$$
$$\Xi^{\cdots\hat{\mathbf{p}}_2\hat{\mathbf{p}}\hat{\mathbf{s}}\hat{\mathbf{s}}_3}_{\cdots\hat{\mathbf{p}}_3\hat{\mathbf{p}}\hat{\mathbf{s}}\hat{\mathbf{s}}_2} = \Xi^{\cdots\hat{\mathbf{p}}_3\hat{\mathbf{p}}\hat{\mathbf{s}}\hat{\mathbf{s}}_2}_{\cdots\hat{\mathbf{p}}_2\hat{\mathbf{p}}\hat{\mathbf{s}}\hat{\mathbf{s}}_3}$$
$$= -3T_6\cos\theta_{ps} + [4T_6 + 2T_7]\cos^3\theta_{ps},$$
$$\Xi^{\cdots\hat{\mathbf{p}}_2\hat{\mathbf{p}}\hat{\mathbf{s}}\hat{\mathbf{s}}_2}_{\cdots\hat{\mathbf{p}}_2\hat{\mathbf{p}}\hat{\mathbf{s}}\hat{\mathbf{s}}_3} = \Xi^{\cdots\hat{\mathbf{p}}_2\hat{\mathbf{p}}\hat{\mathbf{s}}\hat{\mathbf{s}}_3}_{\cdots\hat{\mathbf{p}}_3\hat{\mathbf{p}}\hat{\mathbf{s}}\hat{\mathbf{s}}_2} = \Xi^{\cdots\hat{\mathbf{p}}_2\hat{\mathbf{p}}\hat{\mathbf{s}}\hat{\mathbf{s}}_3}_{\cdots\hat{\mathbf{p}}_2\hat{\mathbf{p}}\hat{\mathbf{s}}\hat{\mathbf{s}}_2} = \Xi^{\cdots\hat{\mathbf{p}}_3\hat{\mathbf{p}}\hat{\mathbf{s}}\hat{\mathbf{s}}_2}_{\cdots\hat{\mathbf{p}}_2\hat{\mathbf{p}}\hat{\mathbf{s}}\hat{\mathbf{s}}_2} = 0,$$
$$\Xi^{\cdots\hat{\mathbf{p}}_3\hat{\mathbf{p}}\hat{\mathbf{s}}\hat{\mathbf{s}}_3}_{\cdots\hat{\mathbf{p}}_3\hat{\mathbf{p}}\hat{\mathbf{s}}\hat{\mathbf{s}}_2} = \Xi^{\cdots\hat{\mathbf{p}}_2\hat{\mathbf{p}}\hat{\mathbf{s}}\hat{\mathbf{s}}_3}_{\cdots\hat{\mathbf{p}}_3\hat{\mathbf{p}}\hat{\mathbf{s}}\hat{\mathbf{s}}_3} = \Xi^{\cdots\hat{\mathbf{p}}_3\hat{\mathbf{p}}\hat{\mathbf{s}}\hat{\mathbf{s}}_2}_{\cdots\hat{\mathbf{p}}_2\hat{\mathbf{p}}\hat{\mathbf{s}}\hat{\mathbf{s}}_3} = \Xi^{\cdots\hat{\mathbf{p}}_3\hat{\mathbf{p}}\hat{\mathbf{s}}\hat{\mathbf{s}}_2}_{\cdots\hat{\mathbf{p}}_3\hat{\mathbf{p}}\hat{\mathbf{s}}\hat{\mathbf{s}}_3} = 0,$$
$$\Xi^{\cdots\hat{\mathbf{p}}\hat{\mathbf{p}}\hat{\mathbf{s}}\hat{\mathbf{s}}_3}_{\cdots\hat{\mathbf{p}}\hat{\mathbf{p}}\hat{\mathbf{s}}\hat{\mathbf{s}}_2} = \Xi^{\cdots\hat{\mathbf{p}}_2\hat{\mathbf{p}}\hat{\mathbf{s}}\hat{\mathbf{s}}}_{\cdots\hat{\mathbf{p}}_3\hat{\mathbf{p}}\hat{\mathbf{s}}\hat{\mathbf{s}}} = \Xi^{\cdots\hat{\mathbf{p}}_3\hat{\mathbf{p}}\hat{\mathbf{s}}\hat{\mathbf{s}}}_{\cdots\hat{\mathbf{p}}_2\hat{\mathbf{p}}\hat{\mathbf{s}}\hat{\mathbf{s}}} = \Xi^{\cdots\hat{\mathbf{p}}\hat{\mathbf{p}}\hat{\mathbf{s}}\hat{\mathbf{s}}_2}_{\cdots\hat{\mathbf{p}}\hat{\mathbf{p}}\hat{\mathbf{s}}\hat{\mathbf{s}}_3} = 0.$$

The coefficients T_i are given by

$$T_1 = -\frac{D^2\nu^2}{945}\frac{335\nu^4 - 1984\nu^3 + 2946\nu^2 - 208\nu - 937}{(1-2\nu)^2},$$
$$T_2 = \frac{D^2\nu}{4725}\frac{31\nu^3 - 139\nu^2 + \nu + 243}{1-2\nu},$$
$$T_7 = \frac{D^2\nu^2(1-2\nu)^2}{945},$$
$$T_3 = \frac{D^2}{945}(1-2\nu)^2(\nu^2 - 18\nu + 63), \tag{63}$$
$$T_4 = \frac{D^2\nu^2}{945}(31\nu^2 - 166\nu + 217),$$
$$T_5 = \frac{D^2\nu}{1890}(1-2\nu)(14\nu^2 - 79\nu + 117),$$
$$T_6 = \frac{D^2}{420}(1-2\nu)^2(7-4\nu),$$

with the constant $D = \frac{16}{3}[(1-\nu)/(2-\nu)(1-2\nu)]2\mu$. The unit vectors $\hat{\mathbf{p}}$, $\hat{\mathbf{p}}_2$, $\hat{\mathbf{p}}_3$ and $\hat{\mathbf{s}}$, $\hat{\mathbf{s}}_2$, $\hat{\mathbf{s}}_3$ used in Eqs. (62) are defined as orthonormal triads, respectively (see Fig. 1). The general compact form of Ξ is not given here. The interested reader may contact the authors for further details.

Using the notation

$$F(\theta_{ps}) = \Xi^{\cdots\hat{\mathbf{p}}\hat{\mathbf{p}}\hat{\mathbf{s}}\hat{\mathbf{s}}}_{\cdots\hat{\mathbf{p}}\hat{\mathbf{p}}\hat{\mathbf{s}}\hat{\mathbf{s}}}, \tag{64}$$
$$M(\theta_{ps}) = \Xi^{\cdots\hat{\mathbf{p}}\hat{\mathbf{p}}\hat{\mathbf{s}}\hat{\mathbf{s}}_2}_{\cdots\hat{\mathbf{p}}\hat{\mathbf{p}}\hat{\mathbf{s}}\hat{\mathbf{s}}_2} + \Xi^{\cdots\hat{\mathbf{p}}\hat{\mathbf{p}}\hat{\mathbf{s}}\hat{\mathbf{s}}_3}_{\cdots\hat{\mathbf{p}}\hat{\mathbf{p}}\hat{\mathbf{s}}\hat{\mathbf{s}}_3} = \Xi^{\cdots\hat{\mathbf{p}}_2\hat{\mathbf{p}}\hat{\mathbf{s}}\hat{\mathbf{s}}}_{\cdots\hat{\mathbf{p}}_2\hat{\mathbf{p}}\hat{\mathbf{s}}\hat{\mathbf{s}}} + \Xi^{\cdots\hat{\mathbf{p}}_3\hat{\mathbf{p}}\hat{\mathbf{s}}\hat{\mathbf{s}}}_{\cdots\hat{\mathbf{p}}_3\hat{\mathbf{p}}\hat{\mathbf{s}}\hat{\mathbf{s}}}, \tag{65}$$
$$N(\theta_{ps}) = \Xi^{\cdots\hat{\mathbf{p}}_2\hat{\mathbf{p}}\hat{\mathbf{s}}\hat{\mathbf{s}}_2}_{\cdots\hat{\mathbf{p}}_2\hat{\mathbf{p}}\hat{\mathbf{s}}\hat{\mathbf{s}}_2} + \Xi^{\cdots\hat{\mathbf{p}}_3\hat{\mathbf{p}}\hat{\mathbf{s}}\hat{\mathbf{s}}_3}_{\cdots\hat{\mathbf{p}}_3\hat{\mathbf{p}}\hat{\mathbf{s}}\hat{\mathbf{s}}_3} + \Xi^{\cdots\hat{\mathbf{p}}_2\hat{\mathbf{p}}\hat{\mathbf{s}}\hat{\mathbf{s}}_3}_{\cdots\hat{\mathbf{p}}_2\hat{\mathbf{p}}\hat{\mathbf{s}}\hat{\mathbf{s}}_3} + \Xi^{\cdots\hat{\mathbf{p}}_3\hat{\mathbf{p}}\hat{\mathbf{s}}\hat{\mathbf{s}}_2}_{\cdots\hat{\mathbf{p}}_3\hat{\mathbf{p}}\hat{\mathbf{s}}\hat{\mathbf{s}}_2} \tag{66}$$

allows the attenuations to be reduced to the form

$$\alpha_{LL} = \frac{1}{4}\frac{\pi\omega^4\varepsilon}{c_L^8}\int \eta^{LL}(\theta_{ps})F(\theta_{ps})d^2\hat{\mathbf{s}}$$
$$= \frac{1}{2}\frac{\pi^2\omega^4\varepsilon}{c_L^8}\int_{-1}^{+1}\eta^{LL}(\theta)F(\theta)d\cos\theta,$$
$$\alpha_{LT} = \frac{1}{4}\frac{\pi\omega^4\varepsilon}{c_L^3c_T^5}\int \eta^{LT}(\theta_{ps})M(\theta_{ps})d^2\hat{\mathbf{s}}$$
$$= \frac{1}{2}\frac{\pi^2\omega^4\varepsilon}{c_L^3c_T^5}\int_{-1}^{+1}\eta^{LT}(\theta)M(\theta)d\cos\theta,$$
$$\alpha_{TL} = \frac{1}{2}\left(\frac{c_T}{c_L}\right)^2\alpha_{LT}, \tag{67}$$
$$\alpha_{TT} = \frac{1}{8}\frac{\pi\omega^4\varepsilon}{c_T^8}\int \eta^{TT}(\theta_{ps})N(\theta_{ps})d^2\hat{\mathbf{s}}$$
$$= \frac{1}{4}\frac{\pi^2\omega^4\varepsilon}{c_T^8}\int_{-1}^{+1}\eta^{TT}(\theta)N(\theta)d\cos\theta.$$

The total attenuations for the longitudinal and transverse waves are given by

$$\alpha_L = \alpha_{LL} + \alpha_{LT}, \quad \alpha_T = \alpha_{TT} + \alpha_{TL}. \tag{68}$$

The appropriate expressions for the tensorial part of the covariance, Eqs. (62), and the final expressions for attenuations, Eqs. (67) and (68), are the main results of this section. The attenuations are expressed as integrations on the unit circle in terms of the spatial transform of the spatial correlation function. Most importantly, the results are expressed in terms of the damage density ε. We see that the attenuations scale linearly with damage factor ε. In the next section, a form for η is assumed and example results presented.

V. EXAMPLE RESULTS

In this section, example results are presented in terms of the dimensionless damage parameter ε for an assumed spatial correlation function. For the example case, the material properties of the uncracked medium used are Young's modulus $E = 2.0\times10^7$ Pa and Poisson's ratio $\nu = 0.16$.

As discussed following Eq. (40), the tensorial and spatial contributions of the material covariance are assumed independent. The spatial correlations were characterized by η. Here it is assumed that η has an exponential form

$$\eta(r) = e^{-r/L}, \tag{69}$$

where L is the spatial correlation length, $L = 2\langle a\rangle$. As discussed by Stanke,[29] an exponential function describes the

correlation of continuous and discrete materials reasonably well. Such a model, with a single length scale, is perhaps oversimplified for materials containing a wide range of crack sizes. However, for many materials, such a model is expected to described the statistics of the material properties well. Other correlation functions, such as that discussed by Markov and Willis,[28] are thought to give similar results for the frequency range considered here. The influence of this choice of correlation function on the attenuations is the subject of future investigations.

In transform space

$$\tilde{\eta}(p)=\frac{L^3}{\pi^2(1+L^2p^2)^2}. \tag{70}$$

With the length scale of the spatial correlation introduced, dimensionless longitudinal and transverse frequencies are defined as $x_L=\omega L/c_L$ and $x_T=\omega L/c_T$. The transform of the difference between two wave vectors is then expressed as

$$\eta_{\alpha\beta}(\chi)=\frac{L^3}{\pi^2(1+x_\alpha^2+x_\beta^2-2x_\alpha x_\beta\chi)^2}. \tag{71}$$

Here the scripts, α, β denote the wave types L or T, and $\chi=\cos\theta_{ps}$. In dimensionless form, the attenuations in Eqs. (67) simplify to

$$\alpha_{LL}H=\frac{x_L^4B^4\varepsilon}{2\mu^2}\int_{-1}^{+1}\frac{h_1+h_2\chi^2+h_3\chi^4}{(1+2x_L^2(1-\chi))^2}d\chi, \tag{72}$$

$$\alpha_{LT}H=\frac{x_L^4\varepsilon}{2B\mu^2}\int_{-1}^{+1}\frac{m_1+m_2\chi^2+m_3\chi^4}{(1+x_L^2+x_T^2-2x_Lx_T\chi)^2}d\chi, \tag{73}$$

$$\alpha_{TT}H=\frac{x_T^4\varepsilon}{4\mu^2}\int_{-1}^{+1}\frac{n_1+n_2\chi^2+n_3\chi^4}{(1+2x_T^2(1-\chi))^2}d\chi, \tag{74}$$

where $B=c_T/c_L$ is the wave speed ratio. The coefficients h_i, m_i, n_i $(i=1,2,3)$ are given as

$$\begin{aligned}
h_1&=T_1+4T_4+4T_7,\\
h_2&=4T_2+4T_4+32T_5+16T_6+16T_7,\\
h_3&=4T_3+16T_6+4T_7,
\end{aligned} \tag{75}$$

$$\begin{aligned}
m_1&=2T_4+4T_5+4T_6+8T_7,\\
m_2&=4T_3+4T_5+20T_6+8T_7,\\
m_3&=-4T_3-16T_6-4T_7,
\end{aligned} \tag{76}$$

$$\begin{aligned}
n_1&=T_3+7T_6+10T_7,\\
n_2&=-3T_3-13T_6-2T_7,\\
n_3&=4T_3+16T_6+4T_7.
\end{aligned} \tag{77}$$

Example calculations using Eqs. (72)–(74) are shown in Fig. 2. The dimensionless longitudinal and transverse attenuations, α_LH and α_TH, respectively, are plotted as a function of dimensionless frequency, x_L, for two values of the damage parameter ε. Equations (72)–(74) are shown to scale linearly with ε such that other values of ε lead to constant shifts in these curves. The attenuations increase with the fourth power of frequency in the low frequency limit as expected. After a transition region, the attenuations increase with the square of frequency. However, it should be noted that the results at higher frequencies are less accurate than those at lower frequencies. This inaccuracy is the result of the truncation of the expansion in Eqs. (20). The longitudinal attenuation is smaller than the transverse attenuation in part due to the wavelengths of the respective waves. However, when the attenuations are plotted in terms of their respective dimensionless frequency, the transverse attenuations remained larger than the longitudinal. Thus, the higher transverse attenuation is a combination of effects of wavelength and interaction with the cracks. As shown in Fig. 2, the ratio of the longitudinal and transverse attenuations is a constant at low frequencies, but changes at higher frequencies. Figure 3 is a plot of the wave speed ratio $B^e=\overline{C_T}/\overline{C_L}$ and $C=(\overline{C_T}/C_T)/(\overline{C_L}/C_L)$, as a function of damage factor ε. As has been observed experimentally, the wave speed changes much less than the attenuation for a given damage level.[30] Thus, the result shown in Fig. 3 is not unexpected.

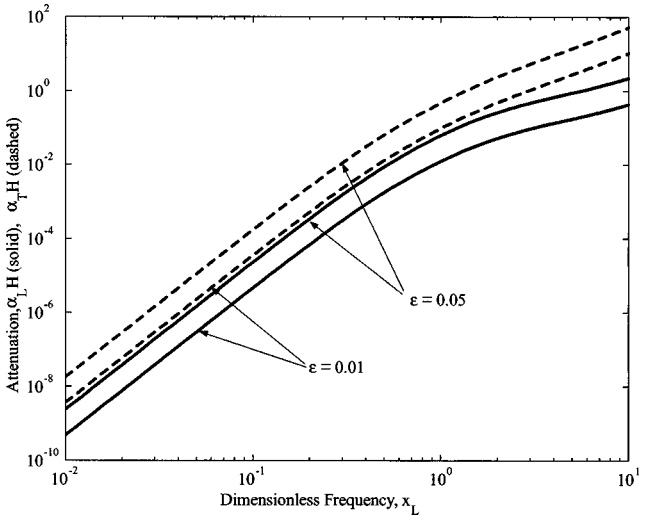

FIG. 2. Dimensionless longitudinal and transverse attenuations, α_LH (solid) and α_TH (dashed), as a function of dimensionless frequency, x_L, for damage factor $\varepsilon=0.01$ and $\varepsilon=0.05$.

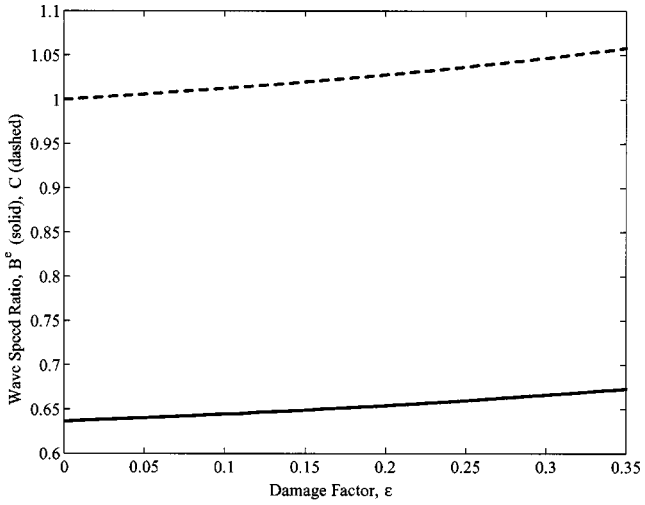

FIG. 3. Wave speed ratio $B^e=\overline{C_T}/\overline{C_L}$ and $C=(\overline{C_T}/C_T)/(\overline{C_L}/C_L)$, as a function of damage factor ε.

VI. DISCUSSION

The propagation and scattering of elastic waves in a homogeneous, isotropic medium with damage from microcracking has been investigated. A generalized tensor-based approach was used such that the results are coordinate free. The effective compliance or stiffness in terms of the damage parameter was discussed. Initially, effective compliance due to a single penny-shaped crack embedded in an infinite elastic solids was examined. The effective properties of a homogenous, isotropic solid in which a large number of microcracks is embedded were then determined by superposition. The modulus fluctuations were then derived relative to these average moduli. The ensemble average covariance of the modulus fluctuations was then derived for randomly oriented cracks. The expressions for the longitudinal and transverse attenuations were derived by considering the Dyson equation, which governs the mean elastodynamic response of the medium. The Dyson equation was solved within the limits of first-order smoothing approximation (FOSA). The final forms of the attenuations have a linear dependency on the damage parameter, which is expected to be valid for low crack densities. The use of the tensor-based approach presented here for studying elastic wave scattering in media with microcracks allowed the attenuation expressions to be reduced to simple forms. These results should be very useful for nondestructive testing and materials characterization research. In particular, the study of wave interactions with aligned cracks, whose evolution is modeled using a damage tensor, will be much more direct. This topic will be examined in the future. The general formulation also is convenient for considering other problems such as studies of backscatter and multiple scattering phenomena.

ACKNOWLEDGMENTS

The support of the National Science Foundation (Grants No. CMS-9978707 and INT-0089548) and the National Bridge Research Organization (NaBRO) is gratefully acknowledged by authors.

[1] J. Achenbach, ''Quantitative Nondestructive Evaluation,'' Int. J. Solids Struct. **37**, 13–27 (2000).
[2] C. Zhang and J. Achenbach, ''Effective Wave Velocity and Attenuation in a Material with Distributed Penny-Shaped Cracks,'' Int. J. Solids Struct. **27**, 751–767 (1991).
[3] A. K. Mal, ''Interaction of Elastic Waves with a Penny-Shaped Crack,'' Int. J. Eng. Sci. **8**, 381–388 (1968).
[4] A. K. Mal, ''A Note on the Low Frequency Diffraction of Elastic Waves by a Griffith Crack,'' Int. J. Eng. Sci. **10**, 609–612 (1972).
[5] M. Piau, ''Attenuation of a Plane Compressional Wave by a Random Distribution of Thin Circular Cracks,'' Int. J. Eng. Sci. **17**, 151–167 (1979).
[6] A. Chatterjee, A. K. Mal, L. Knopoff, and J. Hudson, ''Attenuation of Elastic Waves in a Cracked, Fluid-Saturated Solid,'' Math. Proc. Cambridge Philos. Soc. **88**, 547–561 (1980).
[7] C. Zhang and D. Gross, ''Wave Attenuation and Dispersion in Randomly Cracked Solids-II. Penny-Shaped Cracks,'' Int. J. Eng. Sci. **31**, 859–872 (1993).
[8] V. P. Smyshlyaev and J. R. Willis, ''Linear and Nonlinear Scattering of Elastic Waves by Microcracks,'' J. Mech. Phys. Solids **42**, 585–610 (1994).
[9] S. Hirsekorn, ''The scattering of ultrasonic waves by polycrystals,'' J. Acoust. Soc. Am. **72**, 1021–1031 (1982).
[10] S. Hirsekorn, ''The scattering of ultrasonic waves by polycrystals. II. Shear waves,'' J. Acoust. Soc. Am. **73**, 1160–1163 (1983).
[11] F. E. Stanke and G. S. Kino, ''A unified theory for elastic wave propagation in polycrystalline materials,'' J. Acoust. Soc. Am. **75**, 665–681 (1984).
[12] R. L. Weaver, ''Diffusion of Ultrasound in Polycrystals,'' J. Mech. Phys. Solids **38**, 55–86 (1990).
[13] J. A. Turner, ''Elastic wave propagation and scattering in heterogeneous, anisotropic media: Textured polycrystalline materials,'' J. Acoust. Soc. Am. **106**, 541–552 (1999).
[14] J. Lemaitre, *A Course on Damage Mechanics* (Springer-Verlag, Berlin, 1992).
[15] D. Krajcinovic, *Damage Mechanics* (North-Holland, Amsterdam, 1996).
[16] S. Nemat-Nasser and M. Hori, *Micromechanics: Overall Properties of Heterogeneous Materials* (North-Holland, Amsterdam, 1993).
[17] M. Kachanov, ''Elastic Solids with Many Cracks and Related Problems,'' Adv. Appl. Mech. **29**, 259–445 (1993).
[18] Z. Hashin and S. Shtrikman, ''A Variational Approach to the Theory of the Elastic Behavior of the Multiphase Materials,'' J. Mech. Phys. Solids **11**, 127–140 (1963).
[19] L. V. Gibiansky and S. Torquato, ''Link Between the Conductivity and Elastic Moduli of Composite Materials,'' Phys. Rev. Lett. **71**, 2927–2930 (1993).
[20] U. Frisch, ''Wave Propagation in Random Media,'' in *Probabilistic Methods in Applied Mathematics*, edited by A. T. Barucha-Reid (Academic, New York, 1968), Vol. 1, pp. 75–198.
[21] F. C. Karal and J. B. Keller, ''Elastic, electromagnetic, and other waves in a random medium,'' J. Math. Phys. **5**, 537–547 (1964).
[22] V. Lubarda and D. Krajcinovic, ''Tensorial Representations of the Effective Elastic Properties of the Damaged Material,'' Int. J. Damage Mech. **3**, 38–56 (1994).
[23] I. Kunin, *Elastic Media with Microstructure II* (Springer-Verlag, Berlin, 1983).
[24] J. Walsh, ''The Effect of Cracks on Compressibility of Rocks,'' J. Geophys. Res. **70**, 381–389 (1965).
[25] B. Budiansky and R. J. O'Connell, ''Elastic Moduli of a Cracked Solid,'' Int. J. Solids Struct. **12**, 81–97 (1976).
[26] M. Kachanov, I. Tsukrov, and B. Shafiro, ''Effective Moduli of Solids with Cavities of Various Shapes,'' Appl. Mech. Rev. **47**, 151–174 (1994).
[27] R. W. Zimmerman, ''The Effect of Microcracks on the Elastic Moduli of Brittle Materials,'' J. Mater. Sci. Lett. **4**, 1457–1460 (1985).
[28] K. Z. Markov and J. R. Willis, ''On the Two-Point Correlation Function for Dispersions of Nonoverlapping Spheres,'' Math. Models Methods Appl. Sci. **8**, 359–377 (1998).
[29] F. E. Stanke, ''Spatial autocorrelation functions for calculations of effective propagation constants in polycrystalline materials,'' J. Acoust. Soc. Am. **80**, 1479–1485 (1986).
[30] S. F. Selleck, E. N. Landis, M. L. Peterson, S. P. Shah, and J. D. Achenbach, ''Ultrasonic Investigation of Concrete with Distributed Damage,'' ACI Mater. J. **95**, 27–36 (1998).

Interactive resonant scattering by a cluster of air bubbles in water

Nikolaos C. Skaropoulos[a)]
International Research Centre for Telecommunications-Transmission and Radar, Delft University of Technology, Mekelweg 4, 2628CD, Delft, The Netherlands

Helen D. Yagridou and Dimitrios P. Chrissoulidis[b)]
Department of Electrical and Computer Engineering, Faculty of Engineering, Aristotle University of Thessaloniki, P.O. Box 1562, GR-54124 Thessaloniki, Greece

(Received 28 March 2002; revised 5 March 2003; accepted 17 March 2003)

An exact, analytical solution is developed for the problem of acoustic-wave scattering from a cluster of ideal, gaseous, spherical bubbles in an unbounded, homogeneous, host fluid. This solution takes into account all modes of oscillation of the bubbles as well as all interactions between them; it is applicable to a wide range of bubble sizes and excitation frequencies. In the low frequency regime, the theory of this paper is shown to reduce to the ''monopole'' approximation, the effect of higher-order modes being non-negligible only for very small bubble-to-bubble separations. A numerical study of interactive backscattering from small clusters, comprising up to three ideal bubbles, is presented. Interactions between the bubbles are shown to produce downward shifts in the resonance frequency of the cluster, when the scattering configuration is symmetric. Furthermore, asymmetries of the scattering configuration are shown to generate sharp resonances at frequencies above the resonance of the symmetric mode. The results of this paper agree with previous theoretical and experimental work.
[DOI: 10.1121/1.1572141]

PACS numbers: 43.20.Fn, 43.30.Ft [LLT]

I. INTRODUCTION

Air bubbles are important scatterers of underwater sound, contributing significantly to the ambient noise in the upper ocean and being frequently used as models of fish.[1–4] The properties of a single, spherical, gas bubble in water have been studied extensively.[5,6] When ensonified by a time-harmonic acoustic wave, the bubble is forced to vibrate, thus giving rise to scattering and absorption of sound. The most characteristic feature is a sharp resonance that occurs at the fundamental Minnaert[7] frequency $k_0\alpha \approx 0.013\,35$, where $k_0 = \omega/c_0$ is the incident wave number, ω is the angular frequency of the excitation, c_0 is the speed of sound in the water, and α is the bubble radius. The scattering cross section at resonance exceeds the geometric cross section of the bubble by several orders of magnitude, despite the dampening effect of sound re-radiation, the heat exchange between the bubble and its surroundings, and the viscosity of water.[8,9]

When a gas bubble is in close proximity to other bubbles or to the surface of the sea, the characteristics of the resonance described above are affected because of multiple scattering. Interactions among adjacent bubbles or between a bubble and the sea surface result in shifts of the resonance frequency as well as in variations of the peak amplitude at resonance. Although such phenomena have been addressed in earlier theoretical[4,10–19] and experimental[10,15,16,19] work, their understanding is still incomplete. The present study aims at contributing to the ongoing research on the topic in two particular areas. First, an exact solution to the problem of sound scattering by a general cluster of ideal bubbles is introduced. This solution is applicable to a wide range of bubble sizes and excitation frequencies; in the low frequency regime, it reduces to the self-consistent monopole approximation (i.e., the ''coupled-oscillator'' method). Second, numerical results are presented for simple clusters of identical and nonidentical bubbles. It is worth noting that analytical solutions for clusters of penetrable spheres as well as numerical results for nonidentical bubbles have not, to the authors' knowledge, been considered elsewhere.

Historically, the theoretical treatment of interactions between bubbles has proceeded along two different ways. A great part of earlier work has been based on the ''monopole'' approximation, namely the assumption that bubbles are one-degree-of-freedom, radially pulsating oscillators, in conjunction with the self-consistent, multiple-scattering formulation of Twersky.[20] This approach yields simple and transparent analytical expressions that are easy to implement numerically, wherein the effects of thermal and viscous damping can easily be incorporated. Nevertheless, the aforesaid approach is only applicable in the low-frequency regime and it has not been validated quantitatively in the case of interacting bubbles in close proximity. Relevant work has been done by Tolstoy[11] and Feuillade,[12] who studied the mechanism of superresonances; by Feuillade, who considered scattering by small schools of fish[4] as well as the propagation and attenuation of sound in bubbly media;[13] and by Ye and Feuillade,[14]

[a)]Part of this work has been done while Dr. Skaropoulos was with the Department of Electrical and Computer Engineering, Faculty of Engineering, Aristotle University of Thessaloniki, Thessaloniki, Greece; electronic mail: n.skaropoulos@irctr.tudelft.nl
[b)]Electronic mail: dpchriss@eng.auth.gr; phone/fax: +30-2310-996334.

and Kapodistrias and Dahl,[15] who studied the case of a bubble next to the sea surface.

An alternative approach has been pursued by Gaunaurd *et al.*,[17] who considered two identical, ''soft'' or ''rigid'' bubbles; and by Gaunaurd and Huang,[18] who considered a single bubble next to the sea surface. The problem is therein formulated in terms of infinite modal series, which represent any mode of oscillation of the bubble; multiple scattering is handled by use of the addition theorem of spherical wave functions. This benchmark solution is exact and applicable to a wide range of bubble sizes and excitation frequencies. Nevertheless, the resulting mathematical expressions are complicated, and damping effects are more difficult to incorporate. Furthermore, the numerical implementation of Ref. 18 exhibited a peculiar feature, namely that the peak amplitude at resonance increases when the bubble approaches the surface, which contradicts intuition (see comment to Ref. 18 and Ref. 14).

Here, we extend the methodology of Gaunaurd and coworkers to formulate an exact solution to the problem of time-harmonic, plane, acoustic-wave scattering by an arbitrary cluster of penetrable spheres in an unbounded, homogeneous, host fluid; the analysis is similar to the one by Ioannidou *et al.*,[21] who considered the corresponding electromagnetic problem. Furthermore, we demonstrate how the modal series formulation is linked to the monopole approximation, first by re-deriving the latter as a particular case of the former, and next, by comparing the two formulations numerically. As the focus is on multiple scattering, the problem is otherwise simplified; hence, we do not consider effects associated with the eventual proximity of the cluster to the sea surface or with damping mechanisms, although such effects may be important for naturally occurring resonant bubbles.

We then present a numerical study of interactive backscattering from clusters composed of up to three bubbles. The bubbles, which are not necessarily identical, are located either in a line or at the corners of an equilateral triangle. The results indicate that collective scattering by two or more nearby bubbles results in downward shifts of the resonance frequency, which is in agreement with earlier work.[10–13] New results for asymmetric scattering configurations, namely cases where the bubbles do not experience the same incident and multiply scattered fields, demonstrate that configurational asymmetries are related to sharp resonances at frequencies above the resonance of the ''symmetric'' mode. Finally, we offer an explanation why the theory of collective scattering of Ref. 13 performs less well for polydisperse than for monodisperse size distributions.

II. SCATTERING GEOMETRY

A cluster composed of P homogeneous, not necessarily identical, penetrable spheres in an unbounded, homogeneous fluid is shown in Fig. 1. The host fluid is characterized by density ρ_0, compressibility κ_0, and sound speed c_0, whereas the medium within each sphere is characterized by density ρ_p, compressibility κ_p, and sound speed c_p, where $p=1,2,...,P$. With regard to the spherical coordinate system

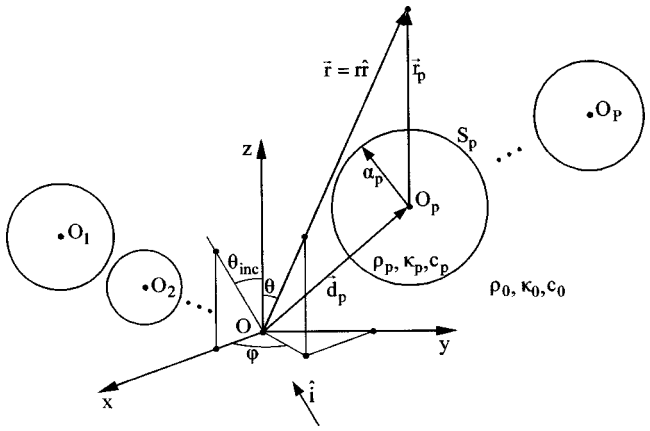

FIG. 1. Geometric configuration.

$(O;r\theta\phi)$, which is attached to an arbitrary point of the host medium close to the cluster, the pth member of the cluster is a penetrable sphere of radius α_p, centered at O_p; the latter is at the tip of the vector $\vec{d}_p$. An individual spherical coordinate system $(O_p;r_p\theta_p\phi_p)$ can be attached to the center of each sphere. A plane acoustic wave, incident from the direction $\hat{i}=\sin\theta_{\rm inc}\hat{x}+\cos\theta_{\rm inc}\hat{z}$ in the xOz plane, is used as excitation. Harmonic time dependence of the type $e^{-j\omega t}$ is assumed for the incident field, the scattered field, and the field within each sphere; the exponential factor $e^{-j\omega t}$ is suppressed throughout the analysis of this paper.

III. ACOUSTIC-WAVE FIELD FORMULATION

The acoustic field in the unbounded host (i.e., exterior) medium is represented by the velocity potential $\psi^{\rm ext}$ which is a solution of the scalar Helmholtz equation $(\nabla^2+k_0^2)\psi=0$; $k_0=\omega/c_0$ is the wave number of the host medium. The exterior field is composed of the incident field (excitation) and the field that is interactively scattered by the cluster of spheres; hence, $\psi^{\rm ext}=\psi^{\rm inc}+\psi^{\rm sca}$ and each term in the right-hand side of this equation is also a solution of the aforementioned scalar Helmholtz equation.

The incident wave, which is of unit amplitude, is represented by the simple closed-form expression $\psi^{\rm inc}=e^{jk_0\hat{i}\cdot\vec{r}}$, but it can also be written as a sum of spherical wave functions

$$\psi^{\rm inc}=\sum_{n=0}^{\infty}\sum_{m=-n}^{n}a_{mn}j_n(k_0r)Y_n^m(\theta,\phi). \tag{1}$$

The radial function $j_n(k_0r)$ is an nth-order spherical Bessel function of the first kind[22] and $Y_n^m(\theta,\phi)=P_n^m(\cos\theta)e^{jm\phi}$ is a spherical harmonic; the latter includes the associated Legendre function $P_n^m(\cos\theta)$.[23] The coefficients

$$a_{mn}=j^n(2n+1)\frac{(n-m)!}{(n+m)!}P_n^m(\cos\theta_{\rm inc}) \tag{2}$$

are the wave amplitudes of the incident wave. In view of the boundary conditions to be applied on the surface of each sphere, it is convenient to express the excitation with respect to the spherical coordinate system $(O_p;r_p\theta_p\phi_p)$, where p

$=1,2,...,P$. Since $\vec{r}=\vec{r}_p+\vec{d}_p$, it follows that $\psi^{\text{inc}}=e^{jk_0\hat{i}\cdot\vec{r}_p}e^{jk_0\hat{i}\cdot\vec{d}_p}$ and therefore

$$\psi^{\text{inc}}=\sum_{n=0}^{\infty}\sum_{m=-n}^{n}a_{mnp}j_n(k_0r_p)Y_n^m(\theta_p,\phi_p), \tag{3}$$

where $a_{mnp}=a_{mn}e^{jk_0\hat{i}\cdot\vec{d}_p}$.

Accordingly, each member of the cluster contributes to the scattered wave as follows:

$$\psi_p^{\text{sca}}=\sum_{n=0}^{\infty}\sum_{m=-n}^{n}b_{mnp}h_n^{(1)}(k_0r_p)Y_n^m(\theta_p,\phi_p). \tag{4}$$

The wave amplitudes b_{mnp} are presently unknown and, although they seem to be associated with a specific sphere, they are implicitly dependent on all members of the cluster, which interactively scatter the incident plane wave. The radial function $h_n^{(1)}(k_0r_p)$ is an nth-order spherical Hankel function of the first kind;[22] if $k_0r_p\gg1$, $h_n^{(1)}(k_0r_p)\approx(-j)^ne^{jk_0r_p}/jk_0r_p$, which is a spherical wave with virtual origin at O_p. Interactive scattering by all spheres is simply obtained by superposition

$$\begin{aligned}\psi^{\text{sca}}&=\psi_1^{\text{sca}}+\psi_2^{\text{sca}}+\cdots+\psi_P^{\text{sca}}\\&=\sum_{p=1}^{P}\sum_{n=0}^{\infty}\sum_{m=-n}^{n}b_{mnp}h_n^{(1)}(k_0r_p)Y_n^m(\theta_p,\phi_p).\end{aligned} \tag{5}$$

Since $h_n^{(1)}(k_0r_p)$ obeys the radiation condition at infinity, so do $\psi_1^{\text{sca}},\psi_2^{\text{sca}},\ldots,\psi_P^{\text{sca}}$. By application of the sagittal approximation $e^{jk_0r_p}/r_p\approx e^{jk_0(r-\vec{d}_p\cdot\hat{s})}/r$, where $\hat{s}$ is the unit vector along the scattering direction, it can be proven that ψ^{sca} obeys the radiation condition, too.

The field ψ_p^{int} in the interior of the pth sphere is obtained by solving $(\nabla^2+k_p^2)\psi=0$; $k_p=\omega/c_p$ is the wave number of that medium. The following expansion in spherical harmonics is used

$$\psi_p^{\text{int}}=\sum_{n=0}^{\infty}\sum_{m=-n}^{n}c_{mnp}j_n(k_pr_p)Y_n^m(\theta_p,\phi_p) \tag{6}$$

and the wave amplitudes c_{mnp} are presently unknown, too.

IV. DETERMINATION OF THE WAVE AMPLITUDES

Both sets of wave amplitudes $b_{mn1},b_{mn2},\ldots,b_{mnP}$ and $c_{mn1},c_{mn2},\ldots,c_{mnP}$ are determined by application of the boundary conditions on the surface of any sphere. Enforcing the continuity of the acoustic pressure and the continuity of the normal component of the particle velocity on S_1, $S_2,\ldots,S_P$ requires use of the translational addition theorem[24,25] for scalar, spherical wave functions $j_n(kr)Y_n^m(\theta,\phi)$ or $h_n^{(1)}(kr)Y_n^m(\theta,\phi)$.

The continuity of the acoustic pressure on S_q, where $q\in[1,P]$, is expressed by $(\psi^{\text{ext}}-\psi_q^{\text{int}})_{r_q=\alpha_q}=0$. By use of Eqs. (3), (5), and (6), the following equation is obtained:

$$\begin{aligned}&\sum_{n=0}^{\infty}\sum_{m=-n}^{n}[a_{mnq}j_n(k_0\alpha_q)+b_{mnq}h_n^{(1)}(k_0\alpha_q)\\&\quad-c_{mnq}j_n(k_q\alpha_q)]Y_n^m(\theta_q,\phi_q)\\&\quad+\sum_{\substack{p=1\\p\neq q}}^{P}\sum_{n=0}^{\infty}\sum_{m=-n}^{n}b_{mnp}\sum_{\nu=0}^{\infty}\sum_{\mu=-\nu}^{\nu}Q_{mn\mu\nu}^{(3)}(r_{pq},\theta_{pq},\phi_{pq})\\&\quad\times j_\nu(k_0\alpha_q)Y_\nu^\mu(\theta_q,\phi_q)=0,\end{aligned} \tag{7}$$

where r_{pq}, θ_{pq}, ϕ_{pq} are the coordinates of O_q with respect to $(O_p;r_p\theta_p\phi_p)$ and the coupling coefficient $Q_{mn\mu\nu}^{(3)}(r_{pq},\theta_{pq},\phi_{pq})$, which is associated with the aforementioned addition theorem, is defined in the Appendix. If $\vec{d}_{pq}=\vec{d}_q-\vec{d}_p$ is the vector from O_p to O_q, then $r_{pq}=|\vec{d}_{pq}|$, θ_{pq} is the angle between $\vec{d}_{pq}$ and the z axis, and ϕ_{pq} is the angle between $\vec{d}_{pq}$ and the x axis. Equation (7) is multiplied by $\overline{Y_l^k(\theta_q,\phi_q)}$, which is the complex conjugate of $Y_l^k(\theta_q,\phi_q)$, and subsequently integrated over S_q, thus taking advantage of the orthogonality of spherical harmonics. The end result is the following equation:

$$\begin{aligned}&a_{klq}j_l(k_0\alpha_q)+b_{klq}h_l^{(1)}(k_0\alpha_q)-c_{klq}j_l(k_q\alpha_q)\\&\quad+j_l(k_0\alpha_q)\sum_{\substack{p=1\\p\neq q}}^{P}\sum_{n=0}^{\infty}\sum_{m=-n}^{n}b_{mnp}Q_{mnkl}^{(3)}(r_{pq},\theta_{pq},\phi_{pq})=0.\end{aligned} \tag{8}$$

The continuity of the normal component of the particle velocity on S_q is expressed by $(\rho_0^{-1}\partial\psi^{\text{ext}}/\partial r_q-\rho_q^{-1}\partial\psi_q^{\text{int}}/\partial r_q)_{r_q=\alpha_q}=0$. By retracing the steps taken above, the following equation is obtained:

$$\begin{aligned}&a_{klq}j_l'(k_0\alpha_q)+b_{klq}h_l'^{(1)}(k_0\alpha_q)-\frac{k_q\rho_0}{k_0\rho_q}c_{klq}j_l'(k_q\alpha_q)\\&\quad+j_l'(k_0\alpha_q)\sum_{\substack{p=1\\p\neq q}}^{P}\sum_{n=0}^{\infty}\sum_{m=-n}^{n}b_{mnp}Q_{mnkl}^{(3)}(r_{pq},\theta_{pq},\phi_{pq})=0,\end{aligned} \tag{9}$$

wherein we have used the convention that a prime over a function name denotes differentiation with respect to the argument.

The wave amplitudes c_{klq} can be eliminated from Eqs. (8) and (9) through multiplying them by $j_l'(k_q\alpha_q)$ and $j_l(k_q\alpha_q)$, respectively, and then subtracting one from the other. The resulting equation involves only the wave amplitudes $b_{mn1},b_{mn2},\ldots,b_{mnP}$ of the interactively scattered wave:

$$\begin{aligned}b_{klq}&=C_l(k_0,k_q,\xi_q,\alpha_q)\\&\quad\times\left[a_{klq}+\sum_{\substack{p=1\\p\neq q}}^{P}\sum_{n=0}^{\infty}\sum_{m=-n}^{n}b_{mnp}Q_{mnkl}^{(3)}(r_{pq},\theta_{pq},\phi_{pq})\right].\end{aligned} \tag{10}$$

The coefficients

$$C_l(k_0,k_q,\xi_q,\alpha_q)$$

$$= -\frac{j_l'(k_0\alpha_q)j_l(k_q\alpha_q)-\xi_q j_l(k_0\alpha_q)j_l'(k_q\alpha_q)}{h_l'^{(1)}(k_0\alpha_q)j_l(k_q\alpha_q)-\xi_q h_l^{(1)}(k_0\alpha_q)j_l'(k_q\alpha_q)}, \tag{11}$$

where $\xi_q=k_q\rho_0/k_0\rho_q$, coincide with those of a single sphere.[18] Hence, in the right-hand side of Eq. (10) the first term in the brackets describes single scattering from the qth sphere, whereas the second term in the brackets incorporates all interactions between the qth sphere and other members of the cluster.

The procedure leading to Eq. (10) can be repeated for any value of the indices $q\in[1,P]$, k, and l, thus yielding an infinite set of linear equations, which can be solved by truncation and matrix inversion. If the condition $n\leqslant N$ is imposed, the number of unknowns is limited to $P(N+1)^2$ and the set of equations can be written in block-matrix form as follows:

$$\begin{bmatrix} \mathbf{\Lambda_{11}} & \mathbf{\Lambda_{12}} & \cdots & \mathbf{\Lambda_{1P}} \\ \mathbf{\Lambda_{21}} & \mathbf{\Lambda_{22}} & \cdots & \mathbf{\Lambda_{2P}} \\ \vdots & \vdots & \ddots & \vdots \\ \mathbf{\Lambda_{P1}} & \mathbf{\Lambda_{P2}} & \cdots & \mathbf{\Lambda_{PP}} \end{bmatrix} \begin{bmatrix} \mathbf{B_1} \\ \mathbf{B_2} \\ \vdots \\ \mathbf{B_P} \end{bmatrix} = \begin{bmatrix} \mathbf{A_1} \\ \mathbf{A_2} \\ \vdots \\ \mathbf{A_P} \end{bmatrix}. \tag{12}$$

$\mathbf{B_q}$, where $q\in[1,P]$, is a $(N+1)^2\times 1$ vector that contains the scattered wave amplitudes b_{mnq} of the qth sphere; its elements are arranged according to the following rule:

$$B_q(j)=b_{mnq}, \quad j=\sum_{\hat{n}=0}^{n}(2\hat{n}+1)+(m-n). \tag{13}$$

$\mathbf{A_q}$, where $q\in[1,P]$, is a $(N+1)^2\times 1$ vector with the following elements:

$$A_q(i)=C_l(k_0,k_q,\xi_q,\alpha_q)a_{klq},$$
$$i=\sum_{\hat{l}=0}^{l}(2\hat{l}+1)+(k-l). \tag{14}$$

The $(N+1)^2\times(N+1)^2$ matrices $\mathbf{\Lambda_{qq}}$ represent noninteractive scattering from the qth sphere, their elements being given by

$$\Lambda_{qq}(i,j)=\delta_{ij}, \tag{15}$$

whereas the matrices $\mathbf{\Lambda_{pq}}$ with $p\neq q$ represent the coupling from the pth to the qth sphere of the cluster; their elements are given below

$$\Lambda_{pq}(i,j)=-C_l(k_0,k_q,\xi_q,\alpha_q)Q^{(3)}_{mnkl}(r_{pq},\theta_{pq},\phi_{pq}), \tag{16}$$

and the indices i, j are specified by Eqs. (14), (13), respectively.

In the particular case where all bubbles are located in a line, it is expedient to orient the z axis of the reference frame $(O;r\theta\phi)$ along the line through all scattering centers. Hence, $\vec{d}_p=d_p\hat{z}$, $p=1,2,...,P$, and Eq. (10) can be simplified as follows:

$$b_{klq}=C_l(k_0,k_q,\xi_q,\alpha_q)$$
$$\times\left[a_{klq}+\sum_{\substack{p=1\\p\neq q}}^{P}\sum_{n=|k|}^{\infty}b_{knp}Q^{(3)}_{knkl}(r_{pq},\theta_{pq},0)\right]. \tag{17}$$

Equation (17) reduces to Eqs. (23) of Ref. 17 in the particular case of two identical "soft" spheres. Evidently, $r_{pq}=r_{qp}=|d_q-d_p|$ and θ_{pq} equals 0 or π, depending on whether O_q is above or below O_p, respectively. The simplified coupling coefficients $Q^{(3)}_{knkl}(r_{pq},0,0)$ and $Q^{(3)}_{knkl}(r_{pq},\pi,0)$ that may appear in Eq. (17) are defined in the Appendix. It is worth noting that Eq. (17) involves only wave amplitudes with the first subscript k. Thus, instead of solving for the $P(N+1)^2$ unknowns b_{mnq}, where $q\in[1,P]$, $n\in[0,N]$, and $m\in[-n,n]$, simultaneously, as was the case for a general cluster of bubbles [see Eq. (10)], it is now possible to break down the problem to $(2N+1)$ smaller ones, each for a particular value of k. The latter problems involve the $P(N-|k|+1)$ unknowns b_{knq}, where $q\in[1,P]$ and $n\in[|k|,N]$. The resulting set of linear equations is given below in block-matrix form

$$\begin{bmatrix} \mathbf{\Lambda^k_{11}} & \mathbf{\Lambda^k_{12}} & \cdots & \mathbf{\Lambda^k_{1P}} \\ \mathbf{\Lambda^k_{21}} & \mathbf{\Lambda^k_{22}} & \cdots & \mathbf{\Lambda^k_{2P}} \\ \vdots & \vdots & \ddots & \vdots \\ \mathbf{\Lambda^k_{P1}} & \mathbf{\Lambda^k_{P2}} & \cdots & \mathbf{\Lambda^k_{PP}} \end{bmatrix} \begin{bmatrix} \mathbf{B^k_1} \\ \mathbf{B^k_2} \\ \vdots \\ \mathbf{B^k_P} \end{bmatrix} = \begin{bmatrix} \mathbf{A^k_1} \\ \mathbf{A^k_2} \\ \vdots \\ \mathbf{A^k_P} \end{bmatrix}. \tag{18}$$

$\mathbf{B^k_q}$ and $\mathbf{A^k_q}$, where $q\in[1,P]$, contain $(N-|k|+1)$ elements which are arranged as follows:

$$B^k_q(j)=b_{knq}, \quad n=|k|+(j-1). \tag{19}$$

$$A^k_q(i)=C_l(k_0,k_q,\xi_q,\alpha_q)a_{klq}, \quad l=|k|+(i-1). \tag{20}$$

Finally, $\mathbf{\Lambda^k_{qq}}$ and $\mathbf{\Lambda^k_{pq}}$ with $p\neq q$ are defined as follows:

$$\Lambda^k_{qq}(i,j)=\delta_{ij}, \tag{21}$$

$$\Lambda^k_{pq}(i,j)=-C_l(k_0,k_q,\xi_q,\alpha_q)Q^{(3)}_{knkl}(r_{pq},\theta_{pq},0), \tag{22}$$

where the indices i and j are defined according to Eqs. (20) and (19), respectively.

V. FAR-FIELD SCATTERING CHARACTERISTICS

Far from the origin of coordinates (i.e., for $k_0r\gg 1$), the scattered wave acquires the form of a diverging spherical wave $\psi^{\mathrm{sca}}=f(\theta,\phi)e^{jk_0r}/r$; the direction-dependent factor $f(\theta,\phi)$ is the scattering amplitude. By use of the asymptotic expression of spherical Hankel functions for large arguments and of the sagittal approximation (see Sec. III), it can be verified from Eq. (5) that

$$f(\theta,\phi)=\frac{1}{k_0}\sum_{p=1}^{P}\sum_{n=0}^{\infty}\sum_{m=-n}^{n}(-j)^{n+1}$$
$$\times b_{mnp}e^{-jk_0\vec{d}_p\cdot\hat{s}}Y^m_n(\theta,\phi), \tag{23}$$

where $\hat{s}$ is the unit vector along the scattering direction (Fig. 1). Subsequently, it is possible to determine the differential scattering cross section $\sigma_d=|f(\theta,\phi)|^2$ and the backscattering cross section $\sigma_b=|f(\pi-\theta_{\mathrm{inc}},\pi)|^2$.

The scattering amplitude, as determined above, takes into account every possible interaction among members of the cluster. It is also useful, for the sake of comparisons, to determine the scattering amplitude in the case of single scattering, that is, when all interactions are omitted. By use of the formulation of Sec. IV [see Eq. (10)], it can be shown that the noninteractive scattering amplitude can be expressed as follows:

$$f_{NI}(\theta,\phi)=\frac{1}{k_0}\sum_{p=1}^{P}\sum_{n=0}^{\infty}\sum_{m=-n}^{n}(-j)^{n+1}e^{jk_0\vec{d}_p\cdot(\hat{i}-\hat{s})}\times C_n(k_0,k_p,\xi_p,\alpha_p)a_{mn}Y_n^m(\theta,\phi). \tag{24}$$

Accordingly, it is possible to define $\sigma_{NI,d}=|f_{NI}(\theta,\phi)|^2$ and $\sigma_{NI,b}=|f_{NI}(\pi-\theta_{\rm inc},\pi)|^2$ as the noninteractive version of the differential and backscattering cross section, respectively.

It is worth noting that although multiple-scattering effects have been ignored in the derivation of Eq. (24), interference effects have been retained. This can better be illustrated by studying the particular case of a linear array of identical equidistant bubbles. If d is the center-to-center separation between adjacent bubbles and $\sigma_{s,b}$ is the backscattering cross section of any single bubble, it can be proven by use of Eq. (24) that the noninteractive backscattering cross section of the aforementioned array, which comprises P bubbles, is given by $\sigma_{NI,b}=P^2\sigma_{s,b}\,\mathrm{sinc}^2(k_0Pd\cos\theta_{\rm inc})/\mathrm{sinc}^2(k_0d\cos\theta_{\rm inc})$, where $\mathrm{sinc}(x)=x^{-1}\sin x$. On endfire incidence ($\theta_{\rm inc}=0°$) the normalized noninteractive backscattering cross section $\sigma_{NI,b}/\sigma_{s,b}$ varies with the normalized center-to-center separation k_0d periodically in the range $[0,P^2]$; the period of those variations is $k_0d=\pi$. On broadside incidence ($\theta_{\rm inc}=90°$) $\sigma_{NI,b}/\sigma_{s,b}$ is equal to P^2 regardless of k_0d.

VI. LOW-FREQUENCY APPROXIMATION

The analysis of the preceding sections has taken into account all modes of oscillation of the bubbles: The incident, scattered, and interior fields [see Eqs. (3), (4), and (6), respectively] have been expanded into infinite sums of spherical harmonics. This general formulation is applicable to a wide range of excitation frequencies and bubble sizes. In the low-frequency regime, wherein the wavelength of the incident wave is much greater than the radius of any bubble in the cluster, it is commonly assumed (see, for instance, Ref. 14) that the bubbles only pulsate radially—i.e., the bubbles are assumed to be one-degree-of-freedom oscillators. This is customarily referred to as the ''monopole'' approximation. The purpose of this section is to demonstrate how the analysis presented in this paper reduces to the monopole approximation in the low-frequency regime.

The case of a single bubble at the origin of coordinates is considered first. By neglecting terms of order higher than zero in Eq. (23), use of the identity $P_0^0(\cos\theta)=1$, and of Eqs. (10) and (2), it can be shown that the scattering amplitude of a single bubble is given by

$$f_1=\frac{1}{jk_0}C_0(k_0,k_1,\xi_1,\alpha_1). \tag{25}$$

Note that the dependence on the angular variables θ and ϕ has vanished—i.e., the scattered field is now omnidirectional. The coefficient C_0, which appears in the right-hand side of Eq. (25), involves Bessel and Hankel functions, as well as derivatives thereof, with arguments $k_0\alpha_1$ or $k_1\alpha_1$ [see Eq. (11)]. In the low-frequency regime, it holds $k_0\alpha_1$, $k_1\alpha_1\ll 1$ and, therefore, the following approximations can be used:

$$j_0(z)\approx 1,\quad j_0'(z)\approx -z/3,\qquad h_0^{(1)}(z)\approx 1-j/z,\quad h_0'^{(1)}(z)\approx -z/3+j/z^2. \tag{26}$$

Substitution of Eqs. (26) into Eq. (11) and some straightforward algebra finally yield

$$f_1=\frac{\alpha_1}{\omega_1^2/\omega^2-1-jk_0\alpha_1}, \tag{27}$$

where

$$\omega_1=\frac{1}{\alpha_1}\sqrt{\frac{3}{\rho_0(\kappa_1-\kappa_0)}} \tag{28}$$

is the resonance frequency of the single bubble. Eqs. (27) and (28) coincide with those derived by use of the monopole approximation[14] in the case of an ideal bubble.

The case of P interactively scattering bubbles is considered next. Neglecting terms of order higher than zero, Eq. (4) yields the following expression for the field scattered by the pth bubble:

$$\psi_p^{\rm sca}=\frac{b_{00p}}{jk_0}\frac{e^{jk_0r_p}}{r_p}. \tag{29}$$

The wave amplitudes b_{00p} can be determined from Eq. (10), which assumes the following form in the low-frequency regime:

$$b_{00p}=C_0(k_0,k_p,\xi_p,\alpha_p)\times\left[a_{00p}+\sum_{\substack{q=1\\q\neq p}}^{P}b_{00q}Q_{0000}^{(3)}(r_{qp},\theta_{qp},\phi_{qp})\right]. \tag{30}$$

By use of Eq. (A1), it can be shown that

$$Q_{0000}^{(3)}(r_{qp},\theta_{qp},\phi_{qp})=h_0^{(1)}(k_0r_{qp})=\frac{e^{jk_0r_{qp}}}{jk_0r_{qp}}. \tag{31}$$

Furthermore, $a_{00p}=e^{jk_0\hat{i}\cdot\vec{d}_p}$ and $C_0(k_0,k_p,\xi_p,\alpha_p)=jk_0f_p$ [see Eq. (25)]. Thus, Eq. (30) can be expressed as

$$\frac{b_{00p}}{jk_0}=f_p\left[e^{jk_0\hat{i}\cdot\vec{d}_p}+\sum_{\substack{q=1\\q\neq p}}^{P}\frac{b_{00q}}{jk_0}\frac{e^{jk_0r_{qp}}}{r_{qp}}\right], \tag{32}$$

which, apart from some differences in notation, coincides with Eq. (10) of Ref. 14. The latter was derived by use of the monopole approximation and of Twersky's self-consistent multiple-scattering formulation.[20] Thus, the results of the monopole approximation for ideal bubbles can be re-derived as a particular case of the general formulation presented herein.

VII. RESULTS AND DISCUSSION

Numerical results for simple clusters of two or three bubbles are presented next. The emphasis is on backscattering from resonant bubbles. Moreover, interest is in the effects of interactions among the bubbles on their resonance frequency as well as in the peak backscattering at resonance of the cluster as a whole. Quantitative information, which, to the authors' knowledge, is not available elsewhere, is provided about the effects of higher-order modes of the modal solution (see Secs. III and VI) and about the behavior of clusters composed of nonidentical bubbles. Wherever applicable, the results documented here are in agreement with previous theoretical and experimental work.

The first set of results (Fig. 2) deals with backscattering from two, identical, resonant-size ($k_0\alpha=0.013\,35$) bubbles. Figure 2(a) depicts the case of endfire incidence. An interference pattern is apparent in the noninteractive case (thin curve). The normalized backscattering cross section of the cluster varies periodically between the values 0 and 4, which correspond to destructive and constructive interference, respectively (see also Sec. V). It is worth noting that the aforesaid interference is constructive at small separations; as the wavelength of the incident wave is much larger than the radius of the bubbles, the bubbles oscillate in phase and, thus, they interfere constructively. In the interactive case (thick curve), the pattern is somewhat more complicated because of multiple-scattering effects. At small separations, multiple scattering results in significant decrease in backscatter (see also Ref. 16, where similar experimental and theoretical findings have been reported for bubbles in the size range $0.2<k_0\alpha<0.35$), whereas at large separations, multiple-scattering effects gradually vanish and the interactive backscattering cross section coincides with the noninteractive one.

On broadside incidence [Fig. 2(b)], the two bubbles always oscillate in phase, regardless of their separation. Thus, there is no interference pattern in the noninteractive backscattering cross section (thin curve), and multiple scattering effects are easier to assess. Because the emphasis in this work is on interactions between bubbles, most of the results that follow deal with interference-free cases. The latter, though, are particular cases: Multiple scattering appears together with interference in most cluster configurations. As in the case of endfire incidence [see Fig. 2(a)], multiple-scattering effects are more evident at small separations, reducing the backscattering cross section. With increasing separation, the interactive backscattering cross section follows an oscillatory pattern with decreasing amplitude. Figure 2(b) also includes two additional curves, which depict interactive scattering by the pair of bubbles at frequencies below and above resonance. Evidently, interactions persist for far greater separations at the resonance frequency than either below or above it.

The curves in Fig. 2 have been produced with truncation number $N=4$, which ensures four-digit convergence of the results. It is interesting to investigate how the aforesaid results compare with those of the monopole approximation, which can be reproduced by setting $N=0$ (see Sec. VI). This comparison is made in Fig. 3, wherein broadside incidence is

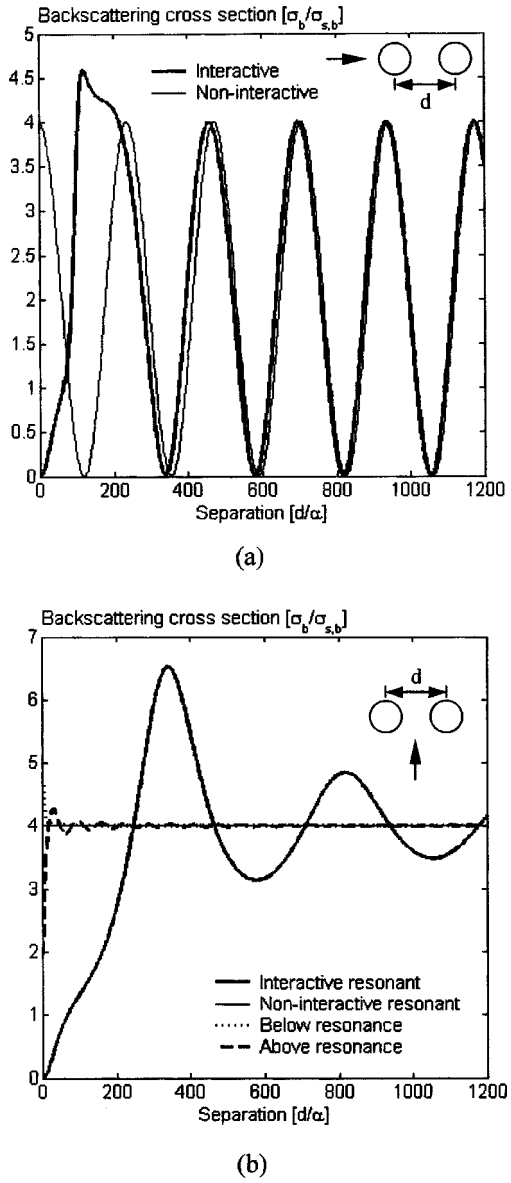

FIG. 2. Normalized interactive ($\sigma_b/\sigma_{s,b}$) and noninteractive ($\sigma_{NI,b}/\sigma_{s,b}$) backscattering cross section of twin, resonant ($k_0\alpha=0.013\,35$) bubbles versus normalized separation d/α; (a) endfire ($\theta_{\text{inc}}=0°$) and (b) broadside ($\theta_{\text{inc}}=90°$) incidence.

considered. Evidently, the effects of higher-order modes vanish at large separations and they are discernible, albeit marginal, only when the bubbles are in close proximity. Thus, the qualitative conclusion of Ref. 14, namely that the assumption of monopole scattering is valid near resonance except possibly when the bubbles are in contact, is herein confirmed quantitatively.

Figure 4 depicts the backscattering cross section of three, identical bubbles. The bubbles are either located at the corners of an equilateral triangle (solid curve) or in a line (dashed curve); in either case, the ensonifying field is normal to the plane of the figure, and, therefore, the bubbles oscillate in phase. On the whole, the behavior of the three-bubble cluster is similar to the two-bubble one, but the amplitude of the fluctuations of the interactive backscattering cross section is now somewhat greater. The more compact configuration (equilateral triangle) favors interactions more than the less

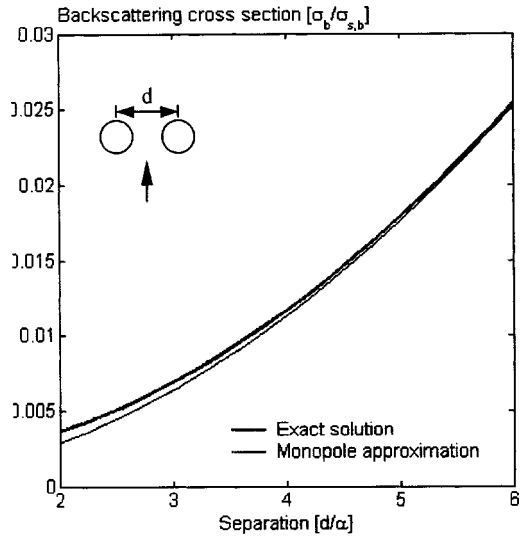

FIG. 3. Normalized interactive ($\sigma_b/\sigma_{s,b}$) backscattering cross section of twin, resonant ($k_0\alpha=0.013\,35$) bubbles; exact formulation of Secs. III–V and monopole approximation; broadside ($\theta_{\text{inc}}=90°$) incidence.

compact one (bubbles in a line). Nevertheless, the two configurations produce almost identical backscattering at small separations; as the incident wavelength is much greater than the size of the cluster as a whole, details of the cluster configuration are not resolved.

The frequency dependence of the backscattering cross section of a pair of bubbles is discussed next (Fig. 5); pairs of identical and nonidentical bubbles are considered. In the former case [Fig. 5(a)], the resonance frequency of the cluster is shifted downwards because of the interactions between the bubbles, the shift being greater the smaller the separation between the bubbles; this is in agreement with results documented by Feuillade[12,13] as well as by Strasberg[10] (case of bubble next to a rigid surface), wherein an experiment has been conducted. The peak amplitude at resonance is less than

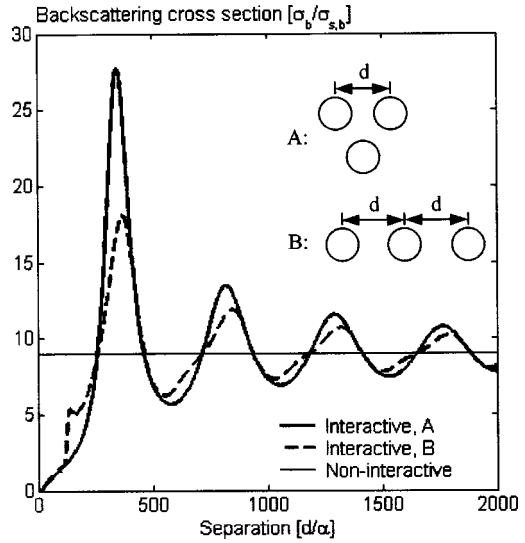

FIG. 4. Normalized interactive ($\sigma_b/\sigma_{s,b}$) and noninteractive ($\sigma_{NI,b}/\sigma_{s,b}$) backscattering cross section of three, identical, equidistant, resonant ($k_0\alpha=0.013\,35$) bubbles versus normalized separation d/α; the direction of incidence is normal to the plane of the figure.

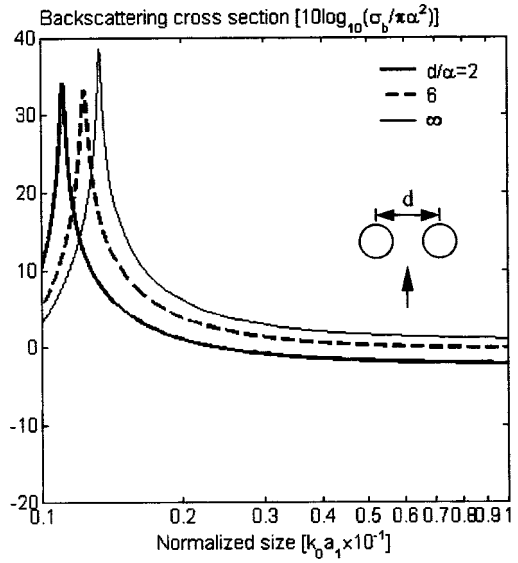

(a)

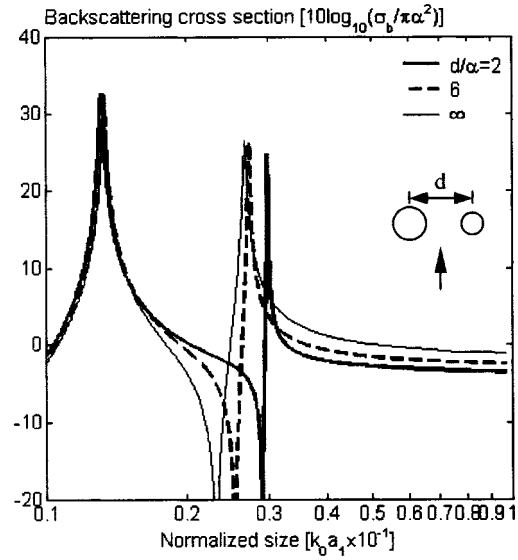

(b)

FIG. 5. Interactive resonance by two bubbles versus $k_0\alpha_1$ for various separations; (a) identical ($\alpha_1=\alpha_2$) and (b) nonidentical ($\alpha_1=2\alpha_2$) bubbles.

that of the case of noninteracting bubbles (i.e., $d/\alpha=\infty$), and it fluctuates with separation.

The cluster of nonidentical bubbles [Fig. 5(b)] exhibits more complex behavior with two resonances that correspond to the big and the small bubble; their nominal positions (i.e., those with the interactions neglected) are at $k_0a_1=0.013\,35$ and $k_0a_2=0.013\,35$, the latter implying that $k_0a_1=0.026\,70$. Interactions between the bubbles affect the resonance frequency of each bubble in a different way. On the one hand, the resonance frequency of the big bubble is shifted downwards, as in the case of identical bubbles, wherein, though, the shift was much more pronounced [see Fig. 5(a)]. On the other hand, the resonance frequency of the small bubble is shifted upwards, the effect being most significant for small separations. It is worth noting that this may partly explain why the theory of collective scattering by Feuillade,[13] which assumes only downwards shifts for

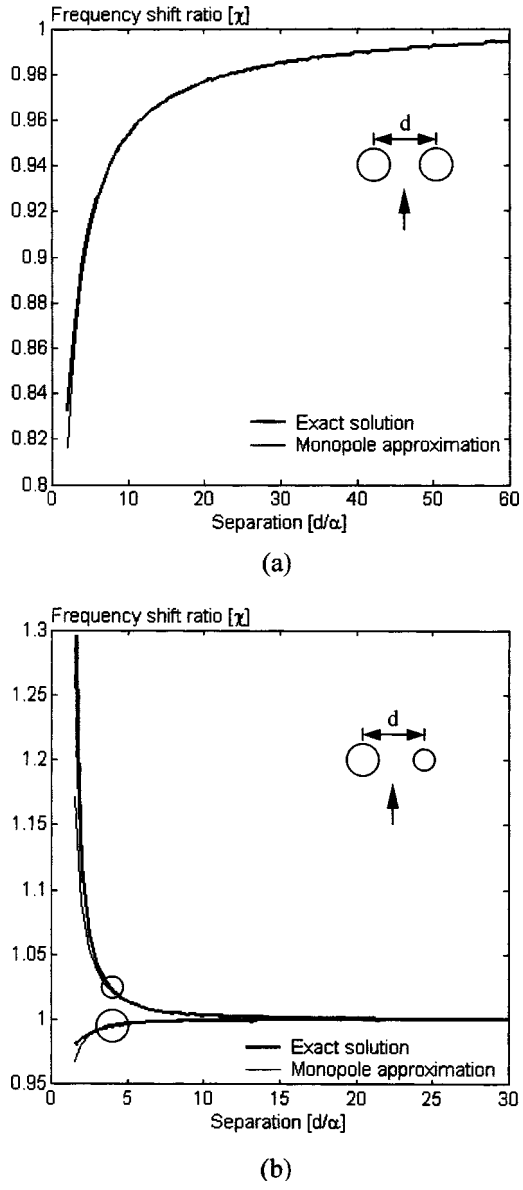

FIG. 6. Frequency-shift ratio χ of two interacting bubbles versus separation; (a) identical ($\alpha_1=\alpha_2$) and (b) nonidentical ($\alpha_1=2\alpha_2$) bubbles.

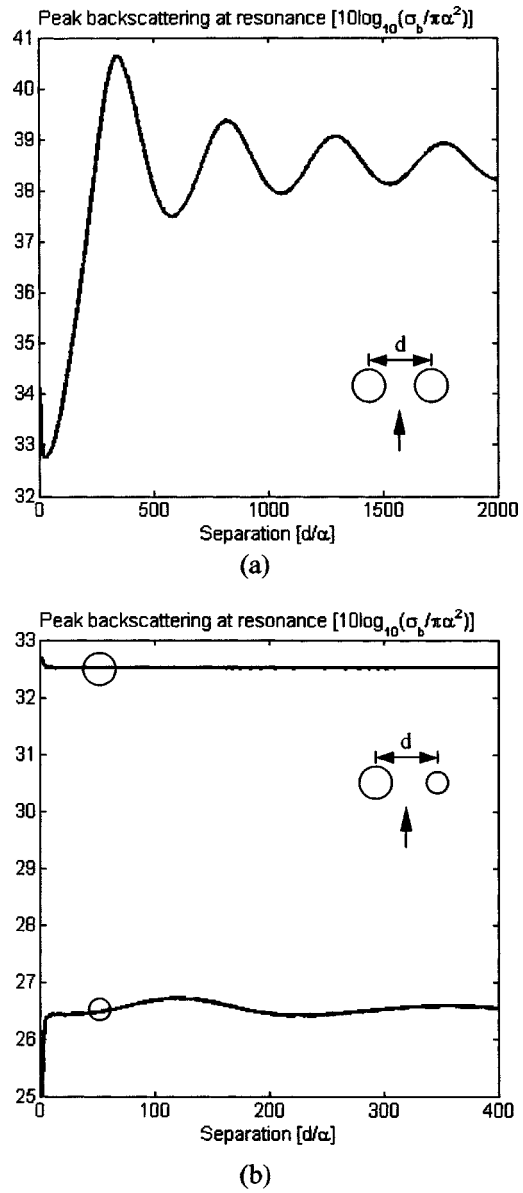

FIG. 7. Peak backscattering cross section at resonance of two interacting bubbles versus separation; (a) identical ($\alpha_1=\alpha_2$) and (b) nonidentical ($\alpha_1=2\alpha_2$) bubbles.

bubbles of any size, performs much better in the monodisperse than in the polydisperse case; this point is discussed further in what follows.

A more detailed view to the dependence on bubble-to-bubble separation of the resonance frequency and of the peak backscattering at resonance of a pair of bubbles is provided by Figs. 6 and 7, respectively. The frequency-shift ratio χ, which is defined as the ratio between the interactive and the noninteractive resonance frequency, is plotted in Fig. 6. When the bubbles are identical [Fig. 6(a)], χ increases monotonously with separation, asymptotically approaching unity for large separations. The same holds for the frequency-shift ratio of the big bubble when the bubbles are nonidentical [Fig. 6(b)], in which case, though, the range of values of χ is smaller and the asymptotic value $\chi=1$ is reached at smaller separations. In contrast, the frequency-shift ratio of the small bubble is always larger than unity and it decreases monotonously with separation. Figure 6 includes results derived by use of the monopole approximation, too. These results agree very well with those of the exact solution, the discrepancies being discernible only when the bubbles are very close to each other. The peak backscattering at resonance can be seen (Fig. 7) to fluctuate with separation, the effect being far more pronounced for identical bubbles [Fig. 7(a)] than it is for nonidentical bubbles [Fig. 7(b)]. As a whole, Figs. 6 and 7 indicate that interactions persist for larger separations when the bubbles are identical, which is in agreement with intuition. In the case of nonidentical bubbles, a resonant bubble, may it be the big or the small one, always interacts with a nonresonant one, which scatters sound much less effectively. In contrast, in the case of identical bubbles, the interactions take place between two resonant bubbles, which are both very effective scatterers of sound.

The last set of results (Fig. 8) focuses on three-bubble clusters. Its purpose is to investigate how the scattering con-

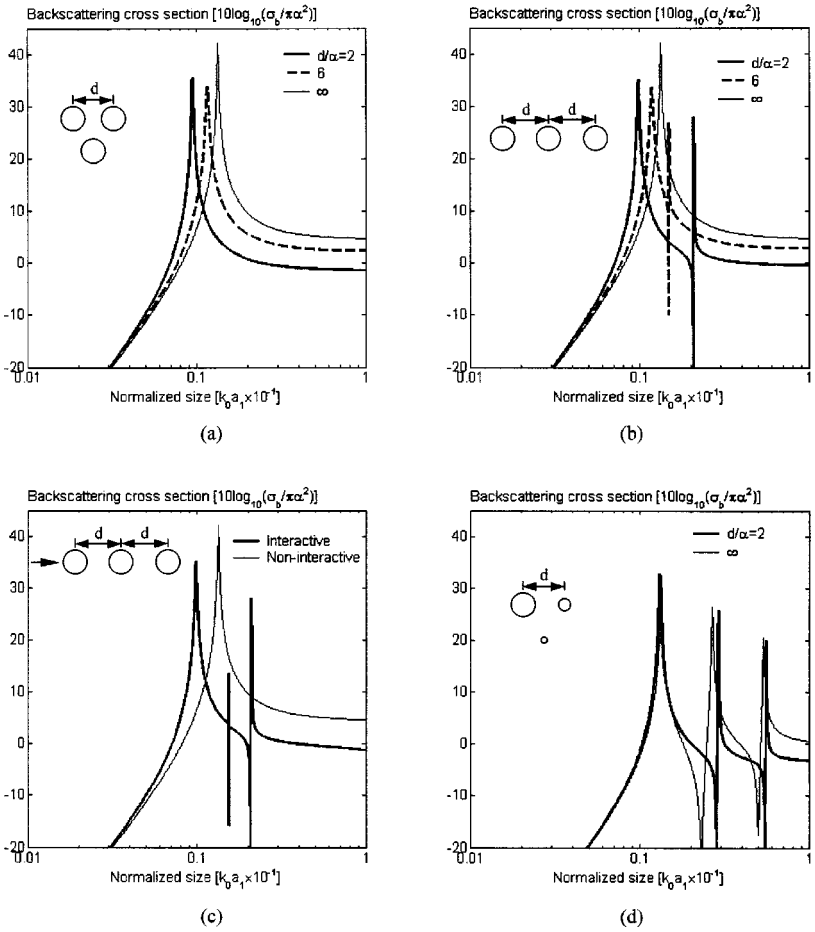

FIG. 8. Interactive resonance by three, equidistant bubbles versus the size parameter $k_0\alpha_1$ of the biggest bubble; (a) identical bubbles ($\alpha_1=\alpha_2=\alpha_3$) at the corners of an equilateral triangle; (b),(c) identical bubbles in a line; (d) nonidentical bubbles ($\alpha_1=2\alpha_2=4\alpha_3$) forming an equilateral triangle; except in (c), incidence is normal to the plane of the figure.

figuration and asymmetries thereof may affect the behavior of the bubbles at resonance. The discussion of the results makes use of the terminology introduced in Refs. 12 and 13, where interactive scattering by clusters of bubbles has been categorized in ''symmetric modes,'' whereby bubbles oscillate in phase, and ''antisymmetric modes,'' whereby bubbles oscillate in antiphase. The first case studied herein [Fig. 8(a)] is that of three identical bubbles that form an equilateral triangle, with the incidence direction perpendicular to the plane defined by their centers. This configuration is perfectly symmetric in the sense that all bubbles experience the same incident and multiply scattered fields. Interactions among the bubbles result in downward shifts of their (common) resonance frequency, in agreement with the findings of Ref. 13. Next, three identical bubbles in a line, either on broadside [Fig. 8(b)] or endfire [Fig. 8(c)] incidence are considered. Both cases are characterized by additional, very sharp, peaks at frequencies above the resonance of the symmetric mode. These peaks are manifestations of asymmetries in the scattering configuration; on broadside incidence, although all bubbles experience the same incident field, the bubble in the middle experiences different multiply scattered field than the bubbles at the edges; on endfire incidence, all three bubbles experience different incident and multiply scattered fields. Similar findings were also documented for pairs of bubbles in asymmetric configurations in a recent experimental work;[19] the antisymmetric peaks reported there are less sharp because of damping effects. It is worth noting that, although the characteristics of the antisymmetric peaks depend strongly on the scattering configuration, those of the symmetric mode are only slightly affected; this is in agreement with Ref. 13, which predicted that the symmetric mode should be dominant in cases where the scattering characteristics are important only in a statistical sense, namely in terms of ensemble averages over all possible configurations. Nevertheless, the assumption that the symmetric mode alone suffices to describe the characteristics of a cluster of bubbles breaks down as soon as bubbles of different sizes are considered. This is apparent in Fig. 8(d), where three different bubbles forming an equilateral triangle are considered. A downward shift of the resonance frequency is observed only for the biggest bubble, and still it is marginal, whereas the resonance frequencies of the smaller bubbles are shifted upwards.

VIII. CONCLUSIONS

An exact solution to the problem of acoustic wave scattering by a general cluster of ideal, not necessarily identical, gas bubbles in an unbounded homogenous host fluid has been developed in Secs. III–V. This solution accounts for all modes of oscillation of the bubbles, as well as for all interactions among the bubbles. Therefore, it can be applied to a wide range of bubble sizes and excitation frequencies.

In the low frequency regime, the above theory reduces to the monopole approximation (Sec. VI), which can, therefore, be perceived as a particular case of the general solution. Numerical comparisons between the two theories have dem-

onstrated that the monopole approximation is well suited for studies of resonating bubbles, even when the bubbles are in close proximity. It is worth noting that the monopole approximation has the additional advantage that it permits easy incorporation of damping terms, which were not discussed in this work.

A numerical study of backscattering from simple clusters, composed of up to three bubbles, has provided new insights into the effects of interactions among the bubbles and on the behavior of the cluster as a whole. Pairs and triplets of identical bubbles have been shown to be dominated by the symmetric mode of collective scattering, which gives rise to downward shifts of the resonance frequency. Nevertheless, antisymmetric resonances may also be present; such resonances are related to asymmetries of the scattering configuration. In contrast, the predominance of the symmetric mode has not been confirmed in cases of clusters of differently sized bubbles; the resonant behavior of such clusters is far more complex. This may partly explain why the theory of collective scattering that was developed in Ref. 14 is less successful for polydisperse bubble distributions than for monodisperse ones.

APPENDIX: COUPLING COEFFICIENT

The coupling coefficient $Q^{(i)}_{mn\mu\nu}(r,\theta,\phi)$ required for the translation of scalar spherical wave functions is defined as follows:

$$Q^{(i)}_{mn\mu\nu}(r,\theta,\phi)=\sum_{l=|n-\nu|}^{n+\nu} j^{l+\nu-n}(2\nu+1)b_l^{(nm\nu\mu)} \times z_l^{(i)}(kr)P_l^{m-\mu}(\cos\theta)e^{j(m-\mu)\phi}, \quad \text{(A1)}$$

where

$$b_l^{(nm\nu\mu)}=(-1)^m(2l+1)\sqrt{\frac{(n+m)!(\nu-\mu)!(l-m+\mu)!}{(n-m)!(\nu+\mu)!(l+m-\mu)!}} \times\begin{pmatrix} n & \nu & l \\ 0 & 0 & 0\end{pmatrix}\begin{pmatrix} n & \nu & l \\ m & -\mu & -m+\mu\end{pmatrix}. \quad \text{(A2)}$$

Equation (A2) involves the Wigner $3-j$ symbols, which are defined as follows:

$$\begin{pmatrix} j_1 & j_2 & j_3 \\ m_1 & m_2 & m_1+m_2\end{pmatrix}=(-1)^{j_1-j_2-m_1-m_2}\Delta(j_1,j_2,j_3)[(j_1+m_1)!(j_1-m_1)!(j_2+m_2)!(j_2-m_2)!(j_3+m_1+m_2)! \times(j_3-m_1-m_2)!]^{1/2}\sum_n (-1)^n[n!(j_1+j_2-j_3-n)!(j_1-m_1-n)!(j_2+m_2-n)!(j_3-j_2+m_1+n)! \times(j_3-j_1-m_2+n)!]^{-1}. \quad \text{(A3)}$$

The sum over n in the right-hand side of Eq. (A3) includes only terms with non-negative arguments for all factorials. The abbreviation

$$\Delta(j_1,j_2,j_3)=\sqrt{\frac{(j_1+j_2-j_3)!(j_1-j_2+j_3)!(-j_1+j_2+j_3)!}{(j_1+j_2+j_3+1)!}} \quad \text{(A4)}$$

has also been used in Eq. (A3).

Translations along the z axis, which arise in the marginal case of a linear cluster, are treated by use of the simplified coupling coefficients

$$Q^{(i)}_{mn\mu\nu}(r,0,0)=\delta_{m\mu}\sum_{l=|n-\nu|}^{n+\nu} j^{l+\nu-n}(2\nu+1)b_l^{(nm\nu m)}z_l^{(i)}(kr), \quad \text{(A5a)}$$

$$Q^{(i)}_{mn\mu\nu}(r,\pi,0)=\delta_{m\mu}\sum_{l=|n-\nu|}^{n+\nu} (-1)^l j^{l+\nu-n}(2\nu+1)b_l^{(nm\nu m)} \times z_l^{(i)}(kr). \quad \text{(A5b)}$$

A detailed description of the addition theorem for scalar spherical wave functions is given in the Appendix of Ref. 18.

[1] R. J. Urick, *Principles of Underwater Sound for Engineers* (McGraw-Hill, New York, 1975).
[2] C. S. Clay and H. Medwin, *Acoustical Oceanography* (Wiley, New York, 1977).
[3] T. G. Leighton, *The Acoustic Bubble* (Academic, London, 1994).
[4] C. Feuillade, R. W. Nero, and R. H. Love, "A low-frequency acoustic scattering model for small schools of fish," J. Acoust. Soc. Am. **99**, 196–208 (1996).
[5] V. C. Anderson, "Sound scattering from a fluid sphere," J. Acoust. Soc. Am. **22**, 426–431 (1950).
[6] P. M. Morse and K. U. Ingard, *Theoretical Acoustics* (Princeton U.P., Princeton, NJ, 1986).
[7] F. M. Minnaert, "On musical air-bubbles and the sounds of running water," Philos. Mag. **16**, 235–248 (1933).
[8] C. Devin, "Survey of thermal, radiation, and viscous damping of pulsating air bubbles in water," J. Acoust. Soc. Am. **31**, 1654–1667 (1959).
[9] R. Y. Nishi, "The scattering and absorption of sound waves by a gas bubble in a viscous liquid," Acustica **33**, 65–74 (1975).
[10] M. Strasberg, "The pulsation frequency of nonspherical gas bubbles in liquids," J. Acoust. Soc. Am. **25**, 536–537 (1953).
[11] I. Tolstoy, "Superresonant systems of scatterers. I," J. Acoust. Soc. Am. **80**, 282–294 (1986).
[12] C. Feuillade, "Scattering from collective modes of air bubbles in water and the physical mechanism of superresonances," J. Acoust. Soc. Am. **98**, 1178–1190 (1995).
[13] C. Feuillade, "The attenuation and dispersion of sound in water containing multiply interacting air bubbles," J. Acoust. Soc. Am. **99**, 3412–3430 (1996).
[14] Z. Ye and C. Feuillade, "Sound scattering by an air bubble near a plane sea surface," J. Acoust. Soc. Am. **102**, 798–805 (1997).
[15] G. Kapodistrias and P. H. Dahl, "On scattering from a bubble located near

a flat air-water interface: Laboratory measurements and modeling,'' J. Acoust. Soc. Am. **110**, 1271–1281 (2001).
[16] G. Kapodistrias and P. H. Dahl, ''Effects of interaction between two bubble scatterers,'' J. Acoust. Soc. Am. **107**, 3006–3017 (2000).
[17] G. C. Gaunaurd, H. Huang, and H. C. Strifors, ''Acoustic scattering by a pair of spheres,'' J. Acoust. Soc. Am. **98**, 495–507 (1995).
[18] G. C. Gaunaurd and H. Huang, ''Acoustic scattering by an air-bubble near the sea surface,'' IEEE J. Ocean. Eng. **20**, 285–292 (1995); M. Strasberg, ''Comments on 'Acoustic scattering by an air-bubble near the sea surface,' '' *ibid.* **21**, 233 (1996); G. C. Gaunaurd and H. Huang, ''Reply to 'Comments on Acoustic scattering by an air-bubble near the sea surface,' '' *ibid.* **21**, 233 (1996).
[19] P. Y. Hsiao, M. Devaud, and J.-C. Bacri, ''Acoustic coupling between two air bubbles in water,'' Eur. Phys. J. E **4**, 5–10 (2001).
[20] V. Twersky, ''Multiple scattering of waves and optical phenomena,'' J. Opt. Soc. Am. **52**, 145–171 (1962).
[21] M. P. Ioannidou, N. C. Skaropoulos, and D. P. Chrissoulidis, ''Study of interactive scattering by clusters of spheres,'' J. Opt. Soc. Am. A **12**, 1782–1789 (1995).
[22] *Handbook of Mathematical Functions*, edited by M. Abramowitz and I. Stegun (Dover, New York, 1970).
[23] I. S. Gradshteyn and I. M. Ryzhik, *Table of Integrals, Series, and Products* (Academic, San Diego, 1980).
[24] O. R. Cruzan, ''Translational addition theorems for spherical vector wave functions,'' Q. Appl. Math. **20**, 33–40 (1962).
[25] S. Stein, ''Addition theorems for spherical wave functions,'' Q. Appl. Math. **19**, 15–24 (1961).

Three-dimensional elastic wave scattering by a layer containing vertical periodic fractures

Seiji Nakagawa,[a] Kurt T. Nihei, Larry R. Myer, and Ernest L. Majer
Earth Sciences Division, Lawrence Berkeley National Laboratory, Berkeley, California 94720

(Received 31 May 2002; revised 29 January 2003; accepted 18 February 2003)

Elastic wave scattering off a layer containing a single set of vertical periodic fractures is examined using a numerical technique based on the work of Hennion *et al.* [J. Acoust. Soc. Am. **87**, 1861–1870 (1990)]. This technique combines the finite element method and plane wave method to simulate three-dimensional scattering off a two-dimensional fractured layer structure. Each fracture is modeled explicitly, so that the model can simulate both discrete arrivals of scattered waves from individual fractures and multiply scattered waves between the fractures. Using this technique, we examine changes in scattering characteristics of plane elastic waves as a function of wave frequency, angle of incidence, and fracture properties such as fracture stiffness, height, and regular and irregular spacing. © *2003 Acoustical Society of America.* [DOI: 10.1121/1.1572139]

PACS numbers: 43.20.Gp, 43.20.Px, 43.58.Ta [DEC]

I. INTRODUCTION

Fractures in sedimentary rock can have a significant impact on the production of gas and liquids in the subsurface. These fractures often are near regularly spaced and near vertical with a preferred orientation in the horizontal plane due to regional geological stresses (Fig. 1). The conventional approach for characterizing these fractures using seismic (elastic) waves treats a fractured rock as an equivalent, homogeneous transversely isotropic medium with the elastic symmetry axis aligned in the fracture-normal direction. This methodology has been adopted by many researchers to examine the seismic properties of fractured rock in physical experiments,[1] theoretical modeling,[2,3] numerical studies using the finite difference method[4] and interpretation of field data.[5] A particularly important result from such research is that a geological unit containing aligned fractures can exhibit azimuthal anisotropy (around a vertical axis) in the velocity and amplitude of scattered elastic waves, which can be used for fracture detection and characterization. This effective medium approach, however, neglects frequency-dependent wave phenomena such as scattering off and wave channeling along discrete fractures, which become increasingly important to consider in high-resolution seismic surveys using higher-frequency waves with wavelengths comparable to the fracture spacing.

Understanding these frequency-dependent effects of fractures on seismic behavior is critical for designing field measurements and collecting data. For the surveys to cover fractures of many scales, a broad range of frequency needs to be employed. Conversely, if fractures of certain size range are to be detected and characterized, a proper frequency range that should be used in the survey needs to be known. These measurements can be performed at many scales, ranging from the well-logging (kilohertz), single-well (hundreds of hertz to kilohertz), cross-well (hundreds of hertz) to the VSP (vertical seismic profiling) and surface seismic (10 to 100 hertz) scales. The data should be collected using multicomponent sensors to capture the effect of fracture anisotropy augmented by wave frequency and fracture scale. These data can help to map and characterize fractures at many scales if the frequency dependent and anisotropic effect of fracture properties on seismic waves is understood. To this end, numerical studies have been performed to examine high-frequency, three-dimensional seismic (elastic) wave scattering by fractures with a range of geometric and material properties.

The scattering of elastic waves off individual fractures can be simulated explicitly using a variety of numerical techniques. For high-frequency wave scattering problems, the boundary element method (BEM) has been used for its accuracy in modeling the stress singularity and wave diffractions generated at the ends of fractures.[6–8] Typically, the BEM computation is performed by modeling a fracture as internal boundaries, and a series of linear systems of equations is solved for unknown crack- (fracture-) opening displacements at each frequency (frequency-domain BEM) or time step (time-domain BEM). Alternatively, for large-scale problems with heterogeneous distribution of material properties in the background medium of fractures, explicit, time-domain finite difference methods (FDM) have been used. This is achieved by modeling individual fractures as thin compliant, orthotropic zones with a thickness equal to a single finite difference cell.[9] Using this method, Schoenberg *et al.*[10] studied two-dimensional elastic wave scattering off an elastic layer containing a large number of aligned vertical fractures. These simulations showed that an incident compressional wave can generate significantly large scattered shear waves when the fracture spacing is on the order of the shear wave wavelength.

However, the direct extension of the existing numerical methods such as the BEM and FDM to three-dimensional fractured systems, which is necessary for studying the azimuthal anisotropy of scattered waves, is still difficult and not commonly performed. This is primarily because the BEM requires a large computing time to solve multiple, linear sys-

[a]Electronic mail: snakagawa@lbl.gov

 0001-4966/2003/113(6)/3012/12/$19.00

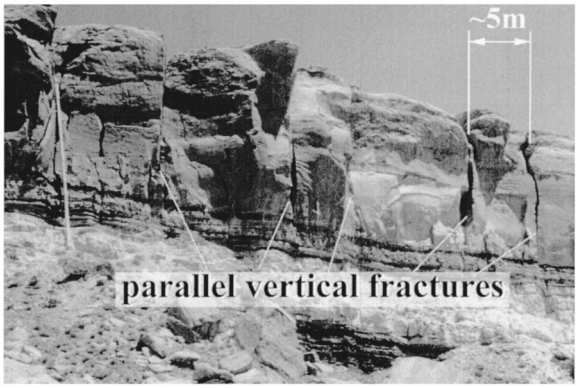

FIG. 1. Near-parallel vertical fractures in sandstone. Chaco Canyon, NM.

tem of equations with a large, densely populated system matrix while the size of available computer memory limits the size of problems solvable using the FDM.

In this paper, we show that if the aligned fractures in a single horizontal layer are periodic and extend infinitely in one of the horizontal directions, the three-dimensional scattering of elastic waves off these fractures can be examined by using an efficient numerical technique that involves only a two-dimensional finite element mesh. The method is based on the numerical technique developed by Hennion *et al.*[11] and Hlakdy-Hennion and Decarpigny[12] for acoustic (pressure) wave scattering by heterogeneous, periodic, and elastic structures. By extending this technique to incident elastic waves, we compute frequency domain responses and subsequently time domain seismograms of plane elastic waves scattered from the periodic, two-dimensional fractured structure for arbitrary angles of incidence.

II. THEORY

A. 3D wave scattering by a 2D periodic structure

In this paper, we examine the scattering of incident plane waves by an array of vertical fractures that extends infinitely in a single horizontal direction within an elastic layer (Fig. 2). The fractured layer is divided into an array of periodic cells in the x, z plane, with a thickness L_z and a width L_x. The Cartesian coordinate system used throughout this paper is defined in the figure with the z direction pointing downward parallel to the fractures and the x direction parallel to the fracture-normal direction. The geometry of such a model is characterized by the continuous translational symmetry in the y direction, and the discrete translational symmetry with a period L_x in the x direction. The homogeneous half-spaces above and below the fractured layer are denoted Ω_- and Ω_+, respectively. A single unit cell within the fractured layer, which can be heterogeneous, is denoted Ω_0, and the surrounding boundaries are defined as $\Gamma_{z+} \equiv \Omega_+ \cap \Omega_0$ and $\Gamma_{z-} \equiv \Omega_- \cap \Omega_0$, and the periodic boundaries on the sides are $\Gamma_{x-} \equiv \Omega_0\,(x=0)$ and $\Gamma_{x+} \equiv \Omega_0\,(x=L_x)$. The numerical technique shown in the following sections models the homogeneous domains Ω_- and Ω_+ using plane wave theory, and the fractured domain Ω_0 using the finite element method (FEM).

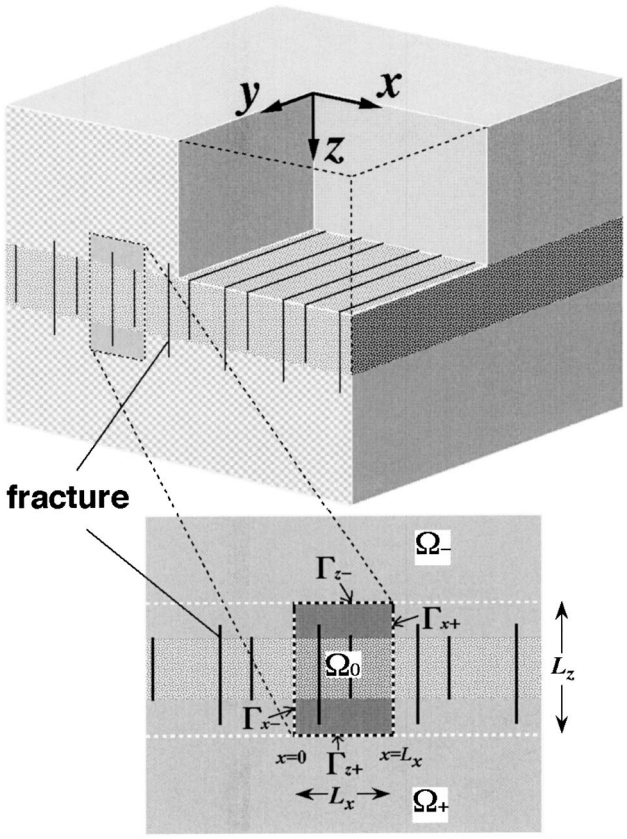

FIG. 2. A model fractured medium containing periodic fractures. The heterogeneous layer containing fractures (domain Ω_0) is modeled using FEM and the bounding homogeneous half-spaces (Ω_+ and Ω_-) are modeled by the plane wave method.

B. Elastic plane wave propagation in a homogeneous domain

In an isotropic and homogeneous elastic medium with P (compressional) and S (shear) wave velocities C_P and C_S, respectively, and material density ρ, the particle displacement of monochromatic plane waves with a frequency ω propagating in the down-going (positive-z) direction is given by

$$
\begin{aligned}
\mathbf{u}^+ &= \begin{bmatrix} u_x \\ u_y \\ u_z \end{bmatrix} \\
&= [\hat{\mathbf{v}}_{Sv} a_{Sv}^+ e^{ik_z^S z} + \hat{\mathbf{v}}_{Sh} a_{Sh}^+ e^{ik_z^S z} + \hat{\mathbf{v}}_P a_P^+ e^{ik_z^P z}] e^{i(k_x x + k_y y - \omega t)} \\
&= \begin{bmatrix} k_x/k & -k_y/k & 0 \\ k_y/k & k_x/k & 0 \\ 0 & 0 & 1 \end{bmatrix} \begin{bmatrix} -k_z^S/k_S & 0 & k/k_P \\ 0 & 1 & 0 \\ k/k_S & 0 & k_z^P/k_P \end{bmatrix} \\
&\quad \times \begin{bmatrix} e^{ik_z^S z} & 0 & 0 \\ 0 & e^{ik_z^S z} & 0 \\ 0 & 0 & e^{ik_z^P z} \end{bmatrix} \begin{bmatrix} a_{Sv}^+ \\ a_{Sh}^+ \\ a_P^+ \end{bmatrix} e^{i(k_x x + k_y y - \omega t)} \\
&\equiv \mathbf{R}^T \mathbf{U}^+ \mathbf{E}^+(z) \mathbf{a}^+ e^{i(k_x x + k_y y - \omega t)}, \qquad (1)
\end{aligned}
$$

where $k_z^P = \sqrt{k_P^2 - k^2}$ and $k_z^S = \sqrt{k_S^2 - k^2}$ are the vertical components of P- and S-wave wave-number vectors with ampli-

tudes k_P and k_S, respectively, k is the horizontal wave number given by $k=\sqrt{k_x^2+k_y^2}$ where k_x and k_y are the x- and y-direction wave numbers each of which is preserved when the wave is scattered by a horizontal boundary. "i" in the exponent is $\sqrt{-1}$. $\mathbf{R}$ is the rotation matrix around the z axis, and the superscript T indicates the matrix transposition. $\mathbf{R}$ rotates the unit particle motion vectors $\hat{\mathbf{v}}_{Sv}$, $\hat{\mathbf{v}}_{Sh}$, and $\hat{\mathbf{v}}_P$ for the three independent wave modes to each column vector in the matrix $\mathbf{U}^+$. Components a_{Sv}^+, a_{Sh}^+, and a_P^+ of the column vector $\mathbf{a}^+$ corresponding to these vectors give the amplitude of individual wave modes, and each mode type is denoted in the subscript, i.e., P for the P wave, Sh for the horizontally polarized S wave, and Sv for the remaining component of the S wave. Superscript "+" indicates down-going waves. Three stress components on a horizontal plane are computed by

$$\boldsymbol{\sigma}^+=\begin{bmatrix}\sigma_{xz}\\ \sigma_{yz}\\ \sigma_{zz}\end{bmatrix}=\mathbf{R}^T\mathbf{S}^+\mathbf{E}^+(z)\mathbf{a}^+e^{i(k_xx+k_yy-\omega t)}, \tag{2}$$

where the matrix $\mathbf{S}^+$ is obtained by applying the elastic Hooke's law to Eq. (1),

$$\mathbf{S}^+\equiv i\omega\rho C_S\begin{bmatrix}-[1-2(k/k_S)^2] & 0 & 2kk_z^P/(k_Sk_P)\\ 0 & k_z^S/k_S & 0\\ 2kk_z^S/k_S^2 & 0 & [1-2(k/k_S)^2]\cdot k_S/k_P\end{bmatrix}. \tag{3}$$

For plane waves propagating in the up-going (negative z) direction, the displacement and stress are obtained by changing the signs of k_z^P and k_z^S in Eqs. (1)–(3).

C. Finite element method for the fractured domain

For the domain containing fractures, the FEM is used to model the displacement and stress fields that can be highly complex due to the scattering of waves. The variational equation of three-dimensional, elastodynamic problems for monochromatic wave propagation can be written as[13]

$$\int_V w_{i,j}C_{ijkl}u_{k,l}\,dV-\omega^2\int_V w_i\rho\,\delta_{ij}u_j\,dV-\int_V w_ib_i\,dV-\int_S w_it_i\,dS=0 \quad (i,j,k,l=x,y,z), \tag{4}$$

where u_j and w_i are the displacement and virtual displacement, b_i and t_i are the body force and surface traction, δ_{ij} is the Kronecker delta and C_{ijkl} is the fourth-rank tensor of elastic moduli. The summation rule applies to the repeated indices in the above equation and the rest of the equations in this section. The domain of integration in space and the domain boundary are denoted V and S, respectively. It is noted that the volumetric integrals in the first and the second terms represent the virtual strain energy and kinetic energy, respectively, and the third and fourth terms are the external virtual work done by the body force and the surface traction.

Because of the continuous translational geometric symmetry in the y direction and of the monochromatic plane incident waves, terms dependent on the parameters y and ω are both factored out of the displacement and force variables u_j, w_i, b_i, and t_i. For example, u_j and w_i can be expressed as

$$u_j(x,y,z,t)=u_j(x,z)e^{i(k_yy-\omega t)}, \tag{5}$$

$$w_i(x,y,z,t)=w_i(x,z)e^{i(k_yy-\omega t)}. \tag{6}$$

"i" ($=\sqrt{-1}$) in the exponent should not be confused with the indices "i" ($=x,y,z$) in the subscript. We introduce the following variables for later use:

$$\tilde{u}_{k,l}=\begin{cases}u_{k,l}(x,z), & l=x,z,\\ ik_y\cdot u_k(x,z), & l=y,\end{cases} \tag{7}$$

$$\tilde{w}_{i,j}=\begin{cases}w_{i,j}(x,z), & j=x,z,\\ ik_y\cdot w_i(x,z), & j=y,\end{cases} \tag{8}$$

where $ik_y=\sqrt{-1}k_y$. When these expressions are introduced into Eq. (4), by denoting the two-dimensional domain Ω and boundary Γ corresponding to the three-dimensional domain V and boundary S,

$$e^{-i\omega t}\int e^{+2ik_yy}\,dy\cdot\left[\int_\Omega \tilde{w}_{i,j}C_{ijkl}\tilde{u}_{k,l}\,d\Omega-\omega^2\int_\Omega w_i\rho\,\delta_{ij}u_j\,d\Omega-\int_\Omega w_ib_i\,d\Omega-\int_\Gamma w_it_i\,d\Gamma\right]=0. \tag{9}$$

Because of the periodicity, the integration in the y direction can be taken for a single period, i.e., $[0,2\pi/k_y]$. The time- and y-coordinate-dependent terms can be dropped off the equation, and the variational equation becomes

$$\int_\Omega \tilde{w}_{i,j}C_{ijkl}\tilde{u}_{k,l}\,d\Omega-\omega^2\int_\Omega w_i\rho\,\delta_{ij}u_j\,d\Omega=\int_\Omega w_ib_i\,d\Omega+\int_\Gamma w_it_i\,d\Gamma. \tag{10}$$

We model fractures explicitly as internal boundaries with surface traction. The stress singularity arising at the ends of the fractures is treated by using the distorted mesh (quarter-node mesh) technique.[14,15] The work term for the boundaries (the second term on the right-hand side of the equation) can be divided into three parts, one for the external

boundary Γ_{ext} and the other two for the fracture surfaces Γ_{f+} and Γ_{f-}.

$$\int_{\Gamma} w_i t_i \, d\Gamma = \int_{\Gamma_{\text{ext}}} w_i t_i \, d\Gamma + \int_{\Gamma_{f+}} w_i^+ \sigma_{ij}^+ n_j^+ \, d\Gamma + \int_{\Gamma_{f-}} w_i^- \sigma_{ij}^- n_j^- \, d\Gamma. \tag{11}$$

The two opposing surfaces of the fracture are labeled with subscripts "+" and "−" and have unit normal vectors n_j^+ and n_j^-, respectively. Using these vectors, we wrote the tractions in terms of the stress components σ_{ij}^+ and σ_{ij}^-. The superscripts on the variables are to emphasize the surface of the fracture on which the variables are defined. Because we assume mathematical fractures that have no thickness, the geometry of the two surfaces is identical, which results in $\Gamma_{f+} = \Gamma_{f-} \equiv \Gamma_f$ and $n_j^- = -n_j^+$. Therefore,

$$\int_{\Gamma} w_i t_i \, d\Gamma = \int_{\Gamma_{\text{ext}}} w_i t_i \, d\Gamma + \int_{\Gamma_f} w_i^+ \sigma_{ij}^+ (-n_j^-) d\Gamma + \int_{\Gamma_f} w_i^- \sigma_{ij}^+ n_j^- \, d\Gamma. \tag{12}$$

For small displacement and stress introduced by wave propagation, boundary conditions on the fracture (the linear slip or displacement-discontinuity boundary conditions) can be stated as

$$\sigma_{ij}^+ = \sigma_{ij}^- \equiv \sigma_{ij}, \tag{13}$$

$$\sigma_{ij} n_j^- = t_i^- = \kappa_{ij}(u_j^+ - u_j^-), \tag{14}$$

where κ_{ij} is the fracture stiffness tensor.[16,17] Using these relationships, the Eq. (12) becomes

$$\int_{\Gamma} w_i t_i \, d\Gamma = \int_{\Gamma_{\text{ext}}} w_i t_i \, d\Gamma - \int_{\Gamma_f} (w_i^+ - w_i^-) \kappa_{ij} (u_i^+ - u_i^-) d\Gamma. \tag{15}$$

The second term on the right-hand side of the equation can now be seen as the internal virtual work (strain energy) stored in the fracture. By introducing Eq. (15) into Eq. (10), the variational equation becomes

$$\int_{\Omega} \tilde{w}_{i,j} C_{ijkl} \tilde{u}_{k,l} \, d\Omega + \int_{\Gamma_f} (w_i^+ - w_i^-) \kappa_{ij} (u_i^+ - u_i^-) d\Gamma - \omega^2 \int_{\Omega} w_i \rho \delta_{ij} u_j \, d\Omega - \int_{\Omega} w_i b_i \, d\Omega - \int_{\Gamma_{\text{ext}}} w_i t_i \, d\Gamma = 0. \tag{16}$$

This equation is discretized using a nodal displacement vector **U** and a virtual nodal displacement vector **W**.[13] In vector notation, the discrete form of the equation is

$$\mathbf{W}^T (\mathbf{K}_b \mathbf{U} + \mathbf{K}_f \mathbf{U} - \omega^2 \mathbf{M} \mathbf{U} - \mathbf{F}) = 0, \tag{17}$$

where $\mathbf{K}_b$, $\mathbf{K}_f$, and $\mathbf{M}$ are the FEM bulk stiffness, fracture stiffness, and mass matrices, respectively, and $\mathbf{F}$ is the FEM load vector, corresponding to each domain and boundary integral in the variational equation. Because $\mathbf{W}^T$ is for arbitrary virtual displacement, it can be dropped and

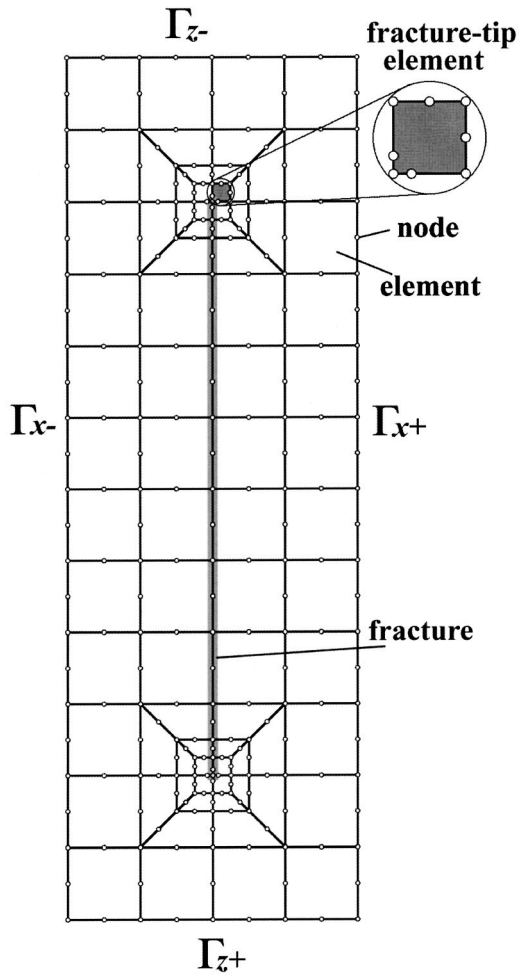

FIG. 3. An example of FE mesh used for computing the wave scattering by equally spaced (4 m spacings), 8 m tall fractures. Both mesh refinement and the distorted mesh (quarter-node) techninque were applied to the ends of the fracture.

$$\mathbf{K}\mathbf{U} \equiv (\mathbf{K}_b + \mathbf{K}_f - \omega^2 \mathbf{M})\mathbf{U} = \mathbf{F}. \tag{18}$$

This is the finite element equation that is solved for unknown nodal displacement. Because the system stiffness matrix **K** and the load vector **F** are computed from numerical integrations within and along the two-dimensional domain Ω, the FEM mesh required for this computation is two-dimensional although each node has three degrees of freedom in displacement (e.g., Fig. 3).

D. Coupling between plane wave fields and FEM mesh

Hannion *et al.*[11] have given a detailed description of the method to couple plane acoustic wave fields and an FEM mesh. Here, we present their method for the elastic case.

Because of the discrete translational symmetry (periodicity) in the x direction and the plane incident waves, the scattered wave field within the half-spaces Ω_- and Ω_+ can be expressed by a superposition of an infinite series of plane waves with discrete x-direction wave numbers. In order to solve the problem numerically, this series is truncated at a finite number M. Therefore the wave number for the nth mode is given by $k_{nx} = k_{0x} + 2\pi(n/L_x)$ $(n = -M, -M$

$+1,...,0,...,+M)$, where k_{x0} is the x-direction wave number for an incident plane wave, which we previously denoted k_x. In this study, the series truncation number M was determined so that the total number of the modes $2M+1$ is equal to the number of FEM nodes along the boundaries Γ_{z+} and Γ_{z-}.

We first examine the plane wave field in the domain Ω_+ along the boundary Γ_{z+}. Since only down-going waves exist in this domain, the displacement and stress are

$$\mathbf{u}^+ = \sum_{n=-M}^{+M} \mathbf{R}_n^T \mathbf{U}_n^+ \mathbf{a}_n^+ e^{ik_{nx}x}, \tag{19}$$

$$\boldsymbol{\sigma}^+ = \sum_{n=-M}^{+M} \mathbf{R}_n^T \mathbf{S}_n^+ \mathbf{a}_n^+ e^{ik_{nx}x}, \tag{20}$$

where $\mathbf{R}_n^T$, $\mathbf{U}_n^+$, $\mathbf{S}_n^+$, and $\mathbf{a}_n^+$ are obtained by substituting k, k_z^P, and k_z^S in Eqs. (1)–(3) by wave numbers k_{nx}, k_{nz}^P, and k_{nz}^S of corresponding modes. The dependency on the term $e^{i(k_y y-\omega t)}$ is understood and dropped from Eqs. (19), (20), and the following derivations. Also, without losing generality, the origin of the z coordinate is defined on Γ_{z+}, which has eliminated $\mathbf{E}^+(z=0)=\mathbf{E}$ (identity matrix) from the equations.

Within the FEM domain Ω_0 along Γ_{z+}, a similar decomposition of the displacement field can be obtained from a truncated Fourier series,

$$\mathbf{u}^+ = \sum_{n=-M}^{+M} \mathbf{c}_n^+ e^{ik_{nx}x}, \tag{21}$$

where the coefficient vectors $\mathbf{c}_n^+$ can be computed from the displacement along Γ_{z+} by

$$\mathbf{c}_n^+ = \frac{1}{L_x} \int_{-L_x/2}^{+L_x/2} \mathbf{u}^+(x) e^{-ik_{nx}x}\, dx. \tag{22}$$

From term-by-term comparison between Eqs. (19) and (21), coefficient vectors $\mathbf{a}_n^+$ can be expressed via $\mathbf{c}_n^+$ as $\mathbf{a}_n^+ = (\mathbf{U}_n^+)^{-1}\mathbf{R}_n\mathbf{c}_n^+$. By introducing this relationship into Eq. (20), the stress (or traction) along the boundary can be computed by

$$\boldsymbol{\sigma}^+ = \sum_{n=-M}^{+M} \mathbf{R}_n^T \mathbf{S}_n^+ (\mathbf{U}_n^+)^{-1} \mathbf{R}_n \mathbf{c}_n^+ e^{ik_{nx}x}. \tag{23}$$

This relationship is important because it explicitly gives the traction along the boundary via displacement, hence eliminating the necessity for the unknown parameters of the plane wave field within Ω_+.

We now write Eq. (23) via nodal displacement. The boundary displacement and traction (or stress) can be expressed by their nodal values as

$$\mathbf{u}_e^+(x) = \sum_{I=1}^{N_{nx}} N_{eI}(x) \mathbf{u}^{+eI}, \tag{24}$$

$$\mathbf{t}_e^+(x)(=\boldsymbol{\sigma}^+) = \sum_{I=1}^{N_{nx}} N_{eI}(x) \boldsymbol{\sigma}^{+eI}, \tag{25}$$

where the summation is performed only for the boundary nodes along a single element e, and $N_{eI}(x)$ are the shape functions for nodes I $(I=1,2,...,N_{nx})$. $\mathbf{u}^{+eI}$ and $\boldsymbol{\sigma}^{+eI}$ are the nodal displacement and stress. The displacement along the boundary is given by a union of the displacement for each element as

$$\mathbf{u}^+(x) = \bigcup_{e=1}^{N_{ex}} \mathbf{u}_e^+(x), \tag{26}$$

where N_{ex} is the number of elements along Γ_{z+}. Therefore the coefficient vectors $\mathbf{c}_n^+$ in Eq. (23) are computed from Eqs. (22) and (26) as

$$\begin{aligned}\mathbf{c}_n^+ &= \frac{1}{L_x} \sum_{e=1}^{N_{ex}} e^{-ik_{nx}x_e} \int_{-h_e/2}^{h_e/2} \mathbf{u}_e^+(x') e^{-ik_{nx}x'}\, dx' \\ &= \frac{1}{L_x} \sum_{e=1}^{N_{ex}} e^{-ik_{nx}x_e} \sum_{I=1}^{N_{nx}} \int_{-h_e/2}^{h_e/2} N_{eI}(x') e^{-ik_{nx}x'}\, dx'\, \mathbf{u}^{+eI} \\ &\equiv \mathbf{A}_n^+ \mathbf{U}^+, \end{aligned} \tag{27}$$

where h_e is the width of each element e $(e=1,2,...,N_{ex})$, x_e is the x coordinate of the element center, and $\mathbf{U}^+$ is a column vector containing the nodal displacement vectors along the boundary. x' indicates the local coordinate defined around x_e $(-h_e/2 \leqslant x' \leqslant h_e/2)$. For the special case when the width of the elements along the boundary is constant $(\equiv h)$ and $N_{nx}=3$, the matrix $\mathbf{A}_n^+$ becomes

$$\mathbf{A}_n^+ = [\,\theta_{n11}^+\mathbf{E}\ \ \theta_{n12}^+\mathbf{E}\ \ (\theta_{n13}^+ + \theta_{n21}^+)\mathbf{E}\ \ \theta_{n22}^+\mathbf{E}\ \ (\theta_{n23}^+ + \theta_{n31}^+)\mathbf{E} \cdots \theta_{nN_{ex}3}^+\mathbf{E}], \tag{28}$$

where $\mathbf{E}$ is the 3×3 identity matrix and

$$\theta_{neI}^+ \equiv \frac{h \cdot e^{-ik_{nx}x_e}}{L_x} \int_{-h/2}^{+h/2} N_I(x') e^{-ik_{nx}x'}\, dx'. \tag{29}$$

The nodal forces on an element e along the boundary Γ_{z+} are computed by

$$\mathbf{f}_{eI}^+ = \int_{-h_e/2}^{h_e/2} N_{eI}(x') \mathbf{t}_e^+(x') dx', \tag{30}$$

where $\mathbf{t}_e^+$ $(=\boldsymbol{\sigma}^+)$ is the boundary traction computed using the plane wave solutions. From Eqs. (23) and (27), these forces can be computed from the nodal displacements on the boundary as

$$\begin{aligned}\mathbf{f}_{eI}^+ = e^{ik_{nx}x_e} \sum_{n=-M}^{M} &\int_{-h_e/2}^{h_e/2} N_{eI}(x') e^{ik_{nx}x'}\, dx' \\ &\cdot \mathbf{R}_n^T \mathbf{S}_n^+ (\mathbf{U}_n^+)^{-1} \mathbf{R}_n \mathbf{A}_n^+ \mathbf{U}^+. \end{aligned} \tag{31}$$

Therefore, the load vector containing nodal force vectors along the boundary is given as a linear function of the nodal displacement. Again, when $h_e = h$ and $N_{nx} = 3$, this is

$$\mathbf{F}^+ = [\mathbf{f}_{11}^{+T}\ \ \mathbf{f}_{12}^{+T}\ \ (\mathbf{f}_{13}^{+T} + \mathbf{f}_{21}^{+T})\ \ \mathbf{f}_{22}^{+T}\ \ (\mathbf{f}_{23}^{+T} + \mathbf{f}_{31}^{+T}) \cdots \mathbf{f}_{N_{ex}3}^{+T}]^T$$

$$= L_x \sum_{n=-M}^{+M} (\mathbf{A}_n^+)^* \mathbf{R}_n^T \mathbf{S}_n^+ (\mathbf{U}_n^+)^{-1} \mathbf{R}_n \mathbf{A}_n^+ \mathbf{U}^+ \equiv \Delta^+ \mathbf{U}^+, \quad (32)$$

where the superscript "*" indicates transposition and complex conjugation of the matrix.

We now discuss the boundary Γ_{z-} for which the effect of the incident wave needs to be considered. Equations corresponding to Eqs. (19) and (20) for the displacement and stress are

$$\mathbf{u}^- = \sum_{n=-M}^{+M} \mathbf{R}_n^T \mathbf{U}_n^- \mathbf{a}_n^- e^{ik_{nx}x} + \mathbf{R}_0^T \mathbf{U}_0^+ \mathbf{a}_{Inc} e^{ik_{0x}x}, \quad (33)$$

$$\boldsymbol{\sigma}^- = \sum_{n=-M}^{+M} \mathbf{R}_n^T \mathbf{S}_n^- \mathbf{a}_n^- e^{ik_{nx}x} + \mathbf{R}_0^T \mathbf{S}_0^+ \mathbf{a}_{Inc} e^{ik_{0x}x}, \quad (34)$$

respectively, where $\mathbf{a}_{Inc}$ is a column vector containing the complex amplitude of an incident plane wave. Again, $\mathbf{E}^-$ was dropped from Eqs. (33) and (34) by defining the origin of the z axis on the boundary Γ_{z-}. From the Fourier expansion of the displacement as in Eq. (21), Eq. (33) yields the relationships

$$\mathbf{c}_n^- = \mathbf{R}_n^T \mathbf{U}_n^- \mathbf{a}_n^-, \quad n \neq 0, \quad (35)$$

$$\mathbf{c}_0^- = \mathbf{R}_0^T (\mathbf{U}_0^- \mathbf{a}_0^- + \mathbf{U}_0^+ \mathbf{a}_{Inc}), \quad (36)$$

where $\mathbf{a}_n^-$ is the amplitude vector for the nth reflected wave. $\mathbf{U}_n^-$ and $\mathbf{S}_n^-$ are obtained by changing the signs of the z-direction wave numbers, i.e., $+k_{nz}^P \rightarrow -k_{nz}^P$ and $+k_{nz}^S \rightarrow -k_{nz}^S$, in the definitions for $\mathbf{U}_n^+$ and $\mathbf{S}_n^+$. By eliminating the unknown reflected plane wave amplitudes $\mathbf{a}_n^-$ using Eqs. (35) and (36), Eq. (34) becomes

$$\boldsymbol{\sigma}^- = \sum_{n=-M}^{+M} \mathbf{R}_n^T \mathbf{S}_n^- (\mathbf{U}_n^-)^{-1} \mathbf{R}_n \mathbf{A}_n^- \mathbf{U}_b^- e^{ik_{nx}x} + \mathbf{R}_0^T [\mathbf{S}_0^+ - \mathbf{S}_0^- (\mathbf{U}_0^-)^{-1} \mathbf{U}_0^+] \mathbf{a}_{Inc} e^{ik_{0x}x}, \quad (37)$$

where $\mathbf{A}_n^-$ is also defined by changing the signs of wave numbers in $\mathbf{A}_n^+$. Finally, the load vector can be obtained through the same procedure as for $\mathbf{F}^+$ but with $\mathbf{t}_e^- = -\boldsymbol{\sigma}^-$, yielding

$$\mathbf{F}^- = \Delta^- \mathbf{U}^- + \overline{\mathbf{F}}, \quad (38)$$

where $\overline{\mathbf{F}}$ is the known term (incident wave term) arising from the second term on the right-hand side of Eq. (37). Terms containing unknown nodal displacement vectors $\mathbf{U}^+$ and $\mathbf{U}^-$ in Eqs. (32) and (38) are absorbed into the stiffness matrix of the FEM equation (18) during the assembly of the matrix.

E. Periodic boundary and matrix condensation

Along the boundaries Γ_{x-} and Γ_{x+}, dynamic periodic boundary conditions are applied by using the Floquet–Bloch theory. If the finite element matrix equation (18) is rearranged as

$$\begin{bmatrix} \mathbf{K}_{11} & \mathbf{K}_{12} & \mathbf{K}_{13} \\ \mathbf{K}_{21} & \mathbf{K}_{22} & \mathbf{K}_{23} \\ \mathbf{K}_{31} & \mathbf{K}_{32} & \mathbf{K}_{33} \end{bmatrix} \begin{bmatrix} \mathbf{U}_1 \\ \mathbf{U}_2 \\ \mathbf{U}_3 \end{bmatrix} = \begin{bmatrix} \overline{\mathbf{F}}_1 \\ \mathbf{F}_2 \\ \mathbf{F}_3 \end{bmatrix}, \quad (39)$$

where subscript "1" denotes nonperiodic displacement and force vectors, and "2" and "3" indicate periodic displacement and load vectors on boundaries Γ_{x-} and Γ_{x+}, respectively. Submatrices relating these vectors are given by $\mathbf{K}_{ij}\,(i,j = 1,2,3)$. The "bar" on the load vector $\mathbf{F}_1$ indicates that this is a known term. It is noted that this equation is underdetermined, and additional constraints (boundary conditions) need to be applied. The dynamic periodic boundary condition leads to the following relationships between nodal displacement and traction on the boundaries Γ_{x-} and Γ_{x+} as

$$\mathbf{U}_3 = \mathbf{U}_2 e^{+ik_{0x}L_x}, \quad (40)$$

$$\mathbf{F}_2 = -\mathbf{F}_3 e^{-ik_{0x}L_x}. \quad (41)$$

Using these relationships, the matrix equation (39) can be condensed as

$$\begin{bmatrix} \mathbf{K}_{11} & \mathbf{K}_{12} + \mathbf{K}_{13} e^{+ik_{0x}L_x} \\ \mathbf{K}_{21} + \mathbf{K}_{31} e^{-ik_{0x}L_x} & \mathbf{K}_{22} + \mathbf{K}_{23} e^{+ik_{0x}L_x} + \mathbf{K}_{32} e^{-ik_{0x}L_x} + \mathbf{K}_{33} \end{bmatrix} \times \begin{bmatrix} \mathbf{U}_1 \\ \mathbf{U}_2 \end{bmatrix} = \begin{bmatrix} \overline{\mathbf{F}}_1 \\ \mathbf{0} \end{bmatrix}. \quad (42)$$

This is the FEM equation that is solved to obtain complex displacements on the FE mesh for a given combination of an incident wave frequency ω and horizontal wave numbers k_x and k_y. From the displacement along the boundaries Γ_{x-} and Γ_{x+}, $\mathbf{c}_n^-$ and $\mathbf{c}_n^+$ can be computed using relationships such as in Eq. (27), and subsequently, the plane wave amplitude coefficients $\mathbf{a}_n^-$ and $\mathbf{a}_n^+$ are obtained [e.g., from Eqs. (35) and (36)]. Finally, the displacement and stress fields for domains Ω_- and Ω_+ are computed by superposition of plane waves with a range of discrete horizontal wave numbers [Eqs. (19), (20), (33), and (34)].

Using this hybrid technique, the elastic wave field within and outside the layer containing periodically spaced fractures can be computed for an incident plane wave. Figure 4 shows snapshots of a compressional wave propagating across a periodically fractured layer as cubes cut out of three-dimensional wave fields. Only the vertical (z) component of displacement is shown. In this particular model, the fracture spacing h is 4 m, the height H is 8 m, and the stiffness is zero, i.e., completely open fractures. Except for the fractures, the entire field is isotropic and homogeneous with P- and S-wave velocities of 3000 m/s and 1731 m/s, respectively, and the material density of 2100 kg/m^3. The incident plane P wave has an azimuthal angle of 45° (measured from the x axis around the vertical z axis) and a dip angle of 60° (measured from the horizontal plane), and is a Ricker wavelet of unit amplitude, with the central frequency of 444 Hz (the wavelength to fracture spacing ratio $\lambda_P/h = 1.69$). The complex scattering behavior of the waves gives rise to the localized and trapped energy within the fractured layer as seen in

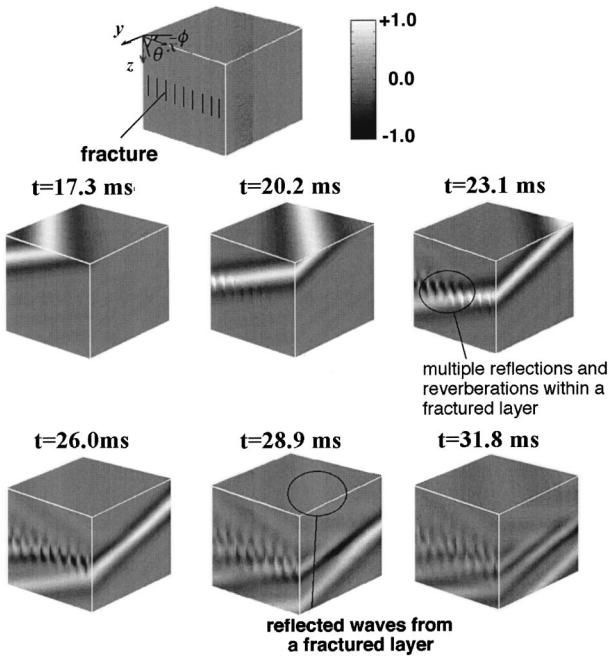

FIG. 4. Three-dimensional snapshots of plane waves propagating through a layer containing equally spaced parallel open fractures. The incident wave is a *P* wave (Ricker wavelet) with a wavelength approximately 1.7 times the fracture spacing.

Fig. 4. The time-retarded radiation of this energy back to the upper half-space manifests itself as the reverberation (coda) in measured reflection seismograms which we will discuss in detail in the following section.

III. EXAMPLES

A. Numerical model

For the remainder of this paper, we examine the scattering of an incident plane elastic wave by a single layer containing an array of plane parallel, periodically spaced fractures using the hybrid numerical technique developed in the preceding section. The analysis focuses on the reflection of an incident *P* wave by a fractured layer. Also, the background medium of the fractured layer is assumed to have the same properties as the surrounding homogeneous half-spaces (i.e., density 2100 kg/m^3 and *P*- and *S*-wave velocities 3000 m/s and 1731 m/s).

The hybrid plane wave–FEM method allows us to propagate a plane wave with arbitrary angles of incidence upon the fractured layer. By numerically simulating the scattering of plane waves propagating at a range of incidence angles, we can examine approximately the changes in the characteristics of reflected waves radiated far from a point source. In applications such as surface seismic surveys for oil and gas exploration, seismic sources and receivers are often located on a surface parallel or near parallel to the fractured layer, and their relative distance and orientation are changed to probe fractures at different depths and orientations. To simulate this, we place a source and receiver pair on a single plane 100 m above the top of the fractured layer and change their locations symmetrically around a vertical axis on the

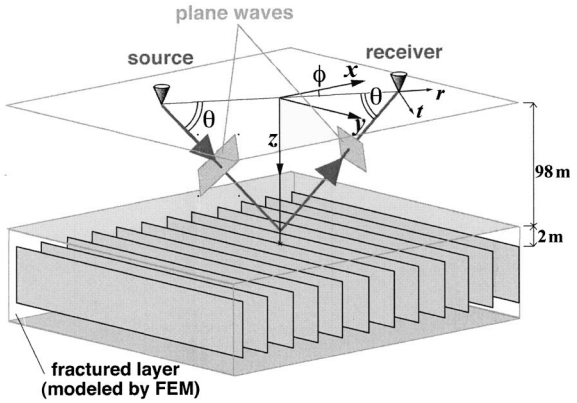

FIG. 5. Source–receiver configuration for the numerical simulations. The locations of the source and the receiver are changed symmetrically around a single vertical axis going through a fracture. For specifying the dip (θ) and azimuthal (ϕ) angles, the point of reflection on the fractured layer is assumed to be located slightly (2 m) above the top ends of the fractures that are 100 m below the source-and-receiver level.

plane. This results in changes in both azimuthal and dip angles (θ and ϕ) of incident waves (Fig. 5).

To minimize numerical dispersion, the central frequency of Ricker wavelets used as incident pulses was chosen such that there were at least 10 nodes of FE mesh per *S*-wave wavelength. Although the FE meshes used for this study were rather coarse (for example, a mesh consisting of 4×12 elements of 1 m$\times$1 m-size, 8-node quadrilateral serendipity elements with the mesh refinement near the fracture tips was used for equally spaced, 8 m tall fractures as shown in Fig. 3), the computed wave forms were in close agreement with the results obtained using finer meshes (e.g., 8×24 element model). We also checked the accuracy of the hybrid method using an accurate, two-dimensional frequency domain elastodynamic boundary element (BE) method.[7] In this exercise, the two methods were compared for waves propagating along the *x*, *z* plane. Because only a finite number of fractures was used in the BE model due to computational limitations, the BE results showed less coda than the results of the hybrid method that assumes an infinite series of fractures. However, early-time wave forms computed at locations near the fractures showed good agreement, indicating that the scattering of waves by individual fractures can be modeled accurately by the hybrid method.

The primary parameters used for the simulations are (1) the central frequency of incident Ricker wavelet (''low'' 111 Hz and ''high'' 332 Hz, corresponding to *P*-wave wavelengths of 27.1 m and 9.03 m), (2) fracture stiffness (for both normal and shear stiffnesses ''soft'' 7.87×10^9 Pa/m and ''stiff'' 15.7×10^9 Pa/m, corresponding to normal incident *P*-wave transmission coefficients of 0.96 and 0.99 at 111 Hz, and 0.77 and 0.92 at 332 Hz), (3) fracture height (''short'' 8 m and ''tall'' 16 m), and (4) irregularity of the fracture spacing (either regular 4 m intervals or irregular, alternating 3 m and 5 m intervals). Because there are still a large number of possible combinations among these parameters, only several illustrative examples of the results are presented in the following sections.

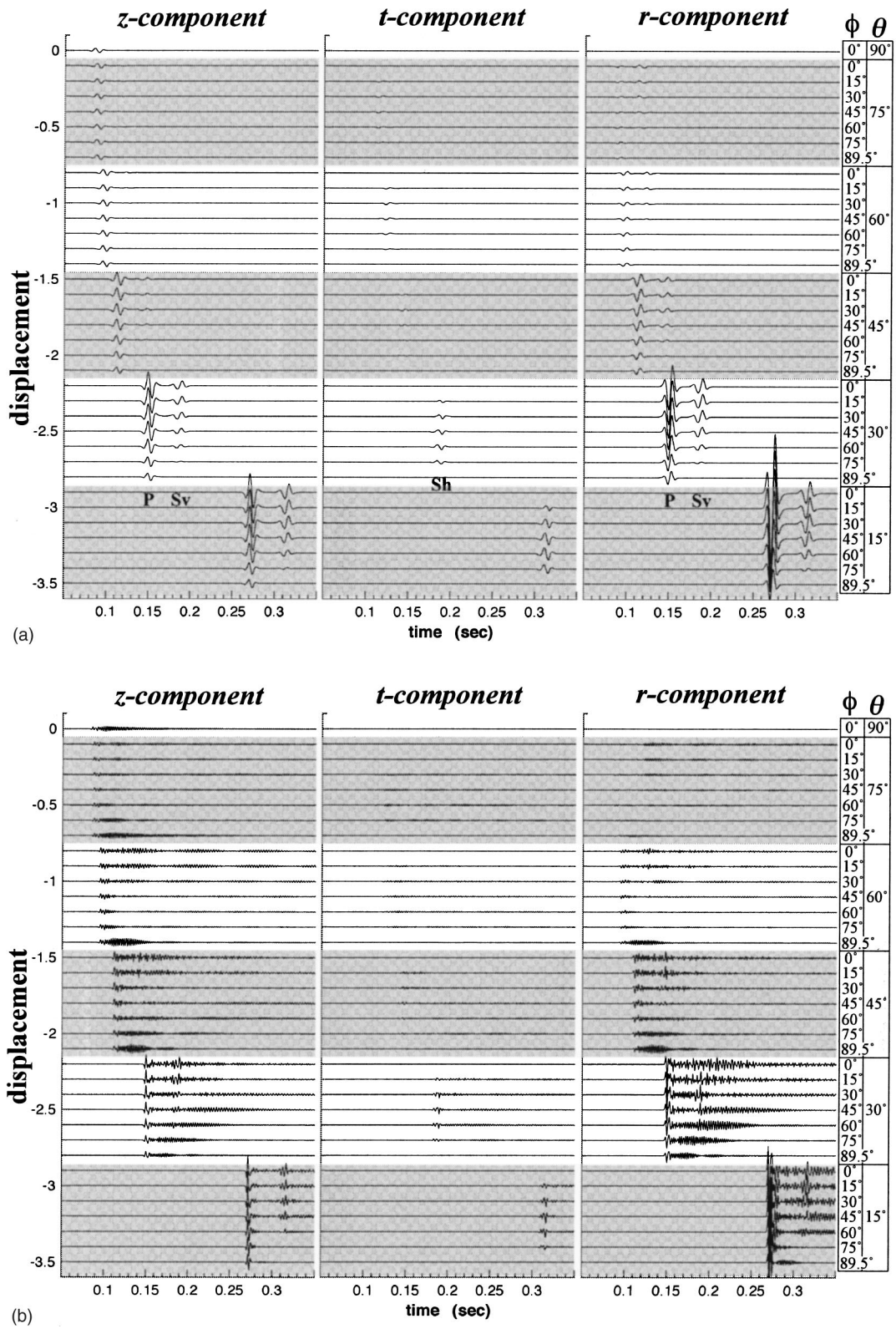

FIG. 6. *z*-, *r*-, and *t*-component seismograms computed for the "low-frequency" cases (a) and the "high-frequency" cases (b). Angles of incidence (θ, dip angle; ϕ, azimuthal angle) are indicated on the right edge of the plots. For the "low-frequency" cases, arrivals of three wave modes are clearly seen (indicated as *P*, *Sv*, and *Sh* below the wavelets for the $\theta=30°$ cases). For the "high-frequency" cases, multiple scattering (coda) dominates the seismograms and *P* and *Sv* waves are difficult to distinguish.

B. Wave forms as a function of incidence angles

For regularly spaced, "soft" 8 m tall fractures, the wave forms of reflected waves for a unit-amplitude incident *P* wave were computed for a range of dip and azimuthal angles. The *z*, *t* (source–receiver azimuth direction) and *r* (source–receiver offset direction) components of the particle displacement, as defined in Fig. 5, are shown in Figs. 6(a)

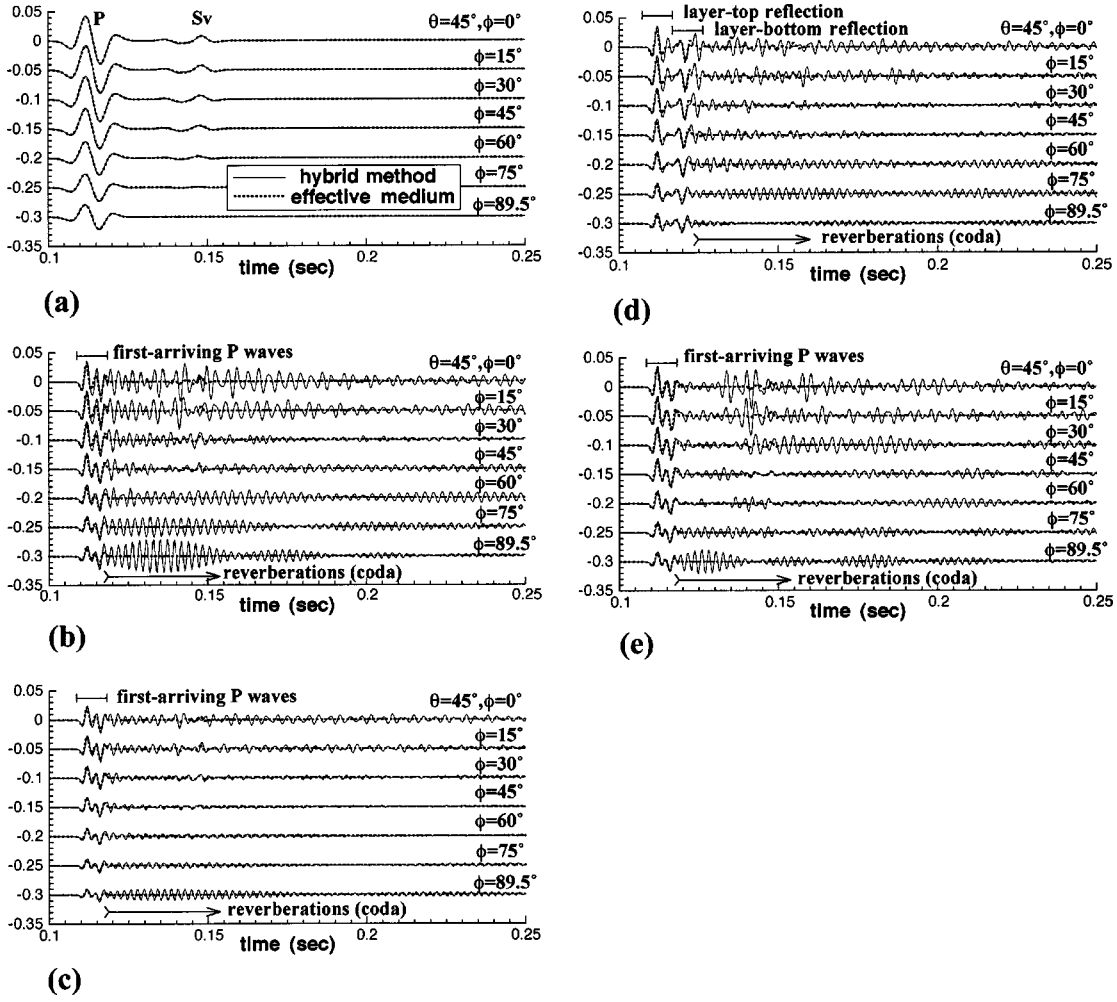

FIG. 7. (a) ''Low-frequency'' wave forms for ''soft, short and regular'' fractures. (b) ''High-frequency'' wave forms for ''soft, short and regular'' fractures. (c) ''High-frequency'' wave forms for ''stiff, short and regular'' fractures. (d) ''High-frequency'' wave forms for ''soft, long and regular'' fractures. (e) ''High-frequency'' wave forms for ''soft, short and irregular'' fractures. Azimuthal changes in the *z*-component wave forms of reflected waves for the incidence dip angle of $\theta=45°$. Direct arrivals (incident waves) are not shown. For comparison, predictions by the static effective medium approximation are shown in dotted lines.

and (b) for both ''low'' and ''high'' frequency incident waves. The wave forms were computed at every 15° of increment in both dip and azimuthal angles. However, because the FEM system stiffness matrix becomes singular and the numerical code becomes unstable for the azimuthal angle of 90°, wave forms for 89.5° are shown instead. The direct waves were ''muted'' from the computed seismograms.

For the low-frequency case, the clear first arrivals in the *z*- and *r*-component seismograms are the reflected *P* waves that are followed by converted *S* waves. Using the notations in the theory, these *S* waves in the *z* and *r* components are the *Sv* waves, and *S* waves in the *t* component are the *Sh* waves. Reflections from the top and the bottom of the fractured layer are overlapping and difficult to distinguish from each other. With decreasing dip angle (measured from the horizontal plane) and increasing the source–receiver distance, amplitudes of the reflected waves increase significantly, making the detection of the fractured layer easier. An increase in the azimuthal angle (measured from the *x* axis) results in decreases in both *P*- and *S*-wave amplitudes. In particular, the amplitude of reflected *Sv* wave vanishes when the incident direction is parallel to the fractures. This can be explained by the source–receiver reciprocity: because no reflection of *P* waves (or *S* waves) occurs for an incident *S* wave with particle motion parallel to the fractures, when the source and the receiver are swapped, no reflection of *S* waves occur for an incident *P* wave. The *Sh* component exhibits finite amplitudes at intermediate azimuthal angles because of the azimuthal anisotropy of the fractured layer, as shown by Schoenberg *et al.*[2]

For the high-frequency case, reflected waves show the same behavior as the low-frequency case. However, each arrival of the primary reflections is followed by coda that last for an extended period of time. Amplitudes of these coda compared to the leading, primary pulses are typically larger for smaller dip angles (i.e., larger incidence angles). We examine the behavior of coda more in detail in the following section.

C. Azimuthal variations of wave forms

From Figs. 7(a)–(e), azimuthal gathers of the *z*-component wave forms at a dip angle of 45° are shown for

fractures with a range of properties. Within each plot, solid lines are computed using the hybrid technique, and the dotted lines are obtained by applying the static effective medium approximation to the fractured layer. In this approximation, the transversely isotropic elastic moduli of the layer containing fractures are computed by adding the compliance of the fractures to the matrix compliance.[18]

For the low-frequency case shown in Fig. 7(a), results of the hybrid method and the effective medium approximation are in excellent agreement. However, the development of coda results in significant differences in the wave forms for the high-frequency cases [Fig. 7(b)]. It is noted that the first-arriving part of the reflected *P* waves shows rather good agreement between the two methods. However, for small azimuthal angles, the distortion of the latter part of the first-arriving wavelet corresponding to the layer-bottom reflection results in an increase in mismatch between the wave forms. The *S*-wave parts in the seismograms are difficult to identify because the amplitude of coda caused by the incident *P* wave is overwhelmingly large.

An increase in the fracture stiffness results in decreases in the amplitudes of reflected waves [Figs. 7(b) and (c)]. The relative effect is larger for the coda part of the wave, resulting in the first-arriving part of the *P* waves becoming easier to identify from the rest of the wave forms.

The simulations show that the relative amplitude of coda be reduced for the ''taller'' fractures as shown in Fig. 7(d) [compare with Fig. 7(b)]. For this case, the *P*-wave reflection from the bottom of the layer is now clearly separated from the reflection from the top. Although the first-arriving parts of the individual reflections show good agreement with the static theory, the later-arriving parts of the wavelets shows significant discrepancies. The decrease in coda amplitude may result because longer fractures increase the forward scattering of an incident wave,[19] which reduces the contributions to the coda by waves scattered by distant fractures.

The periodic geometry and material properties of the fractures can be ''perturbed'' by modeling multiple fractures with a range of properties within a single periodic cell. Here we examine only the case for perturbed fracture spacing. In Fig. 7(e), wave forms are computed for periodic but irregular fracture intervals alternating between 3 m and 5 m in contrast to the regular 4 m intervals in Fig. 7(b). All other parameters are identical. Although the effect is not as strong as the ''stiff'' and ''tall'' fractures, the relative amplitude of the coda was, again, reduced compared to the reference case in Fig. 7(b). This decrease is due to the destructive interference between scattered waves due to the less ordered geometry of the fractures. It is interesting to note that the first-arriving part of the reflected *P* waves are well approximated by the static effective medium theory shown by the dotted lines even for small azimuthal angles. This was also observed for the ''stiff'' fracture case in Fig. 7(c).

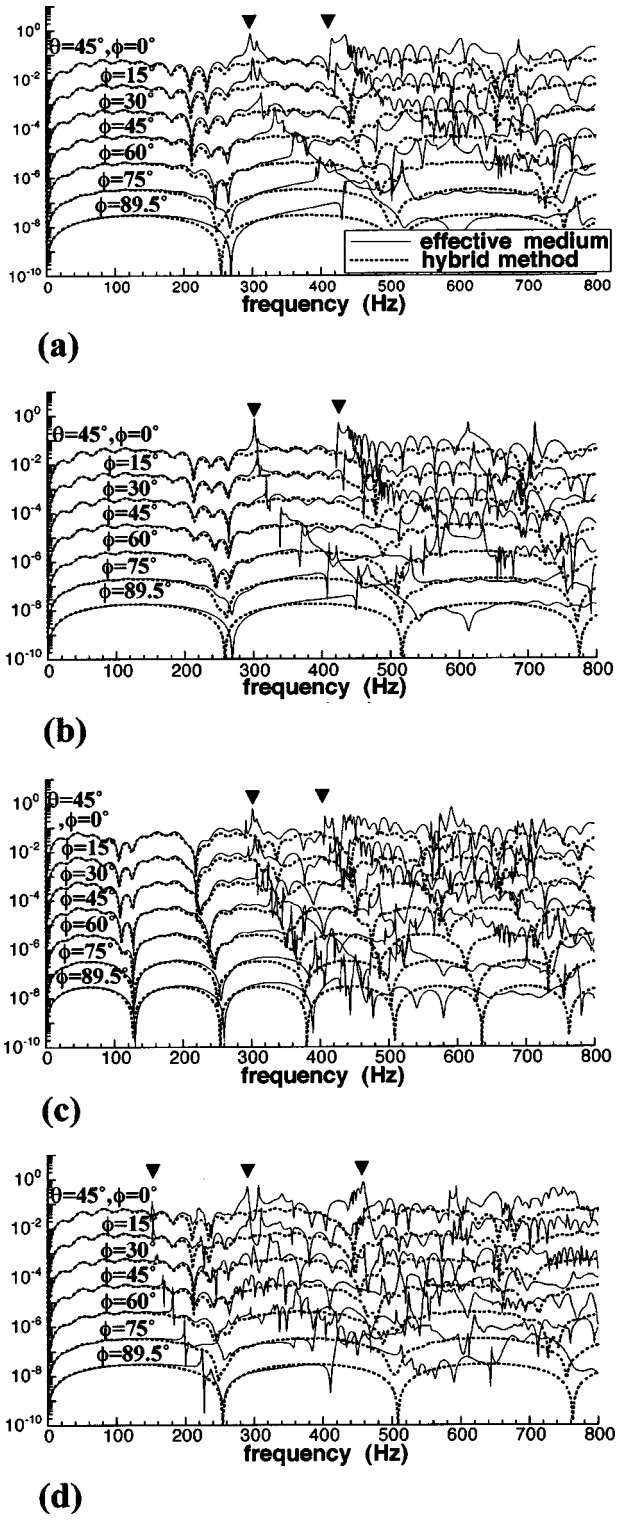

FIG. 8. (a) Frequency response for ''soft, short and regular'' fractures. (b) Frequency response for ''stiff, short and regular'' fractures. (c) Frequency response for ''soft, long and regular'' fractures. (d) Frequency response for ''soft, short and irregular'' fractures. Spectra of wave forms shown in Figs. 6(b)–(e) normalized by the incident wave spectra. All plots exhibit a trend that shows shifts of spectral peaks (as indicated by solid triangles) and valleys to higher frequencies with increasing azimuthal angle.

D. Azimuthal variations of spectra

For the wave forms shown in the preceding section, it is difficult to identify the azimuthal anisotropy due to the fractures using the complicated, seemingly random wave forms of the scattered high-frequency waves. To identify any consistent trends in the multiple scattering or resonance structures of the wave forms, we computed the amplitude spectra of the wave forms shown in Figs. 7(b)–(e) excluding the

direct waves. Each spectrum [Figs. 8(a)–(d)] was normalized by the spectra of the incident wave. Spectra for wave forms computed using the static effective medium approximation are overlaid in dotted lines.

A comparison between the spectra computed by the hybrid plane wave-FEM method and the effective medium theory show that the results start to deviate at frequencies near 200 Hz corresponding to the fracture interval to *P*-wave wavelength ratio of $h/\lambda_P \sim 1/4$. In contrast, the sharp peaks in the spectra that contribute to the coda in the wave forms appear at frequencies above 300 Hz ($h/\lambda_P > 0.4$) for the regularly spaced fractures, and above 150 Hz ($h/\lambda_P > 0.2$) for the irregularly spaced fractures, indicating a strong correlation between the periodicity of the fracture interval and the coda frequency.

Also, for periodic fractures with regular spacings [Figs. 8(a), (b), and (c)], the spectral profiles show a clear trend that shows upward shifts of the peaks (as indicated by solid triangles) with azimuthal angle. This trend becomes less obvious for irregular intervals [Fig. 8(d)], but still noticeable changes as a function of azimuthal angle are present. The regularly spaced notches in the spectra are possibly caused by the tuning effect of the layer because they can be observed for both hybrid and effective medium computations, and also, the intervals of notches are shorter (approximately half) for the ''tall'' fractures [Fig. 8(c)]. These notches show the same shifting behavior as the spectral peaks although the changes in frequency are smaller. These characteristics of the spectra of reflected waves can be used as a diagnostic tool for detecting and characterizing a layer of parallel vertical fractures in the subsurface.

IV. CONCLUSIONS

In this paper, we presented an efficient numerical technique for examining the three-dimensional scattering of plane elastic waves by periodic, two-dimensional structures containing fractures. Using this method, we studied the changes in the characteristics of reflection seismograms as a function of incidence angle, wave frequency, and fracture parameters including fracture height, spacing, and stiffness.

For an incident low-frequency *P* wave, the results of the static effective medium approximation and the explicit simulations by our method were identical. This was somewhat surprising for us because the fractures have a finite height that is relatively small compared to the wavelength, even though the effective medium approximation assumes fractures with an infinite height. For an incident high-frequency wave, the results showed that the scattering from individual fractures and multiple reflections between fractures results in strong reverberations (coda) in seismograms for high-frequency waves. These reverberations indicate the presence of the fractures with spacings similar to the wavelength of the probing waves, and the magnitude of the reverberation is sensitive to both geometry and the stiffness of the fractures. To delineate the contribution of each effect quantitatively, however, further extensive parametric studies should be performed.

Unlike the low-frequency case, the reverberations in the high-frequency seismograms can obscure the azimuthal anisotropy of seismic signatures such as amplitude anisotropy of the scattered *Sh* and *Sv* waves. We demonstrated that for periodic, regular and near-regular fracture spacings, systematic changes can occur in the spectral profiles of high-frequency seismograms as a function of azimuthal angle, which can be an alternative diagnostic tool for identifying the fracture orientations.

Although only limited and simple cases were examined in this paper, we emphasize that more realistic, complex geometry and material properties, such as heterogeneous layering, nonplanar fractures, nonuniform fracture stiffness, can be modeled by modifying the FEM mesh for the unit cell. Thus, this technique provides computationally inexpensive solutions for studying the fundamental characteristics of elastic waves scattered by aligned fractures without resorting to extensive three-dimensional computations.

ACKNOWLEDGMENTS

This work has been supported by the Assistant Secretary for Fossil Energy, Office of Natural Gas and Petroleum Technology, through the National Energy Technology Laboratory of the U.S. Department of Energy under Contract No. DE-AC03-76SF200098.

[1] C.-H. Chang and G. H. F. Gardner, ''Effects of vertically aligned subsurface fractures on seismic reflections: A physical model study,'' Geophysics **62**, 245–252 (1997).
[2] M. A. Schoenberg, S. Dean, and C. M. Sayers, ''Azimuth-dependent tuning of seismic waves reflected from fractured reservoirs,'' Geophysics **64**, 1160–1171 (1999).
[3] M. M. Beretta, G. Bernasconi, and G. Drufuca, ''Linearized inversion of vertically fractured media,'' Geophys. J. Int. **143**, 965–968 (2000).
[4] F. Shen and M. N. Toksoz, ''Scattering characteristics in heterogeneously fractured reservoirs from waveform estimation,'' Geophys. J. Int. **140**, 251–266 (2000).
[5] H. B. Lynn, K. M. Simon, M. Layman, R. Schneider, C. R. Bates, and M. Jones, ''Use of anisotropy in P-wave and S-wave data for fracture characterization in a naturally fractured gas reservoir,'' The Leading Edge **14**, 887–893 (1995).
[6] J. D. Achenbach, M. Kitahara, Y. Mikata, and D. A. Sotiropoulos, ''Reflection and transmission of plane waves by a layer of compact inhomogeneities,'' PAGEOPH **128**, 101–118 (1988).
[7] S. Hirose and M. Kitahara, ''Scattering of elastic waves by a crack with spring-mass contact,'' Int. J. Numer. Methods Eng. **31**, 789–801 (1991).
[8] E. Liu, T. Pointer, J. A. Hudson, and J. H. Queen, ''Numerical modeling of seismic wave propagation in media with distributed inclusions,'' Expanded Abstract, 68th SEG Annual Meeting, New Orleans, 1933–1936, 1998.
[9] R. T. Coates and M. A. Schoenberg, ''Finite-difference modeling of faults and fractures,'' Geophysics **60**, 1514–1526 (1995).
[10] M. A. Schoenberg, K. T. Nihei, S. Nakagawa, and L. R. Myer, ''Scattering from reservoirs with discrete fractures,'' Proc. EAGE/SEG Research Workshop on Reservoir Rocks, Pau, 2001.
[11] A. C. Hennion, R. Bossut, and J. N. Decarpigny, ''Analysis of the scattering of a plane acoustic wave by a periodic elastic structure using the finite element method: Application to compliant tube gratings,'' J. Acoust. Soc. Am. **87**, 1861–1870 (1990).
[12] A.-C. Hladky-Hennion and J. N. Decarpigny, ''Analysis of the scattering of a plane acoustic wave by a doubly periodic structure using the finite element method: Application to Alberich anechoic coatings,'' J. Acoust. Soc. Am. **90**, 3356–3367 (1991).
[13] T. J. R. Hughes, *The Finite Element Method, Linear Static and Dynamic Finite Element Analysis* (Prentice-Hall, Englewood Cliffs, NJ, 1987).
[14] R. D. Henshell and K. G. Shaw, ''Crack tip finite elements are unneces-

sary,'' Int. J. Numer. Methods Eng. **9**, 495–507 (1975).
[15] R. S. Barsoum, ''On the use of isoparametric finite elements in linear fracture mechanics,'' Int. J. Numer. Methods Eng. **10**, 25–37 (1976).
[16] M. A. Schoenberg, ''Elastic wave behavior across linear slip interfaces,'' J. Acoust. Soc. Am. **68**, 1516–1521 (1980).
[17] J.-M. Baik and R. B. Thompson, ''Ultrasonic scattering from imperfect interfaces: A quasi-static model,'' J. Nondestruct. Eval. **4**, 177–196 (1984).
[18] M. A. Schoenberg and C. M. Sayers, ''Seismic anisotropy of fractured rock,'' Geophysics **60**, 204–211 (1995).
[19] S. Krenk and H. Schmidt, ''Elastic wave scattering by a circular crack,'' Philos. Trans. R. Soc. London, Ser. A **308**, 167–198 (1982).

Including dispersion and attenuation directly in the time domain for wave propagation in isotropic media[a)]

Guy V. Norton[b)]
Naval Research Laboratory-Stennis Space Center, Stennis Space Center, Mississippi 39529

Jorge C. Novarini
Planning Systems, Inc., 21294 Johnson Road, Long Beach, Mississippi 39560-9702

(Received 12 July 2002; revised 5 March 2003; accepted 17 March 2003)

When sound propagates in a lossy fluid, causality dictates that in most cases the presence of attenuation is accompanied by dispersion. The ability to incorporate attenuation and its causal companion, dispersion, directly in the time domain has received little attention. Szabo [J. Acoust. Soc. Am. **96**, 491–500 (1994)] showed that attenuation and dispersion in a linear medium can be accounted for in the linear wave equation by the inclusion of a causal convolutional propagation operator that includes both phenomena. Szabo's work was restricted to media with a power-law attenuation. Waters *et al.* [J. Acoust. Soc. Am. **108**, 2114–2119 (2000)] showed that Szabo's approach could be used in a broader class of media. Direct application of Szabo's formalism is still lacking. To evaluate the concept of the causal convolutional propagation operator as introduced by Szabo, the operator is applied to pulse propagation in an isotropic lossy medium directly in the time domain. The generalized linear wave equation containing the operator is solved via a finite-difference-time-domain scheme. Two functional forms for the attenuation often encountered in acoustics are examined. It is shown that the presence of the operator correctly incorporates both, attenuation and dispersion. [DOI: 10.1121/1.1572143]

PACS numbers: 43.20.Hq, 43.20.Bi, 43.30.Es [LLT]

I. INTRODUCTION

Wave propagation in a lossy medium is usually accompanied by dispersion (i.e., except for specific cases, a lossy medium is a dispersive medium). Pulse propagation in such a medium is usually modeled by synthesizing the signal via a Fourier transform of the continuous wave results. On the other hand, experimental measurements are usually carried out using pulses of finite bandwidth. Therefore, direct modeling in the time domain is highly desirable. Previous efforts to include attenuation in the time domain have been carried out mainly in the field of nonlinear acoustics. Most of these methods resort to a form of the parabolic approximation, are restricted to specific functional form for the attenuation, and rely on the hybrid approach of going to the frequency domain to calculate the causal attenuation term. An exception is the work by Tavakkoli *et al.*[1] In that work arbitrary absorption and dispersion are allowed directly in the time domain while not invoking a parabolic approximation. It is based on the use of a second-order operator splitting algorithm. Recently, Szabo[2] proposed a way to include attenuation and dispersion effects into the linear wave equation directly in the time domain through the so-called *causal convolutional propagation operator*. Szabo's operator was defined in the context of a lossy media obeying a frequency power law attenuation. More recently, Waters *et al.*[3] showed that it could be used for a broader class of media. However, direct validation of the theory is still lacking. The operator carries information on both, attenuation and dispersion in a linear medium in the time domain. Hence, it is ideal for use in numerical solutions of the wave equation for pulse propagation in lossy media via the finite-difference-time-domain (FDTD) technique. On the other hand, in the frequency domain, wave propagation occurring in a weakly dispersive media implies that the real and imaginary components of the complex wavenumber are Hilbert transforms of each other. This is usually expressed through the Kramers–Krönig (K-K) relations.[4,5] Analogous expressions were derived by Szabo[2] for use in the time domain. In this work Szabo's approach is investigated by solving the scalar, generalized, inhomogeneous linear wave equation with the inclusion of the causal convolutional propagation operator via a FDTD scheme. Two cases are examined: the first in which the attenuation obeys a power law[2] and the second in which the attenuation follows a more complicated functional form, which serves as an example of attenuation arising in a variety of media.[6–8]

II. BACKGROUND

In what follows, Szabo's approach is reviewed and clarified for use in numerical modeling of pulse propagation directly in the time domain. Assuming that propagation occurs through an isotropic lossy linear medium, the propagation is governed by a modified wave equation of the form

$$\nabla^2 p(r,t) - \frac{1}{c_0^2}\frac{\partial^2 p(r,t)}{\partial t^2} - \frac{1}{c_0} L_\gamma(t) * p(r,t) = \delta(r - r_s)s(t), \tag{1}$$

[a)]Presented at the 143rd meeting of the Acoustical Society of America.
[b)]Electronic mail: norton@nrlssc.navy.mil

 0001-4966/2003/113(6)/3024/8/$19.00

where c_0 is a reference phase velocity, $\delta(r-r_s)$ is the Dirac delta function at the source location, $s(t)$ is a source function, and $L_\gamma(t)$ is the *causal convolutional propagation operator* controlling attenuation and dispersion. It plays the role of a generalized dissipative term in the time domain. This equation is Szabo's Eq. (2)[2] with the addition of a source term and a factor c_0^{-1} in the third term of the lhs arising from dimensional analysis. In the framework of generalized functions, assuming that the pressure field $p(r,t)$ is a distribution and recalling that distributional differentiation is equivalent to a convolution with a derivative of the Dirac delta function $[\delta^{(1)}(t)*f(t)=f^{(1)}(t)]$, the operator can be defined as

$$L_\gamma(t)=\Gamma(t)*\delta^{(1)}(t). \tag{2}$$

The function $\Gamma(t)$ represents a causal time domain propagation factor which accounts for *causal attenuation*, that is, the factor $\Gamma(t)$ has to also govern the dispersion in the system in order to insure causality. Waters *et al.*[3] defined the linear propagation of ultrasonic waves through an isotropic, lossy medium by the following dissipative homogeneous wave equation

$$\nabla^2 p(r,t)-\frac{1}{c_0^2}\frac{\partial^2 p(r,t)}{\partial t^2}-\Gamma(t)\frac{\partial p(r,t)}{\partial t}=0. \tag{3}$$

Starting with this equation and defining the operator as the result of a *product* $[L_\gamma(t)=\Gamma(t)\delta^{(1)}(t)]$ they write the following:

$$\nabla^2 p(r,t)-\frac{1}{c_0^2}\frac{\partial^2 p(r,t)}{\partial t^2}-L_\gamma(t)*p(r,t)=0. \tag{4}$$

It should be pointed out that, in order to go from Eq. (3) to Eq. (4), the product in the third term of Eq. (3) as well as in the definition of $[L_\gamma(t)]$ should be interpreted as convolutions and not as products as stated. It should be understood that the product of a function with a delta function or its derivative is meaningful only upon integration, which implies a convolution. Thus Eq. (3) should be interpreted as being symbolic. Numerical evaluation of Eq. (3) as written (interpreted as a product) does not correctly carry the causal attenuation (and hence dispersion) into the time domain. Defining the operator as in Eq. (2) leads to the following two alternative expressions for Eq. (1),

$$\nabla^2 p(r,t)-\frac{1}{c_0^2}\frac{\partial^2 p(r,t)}{\partial t^2}-\frac{1}{c_0}\left(\Gamma(t)*\frac{\partial p(r,t)}{\partial t}\right)=\delta(r-r_s)s(t) \tag{5}$$

and

$$\nabla^2 p(r,t)-\frac{1}{c_0^2}\frac{\partial^2 p(r,t)}{\partial t^2}-\frac{1}{c_0}\frac{\partial(\Gamma(t)*p(r,t))}{\partial t}=\delta(r-r_s)s(t). \tag{6}$$

The causal propagation factor $[\Gamma(t)]$ of Eq. (2) will now be defined. Considering the medium as a linear filter and excluding nondispersive components of attenuation and phase velocity, the transfer function can be written as

$$T(\omega)=e^{(-\alpha(\omega)+i\beta'(\omega))}=e^{\gamma'(\omega)} \tag{7}$$

with the complex propagation factor given by

$$\gamma'(\omega)=-\alpha(\omega)+i\beta'(\omega), \tag{8}$$

where $\alpha(\omega)$ is the frequency-dependent attenuation and $\beta'(\omega)$ is the relative dispersion. The full complex propagation factor (which now includes both dispersive and nondispersive components) can be written as

$$k(\omega)=-\alpha(\omega)+i\beta(\omega), \tag{9}$$

where $\beta(\omega)=\beta'(\omega)+\omega/c_0$ and thus it follows that

$$\beta'(\omega)=\omega\left[\frac{1}{c(\omega)}-\frac{1}{c_0}\right], \tag{10}$$

where c_0 is the reference phase velocity, usually the velocity at a given circular frequency ω_0, i.e., $c_0=c(\omega_0)$ in the same medium.

The physical assumption made by Szabo, borrowed from linear circuit theory, is that for a real signal to propagate in a real medium, not only should the complex transfer function of the medium be causal, but its logarithm (the complex propagation factor) should also satisfy causality.[9] For wave propagation, this implies that the real and imaginary parts of the complex propagation factor should be related by the Hilbert transform H. Then

$$\beta'(\omega)=H[\alpha(\omega)] \tag{11}$$

and thus

$$\gamma'(\omega)=-1(1-iH)\alpha(\omega). \tag{12}$$

It should be pointed out that for physical systems, the K-K relations relate the real and imaginary part of the generalized susceptibility of the system. It is a complex quantity which connects the generalized displacement in dissipative systems with the generalized force applied to them.[6,10] In acoustics, the suitable descriptor of the physical system to which the K-K are usually applied is the complex compressibility. It connects the change in acoustic density ρ' as the general displacement, and the applied acoustic pressure p' as the generalized force, $\rho'=Kp'$. Since for plane waves $p'=\rho' c^2$ it follows that $K=1/c^2$. Therefore, the compressibility is related to the inverse of the square of a complex phase velocity, or, equivalently, it is proportional to the square of the complex wavenumber. In the limit of $\alpha(\omega)c(\omega)/\omega \ll 1$ (i.e., when the attenuation in Neper per wavelength is small) the K-K relations relate $c(\omega)$ and $\alpha(\omega)$ directly. Otherwise the attenuation and phase velocity are related by a pair of coupled integral equations.[6,10]

In the framework of generalized functions and their transforms, since the nondispersive part is not included in $\gamma'(\omega)$, the Fourier conjugate to ω is the retarded time ($\tau=t-r/c_0$) and defining the causal time domain propagation factor $\Gamma(\tau)$ as the Fourier transform of $\gamma'(\omega)$ we obtain

$$\Gamma(\tau)=FT^{-1}[-(1-iH)\alpha(\omega)]. \tag{13}$$

Recalling that $FT^{-1}[iH]=\mathrm{sgn}(\tau)$ the causal time domain propagation factor reduces to

$$\Gamma(\tau)=-(1+\mathrm{sgn}(\tau))FT^{-1}[\alpha(\omega)], \tag{14}$$

which can be rewritten as

$$\Gamma(\tau) = -2 \;\; 1_+(\tau) FT^{-1}[\alpha(\omega)], \tag{15}$$

where $1_+(\tau)$ represents the step function defined as[11]

$$1_+ = \begin{cases} 0 & \tau < 0, \\ \frac{1}{2} & \tau = 0, \\ 1 & \tau > 0. \end{cases} \tag{16}$$

Once the causal time domain propagation factor has been generated, the causal convolutional propagation operator $L_\gamma(\tau)$ is formed using Eq. (2). It should be pointed out here that in both, the original development by Szabo [Ref. 2, Eq. (43)] and in the review by Waters *et al.* [Ref. 3, Eq. (18)], Eq. (15) was written as though corresponding to the operator L_γ, when, actually, it is strictly concerned with $\Gamma(\tau)$.

As mentioned elsewhere, Szabo's original use of the operator was limited to a power law attenuation form, excluding some values of the exponent. Waters *et al.*,[3] using distributional analysis, show that Eq. (15) is more general and can be applied to any attenuation form for which an associated causal phase velocity exists.

Szabo[2] showed the form that the time domain propagation factor $\Gamma(\tau)$ can take for some specific cases of power law attenuation. Because of the power law nature of the chosen attenuation, the resulting operators involve improper integrals (which can be interpreted in a Cauchy principal value sense), which are difficult to evaluate. Consequently, no numerical evaluation of the resulting time domain integro-differential equations was offered. The purpose of this work is to determine, through high fidelity numerical modeling, the ability of the causal convolutional propagation operator to properly include dispersion and attenuation when modeling pulse propagation directly in the time domain in an isotropic lossy medium (within the weak dispersion regime).

III. MODELING CONSIDERATIONS

In this section several modeling issues that are of interest when implementing the proposed technique will be discussed. The intent of this section is to relay information based on knowledge gained from having implemented the proposed technique and while performing numerical experiments. No attempt is made to perform a sensitivity test with the various available parameters. Instead we choose to determine the validity of the technique when utilizing standard sampling criteria for FDTD modeling and signal processing.

Equations (5) and (6) were implemented utilizing the FORTRAN programming language operating on a multiprocessor computer. It was observed that the derivative of the pressure [Eq. (5)] oscillates quicker than the derivative of the convolution [Eq. (6)]. Therefore, in order to properly depict the changing pressure derivative requires a finer time step (δt) than one would normally require for either defining the time domain propagation factor or satisfying the Courant condition. Even though the equations differ in both derivation and implementation, they both gave identical results. Using Eq. (5) requires more computational time to complete a numerical simulation than using Eq. (6). This is due to the fact that its time step (δt) is smaller than that required for Eq. (6), thus requiring more executions to cover a given time duration. The results presented in Sec. III are therefore based on Eq. (6).

A good review of using the method of finite differences to numerically integrate partial differential equations can be found in Ref. 12. The FDTD scheme utilized is explicit, fourth-order accurate in space and second-order accurate in time. The finite difference approximations to the derivatives of Eq. (6) are

$$\frac{\partial^2 p(r,t)}{\partial t^2} = \frac{p_i^{k+1} - 2p_i^k + p_i^{k-1}}{\delta t^2}, \tag{17}$$

$$\nabla^2 p(r,t) = \frac{-p_{i+2}^k + 16p_{i+1}^k - 30p_i^k + 16p_{i-1}^k - p_{i-2}^k}{12\delta r^2}, \tag{18}$$

$$\frac{\partial(\Gamma(t) * p(r,t))}{\partial t} = \frac{3q_i^{k+1} - 4q_i^k + q_i^{k-1}}{2\,\delta t}, \tag{19}$$

where $q = \Gamma * p$, the superscript k is the time index and the subscript i is the spatial or grid index. The grid spacing and time step are given by δr and δt, respectively. To insure that the edges and corners of the computational grid do not introduce spurious reflections, absorbing boundary conditions were implemented.[13]

A word on the convolution shown in Eq. (19) is in order. The convolution is defined as

$$q(r,t) = \int_{-\infty}^{\tau} \Gamma(\tau) \cdot p(r, t-\tau) d\tau \tag{20}$$

and takes the following discrete form

$$q(r, k\,\delta t) = \sum_{n=0}^{N} \Gamma(n\,\delta t) \cdot p(r, (k-n)\,\delta t)\,\delta t, \tag{21}$$

where N in the maximum number of convolution points [the size of the $\Gamma(\tau)$ array]. In order to expedite the execution of the model, the convolution performed at a spatial grid point occurs only when sufficient time has elapsed (from the time the signal is turned on) to allow the signal to arrive at the grid point. This time is determined by using a phase velocity higher than that expected to be found in the dispersive media to determine the time at which the convolution is allowed to start for each grid point. Once this conditional is met the convolution will be performed for each and every subsequent time step. In addition, each convolution that is performed is not initially equal to the maximum number of propagation factor terms available. The maximum number used in the convolution is used only after the model has time stepped more than this maximum number. The convolution requires that the time history of the pressure be retained for each grid point. The pressure array at each grid point will have the same number of temporal points as the $\Gamma(\tau)$ array. If, for example, 1000 points were the maximum number used in the convolution, then 1000 past pressures need be kept for each grid point.

The explicit FDTD scheme is conditionally stable if the Courant condition $[(c_0 \delta t / \delta r) < 1]$ is satisfied. This, how-

ever, does not guarantee that the solution will achieve the desired accuracy. Typically 15 to 20 grid points per wavelength are required for accurate solutions. Thus the requirement on grid spacing is dependent upon the wavelength of the highest frequency that the source produces. This then puts an upper bound on the time step if the Courant condition is to be satisfied. However, there is another constraint on the time step, it must be small enough to capture the form of the time domain propagation factor.

It was found that the time domain propagation factor determined for a given time step cannot be interpolated and used at a finer time step nor can it be used at a coarser time step. Interpolation to a finer time step will introduce information at frequencies not contained in the attenuation array used to generate $\Gamma(\tau)$. Sampling at a coarser time step will not properly resolve the high and rapid oscillations (in amplitude) occurring at the beginning of its time history. This early time section of the propagation factor array is critical to correctly account for both the attenuation and dispersion. Thus the time domain propagation factor must be determined at the same time step that the finite difference routine uses.

There are other considerations unique to the present method. Since a convolution will be performed at every grid point, a determination of how much time the convolution will span is required: Too short a time and the dispersion effects will not be fully manifest; too long and the computational requirements will be such that obtaining a solution becomes too time consuming even on a computer with parallel processing capabilities. The following condition is used as a guide: that the time span of the convolution must be long enough such that the time domain propagation factor has numerically converged to a constant value. As previously stated, the time domain propagation factor has high and rapid oscillations which exist for a short period of time after which the propagation factor will monotonically converge. For the examples presented in the next section 1000 convolution points were adopted. This number represents a small subset of the total propagation factor determined for both examples. For the first example the propagation factor consisted of 16 384 points and for the second it consisted of 32 768 points.

Another consideration is the overall size of the program. The number and size of the matrices needed to implement this procedure is larger than a typical explicit FDTD program. Normally one needs to store the current and previous pressure values at each grid point in order to solve for the future value. Hence the matrix would have a size of, say, *number of grid points by three*, but now the matrix size would be *number of grid points by number of convolution points*. In addition another matrix of size *number of grid points by three* is required to store the convolution of the time domain propagation factor with the pressure [see Eq. (19)].

IV. VALIDATION

To evaluate the ability of the causal convolutional propagation operator to properly incorporate the effects of attenuation and dispersion, Eq. (6) is solved for the acoustic pressure via finite differences for the case of acoustic pulse propagation in a 1-D isotropic lossy medium. Since the lossy media considered in the examples are also dispersive the two terms lossy and dispersive will be used interchangeably. In addition, for the sake of simplicity, henceforth the numerically calculated pressure at a given location will be referred to as ''the received signals.''

Two numerical experiments will be performed using different environments for each experiment. The environment for the first experiment has a power-law attenuation of the type encountered in a variety of media (liquids, ocean sediments, etc.). The environment for the second experiment has an attenuation that follows a bell-shaped functional form typically found in both ultrasonics[7] and in bubble clouds at sea.[8] Both environments are probed with a broadband doublet signal (source function) of the type

$$s(t) = te^{-\alpha_d t^2}, \tag{22}$$

where α_d is a constant governing the time interval between the negative and positive peaks of the doublet.

The numerically calculated signals obtained from solving Eq. (6) were processed using the technique of broadband spectroscopy.[14] In this case the technique will be applied to propagation between two locations in the same medium. The numerical signals versus time, in the dispersive medium at two different receiver locations (r1 and r2) separated a distance d, were transformed into the frequency domain via the fast Fourier transform (FFT). By taking the ratio of the complex spectra, both attenuation and phase velocity versus frequency were extracted and compared with the expected values. The attenuation (in Np/m) at a given frequency is determined from the spectral components and the path length d as

$$\alpha(f) = \frac{\ln(|P(r_2,f)/P(r_1,f)|)}{d}. \tag{23}$$

The phase velocity is calculated as

$$c(f) = \frac{2\pi f d}{\mathrm{ARG}(P(r_2,f)/P(r_1,f))}, \tag{24}$$

where ARG is the argument of the ratio of the complex spectra, with due regard to phase unwrapping. Notice that neither Eq. (23) nor Eq. (24) explicitly use c_0 to determine the attenuation or phase velocity. The reference velocity is present as a consequence of the governing equation, namely Eq. (6).

For the first numerical experiment, the case of the power law attenuation, $\alpha(\omega) = \alpha_0 \omega^y$, a linear dependence with frequency was chosen $(y=1)$, with $\alpha_0 = 2.35 \times 10^{-5}$ Np/m/rad/s. The constant α_d of the source function Eq. (22) was set equal to 3.15×10^6, leading to a spectral peak $f_p = 400$ Hz for the acoustic signal. The reference sound velocity (c_0) is assumed 1370 m/s.

When the attenuation increases monotonically with frequency (as is the case for the power law with $y=1$) it is necessary to generate the attenuation curve over a wide frequency range. A window function is then applied that leaves invariant the region of interest. This is performed in order to avoid artifacts stemming from the numerical implementation of Eq. (15) via the use of the FFT. Since this case deals with low frequencies, a cosine window centered at zero frequency

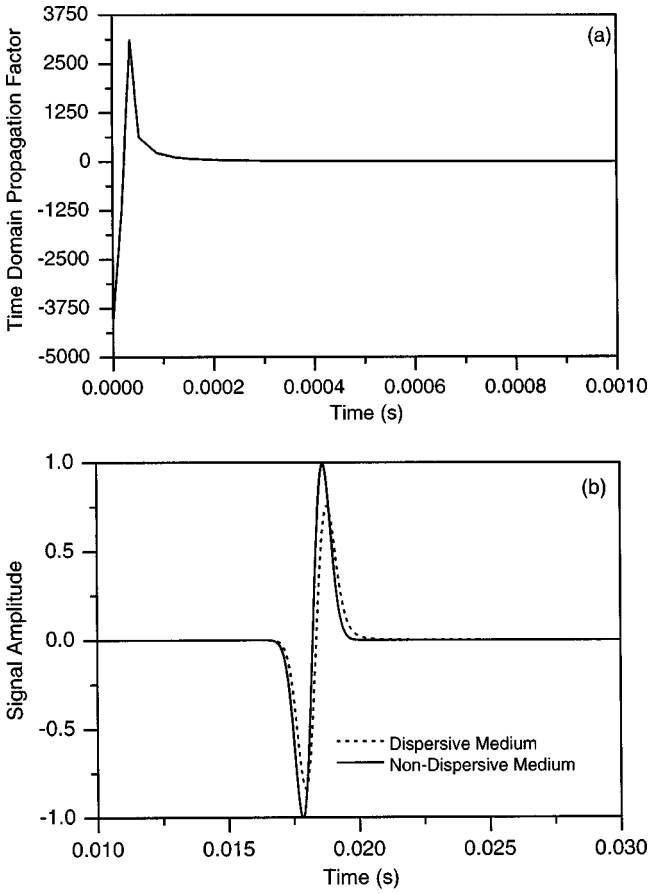

FIG. 1. The (a) time domain propagation factor and (b) the received signals.

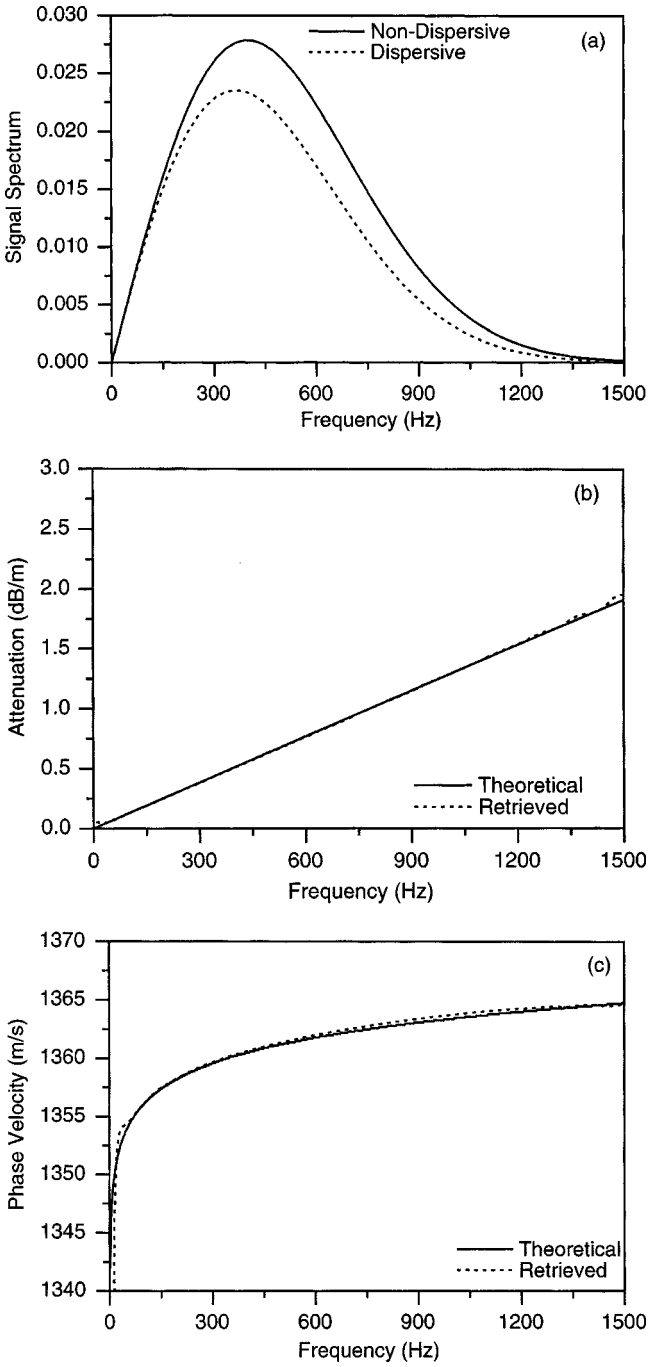

FIG. 2. (a) Signal spectrum for the nondispersive (solid line) and dispersive (dotted line) media versus frequency. (b) Comparison of the original (solid line) and retrieved (dotted line) attenuation. (c) Comparison of the original (solid line) and retrieved (dotted line) phase velocity.

was applied to the power law attenuation over the entire frequency range. This leaves the low-frequency region embraced by the source spectrum essentially invariant, while tapering to zero for the high frequencies. At the maximum frequency of interest (1500 Hz), at which the spectrum of source signal falls 40 dB down, the value of the filtered attenuation is 99.3% of its original value. In generating $\alpha(f)$, 16 384 frequencies are used with a constant frequency spacing of 1.74 Hz. The resulting time step is 1.75×10^{-5} s. The grid spacing δr is 0.1 m. A maximum of 1000 points was used for the convolution. These choices of parameters amply satisfy the stability condition along with providing sufficient accuracy in the finite difference scheme for the frequency content of the pulse. The corresponding time domain propagation factor, obtained as prescribed by Eq. (15) [which provides the amplitude of $L_\gamma(t)$], is shown in Fig. 1(a). Figure 1(b) shows the signal received at a range of 25 m (dotted line). The signal at the same location in a nondispersive medium with $c_0 = 1370$ m/s is also plotted (solid line) for comparison. Note that the signal in the dispersive medium has suffered a loss in strength and has incurred a slight broadening.

Figure 2(a) depicts the signal spectra in both the nondispersive medium (solid line) and in the dispersive medium (dotted line). Note the shape of the signal's spectrum in the dispersive medium. The spectral peak now occurs at approximately 360 Hz, where the original peak was at 400 Hz. Figure 2(b) depicts a comparison of the original values for the attenuation (solid line), used to generate $\Gamma(\tau)$ of Eq. (15), to the retrieved attenuation (dotted line) determined using the model output shown in Fig. 1(b). Note that the retrieved attenuation is in excellent agreement with the expected attenuation. The agreement is good even at the high frequencies where the signal amplitude is very small. Figure 2(c) depicts the comparison between the theoretically predicted (solid line) and retrieved phase velocity (dotted line). The agreement between the two is excellent, demonstrating that the inclusion of the causal convolutional propagation operator in the generalized wave equation incorporates both at-

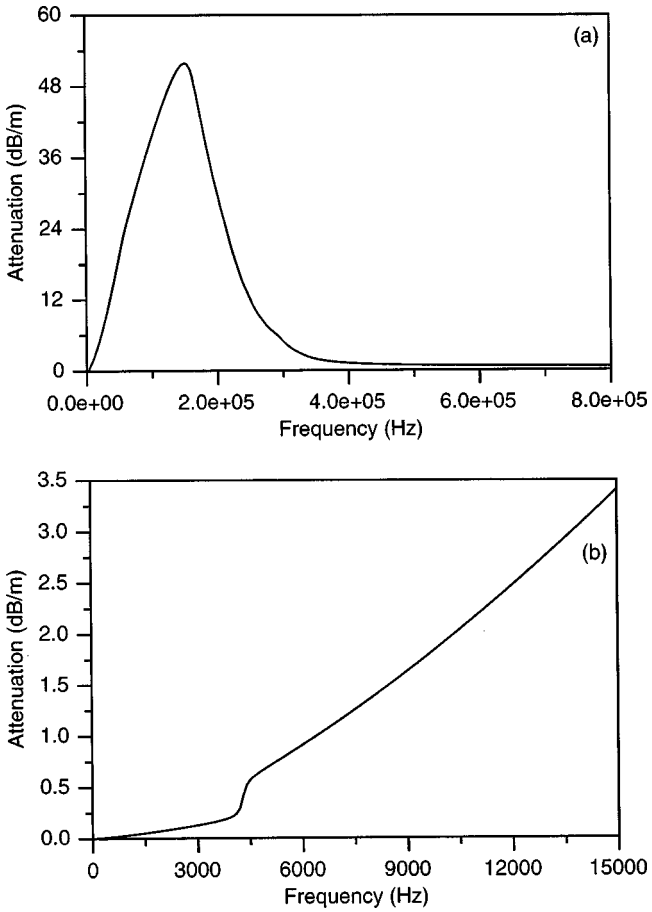

FIG. 3. The (a) original attenuation versus frequency and (b) a close-up of the low-frequency portion of the original attenuation.

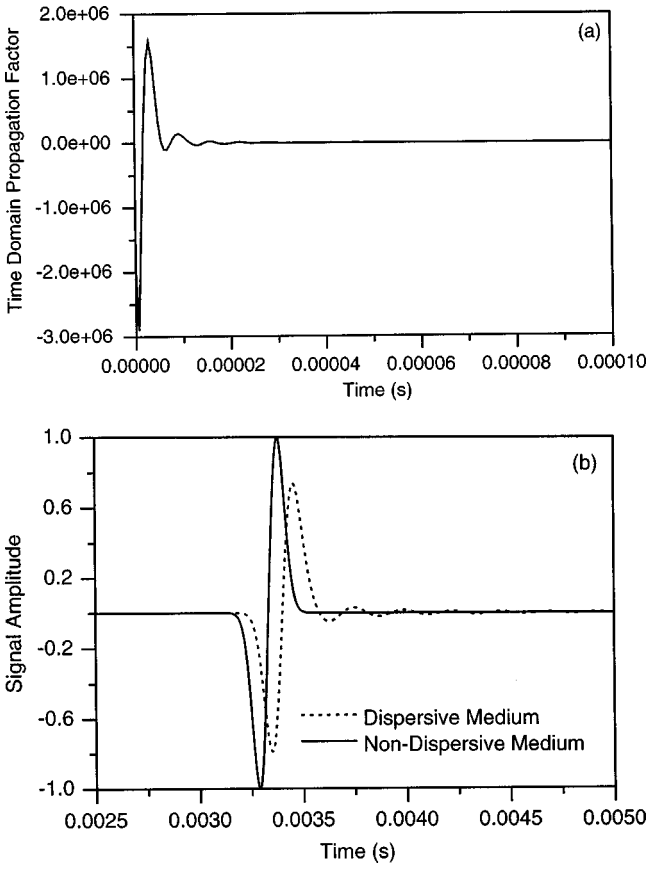

FIG. 4. The (a) time domain propagation factor and (b) the received signals.

tenuation and dispersion in a precise manner.

For the second numerical experiment, the functional form for the attenuation is representative of that found for bubble distributions in liquids (i.e., in ultrasonics[7] and near the sea surface[8]). In those cases measured attenuation increases from a minimum at low frequency to a maximum value and then decreases at high frequencies. In the particular case presented here, the attenuation corresponds to a possible bubble distribution at sea.[8] Underlying the sea surface there are clouds of microbubbles generated by the presence of breaking waves forming typical structures or "plumes." The bubble density and the radii spectrum within a plume varies with depth and wind speed. (See Ref. 8 for a description of typical plumes and numerical parameters.) There is no analytical functional form available for the attenuation for any of the bubble formations. Neither are there available reliable dispersion data curves over a broad band of frequencies. Therefore, the attenuation necessary to generate the convolution operator is calculated from a possible spectrum of bubble radii (derived from direct measurements of bubble population). Then, applying well-known equations for sound propagation in bubbly liquids at low void fractions, the attenuation and phase velocity in the medium are calculated from the complex compressibility. (See Ref. 8 for details.) Next, the attenuation versus frequency is used to generate the propagation factor as prescribed by Eq. (15), needed to form the convolution operator [Eq. (2)]. It also provides the reference solution for the values retrieved from Eq. (23). The phase velocity array derived directly from the compressibility is used to check the dispersion curve retrieved through Eq. (24). The spectrum of bubble radii of the so-call gamma plumes at 1 m below the surface and for a 20-m/s wind speed was adopted. The attenuation over an extended frequency range is shown in Fig. 3(a). Figure 3(b) shows the low-frequency region that the source signal will span. Notice the transition occurring around 4 kHz. This corresponds to the resonance frequency of the largest bubble present in the bubble distribution (800 μm) leading to the attenuation at hand. A portion of the causal time domain propagation factor Γ is shown in Fig. 4(a), obtained using Eq. (15) over the entire frequency range of the attenuation [Fig. 3(a)].

The constant α_d of the source function Eq. (22) is set equal to 2.418×10^8 leading to a spectral peak $f_p=3500$ Hz for the acoustic signal. The time step is 6.1×10^{-7} s. The grid spacing δr is 0.005 m. Again, a maximum of 1000 terms was used for the convolution. Figure 4(b) shows the signal received at a range of 5 m for both the dispersive and non-dispersive medium. Notice that for the signal in the dispersive medium (dotted line) the result is reminiscent of that observed in the previous example. There is an additional effect this time, namely small amplitude oscillations extending in time. This is a direct consequence of the oscillatory nature of the time domain propagation factor. The observed time delay in the dispersive medium with respect to the non-dispersive medium is just a consequence that, for the nondispersive medium, we chose c_0 to be the typical value for the

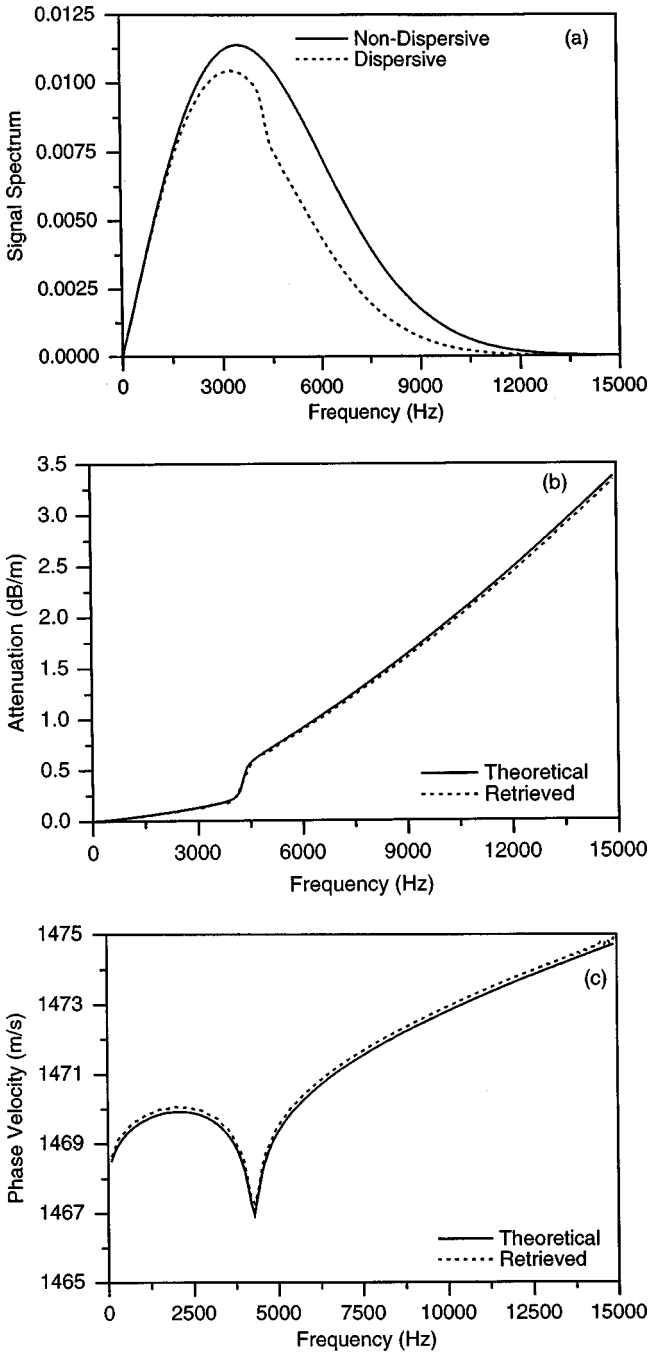

FIG. 5. (a) Signal spectrum for the nondispersive (solid line) and dispersive (dotted line) media versus frequency. (b) Comparison of the original (solid line) and retrieved (dotted line) attenuation. (c) Comparison of the original (solid line) and retrieved (dotted line) phase velocity.

velocity at extremely high frequency (MHz) in bubble free sea water namely, 1500 m/s. Figure 5(a) is similar to Fig. 2(a) comparing the signal spectrum in a nondispersive medium (solid line) to the dispersive medium (dotted line). Figure 2(b) compares the original attenuation (solid line) to the retrieved attenuation (dotted line). Again, note the excellent agreement of the retrieved attenuation compared to the original attenuation. Particularly interesting is that the step observed in the signal spectrum [Fig. 5(a)] for the dispersive medium is due to the step or jump in the attenuation curve [Fig. 2(b)] which is caused by the onset of bubble resonance. This step or jump in the attenuation is accurately recovered, implying that it has been correctly included in the propagation of the pulse. Figure 5(c) compares the phase velocity. The agreement between retrieved and theoretically predicted results is excellent, once again demonstrating that both attenuation and dispersion are accurately included when modeling propagation directly in the time domain utilizing the convolutional propagation operator.

V. CONCLUDING REMARKS

Direct time domain modeling of a 1-D broadband pulse propagating in an isotropic lossy/dispersive medium has been performed via numerical solution of the modified linear wave equation. It is shown that the inclusion of Szabo's causal convolutional propagation operator successfully accounts for attenuation and dispersion in the medium. The fact that a causal convolutional propagation operator can be defined for wave propagation in any weakly dissipative media allows for inclusion of attenuation and dispersive effects directly in the time domain. This is true for any physical process that can be expressed through the scalar linear wave equation (acoustics waves, longitudinal waves, shear waves, elastic waves, polarized electromagnetic waves), and for which Eq. (11) holds. In particular, when dealing with numerical time domain models for wave propagation, the concept of a causal convolutional propagation operator is very attractive because of its simplicity. For attenuation gathered during an experiment, Eqs. (15) and (2) allow for the calculation of the operator via a FFT of the discrete set of values without requiring a specific functional form.

ACKNOWLEDGMENTS

The authors would like to thank one of the anonymous reviewers for bringing to their attention the work by Tavakkoli *et al.* This work has been supported by the Office of Naval Research (Program Element No. 61153N, WU No. 71820500) and by a grant of computer time at the DoD High Performance Computing Shared Resource Center [U. S. Army Engineer Research and Development Center (ERDC), Vicksburg, MS]. This document has been reviewed and is approved for public release.

[1] J. Tavakkoli, D. Cathignol, R. Souchon, and O. A. Sapozhnikov, "Modeling of pulsed finite-amplitude focused sound beams in time domain," J. Acoust. Soc. Am. **104**, 2061–2072 (1998).
[2] T. L. Szabo, "Time domain wave equations for lossy media obeying a frequency power law," J. Acoust. Soc. Am. **96**, 491–500 (1994).
[3] K. R. Waters, M. S. Hughes, G. H. Brandenburger, and J. G. Miller, "On a time-domain representation of the Kramers-Krönig dispersion relations," J. Acoust. Soc. Am. **108**, 2114–2119 (2000).
[4] R. D. L. Krönig, "On the theory of dispersion of X-rays," J. Opt. Soc. Am. **12**, 547–557 (1926).
[5] C. W. Horton, Sr., "Dispersion relationships in sediments and sea water," J. Acoust. Soc. Am. **55**, 547–549 (1974).
[6] S. Temkin, "Attenuation and dispersion of sound in bubbly fluids via the Kramers-Krönig relations," J. Fluid Mech. **211**, 61–72 (1990).
[7] J. N. Marsh, C. S. Hall, M. S. Hughes, J. Mobley, J. G. Miller, and G. H. Brandenburger, "Broadband through-transmission signal loss measurements of Albyunex suspensions at concentrations approaching *in vivo* doses," J. Acoust. Soc. Am. **101**, 1155–1161 (1997).
[8] J. C. Novarini, R. S. Keiffer, and G. V. Norton, "A model for variations in the range and depth dependence of the sound speed and attenuation in-

duced by bubble clouds under wind-driven sea surfaces,'' IEEE J. Ocean. Eng. **23**, 423–438 (1998).
[9] E. A. Guillemin, *Theory of Linear Physical Systems* (Wiley, New York, 1963), Chap. 18.
[10] E. T. O'Donnell, E. T. Jaynes, and J. G. Miller, ''Kramers-Krönig relationship between ultrasonic and phase velocity,'' J. Acoust. Soc. Am. **69**, 696–701 (1981).
[11] R. N. Bracewell, *The Fourier Transform and its Applications*, 2nd ed. (McGraw-Hill, New York, 1986), pp. 57–61.
[12] G. G. O'Brien, M. A. Hyman, and S. Kaplan, ''A Study of the Numerical Solution of Partial Differential Equations,'' J. Math. Phys. (Cambridge, MA) **29**, 223–251 (1950).
[13] R. Clayton and B. Engquist, ''Absorbing boundary conditions for acoustic and elastic wave equations,'' Bull. Seismol. Soc. Am. **67**, 1529–1540 (1977).
[14] W. Sachse and Y. Pao, ''On the determination of phase and group velocities of dispersive waves in solids,'' Appl. Phys. **49**, 4320–4327 (1978).

Prediction and measurement of nonpropagating Lamb modes at the free end of a plate when the fundamental antisymmetric mode A_0 is incident

O. Diligent and M. J. S. Lowe
Department of Mechanical Engineering, Imperial College London, London SW7 2AZ, United Kingdom

E. Le Clézio, M. Castaings, and B. Hosten
Laboratoire de Mécanique Physique, Université Bordeaux 1, UMR CNRS 5469, 351 Cours de la Libération, 33405 Talence Cedex, France

(Received 16 July 2002; revised 13 February 2003; accepted 24 February 2003)

Reflection of Lamb waves when the fundamental mode A_0 is incident at the free end of a plate is studied, in order to identify the extent to which the generation of nonpropagating modes influences the field local to the end of the plate. Semi-analytical predictions, finite element simulations, and experimental measurements are presented for frequencies below the A_2 cutoff. First it is shown, for frequencies below the A_1 cutoff, that reflection of the A_0 mode is accompanied by a delay in phase, and that there is significant additional motion due to nonpropagating modes within about five plate thicknesses of the end. The extend of this additional motion in the vicinity of the end of the plate is demonstrated by subtracting the contribution of the propagating modes from the displacement field. The wave field at frequencies above the A_1 cutoff is more complex because the A_1 as well as the A_0 propagating modes are present at the end of the plate. Nevertheless, it has still been possible, using semi-analytical predictions and finite element simulations, to demonstrate the additional motion due to the nonpropagating modes.
[DOI: 10.1121/1.1568758]

PACS numbers: 43.20.Mv [YHB]

I. INTRODUCTION

The motivation of the work presented here is the ultrasonic inspection (NDE) of plates. There are many engineering structures which are composed of large areas of flat plates, such as petrochemical tanks or pressure vessels. The detection of flaws in such big structures is often tedious and time consuming and thus expensive. Common techniques such as point by point inspection can be replaced by a rapid inspection using ultrasonic Lamb waves which propagate along the plate and may be reflected by defects.

Lamb waves[1] have been very much studied in the past 50 years,[2–4] including work which has identified the potential of using them for inspection.[5–11] It is well known that the reflection of a Lamb wave from the end of a plate is very often accompanied by the generation of additional localized disturbances. These nonpropagating modes, which exist solely in the material near the end of the plate, and which are present only during the time it takes for the Lamb wave to reflect, have indeed been studied and reported quite extensively; see, for example, Refs. 8, 9, 12–18. The work of Torvik[9] is particularly recommended. Very often the interest in considering these modes is in properly accounting for all contributions to the field around a discontinuity when applying normal mode superposition techniques.[12,16,17,19]

The study of the nonpropagating modes which is presented in this paper was conducted in the context of ongoing research by the authors relating to the Non-Destructive Testing (NDT) of plate structures at Imperial College and at the Laboratoire de Mécanique Physique (LMP) of Bordeaux. This collaborative work is to validate finite element as well as semi-analytical models.

The NDT laboratory at Imperial College is interested in the detection of corrosion defects in plate structures, with particular motivation to inspect large shell structures such as oil storage tanks. The aim of the work is to develop a technique which can be used rapidly to assess the integrity of a plate using Lamb waves. The notion is that a transducer unit placed on the plate will generate and receive Lamb waves in controlled directions; processing of the arrival of reflected waves will then allow a map of corrosion anywhere in the plate to be constructed. Some preliminary results of the work on this technique have already been reported.[20,21] The value of the knowledge of the nonpropagating modes for that work is: (1) it is essential when processing received signals to account properly for those which are reflections from the edge of the plate under test; for example, if not understood, phase delays of these reflections could adversely affect the performance of a phased array transducer; (2) it is important to be aware of how far the transducer needs to be from the edge of the plate in order to avoid detecting the additional localized displacements.

The LMP group at Bordeaux University is interested in a modal decomposition method[17,22,23] for establishing semi-analytical solutions for modelling the diffraction of Lamb waves by cracks in plates. The purpose of their study is to understand the scattering problem, and also to build an efficient numerical routine which is much faster than traditional finite element (FE)-based methods. It is planned later to solve the inverse problem, that is to estimate the position and

 0001-4966/2003/113(6)/3032/11/$19.00

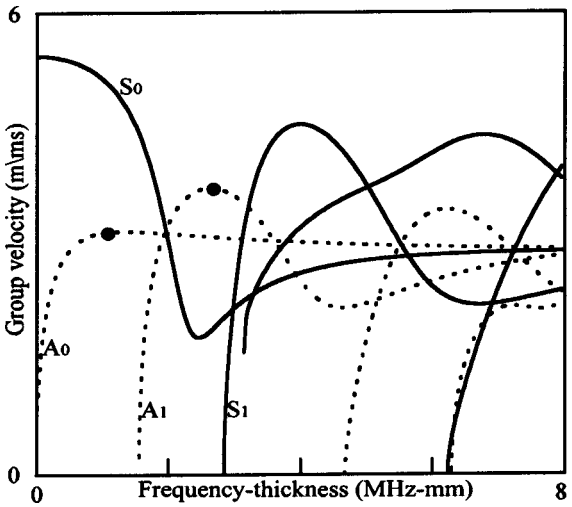

FIG. 1. Group velocity dispersion curves for Lamb waves in an aluminum plate. Solid lines are symmetric modes, dashed lines are antisymmetric modes. The two dots show the two frequencies (1.0 and 2.7 MHz mm) at which the study was carried out.

geometry of a crack from the measured diffracted Lamb modes. An intermediate stage to this work was to solve properly the reflection of Lamb waves at the free edge of a plate.

The principal aim of this paper is then to perform a cross-validation of the model developed in Bordeaux with the FE calculations and experiments undertaken at Imperial College, by comparing results for the reflection of Lamb waves and the generation of nonpropagating modes when the A_0 mode is incident, at frequencies both below and above the A_1 cutoff frequency. The novel measurements of the fields of the nonpropagating modes using a laser interferometer are also included in the validation exercise. Finally, the reflection of the S_0 mode, which is much simpler in its behavior, is considered briefly for completeness.

II. PROPERTIES OF THE ANTISYMMETRIC PROPAGATING AND NONPROPAGATING MODES

Figure 1 shows the group velocity Lamb wave dispersion curves for an aluminum plate. These, and all other dispersion curves and mode shapes in this paper, were plotted using the predictive model DISPERSE.[24,25] Lamb wave dispersion curves are scalable by the product of the frequency and the plate thickness. Thus the curves here show the frequency-thickness on the horizontal axis. The work which is presented here is focused on the A_0 mode at two different frequency-thicknesses: (1) at 1 MHz mm, where it is least dispersive and is also below the A_1 cutoff; (2) at 2.7 MHz mm where both the A_0 and A_1 modes are present as propagating modes (''real modes''), and A_1 is relatively nondispersive. The edge of the plate is assumed to be cut perfectly square, and the A_0 wave is assumed to be normally incident. It follows that at 1 MHz mm there is no mode conversion of the propagating modes: an incident mode of A_0 reflects as A_0 with a reflection coefficient amplitude of unity. On the other hand, at 2.7 MHz mm the incident A_0 mode can be reflected partially as A_0 and partially, by mode conversion, as A_1.

The role of the nonpropagating modes when Lamb waves are reflected from the end of a plate is easily understood by examining the mode shapes of the A_0 and the A_1 modes, shown for frequency-thickness products of 1 MHz mm and 2.7 MHz mm in Fig. 2. The z direction is the direction of propagation of the wave and the x direction is the normal to the plate. Considering for example the A_0 mode at 1 MHz mm, the two components of the stress field of importance here, the normal stress (σ_{zz}) and the shear stress (τ_{xz}), show the characteristic distributions corresponding to the flexural behavior of the wave. Not shown here, but very important, is the phase relationship; in fact although both components vary harmonically in time, τ_{xz} lags 90 deg

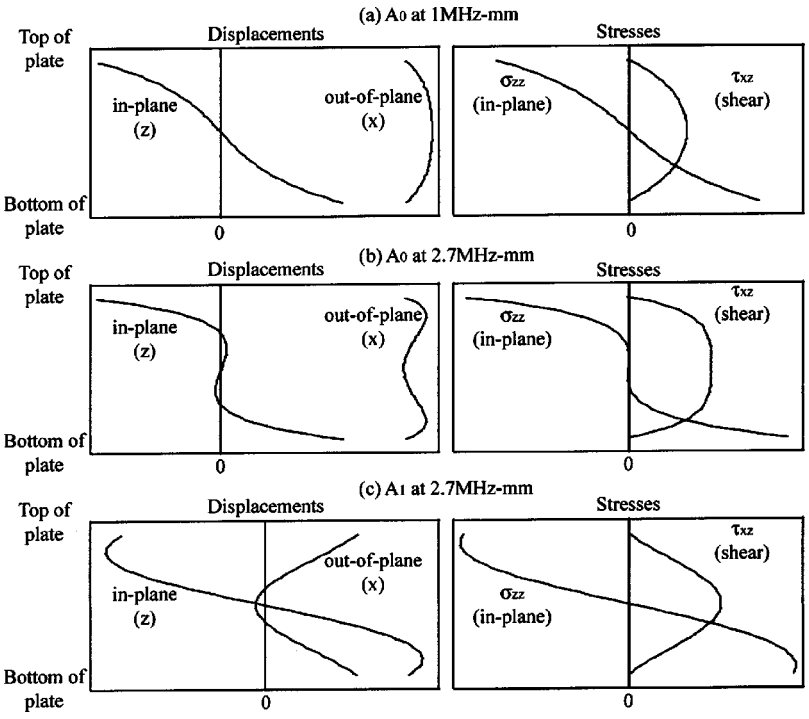

FIG. 2. Mode shapes of the A_0 and A_1 modes in an aluminum plate: (a) A_0 mode at 1 MHz mm; (b) A_0 mode at 2.7 MHz mm; (c) A_1 mode at 2.7 MHz mm.

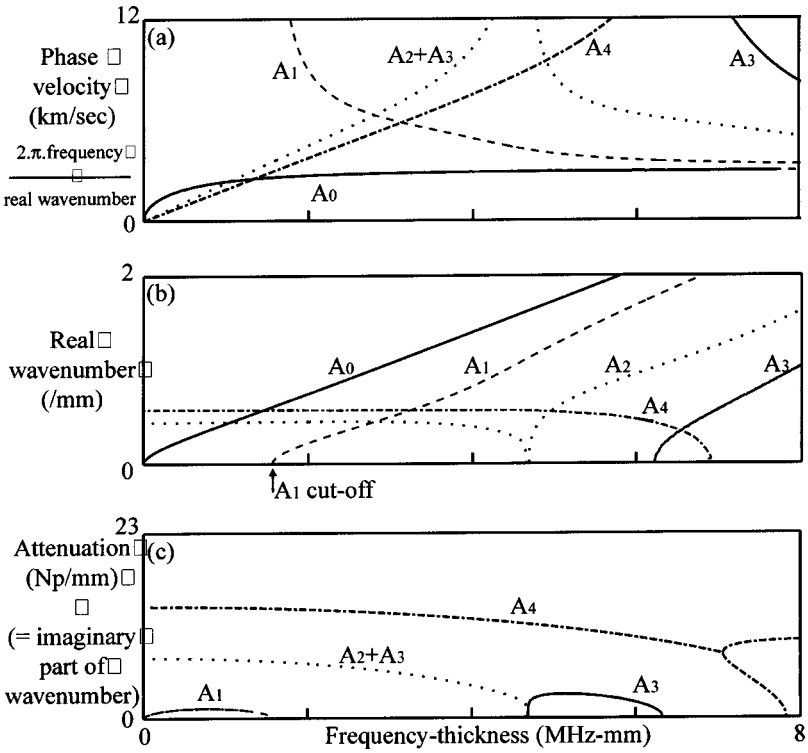

FIG. 3. Dispersion curves for anti-symmetric modes in a 1 mm thick aluminum plate, including nonpropagating branches: (a) phase velocity, (b) real wave number, and (c) imaginary wave number.

in phase behind σ_{zz}. At this frequency, and considering just the propagating modes, it is clear that an A_0 mode incident at the square end of a plate must reflect also in A_0 with unit amplitude reflection coefficient at 1 MHz mm. However, because of the phase difference of the stress components, there is no linear combination of incident and reflected modes which can satisfy the requirement that both σ_{zz} and τ_{xz} are zero across the end of the plate. It is then of course the presence of nonpropagating modes which allow these boundary conditions to be satisfied. The same feature happens at 2.7 MHz mm when A_0 is incident and is partially reflected into A_0 and A_1. There is no combination at the end of the plate to satisfy the boundary condition and hence nonpropagating modes are needed.

Dispersion curves for the anti-symmetric modes in a 1 mm thick aluminum plate, including the nonpropagating branches, are shown in Fig. 3. These show similar information to the well-known curves in Refs. 8, 12, except that those authors present only the symmetric modes, and also we choose here to plot the curves three times with different 2-D projections as an alternative to their 3-D plot. In part (a), the only addition which the nonpropagating modes make to the usual Lamb wave phase velocity curves (the real modes) are the branches labeled A_2+A_3 and A_4 linking the cutoffs to the origin of the plot. These are in fact complex branches whose wave numbers have both real and imaginary parts, as can be seen in parts (b) and (c) of the figure. These complex nonpropagating modes are therefore characterized by a sinusoidal variation of the field along the plate, described by the real part of the wave number, modified by an exponential decay function, described by the imaginary part of the wave number. The imaginary part corresponds to Nepers/mm attenuation along the plate (1 Np/mm = 8.69 dB/mm). The shape of a complex mode is illustrated in the sketch in Fig. 4(b).

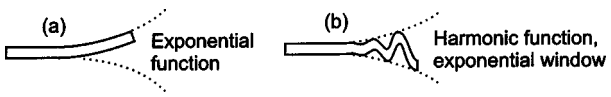

FIG. 4. Illustration of the shapes of the nonpropagating modes at the end of the plate: (a) imaginary modes, (b) complex modes.

The A_1 mode is radically different from A_2 and A_3, its nonpropagating branch being entirely imaginary. Thus it does not appear in the phase velocity plot and it has zero value to the left of the A_1 cutoff in the real wave number plot. Its shape is thus characterized just by an exponential decay, as illustrated in Fig. 4(a).

Torvik[9] demonstrated that neither the imaginary nor the complex modes transport energy along the plate. Thus the imaginary part of the wave number describes, not an attenuation of energy, but simply the spatial shape of the field. Also, this means that calculations of power flow may only be used to equate the energy of the incident and the scattered propagating modes. Although the mode shapes bear a strong resemblance to the mode shapes of vibrations at the end of plate, such a comparison can lead to misunderstanding for two reasons. First, these modes have nonzero stresses at the end of the plate, so it is not possible for them to exist in isolation; they can only be present in combination with other modes. The second point follows from this, that they do not exhibit the ringing of a free vibration mode but exist only while the propagating modes are reflecting.

The stress mode shapes of the first two non-propagating modes are shown in Fig. 5. It is interesting to see here that the shapes of the A_1 mode are very similar to those of the A_0 mode shown in Fig. 2. However, these A_1 shapes differ in that there is no phase shift between the σ_{zz} and τ_{xz} components. On the other hand, the A_2 mode, which is complex,

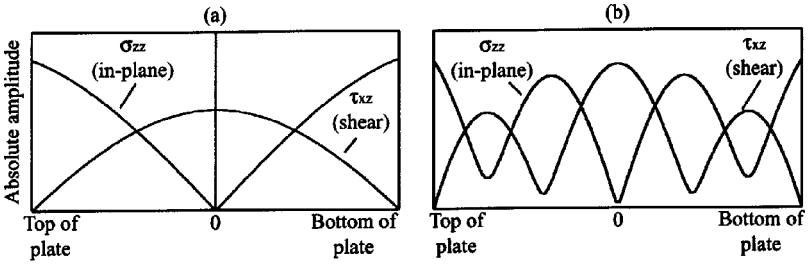

FIG. 5. Stress mode shapes of the nonpropagating modes: (a) A_1 at 1 MHz mm and (b) A_2 at 1 MHz mm.

does have phase shifts between stress components; indeed the phase shift varies according to the position through the thickness of the plate. A_2 also shows an increase, with respect to A_1, in the number of cycles in the shape of the through-thickness distribution, a trend which is continued with the higher nonpropagating modes in the series.

III. PROCEDURE FOR PREDICTION OF THE AMPLITUDES OF THE NONPROPAGATING MODES USING NORMAL MODE ANALYSIS

A normal mode analysis is chosen to solve the reflection of A_0 at the free end of a plate. Every acoustic field that exists in the plate can be developed as an expansion of Lamb waves:

$$V=\sum_n \alpha_n V_n, \tag{1}$$

where $V_n=v_n(x)e^{i(k_n z-\omega t)}$ is the particle velocity field of the nth Lamb mode. In order to be able to represent completely the acoustic phenomena, all of the Lamb modes that can exist in the plate must be considered.[26] Indeed, at a particular frequency-thickness product, only a finite number of propagating (real), a finite number of imaginary, and an infinite number of complex Lamb modes coexist in the plate. As discussed in the preceding section, the imaginary and complex modes do not propagate energy but they create a spatially transient acoustic field in their excitation area. The reflection of a Lamb mode at the free end of a plate requires selecting specific imaginary and complex roots, so that the corresponding modes have a physical meaning. Here we define the z axis to be positive in the direction away from the edge of the plate. With this convention, these imaginary and complex wave numbers must correspond to amplitudes decreasing away from the end[14] according to:

$$\begin{aligned} &k_n=ik_n'', \quad \text{for imaginary modes} \\ &k_n=\pm k_n'+ik_n'', \quad \text{for complex modes.} \end{aligned} \tag{2}$$

The co-existence of real, imaginary and complex Lamb modes at the end of the plate allows the stress-free boundary conditions to be satisfied. To fulfil these conditions, from ten to 25 locations are considered across the thickness at the end. At these points, the total stress field, produced by the superposition of all the propagating modes, all the imaginary modes, and between ten and twenty complex modes, must vanish. To find the complex amplitudes α_n of all these Lamb modes, a linear system is solved. For each point:

$$\bar{\bar{\sigma}}.\bar{e_z}=\begin{cases} \sum_n \alpha_n \sigma_{zz(n)} \\ \sum_n \alpha_n \tau_{xz}(n) \end{cases} = \begin{cases} 0 \\ . \\ 0 \end{cases} \tag{3}$$

An energy balance criterion is used to check the validity of the numerical result. The energy carried by the reflected propagating modes must be as close as possible to the energy of the incident mode. However, if the energy balance is not satisfied, the parameters of computation (i.e., the number of the points through the thickness at the end of the plate and the number of complex modes) are optimised until the best result is obtained. In the results presented in this paper, the energy balance is always correct within 5% error.

When the system is correctly solved, the particle velocity field at the end can be computed by introducing the amplitudes α_n in Eq. (1). The displacement is given by dividing the particle velocity by $i\omega$. Moreover, to compare to the finite element predictions and to the experimental data, the reflection coefficients can be computed as ratios of displacements at the plate surface:

$$R_j^n=\alpha_n\frac{U_j^n(h/2)}{U_j^I(h/2)},$$

where $j=x$,

z indicates the displacement component. (4)

$U_j^I(h/2)$ and $U_j^n(h/2)$ are the displacements, at the plate surface, in direction j, of the incident Lamb mode (I) and of the reflected Lamb mode (n), respectively.

A single frequency computation of the displacement field at the end and the reflection coefficients of the propagating modes takes about thirty seconds. If similar computations were to be done for a range of frequencies, then the computational parameters should be optimised for some frequencies, thus implying a nonlinear increase of the computational time. This method has proved to be numerically stable up to 16 MHz mm. However, the validity of the results obtained for such high frequency-thickness products has not

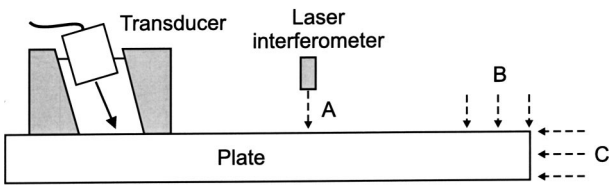

FIG. 6. Schematic illustration of the experimental setup.

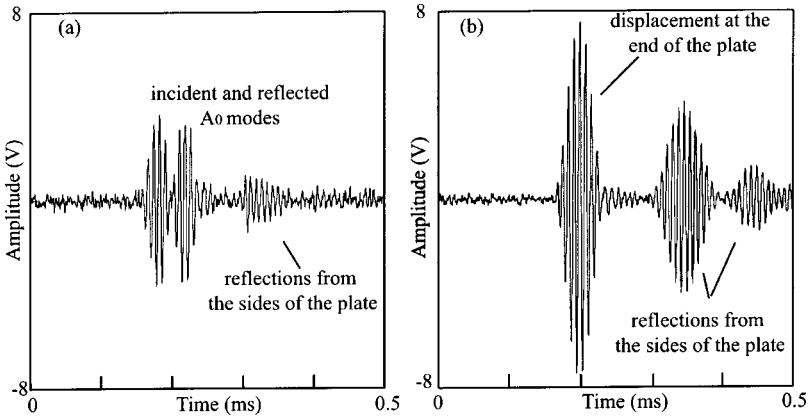

FIG. 7. Typical experimental out-of-plane displacement at location "*B*" when A_0 mode of 1 MHz mm center frequency-thickness is incident; (a) 40 mm from the end of the plate and (b) at the end of the plate.

been confirmed by experimental data, or compared to other numerical predictions. A more thorough description of this model is presented in Refs. 17, 23.

IV. EXPERIMENTAL SETUP FOR MEASUREMENT OF THE NONPROPAGATING MODES

Experimental studies were conducted in order to provide some practical validation for both the semi-analytical and the finite element work. The experimental work was done only with the A_0 mode below the A_1 cutoff frequency. An experimental study of A_0 mode above the A_1 cutoff frequency would require a very long plate because of the existence of reflections of both A_0 and A_1, and this was considered to be impractical. This can be understood by looking at the dispersion curves plotted in Fig. 1, from which it can be seen that the group velocities of A_0 and A_1 are approximately 20% different. At first sight this difference might be expected to be enough to separate the different modes, but unfortunately the A_1 Lamb mode is very dispersive at frequency-thicknesses just below and above 2.7 MHz mm. Hence, many cycles would be needed to limit the dispersion, and then the signal would be lengthened. In order to fully separate these reflected propagating modes, which would be necessary in order to calculate the non-propagating modes (see Sec. V), a 4 m long plate would be needed. Such practical problems of limiting the time duration of dispersive signals have been discussed by Wilcox *et al.*[27]

For practical convenience, an 800 mm$\times$800 mm $\times$8 mm thick aluminum plate was used. A_0 was excited using a piezo-electric transducer (ULTRAN WS100-0.2) aligned at the appropriate coincidence angle ($\simeq$35°) in a local water immersion arrangement (see Fig. 6). The signal was narrow in bandwidth, consisting of a 10 cycle tone burst modified by a Hanning window at 125 KHz (equivalent to 1 MHz for a 1 mm thick plate). This scaling relationship will be exploited so that all the results presented later will correspond to a plate of 1 mm in thickness. The transducer was excited using a WAVEMAKER instrument from Macro Design Ltd (UK). A POLYTEC laser interferometer[28] was used in order to measure the in-plane (motion of the plate in the *z* direction) and out-of-plane (motion of the plate in the *x* direction) displacements at the different locations marked in Fig. 6.

The interferometer system consists of the interferometer itself, a decoder and two probes connected by fibre optic cable to the interferometer. One of the two probes is nominally the measurement probe and the other the reference probe. In order to measure normal displacement the reference probe is simply replaced by a mirror while the measurement probe is aligned normal to the surface of the plate. All of the measurements in this paper were achieved using this approach. However, measurements of tangential displacements were also recorded, and although those results are omitted here for brevity, it is useful to state how such measurements are made. In order to measure the displacement tangential to a surface, both the measurement and the reference probes must be used. They are aligned so that their beams lie in a plane normal to the surface, and both beams strike the surface at the same spot. Within their plane, the two probes are aligned at equal and opposite directions with an angle of $\pm$30° to the normal to the surface of the plate. In this configuration, both displacements measured by the probes contain equal amounts of the normal component of surface displacement and equal and opposite amounts of the tangential component of surface displacement. Hence when

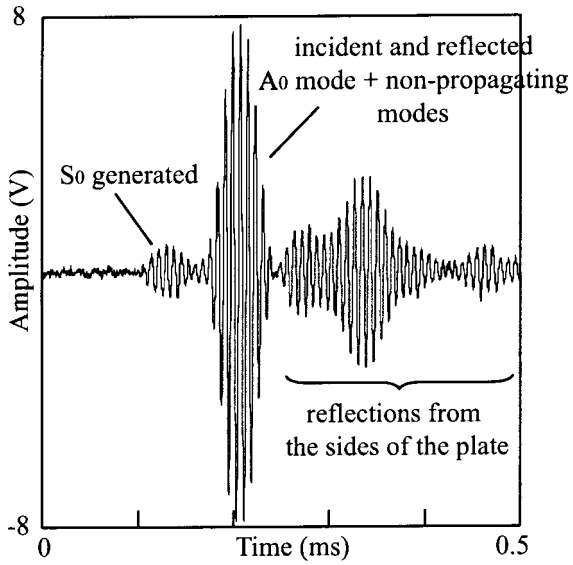

FIG. 8. Typical measured signal of in-plane displacement near the surface of the plate at location "*C*," when A_0 mode of 1 MHz mm center frequency-thickness is incident.

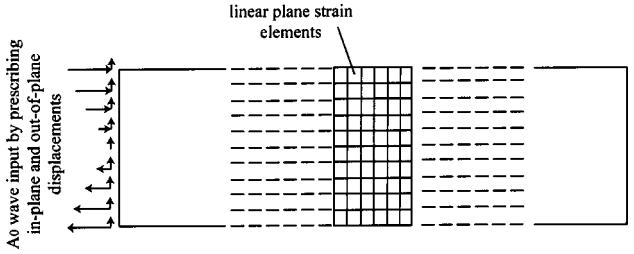

FIG. 9. Schematic illustration of finite element spatial discretization of the plate, with excitation of the A_0 wave.

the reference signal is subtracted from the measurement signal, the normal components of surface displacement cancel out and the tangential components of surface displacement add. Using an angle of $\pm 30°$ for the probes means that the constant of proportionality relating voltage to displacement is equal for both the tangential and normal measurement configurations.

With the interferometer at the location marked *A*, both the incident and the reflected A_0 modes could be monitored remote from the end. Then at the positions *B* and *C* the displacements comprising the sum of the incident and reflected A_0 modes and the nonpropagating modes could be measured. When measuring at *C*, only the displacements in one half of the plate were measured, those in the other half being expected to respect the conditions of anti-symmetry. In-plane (tangential to surface) and out-of-plane (normal to surface) displacements have been measured at locations *A* and *B* whereas only in-plane (normal to surface) displacements have been measured at location *C*. While setting up, the attenuation of the signal due to beam spreading, which is inversely proportioned to the square root of the propagating distance, was measured by detecting the change in amplitude of the incident signal for two different locations near *A*; subsequently all measured amplitudes were adjusted according to the distance travelled so that the results would correspond to those for lossless plane waves.

Figure 7 and 8 show typical experimental time histories. Figure 7 shows out-of-plane displacements measured at location *B* in Fig. 6. Figure 7(a) shows a measurement at 40 mm away from the end of the plate, where the incident and the reflected A_0 modes are just separated but they still include some contribution from nonpropagating modes. This measurement will be used later for the calculation of the spatial attenuation of the nonpropagating modes. Figure 7(b) shows the out-of-plane displacement measured at the end of the plate, on the top surface. Note the increase in amplitude at the end of plate (b) compared to that at the location 40 mm away (a). Figure 7 also shows some unwanted reflections from the sides of the plate. Fortunately these arrive sufficiently late to be gated out; however they indicate the importance of using a plate of significant width in order to achieve the necessary delay.

Figure 8 shows the in-plane displacement at the end of the plate measured at the corresponding location *C* in Fig. 6. Some S_0 mode is visible just before the A_0 wave. This is due to the very strong in-plane displacement of the S_0 mode, which is partially excited by the setup. It did not appear in the out-of-plane measurements because its out-of-plane displacement is very weak, and S_0 is indeed very difficult to excite at this frequency with an out-of-plane forcing technique. The S_0 velocity is much higher than the A_0 velocity (see Fig. 1) and they are easily and safely separated in time when they have travelled along the plate.

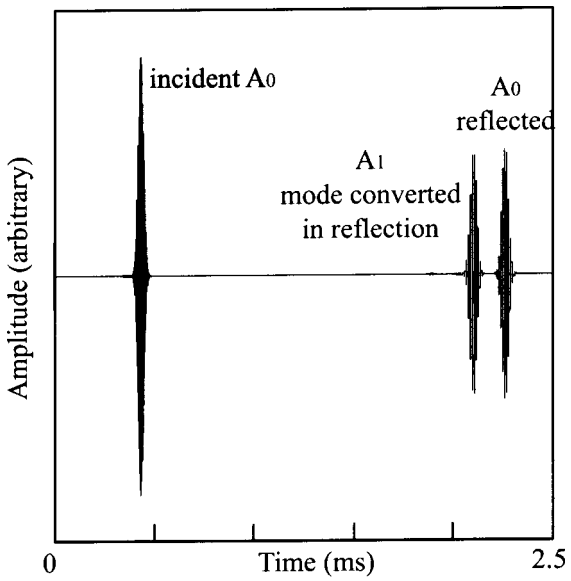

FIG. 10. Typical FE predicted in-plane displacement signal, when the incident A_0 wave has a center frequency-thickness of 2.7 MHz mm, monitored at 3.2 m from the end of the plate, showing separation of the reflected A_0 and the mode converted A_1.

V. PROCEDURE FOR FINITE ELEMENT SIMULATION

The FE simulation is used as a validation in the same way as experiments, and indeed the results will be processed in the same way. In the previous section, the formation of nonpropagating modes above the A_1 cutoff frequency has not been studied experimentally due to the closeness of the group velocities of the A_0 and the A_1 modes. However, the case of a very long plate is possible in the FE model, and so predictions at both of the test frequencies can be made.

We discuss first the general features of the FE approach and then the specific models for the 1 MHz mm and 2.7 MHz mm cases.

A. Discretization

The propagation of straight-crested Lamb waves can be modelled using a two-dimensional spatial discretization. The two-dimensional finite element modelling was performed, with the assumption of plane strain, using the program FINEL which is developed at Imperial College.[29] Rectangular elements, with four nodes and linear shape functions, each node having two displacement degrees of freedom in the plane of computation, were used in the models. The spatial discretisation in both cases was chosen to be certain of satisfying the rule:

$$\lambda_{\min} \geqslant 8\Delta x, \tag{5}$$

where $\lambda_{\min}$ is the shortest wavelength, within the bandwidth of the signal, of any waves which may travel in the structure, and Δx is the biggest dimension across any single element in

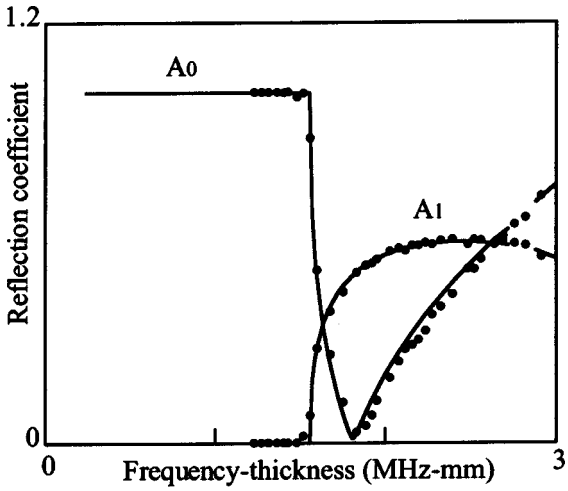

FIG. 11. Predictions of the reflection coefficient spectrum of the A_0 and A_1 modes when the A_0 mode is incident. Solid lines are semi-analytical solution, filled circles are FE results. The reflection coefficient is defined as the ratio of the amplitude of the out-of-plane displacement of the reflected wave to that of the incident A_0 wave, calculated at the surface of the plate.

the model. This rule has been found by the authors to be effective for ensuring accurate modelling; see, for example, Ref. 30.

The program uses a diagonal mass matrix, allowing an efficient explicit time marching algorithm to be exploited. The explicit algorithm is stable provided that the time step δt is short enough to meet the convergence criterion:[31]

$$\delta t \leqslant 0.8 \frac{\Delta s}{c}, \tag{6}$$

where c is the velocity of the wave and Δs is the shortest side-length of any element.

B. Simulations below and above the A_1 cut-off frequency

A schematic illustration of the model is shown in Fig. 9. Plates of 8 mm thickness were modelled, the thickness being chosen for convenience to match the thickness of the plate in the experimental work. In fact, as discussed earlier, the choice of thickness is arbitrary provided that the other spatial dimensions and the frequency are scaled to give the appropriate frequency-thickness product when comparing the results. Accordingly all the results presented later will correspond to a plate of 1 mm in thickness. The models used 16 elements through the thickness of the plate and the elements were defined to be square. Thus the number of elements per wavelength was safely above the 8 elements required, being about 37 elements per wavelength at the frequency-thickness product 1 MHz mm and 20 elements per wavelength at the frequency-thickness product 2.7 MHz mm.

The temporal model for the 1 MHz mm case was chosen to match exactly the experimental A_0 input signal, so a 1 MHz mm 10 cycle tone burst modified by a Hanning window was excited at one end of the plate. This was achieved by prescribing in-plane and out-of-plane displacements at each node across the thickness (see Fig. 9). The model was 800 mm long and several regions were monitored. First the end of the plate through the thickness (location "*C*") was monitored in the in-plane and out-of-plane directions, every 0.5 mm, providing the total field displacement. A second region was monitored through the thickness at 300 mm and 200 mm away from the end of the plate in order to monitor the incident and the reflected A_0 modes when they are fully separated in time. Finally, in order to study the spatial attenuation of the nonpropagating modes, points every 0.5 mm from the end of the plate along the top surface were monitored.

The same model could not be used for frequencies above the A_1 cutoff frequency because then more than one antisymmetric mode exists. The problem is that the A_1 mode is excited by mode conversion at the end of the plate and it propagates back together with the reflected A_0 mode. Since they have very similar values of group velocity, they need to propagate a very long distance before they can be recorded separately. Thus the model was extended to 4 m in length. The separation of these two modes in time is important in order to perform the processing to expose the nonpropagating modes which will be explained in the following section of the paper.

The input A_0 signal for the 2.7 MHz mm case was similar to the 1 MHz mm case, except that a 30 cycle signal was used, in order to minimize dispersion over the long propagation distance. Furthermore, the profile of the displacement field which was imposed at the end of the plate had to be chosen more carefully, since it was essential to avoid generating any A_1 in the incident signal. This was done by imposing displacements which matched exactly the mode shape of the A_0 mode at 2.7 MHz mm.[32]

Monitoring of the 2.7 MHz mm case was done at 3 m and 3.2 m away from the end of the plate, through the thickness of the plate and in both in-plane and out-of-plane directions. Figure 10 shows, by way of example, the monitored in-plane displacement at 3.2 m from the end of the plate; it can be seen that the A_0 and A_1 modes are satisfactorily separated. The end of the long plate was also monitored, in exactly the same way as in the 1 MHz mm case.

VI. PROCEDURE FOR REMOVAL OF THE PROPAGATING MODES FROM THE TOTAL DISPLACEMENT FIELD AT THE END OF THE PLATE

An aim of the analysis in this paper is to illustrate the extent to which the nonpropagating modes contribute to the total displacement field at and near the end of the plate. One way to perform such an illustration is to subtract the contributions of the propagating modes from the total field at the end of the plate, thus leaving only the displacements due to the nonpropagating modes. We explain here the procedure by which we performed that subtraction.

The amplitudes of the incident and reflected propagating modes are known from the remote monitoring at location "*A*" (these will be presented later and are plotted in Fig. 11), so this determines the amplitudes of the fields to be subtracted at the end of the plate. However, the phases of these waves at the end of the plate are not yet known. The following process is applied sequentially and separately to each of the three possible propagating modes: the incident A_0 mode,

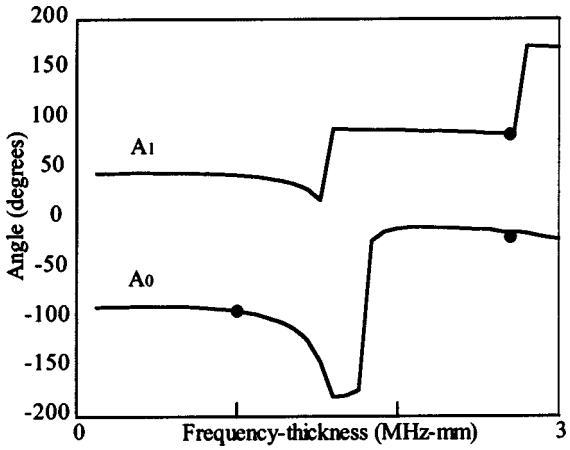

FIG. 12. Predictions of the phase of the reflected A_0 and A_1 modes at the end of the plate when the A_0 mode is incident. Solid lines are semi-analytical solution, filled circles are FE results. The values are the difference between the phase of the out-of-plane displacement of the reflected mode and that of the incident mode.

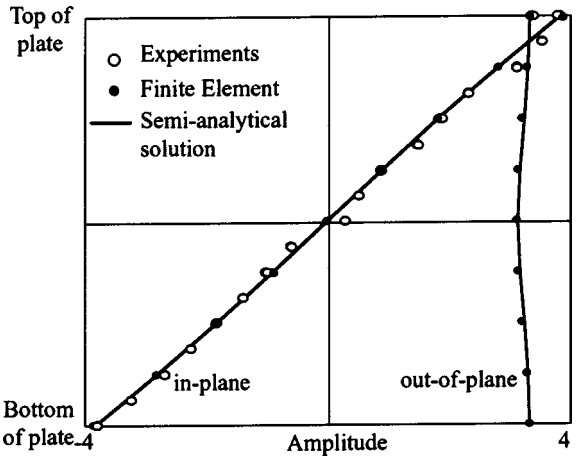

FIG. 14. Total displacement field (all modes) through the thickness at the end of the plate at 1 MHz mm, when the incident A_0 mode has unit amplitude out-of-plane displacement at plate surface. Solid lines are semi-analytical solution, filled circles are FE results, empty circles are experimental measurements.

the reflected A_0 mode and (if present) the reflected and mode converted A_1 mode.

The out-of-plane displacement of the propagating mode is monitored at two separate locations remote from the end of the plate, let us say locations at distances $D1$ ad $D2$ from the end of the plate. The FFT of each of these monitored signals is calculated, giving the amplitude and phase at the chosen calculation frequency (1 or 2.7 MHz mm). The phase, ϕ_{end}, at the end of the plate is then found by linear extrapolation of the phases at $D1$ and $D2$:

$$\phi_{\text{end}} = \phi_{D2} - (\phi_{D2} - \phi_{D1}) * \frac{D2}{D2 - D1}. \tag{7}$$

Having found the amplitude and phase of the propagating wave at the end of the plate, these can be converted to real and imaginary quantities and subtracted from the real and imaginary parts of the total field at the end of the plate. Once this has been performed for all of the propagating modes, the remaining field is that due solely to the nonpropagating modes.

The above calculation corresponds just to the out-of-plane component of displacement at the surface of the plate. In order to process the in-plane displacement, and the values at any other locations through the thickness of the plate, it is a simple matter just to make use of the known mode shape of the mode (Fig. 2). Thus for example, the amplitude of the out-of-plane displacement at a quarter depth in the plate is taken to be the known amplitude at the surface multiplied by the ratio of the amplitudes of the mode shape at quarter-depth and surface. When processing the FE results, an alternative approach was to perform the complete phase extrapolation separately at each depth, since the signals were monitored at all depths at the remote locations. This achieved the same results, confirming agreement between the mode shapes in the FE simulations and those predicted by DISPERSE.

VII. RESULTS

A. Below A_1 cutoff frequency

Figure 11 shows a comparison of the semi-analytical and the finite element predictions of the amplitudes of the reflection coefficients of the A_0 and A_1 modes when the A_0 mode is incident at the free edge of an aluminum plate. The reflection coefficient here is calculated from the out-of-plane component of the displacement at the surface of the plate (at location A in the FE models), and is defined by the ratio of the amplitude of the displacement of the reflected wave to that of the incident wave. This detail is unimportant when considering the A_0 mode, because the identical reflection coefficient would be indicated by considering any component or depth-location of the displacement; however, it will become essential information when considering the A_1 mode because the mode shapes of the A_1 mode are different from those of the incident A_0 mode. Furthermore, it should be emphasized that neither the A_0 nor the A_1 reflection coeffi-

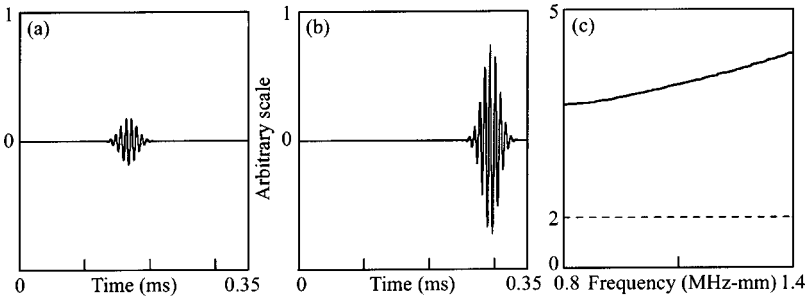

FIG. 13. Prediction of the enhancement of the displacements at the end of the plate caused by the nonpropagating modes: (a) incident A_0 mode; (b) signal at end of plate, consisting of incident and reflected A_0 and nonpropagating modes; (c) ratio (b)/(a) (solid line) and expected ratio (b)/(a) (dashed line) if there were no nonpropagating modes. All results are out-of-plane component of displacement at surface of plate, using signal with center frequency of 1 MHz mm.

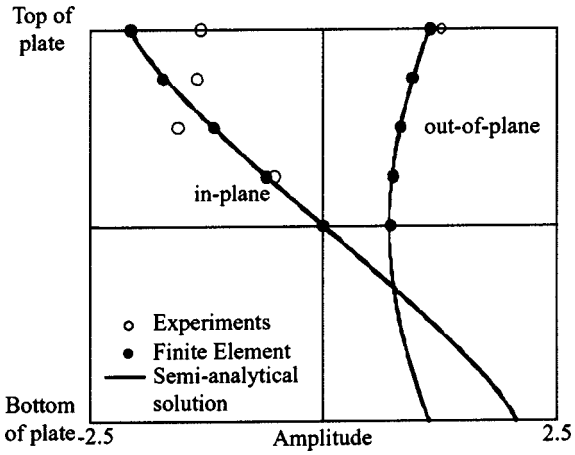

FIG. 15. Displacement field corresponding to Fig. 14, but after removal of the incident and reflected propagating modes, leaving just the nonpropagating modes. Solid lines are semi-analytical solution, filled circles are FE results, empty circles are experimental measurements.

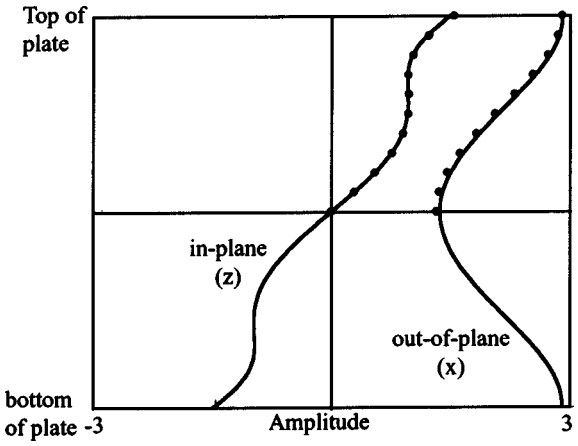

FIG. 17. Total displacement field (all modes) through the thickness at the end of the plate at 2.7 MHz mm, when the incident A_0 mode has unit amplitude of out-of-plane displacement at plate surface. Solid lines are semi-analytical solution, filled circles are FE results.

cient indicates directly the coefficient of the reflection of energy; the A_0-A_0 energy reflection coefficient is given by the square of the value reported here, while the A_0-A_1 reflection coefficient would require a calculation accounting for all of the field through the thickness of the plate. The FE reflection coefficients were calculated in the frequency domain, that is to say the amplitude frequency spectrum of the reflected signal was divided by that of the incident signal. This required a number of simulations with different center frequencies in order to cover the bandwidth of the plot.

Very good agreement is found between the two methods across the full bandwidth, thus confirming consistency in the methodologies of the two techniques. As should be expected, only the A_0 mode is present at frequencies below the A_1 cutoff frequency, and its reflection coefficient is unity. As the frequency is increased above the cutoff, it can be seen that the amplitude of A_0 initially decreases while the amplitude of A_1 increases; then later A_0 rises again. These trends have also been demonstrated experimentally using a water-coupled piezo-electric source transducer and an air-coupled capacitive receiver transducer; full details of that setup and results are given in Ref. 23.

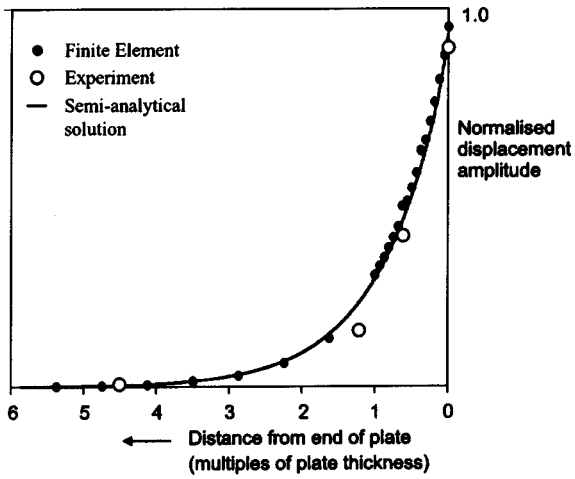

FIG. 16. Out-of-plane displacement field of the nonpropagating modes in the vicinity of the end of the plate, after removal of the incident and reflected A_0 mode, at 1 MHz mm. Solid line is semi-analytical solution, filled circles are FE results, empty circles are experimental measurements.

Figure 12 shows the change of phase of the two propagating modes as they are reflected or mode converted at the end of the plate. The phase was calculated from the out-of-plane component of displacement at the surface of the plate. Thus if the incident mode has zero phase at the moment it arrives at the end of the plate, then the plotted phase is that of the reflected or mode converted mode at the moment it leaves the end of the plate. The sign convention is that negative angles denote a phase delay. Very good agreement is again found between the semi-analytical and the FE predictions.

Figure 13 shows finite element predictions which illustrate the extent to which the displacements at the end of the plate are enhanced by the contributions from the nonpropagating modes. For simplicity the illustration is based on predictions made using a signal with center frequency-thickness equal to 1 MHz mm, when the only propagating mode is A_0. The incident wave was sampled by monitoring the out-of-plane component of the displacement at the surface of the plate at location *A* of Fig. 6, and this is shown in part (a) of Fig. 13. Part (b) then shows the same component of displacement at the end of the plate (surface of plate at location *C*). If this study had been carried out on the reflection of plane bulk waves from the free surface of a semi-infinite half-space, then we would expect the amplitude of the signal in (b) to be exactly twice that of the signal in (a). However, the ratio of these amplitudes, shown in the frequency domain in Fig. 13(c), is clearly very much more than two. The additional displacement amplitude is that of the nonpropagating modes. Similar enhancement of the displacements is found at frequencies above the A_1 cutoff frequency, but for brevity such cases are not shown here.

Further illustration of these enhanced displacements is developed in Fig. 14. This shows the total displacement field through the thickness at the end of the plate at 1 MHz mm. The field comprises the sum of the incident and reflected propagating modes and the nonpropagating modes. The values are scaled such that the amplitude of the out-of-plane

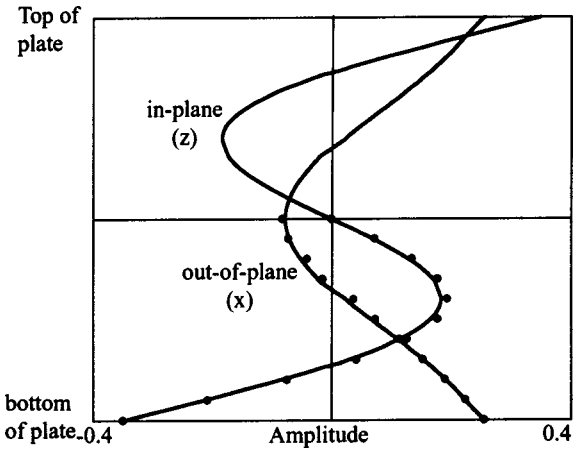

FIG. 18. Displacement field corresponding to Fig. 17, but after removal of the incident and reflected propagating modes, leaving just the nonpropagating modes. Solid lines are semi-analytical solution, filled circles are FE results.

surface displacement of the incident A_0 mode is unity. Each of the two components of the displacement is plotted without phase information, that is to say the displacement profile is shown at the instant during the harmonic cycle when it has its maximum value at the surface of the plate. Excellent agreement is found between the semi-analytical solutions, the FE predictions, and the experimental measurements.

We now present results making use of the method described in Sec. VI to remove the propagating modes from the total displacement field of Fig. 14, leaving the contribution due just to the nonpropagating modes. The results thus processed are shown in Fig. 15. Again the amplitudes are scaled to correspond to unit amplitude of the out-of-plane surface displacement of the (removed) incident A_0 mode. Also, the displacement components are shown without phase information, as in the preceding figure. This process was applied separately to the FE and the experimental data, and both are shown in the plot: FE predictions by filled circles and experimental measurements by empty circles. The sum of the nonpropagating modes from the semi-analytical model are also shown here, plotted as solid lines. In general there is very good agreement between these results, although the measurements show some scatter near the surface of the plate.

An interesting outcome of the study at this particular frequency is that the nonpropagating wave field is dominated by the A_1 nonpropagating mode. This is confirmed by examining the results of the semi-analytical model, revealing that the displacement amplitudes of the A_1 nonpropagating mode are more than one order of magnitude larger than those of any other nonpropagating mode. Indeed plots of the in-plane and out-of-plane displacement mode shapes of A_1 can be practically overlaid on Fig. 15.

A similar approach was applied to the displacement field along the top surface of the plate, in the vicinity of the end (location *B*). After applying the processing to remove the displacements of the incident and reflected A_0 modes, the finite element predictions and the experimental measurements of the nonpropagating modes field are shown in Fig. 16. The plot shows the out-of-plane displacement, the amplitude corresponding as before to unit amplitude of the incident mode. Once again there appears to be good agreement between the finite element and the experimental results. The decay of the nonpropagating modes within about five plate thicknesses of the end of the plate is clearly demonstrated. Also shown in the figure, by a solid line, is the decay profile of the A_1 nonpropagating mode, taken from the imaginary part of the wave number from the semi-analytical model (the DISPERSE prediction shows exactly the same shape). This confirms the observation that the nonpropagating modes field is well described by just the A_1 nonpropagating mode. Indeed it can be seen in Fig. 3(c) that the A_1 nonpropagating mode has much the lowest value of attenuation at 1 MHz mm, and so any other nonpropagating modes present at the end of the plate would have vanishing amplitude within a short distance along the plate.

B. Above A_1 frequency cutoff

We now consider the behavior at 2.7 MHz mm, when both the A_0 and A_1 modes may propagate. For brevity we study just the field across the end of the plate in this case.

Figure 17 shows the total displacement field through the thickness at the end of the plate. This field comprises the sum of the incident A_0 mode, the reflected A_0 mode, the reflected and mode converted A_1 mode, and all the nonpropagating modes. The amplitude scaling and the form of the presentation is exactly the same as was used in the preceding section for the 1 MHz mm case. The results show very good agreement between the FE and the semi-analytical predictions.

Finally, Fig. 18 shows the displacement field through the thickness at the end of the plate, after removal of the three propagating modes. This field is thus the sum of the nonpropagating modes. Good agreement between the FE and the semi-analytical predictions is demonstrated. The shape of the field here is somewhat more complicated than that for the 1 MHz mm case, and indeed the semi-analytical study showed that this field is no longer dominated by a single nonpropagating mode, but by a combination, consisting predominantly of A_2 and A_3.

C. A brief comment on the symmetric mode S_0

As discussed in Sec. II, the nonpropagating modes play a part in the reflection behavior when the traction-free boundary condition at the end of the plate cannot be satisfied by a superposition of propagating modes. At low frequencies the S_0 mode is dominated by its in-plane displacement and stress components, and these allow the traction-free boundary conditions to be satisfied simply by the sum of the incident and reflected S_0 modes. Thus we should expect negligible contributions from nonpropagating modes.

Indeed FE studies of the S_0 mode within the frequency range up to the A_1 cutoff showed no evidence of the phenomena which were observed with the A_0 mode. The displacements at the end of the plate were found to be almost exactly twice the values of the incident mode, thus implying that the amplitude of nonpropagating modes is negligible. There was also no evidence of a phase change when reflecting from the end of the plate.

Nevertheless, it should be noted that this conclusion only applies in this low frequency range; significant amplitudes of nonpropagating modes exist at higher frequencies.[9,17]

VIII. CONCLUSION

The study has demonstrated significantly enhanced displacements in the vicinity of the end of a plate when the A_0 mode is incident. Semi-analytical predictions, finite element simulations, and experimental measurements have been used to investigate these fields at two example values of frequency-thickness, below (1 MHz mm) and above (2.7 MHz mm) the A_1 cutoff. Good agreement has been found between the results of all three techniques. Then, by identification of the amplitudes and phases of the propagating modes, it has been possible to remove these from the displacement fields at the end of the plate, thus revealing the fields due solely to the nonpropagating modes.

In relation to the motivation for the work, the development of NDE techniques for the inspection of plates, there are two important outcomes from the study. The first is that the reflection of the A_0 mode occurs with a change of phase, for example a 90 deg delay in the more useful 1 MHz mm case. It may be necessary to take account of this when dealing with the superposition of multiple reflected signals in an area-inspection technique. The second is that the nonpropagating modes can enhance the displacement field at some distance from the end of the plate, and this indicates the importance of transducer placement for inspection. In the 1 MHz mm case the field is enhanced within a region of about five plate thickness from the end of plate.

[1] H. Lamb, ''On waves in an elastic plate,'' Proc. R. Soc. London, Ser. A **93**, 114–128 (1917).
[2] D. Worlton, ''Ultrasonic testing with Lamb waves,'' Nondestr. Test. (Chicago) **15**, 218–222 (1957).
[3] D. Worlton, ''Experimental confirmation of Lamb waves at megacycle frequencies,'' J. Appl. Phys. **32**, 967–971 (1961).
[4] I. A. Viktorov, *Rayleigh and Lamb Waves* (Plenum, New York, 1970).
[5] T. Mansfield, ''Lamb wave inspection of aluminium sheet,'' Mater. Eval. **33**, 96–100 (1975).
[6] S. Rokhlin, ''Resonance phenomena of Lamb waves scattering by a finite crack in a solid layer,'' J. Acoust. Soc. Am. **69**, 922–928 (1981).
[7] D. Alleyne and P. Cawley, ''The interaction of Lamb waves with defects,'' IEEE Trans. Ultrason. Ferroelectr. Freq. Control **39**, 381–397 (1992).
[8] R. Mindlin, ''Waves and vibrations in isotropic elastic plates,'' in *First Symposium on Naval Structural Mechanics*, edited by N. Goodier (Pergamon, New York, 1960), pp. 199–232.
[9] P. Torvik, ''Reflection and wave trains in semi-infinite plates,'' J. Acoust. Soc. Am. **41**, 346–353 (1967).
[10] M. Lowe and O. Diligent, ''The low frequency reflection characteristics of the fundamental symmetric Lamb wave S0 from a rectangular notch in a plate,'' J. Acoust. Soc. Am. **111**, 64–74 (2002).
[11] M. Lowe, P. Cawley, J.-K. Kao, and O. Diligent, ''The low frequency reflection characteristics of the fundamental anti-symmetric Lamb wave A_0 from a rectangular notch in a plate,'' J. Acoust. Soc. Am. **112**, 2612–2622 (2002).
[12] B. Auld, *Acoustic Fields and Waves in Solids*, Vol. 2 (Krieger, Malabar, FL, 1990).
[13] Y. Cho and J. Rose, ''A boundary element solution for a mode conversion study on the edge reflection of Lamb waves,'' J. Acoust. Soc. Am. **99**, 2097–2109 (1996).
[14] D. Gazis and R. Mindlin, ''Extensional vibrations and waves in a circular disk and a semi-infinite plate,'' J. Appl. Mech. 541–547 (1960).
[15] M. Onoe, ''Contour vibration of thin rectangular plates,'' J. Acoust. Soc. Am. **30**, 1159–1162 (1958).
[16] R. Gregory and I. Gladwell, ''The reflection of a symmetric Rayleigh-Lamb wave at the fixed or free edge of a plate,'' J. Elast. **13**, 185–206 (1983).
[17] E. Le Clézio, M. Predoi, M. Castaings, B. Hosten, and M. Rousseau, ''Numerical predictions and experiments on the free-plate edge mode,'' Ultrasonics **41**, 25–40 (2003).
[18] S. Morse and P. Marston, ''Meridional ray backscattering enhancements for empty truncated tilted cylindrical shells: Measurements, ray model and effects of a mode threshold,'' J. Acoust. Soc. Am. **112**, 1318–1326 (2002).
[19] X.-M. Wang and F. Ying, ''Scattering of Lamb waves by a circular cylinder,'' J. Acoust. Soc. Am. **110**, 1752–1763 (2001).
[20] O. Diligent, M. Lowe, and P. Cawley, ''Reflection and scattering of the S_0 Lamb mode from circular defects in plates,'' in *Review of Progress in Quantitative NDE*, edited by D. Thompson and D. Chimenti (American Institute of Physics, New York, 2001), Vol. 20B, pp. 1134–1141.
[21] P. Wilcox, M. Lowe, and P. Cawley, ''Lamb and *SH* wave transducer arrays for the inspection of large areas of thick plates,'' in *Review of Progress in Quantitative NDE*, edited by D. Thompson and D. Chimenti (Plenum, New York, 2000), Vol. 19, pp. 1049–1056.
[22] E. Le Clézio, M. Castaings, and B. Hosten, ''Réflexion d'ondes de Lamb à l'extrémité de plaque: solution analytique et mesures,'' in *Proceedings of the 5th Congrès Français d'Acoustique* (2000), pp. 177–180.
[23] E. Le Clézio, ''Diffraction des ondes de Lamb par des fissures verticales,'' Ph.D. thesis, Université Bordeaux I (number 2472), spécialité Mécanique (2001).
[24] M. Lowe, ''Matrix techniques for modeling ultrasonic waves in multilayered media,'' IEEE Trans. Ultrason. Ferroelectr. Freq. Control **42**, 525–542 (1995).
[25] B. Pavlakovic, M. Lowe, D. Alleyne, and P. Cawley, ''DISPERSE: A general purpose program for creating dispersion curves,'' in *Review of Progress in Quantitative NDE*, edited by D. Thompson and D. Chimenti (Plenum, New York, 1997), Vol. 16, pp. 185–192.
[26] P. Kirrmann, ''On the completeness of the Lamb Waves,'' J. Elast. **37**, 39–69 (1995).
[27] P. Wilcox, M. Lowe, and P. Cawley, ''The effect of dispersion on long range inspection using ultrasonic guided waves,'' NDT & E Int. **34**, 1–9 (2001).
[28] Vibrometer operator's manual for Polytec Vibrometer OFV 2700, Lambda Photometrics Ltd., Lambda House, Harpenden Hertfordshire AL5 5BZ, U.K. (1999).
[29] D. Hitchings, ''FE77 User Manual,'' Tech. Rep., Imperial College of Science, Technology and Medicine, London, U.K. (1994).
[30] D. Alleyne, M. Lowe, and P. Cawley, ''The reflection of guided waves from circumferential notches in pipes,'' J. Appl. Mech. **65**, 635–641 (1998).
[31] K.-J. Bathe, *Finite Element Procedures in Engineering Analysis* (Prentice-Hall, Englewood Cliffs, NJ, 1982).
[32] B. Pavlakovic, D. Alleyne, M. Lowe, and P. Cawley, ''Simulation of Lamb waves propagation using pure mode,'' in *Review of Progress in Quantitative NDE*, edited by D. Thompson and D. Chimenti (Plenum, New York, 1998), Vol. 17, pp. 1003–1010.

Some extensions of the Gaussian beam expansion: Radiation fields of the rectangular and the elliptical transducer

Desheng Ding,[a] Yu Zhang, and Jinqiu Liu
Department of Electronic Engineering, Southeast University, Nanjing 210096, People's Republic of China

(Received 22 November 2002; revised 5 March 2003; accepted 17 March 2003)

A straightforward extension of Gaussian beam expansion is presented for calculation of the Fresnel field integral [J. J. Wen and M. A. Breazeale, J. Acoust. Soc. Am. **83**, 1752–1756 (1988)]. The source distribution function is expanded into the superposition of a series of two-dimensional Gaussian functions. The corresponding radiation field is expressed as the superposition of these two-dimensional Gaussian beams and is then reduced to the computation of these simple functions. This treatment overcomes the limit that the shape of source is of circular axial-symmetry. The numerical examples are presented for the field of the (uniform) elliptical and the rectangular piston transducers and agree well with the results given by complicated computation. © *2003 Acoustical Society of America.* [DOI: 10.1121/1.1572144]

PACS numbers: 43.20.Rz, 43.20.Bi, 43.20.El [MO]

I. INTRODUCTION

The Fresnel field integral (or Fresnel transform) appears in many relevant problems of diffraction, for instance, the theory of the sound field radiated from an ultrasonic transducer and of the laser beam field diffracted by an aperture. The exact solution of these problems is described by the well-known Rayleigh surface integral in general, or by King's integral in the case of circular axial-symmetry. In practical situations, the Fresnel field integral is often used instead of these two solutions. It is a good approximation when the size of source is much larger than the wavelength (about ten times) and the observation point is located in the paraxial region. For most of the practical ultrasonic transducers, this integral is possibly invalid only in the extremely near region of the transducers. In the most general case, however, the Fresnel field integral, two-dimensional and strongly oscillatory, has to be numerically performed in the evaluation of the field of an arbitrary distributed source. This is always a time-consuming thing. To overcome this difficulty, Cook *et al.* first presented the beam (or function) expansion method that the field integral is expressed as the superposition of Gaussian–Laguerre functions (or Gaussian–Hermite ones in the rectangular coordinate) and obtained a satisfactory result, compared with the numerical solution of the Rayleigh integral, of the sound field from a circular uniform piston transducer.[1,2] Wen and Breazeale made some extensions of the method in which the expansion functions used involve only the Gaussian ones.[3] Since then, many other extensions have been made in various ways.[4–15] An obvious advantage of this approach is that the analytical description for the (linear) sound field distribution, and even for the second-order field nonlinearly generated, is obtainable and thus the computation is greatly reduced. In previous papers, nearly all examples are analyzed for the sound fields with circular axial symmetry, but few are analyzed for the lack of this symmetry.[4]

This paper presents an alternative approach, a further extension of Breazeale's, to evaluate the ultrasonic field of transducers. The source function is generally expressed as the superposition of a series of two-dimensional Gaussian functions. The corresponding sound field is then reduced to the computation of these simple functions. It avoids the limit that the shape of the source is of the circular axial symmetry. Numerical examples are given for the uniform elliptical and rectangular piston transducers and compared with the results in references, demonstrating the high efficiency of our method in computer run time.

II. THEORY

A. Field integral

Here we write only the Fresnel field integral and its alternative form in nondimensional variables. The detailed derivation of this formula and the discussion of its application limits can be found in much of the literature and textbooks. Assume that the source or the aperture is placed in the plane $z=0$ in a rectangular coordinate, and here the quantity $u(x',y')$ is the pressure or normal velocity at the transducer's surface and may be defined as zero in other regions. It may also represent the others, such as the light beam distribution or the components of electromagnetic field intensity. In the Fresnel approximation, the radiated sound field can be expressed by

$$u(x,y,z)=\frac{1}{i\lambda z}\int_{-\infty}^{\infty}\int_{-\infty}^{\infty}\exp\left(\frac{i\pi}{\lambda}\frac{(x-x')^2+(y-y')^2}{z}\right)\times u(x',y')\,dx'\,dy', \tag{1}$$

i.e., the Fresnel field integral. Here λ is wavelength and the propagating factor $\exp[-i(\omega t-kz)]$ has been omitted. With the dimensionless variables

$$\xi=x/\sqrt{S},\quad \zeta=y/\sqrt{S},\quad \text{and}\quad \eta=\lambda z/\pi S, \tag{2a}$$

S being simply related to the area of source, we write Eq. (1) as

[a]Electronic mail: dds@seu.edu.cn

$$u(\xi,\zeta,\eta)=\frac{1}{i\pi\eta}\int_{-\infty}^{\infty}\int_{-\infty}^{\infty}\exp\left(i\frac{(\xi-\xi')^2+(\zeta-\zeta')^2}{\eta}\right)\times u(\xi',\zeta')d\xi'\,d\zeta'. \tag{2b}$$

B. Two-dimensional Gaussian beams

A two-dimensional Gaussian source has the form

$$u(\xi',\zeta')=\exp[-(B_x\xi'^2+B_y\zeta'^2)], \tag{3}$$

where B_x and B_y are generally complex numbers with the real parts greater than zero. The two-dimensional Gaussian beam field, with a special notation G_2, is

$$G_2(\xi,\zeta,\eta;B_x,B_y)=\frac{1}{i\pi\eta}\int_{-\infty}^{\infty}\int_{-\infty}^{\infty}\exp\left(i\frac{(\xi-\xi')^2+(\zeta-\zeta')^2}{\eta}\right)\times\exp[-(B_x\xi'^2+B_y\zeta'^2)]d\xi'\,d\zeta'. \tag{4}$$

Using

$$\int_{-\infty}^{\infty}\exp\left(-\frac{t^2}{4\beta}-\gamma t\right)dt=2\sqrt{\pi\beta}\exp(\beta\gamma^2), \tag{5}$$

and making some arrangements, we have

$$G_2(\xi,\zeta,\eta;B_x,B_y)=\left[\frac{1}{\sqrt{1+iB_x\eta}}\exp\left(-\frac{B_x\xi^2}{1+iB_x\eta}\right)\right]\cdot\left[\frac{1}{\sqrt{1+iB_y\eta}}\exp\left(-\frac{B_y\zeta^2}{1+iB_y\eta}\right)\right]=G_1(\xi,\eta;B_x)\cdot G_1(\zeta,\eta;B_y). \tag{6}$$

In Eq. (6), the G_1's denote the terms in the square brackets and are indeed the expression of a one-dimensional Gaussian beam. When $B_x=B_y=B$, Eq. (6) is just a usual (circular) Gaussian beam.

In one paper by Wen and Breazeale, they expressed the distribution function of an axial-symmetric (circular) source as a linear superposition of complex Gaussian functions and reduced the field solution to the calculation of simple Gaussian functions. Mathematically, this expansion means that a class of functions can be expressed approximately by a sum of a set of Gaussian functions, namely,

$$f(x)=\sum_{k=1}^{N}A_k\exp(-B_kx^2), \tag{7}$$

where the expansion and Gaussian coefficients, A_k and B_k, can be found out by computer optimization. Specially, Wen and Breazeale obtained one of the coefficient sets, containing only ten terms of coefficients ($N=10$), to match the circ function. These coefficients on the right-side of Eq. (7), an approximation of this function, are listed in Table I of Ref. 3; moreover, they calculated the sound field distribution of a uniform circular piston source. It is found that an excellent agreement between a ten-term Gaussian beam solution and the results of numerical integration is obtained throughout the beam field, and discrepancies exist only in the extreme near field (<0.12 times the Fresnel distance). In this paper, we take Eq. (7) as a known result, *an approximation to the circ function*, and we express an arbitrary source function as the superposition of a series of two-dimensional Gaussian functions and show how to apply this approach in the field calculation for the elliptical and rectangular transducers.

C. Rectangular piston

Assume that the center of a rectangular piston transducer, with a uniform distribution excitation, is located at the origin of the coordinates. The source distribution function is then defined as

$$u(x',y')=\begin{cases}1 & \text{if } |x'|\leqslant a,\quad |y'|\leqslant b,\\ 0 & \text{elsewhere.}\end{cases} \tag{8}$$

The quantities a and b are the half-major and half-minor axes of the transducer. Using the nondimensional variables, Eq. (2a), with $S=ab$, we get

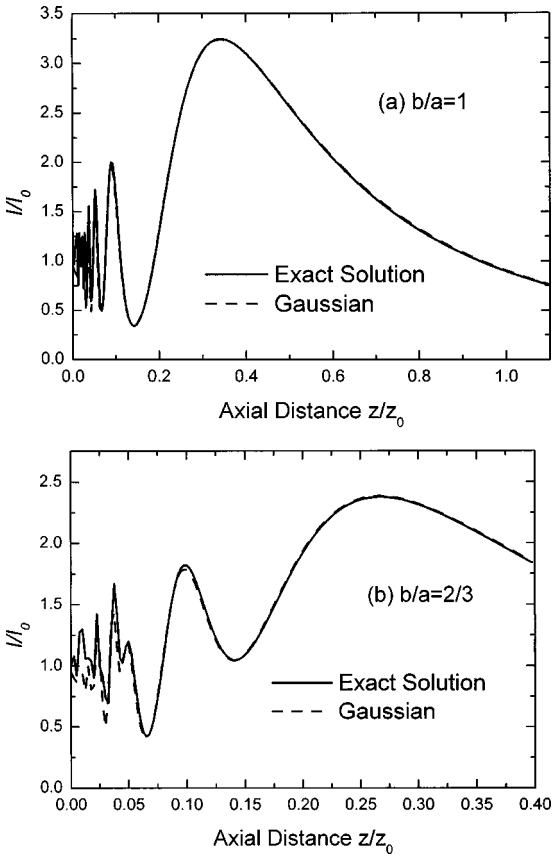

FIG. 1. Comparison of the sound intensity distributions of the rectangular piston along the acoustic axis (z), computed by use of the Gaussian expansion and the exact expression. (a) Square transducer ($b/a=1$); (b) rectangular ($b/a=\frac{2}{3}$). (a) and (b) correspond to Figs. 3 and 5 of Ref. 17. Note that the axial distance is normalized to $Z_0=4a^2/\lambda$.

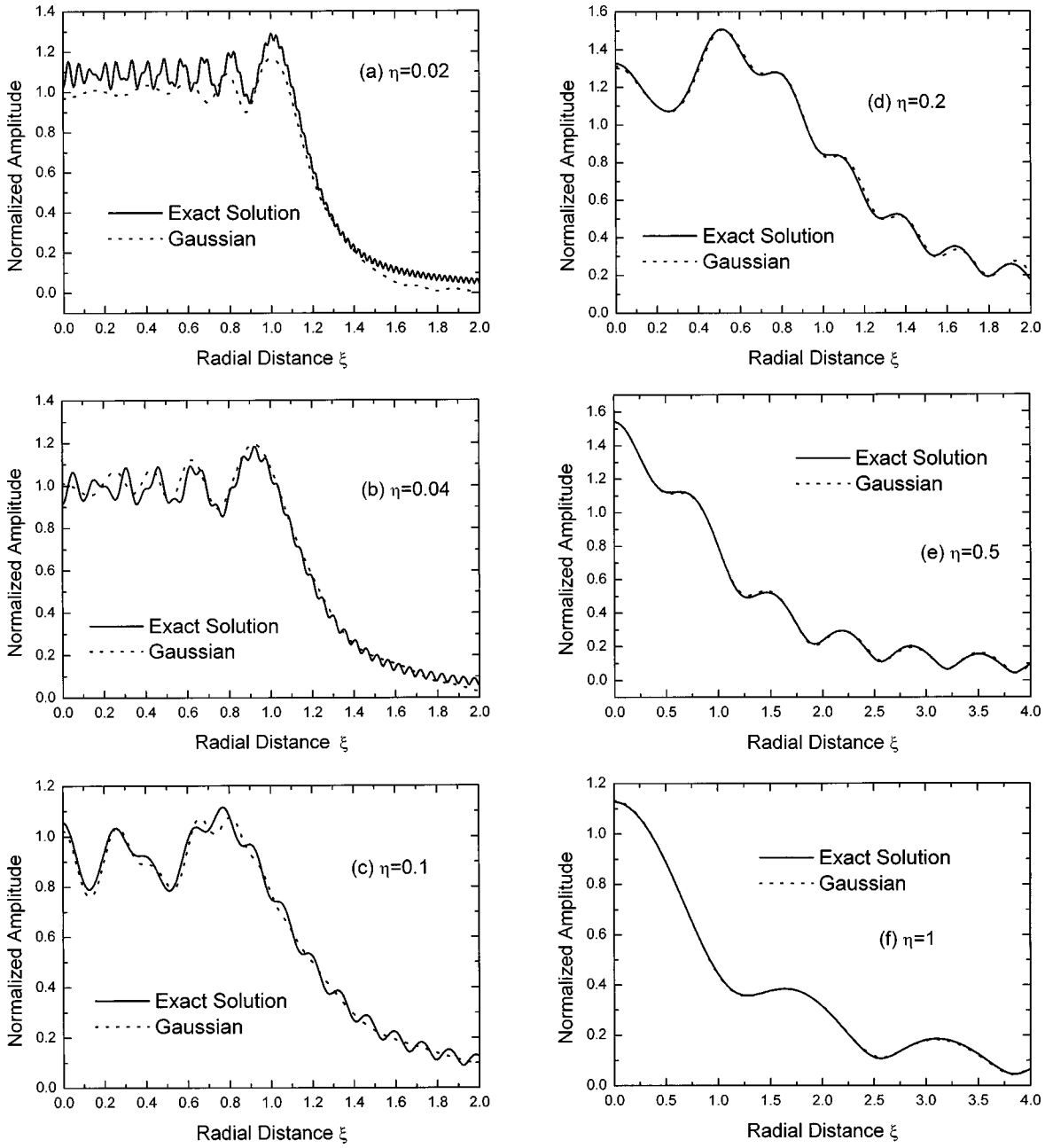

FIG. 2. Comparison of the off-axis pressure field distributions (in the *x*-*z* plane) at the different axial distances. Here η is as defined in the text [Eq. (20)]. No other results may be compared.

$$u(\xi',\zeta')=\begin{cases}1 & \text{if } |\xi'|\leqslant\sqrt{a/b},\ |\zeta'|\leqslant\sqrt{b/a},\\ 0 & \text{elsewhere.}\end{cases} \tag{9}$$

The above function can be written

$$\begin{aligned}u(\xi',\zeta')&=\operatorname{circ}(\sqrt{b/a}\,\xi')\cdot\operatorname{circ}(\sqrt{a/b}\,\zeta')\\&=\left\{\sum_{k=1}^{N}A_k\exp\left[-B_k\left(\frac{b}{a}\right)\xi'^2\right]\right\}\\&\quad\cdot\left\{\sum_{k=1}^{N}A_k\exp\left[-B_k\left(\frac{a}{b}\right)\zeta'^2\right]\right\}.\end{aligned} \tag{10}$$

In the next treatment it is not necessary to further expand this into the formal summation of two-dimensional Gaussian functions like Eq. (3). Using Eq. (6), we express the sound field of the rectangular piston transducer as

$$\begin{aligned}u(\xi,\zeta,\eta)&=\left[\sum_{k=1}^{N}A_kG_1\left(\xi,\eta;\frac{b}{a}B_k\right)\right]\\&\quad\cdot\left[\sum_{k=1}^{N}A_kG_1\left(\zeta,\eta;\frac{a}{b}B_k\right)\right].\end{aligned} \tag{11}$$

The field distribution, directly from Eq. (2), may be expressed by

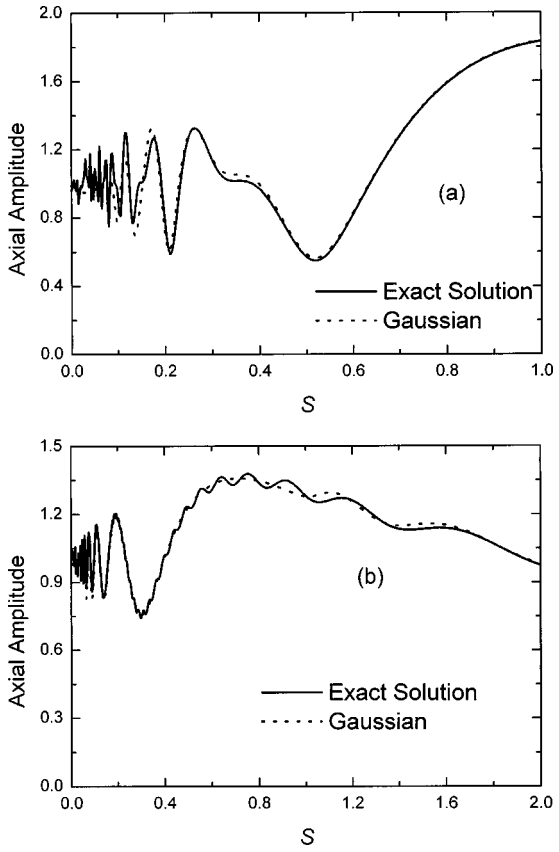

FIG. 3. The on-axis field distributions with different values of $\delta=b/a$. Here the normalized distance S defined by Ref. 4 has the relation with the variable η of Eq. (2a) in the text: $S=(\pi/2)(\delta+1/\delta)\eta$. And $\Delta S/S=(1-\delta^2)/(1+\delta^2)$. (a) $\delta=0.7738$, $\Delta S/S=0.3$; (b) $\delta=0.25$, $\Delta S/S=0.882$. (a) and (b) correspond to Figs. 6(c) and 7(c) of Ref. 4. (a) has some discrepancies in the region of $S\approx 0.3-0.6$ from Fig. 6(c) of Ref. 4; the others presented in Fig. 1 of Ref. 15 agree fairly well with those of Ref. 4.

$$u(\xi,\zeta;\eta)=\frac{1}{i\pi\eta}\int_{\xi'=-\sqrt{a/b}}^{\sqrt{a/b}}\int_{\zeta'=-\sqrt{b/a}}^{\sqrt{b/a}} \times\exp\left[i\frac{(\xi-\xi')^2+(\zeta-\zeta')^2}{\eta}\right]d\xi'\,d\zeta' =\frac{1}{i\pi\eta}\int_{\xi'=-\sqrt{a/b}}^{\sqrt{a/b}}\exp\left[i\frac{(\xi-\xi')^2}{\eta}\right]d\xi' \times\int_{\zeta'=-\sqrt{b/a}}^{\sqrt{b/a}}\exp\left[i\frac{(\zeta-\zeta')^2}{\eta}\right]d\zeta'. \tag{12}$$

One further obtains

$$u(\xi,\zeta;\eta)=\frac{1}{2i}\left[F\left(\sqrt{\frac{2}{\pi\eta}}\left(\xi+\sqrt{\frac{a}{b}}\right)\right)-F\left(\sqrt{\frac{2}{\pi\eta}}\times\left(\xi-\sqrt{\frac{a}{b}}\right)\right)\right]\left[F\left(\sqrt{\frac{2}{\pi\eta}}\left(\zeta+\sqrt{\frac{b}{a}}\right)\right)-F\left(\sqrt{\frac{2}{\pi\eta}}\left(\zeta-\sqrt{\frac{b}{a}}\right)\right)\right]. \tag{13}$$

Here $F(z)=C(z)+iS(z)$ is the Fresnel function, a kind of the special functions widely used in the diffraction problem.

We now give a comparison of the results for the rectangular piston, calculated respectively from Eqs. (11) and (13).

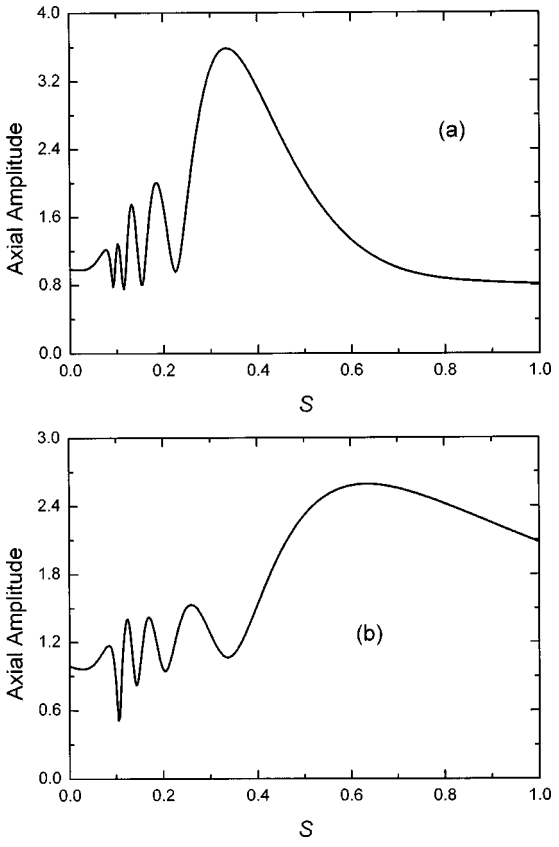

FIG. 4. The axial fields for a cylindrically focused circular piston ($\delta=b/a=1$) obtained from the Gaussian expansion. (a) $F_x\lambda/4a^2=0.372$, $F_y=\infty$; (b) $F_x\lambda/4a^2=0.744$, $F_y=\infty$. F_x and F_y are the focal lengths defined in Ref. 4.

Figure 1 shows the intensity distribution of the on-axis field with the different values of b/a, the ratio of the minor to major side. One can see that the results with the Gaussian expansion technique agree well with those of the analytical solution. Discrepancies exist only in the extreme near-field. To compare with the earlier results[16,17] (see Figs. 3 and 5 of Ref. 17), the calculation parameters in this example are taken the same as in Ref. 17. Figure 2 is typically for the pressure distribution of the off-axis field. In all the graphs, the results are compared with numerical computation of the Fresnel function, Eq. (13). A very good agreement is again obtained, with the exception of little loss of the fine structures in the extreme near-field region.

D. Elliptical piston

For a uniform elliptical piston field, the source function is

$$u(x',y')=\begin{cases}1 & \text{if } (x'/a)^2+(y'/b)^2\leqslant 1,\\ 0 & \text{elsewhere.}\end{cases} \tag{14}$$

Without loss of generality, here a and b are the semi-major and semi-minor axes of an elliptical piston. Letting $S=ab$ and using dimensionless variables, we write

$$u(\xi',\zeta')=\begin{cases}1 & (b/a)\xi'^2+(a/b)\zeta'^2\leqslant 1,\\ 0 & \text{elsewhere.}\end{cases} \tag{15}$$

The source function of the uniform elliptical piston can be written

$$u(\xi',\zeta') = \mathrm{circ}\left(\frac{b}{a}\xi'^2 + \frac{a}{b}\zeta'^2\right) = \sum_{k=1}^{N} A_k \exp\left[-\left(\frac{b}{a}B_k\xi'^2 + \frac{a}{b}B_k\zeta'^2\right)\right]. \quad (16)$$

From Eqs. (6) and (7), the radiated field distribution is thus expressed as

$$u(\xi,\zeta,\eta) = \sum_{k=1}^{N} A_k G_2\left(\xi,\zeta,\eta;\frac{b}{a}B_k,\frac{a}{b}B_k\right). \quad (17)$$

As in the case of a uniform circular piston transducer, there is no analytical expression for the uniform elliptical piston field, except in the far field (Fraunhofer region) where the field distribution may be simply described in terms of the first-order Bessel function of the first kind. An integral representation of the on-axis radiation field from the elliptical transducer is given by Thompson *et al.*[4] This result is reproduced here with our notation,

$$u(0,0,\eta) = \frac{1}{2\pi}\int_0^{2\pi}\left[1-\exp\left[\frac{i2\delta}{\eta[(1+\delta^2)+(1-\delta^2)\cos 2\theta]}\right]\right]d\theta, \quad (18)$$

where $\delta = b/a$ is the ratio of the semi-minor to semi-major axis. For the off-axis field, they expanded it into the superposition of Gaussian–Hermite functions up to about 2000 (for instance, 47×47) terms, using the method of Cook *et al.*

We now present the calculated results for the elliptical piston field. For comparison, all parameters are the same as in Ref. 4. Figure 3 demonstrates the on-axis field of the uniform elliptical pistons with the different values of δ. The exact results from Eq. (18) are also shown in this figure. It is obvious that our results with the only ten-term Gaussian expansion technique are better than those calculated using 47×47- or 41×41-term Gaussian-Hermite functions.[4] (See Figs. 6 and 7 of Ref. 4.) Unfortunately, there is no body of literature for the off-axis near-field of elliptical transducers that permits comparison.

The present method is easy to apply to the case of the sound field of the elliptical piston focused by a bicylindrical lens.[4] The effect of focusing is (approximately) equivalent to a spatial modulation of the plane piston distribution. A procedure fully applicable here has been given in Refs. 8 and 9, although there the field of the circular focused piston transducer was analyzed. We do not repeat here and merely give some results for the focused elliptical pistons, as shown in Fig. 4. In all calculations we apply the ten pairs of coefficients in Table I of Ref. 3.

Finally, it is worth pointing out that the present method may be applied to the other circumstances. For example, the sound field by a strip piston may be included as a special case of the rectangular transducer.[18,19] A more general discussion will be given in the Appendix. Besides, the integral representation of field, Eqs. (1) and (2), appear in many other branches of physics and engineering application involving the problem of diffraction, such as optics, the propagation of electromagnetic fields, etc. It is expected that the present or an improved method is still applicable in these fields.

III. CONCLUSION

In conclusion, we have presented a new approach that treats efficiently the radiation problem for the ultrasonic transducers. It reduces the Fresnel field integral to the superposition of a set of two-dimensional Gaussian beams. The radiated fields of the elliptical and the rectangular piston are exemplified and compared with the results in references, demonstrating the high efficiency of this method. The possibility of the application to the other cases is also discussed.

ACKNOWLEDGMENTS

This work is supported by the National Natural Science Foundation of China under Grant No. C-A040505-19904003 and 10274010. DD would like to express his thanks to Professor M. A. Breazeale. Much work is inspired by his lectures presented at the Institute of Acoustics of Nanjing University many years ago.

APPENDIX: FURTHER EXTENSION

Notice that those several examples given in the text are still very special. The source function has the property $u(x,y) = u(\pm x,\pm y)$, that is, the source (or beam) distribution is always symmetrical with respect of x and y axes. Naturally, the question rises: Is there an expansion similar to Eq. (10) or (16), or does the present method remain applicable, for an arbitrary, real source distribution without this symmetry? To answer this question, we give the following statement.

Let the function $f(x,y)$ be square integrable and (piecewise continuous) in the entire region (x-y plane), i.e., $\int_{-\infty}^{\infty}\int_{-\infty}^{\infty} f^2(x,y)\,dx\,dy < +\infty$. Then this function is always expressed as the summation form of the two-dimensional Gaussian functions, in a sense of an average convergence. In other words, if

$$Q = \int_{-\infty}^{\infty}\int_{-\infty}^{\infty}\left[f(x,y) - \sum_{k=1}^{N} A_k G_2(x-a_k, y-b_k; B_{xk}, B_{yk})\right]^2 dx\,dy, \quad (A1)$$

then $Q\to 0$ when $N\to\infty$. The function G_2 here is the same form as that of Eq. (3), defined by

$$G_2(x-a_k, y-b_k; B_{xk}, B_{yk}) = \exp\{-[B_{xk}(x-a_k)^2 + B_{yk}(y-b_k)^2]\}, \quad (A2)$$

and A_k, B_{xk}, B_{yk}, a_k and b_k are a set of coefficients to be determined for the function $f(x,y)$ given. Further, a_k and b_k are always assumed to be real-valued. There is a geometric explanation for real-valued a_k and b_k. For a Gaussian beam described by Eq. (A2), its center shifts from the point (0,0) to (a_k,b_k). In principle, these coefficients of Eq. (A1) are obtained by computer optimization.[3]

We have some difficulty to mathematically prove this statement. However, the statement seems to hold good from intuition. Under this assumption, the approach presented in the text is extended to a more general case. An arbitrary source function is decomposed to

$$u(\xi,\zeta)=\sum_{k=1}^{N} A_k G_2(\xi-\alpha_k,\zeta-\beta_k;B_{xk},B_{yk}). \tag{A3}$$

The radiation field is calculated from

$$u(\xi,\zeta,\eta)=\sum_{k=1}^{N} A_k G_2(\xi-\alpha_k,\zeta-\beta_k,\eta;B_{xk},B_{yk}) \tag{A4}$$

of G_2 with the same form as Eq. (3).

An example at hand strongly supports the above argument. We assume that the quarter of a uniform, elliptical (or circular) piston is located in the first region of the rectangular coordinate. Its source function, no longer symmetric, is expressed as

$$u(\xi',\zeta')=\begin{cases}1 & (b/a)\xi'^2+(a/b)\zeta'^2\leqslant 1,\ \ \xi'\geqslant 0,\ \ \zeta'\geqslant 0,\\ 0 & \text{elsewhere.}\end{cases} \tag{A5}$$

Note that Eq. (A5) may be written as

$$u(\xi',\zeta')=f_1(\xi',\zeta')f_2(\xi')f_3(\zeta'), \tag{A6a}$$

where

$$f_1(\xi',\zeta')=\mathrm{circ}\left(\frac{b}{a}\xi'^2+\frac{a}{b}\zeta'^2\right)=\sum_{k=1}^{N} A_k \exp\left[-\left(\frac{b}{a}B_k\xi'^2+\frac{a}{b}B_k\zeta'^2\right)\right], \tag{A6b}$$

$$f_2(\xi')=\mathrm{circ}\left(2\sqrt{\frac{b}{a}}\left|\xi'-\frac{1}{2}\right|\right)=\sum_{k=1}^{N} A_k \exp\left[-4B_k\left(\frac{b}{a}\right)\left(\xi'-\frac{1}{2}\right)^2\right], \tag{A6c}$$

and

$$f_3(\zeta')=\mathrm{circ}\left(2\sqrt{\frac{a}{b}}\left|\zeta'-\frac{1}{2}\right|\right)=\sum_{k=1}^{N} A_k \exp\left[-4B_k\left(\frac{a}{b}\right)\left(\zeta'-\frac{1}{2}\right)^2\right]. \tag{A6d}$$

The above coefficients are known from Table I of Ref. 3. Then Eq. (A5) is expressed in the form of Eq. (A3), and its coefficients, although not optimized, are the combination of the known Gaussian and expansion coefficients B_k and A_k, and the parameter $\delta=b/a$.

This is of course an imagined example. Fortunately, the geometry of transducers or sources is nearly (considered) regular in many practical uses and the theory of diffraction problems. We do not say much.

[1] B. D. Cook and W. J. Arnoult III, "Gaussian-Laguerre/Hermite formulation for the nearfield of an ultrasonic transducer," J. Acoust. Soc. Am. **59**, 9–11 (1976).

[2] E. Cavanagh and B. D. Cook, "Gaussian-Laguerre description of ultrasonic fields-Numerical Example: Circular piston," J. Acoust. Soc. Am. **67**, 1136–1140 (1980).

[3] J. J. Wen and M. A. Breazeale, "A diffraction beam field expressed as the superposition of Gaussian beams," J. Acoust. Soc. Am. **83**, 1752–1756 (1988).

[4] R. B. Thompson, T. A. Gray, J. H. Rose, V. G. Kogan, and E. F. Lopes, "The radiation of elliptical and bicylindrically focused piston transducers," J. Acoust. Soc. Am. **82**, 1818–1828 (1987).

[5] D. Ding, J. Lin, Y. Shui, G. Du, and D. Zhang, "An analytical description of ultrasonic field produced by circular piston transducer," Acta Acust. (Beijing) **18**, 249–255 (1993).

[6] D. Ding, Y. Shui, J. Lin, and D. Zhang, "A simple calculation approach for the second harmonic sound field generated by an arbitrary axial-symmetric source," J. Acoust. Soc. Am. **100**, 727–733 (1996).

[7] D. Ding and Z. Lu, "A simplified method to calculate the sound field of pistonlike source," Chin. J. Acoust. **15**, 213–222 (1996), also appearing in Acta Acust. (Beijing) **21** (Suppl. 4), 421–428 (1996).

[8] D. Ding and Z. Lu, "A simplified calculation for the second-order fields generated by axial-symmetric sources at bifrequency," in *Nonlinear Acoustics in Perspective: Proceedings of the 14th International Symposium on Nonlinear Acoustics*, edited by R. J. Wei (Nanjing U. P., Nanjing, 1996), pp. 183–188.

[9] D. Ding, "A simplified algorithm for the second-order sound fields," J. Acoust. Soc. Am. **108**, 2759–2764 (2000).

[10] D. Ding and X. Liu, "Approximate description for Bessel, Bessel-Gauss and Gaussian beams with finite aperture," J. Opt. Soc. Am. A **16**, 1286–1293 (1999).

[11] M. D. Prange and R. G. Shenoy, "A fast Gaussian beam description of ultrasonic fields based on Prony's method," Ultrasonics **34**, 117–119 (1996).

[12] O. B. Matar, J. P. Rernenieras, C. Bruneel, A. Roncin, and F. Patat, "Ultrasonic sensing of vibrations," Ultrasonics **36**, 391–396 (1998).

[13] D. Huang and M. A. Breazeale, "A Gaussian finite-element method for description of sound diffraction," J. Acoust. Soc. Am. **106**, 1771–1781 (1999).

[14] M. Spies, "Transducer field modeling in anisotropic media by superposition of Gaussian base function," J. Acoust. Soc. Am. **105**, 633–638 (1999).

[15] Y. Zhang, J. Liu, and D. Ding, "Sound field calculations of elliptical pistons by the superposition of two-dimensional Gaussian beams," Chin. Phys. Lett. **19**, 1825–1827 (2002).

[16] A. Freedman, "Sound field of a rectangular piston," J. Acoust. Soc. Am. **32**, 197–201 (1960).

[17] J. Marini and J. Rivenez, "Acoustical fields from rectangular ultrasonic transducers for nondestructive testing and medical diagnosis," Ultrasonics **12**, 251–256 (1974).

[18] F. D. Martin and M. A. Breazeale, "A simple way to eliminate diffraction lobes emitted by ultrasonic transducers," J. Acoust. Soc. Am. **49**, 1668–1669 (1971).

[19] M. A. Breazeale, F. D. Martin, and B. Blackburn, "Reply to 'Radiation pattern of partially electroded piezoelectric transducers,'" J. Acoust. Soc. Am. **70**, 1791–1793 (1981).

Local interaction simulation approach to modelling nonclassical, nonlinear elastic behavior in solids

Marco Scalerandi,[a] Valentina Agostini, and Pier Paolo Delsanto
INFM, Dip. Fisica, Politecnico di Torino, C.so Duca degli Abruzzi 24, Torino, Italy

Koen Van Den Abeele
Interdisciplinary Research Center, Fac. of Science, K. U. Leuven Campus Kortrijk, E. Sabbelaan 53, B-8500 Kortrijk, Belgium

Paul A. Johnson
Los Alamos National Laboratory, Nonlinear Elasticity Group, MS D-443, Los Alamos, New Mexico 87545

(Received 16 July 2002; revised 6 February 2003; accepted 10 March 2003)

Recent studies show that a broad category of materials share ''nonclassical'' nonlinear elastic behavior much different from ''classical'' (Landau-type) nonlinearity. Manifestations of ''nonclassical'' nonlinearity include stress–strain hysteresis and discrete memory in quasistatic experiments, and specific dependencies of the harmonic amplitudes with respect to the drive amplitude in dynamic wave experiments, which are remarkably different from those predicted by the classical theory. These materials have in common soft ''bond'' elements, where the elastic nonlinearity originates, contained in hard matter (e.g., a rock sample). The bond system normally comprises a small fraction of the total material volume, and can be localized (e.g., a crack in a solid) or distributed, as in a rock. In this paper a model is presented in which the soft elements are treated as hysteretic or reversible elastic units connected in a one-dimensional lattice to elastic elements (grains), which make up the hard matrix. Calculations are performed in the framework of the local interaction simulation approach (LISA). Experimental observations are well predicted by the model, which is now ready both for basic investigations about the physical origins of nonlinear elasticity and for applications to material damage diagnostics.
[DOI: 10.1121/1.1570440]

PACS numbers: 43.25.Dc, 43.25.Gf, 43.25.Ed [MFH]

I. INTRODUCTION

In the last decade, numerous studies of a diverse class of materials such as earth materials, cement products, concrete, composites, etc., have shown that their elastic nonlinear behavior is significantly different from the classical nonlinear behavior found in ''ordinary'' materials, such as glasses, single crystals, and numerous others.[1–3] Despite their very different structural and chemical properties, these materials share the same nonlinear elastic signatures that can be observed in both quasistatic and dynamic experiments. In the following we shall say that these materials display ''nonclassical'' nonlinearity, while the ''ordinary'' materials, which obey the traditional nonlinear theory of Landau[4,5] shall be called ''classical'' nonlinear.

The fundamental characteristic of nonclassical material behavior in quasistatic experiments is the appearance of stress–strain hysteresis and discrete memory.[6] Differences between nonclassical and classical nonlinear dynamic behavior include: a downshift of the resonance frequency, proportional to the resonance amplitude in the nonclassical case versus a quadratic amplitude dependence in the classical case; nonlinear attenuation versus amplitude independent attenuation; quadratic amplitude dependence of the third harmonic versus cubic in the classical case.[2] Another striking feature observed in the nonclassical nonlinear dynamic response of nonclassical materials is ''slow dynamics,'' i.e., the slow recovery of the linear material properties (wavespeed and attenuation) after a sample has been subjected to a force.[7–9]

Nonclassical nonlinear effects are believed to be due to the presence of soft regions in hard materials (e.g., microcracks, flat pores and soft bonding regions between grains in a granular material). They have been successfully reproduced by a model proposed by Holcomb and, later, by Guyer and McCall,[10] based on a Preisach–Mayergoyz (PM) space representation, in analogy with the treatment of magnetic hysteresis. Such a model provides a simple phenomenological description of the complex elastic behavior of an elementary elastic unit in the composition of an arbitrary material. Each unit is described by an elementary constitutive law that accounts for effects such as nonlinearity, hysteresis and endpoint memory. The collection of all units, each of them with their particular constitutive relations, yields the so called ''PM space,'' which characterizes the material specimen and can be used to predict the static mechanical behavior of rocks in agreement with macroscopic observations. In the case of dynamic problems, Van Den Abeele *et al.*[11] used a quasianalytical approximation of this model for homogeneous and

[a]Author to whom correspondence should be addressed; electronic mail: scalerandi@polito.it

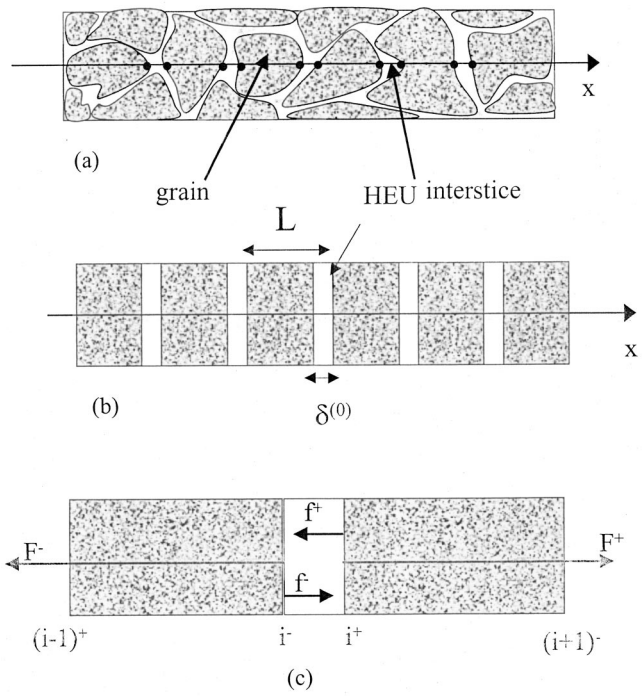

FIG. 1. (a) Representation of a specimen bar with grains and interstices; (b) its 1D schematic representation; (c) representation of the forces acting on the two subnodes delimiting an interstice.

isotropic nonlinear media to evaluate the influence of hysteresis on the propagation of longitudinal waves.

Analytical approaches significantly simplify the problem but may not succeed in reproducing the whole set of observed phenomena. Application of numerical calculations can serve as an alternative for a more complete theoretical analysis, including the extension of a basic one-dimensional model to higher dimensions. Computer models based on a microscopic approach, such as *ab initio* calculations and molecular dynamic techniques[12] are commonly used and allow, for instance, the understanding of atomic-scale effects and material behavior under applied stresses.[13] However, such methods are often of no practical use because of the huge CPU time required, even for simulations over a relatively small number of atoms. Therefore, a bridging between a microscopic and a macroscopic description is extremely useful.

In wave propagation applications, Delsanto *et al.*[14] proposed an approach for numerical simulations of macroscopic wave phenomena in complex heterogeneous media by introducing localized features at the mesoscopic to microscopic scale. The approach is based on the local interaction simulation approach (LISA)[15] in conjunction with a spring model.[16] A very important feature of LISA is, as its name implies, the capability of implementing at the local level even very complex mechanisms, which would be difficult to include in a partial differential equation. In fact the method allows full freedom in the choice of interaction between the nodes which represent the boundaries of the material cells.

It is also possible, by splitting the nodes at the interfaces between different material components into ''subnodes,'' each related to a different component, to include all kinds of microscopic-to-mesoscopic scale features. Such a model was implemented numerically in the LISA framework to simulate the influence of the local nonlinear elastic properties on the one-dimensional dynamic wave propagation in nonclassical materials.[17] To our knowledge, this is the only study to date that explicitly incorporates a macroscopic simulation of dynamic nonlinearity and hysteresis.

One of the drawbacks of numerical simulations is the difficulty of insuring the convergence and stability of the solutions. In this work, we propose a modification of the micromechanical properties of the individual units, as suggested in previous papers,[10] providing both an alternative physical description of the elasticity of the bond system and a more stable numerical treatment.

In Sec. II, we define for each unit the nonanalytical constitutive law provided by the model used as input for the LISA simulation. The main difference with the model of Guyer and McCall[10] is that the units, which represent the interstices between grains, are elastic and therefore not restricted to only two strain states (''open'' and ''closed''). In Sec. III, a generalization of the spring model[16] is introduced for the simulation of the propagation of ultrasonic waves in classical materials, with both rigid and nonrigid interfaces. The approach is then extended to the treatment of nonclassical nonlinearities.

In order to illustrate the applicability of the model, we focus our attention on simulations of a resonant bar experiment (Sec. IV) and show that our model is capable of reproducing all of the observed nonclassical nonlinear features.

II. CONSTITUTIVE RELATIONS

Let us consider a sample of a multigrained material, as shown in Fig. 1(a). For simplicity, we assume that grains are homogeneous and that the distance between two grain centers is L when no pressure is applied to the bar. Likewise we assume that, initially, all the interstices between grains have the same length $\delta^{(0)} \ll L$. The bar may then be represented by the 1D lattice sketched in Fig. 1(b): a sequence of elastic portions separated by soft interstice regions. The latter can be thought of as the bond system between the grains. In the following we will call the combination of elastic grain and interstice elastic unit (EU) or lattice cell.

In the PM space model,[10] the interstice regions can exist only in two states: open or closed. In the open state the interstice has a length δ_0. When the pressure on the interstice increases, it behaves rigidly and remains at the length δ_0 up to a certain pressure P_c. At this pressure level, the interstice instantaneously closes (infinitely soft elasticity for an infinitesimal short time) and assume the length δ_c ($\leqslant \delta_0$). Upon further increase of pressure, the interstice continues to behave rigidly, this time with length δ_c. When decreasing the pressure, the interstice remains at its length δ_c down to a pressure level $P_0 (\leqslant P_c)$, where it instantaneously opens, and remains at the length δ_0 upon further decrease of the pressure. The grains are considered to be purely elastic, represented by a modulus K_g. The corresponding stress–

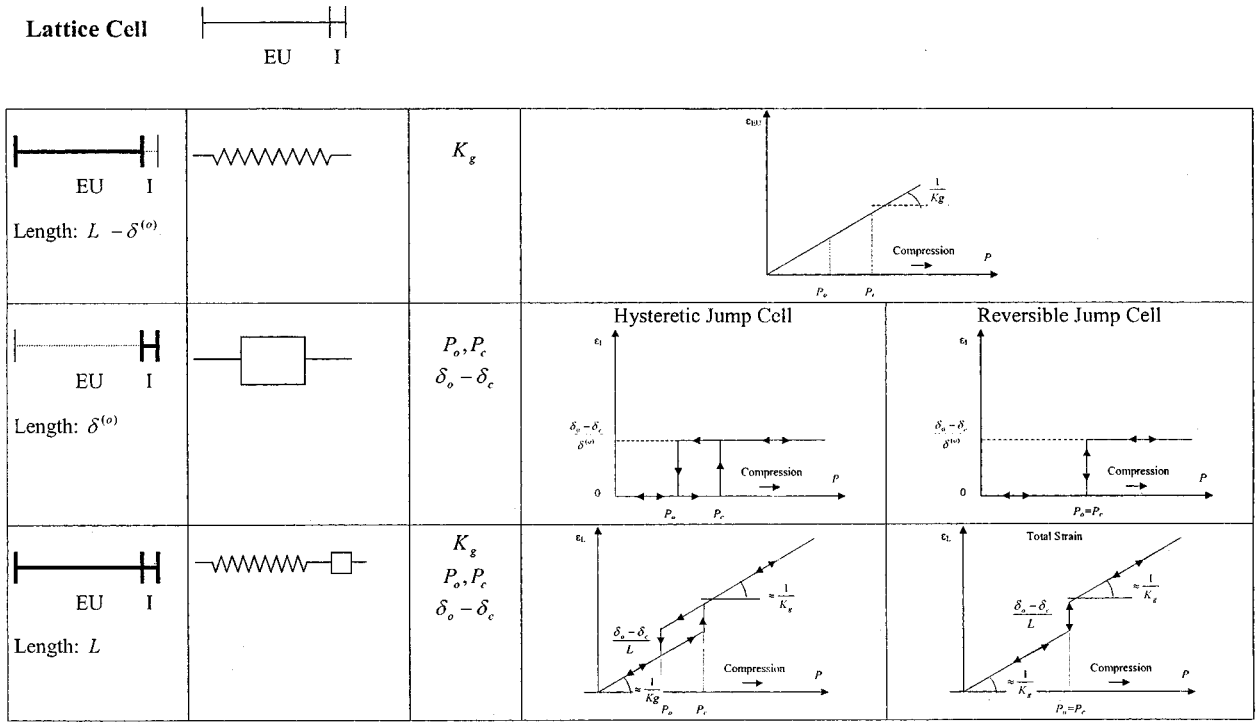

(a)

$$\varepsilon_{EU} = \frac{P}{K_g} \qquad \varepsilon_I = \begin{cases} 0 & \text{if } (P < P_c \text{ and } P \text{ increasing}) \text{ or } (P < P_0 \text{ and } P \text{ decreasing}) \\ \dfrac{\delta_o - \delta_c}{\delta^{(o)}} & \text{if } (P > P_c \text{ and } P \text{ increasing}) \text{ or } (P > P_0 \text{ and } P \text{ decreasing}) \end{cases}$$

$$\varepsilon_L = \frac{L-\delta^{(o)}}{L}\varepsilon_{EU} + \frac{\delta^{(o)}}{L}\varepsilon_I = \frac{L-\delta^{(o)}}{L}\frac{P}{K_g} + \begin{cases} 0 & \text{if } (P < P_c \text{ and } P \text{ increasing}) \text{ or } (P < P_0 \text{ and } P \text{ decreasing}) \\ \dfrac{\delta_o - \delta_c}{L} & \text{if } (P > P_c \text{ and } P \text{ increasing}) \text{ or } (P > P_0 \text{ and } P \text{ decreasing}) \end{cases}$$

$$\text{and thus } \varepsilon_L \approx \frac{P}{K_g} + \begin{cases} 0 & \text{if } (P < P_c \text{ and } P \text{ increasing}) \text{ or } (P < P_0 \text{ and } P \text{ decreasing}) \\ \dfrac{\delta_o - \delta_c}{L} & \text{if } (P > P_c \text{ and } P \text{ increasing}) \text{ or } (P > P_0 \text{ and } P \text{ decreasing}) \end{cases}$$

(b)

FIG. 2. The micromodel of Guyer and McCall (Ref. 10) illustrating the stress–strain behavior of a typical lattice cell composed of an elastic unit and a nonclassical interstice. The grains are purely elastic, the interstices display jump and hysteresis phenomena. Apart from two geometric parameters (L and $\delta^{(0)}$, see Fig. 1), lattice cells are represented by four "elastic" parameters: the elasticity of the grains K_g, the opening and closing pressures P_0 and P_c, and the elementary length change $\delta_0 - \delta_c$. The total strain on a lattice cell can be calculated by a series interaction. A statistical ensemble of such cells represents a microinhomogeneous material.

strain relations are shown in Fig. 2 (we consider the strain ϵ to be positive if the length is decreasing, and pressure is considered positive in compression, negative in tension). The pairs (P_0, P_c) have generally different values for each interstice.

The residual modulus of a lattice cell K_{cell} can be calculated as follows:

$$\frac{1}{K_{\text{cell}}} = \frac{1}{K_g} + \frac{1}{K_I}, \tag{1}$$

where K_I is the interstice modulus, which is infinity (rigid behavior) except at P_0 and P_c. For completeness, we also illustrate in Fig. 2 the elastic response of a single lattice cell, both for $P_0 \neq P_c$ (hysteretic jump cell) and for $P_0 = P_c$ (reversible jump cell).[10] Apart from two geometric parameters (L and $\delta^{(0)}$), lattice cells in this model are thus represented by four "elastic" parameters: K_g, P_0, P_c, and δ_0.

For numerical simulations, the appearance of jumps in the state equation, i.e., i the interstice length, may cause problems of convergence and stability. Also, from a physical point of view, discontinuities in a physical parameter are unrealistic. Ideally, it would be most satisfactory to describe the elastic behavior by means of smooth analytic functions. As an example, the expressions

$$\epsilon=\begin{cases}\dfrac{P}{K_g}+\dfrac{P+P_0-\chi\ln[\cosh((P-P_0)/\chi)]}{2K_I}+\kappa\left(1+\tanh\left(\dfrac{P-P_0}{\chi}\right)\right) & \text{if } P>0,\\ \dfrac{P}{K_g}+\dfrac{P+P_0-\chi\ln[\cosh((P-P_0)/\chi)]}{2K_I}+\left(\kappa+\dfrac{(P_c-P_0)}{K_I}\right)\left(1+\tanh\left(\dfrac{P-P_0}{\chi}\right)\right) & \text{if } P<0\end{cases} \tag{2}$$

yield the elastic stress-strain behavior of the lattice cell illustrated in Fig. 3, i.e., describes the hysteresis loop. Here, a total of six ''elastic'' parameters are involved: K_g, K_I, P_0, P_c, κ, and χ. K_I introduces a difference in elasticity modulus before and after the hysteretic open-closure pressure range; κ reflects the magnitude of the jump in strain at P_c and χ takes into account the smoothness of the transitions at P_c and P_0. The PM space of Ref. 10 can be reproduced in the limit of $K_I\to\infty$ and $\chi=0$, i.e., when there is no change in the elasticity modulus before and after closure, and the closing and opening are instantaneous in pressure.

However, since we are treating the bond system as soft inclusions, it is reasonable to assume that the modulus of a lattice cell alters when the elastic features change states. Therefore, it seems appropriate to retain the interstice softness parameter K_I at a value different from infinity. In order to limit the number of free parameter values to four, as in the original PM space model, we put $\kappa=\chi=0$. In doing so, we have adjusted the micromechanical properties of the bond elements, introducing a state variable which rules the interstice elastic properties. Instead of opening and closing discontinuously in pressure, the interstice element behaves linearly elastic, with modulus $K'=\delta^{(0)}/L^{(0)}K_I$, up to the pressure P_c. At that pressure level, the element becomes rigid (infinite modulus), and it remains rigid for all pressures above. When decreasing the pressure, the interstice remains at a fixed length down to a pressure level P_0, where it instantaneously opens and continues afterwards to increase its length according to Hooke's law,

$$\epsilon_I=\frac{\delta^{(0)}-\delta}{\delta^{(0)}}=\frac{P}{K'}. \tag{3}$$

The sudden decrease in strain (increase in length) of the lattice cell at P_0 amounts to $(P_c-P_0)/K_I$. The corresponding stress–strain behavior of the elastic unit, the interstice element and the total lattice cell are shown in Fig. 4. As in the case of the original PM space model, the micromechanical behavior can be described by piecewise linear functions. If $P_0=P_c$, we talk of a reversible elastic unit (REU). If P_0 differs from P_c, we use the term hysteretic elastic unit (HEU).

The new representation is an alternative model to the PM space model for a possible nonclassical physical mechanism. Of course, the choice of the protocol for the state variable should be dictated by the physical processes involved in the propagation at a microscopic level (work in progress). However, the simple phenomenological protocol used here already yields satisfactory results. It also has the advantage of eliminating the discontinuities of the physical parameter by replacing them with two discontinuities of a state variable, to be defined in the next section. This is important for the stability and convergence of the simulations. In the following section, we implement this type of elastic behavior in the framework of the local interaction simulation approach (LISA). However, the LISA approach can be applied to evaluate the macroscopic dynamic response of systems with any type of local nonclassical nonlinear elasticity.[17] In the present paper, first we consider the case of ''classical phase'' materials with completely rigid bonds, then we introduce linearly elastic bonds, and finally we implement the case of bonds with the assumed nonlinear elasticity, in order to describe the macroscopic dynamic behavior of nonclassical materials.

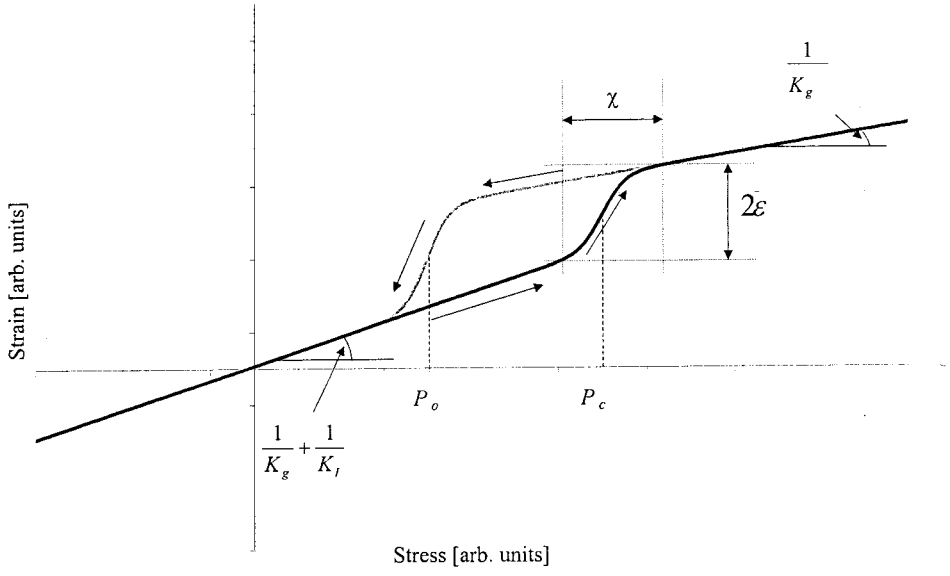

FIG. 3. A continuous micromodel illustrating the stress–strain behavior of a lattice cell characterized by a set of six ''elastic'' parameters: K_g, K_I, P_0, P_c, κ, and χ.

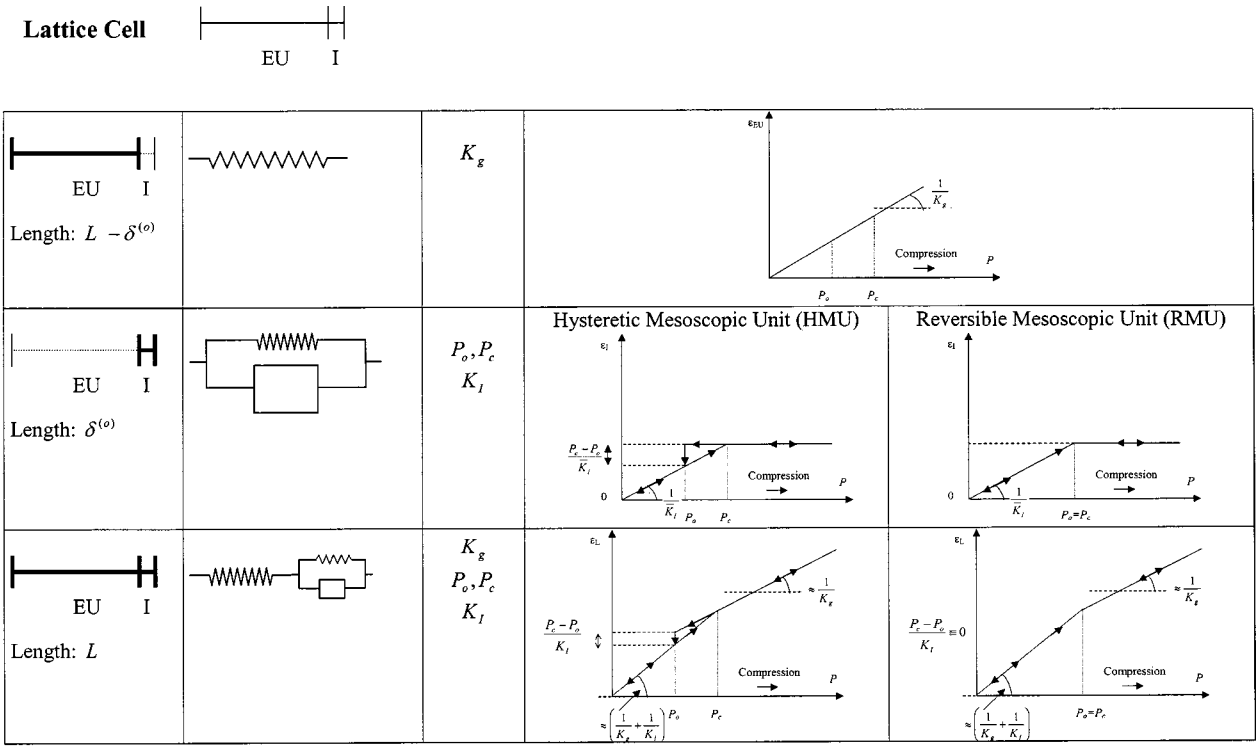

(a)

$$\varepsilon_{EU}=\frac{P}{K_g} \qquad \varepsilon_I=\begin{cases}\dfrac{P}{K_I} & \text{if } (P<P_c \text{ and } P \text{ increasing}) \text{ or } (P<P_0 \text{ and } P \text{ decreasing})\\[2ex] \dfrac{P_c}{K_I} & \text{if } (P>P_c \text{ and } P \text{ increasing}) \text{ or } (P>P_0 \text{ and } P \text{ decreasing})\end{cases}$$

$$\varepsilon_L=\frac{L-\delta^{(o)}}{L}\varepsilon_{EU}+\frac{\delta^{(o)}}{L}\varepsilon_I=\frac{L-\delta^{(o)}}{L}\frac{P}{K_g}+\begin{cases}\dfrac{\delta^{(o)}}{L}\dfrac{P}{K_I}=\dfrac{P}{K_I} & \text{if } (P<P_c \text{ and } P \text{ increasing}) \text{ or } (P<P_0 \text{ and } P \text{ decreasing})\\[2ex] \dfrac{\delta^{(o)}}{L}\dfrac{P_c}{K_I}=\dfrac{P_c}{K_I} & \text{if } (P>P_c \text{ and } P \text{ increasing}) \text{ or } (P>P_0 \text{ and } P \text{ decreasing})\end{cases}$$

$$\text{and thus } \varepsilon_L\approx\frac{P}{K_g}+\begin{cases}\dfrac{P}{K_I} & \text{if } (P<P_c \text{ and } P \text{ increasing}) \text{ or } (P<P_0 \text{ and } P \text{ decreasing})\\[2ex] \dfrac{P_c}{K_I} & \text{if } (P>P_c \text{ and } P \text{ increasing}) \text{ or } (P>P_0 \text{ and } P \text{ decreasing})\end{cases}$$

(b)

FIG. 4. The currently used micromodel illustrating the stress–strain behavior of a typical lattice cell composed of a purely elastic unit and a nonclassical interstice displaying both elasticity and jump and hysteretic phenomena. Apart from the geometric parameters, the lattice cells in this model are represented by four "elastic" parameters: the elasticity of the grains K_g, the opening and closing pressures P_0 and P_c, and the elasticity of the interstices K_I. The total strain on a lattice cell can be calculated by a series interaction. This micromodel derives from the general continuous model by setting both κ and χ equal to zero.

III. THE LISA MODEL

As shown in Fig. 1, each lattice cell consists of an elastic portion (grain) and an interstice element (bond). According to our model, the latter is responsible for the elastic hysteretic response. In order to describe the interstice region between two grains, each grid node i is split into two subnodes $i^{\pm}$ [see Fig. 1(c)]. Since in dynamical experiments the contribution of classical nonlinearity is generally negligible, we assume that the grains are linearly elastic. We confine all the nonlinear behavior to the interstices. Associated with each subnode is a length $L_n=L/2$ (i.e., of half a grain) and a mass $m_n=\rho L_n$, where ρ is the mass density per unit length. The interstices are considered to have zero mass (because $\delta^{(0)}$ is assumed to be very small). We call the combination of two subnodes left and right of a grid node, with their lengths and masses, a GBG cell (grain–bond–grain). Depending on the elastic behavior of the grains and the bond, this cell can be linearly elastic, classical nonlinear or nonclassical nonlinear.

For the simulation of dynamic processes, we also consider a time discretization $t=0,1,2,...$ with a constant time step τ. When referring to lengths (δ), displacements (u) and forces (F,f), the first subscript always refers to the space discretization, whereas the second refers to the time discretization. However, for brevity, starting with Eq. (3), we will

usually omit one or both indices when equal to the ''current'' values of i and/or t.

A. Classical phase materials

Classical phase materials are elastic materials with a classical bond system, i.e., the elastic behavior of both grains and bonds is linear or classically nonlinear. A particular case occurs when all of the interstices behave rigidly, i.e., the length of each interstice remains constant:

$$\delta_{i,t}=\delta_i^{(0)}+u_{i,t}^{+}-u_{i,t}^{-}=\text{const} \quad \forall T_0\leqslant t\leqslant T_1, \tag{4}$$

where T_0 and T_1 represent two arbitrary times and $\delta_i^{(0)}$ is the rest length of the ith interstice. This corresponds to the case of ''perfect contact'' in Ref. 16. In other cases of ''classical phase elasticity'' $\delta_{i,t}$ may be allowed to vary, provided the elastic modulus (i.e., the derivative of the stress with respect to the strain) is a continuous (linear or nonlinear) function of the applied stress.

To describe the general case, we assume that the following forces act on each subnode (we use the convention that forces are positive when pointing to the positive x direction):

An ''external'' elastic force $F_{i,t}^{\pm}$, due to the presence of an excitation of the bar at the interstice i at the time t. Neglecting, as mentioned, the classical nonlinear terms,

$$F_{i,t}^{\pm}=K_g\frac{u_{i\pm1,t}^{\mp}-u_{i,t}^{\pm}}{L}, \tag{5}$$

where K_g is the stiffness of the grains and $u_{i,t}^{\pm}$ is the subnode displacement.

A ''dissipative'' force $\gamma\, du_{i,t}^{\pm}/dt$, which is required in the simulation of dynamic resonance experiments in order to obtain steady state solutions.

An ''internal'' force, which acts on the interstice to keep the two subnodes together and transmits the external excitation through the bar.[16] Since the interstice itself has no mass: $f_{i,t}^{+}=-f_{i,t}^{-}$. These forces represent the ''interaction forces'' in the interstice.

An elastic ''restoring'' force

$$\mathfrak{I}_{i,t}^{\pm}=\mp K_I\,\frac{\delta_{i,t}-\delta_i^{(0)}}{\delta_i^{(0)}} \tag{6}$$

which corresponds to the elastic contribution, analogous to Eq. (5) for the grain.

The equation of motion for the two subnodes is then

$$\rho L_n\ddot{u}^{\pm}=F^{\pm}-\gamma\dot{u}^{\pm}+f^{\pm}+\mathfrak{I}^{\pm}. \tag{7}$$

By subtracting and summing these equations, we obtain the following:

The differential equation of the state evolution of the interstice (describing the hysteretic loop)

$$\rho L_n\ddot{\delta}=P-\gamma\dot{\delta}+2f+\mathfrak{I}^{+}-\mathfrak{I}^{-}. \tag{8}$$

The differential equation describing the pulse propagation

$$\rho L_n\ddot{y}=F-\gamma\dot{y}, \tag{9}$$

where

$$P=F^{+}-F^{-}, \tag{10}$$

$$y=(u^{+}+u^{-})/2, \tag{11}$$

$$F=(F^{+}+F^{-})/2. \tag{12}$$

1. Rigid interstice case

In a time interval $(t,t+1)$ in which the interstice remains rigid, i.e., $\delta_{t+1}=\delta_t$, it follows:

$$\dot{\delta}\approx\frac{\delta_{t+1}-\delta_{t-1}}{2\tau}=\frac{\delta_t-\delta_{t-1}}{2\tau}=\frac{\Delta\delta_{t-1}}{2\tau}, \tag{13}$$

$$\ddot{\delta}\approx\frac{\delta_{t+1}-2\delta_t+\delta_{t-1}}{\tau^2}=-\frac{\Delta\delta_{t-1}}{\tau^2}, \tag{14}$$

where we have applied the usual first order finite difference formalism together with the definition of the forward difference operator

$$\Delta y_k=y_{k+1}-y_k. \tag{15}$$

From Eqs. (6), (8), and (9), it follows

$$f=-\frac{P}{2}-\frac{a}{2}\Delta\delta_{t-1}+K_I(\delta-\delta^{(0)}), \tag{16}$$

where

$$a=\frac{1}{2\tau}\left(\frac{2\rho L_n}{\tau}-\gamma\right). \tag{17}$$

Note that if δ never changes (permanently rigid interface), $\Delta\delta_{t-1}=0$ and $\delta=\delta^{(0)}$ at all times, and therefore

$$f=-P/2 \tag{18}$$

as in Ref. 15. In this case, $u^{+}=u^{-}$ at each time.

2. Classical interstice case

When the interstice is not rigid, the arrival of an external excitation may change its length. Then, at least locally, we must assume that the material is undergoing a change. Accordingly, we modify Eq. (16) by multiplying the three terms on the right-hand side by three bond ''quality'' parameters q, q', and q'' (each of them less or equal to unity), which allow us to specify the quality of the interface bond at the time t:

$$f=-q\frac{P}{2}-q'\frac{a}{2}\Delta\delta_{t-1}+q''K_I(\delta-\delta^{(0)}). \tag{19}$$

In the general case of a ''classical'' interstice, q, q', and q'' are assumed to be constant, but more generally they may depend on the stress in a continuous and reversible way. The rigid interstice phase is recovered by placing all values equal to unity.

Substituting Eq. (19) into Eq. (8), we obtain

$$\rho L_n\ddot{\delta}=rP-\gamma\dot{\delta}-q'a\Delta\delta_{t-1}-2r''K_I(\delta-\delta^{(0)}), \tag{20}$$

where $r=1-q$, $r''=1-q''$. Equation (9) remains unaffected, because it does not involve the internal forces.

Following Eq. (20), the overall elastic properties of the GBG cells are defined by an effective elastic constant, which is a function of the elastic constants of the grain and bond, and of the (instantaneous) values of the bond quality parameters

$$K_{\text{eff}}=\Phi(K_g,K_i,q,q',q''). \tag{21}$$

Since $u^{\pm}=y\pm\delta/2$, we obtain from Eqs. (9) and (20),

$$2\rho L_n \ddot{u}^{\pm} = (1+r)F^{\pm} + (1-r)F^{\mp} - 2\gamma \dot{u}^{\pm} \mp q' a(\Delta u^{+}_{t-1} - \Delta u^{-}_{t-1}) \mp 2r''(u^{+} - u^{-} - \delta^{(0)}). \quad (22)$$

From Eq. (22) and by assuming that L_n and τ are chosen in order to assure optimal convergence,

$$\frac{2L_n}{\tau} = \sqrt{\frac{K_g}{\rho}}, \quad (23)$$

it follows:

$$Bu^{\pm}_{t+1} = (1+r)u^{\mp}_{i\pm1} + (1-r)u^{\pm}_{i\mp1} - 2Au^{\pm}_{t-1} + q'A(u^{\pm}_{t-1} - u^{\mp}_{t-1}) + E(u^{\pm} - u^{\mp}) \pm \frac{2K_i r''}{C}\delta^{(0)}, \quad (24)$$

where

$$C = \frac{2L_n\rho}{\tau^2}, \quad B = 1 + \frac{\gamma}{C\tau}, \quad A = 1 - \frac{B}{2}, \quad E = 1 - r - q'A - \frac{2K_I r''}{C}. \quad (25)$$

We remark here that, when the linear attenuation is not negligible, better convergence is obtained by choosing a frequency dependent time step[18]

$$\frac{2L_n}{\tau} = \sqrt{\frac{\rho}{K_g}}\sqrt{\frac{1+\sqrt{1+4\gamma^2/(\omega^2\rho^2(2L_n)^2)}}{2}}. \quad (26)$$

Equations (25) needs to be correspondingly modified.

B. Nonclassical phase materials

In a classical phase material, the parameters q, q', and q'' at each grid point are smooth single valued functions of the stress. In a nonclassical material, the internal structure may vary discontinuously and nonuniquely as a function of the applied stress. The discontinuous or nonunique stress dependence may be due to various physical mechanisms, e.g., a redistribution of dislocations, crack activation (opening or closing) or frictional forces (jerks). In the case of nonlinear elastic materials it is reasonable to assume that these changes affect only the interstice region. The effects at the mesoscopic–microscopic scale may be conveniently modeled by introducing a more complex dependence of the bond quality parameters q, q', and q'' on the local applied pressure. To describe the dependence of the bond quality parameters on the externally applied driving pressure in a nonclassical phase, we apply an approach similar to the one of Ref. 10, as described in Sec. II. We assign a pair of pressure parameters P_0 and P_c to each GBG cell ($P_0 \leqslant P_c$). When the local pressure applied to the interstice reaches the value P_c, we allow the bond quality parameters to switch from their initial values to unity, i.e., the bond becomes rigid for $P > P_c$. Conversely, when P decreases below P_0, the bond-quality parameters are switched to a value less than unity. The protocol for the bond quality parameter q as a function of the local pressure P is schematized in Fig. 5. Since q' affects only the wave attenuation, which is not relevant in the present context, we keep for simplicity $q'=1$ at all times. Likewise, for simplicity, we set $q''=q$ at all pressures. Other choices of protocol are, of course, possible and might be more suitable in general or in particular situations.

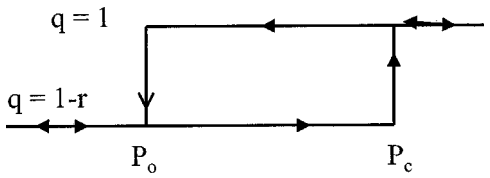

FIG. 5. Representation of the protocol for the dependence of the bond quality factor q on the applied pressure.

In the above described protocol, the specimen is represented as a sequence of GBG cells, each defined by a pair of activation pressures and by an initial bond state configuration. If $P \geqslant P_c$ or $P \leqslant P_0$, there is only one possible state, rigid or elastic, respectively. In the pressure range $P_0 < P < P_c$ two different states are possible, depending on the activation history of the GBG. The distribution of the pair of values (P_0, P_c), represented by the density $\rho_{NC}(P_0, P_c)$ of nonclassical GBG cells (hysteretic and reversible elastic units), can be obtained by inversion of quasistatic stress–strain measurements.[19,20]

The initial q distribution (at $t=0$) is strongly affected by the previous activation history of the specimen. In the following the specimen is assumed to be, at the time $t=0$, com-

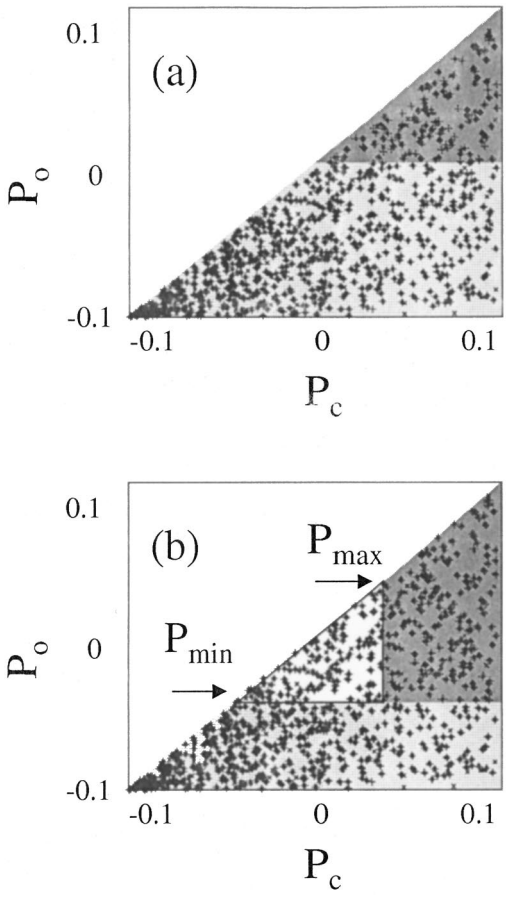

FIG. 6. PM space representation. Each dot represents one HEU or REU. (a) Specimen initially at zero pressure. Units in the dark gray and light gray areas are initially soft or rigid, respectively; (b) specimen under an external sinusoidal driving pressure between p_{min} and p_{max}. Units in the dark gray, light gray, and white areas are permanently soft, permanently rigid and active, respectively.

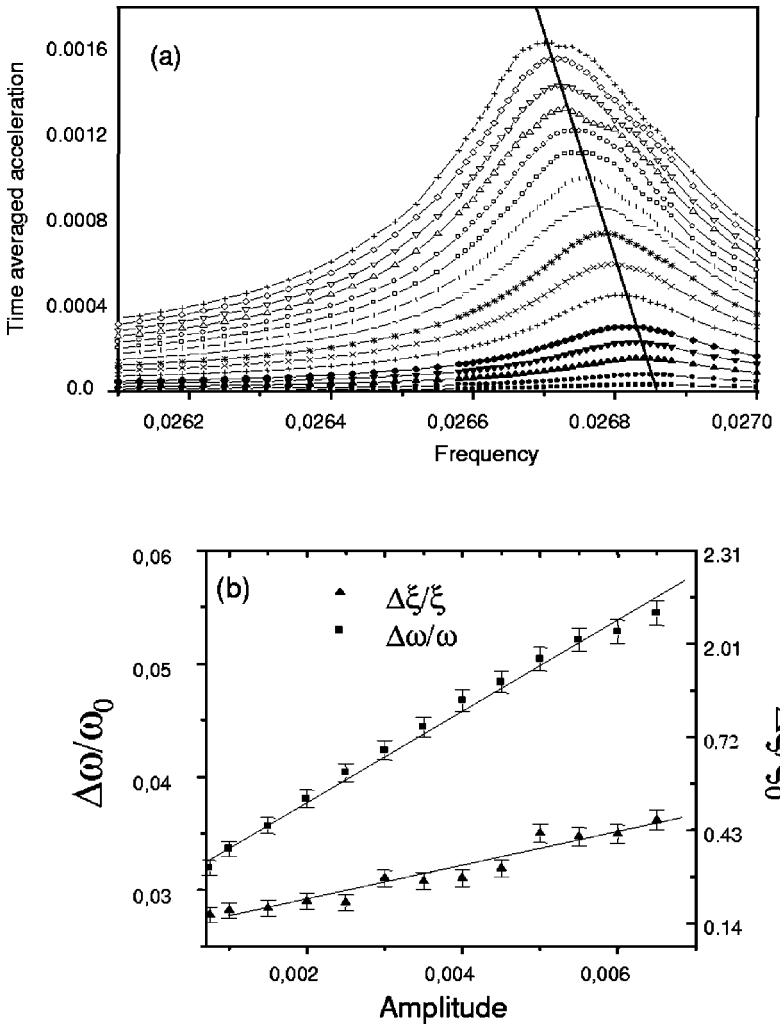

FIG. 7. Result of a resonant dynamic experiment. (a) Time averaged acceleration versus frequency for different driving amplitudes. (b) Normalized frequency shift and attenuation vs output wave amplitude at resonance.

pletely relaxed, i.e., kept at atmospheric pressure ($P=0$ after proper rescaling) and constant temperature for a sufficiently large time interval. The initial conditions then corresponds to the low energy ''equilibrium state'' produced by applying an oscillatory field amplitude slowly decreasing from a very large value to zero.[21] Assuming that random transitions between the elastic and rigid states occur when the applied pressure falls between the opening and closing pressures (see Ref. 9 for more details about the relaxation process), the following initial conditions apply:

$$\begin{aligned} &q=1 \quad \text{if } P_0<0 \quad \text{and } P_c<0,\\ &q=1-r \quad \text{if } P_c>0 \quad \text{and } P_0>0,\\ &q=1 \quad \text{with probability } p_e/(p_r+p_e)\\ &\qquad \text{if } P_c>0 \quad \text{and } P_0<0,\\ &q=1-r \quad \text{with probability } p_r/(p_r+p_e), \end{aligned} \tag{27}$$

where p_e and p_r are the transition probabilities from the elastic to the rigid state and vice versa.

Once the initial configuration is specified and the forcing protocol defined, the iteration equations (24) yield the temporal evolution of the system.

IV. SIMULATIONS OF NONLINEAR RESONANT BAR EXPERIMENTS

In the following we focus our attention on a resonant bar experiment performed on a typical material exhibiting nonclassical nonlinearity.[1] We assume that a rod-shaped specimen is equipped with a transducer generating monochromatic waves of excitation amplitude A_d attached at one end and with an accelerometer attached to the other end. The frequency f_d is swept through the fundamental resonance mode f_0 of the specimen and the time averaged acceleration amplitude A_r (in stationary conditions) is recorded. This procedure of resonance curve tracking is repeated for several different levels of excitation.

In the simulation approach, each elastic unit (HEU or REU) corresponds to a point in the PM space [see Fig. 6(a)]. The dark and light gray areas in the plot correspond to ini-

tially soft and rigid interstices, respectively. In the stationary state of a resonance, the actual pressure P for each HEU/REU oscillates between a minimum and a maximum pressure ($P_{\min}$ and $P_{\max}$, respectively), depending on the external excitation level and its location in the bar [see Fig. 6(b)]. If the HEU/REU is situated within the activation triangle (the PM space area bounded by the diagonal $P_0=P_c$ and the lines $P_0=P_{\min}$ and $P_c=P_{\max}$), the nonlinear properties are activated by the forcing (white area in the plot). As a consequence, the bond will change during the excitation process between rigid and soft.

In all the simulations arbitrary units have been chosen. The values of the parameters are $\rho=1$, $K_g=1$, $K_i=3$, $2L_n=1$, $\delta^{(0)}=1$, $\gamma=0.0001$, $p_e=0.0001$, and $p_r=0$. Simulations have been performed considering 1000 grains. Stationary conditions were usually reached in about 40 round trips of the wave. Results are qualitatively independent from the choice of the transition rates p_r and p_e, provided $p_r<p_e \ll 1$ (see also Ref. 9). Similar behaviors are found for the fundamental resonance and for higher modes.

Figure 7 illustrates a typical numerical simulation of the resonant bar experiment (simulations are performed without letting the system relax to the original initial conditions after each sweep). The time averaged acceleration amplitude on the free edge is plotted vs frequency for several driving amplitudes in Fig. 7(a). From Fig. 7(a) (using a Lorentzian fit), one can determine the resonance frequency and its amplitude. The width of the resonance curve is a measure of the attenuation. In the case of skewed resonance curves the attenuation can be obtained by means of the RTMF method

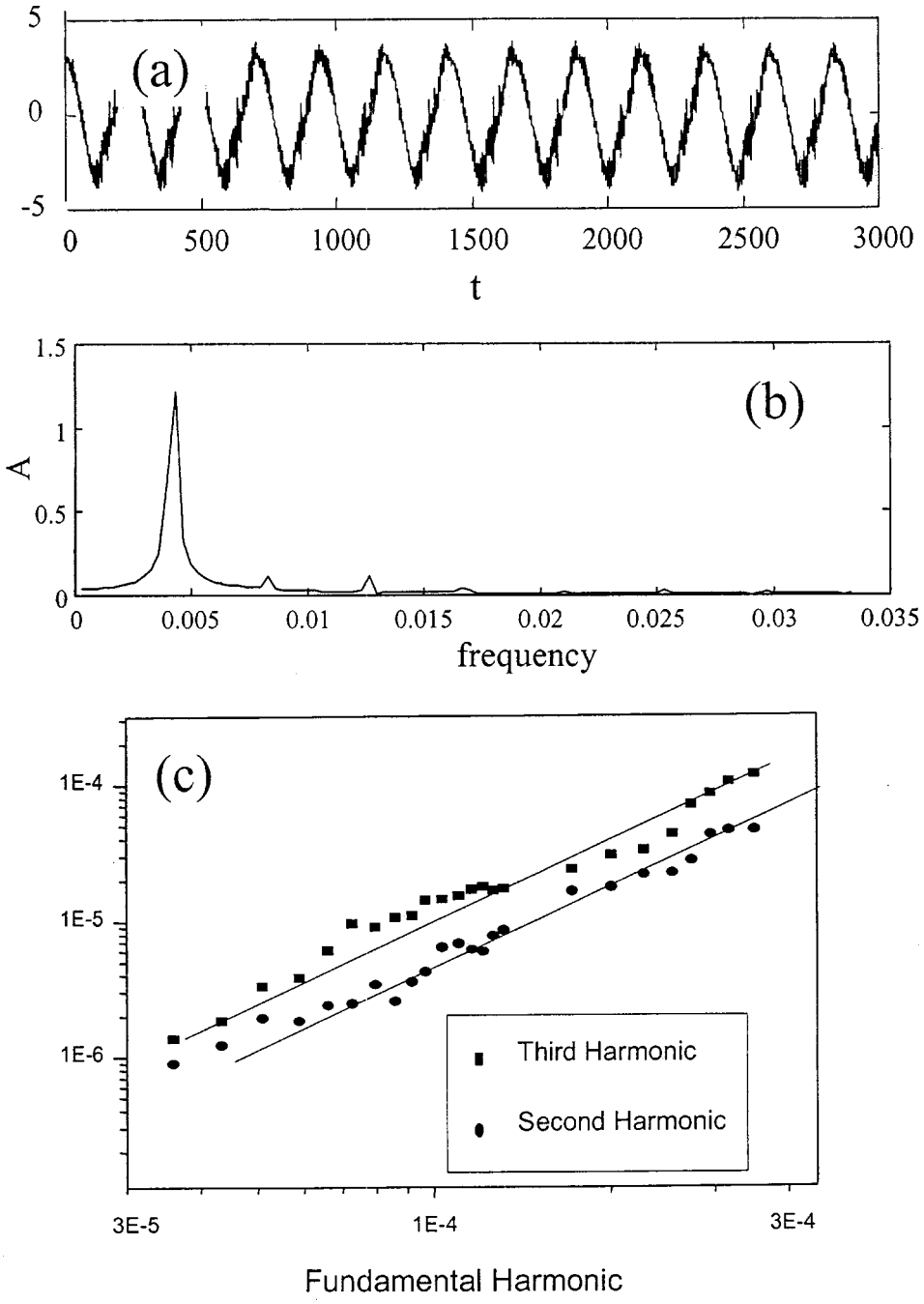

FIG. 8. Generation of higher order harmonics. (a) Temporal signal (acceleration versus time); (b) fast Fourier transform of the signal; (c) amplitudes of the second and third harmonics vs the fundamental one.

proposed by Smith *et al.*[22] The relative changes of frequency ω and attenuation ξ (defined as the half-width of the Lorentzian) vs the resonance amplitude are shown in Fig. 7(b). Both of them display a linear dependence on the amplitude of the output acceleration in resonance, although an initial saturation is observed for the resonance frequency shift, in agreement with experimental data.[23]

The temporal signal in resonance is shown in Fig. 8(a) for a given driving amplitude. The signal (perfectly sinusoidal in the linear case or at very low driving amplitudes) is distorted due to the nonlinearity. The triangular shape betrays the hysteretic behavior of the system. The fast Fourier transform (FFT) of the signal is illustrated in Fig. 8(b). As expected, higher order harmonics (both even and odd) are generated. Even harmonics arise in the present model, since all HEU and REU contribute to both hysteretic and non hysteretic nonlinearity. In fact, the bimodulus feature in $P=P_c$ (see Fig. 4), or more precisely the modulus jump, leads to the formation of higher order harmonics (at any order).

Finally, in Fig. 8(c) we analyze the dependence of the second and third order harmonics on the amplitude of the fundamental one in a log–log plot. Both curves have slope two, in agreement with experimental data. We recall that the expected slopes in the classical nonlinear case are two and three for the second and third harmonics, respectively. The ratio between the amplitudes of the second and third order harmonics depends strongly on the choice of the parameters, but is always less than one. The ratio may range from close to one to almost zero, in agreement with experimental observations on different materials.[24]

V. CONCLUSIONS

We have presented a numerical simulation approach to the study of nonclassical nonlinear effects induced by soft inclusions in a hard matrix. Typical examples of soft inclusions are the interstices among grains in a rock. In our approach they are represented by means of lattice units including portions of the adjoining grains. For each elastic unit we assume that all the nonlinearity is included in the interstice region. The nonclassical nonlinear behavior of the unit arises from transitions between a rigid and a soft state (or vice versa).

The above nonclassical micromodel has been implemented in the framework of a local interaction simulation approach (LISA). As a result it has been possible to reproduce, at least qualitatively, most of the nonclassical nonlinear effects, which have been discovered in recent years in quasistatic and in resonant dynamics experiments. Some of these results are included in the present paper.

A very important effect, the so-called ''slow dynamics,'' which gives rise to a logarithmic increase with time of the resonance frequency and amplitude in a resonant dynamics experiment when the driving force is released, has been ignored, since it requires the further inclusion of additional mechanisms.[9]

Another very important extension of the model concerns the possibility of applying it to the analysis of local or diffused damage.[25] By indentifying the appropriate changes in the density representation of HEU's and REU's, the model can be utilized as a powerful tool for nondestructive evaluation in a large variety of structural or earth materials.

The micromodel and protocol, which have been used to describe the local elasticity, represent, of course, only one of many possible alternatives.[26] The main purpose of the present work is to present a method, which is flexible enough to allow one to adopt any plausible model (even if it includes complex local interaction mechanisms) and to illustrate its implementation by means of a model, which seems to us to be particularly appealing. Another goal is to elicit more detailed experiments, in order to discriminate conclusively between the variety of plausible models and solicit suggestions based on basic mechanisms at the molecular dynamics level.

ACKNOWLEDGMENTS

The work was supported by the INFM Parallel Computing Initiative and by MURST (prot. NM02328989, Italy). The authors also acknowledge support by a University Collaborative Research Program of The Institute of Geophysics and Planetary Physics at the Los Alamos National Laboratory, NM, USA, by the US DOE Office of Basic Energy Science, and by the ESF–PESC program NATEMIS. The authors are grateful to E. Smith (Santa Fe' Institute, NM) and D. Iordache (Univ. of Bucharest, Romania) for fruitful discussions.

[1] R. A. Guyer and P. A. Johnson, ''Nonlinear mesoscopic elasticity: evidence for a new class of materials,'' Phys. Today **52**, 30–36 (1999).
[2] R. A. Guyer, J. A. Tencate, and P. A. Johnson, ''Hysteresis and the dynamic elasticity of consolidated granular materials,'' Phys. Rev. Lett. **82**, 3280–3283 (1999).
[3] J. A. TenCate, K. E.-A. Van Den Abeele, T. J. Shankland, and P. A. Johnson, ''Laboratory study of linear and non linear elastic pulse propagation in sandstone,'' J. Acoust. Soc. Am. **99**, 3334–3345 (1996).
[4] L. D. Landau and E. M. Lifshitz, *Theory of Elasticity* (Pergamon, Oxford, 1986).
[5] K. Van Den Abeele, ''Elastic pulsed wave propagation in media with second-or higher order non linearity,'' J. Acoust. Soc. Am. **99**, 3334–3345 (1996).
[6] R. A. Guyer, K. R. McCall, and G. N. Boitnott, ''Hysteresis, discrete memory and nonlinear wave propagation in rock: a new paradigm,'' Phys. Rev. Lett. **74**, 3491–3494 (1994).
[7] J. A. TenCate and T. J. Shankland, ''Slow dynamics in nonlinear elastic response of Berea sandstone,'' Geophys. Res. Lett. **23**, 3019–3022 (1996).
[8] J. A. TenCate, E. Smith, and R. A. Guyer, ''Universal slow dynamics in granular solids,'' Phys. Rev. Lett. **85**, 1020–1024 (2000).
[9] M. Scalerandi, P. P. Delsanto, and P. A. Johnson, ''Stress induced conditioning and thermal relaxation in the simulation of quasi-static compression experiments,'' J. Phys. D **36**, 288–293 (2003); M. Scalerandi and P. P. Delsanto, ''Modelling nonlinearity, conditioning and slow dynamics in mesoscopic elastic materials,'' Phys. Rev. B (submitted).
[10] J. D. Holcomb, ''Memory, relaxation and microfracturing in dilatant rocks,'' J. Geophys. Res. B **86**, 6235–6248 (1981); K. R. McCall and R. A. Guyer, ''A new theoretical paradigm to describe hysteresis, memory and nonlinear elastic wave propagation in rock,'' Nonlinear Processes Geophysics **3**, 89–101 (1996).
[11] K. Van Den Abeele, P. A. Johnson, R. A. Guyer, and K. R. McCall, ''On the quasi analytic treatment of hysteretic nonlinear response in elastic wave propagation,'' J. Acoust. Soc. Am. **101**, 1885–1898 (1997).
[12] F. Cleri, ''Atomic and electronic structure of high energy grain boundaries in silicon and carbon,'' Comput. Mater. Sci. **20**, 351–362 (2001).
[13] F. Cleri, S. Yip, D. Wolf, and S. R. Phillpot, ''Atomic-scale mechanism of crack-tip plasticity: Dislocation nucleation and crack-tip shielding,'' Phys. Rev. Lett. **79**, 1309–1312 (1999).
[14] P. P. Delsanto, R. Mignogna, M. Scalerandi, and R. Schechter, ''Simulation of ultrasonic pulse propagation in complex media,'' in *New Perspectives on Problems in Classical and Quantum Physics*, edited by P. P.

Delsanto and A. W. Saenz (Gordon & Breach, New Delhi, 1998), Vol. 2, pp. 51–74.
[15] P. P. Delsanto *et al.*, ''Connection machine simulation of ultrasonic waves propagation I: the 1-D case,'' Wave Motion **20**, 295 (1994).
[16] P. P. Delsanto and M. Scalerandi, ''A spring model approach for the simulation of wave propagation across imperfect interfaces,'' J. Acoust. Soc. Am. **104**, 2584–2591 (1998).
[17] M. Scalerandi, E. Ruffino, P. P. Delsanto, P. A. Johnson, and K. Van Den Abeele, ''Simulation of acoustic wave propagation in non classical, non linear mesoscopic media, in *Review of Progress in Quantitative Non Destructive Evaluation*, edited by D. O. Thompson and D. E. Chimenti, Conf. Proc. Vol. 19B (AIP, Melville, NY, 2000), 1393–1399.
[18] R. Courant, K. Friedrichs, and H. Lewy, ''Uber die partiellen differenzgleichungen der mathematischen physik (Partial differential equations in mathematical physics),'' Math. Ann. **100**, 32–38 (1928); D. Iordache *et al.*, ''Simulation of the wave propagation in 1-D Zener attenuative media,'' Nuovo Cimento B **114**, 1413–1426 (1999).
[19] E. Ruffino and M. Scalerandi, ''Analysis of the elastic behavior of nonclassical non linear mesoscopic materials in quasi-static experiments,'' Nuovo Cimento B **115**, 645–652 (2000).
[20] P. A. Johnson and P. N. J. Rasolofosaon, ''Manifestation of non linear elasticity in rock,'' Nonlinear Proc. Geophys. **3**, 89–95 (1996).
[21] G. Bertotti, ''Energetic and thermodynamic aspects of hysteresis,'' Phys. Rev. Lett. **76**, 1739–1742 (1996); G. Zarand *et al.*, ''Using hysteresis for optimization,'' *ibid.* **89**, 150201 (2002).
[22] D. E. Smith and J. A. TenCate, ''Sensitive determination of nonlinear properties of Berea sandstone at low strains,'' Geophys. Res. Lett. **27**, 1985–1988 (2000).
[23] P. A. Johnson *et al.*, ''Resonance and nonlinear elastic phenomena in rock,'' J. Geophys. Res., [Solid Earth] **101**, 11553–64 (1996). See in particular Fig. 5.
[24] B. Zinszner *et al.*, ''Influence of change in physical state on elastic nonlinear response in rock,'' J. Geophys. Res., [Solid Earth] **102**, 8105–8120 (1997) (see in particular Fig. 13); L. A. Ostrowsky and P. A. Johnson, ''Dynamic nonlinear elasticity in geomaterials,'' Riv. Nuovo Cimento **24**, 1–46 (2001) (see in particular Fig. 10); K. Van den Abeele *et al.*, ''Nonlinear elastic wave spectroscopy (NEWS) techniques to discern material damage, Part 1: nonlinear wave modulation spectroscopy,'' Res. Nondestruct. Eval. **12**, 17–30 (2000) (see in particular Figs. 4 and 7).
[25] K. Van Den Abeele, P. A. Johnson, J. Carmeliet, and A. Sutin, ''Microdamage diagnostics using non linear elastic wave spectroscopy,'' NDT & E Int. **34**, 239–248 (2001).
[26] P. P. Delsanto, V. Agostini, M. Scalerandi, and P. A. Johnson, ''Phenomenology and modeling of damaged mesoscopic materials,'' Proceedings of EuroMech Conference, Prague, 2000; B. Capogrosso Sansone and R. A. Guyer, Phys. Rev. B (in press).

Nonlinear coupling of surface and quasitransverse bulk modes in cubic crystals[a)]

R. E. Kumon[b)]
National Institute of Standards and Technology, 325 Broadway, Mail Stop 853, Boulder, Colorado 80305-3328

M. F. Hamilton
Department of Mechanical Engineering, The University of Texas at Austin, Austin, Texas 78712-1063

(Received 4 November 2002; revised 18 January 2003; accepted 10 February 2003)

In crystals the speed of the surface acoustic wave mode may approach that of the lowest-speed quasitransverse bulk mode in some directions of propagation. Under these circumstances, it is possible for energy to be transferred from the surface mode to the bulk mode by nonlinear coupling. In the present paper we investigate the possibilities for mode coupling in the (001), (110), and (111) planes of cubic crystals. A condition is given for determining the range of propagation directions with significant coupling, and numerical results are provided for eight different crystals with a range of anisotropy ratios. It is shown that even for significant excitation amplitudes the coupling is negligible for most propagation directions in the aforementioned surface cuts. © *2003 Acoustical Society of America.* [DOI: 10.1121/1.1566974]

PACS numbers: 43.25.Fe, 43.35.Pt, 68.35.Iv [DEC]

I. INTRODUCTION

Anisotropic media have the property that acoustic wave speeds vary as a function of the direction of propagation. In particular, there exist directions where the lowest speed of a quasitransverse bulk wave approaches the speed of the surface acoustic wave (SAW).[1] In these instances, it is possible for nonlinear coupling (and therefore energy exchange) between the surface acoustic wave and quasitransverse bulk wave to occur. Several theoretical models for the nonlinear propagation of SAWs in anisotropic media[2–4] do not account for this coupling, an observation also made previously in the context of nonlinear Scholte waves.[5] To properly use these theories it is important to quantitatively determine their regions of applicability, a topic that does not appear to have been explored.

In this article we describe the condition under which significant coupling may be expected in crystals. Calculations based on the model of Ref. 4 are presented for eight different cubic crystals with a range of anisotropy ratios for propagation in the (001), (110), and (111) surface cuts. The properties of nonlinear SAWs in the materials and surface cuts presented here have been discussed in detail in previous work,[6–8] and measurements of finite-amplitude SAWs in selected directions in the (001) and (111) planes of crystalline silicon have corroborated the waveform evolution predicted by the model.[9,10] The present calculations show that for practical excitation amplitudes, negligible coupling is expected for most propagation directions.

II. MODE COUPLING CONDITION

Coupling between the surface mode and quasitransverse bulk mode is insignificant when the characteristic nonlinear length scale $\bar{x}$ (e.g., the shock formation distance) is large in relation to the coherence length[11] for the modal interaction. For a SAW of wave number k and speed c, this criterion corresponds to

$$\frac{1}{k\bar{x}} \ll \frac{\Delta c}{c_b}, \tag{1}$$

where $\Delta c = |c - c_b|$ and c_b is the speed of the bulk wave. The characteristic nonlinear length scale is

$$\bar{x} = \frac{1}{|\beta| \epsilon k}, \tag{2}$$

where β is the coefficient of nonlinearity[6] and ϵ is the characteristic acoustic strain. Substituting Eq. (2) into Eq. (1) yields

$$\epsilon \ll \frac{\Delta c}{c_b} \frac{1}{|\beta|}. \tag{3}$$

Equation (3) can be used in two ways to develop limits for negligible mode coupling. First, the range of propagation directions with negligible mode coupling can be determined with a given upper bound on the acoustic strain. In SAW experiments with some of the largest amplitudes,[9,10] the maximum applied acoustic strain is $\epsilon = 0.01$. With this condition, the criterion for negligible mode coupling is given by

$$0.1 < (\Delta c / c_b)/|\beta|, \tag{4}$$

providing for a difference of an order of magnitude between both sides of Eq. (3). The actual range may be larger depending on the value of ϵ for a given data set. Equation (4) is used in Sec. III to evaluate the range of propagation directions

[a)]Contribution of NIST, an agency of the U.S. government; not subject to U.S. copyright.

[b)]Current address: Department of Physics, University of Windsor, 401 Sunset Ave., Windsor, Ontario N9B 3P4, Canada. Electronic mail: ronkumon@kumonweb.com

 0001-4966/2003/113(6)/3060/5/$19.00

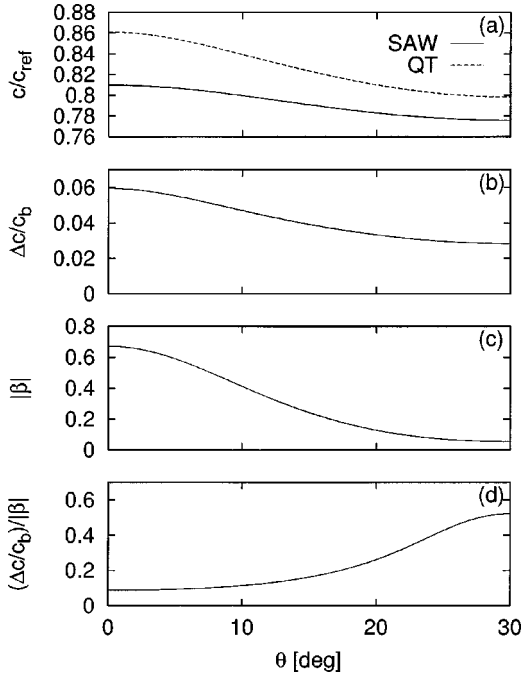

FIG. 1. (a) Scaled SAW and quasitransverse (QT) bulk wave speeds, (b) relative wave speed, (c) nonlinearity coefficient, and (d) ratio of relative wave speed to nonlinearity coefficient as a function of propagation direction for Si in (111) surface cut.

for negligible coupling for a variety of materials and surface cuts. Second, the maximum acoustic strain that ensures negligible mode coupling for all propagation directions is

$$\epsilon_{\max} = \min\left(\frac{\Delta c}{c_b}\frac{0.1}{|\beta|}\right). \tag{5}$$

Values of $\epsilon_{\max}$ for each cut and each material are given in Tables I, II, and III.

III. RESULTS

A. Specific case: Si in (111) plane

To illustrate the analysis in detail, calculations are performed for Si in the (111) plane, and the results are summarized in Fig. 1. Figure 1(a) shows the scaled wave speeds c/c_{ref} of the surface and lowest quasitransverse bulk modes as a function of the angle θ between the propagation direction and $\langle 11\bar{2}\rangle$, where $c_{\text{ref}}=(c_{44}/\rho)^{1/2}$. Only the angular range $0°\leqslant\theta\leqslant 30°$ is considered because the wave speeds are symmetric about $\theta=30°$ and periodic every 60° in this plane. The speeds approach each other as $\theta\to 30°$ but do not converge. Figure 1(b) shows $\Delta c/c_b$ as a function of propagation direction. In accordance with Fig. 1(a), the maximum change in relative wave speed occurs at $\theta=0°$ around 5.9% and decreases to around 2.8% as $\theta\to 30°$. Figure 1(c) shows the magnitude of the nonlinearity coefficient as a function of propagation direction. The magnitude of the nonlinearity coefficient is maximum at $\theta=0°$ and decreases monotonically as $\theta\to 30°$. (As discussed in Ref. 7, the absolute value of the nonlinearity matrix elements and therefore $|\beta|$ are symmetric about $\theta=30°$ and periodic every 60° in this plane.) Finally,

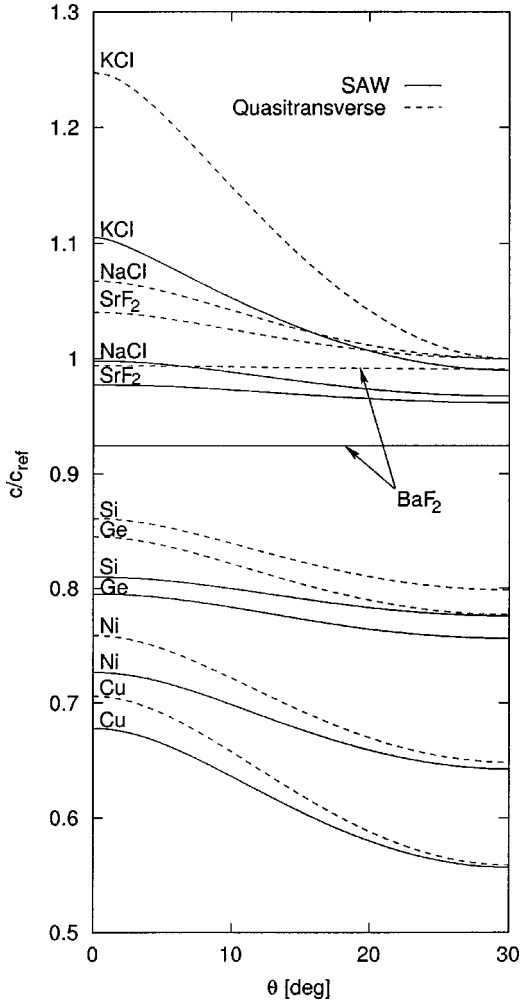

FIG. 2. Scaled SAW (solid) and lowest quasitransverse bulk wave (dashed) mode speeds as a function of propagation direction in the (111) plane.

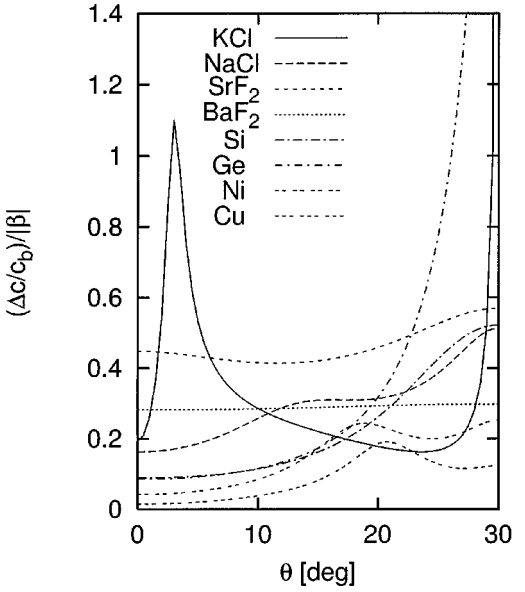

FIG. 3. $(\Delta c/c_b)/|\beta|$ as a function of propagation direction in the (111) plane.

Fig. 1(d) shows $(\Delta c/c_b)/|\beta|$ as a function of propagation direction. While both $\Delta c/c_b$ and $|\beta|$ decrease as $\theta \to 30°$, their ratio actually increases as $\theta \to 30°$. Hence, the limitation on the range of negligible mode coupling is due more to the larger nonlinearity coefficient as $\theta \to 0°$ than to the closeness of the SAW and quasitransverse bulk mode speeds in this region. For this particular case $\epsilon_{max} = 0.0088$ by Eq. (5). However, Fig. 1(d) can be used to evaluate the range of propagation directions with negligible coupling for any given value of ϵ by looking to see where the curve exceeds a horizontal line at that value of the maximum applied acoustic strain.

B. General study

For many materials, the angular dependence of the SAW speed can be conveniently grouped according to the material's anisotropy ratio[1] $\eta = 2c_{44}/(c_{11} - c_{12})$. The ratio is defined such that $\eta = 1$ for isotropic materials. KCl, NaCl, SrF_2, BaF_2, Si, Ge, Ni, and Cu are selected for study here to illustrate the behavior seen for the range of anisotropy ratios $0.373 \leqslant \eta \leqslant 3.20$. The anisotropy ratio for each individual material is listed in the tables.

1. (111) plane

Figure 2 shows the scaled surface and lowest quasitransverse mode wave speeds c/c_{ref} as a function of the propagation direction for the (111) plane. As in Fig. 1, θ is defined as the angle between the propagation direction and $\langle 112 \rangle$. The closest convergence occurs for the materials with $\eta > 1$. Figure 3 shows $(\Delta c/c_b)/|\beta|$ as a function of propagation direction. Table I lists the anisotropy ratios, ϵ_{max}, and the range of directions for negligible mode coupling for values of applied acoustic strain $\epsilon = 0.005$ and $\epsilon = 0.01$. While the ranges decrease as the anisotropy ratio increases, negligible coupling is expected for most directions in most of the materials. As demonstrated in Sec. III A, the directions without negligible mode coupling tend to occur more where the nonlinearity coefficient is strong rather than where the SAW and quasitransverse bulk modes are nearly equal in speed.

2. (001) plane

Next, consider propagation in the (001) plane. Figure 4 shows the scaled surface and lowest quasitransverse mode wave speeds c/c_{ref} as a function of propagation distance. In this section θ is defined as the angle between the propagation direction and $\langle 100 \rangle$. Only the angular range $0° < \theta < 45°$ is

TABLE I. Parameters for mode coupling in the (111) plane.

Material	η	ϵ_{max}	Negligible mode coupling with $\epsilon = 0.005$	$\epsilon = 0.01$
KCl	0.373	0.016	All directions	All directions
NaCl	0.705	0.016	All directions	All directions
SrF_2	0.803	0.041	All directions	All directions
BaF_2	1.02	0.028	All directions	All directions
Si	1.57	0.0088	All directions	$7° < \theta < 30°$
Ge	1.66	0.0085	All directions	$7° < \theta < 30°$
Ni	2.60	0.0042	$5° < \theta < 30°$	$12° < \theta < 30°$
Cu	3.20	0.0014	$12° < \theta < 30°$	$17° < \theta < 30°$

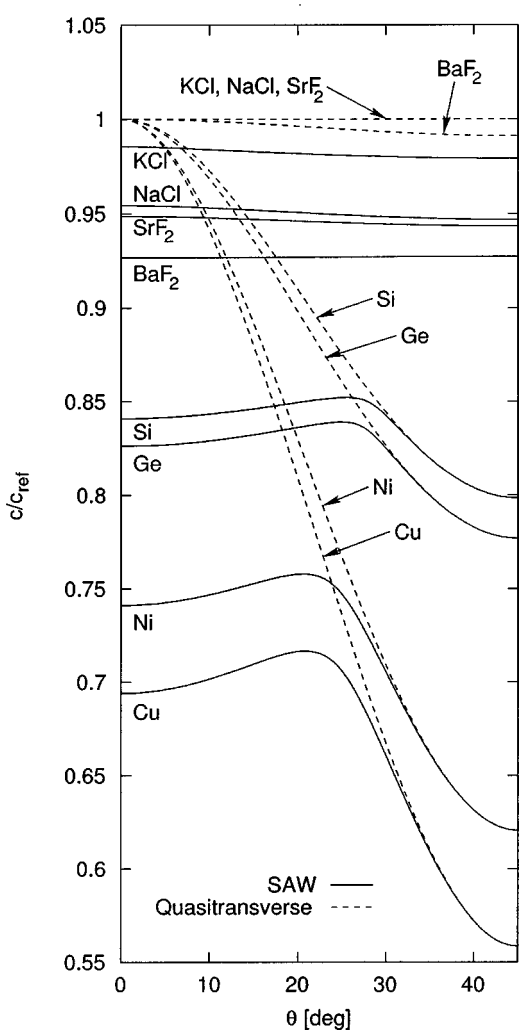

FIG. 4. Scaled SAW and lowest quasitransverse bulk mode speeds as a function of propagation direction in the (001) plane. Note that KCl, NaCl, SrF_2 all have $c/c_{ref} = 1$.

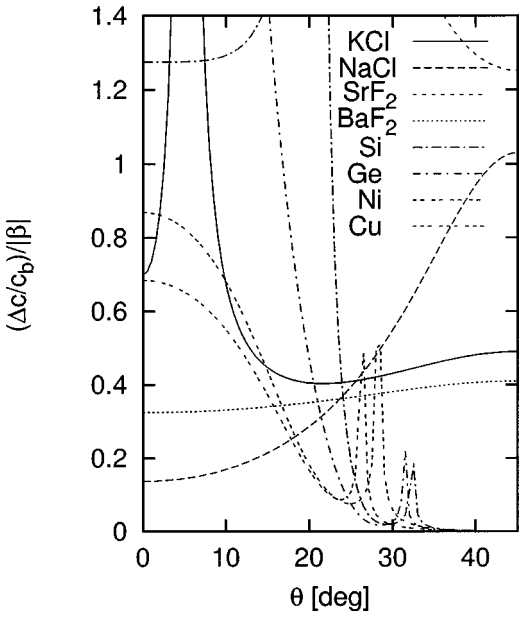

FIG. 5. $(\Delta c/c_b)/|\beta|$ as a function of propagation direction in the (001) plane.

considered because the wave speeds are symmetric about $\theta=45°$ and are periodic every $\theta=90°$. For the materials shown with $\eta>1$, the SAW and lowest quasitransverse bulk modes converge as $\theta\rightarrow 45°$. The pseudosurface wave[1] mode at $\theta=45°$ is not considered in this study.

Figure 5 shows $(\Delta c/c_b)/|\beta|$ as a function of propagation direction. Unlike the (111) plane, β is always real-valued in this plane and can be zero.[6] The zeros are the source of the discontinuities in the slope of $|\beta|$ and therefore also in the curves for Si near $\theta=32°$, Ge near $\theta=31°$, Ni near $\theta=26°$ and Cu near $\theta=28°$ in Fig. 5. [In cases where $|\beta|=0$, Eq. (2) does not apply, although an alternative characteristic nonlinear length scale $\bar{x}$ can be constructed[8] so that Eq. (3) is still valid.] Like Table I, Table II lists the acoustic strains and angular ranges with negligible mode coupling. Negligible coupling occurs for all directions for the materials with $\eta<1$. For the materials with $\eta>1$, $|\beta|\rightarrow 0$, but $(\Delta c/c_b)\rightarrow 0$ faster so that the net result is $(\Delta c/c_b)/|\beta|\rightarrow 0$. As a result, negligible mode coupling occurs only in selected ranges, but still over half the possible angular range. Like the (111) plane, the ranges in the (001) plane decrease as the anisotropy ratio η increases.

3. (110) plane

Finally, consider propagation in the (110) plane. Figure 6 shows the scaled surface and lowest quasitransverse mode wave speeds c/c_{ref}. In this plane, θ is defined as the angle between the propagation direction and $\langle 001\rangle$. Only the angular range $0°<\theta<90°$ is considered because the wave speeds are symmetric about $\theta=90°$ and are periodic every $\theta=180°$. Note that the discontinuities of the slopes of the lowest quasitransverse mode curves in Fig. 6 occur because the quasitransverse mode of lowest speed changes in these directions from one type to another (e.g., see Figs. 11 and 15 in Farnell[1] for plots of both quasitransverse modes for Ni and KCl). The SAW and lowest quasitransverse bulk mode for KCl and NaCl converge only as $\theta\rightarrow 90°$. While a pseudosurface wave mode is possible at $\theta=90°$ for some materials, it is not considered here.

Figure 7 shows $(\Delta c/c_b)/|\beta|$ as a function of propagation direction. As in the (001) plane, β is real-valued and can be zero for certain directions in the materials considered. The zeros or near zeros are the source of the discontinuities in the slope of $(\Delta c/c_b)/|\beta|$ for KCl near $\theta=10°$ and $\theta=70°$, SrF_2 near $\theta=11°$ and $\theta=79°$, Si near $\theta=60°$, and Ge near $\theta=65°$. Table III is the analog of Tables I and II for the (110)

TABLE II. Parameters for mode coupling in the (001) plane.

Material	η	$\epsilon_{\max}$	Negligible mode coupling with $\epsilon=0.005$	$\epsilon=0.01$
KCl	0.373	0.040	All directions	All directions
NaCl	0.705	0.014	All directions	All directions
SrF_2	0.803	0.12	All directions	All directions
BaF_2	1.02	0.032	All directions	All directions
Si	1.57	None	$0°<\theta<27°$	$0°<\theta<26°$
Ge	1.66	None	$0°<\theta<26°$	$0°<\theta<24°$
Ni	2.60	None	$0°<\theta<28°$	$0°<\theta<22°$
Cu	3.20	None	$0°<\theta<30°$	$0°<\theta<22°$

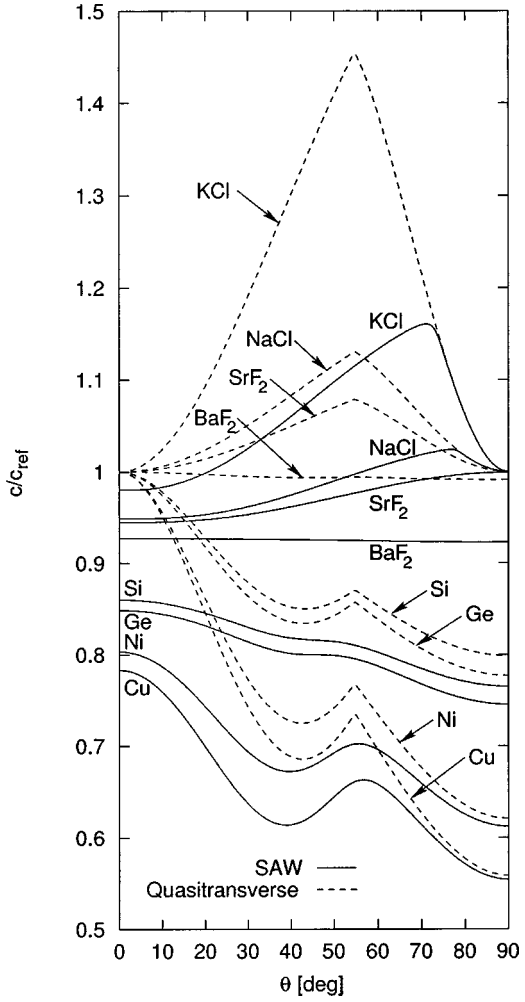

FIG. 6. Scaled SAW and lowest quasitransverse bulk mode speeds as a function of propagation direction in the (110) plane.

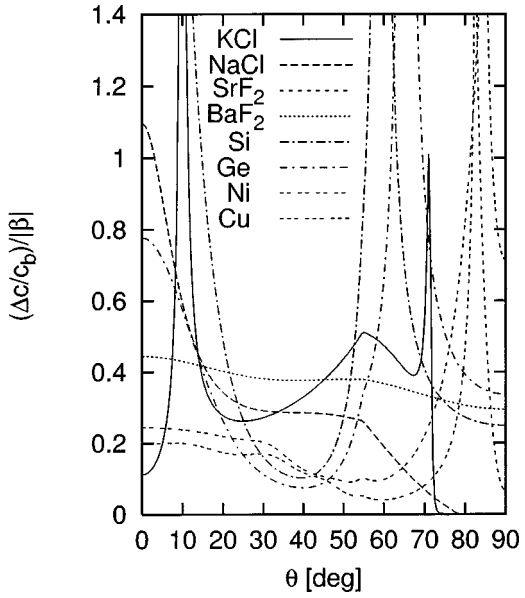

FIG. 7. $(\Delta c/c_b)/|\beta|$ as a function of propagation direction in the (110) plane.

TABLE III. Parameters for mode coupling in the (110) plane.

Material	η	ϵ_{max}	Negligible mode coupling with ϵ=0.005	ϵ=0.01
KCl	0.373	None	$0°<\theta<72°$	$0°<\theta<72°$
NaCl	0.705	None	$0°<\theta<72°$	$0°<\theta<67°$
SrF_2	0.803	0.0064	All directions	$0°<\theta<88°$
BaF_2	1.02	0.029	All directions	All directions
Si	1.57	0.010	All directions	All directions
Ge	1.66	0.0076	All directions	$\theta<32°;\theta>47°$
Ni	2.60	0.0090	All directions	$\theta<48°;\theta>61°$
Cu	3.20	0.0040	$\theta<55°;\theta>65°$	$\theta<45°;\theta>72°$

plane. For KCl and NaCl, $\Delta c/c_b \to 0$ and $|\beta| \to 0$ as $\theta \to 90°$, but the wave speeds converge faster, so that the net result is that the ratio goes to zero. As a result, negligible mode coupling is expected only for propagation directions away from $\theta=90°$, as shown in Table III. For materials with $\eta>1$, negligible coupling is expected for most directions, except for relatively small regions where there is both a strong nonlinearity coefficient and relatively close SAW and quasitransverse wave speeds. As in the previous two planes, the ranges tend to decrease as the anisotropy ratio η increases.

IV. CONCLUSION

The condition for the nonlinear mode coupling between the SAW and lowest quasitransverse bulk mode is defined and examined. Numerical results are presented for the cubic crystals KCl, NaCl, SrF_2, BaF_2, Si, Ge, Ni, and Cu in the (001), (110), and (111) planes. As an example, a detailed study is provided for Si in the (111) plane. Criteria are developed for (1) determining the range of directions of negligible mode coupling for a given acoustic strain and (2) calculating the maximum acoustic strain for which negligible mode coupling occurs in all directions in a given plane.

In the (111) plane, the magnitude of the nonlinearity coefficient tends to determine the range of directions with negligible mode coupling more strongly than the closeness of the SAW and quasitransverse speeds. In the (001) plane, the nonlinearity coefficient also tends to dominate, except for materials such as Si, Ge, Ni, and Cu, where the SAW and quasitransverse modes converge in speed near $\langle 110 \rangle$ ($\theta=45°$). In the (110) plane, regions without negligible mode coupling tend to occur where there is both a relatively strong nonlinearity coefficient and relatively close SAW and quasitransverse wave speeds. Exceptions are KCl and NaCl, where the convergence between the modes in speed near $\langle 110 \rangle$ ($\theta=90°$) dominates. The angular ranges of negligible mode coupling for all three planes tend to decrease in size as the anisotropy ratio increases. For typical excitation amplitudes, the results indicate that negligible mode coupling is expected for most propagation directions in the (001), (110), and (111) planes for the materials considered.

ACKNOWLEDGMENTS

This work was performed while R. E. K. held a National Research Council Research Associateship Award at the National Institute of Standards and Technology. We also gratefully acknowledge discussions with Yu. A. Ilinskii and E. A. Zabolotskaya at The University of Texas at Austin.

[1] G. W. Farnell, "Properties of elastic surface waves," in *Physical Acoustics*, edited by W. P. Mason and R. N. Thurston (Academic, New York, 1970), Vol. 6, pp. 109–166.
[2] D. F. Parker, "Waveform evolution for nonlinear surface acoustic waves," Int. J. Eng. Sci. **26**, 59–75 (1988).
[3] D. F. Parker and E. A. David, "Nonlinear piezoelectric surface waves," Int. J. Eng. Sci. **27**, 565–581 (1989).
[4] M. F. Hamilton, Yu. A. Il'inskii, and E. A. Zabolotskaya, "Nonlinear surface acoustic waves in crystals," J. Acoust. Soc. Am. **105**, 639–651 (1999).
[5] G. D. Meegan, M. F. Hamilton, Yu. A. Il'inskii, and E. A. Zabolotskaya, "Nonlinear Stoneley and Scholte waves," J. Acoust. Soc. Am. **106**, 1712–1723 (1999).
[6] R. E. Kumon and M. F. Hamilton, "Directional dependence of nonlinear surface acoustic waves in the (001) plane of cubic crystals," J. Acoust. Soc. Am. **111**, 2060–2069 (2002).
[7] R. E. Kumon and M. F. Hamilton, "Effects of harmonic phase on nonlinear surface acoustic waves in the (111) plane of cubic crystals," J. Acoust. Soc. Am. **113**, 1293–1303 (2003).
[8] R. E. Kumon, "Nonlinear surface acoustic waves in cubic crystals," Ph.D. dissertation, The University of Texas at Austin, 1999.
[9] R. E. Kumon, M. F. Hamilton, Yu. A. Il'inskii, E. A. Zabolotskaya, P. Hess, A. Lomonosov, and V. G. Mikhalevich, "Pulsed nonlinear surface acoustic waves in crystals," in *Proceedings of the 16th International Congress on Acoustics and 135th Meeting of the Acoustical Society of America*, edited by P. K. Kuhl and L. A. Crum (Acoustical Society of America, Woodbury, NY, 1998), Vol. 3, pp. 1557–1558.
[10] R. E. Kumon, M. F. Hamilton, P. Hess, A. Lomonosov, and V. G. Mikhalevich, "Dependence of surface acoustic wave nonlinearity on propagation direction in crystalline silicon," in *Nonlinear Acoustics at the Turn of the Millennium: Proceedings of the 15th International Symposium on Nonlinear Acoustics*, Vol. 524 of AIP Conference Proceedings, edited by W. Lauterborn and T. Kurz (American Institute of Physics, Melville, NY, 2000), pp. 265–268.
[11] O. V. Rudenko and S. I. Soluyan, *Theoretical Foundations of Nonlinear Acoustics* (Plenum, New York, 1977), pp. 86–87.

Nonlinear interaction of plane ultrasonic waves with an interface between rough surfaces in contact

Claudio Pecorari[a)]
Marcus Wallenberg Laboratory, Department of Aeronautics and Vehicle Engineering, Royal Institute of Technology, 100 44 Stockholm, Sweden

(Received 27 November 2002; revised 28 February 2003; accepted 8 March 2003)

A theoretical investigation of the nonlinear interaction between an acoustic plane wave and an interface formed by two rough, nonconforming surfaces in partial contact is presented. The macroscopic elastic properties of such a nonlinear interface are derived from micromechanical models accounting for the elastic interaction that is characteristic of spherical bodies in contact. These results are used to formulate set of boundary conditions for the acoustic field, which are to be enforced at the imperfect interface. The scattering problem is solved for plane wave incidence by using a simple perturbation approach and the harmonic balance method. Sample results are presented for arbitrary wave polarization and angle of incidence. The relative magnitude of the nonlinear signals and their potential use toward the nondestructive evaluation of imperfect interfaces are assessed. In particular, attention is drawn to the enhanced nonlinear response of an interface insonified by a shear vertical wave in the neighborhood of the longitudinal critical angle. The motivation for this investigation is provided by the need to develop nondestructive methods to detect and localize small, partially closed cracks in metals with coarse microstructures. © *2003 Acoustical Society of America.* [DOI: 10.1121/1.1570437]

PACS numbers: 43.25.Jh, 43.25.Dc, 43.35.Zc [MFH]

I. INTRODUCTION

Stress corrosion cracks affect components operating in chemically harsh environments and to which stress fields of thermal origin or due to external loads are applied. In general, these defects originate at the surface of the material and extend toward its interior through a rather complex path. In fact, they are often branched and have surfaces that are rough both at the scale of the typical grain's dimension and in the submicron region. Furthermore, due to the random nature of the corrosion process, the surfaces of such cracks do not conform to each other at the scale that characterizes the range of action of the chemical forces.

Stress corrosion cracks constitute a serious threat to the structural integrity of nuclear power plants. Unfortunately, conventional methods used during routine inspections may not succeed in this task since partial closure of these cracks may occur following the temporary shut-down of the plant and the consequent removal of tensile stress fields that are responsible for the crack growth. Furthermore, the microstructure of the hosting material, by linearly scattering part of the energy of the inspecting beam, may raise the signal threshold above which the detection of these defects is possible. Thus, the development of novel methods to detect stress corrosion cracks at the earliest possible time is of paramount importance.

In the recent past, considerable evidence has been gathered in laboratory experiments to show that cracks and imperfect interfaces can behave in a nonlinear fashion.[1–9] In particular, by showing that such material discontinuities may act as sources of acoustic waves with spectral features that are distinct from those of the inspecting beam, this experimental effort has opened new possibilities to detect partially closed cracks that otherwise may not be sensed by linear, conventional methods.

On the theoretical front, work on nonlinear scattering from cracks and interfaces has not been carried out to a similar extent.[5,10–17] Boundary conditions that allow an interface or crack to be either completely open or completely closed were considered by a few authors.[10,11,16,17] Such a model hardly seems to provide a convincing description of the defect–wave interaction involving an interface that is only partially closed. In other investigations, the mathematical treatment of the scattering problem, as well as the geometrical description of the crack, appear quite simplistic.[5]

The complexity of real defects and their interaction with acoustic waves remains beyond the reach of current theoretical methods. Nonetheless, well-established results in the area of contact mechanics can be exploited toward improving our understanding of the scattering process by such defects. In particular, they can be used to establish realistic boundary conditions to be enforced at the crack or interface surface. A few attempts to tackle this problem have already been carried out to the extent that the interface behavior under a normal load has been considered.[12,13] For instance, working within the framework of the Greenwood and Williamson approach,[18] Nazarov and Sutin[13] evaluated the effect of a microcrack distribution on the nonlinear elastic properties of a medium. They employed the Hertz's model to describe the interaction between asperities, and assumed the height of the asperities to be distributed exponentially, a distribution that is very convenient from the mathematical point of view, but physically unrealistic. They also treated the

a)Electronic mail: claudio@fkt.kth.se

crack opening displacements as that of an interface of finite extent disregarding the edge effects.

Rudenko and Chin[12] modeled the individual contacts by means of linear springs, the length of which is distributed according to an unknown function to be determined by fitting the model to experimental data. Their analysis of the scattering process neglected mode conversion, casting reasonable doubt on the accuracy of the model. Finally, theoretical models of the nonlinear properties of rough surfaces in contact subjected to an oscillating shear load still remain to be developed.

The purpose of this investigation is threefold. First, realistic models of the nonlinear macroscopic properties of two rough surfaces in contact, and subjected to both a normal load and a shear oscillating force, are derived within the framework of Greenwood and Williamson's approach.[18] In this work, the height of the asperities is assumed to be distributed according to an inverted X^2 distribution function.[19–21] The interaction of the asperities under a compressive load is considered to be Hertzian,[22] while Mindlin and Deresiewicz's analysis is employed to recover the interface properties when the interface is subjected to an oscillating shears load.[23] The second goal is the formulation of suitable boundary conditions that extend those of the quasistatic spring model,[21,24] to the nonlinear case. Finally, the boundary value problem posed by the new boundary conditions is solved by means of a simple perturbation approach, and the numerical results are used to evaluate the relative contribution to the nonlinear scattered field of each nonlinear mechanism considered in this work. The potential relevance of the nonlinear phenomena examined in this work to the nondestructive detection of partially closed cracks is also discussed.

II. INTERFACE MECHANICAL PROPERTIES

A. Normal interfacial stiffness

By using Greenwood and Williamson's model,[18] and Hertz analysis of the contact between two elastic spheres, the relationship between the normal pressure, P, and the relative approach, δ, between the mean planes of the contacting surfaces if found to be[18,20,21]

$$P=\frac{2}{3}n\left\langle\frac{E}{1-\upsilon^2}\right\rangle\langle R^{1/2}\rangle\int_0^{\delta}(\delta-z)^{3/2}\varphi(z;N)dz, \tag{1}$$

In this approach, the load-bearing asperities are assumed to be independent of each other, limiting the validity of the model to those situations in which only a small fraction of the total number of asperities are in contact. From Eq. (1), Baltazar *et al.*[21] derived the following expression for the normal interface stiffness, K_N:

$$K_N=\frac{\partial P}{\partial\delta}=n\left\langle\frac{E}{1-\upsilon^2}\right\rangle\langle R^{1/2}\rangle\int_0^{\delta}(\delta-z)^{1/2}\varphi(z;N)dz. \tag{2}$$

In Eqs. (1) and (2), n is the number of contacts per unit area, E and ν are the Young modulus and the Poisson ratio of the material, respectively, R is the radius of curvature of the asperities, and φ is the height distribution of the asperities of the composite surface. The latter is defined by a linear combination of the profiles of the two surfaces, which maps the actual contacts of the interface onto the asperities of the composite surface.[20] Following Adler and Firman,[19] and Brown and Scholz,[20] this function is properly modeled by an inverted X^2 distribution that depends on an integer parameter, $N\geqslant 2$, known as the ''number of degrees of freedom'' (see also Baltazar *et al.*[21]). For $N=2$, $\varphi(z)$ is an exponential function with an absolute maximum at $z=0$, while it approaches a Gaussian distribution as N increases. Such a choice for $\varphi(z)$ provides the required flexibility to model the topographical properties of the two surfaces. The integration variable z is defined by the transformation $z=Z_0-z'$, where Z_0 is the coordinate of the highest asperities of the composite surface, and z' is the actual coordinate of the asperity measured from the surface mean plane. The nonlinear nature of the dependence of K_N can be accounted for by considering the expansion of K_N in powers of $\Delta\delta$ in which the first-order term is retained,

$$K_N(\delta+\Delta\delta)=K_N(\delta)=\frac{\partial K_N}{\partial\delta}\Delta\delta=K_{N.0}+K_{N.1}\Delta\delta. \tag{3}$$

In Eq. (3), the constant $K_{N.0}(\delta)$ can be evaluated by means of Eq. (2), while $K_{N.1}$ is given by

$$K_{N.1}=\frac{\partial K_{N.0}}{\partial\delta}=\frac{n}{2}\left\langle\frac{E}{1-\upsilon^2}\right\rangle\langle R^{1/2}\rangle\int_0^{\delta}(\delta-z)^{-1/2}\varphi(z;N)dz, \tag{4}$$

The variation of the relative approach $\Delta\delta$ is positive when the distance between the mean planes of the two surfaces decreases. Using Eq. (4), it can be shown that $K_{N.1}$, although more slowly than $K_{N.0}$, tends to zero for vanishing values of δ, i.e., when the contacts are removed.

B. Tangential interfacial stiffness

Mindlin and Deresiewicz[23] derived the relationship between an oscillating tangential force, $F_{\tan}$, and the relative tangential displacement, Δu, of two spheres that are maintained in contact by a normal load, N. Their result, recast in a form suitable for the present work, is

$$\begin{aligned}F_{\tan}=&\frac{4}{3}\frac{E}{1-\upsilon^2}R^{1/2}\delta^{3/2}f\,\mathrm{sgn}\left(\frac{\partial\Delta u}{\partial t}\right)\\&\times\left\{1-\left[1-\frac{1-\upsilon}{2-\upsilon}\frac{1}{\delta f}\left(\Delta u_{\max}+\mathrm{sgn}\left(\frac{\partial\Delta u}{\partial t}\right)\Delta u\right)\right]^{3/2}\right.\\&\left.-\frac{1}{2}\left[1-\left(1-\frac{2(1-\upsilon)}{2-\upsilon}\frac{\Delta u_{\max}}{\delta f}\right)^{3/2}\right]\right\},\end{aligned} \tag{5}$$

where, as before, δ is the relative approach caused by the normal load applied to the two surfaces, f is the material static coefficient of friction, and $\Delta u_{\max}$ is the maximum, positive tangential displacement reached during a cycle. The function sgn(.) is equal to 1 when its argument is positive, and to -1 when it is negative. Equation (5) describes a hysteretic loop, the origin of which rests in the relative partial slipping of the contacting spheres. Such a relative displacement occurs within an annulus that extends from the edge of the contact area toward its center as the strength of the tangential force, $F_{\tan}$, increases. The two spheres undergo com-

plete sliding when $F_{\tan}=fN$. For small tangential displacements, Eq. (5) can be approximated by

$$F_{\tan}\cong \frac{2E}{(1+v)(2-v)}R^{1/2}\delta^{1/2}\Delta u - \frac{2E(1-v)}{(1+v)(2-v)^2}\frac{1}{f}\left(\frac{R}{\delta s}\right)^{1/2} \times\left[(\Delta u^2-\Delta u_{\max}^2)\operatorname{sgn}\left(\frac{\partial \Delta u}{\partial t}\right)+\Delta u\Delta u_{\max}\right]. \quad (6)$$

Note that the tangential force $F_{\tan}$ is not null for $\Delta u=0$. Indeed, it is proportional to $\Delta u_{\max}^2$. Furthermore, to account for the effect of a possible modulation of the normal load, Eq. (6) can be further generalized by including a term that is proportional to the product of $\Delta\delta\Delta u$,

$$F_{\tan}\cong \frac{2E}{(1+v)(2-v)}R^{1/2}\delta^{1/2}\Delta u + \frac{E}{(1+v)(2-v)}\left(\frac{R}{\delta}\right)^{1/2}\Delta\delta\Delta u - \frac{2E(1-v)}{(1+v)(2-v)^2}\frac{1}{f}\left(\frac{R}{8}\right)^{1/2} \times\left[(\Delta u^2-\Delta u_{\max}^2)\operatorname{sgn}\left(\frac{\partial \Delta u}{\partial t}\right)+\Delta u\Delta u_{\max}\right]. \quad (7)$$

Within the framework of the Greenwood and Williamson approach, Eq. (7) can be extended to the whole interface,

$$\Sigma = K_{T,0}\Delta u + K_{T,N}\Delta u\Delta\delta - \frac{1}{2}K_{T,1}\left[(\Delta u^2-\Delta u_{\max}^2)\operatorname{sgn}\left(\frac{\partial \Delta u}{\partial t}\right)+\Delta u\Delta u_{\max}\right], \quad (8)$$

where Σ is the shear stress acting on the interface, and $K_{T,0}$, $K_{T,N}$, and $K_{T,1}$ are defined by

$$K_{T,0}=2n\left\langle\frac{E}{(1+v)(2-v)}\right\rangle\langle R^{1/2}\rangle\int_0^{\delta}(\delta-z)^{1/2}\varphi(z)dz, \quad (9)$$

$$K_{T,N}=n\left\langle\frac{E}{(1+v)(2-v)}\right\rangle\langle R^{1/2}\rangle\int_0^{\delta}(\delta-z)^{-1/2}\varphi(z)dz, \quad (10)$$

$$K_{T,1}=2n\left\langle\frac{E(1-v)}{(1+v)(2-v)^2}\right\rangle\frac{\langle R^{1/2}\rangle}{\langle f\rangle}\int_0^{\delta}(\delta-z)^{-1/2}\varphi(z)dz, \quad (11)$$

respectively. A comparison between Eqs. (4), (10), and (11) shows that $K_{T,N}$ and $K_{T,1}$ are proportional to $K_{N,1}$, although $K_{T,1}$ controls a nonlinear mechanism that is physically independent of those to which $K_{N,1}$ and $K_{T,N}$ are connected. In addition, the expression found for $K_{T,0}$ is found to be identical to that given by Baltazar *et al.*,[21] and, as discussed in that work, requires a correction factor ξ of the order of 0.5. A correction to Eqs. (9)–(11) is necessary to account for the effect of the angle of misalignment between the centers of the spherical contacts with respect to the line of action of the normal load. Furthermore, since sliding occurs at the contacts where the local compressive stress is small, the lowest asperities in contact are expected to support only a fraction of the tangential load.[25] Henceforth, such a factor will be included in the definition of the above-mentioned coefficients.

III. EFFECTIVE NONLINEAR BOUNDARY CONDITIONS

In this section, the boundary conditions to be enforced at a nonlinear interface between two rough surfaces in contact are formulated. They are

$$\sigma_{31}^{+}=K_{T,0}\Delta u-K_{T,N}\Delta v\Delta u - \frac{1}{2}K_{T,1}\left[(\Delta u^2-\Delta u_{\max}^2)\operatorname{sgn}\left(\frac{\partial \Delta u}{\partial t}\right)+\Delta u\Delta u_{\max}\right], \quad (12a)$$

$$\sigma_{33}^{+}=K_{N,0}\Delta v-K_{N,1}\Delta v^2, \quad (12b)$$

$$\sigma_{31}^{+}=\sigma_{31}^{-}, \quad (12c)$$

$$\sigma_{33}^{+}=\sigma_{33}^{-}. \quad (12d)$$

In Eq. (12), the superscripts "+" and "−" refer to the positive and negative sides of the interface, and the subscripts 1 and 3 identify the direction parallel and normal to the interface, respectively. Similarly, u and v are the displacement components parallel and normal to the interface, respectively. The latter is assumed to lie in the plane of equation $x_3=0$. Equation (12a) is derived from Eq. (8) by identifying the variation of the relative approach, $\Delta\delta$, with $-\Delta v$, i.e., the out-of-plane displacement discontinuity at the interface. This equation accounts for the hysteretic behavior of the interface when it is subjected to a shear stress. Equation (12b) describes the behavior of an interface that softens as it opens. The stress fields are continuous at the interface. In Eqs. (12a)–(12d), all the field quantities must be understood to be functions of the position along the x axis, and of time t.

IV. REFLECTION AND TRANSMISSION OF PLANE WAVE

In the following, the boundary value problem posed by Eqs. (12a)–(12d) is solved for an incident plane having an arbitrary angle of incidence and polarization. To this end, a simple perturbation approach is used which exploits the harmonic balance method.

A. Longitudinal wave at normal incidence

Let $v_{\text{in}}(x_3,t)=A_{\text{in}}\hat{x}_3\exp[j(\omega t-k_L x_3)]$ be the incident longitudinal wave of angular frequency ω and wave number $k_L=\omega/C_L$, where C_L is the phase velocity of the wave. Let $v^{-}(x_3,t)$ and $v^{+}(x_3,t)$ be the total displacement fields in the negative ($x_3<0$) and positive ($x_3>0$) half-space, respectively. By introducing these field variables in Eq. (12), and by using appropriate normalization constants, the boundary conditions for this problem become

$$\frac{\partial V^{+}}{\partial X_3}=\frac{\overline{K}_{N,0}}{\kappa^2}(\Delta V-\epsilon_N\Delta V^2), \quad (13a)$$

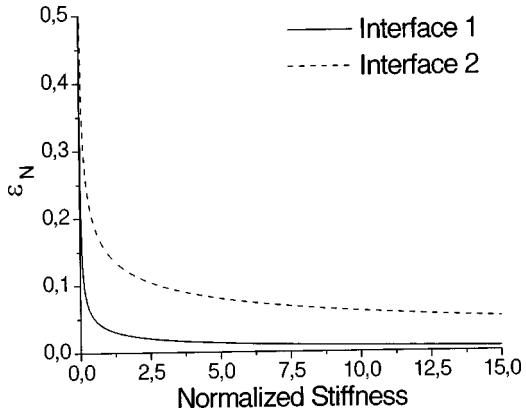

FIG. 1. Dependence of the parameter ϵ_N on the normalized interfacial stiffness for the two interfaces characterized by the parameters of Table I.

$$\frac{\partial V^+}{\partial X_3} = \frac{\partial V^-}{\partial X_3}. \tag{13b}$$

In Eq. (13), $v^{+,-} = A_{\text{in}} V^{+,-}$, $\Delta V = V^+ - V^-$, $\kappa = C_L / C_T$, where C_T is the shear phase velocity, $x_3 = X_3 / k_T$, where $k_T = \omega / C_T$ is the shear wave number, $K_{N,0} = K_{N,0} / Z_T \omega$, where Z_T is the shear acoustic impedance of the medium, and, finally, $\epsilon_N = A_{\text{in}} K_{N,1} / K_{N,0}$. Furthermore, a new normalized time variable, τ, is introduced, which is defined by $\tau = \omega t$. Note that the coefficient ϵ_N does not represent an intrinsic property of the interface. Rather, it measures the variation of the interfacial stiffness caused by a variation of the relative approach, δ, equal to the amplitude of the incident wave, A_{in}. Figure 1 shows plots of ϵ_N versus the normalized interfacial stiffness $\overline{K}_{N,0}$ for two steel interfaces characterized by the parameters in Table I, where the parameter

$$M = \frac{2}{3} n \left\langle \frac{E}{1-v^2} \right\rangle \langle R^{1/2} \rangle.$$

Of the parameters in Table I, those that are related to the interface geometry are obtained from Baltazar *et al.*,[21] while those relating to the material properties have been adapted from the same reference to the case of interest here. The parameters reported by Baltazar *et al.*[21] were obtained by either direct measurements or best fitting experimental results. Therefore, they can be considered as realistic. The quantity ϵ_N is evaluated assuming the amplitude and frequency of the incident wave to be $A_{\text{in}} = 3$ nm, and 1 MHz, respectively. Thus, the strain produced by this wave is of the order of 3.0×10^{-6}. Except for a very small region near the origin within which the interface is essentially open, the parameter ϵ_N is always much smaller than unity. Furthermore, the coefficient ϵ_N increases as the roughness of the surfaces in contact decreases.

TABLE I. Statistical parameters for the interfaces (adapted from Baltazar *et al.*—Ref. 21).

	Roughness (μm)	M[GPa/(μm$^{3/2}$)]	Derees of freedom
Interface 1	0.68	5.4	3
Interface 2	0.23	76.8	5

The solution of this problem is searched in terms of a series expansion of the displacement components in the small parameter ϵ_N:

$$V^{+,-}(\tau) = \sum_{m=0}^{\infty} \epsilon_N^m V_m^{+,-}(\tau). \tag{14}$$

Introducing Eq. (14) into the boundary conditions of Eq. (13), and collecting terms according to their expansion order, m, the following systems of boundary conditions are obtained for the zeroth and first-order solutions, respectively:

$$\frac{\partial V_0^+}{\partial X_3} - \frac{\overline{K}_{N,0}}{\kappa^2} \Delta V_0 = 0, \tag{15a}$$

$$\frac{\partial V_0^+}{\partial X_3} = \frac{\partial V_0^-}{\partial X_3}, \tag{15b}$$

and

$$\frac{\partial V_1^+}{\partial X_3} - \frac{\overline{K}_{N,0}}{\kappa^2} \Delta V_1 = -\frac{\overline{K}_{N,0}}{\kappa^2} \Delta V_0^2, \tag{16a}$$

$$\frac{\partial V_1^+}{\partial X_3} = \frac{\partial V_1^-}{\partial X_3}. \tag{16b}$$

The solutions of the zeroth order system are waves with the same angular frequency as the incident wave, and complex amplitudes that are proportional to the complex reflection and transmission coefficients for an imperfect interface[24]

$$R = -\frac{1}{1 - j 2 \overline{K}_{N,0} / \kappa}, \quad T = -\frac{j 2 \overline{K}_{N,0} / \kappa}{1 - j 2 \overline{K}_{N,0} / \kappa}. \tag{17}$$

The solution of Eq. (16) are determined by the square of the displacement discontinuity between the zeroth-order solutions. The latter can be written as a linear combination of a term that is time-independent and describes an increase of the interface opening, and a second one that is proportional to $\exp(j2\tau)$, i.e., it contains the second harmonic of the incident wave. The complex amplitude of the reflected and transmitted second harmonic can be shown to be equal, and are given by

$$A(2\omega) = \epsilon_N V_1^{+,-} = -\frac{\epsilon_N}{4} \frac{j \dfrac{\overline{K}_{N,0}}{\kappa}}{1 - j \dfrac{\overline{K}_{N,0}}{\kappa}} (T - 1 + R)^2. \tag{18}$$

According to Eq. (18), $A(2\omega)$ is a linear function of A_{in} through ϵ_N. Therefore, the amplitude of the physical solution is proportional to the square of the amplitude of the incident wave, A_{in}^2. Figure 2 illustrates the dependence of the second harmonic amplitude, $A(2\omega)$, on the normalized interfacial stiffness. As expected, after reaching a maximum value in the neighborhood of $\overline{K}_{N,0} = 1$, the nonlinear response of the interface is drastically reduced as the interface becomes stiffer. For the interface with smaller roughness, $A(2\omega)$ reaches values that are only 30 dB below that of the incident wave. Finally, since $\overline{K}_{N,0}$ can be viewed as a function of either R or T, Eq. (18) shows that $A(2\omega)$ is the only

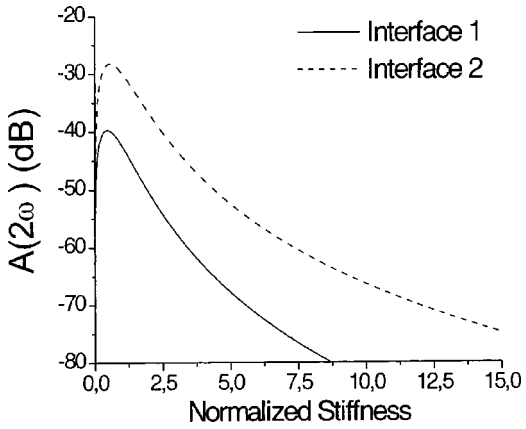

FIG. 2. Amplitude of the second harmonic components, $A(2\omega)$, vs the normalized interfacial stiffness for the two interfaces characterized by the parameters of Table I.

additional quantity that must be determined experimentally in order to estimate the parameter ϵ_N.

The next higher-order components in Eq. (14) can be shown to contain terms that depend on ω and 3ω, and, thus, do not affect the amplitude of the second harmonic. Therefore, the results of Fig. 2 are valid up to the third order in ϵ_N.

B. Shear wave at normal incidence

A shear wave at normal incidence is considered next. The incident wave is given by $u_{\text{in}}(x_3,t)=-A_{\text{in}}\hat{x}_1 \exp[j(\omega t - k_T x_3)]$. As in the previous case, sample results are obtained for $A_{\text{in}}=3$ nm, and $\omega=2\pi$ MHz×rad. The boundary conditions enforced at the interface are

$$\frac{\partial U^+}{\partial X_3}=\overline{K}_T\left[\Delta U-\frac{\epsilon_T}{2}\left[\operatorname{sgn}\left(\frac{\partial \Delta U}{\partial \tau}\right)(\Delta U^2-\Delta U_{\max}^2)+\Delta U\Delta U_{\max}\right]\right], \tag{19a}$$

$$\frac{\partial U^+}{\partial X_3}=\frac{\partial U^-}{\partial X_3}. \tag{19b}$$

To obtain Eqs. (19a) and (19b) from Eqs. (12a) and (12d), the normalization constants used in the previous case have been employed. Here again, the perturbation parameter $\epsilon_T=A_{\text{in}}K_{T,1}/K_{T,0}$ can be shown to be much smaller than unity, and, more precisely, smaller than ϵ_N by a factor of the order of $(1/f)(1-v)/(2-v)$, which, for steel, is roughly equal to 0.7. Given such a link between ϵ_N and ϵ_T, the independence of ϵ_T on the interface condition is shown to closely resemble that in Fig. 1, apart from a proper scaling factor of the vertical coordinates. The nonlinear term proportional to the product $\Delta u\,\Delta v$ is not present in this problem.

The solution is sought be using again the same perturbation expansion as in Eqs. (14), which leads to the following boundary conditions for the zeroth and first order solutions:

$$\frac{\partial U_0^+}{\partial X_3}-\overline{K}_{T,0}\Delta U_0=0, \tag{20a}$$

$$\frac{\partial U_0^+}{\partial X_3}=\frac{\partial U_0^-}{\partial X_3}, \tag{20b}$$

for the zeroth order, and

$$\frac{\partial U_1^+}{\partial X_3}-\overline{K}_{T,0}\Delta U_1=\frac{\overline{K}_{T,0}}{2}\left[\operatorname{sgn}\left(\frac{\partial \Delta U_0}{\partial \tau}\right)(\Delta U_0^2-\Delta U_{0,\max}^2)+\Delta U_0\Delta U_{0,\max}\right], \tag{21a}$$

$$\frac{\partial U_1^+}{\partial X_3}=\frac{\partial U_1^-}{\partial X_3}, \tag{21b}$$

for this first order. In order to obtain Eq. (21a) from Eq. (19a), the function $\operatorname{sgn}(\partial\Delta U/\partial\tau)$ has been approximated by $\operatorname{sgn}(\partial\Delta U_0/\partial\tau)$ on the ground that the first-order solutions are much smaller than those of the zeroth order.

The solutions of the zeroth order system are obtained from those of the previous case [see Eq. (17)] by replacing $\overline{K}_{N,0}/\kappa$ with $\overline{K}_{T,0}$. With these terms, the right-hand side of Eq. (21b) can be evaluated, and its time dependence examined in terms of its harmonic content. Expanded in a Fourier series, this source function is shown to be odd with respect to time. Therefore, no even harmonic of the incident wave is generated upon reflection and transmission of a shear wave at normal incidence. A similar result was found by O'Neil *et al.*[14] for an interface formed by two surfaces coupled by friction. The amplitudes of the odd harmonic waves generated by the nonlinear response of the interface are found by introducing the Fourier representation of the source function on the right-hand side of Eq. (21b) and by solving the partial linear problems into which the original one can be decomposed. The amplitudes are

$$A(n\omega)=-j\epsilon_T\frac{2\overline{K}_{T,0}}{n-j2\overline{K}_{T,0}}C_n, \quad n=1,3,5,\ldots, \tag{22}$$

where C_n is the nth complex coefficient of the Fourier series of the source function. Figure 3 presents plots of the first and higher harmonics generated by the interfaces of Table I. The third harmonic generated by the interface having a rms roughness of 0.68 μm is more than 60 dB below the amplitude of the incident wave, while that generated by the interface with the smaller roughness reaches -50 dB. The reduced nonlinear response of this kind of interface to a shear excitation, compared to the response to longitudinal wave, can be partly explained by the higher order nonlinearity at which the effect appears, and partly by the magnitude of the coefficient ϵ_T compared to ϵ_N. These results indicate that the magnitude of the nonlinear response of interfaces formed by rough surfaces in contact to a longitudinal wave exceeds that to a shear wave by about 20 dB.

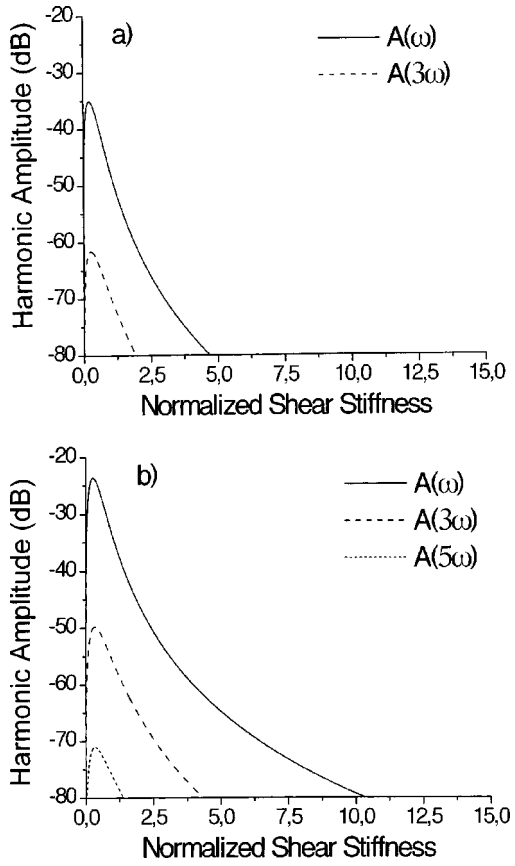

FIG. 3. Amplitude of the first three odd harmonic components, $A(n\omega)$, $n=1,3,5$ vs the normalized interfacial shear stiffness for the two interfaces characterized by the parameters of Table I; (a) interface 1, (b) interface 2.

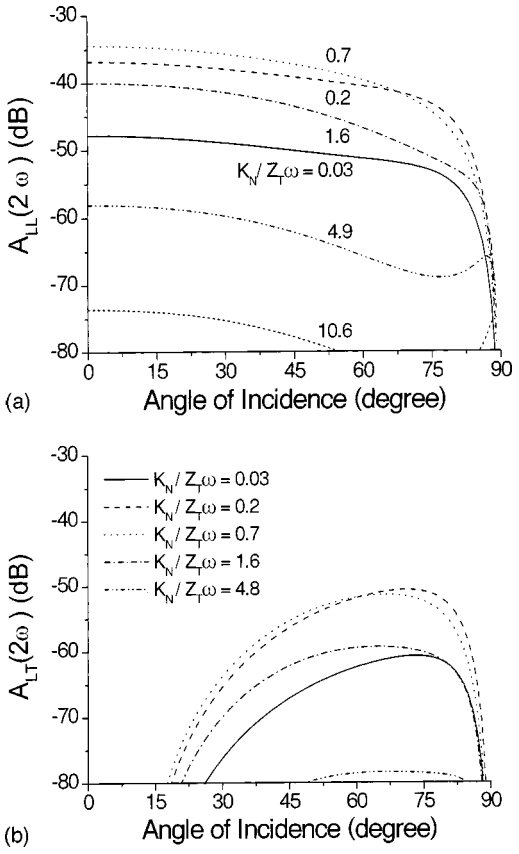

FIG. 4. Longitudinal (a) and shear (b) second harmonic amplitude vs angle of incidence generated upon scattering of a longitudinal incident wave for various values of the normalized normal stiffness.

C. Oblique incidence

In this section, the cases of both longitudinal and shear oblique incidence are considered. For both problems, the boundary conditions for the normalized displacement field are

$$\frac{\partial V^+}{\partial X_3}+\frac{\partial U^+}{\partial X_1}=\overline{K}_T\left[\Delta V-\epsilon_N\Delta U\Delta V-\frac{\epsilon_T}{2}\left[\mathrm{sgn}\left(\frac{\partial\Delta V}{\partial\tau}\right)\times(\Delta V^2-\Delta V_{\max}^2)+\Delta V\Delta V_{\max}\right]\right], \quad (23a)$$

$$\kappa^2\frac{\partial V^+}{\partial X_3}+(\kappa^2-2)\frac{\partial U^+}{\partial X_1}=\overline{K}_{N,0}(\Delta V-\epsilon_N\Delta V^2), \quad (23b)$$

$$\frac{\partial V^+}{\partial X_3}+\frac{\partial U^+}{\partial X_1}=\frac{\partial V^-}{\partial X_3}+\frac{\partial U^-}{\partial X_1}, \quad (23c)$$

$$\kappa^2\frac{\partial V^+}{\partial X_3}+(\kappa^2-2)\frac{\partial U^+}{\partial X_1}=\kappa^2\frac{\partial V^-}{\partial X_3}+(\kappa^2-2)\frac{\partial U^-}{\partial X_1}. \quad (23d)$$

A comparison between Eqs. (12) and (23a) shows that, upon normalization, the coefficient K_{NT} leads to ϵ_N, reducing the number of parameters required to describe the nonlinearities of the interface to two. The solution of the problem is sought by expanding the displacement field components on both sides of the interface in a double series in the small parameters ϵ_N and ϵ_T.

$$U^{+,-}=U_0^{+,-}+\epsilon_N U_{1,N}^{+,-}+\epsilon_T U_{1,T}^{+,-}+O(\epsilon_N,\epsilon_T), \quad (24a)$$

$$V^{+,-}=V_0^{+,-}+\epsilon_N V_{1,N}^{+,-}+\epsilon_T V_{1,T}^{+,-}+O(\epsilon_N,\epsilon_T). \quad (24b)$$

Following the perturbation procedure previously employed, the reflected and transmitted waves can be easily found, though they cannot be given by simple analytical expression.

Figure 4 illustrates the first-order, nonlinear response of the interface with rms roughness equal to 0.23 μm (see Table I) as a function of the angle of incidence. The incident wave is longitudinally polarized. Figure 4(a) refers to the longitudinal second harmonic, while Fig. 4(b) to the shear second harmonic. Similar to the results at normal incidence, the amplitude is shown to initially increase, and rapidly fall as the normalized normal stiffness, $\overline{K}_N$, becomes greater than 1. Of interest is the relatively small variation of the amplitude of the second harmonic longitudinal wave with the angle of incidence, in view of which the angular dependence of the nonlinear response of a partially closed crack may be expected to resemble that of the linear response. As for the second harmonic shear wave [Fig. 4(b)], its amplitude remains below that of the longitudinal component for all the values of the angle of incidence. The same observation can be made for the amplitude of the third harmonics generated by the hysteretic behavior of the interface, which, therefore, seems not to play a relevant role.

Figure 5 presents sample results for a shear incident wave. They illustrate the remarkable feature of the amplitude of the longitudinal second harmonic in the neighborhood of

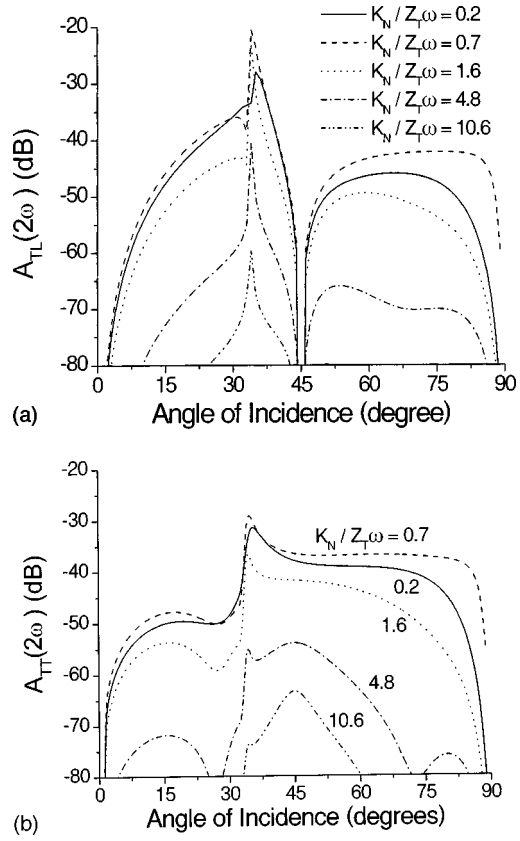

FIG. 5. Longitudinal (a) and shear (b) second harmonic amplitude versus angle of incidence generated upon scattering of a shear incident wave for various values of the normalized normal stiffness.

the longitudinal critical angle, which approaches the −20 dB level below the amplitude on the incident wave [Fig. 5(a)]. Such a result can be explained by the localization of the energy carried by the longitudinal waves in proximity of the interface occurring for values of the angle of incidence near the longitudinal critical angle. Although above the longitudinal critical angle the nonlinear scattered waves may not be used for detection purposes since they do not propagate away from the interface, this result suggests an efficient way to inject energy into the interface in order to enhance its nonlinear response to a second inspecting wave. The shear second harmonic [Fig. 5(b)], on the other hand, maintains its propagating character over the whole range of angles of incidence. A similar phenomenon was previously predicted for a perfect interface between two nonlinear material by Shui *et al.*[26]

V. SUMMARY AND CONCLUDING REMARKS

The micromechanical models presented in this work have been used to establish new effective boundary conditions at the interface between two elastic rough surfaces in contact. The solution of this boundary value problem has shown that the main nonlinear response on the interface is in the form of longitudinal waves having a frequency twice that of the fundamental. In the most favorable conditions, the longitudinal response can reach levels near −20 dB below the amplitude of the incident wave. Such a response is caused by the nonlinearity of the relationship between a normal load and the relative approach of the two rough surfaces, and, in particular, by the distribution of the heights of the asperities. The second nonlinear mechanism considered in this investigation, i.e., the hysteretic behavior of contacts subjected to an oscillating tangential force, was shown to produce third and higher odd harmonics with amplitudes that are considerably lower than that of the incident wave, and, thus, of negligible importance. An examination of the angle dependence of the second harmonic generated by a longitudinal incident wave shows the nonlinear response to be rather insensitive to the angle of incidence. Conversely, upon shear wave incidence, the longitudinal second harmonic displays a distinct peak near the longitudinal critical angle, which approaches −20 dB below the amplitude of the incident wave.

The investigation presented here would suggest that, in searching for a nonlinear signature of defects with faces in partial contact and interacting through elastic forces, the experimental setup should be optimized toward detection of the longitudinal second harmonic. Also, although the scattering directivity of cracks of finite extent is not expected to resemble closely that of an infinite interface, the occurrence of features similar to the maximum in the longitudinal second harmonic generated upon shear incidence near the longitudinal critical angle should be explored and possibly utilized in designing new experimental setups for the nonlinear detection of cracks. Finally, it is hoped that the results of this work may be of help in identifying the mechanisms behind several experimental observations of nonlinear material response to an investigating ultrasonic wave, either directly or by exclusion.

ACKNOWLEDGMENTS

This work was performed as part of the project "Nonlinear scattering from partially closed cracks and imperfect interfaces," No. 14.43-010902,01156, supported by the Swedish Inspectorate for Nuclear Power (SKI).

[1] S. U. Fassbender and W. Arnold, *Measurement of Adhesion Strength of Bonds using Nonlinear Acoustics*, Rev. Prog. Quant. Nondestr. Eval., Vol. 15, edited by D. O. Thompson and D. E. Chimenti (Plenum, New York, 1996), pp. 1321–1328.
[2] I. Y. Solodov, "Ultrasonics of non-linear contacts: Propagation, reflection and NDE-applications," Ultrasonics **36**, 383–390 (1998).
[3] P. B. Nagy, "Fatigue damage assessment by nonlinear ultrasonic material characterization," Ultrasonics **36**, 373–381 (1998).
[4] V. V. Kazakov and A. M. Sutin, "Pulsed sounding of cracks with the use of the modulation of ultrasound by vibrations," Acoust. Phys. **47**, 308–312 (2001).
[5] D. Donskoy, A. Sutin, and A. Ekimov, "Nonlinear acoustic interaction on contact interfaces and its use for nondestructive testing," NDT & E Int. **34**, 231–238 (2001).
[6] I. Y. Solodov, N. Krohn, and G. Busse, "CAN: An example of nonclassical acoustic nonlinearity in solids," Ultrasonics **40**, 621–625 (2002).
[7] V. Y. Zaistev, V. Gusev, and B. Castagnede, "Observation of the 'Luxenburg-Gorky' effect for elastic waves," Ultrasonics **40**, 627–631 (2002).
[8] I. Y. Solodov and B. A. Korshak, "Instability, chaos, and 'memory' in acoustic wave-crack interaction," Phys. Rev. Lett. **88**, 014303-1–014303-3 (2002).
[9] V. Y. Zaistev, V. Gusev, and B. Castanede, "Luxenburg-Gorky effect retooled for elastic waves: A mechanism and experimental evidence," Phys. Rev. Lett. **89**, 105502-1–105502-4 (2002).
[10] M. Comninou and J. Dundrus, "Reflection and refraction of elastic waves in presence of separation," Proc. R. Soc. London **356**, 509–528 (1977).

[11] J. M. Richardson, ''Harmonic generation at an unbounded interface—I. Planar interface between semi-infinite elastic media,'' Int. J. Eng. Sci. **17**, 73–85 (1979).
[12] O. V. Rudenko and A. V. Chin, ''Nonlinear acoustic properties of a rough surface contact and acousto-diagnostics of a roughness height distributions,'' Acoust. Phys. **40**, 593–596 (1994).
[13] V. E. Nazarov and A. M. Sutin, ''Nonlinear elastic constants of solids with cracks,'' J. Acoust. Soc. Am. **102**, 3349–3354 (1997).
[14] B. O'Neil, R. G. Maev, and F. Severin, *Distorsion of Shear Waves Passing through a Friction Coupled Interface*, Rev. Prog. Quant. Nondestr. Eval. Vol. 20, edited by D. O. Thompson and D. E. Chimenti (AIP, New York, 2001), pp. 1261–1267.
[15] S. Hirsekorn, ''Nonlinear transfer of ultrasound by adhesive joints—a theoretical description,'' Ultrasonics **39**, 57–68 (2001).
[16] V. P. Smyshlyaev and J. R. Willis, ''Effective relations for nonlinear dynamics of cracked solids,'' J. Mech. Phys. Solids **44**, 49–75 (1996).
[17] J. D. Achenback and A. N. Norris, ''Loss of specular reflection due to nonlinear crack-face interaction,'' J. Nondestruct. Eval. **3**, 229–239 (1982).
[18] J. A. Greenwood and J. B. P. Williamson, ''Contact of nominally flat surfaces,'' Proc. R. Soc. London, Ser. A **295**, 300–319 (1966).
[19] R. J. Adler and D. Firman, ''A non-Gaussian model for random surfaces,'' Philos. Trans. R. Soc. London, Ser. A **303**, 433–462 (1981).
[20] S. R. Brown and C. H. Scholz, ''Closure of random elastic surfaces in contact,'' J. Geophys. Res., **90**, 5531–5545 (1985).
[21] A. Baltazar, S. I. Rokhlin, and C. Pecorari, ''On the relationship between ultrasonic and micro-mechanic properties of contacting rough surfaces,'' J. Mech. Phys. Solids **50**, 1397–1416 (2002).
[22] K. L. Johnson, *Contact Mechanics* (Cambridge University Press, New York, 1985).
[23] R. D. Mindlin and H. Deresiewicz, ''Elastic spheres in contact under varying oblique forces,'' J. Appl. Mech. **20**, 327–344 (1953).
[24] J. M. Baik and R. B. Thompson, ''Ultrasonic scattering from imperfect interfaces: A quasi-static model,'' J. Nondestruct. Eval. **4**, 177–196 (1984).
[25] S. Björklund, ''A random model for micro-slip between nominally flat surfaces,'' J. Tribol. **119**, 726–732 (1997).
[26] Y. Shui, Y. Mao, W. Jiang, W. Wu, and I. Y. Solodov, ''The second harmonic generation of bulk acoustic waves reflection,'' *Proceedings of the IEEE Ultrasonics Symposium*, edited by B. R. McAvoy (IEEE, New York, 1987), pp. 429–432.

Optimization of acoustic scattering from dual-frequency driven microbubbles at the difference frequency

Matthew Wyczalkowski and Andrew J. Szeri
Department of Mechanical Engineering, University of California at Berkeley, Berkeley, California 94720-1740

(Received 11 May 2000; accepted for publication 14 February 2003)

The second harmonic radiation of acoustically driven bubbles is a useful discriminant for their presence in clinical ultrasound applications. It is useful because the scatter from a bubble at a frequency different from the driving can have a contrast-to-tissue ratio better than at the drive frequency. In this work a technique is developed to optimize the scattering from a microbubble at a frequency different from the driving. This is accomplished by adjusting the relative phase and amplitudes of the components of a dual-frequency incident ultrasound wave form. The investigation is focused primarily on the example of dual-mode driving at frequencies of 1 MHz and 3 MHz, with the scattering optimized at 2 MHz. Bubble radii of primary interest are 0.5 to 2 μm and driving amplitudes to 0.5 atm. Bubbles in this size range are sensitive to modulation of driving. It is shown that an optimal forcing scheme can increase the target response eightfold or more. This suggests new applications in imaging and in bubble detection.
[DOI: 10.1121/1.1570442]

PACS numbers: 43.25.Ts, 43.80.Vj [SGK]

I. INTRODUCTION

Acoustic scattering of ultrasound is used to infer the structure of liquid-filled vessels or cavities and the flow of body fluids such as blood. Because the acoustic response of desired features is difficult to distinguish, ultrasound contrast agents are employed to enhance scattering from blood, in order to facilitate studies of blood flow especially in the microcirculation. By far the most successful contrast agents are microbubbles, though other substances find application as well.[1–6] Microbubbles have the advantage as contrast agents because their compressibility relative to the surrounding tissue is large. This increases the scattering cross section,[6] which is defined to be the scattered ultrasound power divided by the incident ultrasound intensity. There is a further significant enhancement of scattering by bubbles as a consequence of resonant oscillations.

Despite the increased scattering due to the microbubble contrast agent, image quality is not satisfactory in some critical applications such as imaging the microcirculation deep within tissue. There are appreciable echoes from surrounding tissue in addition to the microbubbles at the incident ultrasound frequency. Bubbles, however, display a highly nonlinear response and scatter not only at the main harmonic of a sinusoidal driving frequency, but also at low multiples and simple fractions of the main harmonic. By receiving at the second harmonic of the incident field, the echo from the bubbles is more easily distinguished from that of the surrounding tissue.[7,8] This effect also occurs with commercially available encapsulated microbubble contrast agents.[9–12]

There are limits on the intensity of the incident ultrasound that may be employed. It has been shown that at higher ultrasound intensities, ultrasound contrast agents can facilitate inertial cavitation, both *in vitro*[13,14] and *in vivo*.[15] The high temperatures associated with the characteristic rapid collapses can cause formation of free-radicals and damage similar to that caused by ionizing radiation.[16] Contrast agents can also be destroyed by intense ultrasound. Such concerns indicate the need to increase acoustic back scatter of ultrasound contrast agents at select frequencies without increasing the intensity of the incident ultrasound.

In the present work, we develop a technique for the enhancement of the scattering at a target frequency from ultrasound contrast agents by the use of dual-mode acoustic forcing. As an example, we consider the pair of forcing schema illustrated in Fig. 1. The sinusoidal, or single-mode driving has a frequency of 1 MHz and a pressure amplitude of 0.5 atm. The dual-mode optimal driving of the same intensity (defined below) is an optimal mix of signals at 1 MHz and 3 MHz, combined in such a way so as to maximize the acoustic radiation of a bubble at 2 MHz—the second harmonic of the primary driving frequency and also the difference frequency of the two driving frequencies. The new scheme thus represents a departure from harmonic imaging, where one usually drives at one frequency and receives at twice that frequency. In Fig. 2 we show the radial response of a 1.25 μm (radius) bubble to these two forcing protocols. The scattering at 2 MHz of the bubble is 8.0 times higher for the optimal driving. Such an effect is useful and robust, and allows one to further isolate the acoustic signature of the contrast agent microbubbles.

Other researchers have considered multiple frequency forcing of nonlinear bubble dynamics. Newhouse and Shanker[17] drove a bubble at two frequencies (a low pumping frequency in the resonance range f_p, and a higher frequency f_i) and noted resonance behavior in the side bands $f_i \pm f_p$ when f_p was equal to the resonance frequency. More recently, others have succeeded in increasing the light output from sonoluminescence bubbles by use of multiple frequency drives.[18,19] However, these methods have involved costly searches over parameter space for optimal frequency/

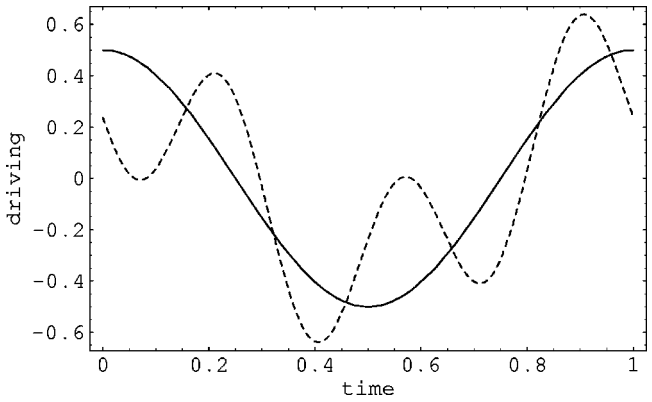

FIG. 1. Dimensionless single-mode (sinusoidal) and optimized driving pressure versus dimensionless time. The single-mode driving is at 1 MHz, and the optimal driving has components at 1 MHz and 3 MHz. The optimal driving is constructed so as to maximize the acoustic scattering at 2 MHz of a 1.25 μm radius bubble. The driving schemes are of the same intensity; $P_f=0.5$ (see text).

amplitude/phase combinations in the absence of a theory for their determination.

The plan of the paper is as follows. We begin with the formulation of the optimal control problem for the increase in scattering at a target frequency by multimode forcing, in the manner of Ref. 20. The resulting equations for the optimal forcing are then solved using the successive continuation strategy of Doedel.[21,22] Finally, we consider a number of results for the responses of a range of bubble sizes. We have relegated mathematical details to the appendix. The focus in this paper is on continuous wave (cw) driving. Pulse driving was the subject of another recent paper.[23]

II. FORMULATION OF THE PROBLEM

A. Bubble dynamics and acoustic scattering

In dimensionless variables, the Rayleigh–Plesset equation which governs the radial response of a strongly collapsing microbubble[24] is

$$\mathcal{G}\equiv R\ddot{R}+\frac{3}{2}\dot{R}^2-\mathrm{Eu}\left(1+M_L R\frac{\mathrm{d}}{\mathrm{d}\tau}\right)(P_L-P_\infty)=0, \qquad (1)$$

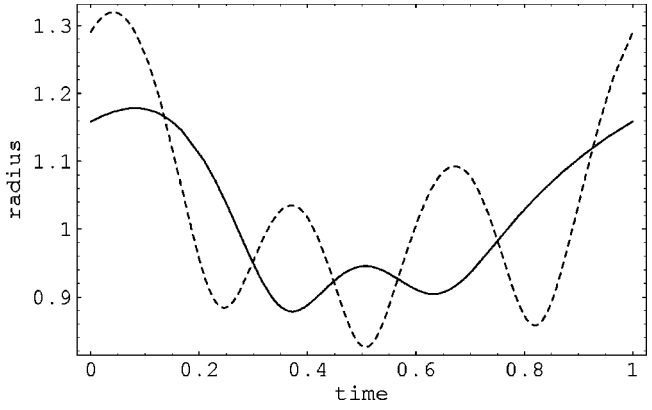

FIG. 2. Dimensionless radial response of a 1.25 μm radius bubble versus dimensionless time, subject to the single-mode and optimal forcing illustrated in Fig. 1. The energy radiated at 2 MHz in response to optimal forcing is 8.0 times greater than for single-mode forcing.

where the pressure in the liquid is

$$P_L=P_g+M_gR\frac{\mathrm{d}}{\mathrm{d}\tau}P_g+P_v-\frac{1}{\mathrm{We}\,R}-\frac{\dot{R}}{\mathrm{Re}\,R},$$

the gas pressure is $P_g=P_{g0}^*R^{-3k}$, $P_\infty=1-F(\tau)$ and $k=1$ when $R>R_0$ and $k=\gamma$ when $R<R_0$. In this equation, R is the bubble radius, made dimensionless with respect to the equilibrium radius R_0. The dots denote differentiation with respect to dimensionless time $\tau=t/T$, where t is time and T is a period (associated with the linear resonance frequency) of a bubble of a given nominal radius R_{nom}. The nominal radius provides a time scale which will later prove convenient. The other dimensionless groups are the Reynolds number $\mathrm{Re}=TP_0/(4\eta)$ formed from the ambient pressure P_0 and the viscosity η; the Weber number $\mathrm{We}=R_0P_0/(2\sigma)$ formed with the surface tension σ; the Mach numbers in the gas and liquid, $M_L=R_0/(c_LT)$ and $M_g=R_0/(3c_gT)$, with c_L and c_g the speed of sound in the medium; and the Euler number $\mathrm{Eu}=P_0T^2/(\rho_LR_0^2)$ where ρ_L is the density of the liquid. For equilibrium, we require $P_{g0}^*=1+1/\mathrm{We}-P_v$ where P_v is the dimensionless vapor pressure. F is the dimensionless acoustic forcing pressure, regarded as a function of τ. Finally, all terms of order two or higher in Mach number are neglected. Other variations of the Rayleigh–Plesset equation may be employed for the analysis we present below; this one was chosen for its more faithful reproduction of the damping observed in experimental results for strong collapses.

The incident acoustic intensity I_{inc}, a dimensionless measure of the energy of the forcing per unit area per unit time, is related to the forcing pressure $F(\tau)$ as[25]

$$I_{\mathrm{inc}}=\int_0^1 F(\tau)^2\,\mathrm{d}\tau. \qquad (2)$$

The energy radiated by the bubble is

$$E_{\mathrm{rad}}=\frac{M_L}{4\pi}\int_0^1 \ddot{V}^2\,\mathrm{d}\tau, \qquad (3)$$

where $V=(4\pi/3)R^3$ is the dimensionless volume of the bubble. The energy radiated by a bubble at the dimensionless frequency n is[26]

$$E_{\mathrm{rad}}^{(n)}=\frac{M_L}{2\pi}\left[\left(\int_0^1 \ddot{V}\cos(2\pi n\tau)\mathrm{d}\tau\right)^2+\left(\int_0^1 \ddot{V}\sin(2\pi n\tau)\mathrm{d}\tau\right)^2\right]. \qquad (4)$$

The scattering cross section of the bubble $\sigma^{(n)}$ at the frequency n is defined as the ratio of the radiated power at that frequency to the incident intensity. It is given in dimensionless terms, as

$$\sigma^{(n)}=\frac{E_{\mathrm{rad}}^{(n)}}{I_{\mathrm{inc}}\pi}. \qquad (5)$$

The dimensional form is $\sigma^{(n)}$ multiplied by the frontal area πR_0^2.

B. Optimal control problem

The goal of the optimal control problem is, subject to reasonable constraints, to maximize the energy scattered by the bubble at a particular target frequency. Specifically, here we wish to find a forcing $F(\tau)$ which yields the largest acoustic response at the dimensionless frequency of 2. The following formulation is valid for all $F(\tau)$, but the problem will shortly be specialized to an $F(\tau)$ consisting of a few specified Fourier modes. Mathematically, we wish to maximize $E_{\mathrm{rad}}^{(2)}$ (4), subject to a constraint on the incident intensity (2) where the intensity I_{inc} is a prescribed constant. We integrate $E_{\mathrm{rad}}^{(2)}$ by parts twice to obtain,

$$E_{\mathrm{rad}}^{(2)} = -\frac{2048}{9}\pi^5 M_L[\mathcal{C}^2+\mathcal{S}^2], \tag{6}$$

where $\mathcal{C}\equiv\int_0^1 R(\tau)^3\cos(4\pi\tau)\mathrm{d}\tau$, and $\mathcal{S}\equiv\int_0^1 R(\tau)^3\times\sin(4\pi\tau)\mathrm{d}\tau$.

In order to formulate the optimization problem, we begin by constructing a cost function J which consists of the quantity to be maximized (6) (with the constants of proportionality dropped), incorporating the constraints to be satisfied:

$$J\equiv\mathcal{C}^2+\mathcal{S}^2-\phi\left(\int_0^1 F(\tau)^2\,\mathrm{d}\tau-I_{\mathrm{inc}}\right)-\int_0^1\lambda(\tau)\mathcal{G}\,\mathrm{d}\tau. \tag{7}$$

$\mathcal{G}\equiv 0$ is the Rayleigh–Plesset equation (1), and J is a functional which associates a scalar cost with the acoustic forcing protocol $F(\tau)$.

In (7), the constraints are incorporated by the use of two Lagrange multipliers ϕ and $\lambda(\tau)$. Because the constraint on the norm of the acoustic forcing (2) is an integral constraint (and therefore not a function of τ), the associated Lagrange multiplier ϕ is a constant. The Rayleigh–Plesset equation $\mathcal{G}=0$ is regarded as a differential constraint. For this reason the associated Lagrange multiplier $\lambda(\tau)$ is time dependent. We note that when the constraints are satisfied, (7) is proportional to the scattered energy at the target frequency.

A necessary condition for J to achieve a maximum is that its variation δJ should be zero. This allows one to determine Euler–Lagrange equations to be satisfied by the unknowns $\{F(\tau),R(\tau),\lambda(\tau),\phi\}$ that are equivalent to the requirement that the variation in J should be zero. One must consider the variations in the forcing protocol $F(\tau)$, with accompanying changes in $R(\tau)$, $\dot{R}(\tau)$, and $\ddot{R}(\tau)$, and in the Lagrange multipliers ϕ and $\lambda(\tau)$. Further details are relegated to the appendix.

Thus far we have assumed a general form of the forcing $F(\tau)$. It is possible to solve for a general $F(\tau)$ directly,[20] but it is more practical from a technological standpoint to consider $F(\tau)$ as a sum of known Fourier components with unknown amplitudes and relative phases.[20] Hence (for simplicity) we restrict ourselves to a dual-mode forcing of the form,

$$F(\tau)=P_f(A_1\cos(2\pi f_1\tau)+A_2\cos(2\pi f_2\tau)+B_2\sin(2\pi f_2\tau)), \tag{8}$$

where P_f is the amplitude of the acoustic driving pressure made dimensionless with respect to P_0, f_1, and f_2 are given frequencies of forcing, and we have the convenient representation

$$A_1=\cos\theta\cos\nu,\quad A_2=\sin\theta\cos\nu,\quad B_2=\sin\nu. \tag{9}$$

Here θ and ν are simply (two) efficient variables to represent the mix of (three) amplitudes. In all cases to be examined f_1 is unity, owing to the nondimensionalization. That is, the driving at f_1 is at the linear resonance frequency of the bubble of radius R_{nom}. We shall defer specification of f_2 to specific examples below. In the example of Figs. 1 and 2, $f_1/T=1$ MHz, $f_2/T=3$ MHz and the scattering at $2f_1/T=2$ MHz was maximized.

C. Solution of the optimal control problem

Equations (12)–(19) of the appendix define the optimal control problem for the case of dual mode forcing (8) and (9). That is, the solution of these equations will yield a forcing protocol and a bubble radial response which maximizes scattering at the target frequency ($2f_1=2$). The corresponding θ and ν, which fully describe the forcing at a given amplitude through (8) and (9), are then *optimal*.

The solution of this system of equations can be very efficiently developed with AUTO 97,[27] software for continuation and bifurcation of ODEs. AUTO enables one to use pseudoarc length continuation to continue a particular branch of solutions to a system of ODEs (plus boundary conditions and integral constraints) as a parameter is varied. An exact initial solution is required. We employ AUTO to satisfy successively the various integral constraints (as well as periodicity conditions and ODEs) to obtain the optimal solution. Thereafter, we can maintain the optimal conditions while varying parameters such as the ambient radius of the bubble R_0 in order to develop response diagrams of various types.

We shall report the results of several different types of calculations. These are (i) (unoptimized) sinusoidal *single-mode forcing* where we vary R_0 to develop a response diagram of $\sigma^{(2)}$ vs R_0, (ii) *optimized dual-mode forcing* where we vary R_0 to develop a response diagram of $\sigma^{(2)}$ vs R_0 that is optimal for each R_0, and (iii) *fixed dual-mode forcing*, where we vary R_0 to develop a response diagram of $\sigma^{(2)}$ vs R_0 that is optimal for only one R_0^*—but suboptimal for other R_0. The latter calculation is intended to show the response of a cloud of bubbles of various sizes to forcing that is optimal for a single sized bubble. Note that a calculation of type (ii) is not feasible for direct application in a real imaging situation where bubbles of various sizes are present; but, pursuit of this helps to delineate what is possible in an ideal case. Details of the AUTO calculation are given in the appendix.

The physical parameters were chosen to model air bubbles in blood,[28–30] see Table I. The forcing frequencies are $f_1=1$, $f_2=3$ (we shall refer to this as 1/3 forcing), and $R_{\mathrm{nom}}=2.961\,05\,\mu$m. We remind the reader that R_{nom} is not the size of any bubble of interest, but rather just a convenient way to refer to the frequencies. A bubble of this radius has a linear resonance frequency of 1 MHz ($T=10^{-6}$ s). The dual-mode forcing then has components at 1 MHz and 3 MHz, and the scattering is to be maximized at 2 MHz, as in the example of Figs. 1 and 2.

TABLE I. Parameter values used in the simulations.

γ	= 1.0
ρ_L	= 1090 kg/m^3
c_g	= 340 m/s
c_L	= 1570 m/s
σ	= 58.89 mN/m
η	= 1.5 cP
P_0	= 101 325 Pa=1 atm

Other forcing schema were investigated but rejected for the present purposes. Forcing at 1/2 resulted in significantly higher scattering at $2f_1$. This is not surprising, because one component of forcing is at the receive frequency. However, in a physical system the second harmonic response of the f_1 component would be indistinguishable from a linear response driven by the f_2 component; this would have unfavorable consequences for the contrast-to-tissue ratio. Forcing at 1/3 seems to be the most effective because the second harmonic of f_1 is also the difference frequency between f_1 and f_2. Forcing at 1/4 forcing resulted in an insignificant increase in the scattering at $2f_1$.

III. RESULTS

In this section we illustrate the response of bubbles of different sizes to various driving protocols. The driving may be single-mode, optimal dual-mode, or fixed dual-mode. In all cases the dual-mode driving is a mixture of frequencies $f_1=1$, $f_2=3$, and the single-mode is entirely at frequency $f_1=1$. The acoustic response of the bubble is expressed in terms of the scattering cross section, which is related to the energy radiated by the relation (5). The scattering cross section, widely adopted in literature,[6,10] gives a measure of the acoustic radiation of a bubble for a given intensity of driving. For any given R_0 and I_{inc} the scattering cross section and the energy radiated $E^{(2)}_{\text{rad}}$ express the same thing; all optimizations with respect to one are valid with respect to the other.

Three driving amplitudes are examined, $P_f=0.1$, 0.25, and 0.5. These correspond to dimensional driving pressures $(P_f \cdot P_0)$ of 0.1, 0.25, and 0.5 atm, and to dimensionless intensities $I_{\text{inc}}=0.005$, 0.031 25, and 0.125. Two categories of plots are shown. The first (Figs. 3–5) illustrate the $\sigma^{(2)}$ response of a range of bubble sizes to two forcing schema, optimal dual-mode and single-mode forcing. Finally, in Fig. 6 we illustrate the response of bubbles to fixed dual-mode driving—driving which is fixed for all radii and which is optimal for only one bubble size.

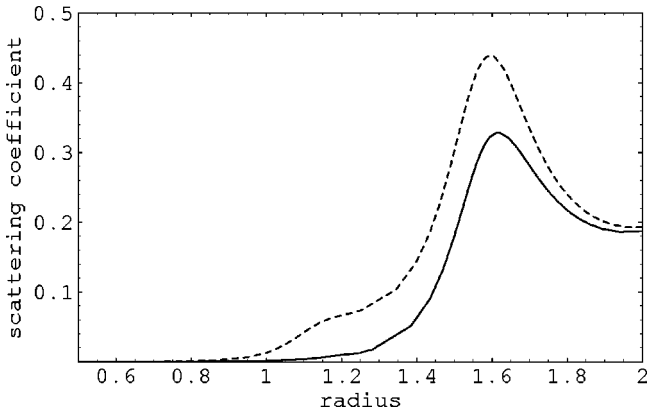

FIG. 3. Dimensionless scattering cross section $\sigma^{(2)}$ of bubbles of range of sizes R_0. The solid curve represents the response of bubbles subject to single-mode driving and the dashed one the response to optimal dual-mode driving. The optimal driving is optimal for every radius R_0. Driving amplitude is $P_f=0.1$.

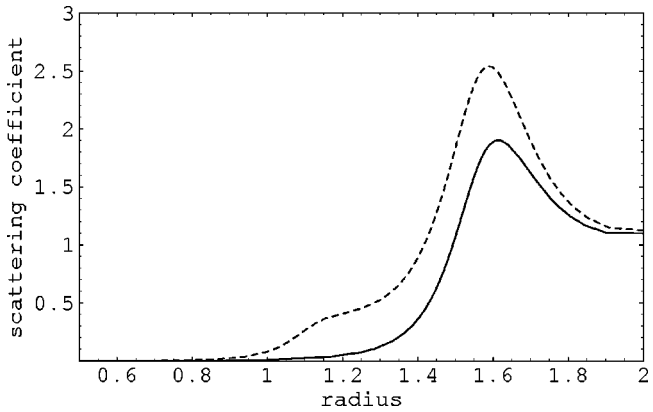

FIG. 4. The dimensionless scattering cross section of a bubble to different driving schema at $P_f=0.25$. Response to single-mode driving is shown as a solid curve, and to optimal dual-mode driving as a dotted curve. Optimal driving is optimal for each R_0.

A. A comparison of single-mode and optimal dual-mode forcing

In Fig. 3 we show the scattering cross section at the target frequency of bubbles ranging in size from 0.5 to 2 μm (radius) driven with a P_f of 0.1. Our investigations focus on bubbles of this size because they will not obstruct microcirculation.[1] The solid curve shows $\sigma^{(2)}$ of bubbles subject to single-mode driving, the dashed curve the response to dual-mode driving that is optimal at each R_0. The optimally driven bubble has a response $\sigma^{(2)}$ which is everywhere greater or equal to the single-mode driven bubble. The response of the optimally driven bubble is relatively greater for sizes $R_0 \sim 1-1.6\,\mu$m. This change illustrates that a significant increase in scattering at the target frequency, at a fixed intensity of driving, is possible.

Two amplitudes of driving were investigated further: $P_f=0.25$ and 0.5. In Figs. 4 and 5 are illustrated $\sigma^{(2)}$ for

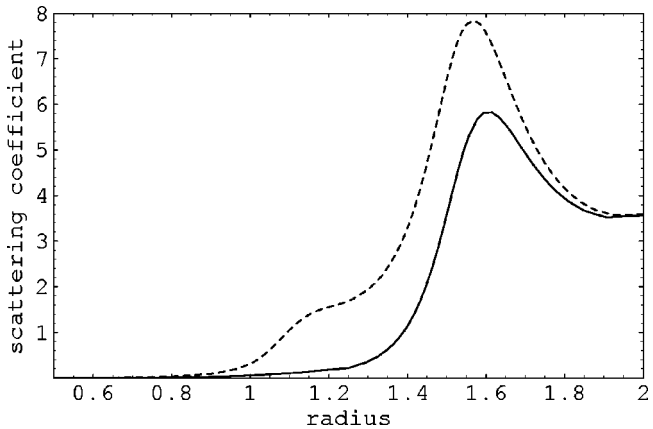

FIG. 5. $P_f=0.5$. As in Fig. 4.

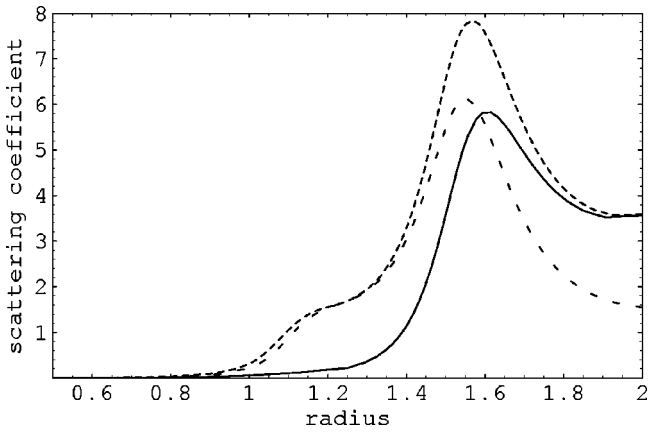

FIG. 6. Response to single-mode forcing (solid), forcing optimal for every R_0 (dashed) and fixed dual-mode forcing (long-dashed), where the fixed dual-mode forcing is optimal for a bubble of size $R_0^* = 1.25\ \mu$m. $P_f = 0.5$.

single-mode and optimal dual-mode driving in the latter two cases. For certain bubble sizes the difference in the response between single-mode and optimal driving is large. The $\sigma^{(2)}$ response of a 1.25 μm bubble driven at $P_f = 0.5$ increases eightfold (see also Figs. 1 and 2).

B. Components of the optimal dual-mode forcing

The mix of frequencies that makes for optimal forcing at a given R_0 depends on R_0. In other words, the values of A_1, A_2, and B_2 (or equivalently of θ and ν) as defined in (8) and (9) for optimal forcing depend on R_0. In a physical situation where a cloud of bubbles with a distribution of sizes is excited by the sound field, the driving is of course of one fixed form for all bubbles. This forcing may be optimal for bubbles of one particular size only, and differently sized bubbles will feel a forcing which is generally suboptimal. Note that the driving pulse may also change shape with propagation owing to frequency dependent attenuation and nonlinear effects, but this is beyond the scope of the present work. To gauge the response of a population of bubbles of a distribution of sizes to a driving which is optimal for a bubble size $R_0 = R_0^*$, we evaluated $\sigma^{(2)}$ for a fixed dual-mode driving with $\theta = \theta^*$ and $\nu = \nu^*$. θ^* and ν^* yield optimal forcing for a bubble of size R_0^*.

In Fig. 6 we show the response for the choice of $R_0^* = 1.25\ \mu$m; nearby choices lead to very similar pictures. For comparison, the responses to single-mode forcing and to forcing optimal for every R_0 are also shown. It is apparent that the increase in $\sigma^{(2)}$ is a robust phenomenon, and a fixed dual-mode driving which is optimal for one size of bubble increases the target response of bubbles for a considerable range of radii. Roughly speaking, such a fixed dual mode driving which is optimal for a size R_0^* increases $\sigma^{(2)}$ significantly above that of single-mode driving for sizes $R_0 \approx R_0^* \pm 0.4\ \mu$m. For R_0 outside of this range, the $\sigma^{(2)}$ is lower than for single-mode driving alone. At other driving pressure amplitudes, the choice of R_0^* near the midpoint of the range over which $\sigma^{(2)}$ is enhanced in the optimization calculation leads to similar results for fixed dual-mode driving which is optimal for one size of bubble.

In this regard, fixed dual-mode driving is size-selective. It will enhance the scattering at the target frequency of bubbles in a window of radii, and suppress it for bubbles outside of this range. This effect could be exploited to formulate a detection scheme, for bubbles in a range of sizes; see[17] for related ideas.

C. Stability of the optimal solutions

In constructing a solution to the problem $\delta J = 0$ one must ensure the solution obtained is physically realizable. There are two issues: the solution may be unstable, or it may require particular initial conditions. The basin of attraction of the optimal solution of the Rayleigh–Plesset equation is the set of all initial conditions which will, in time, converge upon the optimal radial dynamics, given that the optimal forcing (as given by θ and ν) is applied. Figure 2 is an example of such a solution. An unstable solution would never in practice be observed.

To determine the entire basin of attraction of an optimal solution is beyond the scope of this paper. Instead, we determine if one convenient initial condition corresponding to a quiescent bubble, $R(0) = 1$, $\dot{R}(0) = 0$, lies in the basin of attraction. We integrate the Rayleigh–Plesset equation (1) for a number of periods with a given initial condition, $R(0) = 1$, $\dot{R}(0) = 0$ until the periodicity conditions (A3) and (A4) are satisfied. In all cases, given the optimal forcing as prescribed by θ and ν for a given bubble size and driving intensity, we reach the optimal solution, and such convergence occurred in a small number of periods of forcing. We conclude that the optimal solutions described in this paper are stable and that the quiescent initial condition ($R = 1$, $\dot{R} = 0$) falls within their basin of attraction. Furthermore, the solution converges upon the periodic solution rather quickly.

IV. CONCLUSIONS

In this work we have shown how to optimize acoustic scattering from microbubbles at a frequency not contained in the forcing. Specifically, we have maximized the acoustic scattering at the difference frequency by optimizing over the phase and amplitudes of the components of a dual-frequency forcing. Numerical simulations were performed to gauge the effectiveness of the optimal driving scheme. The investigation focused primarily on an example of dual-mode driving with frequencies of 1 MHz and 3 MHz, with the scattering at 2 MHz optimized.

The scattering cross section at the target frequency can be increased considerably with optimal driving. Bubbles are receptive candidates for enhancement of the scattering as a consequence of frequency mixing phenomena; we have demonstrated that an optimal forcing scheme can increase $\sigma^{(2)}$ eightfold or more. Hence, the technique represents a powerful method for increasing the scattering at a target frequency.

It has been demonstrated that encapsulated microbubble contrast agents also scatter at the second harmonic,[9–12] but that their harmonic echoes are much fainter than free microbubbles. (Of course, they can be intentionally ruptured for imaging purposes.) The present methods can be used to enhance the scatter from these commercial contrast agents. The

formulation of the optimization problem in this paper is general. It can be regarded as a strategy to be exploited for other aims in acoustics, in addition to optimization of the scattering at the difference frequency.

ACKNOWLEDGMENTS

This work was supported by a grant from the National Science Foundation Program in Biomedical Engineering and by the University of California Energy Institute.

APPENDIX A: DERIVATION OF EULER–LAGRANGE EQUATIONS

In this appendix we derive differential equations that are equivalent to the (integral) statement of the optimization problem, including constraints. The strategy is to assume one has an optimal solution, and to perturb away from it. The change in the cost function J should be zero, to first order in the departure from the optimal solution.

Hence, we take the variation of J with respect to changes in $F(\tau)$, etc., and integrate by parts to eliminate related variations $\delta\dot{R}(\tau)$ and $\delta\ddot{R}(\tau)$ in favor of $\delta R(\tau)$. The result is

$$\delta J = -[M_L \lambda R\,\delta F]_0^1 + \left[\left(\frac{R\lambda}{\mathrm{Eu}} + \frac{M_L\lambda}{\mathrm{Re}}\right)\delta\dot{R}\right]_0^1 + \left[\left\{\frac{\lambda}{R}\left(\frac{1}{\mathrm{Re}} - \frac{M_L}{\mathrm{We}}\right) + 3k\left(\frac{1}{R}\right)^{3k} P_{g0}^{*}\lambda(M_g + M_L) + 2\lambda\dot{R}\left(\frac{1}{\mathrm{Eu}} - \frac{M_L}{\mathrm{Re}\,R}\right) - \dot{\lambda}\left(\frac{R}{\mathrm{Eu}} + \frac{M_L}{\mathrm{Re}}\right)\right\}\delta R\right]_0^1 - \delta\phi\left[\int_0^1 F^2\,\mathrm{d}\tau - I_{\mathrm{inc}}\right] + \int_0^1 \delta F(\tau)[-2\phi F + \lambda - M_L(\lambda\dot{R} + \dot{\lambda}R)]\mathrm{d}\tau + \int_0^1 \delta\lambda(\tau)\mathcal{G}\,\mathrm{d}\tau + \int_0^1 \delta R(\tau)\mathcal{H}\,\mathrm{d}\tau, \tag{A1}$$

where $\mathcal{H}$ is

$$\mathcal{H} \equiv \left[-\frac{R}{\mathrm{Eu}} - \frac{M_L}{\mathrm{Re}}\right]\ddot{\lambda} + \left[\frac{1}{\mathrm{Re}\,R} - \frac{M_L}{\mathrm{We}\,R} + 3kP_{g0}^{*}R^{-3k}(M_g + M_L) + \dot{R}\left(\frac{1}{\mathrm{Eu}} - \frac{2M_L}{\mathrm{Re}\,R}\right)\right]\dot{\lambda} + \left[\frac{1}{\mathrm{We}\,R^2} - 3kP_{g0}^{*}R^{-1-3k} + M_L\dot{F} + \frac{\ddot{R}}{\mathrm{Eu}} + \frac{M_L}{\mathrm{Re}\,R}\left(\frac{\dot{R}^2}{R} - 2\ddot{R}\right)\right]\lambda + 6R^2(\mathcal{C}\cos(4\pi\tau) + \mathcal{S}\sin(4\pi\tau)). \tag{A2}$$

The goal is to find conditions on $F(\tau)$ necessary for $\delta J = 0$.

We restrict ourselves to the narrow-band problem, where both the forcing $F(\tau)$ and the radial response of the bubble $R(\tau)$ are periodic with a period of unity (equivalently, a dimensional period of T seconds). In other words, we seek the solution to narrow-band forcing in which the transients of the response have died away. This imposes periodicity conditions on the radial response,

$$R(0) = R(1), \quad \dot{R}(0) = \dot{R}(1), \tag{A3}$$

and implies that the variations δR and $\delta\dot{R}$ as well as δF are periodic. The boundary terms in (A1) in turn imply that λ and $\dot{\lambda}$ are periodic with τ, or

$$\lambda(0) = \lambda(1), \quad \dot{\lambda}(0) = \dot{\lambda}(1). \tag{A4}$$

These arguments eliminate the boundary terms in (A1). The Euler–Lagrange equations corresponding to the variational principle are then obtained by assuming that the variations $\delta R(\tau)$ and $\delta\lambda(\tau)$ are arbitrary and independent for all τ; this requires that coefficients of these variations be identically zero for all τ, and we obtain

$$\mathcal{G} = 0, \tag{A5}$$

$$\mathcal{H} = 0. \tag{A6}$$

The assumptions on the form of the forcing (dual-mode in the present work) allow us to rewrite δF, a function of τ, in terms of the variations $\delta\theta$, $\delta\nu$, and δP_f. These variations are assumed to be independent, arbitrary and constant with respect to τ, hence the coefficients of this triad of variations must vanish individually. This leads in the usual way to the Euler–Lagrange equations associated with the variations δP_f, $\delta\theta$, and $\delta\nu$,

$$\int_0^1 \frac{\partial F}{\partial P_f}\left(\lambda - M_L\frac{\mathrm{d}}{\mathrm{d}\tau}(\lambda R)\right)\mathrm{d}\tau - P_f\phi = 0, \tag{A7}$$

$$\int_0^1 \frac{\partial F}{\partial \theta}\left(\lambda - M_L\frac{\mathrm{d}}{\mathrm{d}\tau}(\lambda R)\right)\mathrm{d}\tau = 0, \tag{A8}$$

$$\int_0^1 \frac{\partial F}{\partial \nu}\left(\lambda - M_L\frac{\mathrm{d}}{\mathrm{d}\tau}(\lambda R)\right)\mathrm{d}\tau = 0. \tag{A9}$$

Likewise, $\delta\phi$ is assumed to be an arbitrary constant and we immediately recover the constraint (2), which may be rewritten,

$$P_f^2 = 2I_{\mathrm{inc}}. \tag{A10}$$

In summary, the Euler–Lagrange equations consist of (A5) and (A6) (second order ordinary differential equations in R and λ) with boundary conditions (A3) and (A4), and integral constraints (A7)–(A9).

APPENDIX B: DETAILS OF SOLUTION VIA AUTO

A sequence of three continuations using AUTO is required to reach the optimal solution. In the first continuation the integral constraints (A8) and (A9) are relaxed and the parameters θ and ν are held fixed at some arbitrary value. The solution branch is traced as the driving intensity I_{inc} is increased from zero (corresponding to the known quiescent solution) to a desired value. The parameter ϕ is determined by satisfaction of (A7). For the second continuation the intensity is fixed while the first integral constraint (A8) is driven to zero by adjustment of θ. In the third continuation the integral constraints (A7) and (A8) are enforced while (A9) is forced to be satisfied by adjustment of θ and ν. At the end of the third continuation all the equations (A3)–(A10) are satisfied and the optimal solution is obtained. This is the successive continuation strategy of Doedel.[21,22]

Such an optimized forcing is specific to a bubble of size R_0 (in addition to all other physical parameters). We wish to broaden the scope by considering the response of bubbles of various sizes to optimal forcing. Such a sweep across R_0 is accomplished in a fourth continuation. Satisfaction of the entire system (A3)–(A10) is maintained; hence one obtains the *optimal dual-mode forcing* at each R_0. As the parameter R_0 is varied, this alters the values of the dimensionless groups such as the Reynolds number. The value of R_{nom} is unaltered, however, so the characteristic time T is unchanged. Physically this corresponds to an examination of the response of bubbles of a spectrum of sizes, each one subject to optimal forcing of the same two frequencies.

We are also interested in obtaining the response of bubbles of various sizes to a *fixed dual-mode forcing*, where θ and ν are fixed. This is accomplished in the fifth continuation, where R_0 is varied while θ and ν are held constant; the integral constraints (A8) and (A9) are by necessity relaxed. The particular case of $\theta=\nu=0$ [$A_1=1$, $A_2=B_2=0$ in (9)], which we call *single-mode forcing*, is also evaluated in this manner.

[1] F. G. Balen, C. M. Allen, and W. R. Lees, ''Ultrasound contrast agents,'' Clin. Radiol. **49**, 77–82 (1994).
[2] D. Cosgrove, ''Why do we need contrast agents for ultrasound?,'' Clin. Radiol. **51**, 1–4 (1996).
[3] N. de Jong, ''Improvements in ultrasound contrast agents,'' IEEE Eng. Med. Biol. Mag. **15**, 72–82 (1996).
[4] N. de Jong and F. J. Ten Cate, ''New ultrasound contrast agents and technological innovations,'' Ultrasonics **34**, 587–590 (1996).
[5] B. B. Goldberg, J.-B. Liu, and F. Forsberg, ''Ultrasound contrast agents—a review,'' Ultrasound Med. Biol. **20**, 319–333 (1994).
[6] J. Ophir and K. J. Parker, ''Contrast agents in diagnostic ultrasound,'' Ultrasound Med. Biol. **15**, 319–333 (1989).
[7] B. Schrope and V. L. Newhouse, ''2nd-harmonic ultrasonic blood perfusion measurement,'' Ultrasound Med. Biol. **19**, 567–579 (1993).
[8] B. Schrope, V. L. Newhouse, and V. Uhlendorf, ''Simulated capillary blood-flow measurement using a nonlinear ultrasonic contrast agent,'' Ultrason. Imaging **14**, 134–158 (1992).
[9] P. H. Chang, K. K. Shung, S.-J. Wu, and H. B. Levene, ''2nd-harmonic imaging and harmonic Doppler measurements with Albunex,'' IEEE Trans. Ultrason. Ferroelectr. Freq. Control **42**, 1020–1027 (1995).
[10] N. de Jong, R. Cornet, and C. T. Lancée, ''Higher harmonics of vibrating gas-filled microspheres. 1. Simulations,'' Ultrasonics **32**, 447–453 (1994).
[11] N. de Jong, R. Cornet, and C. T. Lancée, ''Higher harmonics of vibrating gas-filled microspheres. 2. Measurements,'' Ultrasonics **32**, 455–459 (1994).
[12] C. C. Church, ''The effects of an elastic solid-surface layer on the radial pulsations of gas-bubbles,'' J. Acoust. Soc. Am. **97**, 1510–1521 (1995).
[13] C. X. Deng, Q. Xu, R. E. Apfel, and C. K. Holland, ''In vitro measurements of inertial cavitation thresholds in human blood,'' Ultrasound Med. Biol. **22**, 939–948 (1996).
[14] D. L. Miller and R. M. Thomas, ''Ultrasound contrast agents nucleate inertial cavitation in vitro,'' Ultrasound Med. Biol. **21**, 1059–1065 (1995).
[15] C. K. Holland, C. X. Deng, R. E. Apfel, J. L. Alderman, L. A. Fernandez, and K. J. W. Taylor, ''Direct evidence of cavitation in vivo from diagnostic ultrasound,'' Ultrasound Med. Biol. **22**, 917–925 (1996).
[16] R. E. Apfel and C. K. Holland, ''Gaging the likelihood of cavitation from short-pulse, low-duty cycle diagnostic ultrasound,'' Ultrasound Med. Biol. **17**, 179–185 (1991).
[17] V. L. Newhouse and P. M. Shankar, ''Bubble size measurements using the nonlinear mixing of two frequencies,'' J. Acoust. Soc. Am. **75**, 1473–1477 (1984).
[18] J. Holzfuss, M. Ruggeberg, and R. Mettin, ''Boosting sonoluminescence,'' Phys. Rev. Lett. **81**, 1961–1964 (1998).
[19] J. A. Ketterling and R. E. Apfel, ''Using phase space diagrams to interpret multiple frequency drive sonoluminescence,'' J. Acoust. Soc. Am. **107**, 819–826 (2000).
[20] M. M. Fyrillas and A. J. Szeri, ''Control of ultra- and subharmonic resonances,'' J. Nonlinear Sci. **8**, 131–159 (1998).
[21] E. A. Doedel, H. B. Keller, and J. P. Kernevez, ''Numerical analysis and control of bifurcation problems, Part I: Bifurcation in finite dimensions,'' Int. J. Bifurcation Chaos Appl. Sci. Eng. **1**, 493–520 (1991).
[22] E. A. Doedel, H. B. Keller, and J. P. Kernevez, ''Numerical analysis and control of bifurcation problems, Part II: Bifurcation in infinite dimensions,'' Int. J. Bifurcation Chaos Appl. Sci. Eng. **1**, 745–772 (1991).
[23] A. J. Reddy and A. J. Szeri, ''Optimal pulse-inversion imaging for microsphere contrast agents,'' Ultrasound Med. Biol. **28**, 483–494 (2002).
[24] W. C. Moss, J. L. Levatin, and A. J. Szeri, ''A new damping mechanism in strongly collapsing bubbles,'' Proc. R. Soc. London, Ser. A **456**, 1685–1709 (2000).
[25] S. Hilgenfeldt, D. Lohse, and M. Zomack, ''Response of bubbles to diagnostic ultrasound: a unifying theoretical approach,'' Eur. Phys. J. B **4**, 247–255 (1998).
[26] S. Grossman, S. Hilgenfeldt, D. Lohse, and M. Zomack, ''Sound radiation of 3-MHz driven gas bubbles,'' J. Acoust. Soc. Am. **102**, 1223–1230 (1997).
[27] E. J. Doedel, A. R. Champneys, T. F. Fairgrieve, Y. A. Kuznetsov, B. Sandstede, and X. Wang, ''AUTO 97: continuation and bifurcation software for ordinary differential equations,'' ftp://ftp.cs.concordia.ca/pub/doedel/auto
[28] E. Hrncir and J. Rosina, ''Surface tension of blood,'' Physiol. Res. **46**, 319–321 (1997).
[29] W. Welkowitz, *Engineering Hemodynamics: Application to Cardiac Assist Devices* (Lexington Books, Lexington, MA, 1977).
[30] *Wintrobe's Clinical Hematology*, 10th ed., edited by G. R. Lee *et al.* (Williams & Wilkins, Baltimore, 1999).

Influence of viscosity on the diffraction of sound by a circular aperture in a plane screen

Anthony M. J. Davis
Mathematics Department, University of Alabama, Tuscaloosa, Alabama 35487-0350

Raymond J. Nagem[a)]
Department of Aerospace and Mechanical Engineering, Boston University, Boston, Massachusetts 02215

(Received 1 October 2002; revised 17 January 2003; accepted 28 January 2003)

The linearized equations of viscous fluid flow are used to analyze the diffraction of a time-harmonic acoustic plane wave by a circular aperture in a rigid plane screen. Arbitrary aperture size and arbitrary angle of incidence are considered. Sets of dual integral equations are derived for the diffracted velocity and pressure fields, and are solved by analytic reduction to sets of linear algebraic equations. In the case of normal incidence, numerical results are presented for the fluid velocity in the aperture and the power absorption due to viscous dissipation. The theoretical results for power absorption are compared to previously obtained results from high amplitude acoustic experiments in air. The conditions under which the dissipation predicted by linear theory becomes significant are quantified in terms of the fluid viscosity and sound speed, the acoustic frequency, and the aperture radius. © *2003 Acoustical Society of America.* [DOI: 10.1121/1.1562647]

PACS numbers: 43.28.Py [MSW]

I. INTRODUCTION

In a previous paper,[1] the authors began an investigation of the effects of fluid viscosity on acoustic diffraction. Reference 1 considered the problem of diffraction by a half plane, and focused primarily on the determination of the fluid velocity field near the diffracting edge. In the present paper, we analyze the diffraction of an acoustic plane wave by a circular aperture in a viscous fluid. The finite circular aperture considered here allows us to investigate the effects of viscosity on the fluid velocity field, the transmission of energy through the aperture, and the attenuation of acoustic energy by viscous dissipation.

An exact solution for the diffraction of a normally incident plane wave by a circular aperture in a standard inviscid acoustic medium is given by Spence.[2] When the radius of the aperture is small compared to the wavelength of the incident plane wave, Spence's solution agrees with the previous approximate solution of Rayleigh,[3] who derives his result by assuming that the fluid flow in the immediate vicinity of the small aperture is incompressible.

It is clear that fluid viscosity must have an increasingly important effect on sound transmission through an aperture as the aperture size decreases. It has also been shown experimentally that viscous effects in apertures become increasingly significant as the incident sound intensity level is increased.[4,5] A high intensity sound field produces a pulsating jet in the aperture, and this jet leads to the formation of vortex rings which propagate away from the aperture. The vortex rings extract energy from the acoustic field and cause an effective attenuation of sound. The formation of vortex rings and the corresponding attenuation of sound is enhanced by the presence of a steady mean flow. Thus, the diffraction of sound by a circular aperture in the presence of a mean flow has been studied theoretically and experimentally in the context of noise control applications.[6–8]

Here, we give the first complete solution for the linear boundary value problem corresponding to the diffraction of an incident time-harmonic plane wave by a circular aperture in a viscous fluid. We start in Sec. II with the linearized equations for a viscous fluid in the absence of a mean flow, and impose the no-slip condition on the rigid barrier that contains the aperture. We derive dual integral equations for the diffracted velocity and pressure fields that are valid for arbitrary aperture size and arbitrary angle of incidence. In Sec. III, the dual integral equations are transformed analytically into numerically tractable sets of linear algebraic equations. The special case of normal incidence is considered in Sec. IV. The analysis simplifies substantially for normal incidence, and the assumption of normal incidence allows us to develop simple expressions for the power transmission through the aperture and for the far-field transmitted pressure. By considering the ratio of the far-field power transmission to the power transmission through the aperture, we derive an expression for the power absorption due to viscous dissipation. In Sec. V we present numerical results for the case of a normally incident plane wave. The velocity field in the aperture is plotted for inviscid flow, for small viscosity and for fully viscous flow. Our theoretical results for the power absorption are compared with measured absorption values from the aeroacoustic experiments by Salikuddin and Brown.[9] The incident acoustic intensity in these experiments is high enough to induce nonlinear vortex formation in the aperture, and the power absorption predicted here by linear theory is generally small compared to the reported experimental values in Ref. 9. However, our results show that linear dissipation can be significant in some parameter ranges, and our analysis gives a complete determination of the dissipation as a function of fluid properties, acoustic frequency, and aperture size.

[a)]Electronic mail: nagem@bu.edu

 0001-4966/2003/113(6)/3080/11/$19.00

II. THEORY

The standard acoustic equations for linearized flow in a homogeneous viscous fluid are the continuity equation

$$\frac{\partial \rho}{\partial t} + \rho_0 \nabla \cdot \mathbf{v} = 0, \tag{1}$$

the momentum equation

$$\frac{\partial \mathbf{v}}{\partial t} = -\frac{1}{\rho_0} \nabla p + \nu \nabla^2 \mathbf{v} + \frac{\nu}{3} \boldsymbol{\nabla} (\nabla \cdot \mathbf{v}), \tag{2}$$

and the equation of state

$$\frac{dp}{d\rho} = c_0^2, \tag{3}$$

in which $\mathbf{v}$ is the fluid velocity vector, ρ_0 is the ambient fluid density, ρ is the density perturbation, p is the fluid pressure, and ν is the kinematic viscosity. It may be deduced from Eqs. (1)–(3) that the vorticity $\boldsymbol{\Omega} = \boldsymbol{\nabla} \times \mathbf{v}$ satisfies

$$\frac{\partial \boldsymbol{\Omega}}{\partial t} = \nu \nabla^2 \boldsymbol{\Omega}, \tag{4}$$

as in unsteady creeping flow, while ρ, $\boldsymbol{\nabla} \cdot \mathbf{v}$, and p satisfy an acoustic wave equation with viscous damping, namely

$$\frac{\partial^2}{\partial t^2} [\rho, \nabla \cdot \mathbf{v}, p] = \left(c_0^2 + \frac{4\nu}{3} \frac{\partial}{\partial t} \right) \boldsymbol{\nabla}^2 [\rho, \nabla \cdot \mathbf{v}, p]. \tag{5}$$

In particular, an irrotational plane wave has a velocity field of the form

$$\mathbf{v} = \frac{c_0^2}{\omega} \boldsymbol{\nabla} \{ \exp[i(k_a \mathbf{e} \cdot \mathbf{r} - \omega t)] \}, \quad k_a^{-2} = \frac{c_0^2}{\omega^2} - i \frac{4\nu}{3\omega}, \tag{6}$$

where $\mathbf{e}$ denotes a unit vector.

An infinite rigid plate, at which the no-slip condition $\mathbf{v} = \mathbf{0}$ is imposed, is at $z = 0$ but has an aperture at $0 \leqslant r < R$,

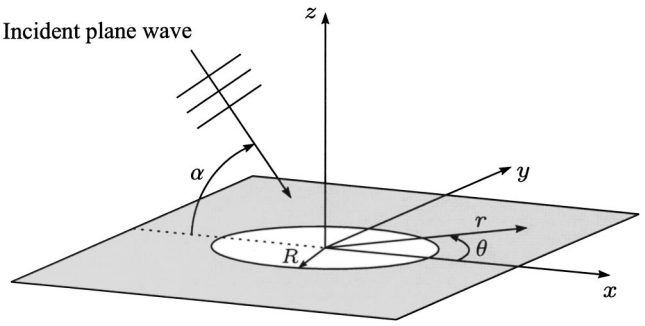

FIG. 1. Geometric configuration for plane wave diffraction through a circular aperture in a viscous acoustic medium.

which generates a three-dimensional disturbance produced by an incident plane wave of period $2\pi/\omega$, as illustrated by Fig. 1. If the viscous decay length $(\nu/\omega)^{1/2}$ is assumed to be much smaller than the acoustic length c_0/ω, as in air or water at normal acoustic frequencies, then the viscous effects are essentially confined to a thin region containing the barrier. However, if the former is of order R, viscosity is expected to restrict the penetration of the disturbance into $z < 0$.

Define

$$k_0 = \frac{\omega}{c_0}, \quad \epsilon^2 = \frac{\omega \nu}{c_0^2} \ll 1, \tag{7}$$

and suppress the time factor $e^{i\omega t}$. Then Eq. (6) yields

$$k_a = \frac{k_0}{\left(1 - \frac{4i}{3} \epsilon^2 \right)^{1/2}}, \tag{8}$$

which lies just above the positive real axis, and a total wave field in the absence of the aperture, regarded as an incident wave and given, for $z > 0$, by

$$\mathbf{v}_{\text{inc}} = (\mathbf{i} \cos\alpha - \mathbf{k} \sin\alpha) c_0 \exp[ik_a(x \cos\alpha - z \sin\alpha)] + (\mathbf{i} \cos\alpha + \mathbf{k} \sin\alpha) c_0 \left[\frac{\left(k_a^2 \cos^2\alpha - \frac{i\omega}{\nu} \right)^{1/2} \sin\alpha + ik_a \cos^2\alpha}{\left(k_a^2 \cos^2\alpha - \frac{i\omega}{\nu} \right)^{1/2} \sin\alpha - ik_a \cos^2\alpha} \right]$$

$$\times e^{ik_a(x \cos\alpha + z \sin\alpha)} - \frac{\left[\mathbf{i} \left(k_a^2 \cos^2\alpha - \frac{i\omega}{\nu} \right)^{1/2} + \mathbf{k} i k_a \cos\alpha \right] 2 c_0 \cos\alpha \sin\alpha}{\left(k_a^2 \cos^2\alpha - \frac{i\omega}{\nu} \right)^{1/2} \sin\alpha - ik_a \cos^2\alpha} e^{-(k_a^2 \cos^2\alpha - i\omega/\nu)^{1/2} z} e^{ik_a x \cos\alpha}, \tag{9}$$

in which $0 < \alpha \leqslant \pi/2$. The final term in $\mathbf{v}_{\text{inc}}$ accounts for the viscous no-slip condition at the wall and implies that the curl of $\mathbf{v}_{\text{inc}}$ is nonzero. For $z < 0$, $\mathbf{v}_{\text{inc}} = \mathbf{0}$. Let the total velocity field be $\mathbf{v}_{\text{inc}} - \mathbf{v}_{\text{sc}}$, with associated pressure field $p_{\text{inc}} - p_{\text{sc}}$, where the negative sign is introduced for later convenience. The scattered field $\mathbf{v}_{\text{sc}}$ must vanish on the barrier in order to maintain the no-slip condition, cancel the stress discontinuities in the aperture associated with $\mathbf{v}_{\text{inc}}$, and vanish as $z \to \pm\infty$. It is calculated by using the modal structure generated by the expansion

$$\exp[ik_a x \cos\alpha] = J_0(k_a r \cos\alpha) + 2 \sum_{n=1}^{\infty} i^n J_n(k_a r \cos\alpha) \cos n\theta, \tag{10}$$

where J_n is the Bessel function[10] of the first kind of order n. From Eqs. (1)–(3), $\mathbf{v}_{sc}$ is governed by

$$\frac{i\omega}{\rho_0 c_0^2} p_{sc} = \nabla \cdot \mathbf{v}_{sc}, \tag{11}$$

$$\left(\nabla^2 + \frac{i\omega}{\nu}\right)\mathbf{v}_{sc} = \frac{1 - \frac{i}{3}\epsilon^2}{\rho_0 \nu} \nabla p_{sc}. \tag{12}$$

The construction of $\mathbf{v}_{inc}$ in Eq. (9) allows the assumption that, at infinity, $\mathbf{v}_{sc}$ has only diffracted waves. Define the dimensionless Fourier coefficients

$$\begin{bmatrix} \mathbf{i}\cdot\mathbf{v}_{sc}/c_0 \\ \mathbf{k}\cdot\mathbf{v}_{sc}/c_0 \\ p_{sc}/\rho_0 c_0^2 \end{bmatrix} = \begin{bmatrix} U_0(r,z) \\ W_0(r,z) \\ P_0(r,z) \end{bmatrix} + 2\sum_{n=1}^{\infty} i^n \begin{bmatrix} U_n(r,z) \\ W_n(r,z) \\ P_n(r,z) \end{bmatrix} \cos n\theta,$$

$$\mathbf{j}\cdot\mathbf{v}_{sc}/c_0 = 2\sum_{n=1}^{\infty} i^n V_n(r,z) \sin n\theta, \tag{13}$$

which, according to Eqs. (11) and (12), are such that

$$\begin{aligned} \frac{i\omega}{c_0} P_0 &= \frac{i}{r}\frac{\partial}{\partial r}[r(U_1 + V_1)] + \frac{\partial W_0}{\partial z}, \\ \frac{i\omega}{c_0} P_1 &= \frac{1}{2i}\frac{\partial U_0}{\partial r} + \frac{i}{2r^2}\frac{\partial}{\partial r}[r^2(U_2 + V_2)] + \frac{\partial W_1}{\partial z}, \\ \frac{i\omega}{c_0} P_n &= \frac{r^{n-1}}{2i}\frac{\partial}{\partial r}\left(\frac{U_{n-1} - V_{n-1}}{r^{n-1}}\right) + \frac{i}{2r^{n+1}}\frac{\partial}{\partial r} \\ &\quad \times [r^{n+1}(U_{n+1} + V_{n+1})] + \frac{\partial W_n}{\partial z} \quad (n > 1), \end{aligned} \tag{14}$$

and

$$\begin{aligned} &\left(\frac{\partial^2}{\partial r^2} + \frac{1}{r}\frac{\partial}{\partial r} + \frac{\partial^2}{\partial z^2} + \frac{i\omega}{\nu}\right)\begin{bmatrix} U_0 \\ W_0 \end{bmatrix} \\ &\quad = \frac{i\omega}{c_0 k_a^2}\left(k_a^2 - \frac{i\omega}{\nu}\right)\begin{bmatrix} \frac{i}{r}\frac{\partial}{\partial r}(rP_1) \\ \frac{\partial P_0}{\partial z} \end{bmatrix}, \\ &\left(\frac{\partial^2}{\partial r^2} + \frac{1}{r}\frac{\partial}{\partial r} - \frac{n^2}{r^2} + \frac{\partial^2}{\partial z^2} + \frac{i\omega}{\nu}\right)\begin{bmatrix} U_n \\ V_n \\ W_n \end{bmatrix} \\ &\quad = \frac{i\omega}{c_0 k_a^2}\left(k_a^2 - \frac{i\omega}{\nu}\right) \\ &\quad \times \begin{bmatrix} \frac{r^{n-1}}{2i}\frac{\partial}{\partial r}\left(\frac{P_{n-1}}{r^{n-1}}\right) + \frac{i}{2r^{n+1}}\frac{\partial}{\partial r}\left(r^{n+1}P_{n+1}\right) \\ \frac{r^{n-1}}{2i}\frac{\partial}{\partial r}\left(\frac{P_{n-1}}{r^{n-1}}\right) - \frac{i}{2r^{n+1}}\frac{\partial}{\partial r}(r^{n+1}P_{n+1}) \\ \frac{\partial P_n}{\partial z} \end{bmatrix} \\ &\quad (n \geq 1). \end{aligned} \tag{15}$$

Since $(\nabla^2 + k_a^2)p_{sc} = 0$, with k_a defined by Eq. (6), the solution for P_n that vanishes as $|z| \to \infty$ is

$$\begin{aligned} P_n &= \int_0^{\infty} k^{-1}[A_n(k) + B_n(k)\mathrm{sgn}(z)] \\ &\quad \times e^{-(k^2 - k_a^2)^{1/2}|z|} J_n(kr)\,dk \quad (n \geq 0). \end{aligned} \tag{16}$$

The solution (16) allows the possibility that P_n or its first derivative with respect to z may be discontinuous at $z = 0$, and is more convenient than the alternative of writing one solution for $z > 0$ and a second solution for $z < 0$. The solution of Eq. (15) that ensures continuity of $\mathbf{V}$ at $z = 0$ is now

$$\begin{aligned} W_n &= \frac{i\omega}{c_0 k_a^2}\int_0^{\infty} \frac{\sqrt{k^2 - k_a^2}}{k}\{[A_n(k)\mathrm{sgn}(z) + B_n(k)] \\ &\quad \times e^{-(k^2 - k_a^2)^{1/2}|z|} - [A_n(k)\mathrm{sgn}(z) + C_n(k)] \\ &\quad \times e^{-(k^2 - i\omega/\nu)^{1/2}|z|}\} J_n(kr)\,dk \quad (n \geq 0), \end{aligned} \tag{17}$$

$$\begin{aligned} U_n \pm V_n &= \frac{\omega}{c_0 k_a^2}\int_0^{\infty}\{[A_{n\mp1}(k) + B_{n\mp1}(k)\mathrm{sgn}(z)] \\ &\quad \times e^{-(k^2 - k_a^2)^{1/2}|z|} - [D_n^{\pm}(k) + B_{n\mp1}(k)\mathrm{sgn}(z)] \\ &\quad \times e^{-(k^2 - i\omega/\nu)^{1/2}|z|}\} J_n(kr)\,dk \quad (n \geq 1), \end{aligned} \tag{18}$$

$$\begin{aligned} U_0 &= \frac{\omega}{c_0 k_a^2}\int_0^{\infty}\{[A_1(k) + B_1(k)\mathrm{sgn}(z)]e^{-(k^2 - k_a^2)^{1/2}|z|} \\ &\quad - [D_0^-(k) + B_1(k)\mathrm{sgn}(z)] \\ &\quad \times e^{-(k^2 - i\omega/\nu)^{1/2}|z|}\} J_0(kr)\,dk. \end{aligned} \tag{19}$$

In Eq. (18), the upper signs and the function D_n^+ are used in the equation for $U_n + V_n$, while the lower signs and the function D_n^- are used in the equation for $U_n - V_n$. The sets of functions, $\{A_n, B_n, C_n, D_n^-; n \geq 0\}$ and $\{D_n^+; n \geq 1\}$, are related by the continuity equation and then determined in the following by applying the mixed conditions at $z = 0$. When Eqs. (16)–(19) are substituted into Eq. (14), it follows that

$$\begin{bmatrix} D_1^+(k) \\ B_0(k) \end{bmatrix} = \frac{1}{k^2}(k^2 - k_a^2)^{1/2}\left(k^2 - \frac{i\omega}{\nu}\right)^{1/2}\begin{bmatrix} A_0(k) \\ C_0(k) \end{bmatrix},$$

$$\begin{bmatrix} \frac{1}{2}[D_{n-1}^-(k) + D_{n+1}^+(k)] \\ B_n(k) \end{bmatrix} = \frac{1}{k^2}(k^2 - k_a^2)^{1/2}\left(k^2 - \frac{i\omega}{\nu}\right)^{1/2}\begin{bmatrix} A_n(k) \\ C_n(k) \end{bmatrix} \quad (n \geq 1).$$

Hence

$$C_n(k) = \left[1 - \frac{K(k)}{(k^2 - k_a^2)^{1/2}}\right]B_n(k) \quad (n \geq 0),$$

$$D_1^+(k) = \left[1 + \frac{\left(k^2 - \frac{i\omega}{\nu}\right)^{1/2}}{k^2}K(k)\right]A_0(k),$$

where

$$K(k)=(k^2-k_a^2)^{1/2}-\frac{k^2}{\left(k^2-\frac{i\omega}{\nu}\right)^{1/2}}. \tag{20}$$

Since the sum $(D_{n-1}^{-}+D_{n+1}^{+})$ is given above in terms of the function A_n, it is convenient to introduce the function $E_n(n\geqslant 1)$ by setting

$$\left.\begin{matrix} D_{n-1}^{-}(k) \\ D_{n+1}^{+}(k) \end{matrix}\right\}=\left[1+\frac{\left(k^2-\frac{i\omega}{\nu}\right)^{1/2}}{k^2}K(k)\right]A_n(k)\pm E_n(k) \quad (n\geqslant 1).$$

When these relations are substituted into Eqs. (17)–(19), the latter can be rearranged as

$$W_n=\frac{i\omega}{c_0k_a^2}\int_0^\infty\left\{\frac{\sqrt{k^2-k_a^2}}{k}[A_n(k)\mathrm{sgn}(z)+B_n(k)]\times[e^{-(k^2-k_a^2)^{1/2}|z|}-e^{-(k^2-i\omega/\nu)^{1/2}|z|}]+\frac{K(k)}{k}\times B_n(k)e^{-(k^2-i\omega/\nu)^{1/2}|z|}\right\}J_n(kr)dk \quad (n\geqslant 0), \tag{21}$$

$$U_0=\frac{\omega}{c_0k_a^2}\int_0^\infty\left\{[A_1(k)+B_1(k)\mathrm{sgn}(z)][e^{-(k^2-k_a^2)^{1/2}|z|}-e^{-(k^2-i\omega/\nu)^{1/2}|z|}]-\left[\frac{\left(k^2-\frac{i\omega}{\nu}\right)^{1/2}}{k^2}K(k)A_1(k)+E_1(k)\right]e^{-(k^2-i\omega/\nu)^{1/2}|z|}\right\}J_0(kr)dk, \tag{22}$$

$$U_n-V_n=\frac{\omega}{c_0k_a^2}\int_0^\infty\left\{[A_{n+1}(k)+B_{n+1}(k)\mathrm{sgn}(z)]\times[e^{-(k^2-k_a^2)^{1/2}|z|}-e^{-(k^2-i\omega/\nu)^{1/2}|z|}]-\left[\frac{\left(k^2-\frac{i\omega}{\nu}\right)^{1/2}}{k^2}K(k)A_{n+1}(k)+E_{n+1}(k)\right]\times e^{-(k^2-i\omega/\nu)^{1/2}|z|}\right\}J_n(kr)dk \quad (n\geqslant 1), \tag{23}$$

$$U_1+V_1=\frac{\omega}{c_0k_a^2}\int_0^\infty\left\{[A_0(k)+B_0(k)\mathrm{sgn}(z)]\times[e^{-(k^2-k_a^2)^{1/2}|z|}-e^{-(k^2-i\omega/\nu)^{1/2}|z|}]-\frac{\left(k^2-\frac{i\omega}{\nu}\right)^{1/2}}{k^2}K(k)A_0(k)e^{-(k^2-i\omega/\nu)^{1/2}|z|}\right\}\times J_1(kr)dk, \tag{24}$$

$$U_n+V_n=\frac{\omega}{c_0k_a^2}\int_0^\infty\left\{[A_{n-1}(k)+B_{n-1}(k)\mathrm{sgn}(z)]\times[e^{-(k^2-k_a^2)^{1/2}|z|}-e^{-(k^2-i\omega/\nu)^{1/2}|z|}]-\left[\frac{\left(k^2-\frac{i\omega}{\nu}\right)^{1/2}}{k^2}K(k)A_{n-1}(k)-E_{n-1}(k)\right]\times e^{-(k^2-i\omega/\nu)^{1/2}|z|}\right\}J_n(kr)dk \quad (n\geqslant 2). \tag{25}$$

The sets of unknown functions $\{A_n(k),B_n(k);n\geqslant 0\}$, $\{E_n(k);n\geqslant 1\}$ are now determined by requiring zero velocity on the barrier and no net stress discontinuities in the aperture. It is readily seen from Eqs. (21)–(25) that $\mathbf{v}_{\mathrm{sc}}$ vanishes on the barrier provided

$$\begin{aligned}
&\int_0^\infty\frac{K(k)}{k}B_n(k)J_n(kr)dk=0 \quad (r>R,n\geqslant 0),\\
&\int_0^\infty\left[\frac{\left(k^2-\frac{i\omega}{\nu}\right)^{1/2}}{k^2}K(k)A_{n+1}(k)+E_{n+1}(k)\right]J_n(kr)dk=0 \quad (r>R,\ n\geqslant 0),\\
&\int_0^\infty\left[\frac{\left(k^2-\frac{i\omega}{\nu}\right)^{1/2}}{k^2}K(k)A_{n-1}(k)-E_{n-1}(k)\right]J_n(kr)dk=0 \quad (r>R,\ n\geqslant 2),\\
&\int_0^\infty\frac{\left(k^2-\frac{i\omega}{\nu}\right)^{1/2}}{k^2}K(k)A_0(k)J_1(kr)dk=0 \quad (r>R).
\end{aligned} \tag{26}$$

Equations valid for $r<R$ are obtained in the following by considering the normal and tangential stresses in the aperture. The normal stress at a $z=$constant plane is given by[11]

$$-p+2\rho_0\nu\left(\frac{\partial v_z}{\partial z}-\frac{1}{3}\nabla\cdot\mathbf{v}\right).$$

However, if $\mathbf{v}$ is continuous, then the normal derivative is equal to the divergence and hence, by virtue of Eq. (11), continuity of pressure suffices to ensure continuity of normal stress.

According to Eq. (9), the pressure discontinuity in the incident field is given by

$$\frac{i\omega}{\rho_0c_0^2}[p_{\mathrm{sc}}]_{z=0-}^{0+}=[\nabla\cdot\mathbf{v}_{\mathrm{sc}}]_{z=0-}^{0+}=2i\omega Qe^{ik_ax\cos\alpha}, \tag{27}$$

where

$$Q=\frac{c_0k_a\left(k_a^2\cos^2\alpha-\frac{i\omega}{\nu}\right)^{1/2}\sin\alpha}{\omega\left[\left(k_a^2\cos^2\alpha-\frac{i\omega}{\nu}\right)^{1/2}\sin\alpha-ik_a\cos^2\alpha\right]}$$

is a dimensionless constant. Thus, according to the Fourier expansions (10), (13) and the solution (16),

$$\int_0^\infty k^{-1}B_n(k)J_n(kr)dk=\frac{1}{2}[P_n]_{z=0-}^{0+}=QJ_n(k_a r\cos\alpha)$$

$$(r<R,\ \ n\geqslant 0), \quad (28)$$

since the total pressure field is $p_{\rm inc}-p_{\rm sc}$. Together with the first of equations (26), Eq. (28) yields, for each $n\geqslant 0$, a pair of dual integral equations for $B_n(k)$ that are disjoint from the other equations.

The tangential stress discontinuities in the incident field are similarly given, from Eq. (9), by

$$\rho_0\nu\left[\frac{\partial}{\partial z}\mathbf{v}_{\rm sc}\cdot\mathbf{i}\right]_{z=0-}^{0+}=\frac{-2i\omega^2\rho_0 Q\cos\alpha}{k_a\left(k_a^2\cos^2\alpha-\dfrac{i\omega}{\nu}\right)^{1/2}}e^{ik_a x\cos\alpha},$$

$$\rho_0\nu\left[\frac{\partial}{\partial z}\mathbf{v}_{\rm sc}\cdot\mathbf{j}\right]_{z=0-}^{0+}=0.$$

But the total velocity field is $\mathbf{v}_{\rm inc}-\mathbf{v}_{\rm sc}$, and thus, according to the Fourier expansions (10), (13) and the solutions (22)–(25),

$$\int_0^\infty\left[\frac{(k^2-k_a^2)^{1/2}}{k^2}A_n(k)+(-i\omega/\nu)^{-1}\left(k^2-\frac{i\omega}{\nu}\right)^{1/2}E_n(k)\right]\times J_{n-1}(kr)dk=\frac{Qk_a\cos\alpha}{\left(k_a^2\cos^2\alpha-\dfrac{i\omega}{\nu}\right)^{1/2}}J_{n-1}(k_a r\cos\alpha)\quad(r<R,\ \ n\geqslant 1),\quad(29)$$

$$\int_0^\infty\left[\frac{(k^2-k_a^2)^{1/2}}{k^2}A_n(k)-(-i\omega/\nu)^{-1}\left(k^2-\frac{i\omega}{\nu}\right)^{1/2}E_n(k)\right]\times J_{n+1}(kr)dk=\frac{Qk_a\cos\alpha}{\left(k_a^2\cos^2\alpha-\dfrac{i\omega}{\nu}\right)^{1/2}}J_{n+1}(k_a r\cos\alpha)\quad(r<R,\ \ n\geqslant 1),\quad(30)$$

$$\int_0^\infty\frac{(k^2-k_a^2)^{1/2}}{k^2}A_0(k)J_1(kr)dk=\frac{Qk_a\cos\alpha}{\left(k_a^2\cos^2\alpha-\dfrac{i\omega}{\nu}\right)^{1/2}}J_1(k_a r\cos\alpha)\quad(r<R).\quad(31)$$

Together with the last of equations (26), Eq. (31) yields a pair of dual integral equations for $A_0(k)$ that are disjoint from the other equations. However, for each $n\geqslant 1$, Eqs. (29), (30) and the rest of equations (26) are identified as coupled pairs of dual integral equations for $A_n(k)$, $E_n(k)$.

III. THE SCATTERED FIELD: SOLUTION BY TRANTER'S METHOD

Such groups of dual integral equations can be converted into coupled integral equations, defined on $r<R$ or $r>R$. But their numerical solution requires discretization and, when rapidly oscillating forcing occurs, as here, the direct reduction to algebraic equations given by Tranter[12] is expected to be preferable. This method starts with the key observation that

$$A(u)=u^\alpha\sum_{m=0}^\infty a_m J_{\nu-\alpha+2m+1}(u)$$

satisfies

$$\int_0^\infty A(u)J_\nu(xu)du=0\quad(x>1),$$

for $|\alpha|<1$. Explicit expressions for the coefficients are available when the integrand for the interval $x<1$ has only the additional factor $u^{-2\alpha}$. Otherwise, the choice of α is determined by the behavior of the additional factor as $u\to\infty$. So, since the stresses introduce a factor k at infinity, $\alpha=-1/2$ here. Thus equations (26) are satisfied by writing

$$\frac{K(k)}{k}B_n(k)=(kR)^{-1/2}\sum_{m=0}^\infty b_{nm}J_{n+2m+3/2}(kR)\quad(n\geqslant 0),\quad(32)$$

$$\frac{\left(k^2-\dfrac{i\omega}{\nu}\right)^{1/2}}{k^2}K(k)A_0(k)=(kR)^{-1/2}\sum_{m=1}^\infty a_{0m}J_{2m+1/2}(kR),\quad(33)$$

$$\frac{\left(k^2-\dfrac{i\omega}{\nu}\right)^{1/2}}{k^2}K(k)A_n(k)\pm E_n(k)=(kR)^{-1/2}\sum_{m=0}^\infty(a_{nm}\pm e_{nm})J_{n+2m+1/2}(kR)$$

$$(a_{n0}=e_{n,0},\ \ n\geqslant 1).\quad(34)$$

After substituting Eq. (32) and writing $u=kR$, $r=R\xi$, Eq. (28) becomes

$$\sum_{m=0}^\infty b_{nm}\int_0^\infty\frac{J_{n+2m+3/2}(u)}{RK(u/R)u^{1/2}}J_n(u\xi)du=QJ_n(k_aR\xi\cos\alpha)\quad(\xi<1,\ \ n\geqslant 0).$$

Tranter's method, described by Sneddon in Sec. 4.6 of Ref. 13, now transforms this functional identity into linear algebraic equations by multiplying by

$$\frac{2^{-1/2}\Gamma(n+l+1)}{\Gamma(n+1)\Gamma(l+3/2)}\xi^{n+1}(1-\xi^2)^{1/2}\mathcal{F}_1(n+3/2,n+1,\xi^2)$$

and integrating over $0<\xi<1$ to obtain

$$\sum_{m=0}^{\infty} b_{nm}\int_0^{\infty}\frac{J_{n+2m+3/2}(u)}{RK(u/R)u^2}J_{n+2l+3/2}(u)\,du$$
$$=\frac{2^{-1/2}\Gamma(n+l+1)Q}{\Gamma(n+1)\Gamma(l+3/2)}\int_0^1\xi^{n+1}(1-\xi^2)^{1/2}$$
$$\times\mathcal{F}_l(n+3/2,n+1,\xi^2)J_n(k_aR\xi\cos\alpha)\,d\xi\quad(l,n\geqslant 0). \tag{35}$$

Here $\mathcal{F}_l$ is a Jacobi polynomial, defined by

$$\mathcal{F}_l(a,b,\xi)={}_2F_1(-l,a+l;b:\xi)$$
$$=\frac{\Gamma(l+1)\Gamma(b)}{\Gamma(l+b)}P_l^{(b-1,a-b)}(1-2\xi)$$
$$=\frac{\Gamma(l+1)\Gamma(b)}{\Gamma(l+a)}\sum_{s=0}^{l}\frac{\Gamma(l+s+a)(-\xi)^s}{\Gamma(s+b)(l-s)!s!}, \tag{36}$$

in which the definition,

$$P_n^{(\alpha,\beta)}(x)=\frac{(-1)^n}{2^n n!}(1-x)^{-\alpha}(1+x)^{-\beta}\frac{d^n}{dx^n}$$
$$\times[(1-x)^{\alpha+n}(1+x)^{\beta+n}],$$

is an obvious extension of Rodrigues' formula for $P_n(x)$.

A set of linear equations for the coefficients in $A_0(k)$ is similarly obtained by substituting Eq. (33) into Eq. (31), multiplying by

$$\frac{2^{-1/2}\Gamma(l+2)}{\Gamma(l+3/2)}\xi^2(1-\xi^2)^{1/2}\mathcal{F}_l(5/2,2,\xi^2)$$

and integrating over $0<\xi<1$. Thus

$$\sum_{m=1}^{\infty} a_{0m}\int_0^{\infty}\left[\frac{u^2-(k_aR)^2}{u^2-\frac{i\omega}{\nu}R^2}\right]^{1/2}\frac{J_{2m+1/2}(u)}{RK(u/R)u^2}J_{2l+5/2}(u)\,du$$
$$=\frac{2^{-1/2}\Gamma(l+2)}{\Gamma(l+3/2)}\frac{Qk_a\cos\alpha}{\left(k_a^2\cos^2\alpha-\frac{i\omega}{\nu}\right)^{1/2}}\int_0^1\xi^2(1-\xi^2)^{1/2}$$
$$\times\mathcal{F}_l(5/2,2,\xi^2)J_1(k_aR\xi\cos\alpha)\,d\xi\quad(l\geqslant 0). \tag{37}$$

Further, for each $n\geqslant 1$, coupled sets of linear equations for the coefficients in $A_n(k)$, $E_n(k)$ are obtained by substituting Eq. (34) into Eqs. (29) and (30), multiplying by

$$\frac{2^{-1/2}\Gamma(n+l)}{\Gamma(n)\Gamma(l+3/2)}\xi^n(1-\xi^2)^{1/2}\mathcal{F}_l(n+1/2,n,\xi^2)$$

and

$$\frac{2^{-1/2}\Gamma(n+l+2)}{\Gamma(n+2)\Gamma(l+3/2)}\xi^{n+2}(1-\xi^2)^{1/2}\mathcal{F}_l(n+5/2,n+2,\xi^2),$$

respectively, and integrating over $0<\xi<1$. Thus

$$\int_0^{\infty}\sum_{m=0}^{\infty}\left\{\frac{1}{K(u/R)}\left[\frac{u^2-(k_aR)^2}{u^2-\frac{i\omega}{\nu}R^2}\right]^{1/2}a_{nm}\right.$$
$$\left.+\frac{\left(u^2-\frac{i\omega}{\nu}R^2\right)^{1/2}}{\left(-\frac{i\omega}{\nu}\right)R}e_{nm}\right\}J_{n+2m+1/2}(u)\frac{J_{n+2l+1/2}(u)}{Ru^2}\,du$$
$$=\frac{2^{-1/2}\Gamma(n+l)}{\Gamma(n)\Gamma(l+3/2)}\frac{Qk_a\cos\alpha}{\left(k_a^2\cos^2\alpha-\frac{i\omega}{\nu}\right)^{1/2}}\int_0^1\xi^n(1-\xi^2)^{1/2}$$
$$\times\mathcal{F}_l(n+1/2,n,\xi^2)J_{n-1}(k_aR\xi\cos\alpha)\,d\xi$$
$$(l\geqslant 0,\ \ n\geqslant 1), \tag{38}$$

$$\int_0^{\infty}\sum_{m=0}^{\infty}\left\{\frac{1}{K(u/R)}\left[\frac{u^2-(k_aR)^2}{u^2-\frac{i\omega}{\nu}R^2}\right]^{1/2}a_{nm}\right.$$
$$\left.-\frac{\left(u^2-\frac{i\omega}{\nu}R^2\right)^{1/2}}{\left(-\frac{i\omega}{\nu}\right)R}e_{nm}\right\}J_{n+2m+1/2}(u)\frac{J_{n+2l+5/2}(u)}{Ru^2}\,du$$
$$=\frac{2^{-1/2}\Gamma(n+l+2)}{\Gamma(n+2)\Gamma(l+3/2)}\frac{Qk_a\cos\alpha}{\left(k_a^2\cos^2\alpha-\frac{i\omega}{\nu}\right)^{1/2}}$$
$$\times\int_0^1\xi^{n+2}(1-\xi^2)^{1/2}\mathcal{F}_l(n+5/2,n+2,\xi^2)$$
$$\times J_{n+1}(k_aR\xi\cos\alpha)\,d\xi\quad(l\geqslant 0,\ \ n\geqslant 1). \tag{39}$$

It may be noted that the function $K(k)$ given by Eq. (20) appeared as the "Wiener–Hopf kernel" in the half-plane diffraction analysis in Ref. 1. This function evidently plays a key role in the acoustic/viscous interaction associated with diffraction problems. It might be described here as the "kernel" of Eq. (35).

For later numerical evaluation of the semi-infinite integrals in Eq. (35) and Eqs. (37)–(39), it is advantageous to identify the asymptotic form of the integrands as $u\to\infty$ and to evaluate the integrals corresponding to this asymptotic form analytically using the identity

$$\int_0^{\infty}\frac{J_{n+2m+3/2}(u)J_{n+2l+3/2}(u)}{u}\,du=\frac{\delta_{ml}}{2n+4m+3}.$$

It is also convenient to rescale the coefficients a_{mn}, b_{mn}, and e_{mn} so as to to remove common factors from the right-hand sides. Thus, on writing

$$[a_{nm},e_{nm}]=-\left[\left(k_a^2+\frac{i\omega}{\nu}\right)\alpha_{nm},\frac{2i\omega}{\nu}\gamma_{nm}\right]R^2\left(\frac{2}{\pi}\right)^{1/2}\times\frac{Qk_a\cos\alpha(n+2m+1/2)}{\left(k_a^2\cos^2\alpha-\frac{i\omega}{\nu}\right)^{1/2}},\tag{40}$$

$$b_{nm}=-\left(k_a^2+\frac{i\omega}{\nu}\right)\beta_{nm}R^2\left(\frac{2}{\pi}\right)^{1/2}Q(n+2m+3/2),$$

and substituting for K from Eq. (20), Eqs. (35), (37)–(39) reduce to

$$\beta_{nl}-\sum_{m=0}^{\infty}(n+2m+3/2)\beta_{nm}\int_0^{\infty}J_{n+2m+3/2}(u)J_{n+2l+3/2}(u)\times\left[\frac{(k_a^2+i\omega/\nu)R^2}{(u^2-k_a^2R^2)^{1/2}-u^2(u^2-iR^2\omega/\nu)^{-1/2}}+2u\right]\frac{du}{u^2}$$
$$=\frac{\Gamma(3/2)\Gamma(n+l+1)}{\Gamma(n+1)\Gamma(l+3/2)}\int_0^1\xi^{n+1}(1-\xi^2)^{1/2}\times\mathcal{F}_l(n+3/2,n+1,\xi^2)J_n(k_aR\xi\cos\alpha)d\xi\quad(l,n\geqslant0),\tag{41}$$

$$\alpha_{0,l+1}-\sum_{m=1}^{\infty}(2m+1/2)\alpha_{0m}\int_0^{\infty}J_{2m+1/2}(u)J_{2l+5/2}(u)\times\left[\frac{(k_a^2+i\omega/\nu)R^2}{(u^2-iR^2\omega/\nu)^{1/2}-u^2(u^2-k_a^2R^2)^{-1/2}}+2u\right]\frac{du}{u^2}$$
$$=\frac{\Gamma(3/2)\Gamma(l+2)}{\Gamma(l+3/2)}\int_0^1\xi^2(1-\xi^2)\mathcal{F}_l(5/2,2,\xi^2)\times J_1(k_aR\xi\cos\alpha)d\xi\quad(l\geqslant0),\tag{42}$$

$$\alpha_{nl}-\sum_{m=0}^{\infty}(n+2m+1/2)\alpha_{nm}\int_0^{\infty}J_{n+2m+1/2}(u)J_{n+2l+1/2}(u)\left[\frac{(k_a^2+i\omega/\nu)R^2}{(u^2-iR^2\omega/\nu)^{1/2}-u^2(u^2-k_a^2R^2)^{-1/2}}+2u\right]\frac{du}{u^2}+\gamma_{nl}$$
$$-\sum_{m=0}^{\infty}(2n+4m+1)\gamma_{nm}\int_0^{\infty}J_{n+2m+1/2}(u)J_{n+2l+1/2}(u)[u-(u^2-iR^2\omega)^{1/2}]\frac{du}{u^2}$$
$$=\frac{\Gamma(3/2)\Gamma(n+l)}{\Gamma(n)\Gamma(l+3/2)}\int_0^1\xi^n(1-\xi^2)^{1/2}\mathcal{F}_l(n+1/2,n,\xi^2)J_{n-1}(k_aR\xi\cos\alpha)d\xi\quad(l\geqslant0,\ n\geqslant1),\tag{43}$$

$$\alpha_{n,l+1}-\sum_{m=0}^{\infty}(n+2m+1/2)\alpha_{nm}\int_0^{\infty}J_{n+2m+1/2}(u)J_{n+2l+5/2}(u)\left[\frac{(k_a^2+i\omega/\nu)R^2}{(u^2-iR^2\omega/\nu)^{1/2}-u^2(u^2-k_a^2R^2)^{-1/2}}+2u\right]\frac{du}{u^2}-\gamma_{n,l+1}$$
$$+\sum_{m=0}^{\infty}(2n+4m+1)\gamma_{nm}\int_0^{\infty}J_{n+2m+1/2}(u)J_{n+2l+5/2}(u)[u-(u^2-iR^2\omega)^{1/2}]\frac{du}{u^2}$$
$$=\frac{\Gamma(3/2)\Gamma(n+l+2)}{\Gamma(n+2)\Gamma(l+3/2)}\int_0^1\xi^{n+2}(1-\xi^2)^{1/2}\mathcal{F}_l(n+5/2,n+2,\xi^2)J_{n+1}(k_aR\xi\cos\alpha)d\xi\quad(l\geqslant0,\ n\geqslant1).\tag{44}$$

For $n\geqslant1$, $a_{n0}=e_{n0}$ implies $(1-ik_a^2\nu/\omega)\alpha_{n0}=2\gamma_{n0}$, which ensures that the number of equations matches the number of unknown coefficients. Note that the forcing terms (right-hand sides) depend on only k_aR while the matrices on the left-hand sides depend on both k_aR and $(\omega/\nu)^{1/2}R$, with emphasis dictated by the magnitudes of these parameters.

In the inviscid limit, only $\{B_n(k);n\geqslant0\}$ and hence one set of equations are required. However, the additional factor in the integral over (0, 1) now behaves like u^{-1}, corresponding to the pressure now playing the role of velocity potential instead of normal stress. Thus, with $\alpha=1/2$, Eq. (32) is modified to

$$\frac{(k^2-k_0^2)^{1/2}}{k}B_n(k)=(Rk)^{1/2}\sum_{m=0}^{\infty}\hat{b}_{nm}J_{n+2m+1/2}(kR)\quad(n\geqslant0),\tag{45}$$

and the resulting system, corresponding to Eq. (35), is

$$\sum_{m=0}^{\infty}\hat{b}_{nm}\int_0^{\infty}\frac{J_{n+2m+1/2}(u)}{(u^2-k_0^2R^2)^{1/2}}J_{n+2l+1/2}(u)du$$
$$=\frac{2^{1/2}\Gamma(n+l+1)}{\Gamma(n+1)\Gamma(l+1/2)}\int_0^1\frac{\xi^{n+1}}{(1-\xi^2)^{1/2}}\times\mathcal{F}_l(n+1/2,n+1,\xi^2)J_n(k_0R\xi\cos\alpha)d\xi\quad(l,n\geqslant0).\tag{46}$$

IV. NORMAL INCIDENCE

In this limiting case, the incident field has the simple form

$$\mathbf{v}_{\rm inc}=c_0\mathbf{k}(-e^{-ik_az}+e^{ik_az}) \quad (z>0)$$

and only P_0, W_0 and $U_1=V_1$ are nonzero. Moreover, the absence of tangential stress in the incident field ensures that $A_0(k)=0$. According to Eqs. (26)–(28), the remaining function $B_0(k)$ satisfies the dual integral equations

$$\int_0^\infty \frac{K(k)}{k}B_0(k)J_0(kr)dk=0 \quad (r>R),$$

$$\int_0^\infty k^{-1}B_0(k)J_0(kr)dk=\frac{c_0k_a}{\omega}=\frac{k_a}{k_0} \quad (r<R),$$

which can be reduced, by writing

$$\frac{K(k)}{k}B_0(k)=-\left(\frac{2}{\pi kR}\right)^{1/2}\left(k_a^2+\frac{i\omega}{\nu}\right)R^2\frac{k_a}{k_0} \times\sum_{m=0}^{\infty}\beta_{0m}(2m+3/2)J_{2m+3/2}(kR), \quad (47)$$

according to Eqs. (32) and (40), to the linear system

$$\beta_{0l}-\sum_{m=0}^{\infty}(2m+3/2)\beta_{0m}\int_0^\infty J_{2m+3/2}(u)J_{2l+3/2}(u) \times\left[\frac{(k_a^2+i\omega/\nu)R^2}{(u^2-k_a^2R^2)^{1/2}-u^2(u^2-iR^2\omega/\nu)^{-1/2}}+2u\right]\frac{du}{u^2} =\frac{\Gamma(3/2)\Gamma(l+1)}{\Gamma(l+3/2)}\int_0^1\xi(1-\xi^2)^{1/2}\mathcal{F}_l(3/2,1,\xi^2)d\xi =\tfrac{1}{3}\delta_{l0} \quad (l\geqslant 0). \quad (48)$$

A. Aperture power transmission

A useful quantity that can be readily calculated here is the power transmitted through the aperture. In terms of the time-dependent fields, the power flow is given, from Eqs. (1) to (3), by the outward flux of the vector field

$$\mathbf{J}=\mathbf{v}\left(1+\frac{\nu}{3c_0^2}\frac{\partial}{\partial t}\right)p-\rho_0\nu\boldsymbol{\nabla}\left(\frac{1}{2}v^2\right). \quad (49)$$

The normal component of $\mathbf{J}$ in the aperture is complicated in the general case of oblique incidence but simplifies enormously when $\alpha=\pi/2$, since then $\mathbf{v}$ has zero tangential component and p varies only in time. Then, with further use of Eq. (1),

$$\mathbf{J}=\mathbf{v}\left(1+\frac{4\nu}{3c_0^2}\frac{\partial}{\partial t}\right)p \quad \text{at } z=0,\ r<R.$$

Using the brackets $\langle\,\rangle$ to denote the time average over one period of the harmonic oscillation, the mean power transmission through the aperture (in the negative z direction) is therefore

$$\mathcal{P}_a=-2\pi\int_0^R\langle\mathbf{J}(r,0)\cdot\mathbf{k}\rangle r\,dr =\pi\Re\left[\frac{k_0^2}{k_a^2}\int_0^R\mathbf{v}_{\rm sc}^*(r,0)\cdot\mathbf{k}(p_{\rm inc}-p_{\rm sc})(r,0)r\,dr\right],$$

where an asterisk denotes a complex conjugate. But, from Eqs. (27) and (28),

$$(p_{\rm inc}-p_{\rm sc})(r,0)=\rho_0c_0^2k_a/k_0,$$

and, from Eqs. (21) and (47),

$$\mathbf{v}_{\rm sc}(r,0)\cdot\mathbf{k}=\left(\frac{2}{\pi}\right)^{1/2}\frac{c_0^2k_0}{\nu k_a}\left(1-\frac{ik_a^2\nu}{\omega}\right)R^2\sum_{m=0}^{\infty}\beta_{0m}(2m+3/2) \times\int_0^\infty\frac{J_{2m+3/2}(kR)}{(kR)^{1/2}}J_0(kr)dk. \quad (50)$$

The r integral in the expression for $\mathcal{P}_a$ is simple and then the identity

$$\int_0^\infty\frac{J_{2m+3/2}(u)}{u^{3/2}}J_1(u)du=\left(\frac{2}{\pi}\right)^{1/2}\frac{1}{3}\delta_{m0}$$

shows that

$$\mathcal{P}_a=\frac{\rho_0c_0^4k_0^2}{\nu|k_a|^2}R^3\Re\left[\left(1+\frac{i(k_a^*)^2\nu}{\omega}\right)\beta_{00}^*\right] =\frac{\omega\rho_0c_0^2R^3}{\epsilon^2}\frac{k_0^2}{|k_a|^2}\Re\left[\left(1-\frac{ik_a^2\epsilon}{k_0^2}\right)\beta_{00}\right]. \quad (51)$$

B. Pressure at infinity

The scattered pressure $p_{\rm sc}$, is given, from Eqs. (13), (16), and (47), by

$$p_{\rm sc}/\rho_0c_0^2=P_0(r,z) =-\,\mathrm{sgn}(z)\left(k_a^2+\frac{i\omega}{\nu}\right)R^2\frac{k_a}{k_0}\int_0^\infty\left(\frac{2}{\pi kR}\right)^{1/2}\frac{1}{K(k)} \times\sum_{m=0}^{\infty}\beta_{0m}(2m+3/2)J_{2m+3/2}(kR) \times e^{-(k^2-k_a^2)^{1/2}|z|}J_0(kr)dk. \quad (52)$$

To obtain a far-field evaluation of the scattered pressure as $z\to-\infty$ and $r\to\infty$, we first express the Bessel function $J_0(kr)$ as a Fourier sine transform in the form

$$J_0(kr)=\frac{2}{\pi}\int_r^\infty\frac{\sin ks}{(s^2-r^2)^{1/2}}ds=\frac{1}{\pi i}\int_r^\infty\frac{e^{iks}-e^{-iks}}{(s^2-r^2)^{1/2}}ds.$$

Since $K(k)$ is an even function of k and $J_{m+3/2}(kR)/(kR)^{1/2}$ is an odd function of k, the semi-infinite integral in Eq. (52) can then be transformed into the double integral

$$\frac{p_\infty}{\rho_0 c_0^2}=\left(k_a^2+\frac{i\omega}{\nu}\right)R^2\frac{k_a}{k_0}\int_r^\infty\frac{ds}{\pi i(s^2-r^2)^{1/2}}\int_{-\infty}^{\infty}dk$$
$$\times\left(\frac{2}{\pi kR}\right)^{1/2}\frac{1}{K(k)}\sum_{m=0}^{\infty}\beta_{0m}(2m+3/2)$$
$$\times J_{2m+3/2}(kR)e^{(k^2-k_a^2)^{1/2}z}e^{iks}. \tag{53}$$

If we set

$$z=-\sqrt{z^2+s^2}\sin\theta,\quad s=\sqrt{z^2+s^2}\cos\theta,$$
$$k=k_a\cos(\theta+it),\quad -\infty<t<\infty,$$

then the exponential in the integrand of Eq. (53) becomes

$$e^{(k^2-k_a^2)^{1/2}z}e^{iks}=e^{ik_a\sqrt{z^2+s^2}\cosh t},$$

so that the exponent has a stationary point at $t=0$ or, equivalently, $k=k_a\cos\theta$. As described in Ref. 14, the equation $k=k_a\cos(\theta+it)$ defines a hyperbola in the complex k plane, and the stationary point $t=0$ lies at the vertex of the hyperbola.

A stationary phase evaluation[15] of the inner integral in Eq. (53) is now applied. Since the stationary value, $k=k_a\cos\theta$, of k is of order k_0 and $k_0R\ll 1$ is of interest here, the $m=0$ term and the small argument approximation

$$\left(\frac{2}{\pi kR}\right)^{1/2}J_{3/2}(kR)\approx\frac{3kR}{3\pi}$$

suffice. Equation (53) becomes

$$\frac{p_\infty}{\rho_0 c_0^2}=\left(k_a^2+\frac{i\omega}{\nu}\right)R^2\frac{k_a}{k_0}\frac{3\beta_{00}}{2}\int_r^\infty\frac{ds}{\pi i(s^2-r^2)^{1/2}}$$
$$\times\frac{2R}{3\pi}\frac{k_a s}{\sqrt{z^2+s^2}}\frac{-ik_a\sin\theta}{K(k_a\cos\theta)}e^{ik_a\sqrt{z^2+s^2}}$$
$$\times e^{i\pi/4}\sqrt{\frac{2\pi}{k_a\sqrt{z^2+s^2}}}.$$

For small $\epsilon^2=\omega\nu/c_0^2$, Eq. (20) shows that $K(k_a\cos\theta)\approx -ik_a\sin\theta$. Setting $s^2=r^2+u^2(z^2+r^2)$, we have

$$\frac{p_\infty}{\rho_0 c_0^2}=\left(k_a^0+\frac{i\omega}{\nu}\right)R^3\frac{k_a}{k_0}\frac{\beta_{00}}{\pi i}\sqrt{\frac{2\pi}{k_a}}e^{i\pi/4}\frac{1}{(z^2+r^2)^{1/4}}$$
$$\times\int_{-\infty}^{\infty}\frac{e^{ik_a\sqrt{z^2+r^2}\sqrt{1+u^2}}}{2(1+u^2)^{3/4}}du. \tag{54}$$

A stationary phase evaluation of the integral in Eq. (54) now gives

$$p_\infty=\rho_0 c_0^2\left(k_a^2+\frac{i\omega}{\nu}\right)R^3\frac{k_a}{k_0}\frac{\beta_{00}}{\pi}\frac{e^{ik_a\sqrt{z^2+r^2}}}{\sqrt{z^2+r^2}}$$
$$=\rho_0 c_0^2\frac{i}{\epsilon^2}\left(1-\frac{ik_a^2\epsilon^2}{k_0^2}\right)k_0^2R^3\frac{k_a}{k_0}\frac{\beta_{00}}{\pi}\frac{e^{ik_a\sqrt{z^2+r^2}}}{\sqrt{z^2+r^2}}. \tag{55}$$

Equation (55) can also be written as

$$p_\infty=-\frac{i\omega}{2\pi}M\frac{k_a^2}{k_0^2}\frac{e^{ik_a\sqrt{z^2+r^2}}}{\sqrt{z^2+r^2}}, \tag{56}$$

where

$$M=-2\pi\rho_0\int_0^R\mathbf{v}_{\rm sc}(r,0)\cdot\mathbf{k}r\,dr$$
$$=-\frac{2\rho_0\omega R^3}{\epsilon^2}\frac{k_0}{k_a}\left(1-\frac{ik_a^2\epsilon^2}{k_0^2}\right)\beta_{00}$$

is the mass flow rate through the hole, evaluated from Eq. (50). Formula (56) displays radiation into a half-space in accordance with Pierce's discussion of flux from a circular aperture in a wall.[16] The factor k_a^2/k_0^2 is seen to be appropriate by writing $\mathbf{v}_{\rm sc}=\nabla\phi_{\rm sc}+\nabla\times\mathbf{\Psi}_{\rm sc}$, whence $p_{\rm sc}/\rho_0 c_0^2=ik_0^2\phi_{\rm sc}/\omega$ whereas the inviscid case has $p/\rho_0 c_0^2=ik_0^2\phi/\omega$.

C. Viscous dissipation

A measure of the viscous dissipation associated with diffraction through the circular aperture can be obtained by comparing the power transmission through the aperture with the power transmission corresponding to the far-field pressure p_∞. The power transmission $\mathcal{P}_a$ through the aperture is given by Eq. (51). The far-field power transmission is obtained by integrating the flux $\mathbf{J}$ in Eq. (49) over the surface of a large hemisphere in the region $z<0$, centered at the origin. If the acoustic field far from the aperture is assumed to be inviscid, then the far-field power transmission $\mathcal{P}_\infty$ is given in terms of the far-field pressure p_∞ in Eq. (54) by[16]

$$\mathcal{P}_\infty=2\pi(r^2+z^2)\frac{|p_\infty|^2}{2\rho_0 c_0}$$
$$=\frac{\omega\rho_0 c_0^2R^3}{\pi\epsilon^4}\frac{|k_a|^2}{k_0^2}k_0^3R^3\left|\left(1-\frac{ik_a^2\epsilon^2}{k_0^2}\right)\beta_{00}\right|^2. \tag{57}$$

Following Salikuddin and Brown,[17] we define the dimensionless power absorption ψ_T as

$$\psi_T=10\log_{10}\frac{\mathcal{P}_\infty}{\mathcal{P}_a}(\text{dB}).$$

Using Eqs. (51) and (57), the power absorption becomes

$$\psi_T=10\log_{10}\left\{\frac{k_0^3R^3}{\pi\epsilon^2}\frac{|k_a|^4}{k_0^4}\frac{\left|\left(1-\frac{ik_a^2\epsilon^2}{k_0^2}\right)\beta_{00}\right|^2}{\Re\left[\left(1-\frac{ik_a^2\epsilon^2}{k_0^2}\right)\beta_{00}\right]}\right\}(\text{dB}). \tag{58}$$

For an inviscid and therefore nondissipative diffraction analysis, the power absorption ψ_T is identically zero, as we have verified using the inviscid results that are derived from the solution of Eq. (45). For the viscous diffraction analysis, the power aborption depends on the dimensionless aperture radius k_0R and the dimensionless viscosity parameter $\epsilon=\sqrt{\omega\nu/c_0^2}$.

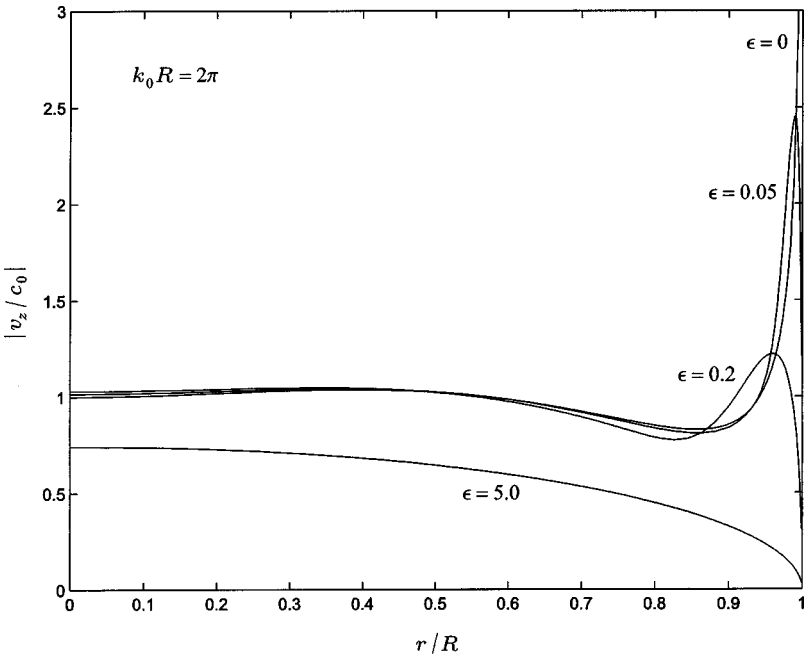

FIG. 2. Magnitude of dimensionless normal velocity component v_z/c_0 in aperture as a function of dimensionless radius r/R for $k_0R=2\pi$.

D. The small aperture limit

In general, the coefficients β_{0m} must be evaluated numerically from the system of linear equations (48). However, when R is small compared to the viscous length $(\nu/\omega)^{1/2}$, the flow through the aperture, having the length scale R, is seen from Eqs. (11) and (12) to be essentially Stokes flow. It is then useful to set $u=(\omega/\nu)^{1/2}R\eta$ in the integrals in Eq. (48), which thus become

$$\beta_{0l}-\sum_{m=0}^{\infty}(2m+3/2)\beta_{0m}\int_0^{\infty}J_{2m+3/2}\left(\sqrt{\frac{\omega}{\nu}}R\eta\right)J_{2l+3/2}\times\left(\sqrt{\frac{\omega}{\nu}}R\eta\right)\left[\frac{i+k_a^2\nu/\omega}{(\eta^2-k_a^2\nu/\omega)^{1/2}-\eta^2(\eta^2-i)^{-1/2}}+2\eta\right]\times\frac{d\eta}{\eta^2}=\frac{1}{3}\delta_{l0}\quad(l\geqslant 0). \tag{59}$$

Evidently, the coefficients $\{\beta_{0m}\}$ now depend weakly on $k_a^2\nu/\omega\simeq\epsilon^2$, with

$$\beta_{0m}=\frac{1}{3}\delta_{m0}+O\left(\frac{\omega}{\nu}R^2\right)\quad(m\geqslant 0), \tag{60}$$

because the matrix with elements

$$\int_0^{\infty}\frac{J_{2m+3/2}(u)J_{2l+3/2}(u)}{u^3}du$$

is tridiagonal.

V. NUMERICAL RESULTS

Numerical results for the case of normal incidence are obtained by truncating the set of linear equations (48) at a finite value N of l and m. The truncation limit N is increased until the coefficients β_{0l} become negligibly small with increasing l. It is found that the required value of N increases with increasing values of the aperture radius R and with decreasing values of the viscosity parameter $\epsilon=\sqrt{\omega\nu/c_0^2}$. For large R and small ϵ, the viscous effects are confined to a small boundary layer near the edge of the aperture, and the modal summations (13) require several terms in order to resolve the velocity and pressure fields in this boundary layer.

Figure 2 shows the magnitude of the dimensionless fluid velocity component $\mathbf{v}_{sc}(r,0)\cdot\mathbf{k}/c_0$, given by Eq. (50), in the aperture as a function of the dimensionless radial coordinate r/R. Note that the incident velocity field in this linear problem is also normalized by c_0. The radius of the aperture is chosen as $k_0R=2\pi$, so that the aperture diameter is equal to two wavelengths of the incident plane wave. Results are displayed for three nonzero values of the viscosity parameter ϵ and for the inviscid case $\epsilon=0$. A nonzero value of the viscosity parameter ϵ eliminates the inviscid singularity at the edge $r=R$. For small values of ϵ, viscous effects are confined to a narrow boundary layer near the edge. For $\epsilon\gg 1$, viscous effects dominate in the aperture, and the velocity distribution becomes that of quasistatic incompressible viscous flow through a circular aperture.[18] This result may be interpreted by noting that $k_0R=(\omega/c_0)R=2\pi$ corresponds to $\epsilon=\sqrt{\omega\nu/c_0^2}=\sqrt{2\pi}/\sqrt{Rc_0/\nu}$, so that $\epsilon\gg 1$ corresponds to small values of the Reynolds number Rc_0/ν.

In Fig. 3 we show the dimensionless power absorption ψ_T as a function of the dimensionless aperture radius k_0R. The solid curves are the results given by Eq. (58) for three different values of ϵ. The power absorption increases rapidly with decreasing aperture size and with increasing values of ϵ.

Figure 3 also contains measured values of the power absorption ψ_T taken from Ref. 9. The aperture in the experimental configuration of Ref. 9 is a circular opening in the end plate of a circular tube. The aperture radius is about one-tenth of the tube radius; we take this to be a reasonable experimental realization of the theoretical model of a circular aperture in an infinite screen. A broadband pulsed plane wave in the tube is generated by a spark source far upstream from the aperture. A pressure transducer in the tube is used to measure the amplitudes of the incident pulse and the pulse

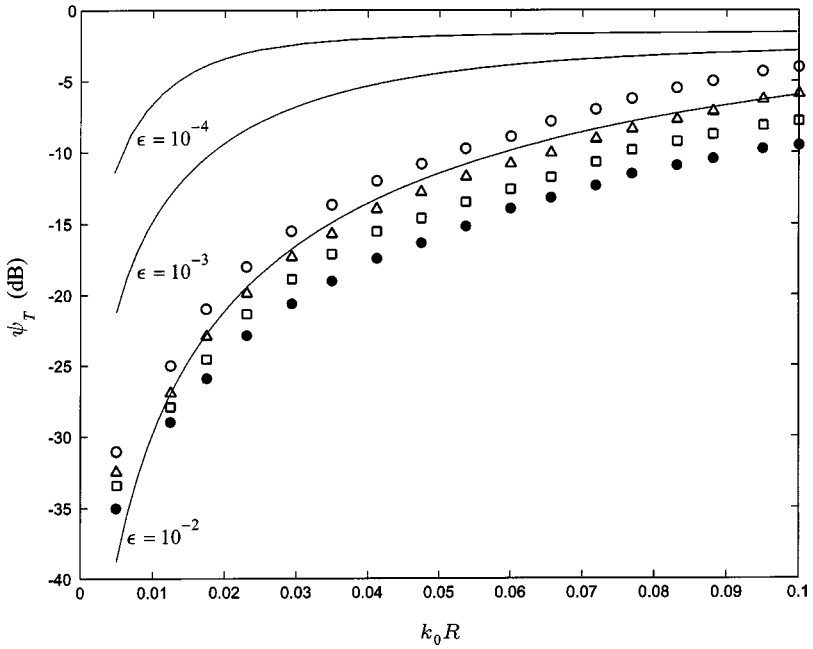

FIG. 3. Power absorption ψ_T as a function of dimensionless aperture radius k_0R. Solid curves are the theoretical linear results derived here. Data points are from the high amplitude aeroacoustic experiments of Ref. 9: (○) 131 dB; (□) 136 dB; (△) 143 dB; (●) 147 dB.

reflected from the tube end plate, and the power transmission through the aperture is computed by considering the difference between the incident energy flux and the reflected energy flux. The far-field power transmission is measured by an array of microphones outside the tube. Frequency domain data are obtained by spectral processing of time domain measurements. The experimental power absorption generally increases as the amplitude of the incident pressure is increased. The incident amplitudes in Fig. 3 are all high enough to induce nonlinear vortex formation in the orifice; flow visualization images of the vortex formation and development are given in Ref. 9.

VI. CONCLUSIONS

For a frequency of $\omega=1000$ rad/s in air, the value of $\epsilon = \sqrt{\omega\nu/c_0^2}$ is approximately 10^{-4}. The results in Fig. 3 thus imply that the theoretical linear dissipation in air at normal acoustic frequencies is small compared to the dissipation produced by the high amplitude nonlinear effects. However, Fig. 3 also shows that linear dissipation becomes comparable to the measured experimental values for $\epsilon \approx 10^{-3}$ and $k_0R \approx 0.1$. For ultrasonic devices that operate at low amplitude levels, the linear viscous effects considered here may represent a significant dissipation mechanism.

Although the analysis in Secs. II and III is valid for arbitrary angle of incidence, we have focused on numerical results for the case of normal incidence, where the relatively simple results for power absorption can be compared with experiment. Viscous effects associated specifically with tangential or grazing flow are distinct and interesting phenomena that will be considered in a subsequent paper on the complementary problem of viscous diffraction by a circular disk.

[1] A. M. J. Davis and R. J. Nagem, "Acoustic diffraction by a half plane in a viscous acoustic medium," J. Acoust. Soc. Am. **112**, 1288–1296 (2002).
[2] R. D. Spence, "The diffraction of sound by circular disks and apertures," J. Acoust. Soc. Am. **20**, 380–386 (1948).
[3] H. Lamb, *Hydrodynamics* (Dover, New York, 1945), Sec. 299.
[4] U. Ingard and S. Labate, "Acoustic circulation effects and the nonlinear impedance of orifices," J. Acoust. Soc. Am. **22**, 211–218 (1950).
[5] U. Ingard and H. Ising, "Acoustic nonlinearity of an orifice," J. Acoust. Soc. Am. **42**, 6–17 (1967).
[6] I. J. Hughes and A. P. Dowling, "The absorption of sound by perforated linings," J. Fluid Mech. **218**, 299–335 (1990).
[7] M. S. Howe, "On the theory of unsteady high Reynolds number flow through a circular aperture," Proc. R. Soc. London, Ser. A **366**, 205–335 (1979).
[8] M. S. Howe, "Damping of sound and vibration by flow nonlinearity in the apertures of a perforated elastic screen," IMA J. Appl. Math. **55**, 221–242 (1995).
[9] M. Salikuddin and W. H. Brown, "Nonlinear effects in finite amplitude wave propagation through orifice plate and perforated plate terminations," J. Sound Vib. **139**, 383–405 (1990).
[10] G. N. Watson, *A Treatise on the Theory of Bessel Functions*, 2nd ed. (Cambridge University Press, New York, 1995), Sec. 2.1.
[11] G. K. Batchelor, *An Introduction to Fluid Dynamics* (Cambridge University Press, New York, 1967), Sec. 3.3.
[12] C. J. Tranter, *Integral Transforms in Mathematical Physics* (Wiley, New York, 1966), Sec. 8.2.
[13] I. N. Sneddon, *Mixed Boundary Problems in Potential Theory* (North-Holland, Amsterdam, 1966), Sec. 4.6.
[14] B. Noble, *Methods Based on the Wiener-Hopf Technique*, 2nd ed. (Chelsea, New York, 1988), Sec. 1.6.
[15] A. Erdélyi, *Asymptotic Expansions* (Dover, New York, 1956), Sec. 2.9.
[16] A. D. Pierce, *Acoustics* (American Institute of Physics, New York, 1994), Secs. 5-3, 7.5.
[17] M. Salikuddin, "Acoustic behavior of orifice plates and perforated plates with reference to low-frequency sound absorption," J. Sound Vib. **139**, 361–382 (1990).
[18] R. A. Sampson, "On Stokes' current function," Philos. Trans. R. Soc. London, Ser. A **182**, 449–518 (1891).

Jet forking driven by pipe tone

B. Karthik, S. R. Chakravarthy, and R. I. Sujith
Department of Aerospace Engineering, Indian Institute of Technology Madras, Chennai-600 036, India

(Received 12 December 2002; revised 17 February 2003; accepted 18 March 2003)

The present work deals with an experimental investigation of flow of air through a square-edged circular orifice at the downstream end of a circular duct. Self-excited acoustic oscillations at the natural duct modes are observed for certain flow velocities when the orifice is sufficiently thick. For a specific Reynolds number based on the orifice diameter and the mean jet velocity ($9150<\mathrm{Re}<9850$), the jet forks into two trains, with the alternating vortices falling into the same branch of the forked train. Whereas this phenomenon has been reported earlier to have occurred when the density ratio of the jet is less than 0.72, the present results show that it is possible for a jet having the same density as the ambient atmosphere. The jet forking is coincident with jump in the acoustic frequency from one natural acoustic mode to another with comparable amplitudes of both the modes. © *2003 Acoustical Society of America.* [DOI: 10.1121/1.1573636]

PACS numbers: 43.28.Ra, 43.50.Ed [MSH]

I. INTRODUCTION

The subject of the present work is the flow of air through a square-edged circular orifice of finite thickness at the end of a circular duct. Audible, sharp tones, referred to as pipe tone, are excited under certain flow and geometric conditions in this case. Pipe tones are not produced outside a critical range of thickness of the orifice for a range of mean flow velocity in the duct. The excited tones also jump from one mode to the other as the flow velocity is varied over a wide range for a given geometry.

The occurrence of these tones has been attributed to the formation and periodic shedding of vortices and their interaction with the duct resonance system.[1] Anderson[1–5] studied this problem extensively, and attributed the excitation of audible tones to periodic fluctuations in the jet cross-sectional area at the orifice.

Audible tones are excited even in the absence of the duct; this phenomenon is referred to as jet tone.[4] It is believed that the mechanism that causes the jet tone is basically the same as the one that causes the pipe tone. The difference lies in the fact that the resonance column of the pipe influences the jet tone to change its frequency. It is hypothesized that the vortex shedding is influenced by the duct acoustics in such a way that a rolled up vortex sheds at the time when the acoustic velocity changes direction against the mean flow, as shown in the studies on pipe side branch tone.[6] In general, it is found that the pipe tone occurs more readily and over a larger range of flow conditions than the jet tone.

The low frequency aeroacoustic response of orifices has recently been predicted theoretically with consideration of the Mach number dependence of the vena contracta, in terms of the scattering matrix connecting the acoustic pressure amplitudes on either side of the orifice, which is treated as a discontinuity.[7] However, the region of sound production lies across the thickness of the orifice. Howe points out that axisymmetric disturbances are generated at the upstream edge of the orifice, which produce sound by the diffraction of the near-field pressure distribution at the downstream edge.[8] A number of other recent investigations related to sound production involving vortex shedding or vorticity fluctuations have been reported in the context of gas flows in pipe systems with closed side branches,[9] vortex-nozzle interactions,[10] and sharp edged open channel ends.[11] In these works, the vortex shedding behavior or vorticity variation has been simulated by means of point vortex method, a single panel method, or the vortex blob method in the two-dimensional potential flow framework in order to retain the simplicity in the analysis, and the Powell–Howe approach[12–14] has been adopted to predict the acoustic power generated. This requires a good physical understanding of the nature of vorticity fluctuation under conditions that excite high amplitude sound.

In the case of the problem considered here, the response of the shear layer originating from the separation point at the upstream edge of the orifice to the self-excited oscillations governs the sound production, and is being optically investigated at this laboratory. However, as a result of this behavior, the near-field vortex roll-up in the free jet just downstream of the orifice is altered by the self-excitation of high amplitude acoustic oscillations in the duct. The vortex roll-up behavior is almost symptomatic of the acoustic excitation inside the duct. The focus of the present paper, specifically, is the phenomenon of jet forking into two trains of vortices at a certain flow Reynolds number coincident with transition of the excited acoustic oscillations from one mode to the other. This has indeed been reported by Anderson,[5] but without any time-resolved visualization and correlation with the acoustic characteristics of the pipe tone. A similar behavior is reported in the absence of duct acoustic resonance with a helium jet issuing out of a nozzle into air.[15,16] This is accompanied by self-excitation of jet tone. Such a phenomenon is reported to be observed only for a density ratio of the jet to the ambient less than 0.72. The present work demonstrates that when pipe tones are excited, it is possible to observe jet forking when the density ratio is unity.

II. EXPERIMENTAL METHOD

A schematic of the experimental setup used in the present study is shown in Fig. 1. It consists of a test section,

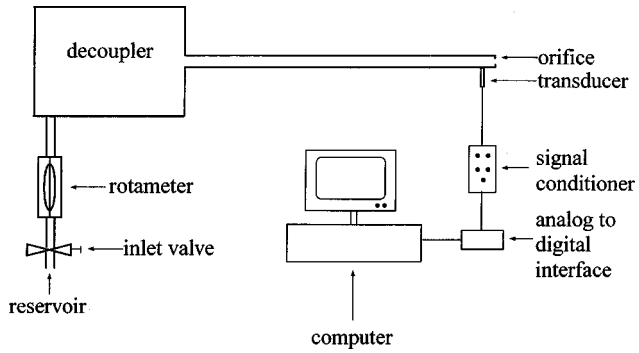

FIG. 1. Schematic of the experimental setup.

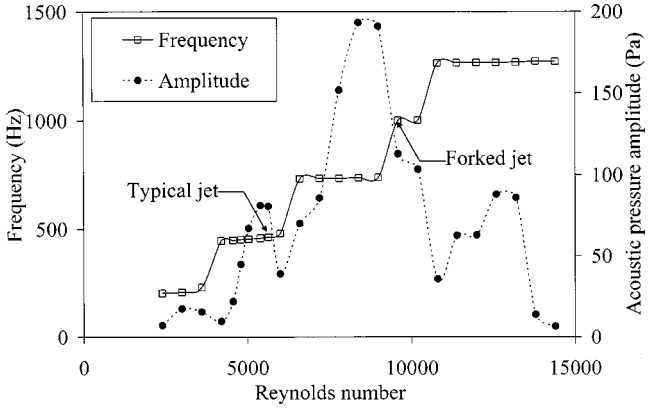

FIG. 2. The variation of the dominant acoustic frequency and the corresponding pressure amplitude with Reynolds number.

which is a circular duct (internal diameter = 50 mm, length = 600 mm) made of mild steel. The orifice had an internal diameter of 10 mm and a thickness of 5 mm. The test section is connected to the air line through an acoustic decoupler with an internal diameter of 300 mm and a length of 270 mm. The decoupler damps out the upstream flow disturbances and acts as an open end for the acoustic oscillations in the duct. One end of the test section is connected to the decoupler and the other end is open to the atmosphere.

The acoustic field in the duct was measured using a piezo-electric transducer (PCB make, model no. 103A12) with a sensitivity of 539 mV/psi (0.08 mV/Pa). The transducer was mounted flush with the wall at a distance of 50 mm upstream of the orifice in the duct. The signals sensed by the PCB transducer could be amplified up to 100 times by a PCB signal conditioner (model no. 441A101). Rotameters with an accuracy of 2% of the full scale were used for volume flow rate measurements. The mean jet velocity at the orifice plane was obtained as the measured volume flow rate measurements divided by the orifice area. The Reynolds number was calculated using the mean jet velocity and the orifice diameter.

Data was acquired on a computer through a software-driven analog-to-digital converter card. Fast Fourier transform (FFT) of the signal was performed to determine the frequency component. In the present work, data was acquired at a sampling frequency of 100 kHz for 0.25 s, with a frequency resolution of 4 Hz.

Instantaneous Mie scattering[17] images of the air jet were acquired using a digital CCD camera with a 12-bit resolution. The jet was seeded by oil droplets generated by an

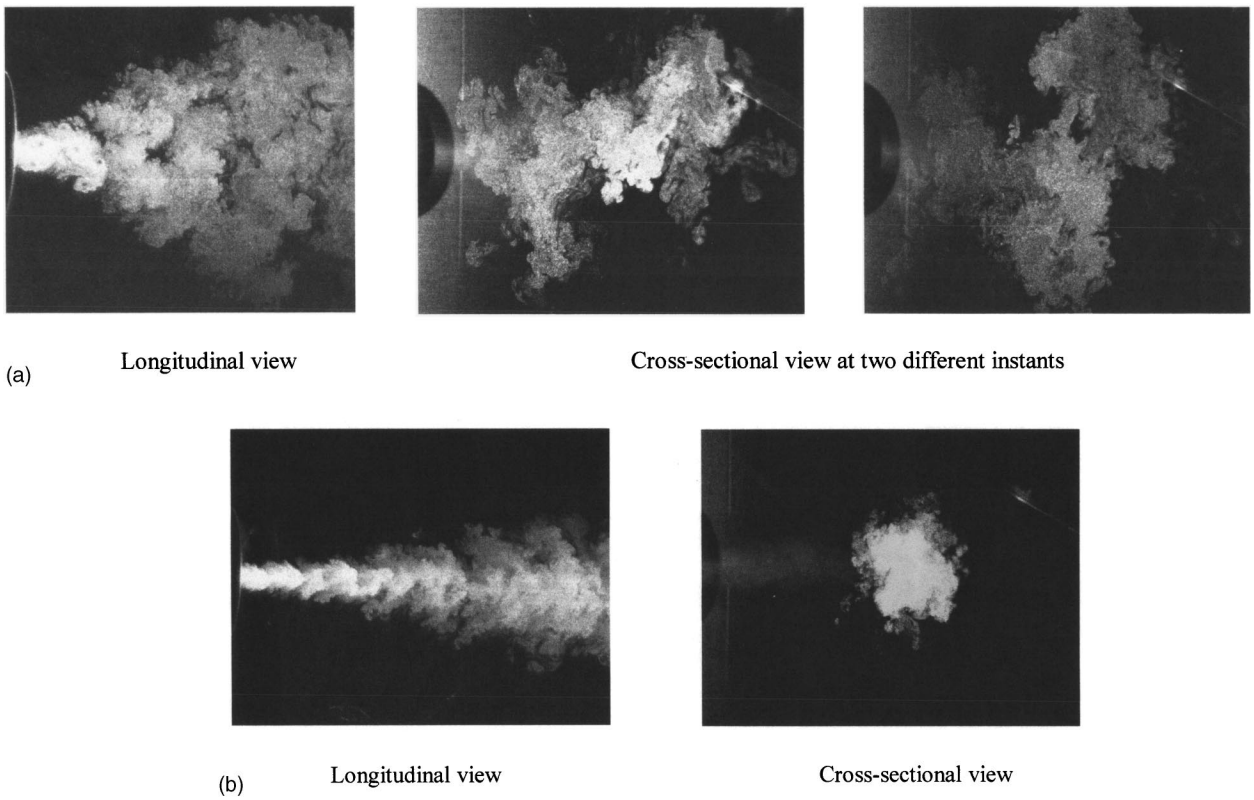

FIG. 3. Planar Mie scattering image of air jet (a) with forking, jet Reynolds number = 9500; (b) typical jet, jet Reynolds number = 5700.

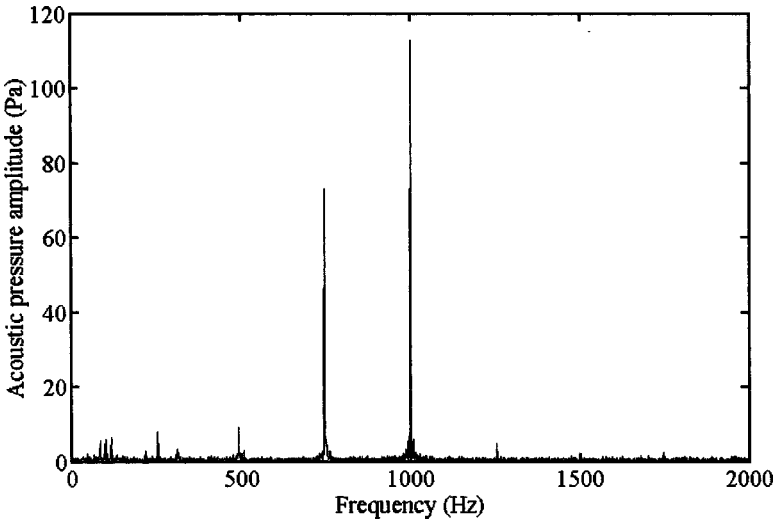

FIG. 4. Fast Fourier transform of the acoustic signal during forking, test conditions same as in Fig. 3(a).

aerosol generator with Laskin nozzles.[18] Olive oil was used in the aerosol generator. Droplet sizes less than 1 μm could be achieved with this aerosol generator.[18] An Nd:YAG pulsed laser with a second harmonic generator (wavelength $=532$ nm) was used to create an instantaneous (6 ns) light sheet for illumination.

III. RESULTS AND DISCUSSION

Figure 2 shows the variation of the dominant acoustic frequency and the corresponding amplitude with the mean jet velocity. As mentioned earlier, the frequency shows a steplike variation with abrupt jumps from one duct mode to the next higher mode. The variation in frequency is similar to the one reported in an earlier paper.[1] The amplitude distribution shows a peak value for any given duct mode. The values are lower during the jump.

For a Reynolds number between 9150 and 9850 the jet issuing out of the orifice is atypical. The jet splits up into two distinct circular vortex trains that make a considerable angle in excess of 60° with each other, with the alternate vortices falling into the same branch of the forked train. This condition is marked in Fig. 2, and condition corresponding to a typical jet for which flow visualization is presented below is also indicated in the figure for comparison. Mie scattering images in planes along and across the jet at this Reynolds number are shown in Fig. 3(a). A typical air jet in the absence of forking but with self-excitation of relatively loud acoustic pressure amplitude (80 Pa) is shown in Fig. 3(b) for comparison. The cross-sectional images in Fig. 3(a) show the rotation of the forked train about the duct axis. Anderson hypothesizes the occurrence of this phenomenon without the support of instantaneous visualization.[5] In the present experiments, the acoustic pressure signal shows the presence of two frequencies of comparable amplitude under these conditions (see Fig. 4). The splitting of the jet occurs during the shift in frequency from one mode to the next higher mode. However, forking does not occur for all such mode shifts. As mentioned earlier, the self-excitation of jet tone has been previously observed to be accompanied by a similar behavior for a jet density ratio of less than 0.72.[15,16]

The present results indicate that the density ratio is not the only parameter for such a behavior. The excitation of sound near the orifice due to duct resonance could be the cause of this phenomenon. In the present case, the mechanism of self-excitation could be due to the periodic oscillations of the vena contracta[1] associated with the shedding of vortices. The density ratio of the jet appears to have a secondary role on the process of excitation. A similar phenomenon of blooming has been reported in the presence of external excitation.[19] Combined axial and azimuthal external excitation of a jet issued into a quiescent flow produced blooming vortex interactions. The vortex rings, generated one after the other in a short time, travels along the jet axis and then separates. However, in the phenomena reported in the current work, the vortex rings fork into two rotating trains right at the jet exit, and the acoustic oscillations are self-excited.

ACKNOWLEDGMENTS

This work was partly supported by the Vikram Sarabhai Space Center of the Indian Space Research Organization, with M. S. Padmanabhan as the technical monitor, and partly by the Defense Research and Development Organization, with V. Siddharta as the technical monitor.

[1] A. B. C. Anderson, "Dependence of pfeifenton (pipe tone) frequency on pipe length, orifice diameter and gas discharge pressure," J. Acoust. Soc. Am. **24**, 675–681 (1952).
[2] A. B. C. Anderson, "Dependence of the primary pfeifenton (pipe tone) frequency on pipe-orifice geometry," J. Acoust. Soc. Am. **25**, 541–545 (1953).
[3] A. B. C. Anderson, "A circular-orifice number describing dependency of primary pfeifenton frequency on differential pressure, gas density, and orifice geometry," J. Acoust. Soc. Am. **25**, 626–631 (1953).
[4] A. B. C. Anderson, "Vortex-ring structure-transition in a jet emitting discrete acoustic frequencies," J. Acoust. Soc. Am. **28**, 914–921 (1956).
[5] A. B. C. Anderson, "Structure and velocity of the periodic vortex-ring flow pattern of a primary pipe tone jet," J. Acoust. Soc. Am. **27**, 1048–1053 (1955).
[6] A. Hirschberg, J. C. Bruggeman, A. P. J. Wijnands, and N. Smits, "The "whistler nozzle" and horn as aero-acoustic sound sources in pipe systems," Acustica **68**, 157–160 (1989).
[7] P. Durrieu, G. Hofmans, G. Ajello, R. Boot, Y. Auregan, A. Hirschberg, and M. C. A. M. Peters, "Quasisteady aero-acoustic response of orifices," J. Acoust. Soc. Am. **110**, 1859–1872 (2001).

[8] M. S. Howe, *Acoustics of Fluid-structure Interactions* (Cambridge U.P., Cambridge, 1998), pp. 485–486.
[9] P. C. Kriesels, M. C. A. M. Peters, A. Hirschberg, A. P. J. Wijnands, A. Iafrati, G. Riccardi, R. Piva, and J. C. Bruggeman, ''High amplitude vortex-induced pulsations in gas transport system,'' J. Sound Vib. **184**, 343–368 (1995).
[10] S. J. Hulshoff, A. Hirschberg, and G. C. J. Hofmans, ''Sound production of vortex-nozzle interactions,'' J. Fluid Mech. **439**, 335–352 (2001).
[11] M. C. A. M. Peters and A. Hirschberg, ''Acoustically induced periodic vortex shedding at sharp edged open channel ends: simple vortex models,'' J. Sound Vib. **161**, 281–299 (1993).
[12] A. Powell, ''Theory of vortex sound,'' J. Acoust. Soc. Am. **36**, 177–195 (1964).
[13] M. S. Howe, ''Contributions to the theory of aerodynamic sound, with application to excess jet noise and the theory of the flute,'' J. Fluid Mech. **71**(1), 625–674 (1974).
[14] M. S. Howe, ''On the absorption of sound by turbulence and other hydrodynamic flows,'' IMA J. Appl. Math. **32**, 187–209 (1984).
[15] C. D. Richards, B. D. Breuel, R. P. Clark, and T. R. Troutt, ''Concentration measurements in a self-excited jet,'' Exp. Fluids **21**, 103–109 (1995).
[16] P. A. Monkewitz, D. W. Bechert, B. Barsikow, and B. Lehmann, ''Self-excited oscillations and mixing in a heated round jet,'' J. Fluid Mech. **213**, 611–639 (1990).
[17] H. C. van de Hulst, *Light Scattering by Small Particles* (Dover, New York, 1981).
[18] M. C. Raffel, C. E. Willert, and J. Kompenhans, *Particle Image Velocimetry: A Practical Guide* (Springer-Verlag, Berlin, 1998), Vol. 16, pp. 20–22.
[19] J. Z. Wu, A. D. Vakili, and J. M. Wu, ''Review of the Physics of enhancing vortex lift by unsteady excitation,'' Prog. Aerosp. Sci. **28**(2), 73–131 (1991).

Examination of time-reversal acoustics in shallow water and applications to noncoherent underwater communications

Kevin B. Smith,[a] Antonio A. M. Abrantes, and Andres Larraza
Department of Physics, Naval Postgraduate School, Monterey, California 93943

(Received 1 October 1999; revised 12 September 2002; accepted 27 February 2003)

The shallow water acoustic communication channel is characterized by strong signal degradation caused by multipath propagation and high spatial and temporal variability of the channel conditions. At the receiver, multipath propagation causes intersymbol interference and is considered the most important of the channel distortions. This paper examines the application of time-reversal acoustic (TRA) arrays, i.e., phase-conjugated arrays (PCAs), that generate a spatio-temporal focus of acoustic energy at the receiver location, eliminating distortions introduced by channel propagation. This technique is self-adaptive and automatically compensates for environmental effects and array imperfections without the need to explicitly characterize the environment. An attempt is made to characterize the influences of a PCA design on its focusing properties with particular attention given to applications in noncoherent underwater acoustic communication systems. Due to the PCA spatial diversity focusing properties, PC arrays may have an important role in an acoustic local area network. Each array is able to simultaneously transmit different messages that will focus only at the destination receiver node. [DOI: 10.1121/1.1570831]

PACS numbers: 43.30.Bp [SAC-B]

I. INTRODUCTION

Traditionally, applications for underwater acoustic (UWA) communication systems were almost exclusively military. In the last 10 years there has been a growing need for UWA communication systems for commercial applications. As a consequence, an increase in research and development of UWA communication systems has occurred. Applications that have received much attention lately are secure military communications, pollution monitoring, and remote control in off-shore oil industry and video telemetry, to name a few. Many of the applications being developed are now calling for near real-time communication with submarines and remotely operated vehicles. As the UWA communications channel has limited bandwidth available, the bandwidth efficiency becomes an important issue for a UWA communication system. There have been several excellent reviews of recent advances in underwater communications and telemetry presented by Baggeroer (1984), Catipovic (1990), Coates *et al.* (1993), and Stojanovic (1996).

The shallow water acoustic communication channel is characterized by strong signal degradation caused by multipath propagation and high spatial and temporal variability of the channel conditions. In any underwater acoustic environment there is limited bandwidth available due to transmission loss which increases with both frequency and range. This is a major constraint in underwater communication systems design. The most important of the difficulties encountered in shallow water acoustics digital communications is considered to be the time-varying multipath propagation. This leads to a requirement for powerful and reliable receiver algorithms for signal processing in shallow water environments. In recent years there has been a large effort made in the design of techniques and algorithms to overcome this problem.

In a digital communication system, multipath propagation causes intersymbol interference (ISI). As an example, in a medium-range, 6-km-long, shallow water (200 m) channel, a typical value for multipath delay spread is 30 ms. If the communication system is signaling at 1 kilosymbol per second, the ISI will extend over 30 symbols, making it difficult for a receiver to recover the original message.

In shallow water regions, multipath is primarily due to reflections at the surface and bottom of the channel but can also be caused by refracted paths under certain environmental conditions. The multipath structure depends on the channel geometry, sound speed structure, frequency of transmitted signals, and on the source and receiver locations. On a small time scale, the most important contribution to channel variability is surface scattering due to waves producing time-varying multipaths. On a larger time scale, channel variations are due to a variety of effects including internal waves, temperature gradients, and currents in the sound speed profile. The temporal variability is also frequency dependent.

The ISI and strong phase fluctuations caused by multipath propagation and temporal channel variability have in the past led to system designs based exclusively on noncoherent detection methods. These systems have poor spectral efficiency and low signaling rates and are still in use when robustness is the principal requirement in system design. To treat the ISI problem, these systems insert delay times between consecutive pulses to ensure that all the reverberation and multipath structure will vanish before each subsequent pulse is received (Stojanovic, 1996). This can significantly reduce the available data throughput.

In recent years, the feasibility of bandwidth-efficient phase-coherent modulation techniques for UWA communications has been proven (Stojanovic *et al.*, 1993, 1994, 1995).

[a]Electronic mail: kbsmith@nps.navy.mil

Several systems have been proposed and implemented using differential and purely coherent detection methods, thereby increasing the data throughput. However, these systems must still treat ISI in the received signal and be able to track any phase variations due to changing channel conditions. Typically these systems employ either some form of array processing, for exploitation of spatial diversity, or equalization or a combination of both.

Array processing at both the source and receiver end have been used for multipath suppression. Coates (1993) and Galvin and Coates (1994) describe an approach that uses transmitter arrays to excite only a single path of propagation. However, long arrays are required and small errors in positioning can degrade performance. In general, this technique was found to be more effective at shorter ranges.

Another approach (Howe *et al.*, 1994; Tarbit *et al.*, 1994; Henderson *et al.*, 1994) is based on adaptive beamforming at the receiver end. It uses a least mean squares (LMS) type of algorithm to adaptively steer nulls in the direction of the surface reflected wave. Naturally, as the multipath structure increases in range, it was found to decrease in performance as the range increases in relation to depth (Tarbit *et al.*, 1994). In order to enhance the performance of the beamformer, an equalizer was proposed by Howe *et al.* (1994) of a decision-feedback type. This system operates under a LMS algorithm with low computational requirements, allowing real-time adaptation at the symbol rate.

A different approach based on purely phase-coherent detection methods is described by Stojanovic *et al.* (1993, 1994, 1995). These methods attempt to counter the effect of phase variations and ISI by combining joint synchronization and equalization. It incorporates spatial signal processing based on combining diversity and a fractionally spaced decision-feedback equalization with a recursive least squares (RLS) algorithm.

From the previous examples of communication systems, it is obvious that complex systems and high computational requirements are needed to handle channel distortion and ISI encountered in the underwater acoustic channel. Such systems can exceed the speeds of available hardware. At high symbol rates, the long ISI requires large adaptive filters, therefore increasing the computational complexity.

The aim of the present paper is to provide an original and relatively simple algorithm to overcome the ISI problem in a shallow water channel. This solution is not based on sophisticated processing algorithms but is equivalent to matched field processing with the filter matched to the impulse response of the ocean. The low computational load required in this technique is due to the fact that it uses the ocean itself as the matched filter for the acoustic propagation between source and receiver. By using rather simple signal processing at the transmitter (suitable for real-time implementation) the multipath structure at the receiver end is virtually absent, allowing a reduced-complexity receiver structure.

This technique uses time-reversal acoustic (TRA) arrays to generate a spatio-temporal focus of acoustic energy at the receiver location, eliminating (or greatly reducing) distortions introduced by channel propagation. The application of TRA to the underwater communications problem has previously been suggested by Jackson and Dowling (1992) and Kuperman *et al.* (1998). The first known application of TRA which developed a signaling scheme for communication purposes was introduced by Abrantes *et al.* (1999). This paper provides the details of much of that work.

The analysis presented here is based purely on numerical modeling results. The numerical model used throughout is the Monterey–Miami Parabolic Equation (MMPE) acoustic propagation model (Smith, 2001), an upgraded version of the University of Miami Parabolic Equation (UMPE) model (Smith and Tappert, 1994). Both versions are available freely on the web at http://oalib.njit.edu/pe.html.

It should be noted that experimental work has been performed which confirms the usefulness of this approach (Heinemann, 2000). The results from that work are presented in a companion article. Additional numerical and experimental work are on-going in the development of more sophisticated signaling techniques.

The remainder of this paper is organized as follows. Section II presents a brief overview of time-reversal acoustics theory. In particular it analyzes the case of time-reversal acoustics in a range-independent channel and a more general static range-dependent channel. In these ideal situations, closed-form solutions for the field at the focus have previously been developed, and some focusing properties can be inferred and may be extrapolated for more general environments. In Sec. III the focusing properties of the time-reversal array are studied through MMPE numerical simulations. It shows how the time-reversal array focusing properties change when the array operates at different carrier frequencies, and when the array length or the array element spacing is altered. Also presented are the frequency characterization of the channel and examples of how range shifting of the focus location can be attained. Section IV describes applications of time-reversal arrays to UWA communications and Sec. V presents a summary of conclusions and identifies some aspects of TRA communications modeling requiring further research.

II. THEORETICAL BACKGROUND AND NUMERICAL EXAMINATIONS

Much of the theoretical development on the phenomenon of time-reversal acoustics has been presented by Jackson and Dowling (1991, 1992), Kuperman *et al.* (1998), and Song *et al.* (1998). The reader is referred to those papers for a more thorough treatment of TRA theory. Each of these previous papers has presented numerical simulations examining various features of the time-reversed field at the position of the focus, including the design of the array. In this section, we shall present specific examples of the focusing properties for our simulated environment and the effects of various array geometries and the implications for communications.

For simplicity, consider a waveguide with pressure-release surface and rigid bottom as depicted in Fig. 1 where the axis from o' to o will be the reference axis for propagation from the receiver array to the source. From the axis location in Fig. 1 the coordinates are related by $z' = z$ and

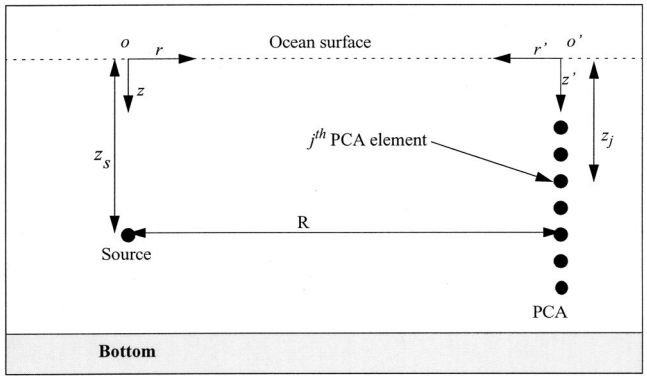

FIG. 1. Waveguide geometry.

$r'=R-r$. In this environment the frequency-domain wave equation, or Helmholtz equation, for a range-independent waveguide can be written as (e.g., Jensen *et al.*, 1994)

$$[\nabla^2+k^2(z)]G(r,z|z_s,\omega)=-\delta(r)\,\delta(z-z_s), \tag{1}$$

where $k(z)=\omega/c(z)$ is the acoustic wavenumber for a waveguide with sound speed $c(z)$, ω denotes the angular frequency, and $G(r,z|z_s,\omega)$ is the frequency-dependent Green's function in cylindrical coordinates at location (r,z) due to a point source located at range $r=0$ and depth $z=z_s$. Note that the depth z is taken positive downward.

From a linear systems theory point of view, the Green's function $G(r,z|z_s,\omega)$ represents the ocean impulse response between a point source located at range $r=0$ and depth $z=z_s$ and a point receiver at location (r,z). It can easily be shown (e.g., Jensen *et al.*, 1994) that $G(r,z|z_s,\omega)$ satisfies the principle of reciprocity,

$$\rho(\vec{r}_s)G(\vec{r}_j|\vec{r}_s,\omega)=\rho(\vec{r}_j)G(\vec{r}_s|\vec{r}_j,\omega), \tag{2}$$

where $\vec{r}_s$ represents the position of a point source and $\vec{r}_j$ indicates the position of a point receiver, i.e., the jth element of the array. Since the density is nearly constant throughout the ocean, this leads to reciprocity of the acoustic field itself. The reciprocity theorem plays a fundamental role in time-reversal acoustics because it implies that the field from an array element propagates to the source location in a reciprocal way as the field from the source to the array element. It is important to note, however, that "time-reversal" only applies to the manipulation of the signal at the time-reversal array elements, and does not imply a reversibility of the propagation itself. This differentiates reciprocity from reversibility. Hence, higher losses incurred along some paths more than others will not be undone via a time-reversal approach.

If a source at position $r=0$, $z=z_s$ transmits a pulse $s(t)$, the jth element of the PCA a distance $r=R$ away records the time-domain signal $p(R,z_j,t)$. The total field back at the original source location, $(r'=0,z_s)$, is given by the superposition of the field produced by each individual array element, which in the time-domain is given by (Kuperman *et al.*, 1998)

$$p_{\mathrm{TRA}}(0,z_s,t)=\frac{1}{(2\pi)^2}\int\left(\sum_{j=1}^{J}\left[\int g_{t'+t''}(R,z_j|z_s,\omega)\times g_{t'}(R,z_s|z_j,\omega)\,dt'\right]s(t''-t+T)\right)dt'', \tag{3}$$

where $g_{t'+t''}(R,z_j|z_s)$ and $g_{t'}(R,z_s|z_j)$ are the time-domain representations of the Green's function. Note that in a time-invariant environment, reciprocity states that these are identical.

The following observations have been made about Eq. (3) (Kuperman *et al.*, 1998):

(i) The integral over t' defines the autocorrelation of the Green's function between the source and the jth element of the PCA. This operation is equivalent to a matched-filter which compresses the time elongation due to multipaths, forming a temporal focus.
(ii) The sum over the array elements is a form of spatial matched filtering, forming a spatial focus.
(iii) The sidelobes of the matched filters for each array element tend to cancel with the sum over the array elements. This is also analogous to broadband matched-field processing results (Brienzo and Hodgkiss, 1993) which further improves temporal focusing.
(iv) The integral over t'' is a convolution of each matched-filtered response with the delayed and time-reversed transmitted pulse. Thus, a slightly degraded and time-reversed version of the original signal is received.

Although the numerical solutions presented in this paper are generated by a parabolic equation model, it is useful in the discussion to consider the field in the context of normal modes. The solutions are then defined in terms of depth-dependent eigenfunctions, or normal modes, and range-dependent Hankel functions. In the frequency domain, Kuperman *et al.* (1998) have shown that a modal decomposition of the time-reversed field in a range-independent environment is given by

$$P_{\mathrm{TRA}}(0,z_s,\omega)\cong\frac{S^*(\omega)e^{i\omega T}}{8\pi RK}\sum_m\frac{\Psi_m(z)\Psi_m(z_s)}{\rho(z_s)}=\frac{S^*(\omega)e^{i\omega T}}{8\pi RK}\,\delta(z-z_s), \tag{4}$$

where $S(\omega)$ is the Fourier representation of the initial transmitted signal $s(t)$, $\Psi_m(z)$ are the depth-separated normal modes of the waveguide, K is a typical horizontal wavenumber component of the propagating modes, $\rho(z_s)$ is the density at the original source location, and $\delta(z-z_s)$ is the Dirac delta function centered at the source location.

This equation shows the vertical focusing performed by the PCA at the range of the original source location due to the closure property of the modes. If the array has only a few elements and cannot properly sample the propagating modes, one can conclude that this focusing will be degraded. As will

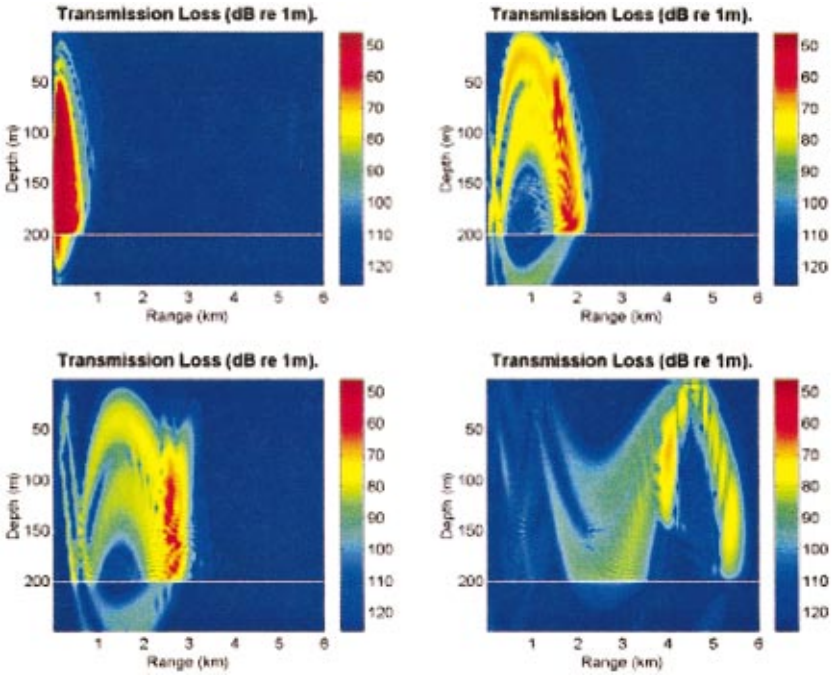

FIG. 2. Single pulse propagation in a shallow water channel.

be confirmed in this paper, numerical simulations indicate that even with a small array aperture, a good quality of temporal focus can still be achieved.

If the environment were range dependent, Kuperman *et al.* (1998) have shown that the time-reversed pressure field satisfies a similar expression. Furthermore, they point out that the focus is independent of the exact nature of the range-independent environment between the source and the PCA. The focus depends only on the local properties of the water column and the sea floor. Therefore, this suggests that, neglecting absorption losses and cylindrical spreading, the focus pattern is independent of the distance between the source and the array. Thus all the general features of a communication scheme based on time-reversal acoustics discussed in this paper should also exist in more general, range-dependent environments.

One should bear in mind, however, that losses due to absorption and scattering are expected to cause attenuation of higher-order modes. As a consequence, the focus is expected to become more blurry than that in the previous ideal lossless situation. Furthermore, as the distance between the array and the focus increases, the focus becomes blurrier due to the strong range and mode number dependence of attenuation. Such influences will not be specifically treated in this analysis.

Figures 2–4 present numerical modeling results of acoustic pulse propagation from the source to the time-reversal array (forward propagation) and the propagation from the time-reversal array to the source (backward propagation). Figure 2 illustrates single pulse propagation from a source located 150 m deep at the origin to a vertical array 6 km away. This pulse has a carrier frequency of 800 Hz and its spectrum spans over 100 Hz with a -3 dB bandwidth of 36.6 Hz. The complete description of this range-independent channel can be found in Sec. III. Figure 3 illustrates the transmitted signal and the multipath arrival structure of the recorded signal by the 150-m-deep array element. Figure 4 represents four snap-shots of the wavefield propagation from the PCA to the source. The spatial focusing at the source location is clearly observable in the lower left panel. Due to the time-reversal transformation at the PCA, the received signal has the time-reversed signature of the signal which was transmitted originally. Similar simulations examining the spatial structure of the focus region have previously been performed by Kuperman *et al.* (1998) and Song *et al.* (1998).

As stated earlier, this phase-conjugation process takes advantage of spatial reciprocity which is a property of wave propagation in a medium with stable refractive index. In general, reciprocity requires a static environment. TRA focusing requires spatial reciprocity in order to construct the exact

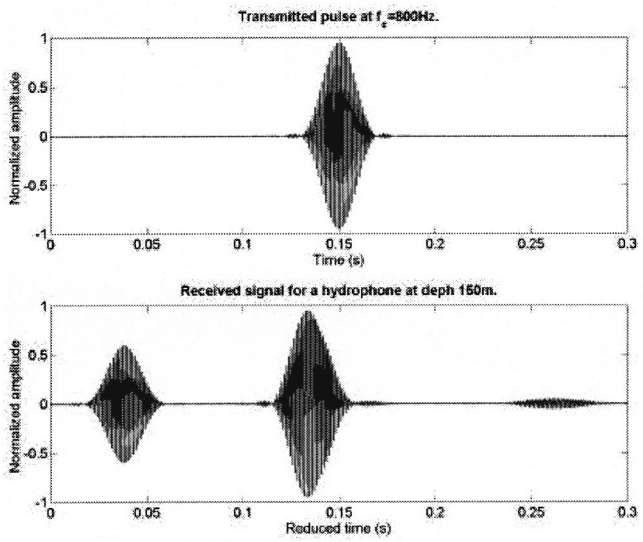

FIG. 3. Transmitted signal from point source 150 m deep (upper panel) and received signal on a single array element at range 6 km and depth 150 m (lower panel).

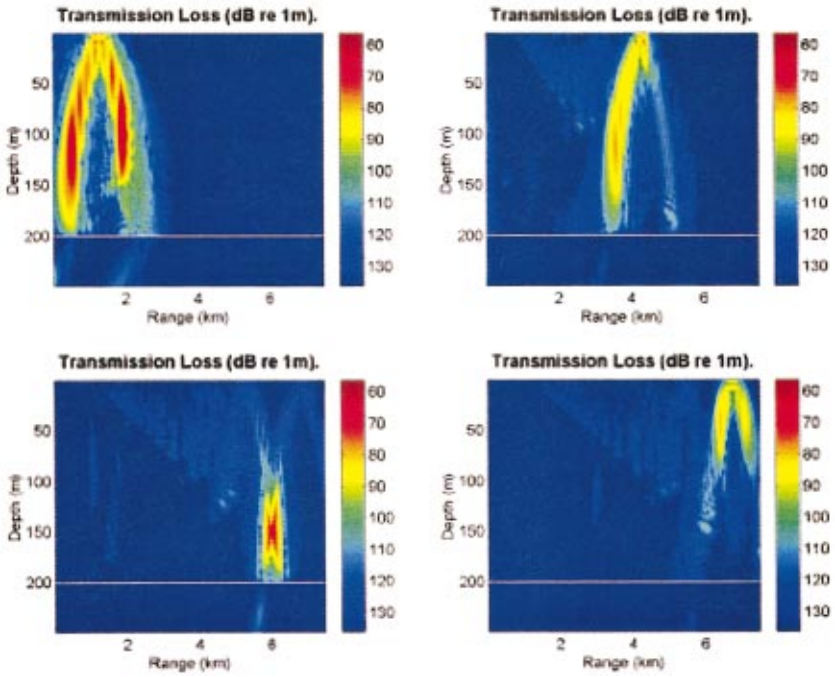

FIG. 4. Time-reversed propagation from the PCA. Note focus appears at original source location, range 6 km, depth 150 m.

time-reversed wavefield that will focus at the original source location. In this way, all the PCA elements transmit back to the source in a reciprocal fashion, and the time-reversed wavefield will have the multipath structure undone at the source location.

Since the PCA only ''learns'' the medium structure that is imprinted in the incoming signal at the instant of its reception, it cannot compensate for refractive fluctuations that occur after reception of the signal, decreasing the focusing properties of the PCA. Also, if the environment or its boundaries change (due to surface waves, internal waves, temperature gradients, receiver or PCA motion, etc.), reciprocity is violated and the focusing properties of the PCA are degraded. To accommodate for temporal changes in the channel, the PCA may need to update the transfer function of the environment with some periodicity that depends on how fast environmental changes affect the focusing properties. Such dynamic interactions would have to be considered in the development of any general communications link.

III. ENVIRONMENTAL INFLUENCES IN TIME-REVERSAL ACOUSTICS

The purpose of the analysis presented here is to examine the features of the focus in the context of a communications algorithm and the influence of variations in the signal and PCA. During the TRA examination process that led to this paper, several other environments were considered. In all these environments it was observed that the PCA has similar focusing properties as the ones described for the UWA channel considered in this section. For conciseness, only the environment described here will be examined because it is the most realistic of the cases considered. The other UWA channels that were considered include channels with different sound speed structures and different range-independent as well as range-dependent bathymetric features.

Roux and Fink (2000) performed similar analysis of the influence of combined array aperture and element spacing parameters on the extent of the focus in depth. Their work employed a ray-based model in a Pekeris waveguide. While some of these results are consistent with their findings, this analysis separates the influence of array aperture and inter-element spacing. A full-wave model is also employed here in an environment with a typical shallow water refractive profile. In addition, the vertical, horizontal, and temporal focusing are examined simultaneously as array parameters are modified.

A. Environmental characterization

The UWA environment used throughout this paper to study the usefulness of TRA in underwater communications is presented in Fig. 5. This UWA channel is range indepen-

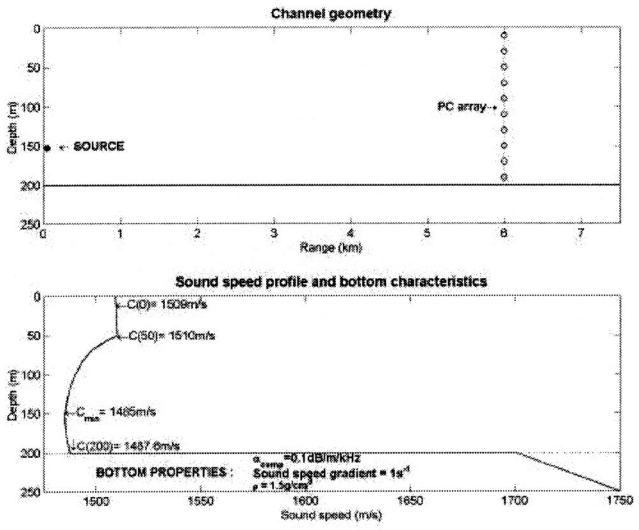

FIG. 5. UWA channel profile.

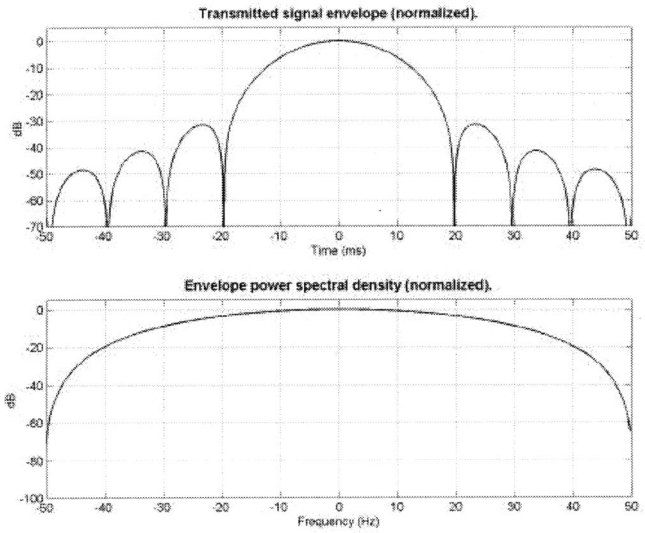

FIG. 6. Transmitted signal envelope.

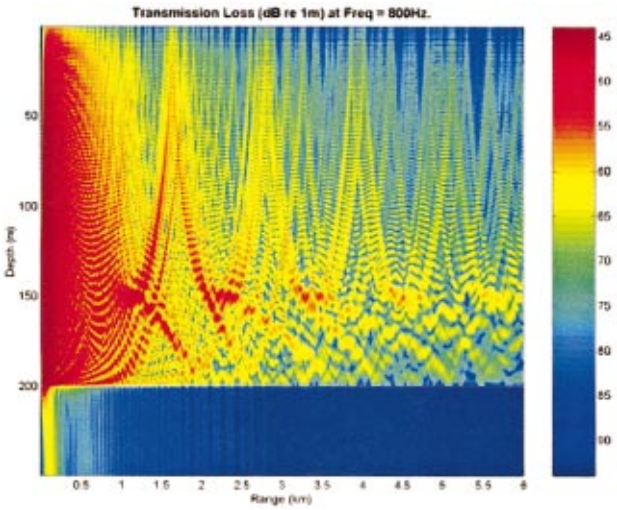

FIG. 7. Ocean response at 800 Hz.

dent in the sound speed profile, bottom bathymetry, and bottom acoustic properties. As depicted in Fig. 5, the source is located at a range of 0 m and a depth of 150 m, and the vertical PC array is located 6 km from the source. Throughout this section several array configurations will be used. In some cases the PC array may have different element spacing, in other cases it has different lengths and in some cases it can span the entire water column. In each instance, the issue to be considered is the impact on communications.

Figure 5 also shows the sound speed profile and the bottom characteristics. This environment has an upward refracting sound speed profile from a depth of 0 to 50 m. From 50 m to the bottom at 200 m, the UWA channel exhibits a sound speed profile similar to a typical shallow ocean sound speed structure with the sound axis located at 150 m in depth. The bottom has compressional attenuation of 0.1 dB/m/kHz, a sound speed gradient of 1 s^{-1}, and a density of 1.5 g/cm^3.

B. Transmitted signal envelope

In most of the TRA numerical simulations presented in this paper, the transmitted pulse has a carrier frequency of 800 Hz. The exceptions are in Sec. III D where carrier frequencies of 400 and 1200 Hz are also considered. In each case, the transmitted pulse has a bandwidth of 100 Hz with a −3-dB effective bandwidth of 36.6 Hz. The MMPE computational bandwidth over which the solutions of the PE field functions are computed includes the full 100 Hz. The envelope characterization of the transmitted pulse is given in Fig. 6. The spectrum of the transmitted pulse envelope is given by the coefficients of a Hanning window (Proakis and Manolakis, 1996). Therefore, the lower panel in Fig. 6 represents a Hanning window (in dB units) that spans 100 Hz in frequency. The time domain representation of the corresponding signal at a carrier frequency of 800 Hz can be found in the upper panel of Fig. 3. For this signal, the −3-dB pulse width is 14.1 ms.

C. Time-reversal acoustics in a range-independent environment

For the environment described in Sec. III A, Fig. 7 represents the magnitude of the ocean response for a time-harmonic acoustic source at a frequency of 800 Hz in a vertical plane defined by the source and the array elements. The ocean frequency response at 800 Hz is represented in terms of transmission loss (dB *re* 1 m). The complex multipath nature of the propagation is evident.

Considering the ocean as a spatial filter, Fig. 7 represents the forward propagation transfer function at the frequency of 800 Hz. The term ''forward propagation'' is used to denote the propagation from the acoustic source. If the source located at a depth of 150 m transmits a pulse at the carrier frequency of 800 Hz with a bandwidth of 100 Hz (−3-dB effective bandwidth of 36.6 Hz), the time arrival structure at the vertical array may be evaluated by Fourier synthesis of single frequency (CW) solutions over the bandwidth of interest. The time and frequency domain characterization of the transmitted pulse was previously described in Fig. 6.

Figure 8 represents the time arrival structure of the received signal envelope at the PCA for the 800-Hz signal with 100-Hz bandwidth. For a given array element, the envelope of the received signal is given by the corresponding horizontal line at the array element depth. The effects of multipath propagation are clearly observed in Fig. 8 where any array element detects several arrivals. From Fig. 8 one can see that the multipath structure is similar between closely spaced array elements. The diversity between array elements can be exhibited by computing the envelope cross-correlation of the time arrival structure represented in Fig. 8. The envelope cross-correlation shown in Fig. 9 was computed with respect to the envelope received by the array element at a depth of 150 m. With respect to this array element one can observe that the other array elements become more decorrelated as the depth difference between array elements increases. In general, as the distance between array elements increases, the multipath structure becomes more decorrelated. This spatial decorrelation between array elements is due to the presence

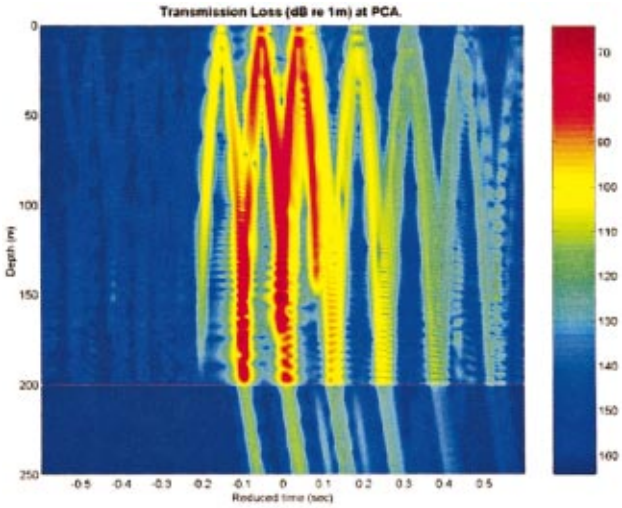

FIG. 8. Time arrival structure at the PCA.

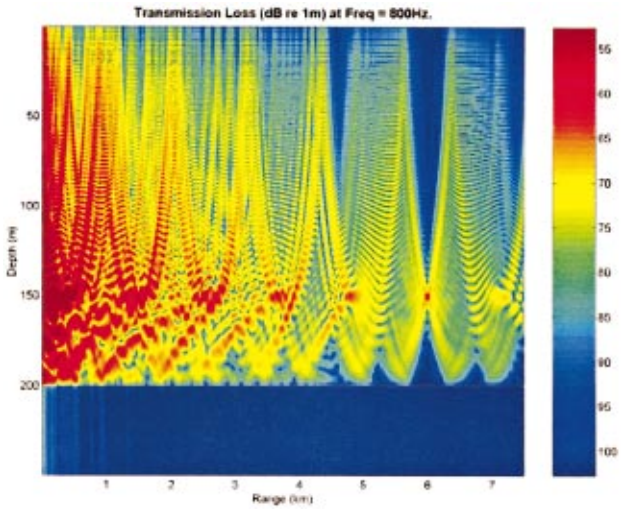

FIG. 10. Backward propagation ocean response at 800 Hz.

of multipaths and is used in communication systems that explore the spatial diversity in the water column.

At the PCA, the received signals are time reversed and transmitted back to the source. Figure 10 represents the ocean frequency response to the time-reversed acoustic field transmitted by the PCA evaluated at 800 Hz. The use of term ''backward propagation'' is meant to describe propagation of the time-reversed signals from the PCA through the reciprocal environment. From this perspective, Fig. 10 represents the backward propagation ocean frequency response at 800 Hz.

In Fig. 10, the propagation is from the left to the right, i.e., the PCA is located at range 0 km and spans the entire water column. In this geometry the original source is located at a range of 6 km and at a depth of 150 m. As expected, the phase conjugation of the 800-Hz frequency component and its consequent propagation through the channel produces a strong spatial focus at the source location.

As described in the previous section, when utilizing TRA the ocean itself behaves much like a spatial matched filter. Due to spatial reciprocity, the only location in space where this spatial filter is matched to the forward propagation function is at the source location. Therefore the output of this spatial filter is maximized at the source location, creating a strong focusing effect because the source location is the spatial location where the backward propagation transfer function matches the forward propagation transfer function. In other words, at the source location all multipath contributions will arrive in phase and add constructively, creating the focusing effect. Using these same arguments, all the other frequency components of the transmitted pulse will focus at the source location.

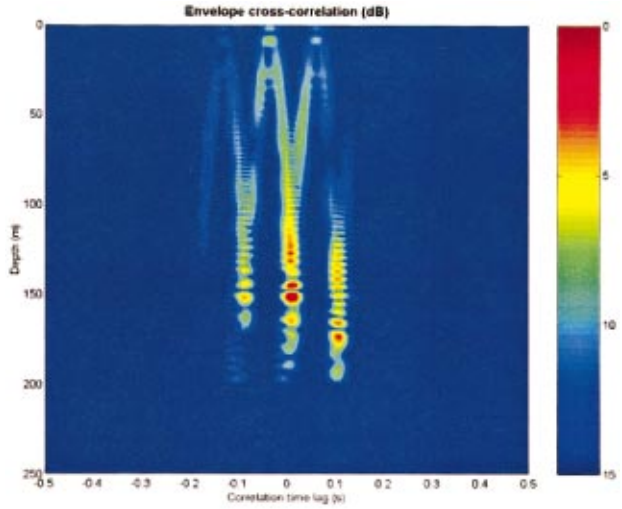

FIG. 9. Envelope cross-correlation across the array elements.

Figure 11 represents the time arrival structure of the backward propagated pulse ($f_c = 800$ Hz, $BW = 100$ Hz) at the source range and the temporal, vertical, and horizontal PCA focusing properties. The data displayed corresponds to the recorded signals of a vertical array of elements that spans the entire water column at the source range. This temporal focusing is also a consequence of the matched filter behavior of the ocean where all frequency components will arrive at the same time at the same location. Previous analysis of such focal regions in a different environment has been performed by Kuperman *et al.* (1998) and Song *et al.* (1998).

In this numerical simulation, the PCA spans the entire water column with an element spacing of $d = 0.244m$ and $\lambda/d = 7.67$, approaching the ideal case of a continuous line of sources. As a consequence, the temporal sidelobes represent the limiting situation that can be achieved in practice. As will be confirmed in this section, decreasing the number of array elements increases the temporal sidelobes.

Also note in Fig. 11 the vertical (along the depth) sidelobes of the focus. As mentioned in Sec. II, the vertical focusing is a consequence of the closure property of the propagating modes. Thus, these sidelobes appear in part because there are higher order modes that decay rapidly in range and do not propagate in the channel. In addition, some propagating modes are attenuated differently by the environment. Thus the focusing extent is dependent on the number of modes allowed in the channel.

Also displayed in Fig. 11 is the horizontal focusing at the source depth. This plot is very representative because it

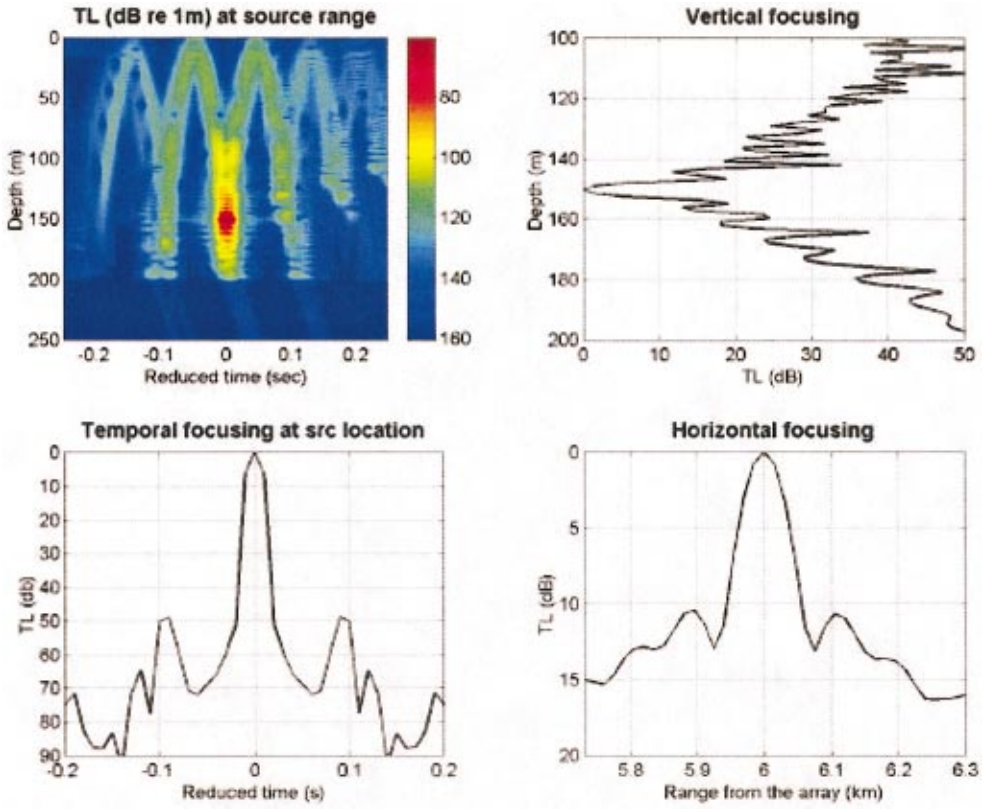

FIG. 11. Time arrival structure focus range. Temporal, vertical, and horizontal PCA focusing properties.

gives the maximum amplitude of the received signal envelope for a given location in range. The main lobe is located at 6 km corresponding to the source range and the −3-dB main lobe width is about 60 m, much larger than the corresponding value along the depth which is 3.3 m.

D. Focusing at different frequencies

In this analysis, three signals with carrier frequencies of 400, 800, and 1200 Hz were used. All these signals have the same bandwidth of 100 Hz that corresponds to a −3-dB effective bandwidth of 36.6 Hz, the same envelope spectral shape as described by Fig. 6, and the PC array spans the entire water column. The temporal, vertical, and horizontal focusing properties for each signal are displayed in Fig. 12.

As can be seen in Fig. 12, the temporal duration of the main arrival is identical for any of these test signals. This is a significant result because it means that use of the same bandwidth at different carrier frequencies achieves the same temporal pulse resolution and consequently the same symbol rates. It appears that the channel frequency response does not change significantly over the bandwidth of each signal and therefore the same temporal resolution exists at these different carrier frequencies. The temporal sidelobes are below 40 dB and decrease with increasing frequency. This is presumably due to the increase in the number of propagating modes at higher frequencies. In addition, the focus dimensions (or ''footprint'') are found to decrease with increasing frequency. This is due to a combination of the increase in the number of propagating modes and the decrease in acoustic wavelength.

E. Effect of interelement spacing

We now evaluate the influence on the focus due to PC arrays with different element spacing. Kuperman *et al.* (1998) previously examined the influence of reduced aperture and interelement spacing (to be considered next) on the focal region for their experimental results in the Mediterranean. A numerical analysis is presented here for our geometry/environment to provide insight into what PCA geometries may be acceptable for an underwater acoustics system.

In this case, the transmitted signal has a carrier frequency of 800 Hz and a bandwidth of 100 Hz. The geometry of the different PC arrays used in this study is given in Fig. 13 where each array is identified by a number from 1 to 6. Associated with each PCA are three numbers giving the number of elements, the distance between consecutive elements in meters, and the distance between consecutive elements in terms of carrier wavelengths. Note that PCA no. 1 has the smallest element spacing and that the distance between array elements doubles between consecutive arrays.

Starting from PCA no. 1 to no. 6, as the element spacing increases, the array cannot provide enough spatial sampling of higher-order propagating modes. Thus, the focusing degrades as a result of the lack of resolution of higher-order modes in the field. This change in focus is the result of removing array elements that are more correlated, i.e., as the array spacing increases it decreases the correlation between array elements.

From Fig. 13, one may conclude that the spatial dimensions of the focus do not change significantly for these PCA

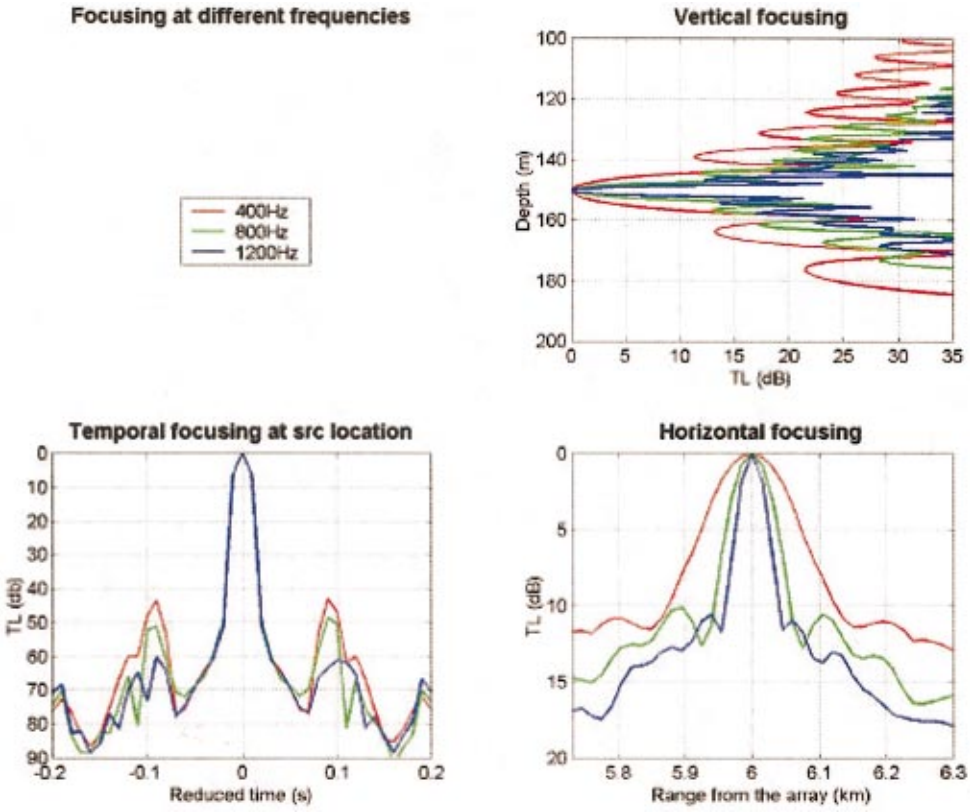

FIG. 12. Focusing at different frequencies.

configurations. Comparing these results to Fig. 11 where the PCA spans the entire water column one should expect an increase in temporal sidelobes because the PC arrays in Fig. 13 only span half of the water column, collecting less information about the channel conditions. Rather remarkably, in the worst case situation (PCA no. 6 with only nine elements), the temporal sidelobes are 25 dB below the main lobe. As the number of array elements increases, the temporal sidelobes improve 10 dB and become more defined.

The results in Fig. 13 seem to indicate that even with a

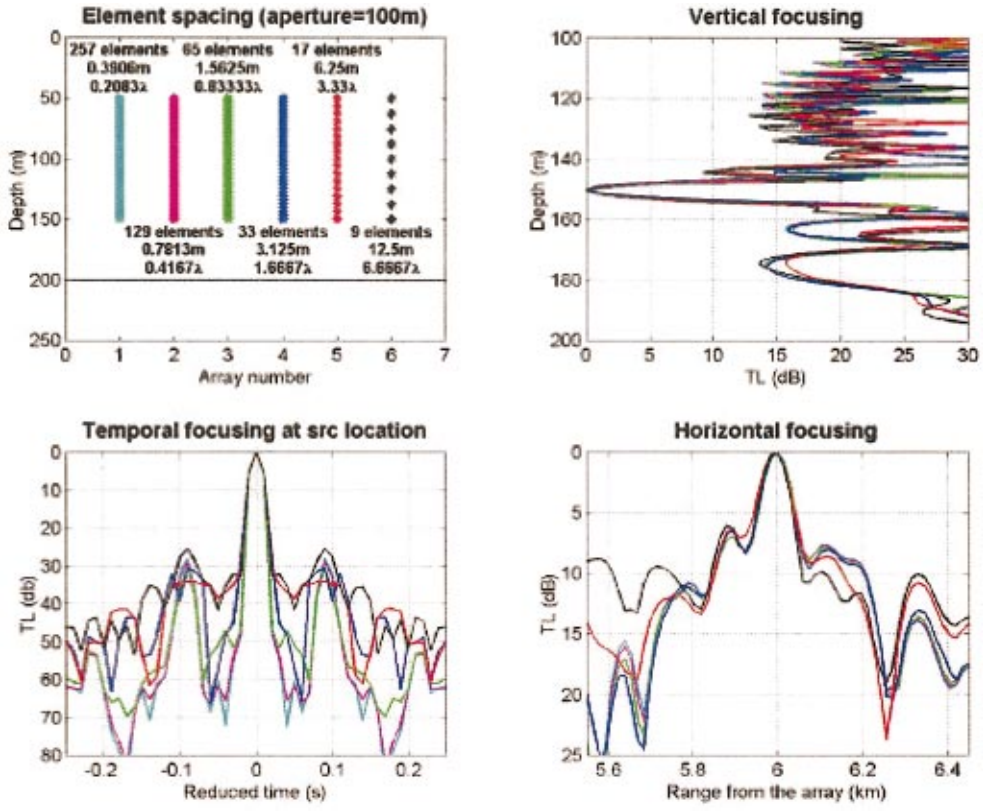

FIG. 13. Focusing properties using PC arrays with different element spacing.

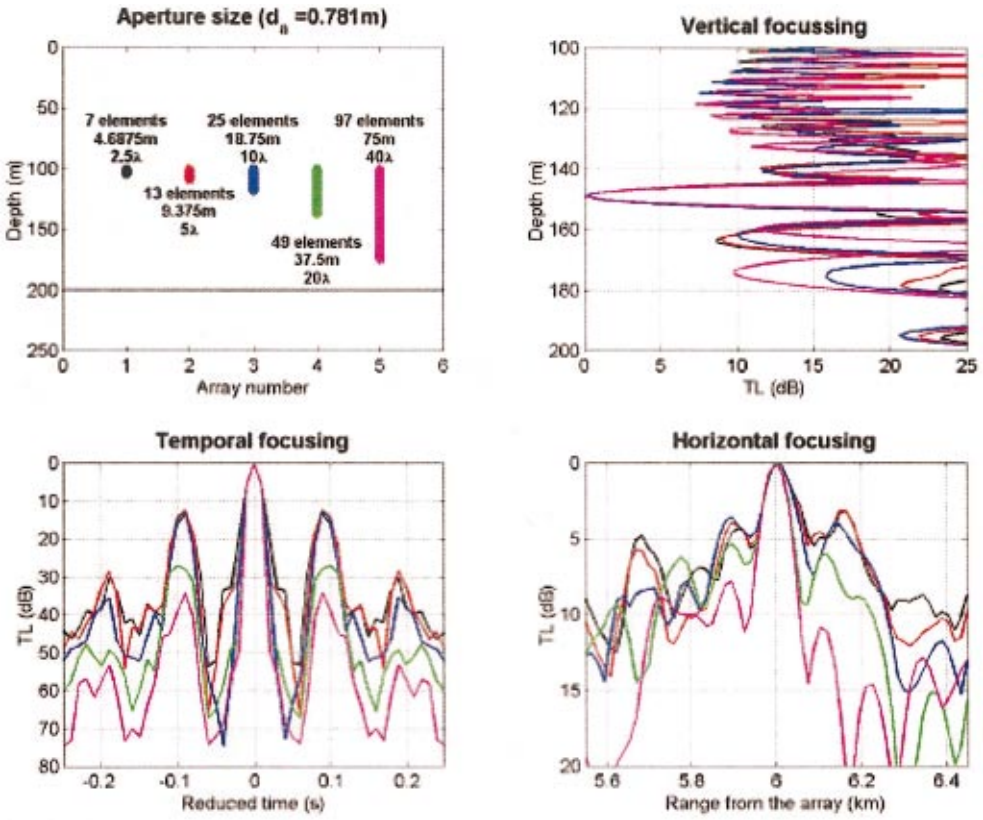

FIG. 14. Focusing properties using PC arrays with different aperture size.

small number of array elements, a good focusing quality, both temporally and spatially, can be achieved provided that the PCA has enough spatial sampling of the propagating modes in the water column. This also suggests that, in this environment, only a small number of the lowest propagating modes dominate the structure of the field and, therefore, the focus. This is important when considering the design of a communications array which employs TRA since the cost increases with the number of elements. Fortunately, it appears that a reduced number of array elements can maintain the temporal resolution, which relates to the data transfer rate at one focal point, and may still be able to take advantage of the spatial diversity of the field at the focal range, allowing multiple focal points in depth to further increase the data rate.

F. Effect of aperture size

In this study, the element spacing is kept constant in order to evaluate the effect that different PCA aperture sizes have on the focus quality. The geometry and spatial location in the water column of the different PC arrays is depicted in Fig. 14. In this figure, each array is designated by a number from 1 to 5. The numbers associated to each array give the number of array elements and the array length in meters and in carrier wavelengths. As the PCA aperture size increases, it can provide a better sampling of the low-order propagating modes. Starting with array no. 1 and going to array no. 5, the changes in focus are due to better spatial sampling of the low-order propagating modes. Thus, one should expect better focusing properties as the aperture size increases because the PCA has more spatial diversity and provides a better sampling of the channel conditions.

Because these PCA arrays cannot properly sample low-order propagating modes, the sidelobes increase in the depth and range coordinates. In Fig. 14, the first three arrays with apertures of $2.5\lambda_c$, $5\lambda_c$, and $10\lambda_c$, respectively, have temporal sidelobes about 12 dB below the main lobe. When the aperture size increases to $20\lambda_c$ the temporal sidelobes decrease to 27 dB below the main lobe. This distinctive behavior of array no. 4 compared to the other three is due to better sampling of the lowest-order propagating modes and therefore better temporal properties.

Presumably, the placement of these arrays in depth will also affect the focus quality. The best quality focus would be expected when the array is placed at a depth which optimally samples the dominant propagating modes. The conclusion that can be drawn is that in a given environment one should evaluate the most important propagating modes and use an array aperture that provides enough sampling of these modes.

IV. APPLICATION OF TIME-REVERSAL ACOUSTICS TO SHALLOW WATER COMMUNICATION SYSTEMS

In this section, we introduce a novel signaling scheme which takes advantage of the focusing properties of TRA system in a point-to-point acoustic link. The communication system described here uses a reduced-complexity noncoherent detector at the expense of increased complexity in the transmitter (PCA). The examples illustrated correspond to a nominal signaling rate of 30.5 symbols/second where 4 bits of information are encoded in each symbol. The channel used for numerical simulations is the one described in Sec.III A

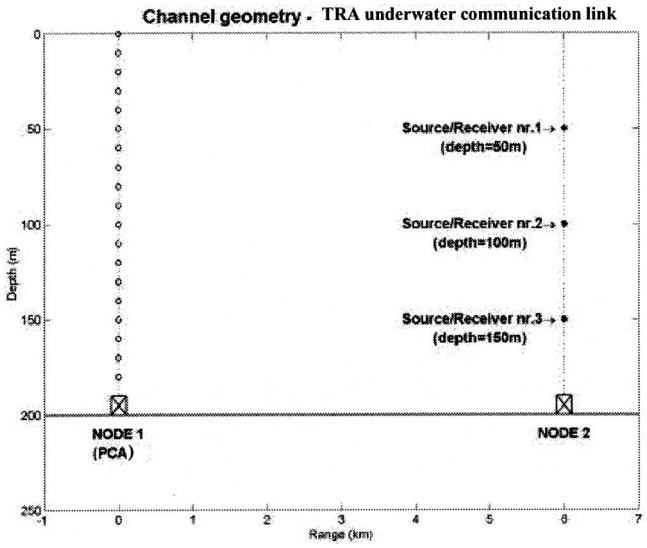

FIG. 15. PCA and channel geometry in a point to point communication link.

A. Using phase-conjugated arrays in underwater acoustic communications

Figure 15 can be used to describe the simplest case of point-to-point communications between two stationary communication nodes. Node 1 of Fig. 15 has a PC array that spans the entire water column, and a single source/receiver element of node 2 is used at a depth of 150 m. (The other source/receiver elements of node 2 will be utilized later.)

The first step towards the focusing of the node 1 PCA requires a probe pulse transmission from the node 2 acoustic source (nr. 3 in Fig. 15). As this probe pulse propagates, it will incorporate channel distortions including multipath. In the next step, the received acoustic signals at each node 1 element are digitized and stored in digital memories. For node 1 transmission (or backpropagation), the recorded signals will be time-reversed and transmitted by each node 1 element. The time-reversal transformation at the PCA is a simple task to perform, requiring the digital memories to be read in a last-in-first-out (LIFO) manner. At the PCA transmission, each element is excited by the output of the corresponding memory where the received signals were recorded. At this point one can consider that the PCA is ''focused'' at the nr. 3 source/receiver location of node 2 because it has recorded the necessary environmental information to generate a spatial focus at the node 2 source/receiver location.

The PCA's focusing procedure is a critical aspect in a TRA communication link. In a real situation, one must take into account the temporal variability of channel conditions. Focusing will degrade with time and will require periodic PCA refocusing. Additionally, the nodes may have some motion in general and the PC array may need to update the environmental information every time the receiver moves out of focus. In such a situation, the range shifting property of PC arrays discussed by Song *et al.* (1998) may be a very useful feature in a UWA communication system. If the receiver is moving slowly, the PCA is able to keep the focus at the receiver location, decreasing the rate at which the UWA communication system updates the environmental information (probing).

As a final remark, the electronic circuitry associated with each PCA element includes a receiver amplifier, an A/D converter, digital filters, memory, a D/A converter and a transmitter amplifier. Until this point no reference was made of the presence of digital filters at each PCA array element. A discussion of filter options is presented in the next section.

B. Signaling scheme

In this signaling scheme, each symbol represents a 4-bit word giving a total of 16 different words in the code. Since this communication system is based on noncoherent detection, the value of each bit within a symbol is given by the detection or lack of detection of the corresponding frequency component. There are 15 different symbols in the code having at least one spectral component. The ''all-zeros'' word corresponds to the case where no carrier frequencies are detected. This signaling scheme corresponds to a four channel ''on-off'' keying modulation scheme. Thus, a simple receiver can be built based on a four-element filter bank followed by an envelope detector. The detection of a given frequency component is achieved when the corresponding envelope detector output is higher than a given threshold.

In this scheme, four frequency components are defined centered at 750, 800, 850, and 900 Hz. Each one of these frequency components spans 100 Hz in frequency and has a -3-dB bandwidth of 36.6 Hz. The least significant bit corresponds to the frequency component centered at 900 Hz and the most significant bit corresponds to the component at 750 Hz.

To simplify the transmissions of the probe signals, assume that each PCA element has a bank of four digital filters centered at 750, 800, 850, and 900 Hz. Each source at node 2 must then transmit a single probe pulse covering the entire bandwidth, 700 to 950 Hz. An alternative approach would be for each source at node 2 to transmit each 100-Hz bandwidth probe pulse separately. If this last approach is chosen, there is no requirement for a digital filter bank in each PCA element but each node must make sure that the probe pulse transmissions will not overlap in time at the PCA.

The choice of which approach to use may be dictated by the temporal variability of the channel conditions that will degrade focusing and will require periodic update of the channel conditions. The filter bank approach has the advantage that it requires only one probe pulse transmission from each node 2 source in Fig. 15. Thus the communication system spends less time in array focusing and higher data throughput can be attained at the expense of a more complex PCA. However, the transmission of each individual probe pulse has the advantage of allowing the use of matched filters at reception. This may provide additional SNR gain and be more robust to signal fading.

C. The phase-conjugated array

In this section, it is assumed that the PCA is able to learn the environmental information in the bandwidth of interest. The PCA is not in a shadow zone and each source transmits

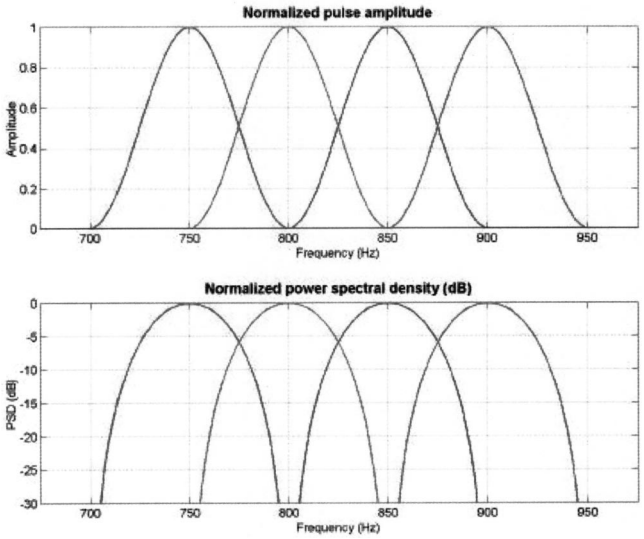

FIG. 16. PCA element filter bank frequency response.

a probe pulse with bandwidth wide enough to accommodate the bandwidth used to transmit all individual frequency components of the signaling scheme.

The signaling scheme described in the previous section requires a four-element filter bank for each PCA element. This four-element filter bank frequency response is given in Fig. 16. All the filters have the same spectral shape but different center frequency, each filter frequency response spanning over 100 Hz, giving a −3-dB bandwidth of 36.6 Hz. The frequency response of each filter is specified by the coefficients of a Hanning window. In Fig. 16, the center frequency of each filter corresponds to the center frequency of one of the frequency components used in the signaling scheme.

After PCA reception and filtering, each PCA element will have recorded four different signals with different center frequencies. Each one of these signals will have the transfer function of the channel imprinted on it. As seen in the previous section, if all PCA elements transmit only the signal component centered at 800 Hz, a pulse with 800 Hz carrier frequency and a −3-dB bandwidth of 36.6 Hz will be received at the node 2 focus location.

D. Point to point message transmission

This section presents a numerical simulation where a message is sent from node 1 to node 2 of Fig. 15. At each PCA element, the transmitted signal corresponding to a given symbol can be obtained by time-domain superposition (i.e., simultaneous transmission) of its different frequency components. Similarly, the signal corresponding to a sequence of symbols can be obtained by superposition of the signals corresponding to the different symbols, properly delayed in the time domain. This time-domain delay corresponds to the signaling period and should be greater than the temporal duration of each symbol at the receiver location to avoid intersymbol interference. In this case, each single frequency component will have at the receiver a −3-dB temporal duration of 14.1 ms and a conservative value of 32.8 ms was chosen for the signaling period.

Figure 17 presents the spectrograms of the signal corresponding to a message composed by the sequence of words from $(0001)_b$ to $(1111)_b$ that is intended to be transmitted from node 1 to the node 2 receiver. The upper panel represents the ideal signal that node 1 wants to focus at the node 2 receiver. The other panels in Fig. 17 present the results from a numerical simulation where node 1 spans the entire water column and transmits the appropriate signals to focus the message at the node 2 receiver. All the signals in Fig. 17 are collected at a depth of 150 m. The middle-left panel represents the signal transmitted from the PCA element located at 150-m depth while the other three correspond to the signal spectrogram at various ranges. Only the lower right panel in Fig. 17 corresponds to the signal spectrogram at the focus location.

In Fig. 17 one can clearly observe that as the pulse backward propagates in the channel the multipath structure becomes less significant as the range approaches the focusing range. It can also be seen that when the pulse approaches the focusing range it increases the power spectral density of its spectral components. This increase in the power spectral density is a consequence of the vertical, horizontal, and temporal PCA focusing properties as the sequence of symbols approaches the focus location.

E. Phase-conjugated array vertical diversity in underwater communications

Presented in this section is an extension of the TRA technique which takes advantage of vertical diversity of the focus. The setup for this TRA experiment is depicted in Fig. 15 with the difference that node 2 has now three source/receiver elements. The extension of the TRA technique presented here exploits node 1 PCA vertical diversity to focus the backward propagated acoustic field at the different node 2 receiver locations. As a result, higher data throughputs can be achieved in the data link from node 1 to node 2.

In this case the PCA focusing process requires probe pulse transmissions from each source/receiver element of node 2. The transmission of probe pulses from node 2 has the constraint that it must allow enough time between consecutive transmissions so each pulse will arrive at node 1 at different time slots and the pulses do not interfere. In this example, node 1 will require a data bank with three times the storage capacity of the one used in node 2 because it has to store the signals received from three probe pulses. The TRA acoustic link from node 1 to node 2 can accommodate three times the data throughput of the case presented in the previous sections. In this case, node 2 has three receivers and node 1 is able to send three different symbols (one for each node 2 receiver) during each symbol period.

At transmission, the PCA will assemble the message intended for each receiver by the superposition of its frequency components stored in its data bank. The signal transmitted by each PCA element will be composed of the superposition of the signals for the different node 2 receivers. Figure 18 represents the desired message signal spectrogram that the PCA wants to focus at each node 2 receiver. Note that these signals do not correspond to the actual signals sent by the node 1 elements.

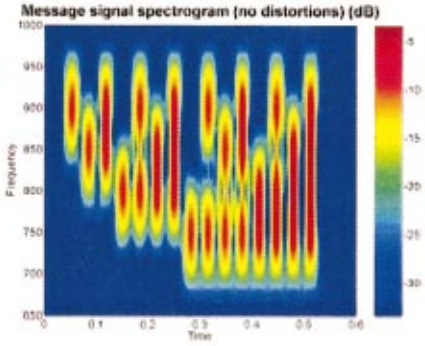

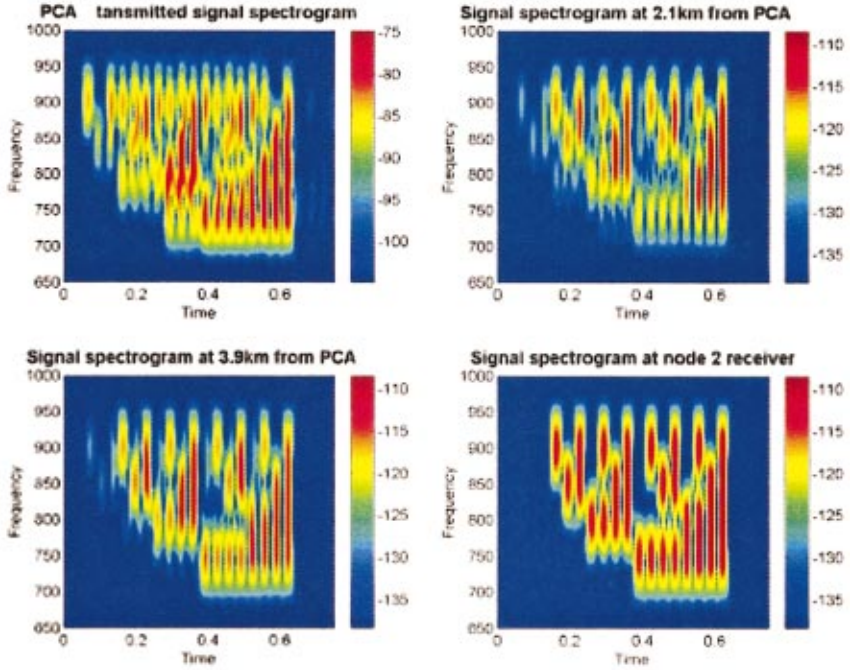

FIG. 17. The central upper panel displays the desired message if no distortions are present in the channel. Other panels display message signal spectrograms at a depth of 150 m dp: (middle left) evaluated at the PCA (transmitted); (middle right and lower left) at two intermediate ranges; and (lower right) at the focus.

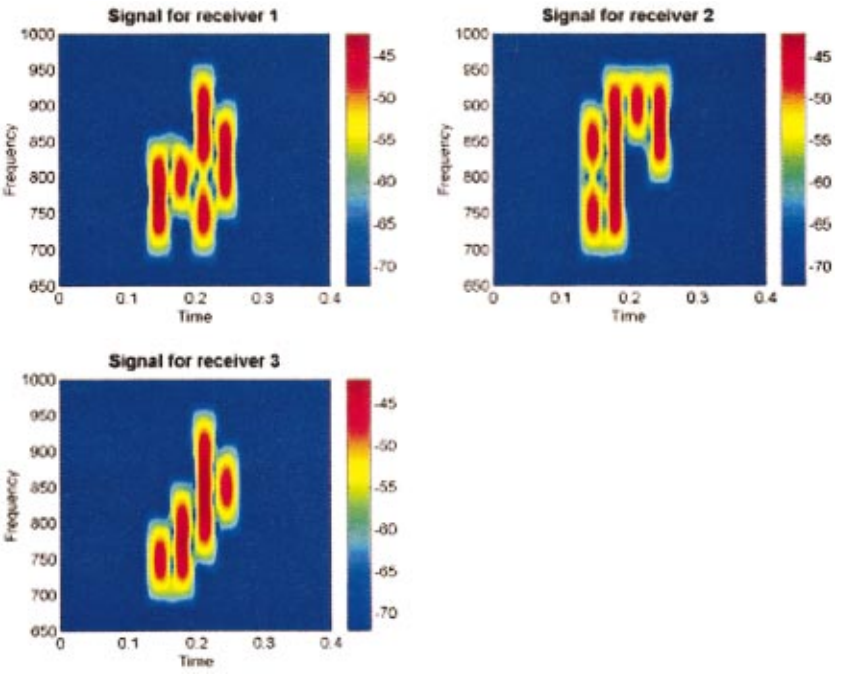

FIG. 18. Desired message signals for node 2 receivers.

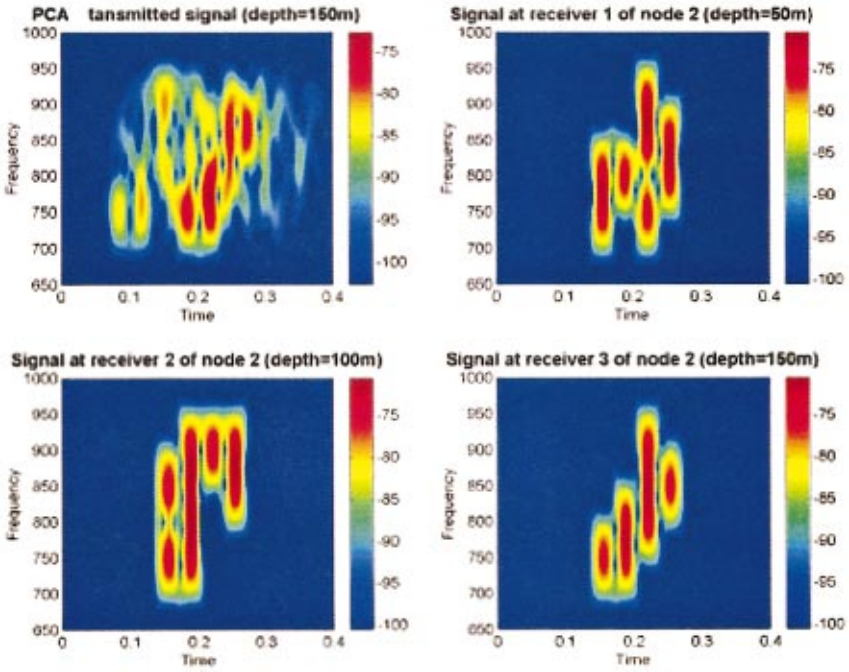

FIG. 19. Transmitted signal by PCA and received signals at node 2 receivers.

Figure 19 presents numerical simulation results of the PCA transmitted signal propagation in which Fig. 18 represents the message that the PCA wants to focus at each receiver location. In this simulation, the PCA spans the entire water column and the upper-left panel of Fig. 19 represents the actual signal sent by the element located at a depth of 150 m. We can observe multipath structure and strong interference between the different transmitted messages. The remaining panels in Fig. 19 represent the signal received by each one of the node 2 receivers. Due to the vertical focusing properties of the PCA, these results show very little message intersymbol interference at each receiver and the desired message can be easily decoded.

With respect to this same numerical simulation, Fig. 20 represents the signal spectrogram at different ranges between node 1 and node 2 collected at a depth of 150 m. The results in this figure show that it will be extremely difficult to decode the original messages at these locations because the different message signals are overlapping both in time and in frequency. These results also show that this TRA vertical diversity technique may have applications to UWA secure communication links. Channel distortions and signal overlap both in time and frequency of the different messages seems to be a very good way to encode digital communication signals with the advantages of a higher data throughput. Such encoding also occurs for the single focus approach described previously but does not exhibit the same level of encryption.

Additional simulations were also performed which took

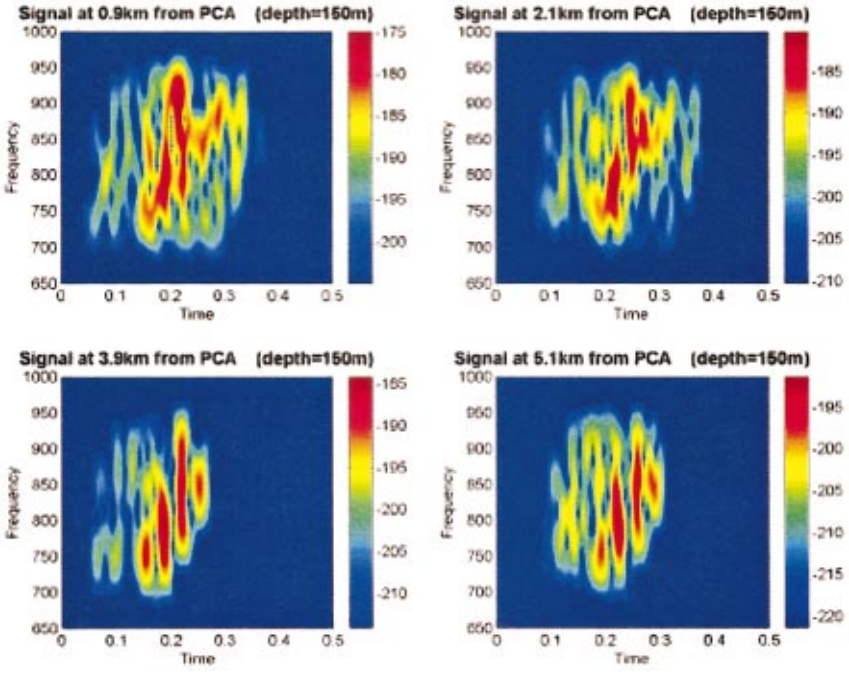

FIG. 20. Received signal spectrogram at depth of 150 m and different ranges from PCA.

advantage of the horizontal spatial diversity of the time-reversed field. Specifically, a network of nodes, separated from the PCA by different ranges, was employed. Similar results were obtained whereby each individual node (some containing multiple receiving elements in depth) received unique focused signals at the particular location for that node. This suggests the potential for an extended area network. However, the signaling schemes for such a configuration would be considerably more complex at the PCA.

V. CONCLUSIONS

In this paper, we numerically explored the influences of a phase-conjugation array design on its focusing properties. Particular attention was given to PCA applications in UWA communication systems. This analysis provides a starting point for a PC array design, and gives support to the planning of further TRA UWA communication experiments both in the laboratory and in an oceanic environment. In the early stages of a TRA UWA communication system design, TRA numerical modeling is very important because it gives insight to the propagation issues that are involved without the need to go out to the ocean and perform very expensive experiments. However, although numerical modeling is an excellent analysis tool, it does not provide complete information about time-variability of the channel conditions.

The numerical analysis of the PCA focusing properties showed that the focus footprint decreases in dimension as the carrier frequency increases. Furthermore, the horizontal dimension is larger than the vertical dimension of the footprint. Therefore vertical motion of the receiver is much more critical than horizontal motion because the receiver can easily move out-of-focus.

Using the same bandwidth and changing carrier frequency, results showed that temporal focusing does not change significantly. However, in a more general situation where a larger pulse bandwidth is used, additional results suggested that for carrier frequencies much higher than 1 kHz, some degradation may occur in the pulse temporal resolution at the focus location since the two-way channel frequency response may change considerably over the bandwidth.

When using PC arrays with different element spacing or with different aperture size, the PCA footprint did not appear to change its dimensions. Keeping constant the aperture size and changing the PCA element spacing, the temporal sidelobes remained approximately at the same level. Keeping constant the PCA element spacing and changing the aperture size, the vertical and horizontal footprint size also did not appear to change significantly. A small improvement in horizontal sidelobes was observed when the aperture length was increased. A dramatic improvement in temporal sidelobes was observed when the aperture size increased to $20\lambda_c$ because the PCA was able to provide better spatial sampling of the lowest propagating modes. In other words, there was more spatial diversity in the PC array.

What may be concluded from this analysis is that aperture size plays a more significant role than the number of array elements in a PC array design, especially for communication applications where temporal resolution of the focus is important. The number of PCA transducers is a critical factor in PC array design because it will drive up the cost. Each PCA transducer has its own electronic circuitry composed of receiver amplifiers, A/D and D/A converters, storage memory, and transmitter. In general, underwater devices rely on batteries to operate their electronic systems and have severe constraints on the amount of power that can be used. Thus, for cost effectiveness one should use a small number of array elements extended over a large aperture size.

For UWA communication systems using noncoherent detection, the use of PC arrays seems promising because there is no requirement of carrier phase tracking. The temporal focusing properties of the PCA overcomes the requirement of guard times between consecutive symbols to ensure that all the reverberation will vanish before each subsequent symbol is received avoiding intersymbol interference at the receiver. Thus some data rate improvement is made because the insertion of idle periods of time results in a reduction of the available data throughput. Array processing is no longer required because the PCA footprint is well defined at the receiver location.

The data throughput can be further improved by taking advantage of the PCA spatial diversity focusing properties. In the cases presented, the PCA was able to focus simultaneously different messages at different receiver locations. The message signal designated for a given receiver only focused at the intended receiver location. At the receiver the corresponding message signal was compressed in time and space and had higher magnitude than the other interfering message signals. As a consequence, each message signal could only be decoded at the desired receiver. Furthermore, this seems to be a good technique for secure UWA communications because the different message signals will be overlapping both in time and frequency at other locations, making it difficult to recover any of the transmitted messages.

Several of the features of this communications algorithm employing time-reversal acoustics have already been implemented experimentally at the Naval Postgraduate School in a controlled tank-scale environment. The results are consistent with those from numerical simulations. These findings will be reported in a companion article. The modeling work is now examining issues related to more realistic environments, while the experimental tank work pursues more sophisticated signaling schemes.

Due to the PC array spatial diversity focusing properties, PC arrays may have an important role in an acoustic local area network. Each array is able to simultaneously transmit different messages that will focus at the destination receiver node. Although the first protocols for acoustic local area networks have been proposed by Brandy and Catipovic (1994) and Talavage *et al.* (1994), the design of an acoustic local area network protocol that accommodates the learning step of the PCAs is still being developed.

In order to achieve high-speed data transmission, the use of TRA bandwidth-efficient phase-coherent communications requires further research. Due to temporal variability of channel conditions, the first step towards the feasibility of TRA phase-coherent communications is the evaluation of the phase-stability (phase fluctuations) at the focus. Once ac-

complished, the receiver structure can be determined and an adaptive equalizer can be designed to accommodate temporal variability of the channel conditions. Other approaches useful in communications should also be explored under these variable conditions, such as increased symbol information through amplitude modulation. Several such issues are currently be investigated at the Naval Postgraduate School.

ACKNOWLEDGMENT

This work was supported by ONR Code 321OA. The authors would like to acknowledge the help and guidance of Professor Monique Fargues, Naval Postgraduate School, for many useful discussions. We also wish to thank Dr. William Kuperman and Dr. William Hodgkiss, Marine Physical Laboratory, UCSD, and Dr. Milica Stojanovic for guiding us through some initial revisions.

Abrantes, A. A. M., Smith, K. B., and Larraza, A. (**1999**). ''Examination of time-reversal acoustics and applications to underwater communications,'' J. Acoust. Soc. Am. **105**, 1364 (joint conference of ASA, EAA, DAGA, 14–19 March, Berlin, Germany).

Baggeroer, A. (**1984**). ''Acoustic telemetry—An overview,'' IEEE J. Ocean. Eng. **9**, 229–235.

Brandy, D. P., and Catipovic, J. A. (**1994**). ''Adaptive multiuser detection for underwater acoustic channels,'' IEEE J. Ocean. Eng. **19**, 158–165.

Brienzo, R. K., and Hodgkiss, W. S. (**1993**). ''Broadband matched-field processing,'' J. Acoust. Soc. Am. **94**, 2821–2831.

Catipovic, J. (**1990**). ''Performance limitations in underwater acoustic telemetry,'' IEEE J. Ocean. Eng. **15**, 205–216.

Coates, R. F. W. (**1993**). ''Underwater acoustic communications,'' in *Proc. OCEANS'93*, Victoria, BC, pp. III.420–III.425.

Coates, R., Owens, R., and Tseng, M. (**1993**). ''Underwater acoustic communications: A second bibliography and review,'' in *Proc. Inst. Acoust.*

Galvin, R., and Coates, R. F. W. (**1994**). ''Analysis of the performance of an underwater acoustic communication system and comparison with a stochastic model,'' in *Proc. OCEANS'94*, Brest, France, pp. III.478–III.482.

Heinemann, M. G. (**2000**). ''Experimental Studies of Applications of Time-Reversal Acoustics to Non-coherent Underwater Communications,'' Naval Postgraduate School, Master's Thesis.

Henderson, G. B., Tweedy, A., Howe, G. S., Hinton, O., and Adams, A. E. (**1994**). ''Investigation of adaptive beamformer performance and experimental verification of applications in high data rate digital underwater communications,'' in *Proc. OCEANS'94*, Brest, France, pp. I.296–I.301.

Howe, G. S., Tarbit, P., Hinton, O., Sharif, B., and Adams, A. (**1994**). ''Subsea acoustic remote communications utilizing an adaptive receiving beamformer for multipath suppression,'' *Proc. OCEANS'94*, Brest, France, pp. I.313–I.316.

Jackson, D. R., and Dowling, D. R. (**1991**). ''Phase conjugation in underwater acoustics,'' J. Acoust. Soc. Am. **89**, 171–181.

Jackson, D. R., and Dowling, D. R. (**1992**). ''Narrow-band performance of phase-conjugate arrays in dynamic random media,'' J. Acoust. Soc. Am. **91**, 3257–3277.

Jensen, F. B., Kuperman, W. A., Porter, M. B., and Schmidt, H. (**1994**). *Computational Ocean Acoustics* (American Institute of Physics, Woodbury, NY).

Kuperman, W. A., Hodgkiss, W. S., Song, H. C., Akal, T., Ferla, C., and Jackson, D. R. (**1998**). ''Phase conjugation in the ocean: Experimental demonstration of an acoustic time-reversal mirror,'' J. Acoust. Soc. Am. **103**, 25–40.

Proakis, J. G., and Manolakis, D. G. (**1996**). *Digital Signal Processing: Principles, Algorithms, and Applications* (Prentice–Hall, Upper Saddle River, NJ).

Roux, P., and Fink, M. (**2000**). ''Time reversal in a waveguide: Study of the temporal and spatial focusing,'' J. Acoust. Soc. Am. **107**, 2418–2429.

Smith, K. B. (**2001**). ''Convergence, stability, and variability of shallow water acoustic predictions using a split-step Fourier parabolic equation model,'' J. Comput. Acoust. **9**, 243–285.

Smith, K. B., and Tappert, F. D. (**1994**). ''UMPE: The University of Miami Parabolic Equation Model, *Version 1.1*,'' MPL Technical Memorandum 432.

Song, H. C., Kuperman, W. A., and Hodgkiss, W. S. (**1998**). ''A time-reversal mirror with variable range focusing,'' J. Acoust. Soc. Am. **103**, 3234–3240.

Stojanovic, M. (**1996**). ''Recent advances in high-speed underwater acoustic communications,'' IEEE J. Ocean. Eng. **21**, 125–136.

Stojanovic, M., Catipovic, J. A., and Proakis, J. G. (**1993**). ''Adaptive multichannel combining and equalization for underwater acoustic communications,'' J. Acoust. Soc. Am. **94**, 1621–1631.

Stojanovic, M., Catipovic, J. A., and Proakis, J. G. (**1994**). ''Phase coherent digital communications for underwater acoustic channels,'' IEEE J. Ocean. Eng. **19**, 100–111.

Stojanovic, M., Catipovic, J. A., and Proakis, J. G. (**1995**). ''Reduced-complexity spatial and temporal processing of underwater acoustic communication signals,'' J. Acoust. Soc. Am. **98**, 961–972.

Talavage, J., Thiel, T., and Brandy, D. (**1994**). ''An efficient store-and-forward protocol for a shallow water acoustic local area network,'' *Proc. OCEANS'94*, Brest, France.

Tarbit, P. S. D., Howe, G., Hinton, O., Adams, A., and Sharif, B. (**1994**). ''Development of a real-time adaptive equalizer for a high-rate underwater acoustic data communication link,'' in *Proc. OCEANS'94*, Brest, France, pp. I.307–I.312.

Experimental studies of applications of time-reversal acoustics to noncoherent underwater communications

M. Heinemann, A. Larraza,[a] and K. B. Smith
Department of Physics, Naval Postgraduate School, Monterey, California 93943

(Received 16 October 2000; accepted for publication 27 February 2003)

The most difficult problem in shallow underwater acoustic communications is considered to be the time-varying multipath propagation because it impacts negatively on data rates. At high data rates the intersymbol interference requires adaptive algorithms on the receiver side that lead to computationally intensive and complex signal processing. A novel technique called time-reversal acoustics (TRA) can environmentally adapt the acoustic propagation effects of a complex medium in order to focus energy at a particular target range and depth. Using TRA, the multipath structure is reduced because all the propagation paths add coherently at the intended target location. This property of time-reversal acoustics suggests a potential application in the field of noncoherent acoustic communications. This work presents results of a tank scale experiment using an algorithm for rapid transmission of binary data in a complex underwater environment with the TRA approach. A simple 15-symbol code provides an example of the simplicity and feasibility of the approach. Covert coding due to the inherent scrambling induced by the environment at points other than the intended receiver is also investigated. The experiments described suggest a high potential in data rate for the time-reversal approach in underwater acoustic communications while keeping the computational complexity low. [DOI: 10.1121/1.1570832]

PACS numbers: 43.30.Bp [SAC-B]

I. INTRODUCTION

For underwater acoustic propagation in shallow water environments, a narrow-band pulse generated by a pointlike source spreads because of multi-path propagation due to reflections at the surface and bottom of the ocean or refractions within the interior. Each propagation path takes a different time, so that the transmitted pulse gives rise to multiple copies of varying magnitude, not equally spaced in time, arriving at a receiver (Fig. 1). The strong signal degradation due to the multipath propagation is further enhanced by high spatial and temporal variability of the channel conditions that exist in a typical underwater acoustic channel in shallow water environments.

In a communication link, the signal degradation due to multipath spreading causes intersymbol interference (ISI) which is the interference between symbols due to multiple arrivals of each transmitted symbol. For example, in a shallow water channel with a multipath spread of 100 ms with 1000 symbols per second, the ISI extends over 100 symbols. Also, as long propagation times decrease data throughput, available bandwidth is severely limited by transmission loss, which increases both in frequency and in range.

A novel technique called time-reversal acoustics (TRA) can environmentally adapt the acoustic propagation effects of a complex medium in order to focus energy at a particular target range and depth. Additionally, estimates show that TRA focusing can be done at useful ranges (30 km) and over reasonable time scales (30 min) without updating the time-reversed signal under certain conditions, as shown by Kuperman *et al.* (1998) in an ocean experiment using 445-Hz frequency signals. Additional experimental data have recently been taken by the same group in the same location at a higher frequency of 3.5 kHz. The TRA technique consists of digitizing the analog signal received by, say, a microphone or a hydrophone, time reversing it, and retransmitting it from a co-located source. If a wide-aperture array of receivers/transmitters is used, the time-reversed signal back at the pointlike source is focused in time and space (Fink, 1997, 1999; Roux *et al.*, 1997; Kuperman *et al.*, 1998). For a small-aperture array, while the time-reversed signal back at the pointlike source does not focus well in space, it still exhibits near-optimal focusing in time.

Because the path back from the array to the original source location is reciprocally identical (barring significant currents or other features which degrade reciprocity), the mode group speeds are also identical. Therefore, all of the modes arrive back at the original source location at the same time and add up constructively. This generates both a temporal and spatial (range and depth) focusing of the propagating field. Thus, using TRA the multipath structure is eliminated because all of the propagation paths add coherently at the source location, which results in a reduced ISI of the communication link. Furthermore, due to spatial and temporal focusing there is a strong enhancement of the field at the focus location, which allows us to increase bandwidth and the transmission range. Also, because the spatial extent of the focus is a few wavelengths of sound, TRA possesses natural encryption for points other than the intended target.

The properties of time-reversal acoustics suggest a potential application in the field of noncoherent acoustic com-

[a]Author to whom correspondence should be addressed. Electronic mail: larraza@physics.nps.navy.mil

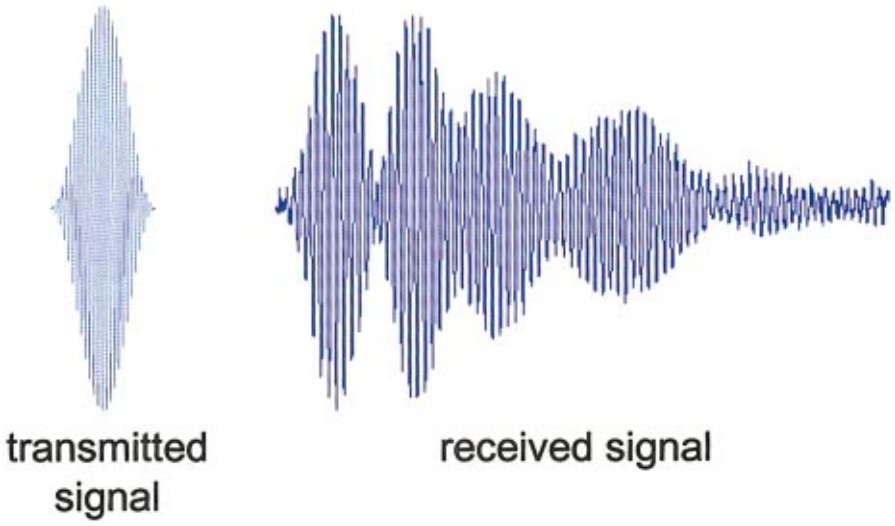

FIG. 1. Example of transmitted and received signal in the multipath propagation environment of a rectangular waveguide. The time scale for both signals is the same.

munications. This has previously been suggested by Jackson and Dowling (1991), Roux *et al.* (1997), Fink (1997), and Kuperman *et al.* (1998). ''Noncoherent'' in this sense is meant to imply that no phase information will be transmitted in the communication signal but instead an energy detector method will be used. A novel communications scheme has been suggested by Abrantes *et al.* (1999) and Smith *et al.* (2003), which employs both the temporal and spatial focusing properties of TRA. In this scheme, two source/receiver systems, **A** and **B**, are used to communicate with one another. A set of distinct signals representing binary bits is agreed upon and known by the **A** and **B** systems. Each signal should have roughly the same temporal resolution. A simple example would be multiple broadband signals with identical bandwidth, Hanning window source spectra, and center frequencies separated by half the bandwidth (allowing for null detection between adjacent signals). The total number of signals within the set is then limited primarily by the bandwidth of the system. For this example, assume that there are four distinct signals (bits) within the set defining a 4-bit character (giving values from 0 to 15). The communications link is achieved when a single element of **A** transmits each signal to **B** with sufficient time between transmissions for all multipath structures to arrive. This provides **B** with the transfer function of the environment for those signals. Then **B** has the ability to transmit binary information to **A** by building 4-bit ''symbols'' out of the time-reversed signals. In addition, the transmission of subsequent symbols can overlap each other significantly. The criterion for the delay between subsequent symbol transmissions is the temporal resolution of the focus back at **A**. For example, if the signals originally transmitted by **A** have a nominal temporal resolution of 10 ms, then **B** is able to transmit the 4-bit symbols at a nominal rate of 100 symbols/s. Furthermore, recall that these focused signals arriving back at **A** have an improved SNR. Thus for a full transmission bandwidth of 1 kHz and a pulse bandwidth of 200 Hz, this scheme can provide a rate of 2000 bits/s. This is comparable to current rates with the added benefits of longer range due to energy focusing and covert coding due to the inherent scrambling induced by the environment at points other than the intended receiver. Now consider that multiple elements in **A** each uniquely transmit the communication signals. Depending upon the spatial focusing properties of the time-reversed signals, multiple symbols may be transmitted from **B** to focus at different locations along **A**.

The aim of this article is to establish the practicality of the method in underwater acoustic communications, and it is organized as follows. In Sec. II, we describe the apparatus. Section III, gives a description of the experiment, the definition of the symbols, and a trial message.

II. APPARATUS

The experiment is conducted in a fiberglass-coated wooden tank made of wooden plates of 18-mm thickness which are sideways reinforced every 65 cm (Fig. 2). The inner dimensions of the tank are 15.32 m long, 1.17 m wide,

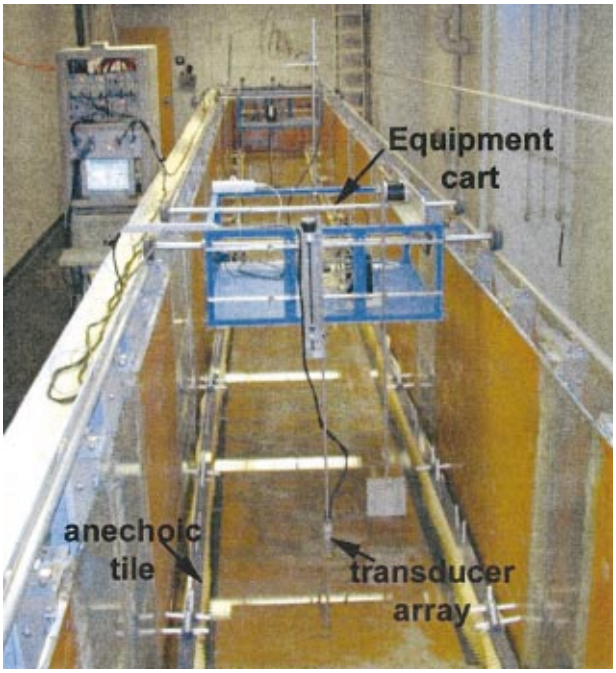

FIG. 2. View from above one end of the tank. The tank has inner dimensions of 15.32-m length, 1.17-m width, and 1.20-m depth. The water level can be raised up to 28 cm, the height of the anechoic material.

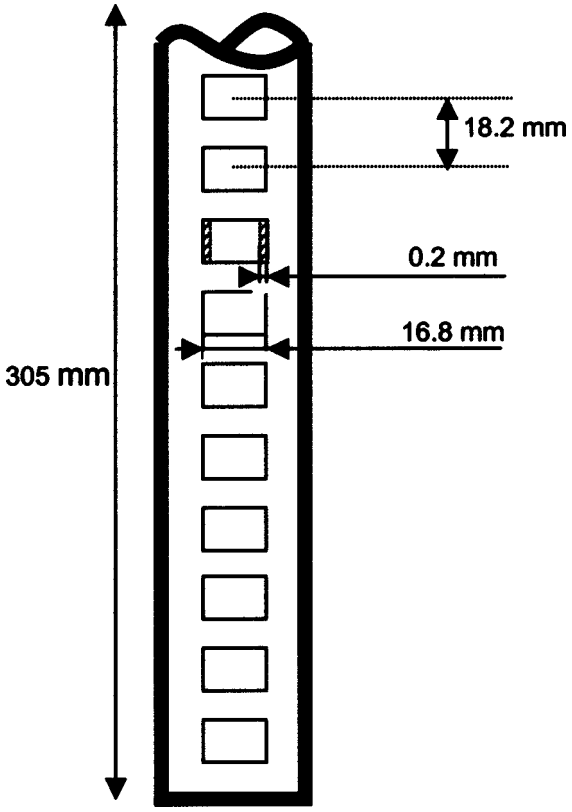

FIG. 3. Design of the ten-element transducer array of dimensions 38-mm diameter and 305-mm length. The hoop mode frequency of all the elements is around 73 kHz. All elements by themselves in both arrays are horizontally omni-directional. The elements are all matched to one another.

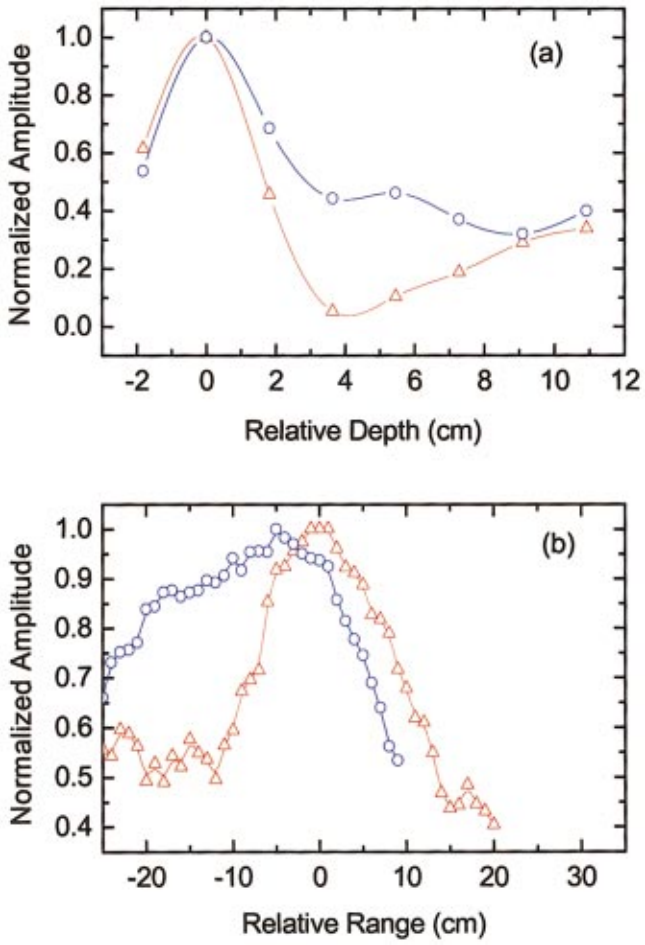

FIG. 4. Normalized, spline curve-fitted amplitude distribution of the focal region. (a) Focal region size as a function of depth for a 50-kHz (up-triangles) and a 65-kHz (open circles) signal. The depth is measured relative to the intended focal point. (b) Focal region size as a function of range for a 50-kHz (up-triangles) and a 65-kHz (open circles) signal. The range is measured relative to the intended focal point.

and 1.20 m deep. For better water sealing the wood is covered with a layer of fiberglass. The tank rests on a concrete floor on foundation level. Seawhisper™ anechoic tiles positioned 8 cm away from the tank walls cover the wall to a height of 28 cm. At normal incidence, the anechoic material reduces the echo reflection by about 25 dB in the frequency range between 20 and 100 kHz. Thus, the tank acts as a horizontally infinite waveguide with almost rigid bottom and pressure release surface. On top of the tank sits a rail system on which two carts can move. The carts are able to carry equipment and hold transducer arrays. One of them is driven by a step-motor, which is steered remotely from a computer system.

The two transducer arrays consist of ten cylindrical piezo-ceramic elements each (see Fig. 3). The elements are aligned vertically along their cylindrical axes within a PVC tube. The dimensions of the arrays are 38-mm diameter and 305-mm length. The hoop mode frequency of all the elements is around 73 kHz. All elements by themselves in both arrays are horizontally omni-directional. The elements are all matched to one another.

The data acquisition and generation are performed by four dual channel CompuScope™ 512 oscilloscope A/D cards and eight CompuGen™ 1100 function generator D/A made by Gage Applied Sciences. Thus a total of eight input and eight output channels are available. The CompuScope cards have a maximum of 5 Msamples per second, 12-bit resolution, and 2-MB memory. They have all features of digital storage oscilloscopes. Synchronicity in the captured signals from all channels is achieved by slaving the cards to a master. The CompuGen cards have a maximum of 80 Msamples per second, 12-bit resolution and up to 16-Msample memory. Synchronicity in the transmission of the signals is also achieved by slaving the cards to a master. The cards are addressed via two MEX-files from Gage Applied Sciences, which are called by MATLAB programs developed at the Naval Postgraduate School. Preamplification of the received analog signals, before they were captured by the oscilloscope cards, was done with a set of eight Stanford SR560 preamplifiers. Preset 6-dB/oct filtering of the incoming signals can be accomplished directly with the built-in filters. To amplify the output of the function generators we used a set of eight HP 467A amplifiers. This allowed us to amplify the signals up to ± 20 V peak to peak.

III. EXPERIMENTAL RESULTS

For the purpose of transmission and reception of multiple frequency signals, we found it best to use a frequency range between 50 and 65 kHz. Below this range, the response of our transducer system was weak. Above the frequency range of operation, the strong response at resonance

TABLE I. The center frequencies used in each symbol.

	Symbol no.														
	1	2	3	4	5	6	7	8	9	10	11	12	13	14	15
Center-frequency 1	×		×		×		×		×		×		×		×
Center-frequency 2		×	×			×	×			×	×			×	×
Center-frequency 3				×	×	×	×					×	×	×	×
Center-frequency 4								×	×	×	×	×	×	×	×

(~73 kHz) overshadowed the response at other frequencies. In the 50- to 60-kHz frequency range, the spacing between elements in the array is bigger than a half-wavelength of sound, and the spatial diversity of modes in depth is not optimally resolved.

Figures 4(a) and (b) show the extent of the focal region both in depth and range for 2-kHz bandwidth signals centered at 50 and 65 kHz. The focal region has an ellipsoidal cross section, with the major axis along the range direction and the minor axis along depth. The extent in depth of the focal region is ±1.5 cm as measured at the half-power point, corresponding to about 0.6 λ. Due to higher attenuation of the higher modes of the 65 kHz signal, the sidelobes at this frequency are stronger. Both frequencies show an increased amplitude at depths close to the rigid bottom, as should be the case. The extent in range of the focal region is larger. For 50 kHz it is about ±3λ, while it is about ±6λ for the 65-kHz signal. The loss of energy and therefore information in the higher modes contained in the higher frequencies leads to a stronger degradation of the focal region.

Because the focal region is limited in size and there are strong sidelobes outside of that region, there exists a natural encryption built into the transmission of messages. The signals do not focus well in time outside of the focal region and intersymbol interference makes it impossible to recover the messages. In order to show this we defined a simple code using the 15 symbols that can be obtained from four center frequencies at 50, 55, 60, and 65 kHz. A symbol is a single

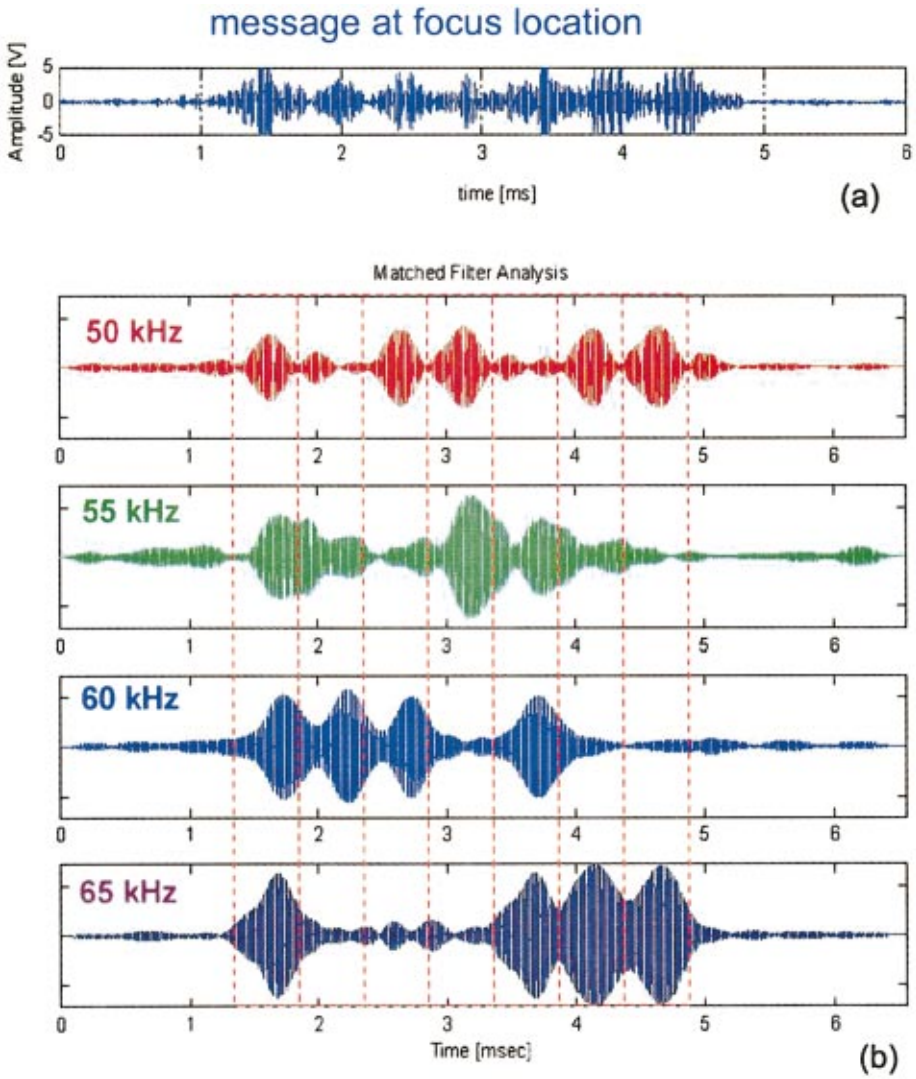

FIG. 5. The spectrograms shown above are the result of a matched-filter analysis on the received messages. Unlike FFT where individual frequency components are synthesized, the matched filtering technique synthesizes predefined signals. In our case the predefined signals are a set of broadband signals with identical bandwidth, and Hanning window source spectra, with a separation between center frequencies twice the signals bandwidth. The spectrogram (b) of the message at the focus location (a) is clearly and easily resolvable. The dashed vertical lines show the symbols with respect to time. Using the accompanied Table I the message reads ''15-4-5-3-14-9-9.''

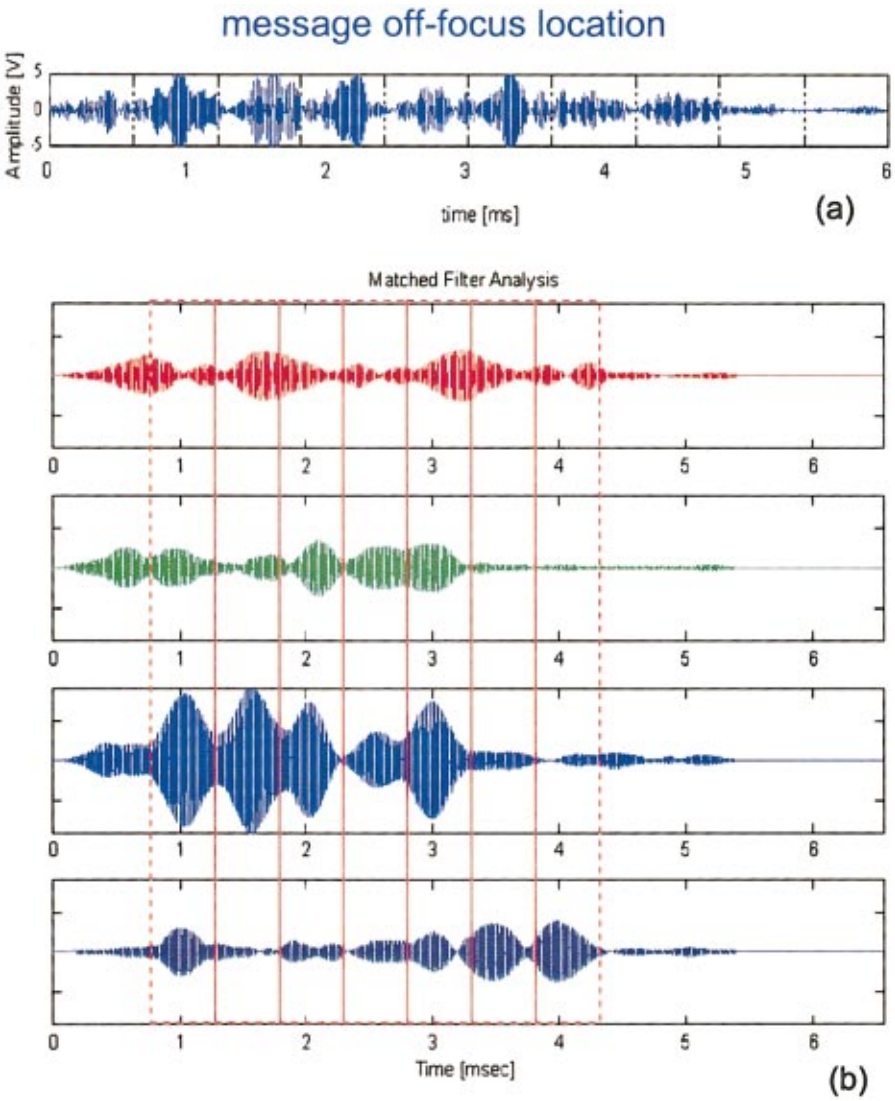

FIG. 6. For the matched-filter analysis of the incoming message outside the focal region (a), shown in the spectrogram (b), using the accompanied Table I the message reads ''4-4-4-0-4-0-0.'' This is not the intended message, indicating natural encryption for points other than the intended receiver.

pulse containing one, two, three, or all four center frequencies. A symbol thus contains information which can be related to a code. Four center frequencies can be combined in 15 different ways, excluding the null symbol which contains no acoustic energy. For each combination we assigned a number between 1 and 15 as shown in Table I.

The three quantities that determine data rates are intersymbol spacing, bandwidth, and center frequency spacing. The bandwidth determines the time span of the symbol, and the frequency spacing determines the resolution of the information contained in a symbol. The intersymbol spacing is mainly determined by the energy of the temporal sidelobes at the focal point. The use of a Hanning window minimized the temporal sidelobes, allowing also for a minimum intersymbol spacing equal to half the temporal width of the signals. This is not the case for a rectangular window. Thus, under this symbol spacing condition it is important to select frequency signals which give a reception that can be resolved in its frequency components. Our criteria for accepting a signal as resolvable is that the sum of two temporal sidelobes must be less than the energy detection threshold corresponding to half the amplitude of the main peaks. This criteria is based on the notion that when the temporal sidelobes of two adjacent symbols are added, the symbol can still be resolved. For a message containing Hanning window signals and with the temporal spacing between symbols as described above, the maximum signal bandwidth is 2.5 kHz, when the received symbols were match filtered with the initial signals whose frequency spacing is 5 kHz. Therefore, using a match filter approach we find a ratio of 2 to 1 for center frequency spacing to bandwidth. With the matched filter the frequency content of all symbols in a message is deciphered at once.

The message we used was ''15-4-5-3-14-9-9.'' The matched filter result of Fig. 5 shows that this message is clearly resolvable at the focal point. This should be contrasted with the matched filter result of Fig. 6, where the message was recorded five wavelengths outside of the focal region. Note that in this case, under the same energy threshold conditions the received message reads ''4-4-4-0-4-0-0.''

IV. SUMMARY

The results presented above show that the TRA approach is suitable to overcome multipath-related problems in underwater acoustic communications. The results show good focusing of energy in time and space at the intended target

location. The focusing extends over a few wavelengths in range. Outside of the focal region multipath propagation leads to scrambling of the message, thus showing that the TRA technique offers natural encryption of the signals. The results also show potential for high data rates in binary data transmissions. For a bandwidth of 2.5 kHz, a transmission of 2500 symbols per second can be realized. Thus, for symbols built out of four possible center frequencies the transmission rate corresponds to 10 kbits per second.

Research in underwater acoustic communications using time-reversal acoustics at the Naval Postgraduate School is ongoing. Current and future efforts will also include studies of more sophisticated schemes and of the sensitivity of such communication systems to temporal and spatial variability of the shallow water acoustic channel. Because TRA relies upon the coherent summation of multipath propagation to produce focusing, rapid fluctuations of the environment may pose serious challenges to such techniques. One example is the short decorrelation times of surface reflected paths. By studying such effects in the controlled conditions of the scale model tank apparatus, we intend to address these issues in a more cost-effective manner before deploying sea trials.

Abrantes, A. A. M., Smith, K. B., and Larraza, A. (**1999**). ''Examination of time-reversal acoustics and applications to underwater communications,'' J. Acoust. Soc. Am. **105**, 1364.

Fink, M. (**1997**). ''Time Reversed Acoustics,'' Phys. Today **March 1997**, 34–40.

Fink, M. (**1999**). ''Time-reversed acoustics,'' Sci. Am. **November 1999**, 91–97.

Jackson, D. R., and Dowling, D. R. (**1991**). ''Phase conjugation in underwater acoustics,'' J. Acoust. Soc. Am. **89**, 171–181.

Kuperman, W. A., Hodgkiss, W. S., Song, H. C., Akal, T., Ferla, C., and Jackson, D. R. (**1998**). ''Phase conjugation in the ocean: Experimental demonstration of an acoustic time-reversal mirror,'' J. Acoust. Soc. Am. **103**, 25–40.

Roux, P., Roman, B., and Fink, M. (**1997**). ''Time reversal in an ultrasonic waveguide,'' Appl. Phys. Lett. **70**, 1811–1813.

Smith, K. B., Abrantes, A. A. M., and Larraza, A. (**2003**). ''Examination of time-reversal acoustics in shallow water and applications to noncoherent underwater acoustic communications,'' J. Acoust. Soc. Am. **113**, 3095–3110.

Measurement and prediction of ultralow frequency ocean ambient noise off the eastern U.S. coast

D. Keith Wilson,[a] George V. Frisk, Timothy E. Lindstrom,[b] and Cynthia J. Sellers
Department of Applied Ocean Physics and Engineering, Woods Hole Oceanographic Institution, Woods Hole, Massachusetts 02543

(Received 13 December 2001; revised 29 January 2003; accepted 31 January 2003)

Ultralow frequency (0.02–2 Hz) acoustic ambient noise was monitored from January to April 1991 at six ocean bottom stations off the eastern U.S. coast. The depths of the stations ranged from about 100 m to 2500 m. The measured spectra are in good agreement with predictions made using Cato's theory [J. Acoust. Soc. Am. **89**, 1076–1095 (1991)] for noise generation by surface-wave orbital motion after extending the calculations to incorporate horizontally stratified environments. Contributions from both the linear, single-frequency (virtual monopole) and the nonlinear, double-frequency (dipole) mechanisms are clearly recognizable in the data. The predictions make use of directional wave data obtained from surface buoys deployed during the SWADE experiment and an ocean bottom model derived from compressional wave speed data measured during the EDGE deep seismic reflection survey. The results demonstrate conclusively that nonlinear surface-wave interactions are the dominant mechanism for generating deep-ocean ULF noise in the band 0.2–0.7 Hz. [DOI: 10.1121/1.1568941]

PACS numbers: 43.30.Nb, 43.30.Lz [DLB]

I. INTRODUCTION

This paper presents results from ECONOMEX, the Environmentally Controlled Ocean-floor NOise Monitoring EXperiment. The overall purpose of ECONOMEX was to study the variability, both with respect to depth and time, of ULF/VLF (0.001–10 Hz) ambient noise in a continental margin region. Six ONR Ocean Bottom Seismometers (OBS's), equipped with differential pressure gauges (DPG's) and three-component seismometers, were deployed from January to April 1991. The sensors were placed off the Virginia coastline in water depths ranging from 95 m to 2600 m.

A more specific goal of the experiment was to determine conclusively whether ULF/VLF noise in the ocean (particularly at deep sites), and the associated seismic activity known as microseisms, are generated by nonlinear interactions of ocean surface waves. It has long been understood that an evanescent pressure wave exists under ocean surface waves, having frequency equal to the surface waves. The seismic waves generated by these pressure disturbances are referred to as *single-frequency microseisms*. Because of its evanescent nature, however, the single-frequency mechanism cannot be the cause of typical ULF/VLF noise levels observed at deep ocean sites. Recognizing this fact, Longuet-Higgins[1] proposed one-half century ago that the primary source of ULF/VLF noise in the deep ocean is a nonlinear interaction between opposing surface wavetrains, which produces a nonevanescent pressure disturbance in the ocean at a frequency twice that of the ocean surface waves. The resulting seismic activity is known as *double-frequency microseisms*.

More recently, Cato[2,3] developed a comprehensive theory, based on Lighthill's analogy, for ocean noise generation by the sea-surface motions. The single-frequency noise field is associated with a time-varying mass flux at the surface, which radiates sound as a distribution of virtual monopoles. The double-frequency noise field is associated with a time-varying momentum flux at the surface, which radiates sound as a distribution of virtual dipoles.

Since the mid-1980s, many authors[3–13] have provided good experimental evidence in support of the Longuet-Higgins theory. (See also the recent review article by Webb.[14]) Most of the initial studies (Refs. 4–8) relied on surface wave spectra estimated from mean wind speed measurements. Kibblewhite and Ewans,[9] however, made simultaneous measurements of seismic waves and surface wave height spectra in 100 m of water. A study by Cato[3] involved simultaneous measurements of noise and surface wave height spectra in a lake. More recently, Babcock *et al.*,[10] Nye and Yamamoto,[11] Herbers and Guza,[12] and Tindle and Murphy[13] performed simultaneous measurements of microseisms and surface wave height spectra in the open ocean. We note that the work described in Refs. 10–12 was part of the ONR Sources of Ambient Microseismic Ocean Noise (SAMSON) experiment, which was conducted in October to November 1990 off the coast of North Carolina.

ECONOMEX, which followed shortly after SAMSON, provided oceanfloor noise measurements in the band 0.02–2 Hz at a wide range of depths over several months. Excellent supporting environmental data were also available. Surface-wave directional spectra were recorded concurrently as part of the SWADE (Surface WAve Dynamics Experiment) project.[15] These data are the essential environmental control needed to test Cato's theory. SWADE also provided meteorological data such as wind speed and direction. In addition to the surface-wave directional spectra, accurate modeling of ULF/VLF noise in the ocean requires profiles of compressional and shear wave speeds deep into the Earth's crust. In this regard, ECONOMEX benefitted from the availability of deep seismic profiles determined during the EDGE survey.[16]

[a]Present address: U.S. Army Cold Regions Research Laboratory, CEERD-RC, 72 Lyme Rd., Hanover, NH 03755-1290.
[b]Present address: Commander, Submarine Squadron 20, 1050 USS Georgia Avenue, Kings Bay, GA 31547

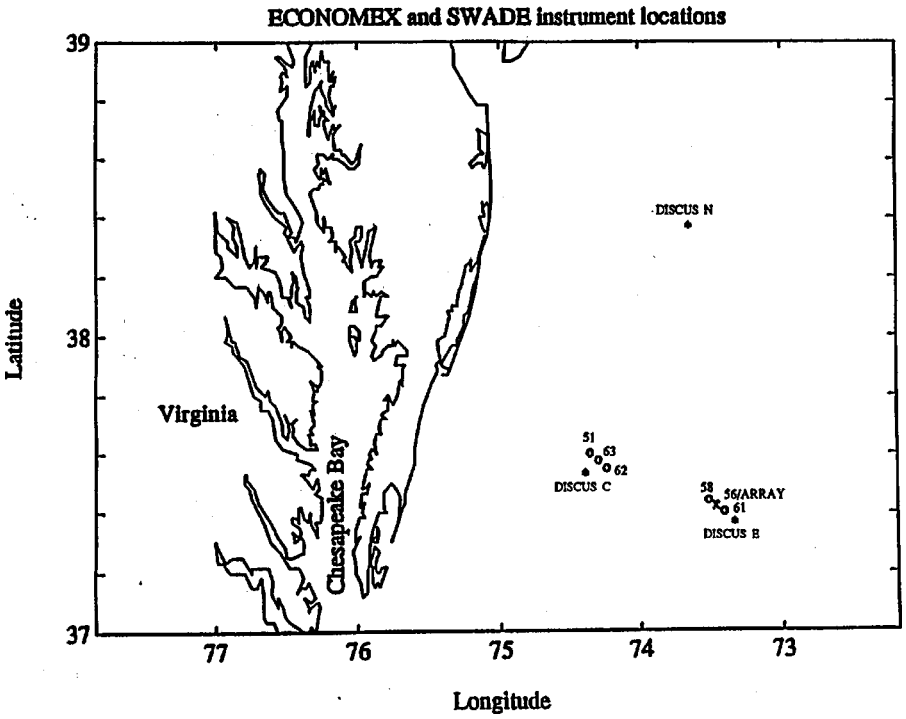

FIG. 1. Approximate locations of the ECONOMEX and relevant SWADE instruments. "*" denotes pitch and roll buoy location, "×" denotes location of one ONR ocean bottom seismometer (OBS) and two hydrophone arrays, and "○" denotes the location of one ONR OBS.

Using the EDGE data, we are able to estimate the compressional and shear wave speed profiles to depths of 10 km, and then incorporate these profiles into a noise prediction model.

The format of the paper is as follows. In Sec. II, we discuss the ECONOMEX data set and the environmental inputs (the SWADE and EDGE data) used by our noise prediction model. Our predictive model for the ULF/VLF spectra, which is based on Cato's theory,[2,3] is described in Sec. III. Last, in Sec. IV, seafloor pressure spectra from ECONOMEX are compared to the model, with special attention given to the relationship between changing wave height conditions and the double-frequency noise field.

II. EXPERIMENT

A. ECONOMEX deployments

ECONOMEX was designed to provide a long-term, high-quality, seismo-acoustic data set that could be coupled to the surface wave and meteorological data of the SWADE experiment. The instrumentation consisted of six Office of Naval Research (ONR) ocean bottom seismometers (OBS's) and two (one vertical and one horizontal) 75 m, six-element hydrophone arrays. The instruments were deployed off the Virginia coast in January 1991, recovered in February 1991 for maintenance, and redeployed from February through

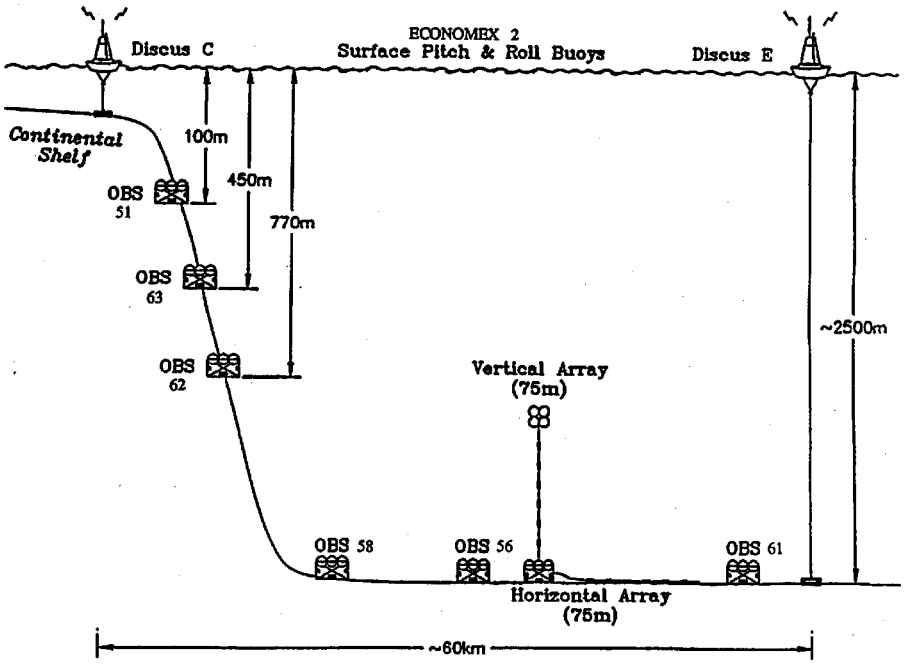

FIG. 2. Schematic arrangement of ECONOMEX and SWADE deployments.

TABLE I. Locations of the ECONOMEX instruments. Positions and depths listed are for the second leg of the experiment; those for the first leg differ only slightly. Also note OBS frames 61 and 62 exchanged positions between the first and second legs, although the instruments on them were exchanged also such that the instruments remained deployed in the same locations.

Instrument name	Lat.	Long.	Depth (m)	Deployment dates (1991)
Vert. array	37° 24.7′ N	73° 26.8′ W	2573	25 Jan–6 Feb; 22 Feb–5 Apr
Horz. array	37° 24.7′ N	73° 26.8′ W	2573	25 Jan–6 Feb; 22 Feb–5 Apr
OBS 56	37° 24.7′ N	73° 26.8′ W	2548	25 Jan–6 Feb; 22 Feb–5 Apr
OBS 58	37° 26.4′ N	73° 31.4′ W	2417	24 Jan–7 Feb; 22 Feb–5 Apr
OBS 61	37° 23.8′ N	73° 24.4′ W	2600	25 Jan–6 Feb; 21 Feb–4 Apr
OBS 62	37° 33.2′ N	74° 14.1′ W	769	11 Jan–6 Feb; 22 Feb–5 Apr
OBS 63	37° 34.1′ N	74° 16.5′ W	443	10 Jan–6 Feb; 22 Feb–5 Apr
OBS 51	37° 35.9′ N	74° 21.3′ W	95	10 Jan–6 Feb; 22 Feb–5 Apr

early April 1991. The instrument locations are shown schematically in Figs. 1 and 2. Precise locations and deployment dates are listed in Table I.

The deployed ONR OBS instruments consisted of a three-component geophone for measuring ground motion in the 0.07 to 80 Hz range, a Cox–Webb differential pressure gauge (DPG) for measuring long-period pressure signals in the water column, and in the original deployment, an OAS hydrophone.[18] In the later deployment, these hydrophones were removed to improve instrument reliability.

The sensors were connected via preamplifiers to an acquisition package consisting of a prewhitening and antialiasing filter, a gain-ranging amplifier to improve dynamic range, and an analog-to-digital converter. The combined filter response is shown in Fig. 3. The acquisition package fed a recording unit consisting of a RAM buffer and an optical disc recording system capable of storing 400 megabytes of data. Most of the OBS's were programmed for continuous 8 Hz recording, with the antialiasing filter set to 2 Hz; however, one of the devices (OBS 56) was set to record at 128 Hz with its antialiasing filter set to 40 Hz.

The 75 m horizontal and vertical arrays each consisted of six OAS hydrophones at 15 m separation. The hydrophone signals were preamplified by a low-noise, wide-range preamplifier and sent to acquisition and recording packages identical to those of the OBS's, with 128 Hz sampling and the antialiasing filter set to 40 Hz. In the second deployment the bottom three hydrophones of the vertical array were not included due to a cable malfunction. The array cable jacket included loose ended fiber strands to reduce strumming noise.

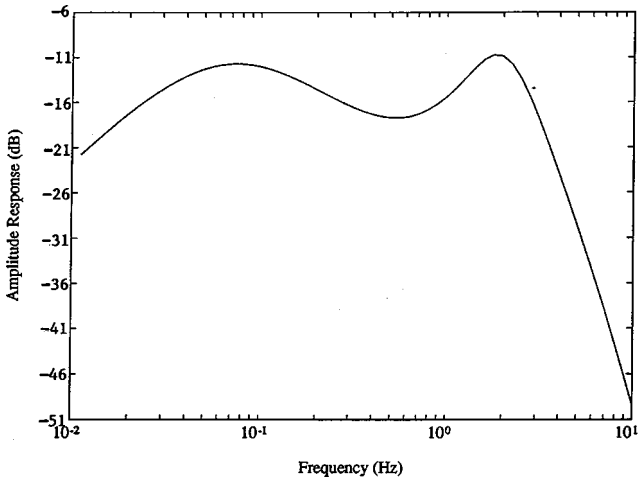

FIG. 3. Amplitude response of the antialiasing and prewhitening filter used in the ECONOMEX instruments with an 8 Hz sampling rate. Response amplitude in dB *re* 1 V.

B. ECONOMEX DPG time series and processing

The focus of this paper is on the DPG time series. Power spectra from these data were computed by partitioning the overall time series into records of 4096 samples, each having 512 s (8.5 min) duration. The responses of the prewhitening and antialiasing filter were then removed from each record. The results, for the entire second observational period of ECONOMEX, are shown in the upper panels of Figs. 4–7. These figures are for OBS 51 (95 m depth), OBS 63 (443 m depth), OBS 62 (769 m depth), and OBS 61 (2600 m depth), respectively. (The gaps in these figures are intervals when data were not acquired.)

The spectra are observed to have a strong depth dependence. Sound pressure levels at the shallowest sensor (OBS 51), in the frequency band 0.06–0.12 Hz, are in the range 150–170 dB *re* 1 $(\mu\text{Pa})^2$/Hz. These are the highest levels recorded at any of the sensors. In roughly the same band, the sound levels recorded by the sensors at the greater depths were all between 70 and 90 dB.

At the next shallowest sensor (OBS 63), levels in the range 120–130 dB are evident below 0.06 Hz. Comparable levels are evident at OBS 62, below 0.04 Hz. No such low frequency energy is evident at the deepest sensor (OBS 61), at least for the frequency range displayed on the spectral plots. The spectral energy below about 0.12 Hz can be confidently attributed to the single-frequency noise field, for which the spectral energy decays exponentially with increasing depth and frequency. As the sensor depth is increased, higher frequencies are unable to penetrate to the bottom.

At the deepest sensor (OBS 61, 2600 m), most of the spectral energy lies in the band 0.2–0.5 Hz. The levels exhibit considerable temporal variability, fluctuating between about 110 and 145 dB. As will become evident when we examine the surface-buoy data, the variability in the pressure field at OBS 61 strongly parallels variations in wave-height power spectrum occurring at one-half the acoustic frequency. The spectral energy in this band must therefore be the double-frequency generation mechanism created by nonlin-

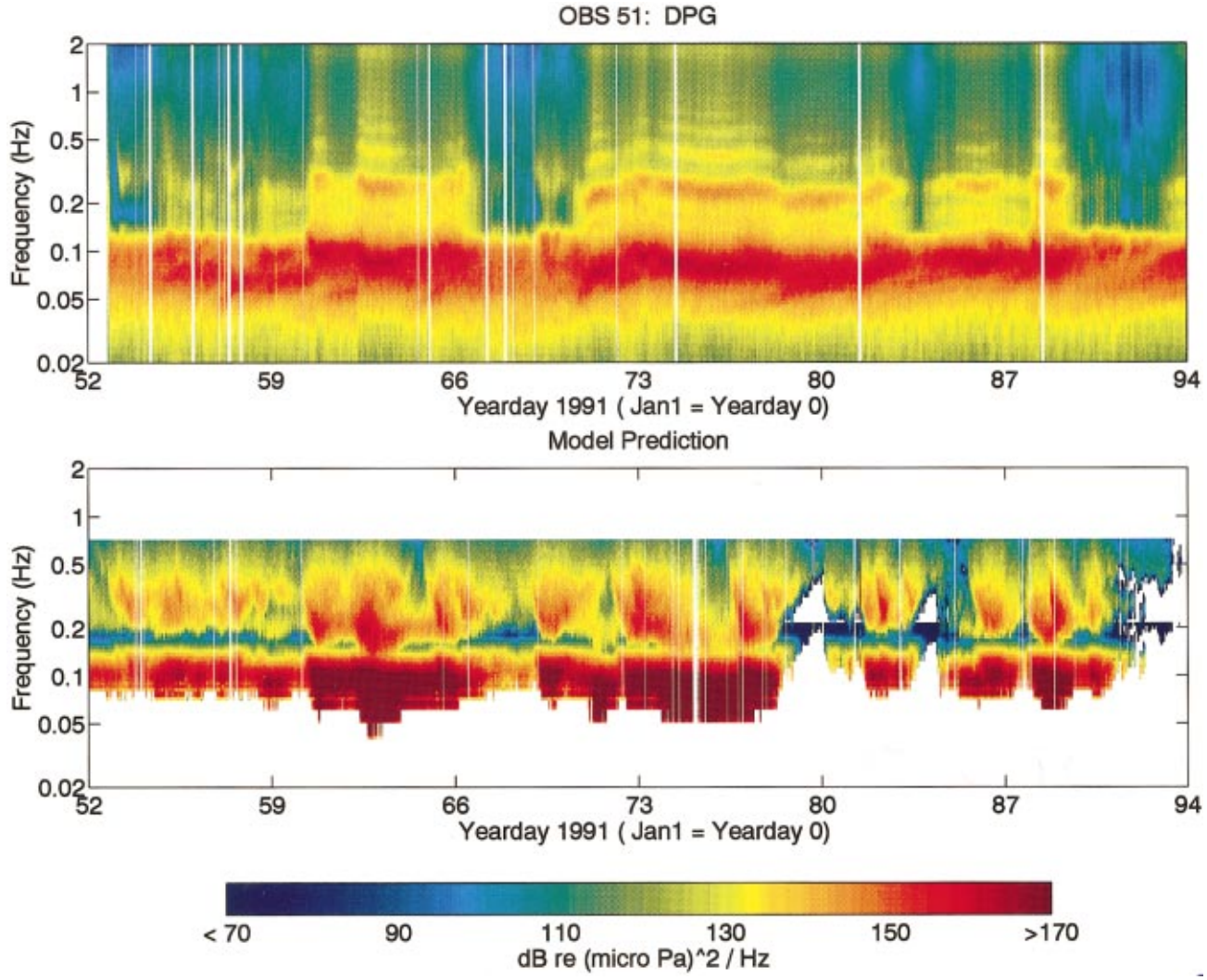

FIG. 4. Differential pressure gauge (DPG) power spectral levels for OBS 51 (95 m depth), second deployment. Upper, measurement. Lower, model prediction.

ear interaction of opposing wavetrains, as was first suggested by Longuet-Higgins.[1] The double-frequency noise, including as it does a nonevanescent component (i.e., a component that does not attenuate with increasing depth), is strong at the deepest sensor, whereas the single-frequency noise, which is evanescent, is not observed there. The nonevanescent nature of the double-frequency noise also explains why it is evident at the other OBS's with approximately the same strength. At OBS 63 and 62 (443 and 769 m), a spectral gap is evident between the single- and double-frequency noise. The gap is not present at OBS 51, since higher frequencies attributable to single-frequency pressure disturbances are able to penetrate to its relatively shallow depth of 95 m. We will develop a quantitative model for these effects in Sec. III.

C. Supporting data

1. SWADE surface wave spectra

The SWADE project was an effort to characterize the sea surface using a variety of sensors and, at the same time, measure other relevant environmental parameters.[15] The project included several pitch and roll surface buoys, satellite radar backscatter measurements, SWATH ship array deployments, and aircraft overflights. The long-term deployment of the pitch-and-roll buoys is the element of the experiment of direct use in our effort to predict noise generated by surface wave motion. In particular, the buoys were used to determine the surface-wave directional spectra required by our noise prediction model. Collection and processing of the SWADE data are discussed in this section.

The SWADE instrument locations are shown together with the ECONOMEX instruments in Figs. 1 and 2. Precise deployment locations of SWADE instruments are listed in Table II. The buoys provided one complete set of measurements (including a spectral estimate) each hour, allowing us to update our estimate of the noise field each hour. The SWADE buoys that were closest to the ECONOMEX instruments were Discus C and Discus E. Figure 8 shows wind speed, time rate-of-change of wind direction, and the wave height power spectrum from Discus E for the duration of ECONOMEX. Periods of elevated activity lasting typically 2–3 days are clearly evident in the spectra. These usually correspond to mid-latitude cyclonic activity in the atmosphere (storms).

The wave-height spectral data from the SWADE buoys were provided for frequencies from 0.03 Hz to 0.34 Hz, in 0.01 Hz bins. For predicting the noise at the deep

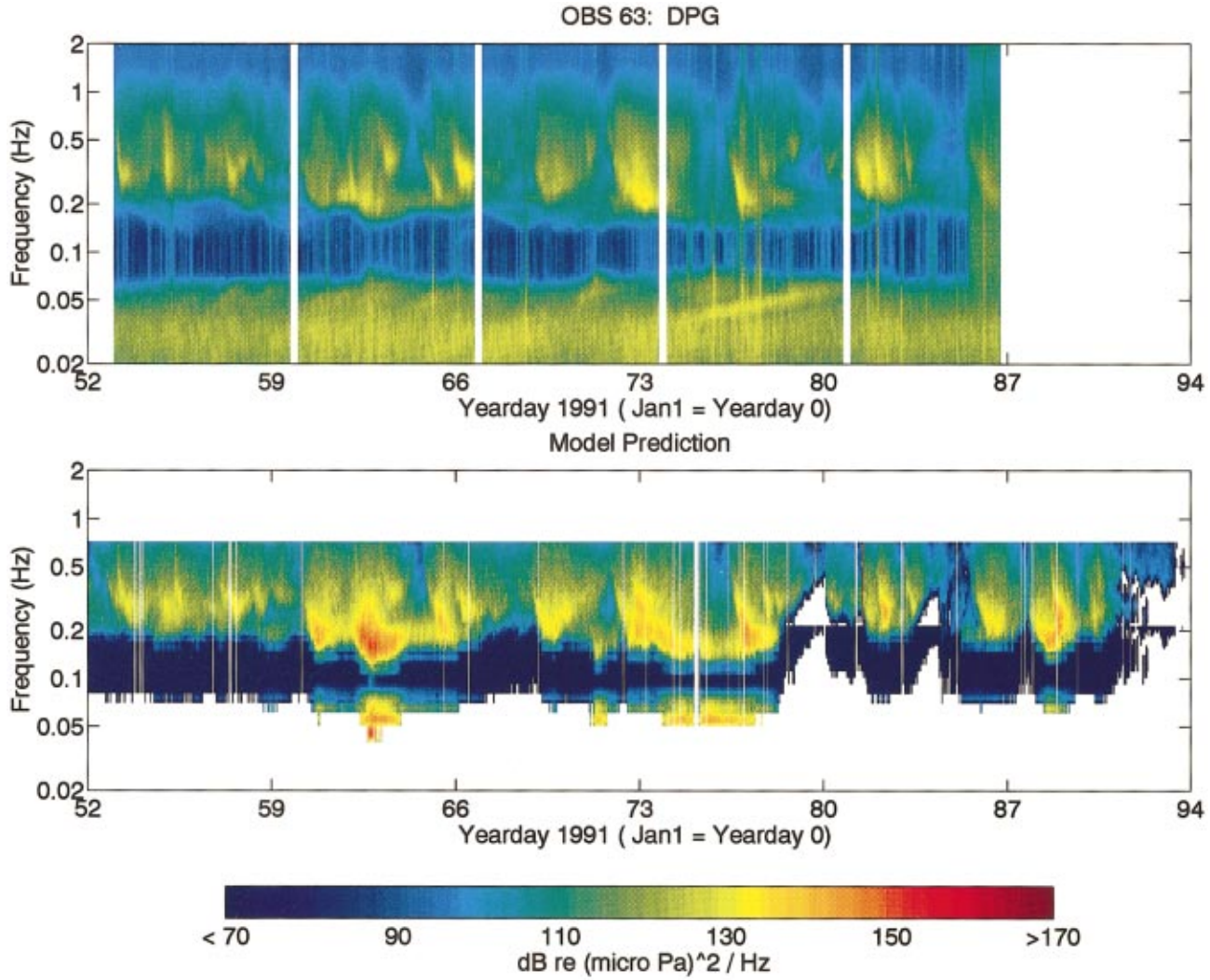

FIG. 5. DPG power spectral levels for OBS 63 (443 m depth), second deployment. Upper, measurement. Lower, model prediction.

ECONOMEX site, the data from Discus E were used, while predictions of noise at the three shallowest ECONOMEX instruments were based on data from Discus C. SWADE had also deployed a SPAR buoy (which had better angular resolution than the Discus buoys) near the shallow ECONOMEX site, but it sank prior to the ECONOMEX deployments.

As is well known, ocean surface waves are dispersive, with the relationship depending on water depth. We should therefore consider the possible effect of using a surface buoy moored in 95 m of water (Discus C) to predict noise at the 443 m and 769 m OBS's. First we note from the measured wave spectra that there is little energy below 0.1 Hz in the wave spectrum. If we calculate $\tanh(kd)$ (the depth-dependent factor of the surface-wave dispersion relation) for the worst case of 0.1 Hz with $d = 95$ m, we find the dispersion factor to be less than 1%. Thus any corrections to the wave spectra measured at Discus C for the 443 m and 769 m OBS's are quite small.

Pitch-and-roll buoys, such as the Discus buoys, can provide only an estimate of the surface-wave directional spectrum. Because our ULF/VLF noise prediction model (Sec. III) depends strongly on the directional spectrum, the method used to estimate the spectrum takes on critical importance. The case of particular interest is when the wind direction changes rapidly in time, creating opposing wavetrains on the sea surface. This situation causes the spreading integral (required for predictions of the double-frequency noise field) to be large. Among the many methods available we have considered are empirical estimates, the Longuet-Higgins *et al.*[17] method, maximum-likelihood (MLM) estimates, and maximum-entropy (MEM) estimates. The reader is referred to the Appendix for a more detailed discussion of our procedures for making the wave-directional estimates.

The four methods of wave-directional spectral estimation are compared in Fig. 9. A simulated bi-directional spectrum was the input. In Fig. 10 we compare estimates of the directional spectra for an actual datum from SWADE: the 0.16 Hz bin from Discus E at 1200 on 27 January 1991. This datum was chosen as illustrative because it occurs after a shift in wind direction, and one would expect the true spectrum to be bi-directional in this case. One can see from the two figures that MEM is most satisfactory in reproducing a sharply peaked, bi-directional distribution. In fact, a bi-directional structure is evident only in the MEM estimate in Fig. 10. Hence we decided to use MEM for our estimates of the wave-directional spectrum.

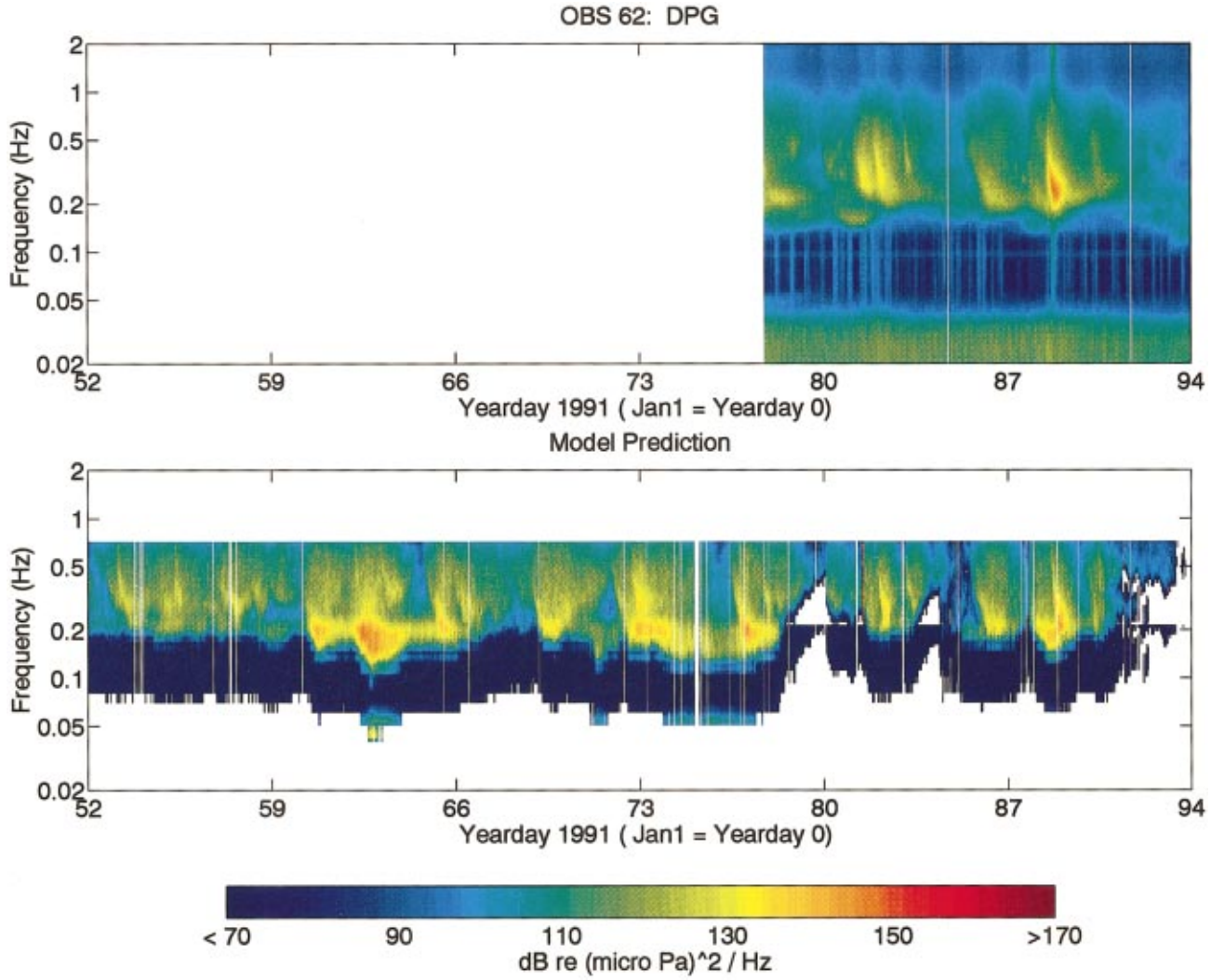

FIG. 6. DPG power spectral levels for OBS 62 (769 m depth), second deployment. Upper, measurement. Lower, model prediction.

2. EDGE profiles

In this section, we discuss our procedure for determining the vertical profiles of the compressional wave speed, shear wave speed, compressional and shear attenuations, and density, as required for input to our noise propagation model. Due to the long wavelengths involved at the very low frequencies of the predictions, the environmental model needs to be as accurate as possible deep into the earth's crust.

As described in the next section, the propagation model is formulated for a horizontally stratified environment. The environment is partitioned into several layers, each having constant seismic properties. The uppermost layer, actually a semi-infinite half space, is the air layer, represented by a vacuum in our model. The next layer down, the water layer, is assumed to have a constant sound speed of 1500 m/s and constant density of 1000 kg/m^3. Approximating the water column as an isovelocity, isodensity layer is quite reasonable for the very low frequencies relevant to the present study.

Below the water layer are 10 to 12 earth layers. Data from a deep seismic reflection study of the U.S. mid-Atlantic continental margin, called EDGE, were used to help determine the seismic profiles. The EDGE experiment[16] involved recording refracted seismic waves of 16 s duration off the Virginia coast, in the same region as the ECONOMEX and SWADE experiments. But because EDGE provided only compressional wave speed data, we were forced to estimate the shear wave speed, compressional attenuation, shear attenuation, and density profiles. Hamilton's[19] data and equations were used for this purpose, and we also benefitted from discussions with other investigators working in the area of geoacoustic modeling.[20,21] The resulting profiles for each of the four water depths (95, 443, 769, and 2600 m) are plotted in Fig. 11.

III. THEORY AND CALCULATIONS

Our method for predicting the pressure field generated by surface wave motion is summarized in this section. Based on Cato's theory,[2] it includes contributions from virtual monopoles and dipoles of all orientations. The surface-distributed monopoles, which are the source of the single-frequency noise field, correspond to a time-varying mass flux across the mean position of the ocean surface. The dipoles, which are the source of the double-frequency noise field, correspond to a time-varying momentum flux.

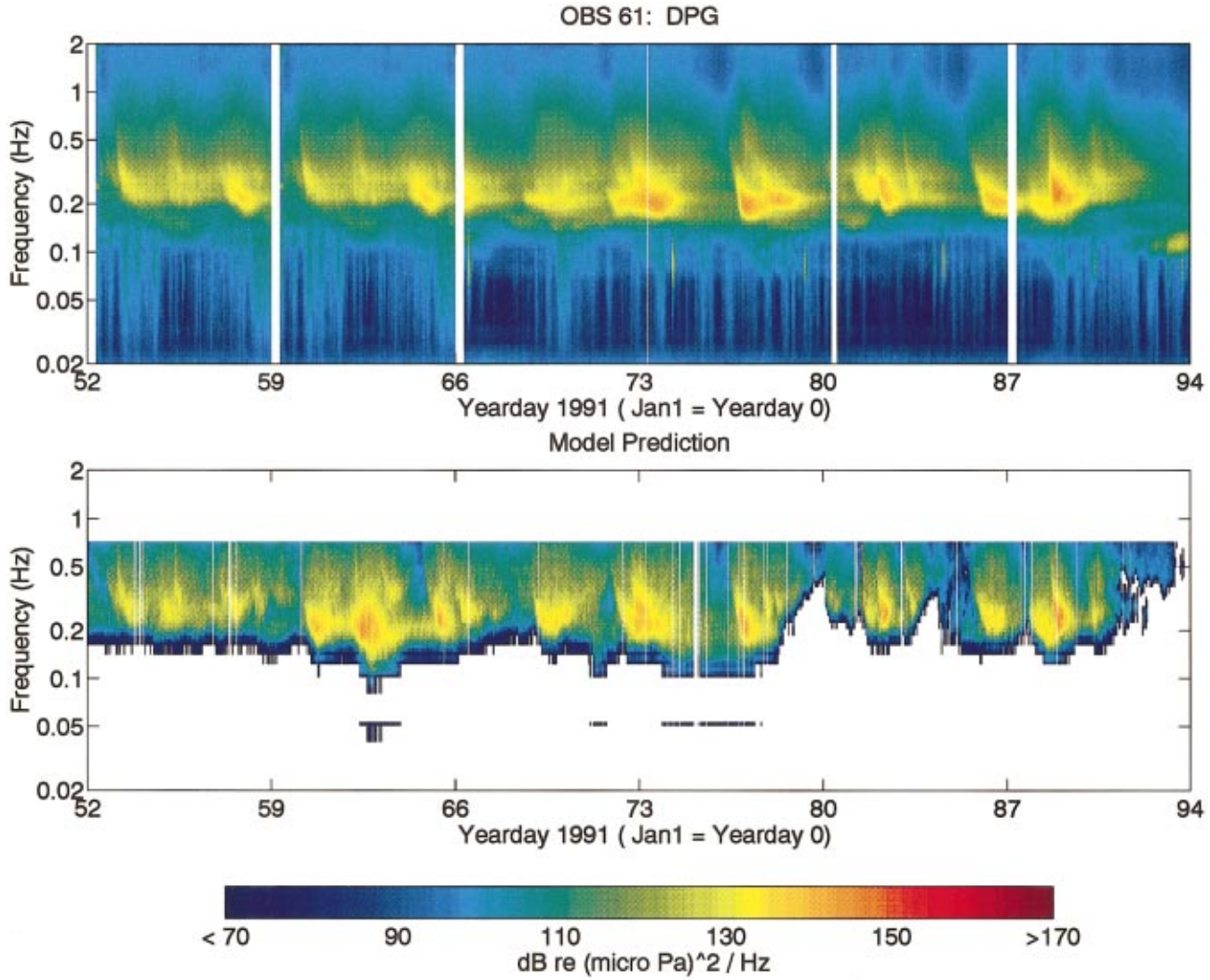

FIG. 7. DPG power spectral levels for OBS 61 (2600 m depth), second deployment. Upper, measurement. Lower, model prediction.

Cato's equation for the double-sided spectral density P_M from the monopoles is

$$P_M(\omega)=\rho^2 c^2 \int_{-\infty}^{\infty} \Psi_{33}(\omega,\mathbf{k}) \times H_0(\omega,\mathbf{k},z) H_0^*(\omega,\mathbf{k},z) \frac{d\mathbf{k}}{(2\pi)^2}, \quad (1)$$

where $\omega=2\pi f$ is the angular frequency, c the sound speed in the water column, $\mathbf{k}$ the horizontal wave number of the surface gravity wave, z the depth, and the superscript asterisk denotes the complex conjugate. The quantity Ψ_{ij} is the cross-spectral density between the velocity components of the surface, u_i and u_j, with subscripts 1 and 2 indicating horizontal axes, and 3 the vertical axis, which originates at the surface and is oriented downward. The quantity H_0, called the monopole coupling factor, includes the effects of interference, source directivity, and spreading. Specifically, for an infinitely deep, cylindrical ocean of radius R, H_0 is given by [Ref. 2, Eq. (72)]:

$$H_0(\omega,k,z)=\frac{\omega}{2c}\int_0^R \frac{\exp(-i\omega r/c)}{r} J_0(k\hat{r})\hat{r}\, d\hat{r}, \quad (2)$$

where $\hat{r}^2=x^2+y^2$ is the horizontal displacement, and $r^2=\hat{r}^2+z^2$ is the total distance from the source to the receiver.

The dipole contributions P_D are given by [Ref. 2, Eq. (48); also Ref. 3, Eqs. (1) and (A7)]

$$P_{D,ij}(\omega)=\rho^2 \int_{-\infty}^{\infty} [\Phi_{i3j3}(\omega,\mathbf{k})+\Phi_{i33j}(\omega,\mathbf{k})] \times H_i(\omega,\mathbf{k},z) H_j^*(\omega,\mathbf{k},z) \frac{d\mathbf{k}}{(2\pi)^2}, \quad (3)$$

where

$$\Phi_{ij\ell m}(\omega,\mathbf{k})=\Psi_{i\ell}(\omega,\mathbf{k}) * \Psi_{jm}(\omega,\mathbf{k}), \quad (4)$$

TABLE II. Locations of the SWADE Discus buoys.

Instrument name	Lat.	Long.	Water depth (m)
Discus E	37° 20.0′ N	73° 23.5′ W	2670
Discus C	37° 32.1′ N	74° 23.5′ W	102
Discus N	38° 22.1′ N	73° 38.9′ W	115

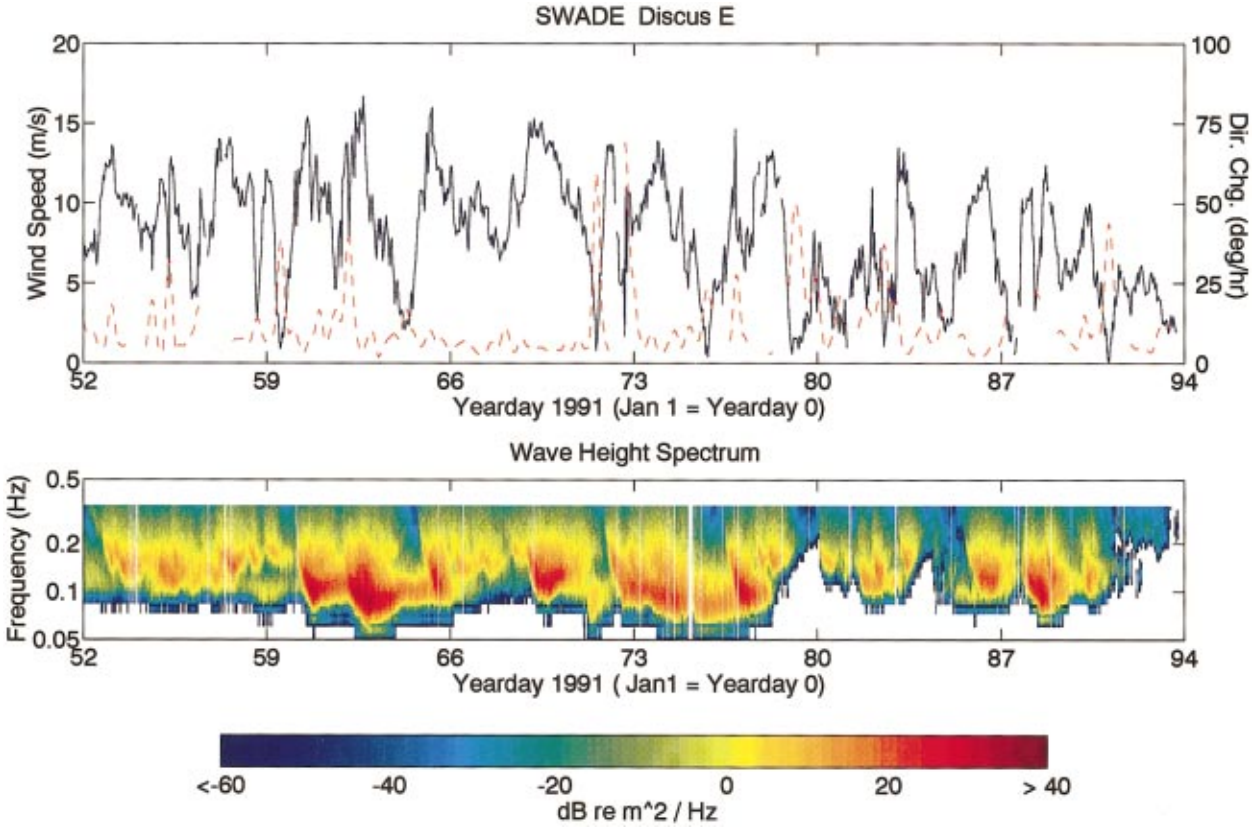

FIG. 8. Data from SWADE Discus E buoy, during the time period of ECONOMEX second deployment. Upper, wind speed (solid line) and rate-of-change of wind direction (dashed line). Lower, wave height power spectrum.

with the asterisk denoting convolution in both frequency and wave number. [No sum over repeated indices is implied in Eq. (3).] The dipole coupling factors are

$$H_1(\omega,\mathbf{k},z) = -i(kc/\omega)\cos\alpha H_0(\omega,k,z), \tag{5}$$

$$H_2(\omega,\mathbf{k},z) = -i(kc/\omega)\sin\alpha H_0(\omega,k,z), \tag{6}$$

$$H_3(\omega,\mathbf{k},z) = \frac{c}{\omega}\frac{\partial}{\partial z}H_0(\omega,k,z), \tag{7}$$

where $\mathbf{k}=(k_x,k_y)=(k\cos\alpha, k\sin\alpha)$.

Using the surface-wave dispersion relation, Eq. (3) can be reduced to[3]

$$P_{D,ij}(\omega) \approx \pi\rho^2 \left[\frac{\hat{\omega}^4}{\hat{k}}\frac{d\hat{\omega}}{dk}\Omega^2(\hat{\omega})\right]_{\hat{\omega}=|\omega/2|} \times I_{ij}(|\omega/2|)K_{ij}(|\omega|,z), \tag{8}$$

where

$$I_{ij}(\omega) = \int_0^{2\pi} G(\omega,\alpha)G(\omega,\pi+\alpha) \times |h_i(\hat{k}(\omega),\alpha)||h_j[\hat{k}(\omega),\alpha]|\,d\alpha \tag{9}$$

is called the surface-wave *spreading integral*, $\Omega(\omega)$ is the surface-wave-height power spectrum, $G(\omega,\alpha)$ is the surface-wave directionality function, $\hat{k}(\omega)$ is the wave number satisfying the surface-wave dispersion relation $\omega^2 = g\hat{k}\tanh\hat{k}h$, $h_1(k,\alpha)=i\cos\alpha\coth(kh)$, $h_2(k,\alpha)=i\sin\alpha\coth(kh)$, $h_3(k,\alpha)=1$, and

$$K_{ij}(\omega,z) = \int_{-\infty}^{\infty} H_i(\omega,\mathbf{k},z)H_j^*(\omega,\mathbf{k},z)\frac{d\mathbf{k}}{(2\pi)^2} \tag{10}$$

is called the *coupling integral*. Working with the definitions of the dipole coupling factors, Eqs. (5)–(7), it is not difficult to show that

$$K_{11}(\omega,z) = K_{22}(\omega,z) = \frac{c^2}{2\omega^2}\int_0^{\infty} H_0(\omega,k,z)H_0^*(\omega,k,z)\frac{k^3\,dk}{2\pi}, \tag{11}$$

$$K_{33}(\omega,z) = \int_0^{\infty} H_3(\omega,k,z)H_3^*(\omega,k,z)\frac{k\,dk}{2\pi}, \tag{12}$$

and $K_{ij}=0$ if $i\neq j$. Hence only the virtual dipoles having $i=j$ contribute to the pressure field, and the total dipole field is given by $P_D = P_{D,11}+P_{D,22}+P_{D,33}$.

Accurate calculations of the spreading integral, Eq. (9), are difficult to achieve in practice. Recall from Sec. II C 1 that we use a maximum-entropy method (MEM) to attempt to improve spreading-integral calculations derived from pitch-and-roll buoys.

Because the ocean bottom can significantly affect the propagation of sound waves in the water column, even particularly at ULF/VLF frequencies, it is worthwhile to extend Cato's analysis to the case of a horizontally stratified ocean and seabed environment. Such an extension is actually quite

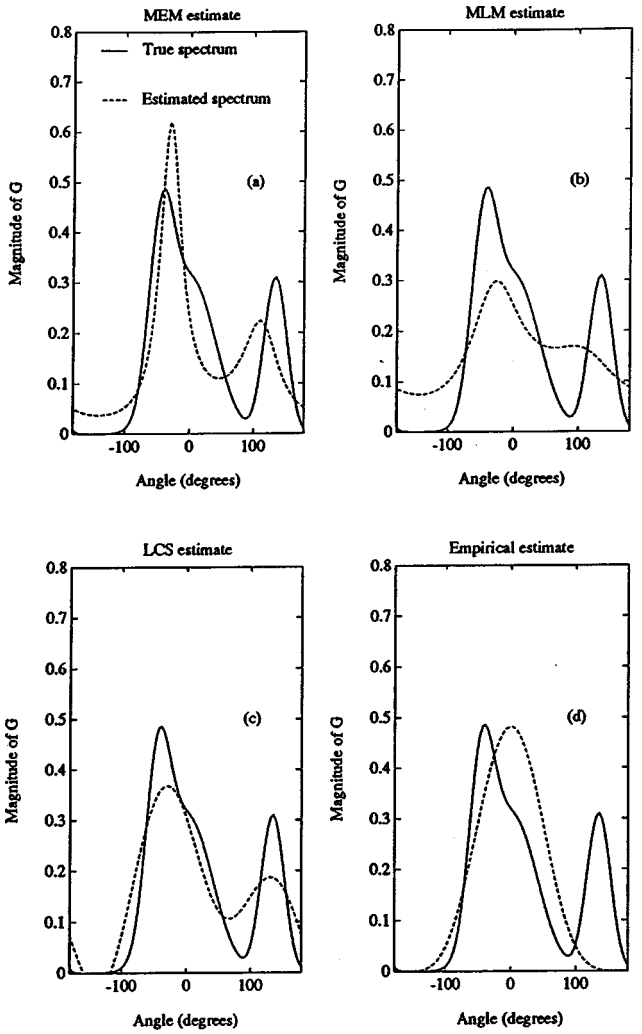

FIG. 9. Estimates of the directional spectrum of $G(\alpha)=N(\cos^8(\alpha/2)+\cos^{10}(\alpha/2+\pi/4))$, where α is the azimuthal angle, and N is chosen to normalize the spectrum. The MEM estimate was made using the Lygre–Krogstad algorithm mentioned in the text. The MLM estimate was made using an algorithm by Lacoss (Ref. 35). The LCS estimate refers to the weighted average of the first five Fourier coefficients suggested by Longuet-Higgins *et al.* (Ref. 17). The empirical estimate was made by estimating the parameter s from the first five Fourier coefficients and using the empirical formula $G(\alpha)=N\cos^{2s}(\alpha/2)$.

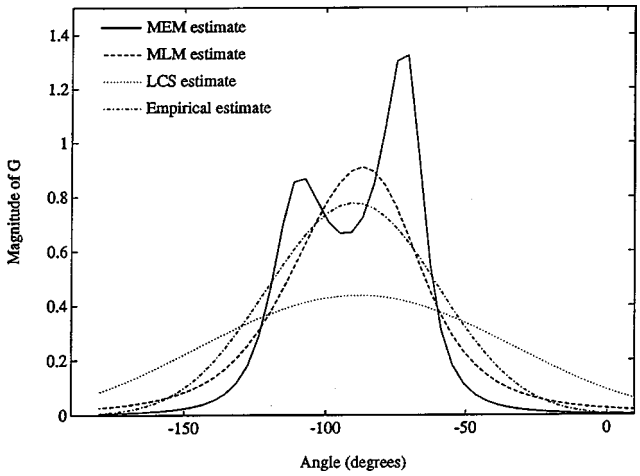

FIG. 10. Estimated spectra derived from the 0.16 Hz data bin from the Discus E buoy on January 27, 1991 at 1200 hours. The estimates were made using the methods discussed in Fig. 9.

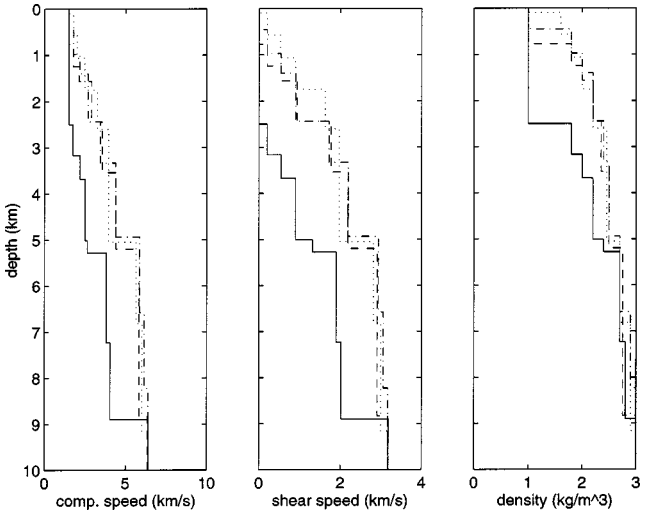

FIG. 11. Profiles used in the ULF/VLF noise model calculations. (a) Compressional wave speed. (b) Shear wave speed. (c) Density. Dotted line, 100 m water depth. Dashed line, 443 m water depth. Dashed–dotted line, 769 m water depth. Solid line, 2600 m water depth.

straightforward when we realize the close relationship between Cato's coupling factors and the depth-dependent Green's functions often employed in ocean acoustics. First we make the observation, that, in Eq. (2), the factor $\exp(-i\omega r/c)/r$ is simply the free-space Green's function for a monopole, G_0, which is the solution to

$$\frac{\partial^2 G_0}{\partial r^2}+(\omega/c)^2 G_0=-4\pi\delta(\mathbf{r}). \tag{13}$$

In fact, for an ocean of infinite radius, Eq. (2) shows that the monopole coupling factor is proportional to the Hankel transform of the Green's function. Hence

$$H_0(\omega,k,z)=\frac{\omega}{2c}g_0(\omega,k,z), \tag{14}$$

where $g_0=\int_0^\infty G_0(\omega,\hat{r},z)J_0(k\hat{r})\hat{r}\,d\hat{r}$ is the depth-dependent Green's function. From Eq. (7), it is evident that H_3 is proportional to the depth-dependent Green's function for a vertical dipole, $g_3=\partial g_0/\partial z$,

$$H_3(\omega,k,z)=\tfrac{1}{2}g_3(\omega,k,z). \tag{15}$$

Equations (1) and (3) can be interpreted physically as follows. To find the pressure spectrum in an infinitely deep ocean, one decomposes the Green's function for the appropriate source type into its horizontal wave number components by calculating the Hankel transform, takes the squared magnitude, multiplies by a source power proportional to the wave height power spectrum (or a convolution product) at each horizontal wave number, and then integrates over the horizontal wave number space. In fact, this procedure for calculating propagation from a surface distribution of noise sources has been given previously for *arbitrarily stratified* environments by Kuperman and Ingenito.[22] Their Eq. (20) becomes, in our notation,

$$P(\omega,z)=\frac{\omega^2}{c^2}\int_{-\infty}^{\infty}\Pi(\mathbf{k})|g(\omega,k,z)|^2 d\mathbf{k}, \tag{16}$$

where P is proportional to the acoustic intensity, Π is the power spectral density of the surface-distributed sources, and g is the depth-dependent Green's function. By setting $\Pi \propto \Psi_{33}$ for the monopoles, and $\Pi \propto \Phi_{i3j3} + \phi_{i33j}$ for the dipoles, it is recognized that Cato's theory provides the spectral density function for Kuperman and Ingenito's general equation for noise generated by surface-distributed sources in a horizontally stratified environment. Alternatively, Cato's expression for the acoustic fields carries over to the case of arbitrary stratification, so long as the appropriate depth-dependent Green's function is used. That is, we can continue to apply Eqs. (1) and (3) to arbitrarily stratified environments, while using Eqs. (14) and (15) to determine the coupling factors.[23]

For the predictions in this paper, the ocean and underlying bottom were allowed to have depth-dependent compressional wave speed and attenuation, shear wave speed and attenuation, and density. The vertical profiles were piecewise constant. The depth-dependent Green's functions corresponding to these profiles were computed using a fast field program (FFP) written by Wilson,[24] which is based on the global-matrix algorithm developed by Schmidt and Tango.[25,26] The FFP can also accommodate monopoles and dipoles that are positioned *on* (as opposed to just below or above) the air/sea interface; this capability is required for predicting the noise from sea-surface motion.

Once the depth-dependent Green's functions for the monopoles and dipoles have been determined by the FFP, they are multiplied by the appropriate forms of the surface-wave directional spectrum (Sec. II C 1) in accordance with Eqs. (1) and (3). The magnitude squared of the Green's function is multiplied by the source strength (surface-wave spectrum), and then integrated over the horizontal wave number space. The final result is pressure as a function of frequency and depth.

IV. ANALYSIS AND DISCUSSION

A. Comparison of the model and measurements

Model predictions, made with the methodology described in the preceding section, are shown in the lower panels of Figs. 4–7. The SWADE spectra usually had a low-frequency cutoff at 0.03 Hz and a high-frequency cutoff at 0.34 Hz (cf. Fig. 8). This limits the predictions for the single-frequency noise field to the frequency range 0.03–0.34 Hz, whereas the double-frequency predictions are limited to 0.06–0.68 Hz. Furthermore, the SWADE spectra were often unavailable at frequencies greater than the 0.03 Hz cutoff (due to difficulties associated with integrating accelerometer data to obtain wave height), thus causing a jagged edge on the low-frequency end of the spectra and further restricting the frequency range of the predictions.

Agreement between the data and the predictions is best for OBS 61, at 2600 m depth. For the most part, the magnitude and spectral shape of the experimental data are accurately predicted. There are cases, however, where the model predicts higher pressures than were measured (e.g., the storms occurring on yeardays 60–64), as well as cases where the model predicts lower pressures (e.g., the storms occurring on yeardays 72–74 and 86–87). The likely causes are the low angular resolution of the surface-wave measurements, and the assumption of uniformity in the horizontal source distribution.

An interesting discrepancy between the predictions and the measurements occurs at the two intermediate depths (OBS's 63 and 62), in the frequency range of the double-frequency noise field. At these depths the predictions have a systematic bias not evident at OBS 61, being about 10 dB higher than the measured levels. This could be caused by the greater bottom slope at the intermediate depths, which may reflect some of the energy away from the continental slope region. (Recall that OBS 61 was located on the continental rise, whereas the other sensors were deployed on the steeper continental slope.) A more sophisticated propagation model incorporating lateral variability might successfully predict this trend.

The model successfully predicts the spectral gap between the single- and double-frequency noise at the intermediate depths, when SWADE data are available for sufficiently low frequencies. Like the double-frequency noise, the levels predicted for the single-frequency noise are somewhat high. However, the relative strengths of the single- and double-frequency noise are well predicted. At the shallowest sensor, OBS 51, the model predicts that a double-frequency noise with strong temporal variability should be evident above about 0.2 Hz. This is not borne out by the experimental spectra, though, which show little temporal variation on time scales associated with storm activity. The model also predicts a narrow spectral gap at slightly below 0.2 Hz, although no such gap is actually observed. During certain periods (e.g., yeardays 71–83), the OBS 51 data exhibit harmonics with spacing of about 0.1 Hz in the band 0.2–0.6 Hz. Kibblewhite and Wu[28] have suggested the existence of mth-frequency microseisms ($m>2$), which, like the double-frequency microseisms, are produced by nonlinear interactions. Although Kibblewhite and Wu indicate that the mth-frequency microseisms will generally be negligible, they are perhaps evident in our data. Or, as pointed out by reviewers of this paper, the harmonics could be caused by shear-wave modes in the sediment or by nonlinear instrument response.

B. Effect of changing wave conditions on the double-frequency noise field

As discussed above, there is good overall agreement between the predicted spectral levels at most frequencies in the band of double-frequency microseisms. In this section we perform more detailed comparisons for selected times during ECONOMEX with differing wind and wave conditions.[27,29]

Figure 12 shows an example of a case where there is particularly good agreement between the predictions and the measurements. The data are for OBS 61, the 2600 meter site. Figure 13 shows similar results at OBS 63, the 443 meter site. Shown with the spectra are the calculations of both the wave-height power spectrum $\Omega(\omega/2)$ and the spreading integral I_{33} from the appropriate SWADE data. While the predicted and observed levels at a given frequency may differ up to 5 dB, there is generally good correspondence between the two. It is interesting that in many of the comparisons

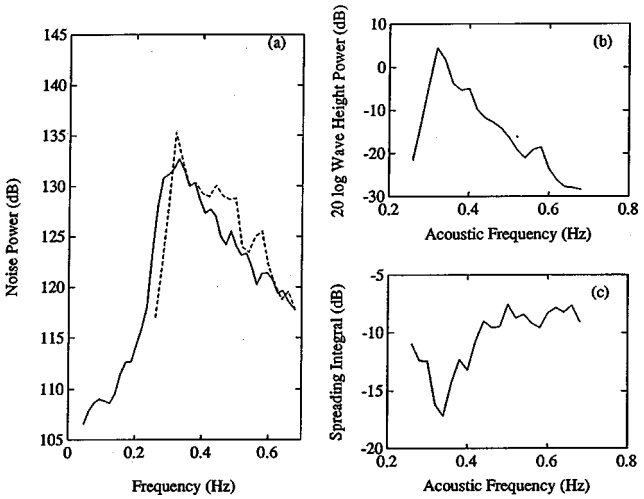

FIG. 12. (a) Observed (solid line) and predicted (dashed line) spectral levels for 1/27/91 at 1800 hours, in dB *re* 1 μPa^2/Hz. Observed spectrum is from the OBS 58 differential pressure gauge (DPG). Predicted spectrum is based on data from the Discus E buoy. (b) Wave height power spectrum in dB, 10 log $\Omega^2(\omega/2)$, where $\Omega(\omega/2)$ has units m^2/Hz. (c) Spreading integral in dB, 10 log $I_{33}(\omega/2)$.

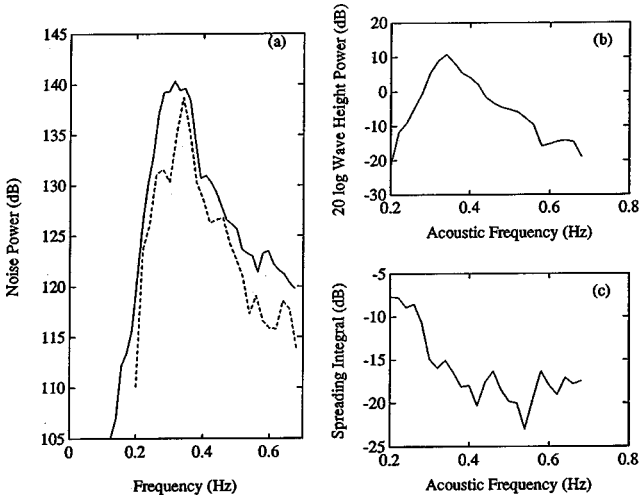

FIG. 14. (a) Observed (solid line) and predicted (dashed line) spectral levels for 2/23/91 at 0700 hours, in dB *re* 1 μPa^2/Hz. Observed spectrum is from the OBS 58 DPG. Predicted spectrum is based on data from the Discus E buoy. (b) Wave height power spectrum in dB, 10 log $\Omega^2(\omega/2)$, where $\Omega(\omega/2)$ has units m^2/Hz. (c) Spreading integral in dB, 10 log $I_{33}(\omega/2)$.

small peaks exist in the observed levels which are present in the predictions at the same frequencies but with different magnitudes. One can see from the inputs that the spreading integral plays a key role in determining the shape and magnitude of the predicted spectra. These two figures represent particularly good agreement between predicted and observed spectra.

More typical of the level of agreement are Figs. 14 and 15, where we can see close agreement at frequencies around the spectral peak, but differences away from the peak of 5 or more dB is sometimes evident. In general, the overall spectral shape is correctly predicted, but the peak is broader or narrower in the observed spectra, giving rise to large differences in the high-slope region on the low-frequency side of the peak. In the predictions from the shallow site, there is a tendency to predict levels that are too high in the band 0.1 Hz to 0.2 Hz. Since this band corresponds to the peak in the bottom response in the shallow case, errors in the bottom model may account for this difference.

The observations show an increase in noise level with wave height, and good agreement between observations and predictions at moderate ($\sim$1 to 3 m) wave heights is evident in Figs. 12–15. At very low predicted noise levels, which correspond to times of low wave height, there is a disparity between predictions and observations. An example of this is the developing wave field of the early hours of January 27 at Discus E, as depicted in Fig. 16. As one can see in Figs. 17 and 18, agreement is good at frequencies corresponding to the peak in the predictions as the wave field develops, but the low levels predicted away from the peak are not confirmed by observation. A possible cause of the error in the predic-

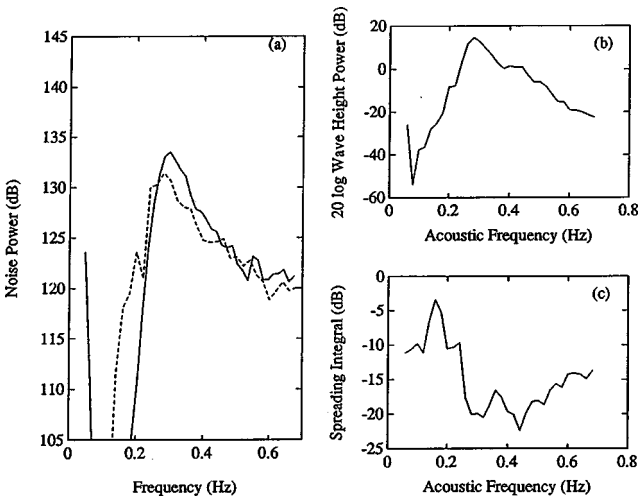

FIG. 13. (a) Observed (solid line) and predicted (dashed line) spectral levels of 2/23/91 at 1400 hours, in dB *re* 1 μPa^2/Hz. Observed spectrum is from the OBS 63 DPG. Predicted spectrum is based on data from the Discus C buoy. (b) Wave height power spectrum in dB, 10 log $\Omega^2(\omega/2)$, where $\Omega(\omega/2)$ has units m^2/Hz. (c) Spreading integral in dB, 10 log $I_{33}(\omega/2)$.

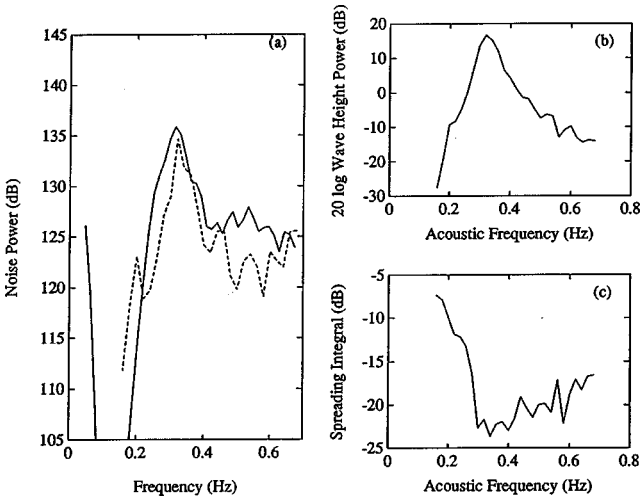

FIG. 15. (a) Observed (solid line) and predicted (dashed line) spectral levels for 2/27/91 at 1500 hours, in dB *re* 1 μPa^2/Hz. Observed spectrum is from the OBS 63 DPG. Predicted spectrum is based on data from the Discus C buoy. (b) Wave height power spectrum in dB, 10 log $\Omega^2(\omega/2)$, where $\Omega(\omega/2)$ has units m^2/Hz. (c) Spreading integral in dB, 10 log $I_{33}(\omega/2)$.

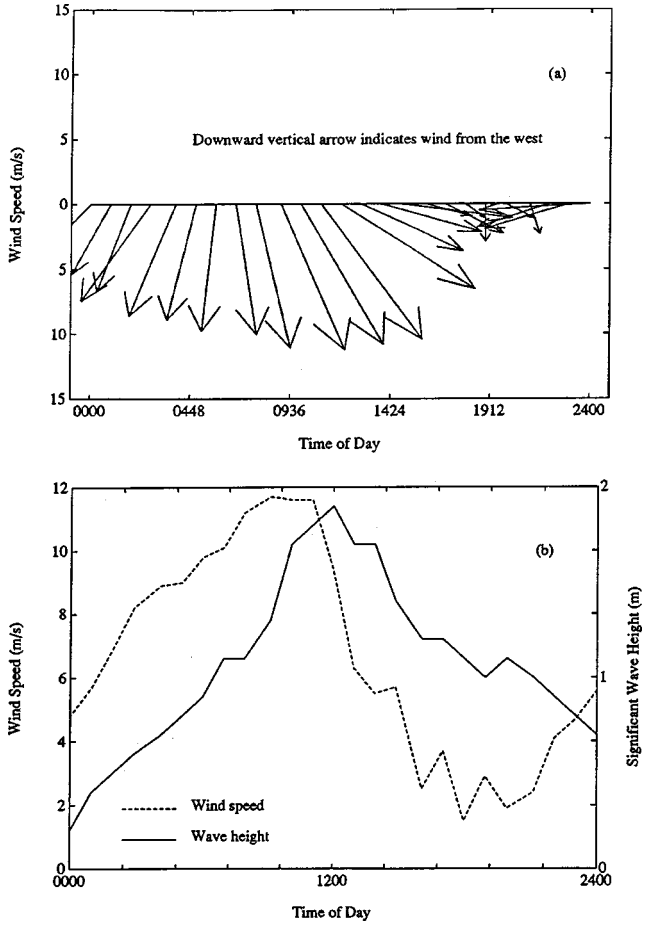

FIG. 16. Meteorological data as measured at Discus E on 1/27/91. (a) Wind vector. The direction of the arrow indicates the direction of the wind, with a downward arrow indicating a wind from the west. The magnitude of the arrow indicates the wind speed with the wind speed scale given on the vertical axis. (b) Wind speed and wave height.

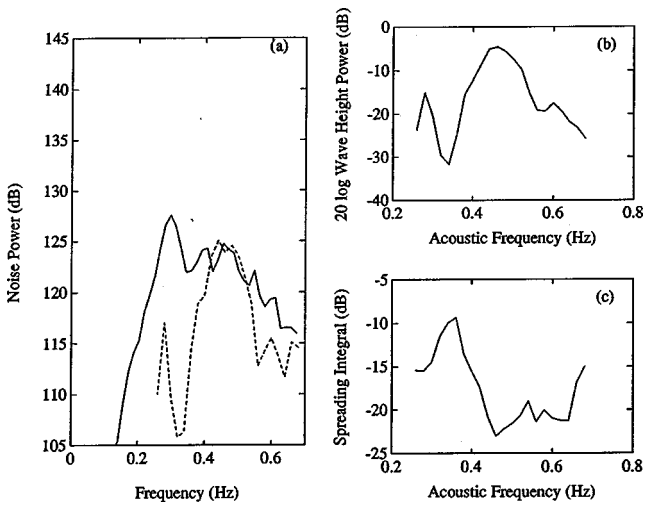

FIG. 17. (a) Observed (solid line) and predicted (dashed line) spectral levels for 1/27/91 at 0600 hours, in dB *re* 1 μPa^2/Hz. Observed spectrum is from the OBS 58 DPG. Predicted spectrum is based on data from the Discus E buoy. (b) Wave height power spectrum in dB, 10 log $\Omega^2(\omega/2)$, where $\Omega(\omega/2)$ has units m^2/Hz. (c) Spreading integral in dB, 10 log $I_{33}(\omega/2)$.

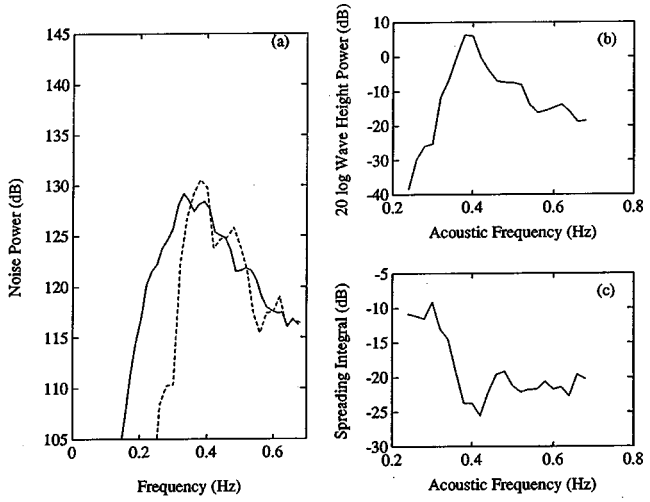

FIG. 18. (a) Observed (solid line) and predicted (dashed line) spectral levels for 1/27/91 at 0900 hours, in dB *re* 1 μPa^2/Hz. Observed spectrum is from the OBS 58 DPG. Predicted spectrum is based on data from the Discus E buoy. (b) Wave height power spectrum in dB, 10 log $\Omega^2(\omega/2)$, where $\Omega(\omega/2)$ has units m^2/Hz. (c) Spreading integral in dB, 10 log $I_{33}(\omega/2)$.

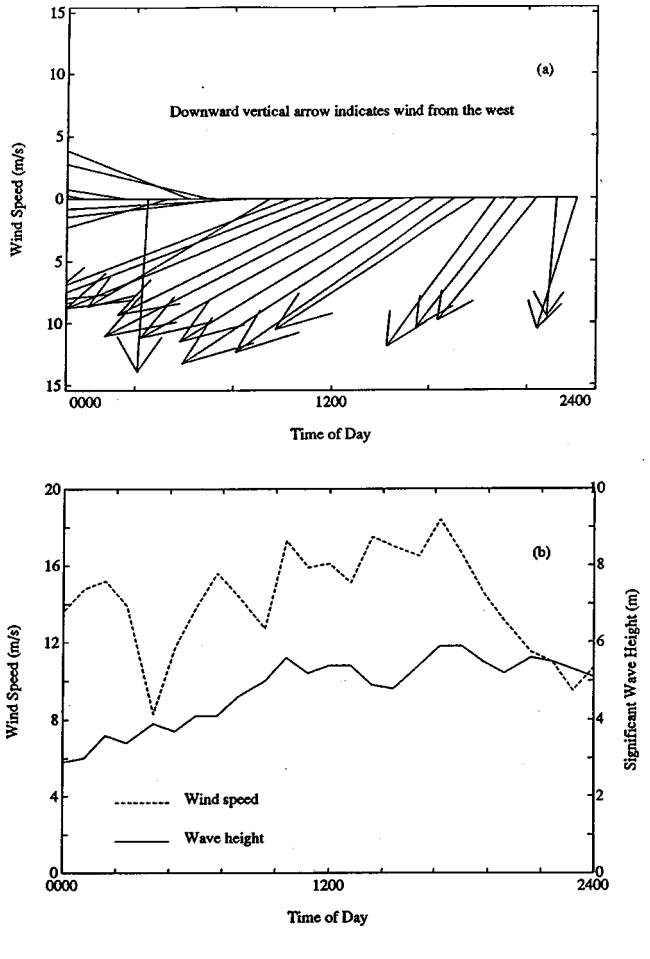

FIG. 19. Meteorological data as measured at Discus E on 3/04/91. (a) Wind vector. The direction of the arrow indicates the direction of the wind, with a downward arrow indicating a wind from the west. The magnitude of the arrow indicates the wind speed with the wind speed scale given on the vertical axis. (b) Wind speed and wave height.

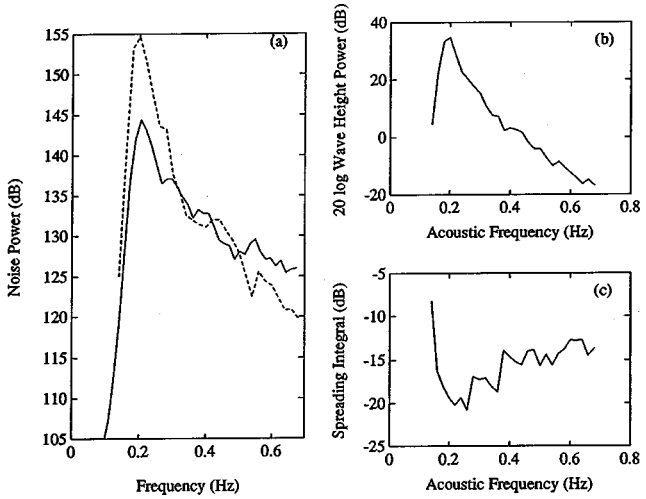

FIG. 20. (a) Observed (solid line) and predicted (dashed line) spectral levels for 3/04/91 at 1000 hours, in dB *re* 1 μPa^2/Hz. Observed spectrum is from the OBS 58 DPG. Predicted spectrum is based on data from the Discus E buoy. (b) Wave height power spectrum in dB, 10 log $\Omega^2(\omega/2)$, where $\Omega(\omega/2)$ has units m^2/Hz. (c) Spreading integral in dB, 10 log $I_{33}(\omega/2)$.

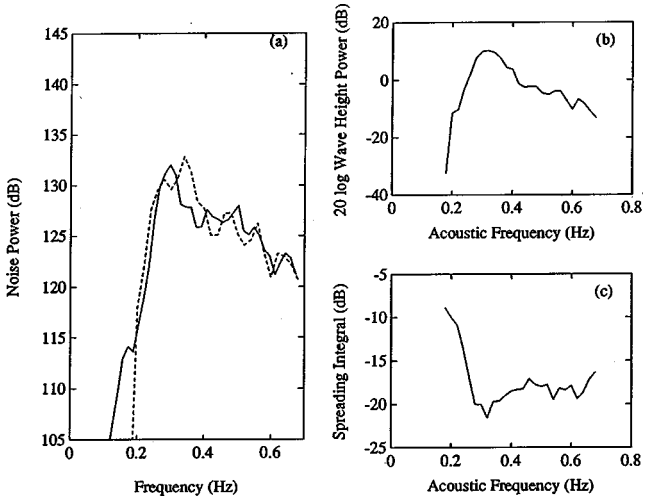

FIG. 22. (a) Observed (solid line) and predicted (dashed line) spectral levels for 2/23/91 at 0300 hours, in dB *re* 1 μPa^2/Hz. Observed spectrum is from the OBS 58 DPG. Predicted spectrum is based on data from the Discus E buoy. (b) Wave height power spectrum in dB, 10 log $\Omega^2(\omega/2)$, where $\Omega(\omega/2)$ has units m^2/Hz. (c) Spreading integral in dB, 10 log $I_{33}(\omega/2)$.

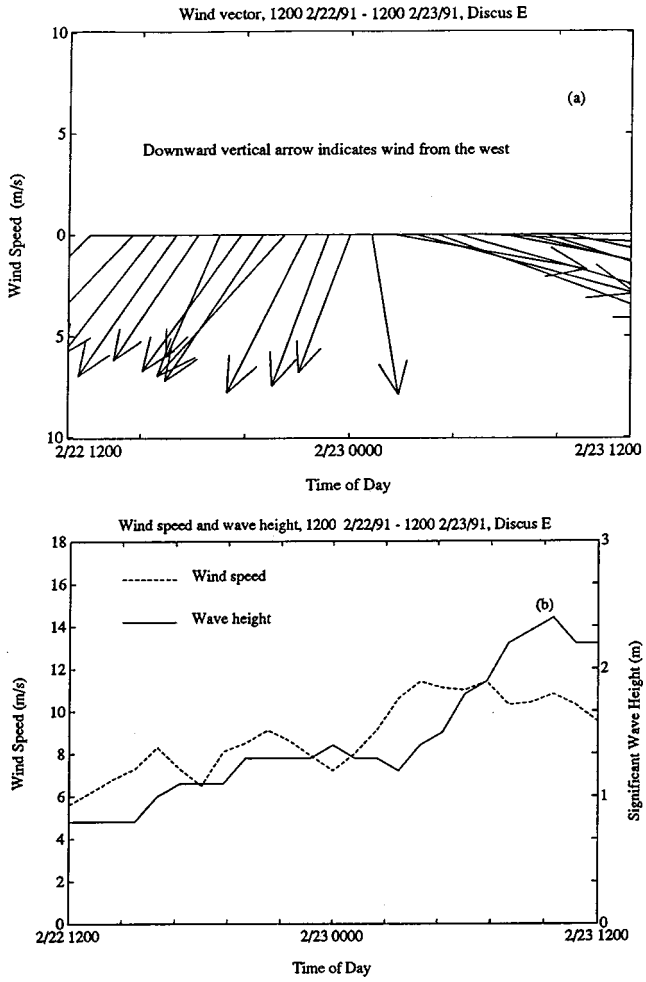

FIG. 21. Meteorological data as measured at Discus E on 2/22/91–2/23/91. (a) Wind vector. The direction of the arrow indicates the direction of the wind, with a downward arrow indicating a wind from the west. The magnitude of the arrow indicates the wind speed with the wind speed scale given on the vertical axis. (b) Wind speed and wave height.

tions at low wave heights is the assumption of spatial homogeneity of the source wave field. Under very low local wave height conditions, it is possible for a much stronger wave field at some distance to dominate the noise field, thus making the predictions made from the local wave field very much in error. Another possible cause of the differences under low wave height conditions is the existence of an unknown source mechanism generating acoustic energy, whose noise is normally dominated by that caused by orbital motion. Under low source strength conditions for the orbital motion noise, this presumed source may now dominate, giving rise to the errors noted above. The predictions in general are in reasonably close agreement when measured significant wave height is above about 1 meter. For the period of the ECONOMEX data, roughly 77% of the wave height measurements are above this threshold.

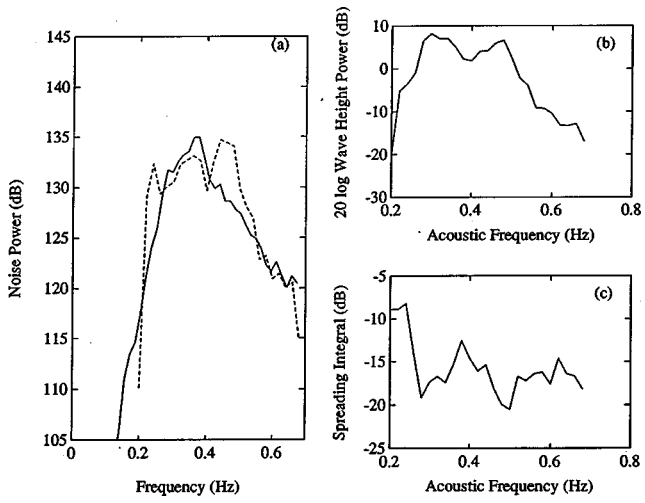

FIG. 23. (a) Observed (solid line) and predicted (dashed line) spectral levels for 2/23/91 at 0400 hours, in dB *re* 1 μPa^2/Hz. Observed spectrum is from the OBS 58 DPG. Predicted spectrum is based on data from the Discus E buoy. (b) Wave height power spectrum in dB, 10 log $\Omega^2(\omega/2)$, where $\Omega(\omega/2)$ has units m^2/Hz. (c) Spreading integral in dB, 10 log $I_{33}(\omega/2)$.

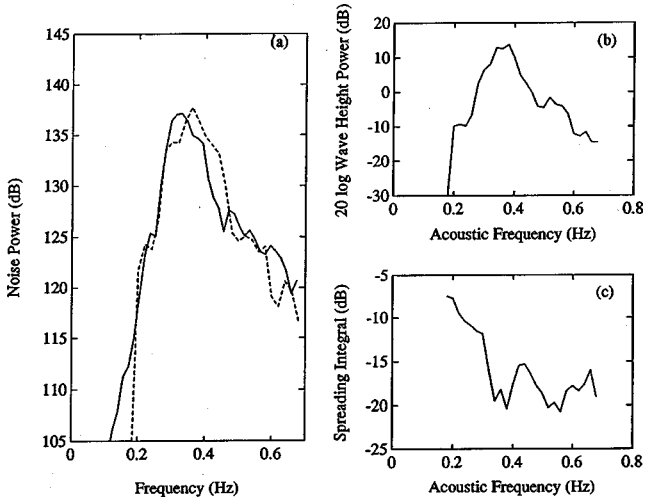

FIG. 24. (a) Observed (solid line) and predicted (dashed line) spectral levels for 2/23/91 at 0500 hours, in dB *re* 1 μPa^2/Hz. Observed spectrum is from the OBS 58 DPG. Predicted spectrum is based on data from the Discus E buoy. (b) Wave height power spectrum in dB, 10 log $\Omega^2(\omega/2)$, where $\Omega(\omega/2)$ has units m^2/Hz. (c) Spreading integral in dB, 10 log $I_{33}(\omega/2)$.

We can see from the data of March 4 (with meteorological conditions shown in Fig. 19 and observed and predicted spectra seen in Fig. 20) that the predictions again deviate at very high wave height conditions corresponding to strong winds at relatively constant direction, with the predictions being higher than the observations. The disagreement at frequencies corresponding to the peak is up to 10 dB under these conditions. There is, however, the same general trend in the observed noise data as exists in the predictions, that of higher levels at higher wave heights and wind speeds. This would tend to indicate the wave directional spectral estimate provided by the MEM technique is overestimating the spreading at these high wave heights. Alternative empirical models, which are based on strong, steady winds, predict less spreading under these conditions than do the MEM estimates (Fig. 9). The observations match the predictions fairly well in the region of frequencies above the peak under high wave height conditions.

The predictions agree quite well with the observed data under conditions of changing wind direction. We can consider the wind shift of February 23 at 0200, depicted in Fig. 21, as typical. The observed and predicted noise levels for subsequent times are shown in Figs. 22–24. The observed noise spectrum changes with time roughly as the predicted spectrum does. Of particular note is the broad peak in the observed spectrum at 0400, and the higher levels seen at the peak from 0300–0500. Again the spreading integral plays a major role in determining the spectral shape.

It is also interesting to examine the predictions and observations during a time of highly variable conditions such as those of the afternoon of January 27, which were depicted in Fig. 16. Observations and predictions are seen in Figs. 12 and 25, for 1800 and 1500, respectively. Again we see relatively close agreement, with the increased spreading adding to the noise as the wave height diminishes to keep the overall noise level fairly constant.

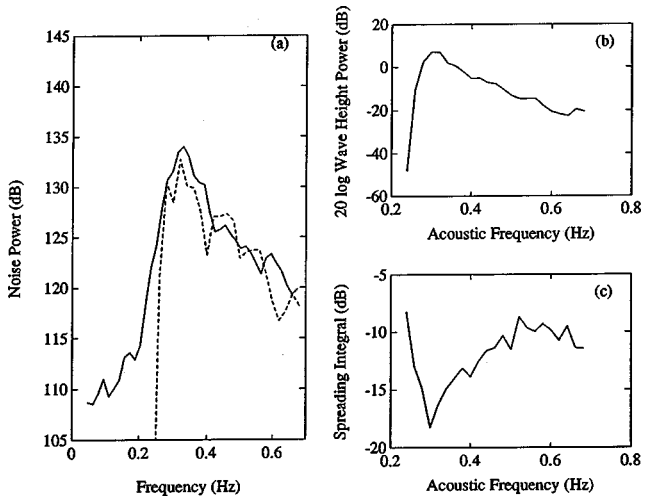

FIG. 25. (a) Observed (solid line) and predicted (dashed line) spectral levels for 1/27/91 at 1500 hours, in dB *re* 1 μPa^2/Hz. Observed spectrum is from the OBS 58 DPG. Predicted spectrum is based on data from the Discus E buoy. (b) Wave height power spectrum in dB, 10 log $\Omega^2(\omega/2)$, where $\Omega(\omega/2)$ has units m^2/Hz. (c) Spreading integral in dB, 10 log $I_{33}(\omega/2)$.

V. CONCLUSIONS

ECONOMEX has provided a unique opportunity to compare ULF noise spectra recorded in different water depths over a 10 week period. The experimental results, and the accompanying model predictions, clearly demonstrate that surface-wave orbital motion is the primary cause of noise in the frequency band 0.02–2 Hz. The fact that the model predictions hold well under conditions of changing wind direction, for which the double-frequency noise is enhanced, demonstrates that wind turbulence acting on the sea surface (which would depend on the wind speed but not the direction) is not a significant mechanism of ULF/VLF sound generation.

The surface-wave motion generates noise via two distinct mechanisms. These are referred to as single-and double-frequency noise fields. The former is due to linearly generated pressure fluctuations following a single surface wavetrain, while the latter results from nonlinear interaction between opposing surface wavetrains. Both mechanisms are clearly evident in the ECONOMEX data.

The single-frequency noise field is strongest at the shallowest sensor (95 m). Levels as high 160 dB *re* 1 μPa^2/Hz were measured, and there appears to be generation of higher harmonics by finite amplitude effects. The intensity and peak frequency of the single-frequency noise decreases rapidly with depth, as would be expected. The single-frequency noise exhibits little temporal variability, relative to the surface wave spectra.

The double-frequency noise field is observed at all depths and exhibits little depth dependence. Also, unlike the single-frequency counterpart, the temporal variations in the double-frequency noise closely track the surface-wave spectra, except at the shallowest sensor. Because the peak frequency of the single-frequency noise diminishes with depth, whereas the peak of the double-frequency noise is relatively constant, a spectral gap whose width increases with depth is observed.

Most features of the data are well predicted by the theory of Cato,[2,3] which we have extended to accommodate a horizontally stratified ocean and seabed. Some of the discrepancies between the data and predictions may be attributable to lateral variability in the environment, particularly since the experiment was performed in a continental shelf/slope region. More sophisticated modeling efforts, accounting for lateral variation in the ocean and seabed as well as the source function (i.e., the surface-wave field), should improve agreement with the data.

The importance of the wave-directional spectrum in determining the overall noise level is apparent from this study. Any models based on empirical relationships using wind speed as their input would have to also include the growth and decay of the wave field resulting from changing wind direction. Models that predict directional wave spectra from a knowledge of wind speed alone are doomed to failure in general, due to their assumption of a fully developed wave field, and to the changing nature of the true wave field.

This work has also demonstrated the key role played by the propagation environment, particularly the geoacoustic bottom model, in determining the overall levels and shape of the acoustic noise spectrum at extremely low frequencies. This observation is consistent with the work of Schmidt and Kuperman.[30] Hence it is imperative that the propagation environment be taken into account if one wishes to compare actual source levels between two different locations. Otherwise differences in the bottom site characteristics could cloud important correlations or lead to incorrect conclusions.

ACKNOWLEDGMENTS

This work was supported by Office of Naval Research Grant No. N00014-90-J-1452, G. M. Purdy and G. V. Fisk, Co-Principal Investigators. They gratefully acknowledge the assistance of the crew of the R/V Oceanus in the acquisition of the data. D. K. Wilson was also supported by a postdoctoral scholarship from the WHOI Education Office. The authors thank J. Collins, D. DuBois, and G. M. Purdy for providing the OBS data in SEGY format, and S. Holbrook for providing the EDGE data. We also thank G. H. Sutton for many helpful discussions. This paper is WHOI Contribution No. 10893.

APPENDIX: DETERMINATION OF THE SURFACE-WAVE DIRECTIONAL SPECTRUM

In this Appendix we consider the angular resolution available from the SWADE Discus buoys. Longuet-Higgins *et al.*[17] were the first to investigate the angular response of such pitch and roll buoys. They pointed out that if the wavelengths of the sea surface motion are large with respect to the buoy diameter, the buoy tends to have the same motion and orientation as the surface. Then, if the vertical displacement and the two angles of pitch and roll are measured, one has three time series: the vertical displacement ζ, and its spatial derivatives $\partial\zeta/\partial x$ and $\partial\zeta/\partial y$. We denote these three quantities as ξ_1, ξ_2, and ξ_3, respectively, in the following discussion.

The vertical displacement may be represented using the following stochastic integral:

$$\xi_1 = \mathrm{Re}\int_S \exp[i(k_x x + k_y y - \omega t)]\,d\mathbf{S}. \tag{A1}$$

Then, since $(k_x, k_y) = (k\cos\alpha, k\sin\alpha)$, we can write our other two time series as

$$\begin{aligned}\xi_2 &= \mathrm{Re}\int_S ik\cos\alpha\exp[i(k_x x + k_y y - \omega t)]\,d\mathbf{S},\\ \xi_3 &= \mathrm{Re}\int_S ik\sin\alpha\exp[i(k_x x + k_y y - \omega t)]\,d\mathbf{S}.\end{aligned} \tag{A2}$$

Next we form co-spectra $C_{ij}(\omega)$ and quadrature spectra $Q_{ij}(\omega)$ from the time series ξ_i and ξ_j, finding

$$\begin{aligned}C_{11}(\omega) &= \int_0^{2\pi} F(\omega,\alpha)\,d\alpha,\\ C_{22}(\omega) &= \int_0^{2\pi} k^2\cos^2\alpha F(\omega,\alpha)\,d\alpha,\\ C_{33}(\omega) &= \int_0^{2\pi} k^2\sin^2\alpha F(\omega,\alpha)\,d\alpha,\\ C_{23}(\omega) &= \int_0^{2\pi} k^2\cos\alpha\sin\alpha F(\omega,\alpha)\,d\alpha,\\ Q_{12}(\omega) &= \int_0^{2\pi} k\cos\alpha F(\omega,\alpha)\,d\alpha,\\ Q_{13}(\omega) &= \int_0^{2\pi} k\sin\alpha F(\omega,\alpha)\,d\alpha,\end{aligned} \tag{A3}$$

where $F(\omega,\alpha) = \Omega(\omega)G(\omega,\alpha)$ is the frequency-directional spectrum of the sea surface elevation. The Fourier coefficients of $F(\omega,\alpha)$ are defined as

$$a_n(\omega) + ib_n(\omega) = \frac{1}{\pi}\int_0^{2\pi} e^{in\alpha}F(\omega,\alpha)\,d\alpha, \tag{A4}$$

where

$$F(\omega,\alpha) = \frac{1}{2}a_0 + \sum_{n=1}^{n=\infty}[a_n\cos(n\alpha) + b_n\sin(n\alpha)]. \tag{A5}$$

Now we can see that the right-hand sides of Eq. (A3) are related to these Fourier coefficients as follows:

$$\begin{aligned}a_0(\omega) &= \frac{1}{\pi}C_{11}(\omega),\\ a_1(\omega) &= \frac{1}{\pi k}Q_{12}(\omega), \quad b_1(\omega) = \frac{1}{\pi k}Q_{13}(\omega),\\ a_2(\omega) &= \frac{1}{\pi k^2}[C_{22}(\omega) - C_{33}(\omega)], \quad b_2(\omega) = \frac{2}{\pi k^2}C_{23}(\omega).\end{aligned} \tag{A6}$$

The pitch and roll buoy hence provides the first five coefficients in the Fourier series describing the directional spectrum of the sea surface elevation, each coefficient being a function of frequency ω. We must now use these five Fourier coefficients to find estimates of the wave-height power spectrum $\Omega(\omega)$ and the directionality function $G(\omega,\alpha)$.

Our estimate of the wave-height power spectrum is obvious from inspection of Eq. (A5) and our definition of the co-spectra:

$$\Omega(\omega)=\int_0^{2\pi} F(\omega,\alpha)d\alpha=\pi a_0(\omega)=C_{11}(\omega). \tag{A7}$$

The best estimate for the directional spectrum is not as simple. An obvious choice would be to try the truncated sum

$$G(\omega,\alpha)=\frac{1}{2\pi}+\frac{1}{\pi a_0}(a_1\cos\alpha+b_1\sin\alpha+a_2\cos 2\alpha + b_2\sin 2\alpha). \tag{A8}$$

This sum is actually a convolution of the true directional spectrum with a weighting function, and considerable smoothing results in the estimated spectrum. Unfortunately, calculations of the spreading integral, I_{33} [Eq. (9)], made using this type of directional spectrum estimate can be shown to be in error by factors as large as 10^3.[27] Other weighted averages of the first five Fourier coefficients can be made, but they also produce an unrealistically smooth estimate.

Several investigators have fit empirical curves to measured directional spectra. Longuet-Higgins *et al.* have suggested the wave directional spectra fit the form[17]

$$G(\omega,\alpha)\propto|\cos^{2s}(\alpha/2)| \tag{A9}$$

where the spreading parameter s is a function of frequency and wind speed. Kibblewhite and Wu[31] used an empirical relationship to find s based on the wind speed and frequency, and then calculated I_{33} analytically. One could also match the measured first five Fourier coefficients to the first five Fourier coefficients of the empirical spectrum $\cos^{2s}\alpha/2$ to estimate the parameter s, as suggested by Longuet-Higgins *et al.*,[17] and hence calculate I_{33}. However, the data used to develop the empirical formula are generally taken under conditions of steady wind speed and direction. In our field data, the wind speed and direction can vary significantly, giving rise to wave fields with different directionality, and in general a broader directional spectrum than that predicted by the empirical formula. Therefore, we would expect predictions of I_{33} calculated from spectra derived from empirical formulas to be lower than the true value under variable meteorological conditions. In particular, if the true directional spectrum is bi-directional (two peaks corresponding to two wave fields generated by winds in different directions) there can be significant energy in opposing wave directions which is not predicted by the cosine power curve. Donelan *et al.*[32] have suggested a better fit to the data is found in a $\mathrm{sech}^2\,\beta\alpha$ distribution with β being the spreading parameter, but estimates of I_{33} based on estimates of β are also too small.

Another approach would be to use a data adaptive spectral estimation technique such as the maximum-likelihood method (MLM), or the maximum-entropy method (MEM). These methods have the common characteristic that the first five Fourier coefficients of the directional spectrum are used to estimate the remaining ones. The MEM technique has been shown by Lygre and Krogstad[33] to give a much more peaked distribution than the MLM technique, and also resolves bi-directional wavefields more satisfactorally. (Examples were given in Sec. II C 1.) Both of these features of the MEM technique are important for accurate calculations of the spreading integral. Hence MEM should give the best results in our application.

Our algorithm for producing MEM estimates largely follows Lygre and Krogstad.[33] We begin by defining a Fourier series for the directional spectrum $G(\alpha)$ (suppressing for now the dependence on ω) on the interval $(-\pi,\pi)$ as

$$G(\alpha)=\frac{1}{2\pi}\sum_{n=-\infty}^{\infty} c_n e^{in\alpha},\quad c_0=1,\ c_{-n}=c_n^*. \tag{A10}$$

The entropy of G is defined by

$$H(G)=1\Big/\int_{-\pi}^{\pi}\log(G(\alpha))d\alpha. \tag{A11}$$

It has been shown by Burg[34] that the function maximizing $H(G)$ subject to the constraint that the coefficients c_n equal some known c_k for $k\leqslant N$ is

$$G(\alpha)=\frac{1}{2\pi}\frac{\theta_e^2}{|1-\phi_1 e^{-i\alpha}-\cdots-\phi_N e^{-iN\alpha}G|^2}, \tag{A12}$$

where $\phi_1\cdots\phi_N$ and θ_e^2 are obtained from the Yule–Walker equations

$$\begin{bmatrix} 1 & c_1^* & \cdots & c_{N-1}^* \\ c_1 & \ddots & \ddots & \vdots \\ \vdots & \ddots & \ddots & c_1^* \\ c_{N-1} & \cdots & c_1 & 1 \end{bmatrix}\times\begin{bmatrix}\phi_1\\ \vdots\\ \vdots\\ \phi_N\end{bmatrix}=\begin{bmatrix}c_1\\ \vdots\\ \vdots\\ c_N\end{bmatrix}, \tag{A13}$$

and

$$\theta_e^2=1-\phi_1 c_1^*-\cdots-\phi_N c_N^*. \tag{A14}$$

In our case we have $N=2$ with $c_1=(a_1-ib_1)/a_0$ and $c_2=(a_2-ib_2)/a_0$. We can now solve this system of equations to find ϕ_n in terms of c_n,

$$\phi_1=(c_1-c_2c_1^*)/(1-|c_1|^2),\qquad \phi_2=c_2-c_1\phi_1. \tag{A15}$$

Finally, we can substitute these into Eq. (A12) to find our directional spectral estimate

$$G(\alpha)=\frac{1-\phi_1c_1^*-\phi_2c_2^*}{2\pi|1-\phi_1e^{-i\alpha}-\phi_2e^{2i\alpha}|^2}. \tag{A16}$$

We now have an estimate of the angular distribution of the wave energy at each frequency which reproduces the first five Fourier coefficients, and uses these coefficients and the Yule–Walker equations to extrapolate the remaining coefficients.

[1] M. S. Longuet-Higgins, "A theory of the origin of microseisms," Philos. Trans. R. Soc. London, Ser. A **243**, 1–35 (1950).

[2] D. H. Cato, "Sound generation in the vicinity of the sea surface: Source mechanisms and the coupling to the received sound field," J. Acoust. Soc. Am. **89**, 1076–1095 (1991).

[3] D. H. Cato, "Theoretical and measured underwater noise from surface wave orbital motion," J. Acoust. Soc. Am. **89**, 1096–1112 (1991).

[4] R. H. Nichols, "Infrasonic ambient ocean noise measurements: Eleuthera," J. Acoust. Soc. Am. **69**, 974–981 (1981).

[5] T. E. Talpey and R. D. Worley, ''Infrasonic ambient noise measurements in deep Atlantic water,'' J. Acoust. Soc. Am. **75**, 621–622 (1984).
[6] R. G. Adair, J. A. Orcutt, and T. H. Jordan, ''Low-frequency noise observations in the deep ocean,'' J. Acoust. Soc. Am. **80**, 633–645 (1986).
[7] G. H. Sutton and N. Barstow, ''Ocean-bottom ultralow-frequency (ULF) seismo-acoustic ambient noise: 0.002 to 0.4 Hz,'' J. Acoust. Soc. Am. **87**, 2005–2011 (1990).
[8] S. C. Webb and C. S. Cox, ''Observations and modeling of seafloor microseisms,'' J. Geophys. Res., [Oceans] **91**, 7343–7358 (1986).
[9] A. C. Kibblewhite and K. C. Ewans, ''Wave-wave interactions, microseisms, and infrasonic ambient noise in the ocean,'' J. Acoust. Soc. Am. **78**, 981–994 (1985).
[10] J. M. Babcock, B. A. Kirkendall, and J. A. Orcutt, ''Relationships between ocean-bottom noise and the environment,'' Bull. Seismol. Soc. Am. **84**, 1991–2007 (1994).
[11] T. Nye and T. Yamamoto, ''Concurrent measurements of the directional spectra of microseismic energy and surface gravity-waves,'' J. Geophys. Res., [Oceans] **99**(C7), 14321–14338 (1994).
[12] T. H. C. Herbers and R. T. Guza, ''Nonlinear wave interactions and high-frequency sea-floor pressure,'' J. Geophys. Res., [Oceans] **99**(C5), 10035–10048 (1994).
[13] C. T. Tindle and M. J. Murphy, ''Microseisms and ocean wave measurements,'' IEEE J. Ocean. Eng. **24**, 112–115 (1999).
[14] S. C. Webb, ''Broadband seismology and noise under the ocean,'' Rev. Geophys. **36**, 105–142 (1998).
[15] R. A. Weller, M. A. Donelan, M. G. Briscoe, and N. E. Huang, ''Riding the crest: a tale of two experiments,'' Bull. Am. Meteorol. Soc. **72**, 163–183 (1991).
[16] R. E. Sheridan, D. L. Musser, L. Glover III, M. Talwani, J. Ewing, S. Holbrook, G. M. Purdy, R. Hawman, and S. Smithson, ''EDGE deep seismic reflection study of the U.S. mid-Atlantic continental margin,'' EOS Trans. Am. Geophys. Union **72**, 273–274 (1991).
[17] M. S. Longuet-Higgins, D. E. Cartwright, and N. D. Smith, ''Observations of the directional spectrum of sea waves using the motions of a floating buoy,'' *Ocean Wave Spectra* (Prentice-Hall, Englewood Cliffs, NJ, 1963).
[18] G. M. Purdy, L. Dorman, A. Schultz, and S. C. Solomon, ''An ocean bottom seismometer for the Office of Naval Research,'' in ULF/VLF (0.001 to 50 Hz) seismo-acoustic noise in the ocean, Proceedings of a workshop at the Institute for Geophysics, University of Texas, Austin, November 29 to December 1, 1988, edited by G. H. Sutton (Office of Naval Research, Arlington, VA, 1990).
[19] E. L. Hamilton, ''Geoacoustic modeling of the sea floor,'' J. Acoust. Soc. Am. **68**, 1313–1340 (1980).
[20] S. Holbrook (private communication).
[21] J. Ewing (private communication).
[22] W. A. Kuperman and F. Ingenito, ''Spatial correlation of surface generated noise in a stratified ocean,'' J. Acoust. Soc. Am. **67**, 1988–1996 (1980).
[23] Our method for predicting noise generated by surface waves, as presented in the text, is valid for stratified environments having infinite horizontal extent. By implication the source distribution also has infinite extent. In this regard our model is less general than Cato's (Ref. 2), who modeled the ocean as a semi-infinite cylinder with finite radius.
[24] D. K. Wilson, ''Sound field computations in a stratified, moving medium,'' J. Acoust. Soc. Am. **94**, 400–407 (1993).
[25] H. Schmidt and G. Tango, ''Efficient global matrix approach to the computation of synthetic seismograms,'' Geophys. J. R. Astron. Soc. **84**, 331–359 (1986).
[26] H. Schmidt, *SAFARI: Seismo-Acoustic Fast Field Algorithm for Range Independent Environments. User's Guide* (SACLANT ASW Research Centre, La Spezia, Italy, 1986), SR 113.
[27] T. E. Lindstrom, ''Predictions and observations of seafloor infrasonic noise generated by sea surface orbital motion,'' Ocean Engineer dissertation, Massachusetts Institute of Technology and Woods Hole Oceanographic Institution, 1991.
[28] A. C. Kibblewhite and C. Y. Wu, ''The theoretical description of wave-wave interactions as a noise source in the ocean,'' J. Acoust. Soc. Am. **89**, 2241–2252 (1991).
[29] The method used to make the theoretical predictions in Sec. IV B is described by Lindstrom (Ref. 27). Lindstrom's method is very similar, but not identical, to the one described in Sec. III. The latter incorporates some corrections for calculation of the effects of the depth-dependent ocean environment on the propagation. However, these corrections affect only the time-independent transfer function between the surface waves and the bottom-based sensors; the time-varying effects of the wave height spectrum and spreading are the same in both models. Therefore the differences between the two methods do not significantly affect the conclusions in Sec. IV B.
[30] H. Schmidt and W. A. Kuperman, ''Estimation of surface noise source level from low-frequency seismoacoustic ambient noise measurements,'' J. Acoust. Soc. Am. **84**, 2153–2162 (1988).
[31] A. C. Kibblewhite and C. Y. Wu, ''The generation of infrasonic ambient noise in the ocean by nonlinear interactions of ocean surface waves,'' J. Acoust. Soc. Am. **85**, 1935–1945 (1989).
[32] M. A. Donelan, J. Hamilton, and W. H. Hui, ''Directional spectra of wind-generated waves,'' Philos. Trans. R. Soc. London, Ser. A **315**, 509–562 (1985).
[33] A. Lygre and H. E. Krogstad, ''Maximum entropy estimation of the directional distribution in ocean wave spectra,'' J. Phys. Oceanogr. **16**, 2052–2060 (1986).
[34] J. P. Burg, ''Maximum entropy spectral analysis,'' Ph.D. dissertation, Stanford University, 1976.
[35] R. T. Lacoss, ''Data adaptive spectral analysis methods,'' Geophysics **36**, 661–675 (1971).

On the use of higher-order azimuthal schemes in 3-D PE modeling

Frédéric Sturm[a)]
Institut National des Sciences Appliquées de Lyon, UMR CNRS 5514 (LMC) and 5585 (MAPLY), Bât. Jean d'Alembert, 20 avenue A. Einstein, 69621 Villeurbanne cedex, France

John A. Fawcett[b)]
DRDC-Atlantic, P.O. Box 1012, Dartmouth, Nova Scotia B2Y 3Z7, Canada

(Received 19 July 2001; revised 11 December 2002; accepted 3 March 2003)

In this paper, the issue of using higher-order finite difference schemes to handle the azimuthal derivative term in a three-dimensional parabolic equation based model is addressed. The three-dimensional penetrable wedge benchmark problem is chosen to illustrate the accuracy and efficiency of the proposed schemes. Both point source and modal initializations of the pressure field are considered. For each higher-order finite difference scheme used in azimuth, the convergence of the numerical solution with respect to the azimuth is investigated and the CPU times are given. Some comparisons with solutions obtained from another 3-D model [J. A. Fawcett, J. Acoust. Soc. Am. **93**, 2627–2632 (1993)] are presented. The numerical simulations show that the use of a higher-order scheme in azimuth allows one to reduce the required number of points in the azimuthal direction while still obtaining accurate solutions. The higher-order schemes have approximately the same efficiency as a FFT-based approach (in fact, may outperform it slightly); however, the finite difference approach has the advantage that it may be more flexible than the FFT approach for various PE approximations. © *2003 Acoustical Society of America.* [DOI: 10.1121/1.1572138]

PACS numbers: 43.30.Bp, 43.30.Dr [DLB]

I. INTRODUCTION

In most realistic oceanic problems the 3-D environmental variability is weak enough to allow two-dimensional (2-D) models to correctly predict sound propagation. The underlying assumption of any 2-D model is that the coupling of the propagating energy from one vertical plane to another is negligible. Models which perform 2-D computations in adjacent planes centered on the source are referred to as N $\times$2-D or pseudo-3-D in the literature. Nevertheless, it has been demonstrated both experimentally and numerically (see, for instance, Refs. 1–3) that in some particular oceanic environments, 3-D effects cannot be neglected and full 3-D models are thus required. The reader is referred to Ref. 4 for an exhaustive review of the available 3-D codes based on mode theory, parabolic equation (PE), rays, and hybrid techniques and to Ref. 5 for a specialized review of existing 3-D PE models.

Most of the 3-D PE models have been derived to handle an isotropic point source and are thus written in cylindrical coordinates r, θ, z with z being the depth below the ocean surface, θ being the azimuthal angle, and r being the horizontal range. In both 2-D and 3-D modeling, parabolic equations are derived using various paraxial approximations of the same basic Helmholtz equation. They are very attractive since their underlying algorithms march the solution outward in range. In a three-dimensional scenario, this means the acoustic field is known on a grid of points in depth and azimuth at a range step and is propagated outward at the next range step. The term that accounts for azimuthal refraction is a differential operator with respect to θ and must be incorporated into the resolution. The standard method consists in splitting the 3-D PE into an N$\times$2-D part and an azimuthal part. Though not used in all 3-D PE models,[6,7] this splitting method leads to relatively fast numerical algorithms (e.g., Refs. 8–10). It offers the possibility to update any 2-D PE code to handle azimuthal coupling, which explains its popularity.

However, solving this azimuthal part (which characterizes full 3-D computations) increases the CPU times. Whereas the computation times are still acceptable at short ranges and low frequencies (in comparison with any 2-D run), any 3-D computation can become unreasonably intensive as the range increases, even at very low frequency. Indeed, to detect any eventual 3-D effect, the user needs to maintain the necessary arclength between adjacent angles. This means that as the desired maximum range increases, the required number of azimuthal points also increases and hence the computational demand can become very large.

The azimuthal part can be solved using either Fourier-based transformation techniques (in particular, FFTs)[10,11] or a finite difference (FD) scheme.[8,9] The azimuthal-FD scheme used in these previous works is the classical second-order approximation. The FFT is very numerically efficient; however, we will show in this paper that by implementing high-order schemes for the azimuthal discretization, a fewer number of azimuthal points are required and accurate solutions can be computed with an efficiency comparable to or better than the FFT-based methods. This is important because there are PE operator expansions for which a FD discretization can be implemented but the FFT approach cannot be used. Also,

a)Electronic mail: frederic.sturm@insa-lyon.fr
b)Electronic mail: john.fawcett@drdc-rddc.gc.ca

 0001-4966/2003/113(6)/3134/12/$19.00

it may be advantageous to consider variable size FD discretizations; e.g., the step size is small where there is rapid azimuthal variation of the solution and larger elsewhere.

This paper deals with the performance of high-order finite difference schemes to handle the azimuthal part in 3-D PE modeling. The aim is to show that by enhancing the order of accuracy of the FD scheme, it is possible to reduce significantly the required azimuthal sampling and thus to significantly improve the computational efficiency over the standard second-order approach, while still maintaining the accuracy of the solution.

The structure of this paper is as follows: In Sec. II, we present the three-dimensional parabolic equation model 3DWAPE[12] which we have chosen to incorporate the higher-order azimuthal schemes and test their efficiencies. Notice that this 3-D PE code was originally configured to use a second-order FD scheme in azimuth. Section III deals with the numerical method chosen to solve the inherent initial- and boundary-value problem. More specifically, the higher-order FD schemes used to handle the azimuthal part are proposed. An *a priori* discussion of their efficiencies is given. To assess the efficiency of the method, we consider in Sec. IV the 3-D penetrable wedge problem. The N×2-D and 3-D solutions are first compared. Three-dimensional solutions are then compared to reference solutions in both up-slope and cross-slope directions. The higher-order accurate FD methods are compared with the classical second-order accurate FD method. In each case, numerical solutions and CPU times are given and compared with the ones obtained using FFTs. The computational efficiency of the method is demonstrated. As a conclusion, the advantages and limitations of this method are discussed.

II. DERIVATION OF 3DWAPE

A multi-layered waveguide composed of one water layer and Q fluid sedimental layers is considered. The geometry of each layer is fully three-dimensional. We work in cylindrical coordinates. A sound field generated by a point harmonic source of frequency f, located at $r=0$ and $z=z_S$, is considered. Assuming a gradual variation of the waveguide both in range and azimuth, the basic equation is the following farfield 3-D Helmholtz equation

$$\frac{\partial^2 p}{\partial r^2}+\frac{1}{r}\frac{\partial p}{\partial r}+\rho\frac{\partial}{\partial z}\left(\frac{1}{\rho}\frac{\partial p}{\partial z}\right)+\frac{1}{r^2}\frac{\partial^2 p}{\partial \theta^2}+(k_0 n_\alpha)^2 p=0 \tag{1}$$

written in cylindrical coordinates, where p is the complex acoustic pressure and $k_0=2\pi f/c_0$ with c_0 a reference sound speed. The terms n_α and ρ represent, respectively, the complex index of refraction and the z-dependent density term. The cylindrical spreading is handled by factorizing the pressure as

$$p(r,\theta,z)=H_0^{(1)}(k_0 r)v(r,\theta,z),$$

where $H_0^{(1)}$ denotes the zeroth-order Hankel function of the first kind. Assuming that r^{-2} approximately commutes with $\partial/\partial r$ for $r\gg 0$, Eq. (1) can be factorized and, assuming only outward propagation in range, the problem is reduced to an initial- and boundary-value problem. We seek a complex-valued function $v=v(r,\theta,z)$, which represents the acoustic field for $r_0\leqslant r\leqslant r_{\max}$, $0\leqslant\theta\leqslant 2\pi$, and $0\leqslant z\leqslant z_{\max}$, and which satisfies the Cauchy problem

$$\begin{aligned}&\frac{\partial v}{\partial r}(r,\theta,z)=\mathrm{i}k_0(\sqrt{\mathcal{Q}}-\mathcal{I})v(r,\theta,z),\\&v(r=r_0,\theta,z)=v^{(0)}(\theta,z).\end{aligned} \tag{2}$$

The function $v^{(0)}$ denotes the initial outgoing field at $r=r_0$ and $\mathcal{Q}$ is the operator defined by

$$\mathcal{Q}=\mathcal{I}+\mathcal{X}+\mathcal{Y}$$

with $\mathcal{I}$ the identity operator and $\mathcal{X}$, $\mathcal{Y}$ defined by

$$\mathcal{X}=(n_\alpha^2-1)\mathcal{I}+\frac{\rho}{k_0^2}\frac{\partial}{\partial z}\left(\frac{1}{\rho}\frac{\partial}{\partial z}\right), \tag{3a}$$

$$\mathcal{Y}=\frac{1}{k_0^2 r^2}\frac{\partial^2}{\partial\theta^2}. \tag{3b}$$

The operator $\mathcal{Y}$ handles the azimuthal diffraction term. Neglecting $\mathcal{Y}$ would lead to an N×2-D (or pseudo-3-D) model which would be unable to predict horizontal refraction of the energy. The acoustic field v satisfies a pressure-release boundary condition at the ocean surface (i.e., at $z=0$) and transmission conditions at each interface between media $q-1$ and q (i.e., at $z=z_q(r,\theta)$, $1\leqslant q\leqslant Q$). An increasing attenuation coefficient in the lower part of the domain is introduced to prevent reflections from an imposed pressure-release boundary condition at $z=z_{\max}$. The acoustic field v also satisfies a 2π-periodicity condition in azimuth.

Now let us turn to the approximation of the square root (pseudo-differential) operator $\sqrt{\mathcal{Q}}$ present in (2). When 3-D effects are sufficiently gradual, one can write

$$\sqrt{\mathcal{Q}}=\sqrt{\mathcal{I}+\mathcal{X}}+\tfrac{1}{2}\mathcal{Y}+O(\mathcal{Y}^2,\mathcal{X}\mathcal{Y}). \tag{4}$$

By neglecting the last term in term in $O(\mathcal{Y}^2,\mathcal{X}\mathcal{Y})$ in Eq. (4), a linear approximation in θ can be made. Following the terminology usually employed, any 3-D PE based on this approximation is called *narrow-angle* in azimuth. Notice that if, as in Ref. 13, a [1/1] Padé expansion (or any higher-order Padé series expansion) was used in azimuth, the approximation would be in $O(\mathcal{Y}^3)$ but still in $O(\mathcal{X}\mathcal{Y})$. The underlying mathematical hypothesis is that $|\mathcal{Y}v|\ll|\mathcal{X}v|$. The associated physical meaning is that any horizontal deviation is small compared to the vertical in-plane deviation of the propagating energy. This assumption is valid for 3-D sound propagation problems for which 3-D effects are slow or gradual. It is clear that this assumption may be inappropriate for problems with large out-of-plane deviations of the outward propagating field. For such problems, one should utilize a three-dimensional parabolic equation that handles wide-angle propagation in both depth and azimuth (see, for instance, the 3-D PE derived by Siegmann *et al.* in Ref. 14).

The following higher-order Padé approximation in depth[15] can be used to approximate the square root operator,[16]

$$\sqrt{\mathcal{I}+\mathcal{X}}=\mathcal{I}+\sum_{k=1}^{n_\mathrm{p}}\frac{a_{k,n_\mathrm{p}}\mathcal{X}}{\mathcal{I}+b_{k,n_\mathrm{p}}\mathcal{X}}+O(\mathcal{X}^{2n_\mathrm{p}+1}) \tag{5}$$

where $a_{k,n_p}=[2/(2n_p+1)]\sin^2(k\pi/2n_p+1)$, $b_{k,n_p}=\cos^2(k\pi/2n_p+1)$ for $1\leqslant k\leqslant n_p$. Notice that complex values of the Padé coefficients can also be used as in Ref. 17 to attenuate Gibb's oscillations when range-dependent environments are considered. This expansion effectively allows for very-wide-angle propagation in depth, the angular limitation depending on the number n_p of Padé terms included in the truncated series. It can be extended to model energy at angles of nearly $\pm 90°$ vertically with respect to the horizontal. By neglecting last term on both right-hand sides of Eqs. (4) and (5), we obtain the following Cauchy problem

$$\frac{\partial v}{\partial r}(r,\theta,z)=ik_0\left(\sum_{k=1}^{n_p}\frac{a_{k,n_p}\mathcal{X}}{\mathcal{I}+b_{k,n_p}\mathcal{X}}+\frac{1}{2}\mathcal{Y}\right)v(r,\theta,z),$$
$$v(r=r_0,\theta,z)=\tilde{v}^{(0)}(\theta,z), \tag{6}$$

where $\tilde{v}^{(0)}$ is an initial field consistent with the paraxial approximation used (see Ref. 18 for more details). This last parabolic equation accounts for refraction effects in the depth direction which are of higher order than those in the azimuthal direction. Thus, the resulting 3-D PE model has a *very-wide-angle* capability in depth (hence the acronym 3DWAPE) and a *narrow-angle* capability in azimuth. Notice that using the following linear approximation both in depth and in azimuth,

$$\sqrt{\mathcal{I}+\mathcal{X}}=\mathcal{I}+\tfrac{1}{2}\mathcal{X}+O(\mathcal{X}^2), \tag{7}$$

leads to the standard 3-D narrow angle parabolic equation proposed by Tappert in Ref. 19:

$$\frac{\partial v}{\partial r}=\frac{ik_0}{2}(n_\alpha^2-1)v+\frac{i}{2k_0}\frac{\partial^2 v}{\partial z^2}+\frac{i}{2k_0r^2}\frac{\partial^2 v}{\partial\theta^2}. \tag{8}$$

For the particular value $n_p=1$, the parabolic equation given in (6) reduces to the Claerbout wide-angle (in depth) PE which can be written as

$$\frac{\partial v}{\partial r}(r,\theta,z)=ik_0\left(\frac{\tfrac{1}{2}\mathcal{X}}{\mathcal{I}+\tfrac{1}{4}\mathcal{X}}+\frac{1}{2}\mathcal{Y}\right)v(r,\theta,z) \tag{9}$$

and which is considered accurate for propagation angle within $\pm 35°$ off the horizontal. The three-dimensional code written and used by Fawcett in Ref. 10 is based on Eq. (9). In the next sections, we will refer to this second three-dimensional code as FFTPE.

For any of the three equations (6), (8), and (9), one can use either Fourier-based transformation techniques (FFTs) or a finite difference scheme to handle the azimuthal derivative term. Any Fourier-based transformation technique can be use directly on each of the three previous parabolic equations since the index of refraction term and the azimuthal derivative term are separated in each equation. However, it is important to note that there are some paraxial approximations of the square root operator that are not amenable to FFTs treatments. For instance, if we denote by $\mathcal{Z}$ the depth-derivative operator

$$\mathcal{Z}=\frac{\rho}{k_0^2}\frac{\partial}{\partial z}\left(\frac{1}{\rho}\frac{\partial}{\partial z}\right),$$

then the square root operator $\sqrt{\mathcal{Q}}$ can be rewritten as

$$\sqrt{\mathcal{Q}}=\sqrt{\mathcal{I}+(n_\alpha^2-1)\mathcal{I}+\mathcal{Z}+\mathcal{Y}}=n_\alpha\sqrt{\mathcal{I}+n_\alpha^{-2}(\mathcal{Z}+\mathcal{Y})},$$

and leads to the following parabolic equation:[20]

$$\frac{\partial v}{\partial r}=ik_0(n-1)v+\frac{i}{2k_0n}\frac{\partial^2 v}{\partial z^2}+\frac{i}{2k_0nr^2}\frac{\partial^2 v}{\partial\theta^2}. \tag{10}$$

Notice that this latter equation can be considered as a 3-D extension of the c_0-insensitive 2-D PE given in Ref. 19, Eq. (1.23b). The reader is referred to Refs. 21 and 22 for more recent works and discussions on c_0-insensitive parabolic equations. Notice, however, that Eq. (10) is amenable to finite difference schemes.

III. NUMERICAL DISCRETIZATION

The previous initial- and boundary-value problem given by (6) is numerically solved using an alternating direction method.[8,9,16] The first step is to split the 3-D parabolic equation into the following system:

$$\frac{\partial v}{\partial r}(r,\theta,z)=ik_0\left(\sum_{k=1}^{n_p}\frac{a_{k,n_p}\mathcal{X}}{\mathcal{I}+b_{k,n_p}\mathcal{X}}\right)v(r,\theta,z), \tag{11a}$$

$$\frac{\partial v}{\partial r}(r,\theta,z)=\frac{i}{2k_0r^2}\frac{\partial^2 v}{\partial\theta^2}(r,\theta,z). \tag{11b}$$

Let Δr, $\Delta\theta$, and Δz be the increments respectively in range, in azimuth, and in depth. We denote

$$v_{i,j}^n=v(r_n,\theta_i,z_j),\quad 1\leqslant n\leqslant N_r,\quad 1\leqslant i\leqslant M,\quad 1\leqslant j\leqslant N,$$

where r_n, θ_i, and z_j are the cylindrical coordinates of a mesh point, and N_r, M, and N are integers indicating the maximum number of mesh points respectively in range, azimuth, and depth. Each of these equations can now be solved separately at any discrete range r_n, $1\leqslant n\leqslant N_r$. If one wishes to use the N×2-D approach, then only the equation (11a) is solved at each single range step. We note that a marching algorithm based on the split-step Fourier (SSF) technique in both depth and azimuth could also be used,[11] since both differential (in depth and azimuth) operators have been separated from the index of refraction term.

A. Solving the N×2-D part

Equation (11a) is solved by using a Crank–Nicolson integration in range and an accurate finite-element/Galerkin method in depth. As we have considered N discrete points in z and M discrete points in θ, the resulting computation procedure requires the inversion, at each single range step, of M algebraic linear systems of order N. A piecewise linear finite-element approximation in depth is used. The resulting matrices (each of order N) are all tridiagonal. Each set of linear equations is solved using a fast and robust Gaussian algorithm optimized for tridiagonal matrices, which requires a number of arithmetic operations $\mathcal{N}_{op}^{G}$ being asymptotically of the order of N, i.e., $\mathcal{N}_{op}^{G}=\mathcal{O}(N)$. The computing cost (in terms of $\mathcal{N}_{op}^{G}$) is thus very efficient in comparison with the classical Gaussian algorithm for full matrices of order N, for which the number of arithmetic operations is in $\mathcal{O}(N^3)$. Notice that when selecting n_p terms in the Padé development of Eq. (11a), each inversion must be repeated n_p times. Conse-

quently, for each single range step, the number of arithmetic operations $\mathcal{N}_{\rm op}^{(a)}$ required becomes asymptotically

$$\mathcal{N}_{\rm op}^{(a)}=\mathcal{O}(n_{\rm p}MN).$$

Thus, the total number of arithmetic operations $\mathcal{N}_{\rm op}^{\rm N\times 2D}$ required to solve Eq. (11a) for all discrete ranges r_n, $1\leqslant n\leqslant N_r$, is

$$\mathcal{N}_{\rm op}^{\rm N\times 2D}=N_r\times\mathcal{N}_{\rm op}^{(a)}$$

and is asymptotically given by

$$\mathcal{N}_{\rm op}^{\rm N\times 2D}=\mathcal{O}(n_{\rm p}N_rMN). \tag{12}$$

B. Higher-order FD schemes in azimuth

In this section, the problem of solving Eq. (11b) is considered. Among the existing numerical techniques, one of the widely used is based on a finite-difference (FD) scheme in azimuth coupled with a Crank–Nicolson-type range-stepping procedure. The three-point stencil scheme given as

$$\left.\frac{\partial^2 v}{\partial\theta^2}\right|_{i,j}^{n}=\frac{v_{i+1,j}^{n}-2v_{i,j}^{n}+v_{i-1,j}^{n}}{\Delta\theta^2}+O(\Delta\theta^2) \tag{13}$$

can be used. This scheme corresponds to a centered FD scheme of second-order of accuracy. In order to optimize the discretization in the θ-direction, one can also use any higher-order centered FD formula. Assuming enough regularity on solution v with respect to the azimuthal variable up to the order 2ℓ, we can prove, using Taylor's expansion, that

$$\left.\frac{\partial^2 v}{\partial\theta^2}\right|_{i,j}^{n}=\frac{\Sigma_{k=1}^{\ell}\gamma_k v_{i+k,j}^{n}-\kappa v_{i,j}^{n}+\Sigma_{k=1}^{\ell}\gamma_k v_{i-k,j}^{n}}{\Delta\theta^2}+O(\Delta\theta^{2\ell}) \tag{14}$$

with $\kappa=2\Sigma_{k=1}^{\ell}\gamma_k$ and with $\gamma_1,\gamma_2,\ldots,\gamma_\ell$ satisfying

$$\begin{aligned}
&\gamma_1+2^2\gamma_2+\cdots+(\ell-1)^2\gamma_{\ell-1}+\ell^2\gamma_\ell=1,\\
&\gamma_1+2^4\gamma_2+\cdots+(\ell-1)^4\gamma_{\ell-1}+\ell^4\gamma_\ell=0,\\
&\gamma_1+2^6\gamma_2+\cdots+(\ell-1)^6\gamma_{\ell-1}+\ell^6\gamma_\ell=0,\\
&\qquad\vdots\\
&\gamma_1+2^{2\ell}\gamma_2+\cdots+(\ell-1)^{2\ell}\gamma_{\ell-1}+\ell^{2\ell}\gamma_\ell=0.
\end{aligned}$$

This $(2\ell+1)$-point stencil scheme corresponds to a higher-order centered FD scheme and can be seen as an extension of the second-order FD scheme given in Eq. (13). Indeed, selecting $\ell=1$, we obtain $\gamma_1=1$ and $\kappa=2$ and then Eq. (14) reduces to Eq. (13). For increasing value of the parameter ℓ, the scheme is more accurate. It is hoped that by using a higher-order FD scheme in azimuth we will be able to significantly reduce the azimuthal sampling. As the mesh has N points in z and M points in θ, the numerical resolution of Eq. (11b) using any higher-order centered FD scheme given in Eq. (14) requires the inversion, at each single range step, of N algebraic linear systems of order M with entries in the upper right and lower left corners of the banded matrices to account for the continuity condition in azimuth. For the sake of simplicity let us concentrate on a three-dimensional problem symmetric about $\theta=0$. The resulting matrices obtained using any higher-order FD formula in azimuth are all banded matrices with no additional terms due to the symmetry condition. Denoting these matrices $\mathbf{B}=(b_{ij})_{1\leqslant j,j\leqslant M}$, it follows that

$$b_{ij}=0 \quad \text{when} \quad j>i+\ell \quad \text{or} \quad i>j+\ell.$$

The bandwidth of $\mathbf{B}$ depends on the parameter ℓ (cf. Table I). Notice that the coefficient given in Eq. (11b) only depends on the range variable. Thus, the resulting matrices depend only on the discrete ranges. To take advantage of this property, we replace the Gaussian algorithm by a *LU*-decomposition and by a forward- and back-substitution. At each single range step, we first complete the *LU*-decomposition and once we have it, we solve the resulting matrix system, one at a time, with each of the N right-hand side vectors. Consequently, for each single range step, the number of arithmetic operations $\mathcal{N}_{\rm op}^{(b)}$ required to invert the N algebraic linear systems of order M writes asymptotically

$$\mathcal{N}_{\rm op}^{(b)}=\mathcal{O}(\ell^2M+\ell NM), \tag{15}$$

where the first term on the right-hand side of Eq. (15) corresponds to the number of arithmetic operations required to perform the *LU*-decomposition and the second term, the number of operations for the forward- and back-substitution for the N systems. The computational cost (in terms of $\mathcal{N}_{\rm op}^{(b)}$) is still small in comparison with the one needed for full matrices of order M on condition $\ell\ll M$. Notice that for $\ell\ll N$, the computational cost needed to perform the forward- and back-substitution at each discrete range step is predominant in comparison with the computing cost needed to complete the *LU*-decomposition. Thus, the total number of arithmetic operations $\mathcal{N}_{\rm op}^{\theta}$ required to solve Eq. (11b) for all discrete ranges r_n, $1\leqslant n\leqslant N_r$, is

$$\mathcal{N}_{\rm op}^{\theta}=N_r\times\mathcal{N}_{\rm op}^{(b)}$$

and is asymptotically given by

$$\mathcal{N}_{\rm op}^{\theta}=\mathcal{O}(N_r(\ell^2M+\ell NM)). \tag{16}$$

In summary, the total number of arithmetic operations $\mathcal{N}_{\rm op}^{\rm 3D}$ required in solving both Eqs. (11a) and (11b) for all discrete ranges is

$$\mathcal{N}_{\rm op}^{\rm 3D}=\mathcal{N}_{\rm op}^{\rm N\times 2D}+\mathcal{N}_{\rm op}^{\theta}. \tag{17}$$

Suppose that using a FD scheme of order ℓ_1 (ℓ_2) we need M_1 (M_2) discrete points in azimuth to get an accurate solution. Selecting ℓ_2 larger than ℓ_1 will lead to $M_2<M_1$. Now let us consider the CPU time which can be estimated considering $\mathcal{N}_{\rm op}^{\rm 3D}$. Both $\mathcal{N}_{\rm op}^{\rm N\times 2D}$ and $\mathcal{N}_{\rm op}^{\theta}$ will accordingly be reduced linearly with respect to M. Unfortunately, using $\ell_2>\ell_1$ introduces additional arithmetic operations (to perform the inversions of the resulting matrices with larger band-

TABLE I. Characteristics of several FD schemes in azimuth.

ℓ	FD scheme	Stencil	Matrix structure
1	second-order	3 points	tri-diagonal
2	fourth-order	5 points	penta-diagonal
3	sixth-order	7 points	hepta-diagonal
4	eighth-order	9 points	nano-diagonal

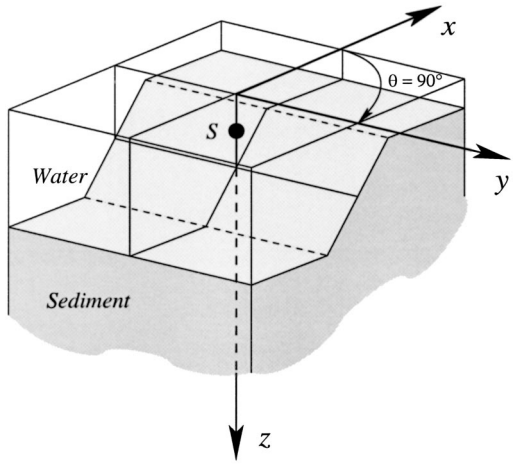

FIG. 1. Geometry of the 3-D (truncated) wedge shaped waveguide. The point source S is located above the sloping bottom.

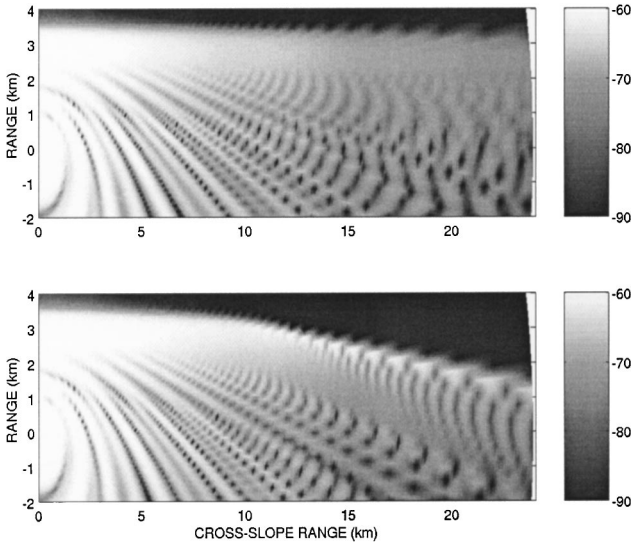

FIG. 2. Transmission loss (horizontal slices at constant depth $z=30$ m) corresponding to N×2-D (upper subplot) and 3-D (lower subplot) calculations. Both solutions have been obtained using 3DWAPE.

width). Hence we will observe an increase of $\mathcal{N}_{\text{op}}^{\theta}$ (mainly linear with $\ell \ll N$ as seen previously) with respect to ℓ. Although it is difficult to state definitely *a priori* whether the total CPU time (estimated by $\mathcal{N}_{\text{op}}^{\text{3D}}$) will be increased or reduced, we believe that the reduction of the azimuthal sampling will be significant enough that the additional operations introduced will be negligible.

IV. NUMERICAL SIMULATIONS

To assess the relative efficiencies of the various three-dimensional PE implementations, we consider the three-dimensional penetrable wedge problem which is now a benchmark problem.[2,10,11,23] The numerical simulations were performed on a 552-MHz mono-processor HP-workstation C3600. Neither vectorization option nor parallel computing have been used. Except when specified explicitly otherwise, all the following numerical results have been obtained running 3DWAPE.

A. Description of the test case

The environment consists of a nonattenuating isovelocity water column, $c_{\text{w}}=1500$ m/s, over an isovelocity half-space bottom, $c_{\text{sed}}=1700$ m/s. The water/bottom interface parametrization is given by $z_{\text{sed}}(r,\theta)=\tilde{z}_{\text{sed}}(x,y)$ with $x=r\cos\theta$, $y=r\sin\theta$ and

$$\tilde{z}_{\text{sed}}(x,y)=\begin{cases} 200(1-x/4000) & \text{if } |x|\leqslant 3600, \\ 20 & \text{if } x\geqslant 3600, \\ 380 & \text{if } x\leqslant -3600. \end{cases}$$

The depth of the water column decreases with increasing x values. It is constant with respect to the y-coordinate. In cylindrical coordinates, it makes an angle of 2.86° with respect to the ocean surface at $\theta=0°$ and has a zero-slope at both $\theta=90°$ and $\theta=270°$ which we will refer to as cross-slope directions (cf. Fig. 1). The density changes at $z=z_{\text{sed}}(r,\theta)$ from $\rho_{\text{w}}=1$ g/cm^3 in the water to $\rho_{\text{sed}}=1.5$ g/cm^3 in the sediment. The bottom attenuation is $\alpha_{\text{sed}}=0.5$ dB/λ. An isotropic point source is placed at range $r_S=0$ and depth $z_S=100$ m. The water depth at the source position is 200 m. The source frequency is 25 Hz. For a constant 200-m water depth, this waveguide has three propagating modes. We use an artificial absorbing layer from $z_{\text{abs}}=450$ m to $z_{\max}=600$ m with a depth-dependent attenuation coefficient $\alpha_{\text{abs}}(z)$ given by $\alpha_{\text{abs}}(z)=\alpha_{\text{sed}}+g_{\text{abs}}\times(z-z_{\text{abs}})$ for $z_{\text{abs}}\leqslant z\leqslant z_{\max}$ with $g_{\text{abs}}=0.05$ (dB/λ)/m. The maximum range of computation is $r_{\max}=24$ km. The reference sound speed is $c_0=1500$ m/s.

B. Comparison of N×2-D and 3-D solutions

We have calculated the N×2-D and 3-D solutions of the three-dimensional wedge problem using the numerical model 3DWAPE. For both calculations, we have used the same values for the depth and range increments ($\Delta r=10$ m and $\Delta z=1$ m). The 3-D solution shown hereafter has been obtained using a second-order accurate FD scheme in azimuth with $M=23\,040$ points. Notice that the N×2-D solution has been calculated using only 360 points in azimuth, which seems reasonable for a horizontal plot of the N×2-D field. Gray-scale images of the transmission loss (TL) (horizontal slices at constant depth $z=30$ m) corresponding to N×2-D and 3-D calculations are shown in Fig. 2. Due to the geometrical symmetry of the problem about the upslope direction, both N×2-D and 3-D solutions are displayed in Fig. 2 as a function of range and azimuth in a limited azimuthal sector, i.e., for $0°\leqslant\theta\leqslant 180°$.

Recall that when calculating the N×2-D solution, only Eq. (11a) is solved. Notice that any N×2-D solution can be θ-dependent if the propagation problem is different from one vertical plane to another. This is the case in the present test case since the bottom slope varies with the azimuth. Though the N×2-D solution includes θ dependence, no 3-D effects due to out-of-plane propagation are present. On the contrary, when calculating the 3-D solution, both Eqs. (11a) and (11b) are solved. Thus, due to the azimuthal coupling term in Eq. (11b), out-of-plane phenomena does appear at various ranges, leading, in the vicinity of the cross-slope direction and at long ranges, to realistic shadow zone and interference

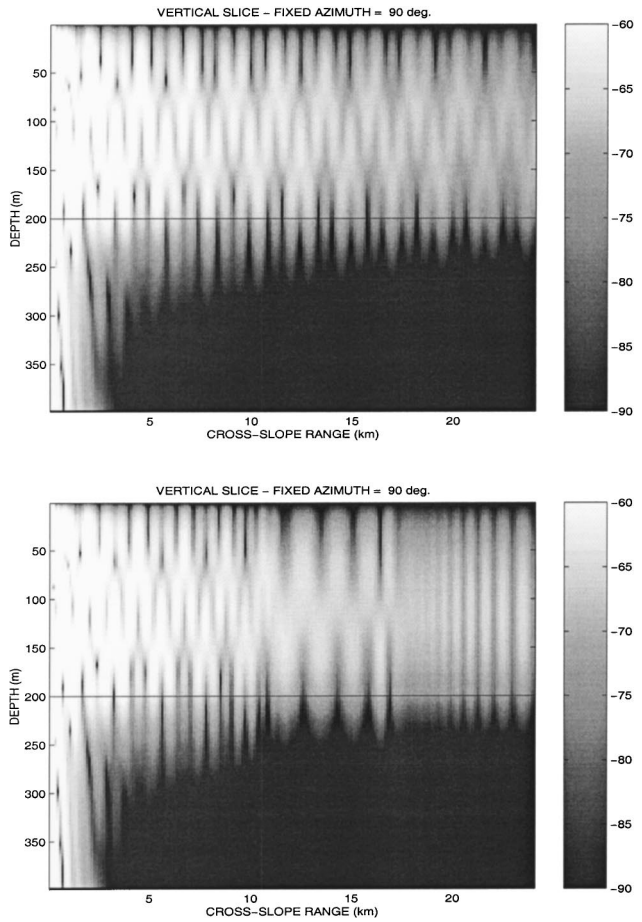

FIG. 3. Transmission loss (vertical slices at constant azimuth $\theta=90°$ across slope) corresponding to N×2-D (upper plot) and 3-D (lower subplot) calculations. Both solutions have been obtained using 3DWAPE.

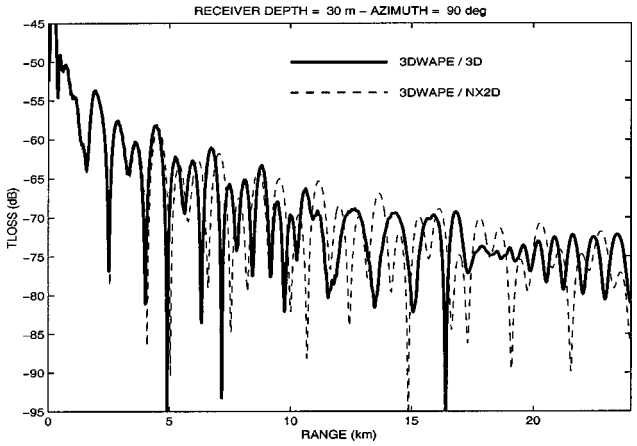

FIG. 4. Transmission loss curves for a receiver at depth $z=30$ m along $\theta=90°$ (across-slope) corresponding to 3-D (bold-solid line) and N×2-D (dashed line) calculations. Both solutions have been obtained using 3DWAPE.

patterns not predicted by a N×2-D calculation. Comparing the two subplots of Fig. 2, we observe that the differences between the N×2-D and 3-D solutions are less for receivers away from the cross-slope direction. We display in Fig. 3 gray-scale images of the transmission loss (vertical slices, across-slope at $\theta=90°$) corresponding to the N×2-D (upper subplot) and 3-D (lower subplot) calculations. TL-versus-range curves corresponding to $z=30$ m and $\theta=90°$ are shown in Fig. 4. After a few kilometers from the source in the across-slope direction, the differences between the N×2-D and 3-D solutions become more and more pronounced as the range r increases. The 3-D effects correspond to intramodal interference effects and can be explained as follows. For a CW-point source emitting at $f=25$ Hz in a 200-m-deep waveguide, three propagating modes are excited at the source position. The geometry of the waveguide in the cross-slope direction (characterized by a zero-slope) is seen by any 2-D or N×2-D model as a classical Pekeris waveguide. Hence, the three initial propagating modes are present in the cross-slope direction for $0\leqslant r\leqslant r_{\max}$. Now, calculating the solution using a 3-D model, the initial propagating modes are horizontally refracted down the slope. Hence, for ranges approximately less than 11 km, three modes are present. Then, due to the 3-D mode shadowing effect of mode 3, only two modes are present for $r\geqslant 11$ km (approximately) until $r\approx 17$ km. After $r\approx 17$ km, there is a mode shadowing effect of mode 2, and only mode 1 is present. The interference pattern in the 3-D solution starting at $r\approx 18$ km corresponds to the 3-D mode self-interference effect of mode 1; that is, there is more than one modal ray path arrival for mode 1 at these points. For all the simulations shown previously, we have used one Padé term in Eq. (11a). Hence, both N×2-D and 3-D solutions correspond to a third-order Claerbout-type wide-angle approximation in depth. It is now interesting to see to what extent the use of higher-order approximations in depth is meaningful when processing 3-D computations. This is examined by 3DWAPE with various values of the parameter n_p in Eq. (11a). We compare in Fig. 5 the 3-D solutions corresponding to different wide-angle approximations in depth. The solid curve corresponds to a third-order Padé 1 approximation ($n_p=1$) and the dashed curve to a fifth-order Padé 2 approximation ($n_p=2$). Also shown in the same plot in dashed-dotted line is the 3-D PE solution corresponding to the narrow-angle Tappert's approximation in depth. The two solutions corresponding to $n_p=1$ and $n_p=2$ agree extremely well. This is not surprising

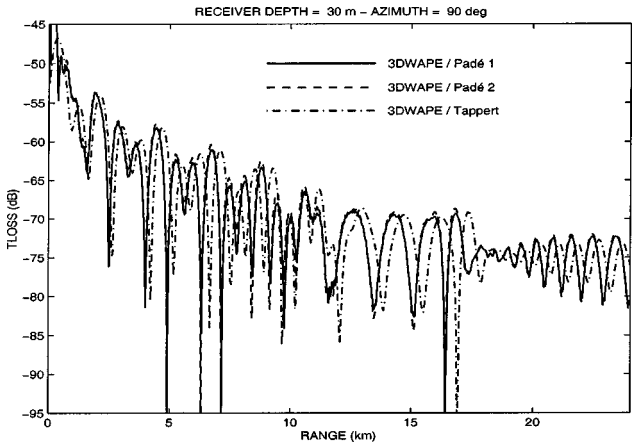

FIG. 5. Transmission loss curves at $z=30$ m and $\theta=90°$ (across-slope) for the 3-D solutions obtained running 3DWAPE with $n_p=1$ (solid curve), with $n_p=2$ (dashed curve) and with a narrow-angle approximation (dashed-dotted curve).

since their limitations in depth exceed the critical grazing angle $\vartheta_c \approx 28°$.

It would be interesting to analyze the influence on sound propagation of using a wide-angle approximation in azimuth. Though this question has not been yet studied quantitatively (and thus remains a question of interest), we are confident that for the penetrable wedge problem considered in this paper, the use of a narrow-angle approximation in azimuth is sufficient to accurately describe all the 3-D effects. Indeed, predicting the horizontal refraction effects using adiabatic mode theory,[24] the horizontal deviation of the energy is relatively slow, the 3-D effects predicted being in good agreement with the ones obtained with a 3-D PE model.[10]

C. Convergence tests using a second-order FD scheme in azimuth

One difficult and time-consuming issue in performing 3-D computations is to know whether or not the discrete solution is close enough to the exact solution. In practice the user needs to perform some convergence tests, i.e., the 3-D model is run several times using different range, azimuthal, and depth increments until the numerical solution starts to stabilize. On the one hand, the values of Δr and Δz required for accurate 3-D computations can be determined using a non-time-consuming N×2-D model. For the present 3-D wedge problem, we have found $\Delta r = 10$ m and $\Delta z = 1$ m, i.e., $\Delta r = \lambda/6$ and $\Delta z = \lambda/60$ where λ denotes the acoustic wavelength. On the other hand, the convergence tests with respect to the azimuthal discretization require much more effort. We first use the second-order FD scheme in azimuth given in Eq. (13) (the use of higher-order azimuthal schemes will be discussed later) with the convergence tests being carried out following the method proposed in Ref. 23: The 3DWAPE method is run using $\Delta\theta = 0.125°$ (i.e., $M = 2880$). This starting value of $\Delta\theta$ corresponds to an arclength increment ΔS of the order of λ at the maximum computation range $r_{\max}$. Then we refine $\Delta\theta$ as many times as necessary until no significant variation is observed for a smaller azimuthal increment. Convergence has been achieved using $M = 23040$, i.e., $\Delta\theta \approx 0.0156°$. This azimuthal increment corresponds to an arclength increment ΔS of the order of $\lambda/10$ at $r_{\max}$. The solutions corresponding to $M = 2880$, $M = 5760$, $M = 11\,520$, and $M = 23\,040$ are shown in the upper (for $0 \leqslant r \leqslant 24$ km) and lower (for $16 \text{ km} \leqslant r \leqslant 24$ km) subplots of Fig. 6. We can make several observations. First, the numerical solutions are in good agreement for $0 \leqslant r \leqslant 16$ km (see upper subplot of Fig. 6) but start to differ at $r \approx 16$ km until $r \leqslant 24$ km. We also observe (see the lower subplot of Fig. 6) that, being less stringent, using $M = 11\,520$ gives also a quite accurate solution (as discussed in Refs. 23 and 25). However, caution must be paid in the interpretation of the other curves. One could easily conclude that they all contain 3-D effects (if compared with the 2-D solution). Nevertheless, these 3-D effects are not the exact ones but only numerical approximations of them. Running 3DWAPE using a second-order accurate FD scheme with only $M = 2880$ or $M = 5760$ appears inappropriate to accurately compute the 3-D effects.

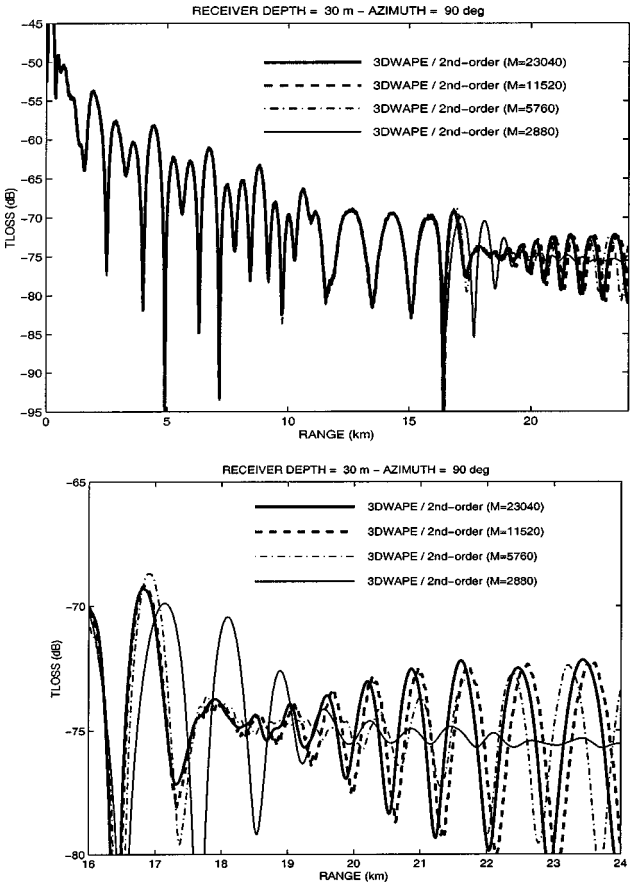

FIG. 6. Transmission loss curves at $z = 30$ m and $\theta = 90°$ (across-slope) obtained running 3DWAPE with $M = 23\,040$ radials (bold-solid line), $M = 11\,520$ (bold-dashed line), $M = 5760$ (dashed-dotted line) and $M = 2880$ (thin-solid line). The second-order FD scheme of Eq. (13) has been used. The lower suplot is a zoom of the upper subplot.

D. Energy-conservation in 3-D PE models

We now compare the 3-D solution obtained running 3DWAPE, with two reference solutions. The first one has been obtained using the 2-D coupled-mode code COUPLE.[26] Notice that in the upslope direction, the 3-D wedge problem corresponds to the classical ASA 2-D benchmark wedge problem. No three-dimensional effect is expected in this particular azimuthal direction (due to the geometrical symmetry of the problem with respect to that particular vertical plane). Since the COUPLE solution has been validated for the ASA wedge problem,[27] it can be used as an exact reference solution when comparing 2-D and 3-D results in the upslope direction. The second reference solution has been obtained using the 3-D PE code of Ref. 10. This three-dimensional code has been previously used in underwater acoustics for intercomparison between 3-D PE models (see for instance Refs. 11, 23, and 13). In that sense, it can be considered as a reference model, though, as we will see it, caution must be paid to its validity in both upslope and cross-slope directions. For the sake of simplicity, we refer to this 3-D code as FFTPE. This reference three-dimensional model uses a splitting of the 3-D parabolic equation given by Eq. (9) into a N×2-D part and an azimuthal part as follows:

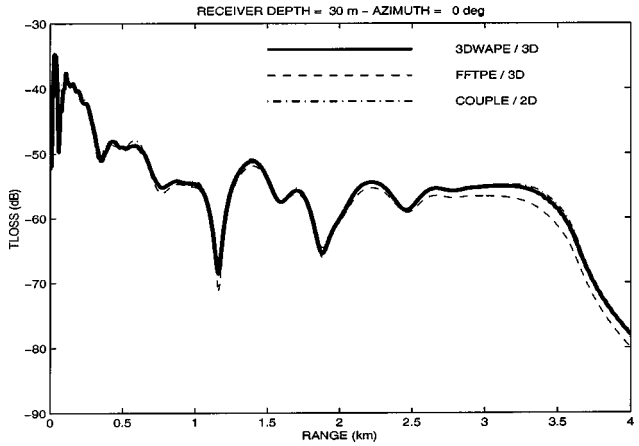

FIG. 7. Transmission loss curves at $z=30$ m and $\theta=0°$ (in the upslope direction) obtained using 3DWAPE (bold-solid line), FFTPE (dashed line) and COUPLE (dashed-dotted line).

$$\frac{\partial v}{\partial r}(r,\theta,z)=\frac{(\mathrm{i}k_0/2)(n_\alpha^2-1)\mathcal{I}+(\mathrm{i}/2k_0)(\partial^2/\partial z^2)}{\mathcal{I}+\frac{1}{4}(n_\alpha^2-1)\mathcal{I}+(1/k_0^2)(\partial^2/\partial z^2)}v(r,\theta,z), \tag{18a}$$

$$\frac{\partial v}{\partial r}(r,\theta,z)=\frac{\mathrm{i}}{2k_0r^2}\frac{\partial^2 v}{\partial\theta^2}(r,\theta,z). \tag{18b}$$

It then solves the N×2-D part given by Eq. (18a) using either a split-step Fourier-based technique or a finite difference method in depth coupled with a Crank–Nicolson range-stepping procedure. At each step in range, the azimuthal part is handled using fast Fourier transforms (FFTs). This means that Eq. (11b) is solved by computing for $1\leqslant n\leqslant N_r$ and $1\leqslant j\leqslant N$,

$$v(r_n+\Delta r,\theta,z_j)=\mathcal{F}_\theta^{-1}\{\Theta\times\mathcal{F}_\theta\{v(r_n,\theta,z_j)\}\}$$

where

$$\Theta=\exp\left(-\frac{\mathrm{i}m^2\Delta r}{2k_0r_n(r_n+\Delta r)}\right),$$

$\mathcal{F}_\theta\{\cdot\}$ denotes the Fourier transform with respect to the azimuth θ, $\mathcal{F}_\theta^{-1}\{\cdot\}$ denotes its inverse transform, and m denotes the azimuthal wavenumber. At each range step, this requires computing N FFT pairs (i.e., a FFT pair for each discrete point in depth) and applying a multiplicative operator at each point of the z, θ-grid. The number of azimuthal FFT components should be an integer power of 2 to take full advantage of the FFT algorithm. We display in Fig. 7 the transmission loss-versus-range curves in the upslope direction (at $\theta=0°$), the receiver depth being $z=30$ m. The solution obtained using the 3-D PE code 3DWAPE is shown as a bold solid line and the reference (exact) solution obtained using the 2-D code COUPLE is shown as a dashed-dotted line. Also plotted (in dashed line) is the solution obtained using the 3-D PE code FFTPE of Ref. 10. As in the majority of the existing 3-D PE models, the varying geometry of the water/sediment interface is approximated in both 3DWAPE and FFTPE by a sequence of stair-steps in each azimuthal direction. It is well known that doing so can lead to energy loss for upslope propagation and energy gain for downslope propagation.[28] In order to avoid this problem of energy conservation, several numerical techniques can be used and have proven to be effective and accurate for 2-D modeling.[17,29–31]

In 3DWAPE a special treatment is done at each vertical interface between range-independent sections. The method used to compute the correct outgoing field is based on a single-scatter formalism and is similar to the one used in Refs. 32 and 30. Depending on the physical problem, one can either use the *narrow angle* approach of Ref. 32 or the *very-wide angle* expansion of Ref. 30. For the present test case, we have used the latter.

This method is satisfying since the 3DWAPE solution (bold-solid line) compares favorably with the reference COUPLE solution (dashed line) in the upslope direction (see Fig. 7). We expected a good agreement between any 2-D and 3-D solutions at $\theta=0°$ since there is no 3-D effect in both the upslope and downslope directions. No special treatment being done in FFTPE, the solution exhibits an energy loss in the upslope direction. In that sense, the FFTPE model is not energy conserving.

Let us turn now to the cross-slope direction. In FFTPE, the numerical convergence has been reached using $\Delta r=10$ m, $\Delta z=1$ m, and 4096 points in azimuth. As mentioned previously, the number of azimuthal FFT components required by FFTPE must be an integer power of 2. The convergence curves (transmission loss-versus-range at depth $z=30$ m and azimuth $\theta=90°$) are shown in Fig. 8. For convenience, the results are displayed for $0\leqslant r\leqslant 24$ km (upper subplot) and 16 km$\leqslant r\leqslant 24$ km (lower subplot). We observe that the 3-D solutions corresponding to 2048 and 4096 azimuthal FFT components are extremely close. The 2048 FFT component solution could also be used as a reference solution for comparison with other numerical solutions.[11]

The 3DWAPE (obtained using a second-order FD scheme with 23 040 points in azimuth) and FFTPE (obtained using 4096 radials) solutions are displayed in Fig. 9 for comparison. Satisfactorily, both 3-D models describe the same three-dimensional effects since the two curves are quite close (see upper subplot of Fig. 9). However, we observe some level differences between the two 3-D solutions, mainly in the prediction at long range of the 3-D self-interference effect of mode 1 (see lower subplot of Fig. 9). In comparison, the shift in the phasing between the two curves is negligible. We have already observed such differences between these two 3-D results in the upslope direction (see Fig. 7). These differences are thus mainly in the levels, which is characteristic of the problem of energy conservation in one-way PE modeling. Unlike 3DWAPE, the FFTPE code is not energy conserving. The energy loss observed directly across-slope in the FFTPE solution is the consequence of the energy-conservation problem present in the upslope direction (i.e., for $\theta=90°$) and in the adjacent azimuthal upslope directions that correspond to $0\leqslant\theta<90°$. Notice that this energy loss is certainly not a problem of energy-conservation in the $\theta=90°$ cross-slope direction since there is no slope in that particular azimuthal direction.

E. Use of higher-order FD scheme in azimuth

Following the approach used in Ref. 10 and later used in Refs. 11 and 23 to characterize the 3-D effects present in the

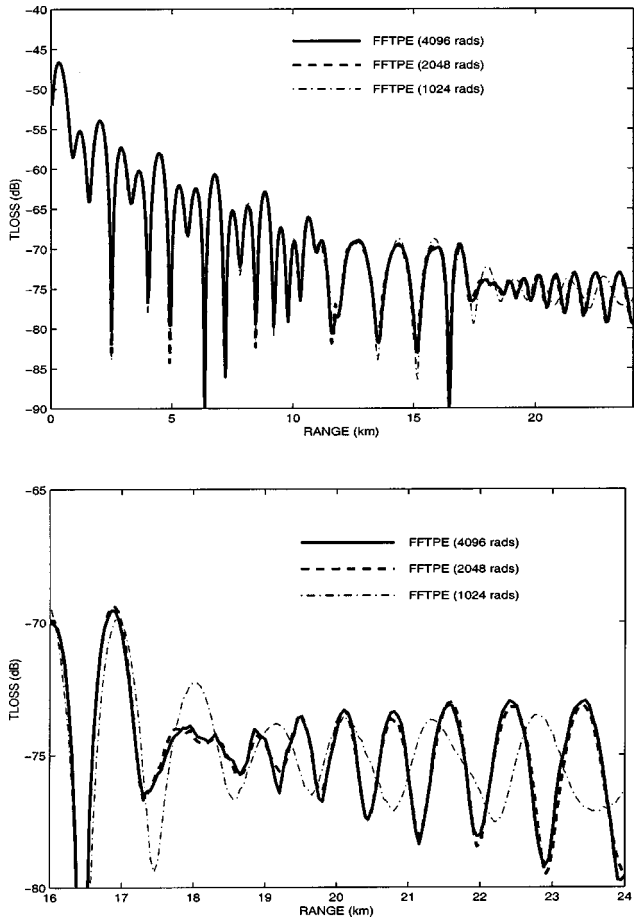

FIG. 8. Transmission loss curves at $z=30$ m and $\theta=90°$ (across-slope) obtained running FFTPE with 4096 radials (bold-solid line), 2048 radials (bold-dashed line), and 1024 radials (dashed-dotted line). The lower suplot is a zoom of the upper subplot.

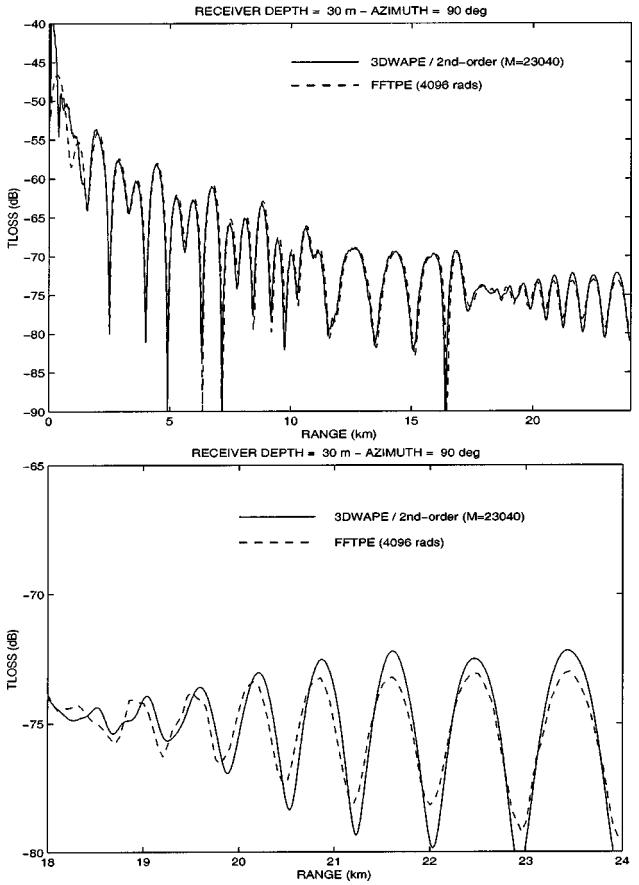

FIG. 9. Transmission loss curves at $z=30$ m and $\theta=90°$ (across-slope) obtained using 3DWAPE with $M=23\,040$ (solid line) and FFTPE with 4096 radials (dashed line). The lower suplot is a zoom of the upper subplot.

waveguide, we excite only mode 1 at the source location and propagate it outward in range. The source field is assumed to be omnidirectional. The 3-D PE marching algorithm is initialized using for all $\theta\in[0,2\pi[$,

$$v(r=0,\theta,z)=\psi(z), \quad 0\leqslant z\leqslant z_{\max},$$

where ψ is defined as

$$\psi(z)=\begin{cases}\mu\sin(k_z z) & \text{for } 0\leqslant z\leqslant H,\\ \mu\sin(k_z H)\mathrm{e}^{-\gamma(z-H)} & \text{for } z>H,\end{cases}$$

and where $H=200$ m is the water depth at the source location. A normalization coefficient μ is introduced such that

$$\int_0^\infty \frac{|\psi(z)|^2}{\rho}dz=1,$$

and $k_z=(\omega^2/c_w^2-k_r^2)^{1/2}$ and $\gamma=(k_r^2-\omega^2/c_{\text{sed}}^2)^{1/2}$. The horizontal wavenumber k_r satisfies

$$\tan(k_z H)=-\frac{\rho_{\text{sed}}\times k_z}{\rho_{\text{w}}\times\gamma}.$$

Solving this latter equation numerically, we find $k_r=0.103\,824\ \text{m}^{-1}$. We display in Fig. 10 TL contour plots (vertical slices at constant azimuth $\theta=90°$) corresponding to N×2-D and 3-D solutions. In order to reduce the phase error inherent to PE models, the reference sound speed used corresponds to the phase velocity of mode 1, i.e., $c_0=\omega/k_r\approx 1512.94$ m/s. While the 2-D solution only includes cylindrical spreading (since the waveguide is range independent in the cross-slope direction), the 3-D solution includes additional three-dimensional effects known as 3-D mode self-interference effects.[25,33–35] We display in Fig. 11 the 3DWAPE numerical solutions obtained using a second-order azimuthal FD scheme with different numbers of points in azimuth. For each simulation, we have used $\Delta r=10$ m and $\Delta z=1$ m. The corresponding CPU times are given in Table II. As a comparison, we also give the CPU times corresponding to N×2-D computations (though it is not necessary to select such a number of points in azimuth when processing N×2-D computations, $M=360$ is sufficient). The solution has converged by $M=23\,040$. The corresponding CPU time is 220 mn 48 s. Running the N×2-D model with $M=360$ took 2 mn 45 s. As expected, the CPU times increase linearly with M for both N×2-D and 3-D computations. Notice that for each value of M, approximately 78% of the total CPU time is devoted to the N×2-D part of the marching algorithm, i.e., only 22% is used to solve Eq. (11b). For comparison, running FFTPE with 2048 (respectively 4096) radials took 40 mn 49 s (respectively 82 mn 47 s) on the same computer, all the other parameters being identical in both codes (e.g., $\Delta r=10$ m, $\Delta z=1$ m, $z_{\max}=600$ m). We now examine the decrease in computation speed that is achieved by

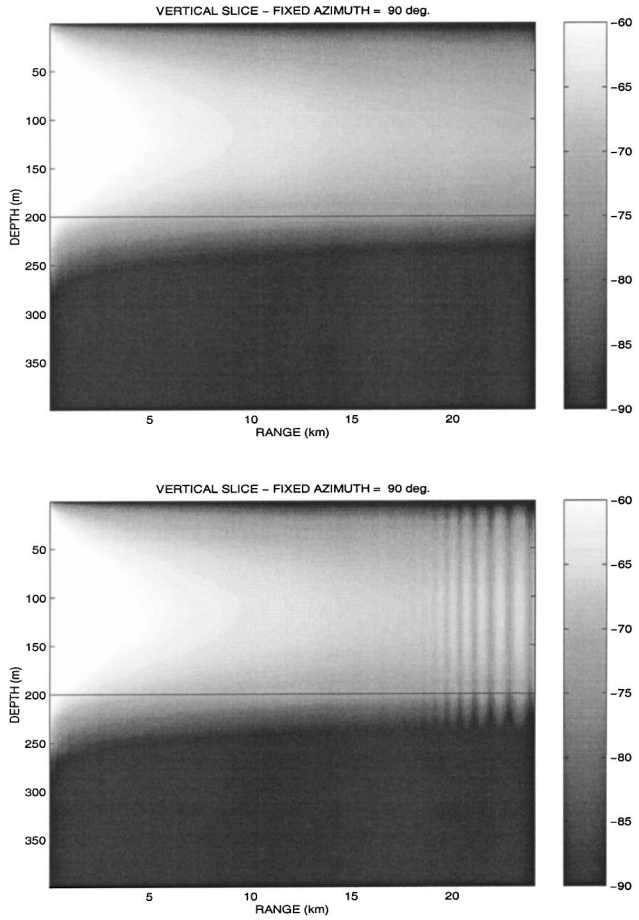

FIG. 10. Mode 1 transmission loss plots (vertical slices at constant azimuth $\theta=90°$). The upper figure corresponds to a N×2-D calculation. The lower figure corresponds to a 3-D calculation. Both results have been obtained using 3DWAPE.

using higher-order FD schemes (with 3DWAPE) in azimuth (up to the eighth order). For each FD scheme considered, the range and depth increments are unchanged and we have performed careful convergence tests with respect to the azimuth. The convergence test is stopped when no significant variation is observed, i.e., when the solution stabilized. The number of points M in azimuth required to achieve the convergence and the corresponding CPU time expended for each run is given in Table III. For each higher-order FD scheme considered, the 3-D solution obtained also agrees very well with the 3-D solution obtained using a second-order FD scheme, which we denote as the ''exact'' numerical solution. For instance, the comparison of the 3-D solutions obtained using a second-order FD scheme (with $M=23\,040$) and an eighth-order FD scheme (with $M=3240$) appears in Fig. 12. Both solutions agree very well, showing that the higher-order accurate scheme introduces no additional artificial dissipation.

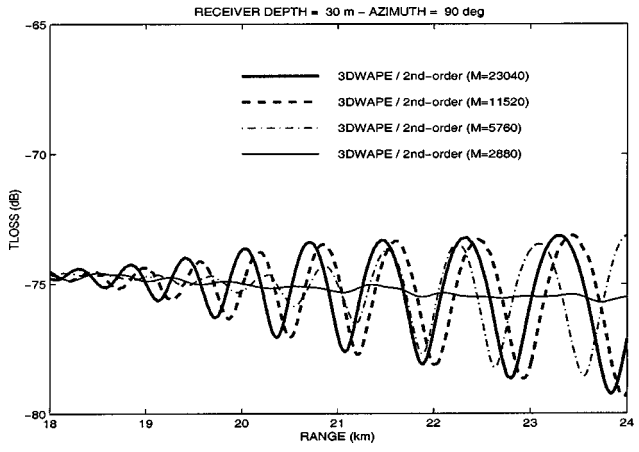

FIG. 11. Mode 1 transmission loss curves at $z=36$ m and $\theta=90°$ (across-slope) obtained using a second-order FD scheme with $M=23\,040$ (bold-solid line), $M=11\,520$ (dashed line), $M=5760$ (dashed-dotted line), and $M=2880$ (thin solid line). These results have been obtained using 3DWAPE.

TABLE II. CPU times expended for 3-D calculations with 3DWAPE using a second-order FD scheme (right column) and for N×2D calculations (middle column) corresponding to an increasing number of points M in azimuth (left column).

M	N×2-D	3-D/second-order
360	2 mn 45 s	3 mn 28 s
2880	21 mn 22 s	27 mn 12 s
5760	43 mn 12 s	54 mn 24 s
11 520	85 mn 12 s	109 mn 12 s
23 040	170 mn 20 s	220 mn 48 s

As expected, using a FD scheme in azimuth with increasing accuracy allows us to reduce significantly the number of points in the azimuthal direction and accordingly enhance the speed-up of the computation. The run using a eighth-order accurate FD scheme only took 37 mn 52 s while it took 220 mn 48 s using a second-order scheme. The CPU time has been reduced by a factor approximately equal to 6. The time of 37 mn 52 s is a little faster than the time 40 mn 49 s for the FFT-based method FFTPE.

As discussed in Section III, the use of higher-order scheme introduces additional operations. For instance, the following result can be derived from the CPU time values given in Table III: when an eighth-order scheme is used, approximately 37% of the total work is devoted to solve Eq. (11b) while, as seen previously, it takes only 22% using a second-order scheme. In any event, the increased computational speed with respect to the classical second-order scheme is so large that the additional operations inherent to the use of higher-order schemes appear negligible. When an eighth-order accurate FD scheme is used, the convergence is reached with an azimuthal increment corresponding to an arclength increment $\Delta S\approx 3\lambda/4$ at $r_{\max}$. It is now interesting to observe the behavior of the 3-D solutions when using larger azimuthal increments. We display in Fig. 13 3-D solutions obtained using the eighth-order FD scheme with vari-

TABLE III. CPU times expended for 3-D calculations using FD scheme with increasing order of accuracy and required to achieve the exact numerical solution.

FD order	M	3-D	N×2-D
second-order	23 040	220 mn 48 s	170 mn 20 s
fourth-order	5760	59 mn 12 s	43 mn 12 s
sixth-order	4320	47 mn 18 s	32 mn 05 s
eighth-order	3240	37 mn 52 s	23 mn 48 s

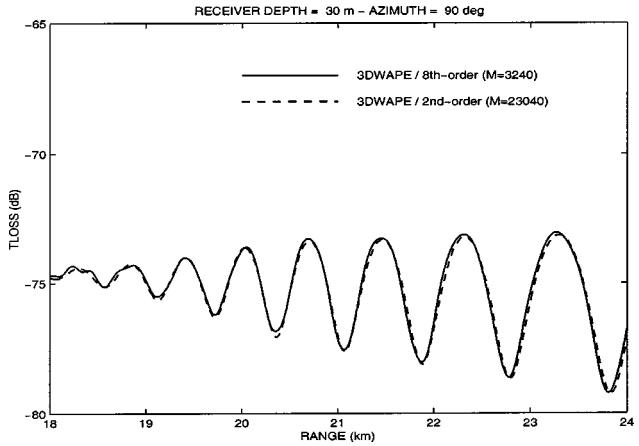

FIG. 12. Mode 1 transmission loss curves at $z=36$ m and $\theta=90°$ (across-slope). The solid curve is a 3-D calculation using a eighth-order FD scheme and $M=3240$. The dashed curve is a 3-D calculation using a second-order FD scheme and $M=23\,040$. These results have been obtained using 3DWAPE.

ous azimuthal increments. The numerical solution obtained running 3DWAPE and using an eighth-order accurate FD scheme with only $M=2880$ agrees quite well with the converged solution except for a shift in the phasing.

V. SUMMARY AND DISCUSSION

In this paper, it has been shown that higher-order finite difference schemes can be very effectively and accurately used in the computation of the azimuthal derivative terms in a three-dimensional parabolic equation model. The required number of azimuthal points is significantly reduced by using a higher-order scheme with a resulting decrease in the computational time. A benchmark wedge case was used for the numerical investigations. The three-dimensional PE codes, with the various orders of azimuthal finite differences, were rigorously tested. The code was also compared with another 3D PE code (FFTPE) which used a FFT evaluation of the azimuthal derivative.

The finite difference and FFT codes predict the same 3-D effects for the same test case, though some level-discrepancies are observed in both upslope and cross-slope directions due to the energy-conservation problem in the particular FFTPE code. It has been confirmed in this paper that the azimuthal discretization technique based on a classical second-order FD scheme is definitely slower than the FFT technique. It has also been shown that the use of higher-order FD schemes can be as efficient as the use of FFT technique. This is important because there are operator expansions and scenarios where the FFT approach cannot be used. In the future, we would also like to consider variable step finite difference schemes where the step size is small in regions where the solution is varying rapidly and larger elsewhere.

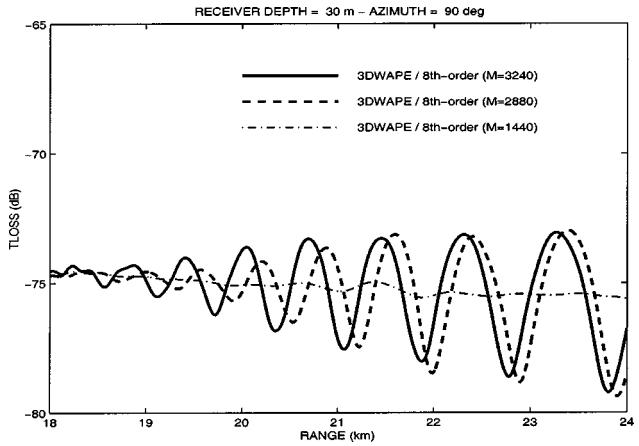

FIG. 13. Mode 1 transmission loss curves at $z=36$ m and $\theta=90°$ (across-slope) obtained using an eighth-order FD scheme with $M=3240$ (bold-solid line), $M=2880$ (dashed line), and $M=1440$ (dashed-dotted line). These results have been obtained using 3DWAPE.

It is not clear under what conditions the higher-order schemes can be accurately used. The higher-order schemes have been derived using Taylor's expansion and thus implicitly assume high levels of regularity of the acoustic field. If the required regularity is absent, the advantages of using such higher-order schemes could eventually break down. However, it is very encouraging to note that this did not occur in the 3-D wedge for which there were significant three-dimensional effects. In this case, the acoustic field had enough regularity with respect to the azimuthal variable to allow the high-order finite difference schemes to be very accurate and efficient.

[1] C. F. Chen, J.-T. Lin, and D. Lee, "Acoustic three-dimensional effects around Taiwan strait: computational results," J. Comput. Acoust. **7**, 15–26 (1999).

[2] G. B. Deane, "The penetrable wedge as a three-dimensional benchmark," J. Acoust. Soc. Am. **103**, 2989 (1998).

[3] S. A. Glegg, G. B. Deane, and I. G. House, "Comparison between theory and model scale measurements of the three-dimensional sound propagation in a shear supporting penetrable wedge," J. Acoust. Soc. Am. **94**, 2334–2342 (1993).

[4] A. Tolstoy, "3-D propagation issues and models," J. Comput. Acoust. **4**, 243–271 (1996).

[5] D. Lee, A. D. Pierce, and E.-C. Shang, "Parabolic equation development in recent twentieth century," J. Comput. Acoust. **8**, 527–637 (2000).

[6] F. Sturm, M.-C. Pélissier, and D. Fattaccioli, "3D Sound propagation modelling with TRIPARADIM," in *Proceedings of the 3rd European Conference on Underwater Acoustics*, Heraklion, Crete, Greece (1996), pp. 243–248.

[7] M. H. Schultz, D. Lee, and K. R. Jackson, "Application of the YALE sparse technique to solve three-dimensional parabolic wave equation," J. Acoust. Soc. Am. Suppl. 1 **78**, S96 (1983).

[8] D. Lee, G. Botseas, and W. L. Siegmann, "Examination of three-dimensional effects using a propagation model with azimuth-coupling capability (FOR3D)," J. Acoust. Soc. Am. **91**, 3192–3202 (1992).

[9] M. D. Collins and S. A. Ching-Bing, "A three-dimensional parabolic equation model that includes the effects of rough boundaries," J. Acoust. Soc. Am. **87**, 1104–1109 (1990).

[10] J. A. Fawcett, "Modeling three-dimensional propagation in an oceanic wedge using parabolic equation methods," J. Acoust. Soc. Am. **93**, 2627–2632 (1993).

[11] K. B. Smith, "A three-dimensional propagation algorithm using finite azimuthal aperture," J. Acoust. Soc. Am. **106**, 3231–3239 (1999).

[12] F. Sturm, "Mise en évidence et analyse d'effets tridimensionnels par utilisation et confrontation de modèles paraboliques 3D," (in French) in *Proc. 4émes Journées d'études Acoustique Sous-Marine*, Brest, France (1998), pp. 1–10.

[13] G. H. Brooke, D. J. Thomson, and G. R. Ebbeson, "PECan: A Canadian Parabolic Equation Model for Underwater Sound Propagation," J. Comput. Acoust. **9**, 69–100 (2001).

[14] W. L. Siegmann, G. A. Kriegsmann, and D. Lee, "A wide-angle three-dimensional parabolic wave equation," J. Acoust. Soc. Am. **78**, 659–664 (1985).

[15] A. Bamberger, B. Engquist, L. Halpern, and P. Joly, "Higher order paraxial wave equation approximations in heterogeneous media," SIAM

(Soc. Ind. Appl. Math.) J. Appl. Math. **48**, 129–154 (1988).
[16] J. I. Arvelo and A. P. Rosenberg, ''Three-dimensional effects on sound propagation and matched-field processor,'' J. Comput. Acoust. **9**, 17–39 (2001).
[17] M. D. Collins and E. K. Westwood, ''A higher order energy-conserving parabolic equation for range-dependent ocean depth, sound speed, and density,'' J. Acoust. Soc. Am. **89**, 1068–1075 (1991).
[18] F. B. Jensen, W. A. Kuperman, M. B. Porter, and H. Schmidt, *Computational Ocean Acoustics*, AIP Series in Modern Acoustics and Signal Processing (AIP, New York, 1994).
[19] F. D. Tappert, ''The parabolic approximation method,'' in *Wave Propagation and Underwater Acoustics*, edited by J. B. Keller and J. S. Papadakis, Lecture Notes in Physics, Vol. 70 (Springer, Berlin, 1977), pp. 224–287.
[20] C. Bernardi and M.-C. Pélissier, ''Spectral approximation of a Schrödinger type equation,'' Math. Models Methods Appl. Sci. **4**, 49–88 (1994).
[21] F. Tappert and G. Brown, ''Asymptotic phase error in parabolic approximations to the one-way Helmholtz equation,'' J. Acoust. Soc. Am. **99**, 1405–1413 (1996).
[22] F. Tappert, J. L. Spiesberger, and L. Boden, ''New full-wave approximation for ocean acoustic travel time predictions,'' J. Acoust. Soc. Am. **97**, 2771–2782 (1995).
[23] F. Sturm and J. A. Fawcett, ''Numerical simulation of the effects of the bathymetry on underwater sound propagation using three-dimensional parabolic equation models,'' SM-342 SACLANT Undersea Research Centre, La Spezia, Italy (1998).
[24] H. Weinberg and R. Burridge, ''Horizontal ray-theory for ocean acoustics,'' J. Acoust. Soc. Am. **55**, 63–79 (1974).
[25] F. Sturm, J. A. Fawcett, and F. B. Jensen, ''Benchmarking two three-dimensional parabolic equation methods,'' J. Acoust. Soc. Am. **103**, 2990 (1998).
[26] R. B. Evans, ''A coupled mode solution for acoustic propagation in a waveguide with stepwise depth variations of a penetrable bottom,'' J. Acoust. Soc. Am. **74**, 188–195 (1983).
[27] F. Jensen and C. M. Ferla, ''Numerical solutions of range-dependent benchmark problems in ocean acoustics,'' J. Acoust. Soc. Am. **87**, 1499–1510 (1990).
[28] M. B. Porter, F. B. Jensen, and C. M. Ferla, ''The problem of energy conservation on one way models,'' J. Acoust. Soc. Am. **89**, 1058–1067 (1991).
[29] G. H. Brooke, D. J. Thomson, and P. M. Wort, ''A sloping boundary condition for efficient PE calculations in range-dependent acoustic media,'' J. Comput. Acoust. **4**, 11–27 (1996).
[30] M. D. Collins and R. B. Evans, ''A two way parabolic equation for acoustic backscattering in the ocean,'' J. Acoust. Soc. Am. **91**, 1357–1368 (1992).
[31] N. A. Kampanis and E. T. Flouri, ''On an energy conserving treatment of variable interfaces in a finite difference PE code,'' Acust. Acta Acust. **85**, 18–23 (1999).
[32] G. H. Brooke and D. J. Thomson, ''A single-scatter formalism for improving PE calculations in range-dependent media,'' in NRL PE WORKSHOP II (Proceedings of the second parabolic equation workshop), edited by S. A. Chin-Bing, D. B. King, J. A. Davies, and R. B. Evans (Naval Research Laboratory, 1993), pp. 126–144.
[33] M. J. Buckingham, ''Theory of three-dimensional acoustic propagation in a wedgelike ocean with a penetrable bottom,'' J. Acoust. Soc. Am. **82**, 198–210 (1987).
[34] R. Doolittle, A. Tolstoy, and M. J. Buckingham, ''Experimental confirmation of horizontal refraction of cw acoustic radiation from a point source in a wedge-shaped ocean environment,'' J. Acoust. Soc. Am. **83**, 2117–2125 (1988).
[35] G. B. Deane and M. J. Buckingham, ''An analysis of the three-dimensional sound field in a penetrable wedge with a stratified fluid or elastic basement,'' J. Acoust. Soc. Am. **93**, 1319–1328 (1993).

Shape identification of underwater objects using backscattered frequency signals

G. R. Liu[a] and Wei Li[a]
Centre for Advanced Computations in Engineering Science, Department of Mechanical Engineering, National University of Singapore, 10 Kent Ridge Crescent, Singapore 119260

X. M. Zhang[b]
Ultrasound Research Laboratory, Mayo Clinic, 200 First Street SW, Rochester, Minnesota 55905

V. K. Varadan
Department of Engineering Science and Mechanics, The Pennsylvania State University, University Park, Pennsylvania 16802

(Received 6 August 2001; revised 19 November 2002; accepted 3 March 2003)

The inverse problems in the area of the acoustic scattering often concern the determination of the size, shape, and orientation of an object using the scattered field data. This paper presents a method to retrieve the shape information of an underwater object using illuminated lengths, which can be obtained from the ramp response signatures of the object. An ellipsoidal object submerged in water is considered. Both the low and high backscattered frequency data have been employed to calculate the illuminated lengths. The calculated results show that the illuminated lengths will be more accurate, if only the high-frequency-range data are employed. For ellipsoidal objects, any three illuminated lengths that are not of a same plane can in theory fully determine the shape of the ellipsoid. As the calculated illuminated lengths contain numerical errors, the calculated results of the three semiaxes of the ellipsoid will deteriorate and become unreliable, especially when the three incident directions of the illuminated lengths become close. The reason is that the condition number of the coefficient matrix becomes big in such situations, which leads to an increase of the relative error upper limit in the calculated results. To avoid such errors in close incident wave cases, it is found that the use of more than three incident waves works very well in the shape identification of an underwater object. [DOI: 10.1121/1.1569937]

PACS numbers: 43.30.Gv, 43.20.Fn [DLB]

I. INTRODUCTION

It is very important to determine the location, size, and shape of an underwater object from available measurement or observation data, such as the far field backscattered frequency spectrum at certain aspects and frequencies. This kind of problem is generally called the inverse acoustics, corresponding to the forward acoustics in which the scattered pressure field needs to be found for given incident acoustic waves and the physical properties of the object. Studies of forward scattering problems have been reported in a large number of publications, and many analytical and approximate methods have been developed. The exact analytic solutions[1,2] can be derived only for objects of simple geometries, such as sphere, infinite cylinder, and spheroid, for which the technique of separation of variables can be used. Approximate methods are thus often used for objects of more general shapes. These methods include the volume integral method,[3] the boundary integral method,[4] the cylinder method,[5] null-field method,[6] and the *T*-matrix method,[7,8] which is based on the extinction theorem.

In 1958, Kennaugh and Cosgriff,[9] in view of the physical optics approximation, found out the linear relationship between the ramp response and the profile function, which is the cross-sectional area versus the distance along the line of sight. In their paper, the ramp response is the second integral of the impulse response of an object, which is the inverse Fourier transform of the complex backscattering frequency spectrum in the frequency domain. Foo and his colleagues[10] extended the technique into the bistatic case in electromagnetic scattering problem. Recently, Chen, Peters, and Nag[11–13] applied this technique for detecting the buried targets, such as mines. In 1985, Tsao[14] introduced the ramp response into the acoustic field and obtained the same linear relationship between the ramp response and profile function for the Neumann boundary or Dirichlet boundary conditions. Zhang *et al.*[15,16] developed a new numerical method to obtain the ramp response for underwater objects in acoustic fluids, which requires less frequency domain data.

An obvious advantage of using ramp response technique to identify the size and shape of the object is that the ramp response is not difficult to be obtained numerically or experimentally. However, this technique requires data that covers the whole frequency domain in order to determine the size and shape of the object. In most cases, this requirement is hard to satisfy. Normally, only parts of the frequency data can be measured, often in a high-frequency domain. Underwater inverse problems are of importance since water occupies more than two-thirds of the surface of the earth. Many objects in water, for example fishes, torpedoes, and subma-

[a]Electronic mail: engp0341@nus.edu.sg
[b]Electronic mail: zhang.xiaoming@mayo.edu

 0001-4966/2003/113(6)/3146/9/$19.00

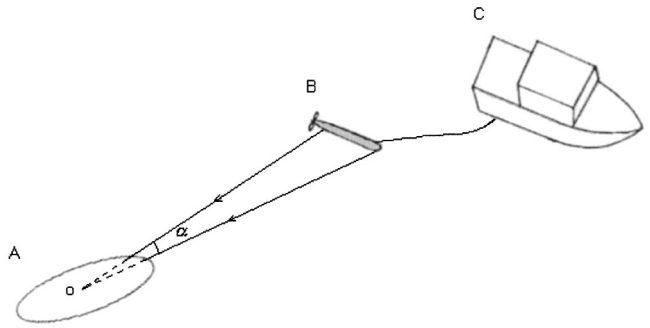

FIG. 1. Sketch of determining underwater object: (a) Underwater object, (b) Tow sonar, and (c) ship. The angle α is the maximum angle for the exploration if only one tow sonar is used.

rines, can be modeled as objects of simple geometries, such as ellipsoids. For an ellipsoid, if we can obtain data for three semiaxes, then the shape of the ellipsoid will be inversely determined.

In this paper, the method, which is used to determine the illuminated length d of an object in a high-frequency domain, was discussed. Theoretically, if three illuminated lengths of an ellipsoid are known in any three incident directions that are not of one plane, then the shape of the ellipsoid can be retrieved. However, when the calculated illuminated lengths contain numerical errors, the semiaxes of the ellipsoid obtained through solving this kind of inverse problem will become less reliable, especially when three incident directions are very close. This is observed as a type of inverse problem.[17] Objects of ellipsoid were first investigated. The relationship between the incident angles and the accuracy of the calculated results was studied. The condition number of the system matrix was introduced to investigate the reasons for the numerical errors in the results. It was found that in order to improve the accuracy of the results, more than three incident directions' frequency domain data should be used in computing the semiaxes of the ellipsoid. The use of the extra incident waves resulted in an overdetermined formulation, which effectively reduces the ill-posedness. The least-squares method was then employed to solve this kind of overdetermined problem.

II. PROBLEM DESCRIPTION

In general, underwater objects are far from the exploration equipment. In this situation, it is very difficult to obtain the backscattered frequency data from the rather wide range of the objects. The exploration range on the objects is very limited. Figure 1 shows the geometry of the underwater inverse problem. The incident wave from the sonar B only can light a small range of the object A. Thus, the backscattered frequency data that we can obtain are limited on the small range. The purpose of this paper is to find a method that can retrieve the shape information of underwater objects, when the directions of incident waves are very close.

In this paper, several basic assumptions have been made. (1) The underwater object is modeled as an ellipsoidal object. (2) The scattering surface is acoustically rigid (Neumann boundary condition). (3) The directions of incident waves are precisely given. The r, θ, ϕ spherical coordinates

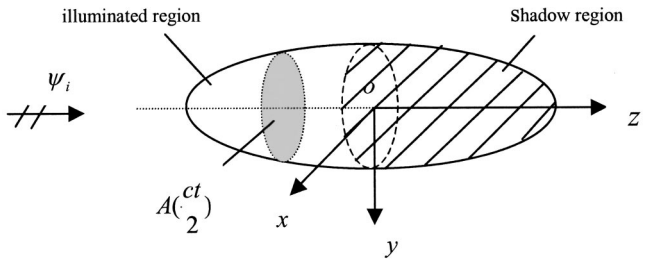

FIG. 2. An incident acoustic wave illuminates an object.

will be used. The origin is assumed, for convenience, to be the centroid of the object. The objective of the inverse problem is reconstructing the shape of the object using the backscattered frequency data for incident waves of different directions that are relatively close.

III. RAMP RESPONSE TECHNIQUES

When an incident pulse (represented by a delta function in time t) encounters an object in a homogeneous, isotropic medium, the phenomenon of wave diffraction or scattering occurs. The incident pulse is scattered in all directions. The waveform scattered in a direction opposite to the direction of incidence is called the backscattered impulse response. The ramp response is defined as a time-domain backscattered signal at a distant observation point in response to an incident ramp signal, where the ramp signal is a function defined to be the second integral of the incident pulse function. In practice, the projector-hydrophone system is used for the ramp response measurement. The projector generates a pulse and sends it out, while the hydrophone is used to receive the backscattered impulse response. Consequently, the backscattered impulse response is integrated twice with respect to time to yield ramp response. As we only need the backscattered signals, the projector and hydrophone should be set together.

In the underwater acoustic far field, based on the physical optics approximation, the ramp response for a rigid object is proportional to the cross-sectional area of the object and can be expressed as below,[9]

$$P_R(t) = \frac{1}{2\pi c} A\left(\frac{ct}{2}\right), \tag{1}$$

where c represents the sound velocity in the water and $A(ct/2)$ is the area of cross section of the object perpendicular to the line of sight. The function $A(ct/2)$ is called a profile function, which is shown in Fig. 2. Here t denotes the propagation time of the acoustic wave. Zero propagation time is defined as when the wave crosses the centroid (geometric center) of the object.

For the acoustically rigid bodies, Eq. (1) shows the linear relationship between the profile function and the ramp response of the object in the medium. If we know the ramp response of an object, the profile function can be obtained easily.

On the other hand, it can be proven that the ramp response $P_R(t)$ and the normalized complex backscattering amplitude $\Gamma(\omega)$ are Fourier transform pairs in the acoustic far field. It is shown as below

$$P_R(t)=\frac{1}{2\pi}\int_{-\infty}^{+\infty}\Gamma(\omega)e^{-i\omega t}\,d\omega. \tag{2}$$

Here the normalized complex backscattering amplitude Γ is defined as[15]

$$\Gamma(\omega)=\frac{S(\omega)+S^*(-\omega)}{(-i\omega)^2}, \tag{3}$$

where $S(\omega)$ is the backscattered frequency spectrum in the acoustic far field. The symbol "*" denotes complex conjugate.

Equation (2) is used to calculate the ramp response of the object. It should be noted that the normalized complex backscattering amplitude Γ is specified completely by scattering information of the object, and describes the frequency dependence of the scattering mechanisms, an inherent property of the object. The ramp response P_R describes the shape, size, and orientation information of the object.

Moreover, Eq. (2) can be further simplified as follows:

$$\begin{aligned}P_R(t)&=\frac{1}{2\pi}\int_{-\infty}^{+\infty}\Gamma(\omega)e^{-i\omega t}\,d\omega\\&=\frac{1}{2\pi}\left[\int_{-\infty}^{+\infty}\frac{S(\omega)}{(-i\omega)^2}e^{-i\omega t}\,d\omega+\left(\int_{-\infty}^{+\infty}\frac{S(\omega)}{(-i\omega)^2}e^{-i\omega t}\,d\omega\right)^*\right]\\&=\frac{1}{\pi}\int_{-\infty}^{+\infty}\frac{1}{-\omega^2}[S_r(\omega)\cos(\omega t)+S_i(\omega)\sin(\omega t)]\,d\omega,\end{aligned} \tag{4}$$

where $S_r(\omega)$ and $S_i(\omega)$ are the real and imaginary parts of $S(\omega)$, respectively.

In the acoustic far field, the relationship between the scattering field potential ψ_s and the backscattered frequency spectrum $S(\omega)$ could be obtained as

$$\lim_{r\to\infty}\psi_s(r)=S(\omega)\frac{e^{ikr}}{r}. \tag{5}$$

The backscattering cross section is given by

$$\sigma_b=|S(\omega)|^2. \tag{6}$$

IV. DETERMINATION OF ILLUMINATED LENGTH

The illuminated length d is defined as the distance between the centroid of the object and the plane that normals to the direction of the incident wave and has tangent with the surface of the object in the illuminated region. It is shown in Fig. 3.

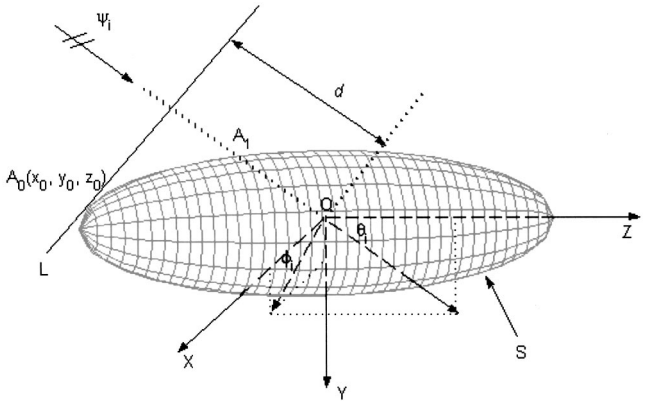

FIG. 3. Scattering geometry from an arbitrary looking angle (S is the surface of the object and L denotes the tangent plane of the S and normals to ψ_i).

In Fig. 3, we can find that the illuminated length d relates the size information of the object. It is, therefore, possible to reconstruct the object if the illuminated length d could be obtained.

Consider an ellipsoid in the water, which is described as below,

$$\frac{x^2}{a^2}+\frac{y^2}{b^2}+\frac{z^2}{c^2}=1, \tag{7}$$

where a, b, c are the three semiaxes of the ellipsoid. As an example, we choose $a=b=0.5$ m and $c=1.0$ m. The distance between the observation point and the centroid of the object r equals 600 m. The calculated nondimensional frequency ka is fixed from 0 to 20 and the incident wave propagates along the z axis. The backscattered frequency data could be generated by employing the T-matrix method,[7] which was originally introduced by Waterman as a method for systematically solving the acoustic scattered problem of arbitrarily shaped targets with Neumann or Dirichlet boundary. Varadan *et al.*[8,19,20] extended the T-matrix method to the elastic wave scattering field first. The computational results are shown in Fig. 4. In Fig. 4(a), the backscattering cross

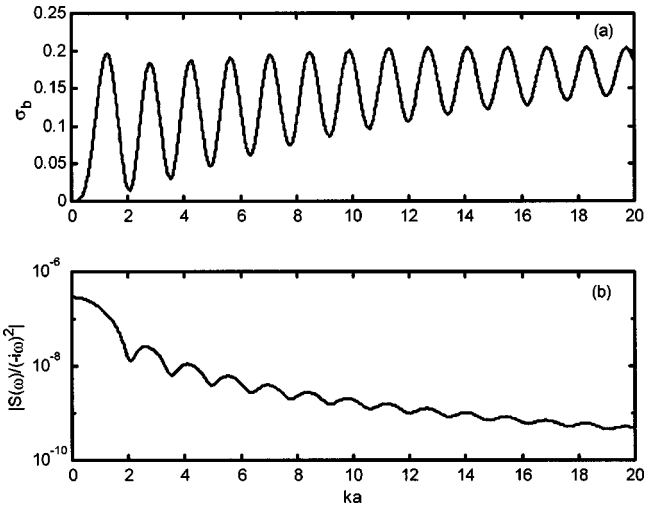

FIG. 4. The backscattering cross-section (a) and the backscattered frequency spectrum $S(\omega)$ weighted by $1/(-i\omega)^2$ (b) of the ellipsoid versus ka.

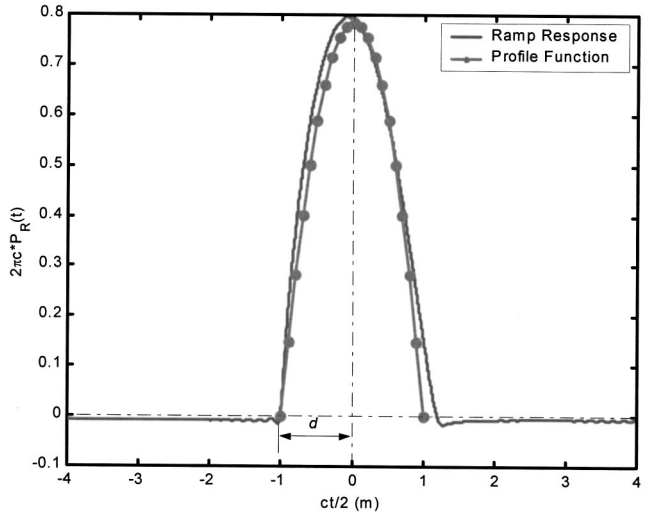

FIG. 5. The ramp response signatures and the exact profile function of the ellipsoid when the incident wave propagates along the z axis. The nondimensional frequency ka is from 0 to 20.

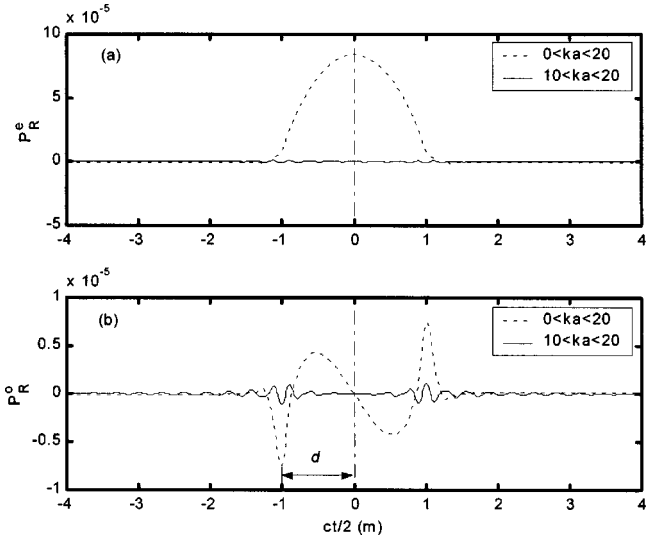

FIG. 6. The functions $P_R^e(t)$ and $P_R^o(t)$ of the ellipsoid when the incident wave propagates along the z axis with the nondimensional frequency $0<ka<20$ (dashed line) and $10<ka<20$ (solid line), respectively.

section for the acoustically hard ellipsoid is plotted as a function of ka. The backscattering cross-section curve fluctuated periodically. When ka increased, the amplitude of the fluctuation decreased. Figure 4(b) shows the amplitudes of backscattered frequency spectrum weighted by $1/(-i\omega)^2$ vs ka. For the purpose of convenience, the log scale was adopted to present the y axis. The amplitudes of $S(\omega)/(-i\omega)^2$ declined quickly, while ka increased. The amplitude at point $ka=0$ was more than 500 times the amplitude at point $ka=20$. Therefore, the values of $S(\omega)/(-i\omega)^2$ nearly vanished when ka increased to 20. Note the fact that the function $S(\omega)/(-i\omega)^2$ is used to compute the ramp response [see Eq. (4)]. Thus the vanishing of $S(\omega)/(-i\omega)^2$ means that $ka=20$ is large enough for our computation. For the underwater acoustic scattering problems in this paper, therefore, when nondimensional frequency ka is from 0 to 20, then it can be regarded as a full frequency domain. Correspondingly, if ka is from 10 to 20, it can be regarded as a high-frequency domain.

The ramp response signatures of the ellipsoid could be calculated and are shown in Fig. 5. Figure 5 showed that the ramp response signatures were very close to the exact profile function. Because of the existence of creeping waves needed to reach the shadow region, the ramp response deviated from the exact profile function as shown in Fig. 5. But the discrepancy was very small. This proves that the ramp response signatures include the size and shape information of the object, and can be used to reconstruct the image of the object, when three or more directions' ramp response data are known. The illuminated length d can be determined through the ramp response signatures (see Fig. 5). However, these conclusions could be made provided an accuracy ramp response can be obtained. Also accuracy ramp response signatures require the full backscattered information in the frequency domain. Unfortunately, in practice, only part of the backscattered frequency domain information can be obtained, especially the high-frequency data. Therefore, how to determine the illuminated length d is the key to solve practical inverse problems when only the high-frequency range data are available.

A method, which gives the illuminated length d from the ramp response signatures whether the backscattered frequency information is full or not, is presented below. This method is very convenient and powerful. First, recall Eq. (4):

$$\begin{aligned} P_R(t) &= \frac{1}{\pi}\int_{-\infty}^{+\infty} \frac{1}{-\omega^2}[S_r(\omega)\ \cos\ (\omega t) \\ &\quad + S_i(\omega)\ \sin\ (\omega t)]\ d\omega \\ &= \frac{1}{\pi}\int_{-\infty}^{+\infty} \frac{1}{-\omega^2} S_r(\omega)\ \cos\ (\omega t) d\omega \\ &\quad + \frac{1}{\pi}\int_{-\infty}^{+\infty} \frac{1}{-\omega^2} S_i(\omega)\ \sin(\omega t)\ d\omega \\ &= P_R^e(t) + P_R^o(t). \end{aligned} \tag{8}$$

In Eq. (8), the ramp response consists of two parts: $P_R^e(t)$ and $P_R^o(t)$. Note that function $P_R^e(t)$ is an even function of t while function $P_R^o(t)$ is an odd function of t. Figure 6 plots these functions $P_R^e(t)$ and $P_R^o(t)$ for the ellipsoid mentioned above, when the backscattered frequency data are obtained with different nondimensional frequency ranges.

In Fig. 6, the dashed line represents the signatures, which are calculated using the full frequency domain data while the solid line indicates the signatures, which are obtained only using the $10<ka<20$ frequency range data. When using the full frequency domain data to calculate the ramp response, the function $P_R^e(t)$ contained the shape information of the object while the function $P_R^o(t)$ contained the size information of the object. However, if only the high-frequency range data were used, $P_R^e(t)$ had no relation with the shape of the object, but $P_R^o(t)$ could still be used to determine the value of the illuminated length d, which is decided by the lowest point of the curve of function $P_R^o(t)$ in the illuminated region. Table I lists the calculated values of

TABLE I. A comparison between the exact values of illuminated length d and the calculated values for different ranges of frequency.

θ_i	Exact values $d_0(m)$	$ka=0-20$ $d(m)$	$ka=0-20$ E_d	$ka=0-10$ $d(m)$	$ka=0-10$ E_d	$ka=10-20$ $d(m)$	$ka=10-20$ E_d
0°	1.0000	1.0138	1.38%	1.0231	2.31%	1.0080	0.80%
10°	0.9886	1.0021	1.37%	1.0108	2.25%	0.9961	0.76%
15°	0.9746	0.9904	1.62%	0.9987	2.47%	0.9839	0.95%
20°	0.9551	0.9693	1.49%	0.9780	2.40%	0.9632	0.85%
30°	0.9014	0.9149	1.50%	0.9237	2.47%	0.9123	1.29%
40°	0.8307	0.8460	1.84%	0.8584	3.33%	0.8371	0.77%
50°	0.7483	0.7651	2.25%	0.7773	3.88%	0.7557	0.99%
60°	0.6614	0.6807	2.92%	0.6992	5.72%	0.6694	1.21%
70°	0.5812	0.6033	3.80%	0.6240	7.36%	0.5883	1.22%
75°	0.5479	0.5701	4.05%	0.5968	8.92%	0.5492	0.24%
80°	0.5221	0.5460	4.58%	0.5761	10.34%	0.5246	0.48%
90°	0.5000	0.5249	4.98%	0.5549	10.98%	0.5070	1.40%

illuminated length d using different ranges of frequency. Since the ellipsoid is a rotational and axial symmetric body, the illuminated length only depends on the axial angle θ_i of the incident wave direction, and $d(\theta_i)=d(180°-\theta_i)$. Therefore, we vary θ_i from 0° to 90°, and fix the azimuthal angle ϕ_i as 0° for convenience. For comparison, the exact values of illuminated length d are also listed in Table I.

In Table I, the error indicator E_d is defined as follows,

$$E_d=\frac{|d_0-d|}{d_0}\times 100\%, \tag{9}$$

where d_0 is the exact value of the illuminated length of the ellipsoid.

From Table I, it was found that if using the data of low-frequency range ($0<ka<10$) to determine the illuminated lengths d, the calculated relative errors were largest in the three kinds of cases for all different incident angles. The calculated results were closer to the exact values when only high frequency ($10<ka<20$) data were employed. The relative errors generated from full frequency data were larger than the results computed from the high-frequency data, although more frequency data were used in full frequency case. The main reason probably is that the illuminated length is not very sensitive to the low-frequency data, as the low-frequency data would lead to larger error when calculating the illustrated length d, which is known as the type II ill-posed problem. Therefore, high-frequency data are better to be used to identify the size of the object. However, the ramp response signatures become unstable in the high-frequency case, while the ramp response signatures are more robust in full frequency case (see Fig. 6).

V. RETRIEVAL OF THE SHAPE INFORMATION

Consider an ellipsoid S, whose expression is shown in Eq. (7). Suppose a plane L (shown in Fig. 3) has tangent with the ellipsoid S at point $A_0(x_0,y_0,z_0)$. Then the plane can be expressed as follows:

$$\frac{xx_0}{a^2}+\frac{yy_0}{b^2}+\frac{zz_0}{c^2}=1. \tag{10}$$

On the other hand, the tangent plane L normals to ψ_i, which has normal vector $(\sin\theta_i\cos\phi_i,\ \sin\theta_i\sin\phi_i,\ \cos\theta_i)^T$. And the distance between the origin point O and the plane is illuminated length d. Thus the plane L can also be expressed as

$$x\sin\theta_i\cos\phi_i+y\sin\theta_i\sin\phi_i+z\cos\theta_i-d=0. \tag{11}$$

Comparing the coefficients of Eqs. (10) and (11) yields

$$d^2=a^2\sin^2\theta_i\cos^2\phi_i+b^2\sin^2\theta_i\sin^2\phi_i+c^2\cos^2\theta_i. \tag{12}$$

Equation (12) indicates that if any three illuminated lengths, which are not of the same plane, are known, then the three semiaxes of the ellipsoid could be solved. In the other words, the shape of the ellipsoid could be determined. In matrix notation, Eq. (12) becomes

$$\mathbf{D}=C\mathbf{X} \tag{13}$$

where $\mathbf{D}$ represents $\mathbf{d}\cdot\mathbf{d}$, in which the symbol "$\cdot$" means scalar product and $\mathbf{d}=(d_1,d_2,d_3)^T$. Similarly, the vector $\mathbf{X}=\mathbf{x}\cdot\mathbf{x}$, in which $\mathbf{x}$ equals $(a,b,c)^T$ and the coefficient matrix C is

$$C=\begin{bmatrix}\sin^2\theta_{i1}\cos^2\phi_{i1} & \sin^2\theta_{i1}\sin^2\phi_{i1} & \cos^2\theta_{i1}\\ \sin^2\theta_{i2}\cos^2\phi_{i2} & \sin^2\theta_{i2}\sin^2\phi_{i2} & \cos^2\theta_{i2}\\ \sin^2\theta_{i3}\cos^2\phi_{i3} & \sin^2\theta_{i3}\sin^2\phi_{i3} & \cos^2\theta_{i3}\end{bmatrix}, \tag{14}$$

where the suffixes $i1$, $i2$, $i3$ denote the three known incident directions.

As an error may exist in the illuminated length vector $\mathbf{d}$ obtained using the ramp response technique, the calculated values of the vector $\mathbf{x}$ will also contain an error. For the purpose of qualitatively investigating the effects of error, we introduce the condition number of a matrix. The condition number of the coefficient matrix C is defined as

$$\mathrm{cond}(C)=\|C\|\|C^{-1}\|, \tag{15}$$

where $\|\cdot\|$ represents the given norm. In this paper, we employ the two-norm. According to the definition of the condition number, $\mathrm{cond}(C)$ must not be less than 1. Assuming an error $\delta\mathbf{D}$ exists in vector $\mathbf{D}$, it must produce an error $\delta\mathbf{X}$ in vector $\mathbf{X}$ when solving Eq. (13). In view of the properties of the norm, an inequality can be proven:[21]

$$\frac{\|\delta\mathbf{X}\|}{\|\mathbf{X}\|}\leqslant\mathrm{cond}(C)\frac{\|\delta\mathbf{D}\|}{\|\mathbf{D}\|}. \tag{16}$$

Obviously, the inequality gives us a relative error upper limit of the vector $\mathbf{X}$ when the vector $\mathbf{D}$ has an estimated error. Suppose there is no rounding error during the solving procedure. In the inequality (16), the condition number plays a role of amplification coefficient of the relative error in vector $\mathbf{D}$. Although the relative errors in vector $\mathbf{D}$ are very small (see Table I), the error in vector $\mathbf{X}$ probably may be very large. In other words, very small relative error in $\mathbf{D}$ may produce large relative errors in $\mathbf{X}$. In this case, the problem of solving Eq. (13) is ill-posed.[17]

TABLE II. Calculated three semiaxes of the ellipsoid when the incident directions are close at the longer and shorter semiaxis ends.

	$\theta_i=(0°,10°,15°)$			$\theta_i=(75°,80°,90°)$		
ϕ_i	$\mathbf{x}(m)$	E_x	cond(C)	$\mathbf{x}(m)$	E_x	cond(C)
(0°,0°,5°)	0.4745,3.1629,1.0080	217.44%	8.9154e+3	0.5036,0.8428,0.9853	28.01%	4.9104e+2
(0°,0°,10°)	0.4745,1.6397,1.0080	93.08%	2.1951e+3	0.5036,0.6071,0.9853	8.84%	1.3062e+2
(0°,0°,15°)	0.4745,1.1550,1.0080	53.53%	9.5232e+2	0.5036,0.5526,0.9853	4.47%	7.5560e+1
(0°,0°,30°)	0.4745,0.7227,1.0080	18.31%	2.1608e+2	0.5036,0.5172,0.9853	1.87%	5.7242e+1
(0°,0°,45°)	0.4745,0.6113,1.0080	9.35%	9.6521e+1	0.5036,0.5104,0.9853	1.50%	5.3069e+1
(0°,0°,60°)	0.4745,0.5694,1.0080	6.07%	7.7638e+1	0.5036,0.5081,0.9853	1.41%	5.0490e+1
(0°,0°,90°)	0.4745,0.5472,1.0080	4.43%	7.7459e+1	0.5036,0.5070,0.9853	1.36%	4.9296e+1

VI. NUMERICAL EXAMPLES

From Sec. IV, it was found that only using the high-frequency data to compute the illuminated length, the calculated results had smaller errors and could be very close to the exact values. Thus, in later discussion, the high-frequency range data are used to compute the illuminated lengths. The nondimensional frequency range is set to be from 10 to 20. The parameters of the ellipsoid are the same as above. The calculated illumination lengths are listed in Table I.

A. Three waves with orthogonal directions

If the directions of three incident waves are orthogonal with each other, then the three illuminated lengths in these directions must satisfy the following relationship,

$$d_1^2+d_2^2+d_3^2=a^2+b^2+c^2, \tag{17}$$

where the d_i $(i=1,2,3)$ are the three arbitrary orthogonal direction illuminated lengths. The a, b, c represent the three semiaxes of the ellipsoid, which are the calculated results. As the relative error of the illuminated lengths is very low, the relative errors of a, b, c are also very low. Consider now a special example. When the axial angles $\theta_i=(10°,100°,90°)$ and the azimuthal angles $\phi_i=(10°,10°,100°)$, then the three incident directions are orthogonal with each other. The corresponding calculated illuminated lengths can be found in Table I, which are (0.9961, 0.5246, 0.5070). Through solving Eq. (13), the calculated results are (0.5020, 0.5072, 1.0076), which are very close to the exact values (0.5, 0.5, 1.0). In this case, cond(C) of the coefficient matrix is 1.0978, which is very close to 1. It indicates the relative error upper limits of the solutions $\mathbf{X}$ are very close to the relative errors of the vector $\mathbf{D}$, which are very low as shown in Table I. Therefore, for the case of three incident waves of three orthogonal directions, the calculated results of the three semiaxes of the ellipsoid are very accurate.

B. Three waves with close directions

However, in practice, it is hard to obtain the backscattered frequency data of an object from three orthogonal incident directions, especially for cases like buried objects or large objects. In these cases, the backscattered frequency data, which could be measured, will have close incident directions. This indicates that the calculated illuminated lengths also have close directions. Similarly, three illuminated lengths can be used to calculate the three semiaxes of the ellipsoid. For the purpose of convenient analysis, the relative errors index of the calculated results E_x is defined as follows,

$$E_x=\frac{\|\mathbf{x}-\mathbf{x}_0\|}{\|\mathbf{x}_0\|}\times 100\%, \tag{18}$$

where $\mathbf{x}_0$ is the exact value (0.5, 0.5, 1.0). For satisfying the general engineering requirement, the maximum tolerant relative error E_x is defined to be within 10%.

When three close incident directions of waves are chosen on both the longer semiaxis end and shorter semiaxis end, respectively, the calculated results are listed in Table II. In Table II, the three axial angles of the incident waves are fixed at the longer $(\theta_i=0°,10°,15°)$ and shorter $(\theta_i=75°,80°,90°)$ semiaxis ends. One of azimuthal angles varies from 5° to 90°. The relative errors E_x and condition numbers of the coefficient matrices for each case are also listed in Table II. From Table II, when the three incident angles were very close, the calculated results were bad, especially when the incident waves focus on the longer semiaxis end. The condition numbers were very large in these cases. However, when one of the azimuthal angles ϕ_i became bigger, the calculated results improved and the values of condition number decreased for both the longer semiaxis end case and the shorter semiaxis end case. Comparing the longer semiaxis end with the shorter semiaxis end case, the results of the shorter semiaxis end case were closer to the exact values and the condition numbers were smaller. The above analysis suggests that if we want to obtain results of three semiaxes with low relative errors E_x, we need to enlarge the difference among the three incident angles, for example fixing the axial angles and enlarging one of the azimuthal angles, which are shown above. Or we could let the incident waves close to the shorter semiaxis end of the ellipsoid. Then the calculated results will have much improvement and the relative errors will decrease rapidly. During the discussion, the condition number played an important role and was used as an indicator, which showed whether the calculated results were good or not. In addition, in Table II, two of three calculated semiaxes were the same just because two of three azimuthal angles were fixed as zeros. These kinds of treatments would not affect validity of the conclusions, which were obtained above.

TABLE III. Calculated three semiaxes of the ellipsoid employing the least-squares method for solving the overdetermined problem, which uses four incident directions data and the four incident directions focus on the longer semiaxis end.

	$\theta_i=[0°,10°,15°,20°]$		
ϕ_i	$\mathbf{x}(m)$	E_x	cond(C)
[0°,0°,5°,0°]	0.5132,2.4328,1.0078	157.82%	4.3722e+3
[0°,0°,10°,0°]	0.5132,1.2992,1.0078	65.27%	1.0984e+3
[0°,0°,15°,0°]	0.5132,0.9512,1.0078	36.86%	4.9240e+2
[0°,0°,30°,0°]	0.5132,0.6597,1.0078	13.10%	1.3031e+2
[0°,0°,45°,0°]	0.5132,0.5910,1.0078	7.54%	6.5557e+1
[0°,0°,60°,0°]	0.5132,0.5663,1.0078	5.56%	4.5452e+1

TABLE IV. Calculated three semiaxes of the ellipsoid employing the least-squares method for solving the overdetermined problem, which uses five incident directions data and the five incident directions focus on the longer semiaxis end.

	$\theta_i=[0°,10°,15°,20°,20°]$		
ϕ_i	$\mathbf{x}(m)$	E_x	cond(C)
[0°,0°,5°,0°,5°]	0.5084,1.3411,1.0080	68.68%	3.0535e+3
[0°,0°,10°,0°,10°]	0.5084,0.8040,1.0080	24.84%	7.5987e+2
[0°,0°,15°,0°,15°]	0.5084,0.6581,1.0080	12.95%	3.3552e+2
[0°,0°,30°,0°,30°]	0.5084,0.5525,1.0080	4.37%	8.2865e+1
[0°,0°,45°,0°,45°]	0.5084,0.5310,1.0080	2.70%	3.8660e+1

C. More than three waves of close directions

From Table II, for the incident waves focused on the shorter semiaxis end case, the calculated results rapidly converged to the exact values when the difference of azimuthal angles increased. If choosing the azimuthal angles $\phi_i=(0°,0°,10°)$, the calculated results $\mathbf{x}$ were good enough and the relative error E_x was 8.84%. However, when the incident waves are located at the longer semiaxes end, the calculated results became very bad. When the three incident directions were very close, such as the azimuthal angles $\phi_i=(0°,0°,5°)$, the relative error E_x of the vector $\mathbf{x}$ was 217.44% (see Table II). In order to reduce the relative error in the solution, the differences in azimuthal angles had to be enlarged. When the azimuthal angles ϕ_i increased to (0°,0°,45°), the relative errors decreased to 9.35%. Nevertheless, due to some practical difficulties mentioned above, it is hard to enlarge the difference among the incident angles. In this situation, an alternative way to get good calculated results with low relative errors is adding the number of incident waves.

When more than three illuminated lengths are used to solve Eq. (13) to obtain the three semiaxes of ellipsoid, this kind of inverse problem becomes overdetermined. Since the system $\mathbf{D}=C\mathbf{X}$ is overdetermined, it cannot generally be satisfied exactly, and there are many possible ways of defining the ''best'' solution in an optimization sense. In this paper, the least-squares method is employed to solve the overdetermined problem, which has the minimum Euclidean length of the residual vector $\mathbf{r}$. It can be proven that the least-squares solution satisfies the normal equations[21]

$$(C^TC)\mathbf{X}=C^T\mathbf{D}, \tag{19}$$

where the superscript ''T'' denotes transpose.

Therefore, the least-squares solution can be easily obtained through solving the normal equations (19). For illustrating the validity of the least-squares method, the four, five, and six incident direction cases are calculated, respectively. The calculated results are listed in Tables III–V.

Comparing Tables III–V with Table II, for the similar incident angles cases, the calculated results were closer to the exact values (0.5, 0.5, 1.0) when using more than three incident directions' data to solve the problem. Moreover, the calculated results in the five incident directions case had less relative errors E_x than those in four incident directions case, while the calculated results in the six incident directions case were more accurate than those in the five incident directions case. These findings indicate that the more incident directions' data are used to solve this inverse problem, the better the results that can be obtained. Meanwhile, the condition numbers of the coefficient matrices C became smaller for the corresponding incident direction cases, when the number of incident waves varied from 3 to 5. However, when the number of incident waves changed from 5 to 6, the condition numbers increased a little, although the calculated results became better. This indicates the condition number is not an absolute criterion to judge which result is better, because it only gives the relative error upper limit. Thus it just gives us a possibility. In order to satisfy the engineering requirement, for four incident directions case, the incident azimuthal angles ϕ_i were equal to (0°,0°,45°,0°) at least, whose relative error was 7.54%. For the five incident directions case, the incident azimuthal angles ϕ_i were equal to (0°,0°,30°,0°,30°), whose relative error E_x was 4.39%. For the six incident directions case, that the incident azimuthal angles ϕ_i were equal to (0°,0°,10°,0°,0°,10°) was enough, and its relative error E_x was 7.70%. These show that it is very effective using more incident waves method to obtain more accurate results, when the directions of the incident waves are limited in a very small range.

In Fig. 3, the illuminated length vector intersects the surface of the ellipsoid at point A_1. When using several illuminated lengths to determine the shape of the ellipsoid that are shown above, then there are several points of intersection A_1^n ($n=1,2,3,\ldots$). Link these points on the surface of the ellipsoid and unfurl the 3-D surface as a plane. The illustration about how to unfurl the surface of the ellipsoid to a plane has been shown in Fig. 7(a). As the ellipsoidal surface cannot be unfurled exactly to a plane without any destruction

TABLE V. Calculated three semiaxes of the ellipsoid employing the least-squares method for solving the overdetermined problem, which uses six incident directions data and the six incident directions focus on the longer semiaxis end.

	$\theta_i=[0°,10°,15°,20°,15°,20°]$		
ϕ_i	$\mathbf{x}(m)$	E_x	cond(C)
[0°,0°,5°,0°,0°,5°]	0.5139,0.7818,1.0082	23.04%	3.1285e+3
[0°,0°,10°,0°,0°,10°]	0.5139,0.5929,1.0082	7.70%	7.7871e+2
[0°,0°,15°,0°,0°,15°]	0.5139,0.5508,1.0082	4.35%	3.4401e+2
[0°,0°,20°,0°,0°,20°]	0.5139,0.5353,1.0082	3.17%	1.9237e+2
[0°,0°,30°,0°,0°,30°]	0.5139,0.5240,1.0082	2.36%	8.5320e+1

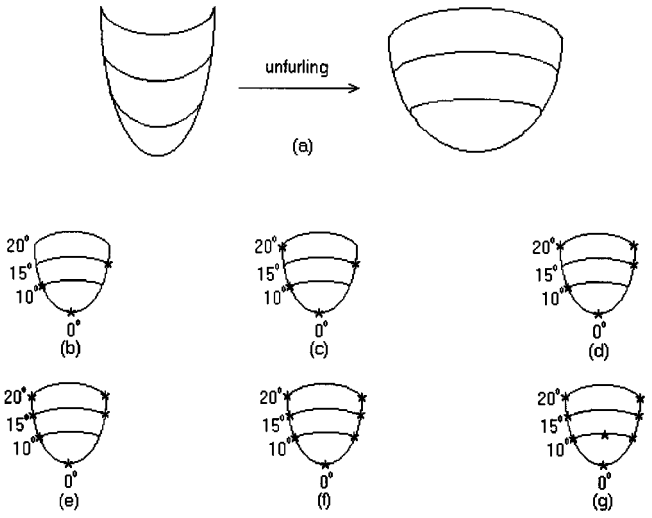

FIG. 7. A sketch of the intersectional distribution on surface of the ellipsoid, where the symbol "*" denotes the point of intersection: (a) the illustration of unfurling, (b) three incident directions case, (c) four incident directions case, (d) five incident directions case, (e) six incident directions case, (f) seven incident directions case, and (g) eight incident directions case.

of the 3-D surface, the unfurling process in this paper is not very precise and its main purpose here is to show the distribution of the intersections roughly. The unfurling figures are shown in Figs. 7(b)–(g).

In Figs. 7(b)–(g), the axial angles are set as 0°, 10°, 15°, 20°, which are labeled in the figure. The 3–6 incident directions cases were computed above, which are shown in Figs. 7(b)–(e), respectively. If using seven incident waves to identify the shape of the ellipsoid, whose points of intersection are shown in Fig. 7(f), then these seven points of intersection symmetrically locate on the surface of the rotational symmetry ellipsoid. In this situation, the calculated results do not depend on the azimuthal angles of the incident waves. The calculated results for the seven directions case are shown in Table VI.

In Table VI, for any azimuthal angles of the incident waves case, as long as these incident waves were symmetrical for the ellipsoid, the calculated results were the same and the relative errors all were 2.27%. The condition numbers still became smaller, when the difference of the azimuthal angles increased, although the calculated results had no change. When using seven incident waves data to identify the shape of ellipsoid, the calculated results **x** were (0.5188, 0.5188, 1.0080), which are very close to the exact values. Therefore, the shape information can be retrieved even when these incident directions are very close, if using enough incident waves data.

TABLE VI. Calculated three semiaxes of the ellipsoid employing the least-squares method for solving the overdetermined problem, which uses seven incident directions data and the seven incident directions focus on the longer semiaxis end.

	$\theta_i=[0°,10°,15°,20°,10°,15°,20°]$		
ϕ_i	$\mathbf{x}(m)$	E_x	cond(C)
[0°,0°,5°,0°,5°,0°,5°]	0.5188,0.5188,1.0080	2.27%	3.3450e+3
[0°,0°,10°,0°,10°,0°,10°]	0.5188,0.5188,1.0080	2.27%	8.3342e+2
[0°,0°,15°,0°,15°,0°,15°]	0.5188,0.5188,1.0080	2.27%	3.6876e+2
[0°,0°,30°,0°,30°,0°,30°]	0.5188,0.5188,1.0080	2.27%	9.2081e+2
[0°,0°,60°,0°,60°,0°,60°]	0.5188,0.5188,1.0080	2.27%	3.1646e+1
[0°,0°,90°,0°,90°,0°,90°]	0.5188,0.5188,1.0080	2.27%	3.0271e+1

VII. CONCLUSIONS

In this paper, a method was addressed to identify the shape information of underwater objects using the finite number of illuminated lengths and waves with very close incident angles. Some useful conclusions were obtained, which are listed as follows:

(1) The function P_R^e was essential to the shape of the object only for the full frequency domain, while the function P_R^o could be used to identify the size information of the object and to calculate the illuminated length in any incident direction whether using the full frequency domain data or only the high-frequency-range data to calculate the ramp response signatures. Moreover, using the function P_R^o to determine the illuminated lengths, the calculated results, which were obtained for the high-frequency-range data, were better than those which were computed for the low-frequency-range data or full frequency domain data.
(2) In theory, only three illuminated lengths can determine the shape of an ellipsoid. As some calculated errors exist in the illuminated lengths, the calculated results of the three semiaxes of the ellipsoid also have errors. The inequality about relative error upper limit was presented, which has a direct relation with the condition number of the coefficient matrix. Therefore, the condition number could be used as an indicator, which shows whether the relative errors in the calculated results are big or not.
(3) For the three orthogonal incident waves, the calculated results had very small errors. However, when the three incident waves directions became close, the calculated results deteriorated unacceptably. In order to avoid the large relative errors in the calculated results, we could enlarge the difference of the three incident waves directions or use more than three incident wave directions data to identify the shape of the ellipsoid, which becomes an overdetermined inverse problem. For solving the overdetermined problem, the least-squares method was employed. The calculated results were satisfying.

The shape identification method for underwater rigid objects, which could be modeled as an ellipsoid, was discussed in this paper. When the method is employed to identify object size, the orientation of object is assumed to be known. Based on this assumption, this identifying problem becomes a linear problem. We need to solve Eqs. (13) or (19) to obtain the solutions of this inverse problem. In practice, however, sometimes we cannot know the orientation of an object in advance. Without the preknowledge of the orientation of an object, the inverse problem becomes a quadratic nonlinear problem. Therefore, how to solve this quadratic nonlinear problem is a challenge and further work will be necessary.

ACKNOWLEDGMENTS

The work received support from the National University of Singapore, Singapore, and Institute of High Performance Computing, Singapore. We greatly appreciate the valuable comments provided by the reviewers.

[1] R. D. Spence and S. Granger, ''The scattering of sound from a prolate spheroid,'' J. Acoust. Soc. Am. **23**, 701–706 (1951).
[2] M. Furusawa, ''Prolate spheroidal models for predicting general trends of fish target strength,'' J. Acoust. Soc. Jpn. **9**, 13–24 (1988).
[3] E. W. Montroll and R. W. Hart, ''Scattering of plane waves by soft obstacles. II. Scattering by cylinders, spheroidals, and disks,'' J. Appl. Phys. **22**, 1278–1289 (1951).
[4] H. A. Schenck, ''Improved integral formation for acoustic radiation problems,'' J. Acoust. Soc. Am. **44**, 41–58 (1968).
[5] M. C. Junger, ''Scattering by slender bodies of revolution,'' J. Acoust. Soc. Am. **72**, 1954–1956 (1982).
[6] M. Ochmann, ''The null-field equations for acoustic radiation and scattering,'' J. Acoust. Soc. Am. **105**, 2574–2584 (1999).
[7] P. C. Waterman, ''New formulation of acoustic scattering,'' J. Acoust. Soc. Am. **45**, 1417–1429 (1969).
[8] V. V. Varadan and V. K. Varadan, ''Scattering matrix for elastic wave. III. Application to spheroids,'' J. Acoust. Soc. Am. **65**, 896–905 (1979).
[9] E. M. Kennaugh and R. L. Cosgriff, ''The use of impulse response in electromagnetic scattering problems,'' in IRE Nat. Conv. Rec., Part 1 (1958).
[10] B. Y. Foo, S. K. Chaudhuri, and W. M. Boerner, ''Polarization correction and extension of the Kennaugh-Cosgriff target-ramp response equation to the Bistatic case and application to electromagnetic inverse scattering,'' IEEE Trans. Antennas Propag. **38**, 964–972 (1990).
[11] C. C. Chen and L. Peters, Jr., ''Ramp response signatures for UXOs,'' in *Geoscience and Remote Sensing Symposium, 2000. Proceedings IGARSS 2000. IEEE 2000 International* (2000), Vol. 4, pp. 1436–1438.
[12] S. Nag and L. Peters, Jr., ''Ramp response signatures of dielectric targets, especially land mines,'' in *Geoscience and Remote Sensing Symposium Proceedings 1998. IGARSS'98 IEEE 1998 International* (1998), Vol. 1, pp. 213–215.
[13] S. Nag and L. Peters, Jr., ''Ramp response signatures for dielectric targets,'' in *Proceedings of SPIE on Detection and Remediation Technologies for Mines and Minelike Targets III* (1998), pp. 703–713.
[14] S. J. J. Tsao, ''Image reconstruction using ramp response signatures,'' Ph.D. dissertation, The Pennsylvania State Univ., The Graduate School Department of Engineering Science and Mechanics (1985), pp. 53–57.
[15] X. M. Zhang, W. Li, and G. R. Liu, ''A new technique in ramp response for acoustic imaging of underwater objects,'' Appl. Acoust. **63**, 453–465 (2002).
[16] X. M. Zhang, W. Li, C. Cai, K. C. Hung, and G. R. Liu, ''Acoustic imaging of underwater objects using ramp response techniques,'' Naval Platform Technology Seminar, Singapore, 10 May 2001.
[17] G. R. Liu and X. Han, *Computational Inverse Techniques in Nondestructive Evaluation* (CRC, Boca Raton, FL, 2003).
[18] V. V. Varadan, Y. Ma, V. K. Varadan, and A. Lakhtakia, ''Scattering of waves by spheres and cylinders,'' in *Field Representations and Introduction to Scattering*, edited by V. V. Varadan, A. Lakhtakia, and V. K. Varadan (Elsevier Science, North-Holland, 1991), pp. 211–273.
[19] V. Varatharajulu and Y.-H. Pao, ''Scattering matrix for elastic wave. I. Theory,'' J. Acoust. Soc. Am. **60**, 556–566 (1976).
[20] J.-H. Su, V. V. Varadan, V. K. Varadan, and L. Flax, ''Acoustic wave scattering by a finite elastic cylinder in water,'' J. Acoust. Soc. Am. **68**, 686–691 (1980).
[21] G. Dahlquist and Å. Björck, *Numerical Methods*, translated by N. Anderson (Prentice–Hall, Englewood Cliffs, NJ, 1974).

Resolution enhancement and separation of reverberation from target echo with the time reversal operator decomposition

Thomas Folégot[a)]
Atlantide, Technopôle Brest-Iroise, BP 80802, 29608 Brest Cedex, France

Claire Prada and Mathias Fink
Laboratoire Ondes et Acoustique, ESPCI, 10, rue Vauquelin, 75005 Paris, France

(Received 2 May 2002; revised 13 February 2003; accepted 24 February 2003)

Time reversal operator (TRO) decompositions are performed in a model of an ocean wave guide containing a target and having different kinds of bottom. The objective is to study the effects of bottom reverberation and absorption by means of ultrasonic experiments. It is shown experimentally that the echo from a target can be separated from the bottom reverberation. Reverberation eigenvectors are back propagated in the wave guide leading to focus on the bottom. An amplitude correction is applied to both reverberation and signal eigenvectors to compensate for bottom absorption and thus to improve target resolution. © *2003 Acoustical Society of America.* [DOI: 10.1121/1.1571541]

PACS numbers: 43.30.Gv, 43.30.Hw, 43.30.Vh [RS]

I. INTRODUCTION

Time reversal techniques have been demonstrated in ultrasonics[1] and underwater acoustics environments.[2–4] A technique resulting from the analysis of the iterative time reversal process[5] has been developed: the DORT (French acronym for ''Decomposition of the Time Reversal Operator'') method is a scattering analysis technique using a source receiver array (SRA).[6,7] This technique shares some of the principles used in eigenvector decomposition techniques for passive source detection.[8,9] These latter techniques however, assume statistically uncorrelated sources and require the averaging of the measured data, whereas the time reversal operator (TRO) decomposition is an active and deterministic method. It was applied to achieve multitarget detection and selective focusing on point like scatterers through heterogeneous media and specifically in an ideal water wave guide with a perfectly rigid bottom. Taking advantage of the multiple reflection at the wave-guide interfaces, the method allows a large improvement in spatial resolution. The super resolution is used to separate the signal coming from close scatterers and then to focus a wave field at any one of them.[10] This procedure has also been simulated in a Pekeris wave guide.[11–13] More recently, Lingevitch *et al.*[14] showed, by a numerical study, that the method can be applied to reverberation signals in order to achieve focusing on the bottom of the wave guide and thus to increase the focused signal level.

The objective of this paper is to describe the consequences of losses and reverberation in the medium, and to show how these effects can be overcome. Thus, three increasingly complex kinds of horizontal bottoms are used in the experiments to reach a more realistic model of an ocean wave guide than the previous ideal configuration (Fig. 1). The first is a steel bottom interface, which induces neither losses nor reverberation and has a very high critical angle. The second is a horizontal Plexiglas plate, which induces absorption and has a low critical angle. Finally, a steel plate covered with a continuous sandy layer is used as the third kind of bottom, which induce reverberation.

The DORT method is first applied to the detection of the targets in presence of bottom absorption, which breaks the time reversal invariance. An amplitude compensation technique is proposed in order to increase the signal to noise ratio at the target while back-propagating the eigenvectors. The benefits of this method, in terms of resolution and signal to noise ratio are evaluated with ultrasonic shallow water experiments.

The effect of noise and reverberation is then studied in the realistic sandy wave-guide model. New eigenvalues appear and their physical meaning is analyzed. After amplitude compensation, the corresponding eigenvector is used in the experiment to focus back on the bottom.

II. GENERALIZED FORMULATION OF TRO DECOMPOSITION

The acoustic configuration consists of a number of targets and a vertical SRA of N transducers in a time invariant medium. Authors[6,7,10,11,14] usually construct the TRO by the direct measurement of the interelement impulse functions $k_{i,j}(t)$ and then Fourier transform these functions to provide the array response matrix $\mathbf{K}(\omega)$. In fact, as already shown by Lingevitch,[14] a more general method consists in emitting signals at the same time by the whole transducers set. It increases up to N times the source level of the system. $\mathbf{K}(\omega)$ can then be measured with any chosen orthogonal family of N signals $\mathbf{E_H}(\omega)$ defined by

$$\sum_{m=1,N} E_{i,m}(\omega)E_{j,m}(\omega)=\delta_{i,j}, \quad 1\leqslant i,j\leqslant N, \tag{1}$$

$\mathbf{R}(\omega)=\mathbf{K}(\omega)\mathbf{E_H}(\omega)$ is a measure of the transfer matrix in the same basis as previously but using another basis of emission. The knowledge of $\mathbf{R}(\omega)$ gives $\mathbf{K}(\omega)=\mathbf{R}(\omega)\mathbf{E_H}(\omega)^{-1}$.

a)Electronic mail: thomas.folegot@ago.fr

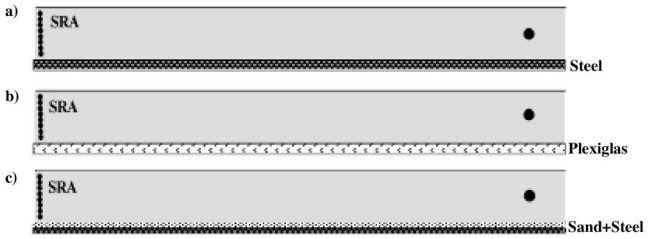

FIG. 1. Three kinds of bottom used for the ultrasonic experiments: (a) Perfectly rigid steel bottom, (b) absorbing Plexiglas bottom, and (c) absorbing and reverberating sand on steel bottom.

To reduce acquisition time and data size, only a subset of M vectors of $\mathbf{E_H}(\omega)$ need be used. As long as M remains much larger than the number of targets in the medium, $\mathbf{R}(\omega)$ provides a good approximation of $\mathbf{K}(\omega)$. The TRO was defined as $\mathbf{K}^{\dagger}(\omega)\cdot\mathbf{K}(\omega)$[6], where $[\ ]^{\dagger}$ denotes the complex conjugate transpose. It is a Hermitian matrix which is diagonalizable at all frequencies.[5,6] Nevertheless, in practice, it is convenient to calculate the singular value decomposition of the transfer matrix, possibly after matched filtering,

$$\mathbf{K}(\omega)=\mathbf{U}(\omega)\mathbf{S}(\omega)\mathbf{V}^{\dagger}(\omega). \tag{2}$$

$\mathbf{S}(\omega)$ is a real diagonal matrix of the singular values, and $\mathbf{U}(\omega)$ and $\mathbf{V}(\omega)$ are unitary matrices. The eigenvalues λ_i of the TRO are the squares of the singular values of $\mathbf{K}(\omega)$ and the eigenvectors are the columns of $\mathbf{V}(\omega)$. At this stage, we notice that if $\mathbf{E_H}(\omega)=E(\omega)\mathbf{I}$, [where $E(\omega)$ is the Fourier transform of the emitted signal and $\mathbf{I}$ is a unitary matrix] the SVD of $\mathbf{K}(\omega)$ is simply related to the SVD of $\mathbf{R}(\omega)$. In this paper, we assume that the target behaves as a discontinuity of compressibility. In this case, the number of ''nonzero'' eigenvalues is exactly the number of independent secondary sources given by the resolved scatterers present in the medium.[7] Eigenvectors are calculated in the time domain using an inverse Fourier transform, as described in Ref. 10.

III. EFFECT OF ABSORPTION

A. Theoretical approach

Let us consider the general ray-based formulation of the time dependent Green function between transducer i and the position of a single pointlike scatterer after multipath propagation (the response of the transducer i is not taken into account):

$$G_i(t)=\sum_r L_{r,i}\delta(t-\tau_{r,i}), \quad -1\leqslant L_{r,i}\leqslant 1, \tag{3}$$

where $\delta(t)$ is equal to 1 at $t=0$ and is zero otherwise, $|L_{r,i}|$ is the loss of the rth arrival received by the ith transducer due to reflections and containing the effect of geometric spreading, and $\tau_{r,i}$ its time delay. Each nonzero temporal eigenvector $V(t)=\{V_i(t)\}_{i=1,N}$ of the TRO has the same multipath structure as $G_i(t)$ and can be written with the same convention as

$$V_i(t)=\sum_r L_{r,i}E\,\delta(t+\tau_{r,i}),$$

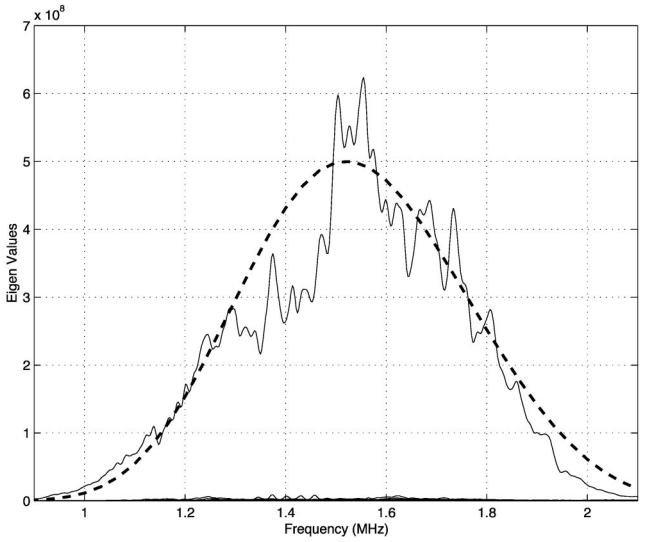

FIG. 2. Experimental evolution of TRO eigenvalues in a rigid wave guide between 1 to 2 MHz. The dotted line represents the frequency response of the system.

where E is the maximum level supported by each source. The pressure at focus location and at focus time $(t=0)$ obtained while transmitting $V(t)$ in the medium is

$$p_f(t=0)=\left(\sum_{i=1,N} G_i(t)\otimes V_i(t)\right)_{t=0}=\sum_{i=1,N}\sum_r L_{r,i}^2E. \tag{4}$$

The time reversal process is affected by losses in the medium and especially at the interfaces. Thus, the losses at each reflection[15] result in an apodization of the virtual array given by the image theory.[1] Consequently, both vertical and horizontal resolutions are degraded.

Tanter *et al.*[16] proposed an amplitude compensation technique in the space domain for attenuated signals through the skull. In their case, only diffraction and absorption affected the propagation. Therefore, the compensation was performed at once for the entire signal received on each transducer. In our case of multipath propagation in a wave guide, the losses affect each arrival differently depending on the number of reflections. Thus, a specific technique has been developed in order to compensate strictly for this effect. In practice, the maximum level supported by each source is $\mathbf{E}$. Therefore, each component $V_i(t)$ of the eigenvector has to be transformed into $\tilde{V}_i(t)$ by multiplying each arrival r by $\min_r(L_{r,i})/L_{r,i}^2$,

$$\tilde{V}_i(t)=\sum_r \frac{\min_r(L_{r,i})}{L_{r,i}}E\,\delta(\tau_{r,i}+t).$$

This transformation provides a uniform amplitude wavefront near the focus, and as a consequence, better time compression and lower side lobes. In this case, the pressure at the focus and at time zero is

$$\tilde{p}_f(t=0)=\left(\sum_{i=1,N} G_i(t)\otimes\tilde{V}_i(t)\right)_{t=0}$$

$$=\sum_{i=1,N}\sum_r \min(L_{r,i})E. \tag{5}$$

Therefore, the signal level at the focus will be very low because of the addition of the environmental losses. The best way to maximize $p_f(t=0)$ in order to maximize the signal to noise ratio at the target location is to normalize the amplitude of each arrival to **E**,

$$\tilde{\tilde{V}}_i(t)=\sum_r E\,\delta(\tau_{r,i}+t).$$

One effect is to minimize virtual array apodization. In this case, the pressure at the focus is

$$\tilde{\tilde{p}}_f(t=0)=\left(\sum_{i=1,N} G_i(t)\otimes\tilde{\tilde{V}}_i(t)\right)_{t=0}=\sum_{i=1,N}\sum_r L_{r,i}E. \tag{6}$$

The pressure is maximized despite higher side lobes. The expected gain is closely related to both the number of array elements and the number of arrivals. In the following sections, we show experimentally the impact of this last weighting technique in comparison with the formal TRO eigenvectors.

In practice, separating the arrivals is not easy. Therefore, after matched filter processing, the envelope of each signal $\mathbf{V}_i(t)$ is calculated. Wave packets above a given threshold are isolated and normalized individually. As a consequence, most of the noise is not increased and the technique guarantees better resolution and better signal to noise ratio.

B. Experimental results

The results we present concern ultrasonic experiments within a water tank in the ultrasonic domain. The 40-element SRA has a 1.5 MHz central frequency and the array pitch is equal to 0.58 mm. For $F \gg D$, where F is the range and D the array aperture, the vertical and horizontal resolutions[15] in free space are $\Re_z \approx \lambda(F/D)$ and $\Re_x \approx 7\lambda(F/D)^2$. The configuration in the experiment gives $\Re_z \approx 14\lambda$.

Two different kinds of bottom are compared [Figs. 1(a) and (b)]. In both cases, the water depth is 27 mm and a single target (a wire of 0.04λ diameter, where λ is the wavelength) is placed in the water column at 330 mm range. For bottom (a), the lower boundary is a water/steel plane interface. The critical angle is very high and the losses of reflected arrivals are due to scattering and diffraction. Bottom (b) is a Plexiglas plate. Only a few bottom-reflected arrivals are above electronic noise because of a low critical angle and the large absorption.

The time reversal operator is measured and decomposed for bottom (a) and (b). In both cases, the first nonzero eigenvalue corresponds to the single target in the water column (Figs. 2 and 3). The temporal eigenvector obtained by an inverse Fourier transform is shown for each kind of bottom in Figs. 4 and 5. Indeed, it presents a series of resolved arrivals and one late unresolved arrival resulting from the interference between the direct rays and the lowest surface bottom reflected rays. The time dispersion of the eigenvectors depends on the absorption as well as on the number of resolved arrivals.

For bottom (a), the high critical angle of steel allows a large number of attenuated arrivals. Attenuation is due to

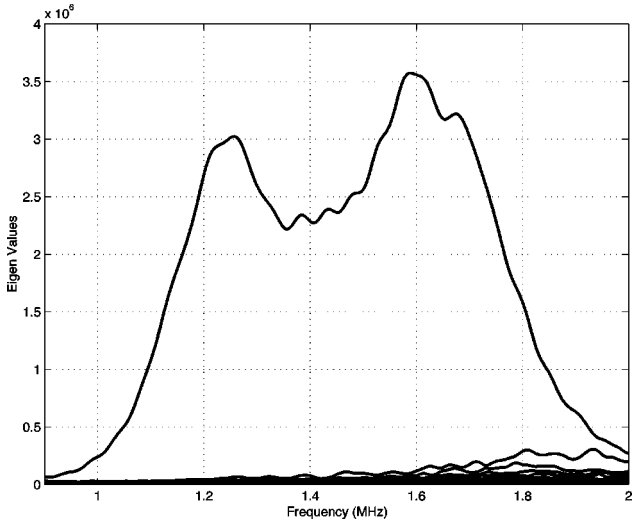

FIG. 3. Experimental TRO eigenvalues versus frequency in a highly absorbing wave guide made of Plexiglas.

scattering on the surface and on the bottom at each reflection. Therefore, the back propagation of this eigenvector gives a pressure profile focusing at the correct depth and range. The observed vertical resolution at the focus, while propagating the first eigenvector without any amplitude compensation, is about 4λ (dotted curve in Fig. 6 right). Therefore, in this case, the gain using the DORT method without amplitude compensation is about 3.5 and the equivalent array aperture in this wave guide (including apodization) is about 3.5 D. Thus, the gain in terms of horizontal resolution is about 12.

Amplitude compensation of the first eigenvector is carried out with the objective of increasing the acoustic pressure on the target as much as possible [Eq. (6)]. As expected, the signal to noise ratio gain is considerable, about 23 dB above the previous case. The vertical resolution is now approaching the diffraction limit value of λ/2 (solid curve in Fig. 6 right).

In the case of a high absorption level, as observed for the bottom (b), the benefit of amplitude compensation is affected by the low number of distinguishable arrivals above noise. The number of resolved arrivals is severely limited by

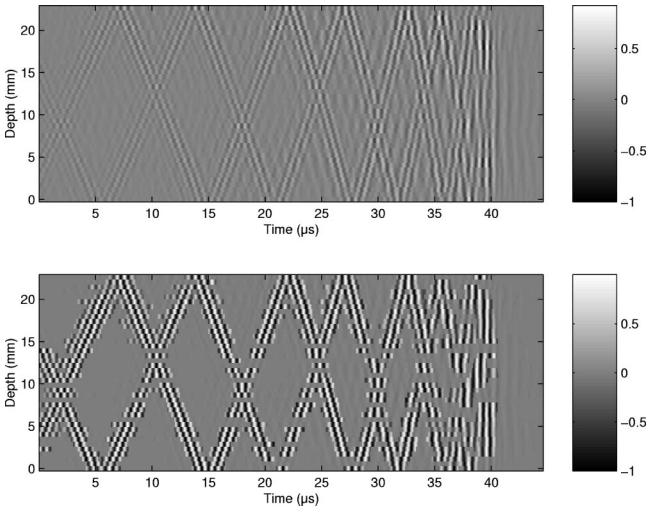

FIG. 4. First eigenvector versus time and depth measured in a perfect rigid wave guide (top) and after amplitude compensation (bottom).

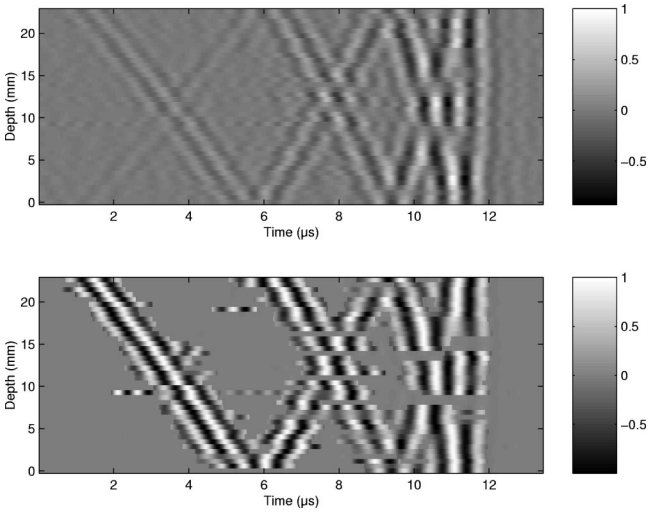

FIG. 5. First eigenvector versus time and depth measured in a wave guide with bottom absorption (top) and after amplitude compensation (bottom).

bottom absorption. However, as the amplitude compensation increases the contribution of the reflected arrivals, the vertical resolution remains good (Fig. 7). The signal to noise ratio at the target increases by 9 to 12 dB after amplitude compensation.

IV. REVERBERATION

Let us consider a single pointlike target in a shallow water environment when electronic noise and bottom reverberation occur. The bottom (c) is a steel base covered by a sandy layer that creates a realistic model of bottom reverberation [Fig. 1(c)]. The grain size of the sand is 0.5 ± 0.2 mm, which is around half a wavelength. For example, at 1 kHz in a real ocean it should correspond more to rocks than a sandy bottom. The reverberation curve in a monostatic configuration has been measured, Fig. 8. It shows that this

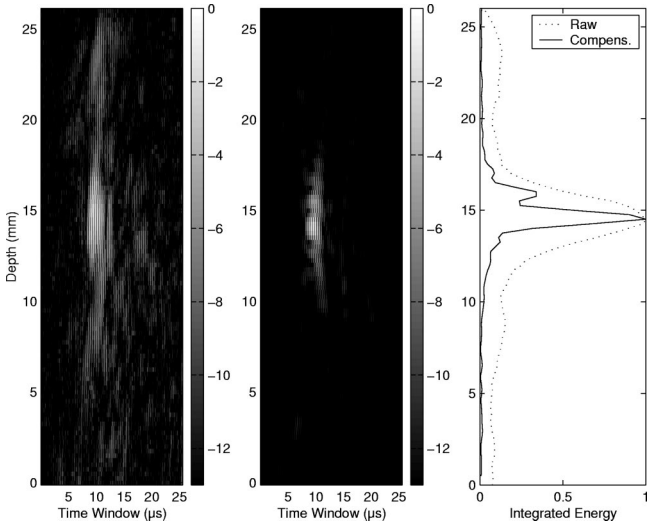

FIG. 6. Effect of amplitude compensation on the focus in a perfect rigid wave guide: the signals versus depth and time are measured while propagating the first eigenvector (left) and the compensated eigenvector (center). The integrated energy versus depth (right) shows the gain of the vertical resolution when amplitude is compensated (solid curve).

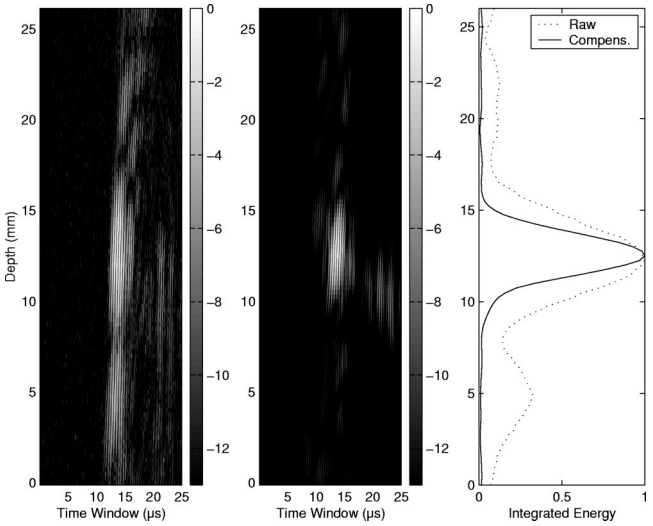

FIG. 7. Effect of amplitude compensation on the focus in an absorbing wave guide: the normalized signals versus depth and time are measured in dB while propagating the eigenvector (left), and the compensated eigenvector (center). The integrated energy versus depth (right) shows an improved vertical resolution when the amplitude is compensated (solid curve).

model provides a realistic representation of a reverberating and absorbing medium.

A. Ambient noise

In Figs. 2 and 3, one observes nonzero singular values, which are the signature of noise. The source level or the emission basis $\mathbf{E_H}$ used for the matrix acquisition will not affect the electronic and ambient noise eigenvalues. Nevertheless, the target eigenvalue levels also improve with the increase of the mean emitted energy. Therefore, the detection threshold should be improved in the same proportions.

B. Reverberation

In a theoretical work, Lingevitch *et al.*[14] extended the DORT method by modelling stochastic reverberation returns

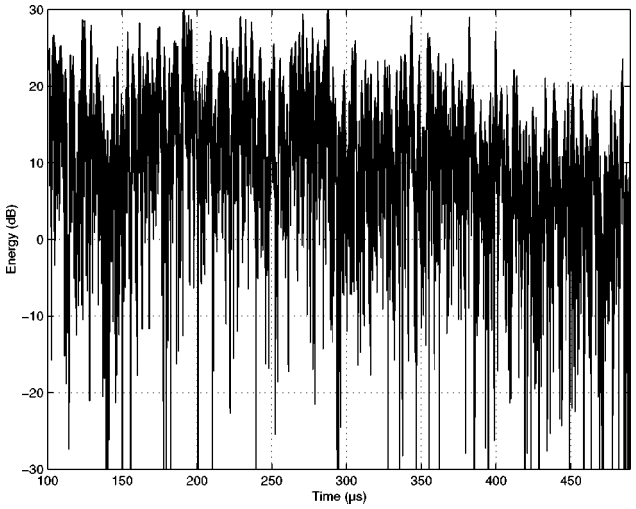

FIG. 8. Monostatic reverberation curve measured for the sand covered steel bottom: the reverberation is due to the sandy layer.

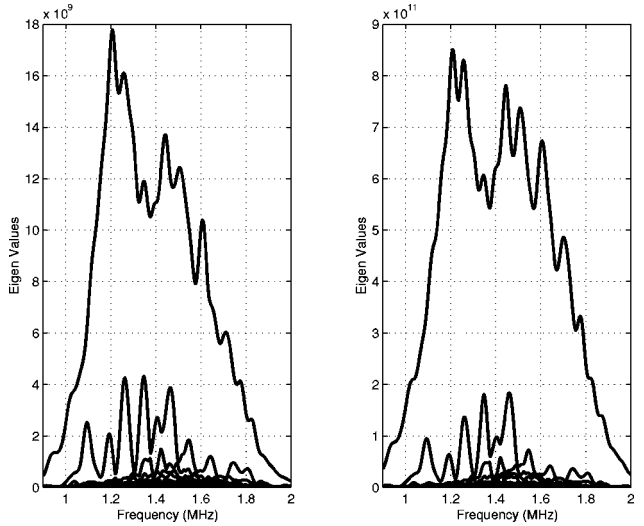

FIG. 9. Singular values versus frequency in a realistic ocean wave guide with absorption and reverberation while $\mathbf{E_H}$ is proportional to identity (left) and while $\mathbf{E_H}$ is proportional to the Walsh matrix (right).

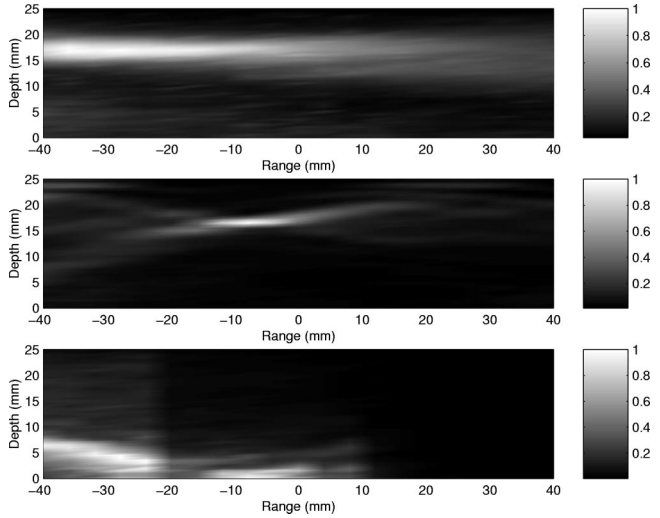

FIG. 11. Range and depth distribution of acoustic energy around the target position by back propagation of the first eigenvector without (top) and with (middle) amplitude compensation and the second eigenvector with amplitude compensation (bottom).

from a rough sediment interface in an ocean wave guide. From their model, they demonstrated that the returned signals focus at the rough bottom interface.

In our experiment, the TRO is constructed in the presence of a single pointlike scatterer at 8.5 mm depth and at 330 mm range in a 25 mm deep sandy wave guide. Figure 9 shows the eigenvalues versus frequency when $\mathbf{E_H}=E(\omega)\mathbf{I}$ (canonical basis) and when $\mathbf{E_H}=E(\omega)\mathbf{H}$, where $\mathbf{H}$ is the Hadamard matrix (Walsh basis[14,17]). Additional nonzero eigenvalues appear in the curves. The magnitude of the singular values are N times higher in the Walsh basis than for the canonical emission (N being the number of array elements) because the source level of the system is N times higher in the Walsh basis. However, at each frequency, the relative magnitudes of the singular values are unchanged, meaning that the second singular value is not due to electronic noise but to an acoustic phenomenonlike reverberation. The differences of shape are unexpected since the Walsh basis is orthonormal and the singular values should be invariant to changes of bases. The coupling between the transducers, which occurs while all the channels are excited simultaneously, implies that the real emitted signals are not strictly orthogonal.

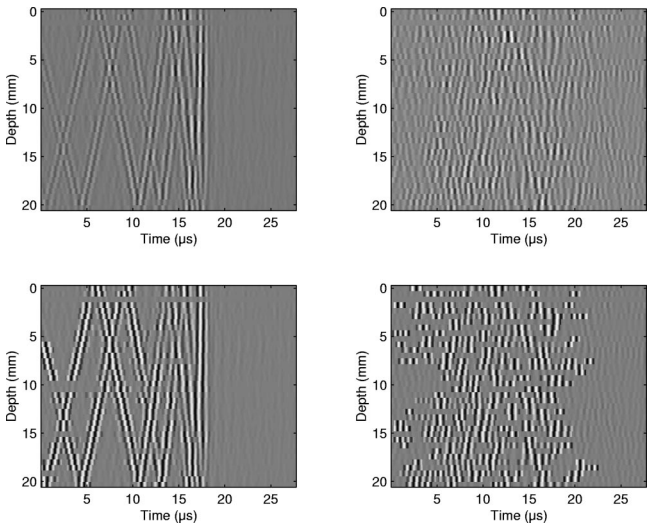

FIG. 10. First (left) and second (right) eigenvectors obtained in the realistic ocean wave guide (top) and after amplitude compensation (bottom).

The time reversal operator is measured with bottom (c) using the canonical basis $\mathbf{E_H}=E(\omega)\mathbf{I}$. The two first eigenvectors are calculated (Fig. 10), compensated as described previously and back propagated. The pressure fields shown in Fig. 11 measured around the target position point out the vertical and horizontal resolution enhancement due to the amplitude compensation. The focusing is achieved on the sandy floor at the same range for the second eigenvector. These results confirm two important properties of the DORT method: first, the ability to take advantage of the environment, of the multipath propagation and of the used returned reverberation signals to increase signal to noise ratio on localized areas, second the ability to separate the reverberation from the target echo and consequently, the ability to focus selectively between reverberation and target.

This result is nontrivial because the spatial dispersion of the bottom speckle and the spatial focus zone are highly dependent on the time window length used in the time reversal operator. In fact, in order to increase the resolution, the method needs to take into account the whole time dispersion of echoes. Nevertheless, the time window must be limited because of the continuity of the target distribution in the bottom. In the experiment, the effective time window is 18 μs. As seen for the first dependent eigenvector associated with the pointlike target (left-hand side of Fig. 10), it allows about eight or nine reflected arrivals. The ranges of focus for both eigenvectors are the same and the focus sizes are both of the same order. The focus occurs at the closest range defined by the beginning of the time window. This can be explained by the greater attenuation of the return signal from longer ranges. The DORT method allows spatial selection on the bottom, and focus on its most reflective part. The characteristic size of the focus on the bottom is given by the

resolution of the complete system, composed of the array, the shallow water environment and the post-processing amplitude compensation.

V. CONCLUSION

These experiments show the ability of the DORT method to separate target echo from the reverberation signal. They also show the huge benefits of amplitude compensation for increasing the signal to noise ratio at the target and improving the vertical and horizontal resolution. The signal to noise ratio gain and the size of focus is directly connected to the array configuration, the environment characteristics and the method of amplitude compensation. Array configuration defines the basic resolution, the range limits of detection and the quality of focus by setting the level of side lobes. Multipath propagation associated with amplitude compensation provides a significant gain in the vertical and the horizontal resolutions and allows the possibility for focusing on the bottom.

ACKNOWLEDGMENTS

The authors would like to thank Didier Cassereau for his helpful upgrade of the acquisition software.

[1] P. Roux, B. Roman, and M. Fink, ''Time-reversal in an ultrasonic waveguide,'' Appl. Phys. Lett. **70**, 1811–1813 (1997).
[2] D. R. Jackson and D. R. Dowling, ''Phase conjugation in underwater acoustics,'' J. Acoust. Soc. Am. **89**, 171–181 (1991).
[3] W. A. Kuperman, T. Akal, C. Ferla, and D. R. Jackson, ''Phase conjugation in the ocean: Experimental demonstration of an acoustic time-reversal mirror,'' J. Acoust. Soc. Am. **103**, 25–40 (1998).
[4] W. S. Hodgkiss, H. C. Song, W. A. Kuperman, T. Akal, C. Ferla, and D. R. Jackson, ''Long-range and variable focus phase conjugation experiment in shallow water,'' J. Acoust. Soc. Am. **105**, 1597–1604 (1999).
[5] C. Prada, J. L. Thomas, and M. Fink, ''The iterative time reversal process: analysis of the convergence,'' J. Acoust. Soc. Am. **97**, 62–71 (1995).
[6] C. Prada and M. Fink, ''Eigenmodes of the time reversal operator: a solution to selective focusing in multiple target media,'' Wave Motion **20**, 151–163 (1994).
[7] C. Prada, S. Manneville, D. Spoliansky, and M. Fink, ''Decomposition of the time reversal operator: detection and selective focusing on two scatterers,'' J. Acoust. Soc. Am. **99**, 2067–2076 (1996).
[8] G. Bienvenu and L. Kopp, ''Optimality of high resolution array processing using the eigensystem approach,'' IEEE Trans. Acoust., Speech, Signal Process. **31**, (1993).
[9] R. O. Schmidt, ''Multiple emitter location and signal parameter estimation,'' IEEE Trans. Antennas Propag. **AP-34**, 276–281 (1986).
[10] N. Mordant, C. Prada, and M. Fink, ''Highly resolved detection and selective focusing in a waveguide using the D.O.R.T. method,'' J. Acoust. Soc. Am. **105**, 2634–2642 (1999).
[11] C. Prada, T. Folégot, N. Mordant, and M. Fink, ''Time reversal operator decomposition in a ocean wave guide,'' Proceedings of the 5th Underwater Acoustics Days, Brest, Session 8-23, France, 2000.
[12] T. Yokoyama, T. Kikuchi, T. Tsuchiya, and A. Hasegawa, ''Detection and selective focusing on scattering using decomposition of time reversal operator method in pekeris waveguide model,'' Jpn. J. Appl. Phys. **40**, (2001).
[13] J. S. Kim, H. C. Song, and W. A. Kuperman, ''Adaptative time-reversal mirror,'' J. Acoust. Soc. Am. **109**, 1817–1825 (2001).
[14] J. F. Lingevitch, H. C. Song, and W. A. Kuperman, ''Time reversed reverberation focusing in a waveguide,'' J. Acoust. Soc. Am. **11**, 2609–2614 (2002).
[15] M. Born and E. Wolf, *Principles of Optics* (Academic, New York, 1970).
[16] M. Tanter, J. L. Thomas, and M. Fink, ''Focusing and steering through absorbing and aberrating layers: Application to ultrasonic propagation through the skull,'' J. Acoust. Soc. Am. **103**, 2403–2410 (1998).
[17] S. Azzaretti, D. Dotti, R. Lombardi, and D. Rossi, ''Echo-graphic images enhanced through walsh functions,'' IEEE Ultrasonics Symposium, 1997, pp. 675–678.

The measurement of A_0 and S_0 Lamb wave attenuation to determine the normal and shear stiffnesses of a compressively loaded interface

Bruce W. Drinkwater[a)]
Department of Mechanical Engineering, University of Bristol, Bristol BS8 1TR, United Kingdom

Michel Castaings and Bernard Hosten
Laboratoire de Mécanique Physique, UMR CNRS 5469, 351 cours de la Libération, Université Bordeaux 1, 33400 Talence, France

(Received 27 September 2002; revised 13 February 2003; accepted 24 February 2003)

Guided waves in an elastic plate surrounded by air propagate with very low attenuation. This paper describes the effect on this propagation of compressively loading an elastomer with high internal damping against one surface of the elastic plate. The propagation of both A_0 and S_0 Lamb modes is considered. The principal effect is shown to be increased attenuation of the guided waves. This attenuation is caused by leakage of energy from the plate into the elastomer, where it is dissipated due to high viscoelastic damping. It is shown that the increase in attenuation is strongly dependent on the compressive load applied across the solid–solid interface. This interface is represented as a spring layer in a continuum model of the system. Both normal and shear stiffnesses of the interface are quantified from the attenuation of A_0 and S_0 Lamb waves measured at each step of the compressive loading. The normal stiffness is also measured independently by normal incidence, bulk longitudinal wave ultrasound. The resulting predictions of wave propagation behavior, such as attenuation, obtained by the model are in excellent agreement with those measured experimentally.
 [DOI: 10.1121/1.1568754]

PACS numbers: 43.35.Cg [YHB]

I. INTRODUCTION

Lamb waves, and other guided waves, have long been known to offer the potential for long range, nondestructive inspection of engineering structures. Recent years have seen these techniques becoming more widely used by industry to solve a number of important inspection problems such as the rapid inspection of pipelines (Alleyne and Cawley, 1996; Rose *et al.*, 1994). The possible uses of Lamb waves are numerous and it is clear that over the coming years a range of new applications will emerge. Due to the complexity of the Lamb wave propagation phenomena, a clear understanding of the wave propagation characteristics must be obtained before any practical testing is initiated. If this understanding is not present, then misinterpretation of the results can easily occur. This paper deals with the topic of the interaction of Lamb waves, more specifically the A_0 and S_0 modes, with a solid–solid interface. This solid–solid interface is the contact between two dry, rough surfaces and could represent a kissing bond in an adhesive joint or the contacting surfaces of a bolted joint. Contact between the surfaces occurs between the peaks of the surface roughness. The ultrasound will ''see'' the solid–solid interface as an array of scatterers, which are the air gaps left between the contacting regions.

The interaction of bulk waves with solid–solid interfaces has been the subject of considerable research effort. Kendal and Tabor (1971) proposed that if the wavelength of the ultrasound was large compared to the scatterers at the interface, then such interfaces could be modeled as a distributed spring. This approach has been validated experimentally (Haines, 1980; Drinkwater *et al.*, 1996; Lavrentyev and Rokhlin, 1998) on a range of different systems. Other models of solid–solid interfaces have also been proposed. Krolikowski and Szczepek (1991) used viscous and hysteretic damping components in a model of a solid interface, though this was not validated experimentally. Baik and Thompson (1984) developed a mass-spring model, which considered the interfaces to have a significant mass component. Margetan *et al.* (1992) validated this mass-spring model on a range of interfaces and showed that, if the interface was thin or its density low, then the mass term could be neglected. Nagy (1992) introduced the concept of a slip boundary condition in which the interface has a normal stiffness and no shear stiffness.

A number of authors have considered the propagation of interface waves along solid–solid interfaces. Rokhlin *et al.* (1981) considered an interface wave propagating along a thin layer of adhesive between two elastic half-spaces. These interface waves were excited by mode conversion from Rayleigh waves which were generated at the free surface of a half space. They showed that the velocity of the interface wave was governed by the elastic properties of the interface layer.

Rokhlin and Wang (1991) demonstrated analytically that such a thin viscoelastic interface layer could be approximated by a spring if the mass of the layer was small. Murty and Kumar (1991) suggested a more general model in which the thin interface layer contained a viscous damping term as

a)Electronic mail: b.drinkwater@bristol.ac.uk

well as an elastic term. Mattei *et al.* (1997) used a laser interferometer to measure the displacement fields of interface waves between two transparent solids. They showed that slip boundary conditions could be used in the case where a thin layer of fluid existed at the interface.

A number of authors (Mal *et al.*, 1989; Kundu and Masalov, 1997; Kundu *et al.*, 1998; Dalton *et al.*, 2001) have suggested that Lamb waves can be used to characterize solid–solid interfaces. Kundu *et al.* measured Lamb wave propagation (phase velocity) in two glass plates, compressively loaded against one another. They suggested that the A_1 mode was particularly sensitive to the interfacial condition. Dalton *et al.* computed the Lamb wave propagation characteristics of a plate coupled to a sealant layer. In the system they considered the sealant to be thick and its attenuation high, so they modeled it as semi-infinite. They showed good agreement between experiment and theory and that the attenuation of the modes was dependent on the properties of the sealant. In this paper, these approaches are extended by considering the case when the coupling between the plate and the half-space is imperfect. The paper has two specific aims; first to show that a spring model of the interface is sufficient to describe the interaction of Lamb waves with a solid–solid interface. The second aim is to demonstrate how, by using the A_0 and S_0 Lamb modes, the normal and shear stiffness of the solid–solid interface between a glass plate and semi-infinite elastomer can be measured.

In Sec. II of this paper experiments are described in which normal incident bulk waves are used to measure the longitudinal stiffness of a glass–elastomer interface. In Sec. III these interfacial stiffness measurements are then used as inputs to a model which predicts the propagation of S_0 and A_0 Lamb modes in a glass–elastomer bi-layer in air. Section IV then describes an experimental study of the interaction of S_0 and A_0 Lamb modes with this system and explains how these measurements can be used to obtain normal and shear interfacial stiffnesses.

II. DETERMINATION OF THE INTERFACIAL SPRING CONSTANTS USING BULK WAVES

A. Apparatus and results

In this section measurements of the reflection coefficient of normal incidence bulk longitudinal waves are used to measure the normal stiffness of the interface. The approach is based on that first developed by Kendal and Tabor (1971). Figure 1 shows the apparatus used to measure the reflection coefficient variation with compressive pressure. A longitudinal wave ultrasonic transducer was coupled to a glass plate

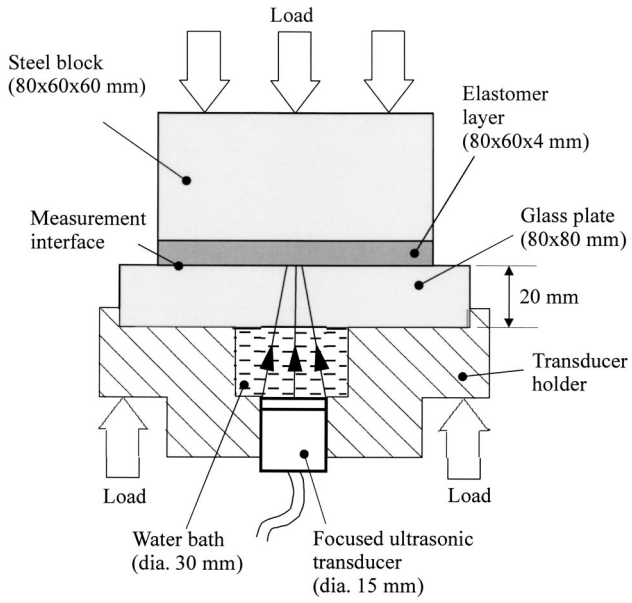

FIG. 1. Schematic diagram of apparatus to measure the normal incidence longitudinal glass–elastomer reflection coefficient.

through a water bath. It was not possible to use the same frequency as in the Lamb (120 and 300 kHz) wave experiments described in Sec. IV as that would have required a glass plate thicker than 200 mm to guarantee separation of the reflections. The stiffness of the interface should not be a function of frequency and so a higher frequency (1 MHz) was chosen, which allowed a 20 mm thick glass plate to be used. The validity of this assumption is explored later in Sec. IV B. The signal reflected from the glass–air interface was recorded as a reference at which the reflection coefficient is known to be equal to unity. An elastomer plate (see Table I for material properties) of identical mechanical properties and surface roughness to that used in the Lamb wave experiments described in Sec. IV was then loaded against the glass plate. The signal reflected from the glass–elastomer interface was recorded as a function of load. For each load increment, the reflection coefficient was calculated by dividing the glass–elastomer measurement by the glass–air measurement in the frequency domain. This gave the reflection coefficient spectrum over the bandwidth of the transducer. Figure 2 shows how the measured 1 MHz longitudinal reflection coefficient varies for a loading and unloading cycle. Note that the applied load was chosen to generate similar contact pressures (0.47 MPa) as used in the Lamb attenuation experiments (0.42 MPa) described in Sec. IV. Figure 2 shows clear hysteresis between the loading and unloading lines which is

TABLE I. Acoustic properties of glass, elastomer, and air used in the modeling. Properties of air are those at 20 °C. The velocities and attenuations of the glass and elastomer were measured at 300 kHz.

Material	Thickness (mm)	Density (kg/m^3)	Longitudinal Velocity (m/s)	Longitudinal Attenuation at 300 kHz (dB/cm)	Shear velocity (m/s)	Shear attenuation at 300 kHz (dB/cm)
Glass	3.9	2460	5880	0	3490	0
Elastomer	8.8	1250	1960	3.5	566	15
Air	⋯	1.225	343	⋯	⋯	⋯

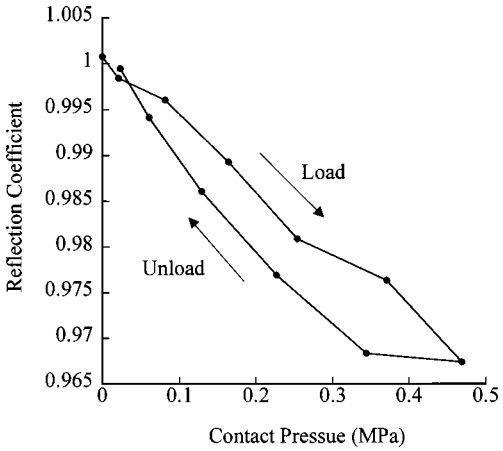

FIG. 2. Measured longitudinal glass–elastomer reflection coefficient variation as a function of contact pressure (1 MHz).

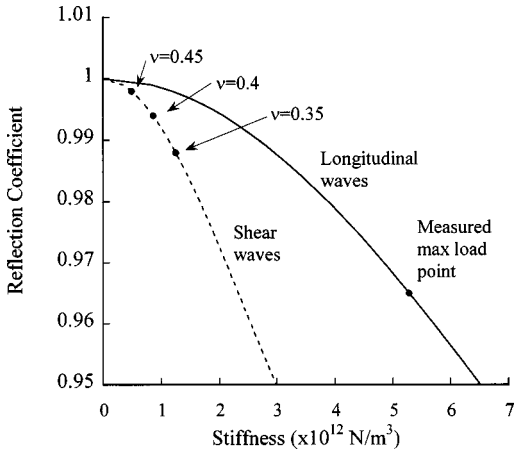

FIG. 3. Spring model prediction of the normal incidence shear and longitudinal reflection coefficient variation as a function of stiffness (1 MHz).

similar to that observed for metal–metal contacts by Drinkwater *et al.* (1996) and explained as contact adhesion. It can also be seen that the reduction in reflection coefficient is very small (≈4%) at the highest contact pressures. However, measurements shown in Fig. 2 are reproducible within 0.5%, thus giving good confidence in these results. This experiment was repeated for a 1 MHz shear transducer coupled to the glass plate with viscous couplant. In this case, no measurable change in the shear reflection was observed and so no meaningful measurement of the shear stiffness was obtained.

B. Discussion

If it is assumed that the solid–solid interface can be modeled as a spring boundary condition, then the measured reflection coefficient, R_{12}, can be used to calculate the interfacial stiffness per unit area, K, from (Drinkwater *et al.*, 1996)

$$K=\omega z_1 z_2 \sqrt{\frac{1-|R_{12}|^2}{|R_{12}|^2(z_1+z_2)^2-(z_1-z_2)^2}}, \tag{1}$$

where z is the acoustic impedance (product of density and wave speed), the subscripts referring to the media either side of the interface, and ω is the angular frequency. It can be seen from Eq. (1) that as the reflection coefficient approaches unity, the calculated stiffness will be sensitive to small reflection coefficient errors. Equation (1) can now be used to demonstrate the difficulties of measuring the shear stiffness using bulk wave reflection coefficients. Figure 3 shows longitudinal bulk wave reflection coefficient plotted as a function of normal stiffness, K_N, and shear bulk wave reflection coefficient as a function of shear stiffness, K_T. Marked on the longitudinal wave graph are the stiffness and reflection coefficient, which correspond to the maximum load point shown in Fig. 2 ($K_N=5.3\times10^{12}$ N/m^3 and RC$=0.965$). Shown on the shear wave line are estimates of the shear stiffness corresponding to this maximum load point. If the interface layer is assumed to be a layer of elastic solid, then the ratio of normal to shear stiffness is governed by Poisson's ratio, ν, by the well-known relation,

$$\frac{K_N}{K_T}=\frac{2(1-\nu)}{1-2\nu}. \tag{2}$$

The three points, which are shown on the shear wave line on Fig. 3, correspond to Poisson's ratios of 0.35, 0.4, and 0.45 which give K_N/K_T ratios of 4.3, 6, and 11, respectively. As can be seen from Fig. 3, these shear stiffness values result in reflection coefficients of greater than 0.985. This means that in order to measure the shear stiffness using bulk wave reflection coefficients at normal incidence (at 1 MHz) would require the measurement of a 1.5% (or less) drop in signal amplitude. Such reflection coefficients are too close to unity to measure accurately with most commercially available apparatus and so no accurate measure of shear stiffness was possible. The physical reason for this is that the shear stiffness of the glass–elastomer contact is very low and so high-frequency bulk shear wave are almost completely reflected. If the interfacial stiffness is higher, then bulk shear wave reflectivity measurements are possible. For example, Baltazar *et al.* (2002) measured the shear interfacial stiffness of an aluminum–aluminium interface using an oblique incidence technique.

III. MODELING OF THE A_0 AND S_0 INTERACTIONS WITH A COMPRESSIVELY LOADED INTERFACE

A. Description of model

The propagation of Lamb modes in a system including a compressively loaded interface was modeled using the surface impedance method (Honein *et al.*, 1991), which is numerically more stable than the standard transfer matrix method and faster than the global matrix method (Lowe, 1995). This method is also convenient in satisfying boundary conditions for different layered media cases and in obtaining modal solutions. The layered system is shown schematically in Fig. 4. The system modeled, was considered as infinitely wide in the direction x_3 normal to the plane of propagation, i.e., the system was in plane strain. Experimentally the dimension of the system in the x_3 direction was large compared to the width of the ultrasonic beams making this assumption reasonable. The plane of propagation was formed by the axis x_1 and x_2, where x_1 is normal to the various

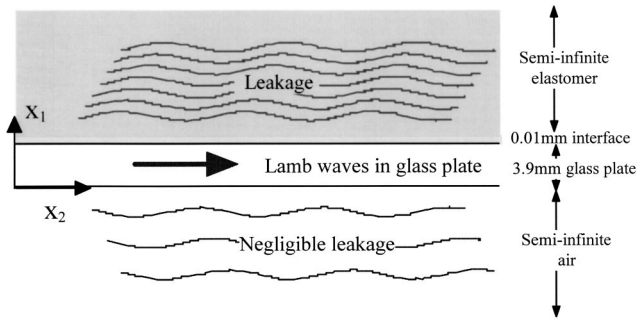

FIG. 4. Schematic diagram of the modeled system consisting of air–glass–"interface layer"–elastomer.

interfaces and x_2 is the direction of propagation for guided modes. The system was modeled as infinitely long in the direction of propagation. As can be seen from Fig. 4 the system modeled was a 3.9-mm-thick glass plate, surrounded by semi-infinite air on one side and semi-infinite elastomer on the other. There was a solid–solid interface between the glass plate and the elastomer and this interface was modeled by a 10 μm thick, isotropic layer, the properties of which are the mass density and elastic moduli. Using the usual notation for the indices (Auld, 1990), only two elastic moduli, C_{11} and C_{66}, are sufficient to represent the mechanical properties of this interface, in the plane of propagation formed by the axis x_1 and x_2, the other C_{ij}'s, C_{22} and C_{12}, being such that $C_{22}=C_{11}$ and $C_{12}=C_{11}-2C_{66}$. The very small thickness of this interface layer meant that the value chosen for the mass density of the interface had a negligible effect on the propagation of modes guided in the system (Pialucha *et al.*, 1993) and so the effect of the interface layer is governed by the elastic moduli, C_{11} and C_{66}. This interface layer approximates a distributed spring interface with the normal and transverse stiffnesses, given by $K_N=C_{11}/h$ and $K_T=C_{66}/h$, respectively. Using this approach, the dispersion curves of modes guided along the glass plate were modeled for the cases of leakage of energy either into two semi-infinite half-spaces of air, or into one semi-infinite half-space of air and into one semi-infinite half-space of elastomer, via the interface. Both the phase velocity and the attenuation of various modes have been predicted using the impedance method. The air, glass, and elastomer properties were fixed (see Table I), while K_N and K_T of the interface were varied in order to fit the experimental attenuation of guided modes.

B. Results and discussion

The modeling approach described in Sec. III A above was used to predict the dispersion curves for a 3.9 mm thick glass plate in air. The resulting dispersion curves are shown in Fig. 5(a). The work in this paper concentrates on the two fundamental modes, A_0 and S_0, and so Fig. 5(a) concentrates on the low frequency-thickness region where these modes are distinct and propagate with very different phase and group velocities. The plotted frequency thickness range corresponds to 0–1 MHz, for the 3.9 mm glass plate. Figure 5(b) shows that the attenuation of these modes is very small, due to the low level of leakage into the surrounding air. Note that for the fundamental modes, the extremely low values of attenuation were too small to be measurable. The crosses in Fig. 6 show the through-thickness displacement fields for the glass plate in air in this low frequency region (A_0 at 300 kHz and S_0 at 120 kHz). From this it can be seen that both modes are composed of a combination of displacement normal to, and in the plane of, the surface of the plate. It can also be seen from Fig. 6 that the A_0 displacement field is mostly normal to the surface whereas that of S_0 is mostly in the plane of the plate. Note that the displacement fields shown in Fig. 6 are similar to those predicted by Seifried *et al.* (2002) for an aluminum–adhesive system.

Figure 7(a) shows the predicted dispersion curves for a 3.9 mm glass plate with semi-infinite air on one side and semi-infinite elastomer on the other (see Table I for material data). A comparison of Fig. 7(a) with Fig. 5(a) shows that the phase velocities of A_0 and S_0 are not significantly changed over the plotted frequency-thickness range except at very low frequency-thicknesses. However, comparison of Figs.

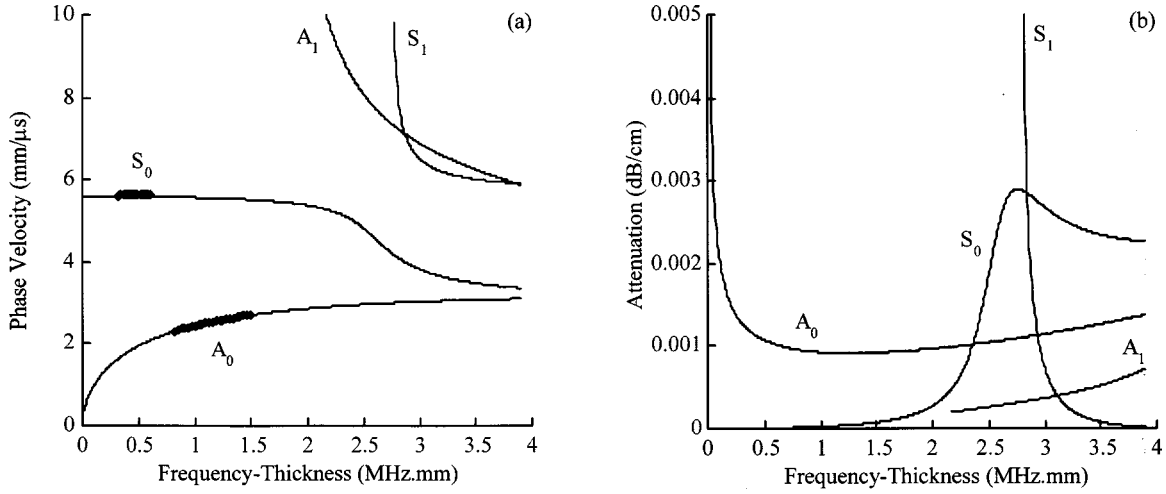

FIG. 5. Dispersion curves for Lamb modes propagating in an air-coupled 3.9-mm-thick glass plate: (a) phase velocity and (b) attenuation: Numerical predictions (———) and experimental data (◆ ◆ ◆).

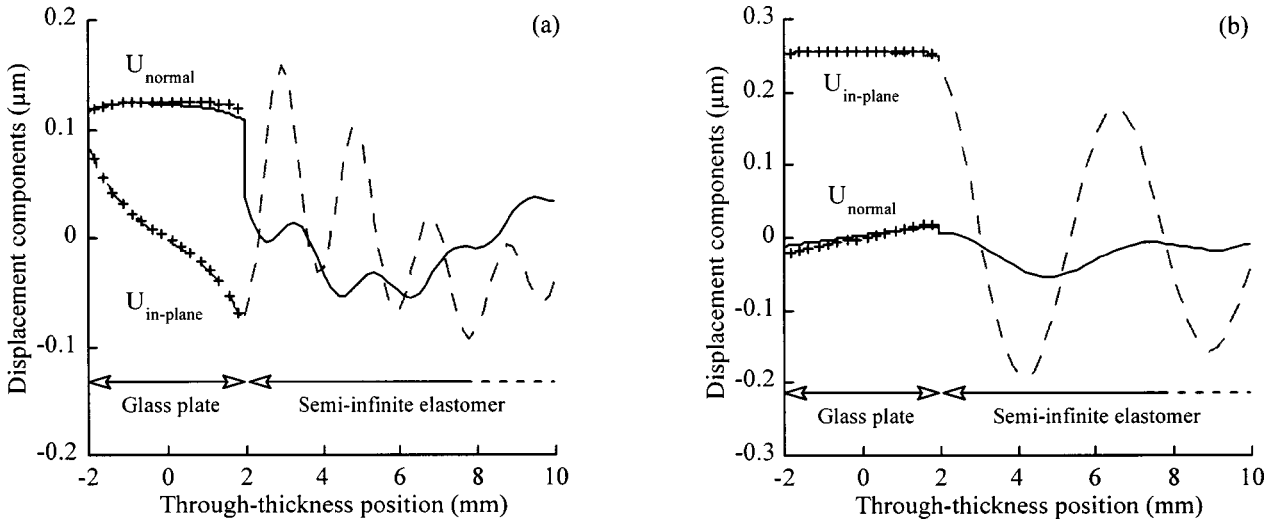

FIG. 6. Through-thickness displacement distributions of power-normalized Lamb modes in an air–glass–elastomer system (3.9-mm-thick glass plate): (a) A_0 mode at 300 kHz and (b) S_0 mode at 120 kHz. Note that the crosses are the displacement distributions for the air–glass–air system.

7(b) and 5(b) shows that the attenuation of the modes is increased by over 300%. If a spring interface layer is now introduced into the model to represent the solid–solid contact, then, depending on the stiffness of that layer, the attenuation dispersion curves can be either as shown in Fig. 5(a) (if stiffness equals zero), as in Fig. 7(a) (if stiffness is infinite), or to have some value in between. It can be seen, then, that changes in the stiffness values of K_N and K_T have negligible effects on the phase velocity dispersion curves but a strong effect on the Lamb mode attenuation. This can be further understood by comparison of the A_0 and S_0 through-thickness displacement fields for a free glass plate and a glass plate loaded with a semi-infinite half-space of elastomer shown in Fig. 6. This figure shows that the glass plate through-thickness fields are almost identical, whether the elastomer is present or not, for A_0 and S_0 in the low frequency-thickness region. This is therefore consistent with the similar phase velocity dispersion curves for A_0 and S_0 shown in Figs. 5(a) and 7(a).

In order to analyze this system further, predictions of the normal and shear stiffness of the glass–elastomer contact at a contact pressure of 0.1 MPa were made. First, the normal stiffness at 0.1 MPa was calculated from the high-frequency, normal incidence experiment (Fig. 2) using Eq. (1). Second, this normal stiffness was used in the dispersion curve prediction software and the shear stiffness varied until the predicted S_0 attenuation (at 120 kHz) was equal to that which was measured experimentally (see Sec. IV for fuller details of the experiments). This gave $K_N = 2.8 \times 10^{12}$ N/m^3 and $K_T = 0.65 \times 10^{12}$ N/m^3. Using these stiffness values as a starting point, Fig. 8 shows the sensitivity of the A_0 and S_0 attenuation to changes in K_N and K_T. For these plots sensitivity has been defined as

$$\text{Sensitivity} = \frac{\alpha_0 - \alpha_{20\%}}{\alpha_0}, \tag{3}$$

where α_0 is the attenuation of the mode at the initial values

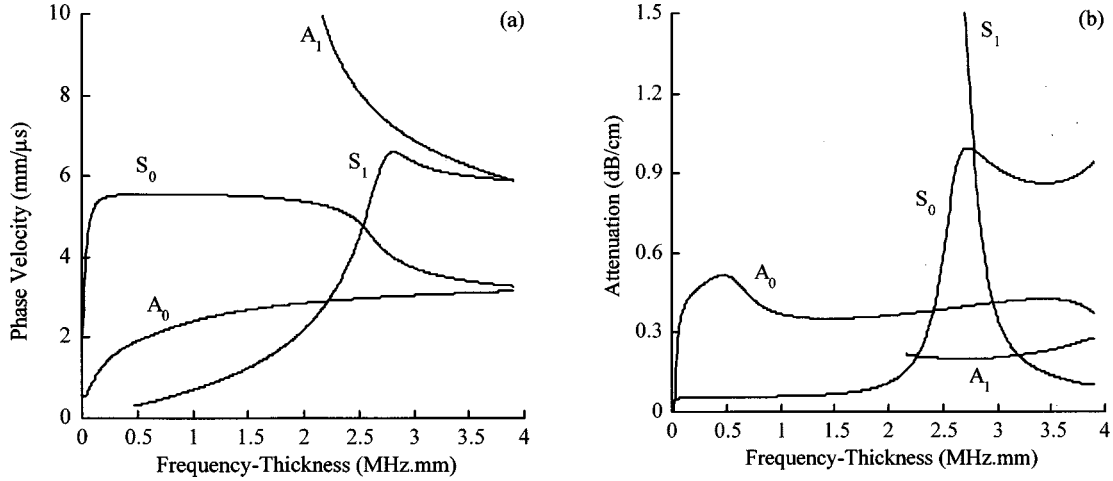

FIG. 7. Dispersion curves for guided waves propagating in an air–glass–elastomer system (3.9-mm-thick glass plate): (a) phase velocity and (b) attenuation.

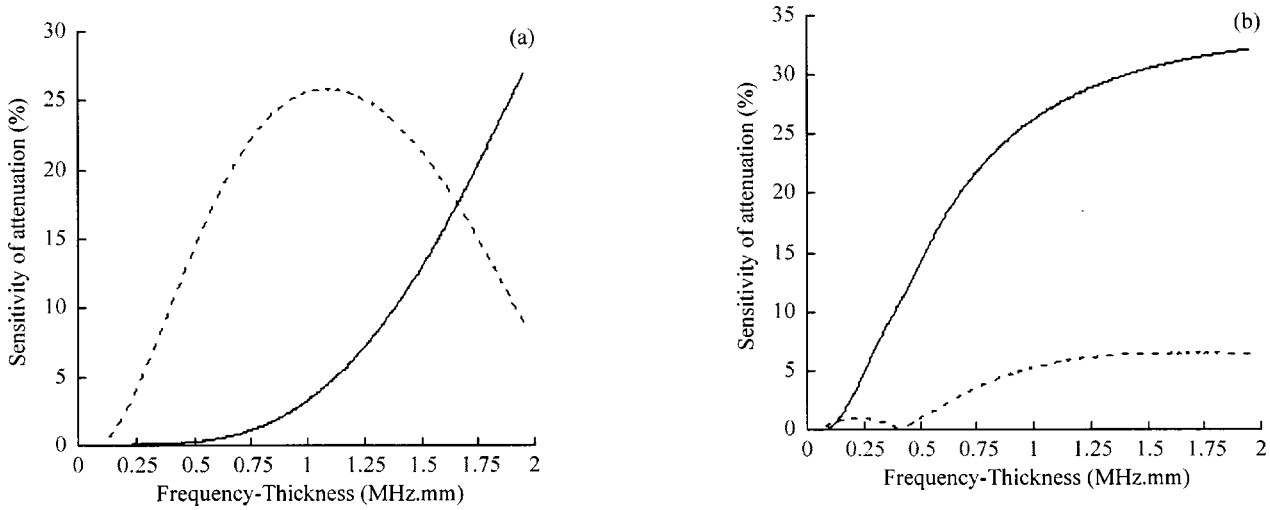

FIG. 8. Sensitivity of Lamb attenuation to an increase of 20% in K_N (———) and K_T (---) stiffnesses of the interface between the glass plate and the elastomer sample: (a) attenuation of S_0 and (b) attenuation of A_0.

of either K_N or K_T and $\alpha_{20\%}$ is the attenuation of the same mode if one of the stiffness is increased by 20% above this initial value. Note that the initial values of K_N and K_T chosen for this sensitivity study do not significantly affect the general result of this sensitivity study. From Fig. 8(a) it can be seen that for S_0, K_T has a significant effect on attenuation across the plotted frequency range and that the influence of K_N increases with frequency. Below 0.5 MHz.mm, the S_0 attenuation is virtually independent of K_N. Conversely, from Fig. 8(b) it can be seen that for A_0, changes in K_N have a significant effect on the attenuation except at very low frequencies, whereas changes in K_T have a much smaller effect across the whole frequency range. These effects can be explained by consideration of the displacement fields shown in Fig. 6 which show that the S_0 displacement field at 0.47 MHz.mm is predominantly in-plane whereas that of A_0 at 1.17 MHz.mm is a combination of normal and in-plane motion, with the normal motion being slightly greater.

This sensitivity study points to an exciting possibility, which is that combined low-frequency S_0 and A_0 attenuation measurements can be used to measure K_T and K_N. Of particular importance is the fact that K_T can potentially be measured with good accuracy whereas such a measurement, as described in Sec. II B was shown to be very difficult using normal incidence bulk waves.

IV. MEASUREMENTS OF THE INTERACTIONS OF A_0 AND S_0 WITH A COMPRESSIVELY LOADED INTERFACE

A. Experimental apparatus and method

The experimental setup shown in Figs. 9 and 10 was used to generate and detect the Lamb waves (A_0 and S_0) in a 3.9 mm glass plate. The plate measured 600 mm by 300 mm. Based on the sensitivity study results shown in Fig. 8 measurement positions were chosen centered on 120 kHz (or 0.47 MHz.mm) for S_0 and 300 kHz (1.17 MHz.mm) for A_0. At 0.47 MHz.mm the aim was to calculate K_T from the S_0 measurement, where there is little sensitivity to K_N. At 1.17 MHz.mm A_0 is sensitive to K_N and so the aim was to use this measurement to calculate K_N, based on the previously measured K_T. For the measurement of A_0 at 300 kHz an air-coupled transmitter and an air-coupled receiver were used. The transducers were capacitive and had an active diameter of 45 mm. Their frequency bandwidth was centered at 200 kHz with −15 dB points at 50 and 400 kHz. A 10-cycle Hanning windowed tone burst was input to the transmitting transducer centered on 300 kHz. Both transducers were inclined at 8°, with respect to the normal of the plate, which was calculated from the dispersion curves shown in Fig. 5(a) using the coincidence principle (Auld, 1990). The

(1) PZT contact transmitter launching S_0 at 120 kHz
(2) Air-coupled transmitter launching A_0 at 300 kHz
(3) Air-coupled receiver
(4) 3.9 mm thick glass plate
(5) 40 mm thick rigid foam sample
(6) 28 mm thick elastomer sample
(7) 60 mm high aluminium block
(8) Load cell
(9) Pressure load rig
(10) Charge level indicator
(11) Goniometers

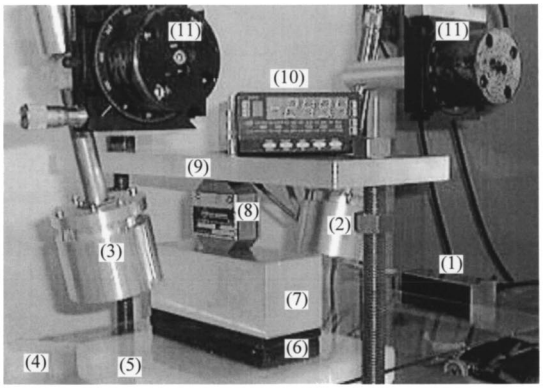

FIG. 9. Photograph of experimental apparatus used for measuring the attenuation of Lamb modes due to leakage through compressively loaded interface.

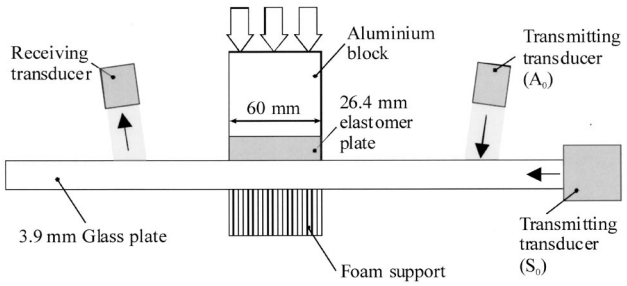

FIG. 10. Schematic diagram of the experimental apparatus used for measuring the attenuation of Lamb modes.

air coupling means that both the transmitter and receiver are sensitive to normal displacement of the plate and insensitive to in-plane displacement. This means that they are ideally suited to the measurement of A_0, which has a large normal displacement component. As S_0 is made up of mostly in-plane displacement, a different experimental setup was used for this measurement. As can be seen in Figs. 9 and 10 a piezoelectric contact transducer (active element size was 100 mm long by 40 mm wide) was placed against the edge of the plate. This generates a large in-plane displacement, strongly exciting S_0. An air-coupled receiver, inclined at 3.5° with respect to the normal of the plate, was then used to detect S_0 by measurement of its small normal displacement. In the cases of both A_0 and S_0 propagating along the plate, the air-coupled receiver was moved away from the transmitter, along a 60 mm long path, by steps of 4 mm. For each position, the temporal signal was captured and signal processing [see Castaings and Hosten (2001) for a fuller description] was used to enable an accurate measurement of the variation with frequency of the phase velocity for each mode. Figure 5(a) also shows the experimentally measured phase velocities for A_0 and S_0 for the glass plate alone from which it can be seen that there is excellent agreement with the predicted dispersion curves.

Experiments were then performed in order to measure the interaction of A_0 and S_0 Lamb waves with a compressively loaded interface. The experimental setup shown in Figs. 9 and 10 was used to perform measurements in which a 26.4 mm thick elastomer plate measuring 160 mm by 60 mm was compressively loaded against the previously described glass plate. The elastomer plate was loaded through a thick (60 mm) aluminum block. This acted as an effectively rigid block and so the load was applied evenly across the top surface of the elastomer plate. The glass plate was supported by a 40 mm thick block of rigid foam. This supporting foam was very porous and had a very low acoustic impedance and so simulated air backing of the glass plate.

The elastomer plate was thick (26.4 mm) and highly attenuative (see Table I), so that any ultrasonic waves transmitted into the elastomer were heavily attenuated. This meant that the amplitudes of the reflections (both longitudinal and shear) from the back face of the elastomer were small (<12% of the transmitted amplitude for a longitudinal wave at 300 kHz) and so the elastomer was modeled as semi-infinite in later analysis.

B. Results

The apparatus shown in Figs. 9 and 10 was used to load the elastomer against the glass plate. The effect of this loading on the propagation of A_0 and S_0 in the glass plate was measured. At each load step the transmitted signal was recorded and transformed to the frequency domain using a fast Fourier transform. The transmission coefficient was then calculated by dividing the spectra of the transmitted pulse by a reference measurement taken when no elastomer was present and the attenuation was known to be zero (hence transmission coefficient equalled unity). All signals were captured at the same distance between transducers (300 mm) and so the geometrical attenuation (beam spreading) was equal in the measured and reference signals. In this way measured transmission coefficient reductions are due to either the leakage of energy into the surrounding media or reflections back from the edges of the elastomer contact. The repeatability of these transmission coefficient measurements was very good with

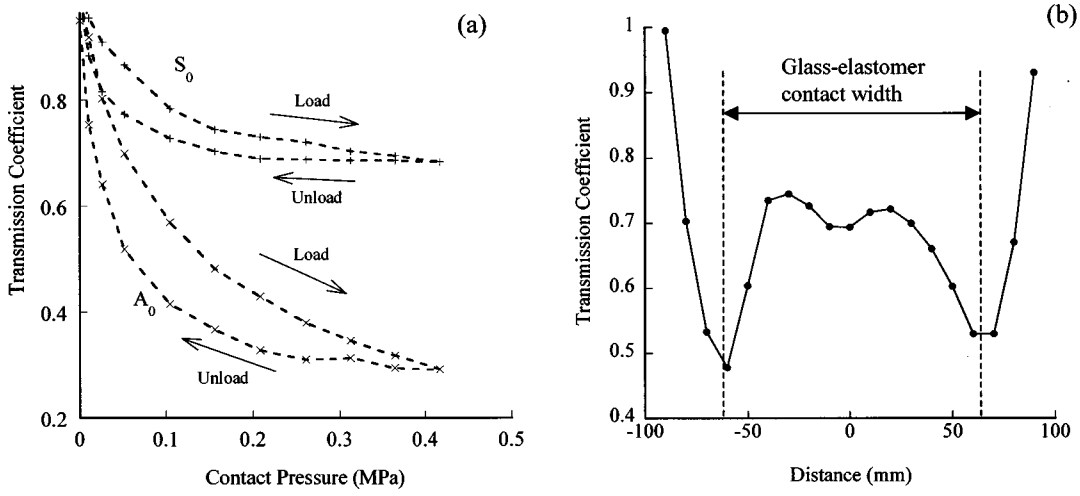

FIG. 11. Experimental measurement of the Lamb wave transmission coefficient: (a) transmission coefficients for A_0 and S_0 as a function of contact pressure and (b) variation in A_0 transmission coefficient across the width of the contact at 4000 N.

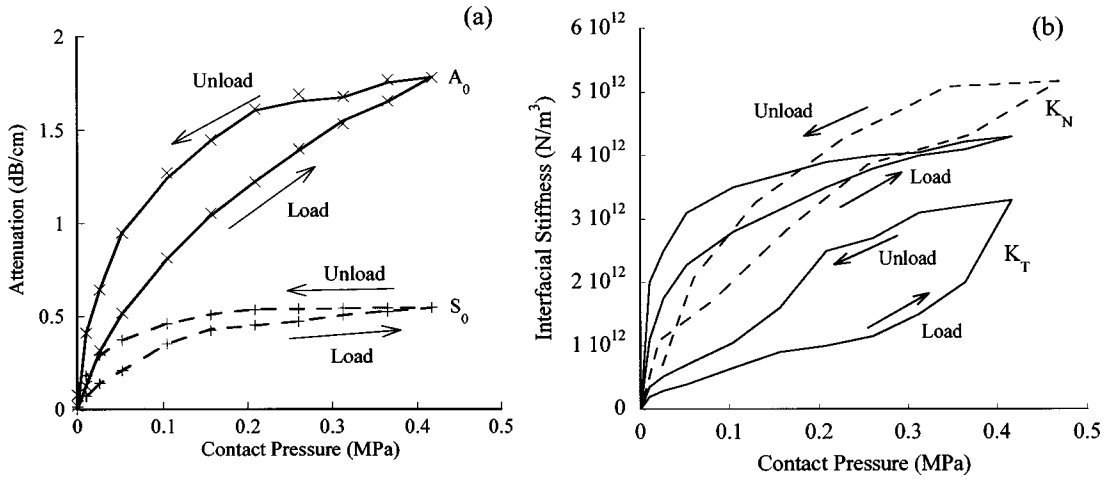

FIG. 12. Variation with contact pressure of (a) the attenuation of A_0 at 300 kHz and S_0 at 120 kHz (experimental data are the points marked with crosses and the predictions are the continuous lines) and (b) stiffnesses of the interface between the glass plate and the elastomer (predictions from Lamb wave attenuation measurements are solid lines whereas that from the normal incidence measurements is dashed).

an error of less than $\pm 3\%$. Figure 11(a) shows how the measured transmission coefficient varied through a cycle of loading and unloading for both A_0 and S_0. From this figure it can be seen that as the load (and hence contact pressure) was increased, so the transmission coefficient decreased. At the maximum contact pressure (0.42 MPa) the transmission coefficient of S_0 had fallen to 0.68 and that of A_0 to 0.29. It can also be seen from Fig. 11(a) that there was a distinct difference between the loading and unloading parts of the cycles. Typically the transmission coefficient at a given pressure on the loading line was higher than on the unloading line. This effect has been observed in earlier work on metal–metal contact (Drinkwater *et al.*, 1996) and was explained as a contact adhesion effect. On loading the contacting asperities (peaks of the surface roughness) adhere to one another. On unloading these adhered asperities tend to maintain the contact area. As it is the solid–solid contact which causes the leakage, and hence the attenuation, a lower transmission coefficient is measured at a given contact pressure on unloading when compared to loading. Figure 11(b) shows how the measured transmission coefficient varies across the width of the elastomer–glass contact. From this it can be seen that the transmission coefficient was uniform over the central portion of the contacting region and that it was slightly smaller towards the edges, increasing to unity when the transmission was made outside the contact area.

To allow the leakage of Lamb waves from the glass plate into the elastomer to be calculated from the measured transmission coefficient it was first necessary to separate losses due to leakage into the elastomer from other possible sources of transmission coefficient reduction. Two potential alternative causes of a reduction in transmission coefficient with load were investigated. First, leakage of S_0 and A_0 into the foam was measured by compressing the glass plate between two blocks of foam. At the highest contact pressure (0.42 MPa) this caused the transmission coefficient to fall by 4.4% to 0.956 for A_0. From this it can be deduced that in the elastomer loading experiments where only one block of foam is present, the leakage due to the foam will be under 2.2% at the highest loads and below that for lower loads. This leakage mechanism was therefore neglected. The second possible source of transmission coefficient reduction is by reflections from the edge of the contact of the elastomer and glass plates. An A_0 reflection experiment was performed in which the receiving transducer was placed close to the transmitting transducers and oriented to receive A_0 reflections. No measurable reflected signals were observed and so this loss mechanism was also neglected. No such experiment has been performed for the incident S_0 mode, but one would expect its reflection from the edge of the elastomer–glass interface to be even lower than that for the incident A_0 mode, since S_0 is usually less sensitive to perturbations at the plate surfaces.

The following procedure was then adopted to determine the normal and shear stiffnesses of the glass–elastomer interface as a function of loading from the experimental data described in Sec. IV A. For each load increment (using $K_N = 2.8\times10^{12}$ N/m^3 and $K_T = 0.65\times10^{12}$ N/m^3 as a starting point) K_T was adjusted until agreement was obtained with the S_0 attenuation measurement at 120 kHz. Using this new value of K_T, K_N was then adjusted until agreement was obtained with the A_0 attenuation measurement at 300 kHz. The result of this K_N and K_T optimization procedure is shown in Fig. 12(a). Figure 12(b) shows how the K_N and K_T values extracted from this procedure varied as a function of loading. Also shown on Fig. 12(b) are the K_N values obtained from the 1 MHz normal incidence measurements. The good agreement between these stiffness measurements for the loading cycle demonstrates that such Lamb wave measurements can be used to measure interfacial stiffness. The unloading data are not directly comparable as the normal incidence experiment was loaded to a higher load and so the hysteresis loop is shifted to the right. Note that the differences at low loads are thought to be due to errors in the normal incidence measurement which is very sensitive to reflection coefficient errors as the reflection coefficient varies over a very small range (between 1.0 and 0.965).

TABLE II. Effect of changes in elastomer properties on leakage of A_0 and S_0 using $K_N = 4.3\times10^{12}$ N/m^3 and $K_T = 3.3\times10^{12}$ N/m^3.

	Initial	Increased $V_L(+12\%)$	Decreased $V_L(-12\%)$	Increased $V_S(+12\%)$	Decreased $V_S(-12\%)$
	$V_L = 1960$ m/s $V_T = 566$ m/s	$V_L = 2191$ m/s $V_T = 566$ m/s	$V_L = 1697$ m/s $V_T = 566$ m/s	$V_L = 1960$ m/s $V_T = 632$ m/s	$V_L = 1960$ m/s $V_T = 489$ m/s
Attenuation of A_0 at 300 kHz (dB/cm)	1.78	1.76 (−1.1%)	1.75 (−1.7%)	1.80 (+1.1%)	1.75 (−1.7%)
Attenuation of S_0 at 120 kHz (dB/cm)	0.546	0.542 (−0.7%)	0.55 (+0.7%)	0.602 (10.3%)	0.48 (12.1%)

A study was also undertaken to assess the effect of errors in the elastic properties of the elastomer on the A_0 and S_0 attenuation predictions. It was estimated that the longitudinal wave velocity was measured to an accuracy of ±5% and the shear velocity ±15%. Table II shows the effect of a ±12% variation of the measured velocities on the predicted attenuation of A_0 and S_0 for constant interfacial stiffnesses ($K_N = 4.3\times10^{12}$ N/m^3 and $K_T = 3.3\times10^{12}$ N/m^3). As can be seen from Table II the A_0 and S_0 attenuation changes which result from this 12% variation in elastomer velocities are small (<12.1%). This means that the measurement of interfacial stiffness by this method is relatively insensitive to the measured properties of the elastomer.

V. CONCLUSIONS

Measurements of the velocity and attenuation of A_0 and S_0 in a glass plate loaded through a solid–solid contact with an effectively semi-infinite elastomer have been made. These measurements were made in the low frequency-thickness region (below the A_1 cutoff frequency) with A_0 measured at 300 kHz (or 1.17 MHz.mm) and S_0 measured at 120 kHz (or 0.468 MHz.mm). These results show that, for both modes, the velocity was virtually unaffected by the elastomer and the applied load whereas the attenuation was strongly dependent on the applied load. This was explained by the similarity of the glass plate through-thickness displacement fields in the air–glass–air system and the air–glass–elastomer system.

It was proposed that the coupling across the solid–solid interface can be modeled by a spring interface having both normal and shear stiffness. As the load across the solid–solid interface is increased, so the interface stiffnesses increases. The dispersion characteristics of this system (air–glass–''spring interface''–elastomer) have been modeled using a multi-layered continuum model. At low frequency-thickness products, the normal stiffness was found to affect the attenuation of A_0 and not that of S_0. Conversely the shear stiffness was found to affect the attenuation of S_0 and not A_0. This fact means that the measurement of A_0 and S_0 can be used to independently quantify both the normal and shear stiffnesses of an interface. Again this finding was explained by consideration of the in-plane and normal surface displacements of the modes (i.e., A_0 is dominated by normal displacement and S_0 by in-plane displacement).

In a separate experiment, high frequency (1 MHz) normal incidence longitudinal wave measurements were used to measure the glass-elastomer interfacial normal stiffness as a function of load. Good agreement was found between stiffness obtained from these normal incidence measurements and stiffness measured via A_0 and S_0 attenuation measurements.

ACKNOWLEDGMENTS

The authors would like to thank Pascale Brassier from EADS-LV, France who supplied the elastomer samples.

Alleyne, D. N., and Cawley, P. (**1996**). ''The Excitation of Lamb Waves in Pipes Using Dry Coupled Piezoelectric Transducers,'' J. Nondestruct. Eval. **15**, 11–20.

Auld, B. A. (**1990**). *Acoustic Fields and Waves in Solids*, 2nd ed. (Krieger, Malabar), Chap. 3, pp. 57–99.

Baik, J-M., and Thompson, R. B. (**1984**). ''Ultrasonic Scattering from Imperfect Interfaces: a Quasi-Static Model,'' J. Nondestruct. Eval. **4**, 177–196.

Baltazar, A., Rokhlin, S. I., and Pecorari, C. (**2002**). ''On the relationship between ultrasonic and micromechanical properties of contacting rough surfaces,'' J. Mech. Phys. Solids **50**, 1397–1416.

Castaings, M., and Hosten, B. (**2001**). ''Lamb and SH waves generated and detected by air-coupled ultrasonic transducers in composite material plates,'' NDT & E Int. **34**(6), 249–258.

Dalton, R. P., Cawley, P., and Lowe, M. J. S. (**2001**). ''The Potential of Guided Waves for Monitoring Large Areas of Metallic Aircraft Fuselage Structure,'' J. Nondestruct. Eval. **20**(1), 29–46.

Drinkwater, B. W., Dwyer-Joyce, R. S., and Cawley, P. (**1996**). ''A Study of the Interaction Between Ultrasound and a Partially Contacting Solid-Solid Interface,'' Proc. R. Soc. London, Ser. A **452**, 2613–2628.

Haines, N. F. (**1980**). ''The Theory of Sound Transmission and Reflection at Contacting Surfaces,'' CEGB Berkeley Nuclear Laboratories, Berkeley, U.K., Report No. RD/B/N4744.

Honein, B., Braga, A. M. B., Barbone, P., and Herrmann, G. (**1991**). ''Wave propagation in piezoelectric layered media with some applications,'' J. Intell. Mater. Syst. Struct. **2**, 542–557.

Kendal, K., and Tabor, D. (**1971**). ''An Ultrasonic Study of the Area of Contact Between Stationary and Sliding Surfaces,'' Proc. R. Soc. London, Ser. A **323**, 321–340.

Krolikowski, J., and Szczepek, J. (**1991**). ''Prediction of Contact Parameters Using Ultrasonic Method,'' Wear **148**, 181–195.

Kundu, T., and Maslov, K. (**1997**). ''Material Interface Inspection by Lamb Waves,'' Int. J. Solids Struct. **34**(29), 3885–3901.

Kundu, T., Maji, A., Ghosh, T., and Maslov, K. (**1998**). ''Detection of Kissing Bonds by Lamb Waves,'' Ultrasonics **35**, 573–580.

Lavrentyev, A. I., and Rokhlin, S. I. (**1998**). ''Ultrasonic spectroscopy of imperfect interfaces between a layer and two solids,'' J. Acoust. Soc. Am. **103**, 657–664.

Lowe, M. J. S. (**1995**). ''Matrix techniques for Modelling Ultrasonic Waves in Multilayered Media,'' IEEE Trans. Ultrason. Ferroelectr. Freq. Control **42**(4), 525–542.

Mal, A. K., Xu, P. C., and Bar-Choen, Y. (**1989**). ''Analysis of Leaky Lamb Waves in Bonded Plates,'' Int. J. Eng. Sci. **27**(7), 779–791.
Margetan, F. J., Thompson, R. B., Rose, J. H., and Gray, T. A. (**1992**). ''The Interaction of Ultrasound with Imperfect Interfaces: Experimental Studies of Model Structures,'' J. Nondestruct. Eval. **11**, 109–125.
Mattei, C., Jia, X., and Quentin, G. (**1997**). ''Direct experimental investigations of acoustic modes guided by a solid-solid interface using optical interferometry,'' J. Acoust. Soc. Am. **120**, 1532–1539.
Murty, G. S., and Kumar, V. (**1991**). ''Elastic Wave Propagation with Kinematic Discontinuity Along a Non-Ideal Interface Between Two Isotropic Elastic Half-Spaces,'' J. Nondestruct. Eval. **10**(2), 39–53.
Nagy, P. B. (**1992**). ''Ultrasonic Classification of Imperfect Interfaces,'' J. Nondestruct. Eval. **11**, 127–139.
Pialucha, T., Lowe, M. J. S., and Cawley, P. (**1993**). ''Validity of Different Models of Interfaces in Adhesion and Diffusion Bonded Joints,'' in *Review of Progress in Quantitative NDE*, Vol. 12, edited by D. O. Thompson, and D. E. Chimenti (Plenum, New York).
Rokhlin, S. I., and Wang, Y. J. (**1991**). ''Analysis of boundary-conditions for elastic wave interaction with an interface between two solids,'' J. Acoust. Soc. Am. **89**, 503–515.
Rokhlin, S. I., Hefets, M., and Rosen, M. (**1981**). ''An Ultrasonic Interface-Wave Method for Predicting the Strength of Adhesive Bonds,'' J. Appl. Phys. **52**(4), 2847–2851.
Rose, J. L., Ditri, J. J., Pilarski, A., Rajana, K., and Carr, F. T. (**1994**). ''A Guided Wave Inspection Technique for Nuclear Steam Generator Tubing,'' NDT & E Int. **27**, 307–330.
Seifried, R., Jacobs, L. J., and Qu, J. (**2002**). ''Propagation of Guided Waves in Adhesive Bonded Components,'' NDT & E Int. **35**, 317–328.

Precise measurements of bulk-wave ultrasonic velocity dispersion and attenuation in solid materials in the VHF range

Jun-ichi Kushibiki,[a] Ryoichi Okabe, and Mototaka Arakawa
Department of Electrical Engineering, Tohoku University, Sendai 980-8579, Japan

(Received 20 November 2001; revised 24 January 2003; accepted 14 February 2003)

A general method was established for precisely measuring velocity dispersion and attenuation in solid specimens with acoustic losses in the very high frequency (VHF) range, using the complex-mode measurement method and the diffraction correction method. Experimental procedures were presented for implementing such a method and demonstrated this measurement method in the frequency range of 50–230 MHz, using borosilicate glass (C-7740) as a dispersive specimen and synthetic silica glass (C-7980) as a nondispersive standard specimen. C-7980 exhibited no velocity dispersion; velocity was constant at 5929.14 ± 0.03 m/s. C-7740 exhibited velocity dispersion, from 5542.27 m/s at 50 MHz to 5544.47 m/s at 230 MHz with an increase of about 2 m/s in the measured frequency range. When frequency dependence of attenuation was expressed as $\alpha = \alpha_0 f^{\beta}$, the results were as follows: $\alpha_0 = 1.07 \times 10^{-16}$ s^2/m and $\beta = 2$ for C-7980 and $\alpha_0 = 5.16 \times 10^{-9}$ s$^{1.25}$/m and $\beta = 1.25$ for C-7740. © *2003 Acoustical Society of America.*
[DOI: 10.1121/1.1568756]

PACS numbers: 43.35.Cg, 43.35.Yb [SGK]

I. INTRODUCTION

In ultrasonic measurements, velocity dispersion and attenuation are the most important quantities to be measured when evaluating materials and studying their physical properties. To conduct research, it is necessary to measure such quantities with higher accuracy in a required frequency range. Various measurement methods using coherent ultrasonic waves have been developed and are broadly divided into three groups: pulse methods, continuous-wave methods, and optical methods.[1,2]

We developed an ultrasonic spectroscopy system using rf tone burst pulses[3] and measured acoustic properties (sound velocity, attenuation, acoustic impedance, and density) of solid materials, liquids, and biological tissues in the VHF and ultrahigh frequency (UHF) ranges. This technology consists of feedback from the technologies related to the previously developed ultrasonic measurement system[4] as well as the technologies of mechanical movement and alignment, and signal processing developed for the line-focus-beam acoustic microscopy system.[5,6] So far, velocity dispersion and attenuation measurements using this system have mainly been performed on liquids and biological tissues.[3,7–9] The system has proven itself to be very useful for obtaining the acoustic properties in the VHF and UHF ranges. This system measures the acoustic properties based on a composite ultrasonic transmission line model. Sound velocities in solid materials are measured using the bulk ultrasonic double-pulse interference method, where they are obtained from the frequency intervals Δf in the interference wave form of the superposed signals when sweeping ultrasonic frequencies. However, the result reflects the average phase gradient in the frequency range analyzed, so the phase velocity at each frequency may not be obtained accurately in the presence of velocity dispersion.

Recently, we have developed a complex-mode measurement method, where the signal amplitude and phase are measured and sound velocity is obtained from the phase, so it is now possible to measure phase velocity at each frequency.[10] Furthermore, we have developed an experimental procedure of correcting diffraction effects on the measured values of sound velocity and attenuation for nondispersive specimens in the VHF and UHF ranges.[10]

In this paper, we establish a general method for precisely measuring velocity dispersion and attenuation in solid specimens using the complex-mode measurement method and the diffraction correction method. This measurement method is demonstrated by taking Pyrex glass (borosilicate glass) as a specimen with velocity dispersion, and synthetic silica glass as a standard specimen with no velocity dispersion in the VHF range.

II. MEASUREMENT METHOD AND SYSTEM

A. Method

The method of precisely measuring sound velocity for nondispersive specimens was presented in detail previously[10] and is extended to apply to dispersive solid specimens. Figure 1 shows the experimental arrangement for measuring acoustic properties of a solid specimen using the complex-mode measurement method. Measurements are performed in the reflection mode in the composite ultrasonic transmission line using rf tone burst ultrasonic pulses. A synthetic silica (SiO_2) glass rod with a transducer mounted on one end is used as the ultrasonic device for longitudinal waves. Ultrasonic plane waves emitted by the transducer are transmitted through a water couplant to the specimen. Let us express signals reflected from the rod end as $\mathbf{V}_1$, from the front face of the specimen as $\mathbf{V}_2$, and from the back face as $\mathbf{V}_3$. By

[a]Electronic mail: kushi@ecei.tohoku.ac.jp

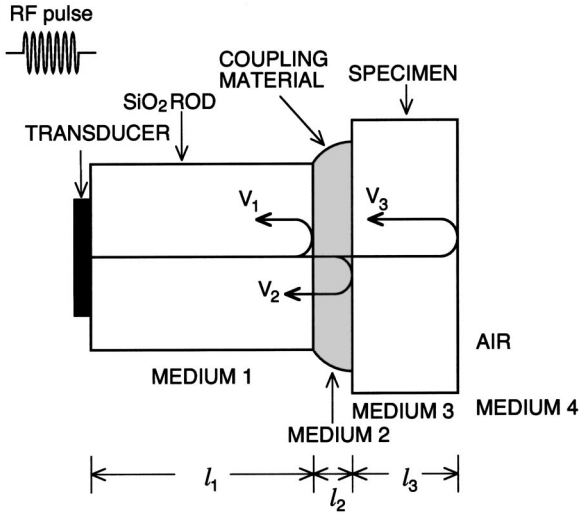

FIG. 1. Experimental arrangement for bulk velocity and attenuation measurements of solid specimens using ultrasonic rf pulses.

properly setting the width of rf pulses, the propagation length in the couplant of l_2, and the thickness of the specimen to an appropriate value l_3, we can separate signals $\mathbf{V}_2$ and $\mathbf{V}_3$ from other spurious signals in the time domain.

To extend the velocity measurement method for dispersive media of the specimen, we have to take into consideration the influence of the acoustic losses in each propagation medium with the complex acoustic impedance Z_i ($i=1$, 2, 3, and 4), especially in the specimen, in the ultrasonic transmission line model. The phase rotation in the specimen needed to determine sound velocity is obtained by normalizing $\mathbf{V}_3$ by $\mathbf{V}_2$ as follows:

$$\frac{\mathbf{V}_3}{\mathbf{V}_2}=\frac{|ATT_3|}{|ATT_2|}\left|\frac{T_{23}T_{32}}{R_{23}}\right|\exp(-2\alpha_3 l_3)\times\exp\{j(-2k_3 l_3+\pi+\Delta\theta+\theta_{\mathrm{TR}})\}. \tag{1}$$

In Eq. (1), ATT_i is the diffraction effect during the propagation of each signal, T_{ij} and R_{ij} are the transmission and reflection coefficients when the ultrasonic wave is incident from medium i to medium j. The reflection coefficient R_{34} at the specimen/air interface is treated to be -1 and the phase rotates by π. α_3 and k_3 are the attenuation and phase constants, and as a function of frequency f, and l_3 is the length of the specimen. The diffraction effect is expressed as

$$ATT_i=|ATT_i|\exp(j\theta_i), \tag{2}$$

where the amplitude and phase are examined separately. In Eq. (1), $\Delta\theta=\theta_3-\theta_2$. The phase of $\mathbf{V}_3/\mathbf{V}_2$ is expressed as

$$\phi=-2k_3 l_3+\pi+\Delta\theta+\theta_{\mathrm{TR}}. \tag{3}$$

As the phase velocity V is ω/k, the sound velocity in the specimen V_3 can be expressed using ϕ by

$$V_3=-\frac{2\omega l_3}{\phi-\pi-\Delta\theta-\theta_{\mathrm{TR}}}. \tag{4}$$

In measuring sound velocity, the difference in phase advance $\Delta\theta$ due to diffraction and the phase change θ_{TR} due to transmission and reflection affect the measured value. When the

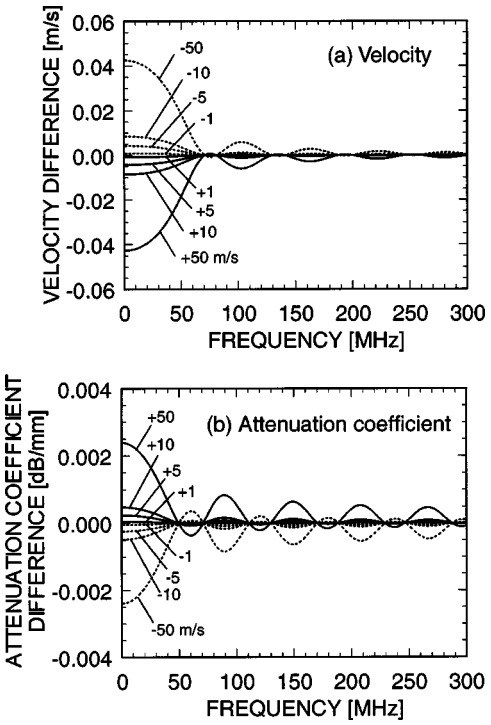

FIG. 2. Errors of velocity and attenuation estimated when making diffraction correction by numerical calculations using different sound velocities with changes of ±1, ±5, ±10, and ±50 m/s.

effect of θ_{TR} on the velocity was examined using the measured values of Pyrex glass obtained in this paper, together with the acoustic properties of synthetic silica glass[10,11] and pure water,[12–14] it was found to be within ±0.003 m/s in the measured frequency range. So, the effect is negligible.

The attenuation coefficient can be obtained in the following expression from Eq. (1):

$$\alpha_3=\frac{1}{2l_3}\ln\left\{\left|\frac{\mathbf{V}_2}{\mathbf{V}_3}\right|\cdot\left|\frac{T_{23}T_{32}}{R_{23}}\right|\right\}-\frac{1}{2l_3}\ln\left|\frac{ATT_2}{ATT_3}\right|. \tag{5}$$

The diffraction loss ratio, $|ATT_2/ATT_3|$, affects the measured value of attenuation coefficient.

To precisely measure velocity dispersion and attenuation, it is essential to compensate for diffraction effects on them. The diffraction effects on sound velocity and attenuation measurements can be compensated[10] through numerical calculations using William's expression.[15]

The validity of this correction method was demonstrated for nondispersive specimens. However, for dispersive media, sound velocity varies depending on the frequency, so this effect must be considered. We numerically investigate the effects on the measurement errors when making the diffraction correction while varying sound velocities of the specimen by ±1, ±5, ±10, and ±50 m/s for the true velocities at each frequency. The calculated results for sound velocities are shown in Fig. 2(a); those for attenuation, in Fig. 2(b). Here, the following parameters were adopted for numerical calculations. The sound velocity for the specimen was assumed as 6000 m/s at each frequency, and thickness, as 5 mm. Using the values in Table I as parameters for the ultrasonic device, the sound velocity of the SiO_2 buffer rod was 5954.1 m/s. The propagation length in the water couplant

TABLE I. Parameters of the ultrasonic device used for measurements.

Center frequency	195 MHz
Transducer material	ZnO
Diameter of transducer	2.5 mm
Rod material	SiO_2
Rod length	9.9827 mm
Diameter of rod	8.4 mm

was 830 μm with a sound velocity of 1491 m/s. Both sound velocity and attenuation tend to include larger errors as the sound velocity used for calculations deviates more from the actual value and as the measurement frequency decreases. For example, when calculations for diffraction correction were made at 50 MHz using sound velocity differences of ± 10 m/s, an error of ± 0.004 m/s was estimated for sound velocity, and an error of ± 0.001 dB/mm for attenuation coefficient. Therefore, we consider the influence of velocity dispersion on the sound velocity and attenuation measurements to be very small.

A flow chart of the procedures for precisely measuring velocity dispersion using the complex-mode measurement method is shown in Fig. 3. First, the amplitudes and phases of signals $\mathbf{V}_2$ and $\mathbf{V}_3$ are measured by scanning the frequencies. The phases are greatly affected by the temperature, so the signals $\mathbf{V}_2$ and $\mathbf{V}_3$ are alternately measured at each frequency under the same temperature condition. $\mathbf{V}_3/\mathbf{V}_2$ given in Eq. (1) is calculated and ϕ including the phase rotation in the specimen is extracted. ϕ involves diffraction effects that must be compensated. In Fig. 3, $V_3(1)$ and $V_3(n)$ are the first and nth calculations of V_3. For $\mathbf{V}_2$ and $\mathbf{V}_3$ signals, the propagation lengths normalized by the Fresnel length for all media are obtained[16] and summed up,[17] for which, first, the

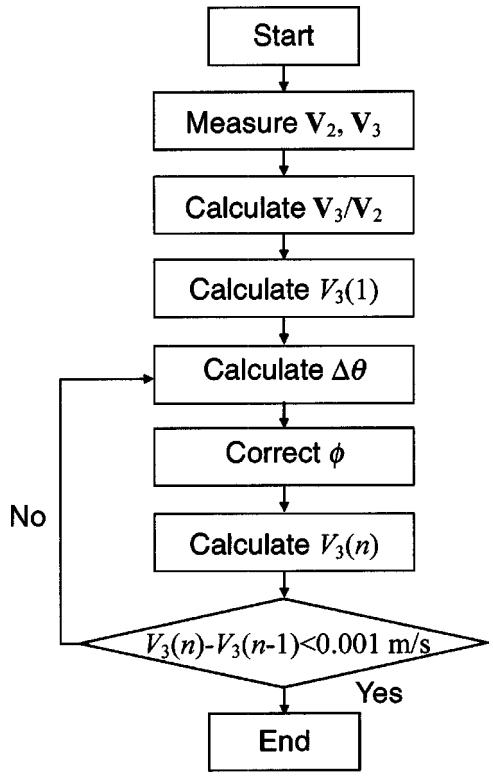

FIG. 3. Experimental procedures for velocity dispersion measurements.

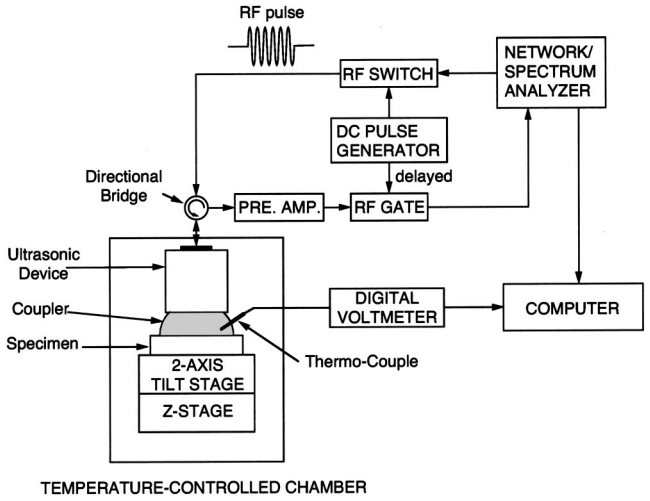

FIG. 4. Block diagram of the bulk ultrasonic spectroscopy system.

sound velocities $V_3(1)$ are determined by ignoring diffraction effects. These values are substituted into William's expression, and the phase advances due to diffraction, θ_2 and θ_3, are calculated to obtain $\Delta\theta$. Obtained $\Delta\theta$ values are substituted into Eq. (4) to obtain the sound velocities $V_3(2)$ corrected for diffraction. Using the corrected sound velocities, the Fresnel length at each frequency is obtained again, diffraction effects are recalculated, and the sound velocities are corrected. This routine is repeated until the sound velocities $V_3(n-1)$ used for numerical calculations coincide with the corrected sound velocities $V_3(n)$ within a difference of less than 0.001 m/s in order to determine precise sound velocities.

For attenuation, $|T_{23}T_{32}/R_{23}|$ in Eq. (5) is calculated and the diffraction losses are numerically calculated, using the sound velocities at each frequency that were determined earlier.

B. System

Measurements were performed using the ultrasonic spectroscopy system.[10] This system enables us to measure the bulk acoustic properties (sound velocity, attenuation, acoustic impedance, and density) of solid materials, liquids, and biological tissues in the VHF and UHF ranges. This system is described in detail in the literature.[3,4,10] A block diagram of the system is shown in Fig. 4. This system is primarily composed of a pulse-mode measurement system[4] and can be broadly divided into the electrical circuit section, ultrasonic device, mechanical operation section, temperature measurement section, and computer.

The ultrasonic device consists of a SiO_2 glass buffer rod with both ends parallel and optically polished and with a ZnO film ultrasonic transducer formed on one end by the dc sputtering method. The radius of the rod was taken to be sufficiently larger than the radius of the transducer to avoid any influences of the waves reflected from the wall of the rod on measurements. The specifications for the ultrasonic device are shown in Table I, and the frequency characteristics of the insertion loss are shown in Fig. 5. The central frequency of operation is around 195 MHz. Figure 5 shows that

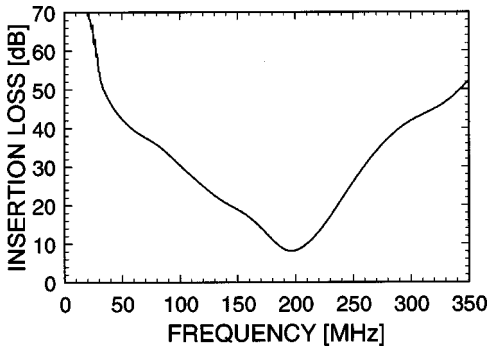

FIG. 5. Frequency characteristics of insertion loss of the ultrasonic device.

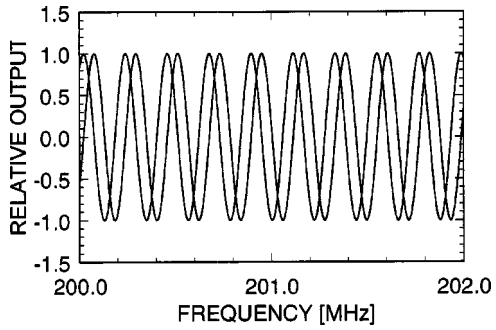

FIG. 6. An example of frequency response of $\mathbf{V}_2$ signal measured in complex mode. Specimen: C-7740.

the frequency range for accurately measuring signals with sufficient S/N is 80–230 MHz, considering the losses due to the use of pure water as the couplant (propagation loss in water and transmission/reflection losses at the interfaces with the solid).

It is very important to stabilize the temperature for phase measurements. Therefore, the whole system was installed in a temperature-controlled room where the temperature is controlled to within $\pm 0.1\,^{\circ}\mathrm{C}$ from the set temperature. To further stabilize the temperature environment around the ultrasonic device and specimen for a long time, they are installed in a temperature-controlled chamber that maintains the temperature within $\pm 0.01\,^{\circ}\mathrm{C}$. The temperature in the couplant when measuring acoustic properties and the temperature around the specimen were measured by a copper–constantan thermocouple (JIS T-model, Class 1, CHINO Co.) calibrated to within $\pm 0.01\,^{\circ}\mathrm{C}$ using a platinum resistance thermometer (model R800-2, CHINO Co.).

In complex-mode measurements, the real (V_{Re}) and imaginary (V_{Im}) parts of complex signals are measured by means of a quadrature detector. V_{Re} and V_{Im} are expressed as follows:

$$V_{\mathrm{Re}} = B\cos\phi, \tag{6}$$

$$V_{\mathrm{Im}} = B\sin\phi, \tag{7}$$

where B is the amplitude and ϕ is the phase. The amplitude and phase are given by

$$B = \sqrt{V_{\mathrm{Re}}^2 + V_{\mathrm{Im}}^2}, \tag{8}$$

$$\phi = \tan^{-1}\left(\frac{V_{\mathrm{Im}}}{V_{\mathrm{Re}}}\right). \tag{9}$$

A typical example of the measured result of $\mathbf{V}_2$ signals (V_{Re},V_{Im}) for a borosilicate glass [C-7740 (Pyrex)] specimen is shown in Fig. 6. The amplitudes and phases of $\mathbf{V}_2$ and $\mathbf{V}_3$ signals are obtained.

III. EXPERIMENTS AND RESULTS

Experiments of precisely measuring velocity dispersion and attenuation were performed for a dispersive specimen of borosilicate glass (C-7740 (Pyrex), Corning Inc.) and a nondispersive specimen of synthetic silica glass (C-7980, Corning Inc.). The C-7980 specimen was used as the reference for this demonstration. The C-7740 specimen has a thickness of 4656.07 μm and a density of 2220.3 kg/m^3. The C-7980 specimen has a thickness of 4985.48 μm and a density of 2199.8 kg/m^3. The specimen thickness was measured using a digital length gauging system with an optical encoder (CERTO, DR. JOHANNES HEIDENHAIN GmbH).[11] The measurement accuracy for thickness is ± 0.06 μm. The specimen density was measured based on the Archimedes method.[18] Both specimens are square plates with a size of 50 mm$\times$50 mm and are optically polished on both sides with a parallelism of less than 4″. Therefore, the influences of the parallelism on the measurement can be ignored. We selected the thicknesses of specimens so that the rf pulse width is at least 500 ns for precise measurements.[4]

The propagation distance in the water couplant between the buffer rod and the specimen was set to about 830 μm to prevent $\mathbf{V}_2$ and $\mathbf{V}_3$ signals from overlapping spurious signals by considering the rod length and the specimen thickness. $\mathbf{V}_2$ and $\mathbf{V}_3$ were measured at $23\pm 0.1\,^{\circ}\mathrm{C}$ and at intervals of 0.06 MHz in the frequency range of 20–250.4 MHz. The temperature deviations during the measurements were within $\pm 0.01\,^{\circ}\mathrm{C}$. According to the literature,[11] variations in sound velocity due to such deviations are estimated to be ± 0.007 m/s or less, which is sufficiently less than the measurement accuracy. The measured results of the amplitude and phase of $\mathbf{V}_3/\mathbf{V}_2$ for the C-7740 specimen are shown in Figs. 7(a) and (b).

A. Velocity

First, let us show that velocity dispersion can be determined from changes in phase. The phase ϕ of $\mathbf{V}_3/\mathbf{V}_2$ varies linearly as seen from Fig. 7(b), so the phase delays of about $605\,^{\circ}$ can be observed as the frequency increases by 1 MHz both for the C-7980 and C-7740 specimens. It is extremely difficult to determine the slight changes in phase due to diffraction and velocity dispersion from those wave forms. Therefore, we drew an approximated straight line (ϕ_a) for the data in the frequency range of 80–230 MHz, where there is a good S/N of the signals, using the least-squares method. We then extrapolated this line to the whole measured frequency range. We obtained the differences from the measured values ϕ, $\Delta\phi$ ($=\phi-\phi_a$), and processed the moving average of the results at ± 4.8 MHz (± 80 points). The results are shown in Fig. 8(a) for the C-7980 specimen and in Fig. 8(b) for the C-7740 specimen. As shown in these figures, both C-7980 and C-7740 have variations in wave form. This is an experimental extraction of the influences of the phase

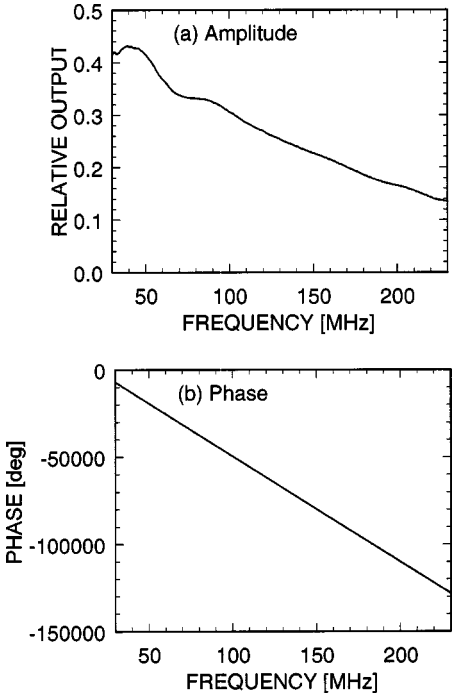

FIG. 7. Measured results for $\mathbf{V}_3/\mathbf{V}_2$ for borosilicate glass (C-7740).

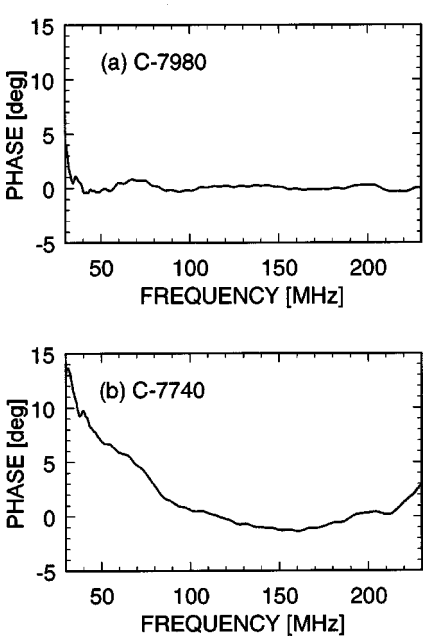

FIG. 9. Phase variations of $\mathbf{V}_3/\mathbf{V}_2$ after diffraction correction by numerical calculations.

advance difference $\Delta\theta$ due to diffraction and the velocity dispersion. It is necessary to obtain $\Delta\theta$ and compensate the results for the C-7980 specimen using the method described in the literature[10] and for the C-7740 specimen using the above-described method. If the corrected phases are expressed as ϕ', then $\phi' = \phi - \Delta\theta = -2k_3 l_3 + \pi$. The wave number k is defined as $k = \omega/V(f)$. If there is no velocity dispersion, $V(f)$ is constant, and wave number k and ϕ' are proportional to the frequency. In contrast, if there is velocity dispersion, ϕ' does not exhibit a linear dependence. ϕ' was obtained for the C-7980 and C-7740 specimens. The results are shown in Figs. 9(a) and (b). For the C-7980 specimen, wave form variations due to diffraction have been almost perfectly removed as shown in Fig. 9(a), and the phases where the approximated straight line was drawn are approximately 0°, demonstrating that ϕ is proportional to the frequency. For the C-7740 specimen, small wave form variations in Fig. 8(b) have been removed as shown in Fig. 9(b), but the phases formed a smooth curve that is convex downward. The phase varies depending on the frequency, showing that velocity dispersion has been determined.

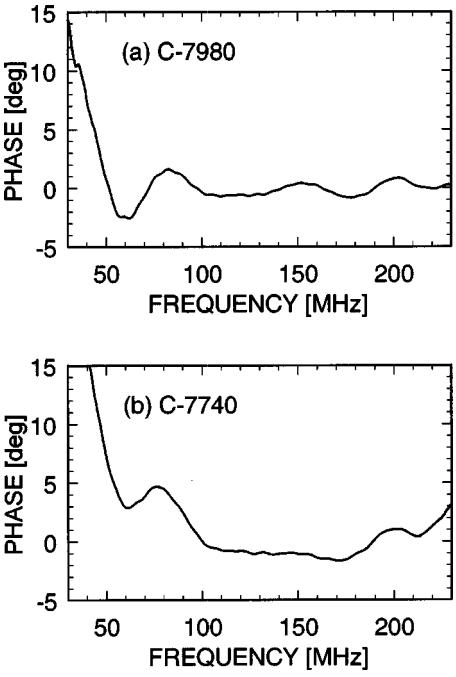

FIG. 8. Phase variations of $\mathbf{V}_3/\mathbf{V}_2$ ($\Delta\phi = \phi - \phi_a$).

Next, the sound velocities were actually determined from ϕ'. The results for the C-7980 and C-7740 specimens are shown in Figs. 10(a) and (b). The dotted lines represent the measured values, i.e., the values obtained directly from ϕ. The solid lines represent the values compensated for diffraction effects, i.e., the values obtained from ϕ'. For the C-7980 specimen, almost constant values were obtained regardless of the frequency, resulting in no velocity dispersion in the measured frequency range. As described previously, the frequency range where the signals can be measured with a good S/N is 80–230 MHz. The frequencies where $S=1$ are 100 MHz for C-7980 and 115 MHz for C-7740. At frequencies exceeding these values, diffraction effects become much less. Therefore, we can consider the frequency range where highly accurate sound velocities are obtained to be 100–230 MHz. From 50 to 100 MHz, slight variations in sound velocity still exist. In any case, from 100 to 230 MHz, the sound velocities for the C-7980 specimen can be obtained as 5929.14 ± 0.03 m/s. From this we can say that the measurement accuracy of sound velocities for the C-7740 specimen shown in Fig. 10(b) after diffraction correction is within ± 0.03 m/s at each frequency between 100 and 230 MHz. The sound velocities of longitudinal waves in C-7740 of borosilicate glass obviously exhibit velocity dispersion.

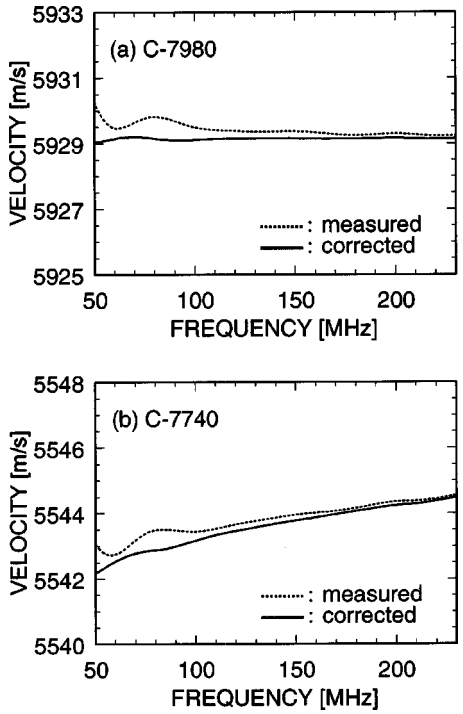

FIG. 10. Compensation of diffraction effects on sound velocity.

B. Attenuation

The measured results of attenuation for C-7740 are shown in Fig. 11. The water density required for calculating the transmission and reflection coefficients was obtained using the temperature during the measurement from the literature.[14] The curve represented by the dotted line represents the measured values of the attenuation coefficient obtained based on the measured results shown in Fig. 7(a) using only the first term of Eq. (5). The dashed-and-dotted curve represents the numerically calculated results of diffraction loss, $\{\ln|ATT_2/ATT_3|/(2l_3)\}$. The attenuation coefficient with diffraction loss compensated by Eq. (5) increases monotonically without a peak around 70 MHz, as seen in the measured results. This demonstrates that the diffraction loss can be compensated through numerical calculations so that accurate attenuation coefficients can be obtained.

The attenuation coefficient can be generally expressed as

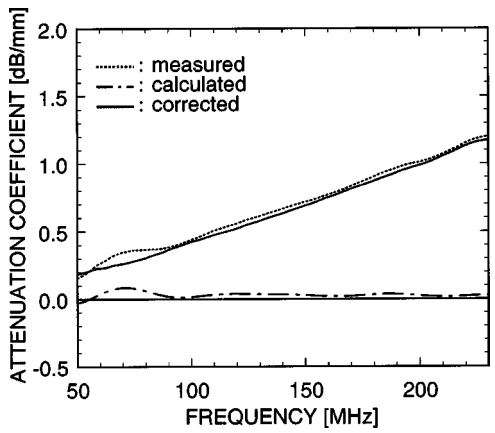

FIG. 11. Compensation of diffraction effects on attenuation coefficient for C-7740 specimen.

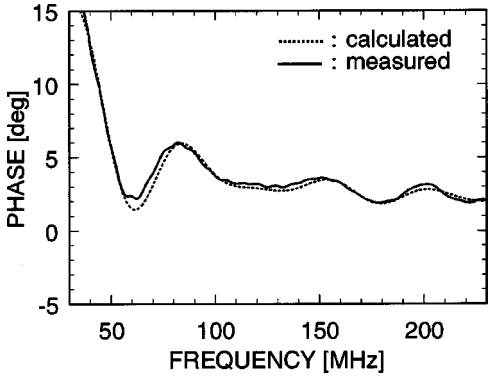

FIG. 12. Measured and calculated results of phase advance difference $\Delta\theta$ for C-7980 specimen.

$\alpha=\alpha_0 f^{\beta}$. When the values of α_0 and β are obtained by the least-squares method, results are $\alpha_0=1.07\times10^{-16}$ s^2/m and $\beta=2$ for the C-7980 specimen and $\alpha_0=5.16\times10^{-9}$ s$^{1.25}$/m and $\beta=1.25$ for the C-7740 specimen.

IV. DISCUSSION

We have shown that velocity dispersion can be precisely determined in a frequency range where the S/N of signals and the propagation distance normalized by the Fresnel length, S, are considered. However, we would like to measure velocity dispersion over a wider frequency range, especially at lower frequencies, to study materials and their physical properties. Therefore, we investigated the variations in sound velocity in the range of 50–100 MHz, which exist even after diffraction correction, and conducted studies for obtaining accurate velocity values even at frequencies below 100 MHz.

For the C-7980 specimen, we compared the experimental results of the phase advance differences $\Delta\theta$ and the calculated results using the parameters in Table I as shown in Fig. 12. The calculated profile is quite similar to the measured one, but is slightly shifted to the right in frequency. This is considered to be the main reason for the slight variations in velocity observed in the frequency range from 50 to 100 MHz as shown in Fig. 10(a), because some of the parameters needed for the calculation of diffraction correction slightly differ from those under the actual experimental conditions, e.g., the actual diameter of the transducer electrode, which was fabricated with a metal mask of 2.5-mm diameter ϕ by evaporation technique, was estimated to be 2.52-mm diameter ϕ. We also examined the disturbance of sound fields because of the insufficient radius of the buffer rod and found its effect to be less than ±0.02 m/s in the measured frequency range by numerically calculating the effects of finite dimensions of the buffer rod using Del Grosso's expression.[19] Therefore, this effect can be ignored. We thus considered that the main cause of the variations was slight differences in some of the parameters for the ultrasonic device. Therefore, we devised the following simple and appropriate compensation method by considering that the variations are due to the frequency characteristics of the total device performance, including the effect of the slightly different diameter on the diffraction correction. First, we ob-

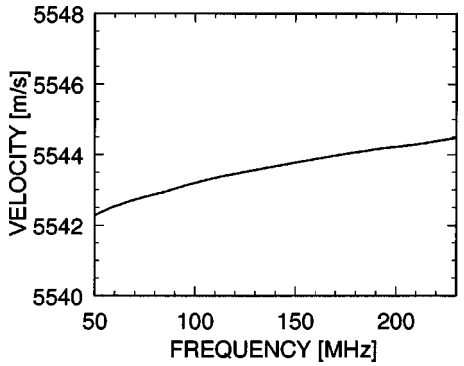

FIG. 13. Velocity dispersion of C-7740 specimen corrected using the sound velocities measured for C-7980 specimen.

tained the sound velocities of the specimen to be compensated $[V(f)]$ and the sound velocities of the reference specimen $[V_{\mathrm{Ref}}(f)]$ that exhibit no velocity dispersion using the same device, within the same frequency range, and at the same frequency steps, according to the diffraction correction method previously described. Next, we normalized $V(f)$ by $V_{\mathrm{Ref}}(f)$ as follows:

$$a(f)=\frac{V(f)}{V_{\mathrm{Ref}}(f)}, \tag{10}$$

where $a(f)$ is the normalized sound velocity. The sound velocity of the reference specimen is constant in the frequency range where the S/N of signals and $S<1$ are considered. We then define that value as V_{R}. By multiplying $a(f)$ by V_{R}, we can obtain the sound velocities $[V'(f)]$ where the device characteristics have been removed,

$$V'(f)=a(f)V_{\mathrm{R}}. \tag{11}$$

This compensation method was applied to the results of the C-7740 specimen. In this case, $V(f)$ represents the sound velocities of the C-7740 specimen, and $V_{\mathrm{Ref}}(f)$, the sound velocities of the C-7980 specimen. V_{R} is the sound velocity of synthetic silica glass (C-7980) as determined in the range of 100–230 MHz, i.e., 5929.14 m/s. The corrected results are shown in Fig. 13. It can be seen that there are much smaller variations in sound velocity in the range of 50–100 MHz. Furthermore, the measured values coincide with the corrected values within a difference of less than 0.03 m/s in the range of 100–230 MHz. We consider that a similar accuracy has been achieved in the extrapolated frequency range and that accurate values have been obtained in the range of 50–230 MHz.

V. CONCLUDING REMARKS

In this paper, we developed a method of precisely measuring velocity dispersion and attenuation for dispersive solid specimens in the VHF range and presented the measurement procedures. We demonstrated that velocity dispersion can be determined as changes in phase using the complex-mode measurement method and that the sound velocities can thus be obtained as a function of frequency. Furthermore, we developed a diffraction correction method for materials having velocity dispersion. By selecting borosilicate glass (C-7740) and synthetic silica glass (C-7980) specimens and measuring velocities and attenuations in the VHF range, we proved that the frequency dependence of sound velocities can be measured to an accuracy of ± 0.03 m/s and thus velocity dispersion can be determined accurately. We also showed that precise values of attenuation can be obtained. Furthermore, we studied a method of compensating the changes in sound velocity, which are considered to be caused by the device characteristics, and successfully obtained precise velocity dispersion over a wider range of frequencies.

This study used pure water as the coupling material, so the measurement frequency range is limited to 300 MHz due to the large propagation attenuation and low acoustic impedance of water. Measurements in the structure of the specimen bonded to the ultrasonic device enable us to obtain velocity dispersion over a higher frequency range.

ACKNOWLEDGMENTS

The authors are very grateful to Y. Okada, Kougakugiken Co., Ltd., for preparing the specimens. This work was supported in part by a Research Grant-in-Aid from the Ministry of Education, Science and Culture of Japan.

[1] M. A. Breazeale, J. H. Cantrell, Jr., and J. S. Heyman, "Ultrasonic wave velocity and attenuation measurements," in *Methods of Experimental Physics*, Ultrasonics, Vol. 19, edited by P. D. Edmonds (Academic, New York, 1981), Chap. 2, pp. 67–135.
[2] J. H. Cantrell and W. T. Yost, "Ultrasonic velocity," in *Encyclopedia of Acoustics*, edited by M. J. Crocker (Wiley, New York, 1997), Vol. 2, Chap. 55, pp. 629–639.
[3] J. Kushibiki, N. Akashi, T. Sannomiya, N. Chubachi, and F. Dunn "VHF/UHF range bioultrasonic spectroscopy system and method," IEEE Trans. Ultrason. Ferroelectr. Freq. Control **42**, 1028–1039 (1995).
[4] J. Kushibiki, T. Sannomiya, and N. Chubachi, "A useful acoustic measurement system for pulse mode in VHF and UHF ranges," IEEE Trans. Sonics Ultrason. **SU-29**, 338–342 (1982).
[5] J. Kushibiki and N. Chubachi, "Material characterization by line-focus-beam acoustic microscope," IEEE Trans. Sonics Ultrason. **SU-32**, 189–212 (1985).
[6] J. Kushibiki, Y. Ono, Y. Ohashi, and M. Arakawa, "Development of the line-focus-beam ultrasonic material characterization system," IEEE Trans. Ultrason. Ferroelectr. Freq. Control **49**, 99–113 (2002).
[7] N. Akashi, J. Kushibiki, N. Chubachi, and F. Dunn, "Acoustic properties of selected bovine tissues in the frequency range 20–200 MHz," J. Acoust. Soc. Am. **98**, 3035–3039 (1995).
[8] N. Akashi, J. Kushibiki, and F. Dunn, "Acoustic properties of egg yolk and albumen in the frequency range 20–400 MHz," J. Acoust. Soc. Am. **102**, 3774–3778 (1997).
[9] N. Akashi, J. Kushibiki, and F. Dunn, "Measurements of acoustic properties of aqueous dextran solutions in the VHF/UHF range," Ultrasonics **38**, 915–919 (2000).
[10] J. Kushibiki and M. Arakawa, "Diffraction effects on bulk-wave velocity and attenuation measurements," J. Acoust. Soc. Am. **108**, 564–573 (2000).
[11] J. Kushibiki, M. Arakawa, and R. Okabe, "High-accuracy standard specimens for the line-focus-beam ultrasonic material characterization system," IEEE Trans. Ultrason. Ferroelectr. Freq. Control **49**, 827–835 (2002).
[12] W. Kroebel and K.-H. Mahrt, "Recent results of absolute sound velocity measurements in pure water and sea water at atmospheric pressure," Acustica **35**, 154–164 (1976).
[13] J. M. M. Pinkerton, "The absorption of ultrasonic waves in liquids and its relation to molecular constitution," Proc. Phys. Soc. Sect. B **62**, 129–141 (1949).
[14] F. E. Jones and G. L. Harris, "ITS-90 density of water formulation for volumetric standards calibration," J. Res. Natl. Inst. Stand. Technol. **97**, 335–340 (1992).
[15] A. O. Williams, Jr., "The piston source at high frequencies," J. Acoust. Soc. Am. **23**, 1–6 (1951).

[16] H. Seki, A. Granato, and R. Truell, ''Diffraction effects in the ultrasonic field of a piston source and their importance in the accurate measurement of attenuation,'' J. Acoust. Soc. Am. **28**, 230–238 (1955).
[17] E. P. Papadakis, ''Ultrasonic attenuation in thin specimens driven through buffer rods,'' J. Acoust. Soc. Am. **44**, 724–734 (1968).
[18] H. A. Bowman and R. M. Schoonover, ''Procedure for high precision density determinations by hydrostatic weighing,'' J. Res. Natl. Bur. Stand., Sect. C **71**, 179–198 (1967).
[19] V. A. Del Grosso, ''Systematic errors in ultrasonic propagation parameter measurements part 2—effective of guided cylindrical modes,'' NRL Report No. 6133, National Research Laboratory, Washington, DC, 1965.

Background noise in piezoresistive, electret condenser, and ceramic microphones[a)]

Allan J. Zuckerwar and Theodore R. Kuhn
NASA Langley Research Center, Mail Stop 493, Hampton, Virginia 23681

Roman M. Serbyn
Physics Department, Morgan State University, Baltimore, Maryland 21251

(Received 2 August 2002; revised 16 March 2003; accepted 17 March 2003)

Background noise studies have been extended from air condenser microphones to piezoresistive, electret condenser, and ceramic microphones. Theoretical models of the respective noise sources within each microphone are developed and are used to derive analytical expressions for the noise power spectral density for each type. Several additional noise sources for the piezoresistive and electret microphones, beyond what had previously been considered, were applied to the models and were found to contribute significantly to the total noise power spectral density. Experimental background noise measurements were taken using an upgraded acoustic isolation vessel and data acquisition system, and the results were compared to the theoretically obtained expressions. The models were found to yield power spectral densities consistent with the experimental results. The measurements reveal that the $1/f$ noise coefficient is strongly correlated with the diaphragm damping resistance, irrespective of the detection technology, i.e., air condenser, piezoresistive, etc. This conclusion has profound implications upon the expected $1/f$ noise component of micromachined (MEMS) microphones. [DOI: 10.1121/1.1572147]

PACS numbers: 43.38.Ar, 43.38.Kb, 43.58.Vb [ADP]

I. INTRODUCTION

The background noise of a measurement microphone is defined as the rms output signal of the microphone in the absence of acoustical excitation. In the past, background noise studies have focused primarily on the air condenser microphone, for which the work is reviewed by Zuckerwar and Ngo[1] and by Gabrielson.[2] The purpose of the present work is to extend the studies to the piezoresistive, electret condenser, and ceramic microphones. Accordingly, the procedure for each microphone is to model the respective noise sources, derive their contributions to the power spectral density, and compare the analytical results with measurements. The models contain several additional noise sources, beyond those considered by Spenser *et al.*[3] for the piezoresistive microphone and by Bevan *et al.*[4] for the electret condenser microphone, that are found here to make significant contributions to the total noise power spectral density. The paper concludes with an analysis of the relationship between the $1/f$ noise coefficient and the diaphragm damping resistance.

II. EXPERIMENTAL METHOD

The methodology underlying the measurements and the salient features of the apparatus, called an ''acoustic isolation vessel,'' are described in an earlier communication.[5] The test microphone was sealed in an inner vessel, the inner vessel suspended in an outer vessel, and the intervening space pumped to a high vacuum. In addition to the test microphone, the inner vessel contained a pressure and a temperature sensor to monitor the microphone environment. The original equipment, however, has been upgraded in several respects. Figure 1 shows the basic components of the measurement system: the vacuum pump, the isolation vessel, and the data-acquisition/signal-processing instrumentation. Substantial improvements were made in each of these subsystems prior to commencing data collection, and the measuring instruments were calibrated against NIST-traceable standards.

First, a major upgrade consisted of replacing the original oil diffusion pump by a more powerful and quieter turbo pump. The new pump proved capable of creating a vacuum better than 10^{-6} Torr in only a few hours. The usual procedure was to perform this step overnight. The sealing of both the inner and the outer vessels, accomplished by means of rubber O-rings compressed between a top plate and the flange terminating the vessel, ensured that the ambient pressure inside the inner vessel remained at atmospheric pressure. The inside temperature remained near 293 K. The vacuum between the two vessels provided a constant level of acoustic isolation during a test, e.g., -155 dB at 40 Hz.

Second, to isolate the vessels and hence the instruments inside from pump vibrations, the original polyethylene tubing used to connect the pump to the outer vessel was replaced by a flexible bellows.

Third, additional vibration isolation was provided by mounting the vessel on an optical table. This measure increased the level of vibration isolation by 20 dB or more over most of the frequency range of the measurements.

Finally, the signal processing capability of the system was greatly augmented by the use of a faster data-acquisition system (B&K type 2035) featuring an extended frequency

[a)]Presented in part at the 143rd Meeting of the Acoustical Society of America.

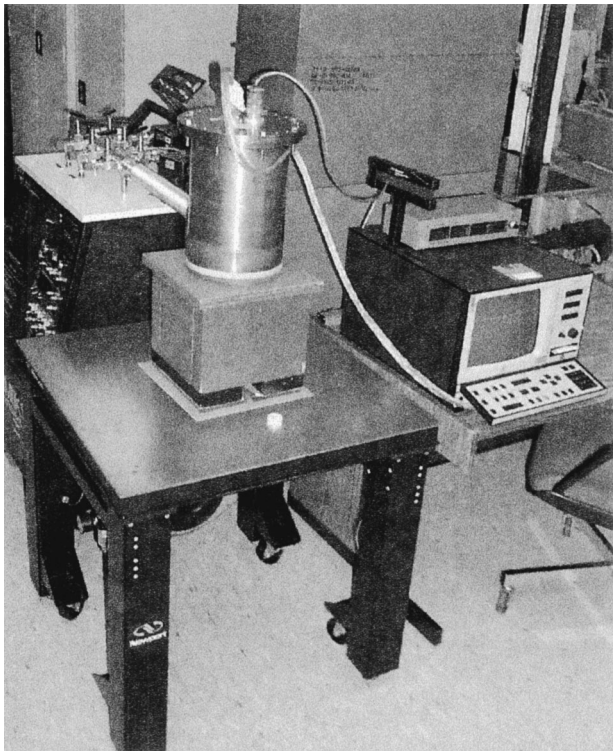

FIG. 1. Acoustic isolation vessel system. The outer vessel in the foreground rests upon a small platform atop an optical table. The vacuum pump is in the background. The signal analyzer and control box for the service instrumentation are to the right.

range (0–102.4 kHz) and retrievable data storage. The latter feature facilitated analysis of the files within the signal analyzer itself or by an external PC. The signal cables connecting the sensors inside the acoustic isolation vessel to outside instrumentation were double-shielded to eliminate rf interference.

Another measure employed to reduce electrical noise consisted of the use of small batteries for the microphones requiring a dc bias or drive voltage, like the piezoresistive or electret condenser microphones. The batteries were enclosed in the inner vessel together with the test microphones. If desired, the terminal voltage of a battery could be monitored continuously, but this was deemed unnecessary because of the short duration of the test runs relative to the battery life.

Prior to installation in the isolation chamber, the test microphone was calibrated by means of a pistonphone at 250 Hz, 124 dB *re*: 20 μPa (B&K type 4228) to determine its sensitivity. The microphone was placed in a specially made adapter that positioned the diaphragm such that a volume correction was not needed. Thus the power spectral density could be read directly in mechanical units (Pa^2/Hz) on the signal analyzer.

III. THE PIEZORESISTIVE MICROPHONE

A. Model

The sensing element in a piezoresistive microphone is a flexible diaphragm containing four strategically located resistors in a Wheatstone bridge configuration. Typically the diaphragm is made of silicon, on which the resistors are formed by deposition or implantation of dopant. An applied pressure P deflects the diaphragm, generates radial and tangential stresses, and causes a change in resistance due to the piezoresistive effect. The open-circuit output voltage of the bridge is

$$V_o = \frac{\delta R}{R} E, \tag{1}$$

where R is the unloaded resistance, δR the change due to the applied stress, and E the bridge excitation voltage. The sensor responds to both static and dynamic pressures.

The model is based on the following assumptions: (1) The diaphragm is a clamped circular plate. (2) The resistors are subjected to the maximum stress found on the diaphragm, i.e., at the periphery. (3) There are no residual stresses in the diaphragm, as may be caused by manufacturing. Then one may write

$$\frac{\delta R}{R} = \pi_p \sigma, \tag{2}$$

where π_p is the piezoresistive coefficient in the direction of the stress σ. Substitution of Eq. (2) into (1) yields

$$V_o = \pi_p \sigma E. \tag{3}$$

The displacement $w(r)$ of a thin vibrating circular plate, excited by an acoustic pressure P, is given by Morse and Ingard:[6]

$$w(r) = \frac{P}{h\rho\omega^2} \frac{I_1(\gamma a)[J_0(\gamma r) - J_0(\gamma a)] + J_1(\gamma a)[I_0(\gamma r) - I_0(\gamma a)]}{I_1(\gamma a)J_0(\gamma a) + J_1(\gamma a)I_0(\gamma a)}, \tag{4}$$

where r is the radial coordinate, and h, a, and ρ are the plate thickness, radius, and density. The J's and I's are Bessel functions and modified Bessel functions of the first kind. The angular frequency ω and the wave number γ are related by the dispersion relation

$$\gamma^4 = \frac{12\omega^2\rho(1-\nu^2)}{Yh^2}, \tag{5}$$

in which Y and ν are the Young's modulus and the Poisson's ratio of the plate taken in the direction of the bridge resistors. The solution satisfies the boundary conditions for a clamped plate:

$$w(a) = 0 \tag{6a}$$

and

$$\frac{dw}{dr}(a)=0. \tag{6b}$$

The relationship between displacement and stress in a plate is given by Timoshenko:[7]

$$\sigma_r=\frac{Yz}{1-\nu^2}\left(\frac{\partial^2 w}{\partial r^2}+\frac{\nu}{r}\frac{\partial w}{\partial r}\right), \tag{7a}$$

$$\sigma_t=\frac{Yz}{1-\nu^2}\left(\nu\frac{\partial^2 w}{\partial r^2}+\frac{1}{r}\frac{\partial w}{\partial r}\right). \tag{7b}$$

In Eqs. (7a)–(7b) σ_r is the radial stress, σ_t the tangential stress, and z the distance from the neutral plane of the plate. Upon substituting Eq. (4) into (7a)–(7b), one finds the surface stress $(z=h/2)$ at the periphery $(r=a)$:

$$\sigma_r(a,h/2)=\frac{Y\gamma^2 P}{2\rho\omega^2(1-\nu^2)}\left[\frac{-I_1(\gamma a)J_0(\gamma a)+J_1(\gamma a)I_0(\gamma a)}{I_1(\gamma a)J_0(\gamma a)+J_1(\gamma a)I_0(\gamma a)}\right], \tag{8a}$$

$$\sigma_t(a,h/2)=\frac{\nu Y\gamma^2 P}{2\rho\omega^2(1-\nu^2)}\left[\frac{-I_1(\gamma a)J_0(\gamma a)+J_1(\gamma a)I_0(\gamma a)}{I_1(\gamma a)J_0(\gamma a)+J_1(\gamma a)I_0(\gamma a)}\right]. \tag{8b}$$

Note that the $\partial w/\partial r$ term contributes nothing to the peripheral stress because of the boundary condition (6b). The applicable stress depends upon the orientation of the resistors on the plate. In the remaining analysis a radial orientation will be assumed, and the effective stress will be somewhat less than that at the periphery. For convenience the stress will be represented simply as σ. Since the stress is a frequency-dependent fraction of the applied pressure, the form of Eqs. (8a) and (8b) suggests the equivalent circuit for the diaphragm shown in Fig. 2. Then the stress σ and volume velocity U are related to the pressure P through the equivalent impedances Z_1 and Z_2:

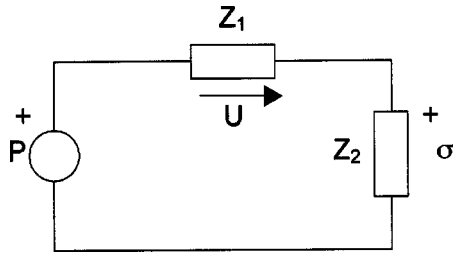

FIG. 2. Representation of the piezoresistive microphone diaphragm.

$$\sigma=\frac{Z_2}{Z_1+Z_2}P, \tag{9}$$

$$U=\frac{P}{Z_1+Z_2}. \tag{10}$$

The volume velocity is the integrated rate of displacement over the area of the diaphragm, which for harmonic time variation becomes

$$U=j\omega\int_0^a w(r)2\pi r\,dr. \tag{11}$$

Upon substituting Eq. (4) into (11), one finds

$$U=\frac{P}{Z_0}\left\{\frac{-[I_1(\gamma a)J_0(\gamma a)+J_1(\gamma a)I_0(\gamma a)]+4\dfrac{I_1(\gamma a)J_1(\gamma a)}{\gamma a}}{I_1(\gamma a)J_0(\gamma a)+J_1(\gamma a)I_0(\gamma a)}\right\}, \tag{12}$$

where

$$Z_0=\frac{h\rho\omega^2}{j\omega\pi a^2}. \tag{13}$$

Comparison of Eq. (12) with (10) and (9) with (8) permits one to determine the impedances Z_1 and Z_2.

At low frequencies, below the plate resonance, the Bessel functions can be approximated by their leading terms:

$$\left.\begin{matrix}J_0(x)\\ I_0(x)\end{matrix}\right\}=1\mp\frac{x^2}{4}+\frac{x^4}{64}\mp\frac{x^6}{2304}+\frac{x^8}{147\,456}\mp\cdots, \tag{14a}$$

$$\left.\begin{matrix}J_1(x)\\ I_1(x)\end{matrix}\right\}=\frac{x}{2}\mp\frac{x^3}{16}+\frac{x^5}{384}\mp\frac{x^7}{18\,432}+\frac{x^9}{1\,474\,560}\mp\cdots, \tag{14b}$$

in which $x=\gamma a\ll 1$. When Eqs. (14a)–(14b) are substituted into Eqs. (8a) and (12), one obtains the following relationships from the leading terms:

$$\sigma=\frac{3a^2P}{4h^2}, \tag{15a}$$

$$U=\frac{P}{\left[\dfrac{16Yh^3}{j\omega\pi a^6(1-\nu^2)}+j\omega\dfrac{9\rho h}{5\pi a^2}\right]}. \tag{15b}$$

Comparison of Eqs. (15a)–(15b) with (8a)–(12) yields the impedances Z_1 and Z_2. Equation (15a) agrees with Timoshenko[7] for a static analysis [Eq. (f), p. 61]. Note that since $a\gg h$, it follows that $\sigma\gg P$, a fact that would appear to contradict the voltage divider relationship Eq. (9). Define

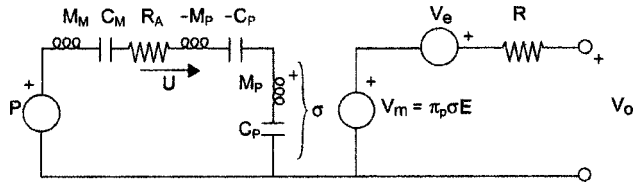

FIG. 3. Noise equivalent circuit of the piezoresistive microphone. A small term $-(\delta R)^2/R$ is omitted from the bridge resistance.

$$C_M=\frac{\pi a^6(1-\nu^2)}{16Yh^3}, \tag{16a}$$

$$M_M=\frac{9\rho h}{5\pi a^2}, \tag{16b}$$

$$C_P=\frac{\pi a^4(1-\nu^2)}{12Yh}, \tag{16c}$$

$$M_P=\frac{27\rho}{20\pi h}. \tag{16d}$$

If the resistors are oriented such that they see a tangential stress, then a factor ν must be added to the numerator of Eq. (15a), in which case the elements of Z_2 become

$$C_P=\frac{\pi a^4(1-\nu^2)}{12Yh\nu}, \tag{16e}$$

$$M_P=\frac{27\rho\nu}{20\pi h}. \tag{16f}$$

Then the impedances can be written:

$$Z_1=j\omega M_M+\frac{1}{j\omega C_M}+R_A-j\omega M_P-\frac{1}{j\omega C_P}, \tag{17a}$$

$$Z_2=j\omega M_P+\frac{1}{j\omega C_P}. \tag{17b}$$

There are two noteworthy features of the impedances Z_1 and Z_2. First, a resistor R_A was added to the plate impedance Z_1 to account for the damping, which was not included in the original plate vibration problem. It can be found from the relation

$$R_A=(2\pi f_R C_M Q)^{-1}, \tag{18}$$

where f_R is the resonance frequency of the diaphragm. Usually the quality factor Q assumes a value near unity. Second, the impedance Z_1 contains the negative of Z_2. This makes the volume velocity independent of Z_2 and permits the condition $\sigma \gg P$ to be fulfilled.

A complete background noise equivalent circuit is shown in Fig. 3. Note that the circuit is representative of a nonreciprocal device; in other words, the application of a voltage to the bridge does not produce a stress in the diaphragm.

Altogether there are four sources of background noise considered in the model:

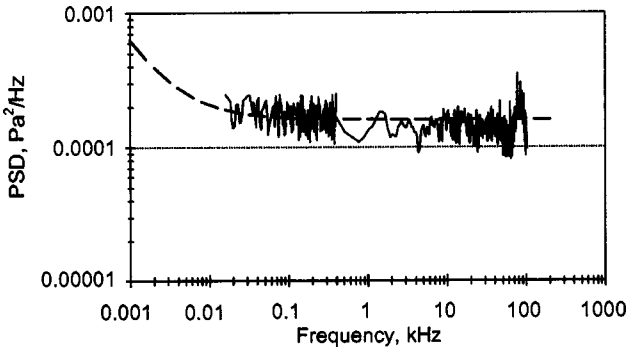

FIG. 4. Noise power spectral density of the Entran Model EPI-411-5P piezoresistive microphone. Solid line: measured. Dashed line: best fit to Eq. (23) with $b_2=0$.

(1) mechanical Johnson noise due to the Brownian motion of air molecules impinging on the diaphragm, as represented by the damping resistor R_A;
(2) $1/f$ noise generated by motion of the diaphragm;
(3) electrical Johnson noise due to random motion of charge carriers in bridge resistors R;
(4) generation-recombination (g-r) noise due to carrier fluctuations in the semiconducting bridge resistors R.

In the absence of an applied pressure the source P represents the mechanical Johnson and $1/f$ noise sources (1) and (2), and the equivalent noise voltage V_e represents the electrical noise sources (3) and (4). The corresponding open circuit voltages V_{0i} $(i=1,...,4)$ at the output are

$$V_{01}=S(4kTR_A\Delta f)^{1/2}, \tag{19a}$$

$$V_{02}=S[(A_m^2/f)\Delta f]^{1/2}, \tag{19b}$$

$$V_{03}=(4kTR\Delta f)^{1/2}, \tag{19c}$$

and the expression for the g-r noise is taken from Mueller,[8] written in the following form:

$$V_{04}=\left[\frac{4I^2R^2}{n_A\Omega}\left(1-\frac{n_A^-}{n_A}\right)\frac{\tau_P}{1+\omega^2\tau_P^2}\Delta f\right]^{1/2}. \tag{19d}$$

In Eqs. (19a)–(19d) k is the Boltzmann constant, T the absolute temperature, Δf the frequency resolution, S the microphone sensitivity, A_m^2 the $1/f$ coefficient, I the current through the bridge resistors, Ω the volume of the bridge resistor, n_A the acceptor concentration, n_A^- the ionized acceptor concentration, and τ_P the hole lifetime. Equation (19d) is written for the case of a p-type semiconductor without traps. At frequencies where $\omega\tau_P \ll 1$, the generation-recombination noise behaves as a white noise source with an equivalent resistance:

$$R_{gr}=\frac{I^2R^2}{kTn_A\Omega}\left(1-\frac{n_A^-}{n_A}\right)\tau_P. \tag{20a}$$

Then

$$V_{04}=(4kTR_{gr}\Delta f)^{1/2}. \tag{20b}$$

The low-frequency microphone sensitivity is obtained from Eqs. (3) and (15a):

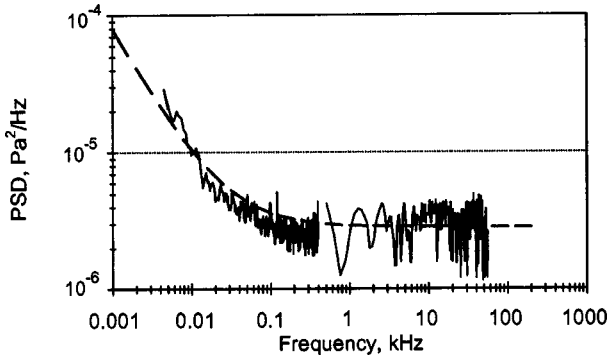

FIG. 5. Noise power spectral density of the Kulite Model XCW-093-5 piezoresistive microphone. Solid line: measured. Dashed line: best fit to Eq. (23) with $b_2=0$.

$$S=\frac{V_o}{P}=\frac{3a^2}{4h^2}\pi_p E, \tag{21a}$$

and the diaphragm resonance frequency from Eqs. (16a) and (16b):

$$f_R=(2\pi\sqrt{M_M C_M})^{-1}. \tag{21b}$$

The power spectral density, then, is the sum of the above contributions:

$$J=\sum_i \frac{|V_{0i}|^2}{\Delta f}. \tag{22}$$

B. Experimental results

Background noise measurements were conducted on two piezoresistive microphones: Entran Model EPI-411-5P and Kulite Model XCW-093-5, both having a nominal rating of 5 psi full scale output. The power spectral densities, expressed in mechanical units of Pa^2/Hz, are shown in Figs. 4 and 5 after subtraction of the internal noise of the analyzer ($\sim$300 nV^2/Hz in electrical units). Measurements were taken over two frequency ranges. The high-frequency range was 102.4 kHz, corresponding to a frequency resolution $\Delta f=128$ Hz. The low-frequency range, chosen to better resolve the $1/f$ noise, was 400 Hz ($\Delta f=0.5$ Hz).

The total noise can be expressed in the following form:

$$J=b_0+b_1/f+b_2/f^2, \tag{23}$$

in which it is assumed that $\omega\tau_p \ll 1$ [see Eq. (19d)]. Further, since the piezoresistive model reveals no $1/f^2$ component, then $b_2=0$. The power spectral density based on the best-fitted values of b_0 and b_1 is shown as a dashed line in the figures.

The Johnson noise sources (in Pa^2/Hz) can be written as

$$b_0=4kT(R/S^2+R_A+R_{gr}/S^2). \tag{24}$$

The only unknown in Eq. (24) is the equivalent generation-recombination resistance R_{gr}, since R is the known bridge resistance and R_A can be estimated from Eq. (18) (with $Q=1$). Pertinent microphone properties are listed in Table I. Accordingly, Eq. (18) yields the values $R_A=3.3\times10^{10}$ and 4.8×10^{10} N·s/m^5 for the Entran and Kulite sensors, respectively, and Eq. (24) then yields $R_{gr}=1123$ and 1121 ohm. The contributions to the Johnson noise are summarized in Table II and the noise coefficients in Table III.

TABLE II. Contributions to the Johnson noise of piezoresistive microphones.

Source of noise	Entran	Kulite
	10^6 Pa^2/Hz	
Mechanical Johnson noise (diaphragm damping)	0.0005	0.0008
Electrical Johnson noise[a] (bridge resistors)	72	1.3
Generation-recombination noise	89	1.5
Total Johnson noise	161	2.8

[a]Bridge voltage=4.8 V for the Entran and 18 V for the Kulite.

IV. THE ELECTRET CONDENSER MICROPHONE

A. Model

The electret condenser microphone (ECM) differs from a conventional air condenser microphone (ACM) in that a prepolarized electret layer provides the polarization electric field between the diaphragm and backplate in place of an applied voltage from an external source. The microphone models are similar, but there are two important differences.[9] First, a high series resistance between the voltage source and backplate in the ACM is eliminated in the ECM. Secondy, the output stage of the ACM preamplifier is a source follower containing a high source resistance; that of the ECM is a conventional common source amplifier with a low output resistance. Thus the parallel combination of two high resistances in the ACM, which serve as sources of electrical Johnson noise, are eliminated in the ECM.

The background noise model[10] of the ECM is shown in Fig. 6. The diaphragm is represented by a mass M_M, com-

TABLE I. Parameters for the evaluation of Johnson noise in piezoresistive microphones.

Parameter	Entran EPI-411-5P	Kulite XCS-093-5
Bridge resistance[a] R, ohm	907	1000
Diaphragm resonance frequency[a] f_R, kHz	125	150
Diaphragm diameter[a] $2a$, cm	0.203	0.096
Sensor sensitivity[b] S, μV/Pa	0.453@4.8 V	3.47@18 V
Diaphragm mass[c] M_M, N·s^2/m^5	4.4×10^4	5.4×10^4
Diaphragm compliance[d] C_M, m^5/N	3.6×10^{-17}	2.0×10^{-17}

[a]Manufacturer's specification.
[b]Determined by pistonphone calibration.
[c]Derived from Eqs. (16b) and (21b).
[d]Derived from Eqs. (16a) and (21b).

TABLE III. Microphone noise coefficients [Eq. (23)].

	Piezoresistive			
	Entran@4.8 V	Kulite@18 V	Electret	Ceramic[a]
Constant b_0, Pa^2/Hz	$1.6\pm0.4\times10^{-4}$	$2.9\pm1.4\times10^{-6}$	$3.5\pm0.2\times10^{-11}$	$6.9\pm0.3\times10^{-9}$
$1/f$ coefficient b_1, Pa^2	$4.7\pm2.1\times10^{-4}$	$7.7\pm4.2\times10^{-5}$	$1.1\pm0.1\times10^{-7}$	⋯
$1/f^2$ coefficient b_2, $Pa^2\cdot Hz$	⋯	⋯	$9.7\pm8.5\times10^{-6}$	⋯

[a]Low-frequency noise ($f<100$ Hz).

pliance C_M, and damping resistance R_A. Further, C_{to} is the diaphragm-backplate capacitance, g_m the FET transconductance, and R_d the drain resistance. The electromechanical transduction factor is defined

$$\psi=\frac{C_{to}\mathcal{E}}{\pi a^2}, \tag{25}$$

where $\mathcal{E}$ is the electric field across the diaphragm-backplate gap, generated by the electret, and a the radius of the diaphragm. The microphone sensitivity, as would be measured by a pistonphone, is

$$S=\left(\frac{\psi C_M}{C_{to}}\right)g_m R_d, \tag{26}$$

which is valid over the operating bandwidth. The acoustical impedance of the diaphragm is

$$Z_M=j\omega M_M+\frac{1}{j\omega C_M}+R_A$$
$$=\frac{1}{j\omega C_M}\left[1-\left(\frac{\omega}{\omega_o}\right)^2+\frac{j\omega}{\omega_o Q}\right], \tag{27}$$

where ω_o and Q are the angular resonance frequency and quality factor of the diaphragm. The sources of background noise are:

(1) mechanical Johnson noise due to the Brownian motion of air molecules impinging on the diaphragm, as represented by the damping resistor R_A, and $1/f$ noise generated by motion of the diaphragm;
(2) thermal channel noise generated in the FET channel;
(3) gate shot noise generated in the FET;
(4) electrical Johnson noise generated in the drain resistor R_d.

Straightforward circuit analysis yields the corresponding open circuit voltages $V_{0i}\,(i=1...4)$ at the output in terms of the sources shown in the figure:

$$V_{01}=-\frac{Sp_m}{[(1-\omega^2/\omega_o^2)^2+(\omega/\omega_o Q)^2]^{1/2}}, \tag{28a}$$

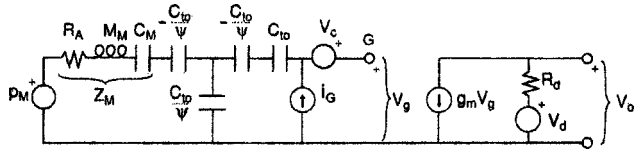

FIG. 6. Noise equivalent circuit of the electret condenser microphone.

$$V_{02}=-g_m R_d V_c, \tag{28b}$$

$$V_{03}=-g_m R_d\frac{i_G}{j\omega C_{to}}, \tag{28c}$$

$$V_{04}=V_d, \tag{28d}$$

where

$$p_m=[4kTR_A\Delta f+(A_m^2/f)\Delta f]^{1/2}, \tag{29a}$$

$$V_c=[4kT(0.65/g_m)\Delta f]^{1/2}, \tag{29b}$$

$$i_G=(2qI_G\Delta f)^{1/2}, \tag{29c}$$

$$V_d=(4kTR_d\Delta f)^{1/2}, \tag{29d}$$

and A_m^2 is the $1/f$ coefficient, q the electronic charge, and I_G the gate leakage current. When Eqs. (28a)–(29d) are substituted into (22), the power spectral density becomes

$$J=\frac{S^2(4kTR_A+A_m^2/f)}{(1-\omega^2/\omega_o^2)^2+(\omega/\omega_o Q)^2}$$
$$+\left[\frac{4(0.65)kT}{g_m}+\frac{2qI_G}{(\omega C_{to})^2}\right](g_m R_d)^2+4kTR_d. \tag{30}$$

Equation (30) reveals two noteworthy features of the power spectral density. First, the gate shot noise term introduces a $1/\omega^2$ component, which is not present in the piezoresistive microphone. Secondly, at frequencies below resonance $\omega \ll \omega_o$ the membrane damping (Brownian) component behaves as a Johnson noise source. Experimental results show that this component dominates over the channel and drain resistor components.

B. Experimental results

A Panasonic Model WM60A microphone cartridge was attached to one end of a circuit board, a three-terminal connector at the other end, and the whole assembly secured in an aluminum tube of 0.0079 m (5/16 in.) diameter. The drain resistor R_d and blocking capacitor were chosen to have values of 5.1 kohm and 0.47 μf, respectively, and the microphone was operated at a supply voltage of 6.8 V. A pistonphone calibration at 250 Hz yielded a microphone sensitivity of $S=18.5$ mV/Pa.

The power spectral density, in Pa^2/Hz, is shown in Fig. 7 after the analyzer noise was subtracted off. The frequency resolution is $\Delta f=128$ Hz over the entire plot. The best-fitted values of the coefficients in Eq. (23) are listed in Table III. The mechanical response of the membrane was accounted for in Eq. (30) using the values $f_R=\omega_o/2\pi=25$ kHz and Q

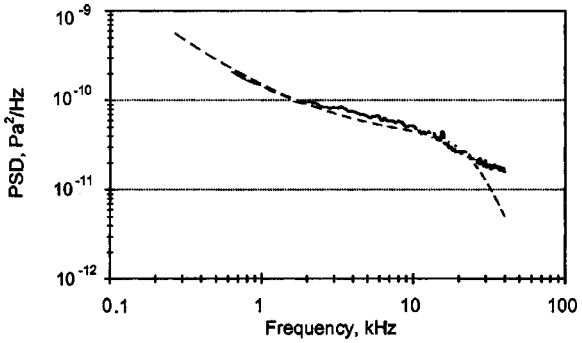

FIG. 7. Noise power spectral density of the electret condenser microphone made with a Panasonic Model WM60A cartridge. Solid line: measured. Dashed line: best fit to Eq. (23).

$=0.707$. It is readily verified that the channel term, even using a high value $g_m=0.01$ mho, and the drain resistor term, using $R_d=5.1$ kohm, together fall far short of accounting for the constant (Johnson) contribution to the power spectral density. Thus one may write (in mechanical units)

$$b_0 \approx 4kTR_A, \tag{31}$$

which yields a value $R_A=2.2\times10^9$ N·s/m^5, or 737 kohm (in electrical units) at $T=293$ K.

V. THE CERAMIC MICROPHONE

A. Model

The ceramic microphone is a low-cost, rugged device, which has lost popularity to the electret microphone, and is included here mainly for historical reasons. The sensing element in a ceramic microphone is a circular flexible diaphragm. Internal to the microphone, one end of a connecting rod is conjoined to the center of the backside of this diaphragm, while the opposite end is connected, via a yokelike clamp, to the center of a flexible rectangular ceramic plate. The ends of the ceramic plate are rigidly clamped to the microphone housing, as shown in Fig. 8. Thus, an applied pressure P deflects the diaphragm, and the deflection is translated to the ceramic plate via the connecting rod. The pressure applied to the entire area of the diaphragm is consequently concentrated on the locations where the connecting rod meets the ceramic plate. This area reduction effectively acts as an impedance matching mechanism to better match the rigidity of the diaphragm to that of the ceramic plate. The deflection of the plate generates a stress, which produces an electric current due to the piezoelectric effect through the electrodes connected to the top and bottom of the plate. Because the current is self-generating and external electronics are not required for microphone operation, both the model and measurements pertain to the microphone cartridge without a preamplifier.

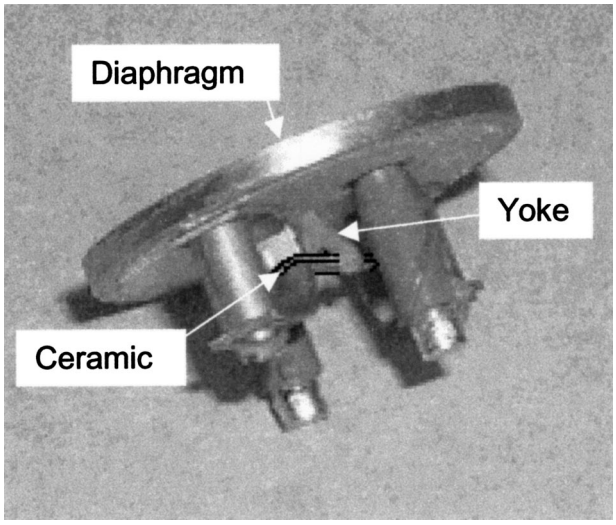

FIG. 8. Internal construction of the General Radio Model 1971-9601 1-in. ceramic microphone [with permission of IET Labs, Inc. (www.ietlabs.com)].

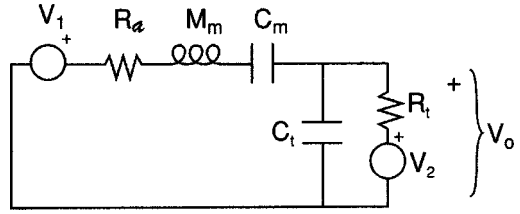

FIG. 9. Noise equivalent circuit of the ceramic microphone.

A noise equivalent circuit of the ceramic microphone[11] is shown in Fig. 9. Here R_a, M_m, and C_m represent the motional elements of the system, transformed to the electrical side of the circuit: $R_a=R_AS^2$ represents the damping of the diaphragm motion due to the Brownian motion of air molecules impinging upon the diaphragm, $M_m=M_MS^2$ the diaphragm mass, and $C_m=C_M/S^2$ the compliance. The electrical elements are R_t and C_t, where C_t is the ceramic plate capacitance, and R_t is the dielectric leakage of the plate. The two noise sources,

$$V_1=(4kTR_a\Delta f)^{1/2}, \tag{32a}$$

$$V_2=(4kTR_t\Delta f)^{1/2} \tag{32b}$$

represent the mechanical and electrical Johnson noise sources, respectively.

Through straightforward circuit analysis, it can be found that the squared magnitude of the noise contributed by V_1 at the output is given by

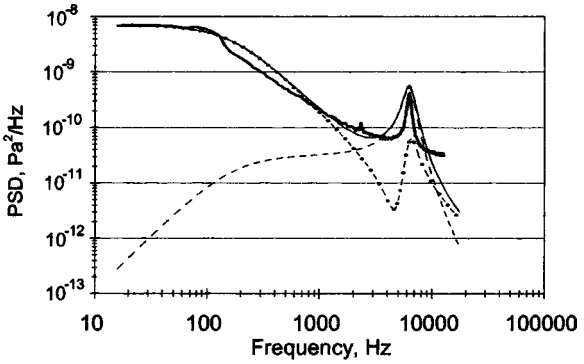

FIG. 10. Noise power spectral density of the General Radio Model 1971–9601 1-in. ceramic microphone in mechanical units. Heavy solid line: measured. Dashed line: fit to Eq. (33a). Dot-dashed line: fit to Eq. (33b). Light solid line: total noise power spectral density [sum of Eqs. (33a) and (33b)].

$$|V_{01}|^2=\left[\frac{(\omega R_tC_m)^2}{\omega^2\left(R_tC_t+R_tC_m+R_mC_m-\frac{\omega^2R_tC_t}{\omega_s^2}\right)^2+\left(1-\omega^2R_tC_tR_mC_m-\frac{\omega^2}{\omega_s^2}\right)^2}\right]V_1^2, \tag{33a}$$

and that contributed by V_2 is given by

$$|V_{02}|^2=\left\{\frac{\left[(\omega R_mC_m)^2+\left(1-\frac{\omega^2}{\omega_s^2}\right)^2\right]}{\omega^2\left(R_tC_t+R_tC_m+R_mC_m-\frac{\omega^2R_tC_t}{\omega_s^2}\right)^2+\left(1-\omega^2R_tC_tR_mC_m-\frac{\omega^2}{\omega_s^2}\right)^2}\right\}V_2^2, \tag{33b}$$

where $\omega_s^2=(M_mC_m)^{-1}$ is the series resonance frequency. To convert the outputs to mechanical units, one must simply divide Eqs. (33a) and (33b) by S^2, where S is the microphone sensitivity.

B. Experimental results

Figure 10 shows the experimental data for the General Radio Model 1971-9601 1-in. ceramic microphone as well as computational results obtained from analysis of the model. The broken lines are the individual contributions V_{01} and V_{02}, based on fitted model parameters appearing in Eqs. (33a) and (33b). Component V_{01} (dashed), associated with the noise generated in motional resistor R_a, starts around $1\times10^{-13}\,\mathrm{Pa^2/Hz}$ at 10 Hz and reaches a peak at about 7 kHz. V_{02} (dot-dashed), associated with the noise generated in dielectric loss resistor R_t, starts just below $1\times10^{-8}\,\mathrm{Pa^2/Hz}$ at 10 Hz and decreases until it describes a smaller peak at a slightly higher frequency. The sum of the individual contributions is shown as the thin solid line. The heavy solid line is the experimentally obtained noise measurements. Because there is no indication of a $1/f$ component appearing above 10 Hz, as can be seen in the figure, this component is not included in the model. Accordingly, the model is seen to account for all of the relevant features of the experimental data, including the resonance around 7 kHz, and the behavior at both ends of the measured spectrum. Model parameters fitted to the data are: $R_t=5.35\,\mathrm{M\Omega}$, $R_a=133.8\,\mathrm{k\Omega}$, $C_t=100\,\mathrm{pf}$, $C_m=74.7\,\mathrm{pf}$, $\omega_s/2\pi=4800\,\mathrm{Hz}$, and $S=3.5\,\mathrm{mV/Pa}$. The low-frequency Johnson noise coefficient b_0, associated with the dielectric loss resistor, is listed in Table III.

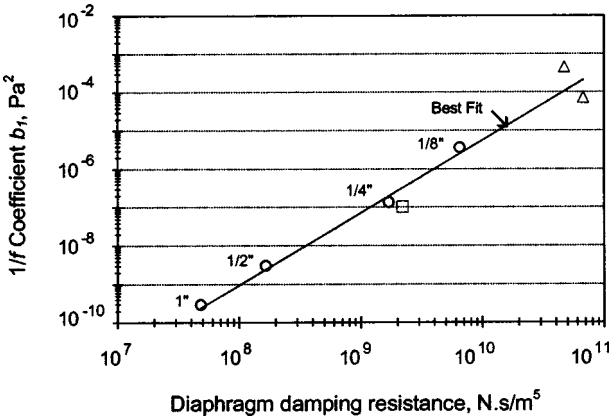

FIG. 11. $1/f$ coefficient versus diaphragm damping resistance. Circles: air condenser microphone (taken from Ref. 1). Square: electret condenser microphone. Triangles: piezoresistive microphone. Solid line: best fit to Eq. (34).

VI. 1/f NOISE COEFFICIENT VERSUS DIAPHRAGM DAMPING RESISTANCE

It was shown in Ref. 1 that the $1/f$ noise coefficient b_1 in air condenser microphones is strongly correlated with the diaphragm damping resistance. Figure 11 reveals that this correlation extends to the piezoresistive and electret condenser microphones. The equation for the best-fitted straight line is

$$\log(b_1)=-24.1+1.89\log(R_A), \tag{34}$$

where R_A represents the diaphragm damping resistance. The correlation coefficient of the fit is 0.9715. This empirical relationship, spanning three orders of magnitude, evidently applies to any diaphragm-based microphone, independently of detection technology. Since the diaphragm damping resistance increases inversely with diaphragm diameter, one may expect a significant $1/f$ component in micromachined (MEMS) silicon sensors. Thus a microphone with a high diaphragm damping resistance can offer only limited performance at low frequencies due to associated $1/f$ noise and deteriorating signal-to-noise ratio.

VII. CONCLUSIONS

The proposed models are found to account for the measured background noise in the microphones considered in this study. As revealed in Table II, the background noise of a piezoresistive microphone decreases strongly with increasing microphone sensitivity, which in turn depends upon the applied bridge voltage. The generation-recombination noise is comparable to the random motional noise in both of the studied microphones. The diaphragm damping contribution, however, is inconsequential in contrast to that of the electrostatic microphones having larger diaphragm diameters.

The electret condenser microphone represents the quietest of all technologies to detect the displacement of a microphone diaphragm. The absence of the polarization voltage resistor makes the electret slightly quieter than a comparable air condenser microphone at low frequencies where its associated $1/\omega^2$ component appears. In fact, the Johnson noise is

almost entirely mechanical in nature. The presence of a drain resistor in the output circuit, having a comparatively low value, makes a negligible contribution to the background noise.

The background noise spectrum of the ceramic microphone is too complex to put into a simple polynomial form. In the low-frequency limit, the noise generated in the dielectric loss resistor approaches the ideal Johnson noise level. It dominates the spectrum at low frequencies and then rolls off well below the diaphragm resonance. The noise generated in the diaphragm damping resistor dominates in the vicinity of the resonance peak. It may be fair to conclude that piezoelectric receivers in general, even those having resonance frequencies well into the MHz range, have a threshold of detectability limited by the Johnson noise generated in the diaphragm damping resistor.

Finally, the correlation between diaphragm damping resistance and $1/f$ noise coefficient is found to be valid for all diaphragm-based microphones, independently of detection technology.

The selection of specific commercial microphones for testing does not imply endorsement by the National Aeronautics and Space Administration.

ACKNOWLEDGMENTS

The authors thank Qamar A. Shams, NASA Langley Research Center, for suggesting several improvements to the acoustical isolation apparatus. Financial support by the American Society for Engineering Education for one of the authors (RMS), who was a Summer Faculty Fellow during the summer of 2001, is gratefully acknowledged.

[1] A. J. Zuckerwar and K. C. Ngo, ''Measured $1/f$ noise in the membrane motion of condenser microphones,'' J. Acoust. Soc. Am. **95**, 1419–1425 (1994).
[2] T. B. Gabrielson, ''Mechanical-thermal noise in micromachined acoustic and vibration sensors,'' IEEE Trans. Electron Devices **40**, 903–909 (1993).
[3] R. R. Spencer, B. M. Fleischer, P. W. Barth, and J. B. Angell, ''A theoretical study of transducer noise in piezoresistive and capacitive silicon pressure sensors,'' IEEE Trans. Electron Devices **35**, 1289–91298 (1988).
[4] W. R. Bevan, R. B. Schulein, and C. E. Seeler, ''Design of a studio-quality condenser microphone using electret technology,'' J. Audio Eng. Soc. **26**, 947–957 (1978).
[5] K. C. Ngo and A. J. Zuckerwar, ''Acoustic isolation vessel for measurement of the background noise in microphones,'' J. Acoust. Soc. Am. **93**, 2974–2980 (1993).
[6] P. M. Morse and K. U. Ingard, *Theoretical Acoustics* (McGraw-Hill, New York, 1968), p. 217.
[7] S. Timoshenko, *Theory of Plates and Shells* (McGraw-Hill, New York, 1940).
[8] R. Mueller, ''Generation-recombination noise,'' in *Noise in Physical Systems*, edited by D. Wolf (Springer-Verlag, Berlin, 1978), pp. 13–25.
[9] V. Tarnow, ''The lower limit of detectable sound pressures,'' J. Acoust. Soc. Am. **82**, 379–381 (1987).
[10] R. S. C. Cobbold, *Theory and Applications of Field-Effect Transistors* (Wiley-Interscience, New York, 1970), pp. 138–143 and 316–342.
[11] L. E. Kinsler and A. R. Frey, *Fundamentals of Acoustics* (Wiley, New York, 1962), p. 345.

The application of smart structures toward feedback suppression in amplified acoustic guitars

Steve Griffin, Steven A. Lane,[a] and Robert L. Clark
Department of Mechanical Engineering and Material Sciences, Duke University, Box 90302, Durham, North Carolina 27708

(Received 4 January 2002; accepted for publication 30 January 2003)

Smart structures technology can be applied to amplified acoustic guitars to prevent instability resulting from acoustic feedback. This work presents a coupled model of the guitar dynamics and the acoustic feedback mechanism, and explains how a simple control loop using a piezoelectric ceramic actuator can be used to reduce the effects of acoustic feedback. In addition to model simulations, experimental results using a real system and a simple controller are presented. The results show that a significantly higher (7 dB) guitar output can be achieved before instability, without detrimentally affecting the amplified and unamplified guitar response. © *2003 Acoustical Society of America.* [DOI: 10.1121/1.1562649]

PACS numbers: 43.38.Ar, 43.40.Vn, 43.75.Tv [SLE]

I. INTRODUCTION

When acoustic guitars are used with loud amplifier systems or with monitoring speakers, there is the potential that feedback can produce unpredictable instabilities that result in loud and annoying noise. This occurs when the sound produced by the amplifier and speakers excite the strings and face-plate (or top-plate) of the guitar and create unstable vibrations. This phenomenon is hard to predict, and is dependent upon many factors including the instrument characteristics, the amplifier and speaker characteristics, and the spatial orientation and position of the musician.

Acoustic feedback is a well-known phenomenon, and there have been several mechanisms developed to avoid the problem. One solution is to add passive damping to the guitar top-plate. This deadens the vibration of the guitar structure and reduces the tendency of oscillations to go unstable. However, when the guitar is used without amplification, its sound is detrimentally affected. Another solution is to use graphic equalizers to reduce the gain in the frequency bandwidth where instability is likely to occur. A more complicated extension of this concept is to employ digital signal processing to ''notch filter'' potentially unstable tones. These solutions are more complex and have the disadvantage of distorting the true sound of the instrument as perceived by the audience or performer. In addition to these ideas, there are also other devices and methods for preventing acoustic feedback in amplified instruments.[1–5] These typically are devices that completely or partially cover the sound hole to prevent feedback destabilization.

There has been considerable analysis of guitar physics, both the structural and acoustic response. Theoretical models have been developed to describe and approximate the vibration of the guitar structure and the corresponding acoustic response.[6–9] However, the authors are unaware of models that have been extended to include the feedback path from the amplifier and monitoring system.

The approach presented in this work to prevent feedback destabilization is to utilize ''smart structure'' technology to actively damp feedback induced vibrations using piezoelectric ceramic sensors and actuators incorporated into the guitar. Active control and smart structures have been applied to other guitar-related issues,[10–12] and offer several advantages over other methods. A key advantage is that with smart structures and inexpensive processing, there is the potential for an adaptive controller whose objective is to make the guitar structural dynamics independent of sound system gain and relative position with respect to monitor speakers. This preserves the original sound quality of the instrument, whether or not it is amplified.

This paper presents a coupled structural-acoustic model of a guitar with a piezoelectric ceramic sensor and actuator, and includes the acoustic feedback path. The model helps explain the mechanisms of feedback-induced instabilities and how the problem can be solved using smart structures. In the following, the development of the coupled structural-acoustic model of the guitar with the acoustic feedback path is presented and cast into state-space form. This is followed by an analysis of the feedback phenomenon and the development of a simple, low-order controller to prevent the instability. Experimental measurements on a guitar are then presented to illustrate the feedback problem, and closed-loop tests are presented to demonstrate the enhanced performance afforded by the control approach. This is followed by a discussion of the advantages and current limitations of this control approach.

II. THEORY

A. Guitar/sound system model

In prior work, the low frequency response of the guitar was modeled as a vibrating piston or plate, coupled with a vented acoustic cavity.[6,7] The model presented here builds on the model developed by Griffin *et al.*[9] illustrated in Fig. 1. The ribs and back of the guitar were assumed to be rigid, while the lower bout of the guitar top-plate was modeled as

[a]Electronic mail: steven.lane@kirtland.af.mil

 0001-4966/2003/113(6)/3188/9/$19.00

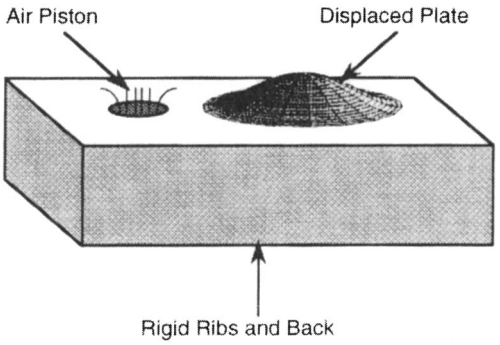

FIG. 1. Low frequency guitar model illustration.

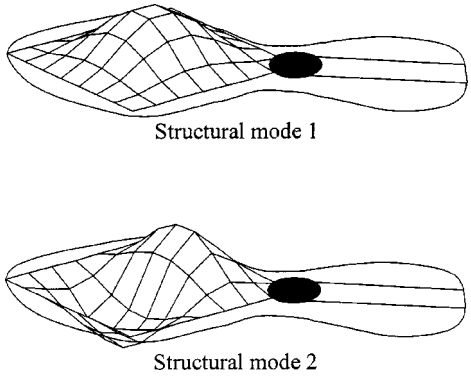

FIG. 2. Structural mode shapes used to model guitar top-plate.

a flexible plate, which was coupled by the guitar cavity to the air piston formed by the guitar rose (the circular vent present in most acoustic guitars). In the model developed by Griffin *et al.*, the vibration of the top-plate lower bout was described using Bessel functions as the uncoupled mode shapes.[9] In the present work, a discrete model was developed using a finite-element model to determine the mode shapes and natural frequencies of the top-plate lower bout. The finite-element model takes into consideration the localized mass and stiffness effects of the piezoelectric ceramic, and greatly simplifies the process of incorporating actuators and sensors into the model. This facilitates the exploration of active control approaches. In this study, a 64 node finite-element model of a rectangular plate represents the motion of the lower bout. The additional assumption was made that, for low frequency behavior, it was sufficient to model the guitar using only two structural modes and the coupled air mode. This assumption is consistent with the previous work of Griffin *et al.* for low frequency behavior. The two structural modes included the first and second plate modes of the guitar. Figure 2 shows the corresponding structural mode shapes and their orientation in the guitar frame of reference.

Using the two structural mode shapes, denoted as $\eta_1(t)$ and $\eta_2(t)$, and the air mode, denoted as $z(t)$, the structural response of the guitar's top-plate with a single piezoelectric ceramic input can be described with the following coupled, ordinary differential equations:

$$\ddot{\eta}_1(t)+2\zeta_1\omega_1\dot{\eta}_1(t)+\omega_1^2\eta_1(t) = \Theta_{A1}v_a(t)+S_{11}\eta_1(t)+W_1z(t), \tag{1}$$

$$\ddot{\eta}_2(t)+2\zeta_2\omega_{32}\dot{\eta}_2(t)+\omega_2^2\eta_2(t)=\Theta_{A2}v_a(t), \tag{2}$$

$$\ddot{z}(t)+\gamma_h\dot{z}(t)+\frac{\beta S_h^2}{m_h}z(t)=\frac{Y_1}{m_h}\eta_1(t), \tag{3}$$

where ζ_1, ζ_2, ω_1, and ω_2 are the modal damping ratios and natural frequencies, respectively, and Θ_{A1} and Θ_{A2} represent the modal coupling of the actuator input, $v_a(t)$, to the plate modes. The coupling of the guitar cavity and the first structural mode is given by S_{11}, and W_1 represents the coupling between the air piston mode and the first structural mode. In Eq. (2), the coupling of both the air cavity and the air piston to the second plate mode is assumed negligible. In Eq. (3), γ_h represents the damping of the air piston, β represents the air compressibility constants, S_h represents the area of the rose, m_h represents the moving mass of the air in the rose, and γ_1 describes the backcoupling between the air piston and the first plate mode. The derivations of the coupling terms in Eqs. (1)–(3) are given in Ref. 13.

Defining the states of the guitar model as

$$\mathbf{x}=\begin{Bmatrix}\eta_1\\ \eta_2\\ z\\ \dot{\eta}_1\\ \dot{\eta}_2\\ \dot{z}\end{Bmatrix}, \tag{4}$$

where the time dependence has been dropped for convenience, a state-space model of the system can be formulated from Eqs. (1)–(3) as

$$\dot{\mathbf{x}}=\begin{bmatrix} 0 & 0 & 0 & 1 & 0 & 0\\ 0 & 0 & 0 & 0 & 1 & 0\\ 0 & 0 & 0 & 0 & 0 & 1\\ -\omega_1^2+S_{11} & 0 & W_1 & -2\zeta_1\omega_1 & 0 & 0\\ 0 & -\omega_2^2 & 0 & 0 & -2\zeta_2\omega_2 & 0\\ \dfrac{Y_1}{m_h} & 0 & -\dfrac{S_h^2\beta}{m_h} & 0 & 0 & -\gamma_h \end{bmatrix}\mathbf{x}+\begin{bmatrix}0\\0\\0\\ \Theta_{A1}\\ \Theta_{A2}\\0\end{bmatrix}\{v_a\}. \tag{5}$$

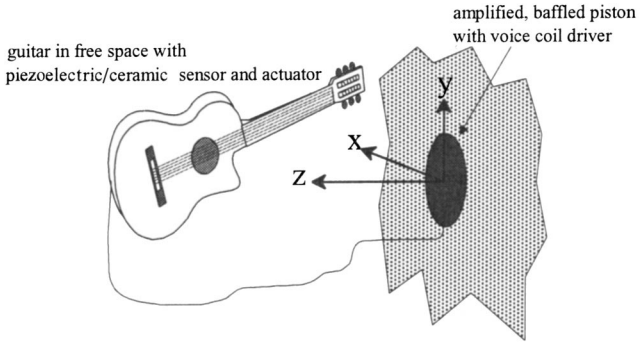

FIG. 3. Components of the feedback instability model.

For a piezoelectric ceramic sensor also mounted on the top-plate, the sensor output voltage, $v_s(t)$, can be expressed as

$$\{v_s\}=[\Theta_{S1} \quad \Theta_{S2} \quad 0 \quad 0 \quad 0 \quad 0]\mathbf{x}+[0]\{v_a\}, \tag{6}$$

where Θ_{S1} and Θ_{S2} represent the modal coupling of the sensor and the plate modes, also given in Ref. 13. From Eqs. (5) and (6), the state-space matrices, **A**, **B**, **C**, and **D** are defined. This model approximates the low frequency response of the guitar as a function of the piezoelectric ceramic actuator input, and can easily be expanded to include exogenous inputs and inputs from string vibration.

Figure 3 illustrates all of the components in the feedback instability model. The guitar response is measured by an electronic pickup, assumed here to be the piezoelectric ceramic sensor, and goes into the amplifier, which then sends the signal to the monitor loudspeaker. In this study, the amplifier gain is modeled as a constant, and the monitor loudspeaker is modeled as a radiating piston mounted in an infinite baffle.[14] It is also assumed that the piston is radiating into an infinite half-space, and that the guitar is located at some point in the half-space. Furthermore, it is assumed that the sound radiated from the guitar is very small compared to the sound radiated by the baffled piston. This allows consideration of only the radiated sound pressure from the piston as a forcing function on the top-plate and rose.

The pickup signal from the guitar model is multiplied by the amplifier gain, denoted as G, and produces an input voltage to the voice coil of the baffled piston, $v_p(t)$, where

$$v_p(t)=Gv_s(t). \tag{7}$$

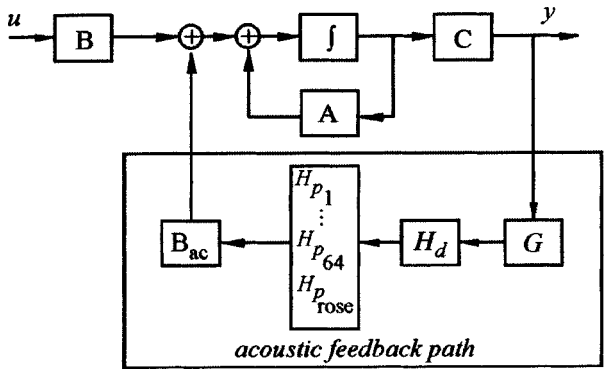

FIG. 4. Block diagram of the feedback instability model.

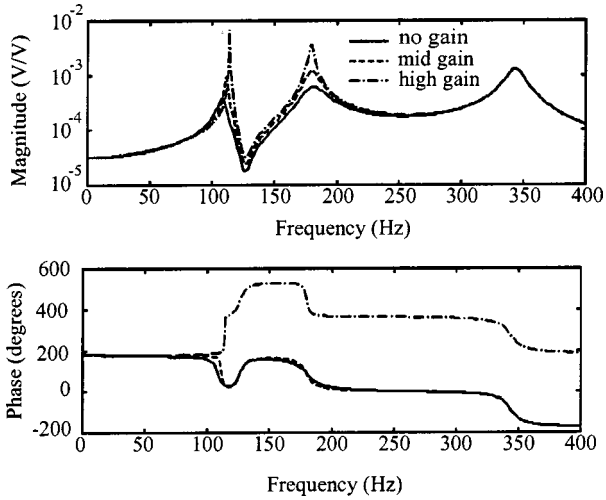

FIG. 5. Effect of piston amplifier gain on guitar dynamics.

The Laplace transform of the transfer function between input voltage, $v_p(s)$, and piston velocity, denoted as $sw(s)$, is given as

$$H_d(s)=\frac{sw(s)}{v_p(s)}=\frac{Bls}{R\left(ms^2+\left(c+\frac{Bl^2}{R_{\mathrm{dc}}}\right)s+k\right)}, \tag{8}$$

where m is the moving mass of the piston, c is the damping constant of the voice coil/piston assembly, k is the stiffness of the voice coil/piston assembly, B is the magnetic field strength, l is the length of the voice coil wire, and R_{dc} is the dc coil resistance. The inductance of the voice coil was ignored, since only the low frequency behavior was under investigation. Once the response of the baffled piston is established, the baffled piston equation can be used to predict the resulting radiated sound pressure on the top-plate at the 64 plate finite-element model node locations and at the guitar rose. Using the equation for far-field pressure radiated by a piston given in Kinsler *et al.*,[14] the transfer function relating pressure to the piston velocity is given as

$$H_p(r,\theta)=\frac{P(r,\theta,t)}{\dot{w}(t)}=\frac{j\rho ck a^2}{2}\,\frac{2J_1(ka\sin(\theta))}{ka\sin(\theta)}\,\frac{e^{-jkr}}{r}, \tag{9}$$

where r is the distance from the center of the piston to the point where the pressure is radiated, θ represents the angle between the center line normal to piston and the same point, ρ is the air density, c is the sound speed, k is the acoustic wave number, a is the piston radius, and $J_1(\cdots)$ represents Bessel functions of the first kind.

To be consistent with the state-space model given by Eqs. (5) and (6), the pressures at the top-plate node locations computed from Eq. (9) must be multiplied by the matrix of mass orthonormalized mode shapes and the corresponding nodal areas before being included in the guitar model. Also, the pressure computed at the rose must be multiplied by the area of the rose and divided by the air mass. These operations on the computed pressure form the definition of $\mathbf{B}_{\mathrm{ac}}$, given as

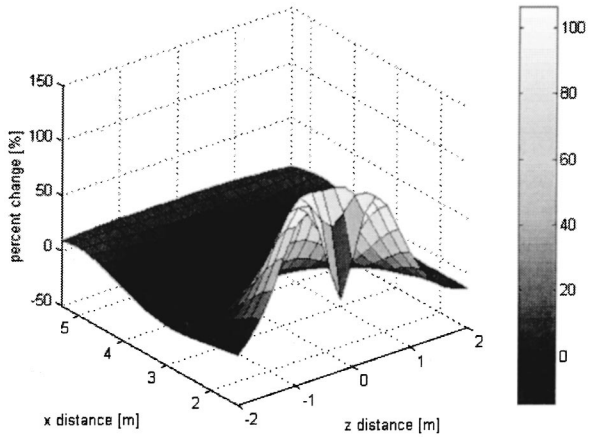

FIG. 6. Fractional change in guitar first mode (air mode) amplitude as a function of relative position.

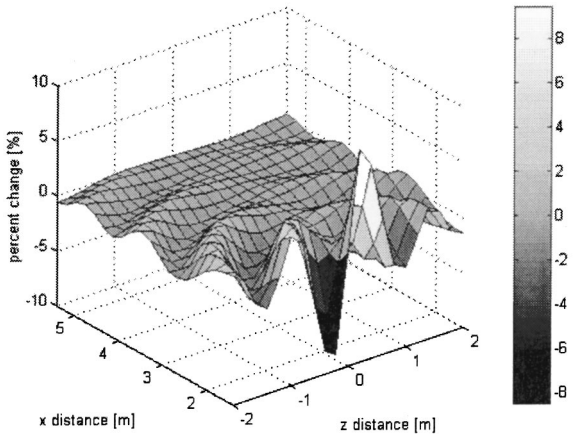

FIG. 8. Fractional change in guitar third mode (second plate mode) amplitude as a function of relative position.

$$\mathbf{B}_{\mathrm{ac}}=\begin{bmatrix} A_1\phi_{11} & A_2\phi_{12} & \cdots & A_n\phi_{1n} & 0 \\ A_1\phi_{21} & A_2\phi_{22} & \cdots & A_n\phi_{2n} & 0 \\ & & & & \\ 0 & 0 & \cdots & 0 & \dfrac{S_h}{m_h} \end{bmatrix}, \tag{10}$$

where A_n are the nodal areas, and $\phi_{m,n}$ are the mass orthonormalized mode shapes with m corresponding to the mode number, and n corresponding to the node location. In the present model, $n=64$, since there were 64 nodes constituting the finite-element model that were capable of out-of-plane motion.

The feedback path from the guitar output, $v_s(t)$, to the inputs acting on the modes of the guitar forms a single-input, three-output system (since $\mathbf{B}_{\mathrm{ac}}$ is $3\times n$), and is illustrated in block-diagram form in Fig. 4. The coupled system represented in Fig. 4 can be solved to predict the changes in the guitar dynamics for given gain and relative position values between the guitar and the speaker (baffled piston). Figure 5 presents the frequency response functions between the guitar sensor and the actuator (i.e., the open-loop system) for varying amplifier gain values, at an initial fixed location directly in front of the baffle. This location is defined by first considering the piston axis of motion to be the global z axis as illustrated in Fig. 3. With the neck of the guitar pointed in the positive x direction and the plane of the guitar top-plate oriented parallel to the plane of the piston, the guitar was centered in the y direction and placed so that the middle of the top plate was 1.4 m from the piston in the z direction. These simulations demonstrate that as the gain is increased, the first mode of the guitar, the air mode, is driven unstable. The change in the phase angle in Fig. 5 at the highest gain values from $-90°$ to $+90°$ of the air mode resonance at approximately 108 Hz indicates the transition from a stable to an unstable mode. The unstable mode forms the feedback instability that ultimately limits the achievable amplified speaker volume for the guitar system.

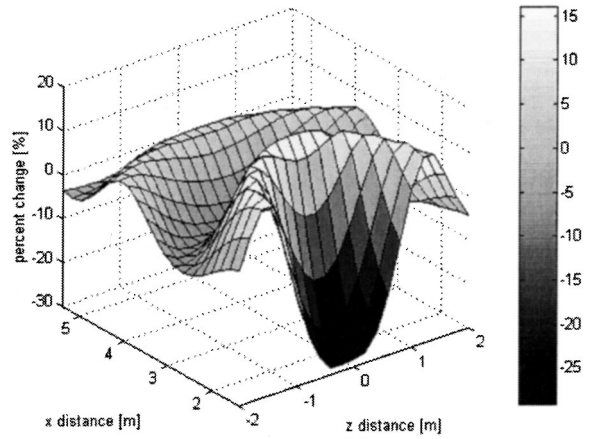

FIG. 7. Fractional change in guitar second mode (first plate mode) amplitude as a function of relative position.

B. Potential solutions to feedback instability

The first solution one might consider to acoustic feedback instability is to change the position of the amplified guitar relative to the amplified piston. The system represented in Fig. 3 can be solved at relatively low gain for many locations in the half-space in front of the piston to help visualize the changes in the guitar structural dynamics as a function of position. Figures 6–8 give a graphic representation of the fractional changes in amplitude of the air mode and the first and second plate modes that form the first three modes in the coupled guitar transfer function, respectively. The fractional change is defined as the difference between the modal amplitudes of the feedback-guitar model evaluated at various positions as compared to the initial position given in Fig. 5. The difference at each position is divided by the modal amplitude at the initial position to get the fractional change. At each new location, the plane of the top-plate is kept parallel to the plane of the piston and the x and z coordinates are varied. These simulations show that the coupling of the acoustic feedback path, and hence the modal amplitude, is highly dependent upon the spatial relationship between the guitar and the monitor loudspeaker. The amplitude of the modal response will determine the gain margins of the system, which indicates the relative stability of the feedback-guitar system.

Another solution to feedback instability is to increase the passive damping in the two plate modes. This solution is implemented in some guitars that are designed to be amplified. The transfer function in Fig. 9 shows the feedback-

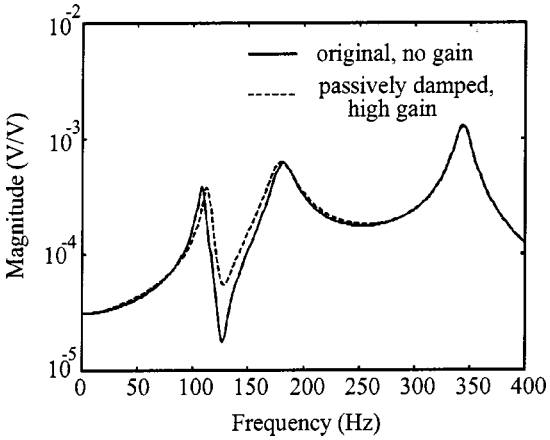

FIG. 9. Effect of adding passive damping to the first and second plate modes to suppress feedback instability.

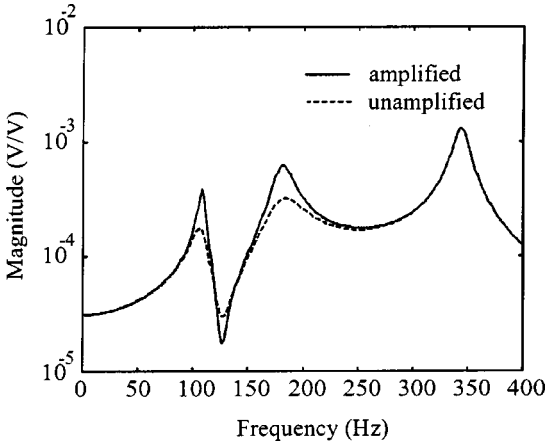

FIG. 10. Passive damping suppresses modes when guitar is not amplified.

guitar model behavior for the highest gain used in Fig. 5 with a multiplication factor increase in modal damping ratio of 1.7 and 2.0, respectively, in the first two plate modes. This is compared to the unamplified response of the feedback-guitar system with no added damping. The modal damping increases were determined so that the first and second mode amplitudes were approximately equal for the amplified and unamplified cases. This illustrates that by damping the plate modes, the system response does not go unstable when amplified. When the guitar is amplified, its response is similar to the response of the original guitar without additional damping.

Aside from the obvious difficulties of adding passive damping to the structural and air modes without detrimentally influencing other aspects of the dynamics like the modal amplitudes and frequencies, a major shortcoming of the passive solution is the behavior when the guitar is not amplified. Figure 10 presents the response of the feedback-guitar system with added modal damping when amplified and unamplified. The amplitude of the guitar response is significantly reduced at the first two modes when the amplifier is off. This shows that the passive damping approach renders the guitar response ''dead'' when it is not amplified.

Another solution is to actively damp the plate and piston modes. In this case, an additional control feedback loop is added to the system to mitigate the effects of the acoustic feedback loop. The advantage of this approach is that the control loop can be turned on, when the guitar is amplified, and turned off when the guitar is not amplified. In this way, the guitar dynamics are similar both amplified and unamplified. Another advantage is that the air mode can be controlled through its structural coupling to the first-plate mode, making it unnecessary to impede or eliminate the air piston dynamics as is done with many existing devices.[1,2,5]

The actual control law implemented will greatly influence the closed-loop performance. The simplest approach is to implement a fixed-gain controller that selectively adds damping to structural modes. Since the amount of damping that needs to be added to each structural mode depends on both the position of the guitar and the amplification of the sound system, this approach would require a calibration step to determine the appropriate control law. It would also require the guitar to remain in the position where it was calibrated to maintain performance. In these limitations, this method is similar to the notch filter approach cited earlier. However, using the active vibration control approach produces a less detrimental effect on the sound from the guitar, since the ideal implementation would not require a decreased sound volume at selected frequencies. A more complex, adaptive controller would offer a more flexible solution and make the active approach more attractive. If the adaptive controller could be configured as a pole-placement filter whose objective was to preserve the unamplified structural dynamics of the guitar top-plate, the guitar could be made insensitive to changes in the sound system gain and position, and would effectively turn off when the guitar was not amplified. In this case, the active control loop would be exactly canceling the acoustic feedback loop.

C. Controller design

To illustrate the concept, a simple, parallel second-order positive-position feedback (PPF) controller was developed to control the modes that are destabilized by the acoustic feedback with the guitar in the initial position. The transfer function of a single PPF controller is given as

$$H_c(s)=\frac{K_1}{s^2+2\zeta_c\omega_c s+\omega_c^2}, \tag{11}$$

where ζ_c and ω_c are the damping ratio and design frequency of the controller, and K_1 is a constant gain. The parallel implementation combines two PPF controllers in parallel with the parameters of each filter designed to add damping to the structural modes. The objective was to add the same amount of damping to the first and second modes of the guitar model as the passive solution previously discussed. The frequency response of the resulting controller is presented in Fig. 11. The open- and closed-loop feedback-guitar model with the PPF controller implemented and no gain on the acoustic feedback path ($G=0$) is shown in Fig. 12. This shows that with the controller turned on and no acoustic feedback, the controller adds damping to the targeted modes as designed. The resulting response using the feedback controller and the previously used destabilizing gain in the

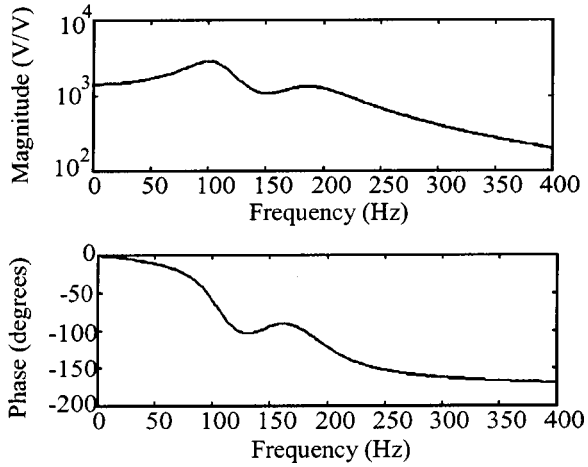

FIG. 11. PPF controller designed to add damping to the first and second guitar modes.

acoustic feedback path is shown in Fig. 13 with the original unamplified open-loop guitar model. This demonstrates that the PPF controller stabilizes the first mode when amplified, and that the responses of the first and second modes are approximately equal to the unamplified case.

Finally, Fig. 14 illustrates the sensitivity of the closed-loop system to changes in position relative to the monitor speaker. The same gains on both the acoustic and control feedback path used in Fig. 13 are maintained, but the guitar position is moved slightly closer to the monitor speaker from 1.4 to 1.1 m. In this case, the first mode goes unstable and the second mode is heavily damped. This result shows that the solution that a fixed-gain controller provides can only be guaranteed to perform at the position for which it was designed.

III. EXPERIMENT

An experiment was designed to show qualitative agreement with the acoustic feedback model. Since the original guitar used in the development of the model did not have a factory-installed pickup and illustration of active feedback suppression on a guitar that was designed for amplification was an important goal of the experiment, it was not used to investigate experimental feedback suppression. The guitar

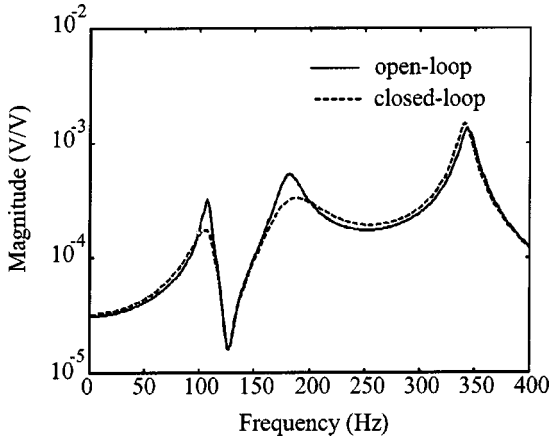

FIG. 12. Effect of closing the control loop on the guitar dynamics.

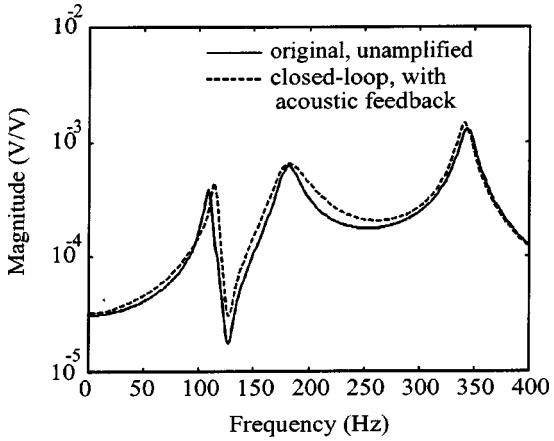

FIG. 13. Effect of both acoustic feedback and the control feedback loops.

used in the experimental investigation of this work was an acoustic/electric Yamaha APX-6N. The major difference in the low frequency behavior of the two guitars was 45° rotation of the second plate mode. Since the FE model was not used directly for actuator location and the feedback controller was designed for the first plate mode, this difference was not significant.

Two piezoelectric ceramic PZT5A actuators were attached to the top-plate of the guitar and the built-in pickup was used as the sensor. The dimensions of the piezoelectric ceramic actuators were 3.8 cm by 6.4 cm by 0.25 mm, and the mass of each actuator was 4.7 g. The actuators were bonded using a quick setting epoxy. The locations of the actuators were selected to couple well with the air and first plate mode of the guitar. Piezoelectric ceramic actuators apply in-plane force, so good coupling locations are regions of high in-plane surface strain for a given mode.[15] Since the air and first plate mode of the guitar top-plate are primarily composed of motion of the lower bout, which approximately matches the first mode shape of a circular plate with fixed boundaries,[16] regions of high in-plane strain were predicted at the edge and in the center of the lower bout. This can easily be verified using the exact solution for the first mode of a plate constrained in this manner.[17] Two convenient actuator attachment locations were selected in these regions.

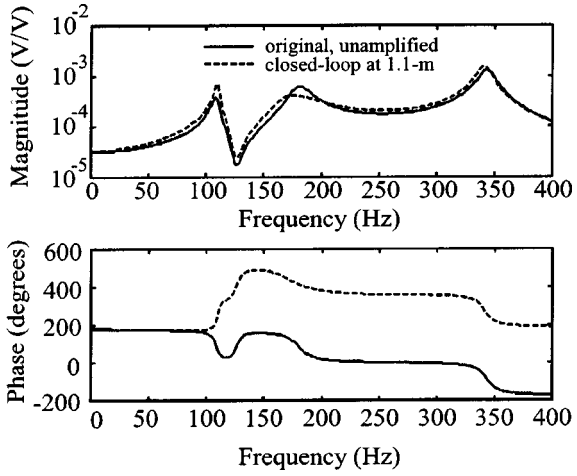

FIG. 14. Effect of changing position on "controlled" guitar.

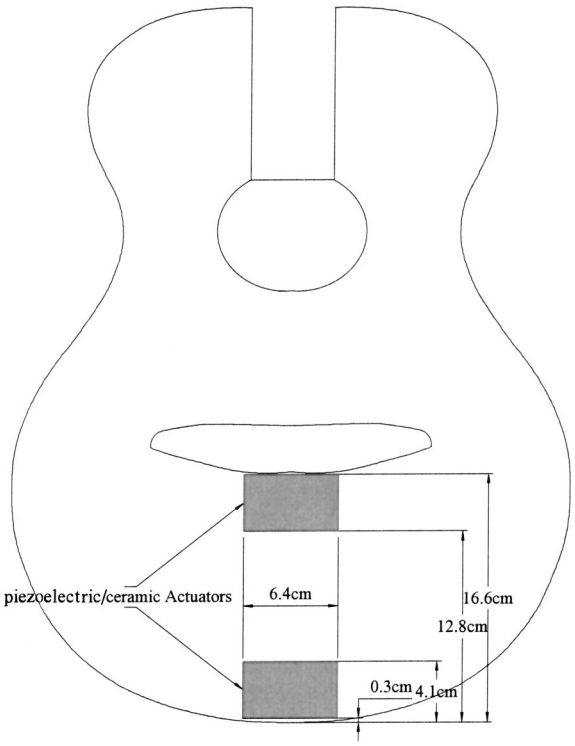

FIG. 15. Actuator locations.

These locations were centered along the shorter dimension of the guitar and are near the bottom of the lower bout and immediately below the bridge, respectively. The actuator locations are shown more nearly precisely in Fig. 15.

The guitar was placed on a 35 cm by 25 cm piece of foam and leaned against a wall, the back of the guitar making an angle of approximately 75° with the foam. This boundary condition was intended to approximate a performance position as opposed to a modal testing position. The strings were not removed or dampened in any way so that their coupled dynamics would also contribute to the response. A 38 cm (15 in.) loudspeaker and amplifier combination was placed directly in front of the guitar at a distance of 2.05 m. A modal survey was conducted using a scanning laser vibrometer as the sensor and the acoustic excitation of the loudspeaker as the input to determine the response of the guitar top-plate with the piezoceramic actuators and the given boundary conditions. A burst-chirp disturbance was played though the amplifier and loudspeaker, and the scanning laser vibrometer measured progressive frequency response functions over a grid of points on the guitar top-plate. The burst chirp measurements were used to prevent overlapping of the data windows resulting from acoustic delays. The mode shapes measured for the air mode at 124 Hz, the first plate mode at 239 Hz, and the second plate mode at 359 Hz are shown in Figs. 16, 17, and 18, and are overlaid on the guitar top-plate.

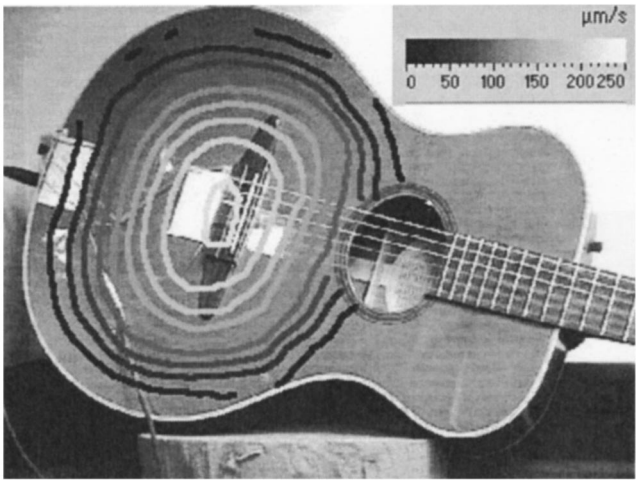

FIG. 17. Experimentally measured first plate mode at 239 Hz.

Next, the guitar pick-up was connected to the amplifier and loudspeaker system. This established an acoustic feedback loop. The gain on the amplifier was increased (without any control loop), until the feedback-guitar system just went unstable. The sound level associated with the instability, is measured by a C-weighted sound level meter 1 m in front of the speaker, reached a maximum of 116 dB. Immediately in front of the speaker, the sound level surpassed the meter's maximum range of 126 dB. A measurement of the modal response, taken at this same gain level, shows that the top-plate response was dominated by the first plate mode shape

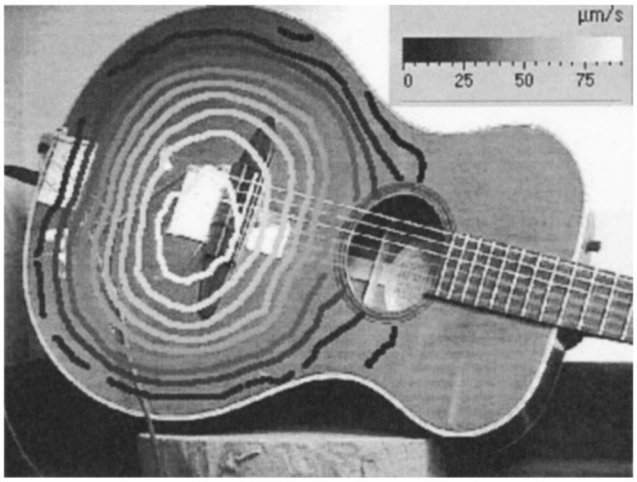

FIG. 16. Experimentally measured response of the air mode at 124 Hz.

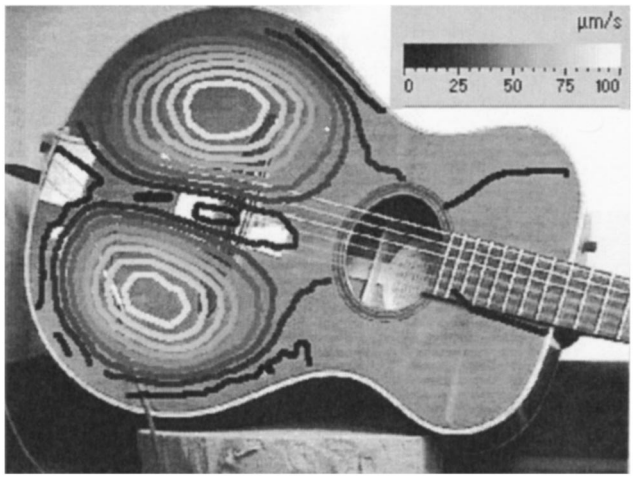

FIG. 18. Experimentally measured second plate mode at 359 Hz.

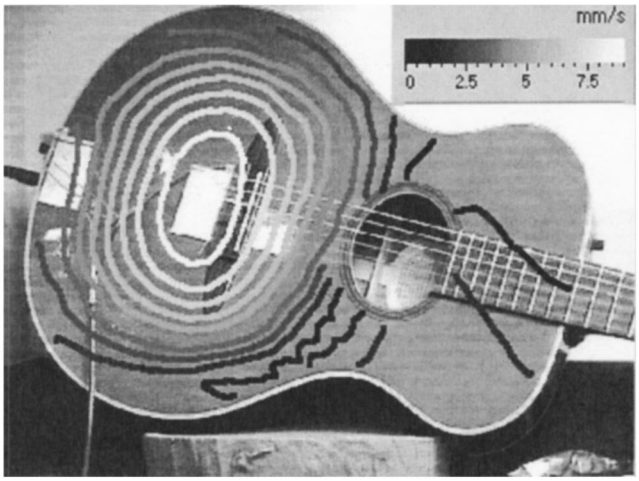

FIG. 19. Experimentally measured response of the unstable mode at 239 Hz.

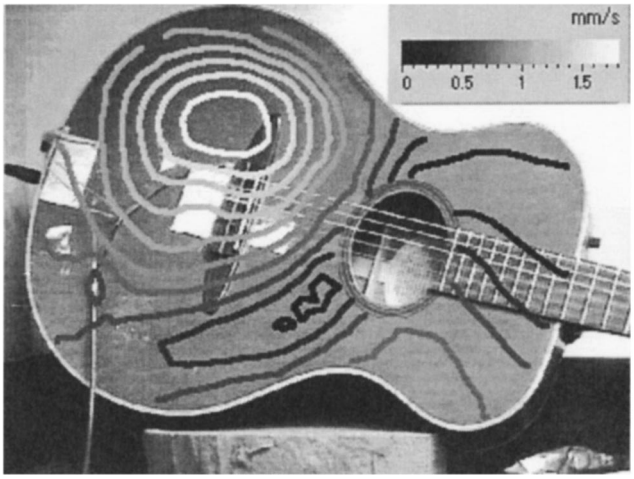

FIG. 21. Predominated motion of the unstable guitar with the control loop closed.

at 239 Hz, which is shown in Fig. 19. This indicates that the first plate mode was going unstable due to the acoustic feedback, and clearly indicates that an active control solution should focus on adding damping to the mode at 239 Hz.

A PPF controller was designed and implemented on a DSPACE Model 1003 digital signal processing system to increase damping at 239 Hz. An additional bandpass filter was put in series with the filter to provide additional gain roll-off in order to prevent control spillover. The measured frequency response function of the controller is presented in Fig. 20. This frequency response function also included some low frequency dynamics introduced by the signal conditioning built into the guitar pickup. With the controller on, the speaker amplifier gain was again turned up until the system went unstable. This time the gain level at which the instability occurred was significantly higher. The motion of the guitar top-plate was remeasured using the vibrometer, and is presented in Fig. 21. Frequency response measurements indicate that, again, the first plate mode goes unstable. Figure 21 has several interesting characteristics when compared to Fig. 19, which showed the predominant motion of the unstable system with no control loop. The control loop radically changed the shape of the first plate mode at high gain. This indicates that there were two potential mechanisms at work that allowed the higher amplifier gain: the active controller added damping to the mode, and the active controller changed the shape of the mode so that it was not as effective at coupling into the acoustic field. Another interesting thing to note about Fig. 21 is that the isolines become discontinuous in the neighborhood of the piezoelectric ceramic actuators that are providing the control force to the guitar, especially the actuator adjacent to the guitar bridge.

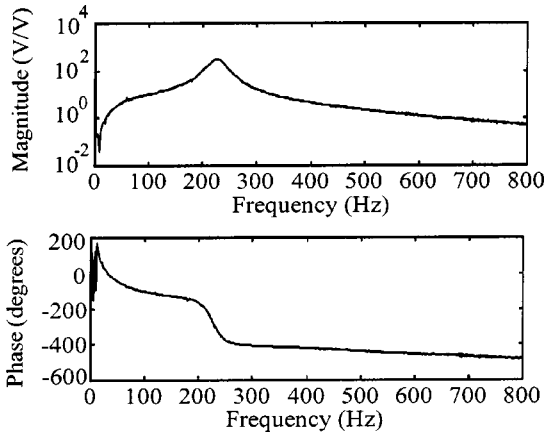

FIG. 20. Measured frequency response of the PPF controller implemented to actively dampen the first plate mode at 239 Hz.

In order to quantify the increase in gain that was achieved with the addition of the active control loop, a frequency response function was measured between the piezoelectric ceramic control actuator and the amplifier output at gain levels just under the gain that caused the instability with and without the active control loop. With the control loop closed, the frequency response function was 7 dB higher than with no controller. This was measured by comparing the average increase in gain over the frequency range from 0 to 800 Hz. The power associated with the control signal to allow the increased gain was quite small. A maximum rms voltage of 2.3 V across the piezoelectric ceramic actuator with the control loop closed was measured using a Fluke ''true rms'' digital volt meter at the highest achievable gain prior to instability with the low E string plucked and allowed to ring down. Assuming a linear amplifier, a conservative estimate of power[18] associated with the primarily capacitive load is

$$P = 2 i_q v_r + \frac{2 \omega C v_r^2}{\pi}. \tag{12}$$

In view of the relatively low rms voltage, a rail voltage, v_r, of 9 V is assumed sufficient. Also assuming quiescent current, i_q, as 60 μA, the measured capacitance, C, of 308 nF, and control effort primarily at 239 Hz, the power using Eq. (12) is 25 mW. Incorporating a safety factor of 3 to account for power requirements of the control electronics, a conservative estimate of power requirements for an analog version of the control electronics is 75 mV. It should also be noted that driving a piezoceramic with a linear amplifier is very inefficient, and that the power requirements could be significantly reduced with a more efficient, switching amplifier

design.[19] Even with a linear amplifier, the maximum power delivery is well within the capabilities of a small integrated circuit and two 9 V batteries, and could be designed to be part of the guitar's pickup.

IV. CONCLUSION

A model was introduced that predicts acoustic feedback instability that results in amplified acoustic instruments at high gain levels. Three potential solutions were proposed, all of which had advantages and disadvantages. Changing relative location with respect to the amplified piston has the potential to decrease the destabilizing effect of the amplified piston on a given mode, but it is likely that the new position will result in destabilizing another mode. Addition of passive damping is simple and effective, but the unamplified dynamics are severely degraded by this solution. Active control can eliminate feedback instability but requires the addition of sensors, actuators, and control electronics. Also, fixed gain active control is only guaranteed to perform at the position it was designed for. A more robust active approach would be a fully adaptive controller that cancels the effect of the acoustic feedback on the guitar dynamics.

An experiment was performed that qualitatively verified the fixed gain, active control approach to suppress feedback instability. A full 7 dB increase in amplifier gain was possible with the incorporation of feedback control. The power necessary for the active controller was approximately 75 mW, indicating the possibility for a relatively small electronics package and battery power.

ACKNOWLEDGMENTS

The authors would like to gratefully acknowledge the United States Air Force Research Laboratory, Space Vehicle's Directorate, Kirtland AFB, NM, for use of laboratory equipment for this work.

[1] P. Damiano, ''Feedback reducer for an acoustic electric guitar,'' U.S. Patent 4,394,830 (1983).
[2] W. Kopp, ''Musical instrument sound quality enhancement device,'' U.S. Patent 4,632,003 (1986).
[3] D. Admiraal and B. Lopes Cardozo, ''Amplifer with automatic inhibition of acoustic feedback,'' U.S. Patent 4,747,144 (1988).
[4] William Staudacher, ''Acoustic feedback cancellation for equalized amplifying systems,'' U.S. Patent 5,533,120 (1996).
[5] Michael Baker, ''Feedback minimizing device,'' U.S. Patent 5,883,322 (1999).
[6] I. M. Firth, ''Physics of the guitar at the Helmholtz and first top-plate resonance,'' J. Acoust. Soc. Am. **61**, 588–593 (1977).
[7] O. Christensen and B. Vistisen, ''Simple model for low-frequency guitar function,'' J. Acoust. Soc. Am. **68**, 758–766 (1980).
[8] G. Caldersmith, ''Designing a guitar family,'' Appl. Acoust. **46**, 3–17 (1995).
[9] S. Griffin, H. Luo, and S. Hanagud, ''Acoustic guitar function model including symmetric and asymmetric plate modes,'' Acustica **84**, 563–569 (1998).
[10] C. Norney, ''Strain-gauge sensors eliminate acoustic feedback in amplified acoustic stringed instruments,'' J. Audio Eng. Soc. **30**, 107–111 (1982).
[11] C. Nourney, ''Infinite sustain through controlled feedback in amplified guitars,'' 75th Convention of the Audio Engineering Society, 27–30 March 1994, Paris, France.
[12] S. Hanagud and S. Griffin, ''Active structural control for a smart guitar,'' Fourth European Conference On Smart Structures and Materials, 6–8 July 1998, Harrogate, U.K.
[13] S. Griffin, ''Acoustic replication in smart structures using active acoustic control,'' Ph.D. thesis, Georgia Tech., Department of Aerospace Engineering, 1995.
[14] L. E. Kinsler, A. R. Frey, A. B. Coppens, and J. V. Sanders, *Fundamentals of Acoustics*, 3rd ed. (Wiley, New York, 1982).
[15] E. Crawley and J. de Luis, ''Use of piezoelectric actuators as elements of intelligent structures,'' AIAA J. **25**, 1373–1385 (1987).
[16] B. Richardson and G. Roberts, The adjustment of mode frequencies in guitars: A study by means of holographic interferometry and finite element analysis,'' Proceedings SMAC 83. Royal Swedish Academy of Music, Stockholm, 1985.
[17] L. Meirovitch, *Analytical Methods in Vibrations* (Macmillan, New York, 1967).
[18] ''General operating considerations—Application note 1,'' Rev. B, Apex Microtechnology, Tuscon, AZ, 1998.
[19] PWM basics—application note 30,'' Rev. B, Apex Microtechnology, Tucson, AZ, 1998.

Optimization and implementation of piezoelectric radiators using the genetic algorithm

Mingsian R. Bai[a] and Chinghong Huang
Department of Mechanical Engineering, National Chiao-Tung University, 1001 Ta-Hsueh Road, Hsin-Chu 300, Taiwan, Republic of China

(Received 27 September 2002; revised 5 February 2003; accepted 25 February 2003)

Very thin and small (45 mm×35 mm×0.35 mm) piezoelectric radiators have been developed in this research. The system is modeled by using the energy method in conjunction with the assumed-modes method. Electrical system, mechanical system, and acoustic loading have all been accounted for during the modeling stage. On the basis of the simulation model, the genetic algorithm (GA) is employed to optimize the overall configurations for a low resonance frequency and a large gain. The resulting designs are then implemented and evaluated experimentally. Performance indices for the experimental evaluation include the frequency response, the directional response, the sensitivity, and the efficiency. It is found in the experimental results that the piezoelectric radiators are able to produce comparable acoustical output with significantly less electrical input than the voice-coil panel speakers. © *2003 Acoustical Society of America.* [DOI: 10.1121/1.1568944]

PACS numbers: 43.38.Fx, 43.38.Ja [AJZ]

I. INTRODUCTION

Miniaturization has been a major trend over the recent years in the so-called 3C industries: computer, communication, and consumer electronics. Like the other components, the loudspeakers are faced with the need to further reduce their sizes, in particular for the 3C products, e.g., personal data assistants (PDAs), mobile phones, MP3 players, etc. The panel speaker offers a potential solution to suit the above need.[1] The panel speaker provides various advantages over the conventional loudspeakers such as omnidirectivity, linearity, insensitivity to room conditions, bipolar radiation.[2] Of particular interest is that the panel speaker is planar, light, and compact, which makes it an attractive feature for many space-constrained applications. A detailed analysis and evaluation of the panel speaker can be found in Ref. 1.

Despite all the advantages, the panel speaker suffers from two drawbacks that may restrict its practical application in the 3C products. First, in the conventional design, the exciter for a panel speaker is generally the voice-coil type. The state-of-art manufacturing voice-coil exciters could reach only approximately 2 mm thickness, which is still considered too thick for many applications, such as the displays of mobile phones. Second, the electroacoustic efficiency of the conventional panel speakers driven by electromagnetic exciters was found to be quite low,[1] which raised the serious concern about the power consumption in mobile electronic products. These physical limitations associated with the conventional exciters hence motivate the development of an alternative way of excitation using a different mechanism. In this paper, planar radiators excited by piezoelectric ceramic (PZT) are proposed in an attempt to overcome the problems encountered in voice-coil exciters.[3,4] Piezoelectric ceramics can be fabricated into various shapes and thicknesses, as desired. In addition, virtually no power is consumed nor heat generated to maintain a piezoelectric actuator in an energized state. As will be manifested in the latter experimental verification, the high efficiency of piezoelectric material makes the proposed radiator an ideal device for many battery-driven products. The conversion of electrical energy into mechanical motion takes place without the generation of any magnetic field or the need for moving electrical contacts. Moreover, piezoelectric devices are capable of response times under a millisecond, limited only by the inertia of the object being moved and the output capability of the electric driver.

This paper is organized as follows. First, the energy method in conjunction with the assumed-modes method is used to derive the dynamic model of the piezoelectric radiator. The electrical system, the mechanical system, and acoustic loading have all been accounted for during the modeling stage. An electromechanical equivalent circuit is obtained for the single mode of the system. Second, on the basis of the above model, the genetic algorithm (GA) is used to optimize the design variables. Third, designs resulting from the optimization are then implemented and evaluated experimentally. Frequency response, directional response, sensitivity, and efficiency are measured in order to evaluate system performance. Finally, technical discussions and a future extension of this work are summarized.

II. DYNAMIC MODELING OF THE PIEZOELECTRIC RADIATOR

In this section, the constitutive equation of piezoelectricity is given, followed by the dynamic modeling using the energy method. Electrical system, mechanical system and acoustic loading are combined into a state-space form. The special case of the single mode of the system will also be presented in terms of an equivalent circuit.

[a]Author to whom correspondence should be addressed. Electronic mail: msbai@mail.nctu.edu.tw; telephone (03)5712121, ext. 55108.

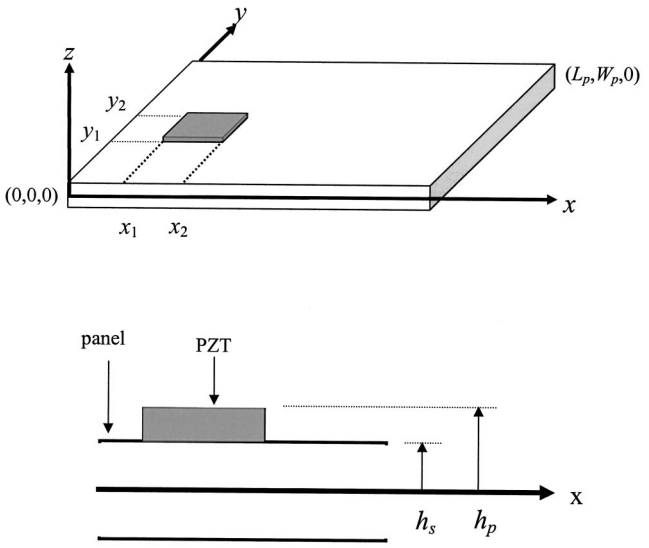

FIG. 1. Schematic diagram of the piezoelectric panel radiator. It consists of a panel and a PZT plate.

A. Energy method based on the variation principle

The model of the piezoelectric planar radiator in Fig. 1 consists of a rectangular panel and a rectangular PZT plate. Assume that the vibration of the system is small such that the nonlinear terms are negligible. The panel is of length L_P and width W_P. Let the transverse displacement of the plate be $w(x,y,t)$. The kinetic energy of the plate is

$$T_p=\frac{1}{2}\int_0^{W_p}\int_0^{L_p}\rho_p w_t^2(x,y,t)\,dx\,dy, \tag{1}$$

where ρ_p is the area density of the panel and the subscript "t" denotes the first partial derivative with respect to the time variable t. The bending strain energy of the plate is[5]

$$U_p=\frac{1}{2}D\int_0^{W_p}\int_0^{L_p}[w_{xx}^2+w_{yy}^2+2\upsilon w_{xx}w_{yy} +2(1-\upsilon)w_{xy}^2]dx\,dy, \tag{2}$$

where $D=Eh^3/12(1-\upsilon^2)$ is the bending stiffness of the panel, $h=2h_s$ is the thickness of the panel, E is the Young's modulus of the panel, and υ is the Poisson's ratio of the panel. The subscript "xx" denotes the second partial derivative with respect to the space coordinate x; a similar rule applies to the other variables. It should be clear from the context, where all subscripts in the following equations that are not in the definition of the variable should be interpreted as differentiation with respect to the variable.

On the other hand, the internal energy of the PZT plate needs to be established. The formulation is based on the h-form constitutive equations. For our problem at hand, the constitutive equations of a hexagonal crystal class (6 mm) PZT plate can be written as

$$\begin{bmatrix}T_1\\T_2\\T_6\\E_3\end{bmatrix}=\begin{bmatrix}c_{11}^D & c_{12}^D & 0 & -h_{31}\\ c_{12}^D & c_{11}^D & 0 & -h_{31}\\ 0 & 0 & c_{66}^D & 0\\ -h_{31} & -h_{31} & 0 & \beta_{33}^S\end{bmatrix}\begin{bmatrix}S_1\\S_2\\S_6\\D_3\end{bmatrix}, \tag{3}$$

where T is the stress, S is the strain D is the dielectric displacement, E is the field strength, h is the piezoelectric voltage constant, c^D is the elastic stiffness under the condition of constant dielectric displacement, and β^S is the impermittivity under the condition of constant strain, the subscripts signify the orientation of electrical and mechanical quantities, and $c_{66}^D=(c_{11}^D-c_{12}^D)/2$. From the thin-plate theory, $S_1=-zw_{xx}$, $S_2=-zw_{yy}$, and $S_6=-2zw_{xy}$. The internal energy of the piezoelectric material U_c can be expressed as[6]

$$\begin{aligned}U_c&=\frac{1}{2}\int_V[(T_1S_1+T_2S_2+T_6S_6)+E_3D_3]dV,\\ &=\frac{1}{2}\left\{\int_{y_1}^{y_2}\int_{x_1}^{x_2}[c_{11}^D I_1(w_{xx}^2+w_{yy}^2)+2c_{12}^D I_1 w_{xx}w_{yy}\right.\\ &\quad+2h_{31}D_3I_2(w_{xx}+w_{yy})+4c_{66}^D I_1 w_{xy}^2]dx\,dy\\ &\quad\left.+\beta_{33}^S V_c D_3^2\right\},\end{aligned} \tag{4}$$

where $I_1=(h_p^3-h_s^3)/3$, $I_2=(h_p^2-h_s^2)/2$, and $V_c=W_cL_c(h_p-h_s)$ is the volume of PZT. W_c and L_c are the width and the length of PZT. The virtual work done by the noninertial forces and the external voltage is written as

$$\begin{aligned}\delta W&=\int_{y_1}^{y_2}\int_{x_1}^{x_2}V_a(t)\,\delta D_3\,dx\,dy\\ &\quad+\int_0^{W_p}\int_0^{L_p}f(x,y,t)\,\delta w\,dx\,dy\\ &=V_a\,\delta D_3\,A_c+\int_0^{W_p}\int_0^{L_p}f(x,y,t)\,\delta w\,dx\,dy,\end{aligned} \tag{5}$$

where $A_c=W_cL_c$, and V_a is the applied voltage to the PZT.

B. Assumed-modes method

The assumed-modes method is then employed in deriving the discretized equation of motion.[7] In this method, the continuous system is approximated as an n-degree-of-freedom system, where the displacement satisfies

$$w(x,y,t)=\sum_{i=1}^{n}\phi_i(x,y)q_i(t), \tag{6}$$

where $\phi_i(x,y)$ are *admissible functions* and $q_i(t)$ are the *principal coordinates*.[7] Using the series expansion, the energy terms shall be discretized in terms of the principal coordinates. The kinetic energy can be expressed as

$$T_p=\frac{1}{2}\sum_{i=1}^{n}\sum_{j=1}^{n}m_{ij}\dot{q}_i(t)\dot{q}_j(t), \tag{7}$$

where

$$m_{ij}=\rho_p\int_0^{W_p}\int_0^{L_p}\phi_i(x,y)\,\phi_j(x,y)\,dx\,dy \tag{8}$$

are symmetric mass coefficients. In a similar fashion, the strain energy of the panel can be written as

$$U_p=\frac{1}{2}\sum_{i=0}^{n}\sum_{j=0}^{n}k_{ij}^{p}q_i(t)q_j(t), \tag{9}$$

where

$$\begin{aligned}k_{ij}^{p}=D\int_0^{W_p}\int_0^{L_p}&[\phi_{i,xx}(x,y)\,\phi_{j,xx}(x,y)\\&+\phi_{i,yy}(x,y)\,\phi_{j,yy}(x,y)+2\upsilon\phi_{i,xx}(x,y)\,\phi_{j,yy}(x,y)\\&+2(1-\upsilon)\phi_{i,xy}(x,y)\,\phi_{j,xy}(x,y)]k\,dx\,dy.\end{aligned} \tag{10}$$

The internal energy of the PZT can also be expressed as

$$\begin{aligned}U_c=&\frac{1}{2}\sum_{i=0}^{n}\sum_{j=0}^{n}k_{ij}^{c}q_i(t)q_j(t)+\frac{1}{2}\sum_{i=0}^{n}\alpha_i q_i(t)D_3\\&+\tfrac{1}{2}V_c\beta_{33}^{S}D_3^2,\end{aligned} \tag{11}$$

where

$$\begin{aligned}k_{ij}^{c}=\int_{y_1}^{y_2}\int_{x_1}^{x_2}I_1\{&c_{11}^{D}[\phi_{i,xx}(x,y)\,\phi_{j,xx}(x,y)\\&+\phi_{i,yy}(x,y)\,\phi_{ji,yy}(x,y)]\\&+2c_{12}^{D}\phi_{i,xx}(x,y)\,\phi_{j,yy}(x,y)\\&+4c_{66}^{D}\phi_{i,xy}(x,y)\,\phi_{j,xy}(x,y)\}dx\,dy,\end{aligned} \tag{12}$$

$$\alpha_i=2h_{31}I_2\int_{y_1}^{y_2}\int_{x_1}^{x_2}[\phi_{i,xx}(x,y)+\phi_{i,yy}(x,y)]dx\,dy. \tag{13}$$

The virtual energy is written as

$$\delta W=A_c V_a\,\delta D_3+\sum_{i=0}^{n}f_i\,\delta q_i(t), \tag{14}$$

where

$$f_i=\int_0^{W_p}\int_0^{L_p}f(x,y,t)\,\phi_i(x,y)\,dx\,dy \tag{15}$$

are modal forces. Let

$$k_{ij}^{t}=k_{ij}^{p}+k_{ij}^{c}, \tag{16}$$

and k_{ij} are symmetric stiffness coefficients. The dielectric displacement $D_3=D_3(t)$ in the z axis is assumed to be constant on the electrodes and is a function of time because in our application the problem can be treated as electrostatic.

C. The Lagrange equation

The introduction of the assumed modes to the energy terms in the early stage rather than to the differential equations offers great convenience. The discretized energy terms are then substituted into the Lagrange equation,

$$\frac{d}{dt}\left(\frac{\partial L}{\partial\dot{q}_i}\right)-\frac{\partial L}{\partial q_i}=f_i,\quad i=1,2,...,n, \tag{17}$$

$$-\frac{\partial L}{\partial D_3}=A_c V_a, \tag{18}$$

where $L=T_p-U_p-U_c$ is the *Lagrangian*. The substitution leads directly to the following dynamic equations:

$$\sum_{j=1}^{n}m_{ij}\ddot{q}_j(t)+\sum_{j=1}^{n}k_{ij}^{t}q_j(t)+\frac{\alpha_i}{A_c}Q=f_i,\quad i=1,2,...,n, \tag{19}$$

$$\frac{1}{A_c}\sum_{j=1}^{n}\alpha_j q_j(t)+\frac{t_c}{A_c}\beta_{33}^{S}Q=V_a, \tag{20}$$

where t_c is the thickness of PZT and $D_3=Q/A_c$, with Q being the electric charges on the electrodes. These equation can be written in a matrix form:

$$\mathbf{M}\ddot{\mathbf{q}}+\mathbf{K}\mathbf{q}+\boldsymbol{\alpha}Q=\mathbf{f}, \tag{21}$$

$$\boldsymbol{\gamma}^T\mathbf{q}+\lambda Q=V_a, \tag{22}$$

where $\mathbf{M}=[m_{ij}]$, $\mathbf{K}=[k_{ij}^{t}]$, $\boldsymbol{\alpha}=[\alpha_i/A_c]$, $\boldsymbol{\gamma}=[\alpha_j/A]$, and $\lambda=t\beta_{33}^{S}/A_c$.

To account for the effects of electrical circuit,

$$V_a=V_s-R\dot{Q}-L\ddot{Q}, \tag{23}$$

where V_s is the source voltage, R and L are the equivalent resistance and the inductance, respectively. Equations (21) and (22) can be assembled into a state-space form:

$$\begin{aligned}\frac{d}{dt}\begin{bmatrix}\mathbf{q}\\Q\\\dot{\mathbf{q}}\\Q\end{bmatrix}=&\begin{bmatrix}0&0&1&0\\0&0&0&1\\-\mathbf{M}^{-1}\mathbf{K}&-\mathbf{M}^{-1}\boldsymbol{\alpha}&0&0\\-\frac{1}{L}\boldsymbol{\gamma}^T&-\frac{\lambda}{L}&0&-\frac{R}{L}\end{bmatrix}\begin{bmatrix}\mathbf{q}\\Q\\\dot{\mathbf{q}}\\Q\end{bmatrix}\\&+\begin{bmatrix}0&0\\0&0\\\mathbf{M}^{-1}&0\\0&\frac{1}{L}\end{bmatrix}\begin{bmatrix}\mathbf{f}\\V_s\end{bmatrix}.\end{aligned} \tag{24}$$

D. Acoustic loading

In addition to the electrical system and the mechanical system, the acoustic loading is also considered in the modeling. In physical coordinates, the relationship between the sound pressure and the surface velocity can be approximated in a discrete form,

$$\mathbf{p}=\mathbf{Z_A}\mathbf{v}, \tag{25}$$

where $\mathbf{p}$ is the sound pressure vector, $\mathbf{v}$ is the surface velocity vector, and $\mathbf{Z_A}$ is the *radiation impedance matrix*:[8]

$$\mathbf{Z_A} = \rho_p c_s \begin{bmatrix} 1-e^{-jk\sqrt{A/\pi}} & \frac{jkA}{2\pi}\frac{e^{-jkr_{12}}}{r_{12}} & \cdots & \frac{jkA}{2\pi}\frac{e^{-jkr_{1n}}}{r_{1n}} \\ \frac{jkA}{2\pi}\frac{e^{-jkr_{21}}}{r_{21}} & 1-e^{-jk\sqrt{A/\pi}} & \cdots & \vdots \\ \vdots & \vdots & \ddots & \vdots \\ \frac{jkA}{2\pi}\frac{e^{-jkr_{m1}}}{r_{m1}} & \cdots & \cdots & 1-e^{-jk\sqrt{A/\pi}} \end{bmatrix}, \tag{26}$$

in which $r_{mn}=r_{nm}$ is the distance from the element m to the element n, $1\leqslant m$, $n\leqslant N$, and $k=\omega/c_s$ is the wave number, with c_s being the speed of sound. A is the area of each element.

Rewrite the assumed-modes expansion of Eq. (6) in the matrix form

$$\mathbf{w}=\mathbf{\Phi q}, \tag{27}$$

where $\mathbf{\Phi}=\lfloor\phi_{ij}(x,y)\rfloor$, in which $\phi_{ij}(x,y)$ is the admissible function of the ijth mode. $\mathbf{w}$ and $\mathbf{q}$ are defined as the physical and modal displacement vectors, respectively, on the panel surface. $\mathbf{\Phi}$ is the transformation matrix that relates the physical space and the modal space. Using the matrix $\mathbf{\Phi}$, Eq. (25) can be transformed into the modal space. Let $\tilde{\mathbf{p}}$ and $\tilde{\mathbf{v}}$ be the surface pressure and velocity in the modal space,

$$\mathbf{p}=\mathbf{\Phi}\tilde{\mathbf{p}}, \tag{28}$$

$$\mathbf{v}=\mathbf{\Phi}\tilde{\mathbf{v}}. \tag{29}$$

Hence, we have

$$\tilde{\mathbf{p}}=\tilde{\mathbf{Z}}_\mathbf{A}\tilde{\mathbf{v}}, \tag{30}$$

where the modal radiation impedance,

$$\tilde{\mathbf{Z}}_\mathbf{A}=\mathbf{\Phi}^{-1}\mathbf{Z_A}\mathbf{\Phi}. \tag{31}$$

To obtain the frequency response function, we let

$$\tilde{\mathbf{v}}=j\omega\mathbf{q}. \tag{32}$$

Substituting Eqs. (30) and (32) into Eqs. (21) and (22) yields the dynamic equations in the modal space:

$$\left[\lambda\left(j\omega\mathbf{M}+\mathbf{MU}+\frac{1}{j\omega}\mathbf{K}+A\tilde{\mathbf{Z}}_A\right)-\frac{1}{j\omega}\boldsymbol{\alpha}\boldsymbol{\gamma}^T\right]\tilde{\mathbf{v}}=-\boldsymbol{\alpha}V_\mathbf{a}, \tag{33}$$

where $\omega_{n,ij}$ is the natural frequency in the ijth mode and an *ad hoc* damping matrix. $\mathbf{U}=\mathrm{diag}\lfloor 2\zeta\omega_{n,ij}\rfloor$ is introduced, with ζ being the damping ratio.

E. Equivalent circuit

To facilitate the ensuing optimal design, a special case, the single-mode system, is considered. For a single mode, generally the fundamental mode, Eqs. (6), (21), and (22), are rewritten as

$$w(x,y,t)=\phi(x,y)q(t), \tag{34}$$

$$m\ddot{q}+kq+\alpha Q=f, \tag{35}$$

$$\alpha q+\lambda Q=V_a, \tag{36}$$

where $m=\rho_p$ if $\|\phi\|_2=1$.

$$k^t=D\int_0^{W_p}\int_0^{L_p}[\phi_{xx}^2+\phi_{yy}^2+2\upsilon\phi_{xx}\phi_{yy}+2(1-\upsilon)\phi_{xy}^2]dx\,dy + \int_{y_1}^{y_2}\int_{x_1}^{x_2}[c_{11}^D I_1\phi_{xx}^2+2c_{12}^D I_1\phi_{xx}\phi_{yy}+c_{11}^D I_1\phi_{yy}^2 + 4c_{66}^D I_1\phi_{xy}^2]dx\,dy, \tag{37}$$

$$\alpha=\frac{\alpha_1}{A_c}=\frac{2h_{31}I_2}{A_c}\int_{y_1}^{y_2}\int_{x_1}^{x_2}(\phi_{xx}+\phi_{yy})dx\,dy, \tag{38}$$

$$\lambda=\frac{h_s-h_p}{A_c}\beta_{33}^S. \tag{39}$$

Assuming a time-harmonic analysis, the velocity and the electric current can be related, respectively, to the displacement and the electric charge,

$$q=\frac{u}{j\omega}, \tag{40}$$

$$Q=\frac{I}{j\omega}. \tag{41}$$

Let $k=1/C_M$, $\tau=\alpha C_E$, and $\lambda=1/C_E$. Equations (35) and (36) become

$$j\omega mu+\frac{1}{j\omega C_M}u+\frac{\tau}{j\omega C_E}I=f, \tag{42}$$

$$\frac{\tau}{j\omega C_E}u+\frac{1}{j\omega C_E}I=V_a, \tag{43}$$

where C_M and C_E denote the mechanical compliance and the electrical capacitance of PZT. Or, in a matrix form,

$$\begin{bmatrix} j\omega m+\frac{1}{j\omega C_M} & \frac{\tau}{j\omega C_E} \\ \frac{\tau}{j\omega C_E} & \frac{1}{j\omega C_E} \end{bmatrix}\begin{bmatrix} u \\ I \end{bmatrix}=\begin{bmatrix} f \\ V_a \end{bmatrix}. \tag{44}$$

As evidenced from the symmetric impedance matrix, the piezoelectric radiator is a ''reciprocal'' transducer. With *ad hoc* damping introduced, the electromechanical equivalent circuit is shown in Fig. 2(a). Reflecting the electrical side to the mechanical side gives Fig. 2(b), where

$$C_M'=\frac{C_M}{1-K^2}, \tag{45}$$

and $K=\sqrt{\alpha^2 C_M C_E}$ being the coupling factor. From the equivalent circuit, the frequency response between the modal velocity and the applied voltage can be expressed as

$$\frac{u}{V_a}=\frac{(j\omega)^2 C_E\tau}{(j\omega)^2 m+(j\omega)(R+Z_A)+\frac{1}{C_T}}, \tag{46}$$

where $C_T=C_E C_M'/(C_E+\tau^2 C_M')$ and $R=2m\zeta\sqrt{1/mC_T}$, with ζ being the damping ratio. This single-mode approximation is apparently a second-order system with the natural frequency,

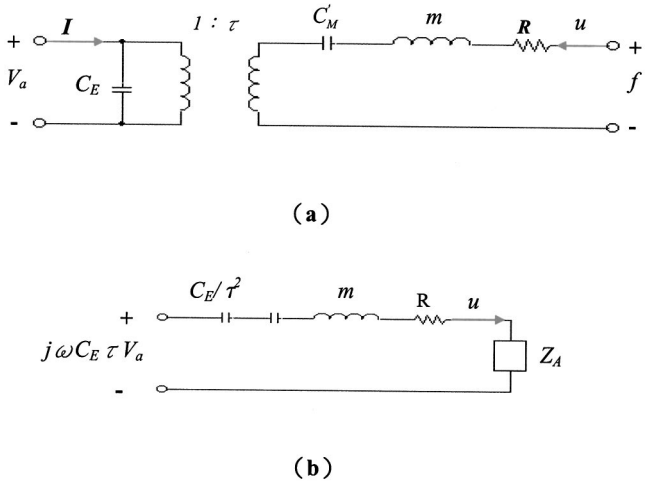

FIG. 2. Electromechanical equivalent circuits of the piezoelectric panel radiator. (a) The electromechanical equivalent circuit; (b) the equivalent circuit referred to as the mechanical side.

$$\omega_0 = \sqrt{\frac{1}{mC_T}}, \tag{47}$$

and a gain beyond resonance

$$g_\infty = \left|\frac{u}{V_a}\right| \approx \frac{C_E \tau}{m}, \quad \omega \gg \omega_0 . \tag{48}$$

An example of the single-mode frequency response of the piezoelectric radiator is illustrated in Fig. 3. For good performance, it is desirable for the resulting design of the radiator to have a low natural frequency ω_0 and high gain g_∞.

III. OPTIMAL DESIGN VIA THE GENETIC ALGORITHM

The genetic algorithm (GA) is an optimization algorithm that is originally motivated by natural selection and evolutionary genetics.[9] The GA has proven to be efficient in many areas such as function optimization and image processing. Unlike the conventional gradient search algorithms, the GA requires no calculation of the gradient and is not susceptible to problems of local minima. In each ''generation,'' three basic genetic operators, *reproduction*, *crossover*, and *mutation*, are performed to generate a new population and *fitness* functions of the *chromosomes* of the population are evaluated. An optimal solution is then obtained, according to the principle of ''survival of the fittest.'' The GA procedure applied to design the piezoelectric radiator is detailed as follows.

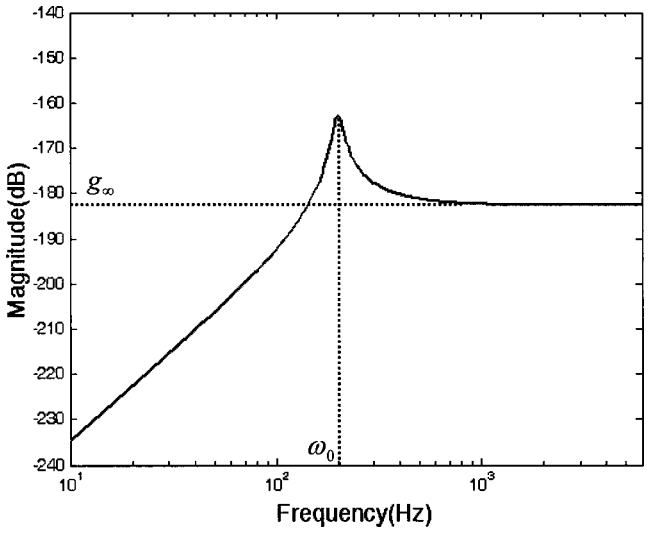

FIG. 3. The example of the single-mode frequency response of the piezoelectric panel radiator. ω_0 is the natural frequency and g_∞ is the gain beyond resonance.

A. Fitness function

Fitness is a measure of the survival rate of a chromosome. A chromosome with high fitness has a high probability of reproducing one or more offspring in the next generation. The ratio of the gain and the natural frequency of the single-mode approximation serves as the fitness function for the GA optimization:

$$f_c = \frac{g_\infty}{\omega_0} = \frac{\dfrac{C_E \tau}{m}}{\dfrac{1}{\sqrt{mC_T}}} = \alpha C_E^2 \sqrt{\frac{C_T}{m}}. \tag{49}$$

The goal of optimization is to search for a design with a low natural frequency and a high gain by maximizing the fitness function f_c. In the single-mode system, parameters relevant to the optimization are

$$m = \rho_p , \tag{50}$$

$$C_E = \frac{1}{\lambda} = \frac{L_c W_c}{t_c \beta_{33}^S}, \tag{51}$$

$$C_T = \frac{C_E C_M'}{C_E + \tau^2 C_M'} = C_M = \frac{1}{k}, \tag{52}$$

$$\alpha = -6 \frac{h_{31}(t_p t_c + t_c^2)}{\sqrt{L_c W_c}} \left[\left(\frac{1}{L_c^2} + \frac{1}{W_c^2} \right) \cos \frac{\pi x_1}{L_c} \cos \frac{\pi y_1}{W_c} \right], \tag{53}$$

$$k^t = \pi^4 \left[D + \left(\frac{1}{2} t_p^2 t_c + t_p t_c^2 + \frac{2}{3} t_c^3 \right) c_{11}^D \right] \left(\frac{1}{L_c^4} + \frac{1}{W_c^4} + \frac{2}{L_c^2 W_c^2} \right). \tag{54}$$

The symbols t_p and t_c are the thickness of the panel and PZT, respectively. Substituting Eqs. (50)–(53) into Eq. (49) gives

$$f_c = \alpha C_E^2 \sqrt{\frac{C_T}{m}} = \eta \frac{t_p + t_c}{t_t} L_c W_c \frac{1}{\sqrt{k}}, \tag{55}$$

where

$$\eta = -6 \frac{h_{31}}{\beta_{33}^S} \sqrt{\frac{L_c W_c}{m}} \left(\frac{1}{L_c^2} + \frac{1}{W_c^2} \right) \cos \frac{\pi x_1}{L_c} \cos \frac{\pi y_1}{W_c}. \tag{56}$$

When $0 \leqslant x_1 \leqslant W_p/2$ and $0 \leqslant x_2 \leqslant L_p/2$, η is a positive constant. It can be readily verified that

$$\partial f_c / \partial L_c > 0, \tag{57}$$

$$\partial f_c / \partial W_c > 0, \tag{58}$$

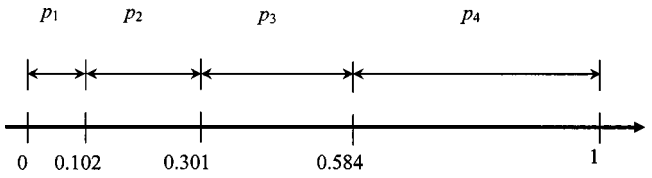

FIG. 4. The reproduction probabilities of four chromosomes, c_1-c_4, with fitness functions, 17, 33, 47, and 69, are concatenated in a real line.

$$\partial f_c/\partial t_c<0. \tag{59}$$

Thus, f_c is a monotonically increasing function of L_c and W_c, and a monotonically decreasing function of t_c. That is, it is generally preferable to have a design using a large and thin PZT, provided no other constraints are of concern. In what follows, the parameter L_c, W_c, and t_c will not be optimized, but were constrained in a certain prescribed range.

B. Encoding and decoding

Suppose that the position of the PZT, (x_1,y_1), on the panel are to be optimized. The variables x_1 and y_1 are encoded into a binary string of length l_i, called a chromosome. The resolution for the string of such length is

$$R_i=\frac{x_i^U-x_i^L}{2^{l_i}-1}, \tag{60}$$

where x_i^U and x_i^L are the upper and lower limits of the parameter. For example, if $0<x_1<4.5$ mm, $0<y_1<3.5$ mm, and the desired resolutions are $R_1=0.145$ and $R_2=0.113$, then $l_1=l_2=5$. If $x_1=1.595$ and $y_1=1.468$, then the chromosome is encoded as [01011 01101].

C. Reproduction, crossover, and mutation

Reproduction directs the search of GA toward the best individuals. The chromosome of the current population is reproduced in the next generation according to the reproduction probability p_i,

$$p_i=\frac{f_c}{\Sigma_1^{P_l} f_c}, \tag{61}$$

where P_l is the population size. Assume there are four chromosomes, c_1-c_4, in the zero generation with fitness functions 17, 33, 47, and 69. From Eq. (61), the reproduction probabilities are $p_1=0.102$, $p_2=0.199$, $p_3=0.283$, and $p_4=0.416$, respectively. The chromosome c_4 is the most likely to reproduce in the next generation. These four reproduction probabilities are then concatenated in the real line, as shown in Fig. 4. In the first generation, four random numbers between 0 and 1 are generated. For example, if the generated random numbers are 0.812, 0.666, 0.111, and 0.501, the candidate chromosomes for reproduction in the next generation will be c_4, c_4, c_2, and c_3, respectively.

Crossover is intended to exchange the information between chromosomes via a probabilistic decision in the mating pool. It proceeds in three steps. First, the crossover rate p_c is specified (usually $0.8<p_c<1$, and we choose $p_c=0.9$). Two chromosomes in the mating pool are selected to cross over at random. Precisely, the entire population in each generation is divided into pairs, e.g., 100 pairs would be required for 200 chromosomes. For each pair, a random number between 0 and 1 is then generated. If the random number is less than the crossover rate p_c, the crossover procedure will take place. Second, a splice point at the chromosome is selected randomly. Third, the genetic codes after the splice point are interchanged. For example, there are two chromosomes c_1 and c_2 with the splice point at the third bit: $c_1=010_\Delta 1010$, $c_2=111_\Delta 1111$. With crossover, two new chromosomes are generated: $\tilde{c}_1=010_\Delta 1111$, $\tilde{c}_2=111_\Delta 1010$.

Reproduction and crossover provide the most search power for GA. However, the gene becomes increasingly homogeneous as one gene begins to dominate after several generations and eventually results in premature convergence. To obviate this problem, mutation is introduced into the GA procedure. Let the probability of mutation be p_m (usually $0<p_m<0.01$, and we choose $p_m=0.01$). This probability determines how many genes are selected for mutation in each generation. In this analysis, where the population was chosen to be 200 at the given 0.01 mutation rate, approximately two genes were presumably selected for mutation in each generation. Mutation is carried out by alternating the gene from zero to one, or from one to zero, with the mutation point determined randomly. For instance, a chromosome c_3 with the mutation point at the third bit is $\tilde{c}_3=10\underset{\Delta}{0}\,101010$. After mutation, the chromosome becomes $\tilde{c}_3=10\underset{\Delta}{1}\,101010$. Note, however, that mutation should be used sparingly. The GA would behave like a random search if the mutation rate is too high.

The aforementioned GA procedure was applied to the design of the piezoelectric radiator. The parameters to optimize include the positions of the PZT and the Young's modulus of the panel. Two kinds of thickness (100 and 150 μm) and five kinds of aspect ratio were examined in the optimization. The results of optimal PZT positions on the panel are

TABLE I. The results of optimal PZT positions on the panel obtained using the GA procedure. Every entry in the table includes three values: the gain beyond resonance, the natural frequency, and the optimal position of the PZT.

		The thickness of PZT	
		100 μm	150 μm
Aspect ratio (length=1.5 cm)	1:(1/3)	−179.520 dB 147.461 Hz (1 cm, 2.75 cm)	−181.886 dB 179.076 Hz (1 cm, 2.81 cm)
	1:(1/2)	−172.512 dB 163.710 Hz (1 cm, 2.65 cm)	−174.870 dB 205.458 Hz (1 cm, 2.61 cm)
	1:1	−160.639 dB 202.512 Hz (1 cm, 2.27 cm)	−163.003 dB 265.580 Hz (1 cm, 2.32 cm)
	1:2	−149.287 dB 248.890 Hz (1 cm, 1.46 cm)	−151.643 dB 335.386 Hz (1 cm, 1.5 cm)
	1:3	−143.437 dB 265.826 Hz (1 cm, 0.75 cm)	−145.812 dB 359.739 Hz (1 cm, 0.78 cm)

summarized in Table I. Every entry in the table includes three values: the gain beyond resonance, the natural frequency, and the optimal position of the PZT. The optimal Young's moduli of the panel are found to vary between 9 and 13 GPa.

IV. NUMERICAL SIMULATION

Although the assumed-modes method, in principle, is applicable to general cases, the modes we assumed are restricted to the eigenfunctions of a simply supported plate that are simple enough for a practical calculation during optimization. The simply supported boundary conditions are

$$w(0,y)=w(L_p,y)=\frac{\partial^2 w}{\partial x^2}(0,y)=\frac{\partial^2 w}{\partial x^2}(L_p,y)=0, \quad 0\leqslant y\leqslant W_p, \tag{62}$$

$$w(x,0)=w(x,W_p)=\frac{\partial^2 w}{\partial y^2}(x,0)=\frac{\partial^2 w}{\partial y^2}(x,W_p)=0, \quad 0\leqslant x\leqslant L_p. \tag{63}$$

The associated eigenfunctions are

$$\phi_{mn}(x,y)=\frac{2}{\sqrt{L_pW_p}}\sin\frac{m\pi x}{L_p}\sin\frac{n\pi y}{W_p}. \tag{64}$$

The natural frequencies are

$$\omega_{mn}=\sqrt{\frac{D}{\rho_p}}\pi^2\left(\frac{m^2}{L_c^2}+\frac{n^2}{W_c^2}\right). \tag{65}$$

Suppose that only M most significant modes are retained in the series expansion. A $M\times M$ transformation matrix $\mathbf{\Phi}$ can be constructed by dividing the panel into M grid points:

$$\mathbf{\Phi}=\frac{2}{\sqrt{L_pW_p}}\begin{bmatrix} \frac{1}{N_1}\sin\frac{m_1\pi x_1}{L_p}\sin\frac{n_1\pi y_1}{W_p} & \cdots & \frac{1}{N_M}\sin\frac{m_M\pi x_1}{L_p}\sin\frac{n_M\pi y_1}{W_p} \\ \vdots & \ddots & \vdots \\ \frac{1}{N_1}\sin\frac{m_1\pi x_M}{L_p}\sin\frac{n_1\pi y_M}{W_p} & \cdots & \frac{1}{N_M}\sin\frac{m_M\pi x_M}{L_p}\sin\frac{n_M\pi y_M}{W_p} \end{bmatrix}, \tag{66}$$

where N_i is the norm of the ith column. Hence, the modal radiation impedance $\tilde{\mathbf{Z}}_{\mathbf{A}}$ is obtained using Eq. (31). The modal velocity vector $\tilde{\mathbf{v}}$ is obtained by solving Eq. (33). The velocity in physical space is then obtained from Eq. (29).

For radiators in a planar baffle, the propagation matrix $\mathbf{E}$ can be written as[8]

$$\mathbf{E}=j\frac{\rho_0 c_s kA}{2\pi}\begin{bmatrix} \frac{e^{-jkr_{11}}}{r_{11}} & \frac{e^{-jkr_{12}}}{r_{12}} & \cdots & \frac{e^{-jkr_{1n}}}{r_{1n}} \\ \frac{e^{-jkr_{21}}}{r_{21}} & \frac{e^{-jkr_{22}}}{r_{22}} & \cdots & \frac{e^{-jkr_{2n}}}{r_{2n}} \\ \vdots & \vdots & \ddots & \vdots \\ \frac{e^{-jkr_{m1}}}{r_{m1}} & \frac{e^{-jkr_{m2}}}{r_{m2}} & \cdots & \frac{e^{-jkr_{mn}}}{r_{mn}} \end{bmatrix}, \tag{67}$$

where A is the area of each element and r_{mn} is the distance from the element n to the field point m. Using the matrix $\mathbf{E}$, we can calculate the farfield pressure,

$$\mathbf{p_f}=\mathbf{Ev}, \tag{68}$$

where $\mathbf{v}$ is the surface velocity vector on the panel.

The data of the PZT and the panel in our simulation are shown in Table II. The dimensions of the panel are 45 mm $\times$35 mm$\times$0.1 mm, which are close to those of a cellular phone. Assume that the panel material is polycarbonate (PC). The size of the PZT is 15 mm$\times$30 mm$\times$0.1 mm. Using the GA procedure with a population size 200, the optimal position of the PZT on the PC panel was found to be at (10.0 mm, 14.6 mm). The learning curve of the GA is shown in Fig. 5. With approximately 100 iterations, the fitness function settles to 2.6×10^{-10}. The computation time was nearly 4 hours for 300 iterations on a Pentium 4 personal computer. The frequency responses for the optimal position and a nonoptimal position (15.0 mm, 10.0 mm) of the PZT, of the on-axis sound pressure at a point 0.5 m away from the panel, were calculated using the forgoing numerical model and compared in Fig. 6. The configuration with the optimal PZT position exhibits significantly better low-frequency response and high-frequency gain as well.

V. EXPERIMENTAL INVESTIGATION

Experiments were undertaken to verify the proposed optimal designs of the piezoelectric panel radiators. Two kinds of panel materials, the polycarbonate and the carbon fiber composite material, are used in the experiment. The parameters of panel materials are listed in Table III. A PU foam and

TABLE II. The data of the PZT and the panel used in the simulation. The dimensions of the panel are 45 mm$\times$35 mm$\times$0.1 mm.

	Parameter	Value
PC plate	Size	0.045 m$\times$0.035 m$\times$0.00025 m
	Density	1200 kg/m^3
	Young's modulus	2.7 GPa
	Poisson's ratio	0.97
PZT	Size	0.0015 m$\times$0.0030 m$\times$0.0001 m
	β_{33}^S	1.94×10^8
	h	-8.1×10^8 V/m
	c_{11}^D	11.73×10^{10} N/m^2
	c_{12}^D	7.77×10^{10} N/m^2
	c_{66}^D	1.98×10^{10} N/m^2

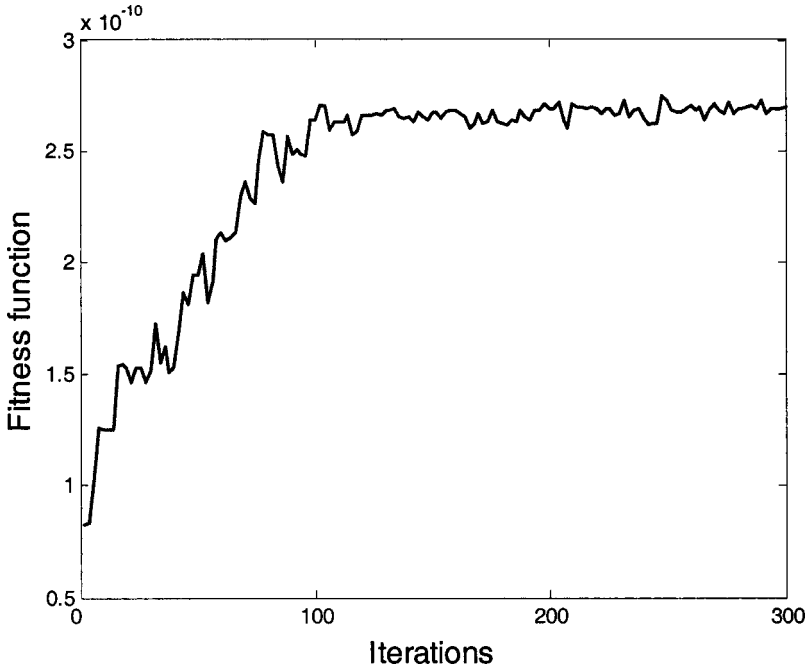

FIG. 5. The learning curve of the GA. With approximately 100 iterations, the fitness function settles to 2.6 $\times 10^{-10}$. The computation time was nearly 4 h for 300 iterations on a Pentium 4 personal computer.

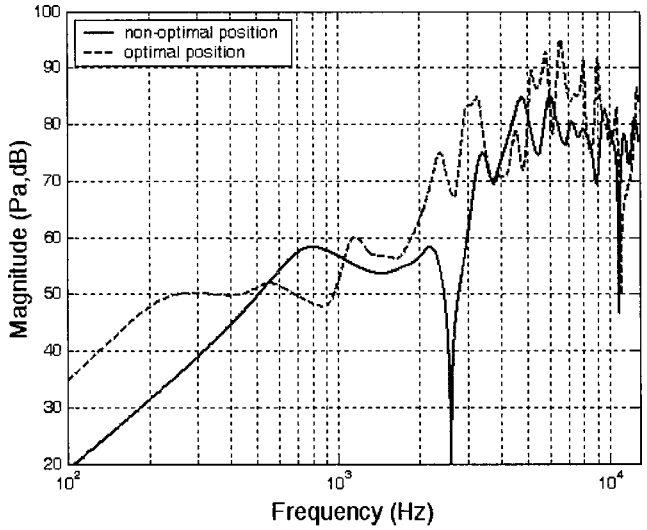

FIG. 6. The simulated on-axis frequency responses for two positions of the PZT, at a point 0.5 m away from the panel. The size of the panel is 45 mm$\times$35 mm$\times$0.25 mm. The size of the PZT is 15 mm$\times$30 mm $\times$0.1 mm. The optimal position of the PZT is at (10.0 mm, 14.6 mm). The nonoptimal position of the PZT is at (15.0 mm, 10.0 mm).

TABLE III. The parameters of the polycarbonate material and the carbon fiber composite material.

	Polycarbonate (PC)	Carbon fiber composite material
Density (ρ, kg/m^3)	1200	1546.37
Young's modulus (E, GPa)	2.7	$E_1=147.564$, $E_2=9.314$
Poisson's ratio (ν)	0.97	0.283
Shear modulus (G, GPa)	0.42	5.702

TABLE IV. Configurations of piezoelectric radiators investigated in the experiment. Two kinds of suspensions, a PU foam and a plastic tape, are tested.

No. of panel	T size (mm)	Panel size (mm)	Material of plate	Material of BC	PZT position
No. 1	15$\times$30$\times$0.1	45$\times$35$\times$0.25	PC	PU foam ($t=1$ mm)	Nonoptimal: (15.0 mm, 10.0 mm)
No. 2	15$\times$30$\times$0.1	45$\times$35$\times$0.25	PC	PU foam ($t=1$ mm)	Optimal: (10.0 mm, 14.6 mm)
No. 3	15$\times$30$\times$0.1	45$\times$35$\times$0.25	Carbon fiber (0°$\times$2)	PU foam ($t=1$ mm)	Optimal: (10.0 mm, 14.6 mm)
No. 4	15$\times$30$\times$0.1	45$\times$35$\times$0.25	Carbon fiber (0°$\times$2)	Adhesive tape	Optimal: (10.0 mm, 14.6 mm)

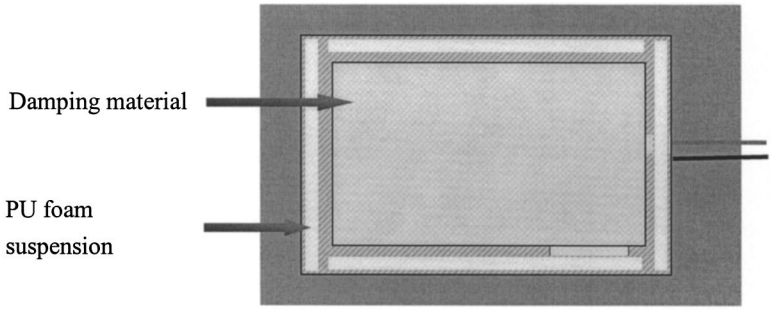

(a)

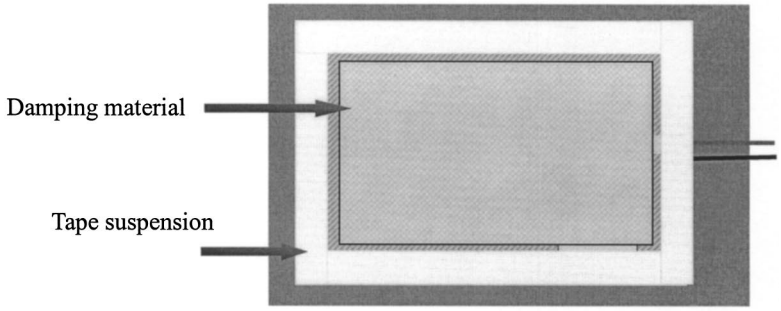

(b)

FIG. 7. Illustrations of the piezoelectric radiators. (a) Nos. 1, 2 and 3; (b) No. 4.

a plastic tape, representing a hard suspension and a soft suspension, are tested. The suspensions are sealed all around the boundary of the panels. With an appropriate combination of these conditions, four configurations of piezoelectric radiators were investigated in the experiment, as summarized in Table IV. The implemented piezoelectric panel radiators are schematically shown in Fig. 7. The panels were treated with some damping. Figure 8 shows the photo of the radiator No. 2. All radiators were embedded in a baffle while testing. The experimental arrangement is shown in Fig. 9. The performance of the panel radiators are measured in an anechoic room and summarized as follows.

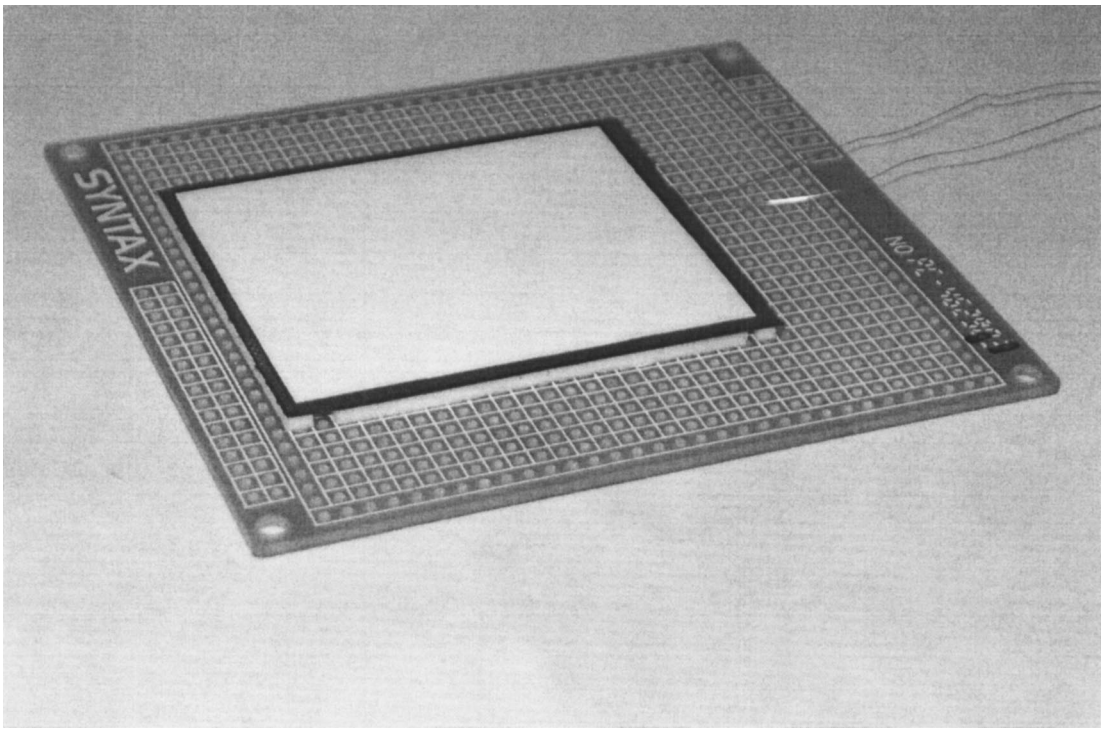

FIG. 8. Photo of the piezoelectric radiator No. 2.

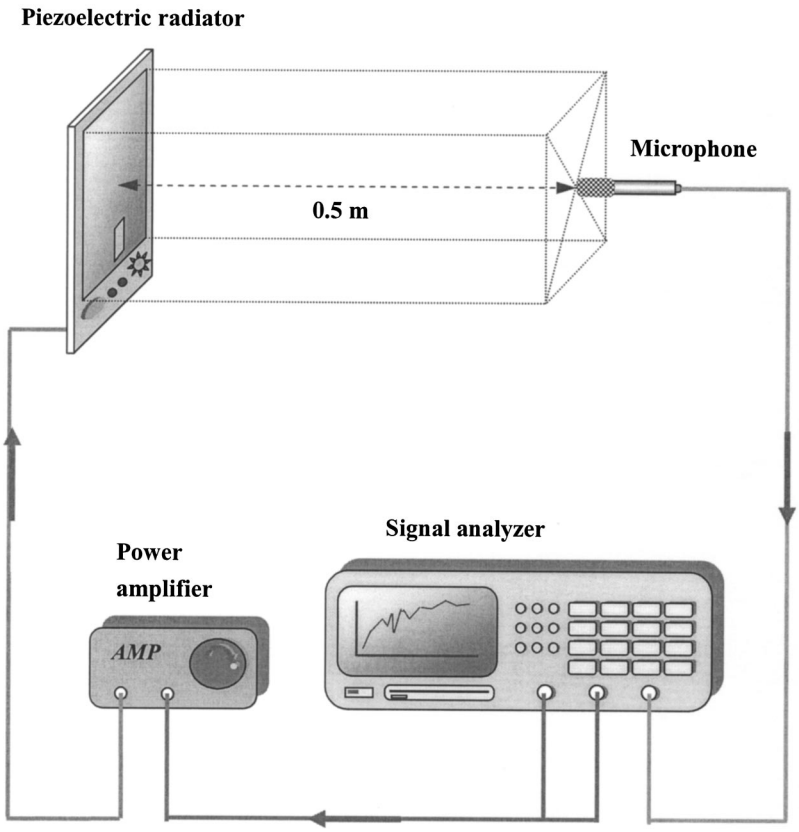

FIG. 9. The experimental arrangement for the performance measurement of the piezoelectric panel radiators. The measurement was conducted in an anechoic room.

A. Frequency responses of farfield pressure

The on-axis pressure responses at 0.5 m from panel speaker were measured. A random signal of 30 V rms, band-limited to 12.8 kHz was used as the input. Figures 10–12 illustrate the performance of various designs. Figure 10 shows the effect of the PZT positions. The design using the optimal position (No. 2) of the PZT produced a better low-frequency response than that using a nonoptimal position (No. 1). In Fig. 11, the frequency responses of the panel radiators, No. 2 and No. 3, are compared. The Young's modulus of the carbon fiber is close to the optimal value obtained from GA. The sound pressure level of the carbon fiber panel is higher than that produced by PC above 700 Hz, which results in a ''brighter'' sound quality of the carbon fiber radiator than the PC. In Fig. 12, we see the frequency responses of panel radiator No. 3 and No. 4. From the result,

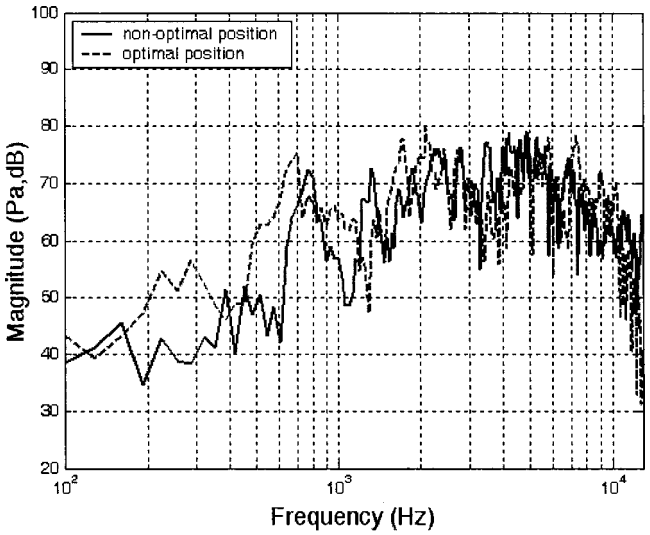

FIG. 10. The frequency responses of the panel radiators Nos. 1 and 2. The effect of the PZT positions on the panel is investigated. The design using the optimal position of the PZT produced a better low-frequency response than that using a nonoptimal position.

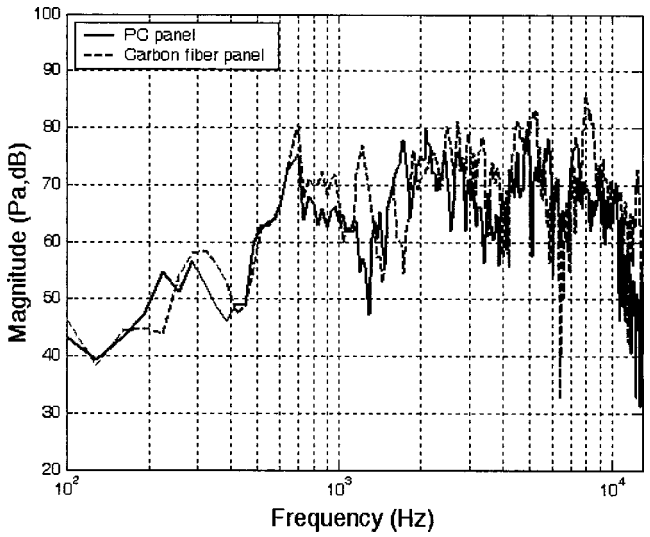

FIG. 11. The frequency responses of the panel radiators, Nos. 2 and 3. The effect of Young's modulus is investigated. The Young's modulus of the carbon fiber is close to the optimal value obtained from GA. The sound pressure level of the carbon fiber panel is higher than that produced by PC above 700 Hz.

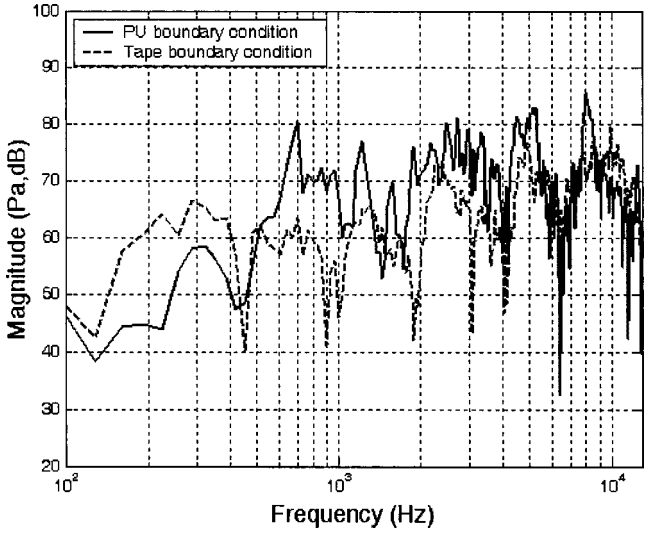

FIG. 12. The frequency responses of the panel radiator Nos. 3 and 4. The effect of the boundary condition is investigated. With a softer suspension, the low-frequency response is enhanced at the expense of the high-frequency output.

the profound effect of the boundary condition is also evidenced. With the soft suspension, the low-frequency response is enhanced at the expense of the high-frequency output.

B. Sensitivity

Sound pressure level is measured on-axis at the distance 0.5 m from the radiator, under the free-field condition. The input signal is the random noise of 30 V rms, bandlimited to 12.8 kHz, which amounts to the input electric power 0.018 W. The measured sensitivities of the No. 3 panel radiator is 76 dB. With this level of acoustic output, speech and music are found to be quite intelligible, even at 1 m distance.

C. Efficiency

The efficiency is defined as the ratio of the radiated acoustical power to the input electrical power. The input electrical power is calculated as

$$W_{\text{in}} \approx \frac{1}{2}\sum_{i=1}^{N} |V|^2 \frac{\text{Re}(Z)}{|Z|^2}\Delta f = \frac{1}{2}\sum_{i=1}^{N} P_{vv}\,\text{Re}\left(\frac{1}{Z}\right)\Delta f, \quad (69)$$

where V and Z are the Fourier transforms of the input voltage and the electrical impedance. P_{vv} is the power spectral density of the input voltage.

In this work, ISO 3745 was employed for measuring the radiated sound power in the anechoic room.[10] The measured efficiency of the No. 3 radiator was 0.767%. In order to appreciate this performance, a panel radiator using identical configurations, except a voice-coil exciter is used, was tested for comparison. The measured efficiency of the radiator driven by the voice-coil exciter was 0.075%. This impressive result indicates that the piezoelectric panel radiator is a very efficient device, which is indeed an attractive feature for many a power-saving applications.

D. Directional response

The directional response[11] of the panel radiator was measured by mounting the radiator on an automated turntable driven by a stepper motor. A 1/2 in. condenser microphone is placed at the distance 0.5 m from the radiator to measure the generated sound pressure under a free-field condition. The panel radiator was rotated at angles from 0° to 180°, with 1° increments. Random noise of 30 V rms, bandlimited to 12.8 kHz, served as the input. The measured results of directional response are shown in Fig. 13. The results indicate that the panel radiator has a relatively omnidirectional response. However, the directional responses are not symmetrical because the PZT is not mounted at the center position.

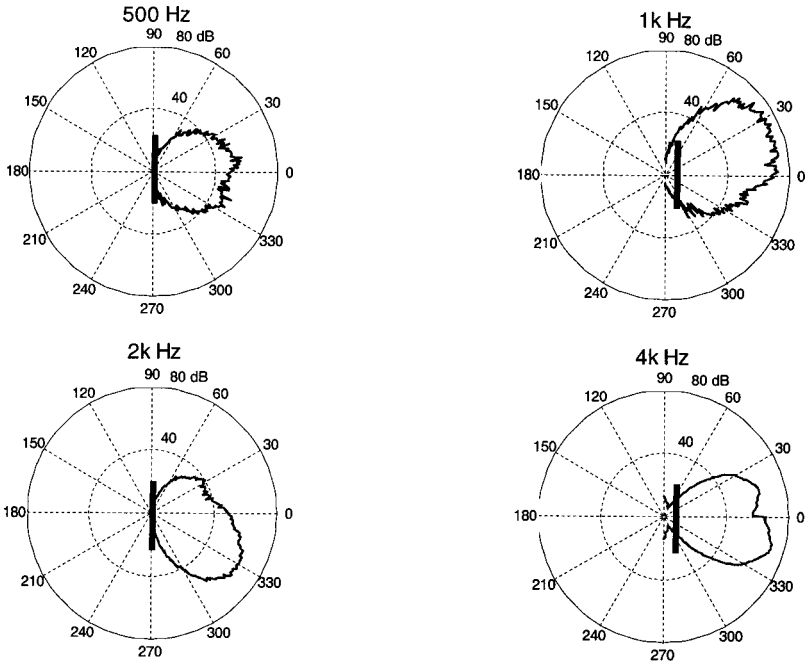

FIG. 13. Directional responses of the piezoelectric radiators at 500, 1, 2 and 4 kHz. The thick line at the center symbolizes the position of the panel.

VI. CONCLUSIONS

A piezoelectric radiator has been proposed in this paper. Although piezoelectrically driven radiators have been around for some time, these devices mainly exist in the form of narrow band acoustic radiators such as buzzers, sounders, sirens, etc., where sound quality is generally not of major concern. By contrast, this work developed an acoustic radiator for a different aim: to meet quality loudspeaker requirements with regard to speech and music listening. The reason why we used piezoelectricity as the driving mechanism lies in our emphasis on the 3C applications, where space and power consumption is critical.

Dynamic modeling of the system was carried out using the energy method and the assumed-modes method. A more elaborate approach than other study is exploited in modeling the acoustic loading and the model is established as a fully coupled system, which is important for a light structure considered here in the paper. Discretization is simplified by assuming a series expansion in energy terms, but not in partial differential equations. The assumed-modes method is employed in the series expansion such that the ensuing optimization process can be carried out in an efficient and practical way.

In this paper we seek to attain an optimal design of the piezoelectric panel speaker, using a ''synergetic'' approach. In particular, a nonconventional optimization algorithm, GA, was employed in this paper to effectively tackle this nonconvex problem. The GA is a multiple starting point algorithm and is not susceptible to the problem of local minima. Performance and adequacy as a broadband loudspeaker of the proposed device is thoroughly investigated. As confirmed by the numerical and experimental results of various indices, the piezoelectric radiator using the optimal configuration indeed produced better performance than the nonoptimal ones. The suspension, the material of the panel, and the mounting positions of PZT are important factors that may contribute to the performance of the radiators. The optimal combination of these parameters can be jointly considered in the GA procedure.

From the experimental investigation, the piezoelectric radiators produced quite impressive efficiency (approximately 10:1) over the panel speakers driven by voice-coil exciters. Furthermore, the thickness of present design of the piezoelectric radiator is 0.35 mm, which is significantly less than the 2.4 mm of the voice-coil panel speaker. In comparison with other conventional means, the piezoelectric radiators are found promising in meeting the increasingly stringent requirements of 3C products.

ACKNOWLEDGMENTS

Thanks are due to the illuminating discussions with NXT, New Transducers Ltd., UK. The work was supported by the *National Science Council (NSC)* in Taiwan, under Project No. NSC 89-2212-E009-057. Special thanks also go to Dr. Meng-Shiun Tsai in Chong-Cheng University for his helpful suggestions on derivations of piezoelectric plates.

[1] M. R. Bai and T. Huang, ''Development of panel loudspeaker system: Design, evaluation and enhancement,'' J. Acoust. Soc. Am. **109**, 2751–2761 (2001).
[2] H. Azima, ''NXT up against wall,'' Audio Magazine 34–41 (Sept., 1998).
[3] J. G. Smits, S. I. Dalke, and T. K. Cooney, ''The constituent equations of piezoelectric bimorphs,'' Sens. Actuators **28**, 41–61 (1991).
[4] J. W. Waanders, *Piezoelectric ceramics—Properties and Applications* (Philips Components Eindhoven, The Netherlands, 1991).
[5] H. L. Langhaar, *Energy Methods in Applied Mechanics* (Wiley, New York, 1962).
[6] H. F. Tiersten, *Linear Piezoelectric Plate Vibration* (Plenum, New York, 1969).
[7] L. Meirovitch, *Elements of Vibration Analysis* (McGraw-Hill, New York, 1986).
[8] A. P. Berkhoff, ''Sensor scheme design for active structural acoustic control,'' J. Acoust. Soc. Am. **108**, 1037–1045 (2000).
[9] J. H. Holland, ''Outline for a logical theory of adaptive system,'' J. Assoc. Comput. Mach. **3**, 297–314 (1962).
[10] ISO 3745, ''Acoustics—Determination of sound power levels of noise sources—Precision methods for anechoic and semi-anechoic rooms,'' 1977.
[11] L. L. Beranek, *Acoustics* (McGraw-Hill, New York, 1986).

Experimental and numerical investigations of axisymmetric wave propagation in cylindrical pipe filled with fluid

Haitao Pan,[a] Kiyoshi Koyano, and Yoshiko Usui
IZUMI Engineering Laboratory Co., Ltd., Yokohama Kanazawa High-Tech Center, Teno-Core 3F, 1-1-1 Fukuura, Kanazawa-ku, Yokohama 236-0004, Japan

(Received 16 November 2001; revised 24 January 2003; accepted 24 February 2003)

Acoustic wave propagation in fluid-filled cylindrical pipe with arbitrary thickness is investigated numerically and experimentally. The vibrational properties of the coupled fluid-pipe system are evaluated by a layerwise approach, which is similar to the finite-strip method. In this approach, the thick cylindrical wall is divided into a number of thin cylindrical layers in the thickness direction. The displacements in the thickness direction for each layer are approximated by linear-shape functions. The governing equation is obtained by using an energy minimization principle. The dispersion curves, distribution of vibrational energy between pipe wall and contained fluid, and displacement fields are examined. The dependence of the dispersion curves on wall thickness is discussed. Two PZT ring transducers adhered to the outer surface of pipe are used as source and receiver, respectively. The propagating waves generated by burst signals are measured. To localize transient signal both in time and frequency domains, the discrete wavelet transform is applied to decomposing the receiving signal into several components. Each component is limited to a narrower bandwidth. Therefore the frequency-dependent group velocity is estimated. The experimental and numerical results are compared.
[DOI: 10.1121/1.1570432]

PACS numbers: 43.40.At, 43.40.Ey, 43.60.Gk [JHG]

I. INTRODUCTION

The vibration of fluid-filled cylindrical pipe is a practical problem widely existing in various fields. There are many demands on the reduction of noise generated from pipe system, measurement of flow rate of internal flow, design of submersible vehicles, and signal transmission among pipe network. When the elastic pipe wall and filled fluid are acoustically coupled, the resulting wave propagation of multiple modes and branches is complex and varies greatly on physical parameters of the system and frequency as well. Consequently, the analysis on the wave behavior and the experimental study are required.

There has been much theoretical research on the vibration of fluid-filled cylindrical pipe by solving wave equations and boundary conditions approximately under some assumptions, mostly on thin-shell theory where the transverse stress and strain components are ignored. Lin and Morgan[1] studied the axisymmetric waves through fluid contained in an elastic thin cylindrical shell. Kumar[2] examined the axisymmetric wave propagation in a fluid-filled cylinder of arbitrary thickness, neglecting high-order terms in a power series expansion in thickness-radius ratio. Fuller *et al.*[3–5] have investigated thin-walled motion of axisymmetric and nonaxisymmetric vibration in terms of Donnel–Mushtari shell equations, where dispersion curves, energy distribution,[3] input mobility,[4] and internal flow's effect[5] have been discussed. The forced vibration in thin pipe has been studied furthermore by Xu and Zhang.[6]

For thick-wall pipe, numerical analysis based on the three-dimensional theory of elasticity is validated to account for all the transverse stress and strain components, which cannot be neglected in thick-wall pipe and high frequency. Several approaches have attempted to solve this problem, such as the Rayleigh–Ritz method,[7,8] finite layer or finite strip method,[9,10] and the perturbation method.[11]

The purpose of the present paper is to examine the wave behaviors in fluid-filled pipe without limitations on wall thickness and frequency. A layerwise approach proposed by Toy and Lam,[10] similar to the finite strip method,[9] is employed to study the vibration of infinitely fluid-filled cylindrical pipe. In this approach, the cylindrical wall is discretized into a number of thin layers in thickness direction. For each layer, the displacements in thickness direction are approximated by linear-shape functions. Using an energy minimization principle, the characteristic eigenvalue equation can be obtained and solved (Sec. II). Consequently, the dispersion curves and energy distribution between contained fluid and pipe wall are given in Sec. IV. The behavior of individual branches and its dependence on wall thickness are discussed.

On the other hand, the experimental investigations on the acoustic wave propagating in pipe have usually been limited to thin-walled pipe and low frequency (below several kilohertz). Seybert[12] used a two-sensor method to measure sound intensity and acoustic impedance in ducts. Kim and Kim[13] measured flow rate in pipe using three accelerometers on the surface of pipe. Hasegawa[14] examined experimentally the propagating velocity and sound absorption in a water-filled silicone rubber tube. The measurement of pipe vibration in high-frequency domain is scarce. The measuring waves with wide frequency band and the appearance of mul-

[a]Electronic mail: ednaxken@ms37.hinet.net

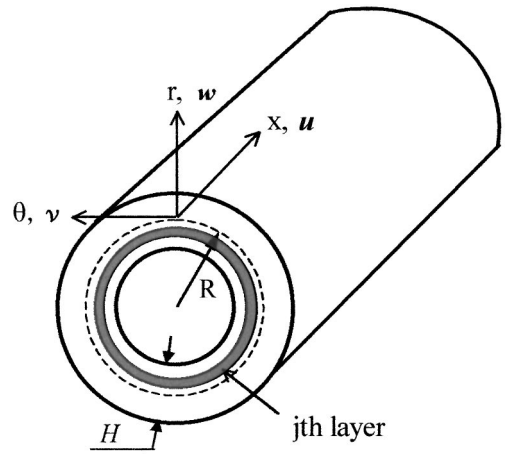

FIG. 1. Geometry of a cylindrical wall with mean radius R and thickness H.

tiple branches at high frequency make the receiving signals complicated.

The propagating waves through a thick-walled, water-filled PFA pipe at high frequency (50–700 kHz) are measured with two PZT ring transducers adhered to the external surface of the PFA pipe (Sec. III). The source transducer is excited by a burst signal with a certain bandwidth. To localize transient signal both in time and frequency domains, the discrete wavelet transform[15] is applied to decomposing the receiving signal into several components (Sec. V). Each component associates to a subband in frequency domain as the filtering response. Therefore the frequency-dependent group velocity would be approximately estimated. The experimental and the numerical results are compared and discussed. The conclusions are drawn in Sec. VI.

II. LAYERWISE FORMULATION

A. Equations of cylinder's motion

Consider an infinitely long cylindrical pipe shown in Fig. 1, which has a uniform thickness H and mean radius R. In the layerwise approach,[10] the cylindrical wall is divided into several number of thin cylindrical layers in thickness direction. For the jth layer, the displacements (u^j, v^j, w^j) of a simple harmonic motion in the (x, θ, r) directions, respectively, can be written as

$$\begin{aligned} u^j(x,r,\theta,t) &= \Re_u^j(r)\cos(n\theta)e^{j(\omega t - kx + \pi/2)}, \\ v^j(x,r,\theta,t) &= \Re_v^j(r)\sin(n\theta)e^{j(\omega t - kx)}, \\ w^j(x,r,\theta,t) &= \Re_w^j(r)\cos(n\theta)e^{j(\omega t - kx)}, \end{aligned} \tag{1}$$

where n is the circumferential mode; $k=\omega/c$ is the wave number; c is the propagating velocity in the coupled system. The present study has focused on the axisymmetric vibration, hence, only $n=0$ is taken into consideration here. The variable functions in the thickness direction are assumed as the linear functions

$$\begin{aligned} \Re_u^j(r) &= \alpha u[j] + \beta u[j+1], \\ \Re_v^j(r) &= \alpha v[j] + \beta v[j+1], \\ \Re_w^j(r) &= \alpha w[j] + \beta w[j+1], \end{aligned} \tag{2}$$

$$\beta = (r - r_j)/h_j, \quad \alpha = 1 - \beta,$$

where h_j is the thickness of the jth layer; r_j is the nearest radial distance of the jth layer; $(u[j], v[j], w[j])$ are the generalized parametric coordinates.

Accordingly, omitting the harmonic term $e^{j(\omega t - kx)}$, the displacement field (u^j, v^j, w^j) in the jth layer can be expressed in a matrix form

$$\mathbf{u} = \mathbf{N}\cdot\mathbf{d}, \tag{3}$$

where

$$\begin{aligned} \mathbf{u}^T &= \{u^j v^j w^j\}, \\ \mathbf{d}^T &= \{u[j]v[j]w[j]u[j+1]v[j+1]w[j+1]\}, \end{aligned} \tag{4}$$

$$\mathbf{N} = [\mathbf{N}_1 \mathbf{N}_2], \tag{5}$$

$$\mathbf{N}_1 = \begin{bmatrix} \alpha\cos(n\theta)e^{j(\pi/2)} & 0 & 0 \\ 0 & \alpha\sin(n\theta) & 0 \\ 0 & 0 & \alpha\cos(n\theta) \end{bmatrix}, \tag{6}$$

$$\mathbf{N}_2 = \begin{bmatrix} \beta\cos(n\theta)e^{j(\pi/2)} & 0 & 0 \\ 0 & \beta\sin(n\theta) & 0 \\ 0 & 0 & \beta\cos(n\theta) \end{bmatrix}. \tag{7}$$

For the jth layer, the stress–strain relation is given by

$$\sigma = [C]\epsilon, \tag{8}$$

$$\begin{aligned} \sigma^T &= \{\sigma_x \sigma_\theta \sigma_r \tau_{\theta r} \tau_{xr} \tau_{x\theta}\}, \\ \epsilon^T &= \{\epsilon_x \epsilon_\theta \epsilon_r \gamma_{\theta r} \gamma_{xr} \gamma_{x\theta}\}, \end{aligned} \tag{9}$$

where $[C]$ is the elastic coefficients matrix.

The elasticity strain-displacement relations are

$$\epsilon = D\cdot\mathbf{u}, \tag{10}$$

$$D = \begin{bmatrix} -jk & 0 & 0 \\ 0 & \frac{1}{R_j}\frac{\partial}{\partial\theta} & \frac{1}{R_j} \\ 0 & 0 & \frac{\partial}{\partial r} \\ 0 & \frac{\partial}{\partial r} - \frac{1}{R_j} & \frac{1}{R_j}\frac{\partial}{\partial\theta} \\ \frac{\partial}{\partial r} & 0 & -jk \\ \frac{1}{R_j}\frac{\partial}{\partial\theta} & -jk & 0 \end{bmatrix}, \tag{11}$$

where R_j is the mean radius of the jth layer; $-jk = \partial/\partial x$.

Substitute Eq. (3) into Eq. (10),

$$\epsilon = B\mathbf{d}, \tag{12}$$

$$B = D\cdot\mathbf{N}. \tag{13}$$

The kinetics energy T_j and potential energy V_j for the jth layer are

$$T_j = \frac{1}{2}\int\int \rho_j[(\dot{u}^j)^2 + (\dot{v}^j)^2 + (\dot{w}^j)^2]R_j\, d\theta\, dr, \tag{14}$$

$$V_j = \frac{1}{2}\int\int (\sigma^T \epsilon) R_j d\theta\, dr, \tag{15}$$

where $\dot{u}^j$, $\dot{v}^j$, $\dot{w}^j$ are the time derivatives of u^j, v^j, w^j, respectively.

Using Eqs. (3), (8), and (12), T_j and V_j can be expressed in a matrix form as

$$T_j = \tfrac{1}{2}\dot{\mathbf{d}}^T M_j \dot{\mathbf{d}}, \tag{16}$$

$$V_j = \tfrac{1}{2}\mathbf{d}^T \cdot K_j \cdot \mathbf{d}, \tag{17}$$

where

$$M_j = \int\int (\rho_j \mathbf{N}^T \cdot \mathbf{N}) R_j d\theta\, dr, \tag{18}$$

$$K_j = \int\int (B^T C B) R_j \mathbf{d}\theta\, \mathbf{dr}. \tag{19}$$

Consequently, the kinetic energy T and potential energy V in the whole cylinder can be expressed as

$$T = \tfrac{1}{2}\dot{\delta}_0^T M \dot{\delta}_0, \tag{20}$$

$$V = \tfrac{1}{2}\delta_0^T K \delta_0, \tag{21}$$

$$\delta_0^T = \{u[0]v[0]w[0]u[1]v[1]w[1]\ldots u[N]v[N]w[N]\}, \tag{22}$$

where δ_0 is the set of generalized coordinates and N is the divided number of the cylinder.

B. Free vibration of the coupled system

Applying the boundary condition[3] of the contained fluid at the pipe wall ($r=a$, a: inner radius of the pipe), the free vibration[3,10] of the coupled system can be presented as

$$\{K - \omega^2 M\}\delta_0 - \rho_f \omega^2 J_0(k_r a)/J_0'(k_r a) w^0 = 0, \tag{23}$$

where

$$k_r^2 = \omega^2\left(\frac{1}{c_f^2} - \frac{1}{c^2}\right);$$

c_f and ρ_f are, respectively, the sound speed and density of the fluid; J_0, J_1 are Bessel functions.

C. Power flow distribution

Acoustic power flux density[3,6] of the jth layer in the axial direction is given by

$$I_x^j = -(\sigma_x^j[\dot{u}^j]^* + \tau_{x\theta}^j[\dot{v}^j]^* + \tau_{xr}^j[\dot{w}^j]^*), \tag{24}$$

where the superscript asterisk means conjugate.

The total time-average power flow of the whole cylinder wall is

$$P_c = \frac{1}{2}\mathrm{Real}\left[\sum_{j=0}^{N-1}\int\int I_x^j R_j d\theta\, dr\right]. \tag{25}$$

The total axial power flow over the cross-sectional area of the contained fluid is

$$P_f = \frac{1}{2}\mathrm{Real}\left(\int\int p v_x^* r d\theta\, dr\right), \tag{26}$$

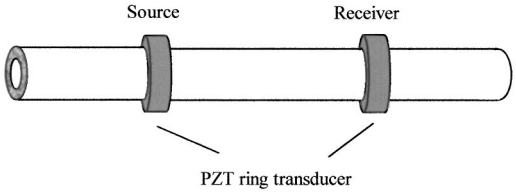

FIG. 2. Measurement of acoustic waves in a water-filled PFA pipe.

where the axial particle velocity is $v_x = -1/(j\rho_f \omega)\partial p/\partial x$.

The ratio of power flow between the fluid and cylinder wall is provided by

$$E_r = P_f / P_c. \tag{27}$$

III. MEASUREMENT CONDITIONS

As shown in Fig. 2, two PZT ring transducers (ϕ7 mm $\times$ ϕ5 mm $\times$ 2 mm$^{\mathrm{H}}$) which acted as source and receiver, respectively, were adhered to a PFA tube (ϕ4 mm $\times$ ϕ2 mm) contained with water. The distance between two transducers was 110 mm. The source transducer was driven by four-cycle burst signal. Transients will cause other frequencies to be generated, which propagate at different velocities due to the dispersion. However, the duration of burst signal cannot be chosen too long. It will make the fast arrival waves overlap with the slower waves, and then, it becomes difficult to separate the received signal into individual dispersion branch. Since the source PZT transducer was excited axisymmetrically, the propagating waves in the coupled system were limited to the circumferential modes $n=0$, meanwhile the circumferential displacement in pipe is: $v(x,r,\theta,t)=0$.

The material properties of the PFA tube are as follows: Young's modulus: $E = 8.75\times10^8$ N/m^2, Poisson ratio: $\nu = 0.45$, Density: $\rho = 2.2\times10^3$ kg/m^3.

The extensional and transverse speed of PFA are $c_e = [E/\rho(1-\nu^2)]^{1/2} = 706$ m/s and $c_t = \sqrt{E/2\rho(1+\nu)} = 370$ m/s, respectively. The sound speed in water is 1500 m/s and its density is 1000 kg/m^3.

IV. NUMERICAL RESULTS AND DISCUSSIONS

The dispersion curves of the above-mentioned water-filled PFA pipe are shown in Fig. 3, which are branches of the frequency-dependent phase velocity expressed in dimensionless form. The acoustic power distributions between the contained fluid and PFA pipe are presented in Fig. 4. To understand the motion of the pipe wall, the normalized displacements u and w of the $s=1$ and 2 branches, at 2, 120, 300, and 500 kHz, respectively, are displayed in Fig. 5.

At low frequency ($ka<1$), the $s=1$ branch corresponds to the Rayleigh wave velocity while the acoustic energy of the coupling system propagates mainly in the contained fluid. The $s=2$ branch is close to the velocity C_k of the

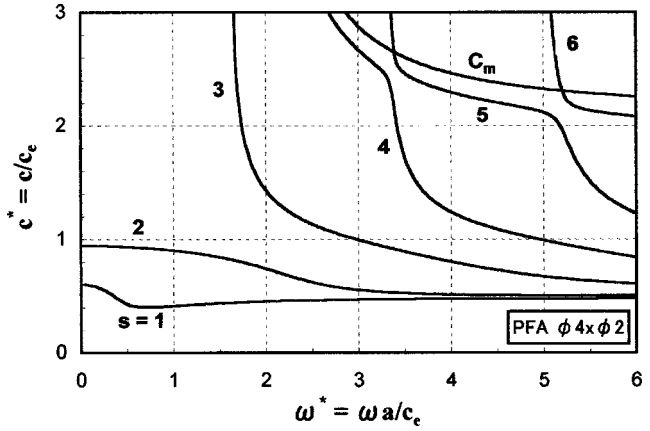

FIG. 3. Dispersion curves for a water-filled PFA pipe of thickness-radius ratio $H/R=0.67$, inner radius $a=1$ mm.

Korteweg–Lamb correction,[16] which expresses a parallel combination of the compressibility of the contained fluid and pipe wall. Here,

$$C_k = c_f[1+2a\rho_f c_f^2/(H\rho_s c_e^2)]^{-1/2} = 664 \text{ m/s}$$

is nearly the same value with $c_{s=2}=665.5$ m/s ($ka\approx 0$) obtained from Eq. (23). The majority of the acoustic energy ($s=2$) distributes in the pipe wall as shown in Fig. 4.

When the frequency is increased, the $s=1$ branch rapidly changes to a wall-type wave. The radial displacement w becomes larger than the axial displacement u, as shown in Fig. 5. The higher the frequency, the acoustic energy becomes more concentrated at the inner surface of pipe wall. The $s=2$ branch also turns into a Rayleigh wave at high frequency, however, u and w motions are concentrated at both the inner and outer surfaces of wall.

At higher frequency ($ka>1$), two types of waves appear. The first type is associated with the *in vacuo* cylinder modes, which has infinite phase velocity as the axial component of the wave number goes to zero. The second type corresponds to the fluid wave in a mass-controlled cylinder wall,[16] which can be approximated by the phase velocity:

$$C_m/c_f = [1-2\rho_f/(\rho k_f^2 Ha)]^{-1/2}, \quad k_f = \omega/c_f.$$

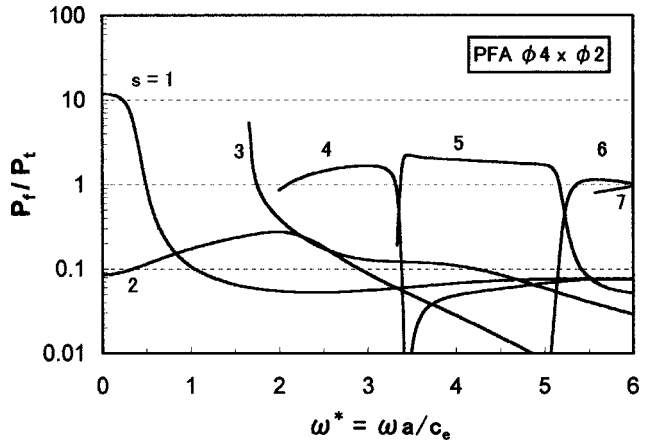

FIG. 4. Energy distribution between the contained fluid and pipe wall; $H/R=0.67$, inner radius $a=1$ mm.

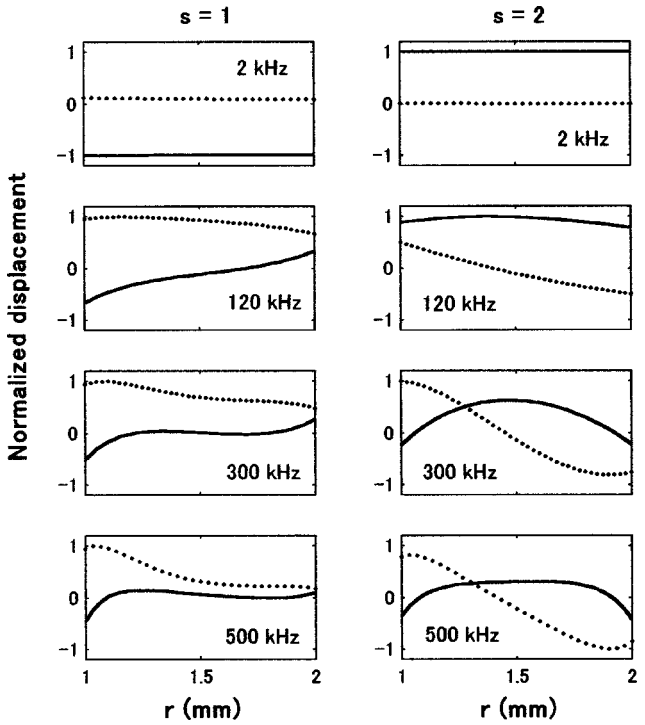

FIG. 5. Distribution of displacements in pipe wall of $s=1,2$; u (—); w (···).

C_m is given in Fig. 3 for comparison with the fluid-type waves for $s\geqslant 3$. These fluid-type waves couple largely with the wall motion, which can be seen clearly from their power distribution in Fig. 4. The corresponding phase velocities are closed to C_m. While one branch enters a fluid-wave plateau, the previous one leaves and converts to an extensional wall wave, and then changes to a Rayleigh wave at higher frequency.

For water-filled PFA pipes with moderate thickness (ϕ3 mm$\times\phi$2 mm) and thin thickness (ϕ2.1 mm$\times\phi$2 mm), the dispersion curves are shown in Figs. 6(a) and (b), respectively, in order to illustrate the dependence of the vibration behavior on wall thickness. The reduction in wall thickness decreases stiffness of the wall structure. As a result, at low frequency, the branch $s=1$ has slower velocity in the coupled system with thinner wall. If a further decrease in wall thickness H makes $H/R\approx 0$, the branch $s=1$ would disappear as in a pressure-release wall. The branch $s=2$ behaves as an extensional wall wave at higher frequency for thinner wall. In other words, as long as the thin wall assumption is available, the branch $s=2$ can be regarded as an extensional wall wave. Fuller[3] has expressed that the branch $s=2$ remains purely extensional throughout the frequency range in a thin-walled rubber-water tube. All higher branches ($s\geqslant 3$) appear at higher frequencies in the coupled system with thinner wall.

V. TIME-FREQUENCY DECOMPOSITION

As a four-cycle burst signal was used to excite the source transducer, the acoustic waves transmitting in the coupled system distribute over a wide frequency range. Figure 7(a) is the received signal at the driving frequency 120

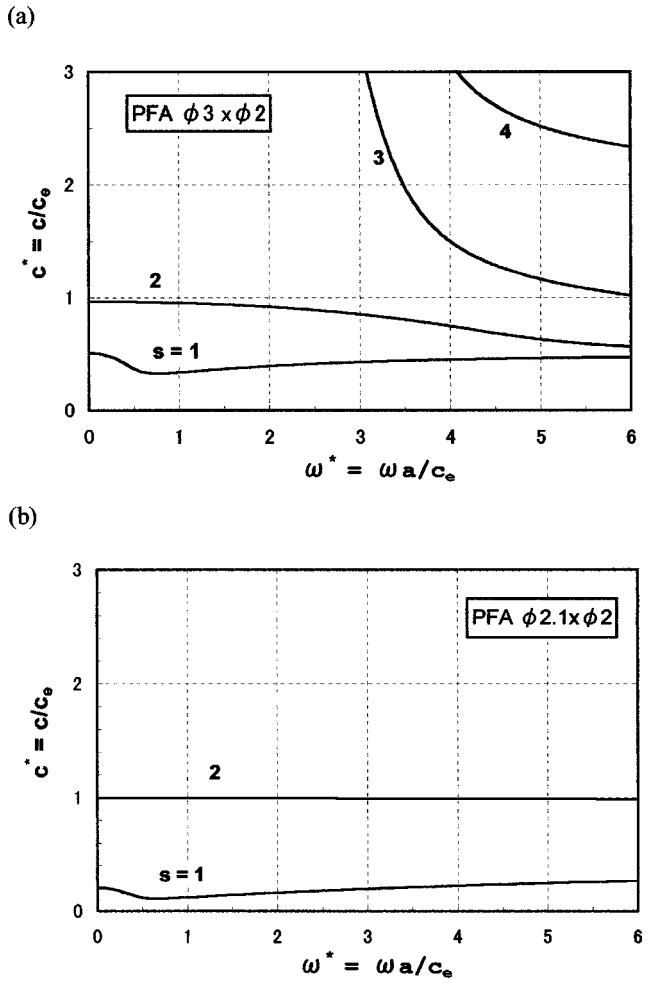

FIG. 6. Dispersion curves for water-filled PFA pipes with: (a) moderate thickness $H/R=0.4$; (b) thin thickness $H/R=0.05$; inner radius $a=1$ mm.

kHz. To estimate the propagating velocities at a certain frequency, it needs to localize the receiving signals both in time and frequency simultaneously with a good resolution. The wavelet transform[15,17] was adopted to decompose the receiving signal into several level components. Each component can be considered as the filtering response within a sub narrower band. Daubechies D4 wavelet[15,18] of a sixth-level decomposition was applied to analyzing the original signal [Fig. 7(a)]. The resulting main components are shown in Figs. 7(b), (c), and (d), which are the approximation coefficient (A6), level 6 (D6), and level 5 (D5) detail coefficients, respectively. Lower level (1–4) detail coefficients are mostly noisy components at high frequency with smaller values, and hence are omitted here. Accordingly, the receiving signal can be regarded approximately as the sum of A6, D6, and D5.

A6 is a lower-frequency component which arrives earlier in time. D5 relates to a higher-frequency wave. Since D6 can be expressed as

$$\text{D6} \approx \text{Original signal} - \text{A6} - \text{D5},$$

D6 will be considered generally as the component located at the central frequency 120 kHz, by removing the lower and higher frequency components from the original signal. Therefore, at 120 kHz, the propagating velocities of the first

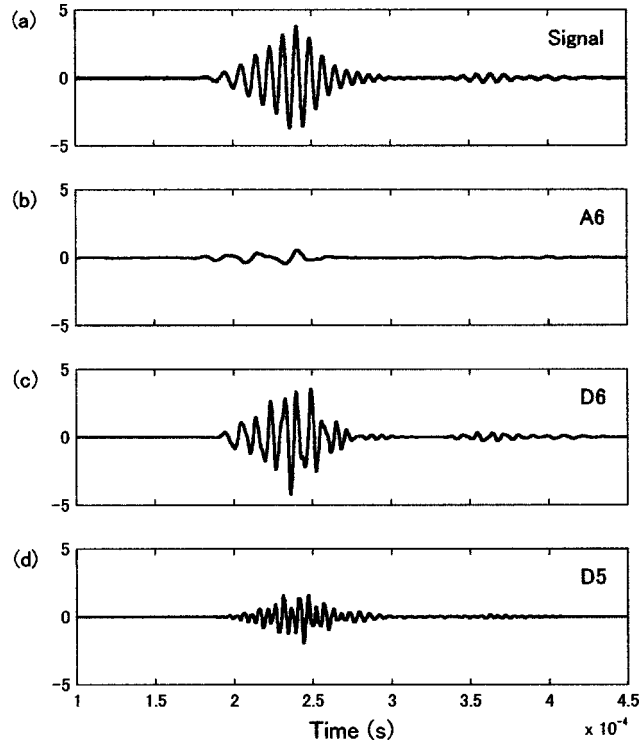

FIG. 7. Wave decomposition of the receiving waves at 120 kHz. (a) Original signal, (b) A6, (c) D6, (d) D5.

($s=2$) and second ($s=1$) arrival waves can be predicted from the arriving time of D6 signal.

Using the above-mentioned approach, the measured velocities at several driving frequencies are evaluated and plotted in Fig. 8. For comparison with the numerical values, the group velocities v_g ($v_g=(d(\omega/v_p)/dw)^{-1}$) calculated from the phase velocity v_p in Fig. 3 are presented in Fig. 8 as well. At 150 kHz, since the second-arrival wave overlapped with the first wave, the prediction of corresponding velocity ($s=2$) failed. At high frequency ($f>370$ kHz), since the ''acoustically'' slower waves were too small to be verified, the velocities of the first arrival wave alone could be estimated. The experimental and numerical values generally coincide well, with 4.3% average error. Although the received waves were analyzed by the discrete wavelet transform, the

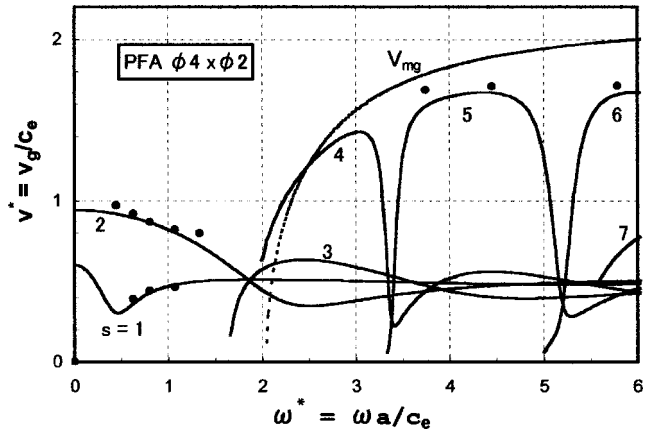

FIG. 8. Dispersed group velocity of a water-filled PFA pipe; cal (—); exp (●); v_{mg} is the group velocity of C_m.

extracted component still distributes at a narrower bandwidth and the resulting velocity might be the larger one within this bandwidth.

VI. CONCLUSIONS

The acoustic wave propagation in cylindrical pipe filled with fluid has been examined numerically and experimentally. The dispersion curves, the energy distribution between the contained fluid and pipe wall, and the distribution of wall motion, have been evaluated by the layerwise approach. The behavior of individual branches for the breathing mode is found to depend greatly on the motion of pipe wall. The acoustic waves in the coupled system generated by burst signals have been measured. To localize transient signal both in time and frequency, the discrete wavelet transform has been applied as decomposition filters to extracting the propagating signal at the driving frequency. Therefore the frequency-dependent group velocity can be estimated from the arrival time of the extracted component. The experimental and numerical results of the dispersed group velocities have a good agreement.

ACKNOWLEDGMENTS

The authors acknowledge Dr. Yoshikazu Koike, Shibaura Institute of Technology, Dr. Sadayuki Ueha and Dr. Kentaro Nakamura, Tokyo Institute of Technology, for their helpful advice.

[1] T. C. Lin and G. W. Morgan, ''Wave propagation through fluid contained in a cylindrical, elastic shell,'' J. Acoust. Soc. Am. **28**, 1165–1176 (1956).
[2] R. Kumar, ''Dispersion of axially symmetric waves in empty and fluid-filled cylindrical shells,'' Acustica **27**, 317–329 (1972).
[3] C. R. Fuller and F. J. Fahy, ''Characteristics of wave propagation and energy distribution in cylindrical elastic shells filled with fluid,'' J. Sound Vib. **81**, 501–518 (1982).
[4] C. R. Fuller, ''The input mobility of an infinite circular cylindrical elastic shell filled with fluid,'' J. Sound Vib. **87**, 409–427 (1983).
[5] B. J. Brévart and C. R. Fuller, ''Effect of an internal flow on the distribution of vibration energy in an infinite fluid-filled thin cylindrical elastic shell,'' J. Sound Vib. **167**, 149–163 (1993).
[6] X. B. Xu and W. H. Zhang, ''Vibrational power flow input and transmission in a circular cylindrical shell filled with fluid,'' J. Sound Vib. **234**, 387–403 (2000).
[7] Y. K. Cheung and C. I. Wu, ''Free vibrations of thick, layered cylinders having finite length with various boundary conditions,'' J. Sound Vib. **24**, 189–200 (1972).
[8] K. Y. Lam and C. T. Loy, ''Effects of boundary conditions on frequencies of a multi-layered cylindrical shell,'' J. Sound Vib. **188**, 363–384 (1995).
[9] Y. K. Cheung, *Finite Strip Method in Structural Analysis*, 1st ed. (Pergamon, Oxford, 1976).
[10] C. T. Loy and K. Y. Lam, ''Vibration of thick cylindrical shells on the basis of three-dimensional theory of elasticity,'' J. Sound Vib. **226**, 719–737 (1999).
[11] X. Y. Jiang, ''3-D vibration analysis of fiber reinforced composite laminated cylindrical shells,'' J. Sound Vib. **119**, 46–51 (1997).
[12] A. F. Seybert and D. F. Ross, ''Experimental determination of acoustic properties using a two-microphone, random excitation technique,'' J. Acoust. Soc. Am. **61**, 1362–1370 (1977).
[13] Y.-K. Kim and Y.-H. Kim, ''A three accelerometer method for the measurement of flow rate in pipe,'' J. Acoust. Soc. Am. **100**, 717–726 (1996).
[14] H. Hasegawa, T. Kmakura, and Y. Kumamoto, ''On the coupling mechanism between sound waves propagating in a thin-walled viscoelastic tube and the wall vibration'' (in Japanese), J. Acoust. Soc. Jpn. **53**, 24–32 (1997).
[15] R. M. Rao and A. S. Bopardikar, *Wavelet Transforms: Introduction to Theory and Applications* (Addison Wesley Longman, Reading, MA, 1998), Chap. 3.
[16] M. C. Junger and D. Feit, *Sound, Structures, and Their Interaction*, 2nd ed. (MIT, Cambridge, 1986), Secs. 2.9, 2.10, and 11.12.
[17] Y. Y. Kim and E.-H. Kim, ''Effectiveness of the continuous wavelet transform in the analysis of some dispersive elastic waves,'' J. Acoust. Soc. Am. **110**, 86–94 (2001).
[18] I. Daubechies, ''Orthonormal bases of compactly supported wavelets,'' Commun. Pure Appl. Math. **41**, 961–996 (1988).

On low frequency sound transmission loss of double sidebranches: A comparison between theory and experiment

S. K. Tang[a] and F. Y. C. Li[b]
Department of Building Services Engineering, The Hong Kong Polytechnic University, Hong Kong, China

(Received 6 September 2002; revised 3 February 2003; accepted 19 February 2003)

The sound power transmission losses of various sidebranches installed along a rectangular duct below the first cut-off frequency of the duct are studied experimentally. Special efforts are made to examine how accurately the plane-wave theory predicts the sound-power transmission loss. Four types of sidebranch impedance are established and their effects to the sound power transmission loss discussed. It is found that under the nonresonant conditions the plane-wave theory can give reasonable prediction when the branch separation is large or the original sound transmission loss of the corresponding single side-branch is weak. The theory always overestimates the sound transmission loss at resonant conditions but gives underestimation if the transmission loss is due to the noise breakout in the sidebranches, especially for short branch separation. © *2003 Acoustical Society of America.* [DOI: 10.1121/1.1568757]

PACS numbers: 43.50.Gf, 43.20.Mv [DKW]

I. INTRODUCTION

Sound propagation inside an air duct and its attenuation is one of the most important issues in building noise control. The problem is more serious at low frequencies because of the poor performance of the dissipative silencer in this frequency range.[1] The low frequency sound attenuation performance of various duct elements has been investigated extensively during the past few decades. They include the expansion chambers and mufflers,[2] the Helmholtz resonators,[3] and different forms of waveguides (for instance, Ref. 4). Formulas for the prediction of low frequency sound transmission loss of some of these conventional passive duct elements are currently available for engineering design purposes.[5] The use of active control for low frequency attenuation in ducts is also possible nowadays.[6]

When engineers calculate the required sound attenuation for a particular air distribution path in a duct system, the transmission losses produced by all the duct elements involved have to be taken into account. Sidebranches, except those specifically installed as a reactive silencer (such as the Helmholtz resonator or simply a cavity[7]), are indispensable as they are important for conveying fresh air from the main air supply duct into different parts in the interior of a building. Similar branches can also be found in the air exhaust system. Though these sidebranches are not designed to provide sound attenuation, they do have contributions in the noise control as they produce a change in the acoustic impedance along a duct.[8] The termination of a sidebranch, its length, and its area relative to that of the main duct cross section affect the overall sound power transmission loss across the branch. For a double sidebranch configuration, the coupling between the two sidebranches and the air mass in between the branches inside the main duct have crucial effects on the overall sound power transmission loss. Optimal design for sound attenuation therefore requires a better knowledge of the acoustical effects associated with branching.

Since it is the low frequency noise that is of concern, the one-dimensional wave theory has been applied to predict the sound power transmission loss, TL, due to sidebranches (for instance, Reynolds[9]). For an infinitely long sidebranch, this approach suggests that the corresponding TL depends solely on the cross-sectional area ratio between the sidebranch and the main duct.[9] For a double sidebranch, the current engineering practice usually ignores the contribution of the air mass inside the main duct bounded by the two sidebranches,[5] though it is included in the theoretical consideration.[9] Despite the importance of the acoustical behaviors of multiple sidebranches on sound propagation inside a duct, a detailed comparison between the predictions from plane-wave theory and experimental results, at least to the knowledge of the authors, is not well documented.

In the present investigation, the experimentally determined sound power transmission loss resulting from double sidebranches is compared with that predicted from the plane-wave theory in detail. The impedance of each sidebranch is estimated from the corresponding complex sound pressure ratios using the plane-wave theory. Different characteristics of the sidebranch impedance are included and their effects discussed. It is hoped that the present results can clarify the extent to which the plane-wave theory can be used to predict the sound power transmission losses of the double sidebranches and provide useful information for building noise control and further modeling.

II. THE EXPERIMENTAL SETUP

Figure 1 illustrates the schematic of the experimental set rig assembly for the present study. The main duct was made of 12.7-mm-thick Perspex and had a rectangular cross sec-

[a]Author to whom correspondence should be addressed; electronic mail: besktang@polyu.edu.hk
[b]Currently at Wo Hing Engineering Limited, 4/F, Telford House, 16 Wang Hoi Road, Kowloon Bay, Hong Kong, China.

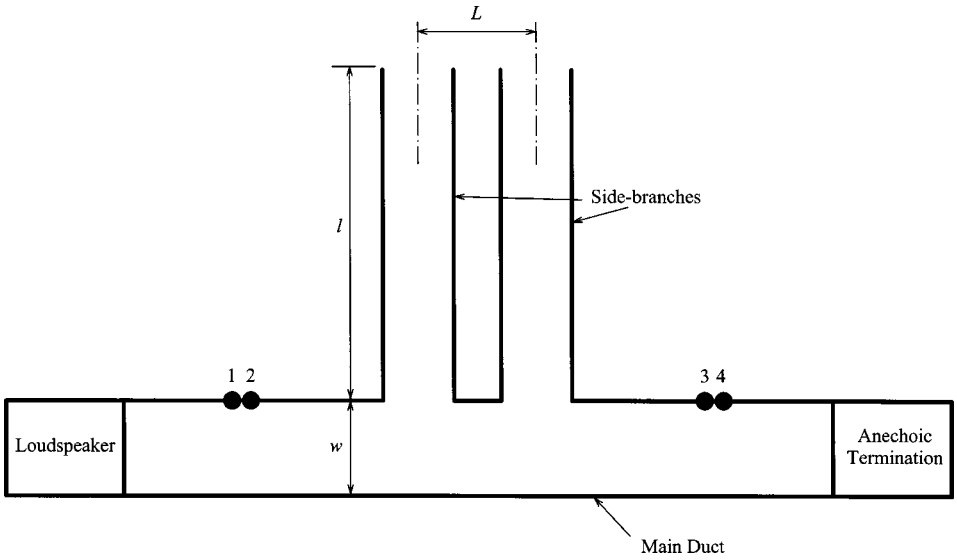

FIG. 1. Schematic diagram for the experiment (not drawn to scale and numbers represent microphones).

tion of dimension 173 mm by 150 mm giving a first cut-off frequency, f_c, of 991 Hz, which was also the highest frequency concerned in the present study. A loudspeaker was mounted at one end of the main duct, while the other end was fitted to an anechoic termination. Owing to the size of the loudspeaker, sound of frequency lower than 100 Hz could not be effectively generated. The sound power reflection coefficient, measured by the two microphone method (discussed later), associated with the anechoic termination shows that this termination basically absorbed 98% of the incident sound energy for frequency at around 180 Hz ($f/f_c=0.18$, Fig. 2). In fact, for $f/f_c>0.22$, the sound power reflection coefficient was less than 0.6%, indicating an anechoic condition was established.

The sidebranches had a cross section of 163 mm by 150 mm. They were made of 5.8 mm Perspex and each of their open ends contained a small flange. Branch length l could be varied and the ends of the sidebranches were either left opened or fitted with anechoic terminations. This was to vary the acoustic impedance of the sidebranch and will be discussed later. The small thickness of the sidebranch allowed a possible noise breakout, which is due to the vibration of the duct walls, somewhere around 450 Hz ($f/f_c\sim0.45$)—a feature specifically introduced for the present investigation to complicate the acoustic impedance of the sidebranches. The exact noise breakout frequency depends on the branch length as well as on the structure of the branch. However, this phenomenon was only important when the branch length was sufficiently long. This will be discussed later. The corresponding noise breakout frequency of the main duct was higher than 1 kHz. One sidebranch was removed during the measurements of single side-branch impedances and the corresponding sound power transmission losses.

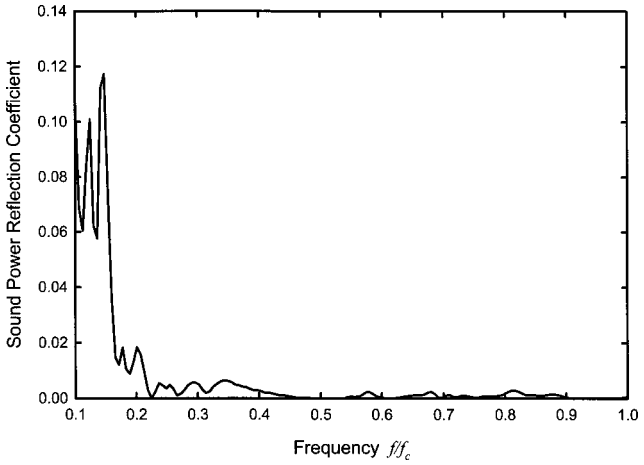

FIG. 2. Sound power reflection coefficients in main duct with anechoic termination.

Sound pressure fluctuations were measured by four Brüel & Kjær 4935 $\frac{1}{4}$ in. microphones with the appropriate signal conditioners. One microphone pair was located on each side of the duct branching and the microphones in each pair were separated by a distance of 20 mm. The locations of measurements were more than two duct widths from the entrance or exit of the branching in order to allow for the decay of all the nonplanar modes.[10] These positions were also more than 0.5 m from the loudspeaker or the anechoic termination. In a preliminary trial test, sound pressure spectra at various points along the centerlines of the main duct cross section were measured by a probe microphone. The variation of spectral densities from 180 to 991 Hz was less than 0.6 dB, confirming that only plane waves were propagating along the main duct within the experimental frequency range. The sound pressure fluctuations from the microphones were simultaneously recorded onto tapes using a SONY PC208Ax digital recorded for later analyses. Sampling rate per channel was 24 kHz and each recording lasted for 30 s.

The experimental investigation was carried out in a large laboratory with a height of around 12 m and a floor area roughly over 100 m^2. There were plenty of scattering objects and the sound absorption was good. The acoustical interaction between the laboratory and the test rig should be insignificant. The laboratory was air-conditioned with air temperature and relative humidity maintained at 23 °C and 60%, respectively.

III. SOUND TRANSMISSION LOSS AND ACOUSTIC IMPEDANCE MEASUREMENTS

The two-microphone transfer function method was employed to calculate the sound transmission loss and the impedance of a single sidebranch. Since the gain and phase responses of the microphones are in general not identical, the sensor-switching technique was used. Though main details of this method for measuring complex sound reflection coefficient can be found in Chung and Blaser,[11] a brief account of it is given in the following for completeness and also as a reference for later derivation of the acoustic impedance measurement and the sound power transmission loss.

The subscripts 1, 2, 3, and 4 denote hereinafter quantities related to microphones 1, 2, 3 and 4, respectively. During each measurement, four complex pressure signals, p_i, can be obtained:

$$\begin{aligned} &p_1(I_u e^{-jkx_1}+R_u e^{jkx_1})e^{j\omega t},\\ &p_2=(I_u e^{-jk(x_1+\Delta x)}+R_u e^{jk(x_1+\Delta x)})e^{j\omega t}J_2 e^{j\phi_2},\\ &p_3=(I_d e^{-jkx_3}+R_d e^{jkx_3})e^{j\omega t}J_3 e^{j\phi_3},\\ &p_4=(I_d e^{-jk(x_3+\Delta x)}+R_d e^{jk(x_3+\Delta x)})e^{j\omega t}J_4 e^{j\phi_4}, \end{aligned} \tag{1}$$

where I and R represent the complex magnitudes of the forward and backward waves, respectively, and the subscripts u and d denote locations upstream and downstream of the duct branching respectively. The separation Δx is 20 mm. J_i and ϕ_i represent the gain and phase response of microphone i relative to those of microphone 1 respectively. Basically, R_d is very weak ($|R_d/I_d|\to 0$) in the present study due to the strong absorption anechoic termination, but it is included here for the sake of completeness. After swapping sensor 1 with sensor 2, and sensor 3 with sensor 4, one obtains another set of recording, p_i', where

$$\begin{aligned} &p_1'=(I_u e^{-jk(x_1+\Delta r)}+R_u e^{jk(x_1+\Delta x)})e^{j(\omega t+\theta)},\\ &p_2'=(I_u e^{-jkx_1}+R_u e^{jkx_1})e^{j(\omega t+\theta)}J_2 e^{j\phi_2},\\ &p_3'=(I_d e^{-jk(x_3+\Delta x)}+R_d e^{jk(x_3+\Delta x)})e^{j(\omega t+\theta)}J_3 e^{j\phi_2},\\ &p_4'=(I_d e^{-jkx_3}+R_d e^{jkx_3})e^{j(\omega t+\theta)}J_4 e^{j\phi_4}, \end{aligned} \tag{2}$$

where θ denotes an unknown but constant phase shift between signals in Eqs. (1) and (2). By rearranging terms in Eqs. (1) and (2), the complex reflection coefficients can be expressed as

$$\begin{aligned} &\frac{R_u}{I_u}=-\frac{\sqrt{H_{21}'H_{12}}-e^{-jk\Delta x}}{\sqrt{H_{21}'H_{12}}-e^{jk\Delta x}}e^{-2jkx_1},\\ &\frac{R_d}{I_d}=-\frac{\sqrt{H_{43}'H_{34}}-e^{-jk\Delta x}}{\sqrt{H_{43}'H_{34}}-e^{jk\Delta x}}e^{-2jkx_3}, \end{aligned} \tag{3}$$

where H_{12} denotes the complex transfer function between p_1 and p_2 and so on. Therefore,

$$\begin{aligned} &p_1=I_u e^{-jkx_1}\left(1-\frac{\sqrt{H_{21}'H_{12}}-e^{-jk\Delta x}}{\sqrt{H_{21}'H_{12}}-e^{jk\Delta x}}\right),\\ &p_3=I_d e^{-jkx_3}\left(1-\frac{\sqrt{H_{43}'H_{34}}-e^{-jk\Delta x}}{\sqrt{H_{43}'H_{34}}-e^{jk\Delta x}}\right)J_3, \end{aligned} \tag{4}$$

so that the complex sound transmission coefficient for the main duct is

$$\frac{I_d}{I_u}=e^{jk(x_3-x_1)}\left(1-\frac{\sqrt{H_{43}'H_{34}}-e^{-jk\Delta x}}{\sqrt{H_{43}'H_{34}}-e^{jk\Delta x}}\right)\Bigg/ \left[H_{31}J_3\left(1-\frac{\sqrt{H_{21}'H_{12}}-e^{-jk\Delta x}}{\sqrt{H_{21}'H_{12}}-e^{jk\Delta r}}\right)\right], \tag{5}$$

where H_{31} is the transfer function between p_3 and p_1 ($H_{31}=p_1/p_3$). J_3 can be obtained by standard microphone calibration. The sound power transmission loss, TL, is thus

$$\mathrm{TL}=20\lg\left|\frac{I_u}{I_d}\right|=20\lg\left|H_{31}J_3\left(1-\frac{\sqrt{H_{21}'H_{12}}-e^{-jk\Delta x}}{\sqrt{H_{21}'H_{12}}-e^{jk\Delta x}}\right)\Bigg/ \left(1-\frac{\sqrt{H_{43}'H_{34}}-e^{-jk\Delta x}}{\sqrt{H_{43}'H_{34}}-e^{jk\Delta x}}\right)\right|. \tag{6}$$

For a single sidebranch with an acoustic impedance Z_b, the plane-wave theory suggests that the complex sound power transmission ratio[3]

$$\frac{I_d}{I_u}=\frac{Z_b}{0.5Z_d+Z_b}\Rightarrow\frac{Z_b}{Z_d}=\left[2\left(\frac{I_u}{I_d}-1\right)\right]^{-1}, \tag{7}$$

where Z_d is the acoustic impedance of the main duct, which equals $\rho c/S$ (c is the speed of sound, ρ the air density, and S the cross-sectional area of the main duct). TL of the double sidebranching formed by coupling two sidebranches of impedance Z_b separated by a distance L is

$$\mathrm{TL}=20\lg\left|\left(1+\frac{Z_d}{2Z_b}\right)^2-\left(\frac{Z_d}{2Z_b}\right)^2 e^{-2jkL}\right|. \tag{8}$$

Equation (7) was used to calculate the experimental acoustic impedance of a single sidebranch from the complex sound pressure ratio obtained using Eq. (5). Predictions from Eq. (8) were then compared with the experimental results associated with the double sidebranching arrangements.

IV. RESULTS AND DISCUSSIONS

This section summarizes the acoustic impedances of the sidebranches involved and compares the TL of the double sidebranch arrangements with the plane-wave theory predictions. All length scales are normalized by the width of the main duct, w, and frequencies by the first cut-off frequency f_c ($w=173$ mm, $f_c=991$ Hz). The acoustic impedances are normalized by that of the main duct, assuming infinitely long (Z_d).

A. Acoustic impedance of single sidebranches

Since the anechoic terminations in the present study absorbed more than 99% of the incident sound energy in the

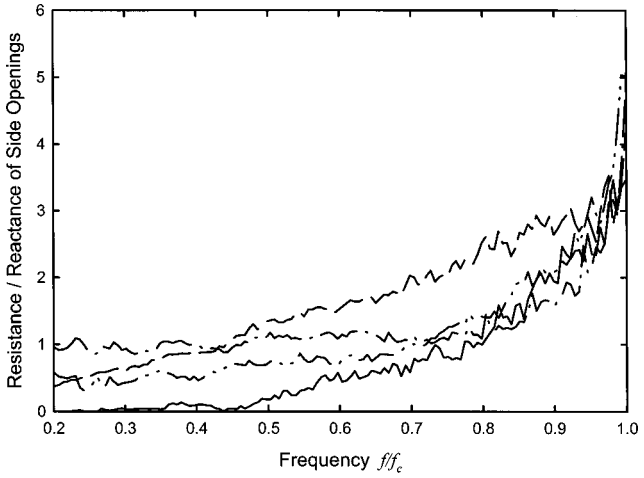

FIG. 3. Acoustic impedance of side opening: (—) resistance without anechoic termination; (— — —) reactance without anechoic termination; (-·-) resistance with anechoic termination; (–·–) reactance with anechoic termination. $l/w=0$.

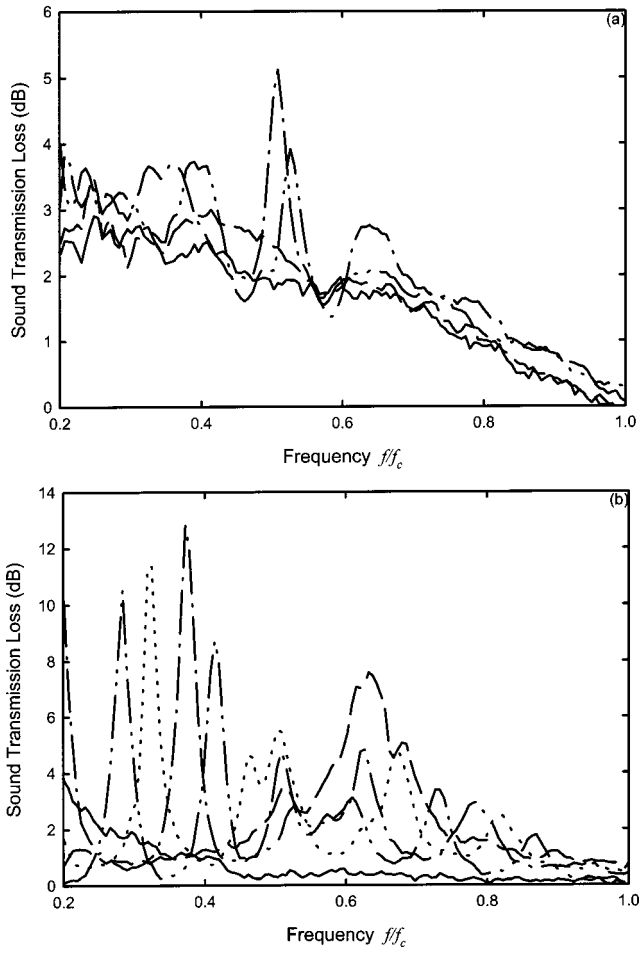

FIG. 4. Effects of length of sidebranch on sound power transmission loss. (a) With anechoic termination; (b) without anechoic termination. (—) $l/w=0$; (— — —) $l/w=0.87$; (-·-) $l/w=4.36$; (···): $l/w=5.23$; (–·–) $l/w=6.10$.

frequency range concerned, they were used to simulate the effect of an infinitely long sidebranch. The magnitude of the acoustic impedance of the sidebranch increases with frequency, even its outlet was fitted with an anechoic termination as shown in Fig. 3 (the case without the anechoic termination will be discussed later). The physical dimension of the branch results in sound diffraction from the main duct into the sidebranch. Such diffraction is less effective at higher frequency,[12] resulting in lower TL as frequency increases [Fig. 4(a)]. It can also be observed from Fig. 4(a) that the length of the sidebranch does not have very significant effect on the acoustic properties of the sidebranch in the presence of the anechoic termination, except for the case where the length is so long that the noise breakout becomes a bit significant. One can notice from Fig. 4(a) that this effect is still very limited with a branch length of $l/w<4$.

The branch length l has significant effects on the acoustical properties and thus the TL of the sidebranch in the absence of the anechoic termination, as shown in Fig. 4(b), mainly because the branch resonance resulted from open-end reflection. The sharpness, and thus the strength, of the resonance becomes distinct for $l/w>2$. It is believed that for short l, the nonplanar acoustic modes scattered at the branch-duct junction will affect the longitudinal resonance in the branch. It should be noted that the resonance frequency is not necessarily the frequency of peak TL. One can notice from Eq. (8) that these frequencies coincide only when the magnitude of Z_b is much smaller than that of the main duct, which is the case of strong resonance. It is noted from Fig. 5(a), which shows the impedance of the first sidebranch with $l/w=5.23$ ($l=905$ mm), that two types of resonance occur (reactance vanishes or small). One of them results in weak Z_b, while the other is accomplished with high resistance magnitude. Only the former can produce a high TL as shown in Fig. 4(b). The frequencies of relatively weak Z_b are approximately $f/f_c=0.16$ (not shown here), 0.32, 0.50, 0.67, and 0.81; those of high resistance being 0.25, 0.42, 0.60, 0.77, and 0.88. One can easily observe that the former and latter frequency series coincide closely with those for resonance along a ''both-ends-opened'' and a ''one-end-closed-one-end-opened'' tube with length of ~1.06 m. The present cross section of the sidebranch was 163 mm by 150 mm, giving an equivalent radius of 88.2 mm. The length correction for open-end reflection, according to existing theory,[2,3] is $8/3\pi\times 88.2$ mm, which equals ~75 mm. Total branch length correction is therefore ~150 mm and the effective branch length for longitudinal resonance is around 905 mm $+150$ mm $=1.055$ m, confirming the occurrence of the above-stated resonance. However, one should note that the junction between the branch and the main duct is not four-side flanged, which would be expected to further increase the length correction somewhat if one follows the increase in end correction from the unflanged to the flanged condition.[3]

The high resistance peaks found under the ''one-end-closed-one-end-opened'' resonance are therefore due to high pressure buildup in the duct-branch junction. The weak impedance at resonance under the ''both-ends-opened'' condition seems to be the result of low pressure at regions close to branch ends. One small peak of resistance can be observed in Fig. 5(a) at $f/f_c\sim 0.47$. This frequency coincides with the fundamental vibration frequency of a four-edge clamped rectangular Perspex plate with dimension 905 mm by 163 mm and thickness 5.8 mm.[13] The small resistance peak is

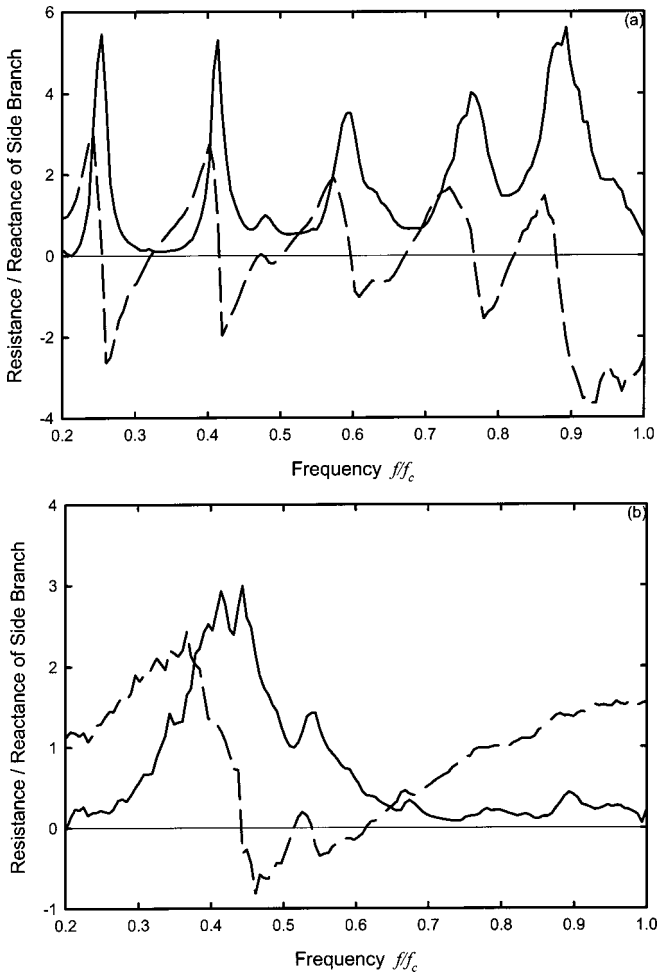

FIG. 5. Variations of acoustic impedance with frequency under resonant conditions. (a) Strong resonance, $l/w=5.23$; (b) weak resonance, $l/w=0.87$. (—) Resistance; (— — —) reactance. Without anechoic termination.

thus due to the noise breakout, which is resistive to sound (dissipation).

Figure 5(b) shows an example of weak sidebranch impedance with $l/w=0.87$ without the anechoic termination ($l=150$ mm). It can be observed that the corresponding impedance magnitude peaks at around $f/f_c\sim0.45$ while the highest TL in the present frequency range of interest is found at f/f_c around 0.63 [Fig. 4(b)]. The large impedance at around $f/f_c\sim0.45$ is probably due to the noise breakout of the sidebranch and is substantially more broadband than those found at strong resonance [Fig. 5(a)]. However, it is not important as the corresponding TL is weak [Fig. 4(b)]. Generally speaking, no significant branch resonance can be observed in this case except at $f/f_c\sim0.51-0.54$, which is in fact not strong. According to existing theory,[2,3] branch resonance in this case will occur at $f/f_c\sim0.29$, 0.58, and 0.87. The wavelength at $f/f_c\sim0.29$ is about 1.2 m, which is much longer than the branch length ($\sim$150 mm) in this case. The chance of the branch air vibrating as a massless piston increases,[3] making longitudinal branch resonance improbable. The diffraction of the acoustic waves into the branch at the duct-branch junction, which results in nonplanar acoustical energy distribution across the branch cross section and violates the plane-wave assumption, is only important when f/f_c approaches unity. One can estimate using mode propagation theory given in standard references (for instance, Refs. 2 and 3) that at $f/f_c=0.87$ there is only a $\sim$7 dB drop in the first higher acoustic mode magnitude along the length of the branch. However, the corresponding magnitude drop reaches $\sim$9.4 dB at $f/f_c=0.7$ and $\sim$12 dB at $f/f_c=0.29$. At zero branch length, which is a very common case in building services engineering, no resonance within the frequency range of the present investigation is therefore possible. This is confirmed in Fig. 3. It can also be observed from Fig. 3 that the acoustic impedance of such opening is weaker than that with the anechoic termination in-place.

The acoustic impedance of the sidebranches can therefore be categorized into four different types. The first type is of broadband high reactance but relatively weak resistance at low frequencies, which corresponds to the case of zero branch length without anechoic termination. The associated TL decreases quickly with frequency. The second one refers to the case of infinitely long sidebranch, which is the case where the end of the branch is fitted with an anechoic termination. This arrangement provides broadband dissipating sound resistance together with reasonable reactance to the main duct, resulting in more significant broadband TL. These two categories are typical high-pass acoustic filters. The third category refers to the case where the sidebranch has weaker acoustic impedance within a narrow frequency band, which is also the case for weak resonance of branch wall. The final one is the case for strong resonance in the branch. The last two categories represent the band-stop/band-pass filters.

B. Sound transmission loss of double sidebranches

Figure 6 illustrates the variation of TL of the present double sidebranch arrangements with frequency. Neglecting the effect of the air mass between the sidebranches suggests, according to Eq. (8), a doubling of the corresponding single sidebranch TL (6.7 dB according to current practice calculation[5]). Figure 6(a) indicates that such assumption, which is used in current engineering practice, is not valid for the case of broadband high sidebranch acoustic reactance even if the TL of the original single sidebranch is less than 1 dB (such as the case of $l/w=0$ without anechoic termination). Better agreement is found at higher frequency where the impedance is large relative to that of the main duct, but the situation at lower frequency is not acceptable. The experimental TL of the double sidebranches, except that at $L/w=1.59$, shows domes at low frequency because of the standing waves set up inside the main duct region between the two sidebranches. The relatively weaker acoustic impedance at lower frequencies amplifies the effect of the factor e^{-2jkL} in Eq. (8). One can find higher TL at frequencies where $e^{-2jkL}\sim-1$ or $-j$. However, unlike the case for the expansion chamber,[2] the magnitudes of the domes decrease with increasing frequency due to the increasing acoustic impedance magnitude of the sidebranches. The resonance inside the region between the sidebranches in the main duct becomes more remarkable as the branch separation L increases. Effects of such resonance are expected to be similar

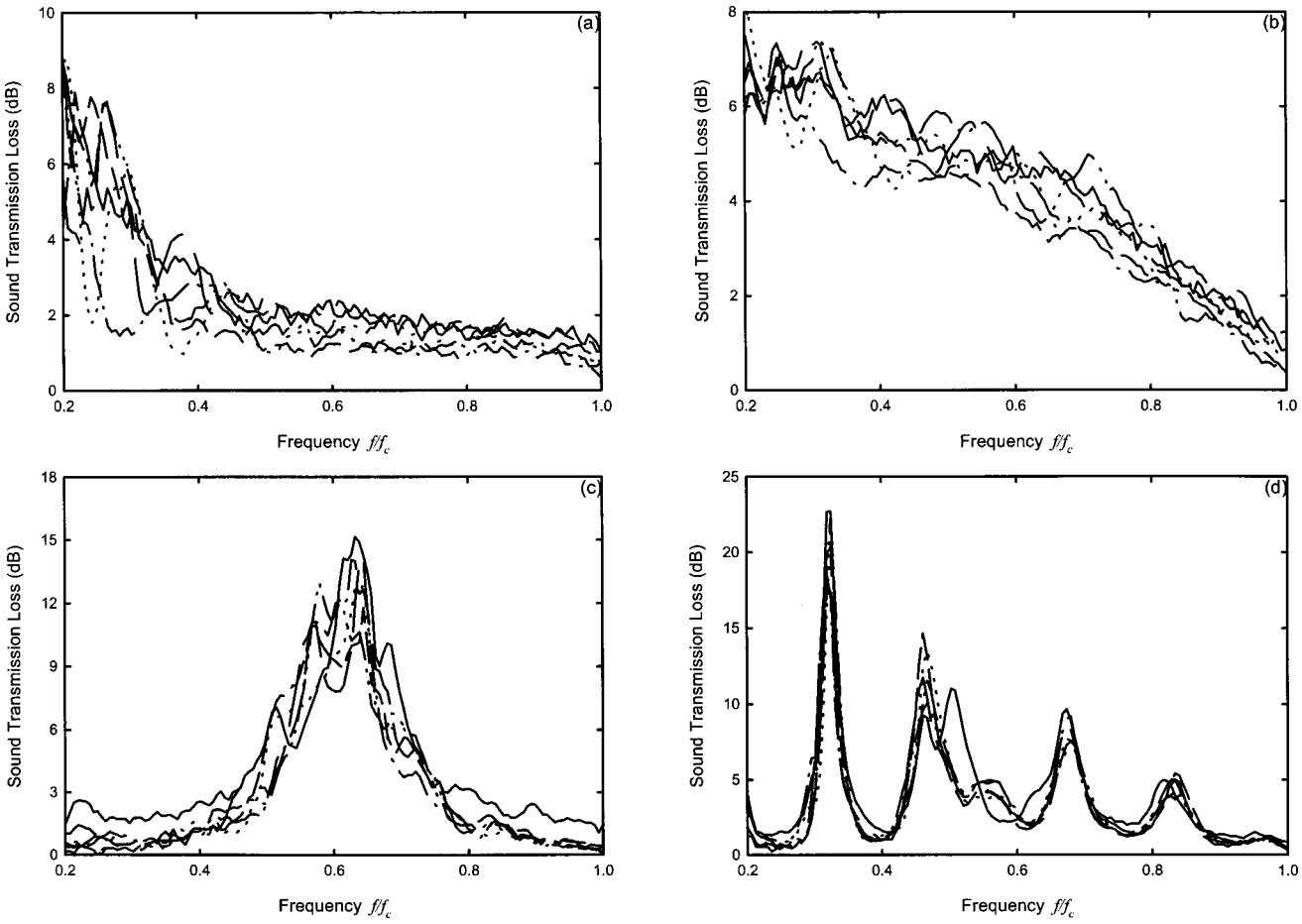

FIG. 6. Variation of sound power transmission loss of double sidebranches with frequency. (a) $l/w=0$ without anechoic termination (broadband high reactance); (b) $l/w=0$ with anechoic termination (broadband high acoustic impedance); (c) $l/w=0.87$ without anechoic termination (weak branch resonance); (d) $l/w=5.23$ without anechoic termination (strong branch resonance). (- - -) $L/w=1.59$; (-·-) $L/w=2.72$; (–·–) $L/w=4.62$; (···): $L/w=7.49$; (–––) $L/w=8.50$; (—) plane-wave theory with effects of L ignored.

to those within an expansion chamber. One can also notice from Fig. 6(a) that the domes become more periodic with sharper regions of low TL as L increases.

Under the broadband high acoustic impedance condition, the effect of neglecting the contribution of the air mass is less remarkable, though one can still anticipate a difference in TL of 2 dB [Fig. 6(b)]. The higher damping (resistive part of Z_b) than in the previous case results in much less perfect wave interference/resonance inside the main duct. The relatively less rapid rate of increase of the impedance magnitude with frequency in this case as indicated in Fig. 3 gives rise to a greater number of domes at a fixed L than in the previous case. Again, the contribution of the standing waves becomes more significant as L increases.

Figure 6(c) illustrates the TLs of double sidebranch arrangements for the case of weak resonance. One finds that the TL of the double sidebranch is more broadband than that of the single branch regardless of L. The variation of TL with frequency appears to be double-peaked, while the relative magnitudes of these peaks depend on L. It is probably because of the moderation produced by the standing waves between the sidebranches. One can notice this immediately by comparing Figs. 6(b) and (c) at locations of peaks and toughs of the domes in Fig. 6(b). This will be further discussed later. Outside the frequency band with significant TL, neglecting L in Eq. (8) results in approximately 2 dB insignificant overestimation.

One can notice from Fig. 6(d) that for the case of strong branch resonance, the effect of L can only be marginally negligible at locations of weak TL or weak higher harmonic resonance. It is expected that the double sidebranch arrangement would result in less than a double increase in TL at frequency of weak Z_b according to Eq. (8). However, the reason for the disappearance of high TL at $f/f_c=0.50$ is unknown. A closer look at Fig. 6(d) reveals the presence of a small ''kick'' at this frequency at $L/w=8.50$ and a point of inflexion at the same frequency at $L/w=7.49$. Further discussion will be given in the next section.

C. Comparison with plane-wave theory predictions

The theoretical sound power transmission losses in this section are calculated from Eqs. (7) and (8) using the experimental results of the single sidebranches. One can observe from Figs. 7(a)–(e) that the plane-wave theory predicts reasonably satisfactorily the TL for the case of zero branch length openings (the case of broadband sidebranch reactance). The experimental TLs show less degree of fluctuations than the predicted ones for all L investigated, showing that the interference between waves in the main duct in re-

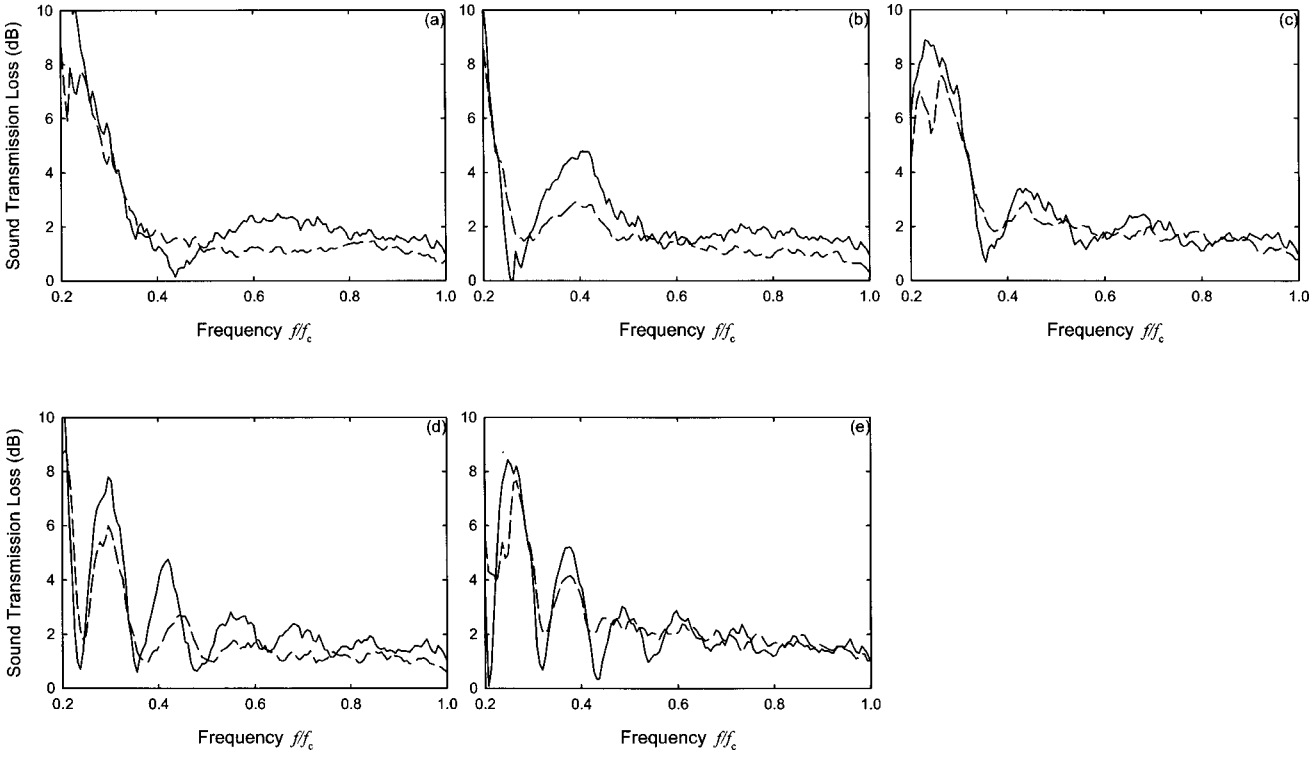

FIG. 7. Comparisons between plane-wave theory predictions and measurements for the case $l/w=0$ without anechoic termination (broadband high reactance). (a) $L/w=1.59$; (b) $L/w=2.72$; (c) $L/w=4.62$; (d) $L/w=7.49$; (e) $L/w=8.50$. (—) Plane-wave theory; (– – –) measurement.

ality is less perfect. This is rather expected. The physical dimension of the branch results in nonuniform acoustic impedance in the corresponding region in the main duct. For small $L/w=1.59$ [Fig. 7(a)], it is found that the standing wave resonance in the main duct, which is expected to occur at $f/f_c\sim 0.42$ according to plane-wave theory, even disappears. The corresponding wavelength is 824 mm ($=4.8w$), which is very long when compared to L in Fig. 7(a). The nonplanar/higher order acoustic wave (evanescent wave) scattered out from the first branch can then result in a highly nonuniform acoustical energy distribution at the proximity of the second branch.[12] This evanescent wave magnitude drops only 7 dB before it reaches the second branch. The separation between the two openings does not have significant influence on the agreement between the experimental results and the theoretical predictions for $L/w\geqslant 2.72$ [Figs. 7(b)–(e)]. At these branch separations, the evanescent waves have died down completely within the duct sections between the two sidebranches. The plane-wave theory predicts the locations of trough and crests of the domes at these separations with acceptable engineering tolerance. The TL cannot go down to 0 dB due to the finite damping offered by the sidebranches.

Figure 8 shows results for sidebranches consisting only with anechoic termination ($l/w=0$). These results demonstrate the introduction of higher resistance and a reduction in the reactance result in higher TL. It is observed that the acceptability of the plane-wave prediction depends substantially on the separation L. In general, one can find that the plane-wave theory predicts peaks of TL at frequency lower than those obtained from experiments. The shorter the distance L, the larger such difference becomes. However, the agreement between plane-wave theory prediction and experiment at $L/w=1.59$ is still better than that in the previous case. The significantly weaker sound transmission produced by this kind of sidebranch at $f/f_c>0.4$ than that in the case without the anechoic termination (Fig. 4) suggests less sound energy reaching the second branch. Weaker influence from the evanescent waves is thus expected.

For the case of weak resonance, the plane-wave theory overestimates the TL nearly over the whole frequency range concerned as shown in Fig. 9. The sound power transmission loss peaks at the frequencies $f/f_c\sim 0.51$ and ~ 0.68, originally found with the single sidebranch of $l/w=0.87$ [Fig. 4(b)], are missing in the double sidebranch arrangement. The plane-wave theory cannot directly explain the moderation discussed earlier and these ''missing peaks'' observation. At $f/f_c\sim 0.68$ in the weak resonance case, $|Z_d/Z_b|\approx 2$, showing that the magnitude of Z_b is not very small. The diffraction and wave scattering at the entrance of each sidebranch suggest that a correction for the branch separation L may be required. Suppose the effective branch separation is given by $L+\varepsilon$, where ε is the correction,

$$\mathrm{TL}=20\ \lg\left|\left(1+\frac{Z_d}{2Z_b}\right)^2-\left(\frac{Z_d}{2Z_b}\right)^2 e^{-2jk(L+e)}\right|. \tag{9}$$

Unlike the case for the sidebranch resonance, the end condition of the region between the side-branches in the main duct is 1/4 flanged and the others are flat. It is believed that ε is likely to exceed 1.7 times the equivalent radius of the main duct cross section. This is because one can observe from Ref. 3 that 1.7 is the factor for a flanged open-end tube and 1.2 is that for the unflanged case, suggesting an increase in this

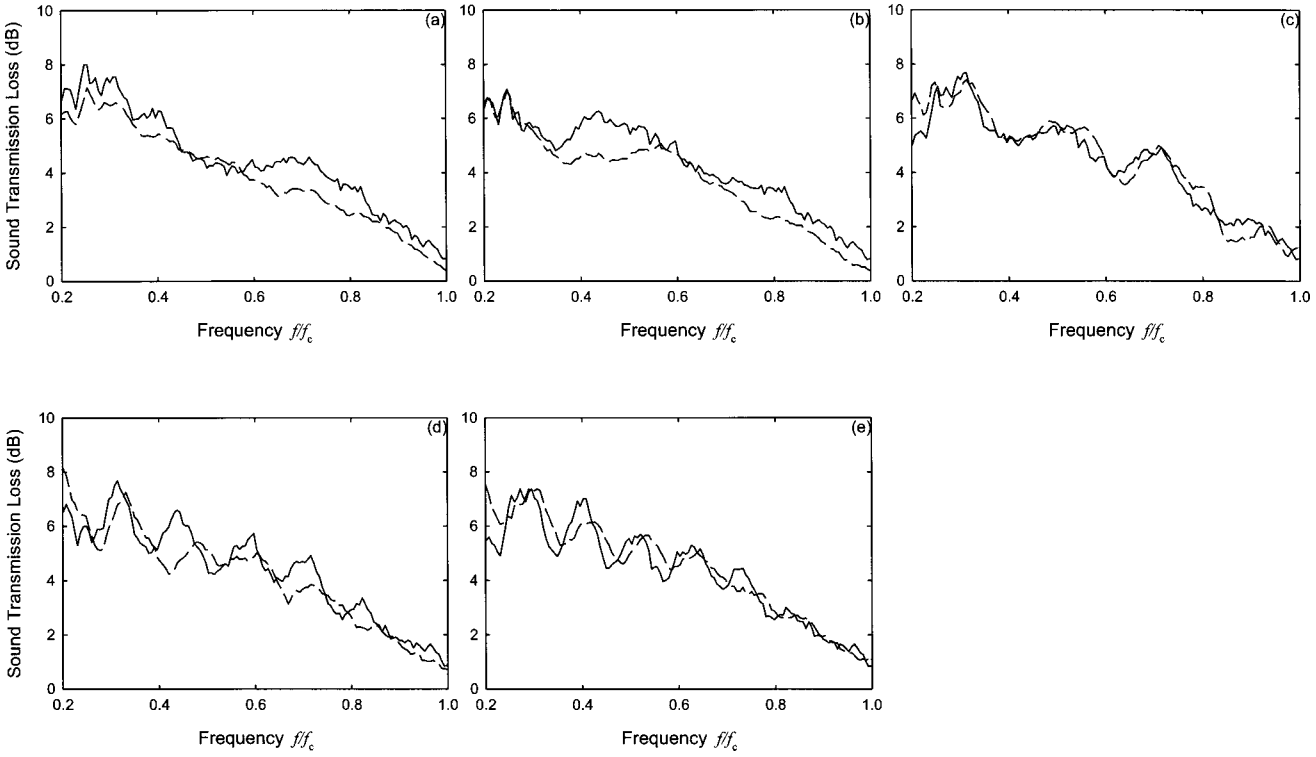

FIG. 8. Comparisons between plane-wave theory predictions and measurements for the case $l/w=0$ with anechoic termination (broadband high acoustic impedance). (a) $L/w=1.59$; (b) $L/w=2.72$; (c) $L/w=4.62$; (d) $L/w=7.49$; (e) $L/w=8.50$. (—) Plane-wave theory; (– – –) measurement.

factor as higher restriction is imposed to the radiation direction at the tube ends. However, a formula or data for determining ε is not known to the authors. The results of Redmore and Mulholland[8] with a single sidebranch do not facilitate the estimation of such factor. Since this factor is increased by 0.5 upon a four-side 50% reduction in the radiation surface, a rough extrapolation here for the factor is $1.7+(1.7-1.2)/4\times 3=2.1$. Equivalent radius of the main duct cross section here is 90.9 mm and thus ε is estimated to be 188.6 mm.

For $L/w=1.59$, 4.62, and 7.49, a drop of 3 to 4.3 dB in

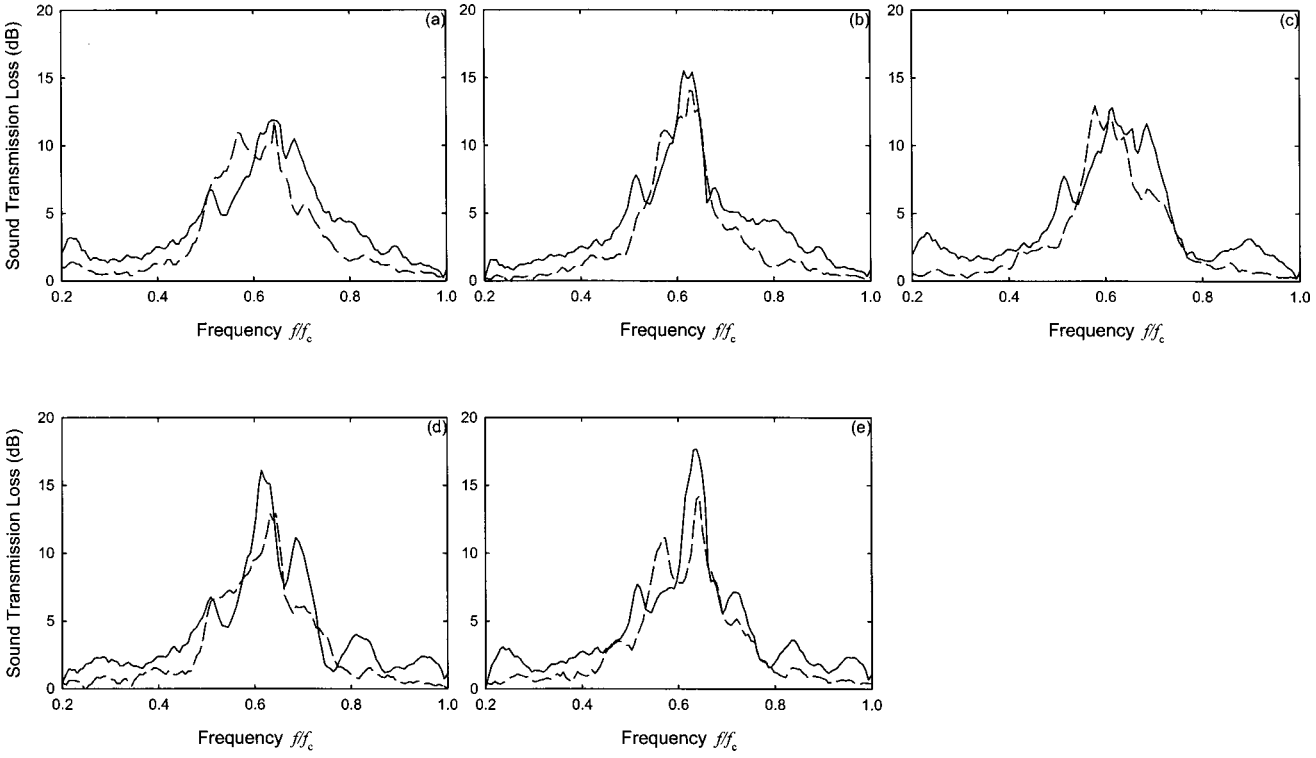

FIG. 9. Comparisons between plane-wave theory predictions and measurements for the case $l/w=0.87$ without anechoic termination (weak branch resonance). (a) $L/w=1.59$; (b) $L/w=2.72$; (c) $L/w=4.62$; (d) $L/w=7.49$; (e) $L/w=8.50$. (—) Plane-wave theory; (– – –) measurement.

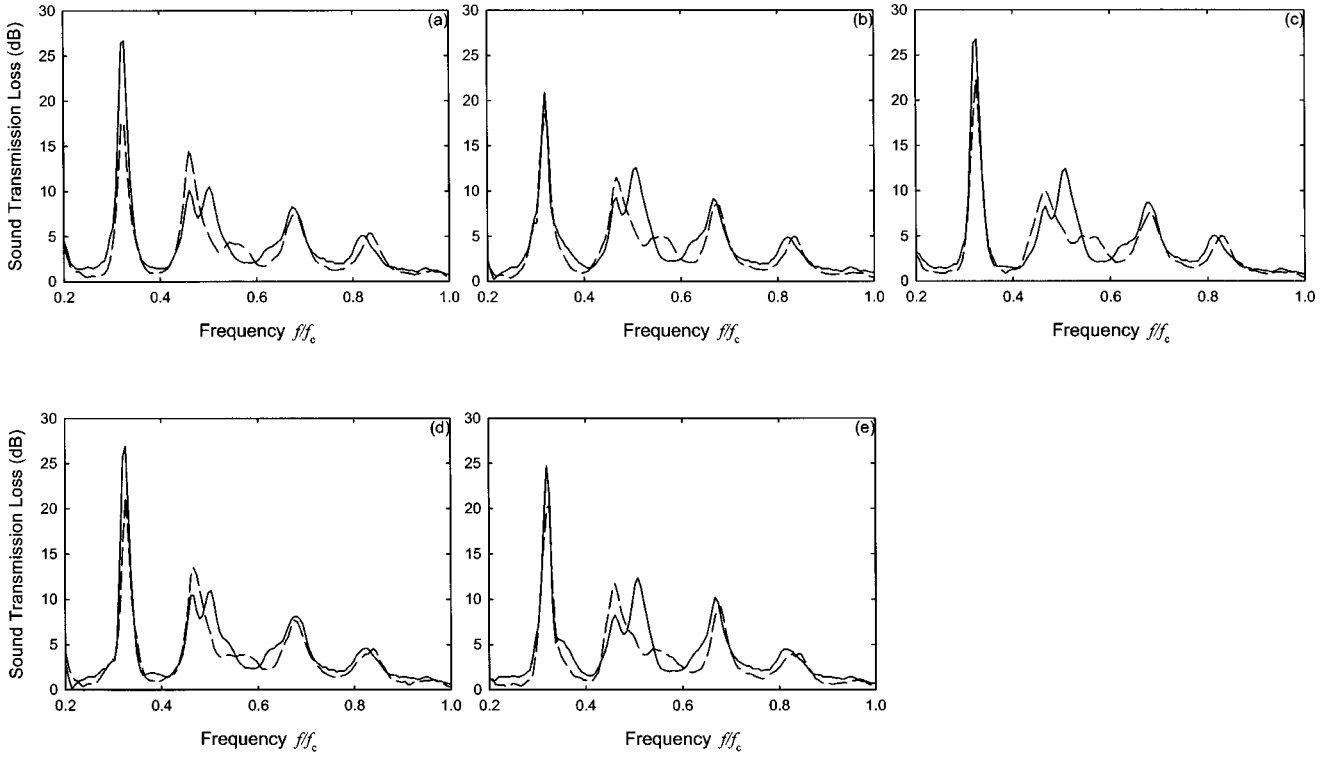

FIG. 10. Comparisons between plane-wave theory predictions and measurements for the case $l/w=5.23$ without anechoic termination (strong branch resonance). (a) $L/w=1.59$; (b) $L/w=2.72$; (c) $L/w=4.62$; (d) $L/w=7.49$; (e) $L/w=8.50$. (—) Plane-wave theory; (– – –) measurement.

the TL prediction can result with such correction ($\varepsilon = 188.6$ mm). This seems able to explain the observation of "missing peak" in Figs. 9(c) and (d). One should note that the evanescent wave scattered out from the entrance of the upstream sidebranch is still relatively strong at that of the downstream sidebranch at $L/w=1.59$ (only a ~2 dB drop in magnitude). The difference in TL drops to ~2 dB after the inclusion of ε. However, such correction does not work when $L/w=2.72$ and 8.50. Indeed, the plane wave theory predicts reasonably the experimental results for these lengths [Figs. 9(b) and (e)] implying no separation correction is required. It is found that these L's are shorter than the nearest integer multiples of half the wavelength at this frequency, while the opposite are observed for the other lengths. This behavior tends to imply that resonance inside the main duct is relatively more difficult to occur at $L/w=2.72$ and 8.5. The resonant condition inside the main duct appears also important for ε. An investigation on the diffraction correction at junction is left to further study. It is believed that the effect of ε still exists in the high pass filter cases, but the broadband gradual variation of the acoustic impedance makes it much less distinguishable.

At $f/f_c \sim 0.51$, $Z_d/Z_b \approx 1$, suggesting a vanishing reactance in Z_b. The plane wave theory without allowance for ε results in more than 3 dB overestimation in TL. Such overestimation is reduced to below 2.6 dB for all L's if a ε of 188.6 mm is included. The overestimation drops below 2.3 dB if $\varepsilon = 163$ mm is taken. This tends to suggest that ε depends on frequency as diffraction does. It may also depend on the branch impedance. Further investigation is essential. It also shows that the measurement error in length, which is at most 2 mm in the present study, is not going to affect the results significantly.

The high of TL at $f/f_c \sim 0.61$ after the introduction of a second sidebranch predicted by the plane-wave theory is not confirmed by the experiment, especially for large L [Figs. 9(d) and (e)]. The introduction of a correction ε of 163 mm to 188.6 mm as before gives prediction 1–3 dB closer to the experimental results for $L/w=2.72$, 4.62, and 7.49, but about 1.5 dB more derivation for $L/w=8.50$. The case for $L/w=1.59$ is exceptional as the evanescent wave is not substantially attenuated in the region bounded by the two sidebranches. One can notice that at this frequency and for $L/w=1.59$ and 8.50, the nominal branch separation L is shorter than the nearest integer multiple of half the wavelength, while the opposite is observed for other L's. This further suggests that the correction ε will depend on the resonant condition along the main duct. The predictions from plane-wave theory without correction in L agree basically with the experimental results at $f/f_c \sim 0.63$.

The plane-wave theory again overestimates TL at frequencies of strong resonance and thus weak Z_b/Z_d (Fig. 10). At $f/f_c=0.32$, an overestimation of about 10 dB is found at $L/w=1.59$ [Fig. 10(a)], while for $L/w \geqslant 2.72$ [Figs. 10(b)–(e)], such difference is capped under 6 dB. Similar situation can be found at $f/f_c \sim 0.16$ (not shown here due to less satisfactory anechoic termination performance, cf. Fig. 2). For short L, the presence of evanescent wave of significant magnitude close to the proximity of the second branch certainly makes the plane-wave assumption less valid (8 dB magnitude drop at $L/w=1.59$, >23 dB at $L/w \geqslant 2.72$). It is again found that the introduction of ε of 188.6 mm into Eq. (9)

reduces considerably the discrepancy between predictions and the experimental results even at $L/w=1.59$. The correction results in only 3 dB TL overestimation except at $L/w=7.49$, but it still gives 1.5 dB better prediction than that without this length correction. In fact, neither a reduction nor an increase of ε from 188.6 mm can produce better results. It is noted that the introduction of ε brings about a 1.5 dB increase of the TL overestimation at $L/w=2.72$. One can observe that for $L/w=2.72$ and 8.50, L is relatively far away from the nearest integer multiple of half the wavelength at $f/f_c=0.32$ than for other values of L/w, suggesting again the resonant condition along the main duct can affect the correction or even the prediction. This is again left to further investigation.

The TL peak at $f/f_c=0.50$ for the single sidebranch of $l/w=5.23$ again disappears upon the introduction of a second sidebranch for all L's investigated in the present study (Fig. 10). However, a small "kick" can be seen at around this frequency on the experimental TL curves for $L/w \geqslant 2.72$ [Figs. 10(b)–(e)]. This large discrepancy in TL of about 6 dB cannot be explained even by including a correction ε of 188.6 mm to L, though such correction improves the prediction by 0.5–3 dB except for $L/w=1.59$ and 7.49 where the TL overestimations are increased by 1.6 and 0.6 dB, respectively. However, this correction still gives the best prediction overall. Anyway, $Z_b/Z_d \sim 0.56+0.04j$ here, which suggests that this is not a frequency of strong branch resonance.

The TL at $f/f_c=0.48$ is amplified by the introduction of a second sidebranch for all L's as shown in Figs. 10(a)–(e). This TL is due to the noise breakout of the sidebranches, which is dissipative to sound in the main duct. This is also the only frequency that the plane-wave theory clearly underestimates TL. Such underestimation reaches 5 dB at $L/w=1.59$ [Fig. 10(a)], drops to about 2 dB at $L/w=2.72$ [Fig. 10(b)], and then gradually increases to about 4 dB at $L/w=8.50$ [Figs. 10(c)–(e)]. The impedance of the branch at this frequency $Z_b/Z_d=1-0.02j$, which is close to that of an infinitely long sidebranch ($\sim$1.06 in the present study theoretically). Though this impedance is nearly the same as that at $f/f_c \sim 0.51$ in the weak resonance case, which is due to a longitudinal resonance in the branches, it is believed that the mechanisms of sound reflection and transmission across the branches in these two cases are different. The sound pressure level drop related to this noise breakout alone accounts for as much as $\sim$30 dB m along this sidebranch (not shown here). One therefore does not expect much reflection from the opened branch end, resulting in an impedance close to that of an infinitely long branch. Some theoretical considerations on the effects of flexible duct walls on TL can be found in Huang.[14] The vibration of branch walls at the breakout frequency is strong and will probably lead to much more vigorous air motion (low sound pressure) at the entrances of the branches than that in the weak resonance case. Higher dissipation of energy by damping at the edges at the entrance of each sidebranch is then expected.

One should also note that the noise broken out from one branch will affect the wall vibration of the other branch.[15] This will lead to some kinds of coordinated wall vibrations, which interferes with the air movement inside the branches and along the main duct. Such interference, which is not considered by the plane-wave theory, can be substantial for short L, due to the direct bombardment of breakout sound waves onto the branch walls, and for L which is close to any integer multiple of half the wavelength at $f/f_c=0.48$. The separation $L/w=8.50$ corresponds to 4.08 times this half wavelength. The higher TLs at $f/f_c \sim 0.48$ shown in Figs. 10(a) ($L/w=1.59$) and Fig. 10(e) ($L/w=8.50$) than in Figs. 10(b)–(d) tend to support the present conjecture. However, further investigations are required to clarify the present observed sound transmission phenomena near the break-out frequency of the sidebranch(es).

Other results, not presented here, show that the TLs of the single or double sidebranch arrangements are not affected very much by in-duct airflow up to a speed of 7 m/s, except that one can find rougher experimental TL curves in the presence of the flow. In the presence of the flow, the loudspeaker was mounted on a wall of the main duct and the anechoic termination determined by Neise *et al.*[16] was used. Though this speed is probably lower than that in actual practice, it has exceeded the 4 m/s recommended by ASHRAE[17] for the present size of the main duct for minimizing frictional loss.

V. CONCLUSIONS

The sound power transmission losses of single and double sidebranch installations along a rectangular duct were studied experimentally by using the two-microphone transfer function method in the present study. Results at frequencies higher than the first cutoff frequency of the main duct were ignored. With the assumption of plane-wave propagation, the acoustic impedance of each single sidebranch was estimated. The corresponding results obtained using the double sidebranch conditions were also compared with the predictions from existing plane-wave theory.

The acoustic impedance of the sidebranches can be categorized into four basic types. The first two types are high pass filters. One is of low resistance at low frequency but a broadband significant reactance, which increases with frequency, and the other possesses higher resistance and reasonable reactance throughout the frequency range concerned. In the former case, the plane-wave theory gives reasonable predictions to the double sidebranch sound power transmission loss. Strong wave interference as in the expansion chamber is observed. However, the magnitudes of the domes decrease quickly with frequency as the magnitude of the acoustic impedance of the sidebranches increases quickly with frequency. Similar observations can be found in the latter case. However, the higher sound power transmission loss for the single branch in this case results in more distinct and periodic domes on the sound power transmission loss curves. Also, the plane-wave theory always predict dome crests/troughs at slightly higher frequency when compared to the experimental results. The prediction becomes closer to the experimental results as the separation distance between the branches increases.

The other two impedance types correspond to the band-stop/band-pass filters. The longitudinal resonance inside the sidebranches is responsible for the high or low impedance

magnitudes. Two types of resonance, one producing weak impedance and the other strong impedance, are identified. They result in high and low sound power transmission loss, respectively. In general, the plane-wave theory overestimates the sound power transmission loss of the double sidebranches at frequencies of high sound transmission loss. It is shown that a specific correction to the branch separation produces better matching between the predictions and the experimental results. However, no exact formula for such correction can be derived from the present results though a rough estimation is given. The scattering of evanescent waves at the branch-duct junctions appears important for short branch separation. Further investigation is required.

When the length of the sidebranch is long, the resistance due to the noise breakout phenomenon becomes significant. The loss due to this breakout is substantial inside the branch, resulting in an acoustic impedance close to that of an infinitely long branch. The plane-wave theory is found to have underestimated the double sidebranch sound power transmission loss around the noise breakout frequency. The underestimation is large for small branch separation. Though the present results provide no clue to explain such observation, it is conjectured that the interaction between the broken out sound and the branch walls, the expected more vigorous airflows at the entrances of the sidebranches and their coherence, are responsible for the unpredictably large sound power transmission loss at this frequency. The exact underlying physics is left to further studies.

ACKNOWLEDGMENTS

Financial support from the Research Grant Council, HKSAR, China and the assistance of C. K. Lau in the data collection are gratefully acknowledged.

[1] C. M. Harris, *Handbook of Noise Control* (McGraw–Hill, New York, 1979).
[2] M. L. Munjal, *Acoustics of Ducts and Mufflers* (Wiley, New York, 1987).
[3] L. E. Kinsler, A. R. Frey, A. B. Coppens, and J. V. Sanders, *Fundamentals of Acoustics*, 4th ed. (Wiley, New York, 2000).
[4] V. Pagneux, N. Amir, and J. Kergomard, ''A study of wave propagation in varying cross-section waveguides by modal decomposition. I. Theory,'' J. Acoust. Soc. Am. **100**, 2034–2048 (1996).
[5] D. D. Reynolds and J. M. Bledsoe, *Algorithms for HVAC Acoustics* (American Society of Heating, Refrigeration and Air-Conditioning Engineers, Atlanta, 1991).
[6] S. K. Tang and J. S. F. Cheng, ''On the application of active noise control in an open end rectangular duct with and without air flow,'' Appl. Acoust. **53**, 193–210 (1998).
[7] P. M. Radavich, A. Selmat, and J. M. Novak, ''A computational approach for flow-acoustic coupling in closed side branches,'' J. Acoust. Soc. Am. **109**, 1343–1353 (2001).
[8] T. C. Redmore and K. A. Mulholland, ''The application of mode coupling theory to the transmission of sound in the sidebranch of a rectangular duct system,'' J. Sound Vib. **85**, 323–331 (1982).
[9] D. D. Reynolds, *Engineering Principles of Acoustics* (Allyn and Bacon, Boston, 1981).
[10] M. C. J. Trinder and P. A. Nelson, ''Active noise control in finite length duct,'' J. Sound Vib. **89**, 95–105 (1983).
[11] J. Y. Chung and D. A. Blaser, ''Transfer function method of measuring in-duct acoustic properties. I. Theory,'' J. Acoust. Soc. Am. **68**, 907–913 (1980).
[12] P. M. Morse and K. U. Ingard, *Theoretical Acoustics* (McGraw–Hill, New York, 1968).
[13] A. Leissa, *Vibration of Plates* (Acoustical Society of America, New York, 1993).
[14] L. Huang, ''A theoretical study of duct noise control by flexible panels,'' J. Acoust. Soc. Am. **106**, 1801–1809 (1999).
[15] M. C. Junger and D. Feit, *Sound, Structures, and Their Interaction* (MIT, Cambridge, MA, 1986).
[16] W. Neise, W. Frommhold, F. P. Mechel, and F. Holste, ''Sound power determination in rectangular flow ducts,'' J. Sound Vib. **174**, 201–237 (1994).
[17] *ASHRAE Handbook: Fundamentals* (American Society of Heating, Refrigeration and Air-Conditioning Engineers, Atlanta, 1993).

Causal impedance matching for broadband hybrid noise absorption

Jing Yuan[a)]
Department of Mechanical Engineering, The Hong Kong Polytechnic University, Hunghom, Kowloon, Hong Kong

(Received 4 October 2002; accepted for publication 17 March 2003)

The complementary strengths and weaknesses of passive and active noise control (ANC) methods have motivated many researchers to develop hybrid noise absorbers that integrate both control strategies. The impedance matching technique (IMT) is the most effective for such a purpose. An unsolved problem with available IMT schemes is the *a priori* reference signal that limits IMT applications. This study proposes the use of the forward wave, available by the two-microphone method, as the reference signal. Due to inevitable errors in wave separation and inlet reflection of the control signal, the absorber becomes a feedback system. A simple and stable ANC is developed for impedance matching without the *a priori* reference signal. The proposed absorber has an absorption coefficient of 0.9 or above in a frequency range of 60–850 Hz. It is stable in the presence of sensor mismatch and robust with respect to significant variation of inlet boundary conditions. [DOI: 10.1121/1.1572148]

PACS numbers: 43.50.Ki, 43.55.Ev [PJR]

I. INTRODUCTION

Passive noise absorption is a well-studied subject with many known analytical and experimental results. The absorption coefficients of available passive noise absorbers can be close to 1 for mid- or high frequency ranges.[1] A common feature of these absorbers is a layer of porous material mounted in front of a cavity. The absorption frequency range of a passive noise absorber is inversely proportional to the physical size of the cavity behind the porous layer. Active noise control (ANC) may be applied in low frequency ranges to reduce the physical size of noise absorbers and improve absorption performance. Since the strengths and weaknesses of passive control and ANC appear to be mutually complementary, many researchers develop hybrid passive/active noise absorbers that integrate both methods.

A natural way to incorporate ANC with a passive absorber is to control the sound field behind the porous layer. Guicking and Lorenz[2] are among the first to study hybrid noise absorbers. Their controller uses a reference signal measured in front of a porous layer to minimize the pressure signal behind the porous layer, hence the name ''pressure-release.'' It leads to almost total absorption over the frequency range of 100–600 Hz. A similar study by Thenail *et al.*[3] releases pressure at the back of a fiberglass absorption layer. Almost total absorption was achieved in the ranges of 200–800 and 500–1400 Hz, respectively, by two controllers implementing the pressure-release method. The optimal thickness of the fiberglass layer was found to be 2 cm by the experiments.

Fuller *et al.* designed an adaptive foam for active control of radiation and reflection waves.[4] It uses identical microphones to separate the incident wave from the reflection wave. The adaptive controller minimizes the reflection wave with an attenuation of up to 40 dB at frequencies above 600 Hz. Beyene and Burdisso[5] proposed the impedance matching technique (IMT). They designed an ANC to minimize the reflection behind the absorption layer, and showed analytically that this strategy is equivalent to impedance matching for the cavity behind the absorption layer. In another study, the IMT was applied to broadband noise absorption with combinations of different cavity depths and absorption layer thickness.[6] The method is generally superior to the pressure-release method and able to achieve an absorption coefficient above 0.9 in a wide range of 100–1000 Hz.

An unsolved problem with available IMT is the reference signal that leads the primary source by 40 samples when the sampling frequency is 3.2 KHz,[6] which is equivalent to 1/80 s. The pioneers of IMT realized the need for a solution to the problem and left it open to different strategies.[6] This study proposes the first IMT without the *a priori* reference. The reference is replaced by the forward wave available by the two-microphone method. This changes the pure feedforward ANC in Refs. 5 and 6 to a feedback one. The feedback effects are due to inevitable sensor mismatch in wave separation and inlet reflection of the control signal. For causal implementation, the sensors must be placed sufficiently away from the actuator, which delays the feedback signal. Stability of a delayed adaptive feedback ANC, like the proposed one, is not a trivial problem. A rigorous stability analysis is conducted on the proposed method. The ANC turns out to be very simple and able to tolerate a reasonable level of sensor mismatch, and the absorber is acoustically encapsulated and analytically independent of inlet boundary conditions.

An experimental study is conducted to verify the analytical results. Since the problem is causality, stability, and robustness, the focus of the experiment is ANC, though it is always possible to combine the test system with passive

a)Electronic mail: mmjyuan@polyu.edu.hk

 0001-4966/2003/113(6)/3226/7/$19.00

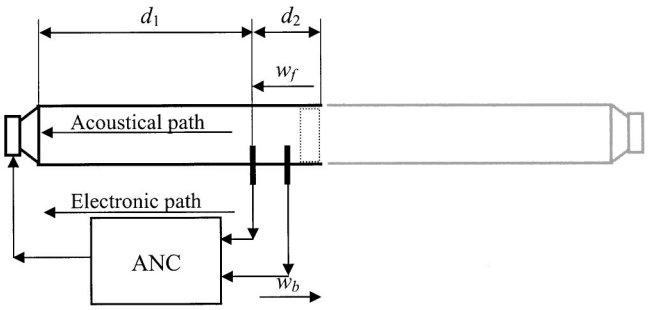

FIG. 1. Hybrid noise absorption by impedance matching.

methods to enhance absorption. In order to assess the performance of the controller, the absorption layer is absent and the interiors of the cavity are made rigid and smooth. The absorber is tested in a range of 0–900 Hz. By active control alone, the absorption coefficient is above 0.9 in a range of 60–850 Hz. The system is stable and robust with respect to significant variation of inlet boundary conditions during the experiment. It has a potential for further enhancement by incorporating passive methods, such as mounting different absorption layers or placing absorption materials in the interiors of the cavity.

II. PROBLEM STATEMENT

The principle of IMT is analytically based on the one-dimensional plane wave model,[5] and only applicable to a noise absorber whose back-cavity is a short duct with a small cross-sectional area as shown in Fig. 1. The absorber, drawn with thick black lines, is terminated with a secondary source at one end, which matches the terminal impedance to the characteristic impedance of the duct by canceling the reflected wave.[5]

The pioneers of IMT have demonstrated the possibility to cancel the reflection waves in a wide frequency range.[5,6] The method has been tested with different combinations of cavity depths, absorption materials, and absorption layer thickness. An unsolved problem is the reference signal that leads the primary source by 1/80 s.[6] The objective of the present study is to design an ANC for IMT without the *a priori* reference signal.

A possible way to avoid the *a priori* reference signal is to substitute the forward wave measured by the identical microphone pair placed behind the absorption layer. This approach, while seemingly simple, faces three obstacles. First, the cavity depth, denoted by d_1 in Fig. 1, must be sufficiently long for the forward wave to pass the controller circuits and catch up with the backward wave. Second, inevitable errors of wave separation could cause delayed feedback or instability to the control loop shown in Fig. 1. Finally, even if the sensors matched perfectly, the duct inlet reflects the control signal that mixes with the incident noise to be the forward wave and threaten closed-loop stability. The design objective is therefore a stable ANC using the forward wave as the reference with a shortest possible cavity depth d_1. The system must be stable in the presence of sensor mismatch and robust with respect to online variation of boundary conditions of the inlet. This is significantly different from Refs. 5 and 6, where a pure feed forward ANC was employed without the feedback problems.

A stability analysis will be presented in Sec. III to address the feedback effects. Meanwhile, an ideal forward wave $w_f(t)$ is assumed available that was free of the effects of sensor mismatch and inlet reflection. There exist two paths for $w_f(t)$ to reach the end of the duct before bouncing back as shown in Fig. 1. The acoustical path takes $\tau_a = d_1/c$ seconds where c is the speed of sound. The electronic path takes $\tau_e = \tau_c + \tau_f$ seconds, where τ_c includes A/D conversion time and computation time; τ_f is the delay due to the anti-alias filter, speaker circuit, and the wave separation circuit.

In order to cancel the backward wave $w_b(t)$, the electronic path must take no more time than the acoustical path does. This means $\tau_c + \tau_f \leqslant d_1/c$ and a lower bound for cavity depth d_1. The actual value of d_1 must be determined by trial and error since it is difficult to estimate $\tau_e = \tau_c + \tau_f$ accurately without experiments. A general way of reducing d_1 is to reduce τ_c and τ_f by optimizing the ANC. In this study, d_1 is reduced to 28 cm while the absorption coefficient is above 0.9 in the frequency range of 60–850 Hz by active control alone.

III. STABILITY ANALYSIS

A major difference between the proposed ANC and the one adopted in Refs. 5 and 6 is the feedback problem due to inevitable sensor mismatch and inlet reflection of the control signal. It is desirable to use inexpensive sensors for wave separation, and the ANC should be able to tolerate sensor mismatch as much as possible. The absorber may be installed in different environments with significantly different boundary conditions of the inlet. The ANC must be robust with respect to significant variation of the inlet boundary conditions. A stability analysis is presented here to investigate these problems.

A. Mathematical model of the absorber

In reality, the process of wave separation introduces inevitable errors. The reference signal, expressed in the z domain, is given by

$$\hat{w}_f(z) = A(z)w_f(z) + B(z)w_b(z), \tag{1}$$

which contains both forward and backward waves. Similarly, the error signal, expressed in the z domain, is given by

$$\hat{w}_b(z) = C(z)w_f(z) + D(z)w_b(z), \tag{2}$$

which is also a mixture of forward and backward waves. Transfer functions $A(z)$, $B(z)$, $C(z)$, and $D(z)$ depend on magnitude and phase match between the two microphones placed behind the absorption layer. The exact expressions of these transfer functions are generally not available analytically. It is not possible to identify these transfer functions experimentally since the true values of w_f and w_b are not measurable by other methods. If the two microphones are well matched, one expects $A(z) \approx 1$, $D(z) \approx 1$, and the magnitudes of $B(z)$ and $C(z)$ can be minimized but are not necessarily zero unless the microphones and conditioners are absolutely identical.

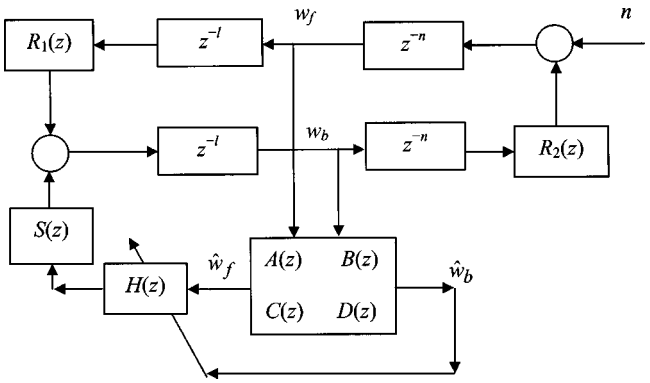

FIG. 2. Block diagram of the absorber system.

The derivations of $A(z)$ and $D(z)$ from identities represent distortions to $\hat{w}_f$ and $\hat{w}_b$ by the wave separation circuit. Such distortions, while not desired, are recoverable if $A(z) \neq 0$, $D(z) \neq 0$ in the frequency range of interest. The derivations of $B(z)$ and $C(z)$ from zeros, on the other hand, represent another kind of wave separation error that causes a small residual w_b in $\hat{w}_f$ and a small residual w_f in $\hat{w}_b$. When $\hat{w}_f$ is the reference signal, the residual w_b causes feedback effect to threaten system stability. The relative contributions of w_b and w_f to $\hat{w}_f$ may be evaluated by a ratio $|A^{-1}(z)B(z)|$. It plays an important role in the stability analysis of the closed-loop system.

When the controller is active, w_b is no longer the reflection wave alone. Instead, it is a combination of reflection wave and the wave generated by the secondary speaker, with an analytical expression

$$w_b(z) = z^{-2l} R_1(z) w_f(z) + z^{-l} S(z) H(z) \hat{w}_f(z), \tag{3}$$

where z^{-l} represents an l-sample delay for the control signal to propagate from the speaker to the sensor pair; $R_1(z)$ describes the reflection effects of the absorber terminal; $S(z)$ and $H(z)$ represent, respectively, transfer functions of the secondary path and the ANC. Similarly, the forward wave contains reflection of the control signal and incident noise from the external noise. Its analytical expression reads

$$w_f(z) = z^{-2n} R_2(z) w_b(z) + z^{-n} n(z), \tag{4}$$

where z^{-n} represents an n-sample delay for the incident noise to propagate from the inlet to the sensor pair; $n(z)$ is the external incident noise and $R_2(z)$ describes the reflection effects of the inlet.

Unlike the feedforward ANC in Refs. 5 and 6, the use of $\hat{w}_f$ as the reference signal makes the absorber practical at the expense of a feedback system described by Eqs. (1)–(4) and the block diagram shown in Fig. 2.

B. Ideal controller transfer function

The ideal objective is to minimize w_b. Since $\hat{w}_b$ is the only available estimate of w_b, the practical objective is to minimize $\hat{w}_b$ as attempted by other researchers.[4–6] Using Eqs. (1)–(3), one may derive

$$\hat{w}_f = \frac{A(z) + z^{-2l} B(z) R_1(z)}{1 - z^{-l} S(z) H(z) B(z)} w_f, \tag{5}$$

and

$$\begin{aligned} \hat{w}_b &= [C(z) + z^{-2l} R_1(z) D(z)] w_f + z^{-l} S(z) H(z) D(z) \hat{w}_f \\ &= \left[C(z) + z^{-2l} R_1(z) D(z) \right. \\ &\quad \left. + z^{-l} S(z) H(z) D(z) \frac{A + z^{-2l} B R_1}{1 - z^{-l} S H B} \right] w_f. \end{aligned} \tag{6}$$

When $\hat{w}_f$ contains broadband noise, it is impossible for a delayed signal $z^{-l}\hat{w}_f$ to cancel the undelayed contribution of w_f. The best possible result of the proposed strategy is the cancellation of the last two terms of Eq. (6). This means the minimization of $\hat{w}_b$ such that $\hat{w}_b = C(z) w_f$ if the ANC function is

$$H(z) = -z^{-l} R_1(z) S^{-1}(z) A^{-1}(z). \tag{7}$$

The ideal ANC function turns out very simple despite the complexity of system model Fig. 2. The stability of $H(z)$ depends on the stability of $S^{-1}(z)$ and $A^{-1}(z)$. This is not a problem since all active controllers require a multiple $S^{-1}(z)$ in the ideal forms and $A(z) \approx 1$ if the two microphones are reasonably well matched. Substituting Eq. (7) into Eq. (6), one may re-write the last two terms of Eq. (6) as

$$\begin{aligned} &z^{-2l} R_1(z) D(z) w_f + z^{-l} S(z) H(z) D(z) \hat{w}_f \\ &\quad = z^{-2l} \left[1 - \frac{A(z) + z^{-2l} B(z) R_1(z)}{A(z) + z^{-2l} B(z) R_1(z)} \right] R_1(z) D(z) w_f, \end{aligned}$$

which cancel each other if $1 > |A^{-1}(z) B(z) R_1(z)|$ for all $z = e^{-j\omega}$ by the small gain theory. This condition may be simplified to $1 > |A^{-1}(z) B(z)|$ since $|R_1(z)| \leqslant 1$ represents passive reflection at the closed end of the absorber.

Recall from Eq. (1), $|A^{-1}(z) B(z)|$ represent the relative contributions of w_b and w_f to the reference signal $\hat{w}_f$. Although the exact forms of $A(z)$ and $B(z)$ are not available, one expects $A(z) \approx 1$ and $|B(z)|$ near zero if the two microphones are well matched. Therefore $1 > |A^{-1}(z) B(z)|$ is a very mild requirement. In practice, it is not difficult to maintain $0.2 > |A^{-1}(z) B(z)|$ in the frequency range of interest with a pair of reasonably matched microphones.

C. Stable adaptation

The ideal ANC function, given by Eq. (7), is not practically available since $A(z)$ is not available. Instead, the well-known filtered-x LMS (FXLMS) algorithm has to be applied to implement the ANC. In the proposed method, the reference signal contains feedback effects as indicated by the denominator of Eq. (5). During the adaptation, the control system must maintain a stable version of the reference signal. This is possible if $|S^{-1}(z) H(z) B(z)| < 1$ by the small gain theory.

One may start with an all zero $H(z)$ that satisfies the stability requirement initially. If the adaptation gain is not too large, $H(z)$ will converge gradually toward its ideal form given by Eq. (7). The system is stable when $H(z)$ converges to the neighborhood of Eq. (7), as explained previously.

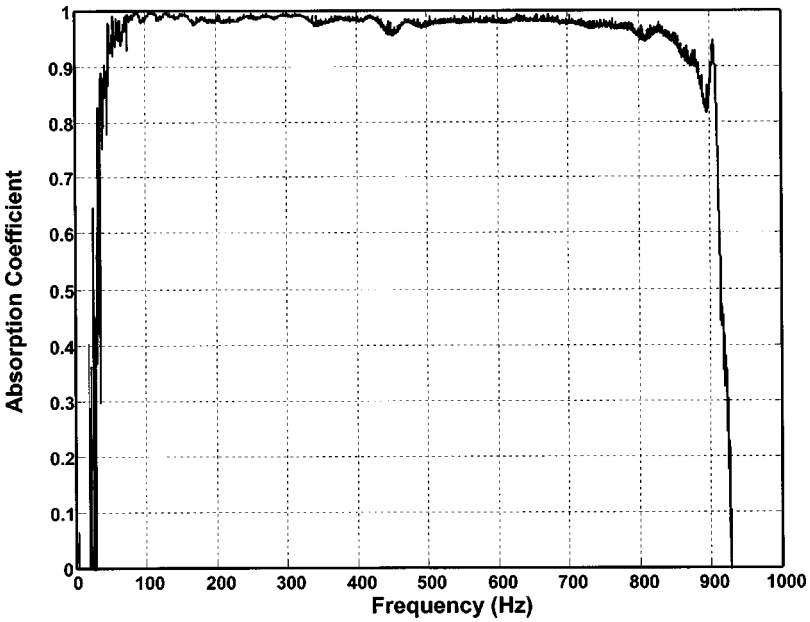

FIG. 3. Performance of the absorber.

The remaining concern is the possible fluctuation of $H(z)$ before its convergence to Eq. (7). Knowing the convergence trend of $H(z)$, one may estimate $|H(z)|$ by a bound

$$|H(z)| \leqslant \alpha_F |S^{-1}(z)A^{-1}(z)R_1(z)|, \tag{8}$$

where $0 < \alpha_F$ describes the possible fluctuation of $|H(z)|$ with respect to its final convergence destination. Substituting Eq. (8), one obtains

$$|S^{-1}(z)H(z)B(z)| \leqslant \alpha_F |A^{-1}(z)B(z)R_1(z)| \leqslant 0.2\alpha_F < 1,$$

where a conservative estimate $0.2 > |A^{-1}(z)B(z)|$ is assumed in the entire frequency of interest, under which condition the proposed system will tolerate a possible fluctuation of $|H(z)|$ as long as it does not exceed the final destination by five times.

In practice the FXLMS algorithm may cause small-level fluctuation of its estimates, however, an overshot of five times in magnitude is very rare with the FXLMS algorithm. From this point of view, the proposed strategy is stable with a comfortable margin. The residual effects of wave separation, represented by $B(z)$ and $C(z)$, respectively, are mainly due to mismatch of the sensor pair. Accurate wave separation only requires near identical response of a sensor pair. This is similar to the requirement for intensity probes[7] and three-dimensional intensity sensors,[8] but much less stringent than the identical sensor array in sonar systems. By improving microphone matching and calibrating the wave separation circuit with due care,[9] it is possible to reduce $|A^{-1}(z)B(z)|$ to a value close to zero. This means the possibility of further relaxing the tolerance margin of the proposed strategy.

IV. EXPERIMENTAL VERIFICATION

An experiment was conducted to verify the feasibility of using $\hat{w}_f$ as the reference for IMT, as well as the stability and robustness of the proposed ANC. The experimental setup was very similar to the diagram of Fig. 1. The passive absorption layer, represented by the dash-line box in Fig. 1, was removed because the focus of the experiment was causality, stability, and robustness of the ANC. The ANC was assessed alone by the experiment.

In the pioneering reports of IMT, the method had been tested in impedance tubes with a small diameter (5 cm) to ensure a one-dimensional plane wave system.[5,6] In this study, a cross section of 12×15 cm^2 was tested to tradeoff between keeping model validity and increasing absorption area. A possible application of the method may be a honeycomb of $N \times M$ absorbers to form an absorption wall. Increasing the area of each individual absorber could lead to the reduction of cost per unit absorption area.

The two microphones are placed $d_1 = 28$ cm from the secondary source. The sampling frequency of the controller is 2463 Hz. The cutoff frequency of the anti-alias filter is 900 Hz, which is close to but lower than the first cross mode frequency of the cavity. The one-dimensional plane wave model is valid for the frequency range of interest. The stop band of the anti-alias filter starts at 1231.5 Hz and the ANC has a frequency range of 0–1231.5 Hz. The space between the two sensors is 14 cm—half the wavelength of the maximum frequency 1231.5 Hz.

A. Causality

The first target is causality when $\hat{w}_f$ is used as the reference signal. When $\hat{w}_f$ is due to broadband noise excitation, its delayed version, after reaching the closed end of the absorber and bouncing back to the microphone pair, is not able to cancel the first term of Eq. (6) contributed by w_f. This turns out to be an advantage of using $\hat{w}_f$ as the reference signal. When the controller is only able to cancel the last two terms of Eq. (6), it actually cancels w_b, as suggested by Eq. (2). The cancellation of the last two terms of Eq. (6) depends on a sufficient cavity depth d_1 as explained in Sec. II. In the experiment, different values of d_1 have been tested. The reduction of d_1 would generally narrow the frequency range of absorption in the high frequency end. The final tradeoff is $d_1 = 28$ cm with an absorption performance shown in Fig. 3.

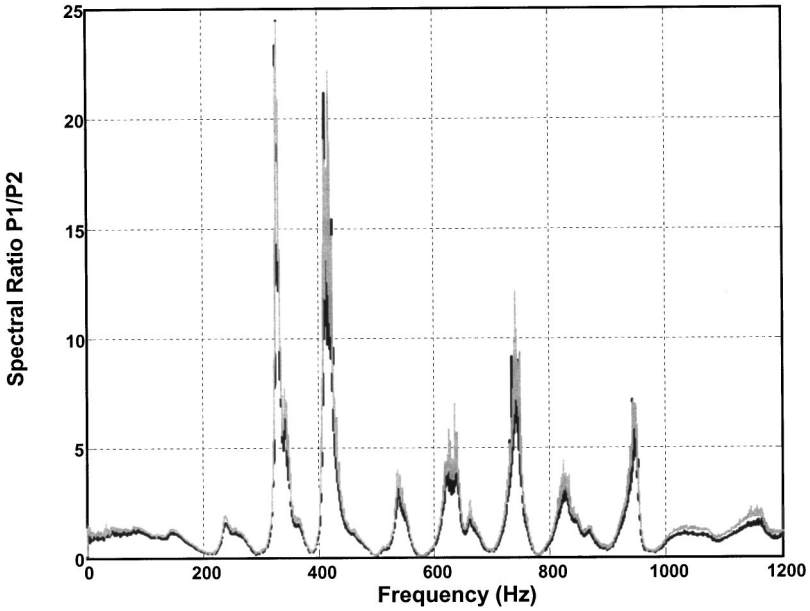

FIG. 4. Sensor mismatch detected by the swapping method.

The absorption coefficient is computed as

$$1-\frac{\hat{P}_b(z)}{\hat{P}_f(z)},$$

where $\hat{P}_b(z)$ and $\hat{P}_f(z)$ are, respectively, power spectral densities (PSD) of $\hat{w}_b$ and $\hat{w}_f$ obtained by MATLAB command "pmtm." The result is above 0.9 for the frequency range of 60–850 Hz. Compared with the cavity depth of $d_1=6$ cm in Refs. 5 and 6, $d_1=28$ cm is significantly longer. Yet this seems to be an inevitable price to pay for a realistic reference signal. After all, $d_1=28$ cm is still significantly shorter than the wavelength of 60 Hz. A passive absorber would require a longer cavity depth[1] to achieve an absorption coefficient of 0.9 in such a low frequency.

B. Stability

Another target of the experiment is stability of the proposed ANC. In the analytical study, the method is believed to tolerate a fluctuation of $|H(z)|$ in the presence of sensor mismatch. In the experiment, two ordinary B&K 4130 microphones were tested. One channel had been repaired from a defect and the swapping method was applied to detect the mismatch effects. Figure 4 plots two sets of spectral ratios of the sensor signals with different colors. The signals were collected under the same experimental conditions with the sensors swapped. Differences of the curves are clearly visible in some frequencies to indicate sensor mismatch. The

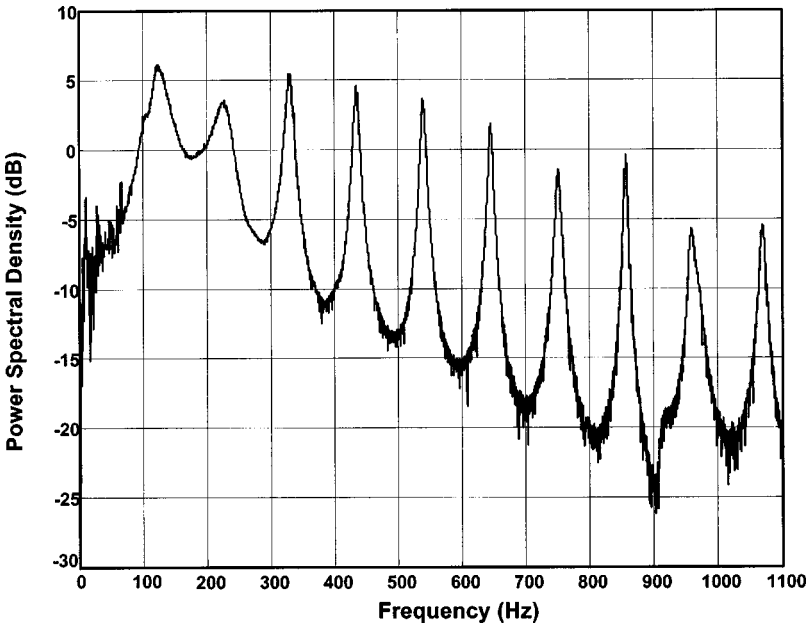

FIG. 5. PSD excited by primary source 1 (equivalent to a "long" duct).

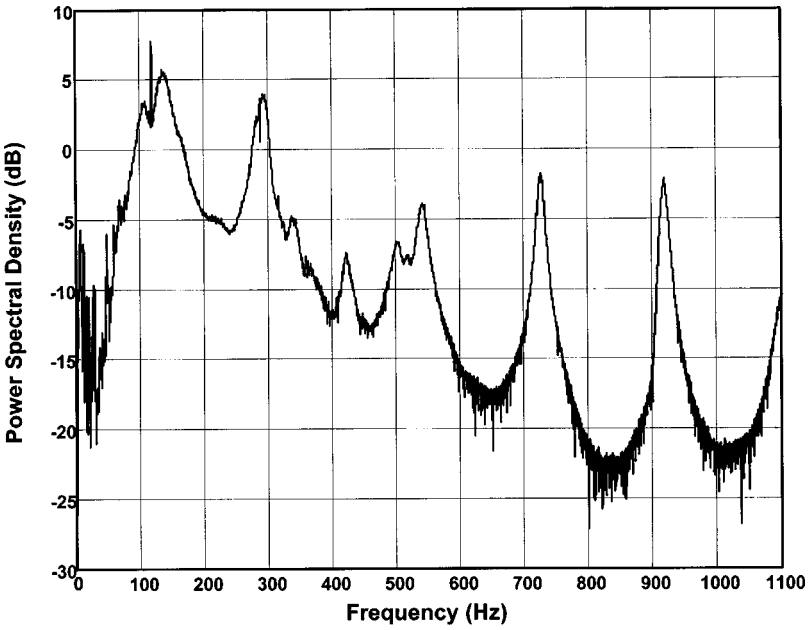

FIG. 6. PSD excited by primary source 2 (equivalent to a "short" duct).

proposed ANC converged very well using these sensors for wave separation. It is able to tolerate a certain level of sensor mismatch, which is analytically $0.2>|A^{-1}(z)B(z)|$ and not too restrictive in practice.

C. Robustness

The third target of the experiment is the robustness of the proposed ANC. Two different primary sources were tested. The first one is a speaker mounted at the end of a duct with identical cross section as the absorber (drawn in Fig. 1 by the gray lines). The second one is a speaker placed in the open space near the absorber inlet. This means different $R_2(z)$'s with different delays in the block diagram of Fig. 2. The system characteristic equation of Fig. 2 is derivable as $1-z^{-2(l+n)}R_1(z)R_2(z)$ without ANC. The variation of z^{-n} and $R_2(z)$ affects the absorber dynamics significantly as demonstrated by the experiment data.

When the first primary source was tested, the primary source extended the length of the absorber to 160 cm. Figure 5 plots the PSD excited by primary source 1 with the ANC off. It shows many resonant peaks due to the relatively long duct effect. When the second primary source was tested, however, the length of the absorber was reduced and its PSD is shown in Fig. 6 (also ANC off). The system has different resonant frequencies because of different boundary conditions at the inlet. These experimental data imply significant change of duct dynamics for different boundary conditions.

The controller was trained with primary source 2 using the FXLMS algorithm. Upon convergence, primary source 2 was replaced by source 1 and the ANC remained stable with its performance shown in Fig. 7. The absorption coefficients did not deteriorate much though the duct dynamics had changed as significantly as shown in Figs. 5 and 6. The de-

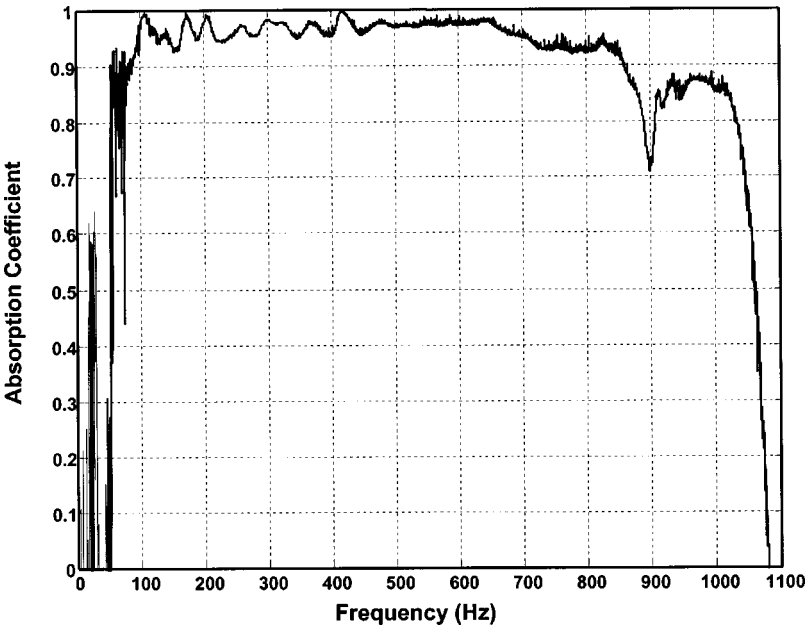

FIG. 7. Performance of the absorber (trained with source 2 and tested with source 1).

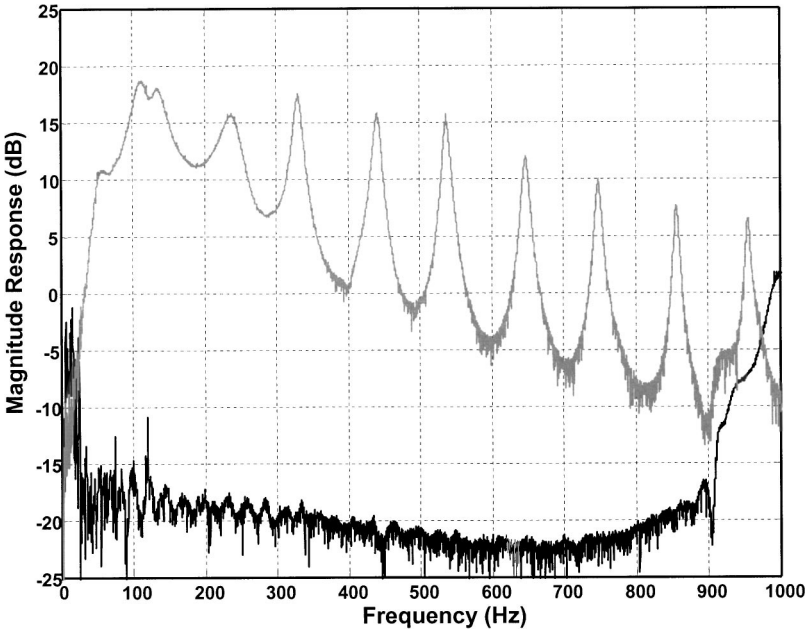

FIG. 8. Magnitude response of the reflection wave for control on (black) and off (gray).

terioration is recoverable by the adaptive ANC after a period of adaptation.

D. Suppression of reflected wave

Finally, the cancellation of the reflected wave is illustrated in Fig. 8, where magnitude responses of the reflection wave are plotted for ANC on (black) and off (gray), respectively. The ANC is not able to cancel low frequency reflection due to limitation of the loudspeaker. Its high frequency cancellation performance is poor because the reduction of d_1 makes it difficult for the high frequency components of $\hat{w}_f$ to pass the ANC in time for cancellation of w_b. A further reduction of d_1 would make the high frequency cancellation even worse. Generally, the ANC managed to cancel the reflection wave reasonably well in the range of 60–850 Hz with $d_1 = 28$ cm.

V. CONCLUSION

A causal impedance match strategy is proposed in this study for broadband hybrid noise absorption. The forward wave $\hat{w}_f$, available by the two-microphone wave separation circuit, is used as the reference signal. Analytical and experimental results are presented to demonstrate the feasibility of the proposed approach. The system is shown, both analytically and experimentally, stable with a comfortable margin. It is also robust with respect to possible variation of boundary conditions at its inlet. Since the reference signal is available inside the absorber, the system is acoustically encapsulated. Its robustness with respect to inlet boundary conditions is an important advantage over other ANC systems. The controller of such an absorber may be trained in factory conditions and work well when the absorber is installed in three-dimensional spaces with different geometric shapes or boundary conditions. This is different from a conventional ANC that depends very much on the specific geometric shape and boundary conditions of the sound field in which it is installed.

ACKNOWLEDGMENT

The work described in this paper was substantially supported by a grant from the Research Grants Council of the Hong Kong Special Administration Region (Project No. PolyU 5175/01E).

[1] U. Ingard, *Notes on Sound Absorption Technology* (Noise Control Foundation, Poughkeepsie, NY, 1994).
[2] D. Guicking and E. Lorenz, "An active sound absorber with porous plate," J. Vibr. Acoust. **106**, 389–392 (1984).
[3] D. Thenail, M. Galland, M. Sunyach, and M. Sunhack, "Active enhancement of the absorbent properties of a porous material," Smart Mater. Struct. **3**, 18–25 (1994).
[4] C. R. Fuller, M. J. Bronzel, C. H. Gentry, and D. E. Whittington, "Control of sound radiation/reflection with adaptive foams," Proceedings of NoiseCon 1994, Fort Lauderdale, FL, pp. 429–436.
[5] S. Beyene and R. Burdisso, "A new hybrid passive/active noise absorption system," J. Acoust. Soc. Am. **101**, 1512–1515 (1997).
[6] J. P. Smith, B. D. Johnson, and R. A. Burdisso, "A broadband passive-active sound absorption system," J. Acoust. Soc. Am. **106**, 2646–2652 (1999).
[7] F. J. Fahy, *Sound Intensity*, 2nd ed. (E & FN Spon, London, 1995).
[8] J. W. Parkins, S. D. Sommerfeldt, and J. Tichy, "Error analysis of a practical energy density sensor," J. Acoust. Soc. Am. **108**, 211–222 (2000).
[9] "Standard test method for impedance and absorption of acoustical materials by the impedance tube method," ASTM C384, Philadelphia, 1990.

On the importance of early reflections for speech in rooms

J. S. Bradley and H. Sato
National Research Council, Ottawa K1A 0R6, Canada

M. Picard
Ecole d'Orthophonie et d'Audiologie, Université de Montréal, Montréal H3C 3J7, Canada

(Received 4 April 2002; accepted for publication 10 March 2003)

This paper presents the results of new studies based on speech intelligibility tests in simulated sound fields and analyses of impulse response measurements in rooms used for speech communication. The speech intelligibility test results confirm the importance of early reflections for achieving good conditions for speech in rooms. The addition of early reflections increased the effective signal-to-noise ratio and related speech intelligibility scores for both impaired and nonimpaired listeners. The new results also show that for common conditions where the direct sound is reduced, it is only possible to understand speech because of the presence of early reflections. Analyses of measured impulse responses in rooms intended for speech show that early reflections can increase the effective signal-to-noise ratio by up to 9 dB. A room acoustics computer model is used to demonstrate that the relative importance of early reflections can be influenced by the room acoustics design. [DOI: 10.1121/1.1570439]

PACS numbers: 43.55.Hy, 43.71.Gv [MK]

I. INTRODUCTION

The beginnings of our understanding of how we perceive sound reflections that arrive within a short time after the direct sound can be traced to the work of Joseph Henry in the 1850s.[1] Work by Haas[2] and Wallach *et al.*[3] showed explicitly how early reflections are integrated with the direct sound to make the direct sound seem to be effectively louder. Lochner and Burger[4] carried out extensive experiments to determine exactly how delayed reflections affected articulation test results as a function of the amplitude and delay time of an early arriving reflection. Although these early results demonstrated an extensive understanding of the benefits of early reflections to speech intelligibility in rooms, they sometimes focussed on the negative effects of early reflections. For example, Haas considered the point at which early reflections became disturbing. Although the early work of Lochner and Burger and others provides a solid basis for the importance of early reflections, they provide little information on the expected improvements to speech intelligibility scores in actual rooms due to early reflection energy.

Lochner and Burger's results suggest that speech energy in early arriving reflections is more or less equivalent to similar amounts of direct speech energy in terms of increasing speech intelligibility scores. They developed the concept of useful-to-detrimental sound ratios in which useful is defined as the sum of the direct and early reflected speech energy and detrimental is the sum of the later-arriving speech reflections and the ambient noise. This concept has been shown to be well correlated with speech intelligibility test scores in a wide range of rooms[5–7] and to be strongly correlated[8] with the newer speech transmission index (STI) concept.

However, Bess[9] has recently claimed that the benefits of early reflections are not experienced by impaired listeners. This is in contradiction with the results of Nábělek and Robinette[10] that indicated normal hearing and impaired listeners benefited equally from a single added early reflection. In addition, the importance of early reflections in rooms is apparently not well appreciated in conventional room acoustics design which is usually based primarily on obtaining a particular preferred reverberation time.[11] A lack of appreciation of the importance of early reflections is no doubt responsible for some recommendations for very short reverberation times for rooms for speech. There is often a misconception that reverberation time must be minimized rather than optimized. Of course, very short reverberation times require increased absorption on room surfaces which is likely to lead to reduced early reflection energy and hence to reduced speech intelligibility.

There are many situations in speech communication in rooms where early reflections would appear to be particularly important such as a teacher talking to students from somewhere in the middle of a classroom or an actor on a thrust stage. Students behind the teacher would receive much reduced direct sound and presumably benefit significantly from early reflections of the speech sounds. In many other situations where the talker directs their attention to some part of a group of listeners, those in other directions benefit from early reflections of the speech sounds. Although we typically include early reflections within the first 50 ms after the direct sound as being useful early reflections, we do not have a quantitative indication of the relative magnitude (and hence importance) of this early reflection energy in typical rooms.

The purpose of the new work reported in this paper was to first confirm the importance of early reflections to speech intelligibility test scores in conditions representative of real rooms. This was done using speech intelligibility tests for both impaired and nonimpaired subjects in simulated sound fields. These simulations allowed comparison of the benefits of added early reflection energy with that of increased direct sound energy for cases with and without reverberant sound. Tests also considered the critical value of early reflections for

TABLE I. Orientation of loudspeakers relative to the listener. Horizontally straight ahead of the listener at ear level is 0 degrees in both planes.

Loudspeaker	Horizontal angle, degrees	Vertical angle, degrees
(1) Center low (direct sound)	0	0
(2) Center high	0	25
(3) Left low	−32	0
(4) Right low	+32	0
(5) Left high	−37	28
(6) Right high	+37	28
(7) Far left	−115	0
(8) Far right	+115	0

situations where the direct sound is reduced in amplitude. The second part of this paper examines the magnitude of the benefit of early reflections in a range of rooms intended for speech communication and illustrates how modern room acoustics computer models can be used to explore various room designs in terms of improved early reflection levels.

II. SPEECH INTELLIGIBILITY TESTS IN SIMULATED SOUND FIELDS

The goal of the speech intelligibility tests in simulated sound fields was first to confirm directly that increased speech energy in early reflections has a similar effect to increased direct speech energy. The second goal was to demonstrate that both hearing-impaired and nonimpaired listeners benefit from early arriving reflections of speech sounds. The benefits of increased early reflections are then shown to be present in more realistic sound fields that also included reverberant sound typical of many rooms for speech communication. Finally, in situations where the direct sound is reduced in level such as when the talker's head is turned, early reflections are shown to be essential to achieving adequate speech intelligibility.

A. Method

1. Sound field simulation procedures

All simulated sound fields were produced using an eight-channel electroacoustic system with loudspeakers arranged around the listener in an anechoic room. The eight loudspeakers were located at a distance of 1.7 m from the listener and their angular locations relative to the listener are described in Table I. Each of the eight channels of electronics included programmable digital equalizers that included time delays and reverberators that could all be changed under computer control via a MIDI interface. The loudspeaker responses were corrected to be flat ±3 dB from 80 Hz to 12 kHz.

The loudspeaker located directly in front of the listener produced the simulated direct sound (first arriving sound) and in some experiments also produced reverberant sound. The other seven loudspeakers each produced one early reflection and in some experiments reverberant sound. The early reflections arrived at the listener within the first 50 ms after the direct sound. Figure 1 illustrates a measured impulse response for a condition that included a direct sound, early reflections and reverberation. Some sound fields included only a direct sound component, others included a direct sound and early reflections and others included a direct sound combined with both early reflections and reverberant sound. Where reverberant sound was included it was delayed to start just after the 50 ms early time interval as seen in the example in Fig. 1. The overall amplitudes of each of these three component groups (direct sound, early reflections, and reverberant reflections) were varied but the arrival times and relative amplitudes of early reflections were not changed.

Each loudspeaker also reproduced simulated ambient noise with a spectrum shape corresponding to that of an NC 40 contour and with a measured overall level at the listener of 47.6 dBA. The noise signals to each loudspeaker were passed through different digital reverberators to ensure that they were not exactly coherent.

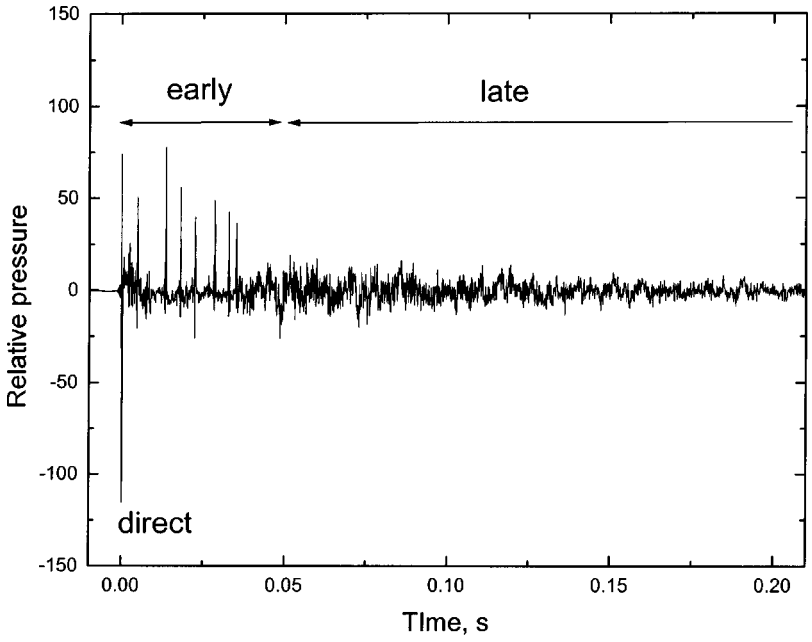

FIG. 1. Illustration of the initial 0.2 s of the measured impulse response of a simulated sound field including a direct sound and seven early reflections followed by a reverberant decay.

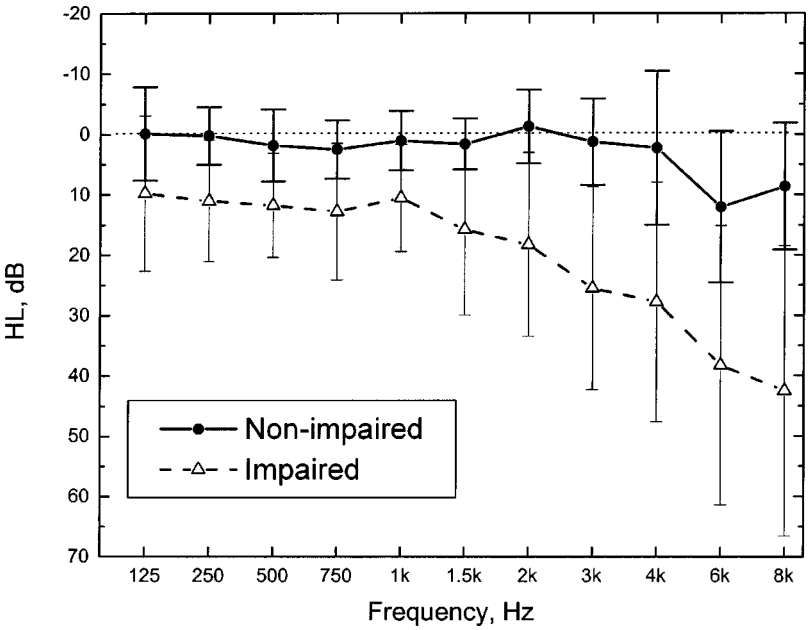

FIG. 2. Average measured hearing loss (HL) (as per ANSI S3.6 1996), ±1 standard deviation for the non-impaired and impaired groups of listeners.

Each experimental condition was measured with our RAMSoft room acoustics measurement software that uses a maximum length sequence signal to obtain impulse responses. A range of standard room acoustics parameters were measured in octave bands and are included here where relevant.

2. Subjects and speech intelligibility tests

Speech intelligibility scores were obtained using a Fairbanks rhyme test as modified by Latham[5] and as used in previous tests.[6–8] The test words were embedded in the sentence ''Word number _ is _ write that down'' and were spoken by a male talker. Each 50 word test took a total of about 2.5 minutes and the speech material was presented at a rate of approximately three syllables per second.

Subjects varied from 20 to 74 years of age. The wide range of ages was intended to ensure subjects included a variety of hearing abilities representative of those typically found for listeners in many rooms for speech. However, no subjects were included who used hearing aids or who had known serious hearing impairment. Many of the younger subjects had excellent hearing with minimal hearing loss. A number of the older listeners had mild to moderate hearing loss typical of many middle-aged listeners.

In some analyses the results of the subjects were divided into two groups according to their measured hearing loss (HL). The group with the least HL will be referred to as nonimpaired and the other group will be referred to as the impaired listeners. Figure 2 plots the average HL (±1 standard deviation) for each group. The nonimpaired (and generally younger) group, on average, showed only very small reductions below threshold at 6 and 8 kHz. They had a mean age of 28 years and their mean hearing loss results shown in Fig. 2 are very similar to the median for this age.[12] The impaired (older) group, on average, showed increasing HL above 1 kHz. Most of the impaired group were apparently unaware that they had any hearing loss. This group had a mean age of 60 years and again their mean hearing loss was similar to the expected median for this age.[12] The high frequency pure tone average (from 3, 4, and 6 kHz results and from both ears) for the nonimpaired listeners was 5.2 dB and 30.5 dB for the impaired group.

B. Results of speech intelligibility tests

1. Comparison of effects of varied direct sound and varied early reflection levels on speech intelligibility scores

The first comparisons were based on the results of tests in which subjects performed speech intelligibility tests for sound fields with varied speech signal-to-noise ratio (S/N) and for two types of reflection conditions. In one series of tests the sound fields consisted of only a direct (speech) sound and varied S/N was obtained by varying the amplitude of the direct speech sound with constant noise level. In the other series of tests the direct speech sound was fixed and S/N was varied by adding increased levels of early reflections in combination with the same constant noise level. Table II showing a summary of the measured conditions for each series of tests, includes *A*-weighted signal-to-noise ra

TABLE II. Summary of acoustical measures for the direct only and direct +early reflections sound field cases. (Noise level 47.6 dBA.)

	Speech level dBA	$S/N(A)$ dB	C_{50} (1 kHz) dB	U_{50} (1 kHz) dB	STI
Direct only					
1	41.8	−5.8	21.9	−5.7	0.32
2	45.4	−2.2	19.3	−2.0	0.44
3	48.8	1.2	19.9	1.5	0.55
4	52.0	4.4	20.1	4.6	0.66
Direct+early					
1	41.8	−5.8	21.9	−5.7	0.32
2	44.9	−2.7	21.1	−2.6	0.41
3	48.1	0.5	21.6	0.5	0.51

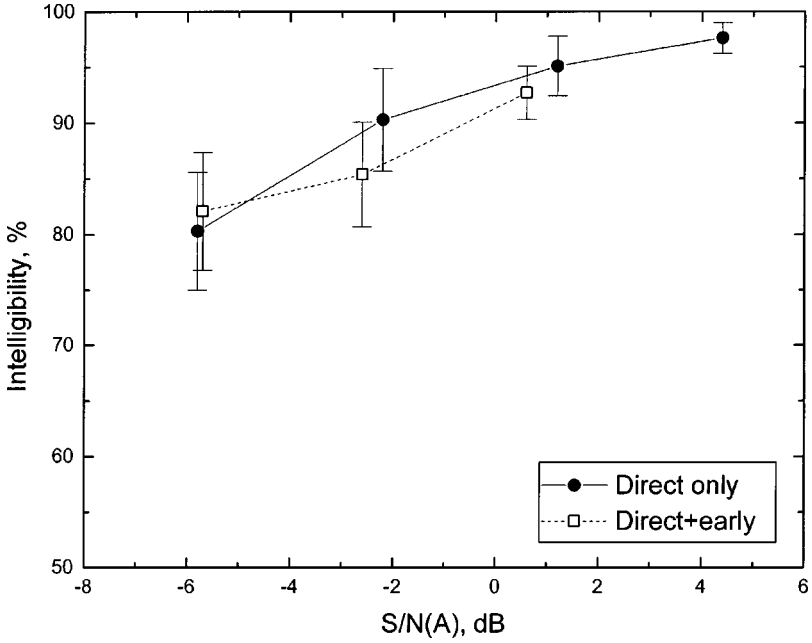

FIG. 3. Mean intelligibility scores ±1 standard deviation for each sound field condition for all listeners for direct only and direct+early reflections cases.

tios, $S/N(A)$, varying from −5.8 to +4.4 dB for the direct sound only cases and −5.8 to +0.5 for the cases with added early reflections. The three added-reflections cases corresponded to increasing the total speech level by 0, 3, and 6 dBA. These were thought to be representative of conditions in typical rooms but later analyses (included in Sec. III) showed that increases of up to 9 dBA can occur in typical rooms for speech.

Results were first considered for all 21 subjects and were not divided according to their level of hearing threshold shift. The complete group of all subjects can be thought of as representing a typical mixed group of listeners in a theatre audience or at a public meeting. Figure 3 plots the mean speech intelligibility scores (±1 standard deviation) for each sound field condition for this combined group of listeners. An analysis of variance test (ANOVA) of the speech intelligibility scores was performed for the comparable $S/N(A)$ cases with and without added early reflections. There was a statistically significant effect of $S/N(A)$ ($p<0.001$) but no significant effect of the two types of reflection conditions (direct sound only versus direct plus early reflections).

For both series of reflection conditions, speech intelligibility scores increased in a statistically significant manner with increasing $S/N(A)$ as was expected. However, there was no identifiable difference between cases where the same increased $S/N(A)$ was due only to varied direct sound and those where it was due to varied added early reflections. In these tests increased early reflection energy had the same effect on speech intelligibility scores as increased direct sound level.

2. Comparison of the effects of varied early reflection levels for impaired and nonimpaired listeners

In a second analysis of the same data, subjects were divided into two almost equal-sized groups according to their measured hearing loss. Eleven subjects were classified as nonimpaired and 10 as impaired. Their average HL characteristics were given in Fig. 2. The mean speech intelligibility scores are plotted versus measured $S/N(A)$ in Fig. 4 separately for the impaired and nonimpaired listeners. As for the combined results in Fig. 3, the mean speech intelligibility scores increase with increasing $S/N(A)$ but for corresponding $S/N(A)$ values the impaired listener group always had lower intelligibility scores. That is, the trends of the results are in agreement with expectation from previous studies that have considered hearing-impaired listeners.[13]

Again the statistical significance of the results was tested using ANOVA on the conditions with similar $S/N(A)$. For the nonimpaired subjects, there was a statistically significant effect of $S/N(A)$ but no effect of the difference between sound fields with only direct sound and those with added early reflections. Exactly the same result was obtained for the impaired listeners' results. However, when impaired and nonimpaired listeners were compared for either condition of direct sound only cases or added early reflections cases, there was a statistically significant effect of the differences in HL.

Therefore these results show that both the impaired and nonimpaired listeners benefit in a similar manner from added reflections. Increasing the $S/N(A)$ by adding early reflections has the same effect as increasing the level of the direct sound on the resulting speech intelligibility scores for both no-impaired and impaired listeners.

These results also reconfirm that hearing impaired listeners need better conditions with higher $S/N(A)$ values to enjoy the same level of speech recognition. The results in Fig. 4 suggest that these particular impaired listeners would require approximately 5 dB higher $S/N(A)$ values to have the same intelligibility scores as the nonimpaired listeners. [For these listeners there was an approximate linear relationship between their measured HL and their speech intelligibility scores. Thus more impaired listeners would appear to require even better $S/N(A)$ for them to be equally able to understand speech as less impaired listeners.]

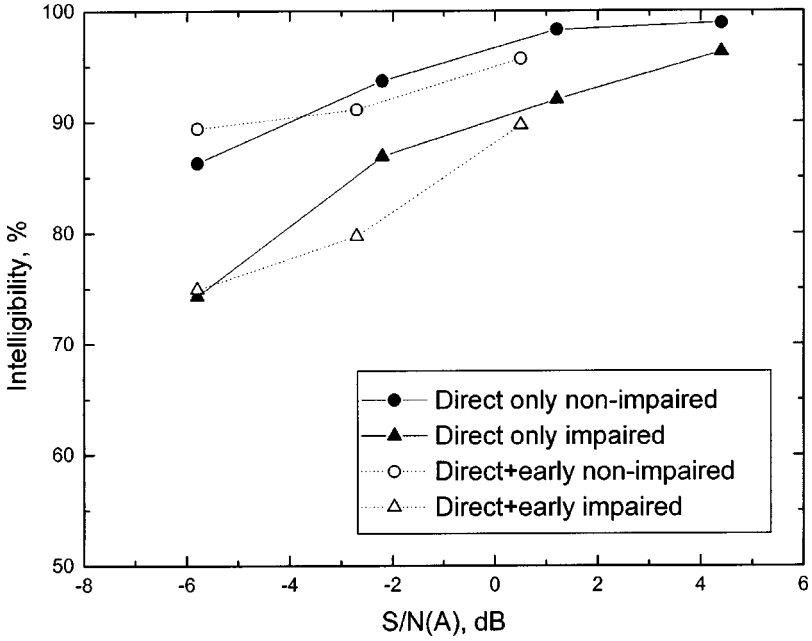

FIG. 4. Mean intelligibility scores for each sound field condition for direct only and direct+early reflections cases plotted for each hearing loss group.

3. Evaluation of the effect of varied early reflection levels in the presence of later arriving speech sounds

It was thought that the benefits of early reflections might be masked or diminished by the presence of reverberant sound which would normally be present in typical rooms intended for speech communication. Therefore, a third series of conditions was created that included varied levels of early reflections in the presence of a fixed level of the direct sound and reverberant sound. These conditions were identical to the previous series of sound fields in which the level of early reflections were varied but with a constant amount of added reverberation as illustrated in Fig. 1. The acoustical measurements of the conditions are summarized in Table III and include reverberation times of 1.1 s representing a realistically reverberant condition for a room intended for speech communication. The speech levels and the $S/N(A)$ values in Table III are termed effective because the speech levels are based on the direct and early reflection energy and do not include the later arriving speech energy. Thus these effective speech levels and $S/N(A)$ values are exactly the same as in the test series where early reflection level was varied without the inclusion of reverberation (given in Table II).

Some subjects in this series of tests were different than in the original tests. There were 10 nonimpaired subjects and six impaired subjects. However, the average HL characteristics of the impaired and nonimpaired groups were very similar to the previous group averages shown in Fig. 2. The group average HL values for the subjects in these tests differed by less than 2 dB at most frequencies with a few differences in higher frequency hearing loss of up to 4 dB.

The mean intelligibility scores are plotted versus effective $S/N(A)$ in Fig. 5 along with the results for the previous tests repeated from Fig. 4. The speech intelligibility scores for the sound fields including reverberation follow similar trends to those of the previous results and there seems to be no significant effect of adding reverberation. Again this was confirmed by ANOVA tests of the significance of the results. There was a highly significant effect of $S/N(A)$ ($p<0.001$) but no significant effect of the differences in the types of reflections present.

These results confirm that the benefits of increased early reflection energy occur for both the impaired and nonimpaired listeners in the presence of a realistic amount of reverberation.

One might expect that adding reverberation would at least reduce intelligibility scores for all listeners. This does not occur because the detrimental effects of the added reverberation were relatively small compared to the negative effects of the simulated ambient noise. This is confirmed by the almost invariant U_{50} values between corresponding cases

TABLE III. Summary of acoustical measures for the direct+early+reverberant reflections sound field cases. Speech level is the total speech level including direct sound, early reflections and late arriving speech sounds. Effective speech level includes only the direct and early reflection speech energy. (Noise level 47.6 dBA.)

	Speech level dBA	$S/N(A)$ dB	Effective speech level dBA	Effective $S/N(A)$ dB	C_{50} (1 kHz) dB	U_{50} (1 kHz) dB	STI	EDT (1 kHz) s	RT (1 kHz) s
Direct+early+reverb									
1	45.5	−2.1	41.8	−5.8	1.4	−5.7	0.31	1.2	1.1
2	47.2	−0.4	44.9	−2.7	4.1	−3.0	0.38	0.9	1.1
3	49.6	2.0	48.1	0.5	7.2	0.0	0.46	0.5	1.1

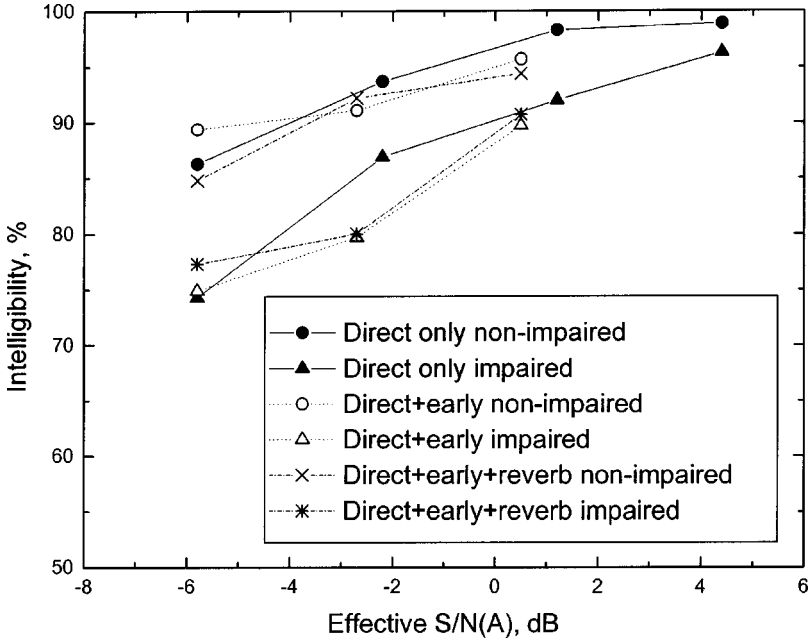

FIG. 5. Mean intelligibility scores for each sound field condition for direct only, direct+early, and direct +early+reverberant reflections cases plotted separately for each hearing loss group. In calculating effective $S/N(A)$ values, the reverberant speech sound was excluded from the signal level.

shown in Table III for sound fields including reverberation and those without reverberation shown in Table II. U_{50} is a useful to detrimental sound ratio[6] where useful is the sum of the direct and early reflection energy arriving in the first 50 ms and detrimental is the sum of later-arriving speech sounds and the ambient noise. Thus the reverberant energy is relatively small compared to the ambient noise energy and therefore its detrimental effect is negligible for these cases. Of course, this is similarly reflected in the almost identical speech transmission index (STI) values in Table III to those in Table II for the corresponding early reflections conditions.

4. Demonstration of the benefits of early reflections when the talker's head is turned

In most situations in rooms the presence of early reflections increases intelligibility by effectively enhancing the direct sound component and hence increasing the signal-to-noise ratio. However, in a number of situations where the direct sound is blocked or reduced in amplitude, the intelligibility of speech is more critically dependent on the presence of early reflection energy. One particular example is when the talker is not pointing directly toward the listener but is directing their speech in some other direction. For example, when a teacher is talking to a class from the middle of the classroom, there are listeners both in front of and behind the talker. Due to the directionality of the human voice, those listeners not directly in front of the talker will experience reduced direct speech sound and this is especially so at the higher frequencies, which are critical for recognizing consonant speech sounds.

The final speech intelligibility tests in simulated sound fields were intended to demonstrate the importance of early reflections when the direct speech sounds are reduced in magnitude. The effect of the talker's head turning were simulated by modifying the spectrum of the direct speech sound to be equivalent to measured speech spectra at angles of 0, 90, and 180 degrees relative to straight ahead of the talker.[14] Subjects listened to speech representing these three talker angles in sound fields with only a direct sound and also in sound fields that also included early reflections. The sequence of early reflections was the same as used in the previous experiments and illustrated in Fig. 1. No attempt was made to estimate changes in early reflections with talker head turning because these would be as likely to increase as to decrease in amplitude and hence to not systematically affect intelligibility.

Figure 6 plots the mean speech intelligibility scores versus talker angle for cases with a direct sound only and also for cases with added constant early reflections. Without early reflections, mean intelligibility decreases dramatically with talker head turning similar to the results of Plomp and Mimpen.[15] However, when early reflections were included, there was only a small reduction in intelligibility even when the taker's head was turned 180 degrees (that is, facing away from the listener). These changes in intelligibility scores can be related to corresponding changes in $S/N(A)$ values. Without early reflections $S/N(A)$ values changed from -2.2 to -8.7 and to -17.5 dB for angles of 0, 90, and 180 degrees. However when early reflections were included the corresponding $S/N(A)$ values were -0.6, -3.9, and -5.4 dB.

The results in Fig. 6 indicate that if there were no early reflections and the talker's head turned 90 degrees, listeners would find it very difficult to understand speech. If the talker's head was turned 180 degrees it would be completely impossible to understand speech without the benefit of early reflections. Clearly in many situations, it is only possible to understand speech in rooms because of the presence of early reflections.

III. THE RELATIVE IMPORTANCE OF EARLY REFLECTION ENERGY IN TYPICAL ROOMS

The results presented in the preceding section have confirmed the benefit of early reflections to obtaining adequate speech intelligibility in rooms for both impaired and nonim-

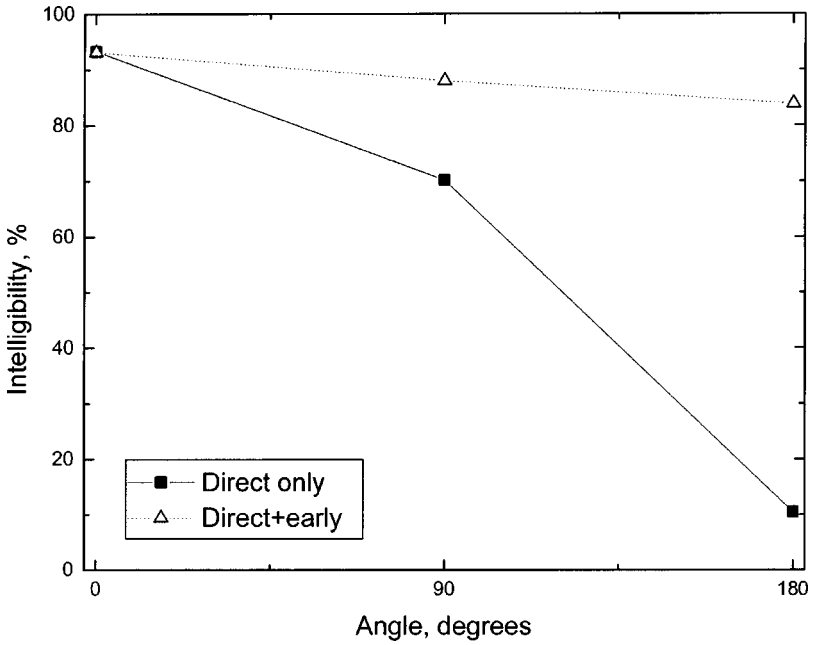

FIG. 6. Mean speech intelligibility scores versus horizontal angle of the talker's head relative to directly pointing towards the listener for sound fields with and without added early reflections.

paired listeners. Early reflections were seen to effectively enhance the direct sound and also to compensate for reduced or weaker direct sound components. This section is intended to provide an initial examination of the relative magnitude of the early reflection energy that is found in actual rooms.

The direct sound energy will decrease with distance so that direct speech levels would frequently be unacceptably low at more distant listening positions in many rooms. In many cases this lack of direct sound energy is compensated for by added early arriving speech reflection energy. The experiments in the previous section confirm that the speech energy in early reflections is equally beneficial to intelligibility as similar speech energy in the direct sound. Thus we can expect speech energy arriving within the first 50 ms after the direct sound (E_{50}) to be useful to increasing intelligibility. If the direct sound is represented approximately by the energy arriving in the first 10 ms (E_{10}), then the ratio of E_{50}/E_{10} is a measure of the benefit provided by early arriving speech reflection energy. Thus the early reflection benefit (ERB) is proposed as a simple measure of the effectiveness of a room's acoustical design obtained by measuring the relative benefit of the early reflection energy,

$$\mathrm{ERB} = 10 \log\{E_{50}/E_{10}\} \ \text{dB}.$$

Values of ERB were determined for several rooms used for unamplified speech communication. The ERB values were calculated from measures of the relative sound level or strength (G) for the first 10 ms (G_{10}) and the first 50 ms (G_{50}) of the impulse responses in each octave band. The relative sound level G is given by

$$G = 10 \log\left\{ \int_0^\infty p^2(t)dt \Big/ \int_0^\infty p_A^2(t)dt \right\} \ \text{dB},$$

where $p(t)$ is the pressure response in the measured impulse response and $p_A(t)$ is the response to the same source in a free field at a distance of 10 m. G_{10} and G_{50} are similarly calculated with the upper limit of the first integration set to 10 and 50 ms, respectively.

The early reflection benefit (ERB) was then calculated as

$$\mathrm{ERB} = G_{50} - G_{10} \ \text{dB}.$$

The current initial analyses were based on averages of the 1 to 4 kHz octave band G_{50} and G_{10} values because these frequencies are most important for the intelligibility of the weaker consonant sounds.

A. Boardroom

Acoustical data from a 390 m^3 boardroom in which impulse response measurements had been made were first considered. The room contained a large elongated table with seating for 22 people. Measurements were made in the unoccupied condition. Figure 7 plots ERB values versus source–receiver distance in this boardroom. These ERB values indicate that with added reflection energy the effective speech level is 2 to 8 dB greater than the direct sound level and that there is a systematic increase in the benefit from early reflections with increasing source–receiver distance. There is some scatter about the mean trend that may have been influenced by the presence of a large glass dome in the ceiling over the boardroom table.

These results suggest that it is quite possible for early reflection energy to increase the effective or useful speech level by as much as 8 dB. This is even greater than the maximum increase of +6 dB included in the speech intelligibility tests in simulated sound fields.

B. Four rooms for speech

The generality of the results from the boardroom were further explored by considering measurements in four other rooms that represent a range of conditions intended for unamplified speech communication. Descriptions of the boardroom mentioned above and the four other rooms are included

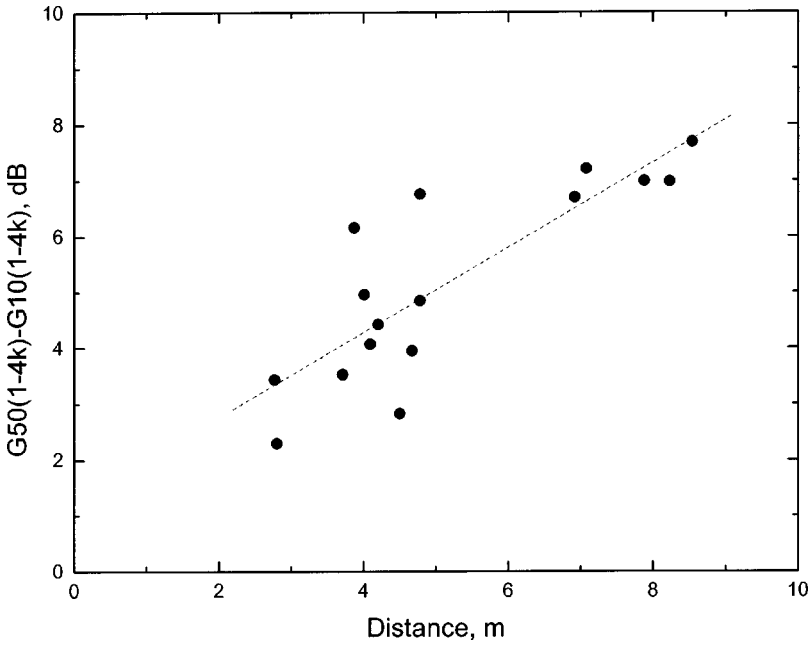

FIG. 7. Measured values of the early reflection benefit in a boardroom.

in Table IV. They varied from a round table meeting room with a considerable amount of added sound absorption (used for teleconferencing) to a small auditorium and a small theatre.

ERB values were again calculated from averages of the 1 to 4 kHz octave-band G_{50} and G_{10} values obtained from impulse response measurements. All measurements were for unoccupied conditions. The resulting ERB values for positions in all four rooms are plotted versus source–receiver distance in Fig. 8. There is again an approximate linear trend for ERB values to increase with increasing source–receiver distance. The maximum ERB values at the largest source–receiver distances are close to +9 dB.

These results indicate that the effect of early reflections in rooms is equivalent to an increase in the direct speech level of up to 9 dB. Increases tend to be greatest for listeners farthest from the talker. That is, rooms naturally tend to help intelligibility most where the help is most needed farthest from the source. Figure 9 compares measured impulse responses at two locations *A* (closer to the source) and *B* (farther from the source) in the Playhouse theatre. In Fig. 8 the ERB at position *B* is seen to be approximately 4 dB greater than at position *A*. The impulse responses in Fig. 9 clearly illustrate the much greater number of significant reflections at the more distant *B* position. Presumably the amount of early reflection benefit can be influenced by the room acoustics design. At the rear of many rooms it may only be possible to understand speech because of the benefits of early reflections. Adding too much absorbing material or inappropriate shaping of reflecting surfaces could reduce the level of beneficial reflections and the related level of speech intelligibility.

The slope of the mean trend for the data from the boardroom in Fig. 7 is steeper than that for the data from the four rooms in Fig. 8. A brief examination of data from larger auditoria indicated even lower slopes. Thus the variation of benefits of early reflections may depend on the overall room size as well as the source–receiver distance. The ERB measure indicates the relative importance of early reflections relative to the direct sound and is not simply related to overall sound levels or strength values (*G*).

IV. DESIGN EXAMPLE CALCULATIONS

This section explores the use of a modern room acoustics computer model to evaluate the effects of room design on the relative strengths of early reflections in rooms for speech. The ODEON (version 4.0) software was used to calculate impulse responses in a small 200 seat lecture theatre with a volume of just over 1000 m^3. The room had a steeply sloping seating area and is illustrated in Fig. 10. It was similar to the room referred to as M50 in Fig. 8 and Table IV.

In the first calculation example, the magnitude of early reflection energy was varied by varying the height of this

TABLE IV. Descriptions of the rooms from which acoustical measurement data were obtained.

Name	Description	Number seats	Volume, m^3	RT(1 kHz), s
Boardroom	Boardroom	22	390 m^3	1.4
Ridgemont	School auditorium	750	2800 m^3	1.2
M50	Lecture theatre	200	1020 m^3	0.6
Playhouse	Small theatre	690	7000 m^3	1.0
RCMP	Round table teleconferencing/ meeting room	15	867 m^3	0.26

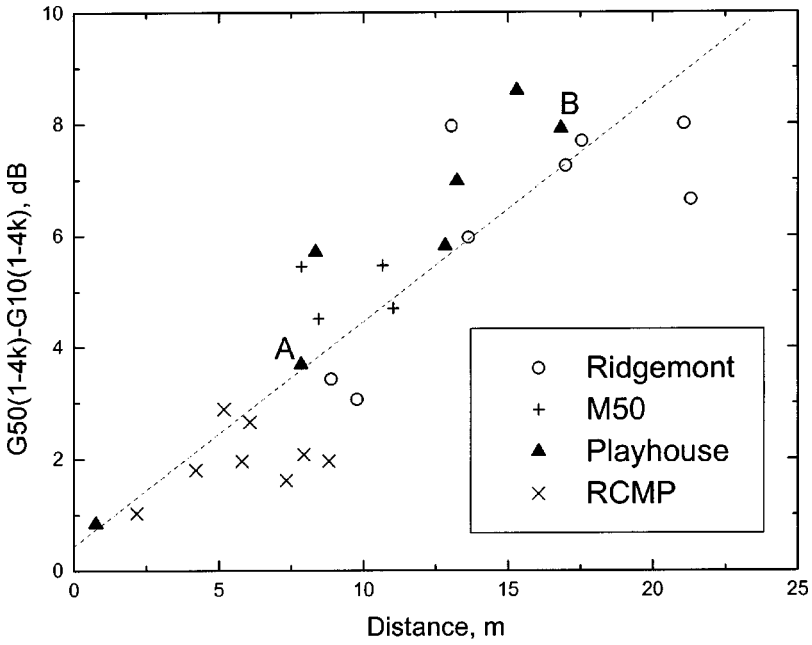

FIG. 8. Measured values of the early reflection benefit in four rooms intended for unamplified speech communication.

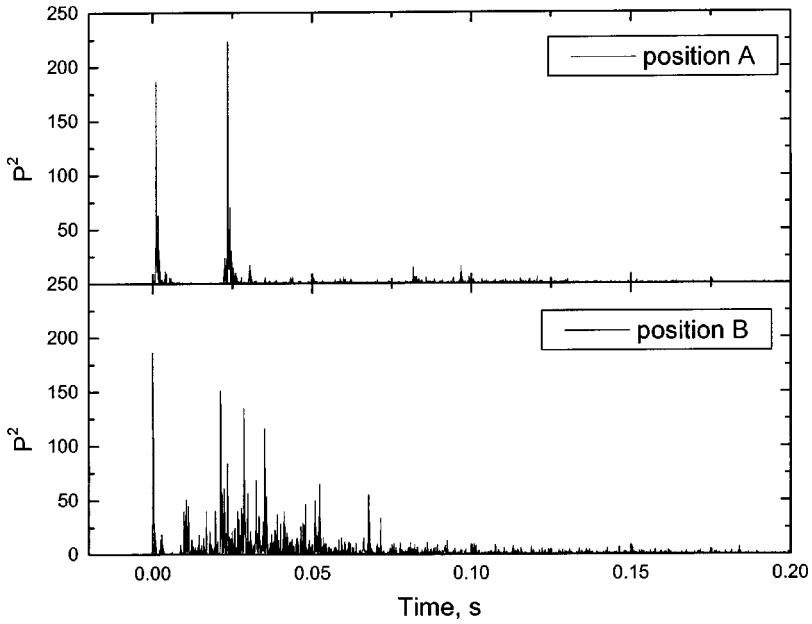

FIG. 9. Measured broadband impulse responses in terms of pressure squared versus time at locations *A* and *B* from Fig. 8 in the Playhouse theatre. They are normalized to the same direct sound amplitude and the same start time to facilitate the comparison.

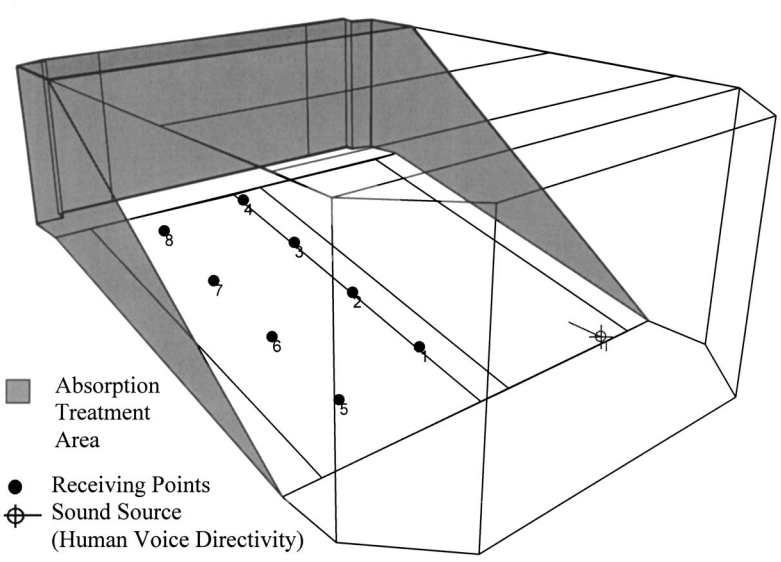

FIG. 10. Sketch of the room used in the calculation examples showing the optimized configuration with a room volume of 1092 m^3. The eight receiver positions (solid circles) and the position of the source (open circle) having the directivity of a human talker are also shown.

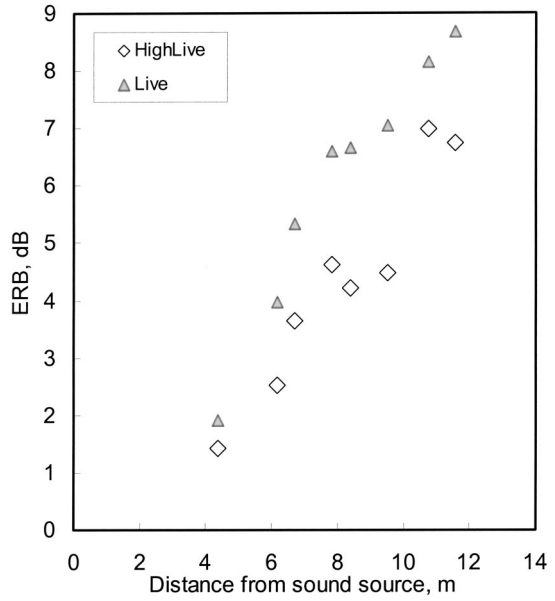

FIG. 11. Calculated 1 kHz ERB values versus source–receiver distance for the high-live (higher ceiling) and live (lower ceiling) room design cases. (Table V includes descriptions of the designs.)

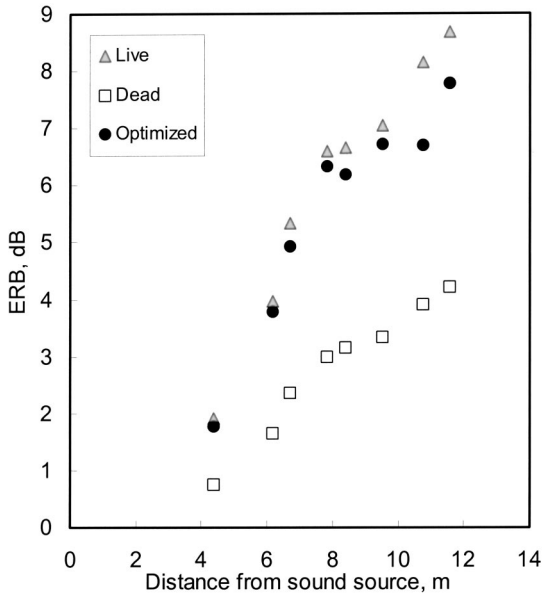

FIG. 12. Calculated 1 kHz ERB values versus source–receiver distance for the live, dead, and optimized room design cases. (Table V includes descriptions of the designs.)

room. The audience seating area was absorptive and the other surfaces were highly reflective. When the ceiling height (at the front of the room) was increased from 7 m to 10 m the volume increased from 1092 m^3 to 1777 m^3. Figure 11 shows the calculated ERB values versus source–receiver distance for both ceiling heights. The details of the design cases are summarized in Table V. The calculated results show that the lower ceiling increases the benefit from early reflections by up to 3 dB. Of course, the lower ceiling case also has a lower reverberation time (see Table V), which would also be preferable for speech.

Figure 12 compares calculated results for the same lower ceiling room shape with varied absorptive treatments. The live case is the same as the lower ceiling case in the previous comparison. Only the audience area was absorptive for this case. The dead case corresponds to adding material that is 60% absorptive to all of the walls and ceiling in addition to the absorptive audience area. The optimized case corresponds to 70% absorptive material added to the shaded areas in Fig. 10. It was hoped that this optimized design would better control reverberant sound without unduly reducing early reflection energy. Figure 12 shows that for a given source–receiver distance the dead case shows much smaller ERB values than the other two cases. That is, when there is too much absorptive treatment, the early reflection energy is reduced by up to 5 dB relative to the live case. However, the ERB values for the optimized case are almost the same as for the live case. Thus, it seems possible to adjust the details of the design to maximize the relative magnitude of early reflection energy.

The measurement results in Figs. 7 and 8 as well as the calculation results in Figs. 11 and 12 show how the relative importance of early reflections tends to increase with increasing source–receiver distance. These types of results can be more completely understood when shown in terms of the total early arriving level. Figure 13 plots results for the same calculations as in Fig. 12 in terms of G_{50} values versus ERB values. For the dead case G_{50} values decrease by 6 dB when moving from nearer to the source to the farthest receiver position. For the live and optimized cases G_{50} values decrease by only 3 dB with increasing source–receiver distance because there are larger amounts of beneficial early reflection energy which lead to larger ERB values. By comparing G_{50} values for the dead case with corresponding values for the optimized case, it is seen that optimizing the absorptive treatment can increase G_{50} values by as much as 4 dB. That is, the effective signal-to-noise ratio was increased by up to 4 dB. In many situations a 4 dB increase in effective signal-to-noise ratio would lead to significant increases in speech intelligibility ratings. (It is interesting to note that if the treated

TABLE V. Details of the calculation examples for the room illustrated in Fig. 10. Treatment corresponds to the shaded area in Fig. 10. Audience areas had a 1 kHz absorption coefficient of 0.8.

Case	Height, m	Volume, m^3	Absorption coefficients (1 kHz)		RT (1 kHz), s
			Walls & ceiling	Treatment	
High-live	10	1777	0.03	None	3.5
Live	7	1092	0.03	None	1.9
Dead	7	1092	0.6	None	0.34
Optimized	7	1092	0.03	0.6	1.1

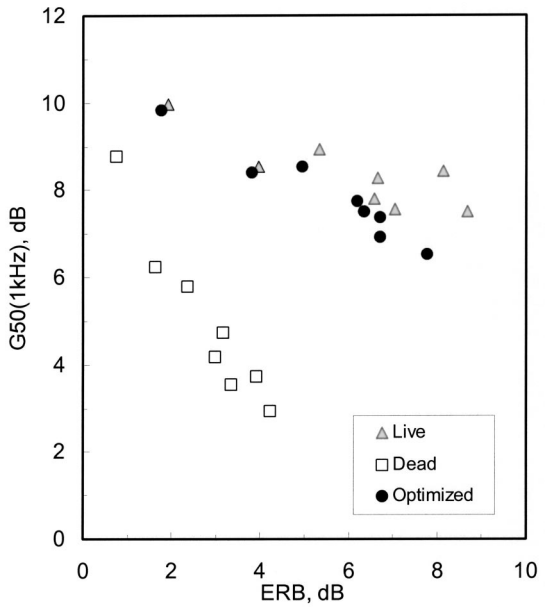

FIG. 13. Plot of the relative early sound level, G_{50} versus ERB for the 1 kHz results shown in Fig. 12.

and untreated surface areas are reversed the same increased ERB does not occur.)

Of course, there are many possible approaches to optimizing a particular room design and larger improvements in ERB values than indicated in these results may be possible. However, the complete room acoustics design process must also include consideration of late-arriving sound levels. Increasing early reflection levels by decreasing the total amount of sound absorption will also tend to increase the later arriving sound levels. The optimum design will also have to consider the level of ambient noise because a truly optimum design must maximize the effective signal-to-noise ratio, which is expected to correspond to maximizing the useful-to-detrimental sound ratios. However, to explore all of the various combinations of room designs and ambient noise conditions is much beyond the scope of this paper.

V. DISCUSSION

These new results have confirmed that early reflections of speech sounds are important for achieving adequate speech intelligibility in rooms and have approximately the same effect as increased direct sound energy for both nonimpaired and impaired listeners. Where the direct sound is particularly weak, such as when the talker's head is turned away from the listener, or at positions towards the rear of many rooms, early reflections are essential to achieving adequate intelligibility.

The impaired subjects in this study were assumed to have peripheral hearing loss due to some combination of presbycusis (as the dominant factor) and noise induced hearing loss. However, the precedence effect is thought to function at a more central cognitive level.[16] There is therefore no reason to expect that subjects with mild to moderate peripheral hearing loss will not benefit fully from the precedence effect. Thus the current results, showing that both impaired and nonimpaired listeners benefited equally from early reflections, are readily explained and lend credence to the belief that the precedence effect is due to higher level processing in the brainstem and auditory cortex.

The early reflection energy can be up to 9 dB greater than that of the direct sound. It is therefore more important than the direct sound and it is of primary importance that the room acoustics design attempts to maximize early reflection energy.

The common practice of focussing on reverberation time as the primary acoustical design parameter can distract us from the more important details of the acoustical design of rooms for speech. Obtaining an optimum reverberation time should not be thought of as a primary design goal but as something that is a consequence of the need to maximize early reflections without including excessive later arriving reflection energy. Ignoring the critical benefits of early reflections would lead to the conclusion that a reverberation time of 0 s. would be preferred. This misconception has been encouraged by experiments in which the positive effects of increased sound levels were either ignored or deliberately controlled (e.g., Ref. 17). A minimum reverberation time is of course not a desirable goal and the added absorption required to achieve very short reverberation times could severely attenuate early reflections that make it possible for us to hear speech in many situations. The result of the real need to maximize early reflection energy without excessive later arriving reflections leads us to a related need for a nonzero optimum reverberation time. The actual optimum reverberation time will vary with room size and ambient noise level. However, there is not a precise optimum value for some particular condition but a relatively broad range of acceptable values.[18]

Although later arriving reflections are undesirable, controlling them should not be the first priority. The first priority for the acoustical design of rooms for speech should be to maximize the total energy in the direct sound and early arriving reflections of the speech sounds. (The live case in Sec. IV is an example of only maximizing the early reflections.) A second priority would be to ensure, that there is not excessive later-arriving reflection energy, usually by determining that conventional goals for optimum reverberation times are approximately met. (The optimum case in Sec. IV is a simple example of combining these first two design steps.) However, it is much more important for designers to focus efforts on maximizing early reflections and hence increased ERB values than on small differences in reverberation times. A room that is slightly too reverberant is probably better for speech than one that is too dead and hence likely to be lacking in critical early reflection energy. Early reflections can increase the effective speech level by up to 9 dB, but even doubling the reverberation time would only increase late arriving sound by only about 3 dB and even this increase in unwanted late arriving sound can be insignificant relative to excessive ambient noise. Of course, achieving adequately low ambient noise levels is usually even more important than any aspect of room acoustics design.[19]

VI. CONCLUSIONS

The results of the new studies presented in this paper show that increased early reflection energy has the same effect on speech intelligibility scores as an equal increase in the direct sound energy. This was true for both nonimpaired listeners and for listeners with mild to moderate hearing threshold shifts. These impaired listeners are thought to be representative of a significant portion of the population.

In typical rooms for speech, early reflection energy increases the effective $S/N(A)$ by up to 9 dB. This would lead to very important increases in speech intelligibility scores in typical rooms for speech. That is, early reflections are important for good speech communication and in many situations where the direct sound is reduced they are essential to satisfactory speech communication. For example, when the talker is not facing the listener or for listeners near the rear of many rooms, it is only due to the benefits of early reflections that we are able to satisfactorily understand speech.

Room acoustics design for speech should focus first on maximizing early reflection energy. Although it is also important to avoid excessive reverberant sound, adding large amounts of absorption to achieve very short reverberations times may degrade intelligibility due to reduced early reflection levels.

The ratio of the early arriving energy in the first 50 ms of impulse responses, to the energy associated with the direct sound is termed the early reflection benefit, ERB, and is proposed as a useful measure of the effectiveness of a room's acoustical design.

While the hearing impaired listeners in this study benefited from added early reflections, there is a need to verify that this is also true for some other special groups. Further studies are required to determine whether younger and older listeners as well as more severely impaired listeners similarly benefit from early reflections.

Much of this is not totally new. In the introduction to a 1964 review paper Lochner and Burger stated,[4] ''...we know that reverberation time in itself gives very little indication of the suitability of a room for speech; rather, given the integration and masking characteristics of the hearing system, the intelligibility of speech will be determined by the reflection pattern of the room.'' Perhaps it is time to make a more serious effort to apply our understanding of the importance of early reflections to the design of rooms for speech.

ACKNOWLEDGMENTS

The authors would like to thank Wai Lyn Wong who carried out many of the speech intelligibility experiments, and also the subjects who volunteered their time.

[1] R. S. Shankland, ''Architectural acoustics in America to 1930,'' J. Acoust. Soc. Am. **61**, 250–254 (1977).

[2] H. Haas, ''Uber den Einfluss des Einfachechos auf die Horsamkeit von Sprache,'' Acustica **1**, 49–58 (1951).

[3] H. Wallach, E. B. Newman, and M. R. Rosenzweig, ''The precedence effect in sound localization,'' Am. J. Psychol. **52**, 315–336 (1949).

[4] J. P. A. Lochner and J. F Burger, ''The influence of reflections on auditorium acoustics,'' J. Sound Vib. **1**, 426–454 (1964).

[5] H. G. Latham, ''The signal-to-noise ratio for speech intelligibility—An auditorium acoustics design index,'' Appl. Acoust. **12**, 253–320 (1979).

[6] J. S. Bradley, ''Predictors of speech intelligibility in rooms,'' J. Acoust. Soc. Am. **80**, 837–845 (1986).

[7] J. S. Bradley, ''Speech intelligibility studies in classrooms,'' J. Acoust. Soc. Am. **80**, 846–854 (1986).

[8] J. S. Bradley, ''Relationships among measures of speech intelligibility in rooms,'' J. Audio Eng. Soc. **46**, 396–405 (1998).

[9] F. H. Bess, ''Classroom acoustics: An overview,'' Volta Review **101**, 1–14 (2001).

[10] A. K. Nábělek and L. Robinette, ''Influence of the precedence effect on word identification by normally hearing and hearing-impaired subjects,'' J. Acoust. Soc. Am. **63**, 187–194 (1978).

[11] Anon, ''American national standard acoustical performance criteria, design requirements and guidelines for schools,'' ANSI Standard S12.60–2002.

[12] Anon, ''Acoustics—Threshold of hearing by air conduction as a function of age and sex for otologically normal persons,'' ISO 7029–1984 (E), International Organisation for Standardisation.

[13] M. Picard and J. S. Bradley, ''Revisiting speech interference and remedial solutions in classrooms,'' Audiology **40**, 221–244 (2001).

[14] W. T. Chu and A. C. C. Warnock, ''Directivity of human talkers,'' J. Acoust. Soc. Am. **110**, 2664 (2001).

[15] R. Plomp and A. M. Mimpen, ''Effect of the orientation of the speaker's head and azimuth of a noise source on the speech-reception threshold for sentences,'' Acustica **48**, 325–328 (1981).

[16] R. Y. Litovsky and H. S. Colburn, ''The precedence effect,'' J. Acoust. Soc. Am. **106**, 1633–1654 (1999).

[17] A. K. Nábělek and J. M. Pickett, ''Reception of consonants in a classroom as affected by monaural and binaural listening, noise, reverberation, and hearing aids,'' J. Acoust. Soc. Am. **56**, 628–639 (1974).

[18] R. D. Reich and J. S. Bradley, ''Optimizing classroom acoustics using computer model studies,'' Can. Acoust. **26**, 15–21 (1998).

[19] J. S. Bradley, R. D. Reich, and S. G. Norcross, ''On the combined effects of signal-to-noise ratio and room acoustics on speech intelligibility,'' J. Acoust. Soc. Am. **106**, 1820–1828 (1999).

An improved water-filled impedance tube

Preston S. Wilson,[a] Ronald A. Roy, and William M. Carey
Department of Aerospace and Mechanical Engineering, Boston University, 110 Cummington Street, Room 101, Boston, Massachusetts 02215

(Received 4 October 2002; revised 28 February 2003; accepted 17 March 2003)

A water-filled impedance tube capable of improved measurement accuracy and precision is reported. The measurement instrument employs a variation of the standardized two-sensor transfer function technique. Performance improvements were achieved through minimization of elastic waveguide effects and through the use of sound-hard wall-mounted acoustic pressure sensors. Acoustic propagation inside the water-filled impedance tube was found to be well described by a plane wave model, which is a necessary condition for the technique. Measurements of the impedance of a pressure-release terminated transmission line, and the reflection coefficient from a water/air interface, were used to verify the system. © *2003 Acoustical Society of America.*
[DOI: 10.1121/1.1572140]

PACS numbers: 43.58.Bh, 43.30.Xm, 43.30.Jx [AJZ]

I. INTRODUCTION

Impedance tubes are commonly used to measure the acoustic properties of materials and structures (wind instruments, acoustical filters, etc.) with air or other gases as the host medium. The technology is mature, as evidenced by an extensive literature (see reviews by Beranek[1] and Dalmont[2]), the availability of standardized techniques,[3,4] techniques for specialized cases,[5,6] and the availability of commercially produced impedance tubes. Despite this maturity, measurement of impedance still requires great care and very careful control of the measurement parameters, such as system temperature and sensor position.[2] Absolute calibration of impedance tube measurements remains difficult. There is currently no accepted material for use as a standard reference.[3] Measurement precision (repeatability) can be reported, but in most cases, accuracy is estimated or inferred by comparison to theory or to the results of other measurement techniques.

The need for acoustic properties measurement also exists for materials or structures with water as the host medium, but there are two additional barriers to the realization of a water-filled impedance tube. The first is the minimization of elastic waveguide effects which result from the coupling between the fill-liquid and the tube walls. The second is the measurement of acoustic pressure without perturbation of the field within the tube and absent of any signal corruption from wall motion.

There have been a number of water-filled impedance tube techniques and measurements reported in the literature. These include pulse tubes,[7,8] active cancellation techniques,[9,10] and two-sensor transfer function techniques.[11,12] Although frequency independent, the water/air interface has been used in two of these works for measurement validation.[7,11] It approximates a pressure-release surface with a reflection coefficient $R=-1=1\angle 180°$. Using a pulse tube technique, and reporting only the phase of the complex reflection coefficient, Kuhl *et al.*[7] reported a maximum deviation of approximately 10° from the expected value of 180°. Adapting the standardized two-sensor transfer function technique for use in water, Corbett[11] reported measurements of reflection coefficient magnitude and phase that deviated from the expected values by as much as 10% and 30°, respectively.

Reported here is a water-filled impedance tube instrument, which utilizes the two-sensor-three-calibration technique[13] and is capable of improved accuracy and precision. Although the present instrument operates between 5 and 9 kHz, the basic technique is not limited to such a small range of operation. The two-sensor-three-calibration technique is reviewed in Sec. II. Performance improvements were achieved through minimization of elastic waveguide effects, discussed in Sec. III, and through use of a nonintrusive wall-mounted acoustic pressure sensor, discussed in Sec. IV. For the two-sensor method to succeed, the acoustic waves traveling within the impedance tube, specifically between the sample and the acoustic sensors, must be plane waves to a high degree of approximation. Experiments used to validate the plane wave behavior of the waveguide used in the impedance tube are presented in Sec. V. In Sec. VI, the impedance tube instrument is described, the performance of the system is reported, a comparison to other systems is made, and the results of a measurement error analysis are presented.

II. METHOD OF IMPEDANCE MEASUREMENT

The standard two-sensor method[3] requires plane wave propagation within a rigid tube and relies on the ability to noninvasively measure acoustic pressure at two positions in the tube. Using the measurement scheme illustrated in Fig. 1 and excitation of the source with random noise, the transfer function is measured between the two acoustic pressure sensors. This transfer function is a complex quantity composed of the amplitude ratio and phase difference between the acoustic pressure measured at positions 1 and 2. From the transfer function measurement, one can calculate either the complex reflection coefficient or the normal specific acoustic impedance at the interface.[3] In the standard method, a cali-

[a]Electronic mail: psw@bu.edu

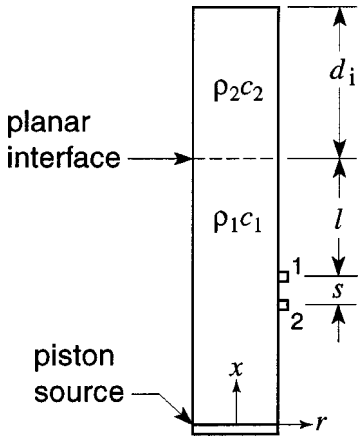

FIG. 1. A schematic diagram of the impedance tube system is shown. A cylindrical tube has a piston-source at the bottom. Acoustic pressure sensors are wall mounted at positions labeled 1 and 2. Below the interface, the tube is filled with distilled water with known properties $\rho_1 c_1$. Above the interface, a material with unknown properties $\rho_2 c_2$ fills the tube to a height d_i. Sensor 1 is positioned a distance l from the interface and sensor separation distance is s. Coordinate axes indicate the longitudinal x and the radial r directions.

bration procedure must also be performed using a sensor switching technique and a strongly absorbing termination. Switching wall-mounted sensors back and forth between the two measurement positions (with the required precision) is impractical with a water-filled tube, as is a strongly absorbing termination. Therefore, the two-sensor-three-calibration method[13] is used, in which no sensor switching or absorptive termination is required. Instead, calibration is achieved through the use of three reference terminations with known impedance values. Otherwise, the method is equivalent to the standard method.

An open-ended, water-filled tube of the same inner diameter and wall thickness as the impedance tube is used as the reference termination. The water height is varied to achieve terminations of three different lengths, which are selected such that resonance and antiresonance are avoided, thereby greatly reducing the importance of a detailed theoretical description of the loss mechanisms.[13] This requirement limits the usable frequency range for any set of three reference terminations to about two octaves. Multiple sets of reference terminations (and hydrophone spacings) are required in order to realize an increased frequency range.

The procedure and theoretical formulation from Ref. 13 for measurement of impedance using the two-sensor-three-calibration technique is summarized below. A complete derivation is given in Ref. 13. The frequency is kept below cutoff for the first higher-order mode, such that only plane waves travel within the tube. The calibration is performed first, with the reference terminations and the impedance tube filled with distilled water with known density ρ_1 and sound speed c_1. One measures the transfer function $y^{(i)}$ for each of the three reference terminations $Z^{(i)}$. Subsequently, measurement of the transfer function y for any unknown termination yields its impedance z in terms of the three calibration transfer functions and $\rho_1 c_1$,[13]

$$\frac{z}{\rho_1 c_1} = \frac{A+B+C}{D+E+F}, \tag{1}$$

where

$$A = Z^{(1)} Z^{(3)} (y^{(1)} - y^{(3)})(y - y^{(2)}),$$
$$B = Z^{(1)} Z^{(2)} (y^{(2)} - y^{(1)})(y - y^{(3)}),$$
$$C = Z^{(3)} Z^{(2)} (y^{(3)} - y^{(2)})(y - y^{(1)}),$$
$$D = Z^{(1)} (y^{(3)} - y^{(2)})(y^{(1)} - y),$$
$$E = Z^{(2)} (y^{(1)} - y^{(3)})(y^{(2)} - y),$$
$$F = Z^{(3)} (y^{(2)} - y^{(1)})(y^{(3)} - y).$$

The reference terminations are modeled as pressure-release-terminated transmission lines, with dimensionless impedances $Z^{(1)}$, $Z^{(2)}$, and $Z^{(3)}$, each given by

$$Z^{(i)} = z^{(i)}/\rho_1 c_1 = i \tan k d_i, \tag{2}$$

where $k = \omega/c_1$, the length of the termination is d_i, and a time dependence $\exp(i\omega t)$ has been assumed. It is reiterated that if the calibration lengths d_i are chosen such that resonance and antiresonance of Eq. (2) is avoided, loss mechanisms can be neglected and a real wave number $k = \omega/c_1$ is sufficient. This is demonstrated in Sec. VI.

III. ELASTIC WAVEGUIDE EFFECTS

The plane wave assumption used in the derivation of Eqs. (1) and (2) is easily satisfied with an air-filled impedance tube at low enough frequencies, because the tube walls are effectively rigid. For acoustic propagation within a water-filled impedance tube with steel walls, a number of elastic waveguide effects can arise, including a dispersive sound speed, radial particle displacement, wavefront curvature, and the existence of at least one higher-order mode at all frequencies.

Del Grosso[14] obtained particle displacement field equations [Eqs. (23), Ref. 14] and a dispersion relation [Eq. (24), Ref. 14] for the axisymmetric modes of an inviscid-liquid-filled cylindrical tube with arbitrary-thickness elastic walls, where the outermost radial boundary condition was approximated as pressure release. These equations were used to evaluate a variety of candidate waveguide dimensions, using stainless steel as the wall material. The calculations indicate that a wall-thickness to inner-radius ratio close to unity results in less than 1% dispersion in the lowest-order mode (labeled ET0 by Del Grosso), up to approximately the rigid waveguide cutoff frequency. The ET0 mode exhibits nearly plane wavefronts and little radial particle motion. The next higher-order mode (ET1) persists down to zero-frequency but it displays about 14 times more wavefront curvature and about 20 times more radial particle motion than ET0. Based on these results, it appears that waves excited by a piston source isolated from the wall of the cylinder should couple well into ET0 and poorly into ET1, leaving only plane-like waves propagating in the waveguide.

Although Del Grosso's results have been experimentally verified for a number of cases,[15] experiments were conducted to confirm the theory for the parameters of interest here. A

TABLE I. Material and geometric parameters of the experimental waveguide discussed in Secs. III–V are shown. The inner liquid was distilled water, with sound speed c_1 calculated from a temperature measurement and density ρ_1. The tube wall material was grade 304L stainless steel, with longitudinal and transverse sound speeds c_l and c_t, respectively,[22] and density ρ_s measured by volumetric displacement of a small sample. Tube dimensions are inner radius a, outer radius b, and length L.

Sound speeds			
Water	304L s.s.	Densities	Dimensions
$c_1=1491$ m/s	$c_l=5640$ m/s $c_t=3070$ m/s	$\rho_1=998$ kg/m^3 $\rho_s=7970$ kg/m^3	$a=2.54$ cm $b=5.08$ cm $L=150.2$ cm

thick-walled stainless steel cylindrical tube was employed with dimensions and material properties shown in Table I. An aluminum piston driven by a mass-loaded piezoelectric element (shown in Fig. 2) was fitted to the bottom of the tube, which was positioned vertically and filled with distilled and degassed water. Time-of-flight measurements were conducted inside the tube using a miniature hydrophone (Brüel and Kjær Model 8103) positioned just under the surface of the water at the open end of the tube. Four cycle sinusoidal pulses were generated and these propagated back and forth between the source and the open end. The hydrophone signal was band pass filtered and recorded using a digital oscilloscope. The pulses were sufficiently separated in time and the time between pulses was extracted using autocorrelation analysis. Results obtained at several frequencies are presented in Fig. 3 and compare favorably with Del Grosso's Eq. (24). The predicted and measured dispersion from 3 to 15 kHz is less than 0.5%, and the speeds are just a few percent below the intrinsic medium sound speed.

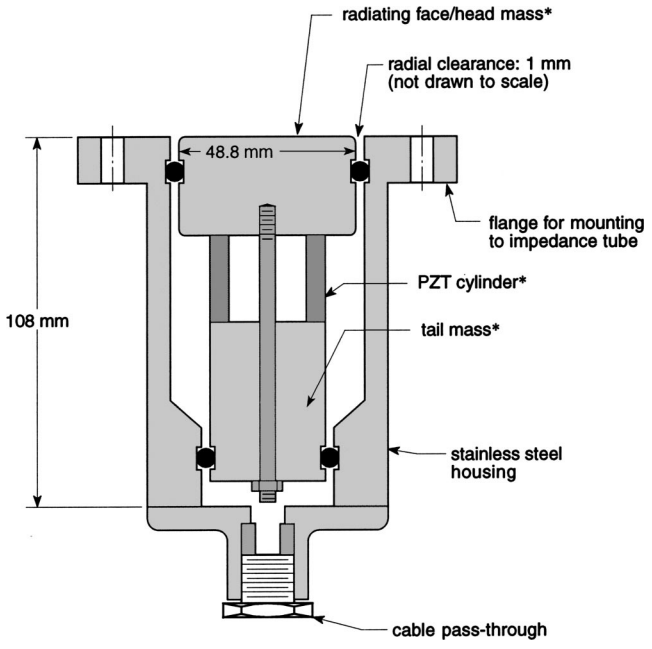

FIG. 2. A schematic diagram of the sound source is shown in a cut-away view. A Tonpilz-type transducer is enclosed and mounted in an air-filled stainless steel housing. The active elements, labeled (*), are decoupled from the housing using rubber o-rings. The housing is sealed to the impedance tube using another o-ring in the flange (not shown). The electrical wiring (not shown) exits the housing through a water-proof cable pass-through.

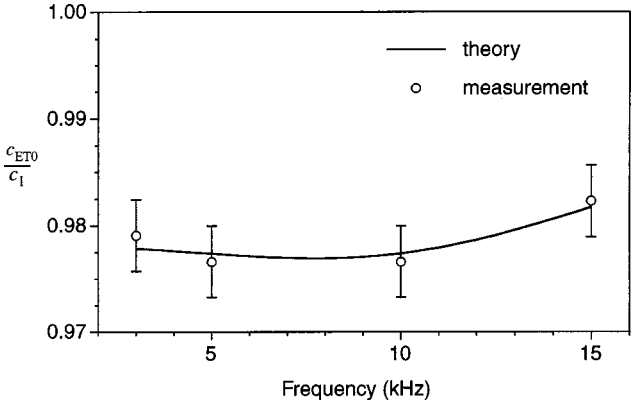

FIG. 3. Measured waveguide phase speed is compared to Eq. (24) from Del Grosso[14] for the planelike ET0 mode. The values are normalized by c_1, the intrinsic sound speed in water for the experimental temperature. Error bars due to ± 0.5 mm uncertainty in waveguide length and 2.5-μs time resolution are shown.

Wavefront curvature was measured by scanning a 1-mm-diam needle hydrophone across the top of the tube, 1 cm below the water surface. Continuous wave excitation was used and rms pressure measurements, made with a digital oscilloscope, were recorded as a function of position. The radial pressure profiles exhibited a concave-up curvature. Deviation between the acoustic pressure at the center of the tube and at the wall was 1% at 5 kHz, 2% at 10 kHz and 5% at 15 kHz, in qualitative agreement with predictions made using Del Grosso's Eqs. (23).

These measurements confirm that the field inside the waveguide is not truly plane. A small amount of dispersion and wavefront curvature is present. It is shown in Sec. V that despite this deviation from plane wave behavior, a plane wave model is sufficient to describe propagation inside this waveguide.

IV. ELIMINATION OF PERTURBATIONS CAUSED BY SENSORS

Corbett[11] reported that hydrophones deployed within a water-filled impedance tube could perturb the acoustic field and, along with sensor location uncertainty, could contribute significantly to impedance measurement error. Wall-mounted sensors could be less invasive and positioned with greater accuracy, but tube wall motion prevented their use. Calculations using Del Grosso's Eqs. (23) and (24) indicated that for the waveguide parameters given in Table I, both radial and longitudinal particle motion is present in the tube wall. A wall-mounted hydrophone with reduced wall coupling in both directions is needed. However, a high impedance in the radial direction must be maintained since the wall-mounted sensor must not appear as an acoustically soft region in the wall.

This was achieved using a lead-zirconate-titanate (PZT) disc transducer mounted in a cylindrical steel housing, as shown in Fig. 4.[16] The two parts of the housing are threaded together and compress the mica/PZT/mica layered stack between the steel window and the base of the housing, which results in sensitivity to acoustic pressure at the center of the steel window. The mica layers electrically isolate the PZT

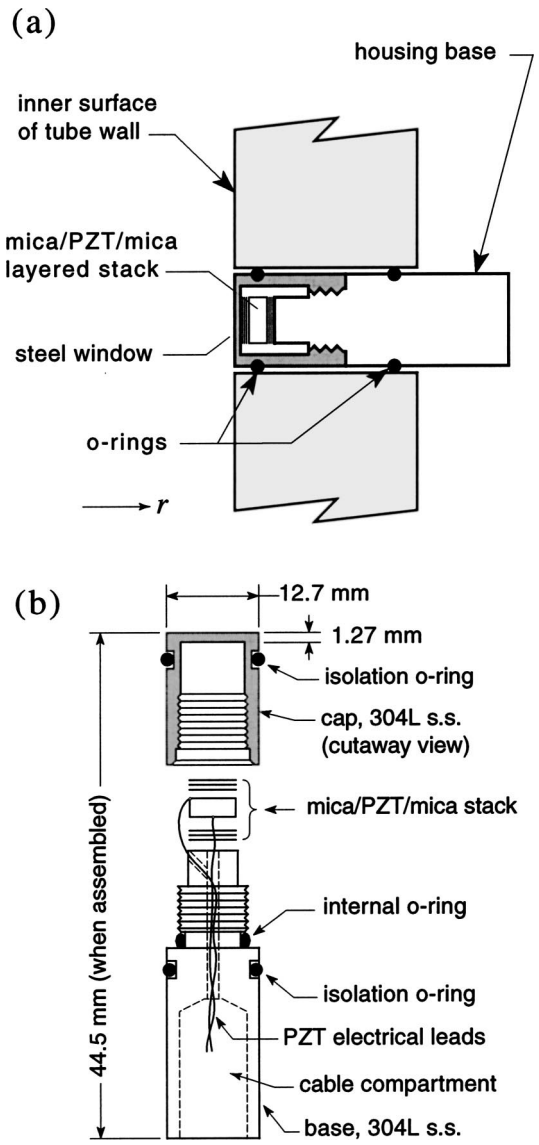

FIG. 4. (a) A schematic diagram of the wall-mounted hydrophone is shown in a cut-away view. The radial direction is indicated with an arrow and the letter r. (b) A more detailed schematic of the hydrophone is shown in exploded view. The dimensions of the disk-shaped PZT element are: 6.35 mm diameter×2.54 mm thick. A shielded cable (not shown) is potted into the cable compartment. Mechanical drawings and additional details are available.[16] Hydrophone sensitivity is -233 ± 3 dB re 1 V/μPa from 1 to 20 kHz.

element and help to decouple shearing motion between the sensor housing and the PZT element, yet stiffness in the radial direction is maintained. Isolation from wall motion is primarily provided by the two rubber o-rings. Despite being free to move in the radial direction in response to a *constant* radial force, the density and stiffness of the hydrophone results in a high *acoustical* input impedance. Some clearance must be present between the sensor and the mounting hole, so that the o-rings provide isolation. However, too much clearance results in acoustic energy loss. A mounting hole with a diameter 0.4%–0.8% larger than the hydrophone's diameter was found to be sufficient.

An experiment was conducted to verify that the presence of these hydrophones did not significantly perturb the acoustic field inside the impedance tube. Using the same arrangement described in Sec. III, the source was excited with a broadband signal and a spectrum analyzer was used to measure the acoustic pressure as a function of frequency. Spectra were measured in the tube before the mounting holes were drilled and again after the hydrophones were installed. The average deviation between the before and after spectra was approximately 0.5 dB in the operating range of the impedance tube, 5–9 kHz.

Air trapped in the clearance gap and in the o-ring grooves can also introduce acoustic energy loss and alter the boundary conditions at tube wall. It is difficult to prevent this unless the insertion of the hydrophones into the mounting holes is done underwater. If this is not possible, wetting of the phones in degassed water prior to insertion is helpful. Subsequent filling of the impedance tube with degassed water will then allow for the dissolution of any trapped air. In practice, this can take a number of hours but the effect of trapped air is easily detectable. With a highly reflective water/air interface terminating the impedance tube, the measured transfer function between the hydrophones will exhibit sharp peaks and nulls in a properly functioning and air-free system. These extrema are due to nulls in the pressure field which occur at integer multiples of a half wavelength from the top of the tube. The presence of even minute air bubbles will change the effective sound speed and induce acoustic energy loss and thereby shift the frequency and reduce the sharpness of these extrema.

V. VERIFICATION OF PLANE WAVE PROPAGATION

Two experiments were conducted to determine if a plane wave model was sufficient to describe acoustic propagation in the impedance tube. Furthermore, propagation measurements serve as an additional check that the wall-mounted sensors do not perturb the field.

In the first experiment, the frequency response of the open water-filled tube was measured, as described in Sec. IV, and the resonance frequencies were obtained. A piston driven by an electromagnetic shaker was used as a source in this experiment. Modeling it as a simple harmonic oscillator with constant force input, suspension stiffness s and piston mass m, resonance of the combined source/tube system occurs when[17]

$$\omega m - s/\omega + \rho_1 c_{\text{eff}} S \tan k_{\text{eff}} L = 0, \tag{3}$$

where ω is the angular frequency, S is the cross-sectional area, L is the length of the tube and $k_{\text{eff}} = \omega/c_{\text{eff}}$. The phase speed predicted by Del Grosso's Eq. (24) averaged across the experimental frequency range was used as the effective sound speed c_{eff} in the tube, which was 1463 m/s for the experimental temperature of 25.5 °C. Equation (3) was solved numerically, using the parameters from Table I and previously measured[16] source parameters $m = 0.187$ kg and $s = 3500$ N/m. The results are shown in Fig. 5. Once the dynamics of the source are considered, a plane wave model with an effective sound speed based on the properties of the elastic waveguide is sufficient to make accurate resonance predictions.

The experiment was repeated at a 51 different positions down the center of the tube, which yielded measurements of

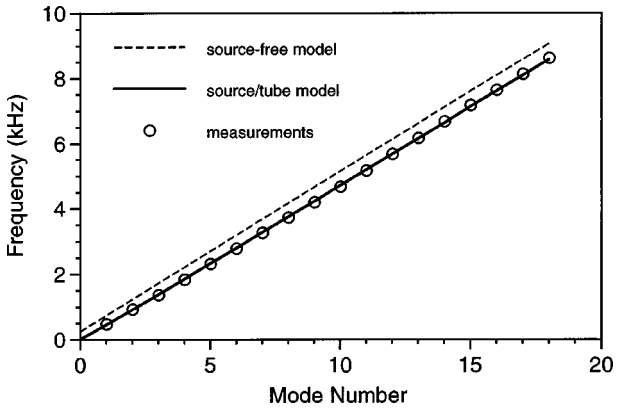

FIG. 5. Measured resonance frequencies of the open, water-filled tube are shown and compared to the model. The solid line is drawn through the resonances predicted by Eq. (3) for the combined source/tube system. The dashed line is drawn through the resonances predicted by Eq. (3) with $m=s=0$, representing the acoustics of the tube with no source.

the standing wave pattern at a number of frequencies. The pressure amplitude of standing plane waves in a tube with a velocity boundary condition at $x=0$ and vanishing pressure at $x=L$ is given by

$$p(x)=A_0\frac{\sin[k_{\text{eff}}(L-x)]}{\cos k_{\text{eff}}L}, \tag{4}$$

where A_0 is an amplitude factor proportional to piston velocity, and $k_{\text{eff}}=\omega/c_{\text{eff}}-i\alpha_0$. Agreement between measurement and Eq. (4) is seen in Fig. 6, where the measured data have been normalized by the maximum pressure at each frequency, A_0 was set to unity, the predicted effective sound speed was $c_{\text{eff}}=1450$ m/s at the experimental temperature of 20.6 °C, and $\alpha_0=0.09\ \text{m}^{-1}$ was obtained from the best fit between measurement and Eq. (4) at the pressure null near $x=0.4$ m in the bottom frame of Fig. 6.

The experimental results shown in Figs. 5 and 6 indicate that a plane wave model, suitably modified by the use of an effective sound speed, is capable of describing the resonance frequencies and standing wave patterns of the current water-filled waveguide. There is a small amount of attenuation in the system but the imaginary part of the wave number is less than $\frac{1}{2}$% of the real part above 5 kHz.

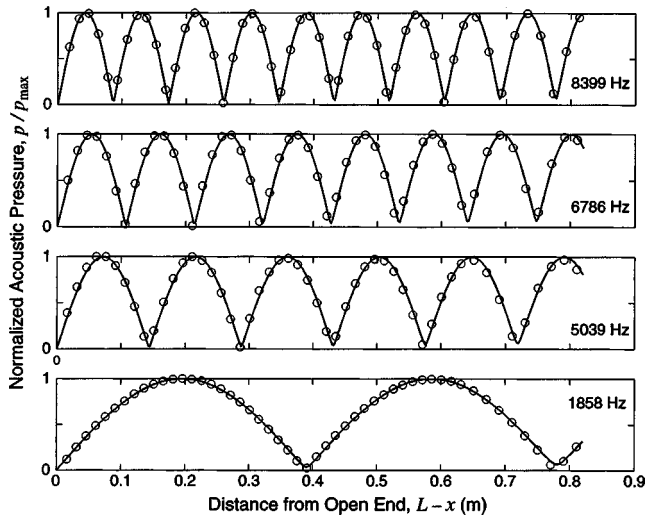

FIG. 6. The standing wave pattern within the impedance tube at four frequencies: Measurement (open circles) and Eq. (4) (solid line).

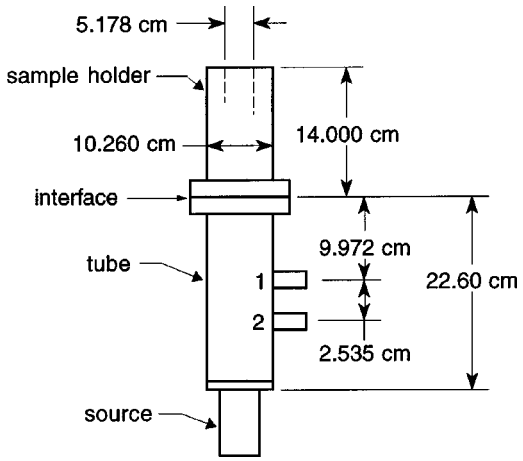

FIG. 7. The dimensions of the impedance tube and sample holder are shown. The material is 304L stainless steel. The two sections are attached using flanges. If needed, a thin mylar sheet can be fitted between the sample holder and the tube, to separate the sample from the water below the interface.

VI. IMPEDANCE TUBE INSTRUMENT

The length of the tube already described was appropriate for propagation studies but the effects of attenuation, already seen to be small, are further reduced by minimizing the tube length. Following tube length and sensor separation distance guidelines given in the ASTM standard document,[3] an impedance tube and sample holder were constructed using tube radii nominally the same as those already discussed. Tube dimensions are presented in Fig. 7 and a schematic diagram of the instrumentation and supporting equipment appears in Fig. 8. The piezoelectric-driven piston source described in Fig. 2 was used but any piston-type source is sufficient, as long as it is decoupled from the tube wall and excites plane waves with a signal to noise ratio greater than 10 dB.[3] Note that increasing the sensor separation distance s lowers the minimum usable frequency of the instrument and decreasing the inner radius of the tube increases the maximum usable frequency.[3,13]

A. Measurement procedure

The first step in the procedure involves measurement of the effective propagation speed in the tube. System calibration is sensitive to small changes in the speed of sound in the tube and therefore sensitive to temperature, which is monitored using a digital multi-meter and a thermocouple attached to the outside of the tube. Calibration and sound speed measurement must be repeated if the temperature of the tube changes by about 0.5 °C but the higher heat capacity of water makes the water-filled impedance tube less sensitive to room temperature changes than an air-filled tube.

The tube is filled with distilled and degassed water, preferably several hours before operation. This insures temperature equilibrium and the dissolution of any air trapped between the sample holder and the tube, around the source

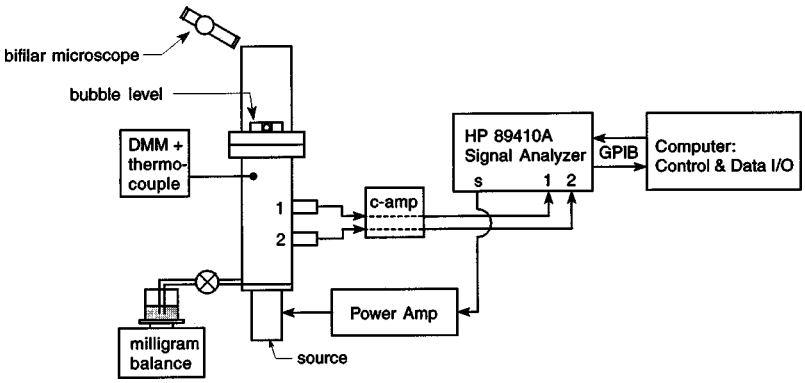

FIG. 8. The impedance tube system, including support equipment and instrumentation, is shown in a schematic diagram. Signals from the acoustic pressure sensors (labeled 1 and 2) are conditioned with a charge amplifier and recorded with a Hewlett-Packard 89410A signal analyzer, which also generates the excitation signal. A power amplifier increases the voltage of the excitation signal. A bifilar microscope is used to measure the height of the fluid column relative to the top of the tube. Additional details are given in the text.

piston, or around the hydrophones. The water level is obtained to approximately 0.05 mm accuracy by using the bifilar microscope to measure the distance from the water surface to the top of the tube. Signal generation and transfer function measurement is performed by a Hewlett-Packard 89410A signal analyzer. The sound source is driven with 5-9-kHz periodic chirps or band-limited pseudorandom noise; chirps are useful for single short-time measurements and noise is useful for time-averaged measurements. The transfer function y_0 between the two wall-mounted hydrophones is measured and from the position of nulls and peaks, the *in situ* sound speed c_{eff} can be calculated based on the water level.

The system is now ready for the three calibration measurements to be performed. The lengths 1.5, 2.5 and 3.5 cm are selected to avoid any extrema, as previously mentioned. The appropriate volume of water is removed by monitoring the milligram balance and a transfer function ($y^{(1)}$, $y^{(2)}$, $y^{(3)}$) is measured for each length (d_1, d_2, d_3). This completes the calibration procedure. The unknown material is installed and the transfer function y is measured. The unknown impedance is then calculated using the three calibration measurements ($y^{(1)}$, $y^{(2)}$, $y^{(3)}$) and Eq. (1). In order to minimize bias error in the transfer function measurements, the resolution bandwidth is minimized and a sufficient number of averages obtained.[18] If a membrane is used to separate the sample from the water below the interface, the lengths of the calibration terminations must be set by removal of water from the top of the tube with a volumetric pipette.

The calibration can be verified efficiently by using the first transfer function measurement y_0 as a test case. This corresponds to a fourth length of fluid d_0, which can be considered a pressure-release-terminated transmission line, whose length is known from the microscope measurement.

B. Verification of impedance tube system

The pressure-release-terminated transmission line described by Eq. (2) has a complex, frequency dependent input impedance. Short lengths with no resonances or antiresonances are used as calibration terminations and losses are neglected. Longer transmission lines do contain extrema and serve as a difficult test for any impedance tube because their input impedances can vary over several orders of magnitude. Verification measurements are compared to a model in which propagation in the bulk fluid is still considered lossless but interaction with the walls will be accounted for using a complex wave number

$$\hat{k}=\frac{\omega}{c_{\text{eff}}}+(1-i)\,\alpha_{\text{walls}}. \tag{5}$$

The approximation $\omega/c_{\text{eff}} \gg \alpha_{\text{walls}}$ is assumed and thermal losses are considered negligible compared to viscous losses, which are characterized by[19]

$$\alpha_{\text{walls}}=\frac{1}{a}\sqrt{\frac{\mu\omega}{2\rho_1 c_{\text{eff}}^2}}, \tag{6}$$

where a is the inner radius of the tube and the viscosity of distilled water is taken to be $\mu=0.907\times10^{-3}$ kg/(m·s), $\rho_1=997$ kg/m^3, $c_{\text{eff}}=1457$ m/s, all at the experimental temperature of 24.0 °C.

Energy also leaves the system via the water/air interface at the open end of the sample holder. Approximating this as a piston in an infinite baffle and using Eq. (8.68b) in Ref. 17, one finds that in the 5-9-kHz frequency range, the magnitude of the radiation impedance varies about the progressive plane wave value $(\rho c)_{\text{air}}$ and possesses an average value within 6% of $(\rho c)_{\text{air}}$. The sample holder was therefore modeled as a layer of water terminated with an infinite length air-filled transmission line, with input impedance

$$z=\rho_1 c_{\text{eff}}\frac{1+R}{1-R}, \tag{7}$$

where the three-medium reflection coefficient is[17]

$$R=\frac{(1-r_1/r_3)\cos\hat{k}d+i(r_2/r_3-r_1/r_2)\sin\hat{k}d}{(1+r_1/r_3)\cos\hat{k}d+i(r_2/r_3+r_1/r_2)\sin\hat{k}d}. \tag{8}$$

Losses are neglected for the water below the sample holder and for the air outside, therefore $r_1=\rho_1 c_{\text{eff}}$ and $r_3=(\rho c)_{\text{air}}=411$ Pa·s/m at 24.0 °C. Losses are accounted for within the sample holder using $\hat{k}$ and $r_2=\rho_1\,\omega/\hat{k}$. The height of the water within the sample holder is d.

Two verification measurements are shown in Fig. 9 and compared with predictions given by Eqs. (5)–(8). Pseudorandom noise excitation was used, with a Hann window, a resolution bandwidth of 5 Hz, and 50 averages.

To verify that the lossless description of the reference terminations used in the calibration was appropriate, the formulation given by Eq. (7) was compared to Eq. (2) for the

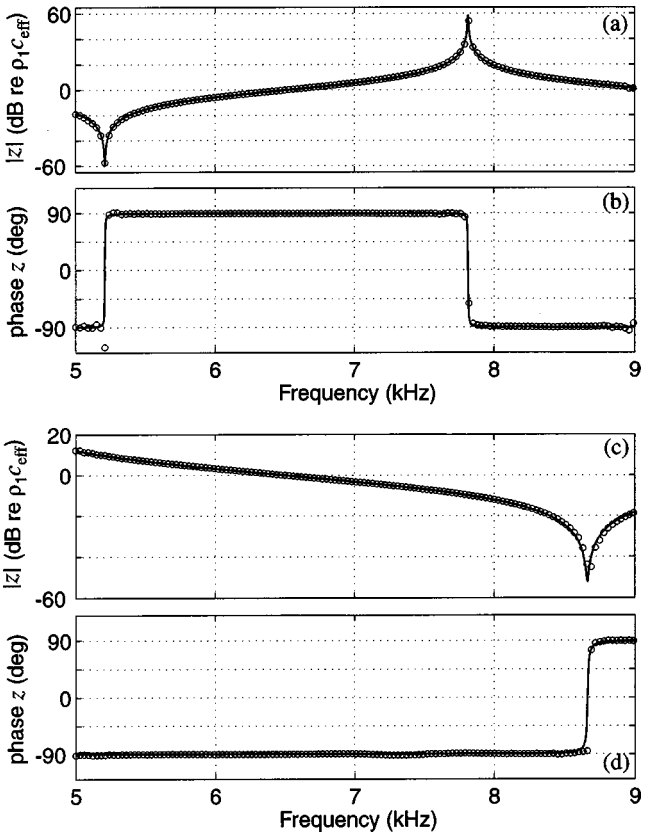

FIG. 9. The system was verified by measuring the impedance z of two different air-terminated transmission lines. The theoretical prediction given by Eq. (7) is shown with solid lines and measurements are shown with open circles. Magnitude and phase for $d=13.98$ cm appears in (a) and (b), and for $d=8.40$ cm in (c) and (d). Only every sixth measurement data point is shown, so that the theoretical curves remain visible.

three reference termination lengths and found to differ in magnitude by at most 8 parts in 10 000 and typically by less than 2 parts in 10 000. In addition, Eq. (7) was substituted for Eq. (2) and then Eq. (1) was recalculated for the $d=13.98$ cm case. The difference between this and the measurement result shown in Fig. 9, averaged across 5–9 kHz, was less than 0.0012 dB. The greatest difference, which only occurred at a few data points immediately surrounding the extrema, was less than 1 dB.

The reflection coefficient of a water/air interface was used for further system verification. The impedance z was measured from a water/air interface and converted to a reflection coefficient by using $R=(z-\rho_1 c_{\text{eff}})/(z+\rho_1 c_{\text{eff}})$. The result is shown in Fig. 10 and should be compared to the expected value of $R\simeq 1\angle 180°$. The increased scatter below 6 kHz is due to reduction of signal-to-noise ratio caused by the limited frequency range of the source used in this system. This is most apparent in Fig. 10, but can also be seen in the phase measurement for the 14-cm case in Fig. 9.

In order to compare this reflection coefficient measurement to the two others that were found in the literature,[7,11] phase and magnitude values were averaged across the 5-9-kHz frequency range to obtain mean values, representing accuracy. Measurement range was used to create error bars, representing precision. The three are compared in Fig. 11. It is clear that for this particular case, the present impedance

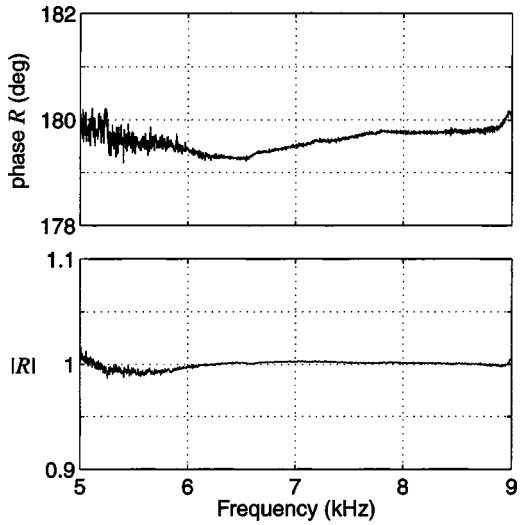

FIG. 10. The measured phase and magnitude of the reflection coefficient of a water/air interface is shown.

tube yields the most accurate and precise measurement.

The repeatability of the instrument was examined by obtaining 50 impedance measurements of the 14-cm length air-terminated transmission line over the course of 35 min. Each of the individual measurements was made as described for Fig. 9, except a periodic chirp was used as the excitation signal. It was found that the measured impedance was changing over time in a manner quantitatively consistent with a length change due to evaporation of water from the open end of the sample holder. This trend was removed and the standard deviation of the magnitude and phase of the impedance at each frequency bin was calculated and then averaged over the 5-9-kHz frequency range. The result, representing frequency-averaged repeatability, was ± 0.0035 dB $re\ \rho_1 c_{\text{eff}}$ in impedance magnitude and $\pm 0.027°$ in impedance phase.

C. Measurement error

A number of authors have analyzed the sources of error in the two-sensor impedance tube measurement tech-

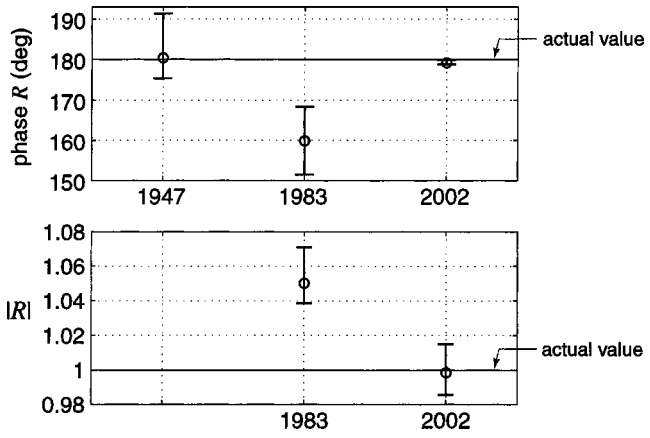

FIG. 11. Accuracy and precision of three impedance tube systems as expressed in the measurement of the reflection coefficient of a water–air interface. Open circles represent the average measurement values and the error bars represent the measurement ranges for the 5–9-kHz frequency range. The 1947 and 1983 data were obtained from Ref. 7 (p. 429) and Ref. 11 (p. 91), respectively. Only phase data was reported in Ref. 7.

nique.[18,20,21] There are two classes: errors associated with the measurement of transfer functions and errors associated with the other measured parameters (sensor position, length of the reference terminations, speed of sound within the impedance tube). Approximate analytical formulations exist for the prediction of the former class of error, which is proportional to the magnitude of the reflection coefficient. Highly reflective terminations, such as those used here, are subject to the maximum error. Direct numerical simulation is used for the later class. A theoretical analysis of error using these techniques was done for this impedance tube[16] and the results are reported here, in terms of rms error in magnitude and phase of impedance, averaged across the 5-9-kHz frequency range. The approximate predicted impedance measurement error for a 14-cm-long pressure-release-terminated transmission line is 0.190 dB in magnitude and 0.42° in phase. Assuming that the theoretical curves shown in part (a) and (b) of Fig. 9 represent the true impedance, the actual measurement error was 0.28 dB in magnitude and 0.95° in phase, which is in reasonable agreement with the predicted error.

VII. CONCLUSIONS

The two-sensor-three-calibration impedance measurement technique has been implemented in a water-filled impedance tube. For the technique to be successful, propagation within the tube must be limited to plane waves and measurement of acoustic pressure must be achieved without perturbation of the acoustic field within the tube. The first criterion was met by minimization of the elastic waveguide effects which are inherent in a liquid-filled tube. Using an elastic waveguide model for a cylindrical tube, inner and outer wall radii were found which minimized these effects over the frequency range of interest, 5–9 kHz. The second criterion was met by using a vibration isolated, wall-mounted acoustic pressure sensor, with a high acoustic input impedance that maintained the sound-hard boundary condition along the tube wall.

Using a water/air interface as a reference termination, the performance of the present water-filled impedance tube system was compared to the performance of earlier systems and increased measurement accuracy and precision was found. Although the present instrument was designed for a particular range of frequencies, tube radii and sensor positions could be modified for use at other frequencies.

ACKNOWLEDGMENTS

This work was supported by the U. S. Navy Office of Naval Research Ocean Acoustics Program and Boston University.

[1] L. L. Beranek, *Acoustical Measurements* (Acoustical Society of America, Woodbury, NY, 1988), Chap. 7, pp. 294–353.
[2] J. P. Dalmont, ''Acoustic impedance measurement, Part I: A review,'' J. Sound Vib. **243**, 427–439 (2001).
[3] ASTM, ''Standard test method for impedance and absorption of acoustical materials using a tube, two microphones, and a digital frequency analysis system,'' ASTM E 1050-98 (American Society for Testing and Materials, West Conshohocken, PA, 1998).
[4] ASTM, ''Standard test method for impedance and absorption of acoustical materials by the impedance tube method,'' ASTM C 384-95 (American Society for Testing and Materials, West Conshohocken, PA, 1995).
[5] M. Åbom and H. Bodén, ''Error analysis of two-microphone measurements in ducts with flow,'' J. Acoust. Soc. Am. **83**, 2429–2438 (1988).
[6] Y. Champoux and M. R. Stinson, ''Measurement of the characteristic impedance and propagation constant of materials having high flow resistivity,'' J. Acoust. Soc. Am. **90**, 2182–2191 (1991).
[7] W. Kuhl, E. Meyer, H. Oberst, E. Skudrzyk, and K. Tamm, *Sound Absorption and Sound Absorbers in Water* (Dept. of the Navy, Bureau of Ships, Washington, DC, 1947), Vol. 1, Chap. IX, pp. 381–453.
[8] G. A. Sabin, ''Acoustic-impedance measurements at high hydrostatic pressures,'' J. Acoust. Soc. Am. **40**, 1345–1353 (1966).
[9] D. M. Kenney, ''A short water-filled pulse tube for the measurement of the acoustic properties of materials at low frequencies,'' Technical Report No. NSWCCD-TR-97/029 (Naval Surface Warfare Center Carderock Division, West Bethesda, MD, 1997).
[10] J. C. Piquette and S. E. Forsythe, ''Low-frequency echo-reduction and insertion-loss measurements from small passive-material samples under ocean environmental temperatures and hydrostatic pressures,'' J. Acoust. Soc. Am. **110**, 1998–2006 (2001).
[11] S. S. Corbett III, ''A Two-Hydrophone Technique for Measuring the Complex Reflectivity of Materials in Water-Filled Tubes,'' M.S. thesis, Pennsylvania State University, 1983.
[12] J. I. Dunlop, ''Measurement of acoustic attenuation in marine sediments by impedance tube,'' J. Acoust. Soc. Am. **91**, 460–469 (1992).
[13] V. Gibiat and F. Laloë, ''Acoustical impedance measurements by the two-microphone-three-calibration (TMTC) method,'' J. Acoust. Soc. Am. **88**, 2533–2545 (1990).
[14] V. A. Del Grosso, ''Analysis of multimode acoustic propagation in liquid cylinders with realistic boundary conditions–application to sound speed and absorption measurements,'' Acustica **24**, 299–311 (1971).
[15] L. D. Lafleur and F. D. Shields, ''Low-frequency propagation modes in a liquid-filled elastic tube waveguide,'' J. Acoust. Soc. Am. **97**, 1435–1445 (1995).
[16] P. S. Wilson, ''Sound Propagation in Bubbly Liquids,'' Ph.D. dissertation, Boston University, 2002, pp. 62–145 and 257–268.
[17] L. E. Kinsler, A. R. Frey, A. B. Coppens, and J. V. Sanders, *Fundamentals of Acoustics*, 3rd ed. (Wiley, New York, 1982), pp. 128 and 210–214.
[18] J. S. Bendat and A. G. Piersol, *Engineering Applications of Correlation and Spectral Analysis*, 2nd ed. (Wiley, New York, 1993), Sec. 5.2, pp. 113–124.
[19] A. D. Pierce, *Acoustics: An Introduction to Its Physical Principles and Applications* (Acoustical Society of America, Woodbury, NY, 1994), Sec. 10-5, pp. 531–534.
[20] A. F. Seybert and B. Soenarko, ''Error analysis of spectral estimates with application to the measurement of acoustic parameters using random sound fields in ducts,'' J. Acoust. Soc. Am. **69**, 1190–1199 (1981).
[21] H. Bodén and M. Åbom, ''Influence of errors on the two-microphone method for measuring acoustic properties in ducts,'' J. Acoust. Soc. Am. **79**, 541–549 (1986).
[22] ASM International, *Metals Handbook*, 9th ed. (ASM International, Materials Park, OH, 1989), Vol. 17, p. 235.

Short-time fractional Fourier methods for the time-frequency representation of chirp signals[a)]

Chris Capus[b)] and Keith Brown
Ocean Systems Laboratory, School of Engineering & Physical Sciences, Mountbatten Building, Heriot-Watt University, Riccarton, Edinburgh, United Kingdom

(Received 26 February 2002; revised 3 March 2003; accepted 3 March 2003)

The fractional Fourier transform (FrFT) provides a valuable tool for the analysis of linear chirp signals. This paper develops two short-time FrFT variants which are suited to the analysis of multicomponent and nonlinear chirp signals. Outputs have similar properties to the short-time Fourier transform (STFT) but show improved time-frequency resolution. The FrFT is a parameterized transform with parameter, α, related to chirp rate. The two short-time implementations differ in how the value of α is chosen. In the first, a global optimization procedure selects one value of α with reference to the entire signal. In the second, α values are selected independently for each windowed section. Comparative variance measures based on the Gaussian function are given and are shown to be consistent with the uncertainty principle in fractional domains. For appropriately chosen FrFT orders, the derived fractional domain uncertainty relationship is minimized for Gaussian windowed linear chirp signals. The two short-time FrFT algorithms have complementary strengths demonstrated by time-frequency representations for a multicomponent bat chirp, a highly nonlinear quadratic chirp, and an output pulse from a finite-difference sonar model with dispersive change. These representations illustrate the improvements obtained in using FrFT based algorithms compared to the STFT. [DOI: 10.1121/1.1570434]

PACS numbers: 43.60.Cg, 43.60.Lq, 43.80.Ka, 43.30.Zk [JCB]

I. INTRODUCTION

This paper introduces two methods for short-time implementation of the fractional Fourier transform (FrFT). These methods produce time-frequency representations with similar properties to the spectrogram or short-time Fourier transform (STFT), but provide better joint resolution for chirp signals than the conventional representations.

The FrFT is ideally suited to the analysis and synthesis of linear chirp signals. The linear chirps are signals which exhibit a linear change in instantaneous frequency with time and are of particular interest for sonar systems, acoustic communications and channel characterization.

Following a brief introduction to the FrFT, recovery of time-frequency information directly from the transform parameters is considered and an optimal-order fractional Fourier transform for a known linear chirp signal is defined.

The FrFT of the Gaussian function has Gaussian support in all fractional domains. Comparative variance measures are introduced for the FrFT and ordinary Fourier transforms of Gaussian windowed linear chirp signals. These are used to estimate the processing gain in using the FrFT over the conventional Fourier transform with chirp signals. An uncertainty relationship is given for Gaussian windowed linear chirp signals processed using the FrFT. This is seen as the most natural extension of the conventional inequality and is minimized for the two orthogonal domains in which the signal finds its narrowest and widest spread.

The piecewise linear description of a nonlinear chirp signal is demonstrated using a series of nonoverlapping short-time FrFTs. The use of maximally overlapping transforms to estimate instantaneous frequencies is discussed and two fully automated short-time fractional Fourier transforms are put forward, which differ only in their optimization procedures.

These short-time methods can produce time-frequency representations for general non-stationary signals, but are most effective in the analysis of signals which contain continuously varying frequencies. For example, FM components in the vocalization of the Minke whale[1] and bottlenose dolphin whistles[2] would be well suited to FrFT analysis. These techniques will also be of value in analyzing acoustic characteristics of channels and systems excited by chirp signals.

The value of chirp-based methods to acousticians is illustrated by related techniques which have been recently reported. Where speed is of vital importance, the Fourier extension method[3] is likely to be of interest. This technique, similar in principle to the FrFT, involves premultiplication of an input signal by a complex chirp, followed by transformation using the FFT. The process can be tuned to the detection of particular signals through choice of the chirp parameters. Time-frequency information has been recovered from the outputs alongside further practical research on the time and rate resolutions available in discrete domains.[4] Another chirp-based method, of interest for its generality, resolution and low computational cost, is Gribonval's fast matching pursuit algorithm which builds a time-frequency signal representation from a set of chirp-modulated Gabor atoms.[5]

The data presented in this paper have been selected to illustrate the range of applications and complementary strengths of the short-time FrFTs and include a multicompo-

[a)]Based in part on a paper given at the 142nd Meeting of the Acoustical Society of America, Ft. Lauderdale, Florida, 2001.
[b)]Electronic mail: C.Capus@hw.ac.uk

nent bat echolocation pulse, a synthetic quadratic chirp, and a pulse from a finite difference sonar simulation model with suspected dispersive change.

II. THE FRACTIONAL FOURIER TRANSFORM

The FrFT has received much attention in the optics literature since its proposal by Namias,[6] though it remains little used in acoustics. The FrFT formula below, Eq. (1), is a slightly modified form of that given by McBride and Kerr,[7]

$$\mathcal{F}^{\alpha}f(x)=\frac{\exp[-j(\frac{1}{4}\pi\hat{\varphi}-\frac{1}{2}\varphi)]}{(2\pi|\sin\varphi|)^{1/2}}\exp\left(\frac{1}{2}jy^2\cot\varphi\right)\times\int_{-\infty}^{\infty}\exp\left(-\frac{jxy}{\sin\varphi}+\frac{1}{2}jx^2\cot\varphi\right)f(x)dx, \qquad (1)$$

where, α: $\{0.0<\alpha<1.0\}$ defines the transform order, $\varphi=\alpha(\pi/2)$, and $\hat{\varphi}=\operatorname{sgn}\varphi$. There are two special cases: $\mathcal{F}^0 f(x)$ is the identity transform, returning the input signal; $\mathcal{F}^1 f(x)$ is equivalent to the ordinary Fourier transform.

The variables x and y emphasize the generality of the transform, rather than assuming time and frequency for the domains. Even with an input time signal, except for the special cases of $\mathcal{F}^0 s(t)$ and $\mathcal{F}^1 s(t)$, the transform output lies in neither the time domain nor the frequency domain.

A. Time-frequency interpretation of the FrFT output

Almeida[8] has provided a set of steps to describe computation of the FrFT, which can be related to the integral transform as follows:

$$\mathcal{F}^{\alpha}f(x)=\underbrace{\frac{\exp[-j(\frac{1}{4}\pi\hat{\varphi}-\frac{1}{2}\varphi)]}{(2\pi|\sin\varphi|)^{1/2}}}_{\text{step 4}}\underbrace{\exp\left(\frac{1}{2}jy^2\cot\varphi\right)}_{\text{step 3}}\times\int_{-\infty}^{\infty}\exp\left(\underbrace{-\frac{jxy}{\sin\varphi}}_{\text{step 2}}+\underbrace{\frac{1}{2}jx^2\cot\varphi}_{\text{step 1}}\right)f(x)dx.$$

(1) Step 1. Multiply the input signal $f(x)$ by the linear chirp $\exp(\frac{1}{2}jx^2\cot\varphi)$, whose rate is determined by the transform order.
(2) Step 2. Perform a scaled Fourier transform, $\int\exp(-jxy/\sin\varphi)f(x)\mathrm{d}x$. The scaling factor, $1/\sin\varphi$, is also dependent on the fractional transform order.
(3) Step 3. A second chirp multiplication, which occurs in the transform domain—indicated by the change of variable, $\exp(\frac{1}{2}jy^2\cot\varphi)$.
(4) Step 4. The last step involves multiplication by the complex scalar, $\exp^{-j[(1/4)\pi\hat{\varphi}-(1/2)\varphi]}/(2\pi|\sin\varphi|)^{1/2}$.

The two chirp multiplication stages have been described in terms of sequential shearing of the time-frequency plane parallel to the time and frequency axes.[9] The resultant discrete representation is characterized by a set of rhombic elements produced by shearing of the time-frequency lattice by $\cos\varphi$ parallel to the time axis and $\sin\varphi$ parallel to the frequency axis, see Fig. 1. Combination of these shear operations produces a rotation of the conventional time-frequency axes, with the rotation angle, φ, dependent on transform order.

Overall these steps result in integration across the time-frequency plane parallel to the rotated time axis. Calculation of the ordinary Fourier transform can be similarly described as integration in the time-frequency plane over all time, with no axis rotation.

B. Discrete implementation of the FrFT

A number of discrete implementations of the FrFT have been put forward. The most satisfactory, consistent with the important properties of index additivity, unitarity and reduction to discrete Fourier transform (DFT) for unit order, are those based on the discrete Hermite–Gaussian functions.[10,11] To date there is no fast algorithm for exact computation of the discrete FrFT. However, a fast $\mathcal{O}(N\log N)$ algorithm has been proposed, which calculates an approximation to the discrete samples of the FrFT with sufficient accuracy for many applications.[12] A definitive fast FrFT will be a welcome addition to the signal processing canon, but is not necessary for demonstration of the short-time algorithms in this paper. Where consideration is given to differences in execution times, these are between short-time methods, rather than due to the particular discrete FrFT implementations used.

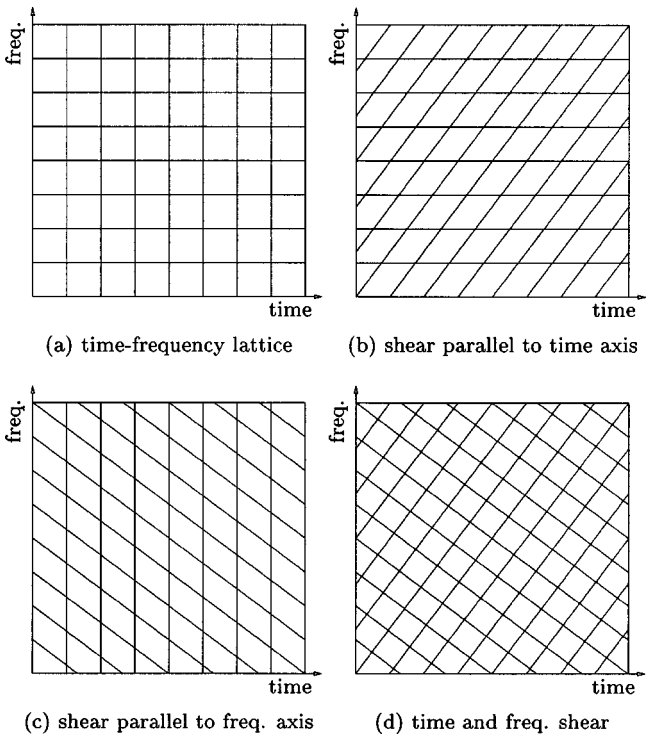

FIG. 1. Shearing in the time-frequency plane and discrete FrFT elements: (a) Conventional time-frequency lattice with rectangular elements; (b) shear of (a) parallel to time axis by $\cos\varphi$; (c) shear of (a) parallel to frequency axis by $\sin\varphi$; (d) combination of (b) and (c) equivalent to rotation by φ.

III. TRANSFORM OPTIMIZATION

The FrFT parameter α is used to tune the transform to provide an optimal response to a given linear chirp signal. When the axis rotation depicted in Fig. 1 is matched to the chirp rate of the signal, the magnitude response reaches its maximum.

In the general linear chirp formula, $e^{j(at^2+bt+c)}$, it is the rate parameter a to which the transform order is matched. The matching process is described geometrically through a plot of the signal's instantaneous frequency, $\phi'(t)=2at+b$, calculated as the derivative of its phase function,[13] see Fig. 2.

Integration across the time-frequency plane for the α-order FrFT produces a signal representation in the domain defined by the u_α axis in Fig. 2. Two transform orders having this same output domain are shown, with axis rotations $\alpha(\pi/2)$ and $(2-\alpha)(\pi/2)$. Taking the simplest case, the optimal order for this signal is defined by

$$\alpha_{\text{opt}}=\frac{2}{\pi}\varphi=-\frac{2}{\pi}\tan^{-1}\left(\frac{1}{2a}\right). \tag{2}$$

The time-frequency discretization for a sampled signal, with time measured in seconds and frequency in Hz, is most easily treated using the linear chirp formula $e^{j2\pi(at^2+bt+c)}$. Under these conditions the geometry of Fig. 2 gives

$$\alpha_{\text{opt}}=-\frac{2}{\pi}\tan^{-1}\left(\frac{\delta f/\delta t}{2a}\right), \tag{3}$$

where

$\delta f=\text{frequency resolution}=f_s/N$ and

$\delta t=\text{time resolution}=1/f_s$,

$f_s=\text{sampling frequency}$,

$N=\text{number of samples}$.

Hence,

$$\alpha_{\text{opt}}=\frac{2}{\pi}\varphi=-\frac{2}{\pi}\tan^{-1}\left(\frac{f_s^2/N}{2a}\right). \tag{4}$$

Equation (4) is used to calculate the optimal order FrFT for a sampled linear chirp signal with known chirp rate. Conversely, Eq. (4) can be rearranged to estimate a signal's chirp rate once the optimal order FrFT has been found.

The position of the maximum peak within the optimal fractional Fourier domain is related to the signal's center frequency. Once again, from the geometry of Fig. 2,

$$\beta=b\sin\varphi=b\sin\left(\alpha\frac{\pi}{2}\right). \tag{5}$$

In the discretely sampled domains the relationship is given by

$$M_\alpha=M_f\sin\varphi=\frac{b}{\delta f}\sin\varphi=\frac{bN}{f_s}\sin\varphi, \tag{6}$$

where M_α and M_f are the numbers of samples offset from the centers of the fractional and frequency domains, respectively. The angle $\varphi=\alpha\pi/2$ is that calculated using Eq. (2) or Eq. (4), for the optimal order transform.

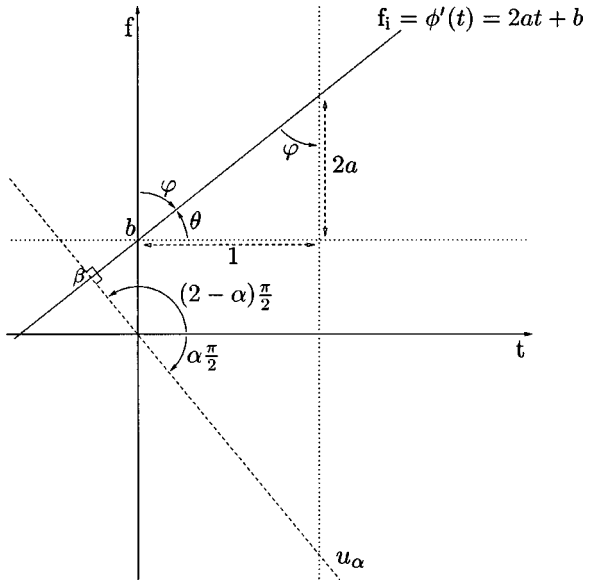

FIG. 2. Geometric interpretation of the relationship between linear chirp rate, a, and fractional Fourier transform order, α.

IV. MEASURING PROCESSING GAIN

Transform optimization maximizes the response to a given linear chirp signal and the FrFT with order α_{opt} provides the most compact fractional domain representation for that linear chirp signal. As with the ordinary Fourier transform, choice of a windowing function is an important factor in determining output resolution. In signal processing, the Gaussian window is commonly used for a number of practical reasons. First, the Fourier transform of the Gaussian is itself Gaussian. Second, the Gaussian minimizes the time-frequency uncertainty relationship with regard to the Fourier transform.[14]

The short proof given in the Appendix shows that similar conditions apply under the FrFT. The extension to discrete domains is made through consideration of the discrete sampling relationships between orthogonal domains and a method is given for calculation of the spread of the Gaussian windowed linear chirp signal in any fractional domain. This provides a measure which is used in Sec. VII for quantitative comparisons between short-time fractional Fourier methods and the STFT.

A. The uncertainty principle in fractional domains

The fractional domain variance formula derived in the Appendix describes the spread of the Gaussian in terms of the standard deviation in the time domain, σ_t,

$$\sigma_\alpha^2=\frac{\sin^2\varphi}{\sigma_t^2}+\sigma_t^2\cos^2\varphi. \tag{7}$$

This is closely related to the uncertainty principle, which in signal processing is usually defined in terms of the signal's energy density, the magnitude squared.[13,14] In this case the relationship is

$$\sigma_\alpha^2 = \frac{\sin^2 \varphi}{4\sigma_t^2} + \sigma_t^2 \cos^2 \varphi. \tag{8}$$

For a signal that is relatively wide in the time domain, $\sigma_t > 1.0$, the value of σ_α^2 is minimized for $\alpha = 1.0 \Rightarrow \varphi = \pi/2$, which defines the Fourier transform. This gives $\sigma_\alpha = \sigma_\omega = 1/2\sigma_t$, and corresponds to the case for which the uncertainty relationship, given in Eq. (9), reaches equality,

$$\sigma_t \sigma_\omega \geqslant \tfrac{1}{2}. \tag{9}$$

Recall that α_{opt} defines the fractional domain providing the most compact representation for a linear chirp signal. The terms $\alpha_{\max}$ and corresponding $\varphi_{\max}$ define the domain with the broadest signal representation. These two orthogonal domains lie $\alpha = 1.0$ apart, with $\alpha_{\max} = \alpha_{\text{opt}} - 1.0$, and are linked by the ordinary Fourier transform.

The value of σ_α is minimized when $\varphi = \varphi_{\text{opt}}$. This is consistent with the uncertainty relationship previously derived for the product of the spreads of a real signal in two arbitrary fractional domains.[15] The inequality is in fact minimized for any Gaussian windowed linear chirp signal represented in the two orthogonal domains $\sigma_{\max}$ and σ_{opt}, with transform orders dependent on chirp rate. Indeed under these conditions the relationship reduces to a generalized form of Eq. (9),

$$\sigma_{\max} \sigma_{\text{opt}} \geqslant \tfrac{1}{2}. \tag{10}$$

The variance of the FrFT of a Gaussian windowed linear chirp can now be calculated in any fractional domain and consequently the variance of the ordinary Fourier transform of a Gaussian windowed linear chirp can also be calculated. For these restricted classes of signal, Eqs. (A6) and (A7) provide comparative compression measures for the ordinary and fractional Fourier transforms in both the continuous and discrete cases.

While these measures apply specifically to the transforms of linear chirp signals, they are also appropriate for estimation of the spread of the transforms of Gaussian windowed nonlinear chirp signals. The accuracy of the estimate will depend on the length of window used, which must be small enough to ensure a reasonable linear approximation to the signal over that time duration.

V. SHORT-TIME FRACTIONAL FOURIER TRANSFORMS

The requirement for transform optimization leads to several possibilities for short-time implementation of the FrFT. Two automated variants of the short-time fractional Fourier transform (STFrFT) are described below.

These implementations have some factors in common. Both use overlapping short-time windows which tend to smooth the output and further smoothing is achieved through choice of an appropriate windowing function. In the following examples a Gaussian window is applied for the reasons outlined in Sec. III. Values are calculated only for the time center of each window. This approach, with maximally overlapping short-time windows, provides frequency information

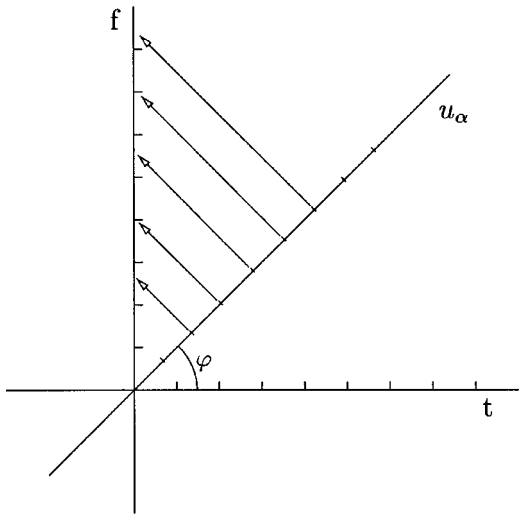

FIG. 3. Projection of the FrFT output perpendicular to the u_α axis in the time-frequency plane provides an instantaneous frequency distribution at the window's time center.

at each time instant through calculation of the projection of the u_α output domain onto the vertical frequency axis, see Fig. 3.

Surprisingly, this procedure simplifies the transform calculation, since the implied rescaling in projection from the fractional domain to the frequency domain is achieved through removal of the $1/\sin \varphi$ scaling factor from the transform definition, Eq. (1). Furthermore, computing only the central column of data for the time-frequency representation eliminates the need to calculate rotation factors and the need to average over several transforms which may have different orders. These are important considerations in the realization of practical short-time transforms, giving improved execution times through reduced computational complexity.

The differences between the short-time implementations lie in the automated transform optimization procedures, which involve finding an α value for each of the short-time transforms that reflects the chirp rate of the input signal. The first method utilizes a global optimization procedure. The second is based on local optimization.

A. Globally optimized STFrFT

The globally optimized STFrFT uses an identical transform order for each short-time section and provides the fastest method for implementing a short-time FrFT. If the signal characteristics are known in advance, the order can be precalculated and supplied as a parameter to the algorithm, obviating the requirement for optimization altogether. Optimization aside, use of a discrete FrFT with $\mathcal{O}(N \log N)$ complex multiplications would allow the globally optimized STFrFT output to be calculated in similar time to the conventional STFT.

The fractional Fourier domain space lends itself well to hill-climbing searches. When signal characteristics are not known in advance a simple automated optimization routine is used to find the transform order giving the global maximum response for the entire input signal.

The algorithm automatically recalculates the transform order for the length of the specified short-time windows. The

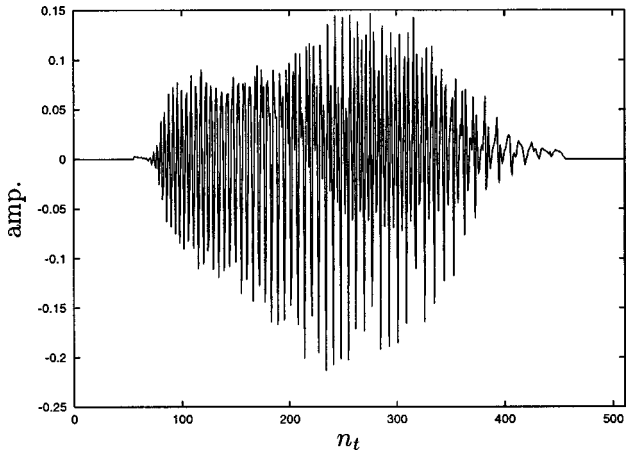

FIG. 4. 2.5 ms echolocation pulse from the Big Brown Bat, *Eptesicus fuscus*.

required recalculation, derived from Eq. (4), follows from the dependence of α_{opt} on the number of samples in the transform frame:

$$\alpha_{\text{opt(M)}} = \frac{2}{\pi}\tan^{-1}\left[\frac{N}{M}\tan\left(\alpha_{\text{opt}(N)}\frac{\pi}{2}\right)\right], \tag{11}$$

where, $\alpha_{\text{opt}(N)}$ defines the optimal transform order for the complete N-sample signal and $\alpha_{\text{opt(M)}}$ defines the equivalent order for the short-time window with M samples in the transform frame.

B. Locally optimized STFrFT

The alternative to global optimization is to search for a separate optimal order for each short-time window. The locally optimized STFrFT uses an exhaustive search routine, which calculates many FrFTs at different α values for each section and searches for the one giving the maximum magnitude response. It is far more time consuming than the globally optimized STFrFT, requiring calculation of $N-M$ times as many FrFTs, where N is the number of samples in the complete signal and M is the number of samples in the short-time transform frame. The actual number of calculations required for either method is dependent on the desired precision in transform order. A more sophisticated search routine could be used to reduce the computational overhead to some degree.

These two short-time approaches are compared with the STFT for a number of signals below.

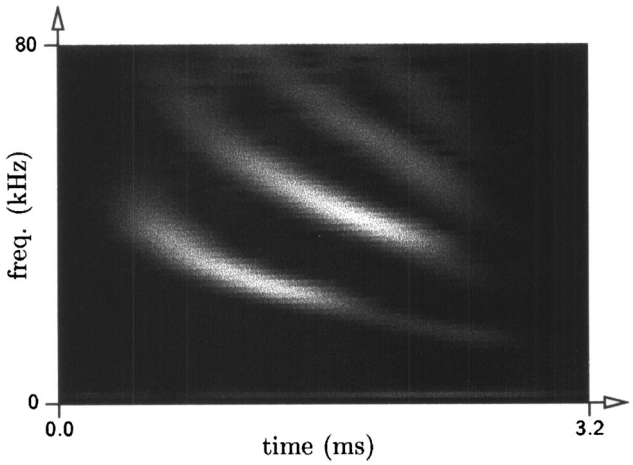

FIG. 6. Short-time Fourier transform of the bat signal calculated using a 128-point sliding Gaussian window.

VI. BIOACOUSTICS: THE BAT CHIRP

An echolocation pulse from the Big Brown Bat is given in Fig. 4. The FrFT has previously been used in a four-parameter atomic decomposition algorithm, showing this signal to contain three strongly linear chirp components.[16] Fractional domain filtering techniques have also been used to find and separate four near linear chirp components in the signal.[17] A time-frequency plot showing these components is reproduced in Fig. 5 and gives a good linear interpretation of the time-frequency localization of the four constituent chirps.

The four-component interpretation of the bat signal is backed up by the STFT, though the magnitude image in Fig. 6, produced with a 128-sample sliding Gaussian window, suggests some nonlinearity in the their time-frequency representations. For further investigation, consideration is initially only given to the largest component. The filtered single chirp is shown in Fig. 7.

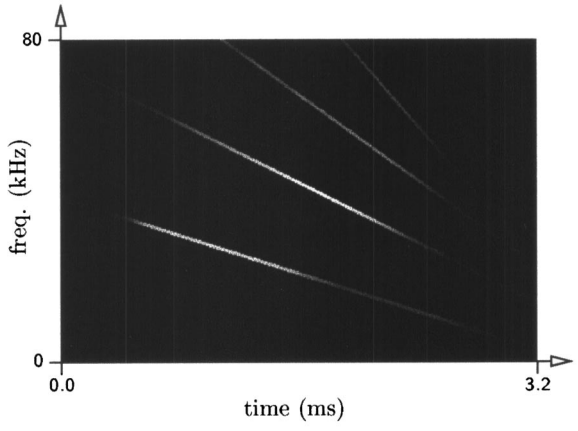

FIG. 5. The bat signal described as four linear chirp components in the time-frequency plane.

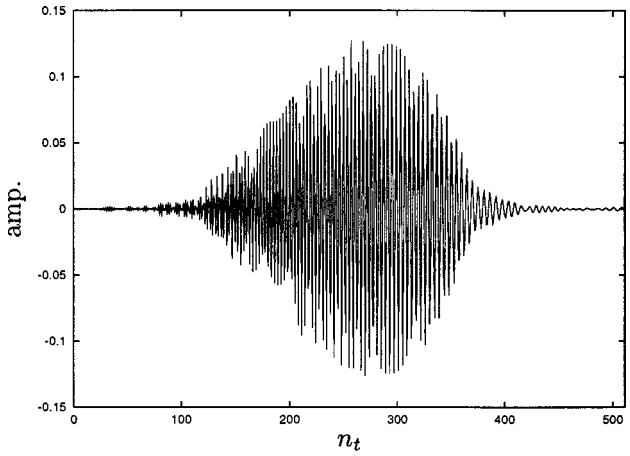

FIG. 7. Time-domain representation of the largest of the bat chirp components.

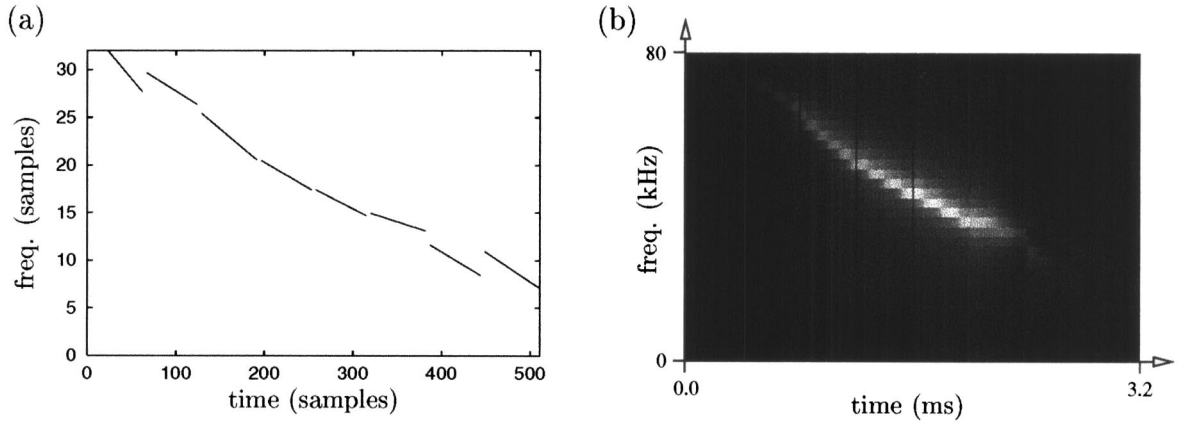

FIG. 8. Fitting the nonlinearities in a single chirp component: (a) Linear chirp segments showing best fit to the signal over 64 sample subframes; (b) amplitude scaled representation illustrating time-frequency resolution obtainable with the narrow 64-sample time window.

The input signal is subdivided into nonoverlapping 64-sample subframes and the optimal FrFT is calculated for each, yielding the best-fit piecewise linear approximation in Fig. 8(a). The lines have been plotted using values calculated from the optimal transforms using Eqs. (4) and (6) and give correct time-frequency plots relative to the time centers of each subframe. This representation demonstrates the emergence of some of the nonlinearity, though the pattern breaks up at the edges where there is little signal energy.

Figure 8(b) provides an alternative representation of the signal by projecting the entire transform for each subframe across the time-frequency plane. The rotation angle for each section is calculated from the optimal transform order. This gives an indication of the spread in frequency which accompanies the use of a 64-sample time window. The output has been scaled using the magnitude of the filtered component chirp in the time domain.

A similar approach has been put forward for an optical adaptive windowed FrFT for spatial filtering.[18] Spatial separation into nonoverlapping regions was achieved using a periodic grating, with the transform order for each region determined by the focal lengths of a series of lenses separated by free space. For signal analysis, the FrFT-based algorithms presented in this paper have the advantage that they give time-frequency information directly rather than providing a fractional domain representation of the signal at each time instant.

Globally and locally optimized STFrFT outputs for the entire bat signal using a 128-point sliding Gaussian window are given in Figs. 9 and 10, respectively. These images show output magnitude only and have been scaled to use the entire 8-bit dynamic range of the image format.

Both outputs show enhanced time-frequency resolution over the STFT, given in Fig. 6. The degree of improvement can be seen more readily through comparison of data for single columns from each image. Figure 11 depicts the data from the central column of each of the short-time transform images. There are visibly tighter bounds on the spreads of the signal energy corresponding to the largest components in the two FrFT based methods. These overlap and are indistinguishable in the figure.

For this multicomponent signal, in which the deviation from linearity is relatively small, the globally optimized STFrFT output is likely to be preferred. In the locally opti-

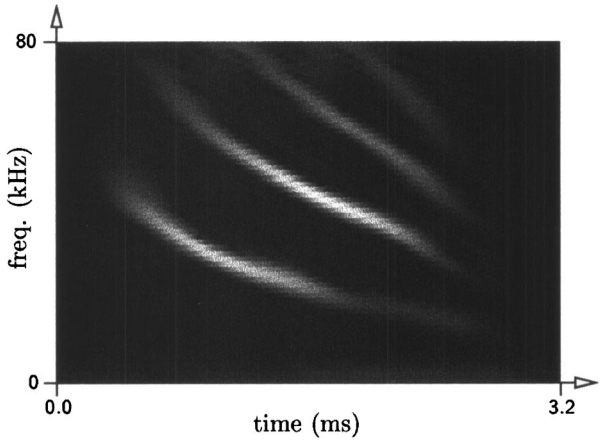

FIG. 9. Globally optimized short-time fractional Fourier transform of the bat signal using 128-point sliding Gaussian window. The optimal $\alpha=0.773$ order for the full signal translates into $\alpha=0.9409$ for the windowed sections.

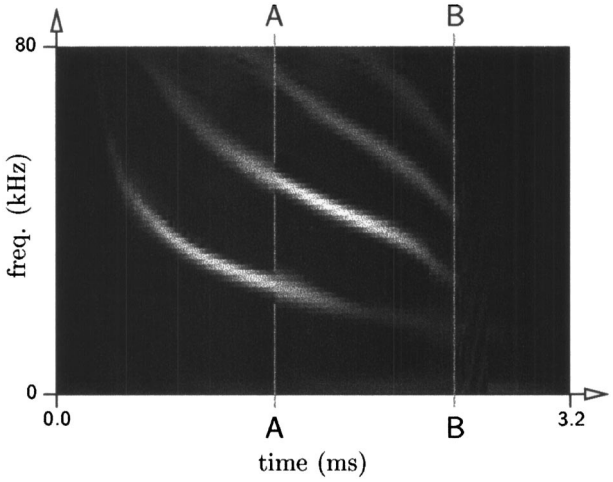

FIG. 10. Locally optimized short-time fractional Fourier transform of the bat signal using 128-point sliding Gaussian window. Discontinuities are seen at positions marked **A–A** and **B–B**.

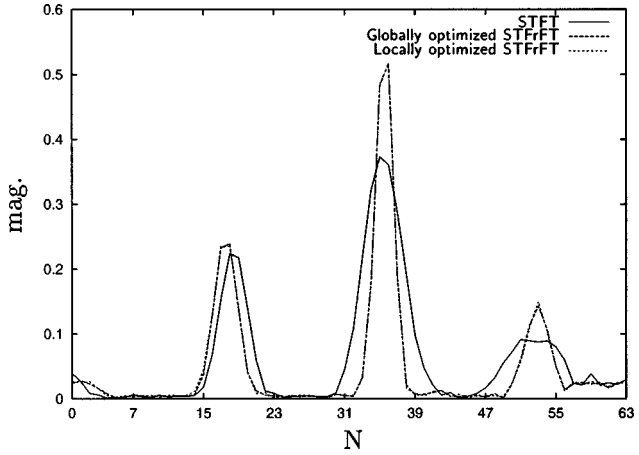

FIG. 11. Data from central columns of the bat chirp STFT, globally optimized STFrFT and locally optimized STFrFT images plotted for comparison. The lines for the globally optimized STFrFT and locally optimized STFrFT outputs are nearly coincident.

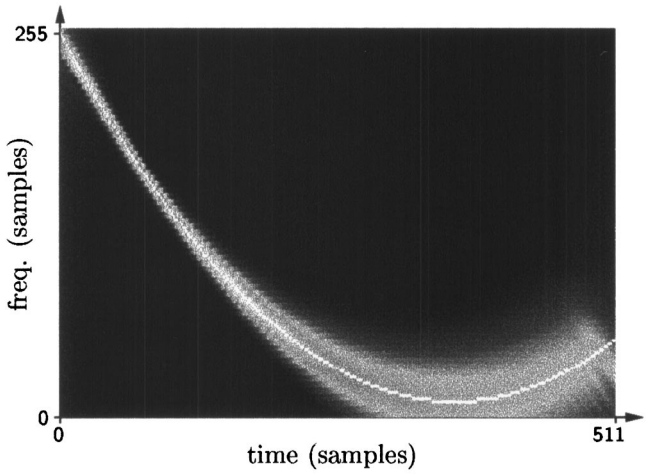

FIG. 13. Globally optimized short-time fractional Fourier transform of the quadratic chirp using 128-point sliding Gaussian window.

mized STFrFT output a number of discontinuities are seen as optimization switches from one component to another, reflecting changes in the distribution of signal energy over time. One such discontinuity is seen at **A–A** in Fig. 10 with a sudden decrease in intensity in the first component, accompanied by a sudden increase in intensity in the second component. The switch has occurred as a result of the change in their relative contributions to the overall signal energy. The discontinuity marked **B–B** arises because the optimization procedure has difficulty locking onto any one signal component in the low-energy tails of the signal.

VII. THE QUADRATIC CHIRP

The outputs of the two short-time FrFTs for a synthetic quadratic chirp are contrasted below with the STFT for the same signal. The signal, nominally $e^{j2\pi(160t^3-100t^2+30t)}$, is sampled in the range $\{t(\mathrm{s}):-0.5\leqslant t<0.5\}$ at a sampling rate of 512 Hz. Use of a synthetic signal, with a known functional form, allows the instantaneous frequency for the input signal to be plotted over the various time-frequency representations. The instantaneous frequency, calculated as the derivative of the signal's phase is indicated by the white line in each image. Figures 12–14 give the STFT, globally optimized STFrFT, and locally optimized STFrFT, respectively.

The globally optimized STFrFT, having optimized on a point early on in the signal, is unable to provide a good description of the rising part of the quadratic. Similarly, the STFT describes only a small part of the signal with good accuracy, around the nadir of the quadratic.

This highly nonlinear chirp is described most accurately by the locally optimized STFrFT. The differences can again be more readily appreciated in graphed data. The plots in Fig. 15 have been taken from the central column of each image.

At this point the optimal transform order returned by the locally optimized STFrFT is $\alpha_{\mathrm{opt}}=0.938$. This is used, in conjunction with the Gaussian support measures derived in the Appendix, to check that the plotted values accurately mirror the expected behavior of the transforms.

With a $6\sigma_t=128$ sample Gaussian window, $\sigma_{\max}\approx 21.4$ samples, estimated using Eq. (A8). For the discrete signal, Eq. (A7) is used to calculate the expected variance in the transform domain.

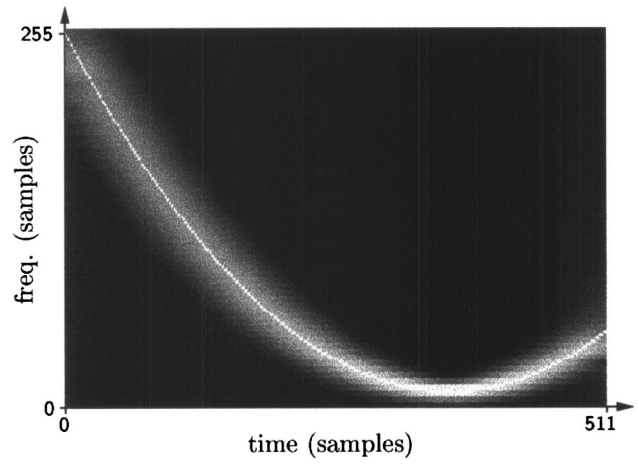

FIG. 12. Short-time Fourier transform of the quadratic chirp using 128-point sliding Gaussian window.

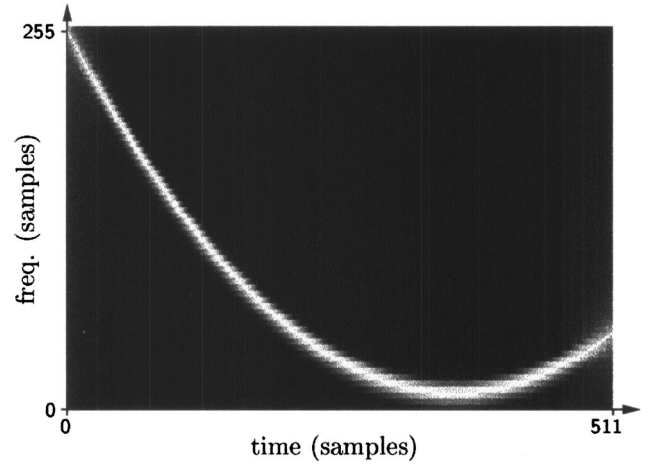

FIG. 14. Locally optimized short-time fractional Fourier transform of the quadratic chirp using 128-point sliding Gaussian window.

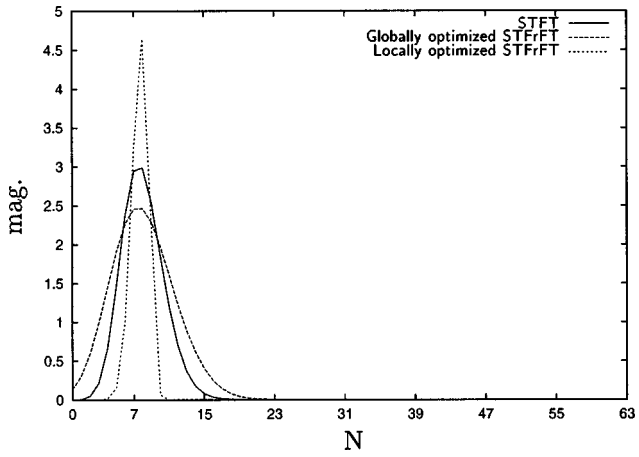

FIG. 15. Data from the central columns of the STFT, globally optimized STFrFT and locally optimized STFrFT images for the quadratic chirp signal plotted together for comparison of the degree of frequency localization for each method.

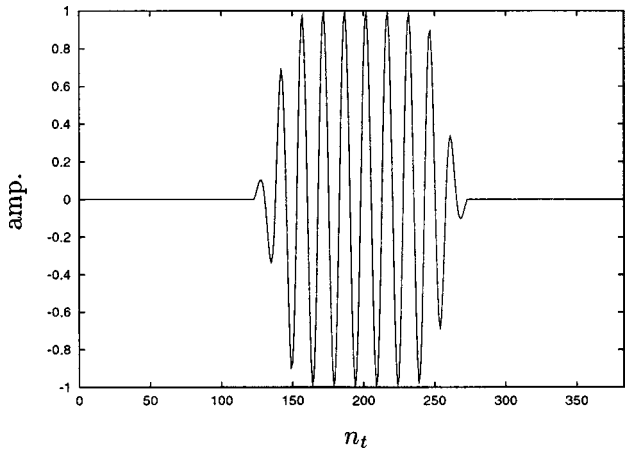

FIG. 16. Input pulse to the FDTD sonar model.

First for the STFT, in which $\varphi=\pi/2.0$ and $\varphi_{\max}=[(\alpha_{\text{opt}}-1.0)\pi/2.0]\approx-0.097\,39$,

$$\sigma_\alpha^2=\frac{128^2\sin^2(1.5708+0.097\,39)}{4\pi^2 21.4^2}+21.4^2\cos^2(1.5708+0.097\,39)$$
$$=0.8976+4.3303=5.2279\Rightarrow\sigma_\alpha\approx 2.2865. \tag{12}$$

Second for the optimal FrFT used in the locally optimized STFrFT algorithm, in which $\varphi=\varphi_{\text{opt}}$, giving $\varphi-\varphi_{\max}=\pi/2.0$,

$$\sigma_\alpha^2=\frac{128^2\sin^2(\pi/2)}{4\pi^2 21.4^2}+21.4^2\cos^2(\pi/2)$$
$$=\frac{128^2}{4\pi^2 21.4^2}=0.9062\Rightarrow\sigma_\alpha\approx 0.9520. \tag{13}$$

Allowing for the $1/\sin\varphi$ scaling factor gives an expected value for the frequency spread derived from the FrFT in this latter case of $\sigma_f\approx 0.9565$. This gives expected 6σ widths in the STFT and locally optimized STFrFT of approximately 14 samples and 6 samples, respectively. These match the plotted values well, indicating a good linear approximation to the quadratic over this interval.

VIII. DETECTING DISPERSIVE CHANGE

Detection of changes in frequency with time can yield important information regarding frequency-dependent dispersion. Figure 16 shows an input to a finite-difference time-domain (FDTD) sonar model. The model was expected to introduce some numerical dispersion.

The output response, after some 15 ms of model time, is shown in Fig. 17(a). A crude estimate of the time-frequency content of this pulse is obtained by plotting peak-to-peak intervals against the central time point for each complete period in the signal, Fig. 17(b).

STFT and locally optimized STFrFT magnitude images, produced with a 128-point sliding Gaussian window, are reproduced in Figs. 18(a) and (b). This length of short-time window provides the clearest indication of any frequency change possible using the STFT. It would be difficult to argue that this image provides convincing evidence of rising frequency with time. The locally optimized STFrFT output, using the same window, provides better resolution of the frequency changes in the tails of the signal. The discontinuities in Fig. 18(b) represent changes in the optimal rate determined by the algorithm. A smoother output could be ob-

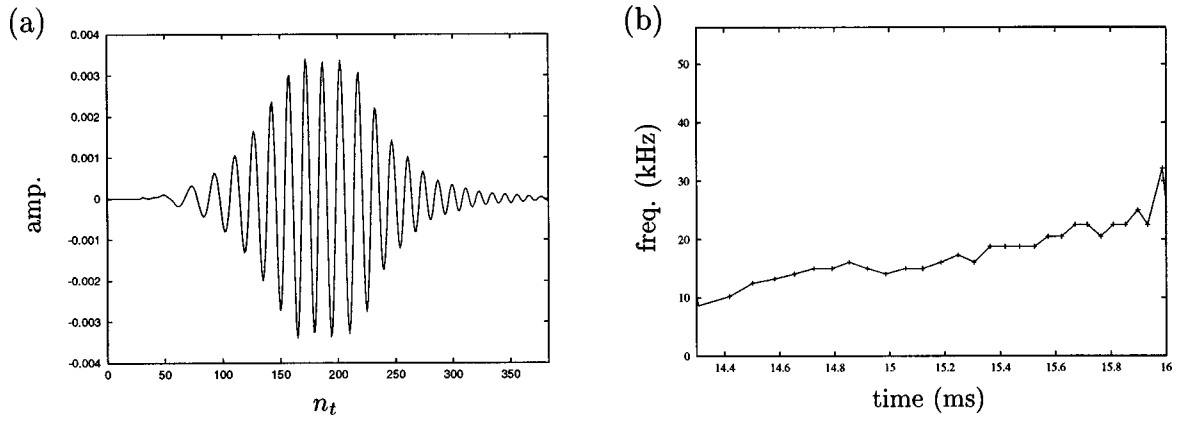

FIG. 17. FDTD sonar model: (a) Post propagation pulse; (b) time-frequency plot generated from peak-to-peak spacings.

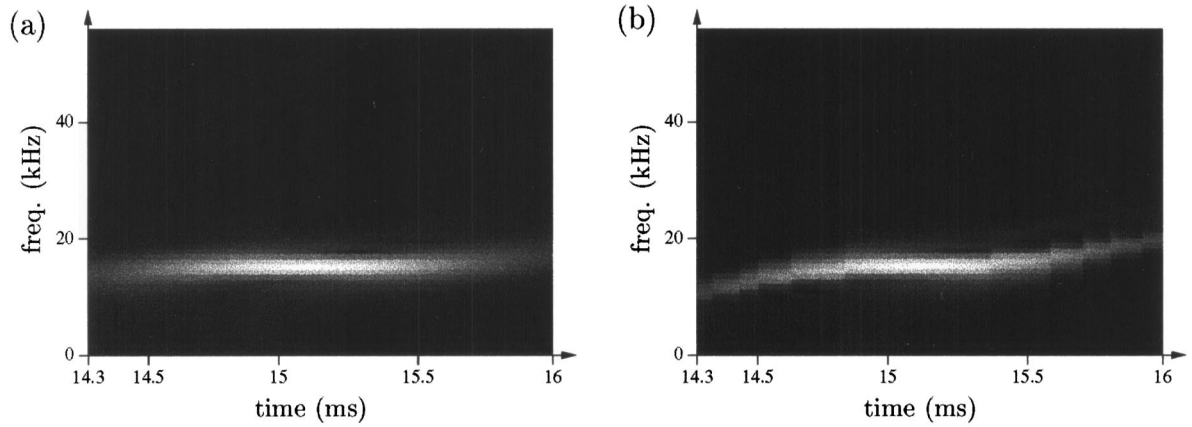

FIG. 18. Time-frequency representations for FDTD post-propagation pulse: (a) STFT using 128-point sliding Gaussian window; (b) locally optimized STFrFT using 128-point sliding Gaussian window.

tained by allowing a finer resolution in transform order, though this would be at the expense of additional computation time.

The globally optimized STFrFT output is not presented because it is indistinguishable from the STFT. The bulk of the signal energy and hence the appropriate point for global optimization lies in the central section where the best approximation is provided by a fixed frequency sinusoid.

IX. CONCLUSIONS

The fractional Fourier transform has been introduced as an optimal approach to the analysis of linear chirp signals. Analytic expressions for calculation of comparative variance measures for the FrFTs and ordinary Fourier transforms of Gaussian windowed linear chirps have been defined. These have provided estimates of the performance of the FrFT-based methods for comparison with the STFT. They have also been related to the uncertainty principle for the spread of real signals under the FrFT. It has been demonstrated that this uncertainty relationship is minimized for Gaussian windowed linear chirp signals represented in the orthogonal fractional domains exhibiting maximum and minimum spread.

Relationships between the FrFT output domains and the time-frequency plane have been used to generate narrower frequency distributions for windowed chirp signals than can be obtained using the ordinary Fourier transform. This has led to the specification of two short-time fractional Fourier implementations. These provide time-frequency representations with similar properties to the STFT, but offer improved performance in the analysis of a variety of nonstationary signals. They are particularly well suited to the analysis of single and multiple, linear and nonlinear chirps. The improvement in performance over the STFT has been illustrated by the analysis of a bat echolocation pulse containing four chirp components which overlap in both time and frequency domains.

The globally optimized STFrFT has been proposed and its effectiveness in highlighting the time-frequency structure of the multiple chirp bat signal has been demonstrated. This algorithm can be executed with an automatic global optimization step to calculate the appropriate optimal transform order for the short-time windows. Alternatively, it can be used with the order supplied as a parameter. In the latter case the algorithm could be executed in similar time to the ordinary STFT, using an $\mathcal{O}(N \log N)$ discrete FrFT.

A locally optimized STFrFT has been developed which calculates separate optimal orders for each short-time window. The speed of this algorithm is highly dependent upon the accuracy with which the transform orders are calculated and the sophistication of the search routines used. However, it remains a time-consuming approach compared to the globally optimized STFrFT. Its advantage lies in its ability to better represent strongly nonlinear chirp signals, demonstrated by the analysis of a quadratic chirp. It is also more sensitive to subtle changes in frequency and chirp rate in regions with relatively low signal energy, as shown in its ability to highlight dispersive change introduced by an FDTD sonar model. With multicomponent signals, discontinuities in the output are possible as optimization shifts from one component to another reflecting changes in the distribution of signal energy.

In conclusion the two short-time FrFT algorithms have been shown to perform well for the analysis of a variety of chirp and multiple chirp signals.

ACKNOWLEDGMENTS

The authors wish to thank Curtis Condon, Ken White, and Al Feng of the Beckman Institute of the University of Illinois for the bat data and for permission to use it in this paper. Thanks to Judith Bell of Heriot-Watt University and Gareth Elston of the University of New Hampshire for permission to use the FDTD model data. This research has been supported by the EPSRC, DERA and the Wellcome Trust.

APPENDIX: PERFORMANCE MEASURES FOR FRACTIONAL DOMAINS

For performance comparisons involving the FrFT it is useful to have a measure which is consistent throughout all fractional Fourier domains. One such measure is provided by

the variance of the Gaussian windowing function. Equation (A1) gives a general formula for the fractional Fourier transform of the Gaussian,[8]

$$\mathcal{F}^{\alpha}\exp\left(-c\frac{t^2}{2}\right)=\sqrt{\frac{1-j\cot\varphi}{c-j\cot\varphi}}\exp\left(j\frac{u^2}{2}\frac{(c^2-1\cot\varphi)}{c^2+\cot^2\varphi}\right)\times\exp\left(-\frac{u^2}{2}\frac{(c\csc^2\varphi)}{c^2+\cot^2\varphi}\right). \tag{A1}$$

For current purposes a relationship is sought between the spread of the function in the time domain and the spread in the fractional domain. The first term in Eq. (A1), $\sqrt{(1-j\cot\varphi)/(c-j\cot\varphi)}$, is a complex scalar, an amplitude and phase shift, which does not affect the spread of the signal representation in the transform domain. Likewise, the second term $\exp[j(u^2/2)(c^2-1\cot\varphi)/(c^2+\cot^2\varphi)]$ is a quadratic phase factor which does not alter the spread of the transformed signal. The spread of the transform magnitude is dependent only on the third term in Eq. (A1), which is a Gaussian function with a complicated variance.

This variance term, $(c\csc^2\varphi)/(c^2+\cot^2\varphi)$, is rearranged as follows:

$$\frac{(c\csc^2\varphi)}{c^2+\cot^2\varphi}=\frac{\dfrac{c}{\sin^2\varphi}}{c^2+\cot^2\varphi}=\frac{c}{\sin^2\varphi(c^2+\cot^2\varphi)}=\frac{1}{c\sin^2\varphi+\dfrac{\cos^2\varphi}{c}}. \tag{A2}$$

Bearing in mind that c, seen on the left-hand side of Eq. (A1), is equivalent to $1/\sigma_t^2$ in the standard definition of the Gaussian,[19] the variance of the signal in the transform domain can be written as

$$\sigma_{\alpha}^2=\frac{\sin^2\varphi}{\sigma_t^2}+\sigma_t^2\cos^2\varphi. \tag{A3}$$

The extension to discrete signals can be made through consideration of the discretization in both time and frequency with respect to the DFT. The sample spacings in time and frequency are $\delta t=1/f_s$ seconds and $\delta f=f_s/N$ Hz, respectively. So, for $\sigma_t=m$ samples,

$$\begin{aligned}\sigma_t&=m \quad \text{samples}\\ &\equiv m\,\delta t=\frac{m}{f_s} \quad \text{seconds},\\ \sigma_u&=\frac{1}{\sigma t}=\frac{f_s}{m} \quad \text{rads s}^{-1}\\ &\equiv\frac{f_s}{2\pi m} \quad \text{Hz}\\ &\equiv\frac{f_s}{2\pi m}\div\delta f=\frac{f_s}{2\pi m}\cdot\frac{N}{f_s}=\frac{N}{2\pi m} \quad \text{samples}.\end{aligned} \tag{A4}$$

The discrete Gaussian in the frequency domain has standard deviation $\sigma_u=N/2\pi m$ samples, where m is the standard deviation in samples of the Gaussian in the time domain.

This version of σ_u can be substituted for $1/\sigma_t$ in Eq. (A3). The revised formula, Eq. (A5), redefines the FrFT variances for the discrete fractional Fourier transform of the Gaussian, relative to the time domain variance. The resulting values for σ_{α} give the FrFT Gaussian widths measured in samples appropriate to the fractional domain in question,

$$\sigma_{\alpha}^2=\frac{N^2\sin^2\varphi}{4\pi^2\sigma_t^2}+\sigma_t^2\cos^2\varphi. \tag{A5}$$

Equation (A3) provides the variance for both the FrFT of the Gaussian itself and also for the FrFT of a Gaussian windowed fixed frequency sinusoid. The expression must be modified, however, to account for the fractional domain spread of a Gaussian windowed linear chirp signal. In this case the optimal domain is neither the time nor the frequency domain. The revised expression for the fractional domain variance[20] is

$$\sigma_{\alpha}^2=\frac{\sin^2(\varphi-\varphi_{\max})}{\sigma_{\max}^2}+\sigma_{\max}^2\cos^2(\varphi-\varphi_{\max}) \tag{A6}$$

or in the discrete case

$$\sigma_{\alpha}^2=\frac{N^2\sin^2(\varphi-\varphi_{\max})}{4\pi^2\sigma_{\max}^2}+\sigma_{\max}^2\cos^2(\varphi-\varphi_{\max}), \tag{A7}$$

where $\varphi_{\max}=(\alpha_{\text{opt}}-1.0)(\pi/2)$ can be calculated from Eq. (2). A good approximation to $\sigma_{\max}$, which improves with increasing N,[20] is given by

$$\sigma_{\max}\approx\left|\frac{\sigma_t}{\cos(-\varphi_{\max})}\right|. \tag{A8}$$

[1] J. Gedamke, D. Costa, and A. Dunstan, "Localization and visual verification of a complex minke whale vocalization," J. Acoust. Soc. Am. **109**, 3038–3047 (2001).

[2] J. Buck, H. Morgenbesser, and P. Tyack, "Synthesis and modification of the whistles of the bottlenose dolphin, *Tursiops truncatus*," J. Acoust. Soc. Am. **108**, 407–416 (2000).

[3] L. Linnett, S. Morrison, and P. Nicholson, "The analysis of signals containing mixtures of linear chirps," Proc. Inst. Acoust. **23**, 55–62 (2001).

[4] I. Stevenson, P. Nicholson, L. Linnett, and S. Morrison, "A method for the analysis of chirp signals insonifying layered media for sub-bottom profiling," in *MTS/IEEE Oceans 2001* (IEEE, Honolulu, HI, 2001), pp. 2608–2615.

[5] R. Gribonval, "Fast matching pursuit with a multiscale dictionary of Gaussian chirps," IEEE Trans. Signal Process. **49**, 994–1001 (2001).

[6] V. Namias, "The fractional order Fourier transform and its application in quantum mechanics," J. Inst. Math. Appl. **25**, 241–265 (1980).

[7] A. McBride and F. Kerr, "On Namias's fractional Fourier transforms," IMA J. Appl. Math. **39**, 159–175 (1987).

[8] L. Almeida, "The fractional Fourier transform and time-frequency representations," IEEE Trans. Signal Process. **42**, 3084–3091 (1994).

[9] H. Ozaktas, Z. Zalevsky, and M. Kutay, *The Fractional Fourier Transform with Applications in Optics and Signal Processing* (Wiley, Chichester, UK, 2001), pp. 99–107.

[10] S.-C. Pei and M.-H. Yeh, "Improved discrete fractional Fourier transform," Opt. Lett. **22**, 1047–1049 (1997).

[11] Ç. Candan, M. A. Kutay, and H. M. Ozaktas, "The discrete fractional Fourier transform," IEEE Trans. Signal Process. **48**, 1329–1337 (2000).

[12] H. Ozaktas, O. Arikan, M. Kutay, and G. Bozdaği, "Digital computation

of the fractional Fourier transform,'' IEEE Trans. Signal Process. **44**, 2141–2149 (1996).
[13] L. Cohen, *Time-Frequency Analysis* (Prentice-Hall, New Jersey, 1995), pp. 15–17, 39–48.
[14] D. Gabor, ''Theory of communication,'' J. Inst. Electr. Eng., Part 3 **93**, 429–457 (1946).
[15] S. Shinde and V. Gadre, ''An uncertainty principle for real signals in the fractional Fourier transform domain,'' IEEE Trans. Signal Process. **49**, 2545–2548 (2001).
[16] A. Bultan, ''A four-parameter atomic decomposition of chirplets,'' IEEE Trans. Signal Process. **47**, 731–745 (1999).
[17] C. Capus, Y. Rzhanov, and L. Linnett, ''The analysis of multiple linear chirp signals,'' *IEE Symposium on Time-Scale and Time-Frequency Analysis and Applications* (IEE, London, 2000), pp. 4/1–4/7.
[18] D. Mendlovic, Z. Zalevsky, A. Lohmann, and R. Dorsch, ''Signal spatial-filtering using the localized fractional Fourier transform,'' Opt. Commun. **126**, 14–18 (1996).
[19] M. Abramowitz and I. Stegun, *Handbook of Mathematical Functions* (Dover, New York, 1970), pp. 927–931.
[20] C. Capus, ''Time-frequency methods based on the fractional Fourier transform,'' Ph.D. thesis, Heriot-Watt University, Edinburgh, UK, 2002, pp. 48–69.

A nonlinear filter-bank model of the guinea-pig cochlear nerve: Rate responses

Christian J. Sumner[a] and Lowel P. O'Mard
Centre for the Neural Basis of Hearing at Essex, Department of Psychology, University of Essex, Colchester CO4 3SQ, United Kingdom

Enrique A. Lopez-Poveda
Centro Regional de Investigación Biomédica, Facultad de Medicina, Universidad de Castilla-La Mancha, Campus Universitario, 02071 Albacete, Spain

Ray Meddis
Centre for the Neural Basis of Hearing at Essex, Department of Psychology, University of Essex, Colchester CO4 3SQ, United Kingdom

(Received 15 March 2002; revised 13 February 2003; accepted 3 March 2003)

The aim of this study is to produce a functional model of the auditory nerve (AN) response of the guinea-pig that reproduces a wide range of important responses to auditory stimulation. The model is intended for use as an input to larger scale models of auditory processing in the brain-stem. A dual-resonance nonlinear filter architecture is used to reproduce the mechanical tuning of the cochlea. Transduction to the activity on the AN is accomplished with a recently proposed model of the inner-hair-cell. Together, these models have been shown to be able to reproduce the response of high-, medium-, and low-spontaneous rate fibers from the guinea-pig AN at high best frequencies (BFs). In this study we generate parameters that allow us to fit the AN model to data from a wide range of BFs. By varying the characteristics of the mechanical filtering as a function of the BF it was possible to reproduce the BF dependence of frequency-threshold tuning curves, AN rate-intensity functions at and away from BF, compression of the basilar membrane at BF as inferred from AN responses, and AN iso-intensity functions. The model is a convenient computational tool for the simulation of the range of nonlinear tuning and rate-responses found across the length of the guinea-pig cochlear nerve. [DOI: 10.1121/1.1568946]

PACS numbers: 43.64.Bt, 43.66.Ba [LHC]

I. INTRODUCTION

Models of signal processing in the auditory periphery are important tools for advancing our understanding of hearing. For example, in psychophysics, models of the cochlea are important components in theories of the perception of pitch (Meddis and Hewitt, 1991a, b; Patterson *et al.*, 1995; Pressnitzer *et al.*, 2002), the segregation of concurrent vowels (Assman and Summerfield, 1990; Meddis and Hewitt, 1992), and binaural precedence (Hartung and Trahiotis, 2001). Computational models of auditory scene analysis also include auditory peripheral models as front-ends (Brown and Cooke, 1994; Ellis, 1996). In audio engineering applications, compression algorithms employ models of psychophysical masking, to decide which parts of a signal can be safely removed (e.g., Brandenburg, 1996; Brandenburg and Bosi, 1997). Speech recognition systems also benefit from employing auditory models, as front-ends in noisy environments (e.g., Ghitza, 1988; Hermansky, 1998; Tchorz and Kollmeier, 1999).

In physiology, computational models of the AN are a useful tool for investigating cochlear processing itself. Some models, like the one here, attempt to reproduce complete peripheral responses (Deng and Geisler, 1987; Jenison *et al.*, 1991; Carney, 1993; Giguere and Woodland, 1994; Robert and Eriksson, 1999; Zhang *et al.*, 2001). Such models integrate facts and theories from a wide range of research in the cochlea. They allow the investigation of speech coding in the auditory periphery (e.g., Deng and Geisler, 1987; Jenison *et al.*, 1991) without the need for animal experimentation. A suitably flexible model, such as presented here, can also be used to simulate cochlear pathology (e.g., Schoonhoven *et al.*, 1994; Giguere and Smoorenburg, 1998; Lopez-Poveda and Meddis, 2001b) and the responses to noise trauma (Sachs *et al.*, 2002), and thus has the potential to inform hearing aid development. Peripheral models are also an essential prerequisite for the modeling of *in vivo* responses in the brainstem (e.g., Hewitt and Meddis, 1992).

Tuning in the cochlea is nonlinear (Rhode, 1971). However, the mechanical filtering of the cochlea has traditionally been modeled as a bank of parallel linear band-pass filters (Patterson *et al.*, 1988). Recently, there have been several attempts to extend computational models to capture the known nonlinear effects (Jenison *et al.*, 1991; Robert and Erikson, 1999; Zhang *et al.*, 2001; Goldstein, 1990, 1995; Irino and Patterson, 2001).

Meddis *et al.* (2001) have also described an architecture for modeling nonlinear mechanical filtering: the dual resonance nonlinear (DRNL) filter. The DRNL filter has been

[a]Author to whom correspondence should be addressed. Current address: Kresge Hearing Research Institute, University of Michigan, Ann Arbor, MI 48109-0506. Electronic mail: cjsumner@umich.edu

shown, by use of different parameter sets, to reproduce the different tuning and nonlinear basilar membrane (BM) input–output (I/O) functions at different locations along the cochlea. It also reproduces variations in phase response with frequency and level, two-tone suppression, local distortion products, and impulse responses on the BM. Using this filter architecture, Lopez-Poveda and Meddis (2001a) modeled human psychophysical measures of tuning and compression at different BFs.

Cochlea nonlinearities can also be measured at the level of the AN (Yates *et al.*, 1990; Sachs and Abbas, 1974) where they affect the shape of rate-intensity (RI) functions. In the guinea-pig, there are three types of RI function: (a) ''saturating:'' having high SR, low thresholds, steep RI functions and small (~20 dB) dynamic ranges; (b) ''sloping saturation'' which have less spontaneous activity, higher thresholds, and do not saturate completely, but show a sloping-saturation; and (c) ''straight'' which have little or no SR, high thresholds and no steep part in their RI function, just a long slope (Winter *et al.*, 1990). Sumner *et al.* (2002) recently described a thorough revision to the Meddis (1986, 1988) inner-hair-cell (IHC) model. When used with a DRNL filter, this model has been shown to reproduce accurately much of the variety of responses seen in the guinea-pig IHC and AN at high best frequencies (BFs; ~18 kHz). This includes the variation of rate-intensity functions for different fiber types, variation with stimulus frequency, the fall off of phase locking with stimulus frequency, adaptation (Sumner *et al.*, 2003), and the stochastic release of neurotransmitter.

We will describe the integration of the DRNL model of mechanical filtering (Meddis *et al.*, 2001) and the new model of inner-hair-cell transduction (Sumner *et al.*, 2002) to produce a complete filterbank model of the guinea-pig cochlea. Previous studies (Meddis *et al.*, 2001; Sumner *et al.*, 2002, 2003) did not place the filters within a filterbank framework, but instead changed parameters individually at different best frequencies. This model seeks to reproduce AN responses at all BFs, using parameters that change smoothly along the full length of the cochlea. Meddis *et al.* (2001) reproduced the responses of the BM at three BFs, 800 Hz, 9 kHz, and 18 kHz. This leaves a considerable gap at frequencies vital for understanding auditory processing of speech and music. Below 5 kHz, there are considerable changes in tuning and compression with BF. The BM data were also taken from more than one species. Furthermore, it is well known that such preparations are physiologically very vulnerable. This limits the collection of the data, and the measurements may not reflect the intact cochlea accurately. Here we have used AN data, which is less invasive, comes from a wide range of BFs including those relevant to speech, and is from a single species.

We will focus here on four different aspects of the responses to single tones: threshold tuning curves; BM compression as measured from AN responses; variation of tuning with level; and RI functions from different types of fibers and the relationship between SR and threshold. For all these, we are especially concerned to accurately represent the changes along the length of the cochlear partition. We intend the model, which is publicly available as part of an extensive suite of auditory modeling tools,[1] for use both as an input to larger scale models of auditory processing in the brain-stem and beyond, and as a predictor of AN responses. It may additionally help to refine of our understanding of signal processing in the cochlea.

II. THE MODEL

A. Middle-ear filtering

The response of the middle ear is modeled by a cascade of two linear band-pass Butterworth filters. This replaces the single band-pass filter used previously (Sumner *et al.*, 2002, 2003). The change was necessary to reproduce the thresholds found by Evans (1972). One filter is second order with an upper cutoff of 25 kHz and a lower cutoff of 4 kHz. The other filter is third order with upper and lower cutoffs of 30 kHz and 700 Hz. Both have unity gain in the passband. The input to the filter is sound pressure (μPa). This is scaled by a factor of 1.4×10^{-10} so that the filter outputs, $x(t)$, reflect measured stapes velocities (Nuttall and Dolan, 1996) in ms^{-1}. Additionally, a variable gain, G_{me}, is introduced at this stage. This is necessary to reproduce overall sensitivity differences between different preparations. G_{me} is 0 dB unless stated.

B. Mechanical filtering: DRNL filter

The filtering of the BM is modeled with a ''dual-resonance-non-linear'' (DRNL) filter architecture that has been described and evaluated more fully elsewhere (Meddis *et al.*, 2001). Only the parameter values vary from the model that was presented previously. Figure 1 shows the architecture. It consists of two parallel pathways, one linear (upper pathway in Fig. 1) and the other nonlinear (lower pathway), whose outputs are summed to produce the filter output, $v(t)$. The compression in the nonlinear pathway is described by

$$y[t]=\mathrm{SIGN}(x[t])\times\mathrm{MIN}(a|x[t]|,b|x[t]|^{v}), \tag{1}$$

where a, b and v are parameters determining the exact behavior.

Meddis *et al.* (2001) showed that the model could be fit to BM laser-interferometry data for three different BFs, by varying the DRNL filter parameters. Figures 2(a) and (b) show the effects of the parameters. At high-BFs the nonlinear pathway has a higher center frequency ($\mathrm{CF_{lin}}<\mathrm{CF_{NL}}$), narrower bandwidth ($\mathrm{BW_{NL}}<\mathrm{BW_{lin}}$) and higher gain ($a>G_{\mathrm{lin}}$) than the linear path. The result at threshold is a narrowly tuned filter, with a wide-bandwidth low-frequency tail. Also, the response at $\mathrm{CF_{NL}}$ is compressed over a large dynamic range. At low BFs the two pathways are very close in center-frequency ($\mathrm{CF_{lin}}\sim\mathrm{CL_{NL}}$) and gain ($a\sim G_{\mathrm{lin}}$). The nonlinear pathway dominates the BF response only at low levels. At high levels the linear pathway dominates the BF response, and at intermediate levels the output is a mix of the two. Thus the variation in measured compression with BF can emerge without any change in the compression exponent v.

To implement the filterbank, we adopted the scheme of Lopez-Poveda and Meddis (2001a). The values of the parameters a, b, the bandwidths of both pathways ($\mathrm{BW_{lin}}$ and

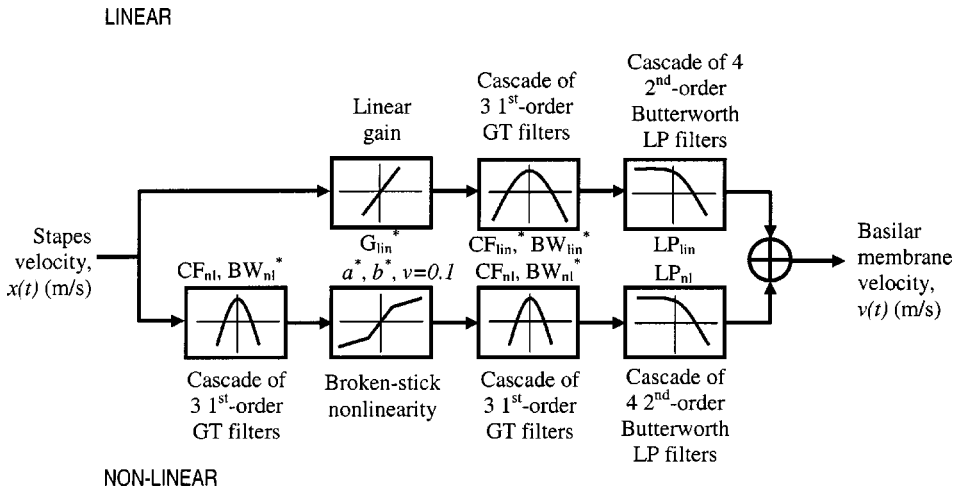

FIG. 1. Schematic of the DRNL filter architecture. The filter output is a sum of a linear and a nonlinear pathway. The linear (upper) pathway is a gain followed by a gammatone filter (GT; Patterson *et al.*, 1988) and a low-pass (LP) filter. The nonlinear (lower) pathway consists of the following cascade; a gammatone filter, a compression function, a second gammatone filter, and a low-pass filter. Parameters which are allowed to vary with BF are indicated with an asterisk (*). Bandpass center frequencies and low-pass filter cutoffs are of the same frequency within a single pathway, i.e., $LP_{NL}=CF_{NL}$ and $LP_{lin}=CF_{lin}$. All filters have unity gain in the pass-band. CF_{NL} is always set to the specified BF of the filter.

BW_{NL}), the gain of the linear filter (G_{lin}), and the center frequency of the linear filter (CF_{lin}) were made to vary linearly on a log-log scale as a function of best frequency (BF):

$$\log(\text{parameter}) = p_0 + m \log(\text{CF}), \tag{2}$$

where p_0 determines the parameter values at a theoretical BF of 1Hz, and m determines the slope of the parameter with BF on a log-log scale. All the parameter values are given in Table I. The parameters that vary with BF are also indicated with an asterisk (*) in Fig. 1. The remaining parameters, which are order of the filter cascades and the compression exponent, were fixed across the entire filter bank. These values are given explicitly in Fig. 1 as well as Table I. The nonlinear pathway center frequency (CF_{NL}) is set equal to BF.

C. Transduction: IHC

The IHC transduction model has been described in detail by Sumner *et al.* (2002, 2003). The first stage is a simple biophysical model of the cilia transduction and receptor potential (RP) response (modified from Shamma *et al.*, 1986). The second stage of transduction simulates the presynaptic calcium processes that lead to the release of neurotransmitter. Two parameters at this stage determine the fiber type. The third IHC stage models the manufacture, release, loss, and reuptake of neurotransmitter vesicles at the synapse. This is a quantal version of the model of adaptation proposed by Meddis (1986). The refractory stage then imposes an absolute and relative refractory period, reducing the probability that a vesicle will trigger an action potential.

Sumner *et al.* described how the model AN fiber response depends on the choice of the two calcium parameters: G_{Ca}^{max}, the maximum calcium conductance in the vicinity of the synapse, and $[Ca^{2+}]_{thr}$, the threshold concentration of calcium required for release. The effects of the parameters are shown in Fig. 2(c). In terms of gross characteristics, a large value of G_{Ca}^{max} (~6–7 nS) will result in a fiber with high-spontaneous-rate (HSR) type characteristics, while a small value (~1–3 nS) produces a low-spontaneous-rate (LSR) fiber. The continuous lines in Fig. 2(c) show this. $[Ca^{2+}]_{thr}$ affects primarily the low intensity responses, and thus affects the spontaneous rate (SR) and threshold of the unit. The dotted lines in Fig. 2(c) show this. An additional parameter, M, in the synapse, scales the vesicle release rate linearly. It is varied to determine the overall firing rate of model fiber responses. The effect of M on RI functions is shown fully in Sumner *et al.* (2002).

The relationship between the parameters and the spontaneous rate can be described analytically:

$$\text{SR} = \frac{10 M k_{\text{SR}}}{10 + 0.28 k_{\text{SR}}}, \tag{3}$$

where

$$k_{\text{SR}} = \max(\lfloor 4.65\times 10^{25}(G_{Ca}^{max})^3 - 20\times 10^{31}([Ca^{2+}]_{thr})^3 \rfloor, 0).$$

The relation of threshold with spontaneous rate is examined in Sec. III D.

D. Model implementation and development

The development of model parameters started with those of previous studies. The initial DRNL filterbank parameters were taken from Lopez-Poveda and Meddis (2001b). The compression exponent, v, was changed from 0.25 to 0.1 dB/dB across all BFs, to reflect the compression estimated by Cooper and Yates (1994) and Yates *et al.* (1990) in the guinea-pig. The DRNL filter parameters were refined progressively from the starting values. For each BF, we looked for a single set of parameters to fit the frequency-threshold tuning curves of Evans (1972) and the RI functions of Cooper and Yates (1994). We then fitted Eq. (2) to these parameter values and reevaluated the complete filterbank. Following previous studies, the orders of the filters were the same for all BFs, but as global parameters they were allowed to vary. The model was fitted by hand. The goal was to arrive at a single set of parameters that gave a good compromise be-

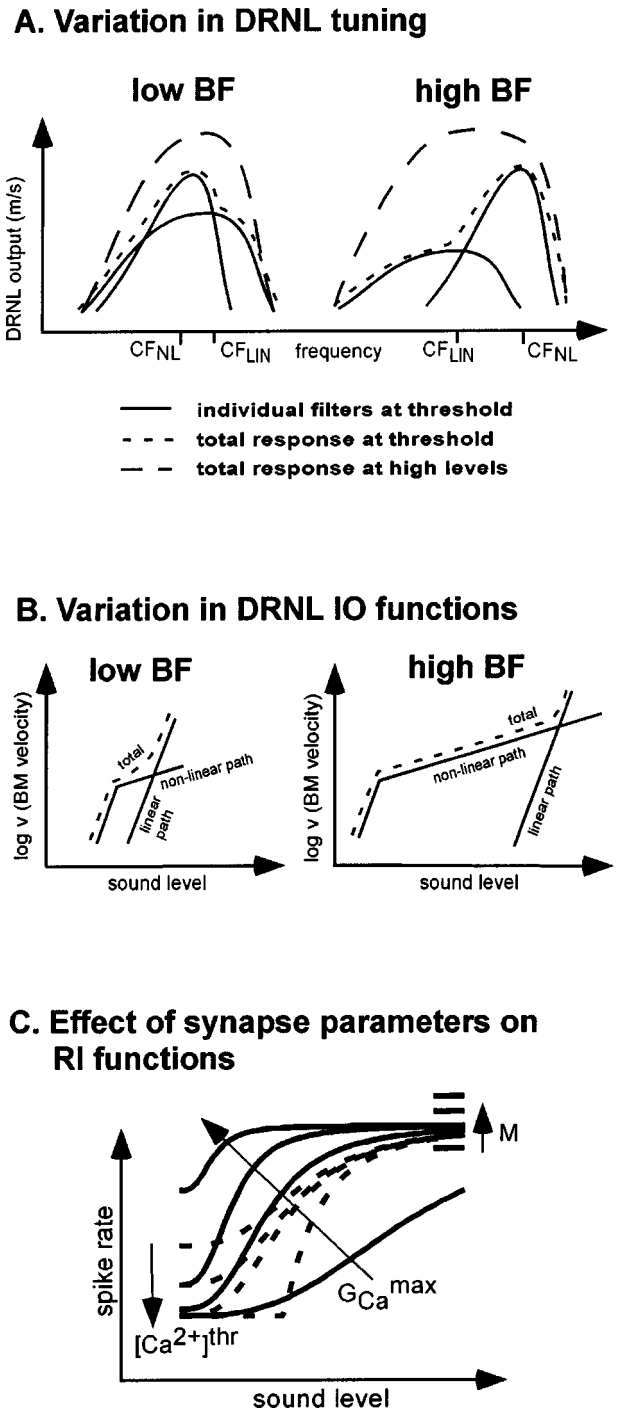

FIG. 2. How model parameters determine the response characteristics. (a) The variation in DRNL filter tuning with level and BF. Continuous lines show the frequency response of the linear and nonlinear pathways at threshold. CF_{NL} and CF_{lin} indicate the center frequencies of the nonlinear and linear paths, respectively. The dotted lines show the combined response at threshold, and the dashed lines show the response at high stimulus levels. (b) Variation in the DRNL filter IO function with BF in response to stimulation at BF. Continuous lines indicate the responses of the linear and nonlinear pathways. Dotted lines indicate the combined DRNL filter output. (c) Effect of varying synapse parameters G_{Ca}^{max} (continuous lines), $[Ca^{2+}]_{thr}$ (dotted lines) and M. For all panels, arrows show the direction of function change for an increase in each parameter value. M scales the response rate linearly across the entire dynamic range [see Eq. (3) and also Sumner *et al.* (2002)].

tween the different data sets. The filterbank was further tuned in light of the result of evaluation against four AN fiber iso-intensity response maps at three different BFs. Two of the fibers were collected by Winter and Robertson (personal communication) at our request. The other two AN fiber responses were taken from Müller and Robertson (1991). The final set of parameters found is given in Table I.

The initial IHC parameters were taken from Sumner *et al.* (2002). However, the parameters that determine fiber type were varied (see Sec. II C). For simulations involving the whole filterbank, the IHC parameters were fixed across all BF, creating generic high-, medium-, and low-spontaneous rate responses. The values are given in Table I. For the fitting of frequency threshold tuning curves, the IHC parameters were fixed at the values given for the generic HSR fiber in Table I. For the fitting of rate-intensity and iso-intensity functions, these parameters were allowed to vary from fiber to fiber. Additionally, the middle-ear-gain parameter, G_{me}, was varied between data from different animals. This was found to be necessary to model differences in overall response with level. Fitting of these parameters was done by hand, guided by the principles shown in Sec. II C and Fig. 2(c). Parameters for individual fibers are given in the figure legends.

Frequency tuning curves (FTCs) were generated using a two-down–one-up-tracking procedure, as described by Relkin and Pelli (1987). RI functions were generated using 100-ms tone pips with 2.5-ms linear ramps. They were presented at a range of sound levels, and often at a range of stimulus frequencies. For each stimulus condition, the stochastic stages of the model were run 20 times to produce a reliable measure of firing rate. Firing rate was calculated over the full period of stimulus presentation.

Cooper and Yates (1994) have inferred BM IO functions at BF from animal AN fibers using a technique described by Yates *et al.* (1990). We have applied their methods to the RI functions produced by the model, in so far as was practical. For each point on the BF RI function, we calculate the sound level required for an off-BF tone to produce the same firing rate. Plotting the off-BF sound level versus BF sound level for a given firing rate yields the BM IO function. The exact off-BF level was calculated by linearly interpolating between the two adjacent off-BF sound levels. Average slopes of model IO functions were calculated by the fitting of a straight line using least squares regression. When the gradient of the function above and below the threshold for compression were clearly different, the fitting of the line was restricted to the high-level portion above any abrupt change in slope associated with the compression threshold.

All the model code has been implemented in C, and is available publicly as source code.[1] MATLAB was used as a harness for control of executables, manipulation of parameters, and analysis of output.

III. EVALUATION OF THE MODEL

A. Filter tuning characteristics at threshold

The tuning characteristics of the AN at threshold are typically described by a frequency-threshold-curve (FTC).

TABLE I. Model parameters.

DRNL filter parameters that are fixed across all BFs	
Compression exponent, ν (dB/dB)	0.1
Gammatone cascade of nonlinear path	3
Low-pass filter cascade of nonlinear path	4
Center frequency of nonlinear path, CF_{NL}	Set equal to BF
Low-pass cutoff of nonlinear path, LP_{NL}	Set equal to BF
Gammatone cascade of linear path	3
Low-pass filter cascade of linear path	4
Low-pass cutoff of linear path, LP_{lin}	Set equal to CF_{lin}

DRNL filter parameters that vary with BF: $p(\mathrm{BF}) = 10^{p_0 + m \log_{10}(\mathrm{BF})}$	Filter-bank coefficients		Single filter at 6 kHz BF [in Fig. 5(b)]. Filterbank values shown in brackets.
	p_0	m	
Bandwidth of nonlinear path, BW_{NL} (Hz)	0.8	0.58	980 (unchanged)
Compression parameter, a	1.87	0.45	251 (3716)
Compression parameter, b	−5.65	0.875	4.52×10^{-3} (unchanged)
Center frequency of linear path, CF_{lin} (Hz)	0.339	0.895	2961 (5253)
Bandwidth of linear path, BW_{lin} (Hz)	1.3	0.53	634 (2006)
Linear path gain, G_{lin}	5.68	−0.97	103 (unchanged)
IHC parameters	HSR	MSR	LSR
$[Ca^{2+}]^{thr}$ threshold Ca^{2+} conductance	0	3.35×10^{-14}	1.4×10^{-11}
M, max. free transmitter quanta	10	10	10
G_{Ca}^{max}, max. Ca^{2+} conductance (nS)	7.2	2.4	1.6

Figure 3(a) shows the FTCs for a selection of guinea-pig AN fibers (Evans, 1972). The tuning clearly shows characteristic tip and tail regions at high BFs. At low BFs the tip is much less prominent, and thresholds are higher. Figure 3(b) shows FTCs generated by the model using the DRNL filterbank. The filterbank parameters were created by applying the coefficients p_0 and m in Table I to Eq. (2). The IHC model used the generic ''HSR'' parameter set given in Table I. The model FTCs agree reasonably well with the data.

Evans summarized the characteristics of the tips of the tuning curves for a large population of AN fibers. Figure 4 shows the animal data statistics (dots), compared with the behavior of the model (continuous lines). Figure 4(a) shows the filter Q-factor (filter BF divided by bandwidth) for 10 dB above the BF threshold (Q_{10}). This is a measure of the sharpness of tuning. In the data Q_{10} rises with BF, from around 1 at 200 Hz to between 3 and 10 at 10 kHz. Figures 4(b) and (c) show the slopes of the tuning curves above and below the unit BFs, calculated for stimulus frequencies whose thresholds lay within 25 dB of the BF threshold. Overall, the model conforms well to the measured data. There are some discrepancies in the shapes of the FTCs and the agreement with the summary statistics. The fit to FTCs has been compromised in order to fit the RI functions of Cooper and Yates (1994), using the same DRNL filterbank parameter set.

B. Compression characteristics across the cochlear nerve

Yates *et al.* (1990) have proposed a method for deriving BM IO functions from AN fiber measurements. AN rate responses are recorded both at BF and also at a stimulus frequency below BF. Below BF, the IHC is assumed to be driven by a linear BM. Thus any nonlinearities evident in the AN response to a below BF stimulus must be associated with the transduction process. It is also assumed that the frequency of stimulation does not affect the transduction nonlinearity. By equating firing rates for on-and off-BF responses, a putative BM IO function at BF can be derived (see Yates *et al.*, 1990, and also Sec. II D, for more details). A derived IO function is limited to within the dynamic range of the fiber at BF.

Cooper and Yates (1994) derived BM IO functions from AN rate responses across a wide range of BFs in a single animal. Figures 5(a)–(c) show three BM IO slopes that they derived (unconnected squares). At high BFs (6 and 23 kHz), the BM IO function is linear at low levels and highly compressed at high levels (0.1 dB/dB). However, at low BF (1800 Hz), the BM IO function is less compressive and almost straight, with a slope of 0.5 dB/dB. The derived IO slopes of the model (thick continuous lines) using the filterbank parameters given in Table I are shown on the same axes as the data. In Figs. 5(a) and (c) they agree well with the animal data of Cooper and Yates. In Fig. 5(b), at 6 kHz BF, the model IO function retains the same shape as the data below about 80 dB, but is shifted to lower intensities. Above 80 dB the model IO function rises again. This reflects the linear pathway, contributing to the high-level response at BF. The dashed line shows the response of the model for a single DRNL filter that has been modified to fit the data. The parameters which give a good fit to the BF response are in Table I. These are the actual parameter values for a single BF, rather than the values for Eq. (2). The main parameter change is the reduction in a, the gain of the low-intensity linear part of the DRNL filter broken-stick function [see Fig. 2(b)]. This lowers the gain of the tip of the tuning curve,

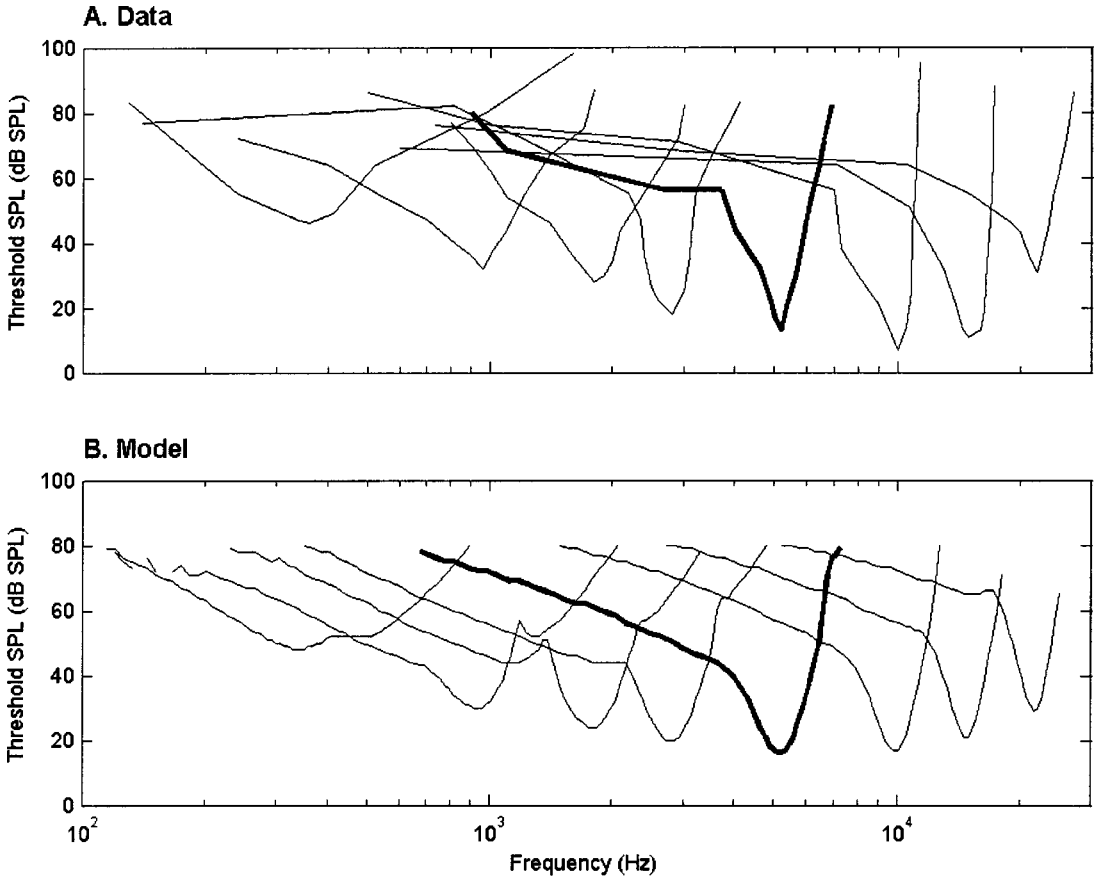

FIG. 3. Frequency threshold tuning curves (FTCs). (a) Guinea-pig AN (Evans, 1972). (b) Model using filter-bank DRNL filter parameters and ''HSR'' synapse parameter set (Table I).

raising the level at which the IHC reaches threshold, and the level at which the DRNL filter response becomes compressed. The contribution of the linear pathway at BF has also been reduced to remove the high-level return to linearity.

A more rigorous test of the model than the derivation of BM IO functions was to fit the RI functions from which the IO functions were derived. Figures 5(d)–(f) show this. On each axis two RI functions are plotted from a single guinea-pig fiber: one at BF (open squares) and one somewhat below BF (dots). The continuous lines show the fits of the model to the RI functions using the filterbank parameters of Table I. It was from these that the continuous lines in Figs. 5(a)–(c) were calculated. A good fit of the data RI functions must lead to a good fit of the data IO functions. The IHC parameters ($G_{\mathrm{Ca}}^{\max}$, $[\mathrm{Ca}^{2+}]_{\mathrm{thr}}$ and M) were allowed to vary between fibers. The parameters used are given in the figure legend. In Fig. 5(e), like Fig. 5(b), the fit of the filterbank at BF is poor. This is because the BF response of the filterbank model is much more sensitive than these data. Note that this is not a failure of the model. There is a clear disparity among the different data sets. In Fig. 5(e) the difference in thresholds between the BF and 2 kHz is about 20 dB. In Fig. 3(a), at a similar BF (marked) the difference between the thresholds

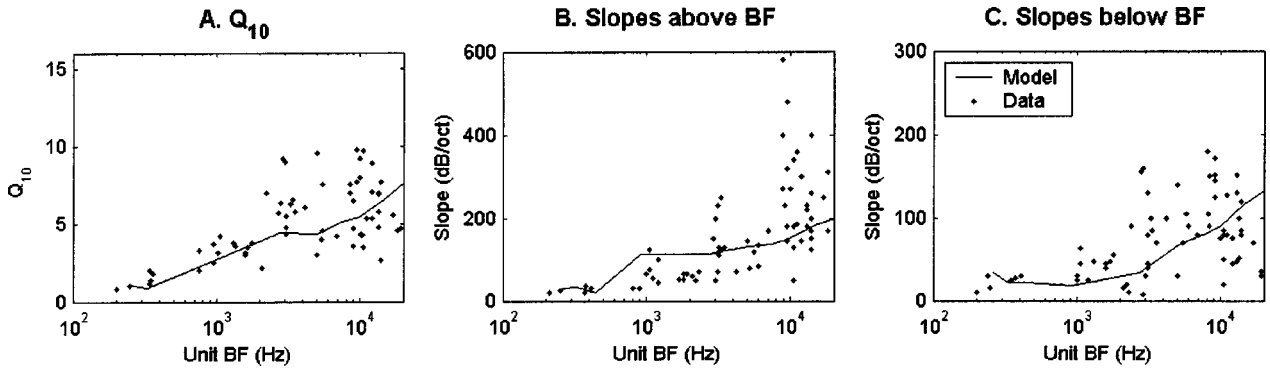

FIG. 4. Summary statistics describing the shapes of the tuning curves. Dots indicate data (Evans, 1972) and continuous lines indicate the behavior of the model. (a) Filter Q_{10} (BF/bandwidth at 10 dB above BF threshold). (b) Slopes of the tuning curves above the unit BF, within 25 dB of BF threshold. (c) Slopes of the tuning curves below the unit BF, within 25 dB of BF threshold.

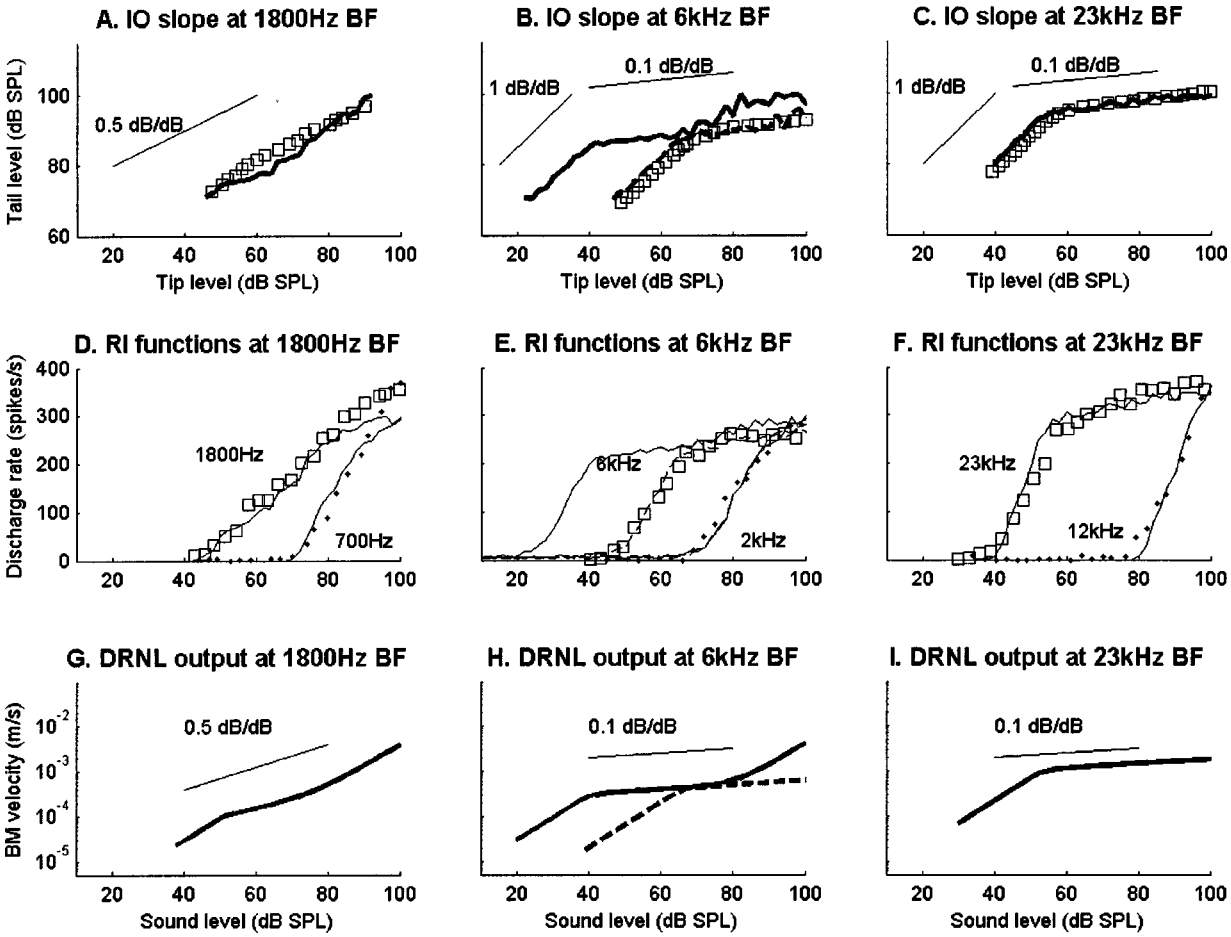

FIG. 5. (a)–(c) IO functions derived from AN responses. Unconnected squares are derived IO functions from Cooper and Yates (1994). Continuous lines are the responses of the model. The dashed line in (b) shows the IO function for the model that fits the RI functions in (e). (d)–(f) The RI functions for the medium spontaneous rate fibers from which the IO functions in (a)–(c) were derived. Unconnected squares are the data points at BF (Cooper and Yates, 1994, Fig. 2, panels A, C and F); unconnected dots are the data below BF; continuous and dashed lines indicate the fits of the model to the data. Model results are generated using the DRNL filter-bank parameters, except the dashed lines in (b) and (e), which use the individual "single filter at 6 kHz BF" DRNL filter parameters given in Table I. Synapse parameters used in (a) and (d): $G_{Ca}^{max}=1.27$ nS, $[Ca^{2+}]_{thr}=3\times10^{-11}$, $M=14$; in (b) and (e): $G_{Ca}^{max}=3$ nS, $[Ca^{2+}]_{thr}=1.4\times10^{-11}$, $M=9$; in (c) and (f): $G_{Ca}^{max}=2.9$ nS, $[Ca^{2+}]_{thr}=2.5\times10^{-11}$, $M=15$. In all cases, $G_{ME}=0$. (g)–(i). The outputs from the DRNL filters in response to BF stimuli, before they are input to the IHC stage. BM velocity is computed as the maximum response during the stimulation period. The continuous lines are for the DRNL filter-bank parameters. The dashed lines in (h) show the response of the "single filter at 6 kHz BF" parameter set in Table I.

for a BF tone and for a 2 kHz tone is about 40 dB. The reduction of a enables us to fit the BF RI function at the same time as the off-BF function in Fig. 5(e) (dashed line).

Figures 5(g)–(i) show the outputs from the DRNL filter at BF. This allows us to compare the real IO function of this stage of the model with the derived IO functions in Figs. 5(a)–(c). At 6- and 23-kHz BFs, the DRNL filter output at BF shows clear regions of linearity and compression which correspond excellently with those of the derived IO functions. In Fig. 5(g), the 1800-Hz BF output from the DRNL filter shows a region of compression between 50 and 80 dB SPL. Within that region the compression is slowly changing. This trend is less obvious in the output from the model AN fiber [Fig. 5(d)]. Stochasticity makes small features harder to see. It is also the case that the derived slopes become less well defined in a statistical sense, near to threshold and close to saturation (see Winter and Palmer, 1991).

The derived high-intensity BM IO slopes of more guinea-pig AN data from Cooper and Yates are shown in Fig. 6 (open squares). Above 5 kHz, derived IO slopes are around 0.1 dB/dB. Below there, there is an increase in the derived slope, to around 0.5 dB/dB. Figure 6 also shows the derived AN IO slopes for the model (continuous line). RI functions were all generated using the DRNL filterbank parameter set (Table I), and the "LSR" synapse parameter set (Table I). The model shows good agreement with the data.

C. Nonlinear tuning characteristics

The model was tuned to reflect two different data sets that are almost independent measures of threshold tuning and compression. However, the frequency dependence of the derived IO slope affects the variation of tuning with level. Figures 7(a)–(d) show rate responses of four different AN fibers, as iso-intensity contours. Each line shows how firing rate depends on stimulus frequency at a given level. At low BFs [400 Hz, Fig. 7(a); data was provided by Donald Robertson and Ian Winter], the response is broad and almost symmetrical. However, at high sound levels, firing rates are higher at frequencies above BF than below BF. At 3-kHz BF [Fig. 7(b); data provided by Donald Robertson and Ian Winter] the response is almost symmetrical at low levels but the activity

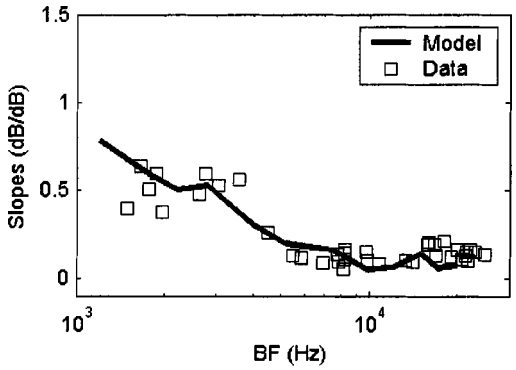

FIG. 6. The variation with BF of the slopes of derived input–output functions at high intensities. Squares are data from the guinea-pig (Cooper and Yates, 1994); continuous line is the model data.

now spreads to lower frequencies at high levels. Figures 7(c) and (d) (reproduced from Müller and Robertson 1991, Fig. 7) show the responses of two fibers from around 9-kHz BF in a single animal, having low- and high-SR fibers, respectively. At high BFs, the response has a pronounced tip, with the activity spreading clearly downwards at high levels. Figures 7(e)–(h) show the response of the model to these stimuli. The DRNL filter stage used the filterbank parameters of Table I, and the IHC parameters were manipulated as in Sec. III B. The parameter values are given in the figure legend. The model reproduces most of the effects observed in the data, including the shift of BF with level. In the model, the direction of the shift with BF depends on the relative center frequencies of the linear and nonlinear DRNL filter pathways. As the level rises, the BF shifts towards the center frequency of the linear path. At high BFs the response shifts down to lower frequencies as level rises. At BFs below 1 kHz the response shifts up to higher frequencies as the level increases. This general trend is also consistent with the directions of frequency glides in cat AN impulse responses (Carney *et al.*, 1999).

D. RI characteristics for different fiber types

AN fiber rate-responses differ within a given BF range as well as along the length of the cochlea (Yates *et al.*, 1990; Sachs and Abbas, 1974). Here we are particularly interested in how RI shape varies with BF. In the guinea-pig, the basic three shapes are found across most of the BF range (Winter *et al.*, 1990). However, Winter and Palmer (1991) report finding no straight RI functions below 1.5 kHz. No straight RI functions have ever been reported in the cat.

Figure 8 shows RI responses from the filterbank for the three different generic IHC settings in Table I, both for stimulus frequencies at BF (continuous lines) and one octave below (dashed lines). The three models differ only in the values of IHC parameters $G_{\mathrm{Ca}}^{\max}$ and $[\mathrm{Ca}^{2+}]_{\mathrm{thr}}$. $G_{\mathrm{Ca}}^{\max}$ decreases and $[\mathrm{Ca}^{2+}]_{\mathrm{thr}}$ increases as SR decreases. These values are the same at all BFs. Each fiber type shows the correct characteristic RI function at BF. The responses to stimuli an octave below BF do not show compression. As low as 3 kHz, the LSR RI functions are of the straight type. Below this, only saturating and sloping-saturation RI functions exist. The RI functions at 12-kHz BF [Figs. 8(b) and (c)] are nonmonotonic, and actually fall at levels above 90 dB. The outputs from the two filter pathways are out of phase and cancel each other out. Such features have been observed in the auditory nerve fibers of cats, and are associated with a 180°

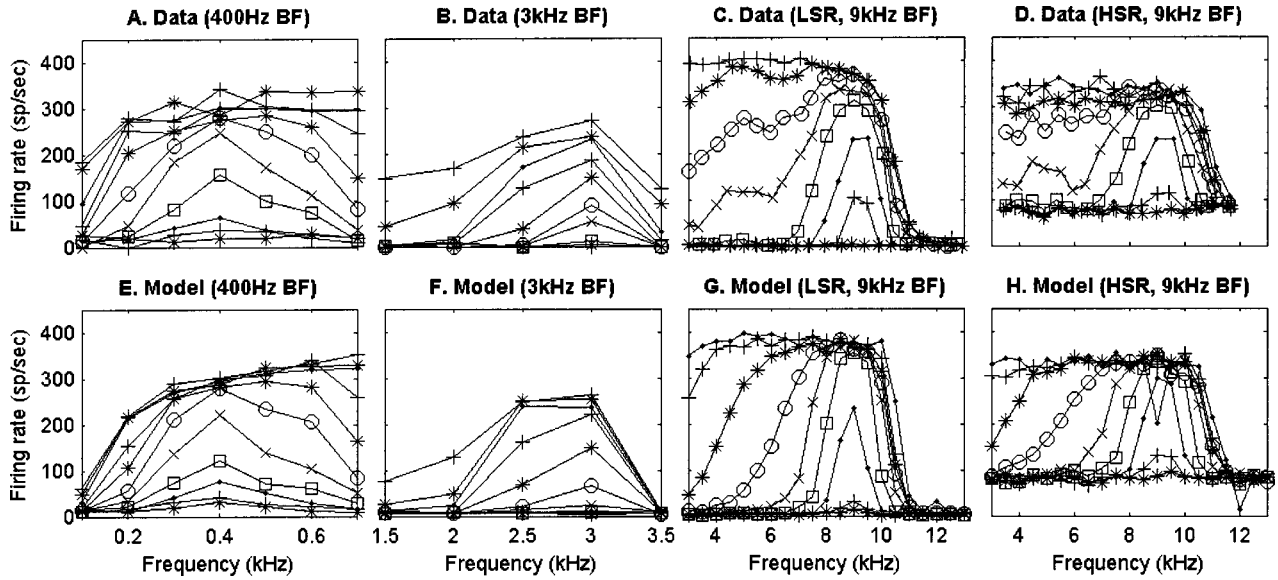

FIG. 7. Iso-intensity rate-responses of guinea-pig AN fibers and the model, for various BFs and SRs. (a)–(d). Guinea-pig AN responses provided by Winter and Robertson (a, b) and reproduced from Müller and Robertson (1991) (c, d). (e)–(h) Model AN fiber responses to the same stimuli and BFs as (a)–(d). All use the DRNL filterbank parameter set (Table I), with IHC parameters and middle ear gain varied to obtain best fit as described in text. (a) Guinea-pig AN fiber with a BF of 400 Hz. Each connected set of symbols has a constant stimulus level, ranging from 35 to 85 dB SPL in 5-dB increments. (b) Guinea-pig AN fiber with a BF of 3 kHz. Stimulus levels range from 41 to 91 dB SPL in 5-dB increments. (c) Low-SR guinea-pig AN fiber with a BF of 9 kHz. Stimulus levels range from 30 to 100 dB SPL in 10-dB increments. (d) High-SR guinea-pig AN fiber with a BF of 9 kHz. Stimulus levels range from 20 to 100 dB SPL in 10-dB increments. (e) Model with a BF of 400 Hz and $G_{\mathrm{Ca}}^{\max}=8.3$ nS, $[\mathrm{Ca}^{2+}]_{\mathrm{thr}}=5\times10^{-11}$, $M=12$, and $G_{\mathrm{me}}=0$. (f) Model with a BF of 2820 Hz and $G_{\mathrm{Ca}}^{\max}=2.7$ nS, $[\mathrm{Ca}^{2+}]_{\mathrm{thr}}=1.2\times10^{-11}$, $M=14$, and $G_{\mathrm{me}}=-30$ dB. (g) LSR model with a BF of 9 kHz and $G_{\mathrm{Ca}}^{\max}=5$ nS, $[\mathrm{Ca}^{2+}]_{\mathrm{thr}}=3\times10^{-11}$, $M=14$, and $G_{\mathrm{me}}=-10$ dB. (h) HSR model with a BF of 9 kHz and $G_{\mathrm{Ca}}^{\max}=8.5$ nS, $[\mathrm{Ca}^{2+}]_{\mathrm{thr}}=4.48\times10^{-11}$, $M=12$, and $G_{\mathrm{me}}=-10$ dB.

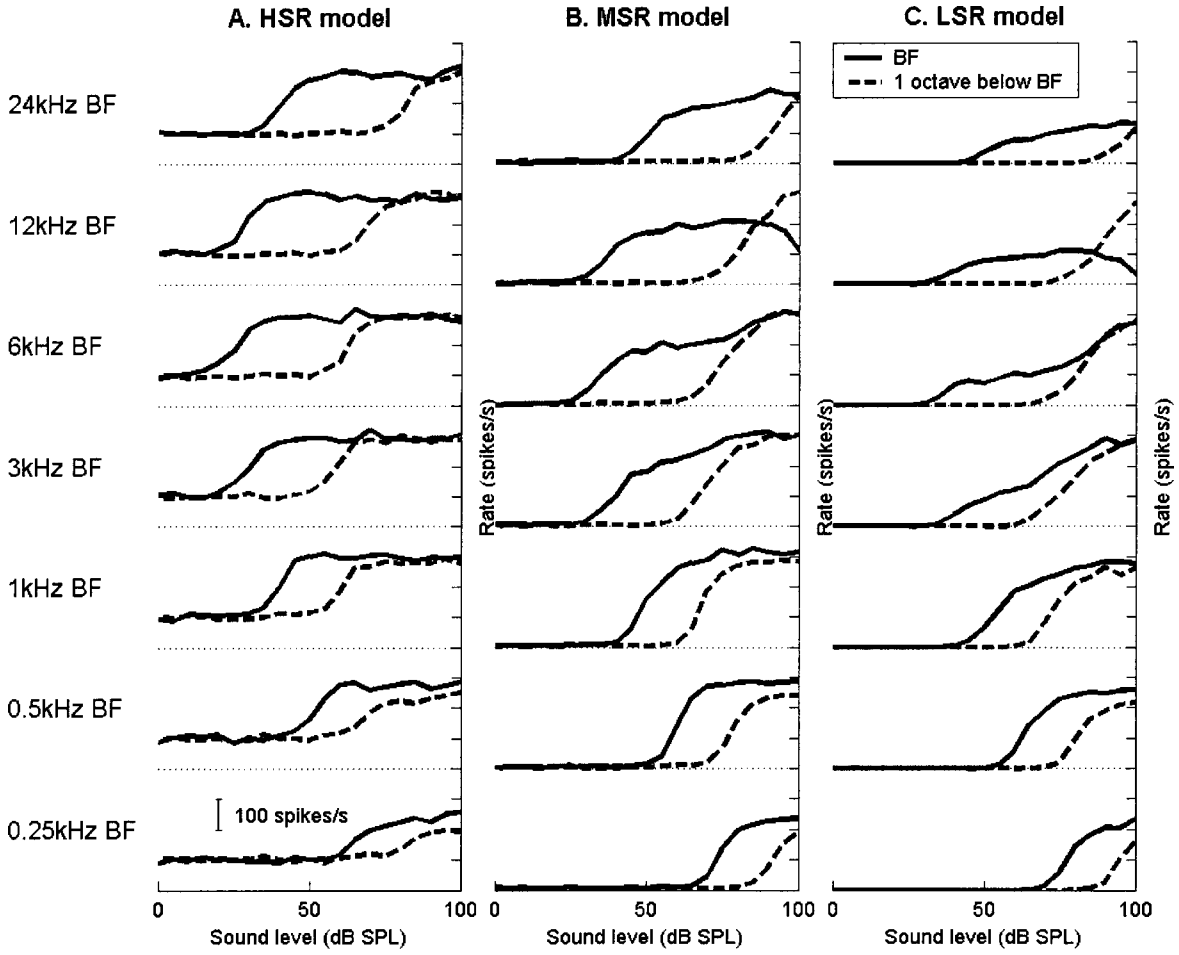

FIG. 8. RI functions from across the filter-bank for (a) high, (b) medium, and (c) low-spontaneous rate fiber types. Continuous lines are the responses at BF (indicated to the left of the panels) and dashed lines are the response for the same filter-bank channel, stimulated at one octave below its BF. All responses use the DRNL filterbank, and the synapse parameters are the ''HSR,'' ''MSR,'' and ''LSR'' parameter sets given in Table I.

phase shift in the period histograms (e.g., Liberman and Kiang, 1984).

Figure 9 shows how the threshold and spontaneous rate vary with $G_{\mathrm{Ca}}^{\max}$. Figure 9(a) shows how the threshold varies with SR in the model, for BF stimulation at two different frequencies (solid lines). The threshold is calculated from rate-level functions as the point at which the rate is 20 spikes/s above the spontaneous rate. The threshold first drops steeply, and then more slowly as the spontaneous rate grows. This trend is compared with the data of Winter and Palmer (1991; dots). In order to satisfy the multiple constraints of SR, threshold, and the shape of the RI function, it was necessary to co-vary $[\mathrm{Ca}^{2+}]_{\mathrm{thr}}$ with $G_{\mathrm{Ca}}^{\max}$:

$$[\mathrm{Ca}^{2+}]_{\mathrm{thr}}=\frac{4.5\times10^{-11}}{[1+e^{8\times10^{9}(G_{\mathrm{Ca}}^{\max}-1.5\times10^{-9})}]}. \tag{4}$$

The model threshold does not appear to change at low SRs. Due to the calcium threshold, at low values of $G_{\mathrm{Ca}}^{\max}$ the SR becomes zero. However, the threshold continues to shift. Figure 9(b) shows how spontaneous rate varies with the maximum-calcium-conductance parameter, $G_{\mathrm{Ca}}^{\max}$. $[\mathrm{Ca}^{2+}]_{\mathrm{thr}}$ is set according to Eq. (4). The continuous line shows the theoretical values calculated from Eq. (3). The single points indicate the values calculated from the model outputs.

IV. DISCUSSION

We have presented a nonlinear filterbank fitted, as far as possible, to guinea-pig AN data for threshold tuning curves, RI functions and compressive nonlinearities. The model is adequate to provide useful responses to pure tones, across a wide range of BFs and stimulus frequencies. It should prove useful as an input to models of more central processes that require nonlinear cochlear properties that vary appropriately with BF. It is especially suited for studying level dependent rate effects, differences between different fiber types, and differences in AN rate responses along the cochlear partition.

There are many response characteristics that have not been considered here. We have restricted the study to rate responses only. Other characteristics of the DRNL filter and IHC models have been considered individually elsewhere (Meddis *et al.*, 2001; Sumner *et al.*, 2002, 2003). These include tuning and nonlinearity at the level of the BM, local distortion products, impulse responses, phase locking, discharge history effects, adaptation, and the variation of pure tone PSTHs with fiber type.

In order to simplify the implementation, the compression exponent and filter orders were fixed across all BFs. It is especially interesting that the same highly compressive exponent value of 0.1 dB/dB could be used at all BFs. The

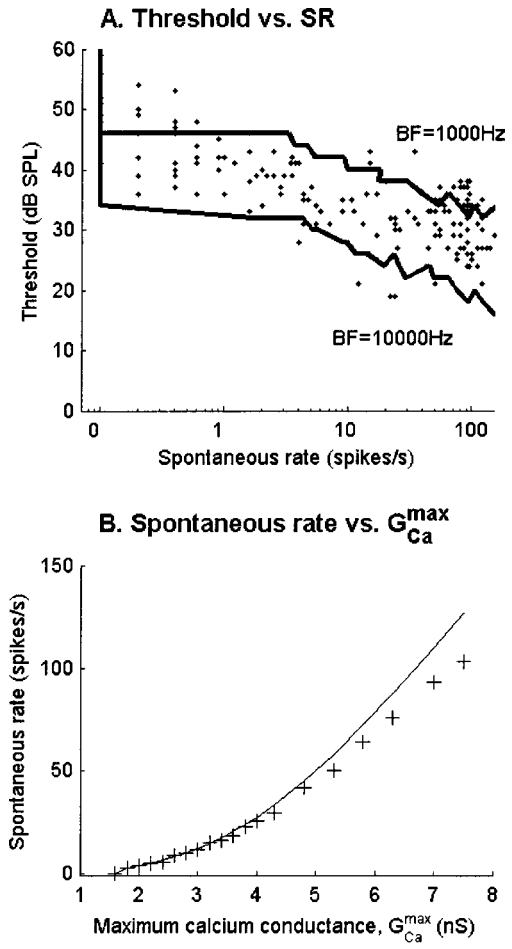

FIG. 9. (a) The relationship between threshold and SR. The solid line show the response of the model for BF stimulation at two different frequencies lines. The dots show the data of Winter and Palmer (1991). Threshold in the model is defined as the point at which the rate reaches 20 s^{-1} above the spontaneous firing rate. (b) The relationship between SR and G_{Ca}^{max}. $[Ca^{2+}]_{thr}$ co-varies with G_{Ca}^{max} as described in the text. The continuous line shows the value predicted by Eq. (3). Crosses show the value calculated at the output of the AN model.

regions with a derived IO slope of greater than 0.1 arise because at lower BFs the I/O slope is a function of the output of both linear and nonlinear pathways. Thus a functional variation in compression emerges from changes in the relative contributions of the pathways at BF. Below 1 kHz the BF IO function of the model is mostly linear. However, distortion products are still produced by the nonlinear pathway and are thus present in its response. The variation in measured nonlinearity could have been achieved by varying the compression exponent, ν, with BF. However, we sought to vary the smallest number of parameters possible, and it was not necessary to vary ν here. The filter orders were fixed across the whole filterbank, and this has compromised the fit of the model in some cases. The logarithmic function of linear path gain with BF was another limitation. A better fit to all BFs would have been possible with a more complicated scheme. However, we felt that this could not be justified without a larger data set.

The IO function of the mechanical filtering was assumed to be linear for stimulation frequencies well below BF. This is supported by BM laser interferometry results (Ruggero *et al.*, 1997; Nuttall and Dolan, 1996) at high BFs. At very low BFs (~250 Hz), BM IO functions are mostly linear at all stimulus frequencies (Cooper and Rhode, 1995). However, what nonlinearity there is seems to extend across a wide range of frequencies. If the BM is compressed at the below-BF stimulus frequency, the resulting derived IO function for the BF response will be less compressed than the underlying mechanical input. At BFs in the range of 1–5 kHz, there are no direct BM measurements. Therefore it is difficult to assess the validity of the assumption here. The shapes of AN FTCs change rapidly with BF when the fiber BFs are below a few kilohertz. It seems probable that IO functions are also varied. We can only comment that the response of the model presented here is linear at 700 Hz for a BF of 1800 Hz and fits the RI functions quite well [Fig. 5(d)]. Therefore it seems to be a reasonable assumption in this instance.

ACKNOWLEDGMENTS

We would like to thank Ian Winter and Donald Robertson for collecting AN data from several animals at our request, and Ian Winter for numerous fruitful discussions. The data were obtained in The Auditory Laboratory at The University of Western Australia, with funding support from The National Health and Medical Research Council of Australia. We would also like to thank Alan Palmer for data collected, which although was not presented, helped to inform this study. This research was supported by the Wellcome foundation (Grant Ref. 003227), and also the Consejería de Sanidad of the Junta de Comunidades de Castilla-La Mancha (Ref. 01044).

[1]The software is available in two forms. DSAM (development system for auditory modelling) is a C library containing an extensive collection of auditory model components, and support routines. AMS (auditory model simulator) is a cross-platform application, providing a flexible GUI interface for all the models supported by DSAM. These can be downloaded from www.essex.ac.uk/psychology/hearinglab/dsam, together with the simulation scripts required to configure the model correctly.

Assman, P., and Summerfield, Q. (**1990**). "Modelling the perception of concurrent vowels: Vowels with different fundamental frequencies," J. Acoust. Soc. Am. **85**, 327–338.

Brandenburg, K. (**1996**). "Introduction to Perceptual Coding," in *Collected Papers on Digital Audio Bit-Rate Reduction*, edited by N. Gilchrist and C. Grewin, Audio Eng. Soc. ISBN 0-937803-33-2.

Brandenburg, K., and Bosi, M. (**1997**). "Overview of MPEG Audio: Current and Future Standards for Low-Bit-Rate Audio Coding," J. Audio Eng. Soc. **45**, 4–21.

Brown, G. J., and Cooke, M. (**1994**). "Computational auditory scene analysis," Comput. Speech Lang. **8**, 297–336.

Carney, L. H. (**1993**). "A model for the responses of low-frequency auditory-nerve fibers in cat," J. Acoust. Soc. Am. **93**, 401–417.

Carney, L. H., McDuffy, M. J., and Shekhter, I. (**1999**). "Frequency glides in the impulse response of auditory nerve-fibers," J. Acoust. Soc. Am. **105**, 2384–2391.

Cooper, N. P., and Rhode, W. S. (**1995**). "Nonlinear mechanics at the apex of the guinea-pig cochlea," Hear. Res. **82**, 225–243.

Cooper, N. P., and Yates, G. K. (**1994**). "Non-linear input-output functions derived from the responses of guinea-pig cochlear nerve fibres: Variations with characteristic frequency," Hear. Res. **78**, 221–234.

Deng, L., and Geisler, C. D. (**1987**). "A composite model for processing speech sounds," J. Acoust. Soc. Am. **82**, 2001–2012.

Ellis, D. P. W. (**1996**). "Prediction-driven computational auditory scene analysis," Ph.D. Thesis, MIT.

Evans, E. F. (**1972**). ''The frequency response and other properties of single fibers in the guinea-pig cochlear nerve,'' J. Physiol. (London) **226**, 263–287.
Ghitza, O. (**1988**). ''Temporal non-place information in the auditory-nerve firing patterns as a front-end for speech recognition in a noisy environment,'' J. Phonetics **16**, 109–123.
Giguere, C., and Smoorenburg, G. F. (**1998**). ''Computational modeling of outer hair cell damage: implications for hearing and signal processing,'' in *Psychophysics, Physiology and Models of Hearing* (World Scientific, Singapore), pp. 155–164.
Giguere, C., and Woodland, P. C. (**1994**). ''A computational model of the auditory periphery for speech and hearing research I. Ascending path,'' J. Acoust. Soc. Am. **95**, 331–342.
Goldstein, J. L. (**1990**). ''Modeling rapid waveform compression on the basilar membrane as multiple-bandpass-nonlinearity filtering,'' Hear. Res. **49**, 39–60.
Goldstein, J. L. (**1995**). ''Relations amount compression, suppression and combination tones in mechanical responses of the basilar membrane: data and MBPNL model,'' Hear. Res. **89**, 52–68.
Hartung, K., and Trahiotis, C. (**2001**). ''Peripheral auditory processing and investigations of the ''precedence effect'' which utilize successive transient stimuli,'' J. Acoust. Soc. Am. **110**, 1505–1513.
Hermansky, H. (**1998**). ''Should recognizers have ears?'' Speech Commun. **25**, 3–24.
Hewitt, M. J., and Meddis, R. (**1992**). ''Regularity of cochlear nucleus stellate cells: A computational modeling study,'' J. Acoust. Soc. Am. **93**, 3390–3399.
Irino, T., and Patterson, R. D. (**2001**). ''A compressive gammachirp auditory filter for both physiological and psychological data,'' J. Acoust. Soc. Am. **109**, 2008–2022.
Jenison, R. L., Greenberg, S., Kleunder, K. R., and Rhode, W. S. (**1991**). ''A composite model of the auditory periphery for the processing of speech based on the filter functions of single auditory-nerve fibers,'' J. Acoust. Soc. Am. **90**, 773–785.
Liberman, M. C., and Kiang, N. Y. S. (**1984**). ''Single-neuron labeling and chronic cochlear pathology. IV. Stereocilia damage and alterations in rate- and phase level-functions,'' Hear. Res. **16**, 75–90.
Lopez-Poveda, E. A., and Meddis, R. (**2001a**). ''A human nonlinear cochlear filterbank,'' J. Acoust. Soc. Am. **110**, 3107–3118.
Lopez-Poveda, E. A., and Meddis, R. (**2001b**). ''A human nonlinear cochlear filterbank,'' #827, ARO Midwinter research meeting, Florida.
Meddis, R. (**1986**). ''Simulation of mechanical to neural transduction in the auditory receptor,'' J. Acoust. Soc. Am. **79**, 702–711.
Meddis, R. (**1988**). ''Simulation of auditory-neural transduction: Further studies,'' J. Acoust. Soc. Am. **83**, 1056–1063.
Meddis, R., and Hewitt, M. J. (**1991a**). ''Virtual pitch and phase sensitivity of a computer model of the auditory periphery. I. Pitch Identification,'' J. Acoust. Soc. Am. **89**, 2866–2882.
Meddis, R., and Hewitt, M. J. (**1991b**). ''Virtual pitch and phase sensitivity of a computer model of the auditory periphery. II. Phase sensitivity,'' J. Acoust. Soc. Am. **89**, 2883–2894.
Meddis, R., and Hewitt, M. J. (**1992**). ''Modeling the identification of concurrent vowels with different fundamental frequencies,'' J. Acoust. Soc. Am. **91**, 233–245.
Meddis, R., O'Mard, L. P., and Lopez-Poveda, E. A. (**2001**). ''A computational algorithm for computing nonlinear auditory frequency selectivity,'' J. Acoust. Soc. Am. **109**, 2852–2861.
Müller, M., and Robertson, D. (**1991**). ''Relationship between tone burst discharge pattern and spontaneous firing rate of auditory nerve fibers in the guinea-pig,'' Hear. Res. **57**, 63–70.
Nuttall, A. L., and Dolan, D. F. (**1996**). ''Steady-state sinusoidal velocity responses of the basilar membrane in guinea-pig,'' J. Acoust. Soc. Am. **99**, 1556–1565.
Patterson, R. D., Allerhand, M. H., and Giguére, C. (**1995**). ''Time domain modeling of peripheral auditory processing: A modular architecture and a software platform,'' J. Acoust. Soc. Am. **98**, 1890–1894.
Patterson, R. D., Nimmo-Smith, I., Holdsworth, J., and Rice, P. (**1988**). ''Spiral vos final report, Part A: The auditory filterbank,'' Cambridge Electronic Design, Contract Rep. (Apu 2341).
Pressnitzer, D., Cheveigne, A., and Winter, I. M. (**2002**). ''Perceptual pitch shift for sounds with similar waveform autocorrelation,'' Acoustic Research Letters On-line **3**(1).
Relkin, E. M., and Pelli, D. G. (**1987**). ''Probe tone thresholds in the auditory-nerve measured by 2-interval forced choice procedures,'' J. Acoust. Soc. Am. **82**, 1679–1691.
Rhode, W. S. (**1971**). ''Observations for vibration of the basilar membrane using the Mossbauer technique,'' J. Acoust. Soc. Am. **49**, 1218–1231.
Robert, A., and Eriksson, J. L. (**1999**). ''A composite model of the auditory periphery for simulating responses to complex sounds,'' J. Acoust. Soc. Am. **106**, 1852–1864.
Ruggero, M., Rich, N. C., Recio, A., Narayan, S. S., and Robles, N. (**1997**). ''Basilar membrane responses to tones at the base of the chinchilla,'' J. Acoust. Soc. Am. **101**, 2151–2163.
Sachs, M. B., and Abbas, P. J. (**1974**). ''Rate versus level functions for auditory-nerve fibers in cats: tone burst stimuli,'' J. Acoust. Soc. Am. **56**, 1835–1847.
Sachs, M. B., Bruce, I. C., Miller, R. L., and Young, E. D. (**2002**). ''Biological basis of hearing aid design,'' Ann. Biomed. Eng. **30**, 157–168.
Schoonhoven, R., Keijzer, J., Versnel, H., and Prijs, V. F. (**1994**). ''A dual filter model describing single-fiber responses to clicks in the normal and noise-damaged cochlea,'' J. Acoust. Soc. Am. **95**, 2104–2121.
Shamma, S. A., Chadwick, R. S., Wilbur, W. J., Morrish, K. A., and Rinzel, J. (**1986**). ''A biophysical model of the cochlear processing: Intensity dependence of pure tone responses,'' J. Acoust. Soc. Am. **80**, 133–145.
Summer, C. J., Lopez-Poveda, E. A., O'Mard, L. P., and Meddis, R. (**2002**). ''A revised model of the inner-hair-cell and auditory nerve complex,'' J. Acoust. Soc. Am. **111**, 2178–2188.
Sumner, C. J., Lopez-Poveda, E. A., O'Mard, L. P., and Meddis, R. (**2003**). ''Adaptation in a revised inner-hair cell model,'' J. Acoust. Soc. Am. **113**, 893–901.
Tchorz, J., and Kollmeier, B. (**1999**). ''A model of auditory perception as a front end for automatic speech recognition,'' J. Acoust. Soc. Am. **106**, 2040–2050.
Winter, I. M., and Palmer, A. R. (**1991**). ''Intensity coding in low-frequency auditory-nerve fibers of the guinea-pig,'' J. Acoust. Soc. Am. **90**, 1958–1967.
Winter, I. M., Robertson, D., and Yates, G. K. (**1990**). ''Diversity of characteristic frequency rate-intensity functions in guinea pig auditory nerve fibers,'' Hear. Res. **45**, 191–202.
Yates, G. K., Winter, I. M., and Robertson, D. (**1990**). ''Basilar membrane nonlinearity determines auditory nerve rate-intensity functions and cochlear dynamic range,'' Hear. Res. **45**, 203–220.
Zhang, X. D., Heinz, M. G., Bruce, I. C., and Carney, L. H. (**2001**). ''A phenomenological model for the responses of auditory-nerve fibers: I. Non-linear tuning with compression and suppression,'' J. Acoust. Soc. Am. **109**, 648–670.

Further efforts to predict pure-tone thresholds from distortion product otoacoustic emission input/output functions

Michael P. Gorga,[a] Stephen T. Neely, Patricia A. Dorn, and Brenda M. Hoover
Boys Town National Research Hospital, 555 North 30th Street, Omaha, Nebraska 68131

(Received 28 October 2002; revised 5 March 2003; accepted 6 March 2003)

Recently, Boege and Janssen [J. Acoust. Soc. Am. **111**, 1810–1818 (2002)] fit linear equations to distortion product otoacoustic emission (DPOAE) input/output (I/O) functions after the DPOAE level (in dB SPL) was converted into pressure (in μPa). Significant correlations were observed between these DPOAE thresholds and audiometric thresholds. The present study extends their work by (1) evaluating the effect of frequency, (2) determining the behavioral thresholds in those conditions that did not meet inclusion criteria, and (3) including a wider range of stimulus levels. DPOAE I/O functions were measured in as many as 278 ears of subjects with normal and impaired hearing. Nine f_2 frequencies (500 to 8000 Hz in $\frac{1}{2}$-octave steps) were used, L_2 ranged from 10 to 85 dB SPL (5-dB steps), and L_1 was set according to the equation $L_1 = 0.4L_2 + 39$ dB [Kummer *et al.*, J. Acoust. Soc. Am. **103**, 3431–3444 (1998)] for L_2 levels up to 65 dB SPL, beyond which $L_1 = L_2$. For the same conditions as those used by Boege and Janssen, we observed a frequency effect such that correlations were higher for mid-frequency threshold comparisons. In addition, a larger proportion of conditions not meeting inclusion criteria at mid and high frequencies had hearing losses exceeding 30 dB HL, compared to lower frequencies. These results suggest that DPOAE I/O functions can be used to predict audiometric thresholds with greater accuracy at mid and high frequencies, but only when certain inclusion criteria are met. When the SNR inclusion criterion is not met, the expected amount of hearing loss increases. Increasing the range of input levels from 20–65 dB SPL to 10–85 dB SPL increased the number of functions meeting inclusion criteria and increased the overall correlation between DPOAE and behavioral thresholds. [DOI: 10.1121/1.1570433]

PACS numbers: 43.64.Ha, 43.64.Jb [BLM]

I. INTRODUCTION

The auditory system behaves nonlinearly under normal conditions. Evidence of this nonlinearity can be found in a number of different phenomena, including the production of distortion product otoacoustic emissions (DPOAEs). DPOAEs are observed when two sounds (f_1 and f_2, f_2 slightly higher in frequency than f_1) are presented to the normal ear. These sounds interact in the cochlea at a place close to the best place for the higher of the two frequencies (f_2), producing intermodulation distortion, the largest component of which occurs at a frequency equal to $2f_1$-f_2. It is thought that these nonlinear phenomena are produced by forces exerted by the outer hair cells (OHCs) on basilar membrane mechanical responses (e.g., Brownell, 1990). When cochlear damage exists that affects the OHCs, thresholds are elevated and nonlinear behaviors are reduced or eliminated (e.g., Dallos *et al.*, 1980). Therefore, it is not surprising that DPOAEs are reduced or eliminated by OHC damage as well. These observations have led to the application of DPOAE measurements in efforts to determine auditory status (e.g., Martin *et al.*, 1990; Gorga *et al.*, 1993, 1997, 2000; Kim *et al.*, 1996). With few exceptions, DPOAE measurements have been used to make dichotomous decisions, in which an ear is classified as having either normal hearing or hearing loss. The results from these studies are similar in that DPOAE measurements classify ears dichotomously with greater accuracy for mid and high frequencies, compared to the accuracy that is achieved at lower frequencies.

Several studies have attempted to go beyond this simple, two-state classification scheme and predict auditory thresholds from DPOAE measurements. For example, Martin *et al.* (1990) and Gorga *et al.* (1996) related DPOAE threshold to audiometric threshold. While both studies showed a relationship between the two threshold measurements, these measurements have not been applied clinically, presumably because estimates of DPOAE threshold require several measurements above and below threshold, and the conditions under which these measurements would be made are characterized by poor signal-to-noise ratios (SNR) because DPOAE level is small. Thus, the reliability of direct DPOAE threshold measurements is reduced by the increased uncertainty in response measurements at threshold.

In other attempts to estimate pure-tone thresholds from DPOAE data, DPOAE level or SNR for suprathreshold eliciting stimuli have been correlated with behavioral thresholds for ears with normal hearing (Allen and Levitt, 1992; Dorn *et al.*, 1998) and for ears in which hearing loss existed (Martin *et al.*, 1990; Gorga *et al.*, 1996, 1997, 2002; Janssen *et al.*, 1998; Kummer *et al.*, 1998). Typically, DPOAE level was measured for fixed, moderate-level primaries that produced responses that were well above DPOAE threshold, at least for ears with normal hearing. These DPOAE levels and/or the SNR were then correlated with audiometric thresholds. While DPOAE level or SNR decreased as audio-

[a]Electronic mail: gorga@boystown.org

metric thresholds increased, the relationship was variable, thus reducing the accuracy with which predictions of behavioral thresholds could be made from DPOAE level. Efforts to include several variables in a prediction model did not result in significant improvements in predictive accuracy (Kimberley *et al.*, 1994, 1997).

More recently (Boege and Janssen, 2002; Oswald *et al.*, 2002), DPOAE input/output (I/O) functions have been used to provide estimates of DPOAE thresholds, which were then correlated with behavioral thresholds. In this approach, DPOAE level (in dB SPL) was measured for levels ranging from 20 to 65 dB SPL, with primary levels chosen to optimize response level (Kummer *et al.*, 1998; Janssen *et al.*, 1998). If an SNR inclusion criterion (6 dB) was met for at least three points on the I/O function, these data were converted into pressure (in μPa) and fit with a linear equation. If the linear solutions met some additional inclusion criteria (related to slope of the best fit line and variability), the data were used to determine DPOAE threshold (defined as the extrapolated DPOAE level at which the pressure equaled 0 μPa). Significant correlations were observed between pure-tone and DPOAE thresholds, although estimates of DPOAE threshold were not possible in a percentage of cases. Oswald *et al.* (2002) noted larger discrepancies between DPOAE and behavioral thresholds at 2000 and 8000 Hz, compared to other frequencies, although the effects of frequency were not described in detail. They also observed a tendency to underestimate behavioral threshold by increasing amounts as behavioral threshold increased.

The present study was designed to replicate and extend the work of Boege and Janssen (2002) and Oswald *et al.* (2002). Specifically, DPOAE I/O functions were analyzed using the same stimulus conditions and inclusion criteria as those used in these previous studies. Following a replication of the results observed by Boege and Janssen, the present study extended the previously reported findings by evaluating DPOAE predictions of pure-tone thresholds as a function of frequency. In addition, the audiometric thresholds of those ears not meeting inclusion criteria were evaluated in order to provide information regarding the conditions under which the Boege and Janssen approach did not fit. Finally, additional stimulus conditions and inclusion criteria were tested in order to determine if predictive accuracy could be improved.

II. METHODS

A. Subjects

Ninety-seven subjects with normal hearing and 130 subjects with hearing loss participated in these studies. Depending on frequency and level, DPOAE and audiometric data were available on as many as 278 ears from these subjects. All subjects had normal middle-ear function at the time of the DPOAE measurements, as determined by tympanometry. For the subjects with hearing loss, the site of lesion was assumed to be the cochlea, based on clinical history and other special audiological tests, including measures of speech reception, acoustic reflex thresholds, and auditory brainstem responses. However, specific etiology was frequently undetermined, which is not an uncommon occurrence for clinical studies.

B. DPOAE stimuli

Custom-designed software was used for data collection (EMAV, Neely and Liu, 1994). DPOAE stimuli were produced and responses were recorded by a high-quality soundcard (CardDeluxe, Digital Audio Labs) housed in a PC. The sampling rate was 32 kHz and the sample resolution was 24 bits. Separate channels of the soundcard were used to produce each of the two primary tones. The outputs from each channel were fed to separate loudspeakers housed in a probe-microphone system (Etymotic ER-10C), which had been modified to remove 20 dB of attenuation. A microphone housed in the same probe unit was used to calibrate stimulus level and to record ear-canal responses and noise. While this calibration procedure may introduce errors associated with standing waves (Siegel, 1994, 2002), it represents common practice for DPOAE measurements and was viewed as a reasonable compromise, given the current status of calibration procedures (Neely and Gorga, 1998).

DPOAEs were elicited in response to pairs of primary tones (f_1, f_2), with f_2/f_1 approximately equal to 1.22 for all test conditions, which differs slightly from the 1.20 frequency ratio used by Boege and Janssen (2002). The higher frequency in each primary pair (f_2) varied from 500 to 8000 Hz in $\frac{1}{2}$-octave steps. These frequencies were chosen, in part, because they correspond to the frequencies at which pure-tone audiometric thresholds were measured in the clinic. Given the sampling rate (32 kHz), the duration of the buffer (64 ms), and the number of points in each sample (2048), the frequency resolution was 15.6 Hz. The f_2 frequency was set exactly at the octave and interoctave frequencies described above. The frequency of f_1, however, did not always exactly equal the frequency defined by a primary ratio of 1.22, but was never more than 15.6 Hz away from that frequency. Primary levels (L_1, L_2) were set according to the equation, $L_1 = 0.4\ L_2 + 39$ dB (Kummer *et al.*, 1998; Janssen *et al.*, 1998) for L_2 levels up to 65 dB SPL. Beyond this level, equal-level primaries were used ($L_1 = L_2$). L_2 varied in 5-dB steps from 10 to a maximum of 85 dB SPL. Measurements in four different cavities, validated against measurements in subjects with cochlear implants, were used to determine the level of system distortion [see Dorn *et al.* (2001) for a more complete description of the approach that was taken to estimate system distortion].

C. Audiometric procedures

Pure-tone audiometric data were collected using routine clinical techniques. All measurements were made in a sound-treated booth, using either TDH39 supra-aural earphones or ER-3A insert earphones. Both earphones were calibrated according to their respective standards (ANSI, 1996). Audiometric test frequencies varied from 500 to 8000 Hz in $\frac{1}{2}$-octave steps. The manner in which audiometric stimuli were calibrated and the conditions under which audiometric thresholds were measured represent a potentially important

distinction between the present results and those reported by Boege and Janssen (2002), who used the same system and approach to calibration for both DPOAE and audiometric measurements. Furthermore, they measured behavioral thresholds with 1-dB precision, in contrast to the present measurements, in which 5-dB steps were used.

D. DPOAE procedures

DPOAE data were collected in the form of I/O functions. For each f_2 frequency, stimulus level was initiated at the highest level ($L_2 = 85$ dB SPL). L_2 was then decreased in 5-dB steps until the response was no longer measurable above the noise floor (or the level at which system distortion occurred). Both DPOAE and noise level were measured in the same frequency bin, using a subtraction technique, in which data were collected into two separate buffers, alternating between the two on successive samples. The contents of the two buffers were summed in order to provide an estimate of DPOAE level. Their contents were subtracted in order to provide an estimate of the noise level. Both signal and noise were estimated at the $2f_1$-f_2 distortion frequency. This approach has the advantage of estimating signal and noise levels at the same frequency. However, it has the disadvantage of introducing greater variability in noise estimates, compared to paradigms in which noise is derived from the average level in several frequency bins on either side of $2f_1$-f_2.

Measurement-based stopping rules were used during data collection. Data collection stopped if either of two criteria were met. The first stopping criterion was met when the noise floor was less than -25 dB SPL for L_2 levels of 65 dB SPL or less. For higher-level primaries, the test stopped once the ''noise level'' was less than the level at which system distortion occurred (Dorn *et al.*, 2001). This level increased with primary levels above 65 dB SPL. In both cases, the aim was to measure DPOAEs over the widest range possible without running the risk of misinterpreting system distortion for biological distortion. The second stopping criterion was met when 32 s of artifact-free averaging time had been devoted to that condition, even if the noise-floor criterion was not met. This stopping criterion was necessary to avoid prolonged averaging times for any one condition, as there were many conditions for each subject.

E. Inclusion criteria

Boege and Janssen (2002) set four inclusion criteria for their analyses, one of which related to the reliability of the DPOAE measurements, the other three of which related to the characteristics of linear fits to the DPOAE I/O functions. First, there needed to be at least three points on the DPOAE I/O function with SNR$\geqslant$6 dB. If this criterion was not met, that function was not included in further analyses. If the SNR criterion was met, then DPOAE levels (dB SPL) were converted into pressure (μPa), and the data for each I/O function were fit with a linear equation. Data were included in the next level of analyses only if the slopes of the individual linear regressions were $\geqslant$0.2 μPa/dB,[1] the variance accounted for (r^2) was $\geqslant$0.8, and the standard error was $\leqslant$10 dB. If these criteria were met, the equations were solved for the DPOAE stimlus level (in dB SPL) at which the DPOAE amplitude equaled 0 μPa. This stimulus level was defined as DPOAE threshold, which was then correlated with behavioral thresholds. If these criteria associated with the linear fits to the DPOAE I/O functions were not met, the data were excluded from further analyses. We chose the same inclusion criteria in our first level of analyses in order to obtain results that were comparable to those observed by Boege and Janssen (2002). In additional analyses, we varied these inclusion criteria to determine if more accurate predictions of threshold could be achieved.

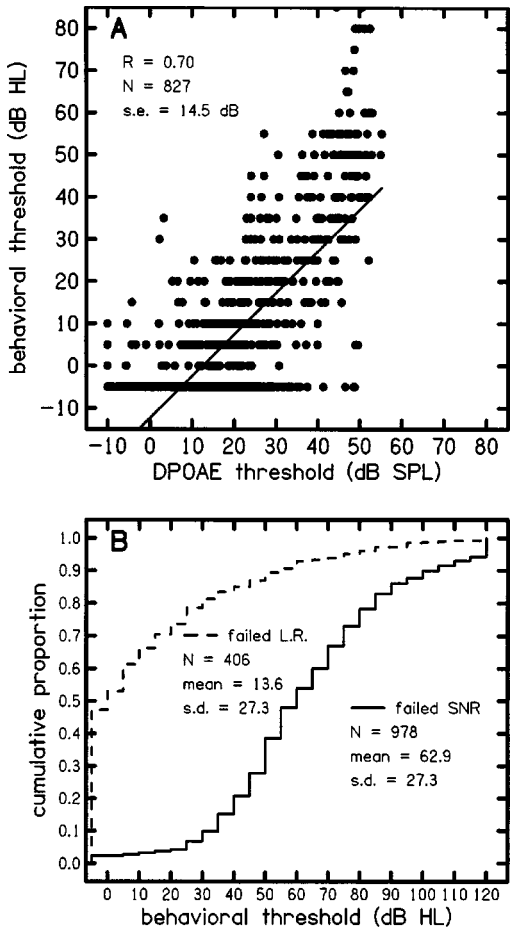

FIG. 1. (a) Behavioral threshold (dB HL) as a function of predicted DPOAE threshold (dB SPL). DPOAE thresholds were predicted from linear fits to individual DPOAE I/O functions (see text for details). The solid line in the figure represents the best-fit line to the behavioral and DPOAE thresholds. Also shown is the correlation coefficient, the number of threshold comparisons (i.e., the number of I/O functions meeting all inclusion criteria), and the standard error. (b) Cumulative proportions of the number of conditions that failed to meet the SNR criterion (solid line) or the inclusion criteria associated with the linear regressions (dashed line) as a function of behavioral threshold (dB HL). See text for details regarding the inclusion criteria. Also shown in this panel are the number of conditions represented on each distribution, the mean behavioral thresholds, and the standard deviations.

III. RESULTS

A. Comparison to Boege and Janssen (2002)

Figure 1(a) plots behavioral pure-tone thresholds (in dB HL) as a function of estimated DPOAE thresholds; recall that DPOAE thresholds (in dB SPL) were defined as the extrapolated stimulus level for which the DPOAE response

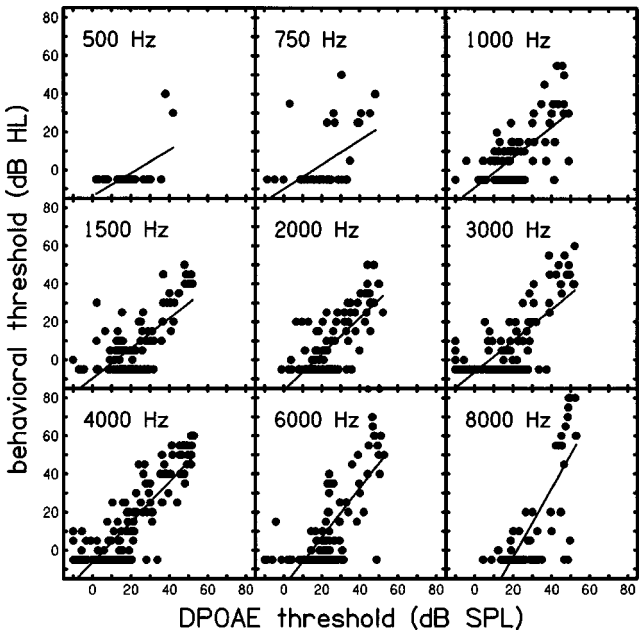

FIG. 2. Behavioral threshold (dB HL) as a function of DPOAE threshold (dB SPL) for each of nine frequencies. Solid lines represent the best-fit line to the data in each panel. See Table I for information regarding correlation coefficients, standard errors, and the number of observations in each panel.

was 0 μPa. For this analysis, primary levels (L_2) were restricted to the range from 20 to 65 dB SPL, which is the same range used by Boege and Janssen (2002). The data included in this figure were collapsed across all nine frequencies, and include only those cases meeting the inclusion criteria previously selected by Boege and Janssen and described above. Thus, these data were derived from DPOAE I/O functions in which at least three points had SNRs$\geqslant$6 dB, and for which the linear fits after converting DPOAE levels to pressure had slopes $\geqslant$0.2 μPa/dB, $r^2 \geqslant 0.8$, and standard errors $\leqslant$10 dB. After applying all of these inclusion criteria, only 827 of 2211 DPOAE I/O functions (37.4%) were selected for further analyses. This percentage is less than the percentage of I/O functions that met criteria in the Boege and Janssen study. One reason for this difference might relate to the distribution of thresholds in the present study, which extended to greater hearing losses, compared to the subjects in the Boege and Janssen study. It is likely that a high proportion of the cases with greater losses did not meet inclusion criteria, especially the SNR criterion. A linear fit to these data is shown as the solid line in Fig. 1(a). The correlation coefficient (r) for these data was 0.70, which is similar to the correlation previously observed by Boege and Janssen ($r = 0.65$). Thus, it would appear that, when analyzed in the same way, the present results are similar to those obtained by Boege and Janssen (2002).

Figure 1(b) plots the cumulative proportions of conditions in which either the SNR criterion was not met (solid line) or, after meeting the SNR criterion, the inclusion criteria associated with the linear regressions were not met (dashed line). These plots are noteworthy for several reasons. Of the total sample of 2211 DPOAE I/O functions, 978 (44.2%) failed to meet the SNR inclusion criterion (i.e., at least three points on the I/O function with a SNR of at least 6 dB). Of these 978 I/O functions, 90% (880) had behavioral thresholds exceeding 30 dB HL, with a mean threshold for these conditions of 62.9 dB HL (SD = 27.3 dB). Thus, it was highly likely that an ear failing the SNR inclusion criterion had hearing loss. An additional 406 DPOAE I/O functions (18.4% of the total sample of 2211) failed to meet the inclusion criteria associated with the linear regressions (slope, correlation coefficient, standard error). Behavioral thresholds exceeded 30 dB HL in only 19% of these cases (77 out of 406 I/O functions not meeting the linear regression criteria). This means that the linear regression inclusion criteria associated with these fits were not met in 329 cases in which normal or near-normal hearing existed. This number represents 14.9% of the total number of I/O functions that were available for analyses. In order to provide a number that shares some characteristics with the false-positive rate, these ears could be added to the number that failed the SNR criterion but had thresholds $\leqslant$30 dB HL (98). Thus, 427 conditions with normal hearing failed to meet criteria; if these cases can be viewed as false positives, then this translates into a false-positive rate of 19.3%.

B. Frequency effects

Figure 2 plots behavioral thresholds (in dB HL) as a function of the predicted DPOAE threshold (in dB SPL) when the data were separated by frequency. Each panel shows the data for a different frequency, going from 500 Hz (upper left panel) to 8000 Hz (lower right panel). In all other respects, the convention followed in Fig. 1(a) is followed here. As a general rule, there were fewer DPOAE data available (and, therefore, fewer opportunities for comparisons between behavioral thresholds and DPOAE thresholds) at lower frequencies. The reduced numbers at low frequencies is a direct result of the fact that noise levels increased as frequency decreased during DPOAE measurements. Thus, fewer DPOAE I/O functions were available that had three points meeting the SNR criterion for lower f_2 frequencies. As a consequence, data are sparse in some panels in Fig. 2 (in particular, those associated with 500 and 750 Hz). Because of this, caution should be exercised when interpreting data in these cases. Reliable predictions are not possible, given the paucity of data at 500 and 750 Hz. At other frequencies, however, a relationship exists between behavioral and DPOAE threshold estimates.

Table I provides a summary that includes the number of observations meeting inclusion criteria for each of the nine test frequencies, along with the slopes, correlations, intercepts, and the standard errors for the linear regressions of behavioral threshold onto DPOAE threshold. In addition to the increase in the number of conditions for which data were available, the correlation between behavioral thresholds and predicted DPOAE thresholds increased as frequency increased. With the exceptions of 500, 6000, and 8000 Hz, the standard errors were relatively constant as a function of frequency. The small standard error at 500 Hz likely results from the fact that, regardless of DPOAE threshold, the vast majority of the cases meeting inclusion criteria had normal behavioral thresholds at this frequency. The reasons for the higher standard errors at 6000 and 8000 Hz are less obvious.

TABLE I. The number of conditions meeting all inclusion criteria, along with the slopes, correlations, and standard errors when behavioral thresholds were predicted from DPOAE thresholds at each of nine frequencies (see Fig. 2).

Frequency (Hz)	No. of conditions meeting inclusion criteria	Slope	Intercept	Correlation	Standard error (dB)
500	27	0.6	−14	0.57	9.0
750	48	0.7	−10	0.49	13.8
1000	88	0.8	−9	0.66	11.6
1500	98	0.8	−10	0.68	11.2
2000	110	1.0	−16	0.74	10.6
3000	103	0.8	−6	0.74	12.5
4000	149	1.1	−6	0.85	11.2
6000	118	1.3	−19	0.74	16.3
8000	81	1.8	−39	0.76	19.2

At 8000 Hz, this effect could be the result of the paucity of observations in which behavioral thresholds were between 20 and 40 dB HL. In addition, the larger standard errors at 6000 and 8000 Hz might have been due to standing-wave problems during DPOAE measurements, although one might predict that these problems would be more likely at 4000 Hz (Siegel, 1994, 2002), a frequency at which performance was particularly good. In general, the correlations increase as frequency increases, achieving a maximum of 0.85 at 4000 Hz, decreasing slightly at 6000 and 8000 Hz.

Following the convention used in Fig. 1(b), Fig. 3 plots the cumulative proportions for those cases failing to meet the SNR criterion and the inclusion criteria associated with the results of the linear regressions. Table II provides a summary of the number of conditions for which the SNR criterion was not met, the percentage of cases in which inclusion criteria were not met *and* threshold ⩽30 dB HL, and the mean thresholds (and standard deviations) for these conditions. The trends in Fig. 3 and Table II are similar to those observed in Fig. 1(b), when all of the data were combined. The

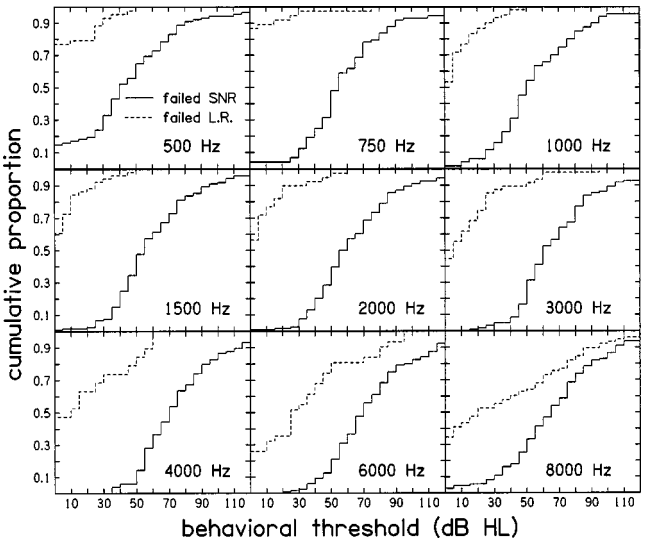

FIG. 3. Cumulative proportions of the number of conditions that failed to meet the SNR criterion (solid lines) or the inclusion criteria related to the linear regressions of individual DPOAE I/O functions (dashed lines) as a function of behavioral threshold (in dB HL). See Table II for a listing of the number of conditions represented on each function, along with the mean behavioral thresholds and their accompanying standard deviations.

TABLE II. The number of conditions failing to meet SNR criterion, the percentage of conditions for which behavioral thresholds were less than or equal to 30 dB HL, and the mean and standard deviations for these conditions at each of nine frequencies (see solid lines, Fig. 3).

Frequency (Hz)	No. of conditions failing SNR criterion	% of thresholds ⩽30 dB HL	Mean thresholds	Standard deviation
500	88	33	44.2	31.3
750	73	12	57.7	26.3
1000	120	16	55.3	26.0
1500	122	7.5	59.4	24.6
2000	124	7.5	63.1	25.1
3000	122	5	67.5	23.8
4000	104	0	74.2	22.5
6000	120	3	73.3	25.0
8000	111	11	65.6	29.0

majority of ears that failed to produce at least three points on the DPOAE I/O function for which the SNR⩾6 dB had behavioral pure-tone thresholds exceeding 30 dB HL. A smaller number of cases were not included because they failed to meet the inclusion criteria associated with the linear fits to individual I/O functions. Thus, hearing loss existed in the majority of conditions in which we could not reliably measure DPOAEs above the noise floor for at least three points on an I/O function.

This point is perhaps made more clearly in Fig. 4, in which the cumulative distributions describing the conditions in which the SNR criterion was not met are superimposed in one plot for the octave frequencies from 500 to 4000 Hz. These are the same distributions that were shown in the appropriate panels of Fig. 3. Note that there is systematic shift of these distributions towards higher behavioral thresholds as frequency increases. Thirty-three percent of the cases in which the SNR was not met at 500 Hz had thresholds better than 30 dB HL, reflecting the difficulty in making DPOAE measurements at such low frequencies. At 1000, 2000, and 4000 Hz, this number was 16%, 7.5%, and 0%, respectively.

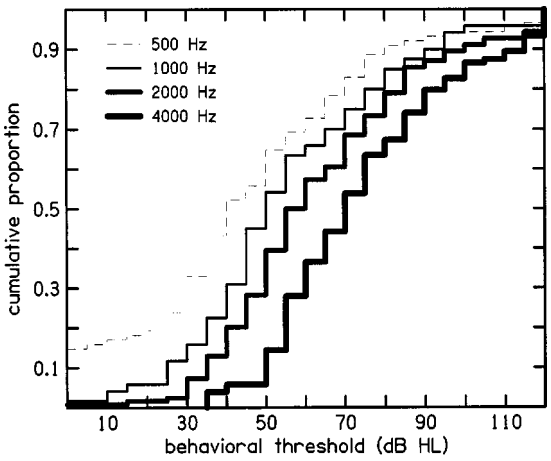

FIG. 4. Cumulative proportions of the behavioral thresholds for those conditions in which the SNR criterion (three points on the I/O function with SNRs⩾6 dB) was not met. These functions are the same data as was shown in the appropriate panels of Fig. 3, only here they are superimposed for the four octave frequencies from 500 to 4000 Hz.

TABLE III. The number of conditions failing to meet criteria associated with linear regressions (LR) for individual DPOAE I/O functions, the percentage of conditions for which behavioral thresholds were less than or equal to 30 dB HL, and the mean and standard deviations for these conditions at each of nine frequencies (see dashed lines, Fig. 3).

Frequency (Hz)	No. of conditions failing LR criteria	% of thresholds ≤30 dB HL	Mean thresholds	Standard deviation
500	43	93.0	3.1	15.7
750	37	97.0	−0.3	14.9
1000	60	93.5	5.2	13.8
1500	51	94.0	3.9	13.4
2000	39	90.0	6.2	16.3
3000	47	87.0	12.4	21.9
4000	19	74.0	17.1	24.6
6000	31	55.0	32.1	31.3
8000	78	55.0	34.6	39.1

Thus, the proportion of time the SNR criterion was not met in normal ears decreased as frequency increased. At 4000 Hz, every condition failing to meet the SNR criterion had thresholds exceeding 30 dB HL. As would be expected from these distributions, there also was a systematic, monotonic increase in mean thresholds as frequency increased, going from 44.2 dB HL at 500 Hz to 74.2 dB HL at 4000 Hz (see Table II).

In comparison to the number of times the SNR criterion was not met, a smaller number of conditions did not meet the inclusion criteria associated with the linear regressions, and the majority of this subset of cases had normal hearing. Table III provides a summary of the number of times this occurred, the percentage of those cases with thresholds ≤30 dB HL, and the mean and standard deviations of the behavioral thresholds for these distributions at each of nine frequencies. In contrast to the behavioral thresholds for those DPOAE I/O functions not meeting the SNR criterion, the majority of the subset of cases not meeting the inclusion criteria associated with the linear regressions had normal hearing.

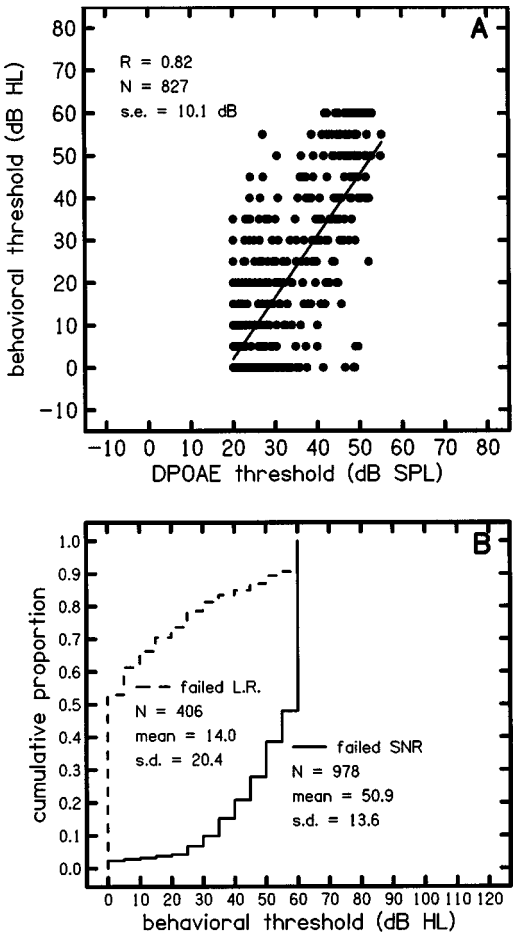

FIG. 5. (a) Behavioral threshold (dB HL) as a function of predicted DPOAE threshold (dB SPL). The analysis here used the same inclusion criteria as was used in the analysis shown in Fig. 1. However, any DPOAE threshold prediction less than 20 dB SPL was arbitrarily set to 20 dB SPL, any behavioral thresholds less than 0 dB HL were set to 0 dB HL, and any behavioral thresholds exceeding 60 dB HL were set to 60 dB HL. (b) Cumulative proportions for the conditions failing to meet the SNR criterion (solid line) or the inclusion criteria associated with the linear regressions (dashed line). Also shown are the number of conditions represented on each distribution, the mean behavioral thresholds and their standard deviations.

C. Extended analyses

Several additional analyses were performed in an effort to (1) improve upon the accuracy with which the data from DPOAE I/O functions predicted behavioral thresholds and (2) increase the number of conditions in which the inclusion criteria were met. In the two analyses described below, data were collapsed across the nine test frequencies. In this respect, these analyses are similar to the approach taken in Fig. 1. Using the same stimulus conditions and inclusion criteria that were used by Boege and Janssen (2002), data were reanalyzed with three added constraints: (1) any DPOAE threshold predictions that were less than 20 dB SPL were arbitrarily set to 20 dB SPL, (2) any behavioral thresholds less than 0 dB HL were arbitrarily set to 0 dB HL, and (3) any behavioral thresholds exceeding 60 dB HL were similarly set to 60 dB HL. The DPOAE threshold limit was based on the view that DPOAE thresholds lower than this would be difficult to measure because of problems associated with the noise floor. The lower behavioral threshold limit was based on the view that it is uncommon to measure behavioral thresholds less than 0 dB HL. The upper limit on behavioral thresholds was based on the hypothesis that DPOAEs are produced by OHCs, and that complete loss of OHCs (with completely normal inner hair cells) will produce no more than about 60 dB of hearing loss. The combined effect of these three constraints was to restrict the threshold predictions to the range where the relation between DPOAE thresholds and behavioral thresholds appears to be most linear. A scatter plot depicting this analysis is shown in Fig. 5(a). This figure follows the convention that was used in Fig. 1(a), with behavioral thresholds plotted as a function of predicted DPOAE thresholds in Fig. 5(a). Cumulative distributions for the cases not meeting either the SNR criterion or the inclusion criteria based on linear regressions are shown in Fig. 5(b). As expected, there was no change in the number of conditions that met the inclusion criteria, as these criteria were not changed in this analysis. Thus, the percentage of ears with normal hearing failing to meet criteria are identical to those described in association with Fig. 1(b). However, the

correlation increased to 0.82 and the standard error decreased to 10.1, both of which represent improvements over what was achieved in the analysis summarized in the top panel of Fig. 1, where there were no constraints on either behavioral or predicted DPOAE thresholds.

In the final analyses, behavioral thresholds and predicted DPOAE thresholds were restricted to the same range that was used for the analysis described in Fig. 5. However, the primary levels (L_2) were expanded to include the range from 10 to 85 dB SPL. This rule was modified so that, for any individual DPOAE I/O function, fits were performed for a maximum range of primary levels of 40 dB, starting at the lowest L_2 level that achieved a 10-dB SNR. The SNR criterion was increased to 10 dB, in part to assure that the DPOAE levels measured for high-level stimuli were not affected by system distortion. The increase in SNR criterion from 6 to 10 dB and the inclusion of higher primary levels might have resulted in a less frequency-specific response, compared to conditions in which the SNR$=6$ dB and primary levels were restricted to 65 dB SPL or less. However, as will be seen below, the correlation was unaffected by these changes. Finally, the criteria based on the linear regressions were altered, such that the slope had to be at least 0.1 μPa/dB, the correlation coefficient had to be $\geqslant 0.7$, and the standard error had to be $\leqslant 9$ dB. In total, these new criteria were selected such that more I/O functions would meet inclusion criteria while the correlation would remain the same or increase. Other criteria also were evaluated (such as returning to the SNR criterion of 6 dB). While other criteria resulted in the inclusion of more I/O functions, they did so at the expense of a reduction in the correlation.

The results of this analysis are summarized in Fig. 6, following the convention used in Figs. 1 and 5. This analysis resulted in the highest correlation (0.83) of any of the three analyses that evaluated the data collapsed across frequency, while the standard error for this condition (10.7) was slightly higher than the standard error observed in one of the previous two analyses (10.1). However, inclusion criteria were met for more than 100 additional conditions in this case. Thus, the inclusion of a wider range of stimulus levels and a slight alteration of the inclusion criteria resulted in an increase in the number of conditions in which the approach proposed by Boege and Janssen (2002) could be applied. Any loss in frequency specificity (due to the increased primary levels and SNR criterion) did not negatively impact the correlation.

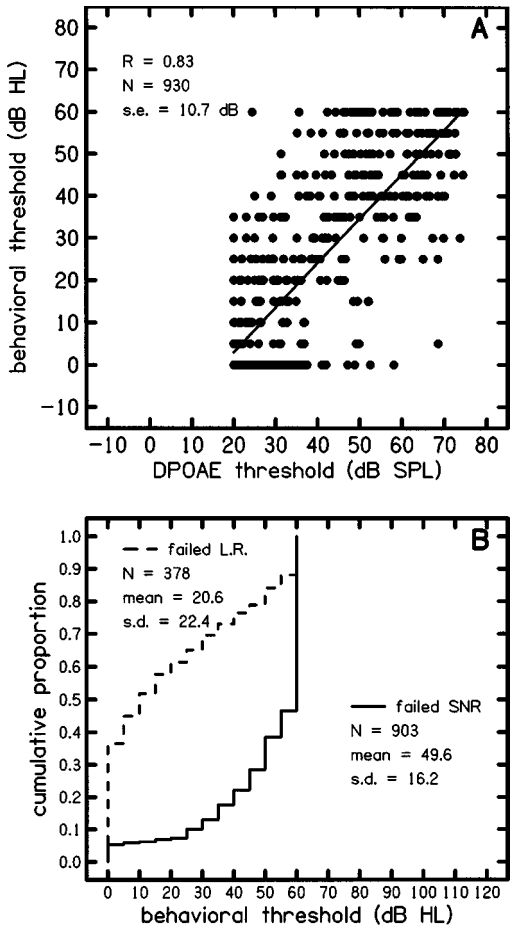

FIG. 6. (a) Behavioral threshold (dB HL) as a function of predicted DPOAE threshold (dB SPL). The range of stimulus levels was increased from 20–65 dB SPL to 10–85 dB SPL; however, only a 40-dB range of stimulus levels was used when fitting linear equations to individual DPOAE I/O functions. In addition, the SNR criterion was changed to 10 dB, and the criteria associated with the linear regressions were relaxed (see text for details). Both DPOAE threshold prediction and behavioral thresholds were restricted in the same way as they were restricted for the analyses shown in Fig. 5. (b) Cumulative proportions for the conditions failing to meet the SNR criterion (solid line) or the inclusion criteria associated with the linear regressions (dashed line). Also shown are the number of conditions represented on each distribution, the mean behavioral thresholds, and their standard deviations.

IV. DISCUSSION

To summarize the results of the first part of this study, the results reported by Boege and Janssen (2002) were essentially replicated, using the same stimulus conditions and inclusion criteria that were used by them. When evaluating the results collapsed across frequency, similar results were observed for the present data compared to the previously reported correlations between behavioral thresholds and predicted DPOAE thresholds, based on linear regressions of DPOAE amplitude (μPa) onto DPOAE stimulus level (dB SPL). The previous results were extended in a number of different ways. First, we evaluated the auditory thresholds among those ears that failed to meet inclusion criteria. The majority of the cases failing to meet a SNR criterion had hearing loss. A smaller number of ears failing to meet inclusion criteria associated with the linear regressions of individual DPOAE I/O functions also had hearing loss. In another extension of the previous work, we evaluated the effect of frequency on the accuracy with which audiometric thresholds could be estimated. The best performance was observed at 4000 Hz. Best performance was defined as the frequency for which the correlation between threshold estimates was highest, the standard error was the lowest, and the percentage of ears not meeting inclusion criteria that also had hearing loss was highest. At low frequencies, performance was particularly poor, but poor performance also was observed at 8000 Hz. Finally, inclusion criteria were adjusted in efforts to determine if better test performance could be achieved with a different set of rules than those proposed by Boege and Janssen (2002). Taking measurements for a wider range of levels and slightly altering the inclusion criteria resulted in

an improvement in test performance. That is, a larger number of conditions met inclusion criteria and a higher correlation was observed between behavioral thresholds and predicted DPOAE thresholds.

It may be important to note that the present results could be specific to the conditions of these measurements, especially the way in which L_1 varied in relation to L_2 (Kummer *et al.*, 1998). It is unclear whether similar results would be observed if a constant primary-level difference of 0, 10, or 15 dB were used. The present data do not allow us to address this issue. In addition, audiometric threshold (in dB HL) was predicted in the present study, whereas Boege and Janssen (2002) predicted behavioral thresholds in dB SPL. Audiometric thresholds were chosen in the present study because of their use in clinical assessments. In addition, converting the present audiometric thresholds to dB SPL would have no influence on the correlations for individual frequencies, since the conversion would amount to adding the same constant to audiometric thresholds in each panel of Fig. 2, even though that constant would vary across frequency. The threshold reference could have had an influence on the correlations between behavioral and DPOAE thresholds when data were collapsed across frequency (Figs. 1, 5, and 6). However, in the condition in which the most direct comparisons could be made between the present results and those reported by Boege and Janssen (see Fig. 1), similar correlations were observed. Thus, there was no apparent detrimental affect of threshold reference on the correlation.

Boege and Janssen (2002) related their DPOAE I/O pressure functions to previous measurements of basilar-membrane motion, described by Ruggero *et al.* (1997). While it is attractive to relate the shape of the DPOAE functions to underlying physiological response properties, it is unclear that such effort was necessary or adds to the practical value of the observations they made. In the end, the success of their approach relies on an empirical evaluation of the extent to which behavioral thresholds can be predicted from DPOAE I/O functions. Their efforts in this regard make an important contribution to the continuing evolution of the clinical application of DPOAE measurements.

Our approach has been to follow a similar empirical evaluation of the extent to which DPOAE measurements can be used to predict behavioral pure-tone thresholds. We were able to essentially replicate the work of Boege and Janssen. If at least three points on the DPOAE I/O function are characterized by a SNR $\geqslant$6 dB, DPOAE levels, converted to pressure and fit with a linear equation of pressure onto stimulus level, can be used to extrapolate to a DPOAE threshold that itself can be used to predict behavioral pure-tone thresholds. An advantage of using supra-threshold values on the DPOAE I/O function is that the measurements can be made in conditions for which a favorable SNR might be observed. Contrast this case with one in which DPOAE thresholds are estimated from direct measurements in which stimulus levels are used that range from being just above to just below DPOAE threshold. Under these latter conditions, the SNR, by definition, will be low in every case, which will affect the reliability of the measurement and make response detection difficult. Thus, supra-threshold DPOAE measurements provide an opportunity for more reliable and potentially quicker measurements than DPOAE threshold measurements. In turn, this could lead to behavioral threshold predictions that might be accomplished under routine clinical conditions.

Our initial, combined-frequency correlation coefficient (0.70) exceeded the correlation reported by Boege and Janssen (0.65) despite our having two additional sources of variability. First, we did not use the same earphone for behavioral threshold and DPOAE measurements, as was done in the previous study. Second, our subjects had a wider range of hearing thresholds. Our observation of a higher correlation may have been due to our use of measurement-based stopping rules, which resulted in longer averaging times for those DPOAE measurements in which the noise level was high.

Several studies have examined the relationship between DPOAE measurements and behavioral thresholds (Martin *et al.*, 1990; Allen and Levitt, 1992; Kimberley *et al.*, 1994, 1997; Gorga *et al.*, 1996, 1997, 2002; Dorn *et al.*, 1998). These studies observed varying degrees of success in relating the two measures. In the end, however, DPOAE measurements have been used almost exclusively to make a dichotomous decision as to whether hearing is normal or impaired, without regard to the magnitude of the hearing loss (e.g., Gorga *et al.*, 1993, 1997, 2000; Stover *et al.*, 1996; Kim *et al.*, 1996). Most multivariate estimates also were concerned with determining if hearing was normal or impaired (Dorn *et al.*, 1999; Gorga *et al.*, 1999), although the work of Kimberley *et al.* (1994, 1997) represents an exception to that rule. The approach described by Boege and Janssen (2002) and Oswald *et al.* (2002) makes use of the entire DPOAE I/O function in deriving an estimate that goes beyond a dichotomous decision and predicts behavioral threshold. Although variable, it was the case that behavioral thresholds could be predicted from DPOAE data, an observation that was replicated in the first part of the present experiment.

Unfortunately, not all DPOAE data met the initial SNR inclusion criterion for a sufficient number of points. Clinically, it is of interest to understand what proportion of the time this occurred and, more importantly, what was the auditory status in those cases when the SNR criterion was not met. Using the same criterion that was used by Boege and Janssen (2002), 44.2% of all DPOAE I/O functions (collapsed across frequency) did not meet the SNR inclusion criterion. However, 90% of these cases had accompanying behavioral thresholds greater than 30 dB HL, and the mean threshold for the entire group failing to meet the SNR criterion was 62.9 dB HL (s.d.$=$27.3 dB) [see Fig. 1(b)]. While it was not possible to predict behavioral threshold from the DPOAE data when the SNR criterion was not met, hearing loss was present in the majority of these cases. From a clinical perspective, this is important information in that the hearing loss was identified by the technique, even if it was not quantified. On the other hand, 18.4% of the total sample of DPOAE I/O functions failed to meet the inclusion criteria associated with the linear regression of DPOAE pressure (μPa) onto DPOAE stimulus level (dB SPL). Eighty-one percent of this subgroup (329 DPOAE I/O functions) had thresholds better than 30 dB HL. In a sense, these cases represent a ''false-positive'' condition, in which normal ears

failed to meet criteria. When added to the number of conditions for which the SNR criterion was not met among ears with thresholds less than or equal to 30 dB HL (98 conditions), one derives an overall ''false-positive'' rate of 19.3% ((329+98)/2211). Obviously, reducing this number would be of clinical interest.

Errors in prediction were not uniformly distributed across frequency. The best performance was observed for mid-to-high frequencies, with poorer performance at lower frequencies, 8000 Hz, and perhaps 6000 Hz (see Figs. 2–4, and Tables I–III). For example, the correlations were higher and the standard errors were typically lower at 2000, 3000, and 4000 Hz, compared to higher and lower frequencies. Furthermore, the percentage of cases with behavioral thresholds less than or equal to 30 dB HL that did not meet the SNR criterion were lower at these frequencies (7.5% at 2000 Hz, 5% at 3000 Hz, and 0% at 4000 Hz). Thus, there was a smaller percentage of cases at 2000, 3000, and 4000 Hz for which the SNR criterion was not met *and* hearing was normal. Finally, one can also estimate something akin to a ''false-positive'' rate by adding the number of cases with behavioral thresholds $\leqslant$30 dB HL that failed to meet either the SNR criterion or the inclusion criteria associated with the linear regression, and divide this number by the total number of DPOAE I/O functions for these three frequencies. This results in a ''false-positive'' rate of 12.9%, which is less than the similarly calculated percentage collapsed across all frequencies (19.3%). These observations are not unexpected, given previous results that have demonstrated that DPOAE test performance in a dichotomous pass/fail decision is better at mid and high frequencies, compared to lower frequencies (e.g., Gorga *et al.*, 1993, 1997, 2000; Kim *et al.*, 1996; Stover *et al.*, 1996).

Finally, overall performance was improved if the range of predicted DPOAE thresholds and the range of behavioral thresholds were restricted. These restrictions resulted in an increase in the correlation from 0.70 to 0.82. Additionally, including a wider range of stimulus levels and altering the inclusion criteria associated with the linear regressions resulted in a slight further increase in the correlation between behavioral thresholds and predicted DPOAE thresholds. More importantly, these changes in inclusion criteria allowed for predictions of behavioral thresholds in a larger percentage of DPOAE measurements. Some of these manipulations are based in an understanding of both DPOAE responses and behavioral thresholds, and others are more arbitrary. However, these results suggest that further improvements in accuracy might be achieved through additional efforts to optimize predictions of behavioral thresholds from DPOAE data (see also Oswald *et al.*, 2002).

ACKNOWLEDGMENTS

This work was supported by a grant from the NIH (NIDCD R01 DC2251). Portions of this work were presented at the 2003 Midwinter Meeting of the Association for Research in Otolaryngology. We thank two anonymous reviewers for their helpful suggestions on an earlier version of this manuscript.

[1]This slope criterion value differs from the 0.1 μPa/dB criterion reported by Boege and Janssen (2002) in their Eq. (4), but agrees with the value shown in their Fig. 8(b). The slope criterion listed in their Eq. (4) (0.1 μPa/dB) represents a typographical error. The actual slope criterion was 0.2 μPa/dB, which is what was used in their Fig. 9 (Boege, 2002), which represents the summary to which the present data are compared.

Allen, J. B., and Levitt, H. (**1992**). ''A comparison of pure tone audiometric and distortion product otoacoustic emission thresholds,'' unpublished manuscript.

ANSI(**1996**). ANSI S3.6, ''Specifications for Audiometers'' (American Institute of Physics, New York).

Boege, P. (**2002**). Personal communication.

Boege, P., and Janssen, T. (**2002**). ''Pure-tone threshold estimation from extrapolated distortion product otoacoustic emission I/O functions in normal and cochlear hearing loss ears,'' J. Acoust. Soc. Am. **111**, 1810–1818.

Brownell, W. E. (**1990**). ''Outer hair cell electromotility and otoacoustic emissions,'' Ear Hear. **11**, 82–92.

Dallos, P. J., Harris, D. M., Relkin, E., and Cheatham, M. A. (**1980**). ''Two-tone suppression and intermodulation distortion in the cochlea: Effect of outer hair cell lesions,'' in *Psychophysical, Physiological and Behavioral Studies of Hearing*, edited by G. van den Brink and F. A. Bilsen (Delft U. P., Delft, The Netherlands), pp. 242–252.

Dorn, P. A., Piskorski, P., Gorga, M. P., Neely, S. T., and Keefe, D. H. (**1999**). ''Predicting audiometric status from distortion product otoacoustic emissions using multivariate analyses,'' Ear Hear. **20**, 149–163.

Dorn, P. A., Piskorski, P., Keefe, D. H., Neely, S. T., and Gorga, M. P. (**1998**). ''On the existence of an age/threshold/frequency interaction in distortion product otoacoustic emissions,'' J. Acoust. Soc. Am. **104**, 964–971.

Dorn, P. A., Konrad-Martin, D., Neely, S. T., Keefe, D. H., Cyr, E., and Gorga, M. P. (**2001**). ''Distortion product otoacoustic emission input/output functions in normal-hearing and hearing-impaired human ears,'' J. Acoust. Soc. Am. **110**, 3119–3131.

Gorga, M. P., Neely, S. T., and Dorn, P. A. (**1999**). ''DPOAE test performance for a priori criteria and for multifrequency audiometric standards,'' Ear Hear. **20**, 345–362.

Gorga, M. P., Neely, S. T., and Dorn, P. A. (**2002**). ''Distortion product otoacoustic emissions in relation to hearing loss,'' in *Otoaccoustic Emissions: Clinical Applications*, 2nd ed., edited by M. S. Robinette and T. J. Glattke (Thieme Medical, New York), pp. 243–272.

Gorga, M. P., Stover, L. J., and Neely, S. T. (**1996**). ''The use of cumulative distributions to determine critical values and levels of confidence for clinical distortion product otoacoustic emission measurements,'' J. Acoust. Soc. Am. **100**, 968–977.

Gorga, M. P., Nelson, K., Davis, T., Dorn, P. A., and Neely, S. T. (**2000**). ''Distortion product otoacoustic emission test performance when both 2f1-f2 and 2f2-f1 are used to predict auditory status,'' J. Acoust. Soc. Am. **107**, 2128–2135.

Gorga, M. P., Neely, S. T., Ohlrich, B., Hoover, B., Redner, J., and Peters, J. (**1997**). ''From laboratory to clinic: A large scale study of distortion product otoacoustic emissions in ears with normal hearing and ears with hearing loss,'' Ear Hear. **18**, 440–455.

Gorga, M. P., Neely, S. T., Bergman, B. M., Beauchaine, K. L., Kaminski, J. R., Peters, J., and Jesteadt, W. (**1993**). ''Otoacoustic emissions from normal-hearing and hearing-impaired subjects: Distortion product responses,'' J. Acoust. Soc. Am. **93**, 2050–2060.

Janssen, T., Kummer, P., and Arnold, W. (**1998**). ''Growth behavior of the 2f1-f1 distortion product otoacoustic emission in tinnitus,'' J. Acoust. Soc. Am. **94**, 2659–2669.

Kim, D. O., Paparello, J., Jung, M. D., Smursynski, J., and Sun, X. (**1996**). ''Distortion product otoacoustic emission test of sensorineural hearing loss: Performance regarding sensitivity, specificity, and receiver operating characteristics,'' Acta Octolaryngol. (Stokh.) **116**, 3–11.

Kimberley, B. P., Hernadi, I., Lee, A. M., and Brown, D. K. (**1994**). ''Predicting pure-tone thresholds in normal and hearing-impaired ears with distortion product emission and age,'' Ear Hear. **15**, 199–209.

Kimberley, B. P., Brown, D. K., and Allen, J. B. (**1997**). ''Distortion product emissions and sensorineural hearing loss,'' in *Otoacoustic Emissions: Clinical Applications*, edited by M. S. Robinette and T. J. Glattke (Thieme Medical, New York), pp. 181–204.

Kummer, P., Janssen, T., and Arnold, W. (**1998**). ''The level and growth

behavior of the $2f_1$-f_2 distortion product otoacoustic emission and its relationship to auditory sensitivity in normal hearing and cochlear hearing loss,'' J. Acoust. Soc. Am. **103**, 3431–3444.

Martin, G. K., Ohlms, L. A., Franklin, D. J., Harris, F. P., and Lonsbury-Martin, B. L. (**1990**). ''Distortion product emission in humans. III. Influence of sensorineural hearing loss,'' Ann. Otol. Rhinol. Laryngol. Suppl. **147**, 30–42.

Neely, S. T., and Gorga, M. P. (**1998**). ''Comparison between intensity and pressure as measures of stimulus level in the ear canal,'' J. Acoust. Soc. Am. **104**, 2925–2934.

Neely, S. T., and Liu, Z. (**1994**). ''EMAV: Otoacoustic emission averager,'' Tech. Memo No. 17 (Boys Town National Research Hospital, Omaha, NE).

Oswald, J. A., Muller, J., and Janssen, T. (**2002**). ''Audiometric threshold estimation in cochlear hearing loss ears by means of weighted extrapolated DPOAE I/O functions,'' presented at the Twenty-Fifth Annual Midwinter Research Meeting of the Association for Research in Otolaryngology, St. Petersburg Beach, FL.

Ruggero, M. A., Rich, N. C., Recio, A., Narayan, S. S., and Robles, L. (**1997**). ''Basilar-membrane responses to tones at the base of the chinchilla cochlea,'' J. Acoust. Soc. Am. **101**, 2151–2163.

Siegel, J. H. (**1994**). ''Ear-canal standing waves and high-frequency sound calibration using otoacoustic emission probes,'' J. Acoust. Soc. Am. **95**, 2589–2597.

Siegel, J. H. (**2002**). ''Calibrating Otoacoustic Emission Probes,'' in *Otoacoustic Emissions: Clinical Applications*, 2nd ed., edited by M. S. Robinette and T. J. Glattke (Thieme Medical, New York), pp. 416–441.

Stover, L., Gorga, M. P., Neely, S. T., and Montoya, D. (**1996**). ''Towards optimizing the clinical utility of distortion product otoacoustic emission measurements,'' J. Acoust. Soc. Am. **100**, 956–967.

Amplitude and phase of distortion product otoacoustic emissions in the guinea pig in an (f_1, f_2) area study

Sandra Schneider, Vera F. Prijs,[a] and Ruurd Schoonhoven[b]
Leiden University Medical Center, Department of ENT/Audiology, P.O. Box 9600, 2300 RC Leiden, The Netherlands

(Received 28 June 2002; revised 14 February 2003; accepted 18 February 2003)

Lower sideband distortion product otoacoustic emissions (DPOAEs), measured in the ear canal upon stimulation with two continuous pure tones, are the result of interfering contributions from two different mechanisms, the nonlinear distortion component and the linear reflection component. The two contributors have been shown to have a different amplitude and, in particular, a different phase behavior as a function of the stimulus frequencies. The dominance of either component was investigated in an extensive (f_1, f_2) area study of DPOAE amplitude and phase in the guinea pig, which allows for both qualitative and quantitative analysis of isophase contours. Making a minimum of additional assumptions, simple relations between the direction of constant phase in the (f_1, f_2) plane and the group delays in f_1-sweep, f_2-sweep, and fixed f_2/f_1 paradigms can be derived, both for distortion (wave-fixed) and reflection (place-fixed) components. The experimental data indicate the presence of both components in the lower sideband DPOAEs, with the reflection component as the dominant contributor for low f_2/f_1 ratios and the distortion component for intermediate ratios. At high ratios the behavior cannot be explained by dominance of either component. [DOI: 10.1121/1.1568753]

PACS numbers: 43.64.Jb, 43.64.Kc [BLM]

I. INTRODUCTION

Distortion product otoacoustic emissions have, since their first appearance in literature in 1979 (Kemp, 1979), been of great interest to researchers in the field of cochlear mechanics. In the past several years, the main focus has been on the generation mechanisms of the DPOAE and the places in the cochlea involved in the generation. Evidence for the two-source model of DPOAE generation, first proposed by Kim (1980), was collected and there is now a solid basis for Kim's theory that the lower sideband DPOAEs (with $f_{dp} < f_1, f_2$) consist of at least two components, one coming from the overlap region of the primaries near X_2 and one coming from the DP characteristic place X_{dp} (Kummer *et al.*, 1995; Brown *et al.*, 1996; Heitmann *et al.*, 1998; Mauermann *et al.*, 1999; Talmadge *et al.*, 1999; Shera and Guinan, 1999). However, Shera and Guinan (1999) and Kalluri and Shera (2001) have argued that the fundamental difference between the two components that contribute to the DPOAE in the ear canal is in the mechanism, not just in the location of the source. Instead of ''two-source model,'' they use the term ''two-mechanism model.'' In this model, nonlinear distortion at the overlap region near X_2 generates the initial component that travels both basally and apically, while linear coherent reflection at the apical DP place results in the second backward traveling component (Talmadge *et al.*, 1998; Shera and Guinan, 1999; Kalluri and Shera, 2001). Together with multiple internal reflections they add up to the DPOAE in the ear canal. Note that the dichotomy between distortion component and reflection component breaks down in the limit of f_2/f_1 approaching 1. In this limit, the lower sideband DPOAEs are not reflected, but actually generated near their resonance place.

The less studied upper sideband DPOAEs (with $f_{dp} > f_1, f_2$) cannot be described by the two-mechanism model, at least not with a distortion source at X_2 and a reflection at X_{dp}, since the distortion product cannot propagate as a wave on the basilar membrane from X_2 to the basal X_{dp}. If the upper sideband DPOAEs are generated by nonlinear distortion at X_2, the basilar membrane might be driven at X_{dp} by a different mechanism (e.g., fluid coupling or evanescent waves), so the distortion product is reemitted at X_{dp}. Data suggesting that these DPOAEs arise directly from around the DP frequency place was presented by Martin *et al.* (1987, 1998).

The nonlinear distortion mechanism has proven to be a wave-fixed mechanism, meaning that the source location is fixed to the traveling wave pattern, in this case of f_2 (Kemp, 1986; Shera and Guinan, 1999). On the other hand, linear reflection is a place-fixed phenomenon, occurring at irregularities in the mechanics of the cochlea around the DP characteristic place (Shera and Guinan, 1999). Originally, the terms place-fixed and wave-fixed were not coupled to the two distinct locations in the cochlea but were seen as two possible mechanisms for DPOAE generation at X_2 (Kemp, 1986; O'Mahoney and Kemp, 1995; Moulin and Kemp, 1996).

The distortion component and the reflection component show a different phase behavior as a function of frequency, which is the main reason they were recognized as being the

[a]Current affiliation: Department of Otolaryngology/Audiology, VU Medical Center, P.O. Box 7057, 1007 MB Amsterdam, The Netherlands.
[b]Author to whom correspondence should be addressed. Current affiliation: Department Clinical Physics and Informatics, VU Medical Center, P.O. Box 7057, 1007 MB Amsterdam, The Netherlands. Electronic mail: r.schoonhoven@vumc.nl

result of two such different mechanisms (Talmadge *et al.*, 1998; Knight and Kemp, 2000; Kalluri and Shera, 2001). Phase versus frequency measurements can be used to determine the presence of the different components. Several experimental paradigms are in use for measuring DPOAE phase behavior. Phase versus frequency curves have been measured with f_1-sweep or f_2-sweep (respectively, fixing f_2, varying f_1 and fixing f_1, varying f_2) but also with constant f_2/f_1 (Kimberley *et al.*, 1993; O'Mahoney and Kemp, 1995; Knight and Kemp, 1999; Shera *et al.*, 2000). Comparing the results of these paradigms is difficult due to the fact that the place of generation, tightly linked to the envelope of the f_2-wave, remains fixed in an f_1-sweep, but moves in different ways along the basilar membrane in the other sweep paradigms (Tubis *et al.*, 2000; Prijs *et al.*, 2000). Phase slope delays of lower sideband DPOAEs measured with f_2-sweep, at intermediate frequency ratios, are larger than delays measured with f_1-sweep (O'Mahoney and Kemp, 1995; Moulin and Kemp, 1996; Schneider *et al.*, 1999). This observation can be understood by considering the shift of generation site in the f_2-sweep paradigm in the wave-fixed model, combined with the assumption of scaling invariance of the cochlea (Schneider *et al.*, 2000; Prijs *et al.*, 2000; Shera *et al.*, 2000; Talmadge *et al.*, 2000; Tubis *et al.*, 2000). When measuring the DPOAEs by varying both f_1 and f_2 in small frequency steps and so mapping part of the (f_1,f_2) plane in detail, phase slope delays in all directions like constant f_1, constant f_2, and constant f_2/f_1 can be deduced (Knight and Kemp, 2000). This gives a more detailed view of the DPOAE phase behavior than single sweeps.

The phase of the nonlinear distortion component is roughly constant when measured with constant frequency ratio f_2/f_1, which can be understood by assuming cochlear scale invariance, since in that case the relative phases of the three components f_1, f_2, and f_{dp} remain unchanged (Talmadge *et al.*, 1998; Shera and Guinan, 1999; Knight and Kemp, 2000; Shera *et al.*, 2000). Using their unmixing strategy, Kalluri and Shera (2001) showed that the phase of the reflection component, analogous to the SFOAE, changes fast with frequency in a constant f_2/f_1 paradigm. Interference of the two components with different phase behavior, the distortion component with the shallow phase gradient and the reflection component with the steep phase gradient, results in fine structure in the DPOAE amplitude (Talmadge *et al.*, 1998, 1999; Heitmann *et al.*, 1998). Suppression of the reflection component by using a third tone close to f_{dp} yields a shallow phase gradient and a smooth DPOAE amplitude (Heitmann *et al.*, 1998; Talmadge *et al.*, 1999; Kalluri and Shera, 2001). The relative contribution of each component to the total DPOAE varies with stimulus parameters, especially frequency ratio f_2/f_1 (Knight and Kemp, 2000) and stimulus level (Fahey and Allen, 1997). Knight and Kemp (2000) found shallow phase gradients for intermediate ratios ($f_2/f_1=1.1-1.3$) and steep phase gradients for a small ratio (1.05). Which of the two components dominates the total DPOAE as a function of stimulus parameters is an important question, for instance for the interpretation of clinical DPOAE data, and obviously DPOAE phase behavior is an important clue in answering this question.

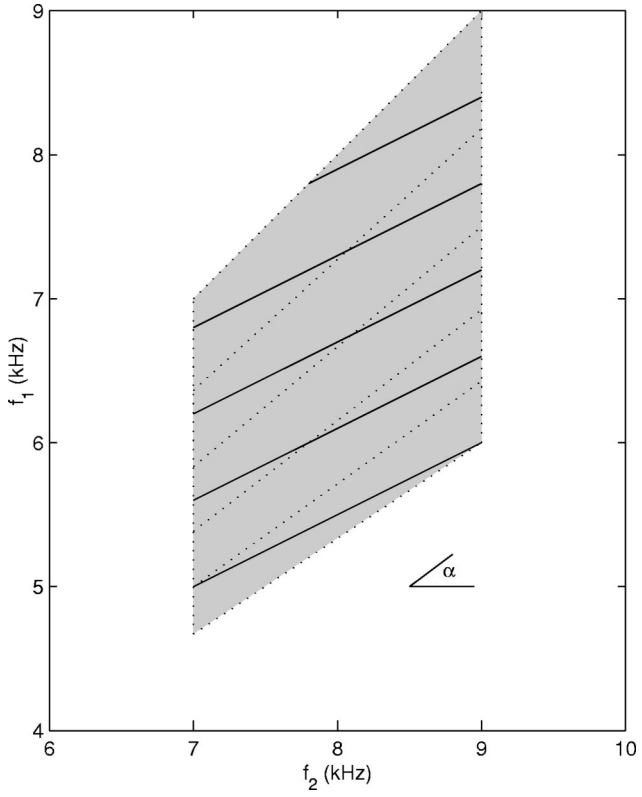

FIG. 1. The (f_1,f_2) area representation. Amplitude and phase will be plotted on this empty (f_1,f_2) matrix. Lines of constant f_{dp} are parallel in this representation, and are shown for the $2f_1-f_2$ distortion product (solid). Their slope depends on DPOAE order. Lines of constant f_2/f_1 (dashed) radiate from the origin (0,0).

In this study we report extensive measurements of guinea pig DPOAE amplitude and phase in an (f_1,f_2) area. The measurements are an extension of some of our previous work (Schneider *et al.*, 1999, 2001), in which we presented DPOAE phase-frequency and amplitude-frequency data measured with f_1- and f_2-sweeps, and group delays determined at optimum ratio only. In several respects, the data and their analysis are also an extension and further elaboration of the work of Knight and Kemp (2000, 2001). Because of the higher signal-to-noise ratio in the guinea pig (Schneider *et al.*, 1999) more detailed information could be obtained on higher order DPOAEs. Besides the presentation of amplitude and phase maps, several more quantitative ways of analyzing the data are elaborated, concentrating on group delays and their mutual relations as a function of f_2/f_1 ratio. To investigate the influence of stimulus level ratio on the relative contribution of the distortion and reflection components, we used two sets of stimulus levels. Finally, some interesting results on fine structure in guinea pig DPOAEs are considered.

II. THEORY

The (f_1,f_2) area representation that we use in this paper is schematically shown in Fig. 1, as an empty (f_1,f_2) matrix on which amplitude and phase can be plotted. Both upper and lower sideband DPOAEs ($f_{dp}>f_1,f_2$ and $f_{dp}<f_1,f_2$,

respectively) will be shown in the same representation, with f_2 on the horizontal axis. Lines of constant DP frequency are parallel in this representation, and shown for the cubic distortion product $2f_1-f_2$ (solid). Their slope depends on DPOAE order. Lines of constant frequency ratio f_2/f_1 (dashed) radiate from the origin (0,0). When DPOAE phase is known in all points neighboring (f_1,f_2) in this representation, phase slope delays in all desired directions can be obtained. Phase slope delay (often called group delay) is defined as

$$D=-\frac{1}{2\pi}\frac{d\varphi_{\mathrm{dp}}}{df_{\mathrm{dp}}} \tag{1}$$

with φ_{dp} the phase of the distortion product and $f_{\mathrm{dp}}=(n+1)f_1-nf_2$ (n integer, and $f_1<f_2$). A group delay is usually measured by changing the DPOAE frequency f_{dp} in one of three controlled manners; by changing f_1 while keeping f_2 fixed (f_1-sweep), by changing f_2 while keeping f_1 fixed (f_2-sweep), and by changing both f_1 and f_2 at a fixed frequency ratio. We term the resulting delays, respectively, D_1, D_2, and $D_{12|\mathrm{R}}$. In the (f_1,f_2) area representation, trigonometrical relations hold between the phase gradients in the two perpendicular directions and the phase gradient in an oblique direction at angle α (see Fig. 1). However, these phase gradients are not derivatives to the DPOAE frequency f_{dp}. The f_1- and f_2-sweep group delays can be calculated from the phase gradients as follows:

$$D_1=-\frac{1}{2\pi}\frac{d\varphi}{df_{\mathrm{dp}}}\bigg|_{f_2}=-\frac{1}{2\pi}\frac{1}{n+1}\frac{\partial\varphi}{\partial f_1}, \tag{2}$$

$$D_2=-\frac{1}{2\pi}\frac{d\varphi}{df_{\mathrm{dp}}}\bigg|_{f_1}=\frac{1}{2\pi}\frac{1}{n}\frac{\partial\varphi}{\partial f_2}. \tag{3}$$

The group delay in any direction α can be calculated by expressing the DPOAE phase change and frequency change as a function of α and the change in f_2. At constant α the DPOAE phase change is given by

$$\begin{aligned} d\varphi|_\alpha&=\left(\frac{\partial\varphi}{\partial f_1}\cdot\tan\alpha+\frac{\partial\varphi}{\partial f_2}\right)df_2\\ &=-2\pi((n+1)\cdot\tan\alpha\cdot D_1-n\cdot D_2)df_2 \end{aligned} \tag{4}$$

while the associated DPOAE frequency change is given by

$$df_{\mathrm{dp}}|_\alpha=((n+1)\cdot\tan\alpha-n)df_2. \tag{5}$$

Combining Eqs. (1), (4), and (5) results in the group delay for constant α in a point (f_1,f_2), which depends on the f_1- and f_2-sweep group delays D_1 and D_2 according to

$$\begin{aligned} D(\alpha)&=-\frac{1}{2\pi}\frac{d\varphi}{df_{\mathrm{dp}}}\bigg|_\alpha\\ &=\frac{(n+1)\cdot\sin\alpha\cdot D_1-n\cdot\cos\alpha\cdot D_2}{(n+1)\cdot\sin\alpha-n\cdot\cos\alpha}. \end{aligned} \tag{6}$$

This reduces to the f_1-sweep group delay D_1 for $\alpha=90°$ and the f_2-sweep group delay D_2 for $\alpha=0°$. For a sweep with constant frequency ratio f_2/f_1, the group delay $D_{12|\mathrm{R}}$ can be derived from D_1 and D_2 by applying Eq. (6) using $\alpha=\arctan(f_1/f_2)$ and

$$\rho_n=\frac{n+1}{nR} \tag{7}$$

with $R=f_2/f_1$. This results in

$$D_{12|\mathrm{R}}=\frac{\rho_n\cdot D_1-D_2}{\rho_n-1}. \tag{8}$$

This expression, which is independent of any model or generation mechanism, relates the three phase-gradient delays, and is in fact the same relation Shera *et al.* [Shera *et al.* (2000), Eq. (22)] have derived.

A. Distortion component

For the distortion component (or wave-fixed DPOAE component), under the assumptions of a logarithmic place-frequency map and frequency-shift invariance, the phase profiles of the components involved in DPOAE generation are fixed when the frequency ratio f_2/f_1 is kept constant (Talmadge *et al.*, 1998; Prijs *et al.*, 2000). This implies that changing the DPOAE frequency in a fixed-ratio-sweep yields a flat phase versus frequency curve for the distortion component, resulting in

$$D_{12|\mathrm{R}}=0. \tag{9}$$

Combining Eqs. (8) and (9) gives the previously derived relation between D_1 and D_2 for the wave-fixed model (Schneider *et al.*, 2000; Talmadge *et al.*, 2000; Prijs *et al.*, 2000)

$$\frac{D_2}{D_1}=\frac{n+1}{n}\frac{f_1}{f_2}=\rho_n. \tag{10}$$

So, the group delays of a DPOAE consisting only of the distortion component (a wave-fixed emission) are expected to obey Eqs. (9) and (10), which express exactly the same feature as isophase contours in the direction of constant f_2/f_1 in the area representation. This holds for both lower sideband and upper sideband DPOAEs, with a distortion component generated at any place along the basilar membrane.

B. Reflection component

When the reflection component (a place-fixed emission) dominates the total lower sideband DPOAE, the phase is expected to be constant in a direction of constant f_{dp} (Knight and Kemp, 2000), implying

$$D(\alpha)=0 \tag{11}$$

with $\tan(\alpha)=n/(n+1)$. Substituting this in Eq. (6) results in

$$\frac{D_2}{D_1}=1. \tag{12}$$

Subsequently, with Eq. (8) this results in

$$D_{12|\mathrm{R}}=D_1=D_2. \tag{13}$$

This relation, for the case of a dominant reflection component, has also been predicted by Tubis *et al.* (2000).

A similar analytical treatment of the upper sideband DPOAEs based on their reemission at the more basal X_{dp} has not been derived so far, albeit that for the USB reemission component $D_{12|R}$ will be different from zero. In addition, Eqs. (12) and (13) will hold for $f_2/f_1=1$ and large f_2/f_1. Possible small deviations may occur for midrange ratios (Knight and Kemp, 2000).

III. METHODS

A. Animal care and preparation

The results presented in this study have been obtained from acute experiments in six female albino guinea pigs with a body weight of 440–545 g ($n=5$) or 900 g ($n=1$). They all showed healthy middle ears upon otoscopic inspection and positive Preyer's reflexes. The guinea pigs were premedicated with atropine-sulphate (75 μg/kg, intramuscular) and anaesthetized with an intramuscular injection of thalamonal (1.6 ml/kg), which is a combination of fentanyl (0.05 mg/ml) and droperidol (2.5 mg/ml), followed 15 min later by nembutal (23 mg/kg, intraperitoneal). Supplementary doses were administered approximately every 60 min (fentanyl, 0.08 mg/kg) and every 80 min (nembutal, 2.7 mg/kg). Body temperature was maintained at 38 ± 0.5 °C using a thermostatically controlled heating pad. The guinea pigs were tracheotomized and the trachea was cleared at least every hour. The ear with the highest $2f_1-f_2$ amplitude at $f_2=8$ kHz (with $f_2/f_1=1.3$, $L_1=65$ dB SPL, $L_2=55$ dB SPL) was used in the experiments. The pinna of this ear was removed, leaving a small part of the external auditory meatus. The head was stabilized with a bite-ring, an earbar in the contralateral external auditory meatus, and a probeholder in the ipsilateral external auditory meatus (with removed pinna). The microphone probe assembly was sealed into the external auditory meatus through the probeholder. This experimental approach was chosen because of the desired stable recording conditions over a long duration of data collection. Procedures were approved by the animal care committee of the Leiden University.

B. Material

DPOAEs were measured using a Tucker Davis Technologies (TDT) system, consisting of a signal processing board, AD- and DA-converters, a trigger device, a clock-generator, headphone buffers, and programmable attenuaters. Customized software, developed in Delphi (Borland) was used. The clock-generator provided a clock rate of 100 kHz, which synchronized the trigger device, AD-, and DA-converters and served as the sample rate for both AD and DA conversion. Stimulus tones f_1 and f_2 were played from two separate DA channels, attenuated separately and delivered to separate ER2 transducers (Etymotics Research). A low-noise microphone ER10-B (Etymotics Research), housed in a customized probe, recorded the frequency response in the ear canal. The microphone signal was preamplified 40 dB.

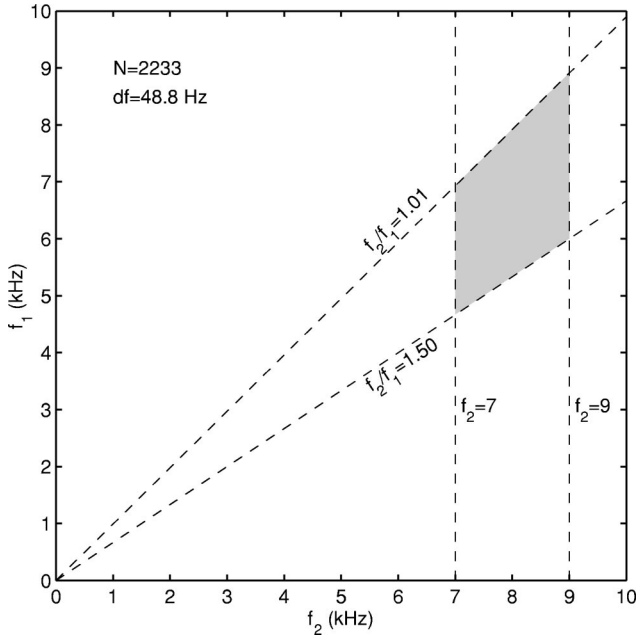

FIG. 2. Area (shaded) of frequency combinations in the (f_1,f_2) plane at which the DPOAE measurements were done. Frequency f_2 varied from 7 to 9 kHz, ratio f_2/f_1 from 1.01 to 1.50. With a frequency spacing of 48.8 Hz in both directions, the area contains 2233 stimulus frequency pairs.

C. DPOAE recording paradigms

DPOAEs were measured at 2233 stimulus frequency combinations arranged in the (f_1,f_2) plane as indicated in Fig. 2. Frequency f_2 varied between 7 and 9 kHz, and the frequency ratio f_2/f_1 was kept between 1.01 and 1.50. In both directions, frequency steps were 48.8 Hz. These stimulus frequency combinations were played as f_1-sweeps from low to high frequency ratio, starting with a fixed f_2 of 7 kHz and ending with f_2 at 9 kHz. First, DPOAEs were measured for all 2233 combinations at stimulus levels $L_1=65$ dB SPL, $L_2=55$ dB SPL. Including intermittent calibrations and DPgrams, this took about 4.5 h for one guinea pig ear. Second, the procedure was repeated in the same ear for stimulus levels $L_1=55$ dB SPL, $L_2=65$ dB SPL. At each (f_1,f_2) stimulus tones were played continuously during 204 windows of 20.48 ms. After an onset of 4 windows, 200 windows were averaged, adding up to a total recording time of 4.096 s per stimulus frequency combination. Phase changes in the probe were corrected by subtracting $2\varphi_1-\varphi_2$ from the measured DPOAE phase (for $f_{dp}=2f_1-f_2$) where φ_1 and φ_2 are the phases of f_1 and f_2 at the location of the microphone. During the entire experiment, at regular intervals a calibration procedure was performed, to set the levels of the stimulus tones. Also $2f_1-f_2$ DPgrams were measured at $f_2=4$, 5.6, and 8 kHz, with $f_2/f_1=1.3$ and $L_1,L_2=65,55$ dB SPL. When the DPOAE amplitude at 8 kHz differed more than 3 dB from the previously measured DPgram, the ear canal was checked and the probe replaced. Stable recordings over the entire measurement time could be obtained in most ears, although in rare occasions an apparent change in the response over time could not be explained. The six animals for which data are elaborated here represent the more stable recordings in a larger group of animals.

TABLE I. Percentage of (f_1,f_2) combinations at which the signal-to-noise ratio >6 dB. Averaged results of six experiments, with standard deviations.

DPOAE	$L_1,L_2=65,55$	$L_1,L_2=55,65$
$2f_1-f_2$	96±2%	90±4%
$3f_1-2f_2$	85±2%	53±10%
$4f_1-3f_2$	55±3%	23±4%
$2f_2-f_1$	76±10%	89±5%
$3f_2-2f_1$	29±2%	79±5%

D. Data analysis

Apart from online processing in Delphi (Borland) to monitor the course of the experiment, data analysis was done offline with custom-designed MATLAB routines. From the averaged acoustic response for each (f_1,f_2) the amplitude and phase spectra were calculated using a FFT algorithm. For five distortion products ($2f_1-f_2$, $3f_1-2f_2$, $4f_1-3f_2$, $2f_2-f_1$, and $3f_2-2f_1$) the amplitudes, noise levels, and phases were taken from those spectra. Noise level was defined as the average amplitude of the six frequency bins closest to the DPOAE frequency. For each distortion product, amplitude and phase were represented in an (f_1,f_2) area plot. The phase was unwrapped in two dimensions (f_1 and f_2), to eliminate 2π phase jumps. Due to phase jumps of approximately π, and missing points that did not meet the signal-to-noise criterion, unwrapping in two dimensions is sometimes ambiguous and then the outcome depends on the order in which the (f_1,f_2) plane is crossed. Care was taken to unwrap the phase plane as neatly as possible, especially at the small ratio side. In each (f_1,f_2) point, the slope of the phase plane was determined in two directions (constant f_1 and constant f_2), by fitting a linear regression line over three points [(f_1,f_2) and the two neighboring points]. This was only done if the amplitudes in all three points met the signal-to-noise criterion of 6 dB. To prevent phase irregularities due to unwrapping or other problems to contaminate the results, the phase slope was excluded from further analysis if the correlation coefficient was smaller than 0.988 (corresponding to $p=0.10$). From the phase slopes in the two perpendicular directions in the (f_1,f_2) plane, group delays D_1 and D_2 were calculated [with Eqs. (2) and (3)]. Note that the difference with the slopes is that the group delays are phase derivatives to f_{dp} instead of f_1 or f_2. Equation (8) was used to determine $D_{12|R}$, the group delay for fixed frequency ratio. The criterion for the correlation coefficient was estimated to lead to maximum errors in $D_{12|R}$ in the order of 0.2 ms.

IV. RESULTS

A. Incidence of the different DPOAE orders

For all five DPOAEs and the two sets of stimulus levels the percentage of (f_1,f_2) combinations at which the signal-to-noise ratio was larger than 6 dB was calculated, as a measure for the relative incidence of the DPOAE orders. Table I shows the averages of six experiments with standard deviations. All percentages are referenced to 2233, the maximum number of (f_1,f_2) points in the chosen area. Note that the DPOAE frequency $4f_1-3f_2$ is negative for frequency ratios above 1.33, so the maximum number of (f_1,f_2) combinations for that DPOAE is 1638 which corresponds to 73%. Table I shows that at stimulus levels $L_1=65$, $L_2=55$ dB SPL the lower sideband DPOAE $2f_1-f_2$ performs best. When stimulus levels $L_1=55$, $L_2=65$ dB SPL are used, which are not considered optimal for the $2f_1-f_2$ DPOAE, a decrease is seen in the incidence of all lower sideband DPOAEs but a dramatic increase occurs in the incidence of the upper sideband DPOAEs, especially for $3f_2-2f_1$. With $L_1=55$, $L_2=65$ dB SPL $2f_1-f_2$ and $2f_2-f_1$ are equally well represented.

B. Amplitude and phase characteristics in the (f_1,f_2) plane

1. Stimulus levels $L_1,L_2=65,55$ dB SPL

In Fig. 3 amplitude and unwrapped phase of the lower sideband DPOAEs $2f_1-f_2$, $3f_1-2f_2$, and $4f_1-3f_2$, measured in one guinea pig (GP55), are shown in the (f_1,f_2) area representation. These results are obtained with stimulus levels $L_1=65$, $L_2=55$ dB SPL. Only data with a signal-to-noise ratio better than 6 dB are shown. The area where the amplitude is maximum runs approximately in the direction of a constant frequency ratio [Figs. 3(a), (c), and (e); cf. Fig. 1]. There are also some valleys, e.g., in Fig. 3(a) for small frequency ratios, that run in a different direction, approximately constant f_{dp}. Note that these amplitude valleys seem to have corresponding isophase profiles [Fig. 3(a) vs (b)]. Generally, however, isophase contours run in the directions of constant frequency ratio, as do the amplitude maxima.

The amplitude and phase data of the upper sideband DPOAE $2f_2-f_1$ measured in GP70 are plotted in Fig. 4. Stimulus levels were again $L_1=65$, $L_2=55$ dB SPL. Constant phase now appears to be in a completely different direction than in Fig. 3 for the lower sideband DPOAEs. Isophase contours approximately follow the direction of constant DPOAE frequency. Again there is a correspondence between amplitude and phase patterns. The results shown in Figs. 3 and 4 for GP55 and GP70 were representative for all other animals.

2. Stimulus levels $L_1,L_2=55,65$ dB SPL

Figure 5 shows the amplitude and phase patterns of the lower sideband DPOAEs measured with the second set of stimulus levels, $L_1=55$, $L_2=65$ dB SPL, in GP55. With this set of stimulus levels there is only a small portion of the (f_1,f_2) area in which $4f_1-3f_2$ has a good signal-to-noise ratio (see also Table I). When the amplitude pattern of the $2f_1-f_2$ DPOAE with these stimulus levels is compared with the $2f_1-f_2$ amplitude at $L_1,L_2=65$, 55 dB SPL [Fig. 3(a)] it is evident that the overall DPOAE amplitude is smaller but also that the maximum amplitude occurs in a different region and, notably, follows the direction of constant f_{dp} instead of constant f_2/f_1 as in Fig. 3. Now the maximum amplitude and isophase contours are generally not in the same direction; isophase contours still follow the direction of constant frequency ratio, as in Figs. 3(b), (d), and (f) with stimulus levels $L_1,L_2=65,55$ dB SPL.

In Fig. 6 the amplitude and phase of the upper sideband DPOAE $2f_2-f_1$ are shown, measured in GP70 with stimu-

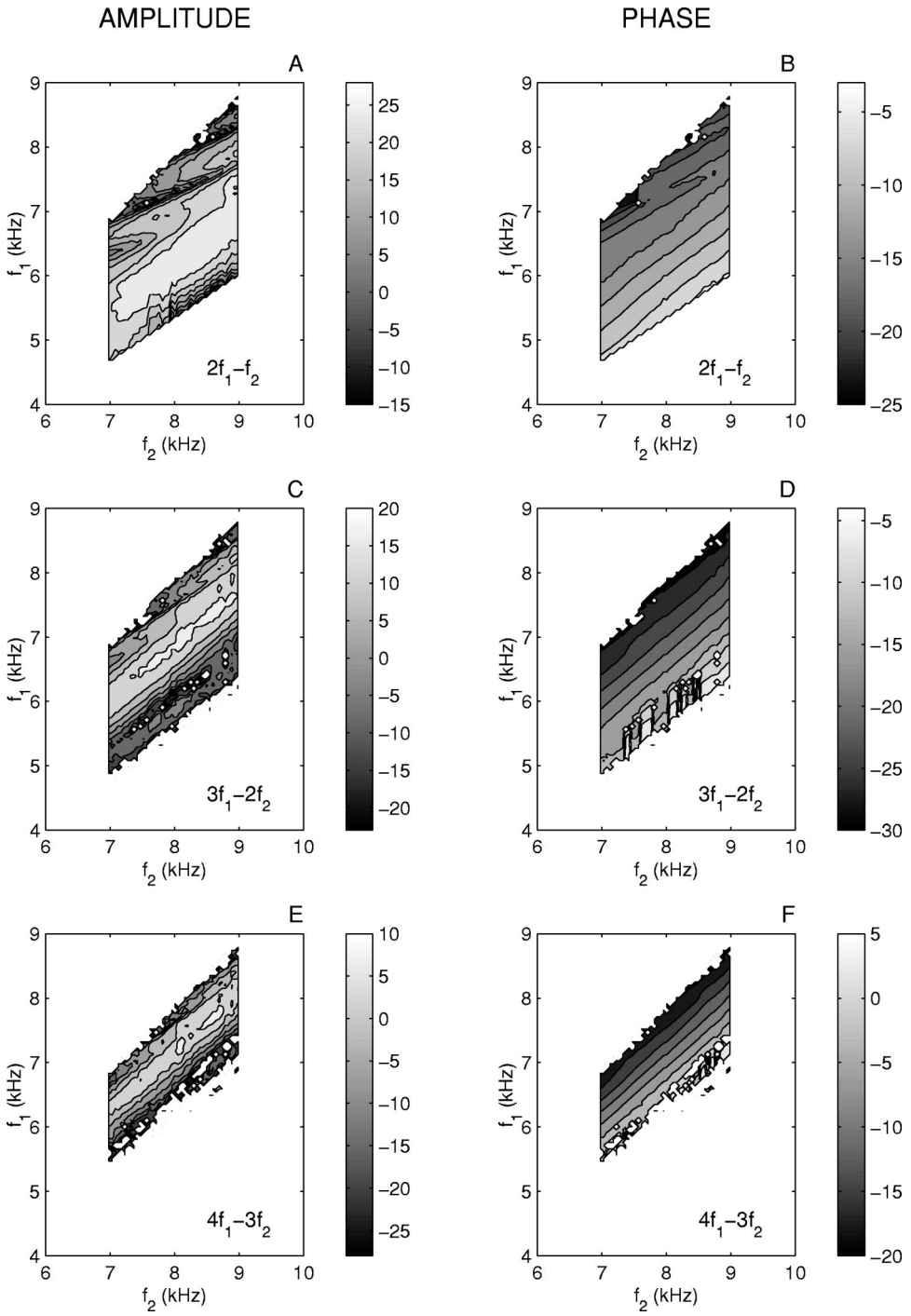

FIG. 3. Amplitude (left) and unwrapped phase (right) of the three lower sideband DPOAEs in the (f_1, f_2) area representation. Measured at $L_1, L_2 = 65,55$ dB SPL, in GP55. Grayscales indicate amplitude in dB SPL and phase in radians.

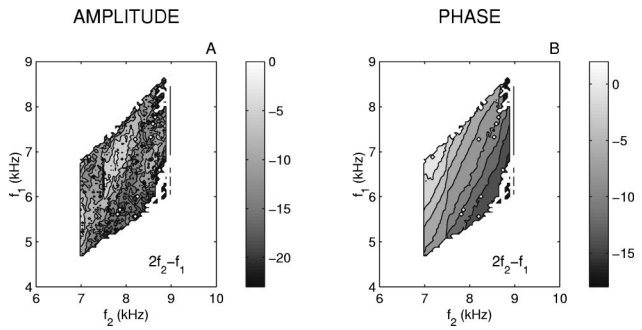

FIG. 4. Amplitude (left) and unwrapped phase (right) of the upper sideband DPOAE $2f_2-f_1$, measured in GP70 at $L_1, L_2 = 65,55$ dB SPL.

lus levels $L_1 = 55$, $L_2 = 65$ dB SPL. Maximum amplitude and constant phase follow lines in the direction of constant DPOAE frequency, as with the first set of stimulus levels in Fig. 4.

C. Group delays

From all phase planes, group delays D_1 and D_2 were determined at every combination (f_1, f_2), and $D_{12|R}$ derived using Eq. (8). In Fig. 7(a), pooled $D_{12|R}$ data is plotted as a function of f_2/f_1 for the lower sideband DPOAE $2f_1-f_2$, with $L_1 = 65$, $L_2 = 55$ dB SPL. Only group delays from fits with a correlation coefficient $r > 0.988$ (corresponding to

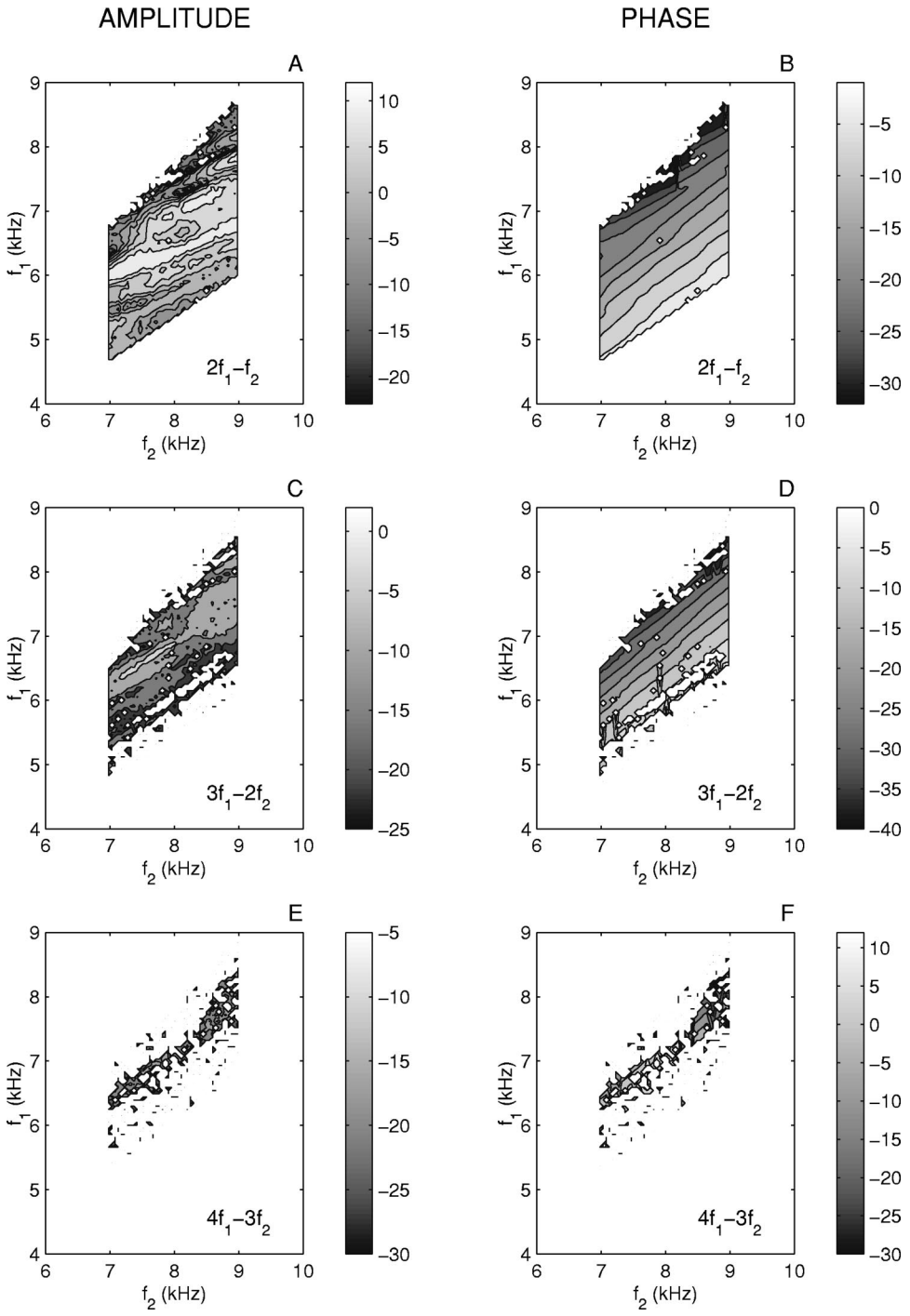

FIG. 5. Amplitude (left) and unwrapped phase (right) of the three lower sideband DPOAEs measured in GP55, with $L_1, L_2 = 55,65$ dB SPL.

$p < 0.10$) are shown. The solid line at $D_{12|R} = 0$ is the prediction from the wave-fixed model, describing the nonlinear distortion component [Eq. (9)]. The wave-fixed hypothesis is met for the intermediate frequency ratios, but not for f_2/f_1 below approximately 1.20 and not towards the higher ratios that were explored (>1.35). As was shown in Sec. II, the relation between $D_{12|R}$, D_1 and D_2 implies that if $D_{12|R} = 0$, Eq. (10) holds for D_2/D_1. In Fig. 7(b), D_2/D_1 vs f_2/f_1 is shown for the same DPOAE together with the prediction from Eq. (10), and again it is clear that the wave-fixed hypothesis is met in a limited intermediate range of f_2/f_1. For small frequency ratios D_2/D_1 approaches 1, in accordance with Eq. (12), indicating that for f_2/f_1 close to 1 the reflec-

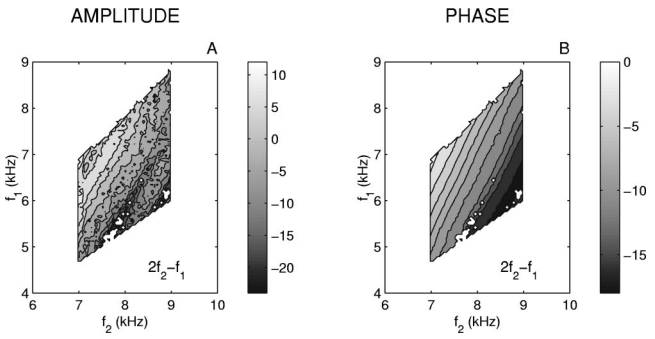

FIG. 6. Amplitude (left) and unwrapped phase (right) of the upper sideband DPOAE $2f_2 - f_1$, measured in GP70 with stimulus levels $L_1, L_2 = 55,65$ dB SPL.

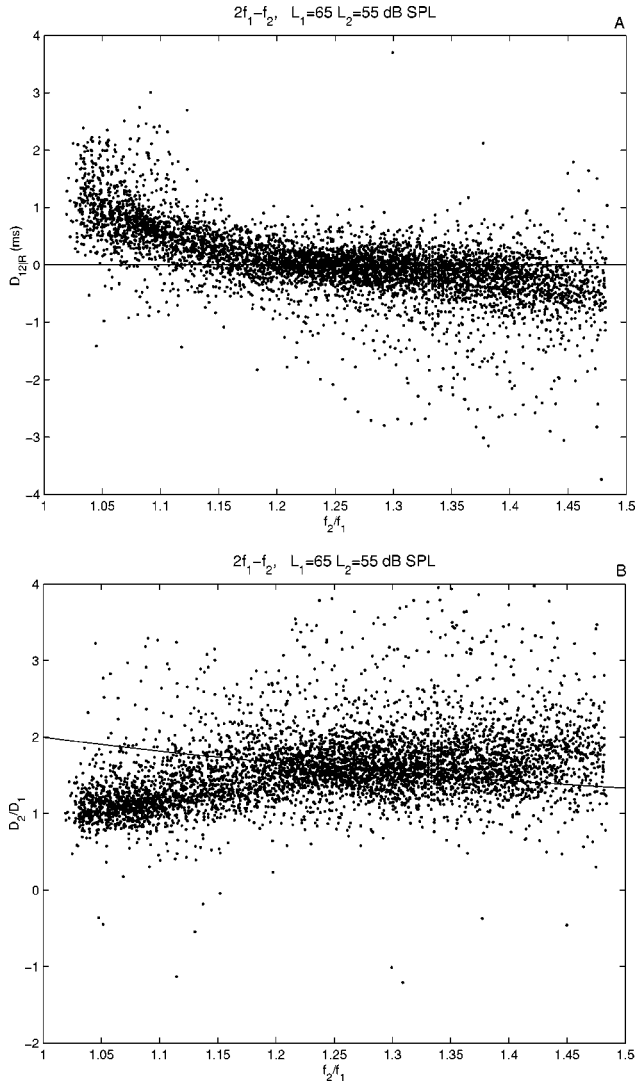

FIG. 7. (a) Group delay $D_{12|R}$ (constant frequency ratio) as a function of f_2/f_1. Pooled data from six experiments, $L_1, L_2 = 65,55$ dB SPL. (b) Ratio of f_2- and f_1-sweep group delays D_2/D_1 plotted as a function of frequency ratio f_2/f_1. Again for the DPOAE $2f_1-f_2$, pooled data, with $L_1, L_2 = 65,55$ dB SPL. Solid lines in (a) and (b) represent predictions of the wave-fixed model.

tion component is dominant. Note that the same data was used for Figs. 7(a) and (b), and that the results are equivalent as expected from Sec. II.

For Fig. 8, the f_2/f_1 axis was divided into segments of width 0.02. In all segments the mean D_2/D_1 over all tested ears was calculated as well as the standard error of the mean (s.e.m.). The error bars indicate plus and minus twice the s.e.m. In the left column, the results for four DPOAEs are given, measured with $L_1 = 65$, $L_2 = 55$ dB SPL, and in the right column the same is done for stimulus levels $L_1 = 55$, $L_2 = 65$ dB SPL. In each subplot, the prediction from the wave-fixed hypothesis [Eq. (10)] is given with a solid line. For the higher order DPOAEs with stimulus levels $L_1 = 65$, $L_2 = 55$ dB SPL [Figs. 8(c) and (e)], the error bars are quite large at high frequency ratios. This is due to the fact that the DPOAE frequency approaches zero (for $3f_1-2f_2$ at $f_2/f_1 = 1.50$ and for $4f_1-3f_2$ at $f_2/f_1 = 1.33$) which gives a poor signal-to-noise ratio. In Fig. 8(f) it is clear that no conclusions can be drawn for the $4f_1-3f_2$ component measured with $L_1 = 55$, $L_2 = 65$ dB SPL, also due to a bad signal-to-noise ratio (see also Table I). Based on a strict reasoning with the 95% confidence interval, the wave-fixed model is obeyed only for $f_2/f_1 = 1.19–1.27$ [$2f_1-f_2$, with $L_1, L_2 = 65,55$ dB SPL, Fig. 8(a)]. The frequency ratio range where the data fits the wave-fixed prediction is centered at lower ratios for higher order DPOAEs [Figs. 8(c) and (e)]. With the second set of stimulus levels, the range of the agreement with the wave-fixed prediction is wider, from 1.15 to 1.35 for the $2f_1-f_2$ [Fig. 8(b)]. The higher order DPOAE $3f_1-2f_2$ obeys the wave-fixed prediction for a wider range of f_2/f_1, starting at a lower value. In Figs. 8(g) and (h) the results for the upper sideband DPOAE $2f_2-f_1$ are shown. For both stimulus level combinations the delay ratio D_2/D_1 is close to one, independent of frequency ratio.

D. Fine structure

In Fig. 9 data from GP55 are presented as a series of f_1-sweeps. In the upper panels the DPOAE amplitude ($2f_1-f_2$) is plotted; for each successive f_1-sweep ($f_2 = 7$ kHz at the bottom and 9 kHz at the top of the chart) the amplitude is shifted by an amount of 2 dB for presentation purposes. In the lower panels the corresponding phase versus frequency curves are shown, with each curve shifted by 2 radians. The notches in the DPOAE amplitude are approximately aligned at the same f_{dp} [Figs. 9(a) and (b)]. These amplitude notches are accompanied by irregularities in the DPOAE phase as can be seen by comparing the upper and lower panels. Sometimes these phase irregularities equal π, resulting in ambiguities with phase unwrapping. In Fig. 9(b) there are also amplitude irregularities aligned in an oblique direction, not comprehensibly related to f_{dp} or one of the stimulus frequencies. Figure 10 shows another example of a series of f_1-sweeps (as in Fig. 9), now measured in GP70. Again, the irregularities in amplitude are accompanied by phase irregularities, aligned at f_{dp} for stimulus levels $L_1, L_2 = 65,55$ dB SPL [Figs. 10(a) and (c)]. At the second set of stimulus levels however [Figs. 10(b) and (d)], the pattern of fine structure is approximately aligned at a fixed frequency ratio ($f_2/f_1 \approx 1.10$).

V. DISCUSSION

A. Incidence of the different DPOAE orders

Optimal detectability of DPOAEs is commonly assumed to occur when the amplitudes of the basilar membrane vibrations for the two primaries at the site of generation is similar, because then nonlinear interaction is largest. Indeed, many studies indicate that taking L_1 larger than L_2 is optimal for the detection of the most commonly studied $2f_1-f_2$, both at the generally used primary levels in the order of 60 dB SPL and at lower levels (Kummer *et al.*, 2000). Higher order lower sideband (LSB) DPOAEs have lower amplitudes and are therefore less detectable against the background noise. Our findings summarized in Table I agree with these literature data for the LSB components, in that detectability decreases for higher order components, and is better for the $L_1, L_2 = 65,55$ than for the $L_1, L_2 = 55,65$ condition. For the

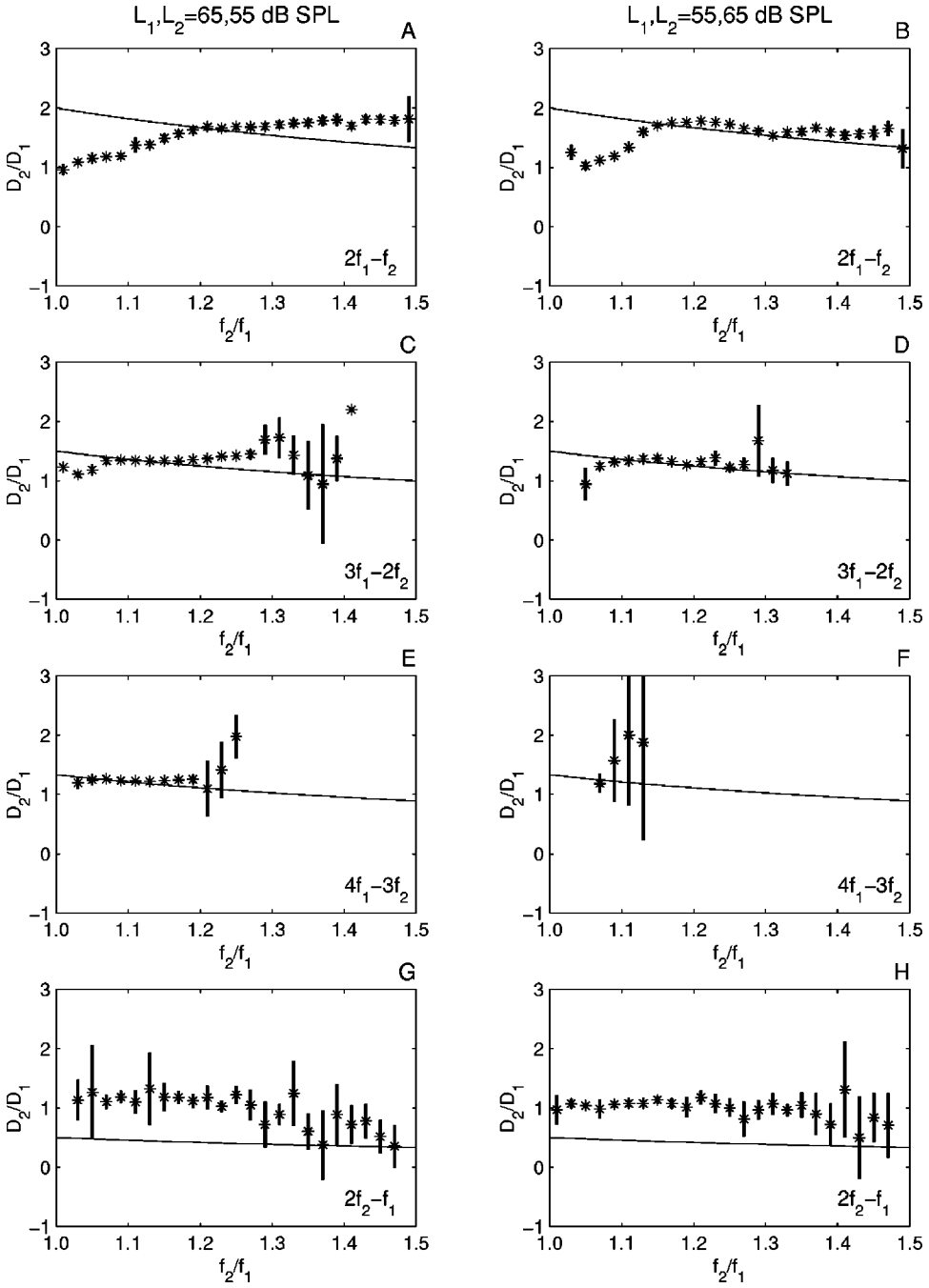

FIG. 8. Averaged D_2/D_1 with $\pm$ twice the s.e.m., for the DPOAEs $2f_1-f_2$, $3f_1-2f_2$, $4f_1-3f_2$, and $2f_2-f_1$. Left column: Stimulus levels $L_1,L_2=65,55$ dB SPL. Right column: $L_1,L_2=55,65$ dB SPL. Solid lines indicate the prediction from the wave-fixed model. For many data the s.e.m. is small and therefore the error bar seemingly absent.

upper sideband (USB) components detectability also decreases with increasing order of the component but, contrary to the LSB DPOAEs, is significantly better for the $L_1,L_2=55,65$ than for the $L_1,L_2=65,55$ condition (Table I). The cause of this difference could possibly be found in the difference in components (distortion, reflection, reemission or other) that contribute to the LSB and USB DPOAEs.

B. Amplitude and phase characteristics in the (f_1,f_2) plane

The presentation of our data was given in a different format from the main other area study published, that by Knight and Kemp (2000). In our area representation, the stimulus parameters f_1 and f_2 are fixed on the *y* and *x* axis, respectively, so all DPOAEs are shown in separate plots. One of the formats used by Knight and Kemp (2000), with the DP frequency on the *x* axis and f_2/f_1 on the *y* axis, is convenient for showing features that align either with f_{dp} or with f_2/f_1 because such patterns are exactly horizontal or vertical. However, this requires a different set of stimulus frequencies, with a quite large range of f_1 and f_2. Since we are interested in the full range of frequency ratios from 1.01 to 1.50, but needed to take care not to use too large a range of f_2 [especially around $f_2=4$ kHz some unexplained anomalies were found to occur in guinea pig DPOAEs, Schneider *et al.* (2000)], we could not use the same $(f_{dp},f_2/f_1)$ representation that Knight and Kemp (2000) did.

In this DPOAE area study in the guinea pig, features of the DPOAE amplitude and phase generally correspond to

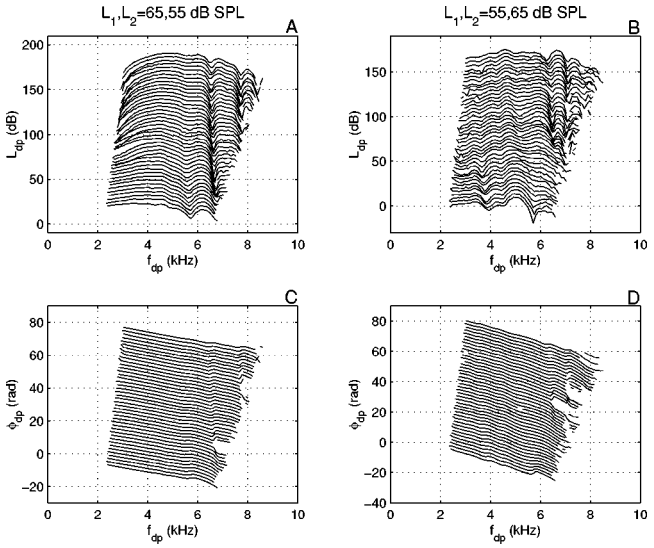

FIG. 9. DPOAE amplitude and phase as a function of f_{dp} from successive f_1-sweeps, for the lower sideband DPOAE $2f_1-f_2$, measured in GP55. The amplitude curves of successive sweeps (with increasing f_2) were shifted to 2 dB, phase curves 2 rad. Stimulus levels were $L_1, L_2 = 65,55$ dB SPL (left) and $L_1, L_2 = 55,65$ dB SPL (right).

characteristics found by Knight and Kemp (2000) in their human area study. In both studies, amplitude valleys were found for $2f_1-f_2$ that follow lines of approximately constant DP frequency. In addition, notches in phase were found to coincide with amplitude valleys, which is a characteristic of two-wave mixing. Except at low ratios, isophase contours for LSB DPOAEs run in the direction of constant frequency ratio, while for USB DPOAEs those contours follow lines of constant DP frequency at all frequency ratios. The transition for $2f_1-f_2$ occurs at a ratio of 1.1 to 1.15 in the study by Knight and Kemp (2000); in the present study that ratio is slightly larger (1.15 to 1.20) and depends on the stimulus levels. Both studies showed that the transition occurs at smaller ratios for higher order LSB DPOAEs.

A disadvantage of the (f_1, f_2) representation we chose seems to be that it is difficult to see the alignment of constant phase or amplitude with f_{dp} or f_2/f_1. Isophase lines in these directions are oblique in our representation. Therefore, instead of only qualitatively studying the phase maps, one could quantitatively analyze the direction of constant phase by calculating the angle in the (f_1, f_2) area at which the phase gradient equals zero. This angle β can be shown to be directly related to the DPOAE order and the f_1- and f_2-sweep group delays D_1 and D_2 as follows:

$$\beta = \arctan\left(\frac{n}{(n+1)}\frac{D_2}{D_1}\right). \tag{14}$$

Therefore, instead of analyzing the angle β of the isophase lines, it is equivalent to consider D_2/D_1 and this is exactly what we did in Figs. 7(b) and 8. The prediction of Knight and Kemp (2000) that the phase change of the reflection component is zero for constant f_{dp} can be translated to $\beta = \arctan[n/(n+1)]$, which, by Eq. (14), results in $D_2/D_1 = 1$.

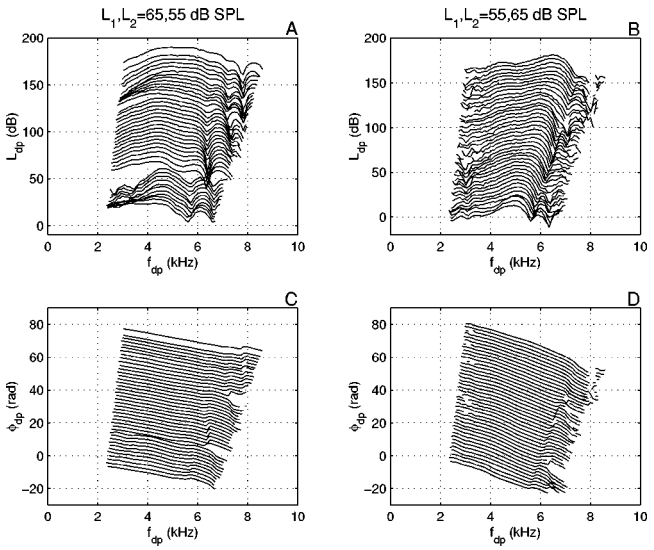

FIG. 10. Similar to Fig. 9, but now for GP70.

C. Group Delays

In this and many other studies the term group delay is used for DPOAE phase slope delays. These delays are not true time delays, since the DPOAE phase also depends on the behavior of the generation place during the sweep paradigm and on interference of several components in the cochlea. As a result, DPOAE phase slope delays can even be zero or negative under certain experimental conditions.

In line with earlier reports (Schneider *et al.*, 1999; Prijs *et al.*, 2000; Schoonhoven *et al.*, 2001) we concentrated our analysis not on D_1 and D_2 as such, but rather on their ratio D_2/D_1 [Figs. 7(b) and 8] and on $D_{12|R}$ [Fig. 7(a)] as quantities that potentially distinguish between different DPOAE generation mechanisms. It should be noted that, for each (f_1, f_2) combination, only conclusions about the dominant DPOAE component are obtained, unlike the analysis of Knight and Kemp (2001) in which the two components were separated through a frequency domain analysis and inverse Fourier transforms. From the theoretical analysis, $D_{12|R} = 0$ for the distortion component with the wave-fixed character. In Fig. 7(a) this property is observed for the $2f_1-f_2$ DPOAE for f_2/f_1 ratios from about 1.20 to 1.35, from a rough visual estimation. This range is slightly narrower than the 1.1–1.35 range reported for humans by Knight and Kemp (2001), though the statistical significance of the data in Fig. 7(a) may not be unequivocal. Similar conclusions can be drawn in a different way from Fig. 7(b), which shows that the D_2/D_1 ratio follows the theoretical wave-fixed relation for f_2/f_1 from 1.20 to 1.35. For the smaller f_2/f_1 ratios D_2/D_1 approaches a value of 1, the prediction for the reflection component, and towards higher f_2/f_1 ratios D_2/D_1 becomes larger than the prediction for the wave-fixed model, corresponding to $D_{12|R} < 0$ in Fig. 7(a). The uncertainties in $D_{12|R}$ and D_2/D_1, based on the uncertainties in the phase slopes with the criterion of a correlation coefficient >0.988, are on the order of 0.2 ms and 14%, respectively, which is much smaller than the variability in the data of Figs. 7(a) and (b). From this we conclude that the scatter in Figs. 7(a) and (b) is of biological origin. To allow for more statistically

solid conclusions, mean D_2/D_1 is plotted in Fig. 8 together with twice the standard errors, not only for $2f_1-f_2$ but also for the other LSB and USB components, and for both combinations of primary levels. From Fig. 8(a) follows that the range over which the $2f_1-f_2$ data at $L_1,L_2=65,55$ dB SPL follow the wave-fixed model in the strict sense of a 95% confidence interval is actually quite small, with f_2/f_1 from 1.19 to 1.27. For the higher order DPOAEs similar conclusions can be drawn, i.e., D_2/D_1 following the wave-fixed prediction for an intermediate range of primary frequency ratios, with D_2/D_1 smaller for lower, and larger for higher f_2/f_1 [Figs. 8(c) and (e)]; note that the associated range of f_2/f_1 ratios shifts to lower values which is directly related to the observation that DPOAE characteristics at different orders line up with f_{dp}, i.e., at increasingly smaller f_2/f_1 ratios for the higher order component (Schneider *et al.*, 2001; Talmadge *et al.*, 1998). When considering the $L_1,L_2=55,65$ condition [Figs. 8(b), (d), and (f)] similar observations are made, the most notable difference being that the wave-fixed prediction is followed to f_2/f_1 ratios as high as about 1.35 for the $2f_1-f_2$ component, and associated high ratios for the $3f_1-2f_2$ component. So the range of frequency ratios where the distortion component dominates the DPOAE is different with these stimulus levels. A possible explanation could be that the frequency ratio where the dominance of the distortion component changes into dominance of the reflection component depends on the overlap of the excitation patterns of f_1 and f_2 on the basilar membrane. That overlap is quite different with stimulus levels $L_1,L_2=55,65$ dB SPL, which could explain that the change from wave-fixed (distortion component dominant) to place-fixed (reflection component dominant) occurs at a different f_2/f_1. Once again, the behavior of the $2f_2-f_1$ USB component in its D_2/D_1 ratio is different from the LSB components [Figs. 8(g) and (h)]: D_2/D_1 takes a value of about one, independent of f_2/f_1, and never follows the wave-fixed prediction (see Sec. II B). These findings suggest that the USB DPOAE is not ruled by the distortion component, corresponding to the results of Knight and Kemp (2000) in humans.

D. Fine structure

Unlike prior statements (Brown and Gaskill, 1990) guinea pigs do exhibit fine structure. Note that in the guinea pig the modulations in amplitude are rather coarse, compared with the fine structure in human subjects. Fine structure is considered to be the result of interference of at least two DPOAE components, a nonlinear distortion component from the X_2 place and a linear reflection component from the X_{dp} place (Talmadge *et al.*, 1998, 1999). As reported in earlier human studies, the patterns in phase and amplitude are correlated; abrupt changes in amplitude often coincide with jumps in the phase spectrum, which is considered an indicator of interference between the two different contributing sources (Talmadge *et al.*, 1998, 1999; Mauermann *et al.*, 1999). In the present study, such covarying patterns were found to have several alignment modes: with f_{dp} [Figs. 9(a) and (b) and Fig. 10(a)], with f_2/f_1 [Fig. 10(b)] and other directions [Fig. 9(b)]. Alignment with f_{dp} has been predicted and measured before (Talmadge *et al.*, 1998, 1999; Mauermann *et al.*, 1999). The relative phase difference between the two components contributing to the DPOAE in the ear canal mainly depends on f_{dp} through the fast rotating phase of the reflection component, which gives rise to a fine structure that is aligned with f_{dp}. We cannot yet give such a simple interpretation for the other observed alignment modes.

ACKNOWLEDGMENTS

We wish to thank two anonymous reviewers for their helpful comments on the manuscript. This study was supported by the Netherlands Organization for Scientific Research and by the Heinsius Houbolt Fund.

Brown, A. M., and Gaskill, S. A. (**1990**). "Measurement of acoustic distortion reveals underlying similarities between human and rodent mechanical responses," J. Acoust. Soc. Am. **88**, 840–849.

Brown, A. M., Harris, F. P., and Beveridge, H. A. (**1996**). "Two sources of acoustic distortion products from the human cochlea," J. Acoust. Soc. Am. **100**, 3260–3267.

Fahey, P. F., and Allen, J. B. (**1997**). "Measurement of distortion product phase in the ear canal of the cat," J. Acoust. Soc. Am. **102**, 2880–2891.

Heitmann, J., Waldmann, B., Schnitzler, H.-U., Plinkert, P. K., and Zenner, H.-P. (**1998**). "Suppression of distortion product otoacoustic emissions (DPOAE) near $2f_1-f_2$ removes DP-gram fine structure—Evidence for a secondary generator," J. Acoust. Soc. Am. **103**, 1527–1531.

Kalluri, R., and Shera, C. A. (**2001**). "Distortion-product source unmixing: A test of the two-mechanism model for DPOAE generation," J. Acoust. Soc. Am. **109**, 622–637.

Kemp, D. T. (**1979**). "Evidence of mechanical nonlinearity and frequency selective wave amplification in the cochlea," Arch. Oto-Rhino-Laryngol. **224**, 37–45.

Kemp, D. T. (**1986**). "Otoacoustic emissions, travelling waves and cochlear mechanisms," Hear. Res. **22**, 95–104.

Kim, D. O. (**1980**). "Cochlear mechanics: implications of electrophysiological and acoustical observations," Hear. Res. **2**, 297–317.

Kimberley, B. P., Brown, D. K., and Eggermont, J. J. (**1993**). "Measuring human cochlear traveling wave delay using distortion product otoacoustic emission phase responses," J. Acoust. Soc. Am. **94**, 1343–1350.

Knight, R. D., and Kemp, D. T. (**1999**). "Relationships between DPOAE and TEOAE amplitude and phase characteristics," J. Acoust. Soc. Am. **106**, 1420–1435.

Knight, R. D., and Kemp, D. T. (**2000**). "Indications of different distortion product otoacoustic emission mechanisms from a detailed f_1,f_2 area study," J. Acoust. Soc. Am. **107**, 457–473.

Knight, R. D., and Kemp, D. T. (**2001**). "Wave and place fixed DPOAE maps of the human ear," J. Acoust. Soc. Am. **109**, 1513–1525.

Kummer, P., Janssen, T., and Arnold, W. (**1995**). "Suppression tuning characteristics of the $2f_1-f_2$ distortion product otoacoustic emission in humans," J. Acoust. Soc. Am. **98**, 197–210.

Kummer, P., Janssen, T., Hulin, P., and Arnold, W. (**2000**). "Optimal L_1-L_2 primary tone level separation remains independent of test frequency in humans," Hear. Res. **146**, 47–56.

Martin, G. K., Jassir, D., Stagner, B. B., Whitehead, M. L., and Lonsbury-Martin, B. L. (**1998**). "Locus of generation for the $2f_1-f_2$ vs $2f_2-f_1$ distortion-product otoacoustic emissions in normal-hearing humans revealed by suppression tuning, onset latencies, and amplitude correlations," J. Acoust. Soc. Am. **103**, 1957–1971.

Martin, G. K., Lonsbury-Martin, B. L., Probst, R., Scheinin, S. A., and Coats, A. C. (**1987**). "Acoustic distortion products in rabbit ear canal. II. Sites of origin revealed by suppression contours and pure-tone exposures," Hear. Res. **28**, 191–208.

Mauermann, M., Uppenkamp, S., van Hengel, P. W. J., and Kollmeier, B. (**1999**). "Evidence for the distortion product frequency place as a source of distortion product otoacoustic emission (DPOAE) fine structure in humans. I. Fine structure and higher-order DPOAE as a function of the frequency ratio f_2/f_1," J. Acoust. Soc. Am. **106**, 3473–3483.

Moulin, A., and Kemp, D. T. (**1996**). "Multicomponent acoustic distortion product otoacoustic emission phase in humans. II. Implications for distor-

tion product otoacoustic emissions generation,'' J. Acoust. Soc. Am. **100**, 1640–1662.
O'Mahoney, C. F., and Kemp, D. T. (**1995**). ''Distortion product otoacoustic emission delay measurement in human ears,'' J. Acoust. Soc. Am. **97**, 3721–3735.
Prijs, V. F., Schneider, S., and Schoonhoven, R. (**2000**). ''Group delays of distortion product otoacoustic emissions: Relating delays measured with f_1- and f_2-sweep paradigms,'' J. Acoust. Soc. Am. **107**, 3298–3307.
Schneider, S., Prijs, V. F., and Schoonhoven, R. (**1999**). ''Group delays of distortion product otoacoustic emissions in the guinea pig,'' J. Acoust. Soc. Am. **105**, 2722–2730.
Schneider, S., Prijs, V. F., Schoonhoven, R., and van Hengel, P. W. J. (**2000**). ''f_1- versus f_2-sweep group delays of distortion product otoacoustic emissions in the guinea pig; experimental results and theoretical predictions,'' in *Recent Developments in Auditory Mechanics*, edited by H. Wada, T. Takasaka, K. Ikeda, K. Ohyama, and T. Koike (World Scientific, Singapore), pp. 360–366.
Schneider, S., Schoonhoven, R., and Prijs, V. F. (**2001**). ''Amplitude of distortion product otoacoustic emissions in the guinea pig in f_1- and f_2-sweep paradigms,'' Hear. Res. **155**, 21–31.
Schoonhoven, R., Prijs, V. F., and Schneider, S. (**2001**). ''DPOAE group delays versus electrophysiological measures of cochlear delay in normal human ears,'' J. Acoust. Soc. Am. **109**, 1503–1512.
Shera, C. A., and Guinan, J. J. (**1999**). ''Evoked otoacoustic emissions arise by two fundamentally different mechanisms: A taxonomy for mammalian OAEs,'' J. Acoust. Soc. Am. **105**, 782–798.
Shera, C. A., Talmadge, C. L., and Tubis, A. (**2000**). ''Interrelations among distortion-product phase-gradient delays: Their connection to scaling symmetry and its breaking,'' J. Acoust. Soc. Am. **108**, 2933–2948.
Talmadge, C. L., Long, G. R., Tubis, A., and Dhar, S. (**1999**). ''Experimental confirmation of the two-source interference model for the fine structure of distortion product otoacoustic emissions,'' J. Acoust. Soc. Am. **105**, 275–292.
Talmadge, C. L., Tubis, A., Long, G. R., and Piskorski, P. (**1998**). ''Modeling otoacoustic emission and hearing threshold fine structure,'' J. Acoust. Soc. Am. **104**, 1517–1543.
Talmadge, C. L., Tubis, A., Tong, C., Long, G. R., and Dhar, S. (**2000**). ''Temporal aspects of otoacoustic emissions,'' in *Recent Developments in Auditory Mechanics*, edited by H. Wada, T. Takasaka, K. Ikeda, K. Ohyama, and T. Koike (World Scientific, Singapore), pp. 353–359.
Tubis, A., Talmadge, C. L., Tong, C., and Dhar, S. (**2000**). ''On the relationships between the fixed- f_1, fixed-f_2, and fixed-ratio phase derivatives of the $2f_1-f_2$ distortion product otoacoustic emission,'' J. Acoust. Soc. Am. **108**, 1772–1785.

Children's detection of pure-tone signals: Informational masking with contralateral maskers

Frederic L. Wightman,[a] Michael R. Callahan, Robert A. Lutfi,[b] Doris J. Kistler, and Eunmi Oh[c]

Waisman Center, University of Wisconsin, Madison, Wisconsin 53705

(Received 19 July 2002; accepted for publication 3 March 2003)

When normal-hearing adults and children are required to detect a 1000-Hz tone in a random-frequency multitone masker, masking is often observed in excess of that predicted by traditional auditory filter models. The excess masking is called informational masking. Though individual differences in the effect are large, the amount of informational masking is typically much greater in young children than in adults [Oh *et al.*, J. Acoust. Soc. Am. **109**, 2888–2895 (2001)]. One factor that reduces informational masking in adults is spatial separation of the target tone and masker. The present study was undertaken to determine whether or not a similar effect of spatial separation is observed in children. An extreme case of spatial separation was used in which the target tone was presented to one ear and the random multitone masker to the other ear. This condition resulted in nearly complete elimination of masking in adults. In young children, however, presenting the masker to the nontarget ear typically produced only a slight decrease in overall masking and no change in informational masking. The results for children are interpreted in terms of a model that gives equal weight to the auditory filter outputs from each ear. © *2003 Acoustical Society of America.* [DOI: 10.1121/1.1570443]

PACS numbers: 43.66.Dc, 43.66.Ba [MRL]

I. INTRODUCTION

The research reported here addresses the general question of how children segregate and attend to target sounds in noisy backgrounds such as classrooms. A previous article (Oh *et al.*, 2001) described an experiment in which preschool children and adults were asked to detect a 1000-Hz sinusoid that was masked by a random multitone complex. The adult results confirmed many earlier reports (e.g., Lutfi, 1993; Neff and Green, 1987; Oh and Lutfi, 1998; Spiegel *et al.*, 1981) that random frequency multitone maskers produced considerably more masking than predicted by traditional auditory filter models. This excess masking, thought to be a central effect produced mainly by the uncertainty of the masker, has been called ''informational masking'' to distinguish it from the ''energetic masking'' predicted by filter models of the auditory periphery. As earlier studies showed (e.g., Neff and Dethlefs, 1995; Oh and Lutfi, 1998), informational masking varied non-monotonically with the number of masker components and was as great as 60 dB in some adult listeners. The data from the children produced a similar pattern, but with considerably greater amounts of informational masking. Individual differences were large, as in most previous studies (e.g., Neff and Dethlefs, 1995).

Simple modifications of the traditional auditory filter model that presume broader auditory filters in children (e.g., Allen *et al.*, 1989) fail to account for either the magnitude of the informational masking effect or its non-monotonicity with number of masker components. In contrast, the component-relative-entropy model (CoRE) proposed by Lutfi (1993) provides good fits to the data from both children and adults in the Oh *et al.* (2001) study. The CoRE model proposes that masking is determined by the variance of the outputs (in dB) of a number of peripheral auditory filters, not just the filter centered at the target frequency. The number of filters monitored (n) and the range of their center frequencies (W) are the two free parameters of the model. Thus, informational masking is the result of the inability of the listener to ignore all filter outputs except the one centered at the target frequency. According to the CoRE model, the adult–child differences are a result of the tendency of children to integrate information over a larger number of auditory filters than adults and not simply a result of wider auditory filters in children.

Efforts to understand the mechanisms and processes underlying the informational masking effects have led some researchers to explore stimulus manipulations that might reduce the size of the effect. Kidd *et al.* (1994, 1998) and Neff (1995), for example, suggested that informational masking in adults may result from an inability to segregate signal and masker perceptually. Kidd *et al.* (1994) reduced adult informational masking by as much as 40 dB by altering the stimulus presentation scheme, making the masker less ''signal-like,'' in order to enhance signal-masker segregation. Neff (1995) reported similar results, noting in addition the large individual differences in the extent to which the stimulus manipulations were successful in reducing informational masking. Some of the successful alterations reported in both the Kidd *et al.* (1994) and Neff (1995) studies amounted to attempts to separate the signal and masker spatially. One was achieved by presenting the masker to both ears and the signal to one ear (Kidd *et al.*, 1994), presumably producing a per-

[a]Also at the Department of Psychology. Electronic mail: Wightman@waisman.wisc.edu
[b]Also at the Department of Communicative Disorders.
[c]Current address: Samsung AIT, P.O. Box 111, Suwon, Korea 440-600.

cept in which the masker was lateralized in the middle of the head and the signal at one ear. Others involved presenting the masker in phase to both ears with the signal phase inverted at one ear (masker probably perceived in the middle of the head and signal at the two ears) or presenting signal and masker to different ears (Neff, 1995). Kidd explored the spatial separation manipulation more directly in a later study (Kidd *et al.*, 1998) in which signals and maskers were presented from loudspeakers in an acoustically treated room. Spatial separation reduced informational masking by as much as 20 dB in this latter study. However, the results of at least one previous study would argue that the informational masking effects observed in children might be resistant to manipulations that would normally reduce or eliminate informational masking in adults. In a study of masking in infants, Werner and Bargones (1991) measured the detection threshold for a 1-kHz tone in quiet and in the presence of a 4–10-kHz noise band. A noise band two octaves above the signal frequency would not be expected to create any masking in adult listeners. In the infants, however, the noise raised detection threshold by about 10 dB. The effect could not be attributed to wider auditory filters in the infants, since increasing the level of the noise band by 10 dB caused only a 1–2-dB change in threshold. A pure tone and a high-frequency noise band are perceptually quite distinct, so one would expect the two stimuli to be readily segregated. However, for the infants in this study, a strong distraction or informational masking effect was evident. This suggests that those stimulus manipulations that reduce informational masking in adults may be less effective in children.

It is important to understand the impact on informational masking of spatial separation of target and masker if one is to relate informational masking data to a child's task of segregating and attending to auditory targets in a noisy classroom. In a typical classroom distracting sounds are spatially distributed and the target sound (the teacher's voice) usually originates from a fixed location. The signals, maskers, and listening environments used in most studies of informational masking have little in common with the classroom situation. Thus, this study was motivated, as others have been, by the desire to approximate classroom listening conditions more closely. Here we study the impact of a simple kind of ''spatial'' separation of target and masker on informational masking in children. We achieve spatial separation, as did Neff (1995) in the ''cross-ear'' condition of her study of adult listeners, by presenting the target signal to one ear and the multitone masker to the other. Our rationale for this approach is twofold. First, it is easy to implement, and since the task remains essentially the same, no additional training of the children is required. Second, the CoRE model can easily be modified to predict the results by adding a second set of auditory filters to be monitored and a weighting parameter for the nontarget ear. To minimize ''central masking,'' the known cross-ear masking effect that is presumably unrelated to informational masking (Wegel and Lane, 1924; Zwislocki *et al.*, 1968; Mills *et al.*, 1996), we present low-level (60 dB SPL) maskers that consist of frequencies remote from that of the signal.

II. METHODS

A. Listeners

Seven preschool children participated in this study. Five of the seven had been tested in the earlier study of informational masking in children (Oh *et al.*, 2001) and two had participated in the earlier study of individual differences (Lutfi *et al.*, 2003). All the preschool children were selected from the Waisman Center Early Childhood Program on the basis of their parents' consent and their own willingness to participate. At the time of testing their ages ranged from 4.2 to 5.6 years. All eight of the previously tested adults (UW—Madison students) also participated in this study. In addition, 28 school-aged children participated. These children, aged 6.7–16.2 years, had been recruited from families of Waisman Center employees into the study of individual differences (Lutfi *et al.*, 2003) in which the identical stimulus conditions as in Oh *et al.* (2001) were presented. The adults and school-aged children were paid for their participation, and the preschoolers were rewarded at the end of each session with small toys.

All listeners demonstrated normal hearing, as indicated by pure-tone thresholds less than 15 dB HL (ANSI, 1989) at octave frequencies from 250 to 4000 Hz. Because middle ear problems are common in young children, tympanometry was performed on each child (preschoolers only) prior to each session using a screening tympanometer (GSI-27A Auto-Tymp) calibrated to ANSI specifications (ANSI, 1987). The child was allowed to continue only if peak-compensated static admittance was normal. Other listeners were not tested on days when they reported having a cold or other upper-respiratory problem.

B. Stimuli

As in the previous study (Oh *et al.*, 2001), the signal was a 1000-Hz tone burst, presented simultaneously with a multitone masker that was derived from a sample of Gaussian, bandpass filtered (0.1 to 10 kHz) noise. A given masker was generated by selecting one noise sample (randomly with equal probability) from a pool of 100 and computing its discrete magnitude and phase spectrum. Then, depending on the condition being tested, a specific number of its frequency components was selected randomly, and those components were summed, using the original magnitudes and phases. The number of masker components (2, 10, 20, 40, 200, 400, or 906) was varied across different experimental conditions but was fixed within an experimental session. A ''broadband'' condition was included in which the actual selected noise burst was presented as a masker (roughly equivalent to 3700 components). In all conditions masker components within a 160-Hz band arithmetically centered at 1000 Hz were excluded. A ''quiet'' condition was also included, with no masker presented, to estimate absolute threshold for the 1000-Hz signal.

Both signal and masker were gated on and off together with 10-ms, $\cos^2$ onset/offset ramps for a total duration of 370 ms. The rms level of the masker was 60 dB SPL in all conditions. In the broadband condition the spectrum level of the noise was approximately 20 dB SPL. The dB levels of

the individual masker components were random, approximately normally distributed (component amplitudes were Rayleigh distributed) with a standard deviation of 5.6 dB. Since the overall level of the masker was constant, the average levels of the individual components would vary inversely with the number of components. The maximum level of the signal was limited to 84 dB SPL. The signal and the masker were computer generated and played over a 16 bit digital-to-analog converter (Tucker-Davis Technologies DD1) at a sampling rate of 44.1 kHz. All stimuli were presented monaurally, the signal to the listener's left ear and the masker to the right ear, through Sennheiser model HD-414 headphones. The sound levels produced by the Sennheiser headphones were estimated with a loudness balancing procedure using calibrated TDH-49 heaphones and adult listeners.

C. Procedure

A staircase, cued two-interval, forced-choice (2AFC) procedure was used to estimate signal threshold. Each trial was preceded by a cue, which consisted of the presentation of a bird picture on a computer screen and a simultaneous unmasked stimulus tone at 60 dB SPL. The child was told that the tone was a ''bird sound.'' Note that the ''bird sound'' was always presented monaurally to the left ear. Two successive stimulus intervals were then presented with a 700-ms silent interval between them. Each stimulus interval was marked (on the computer screen) by a flashing square with the numeral ''1'' or ''2'' on it. One of the two intervals contained a masker sample and the other contained a different masker sample with the signal added to it. The signal occurred in the first or second interval with equal probability. The listener's task was to select the interval that contained the signal. The instructions were ''Listen to the two sounds presented with the two boxes and point to the box that has the bird sound.'' Correct responses were reinforced by presenting a few pieces of a picture puzzle. The listener was allowed to choose pictures for the puzzle (cartoon characters, animals, his/her own pictures, etc). The goal was to complete the puzzle within a block of trials.

The starting signal level was selected so as to make the signal clearly audible to the listener. On each of the next four trials the signal level was decreased in 8-dB steps and then was increased in 8-dB steps back to the starting level. This up–down pattern was continued for a total of 40 trials, producing five trials at the highest and lowest levels and ten trials at each of the three intermediate levels. The signal level was varied by a programmable attenuator (Tucker Davis Technologies PA4). At least three blocks of trials were completed for an experimental condition. If performance levels near 100% and 50% (chance) were not obtained for the highest and lowest signal levels, an additional block of trials was obtained (in some, but not all cases) with the starting level adjusted either up or down so that desirable performance levels were observed at both extremes.

Each listener was tested in a double-walled, sound-attenuating chamber. Two experimenters accompanied a child listener. One experimenter set up an appropriate starting level, initiated stimulus presentation when the child was ready for the next trial, and entered a ''1'' or ''2'' when the child made a response by touching one of the boxes on the screen or by calling out the number. The other experimenter was present to satisfy security regulations. The experimenters interacted with the child in an attempt to hold his/her interest during the session and to remind the child that the target sound was the monaural ''bird sound.''

Practice trials were given until the listener appeared familiar with the task. The children completed three or fewer blocks of 40 trials each day, depending on their willingness to continue and time availability. It took the preschool children 8–10 min to complete a block of trials and they participated for no longer than 30 min on any single day. School-aged children and adults were tested in the same conditions as the preschool children and required approximately 5 min to complete each block of 40 trials. The school-aged children participated for a minimum of an hour on each day, and the adult listeners (and some of the older school-aged children) participated for 2 h on each day. All listeners first completed the condition in which the signal was presented alone (''quiet'' condition), and then the condition involving the broadband noise masker. Next they completed the experimental conditions in which the signal was presented with the multitone maskers. These latter experimental conditions were presented in random order. Finally, all the listeners in the current study were tested after they had participated in a similar study of informational masking in which identical signal and masker stimuli had been presented. In those previous studies signal and masker had been presented to the same ear (Oh *et al.*, 2001; Lutfi *et al.*, 2003).

D. Data analysis

A three-parameter logistic function was fit to the data relating percentage of correct responses to signal level for each listener in each condition using a maximum likelihood criterion. The three parameters of the logistic were used to derive the slope, the signal level at which the function crossed 75% correct, and the upper asymptote. This third parameter allowed estimation of the extent to which performance (especially for the children) would not reach 100% correct at the highest signal levels. The fitting procedure was implemented exactly as described by Wichmann and Hill (2001a, b). In addition to providing estimates of the three parameters of the fitted function, the procedure included a ''bootstrapping'' or simulation phase that provides estimates of confidence limits on all three parameters. The simulation phase estimated the sampling distributions of the three logistic parameters. Using the values of percent correct at each signal level from the fitted function as means, and assuming binomially distributed percent correct values, a simulated percent correct at each signal level was randomly drawn and a logistic was fit to these values. This was repeated 10 000 times to provide 10 000 estimates of each of the three logistic parameters. The 2.5% and 97.5% points from these sampling distributions were then taken as the 95% confidence limits. The sampling distribution of the threshold parameter (signal level at 75% correct) was asymmetric in many cases, thus producing asymmetric confidence intervals in these cases. Since the amount of data obtained from children was quite limited, and since individual differences were large, we

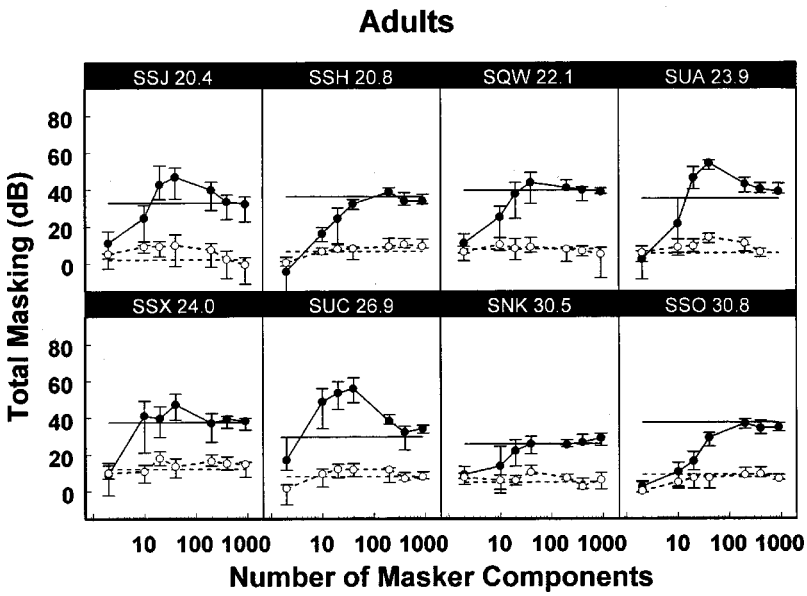

FIG. 1. Masking functions showing total masking as a function of the number of masker components for each of the eight adult listeners in this study. Total masking is defined as the dB difference between the target threshold (75% correct in 2AFC) in quiet and in the presence of a masker. The horizontal lines represent total masking with a broadband noise masker. Solid symbols connected by solid lines (and the solid horizontal line) refer to masking with the ipsilateral masker. The open symbols connected by dashed lines (and the horizontal dashed line) refer to masking with the contralateral masker. The error bars around each data point represent the 95% confidence intervals determined by the bootstrapping technique described in the text. Each panel is labeled with the 3-letter listener code and the listener's age, given in decimal years. Note that the data from the ipsilateral condition are a reanalyzed version of the data shown in Oh *et al.* (2001).

viewed the estimation of confidence limits on psychometric function parameters from each listener in each condition as a critical component of the data analysis procedures. The Wichmann and Hill (2001b) procedure is the first of which we are aware that offers confidence limit estimates that are not dependent on asymptotic normality assumptions.

III. RESULTS

All of the listeners in this study had also participated in earlier studies (Oh *et al.*, 2001; Lutfi *et al.*, 2003) that used identical procedures and nearly identical stimulus conditions. In the previous experiments the target signal and the maskers were presented to the same ear (ipsilateral masker), and in the current study the signal is presented to one ear and the masker is presented to the other (contralateral masker). Since the main purpose of the experiment reported here is a comparison of results from the ipsilateral and contralateral conditions, the data from the previous articles are reproduced here (after reanalysis according to the procedures described above) for the reader's convenience.

Figure 1 shows the data from the adult listeners. Listener ages are given at the top of each panel. In this figure, total masking is defined as the dB difference between signal threshold in quiet and threshold in the presence of a masker. Each data point (and associated 95% confidence interval) represents total masking for a fixed number of masker components. Filled symbols are data from the ipsilateral masker condition (previously reported in Oh *et al.*, 2001, and reanalyzed for presentation here), and open symbols are data from the contralateral masker condition. The horizontal dashed lines in each panel show the listener's threshold for the signal with a broadband noise masker (solid: ipsilateral; dashed: contralateral). Informational masking is revealed by thresholds higher than those predicted on the basis of a simple filter model. Since no masker included energy within a 160-Hz rectangular band centered at the target frequency, most of the masking, especially for small numbers of masker components, is thought to be informational. A very conservative view is that any threshold higher than that obtained with broadband noise reflects the contribution of informational masking (Oh and Lutfi, 1998). Here, that means that any threshold above the horizontal dashed lines includes a significant informational masking component. Of course, even the masking produced by broadband noise may contain some informational masking, as has been argued by Lutfi (1990), but the extent to which thresholds exceed the broadband noise threshold would be expected to reflect additional informational masking. Note that using this criterion only three of the eight adults in this study show significant amounts of informational masking and only in the ipsilateral condition. Large individual differences in amounts of ipsilateral informational masking are typical of past work (e.g., Neff and Dethlefs, 1995), and when the current results are considered in a broader context they should not be considered unusual. For example, Lutfi *et al.* (2003) collected complete ipsilateral masking functions from 84 listeners, including nearly 50 adults, 8 of whom also participated in the current study. Those 8 adults did not represent the extremes of the larger group.

For the adults, the most dramatic results is the fact that there is little if any masking in the contralateral condition (signal and maskers in opposite ears). Thus, putting the masker in the opposite ear not only eliminated informational masking for the adults, but it eliminated nearly all masking. This result is consistent with previous studies of central masking (e.g., Mills *et al.*, 1996), all of which show that central masking is a very small effect when maskers do not overlap spectrally with the signal and are presented at moderate levels. It is also consistent with the results from the contralateral-masking condition in the informational masking study reported by Neff (1995).

Figure 2 shows the data obtained from the preschoolers, plotted as in Fig. 1. Note that the preschoolers [ipsilateral data previously shown in Oh *et al.* (2001) and reanalyzed for presentation here] show large amounts of informational masking in the ipsilateral condition (solid symbols above the solid horizontal line) and large individual differences. More importantly for the purpose of the present study, note that the

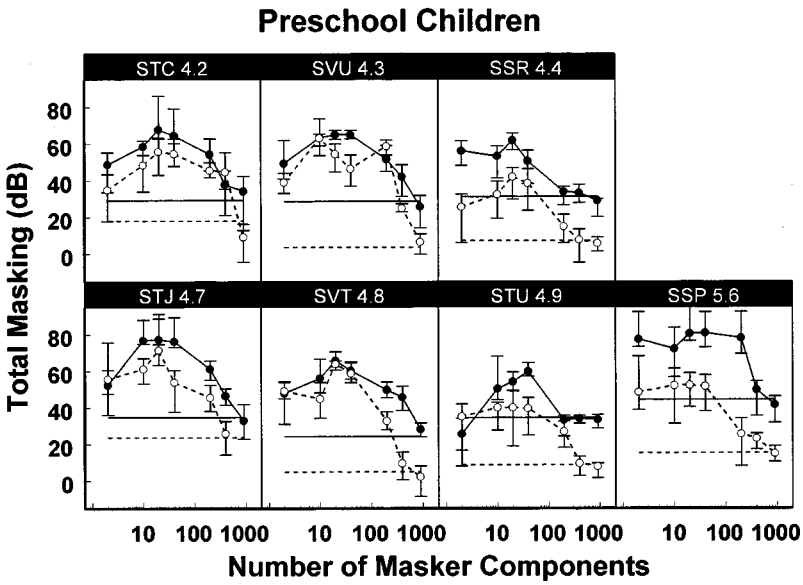

FIG. 2. Same as Fig. 1, but for the listeners in the preschool group.

impact of presenting signal and masker contralaterally is not to eliminate masking, as occurs in adults, but simply to reduce it by an average of 20 dB. In other words, although masking is reduced overall in the contralateral condition, the same masking pattern (masking as a function of the number of masker components) is observed in the contralateral condition as in the ipsilateral condition; informational masking, defined here as the dB difference between masking in a given condition and masking in the broadband condition, is not reduced at all. The large individual differences that are apparent in the data shown in Fig. 2 are particularly striking when one considers the differences between the ipsilateral and contralateral results. For example, listener STJ's threshold with a broadband noise masker is lowered only about 10 dB by placing the masker in the opposite ear, and this contralateral threshold is still more than 20 dB above quiet threshold for this listener. In contrast, listener SVU's contralateral broadband threshold, which is 30 dB lower than the comparable ipsilateral threshold, is very near quiet threshold. In both listeners, however, large amounts of informational masking are evident in both ipsilateral and contralateral conditions. The fact that masking persists with a contralateral broadband masker is difficult to explain if one assumes that the masking produced by broadband noise is energetic, i.e., predictable by a simple auditory filter model.

Figures 3(a) and (b) show the results obtained from the 28 school-aged children. The individual masking functions have been divided into two groups according listener age. The ''younger school-age'' group includes listeners aged 6.7–10.4 years and the ''older school-age'' group includes those aged 10.5–16.4 years. Visual inspection of the ipsilateral data in the two groups [previously reported in Lutfi *et al.* (2003), and reanalyzed for presentation here] reveals few obvious group differences and large individual differences in each group. In both groups there are listeners with large amounts of informational masking in both the ipsilateral and contralateral conditions. There are several listeners in the younger school-age group (e.g., SVP, SUV, SUX) who produced adultlike masking functions, with little or no masking in the contralateral condition and modest informational masking in the ipsilateral condition. There are also several listeners in the older school-age group (e.g., SVF, SVN, SVK) who produced masking functions similar to those from the preschoolers, with large amounts of informational masking in both ipsilateral and contralateral conditions.

The large individual differences in the amounts of masking and in the shapes of the masking functions would lead one to be very cautions with summary data. Nevertheless, plots of the mean amounts of total masking in the two conditions for each of the four listener groups reveals some interesting trends. Figure 4 shows the mean masking functions, with 95% confidence intervals plotted around each mean to allow visual interpretation of the statistical significance of differences.

Note first that the mean amounts of masking with a broadband noise masker are roughly the same in all four groups, in both the ipsilateral and contralateral conditions. In the ipsilateral condition the mean amount of masking with a broadband noise masker is about 35 dB, for the preschoolers, the younger and older school-age children, and for the adults. In the contralateral condition, the mean amount of masking with the broadband masker is only about 6 dB, consistent with previous results from studies of central masking. These are important results since they suggest that in this one condition, with a more or less nonvarying broadband masker, children and adults are performing the task at about the same level of proficiency. Thus, the data from the broadband conditions reveal little evidence of adult–child differences in auditory function.

In contrast, a clear age effect is evident in the mean masking functions from both the ipsilateral and contralateral conditions. In the ipsilateral conditions the age effect is manifest by decreases with increasing age of both the amount of masking with small numbers of masker components and the maximum amount of informational masking (masking above the solid horizontal line). The same is true of the masking functions from the contralateral conditions, although in this case there is an especially dramatic decrease in

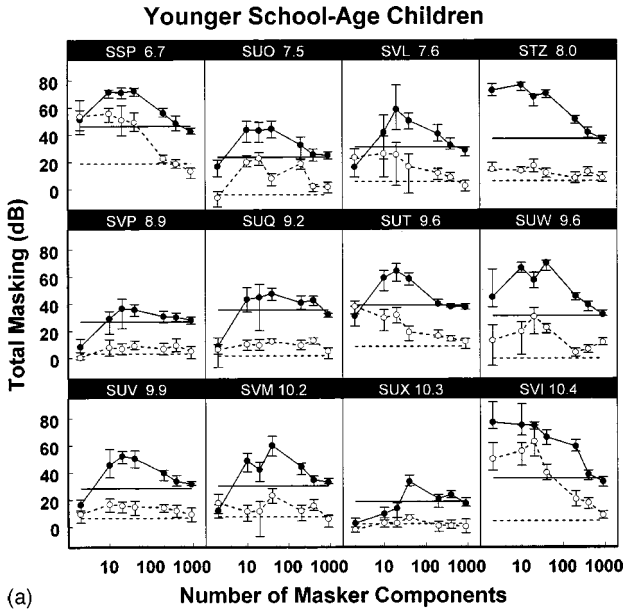

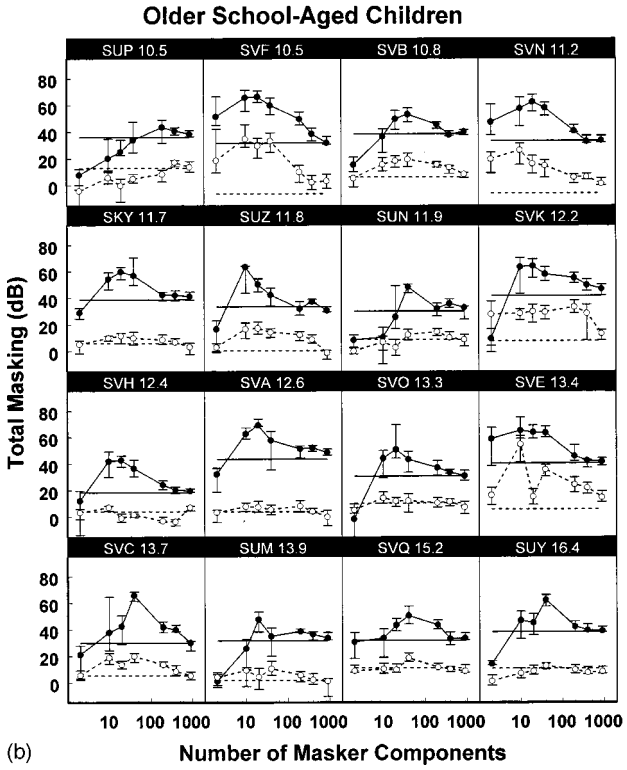

FIG. 3. (a) Same as Fig. 1, but for the listeners in the younger school-age group. For these listeners, the data from the ipsilateral condition are a reanalyzed version of the data shown in Lutfi *et al.* (2003). (b) Same as (a), but for the listeners in the older school-age group.

both amount of masking and maximum informational masking between the preschool and younger school-age group.

The psychometric function fitting procedures used in this study provided estimates of threshold, slope, and upper asymptote. Thus far we have discussed only the threshold estimates. The slopes of the psychometric functions, which are indicative of the variance of the decision variable, varied considerably across both conditions and age groups. The CoRE model makes specific predictions about how the slope parameter should vary with these two variables. A full explanation of how those predictions are generated and the extent to which they are consistent with the data described here will be the subject of a forthcoming article.

The upper asymptote parameter of the fitted psychometric functions estimates the extent to which performance on each individual run would fail to reach 100% correct at the highest signal levels. In the past we and others have argued that an upper asymptote less than 100% might indicate that on a certain fraction of trials the child is inattentive, and thus simply ''guessing'' (e.g., Wightman and Allen, 1992; Lutfi and Wightman, 1996). In the current study, however, guessing is not the only response strategy that would lower the upper asymptote. Attending only to the nontarget auditory filters on a fraction of the trials would have the same impact on the psychometric function as guessing (Lutfi and Wightman, 1996), and it is impossible from threshold estimates alone to tease apart the two strategies. The estimated upper asymptotes were less than 95% (never less than 80%) on 24% of the runs obtained from the preschool children, 11% of the runs from younger school-aged children, 12% of the runs from older school-aged children, and 6% of the runs from adults.

IV. DISCUSSION

This experiment was motivated by the possibility that the large amounts of informational masking previously observed in young children would be reduced if the target and the maskers were spatially separated, as in most everyday listening situations. Previous research with adult listeners (Kidd *et al.*, 1994, 1998) suggested that large reductions in informational masking could be obtained by spatial separation. If the same were true with children, concerns about large informational masking effects in classroom environments could be somewhat alleviated.

In an attempt to simplify the stimulus generation procedures and to allow more complete interpretation of the results by application of the CoRE model, we chose to study

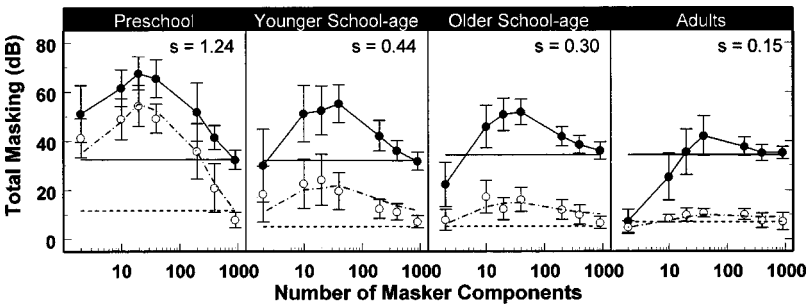

FIG. 4. Mean masking functions for listeners in the four age groups. The meanings of the symbols and the solid and dashed lines are the same as in Fig. 1. However, the dash-dot lines are predictions of the CoRE model, and the *s* values are the scale factors discussed in the text. The error bars represent the 95% confidence intervals computed in the traditional way from the variance of individual threshold estimates, assuming they are normally distributed.

an extreme kind of ''spatial'' separation, namely contralateral presentation of target and maskers. This stimulus configuration, and the percepts that it produces, are not representative of everyday listening, but we feel that it is a reasonable starting point. Our working hypothesis, yet to be tested, is that the reduction in informational masking listeners achieve with contralateral presentation would probably represent an upper bound on the reduction they would achieve in more realistic listening conditions.

For the adult listeners in our study, contralateral presentation of target and masker eliminated not only informational masking but nearly all masking. This result was not entirely unexpected, given the history of work on central masking. For the preschool children, contralateral presentation produced almost no reduction in informational masking, although total masking was reduced by about 20 dB on average. Some of the preschool children produced large amounts of masking in the contralateral broadband condition as well, which might indicate that some masking by broadband noise is informational (Lutfi, 1990). The school-aged listeners produced results that spanned the entire range between the adult and preschool results.

It is possible that aspects of training and prior experience may have contributed to the large individual differences, especially in the data from the children. Although training can exert a significant impact on adult performance (Watson, 1980; Leek and Watson, 1984; Watson and Foyle, 1985), improvements are observed only after extensive training over long time periods. Moreover, the adults in this study performed optimally in the contralateral conditions, and the performance of the children when the masker was broadband noise was almost the same as that of adults in both ipsilateral and contralateral conditions. Whether or not the children might have benefitted from more training with fewer numbers of masker components is not known, but in this context it should be mentioned that one listener in the cross-ear condition of the Neff (1995) study apparently required eight to ten runs to achieve asymptotic performance, so training in conditions such as ours may be an important issue. It is also possible that children may have required more elaborate instructions (emphasizing the fact that the target was only in the left ear), or may have achieved better performance given a different order of conditions (e.g., contralateral first). These are important questions, the answers to which must await further research. However, with regard to the instructions issue, there is every reason to think that the children were fully aware that the target was monaural and in the left ear. An unmasked target was presented on each trial as a cue, and the paradigm insured that a high S/N ratio target would be presented periodically throughout the run. With regard to the condition order issue, nothing can be said, since for all listeners, the ipsilateral conditions were tested before the contralateral conditions. Adults obviously adjusted their listening strategy to focus on the target ear in the contralateral conditions, and children did not. The practice trials and the unmasked cue presentations were included to encourage children to adjust their listening strategy appropriately, but the effectiveness of these procedures is unknown.

The component-relative-entropy (CoRE) model proposed by Lutfi (1993) offers a context in which the current results can be understood. According to this model, listeners are assumed to detect a target signal by implementing a decision rule based on the level outputs of n auditory filters. An ideal observer would monitor the output of only one auditory filter, the one centered on the target frequency. The inability to ignore masker tones, which produces the informational masking effect, is represented by monitoring additional auditory filters, the outputs of which are independent of target presence or absence. Most of the variance (82%) in the masking functions for all age groups in the ipsilateral condition can be accounted for by the value of n (Lutfi *et al.*, 2003). A similar approach can be used to explain masking in the contralateral condition without adding additional parameters to the model. To the extent that listeners can focus attention on the target ear, placing the masker in the opposite ear could be expected to reduce n, the number of attended auditory filters. A change in n has the effect of scaling the predicted masking function, leaving the threshold with a broadband masker unchanged. Thus, the model makes a simple prediction about the relationship between the ipsilateral and contralateral masking functions: the contralateral function should be a scaled version of the ipsilateral function. The best fitting scale factor would indicate the extent to which n was reduced by placing the masker in the opposite ear. In fact, the square root of the scale factor is equal to the proportion by which n is reduced. Scale factors greater than 1.0 would suggest that n was actually larger in the contralateral condition. The dot-dashed lines in Fig. 4 show the predictions of the model applied to the group mean contralateral data. The best fitting scale factor (shown in the figure for each group) is slightly greater than 1 for the preschoolers and close to 0 for the adults. In other words, the model predicts that the impact of placing the masker in the contralateral ear is actually to increase the number of monitored auditory filters for preschoolers and effectively to reduce to 1 the number of monitored filters for adults. Increasing the width of the auditory filters in the model cannot account for either the ipsilateral or the contralateral results.

The concept of selective attention is implicit in the CoRE model. The basic assumption of the model, that decisions are based on the outputs of ''monitored'' auditory filters, requires an attentional mechanism to guide the monitoring. Thus, informational masking, which can be characterized as an inability to ignore irrelevant auditory information, might be viewed as a failure of selective attention. Given the considerable literature on selective attention in children, it may be revealing to consider the current informational masking results in the context of psychological research on attention and the development of attention.

The early years of a child's life are marked by several developmental transitions in attention that have been revealed primarily by studies of the child's pattern of looking at the world. These transitions, most of which occur before age 4–5, reflect the development of a two-stage attentional system (Neisser, 1967; Ruff and Rothbart, 1996). The first stage is characterized by orienting and investigating, and the second by higher level control. There is both behavioral and physiological evidence supporting the development of these

two ''anatomically and functionally separate'' stages of selective attention (Ruff and Rothbart, 1996, Chap. 3).

It is the role of the first stage (orienting, or preattentive) to discriminate among task-relevant and task-irrelevant stimuli (Hagen and Hale, 1973). The second stage (higher level control, or focal) controls what is selected for further processing. The high levels of informational masking observed in children could reflect immaturity of either the first or second stage. Evidence from a series of ''central-incidental learning'' studies leads us to speculate that it may be the second stage that is the source of informational masking.

In an auditory version of the central-incidental learning paradigm (Doyle, 1973), children were asked to repeat target words spoken by a male and presented simultaneously with distracter words spoken by a female. The number of target words correctly repeated was the main performance measure. Retention of both the target and the distracter words was also measured. The main results were that the distracter impaired the word-repeating performance of the younger children (age 8 years) more than that of the older children (age 14), that retention of the target words increased with age, and that retention of the distracter words remained constant across the age groups. Because retention of the distracter words remained constant, the results were interpreted to suggest that the better performance of older children was ''...due not to a greater ability to filter out distracting material at an earlier stage of processing, but in large part to an ability to inhibit intrusions from the distracting material...'' Along similar lines, Humphrey (1982) reported a dramatic decrease in the impact of distracters on performance in visual recognition and recall tasks between age 4 and age 11, reflecting, perhaps, maturation of the second stage of the selective attention system. Although most of the research on the development of selective attention has focused on the visual modality, an important study by Conroy and Weener (1976), using the central-incidental learning paradigm, provided results that argued for parallel developmental trajectories for visual and auditory selective attention. Although the connection between informational masking and selective attention may be speculative, the fact that the processes underlying both seem to develop well into the school years is suggestive. The decrease in distraction effects between ages 4 and 11 reported by Humphrey (1982) in a visual task may reflect maturation of the same processes that modulate informational masking, which also decreases dramatically in that same age range (cf. data from Preschool and Younger School Aged groups in Fig. 4).

The research reported in this paper examined the impact of spatial separation of targets and distracters with the aim of contributing to our understanding of the process of stimulus segregation in noisy backgrounds such as classrooms. The previous research on selective attention in preschool and school-aged children is clearly relevant to the stimulus segregation issue. Nearly all of this research suggests that selective attention is not at adult levels until early adolescence, or even later. The results reported here are consistent with the previous selective attention results. Although the generalizability of the current contralateral target and masker configuration to everyday listening situations is tenuous, the previous selective attention results, combined with the results reported here, do not lead to optimistic predictions about the ability of young children to reduce the masking effect of uncertain maskers by spatial separation. Nevertheless, the prediction of little or no reduction in masking effectiveness with spatial separation should be tested in more natural listening environments which afford all the usual cues to spatial position (interaural differences, etc.). In addition, the potential advantage for children of other sound source segregation techniques should be studied. For example, Kidd *et al.* (1994) showed that stimulus configurations that made the maskers less ''signal-like'' presumably allowed listeners to segregate target from maskers and thus led to reductions in informational masking for his adult listeners. It is entirely possible that although children do not seem to be able to take advantage of spatial cues to segregate target and maskers, they may be able to use some of these other segregation cues (cf. Werner and Bargones, 1991).

ACKNOWLEDGMENTS

The authors would like to thank Jen Junion Dienger and the teachers in the Waisman Early Childhood Program for their contributions to the research. The research was supported financially by grants from the National Institutes of Health (Grant Nos. R01-HD23333, R01-CD01262, and P30-HD03352).

Allen, P., Wightman, F., Kistler, D., and Dolan, T. (**1989**). ''Frequency resolution in children,'' J. Speech Hear. Res. **32**, 317–322.

ANSI (**1987**). ANSI S3.9-1987, ''American National Standards specification for instruments to measure aural acoustic impedance and admittance (aural acoustic immittance)'' (American National Standards Institute, New York).

ANSI (**1989**). ANSI S3.9-1989, ''American National Standards specification for audiometers'' (American National Standards Institute, New York).

Conroy, R. L., and Weener, P. (**1976**). ''The development of visual and auditory selective attention using the central-incidental paradigm,'' J. Exp. Child Psychol. **22**, 400–407.

Doyle, A. (**1973**). ''Listening to distraction: a developmental study of selective attention,'' J. Exp. Child Psychol. **15**, 100–115.

Hagen, J. W., and Hale, G. H. (**1973**). ''The development of attention in children,'' in *Minnesota Symposia on Child Psychology*, edited by A. D. Pick (Univ. of Minnesota, Minneapolis), pp. 117–140.

Humphrey, M. M. (**1982**). ''Children's avoidance of environmental, simple task internal, and complex task internal distractors,'' Child Dev. **53**, 736–745.

Kidd, Jr., G., Mason, C. R., Rohtla, T. L., and Deliwala, P. S. (**1998**). ''Release from masking due to spatial separation of sources in the identification of nonspeech auditory patterns,'' J. Acoust. Soc. Am. **104**, 422–431.

Kidd, Jr., G., Mason, C. R., Deliwala, P. S., Woods, W. S., and Colburn, H. S. (**1994**). ''Reducing informational masking by sound segregation,'' J. Acoust. Soc. Am. **95**, 3475–3480.

Leek, M. R., and Watson, C. S. (**1984**). ''Learning to detect auditory pattern components,'' J. Acoust. Soc. Am. **76**, 1037–1044.

Lutfi, R. A. (**1990**). ''How much masking is informational masking?'' J. Acoust. Soc. Am. **88**, 2607–2610.

Lutfi, R. A. (**1993**). ''A model of auditory pattern analysis based on component-relative-entropy,'' J. Acoust. Soc. Am. **94**, 748–758.

Lutfi, R. A., and Wightman, F. L. (**1996**). ''Guessing or confusion? Analytic predictions for two models of target-distracter interference in children,'' Abst. Assoc. Res. Otolaryngol. **19**, 142.

Lutfi, R. A., Kistler, D. J., Oh, E. L., Wightman, F. L., and Callahan, M. R. (**2003**). ''One factor underlies age-related differences in auditory informational masking,'' Percept. Psychophys. **65**(3), 396–406.

Mills, J. H., Dubno, J. R., and He, N. (**1996**). ''Masking by ipsilateral and contralateral maskers,'' J. Acoust. Soc. Am. **100**, 3336–3344.

Neff, D. L. (**1995**). ''Signal properties that reduce masking by simultaneous, random-frequency maskers,'' J. Acoust. Soc. Am. **98**, 1909–1920.
Neff, D. L., and Dethlefs, T. M. (**1995**). ''Individual differences in simultaneous masking with random-frequency, multicomponent maskers,'' J. Acoust. Soc. Am. **98**, 125–134.
Neff, D. L., and Green, D. M. (**1987**). ''Masking produced by spectral uncertainty with multicomponent maskers,'' Percept. Psychophys. **41**, 409–415.
Neisser, U. (**1967**). *Cognitive Psychology* (Appleton, New York).
Oh, E. L., and Lutfi, R. A. (**1998**). ''Nonmonotonicity of informational masking,'' J. Acoust. Soc. Am. **104**, 3489–3499.
Oh, E. L., Wightman, F. L., and Lutfi, R. A. (**2001**). ''Children's detection of pure-tone signals with random multitone maskers,'' J. Acoust. Soc. Am. **109**, 2888–2895.
Ruff, H. A., and Rothbart, M. K. (**1996**). *Attention in Early Development* (Oxford U.P., New York).
Spiegel, M. F., Picardi, M. C., and Green, D. M. (**1981**). ''Signal and masker uncertainty in intensity discrimination,'' J. Acoust. Soc. Am. **70**, 1015–1019.
Watson, C. S. (**1980**). ''Time course of auditory perceptual learning,'' Ann. Otol. Rhinol. Laryngol. Suppl. **74**, 96–102.
Watson, C. S., and Foyle, D. C. (**1985**). ''Central factors in the discrimination and identification of complex sounds,'' J. Acoust. Soc. Am. **78**, 375–380.
Wegel, R. L., and Lane, C. E. (**1924**). ''The auditory masking of one pure tone by another and its probable relation to the dynamics of the inner ear,'' Phys. Rev. **23**, 266–285.
Werner, L., and Bargones, J. (**1991**). ''Source of auditory masking in infants: distraction effects,'' Percept. Psychophys. **50**, 405–412.
Wichmann, F. A., and Hill, N. J. (**2001a**). ''The psychometric function: I. Fitting, sampling, and goodness of fit,'' Percept. Psychophys. **63**, 1293–1313.
Wichmann, F. A., and Hill, N. J. (**2001b**). ''The psychometric function: II. Bootstrap-based confidence intervals and sampling,'' Percept. Psychophys. **63**, 1314–1329.
Wightman, F., and Allen, P. (**1992**). ''Individual differences in auditory capability among preschool children,'' in *Developmental Psychoacoustics*, edited by L. A. Werner and E. W. Rubel (American Psychological Association, Washington, DC), pp. 113–133.
Zwislocki, J. J., Buining, E., and Glantz, J. (**1968**). ''Frequency distribution of central masking,'' J. Acoust. Soc. Am. **43**, 1267–1271.

Perceptual weights in auditory level discrimination[a)]

Reinier Kortekaas[b)]
Institute of Hearing, Speech & Language and Department of Speech-Language Pathology & Audiology (106A FR), Northeastern University, Boston, Massachusetts 02115

Søren Buus[c)]
Institute of Hearing, Speech & Language and Communications & Digital Signal Processing Center, Department of Electrical & Computer Engineering (440 DA), Northeastern University, Boston, Massachusetts 02115

Mary Florentine[d)]
Institute of Hearing, Speech & Language and Department of Speech-Language Pathology & Audiology (106A FR), Northeastern University, Boston, Massachusetts 02115

(Received 16 June 2000; revised 22 January 2003; accepted 5 March 2003)

Perceptual weights in level discrimination (also called intensity discrimination) were determined for 3-, 7-, 15-, and 24-component tone complexes with flat spectral envelopes using a correlational paradigm. Each frequency component was randomly and independently perturbed in level on each presentation. For the target interval, frequency-component levels were additionally increased by the level increment to be detected, ΔL $[=20\log_{10}((p+\Delta p)/p)$, where p is pressure]. Weights were calculated from the across-trial correlation between the level perturbations for each frequency component and the interval chosen by the listener. Two conditions were investigated: (1) ΔL was equal across frequency components, and (2) ΔL increased progressively across frequency components. For both conditions, data for four listeners usually showed the greatest weight for the highest frequency component. The two-to-four highest frequency components generally were most important for level discrimination. The effect of increasing ΔL progressively with frequency was small and inconsistent. Additional measurements showed that flanking noise maskers designed to mask spread of excitation caused only small and generally unsystematic changes to the weights. Overall, these results indicate that listeners combine information across a wide range of auditory channels to arrive at a decision for level discrimination, but the weighting of channels appears to be suboptimal. [DOI: 10.1121/1.1570441]

PACS numbers: 43.66.Fe, 43.66.Ba [MRL]

I. INTRODUCTION

Level discrimination (also called intensity discrimination) is a basic property of hearing that has been studied extensively for many decades (for a review see, e.g., Plack and Carlyon, 1995). Many studies have reported just noticeable increments, or difference limens (DLs), in level or intensity measured with a pulse-comparison paradigm (e.g., McGill and Goldberg, 1968; Viemeister, 1972; Jesteadt *et al.*, 1977; Florentine *et al.*, 1987). Although these data inform about the auditory system's ability to resolve level differences, they provide relatively little information about how listeners process level information across critical bands. For instance, pure-tone level discrimination is generally thought of as a two-stage process of first determining the increase in excitation caused by the level increment for each critical band separately, and second combining the information from all auditory channels in some way to decide which stimulus had the higher level (e.g., Florentine and Buus, 1981). In other words, level information is not confined to a single frequency-selective channel. Listeners are able to make use of spread of excitation to obtain several ''samples'' of the increment in excitation level. Indeed, experiments using high- and low-pass noises to mask the spread of excitation show that masking enlarges the DLs at high levels (e.g., Viemeister, 1972, 1974; Moore and Raab, 1974, 1975; Florentine and Buus, 1981; Florentine, 1983) and that the DLs are nearly independent of level when the excitation is confined to a fixed number of channels (e.g., Viemeister, 1974; Moore and Raab, 1974; Florentine and Buus, 1995; Buus and Florentine, 1995). Whereas it is quite clear that level discrimination depends on information across a range of auditory channels, it is largely unknown whether listeners pay equal attention to all excited critical bands or focus on some channels at the expense of ignoring information in others.

Florentine and Buus (1981) presented a model for level discrimination in which the information in all critical bands was optimally combined such that

$$d' = \left(\sum_i d_i'^2 \right)^{1/2}, \tag{1}$$

[a)]Part of this work was presented at the 139th Meeting of the Acoustical Society of America in May 2000 [Buus *et al.*, J. Acoust Soc. Am. **107**, 2820(A) (2000)].

[b)]Present address: Siemens Audiologische Technik GmbH, Gebbertstraße 125, D-91058 Erlangen, Germany. Electronic mail: reinier.kortekaas@siemens.com
[c)]Author to whom correspondence should be addressed. Electronic mail: buus@neu.edu
[d)]Electronic mail: florentin@neu.edu

where d' is the overall sensitivity of the listener, and d_i' is the sensitivity associated with critical band i. The index i indicates the critical-band number and takes values from 1 to 24. Within a critical band, d_i' was determined by a constant variance and by the difference between the excitation levels caused by the pedestal and by the pedestal-plus-increment. Excitation levels were derived from Zwicker's (1958) masking patterns. Furthermore, critical-band channels were assumed to be independent and the sensitivity-per-Bel was assumed to be constant across channels and independent of level. If the increase in excitation level is the same in all critical bands, then a model observer who pays equal attention to all critical-band channels performs optimally. If the increase in excitation level is larger in some channels than in others, more attention or weight should be given to the critical-band channels in which the excitation-level increases are larger. Assuming equal variance in all channels, the optimal weight is proportional to the increase in excitation level produced by the level increment. Such a strategy will be termed the optimal decision rule.

The model's assumption of optimal combination of information across auditory channels cannot be readily tested. However, some insight into the way listeners combine information across channels may be obtained by perceptual-weight analysis (e.g., Ahumada and Lovell, 1971; Berg, 1989; Berg and Green, 1990; Richards and Zhu, 1994; Lutfi, 1995; Buus *et al.*, 1996). Perceptual weights quantify how much individual components of complex stimuli contribute to a listener's decisions. To this end, individual components are randomly varied, or perturbed, in the dimension of interest on each presentation. For example, the dimension of interest may be component frequency, duration, or, in the present study, component level. The listener's responses are tracked as functions of the perturbation given to each component of the stimulus. If the listener gives a particular component a high weight—i.e., if its contribution to the decision is important—then the responses will be highly dependent on the perturbation of that frequency component. Conversely, if the component contributes little to the listener's decision, the perturbation will not affect the responses. Thus, the strength of the relation between the perturbation of a component and the listener's response reveals how important any particular component is to the listener's performance. Several methods have been proposed to determine perceptual weights, such as conditional-on-a-single-stimulus (COSS) analysis (Berg, 1989) and trial-by-trial correlational analysis (Richards and Zhu, 1994; Lutfi, 1995). The present study adopted the latter analysis, and derived weights from the point bi-serial correlation between the level-perturbation difference of individual frequency components in the two observation intervals and the interval chosen by the listener.

Doherty and Lutfi (1996) used COSS analysis to determine perceptual weights for level discrimination. Their stimuli were tone complexes consisting of pure tones at octave frequencies between 250 and 8000 Hz. On each trial, the frequency-component levels were randomly and independently varied about one of two mean values, with levels for the target interval selected from the higher mean. For normal-hearing listeners, the weights averaged across listeners were reasonably uniform across frequency components. Some listeners, however, showed a bowl-shaped pattern suggesting greater weights for the lowest and highest frequency components. In a subsequent study, Doherty and Lutfi (1999) showed that listeners generally focused on the target component, when only one of the six components was incremented in the signal interval, but were unable to completely ignore nontarget components. Willihnganz *et al.* (1997) applied the trial-by-trial correlational method to determine perceptual weights for tone complexes composed of frequency components at 250, 1000, and 4000 Hz. For their control group of normal-hearing, adult listeners, the highest frequency component consistently was most important to the decision for three out of six listeners. The weight patterns for the remaining three listeners showed substantial interindividual differences and differed across sets of trials.

The studies of Doherty and Lutfi (1996, 1999) and Willihnganz *et al.* (1997) inform about how normal-hearing listeners use level information associated with individual frequency components, but these data do not directly address the question of how listeners combine information from individual critical bands. First, because the frequency components were spaced several critical bands apart, it is likely that level information in adjacent critical bands was highly correlated. For instance, an increase in level for a particular frequency component probably resulted in a concomitant increase in excitation level in several adjacent critical bands. Second, the number of critical bands in which the information was dominated by a particular frequency component is likely to differ somewhat across frequency components. The lowest and highest frequency components can be expected to excite more critical bands than the remaining frequency components due to spread of excitation. Thus, it is unclear to what extent the variation in weights across frequency reflects the weight of a single auditory channel tuned to the frequency of a particular frequency component.

The present study aimed to minimize the correlation in level information among most auditory channels by using tone complexes with frequency components spaced one critical band apart. This frequency spacing allows the weights associated with individual critical bands to be characterized, because the excitation level in each critical band is governed primarily by one component.[1] In experiment I, weights were determined as a function of level and number of frequency components in the complexes. As the level increases, the effect of spread of excitation is expected to become more prominent (Zwicker, 1958). As a consequence, the lowest and highest frequency components were expected to become more important for the listener's decision at higher levels. By using complexes with different numbers of frequency components, we aimed to determine the number of frequency components that listeners attend to. In addition, the use of complexes with many components offer another way of examining the influence of spread of excitation. For instance, when the stimulus consists of 24 frequency components, level information is present over almost the entire range of audible frequencies, leaving little opportunity for spread of excitation to play a role. Two level-increment conditions were tested: one in which all frequency components received

the same level increment, and one in which the level increment increased progressively across frequency components such that the highest frequency component received the largest level increment. The latter condition was included to investigate whether the weights would increase in auditory channels with an increased excitation-level difference, as required by the optimal decision rule discussed earlier.

To further examine how spread of excitation may affect the weights with which frequency components enter the listener's decision, flanking noise maskers were used for a limited number of conditions in experiment II. Weights were determined for the maskers as well as for the frequency components of the signal to determine whether the effect of the maskers, if any, arises from elimination of spread of excitation or from injecting irrelevant information into the listener's decision.

II. EXPERIMENT I: EFFECTS OF LEVEL, BANDWIDTH, AND ACROSS-FREQUENCY DIFFERENCES IN LEVEL INCREMENT

A. Method

1. Listeners

Four listeners with normal hearing participated. Their ages ranged from 22 to 31 years and their audiometric thresholds in the test ear were better than 15 dB HL (ANSI, 1989) at all octave frequencies between 0.25 and 8 kHz. Before participating in the present study, all listeners had participated in a similar level-discrimination experiment lasting about 20 h. In addition, listeners L3 and L4 (the first author) had ample listening experience in psychoacoustic testing.

2. Stimuli

The stimuli were tone complexes consisting of 3, 7, 15, or 24 frequency components that were 1 Bark apart and centered at $z_c = 11.5$ Barks (1600 Hz) on a critical-band scale (Zwicker, 1961; Zwicker and Feldtkeller, 1967; Scharf, 1970; Scharf and Buus, 1986). The initial phase of each frequency component was chosen at random on each presentation. The duration was 500 ms measured between the half-amplitude points of the 20-ms raised-cosine rise and fall.

The standard stimulus consisted of frequency components whose average levels L—i.e., the levels in the absence of level perturbations—were equal. To examine whether stimulus level affected the weights, the 3- and 7-tone complexes were tested at several standard frequency-component levels: 30, 60, and 80 dB SPL for the 3-tone complexes and 30, 60, and 75 dB SPL for the 7-tone complexes. (The highest level was lowered for the 7-tone complexes to avoid uncomfortable overall loudness levels.) To reduce the number of measurements, the 15- and 24-tone complexes were tested only at a frequency-component level of 60 dB SPL. The target stimulus had the level of all frequency components raised to $L + \Delta L$. Here, $\Delta L = 20 \log_{10}((p + \Delta p)/p)$, where p is the pressure of the standard, and Δp is the pressure increment. In some conditions, the increment in level, ΔL, was the same for all frequency components; in other conditions, ΔL increased progressively across frequency components (see below).

To determine perceptual weights, the frequency-component levels were independently perturbed on each presentation. The perturbations had a Gaussian distribution with a 0-dB mean and standard deviation, σ, of 2 dB, but were limited not to exceed ± 6 dB.

3. Procedure

In experiment I, measurements of difference limens for level, ΔL_{DL}'s, for the tone complexes preceded the measurements of perceptual weights. These initial measurements served to practice the listeners on level discrimination and to help choose ΔL's that would yield about 80% correct responses.

The ΔL_{DL}'s were measured in a two-alternative, forced-choice (2AFC) paradigm. Each trial included two intervals, one of which contained the level increment. The listener's task was to indicate on a response box which interval had the incremented stimulus. Lights on the response box provided correct-answer feedback. A three-down, one-up procedure was used to estimate the ΔL_{DL}'s. As in previous studies from this lab, each block of trials consisted of three interleaved adaptive tracks [see Buus *et al.* (1997) for a more detailed description]. For each track, the level of an in-phase pressure increment, $20 \log_{10}(\Delta p/p)$, decreased after three consecutive correct responses, and increased after every incorrect response. The initial value of $20 \log_{10}(\Delta p/p)$ was chosen to be easily audible. It changed in steps of 5 dB until the first downward reversal, after which the step size was reduced to 2 dB. This procedure converged on the pressure-increment level necessary to obtain 79.4% correct responses (Levitt, 1971). The DL estimate for each of the three tracks, expressed as $20 \log_{10}(\Delta p_{DL}/p)$, was computed as the arithmetic mean of the pressure-increment levels at the last two of a total of five reversals. Subsequently, the three DL estimates were averaged and the resulting value of $20 \log_{10}(\Delta p_{DL}/p)$ was converted to $\Delta L_{DL} (= 20 \log_{10}([p + \Delta p_{DL}]/p)$. As training for the task, each listener completed at least two blocks of adaptive measurements of the ΔL_{DL} for each condition (i.e., number of components, component level, and increment condition; see below and Table I). This totaled about four hours of listening. The data reported here are the geometric means of ΔL_{DL} from three blocks of trials (for a total of nine adaptive tracks) for each condition obtained after training was completed.[2] Measurements were obtained with the ten conditions presented in mixed order.

Perceptual weights were determined by a modified method of constant stimuli. Here, the term constant refers to ΔL being fixed during all trials for a given condition, rather than to the stimuli being identical across trials; the random level perturbation of each frequency component introduced differences between intervals (and across trials) other than ΔL. Again, the listeners' task was to indicate on a response box which of the two intervals contained the level increment and lights on the response box provided correct-answer feedback after each trial. Listeners were informed that the visual feedback might occasionally be clearly counterintuitive. Ow-

TABLE I. Test conditions and outcome of chi-square tests in experiment I. The first column shows the H_0 hypothesis under test: (1) weights are equal for the first and second set of trials, (2) weights are equal to the optimal weights, and (3) weights are equal for $k=1$ and $k=1.1$. The second column shows the figures to which the analysis pertains and the comparison data, if any. The third to sixth columns specify the stimulus. The seventh column shows the parameter that differs for comparisons between two stimulus conditions. Columns 8–11 show the χ^2 values and the level of significance ([a] for $p<0.05$; [b] for $p<0.01$; and [c] for $p<0.001$) for each of the four listeners. The next two columns show the 95% confidence limits (CL) for weights of zero averaged across listeners and their standard deviation. Finally, the last column shows the few conditions for which a different ΔL_0 was used for a particular listener, or for which the 95% confidence limit for a particular listener is not included in the average.

H_0	Figure	Component level (dB SPL)	N	k	ΔL_0 (dB)	Comparison	L1	L2	L3	L4	CL	SD	Remarks
First and	2	30	3	1	2		6.0[a]	3.8	17.0[c]	0.9	0.10	0.009	
second	2	60	3	1	2		0.1	0.1	1.4	5.2	0.096	0.004	
set of	2	80	3	1	1.5		0.2	3.0	18.7[c]	6.9[a]	0.075	0.006	
trials are	3	30	7	1	2		14.5[a]	6.3	6.2	3.7	0.10	0.021	
equal	3	60	7	1	2		10.7	3.9	8.3	1.1	0.08	0.005	
	3	75	7	1	1.5		5.6	3.3	7.7	10.6	0.09	0.007	
	4	60	15	1	1.5		17.1	13.5	18.5	12.4	0.07	0.008	
	5	60	24	1	1.5		24.3	20.0	95.8[c]	35.4[a]	0.077	0.019	CL=0.199 for L4
	6	60	7	1.1	0.7		5.7	4.8	6.4	5.0	0.068	0.015	ΔL_0=0.5 dB for L2
	6	60	15	1.1	0.7		13.8	15.4	23.6	10.9	0.096	0.030	ΔL_0=0.5 dB for L2
Weights	2	30	3	1	2		8.4[a]	13.9[c]	6.5[a]	10.7[b]	0.10	0.009	
are	2	60	3	1	2		34.0[c]	30.1[c]	108.7[c]	8.2[a]	0.096	0.004	
optimal	2	80	3	1	1.5		55.6[c]	16.3[c]	58.3[c]	5.2	0.075	0.006	
	3	30	7	1	2		5.7	15.0[a]	21.0[b]	16.2[a]	0.10	0.021	
	3	60	7	1	2		72.0[c]	9.7	51.5[c]	28.1[c]	0.08	0.005	
	3	75	7	1	1.5		180.1[c]	70.9[c]	137.3[c]	50.5[c]	0.09	0.007	
	4	60	15	1	1.5		99.1[c]	27.5[a]	66.3[c]	62.9[c]	0.07	0.008	
	5	60	24	1	1.5		34.3	16.2	91.4[c]	46.5[b]	0.077	0.019	CL=0.199 for L4
	6	60	7	1.1	0.7		59.5[c]	85.5[c]	148.1[c]	122.7[c]	0.068	0.015	ΔL_0=0.5 dB for L2
	6	60	15	1.1	0.7		19.9	52.7[c]	29.8[b]	40.1[c]	0.096	0.030	ΔL_0=0.5 dB for L2
$k=1$ equal	3 & 6	60	7	1.1		$k=1$	3.1	10.8	14.3[a]	20.0[b]			
to $k=1.1$	4 & 6	60	15	1.1		$k=1$	10.8	12.6	36.9[c]	21.6			

ing to the random nature of the signals, it was possible that the target stimulus—despite its incremented average level—would have an overall level less than that of the reference stimulus. In addition, listeners were instructed to ignore any differences in spectral shape between intervals, and to concentrate on differences in overall level. Each block of trials comprised 100 constant-stimulus trials interleaved with ''orientation trials,'' which provided the listener with a more audible level increment of $2\Delta L$ whenever two incorrect responses occurred consecutively. During each block, the listener's responses and the perturbation level of each frequency component in the constant-stimulus trials were stored for later processing. Data for the orientation trials were discarded. Ten blocks of trials, or a total of 1000 constant-stimulus trials, were gathered for determining perceptual weights for each condition. Listening usually was performed in one- to two-hour sessions several times a week.

The orientation trials were intended to refocus the listener on the task. As expected when the performance averages 80% correct, the percentage of orientation trials was about 4% and appeared to vary unsystematically across conditions. To prime the listener for the task, each run started with four orientation trials. This procedure was adopted as an economical alternative to the procedure developed by Berg and Green (1990), who used a combination of an adaptive procedure and a constant-stimuli procedure to estimate perceptual weights in spectral profile analysis. The constant-stimuli trials yielded the data for weight analysis, while the adaptive trials helped the listeners maintain constant performance. This procedure required approximately 204 trials to yield 100 trials suited for weight estimation, whereas the present procedure required only about 108 trials.

To test whether listeners could adjust their weights if the optimum strategy so required, ΔL in the signal interval was chosen as

$$\Delta L(z) = \Delta L_0 \cdot k^{(z-z_l)}, \tag{2}$$

where $\Delta L(z)$ is the level increment for the frequency component at critical-band rate z (Barks), ΔL_0 is the nominal level increment, and z_l is the critical-band rate of the lowest frequency component in the tone complex. Note that z_l varies with the number of frequency components in the tone complexes because the center frequency is fixed at 11.5 Barks. In the baseline condition, k was equal to 1 so that all frequency components received the same increment in the signal interval. In this case, the optimal decision rule requires equal weights on all frequency components, provided that possible effects of spread of excitation are negligible and that the listener's sensitivity to a change in excitation level is independent of frequency. To produce conditions in which the optimal weights should vary across frequency, k was set to 1.1 in other conditions. In this case, the optimum decision rule requires the weights to increase with frequency because $\Delta L(z)$ increases with frequency. Listeners completed the conditions with $k=1$ before starting the conditions with k

$=1.1$. No training was provided between conditions. Except for the first author (L4), listeners were not informed about the difference between conditions.

Table I lists the ΔL_0's used for each condition. For reasons of simplicity, the ΔL_0's were identical for all listeners unless the performance differed dramatically from 80% correct for an individual listener. The two exceptions are noted in Table I.

4. Apparatus

Stimuli were generated digitally with a 50-kHz sample rate using a TDT AP II array processor, D/A converted (TDT DD1), attenuated (TDT PA4), low-pass filtered with a cutoff frequency of 20 kHz (TDT FT5), attenuated again (TDT PA4), and presented to the listener through one earpiece of a Sony MDR-V6 headphone, which was driven by a headphone buffer (TDT HB6). Level increments were produced digitally by adjusting the amplitudes of the frequency components. Listeners were seated in a double-walled, sound-attenuating booth.

5. Data analysis

Perceptual weights were determined using the correlation method described by Lutfi (1995). This method calculates the point bi-serial correlation between the interval chosen by the listener and the level difference between the perturbations in intervals 2 and 1. The correlation was calculated across trials for each frequency component separately. The correlation coefficients, ρ_i, were normalized such that the weights, a_i, added to a sum of unity—i.e., $a_i = \rho_i / \Sigma_j \rho_j$.[3]

To examine the significance of differences between weight patterns, such as the difference between the observed and the theoretically optimal weights, a chi-square test was devised. A test statistic χ^2 was formed as $\Sigma_i(\Delta w_i / \sigma_{\Delta w})^2$, where Δw_i is the difference between the two patterns for perceptual weight i, and $\sigma_{\Delta w}$ is the standard deviation of the distribution of these differences. If the Δw_i's are normally distributed and independent, then χ^2 is a sum of squared z-scores. Consequently, χ^2 is chi-square distributed with $v = M-1$ degrees of freedom, where M is the number of weights in the pattern. The variance associated with the correlation coefficients, ρ_i, however, is not constant but depends on the true value of the correlation coefficient. To homogenize the variance of the ρ_i estimates, a Fisher z-transform was applied to ρ_i before calculating the weights, w_i. (Note that the figures show the weights a_i, which are based on the normalized raw correlation estimates, rather than w_i, which are used only for statistical testing.) Simulations suggested that for (absolute) ρ_i values smaller than about 0.5, the variance of the transformed coefficients indeed corresponded to the expected variance based on the Fisher z-transform. Third- and fourth-order moments also agreed with expectations. For ρ_i values outside this range, both the mean and the variance were strongly biased [cf. footnote 3 in Richards and Zhu (1994)]. In the present study, all ρ_i's had absolute values less than 0.5, so biases are not a concern. The standard deviation $\sigma_{\Delta w} = \sqrt{(c_1^2 + c_2^2)}\sigma_\rho$, where $\sigma_\rho = \sqrt{1/(N_t - 3)}$ is the standard deviation of the Fisher z-transformed ρ_i, N_t is the number of trials, and c_1 and c_2 are the sums of the Fisher z-transformed ρ_i for weight patterns 1 and 2, respectively. For comparisons between measured weights and the optimal weights, the contribution of the optimal pattern to the total variance was set to zero (i.e., $\sigma_{\Delta w} = c_1 \sigma_\rho$). Whereas Δw_i reasonably can be assumed to have a normal distribution, we cannot readily prove that they are independent. However, an analysis of how weights in a particular band are affected by the level perturbation in neighboring bands indicates little interaction between neighboring critical bands (see Sec. IV C), which makes it reasonable to assume that the weights obtained for different stimulus components are, at least, nearly independent. In the following, a confidence level of $p < 0.05$ will be regarded as statistically significant.

B. Results

The description of the results begins with the presentation of the ΔL_{DL}'s measured by the adaptive procedure and the predictions by the multiband excitation-pattern model (Florentine and Buus, 1981). Then, the weights obtained for the stimuli with uniform level increments are shown. Finally, the weights obtained for the stimuli with nonuniform level increments are presented.

1. Estimates of ΔL_{DL}'s

The left panel of Fig. 1 shows the ΔL_{DL}'s obtained with the adaptive procedure for stimuli without level perturbations. Because the data were relatively similar for the four listeners, the ΔL_{DL}'s are the geometric means across listeners, which also provide the best comparison with model predictions. The ΔL_{DL}'s are plotted as functions of the number of frequency components in the tone complexes. The vertical error bars show standard errors. Note that the ΔL_{DL}'s are shown on a logarithmic axis to preserve ratios between ΔL_{DL}'s [see Buus and Florentine (1991) for discussion]. The right panel of Fig. 1 shows the ΔL_{DL}'s predicted by an excitation-pattern model, which will be discussed later.

On the average, the measured ΔL_{DL}'s for the 3- and 7-tone complexes with $k=1$ decrease by a factor of 2 to 3 as the pedestal level of the frequency components increases from 30 to 75 or 80 dB SPL (left panel). This finding is in accord with the ''near-miss'' to Weber's law (McGill and Goldberg, 1968; Viemeister, 1972; Jesteadt *et al.*, 1977; Florentine *et al.*, 1987). As for the effect of the number of frequency components, the data for the 60 dB SPL frequency-component level show that the average ΔL_{DL}'s are nearly independent of the number of frequency components. The left panel of Fig. 1 also shows average ΔL_{DL}'s for the 7- and 15-tone complexes with $k=1.1$ (diamonds). For the 15-tone complexes, the average ΔL_{DL} for $k=1.1$ is a factor of 3 smaller than that for $k=1$. This finding suggests that the highest frequency components make substantial contributions to the listeners' decision; the level increment for the highest frequency component is k^{14} (≈ 3.8 when $k=1.1$) times the baseline increment, ΔL_0. For the 7-tone complexes, the average ΔL_{DL} for $k=1.1$ is a factor of about 1.5 smaller than that for $k=1$. In this case, the level increment

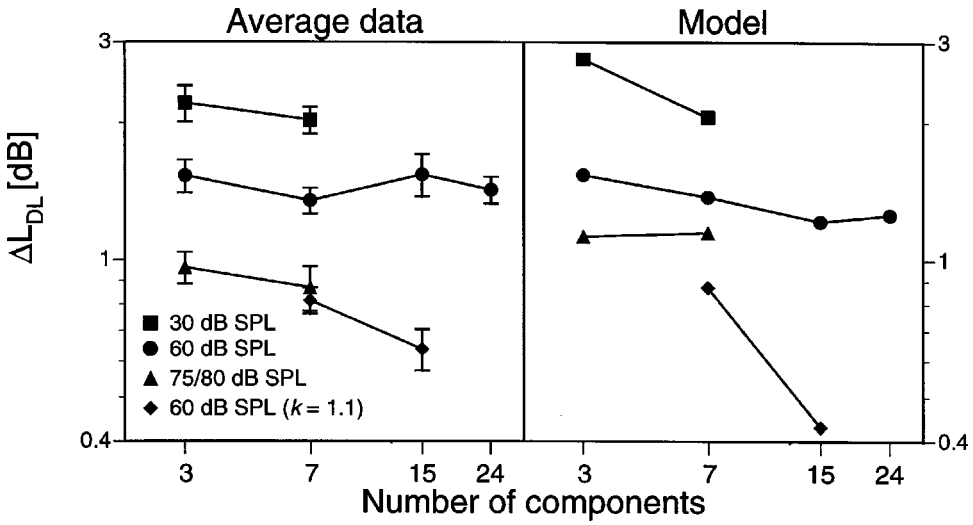

FIG. 1. Measured (left panel) and predicted (right panel) ΔL_{DL}'s are shown as functions of the number of frequency components. For the measured ΔL_{DL}'s, the error bars indicate standard errors of the geometric means. Symbols represent different conditions and are listed in the legend.

for the highest frequency component is k^6 ($\approx$1.77 when $k = 1.1$) times ΔL_0, again suggesting a substantial contribution of the highest frequency components.

The right panel in Fig. 1 shows the ΔL_{DL}'s predicted by Florentine and Buus's (1981) excitation-pattern model. The single free parameter in the model—i.e., the sensitivity to a change in excitation level within a critical band—was chosen to make the geometric means across all conditions identical for the measured and predicted ΔL_{DL}'s. Although some differences are apparent between the measured and predicted ΔL_{DL}'s, the model clearly captures the general trends of the data. The model predicts that the ΔL_{DL}'s ought to decrease only slightly as the number of 60 dB SPL frequency components increases, which agrees with the virtually constant ΔL_{DL}'s obtained. In addition, the predicted effect of level for the 3-tone complexes closely matches the data. However, the effect of level for the 7-tone complexes appears smaller in the model predictions than in the data and the model somewhat overpredicts the effect of having the level increments increase with frequency for the 15-tone complexes with $k = 1.1$. Overall, however, the discrepancies between the predicted and measured ΔL_{DL}'s are relatively minor and the overall patterns of results are very similar for the model predictions and the data.

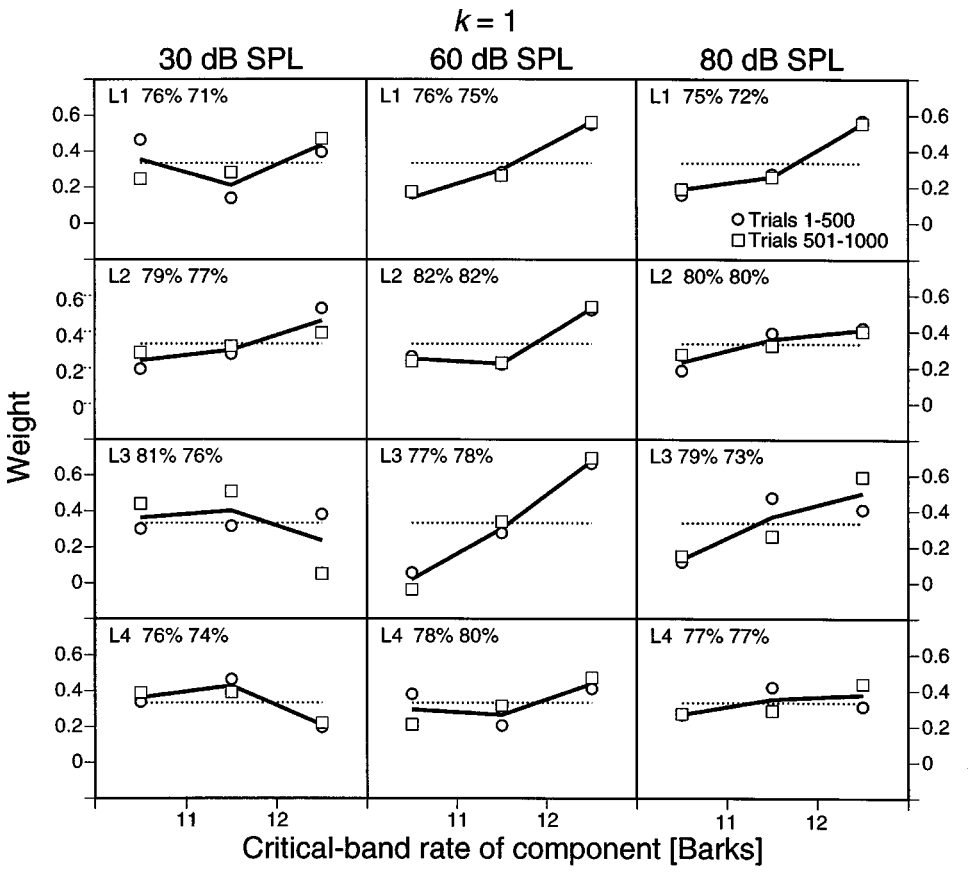

FIG. 2. Weights for 3-tone complexes with $k = 1$. Each column represents a frequency-component level. The circles show the weights obtained for the first 500 trials and the squares show those obtained for the last 500 trials. The solid lines show the overall weights based on 1000 trials. The dotted lines show the optimal weights. The two numbers in each panel indicate the percentages of correct responses obtained in the first and second set of trials.

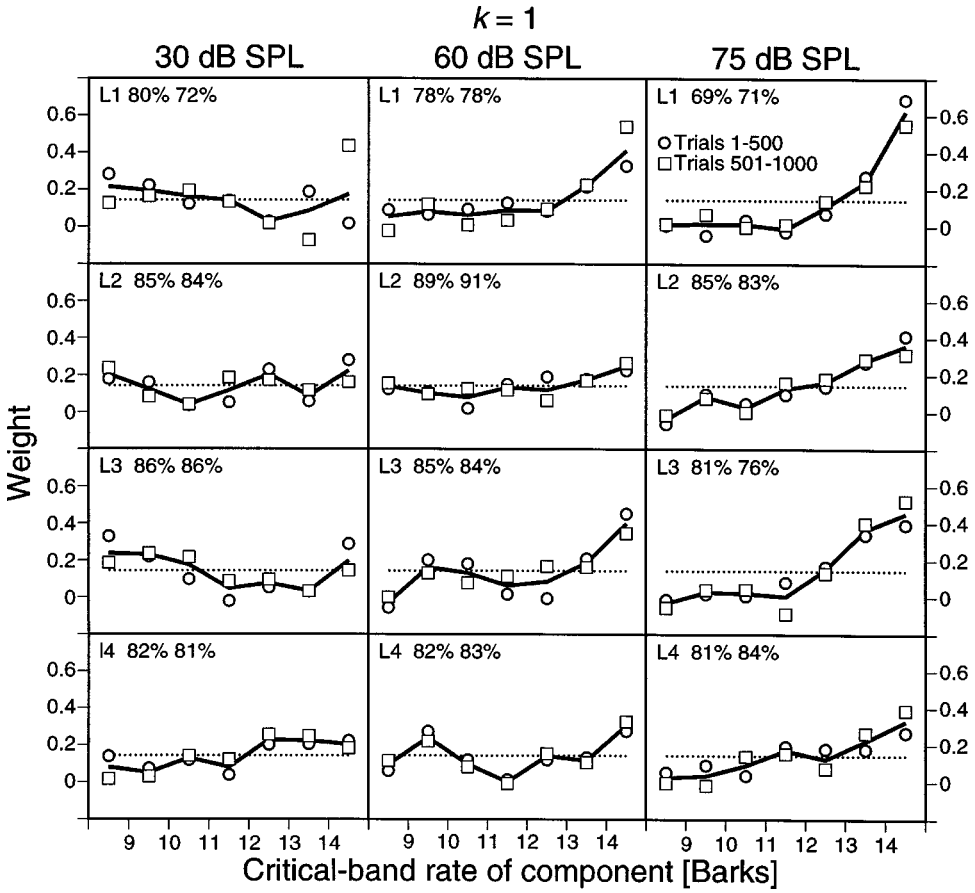

FIG. 3. Weights for 7-tone complexes with $k=1$ are plotted in the same manner as Fig. 2.

2. Perceptual weights

a. Uniform level increments (k=1). Figure 2 shows the individual listeners' perceptual weights for the 3-tone complexes. Solid lines represent the overall weights based on all 1000 trials, whereas the circles and squares represent weights based on the first and last 500 trials, respectively. The dotted lines show the ideal, uniform weights that would result if each frequency component were equally important for the listener's decision. (Throughout the description of the results, the derivation of ideal weights considers only information contained in the acoustic stimulus and ignores any possible effects of auditory processing such as spread of excitation and variability added by the auditory system.) The two numbers in each panel indicate the percentages of correct responses for the first and second set of trials. Clearly, the listeners' overall performance was quite stable over the course of the experiment and generally was between 75% and 80% correct responses. As shown in Table I, the chi-square test described in Sec. II A 5 indicated that the weights generally did not differ significantly between the first and second set of trials. The exceptions are listeners L1 and L3 at 30 dB SPL and listeners L3 and L4 at 80 dB SPL. For these cases, the overall weights are probably less reliable than those in the remaining conditions. Table I also shows the 95% confidence limits for weights of zero averaged across listeners. Based on these confidence limits, almost all the weights shown in Fig. 2 are significantly larger than zero. The only exception is L3's small weight for the 10.5-Bark component at 60 dB SPL.

The weights obtained at 30 dB SPL are reasonably close to the ideal, uniform weights considering that the observed-to-ideal-weight ratio—rather than absolute deviation—is the important metric. For the overall weights, observed-to-ideal-weight ratios range from 0.6 to 1.3 (L1), 0.7 to 1.4 (L2), 0.7 to 1.2 (L3), and 0.6 to 1.3 (L4). Nevertheless, the statistical analysis indicates that the weights vary significantly across frequency for all four listeners, as shown in the second section of Table I. As is evident in the left column of Fig. 2, the patterns of weights differ somewhat among listeners. For listeners L1 and L2, the highest frequency component is most important. For listeners L3 and L4, the center frequency component appears to be most important.

At 60 dB SPL, the highest frequency component is most important for all listeners (see middle column of Fig. 2). The weights for listener L3, for instance, differ dramatically from what would be considered ideal. Again, Table I shows that the weights differ significantly from the ideal, uniform weights for all four listeners. At 80 dB SPL, listeners L1 and L3 show weights similar to those obtained at 60 dB SPL. The weights for L2 and L4 are close to ideal. However, the weights for listener L4 are the only ones that do not differ significantly from the ideal, uniform weights (see Table I). Nevertheless, the variation of weights across frequency is relatively modest for all listeners. In summary, the weights at all three levels usually differ from the ideal, uniform weights, but all three frequency components make substantial contributions to the listeners' decisions. At the higher levels, the highest frequency component contributes the most to the listeners' decisions.

Figure 3 shows the weights for the 7-tone complexes

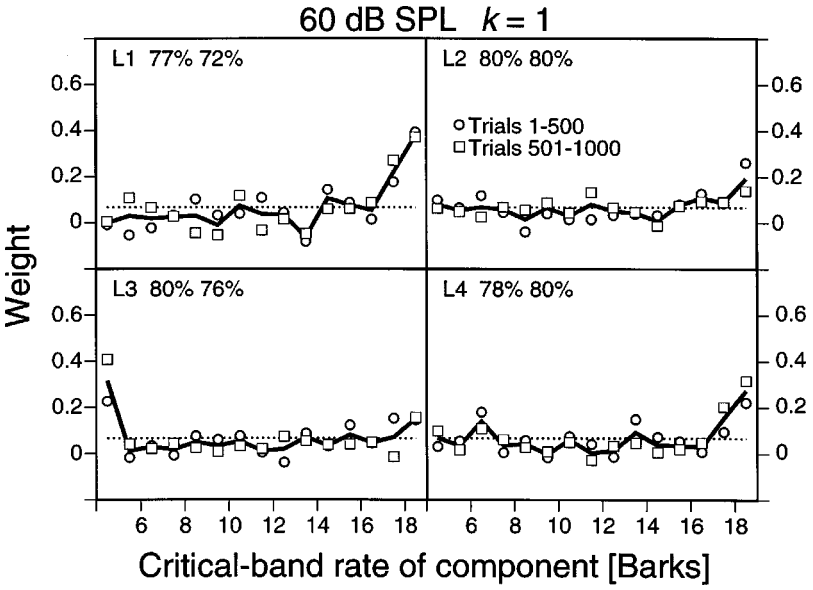

FIG. 4. Weights for 15-tone complexes with $k=1$ are plotted in the same manner as Fig. 2.

plotted in the same manner as Fig. 2. As shown in Table I, the weights did not differ significantly between the first and second set of trials, except for listener L1 at 30 dB SPL. At this level, four to six frequency components contribute substantially to the listeners' decisions as indicated by their being significantly larger than zero (see Table I), but some frequency components contribute little. At 60 dB SPL, the highest frequency component is most important for all listeners, but four to six frequency components make substantial contributions to the decision for all listeners. At 75 dB SPL, the weights are quite similar for the four listeners. The two or three highest frequency components are most important and two to four lower frequency components appear to have almost no effect on the decision. Overall, the weights for the 7-tone complexes generally vary significantly across frequency, and thus from the ideal pattern of weights. As shown in Table I, the only exceptions are L1 at 30 dB SPL and L2 at 60 dB SPL.

Figure 4 shows the weights for the 15-tone complexes at 60 dB SPL plotted in the same manner as Fig. 2. As shown in Table I, no significant differences were found between the first and second set of 500 trials, but the overall weights differed significantly from the ideal, uniform weights for all listeners. Only between three and eight components for each listener show weights that are significantly larger than zero. The highest frequency component had the greatest weight for three of the four listeners. Listeners L1 and L4 also showed a fairly high weight for the second-highest frequency component. In contrast, listener L3 showed the highest weight for the lowest frequency component, but this listener also showed a relatively large weight for the highest frequency component. Although the weights varied considerably across frequency, all listeners showed substantial weights on a majority of the frequency components.

Finally, Fig. 5 shows the weights for the 24-tone complexes, which encompass almost the entire range of audible frequencies and allow little influence of spread of excitation. Only between two and seven components for each listener show weights that are significantly larger than zero. The weights differed significantly between the first and second

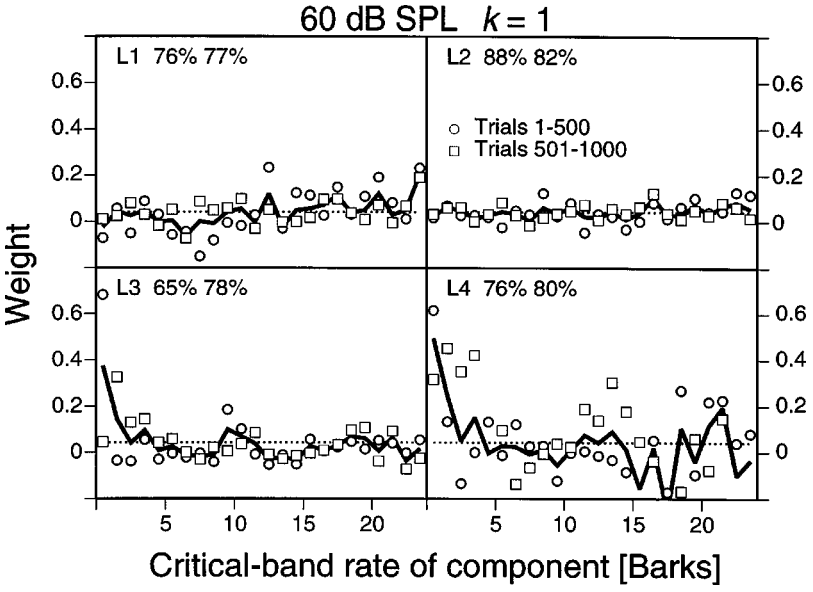

FIG. 5. Weights for 24-tone complexes with $k=1$ are plotted in the same manner as Fig. 2.

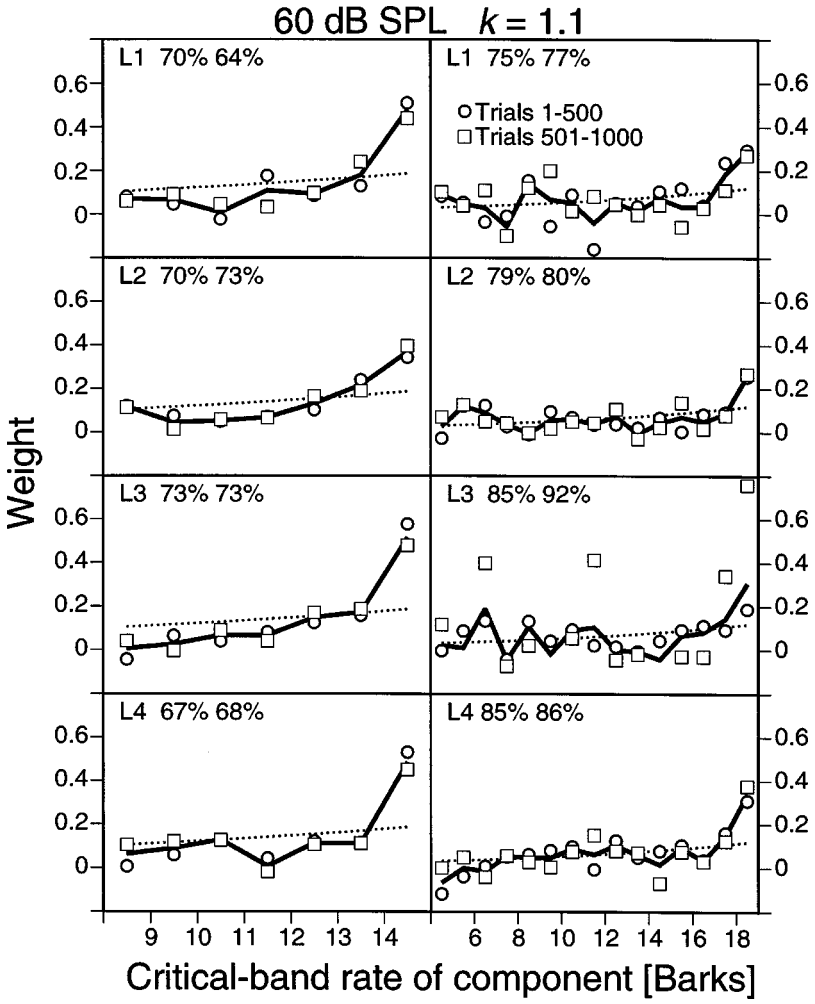

FIG. 6. Weights for 7- (left column) and 15-tone complexes (right column) at 60 dB SPL with $k=1.1$ are plotted in the same manner as Fig. 2.

set of trials for listeners L3 and L4. Disregarding the large variation in weights between the two sets of trials, their decisions were most influenced by the level perturbations of the lowest frequency components. Not surprisingly, the weights were significantly different from uniform weights for both L3 and L4. For listener L1, the highest frequency component was most important, but weights for this listener did not differ significantly from uniform weights. Listener L2 showed close-to-ideal weights that did not vary significantly across frequency. As expected, the observed-to-ideal weight ratios vary dramatically across listeners: -1.5 to 5.0 (L1), 0.1 to 2.5 (L2), -0.9 to 9.0 (L3), and -6.3 to 11.8 (L4).

In summary, the weights for tone complexes with equal ΔL's on all frequency components indicate that listeners are able to combine information from a number of simultaneous frequency components. Although there are some instances for which the observed weights do not differ significantly from the ideal, uniform weights, this is not the usual case. Generally, the weights are significantly different from uniform and the deviations from ideal (as indicated by the observed-to-ideal-weight ratios) tend to increase as the number of components increases. For 7- and 15-tone complexes, much of the deviation from the ideal, uniform weights occurs at the highest frequency components. For 24-tone complexes, the most obvious deviations from uniform weights appear to result from high weights on the lowest frequency components.

b. Nonuniform level increments (k=1.1). Figure 6 shows the weights obtained with $k=1.1$ plotted in the same manner as Fig. 2. In this condition, the level increment increased progressively with the component frequency. Thus, one might expect the high-frequency components to make the largest contributions to the listeners' decisions. The dotted lines indicate the ideal weights that would result if the listener's decision were optimal and unaffected by spread of excitation and noise in the auditory system. They were calculated using the fact that d' is proportional to ΔL (Buus and Florentine, 1991; Buus *et al.*, 1995). Accordingly, the ideal weight for a given frequency component is proportional to its $\Delta L(z)$; for example, the ideal weight on the highest frequency component exceeds that on the lowest frequency component by a factor of 1.77 for the 7-component complexes and by a factor of 3.8 for the 15-component complexes.

For the 7-tone complexes (left panels), the weights obtained when k was 1.1 did not differ significantly between the first and second set of trials for any listener. Each listener has between four and six components with weights that are significantly larger than zero. The weights differed significantly from the ideal weights for all listeners and were gen-

TABLE II. Test conditions, outcome of chi-square tests, and confidence limits for experiment II shown in the same manner as in Table I. The additional H_0 hypothesis pertains to weights being equal with and without masking.

H_0	Figure	Component level (dB SPL)	N	k	ΔL_0 (dB)	Comparison	L1	L2	L3	L4	CL	SD	Remarks
First and	7	60	7	1	2		22.8[c]	3.0	10.1	8.9	0.122	0.034	
second	7	60	15	1	2		12.7	5.9	16.0	7.8	0.099	0.012	
set of	8	60	7	1.1	1.5		2.1	12.2		9.7	0.126	0.043	
trials are	8	60	15	1.1	1.3		11.3	11.5		12.4	0.124	0.041	$\Delta L_0 = 0.75$ dB for L4
equal													
Weights	7	60	7	1	2		28.6[c]	21.0[b]	37.9[c]	63.7[c]	0.122	0.034	
are	7	60	15	1	2		18.6	15.7	57.0[c]	28.0[a]	0.099	0.012	
optimal	8	60	7	1.1	1.5		7.6	30.6[c]		51.0[c]	0.126	0.043	
	8	60	15	1.1	1.3		7.0	13.3		43.3[c]	0.124	0.041	$\Delta L_0 = 0.75$ dB for L4
$k=1$ and	7 & 8	60	7	1.1		$k=1$	9.4	3.2		4.9			
$k=1.1$ are	7 & 8	60	15	1.1		$k=1$	17.3	5.3		25.9[a]			
equal													
Weights	3 & 7	60	7	1		unmasked	12.5	5.4	29.1[c]	20.0[b]			
are equal	4 & 7	60	15	1		unmasked	54.0[c]	8.0	16.9	30.3[b]			
with and	6 & 8	60	7	1.1		unmasked	8.9	2.7		19.1[b]			
without masking	6 & 8	60	15	1.1		unmasked	7.1	21.9		16.8			

erally similar to those obtained when k was 1 (Fig. 3, middle panels). Nevertheless, significant differences between the two conditions were found for listeners L3 and L4 (see Table I). These differences probably are caused by an increased weight for the highest frequency component when k is 1.1, as would be expected given the enlarged level increments on the higher frequency components. However, the second and third highest frequency components show little difference between $k=1.1$ and $k=1$, which is at odds with the optimal decision rule. Overall, the effect of progressively increasing the ΔL's is relatively small and the changes that do occur are not always in favor of the highest frequency components.

The right panels of Fig. 6 show the weights for the 15-tone complexes with $k=1.1$. The weights did not differ significantly between the first and second set of trials for any listener. Only between three and seven components for each listener show weights that are significantly larger than zero. The overall weights differed significantly from the ideal weights for all listeners, except L1. Again, the weights for $k=1.1$ generally are similar to those for $k=1$ (see Fig. 4). In fact, the weights differed significantly between $k=1.1$ and $k=1$ only for L3 (see Table I). Although listener L3 shows some increase of the weight on the highest frequency component when $k=1.1$, the most obvious change is a marked decrease of the weight on the lowest frequency component.

In summary, progressive increases to the level increment across frequency components had only a small, unsystematic effect on the weights. When a difference between $k=1$ and $k=1.1$ was observed, it occurred primarily for the highest frequency component and was not apparent for other frequency components that also had enlarged increments. The similarity of the weights obtained with $k=1.1$ and with $k=1$ indicates that listeners may have limited freedom to vary the weights as required to follow an optimal decision rule.

III. EXPERIMENT II: EFFECT OF SPREAD OF EXCITATION ON WEIGHTS

The results of experiment I indicate that the highest and, sometimes, the lowest frequency components tend to weight heavily in the listeners' decisions. Experiment II aimed to determine the extent to which spread of excitation affects the weights by masking it with flanking noises. To evaluate whether the effect of the maskers, if any, resulted from the listeners using masker excitation as input to the decision, the weight for the maskers was also determined.

A. Method

The characteristics of the 7- and 15-tone complexes tested in experiment II are shown in Table II. Level increments required to yield about 80% correct responses were estimated on the basis of the ΔL_{DL}'s measured in experiment I and on the basis of ΔL_{DL}'s reported in the literature. Flanking noise bands were used to mask upward and downward spread of excitation into auditory channels not tuned to the frequency components of the tone complexes (cf. Florentine and Buus, 1995; Buus and Florentine, 1995). The noise bands were 3 Barks wide. For the noise band below the complex, the high cutoff frequency was 0.5 Bark below the lowest frequency component in the complex. For the noise band above the complex, the low cutoff frequency was 0.5 Bark above the highest frequency component in the complex. The levels of the noise bands, as measured in the critical band adjacent to the frequency components of the complex, were -5 dB relative to the (average) frequency component level. To determine the contribution, if any, that the maskers make to the listeners' discrimination decisions, the overall masker level was perturbed on each presentation. The perturbation was normally distributed with 0-dB mean and a standard deviation, σ_{M}, of 5 dB, but was limited not to exceed ± 15 dB. Apart from allowing estimation of the masker's

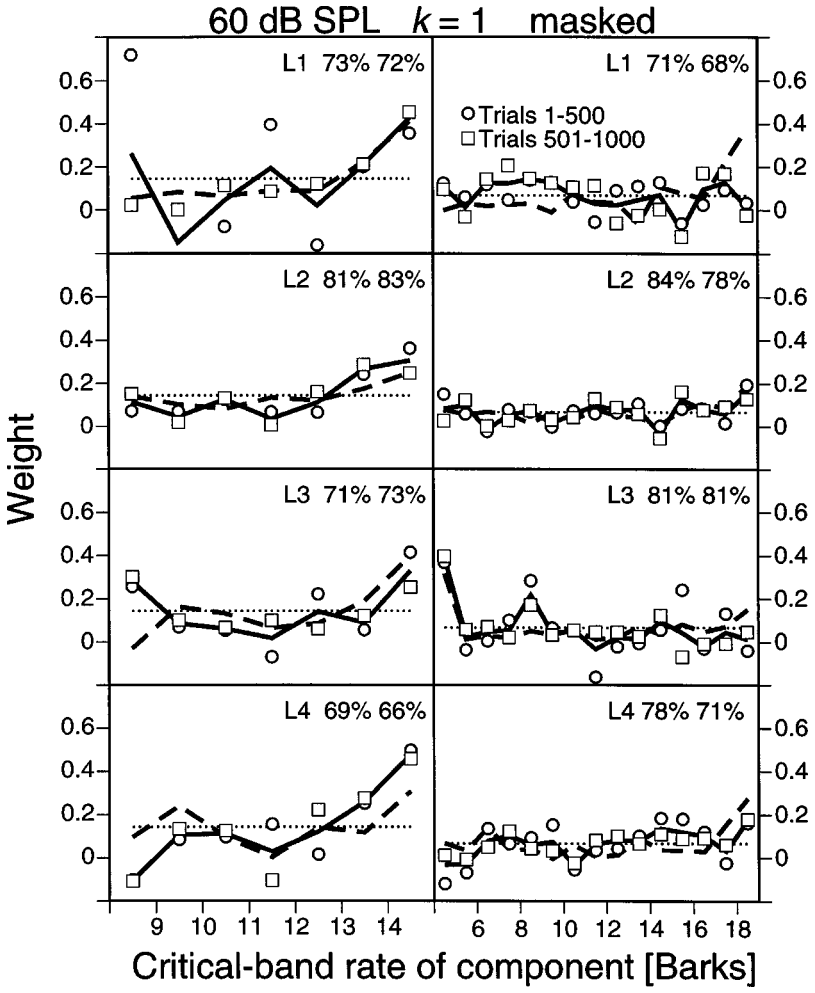

FIG. 7. Weights for 60 dB SPL 7- (left column) and 15-tone complexes (right column) with $k=1$ in the presence of flanking maskers. The figure is plotted in the same manner as Fig. 2, except that the thick dashed lines show the weights obtained without the masker, replotted from Figs. 3 and 4.

contribution to the listeners' decision, the masker-level perturbation also discouraged listeners from using profile analysis cues (Florentine and Buus, 1995). As in Florentine and Buus (1995), the masker's onset was 200 ms before the onset of the tone complex, and its offset was 50 ms after the offset of the complex. Accordingly, the total masker duration was 750 ms measured between the half-amplitude points of its 20-ms raised-cosine rise and fall.

B. Results

1. Perceptual weights

The panels in the left column of Fig. 7 show the weights obtained for the 7-tone complexes with $k=1$ in the presence of the flanking maskers. They are plotted in the same manner as Fig. 2. For comparison, the weights obtained without the flanking maskers are shown by the dashed lines, which are replotted from Fig. 3. As shown in Table II, the weights for the first and second set of trials did not differ significantly, except for listener L1. The weights for this listener's first set may reflect a distraction caused by the noise maskers; the weights for the second set are much more orderly. Between three and five components have weights that are significantly larger than zero for each listener. Table II also shows that the weights were significantly different from the ideal, uniform weights for all four listeners. The effects of the masker can be gauged by comparing the weights obtained with (solid lines) and without the masker (dashed lines). The weights obtained for listener L1 in the second 500 trials are remarkably similar to those obtained without the masker. The weights obtained with and without the masker also are strikingly similar for listener L2 and, to a lesser extent, for listeners L3 and L4. In fact, the effect of the masker is significant for listeners L3 and L4, but not for listeners L1 and L2 (see Table II). Overall it appears that masking the spread of excitation had relatively little effect on the weights and did not eliminate the high weights on the highest frequency component.

Point bi-serial correlations were also calculated for the masker-level perturbation difference between the second and first interval and the interval chosen by the listener. The calculation was identical to that for the frequency-component correlations. The point bi-serial correlations were 0.0064 (L1), −0.0716 (L2), 0.0189 (L3), and 0.0394 (L4). The critical value at the $p<0.05$ level is 0.0621. Thus, it appears that listener L2 had a tendency to choose the interval for which the level of the masker was lowest. The other listeners did not seem to base their decisions on the trial-by-trial masker-level differences between intervals.

The weights obtained for the masked 15-tone complexes with $k=1$ in the presence of the flanking maskers are shown by the symbols and solid lines in the right panels of Fig. 7. For comparison, the weights obtained without the masker are shown by the dashed lines, which are replotted from Fig. 4.

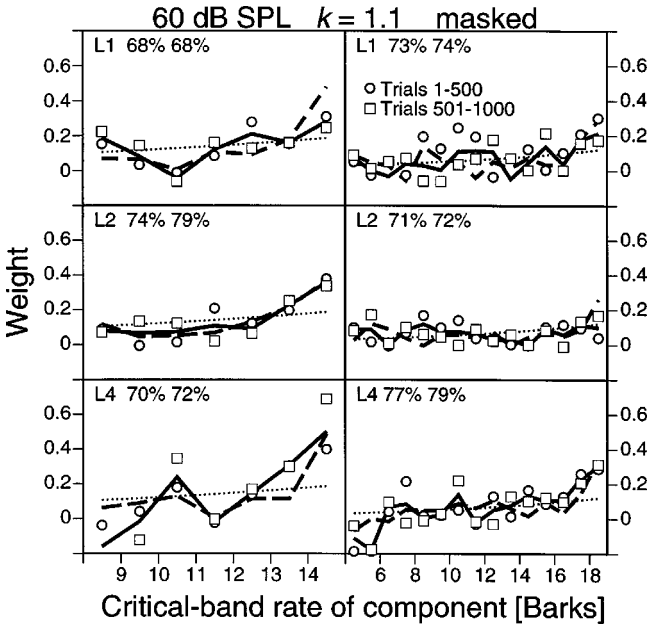

FIG. 8. Weights for 60 dB SPL 7- (left column) and 15-tone complexes (right column) with $k=1.1$ in the presence of flanking maskers. The figure is plotted in the same manner as Fig. 7. The thick dashed lines are replotted from Fig. 6.

Again, the weights obtained for the first and second set of trials did not differ significantly (see Table II). Each listener has between three and five components with weights that are significantly larger than zero. As shown in Table II, the weights did not differ significantly from the ideal uniform weights for listeners L1 and L2, whereas the weights varied significantly across frequency for listeners L3 and L4. A comparison of the weights obtained with and without masking reveals that the flanking noise tended to reduce the weight for the highest frequency component of the 15-tone complexes. The effect of the masker on the weights is significant for listeners L1 and L4 and is most pronounced for listener L1. In the presence of the masker, this listener shows a weight close to zero for the highest frequency component and the weights are highest for frequency components below the center frequency, especially for the second set of trials. For listener L4, the effects of the masker were generally small—although they were significant. For listener L3, the masker did not change the weights significantly, but it appears to reduce the weight on the highest frequency component to be close to zero and to increase the weight on the frequency component at 8.5 Barks (i.e., 1000 Hz) considerably. For listener L2, the effect of the masker was not significant and none is apparent. Altogether the masker changed the high weights on the extreme frequency components only for listener L1. The highest weight remained on the highest frequency component for listeners L2 and L4 and on the lowest frequency component for listener L3. The point biserial correlations between the listener's responses and the masker-level perturbations were 0.0282 (L1), 0.0049 (L2), 0.0119 (L3), and 0.0035 (L4). These small correlations do not differ significantly from zero, which indicates that the masker-level perturbations did not affect the decision for any of the listeners.

Finally, Fig. 8 shows the weights obtained with $k=1.1$ in the presence of the flanking masker. Results are shown only for listeners L1, L2, and L4, because listener L3 was no longer available. For the 7-tone complexes (left panels), the weights did not differ significantly between the first and second 500 trials for any listener. Four or five components have weights that are significantly larger than zero for each listener. The overall weights differed significantly from the ideal weights for listeners L2 and L4, but not for listener L1. On the other hand, no listener showed a significant difference between $k=1$ and $k=1.1$ with the flanking masker. All three listeners showed relatively high weights on the two or three highest frequency components and the highest weight was on the highest frequency component. The dashed lines show the weights obtained without the masker, replotted from Fig. 6. The effects of the masker are modest and are significant only for listener L4 (see Table II) for whom they appear quite unsystematic. Certainly, the masker did not reduce the weight on the highest frequency component for listener L4.

For the 15-tone complexes (right panels), there also was no significant difference between the weights for the first and second set of trials for any listener. Only between two and four components have weights that are significantly larger than zero for each listener. The overall weights obtained for listeners L1 and L2 when k was 1.1 did not differ significantly from the ideal weights, nor did they differ significantly from those obtained when k was 1. For listener L4, on the other hand, the weights obtained with $k=1.1$ differed significantly from the ideal weights and from those obtained with $k=1$. In the presence of the flanking masker, listener L4's weights were more or less uniform when $k=1$ (see Fig. 7), but were high for the two highest frequency components when $k=1.1$. A comparison between the dashed and solid lines shows that the masker had no obvious effect for any of the listeners. This is confirmed by the nonsignificant chi-square values shown in the last line of Table II.

Altogether, the effects of the masker are surprisingly small whether $k=1$ or $k=1.1$. Although they were significant in some instances, the effects of the masker usually were not systematic. Certainly, the masker generally did not cause any substantial change to the weights on the highest and lowest frequency components. This finding appears inconsistent with the high weight on these frequency components being due to spread of excitation into multiple auditory channels. It also is noteworthy that the differences between $k=1$ and $k=1.1$ generally were small.

IV. GENERAL DISCUSSION

Four issues are central to a discussion of the experimental weights presented here. First, the definition of theoretically optimal weights depends on whether optimality is considered only in terms of the *acoustic information* physically present in the stimuli, or in terms of the *auditory processing* of this information—in particular, the addition of variance by the auditory system and spread of excitation. Second, the listeners' decision on each trial may be based on *weighting* the information in each auditory channel, or on *selecting* certain channels while ignoring others (Buus *et al.*, 1986). Third, the weight-analysis model was based on the assump-

tion of independent processing of the level information of the individual Bark-spaced frequency components, which were assumed to fall within different auditory channels. To test this assumption, a conditional, trial-by-trial correlational method will be discussed and evaluated for a subset of the data. Finally, listening strategies other than using the information from particular frequency components and/or auditory channels consistently, and other than comparing the two observation intervals will be discussed.

A. Optimal weights

In terms of *acoustic information*, theoretically optimal weights were proportional to ΔL because the standard deviation in level perturbation was constant across stimulus frequency components. Accordingly, optimal weights were considered to be uniform across frequency components for $k=1$, and to increase progressively with frequency for $k=1.1$. Weights close to optimal were observed occasionally (e.g., for listeners L1 and L2 with the 24-tone complexes and $k=1$; see Fig. 5). However, even if these weights did not differ significantly from optimal, they appear to be essentially zero for a number of frequency components, which is not in accord with optimal weighting. Moreover, even the nonzero weights obtained in the present study generally differed from the optimal weights defined by the acoustic information. In many cases, the two or three highest frequency components contributed substantially more to the decision than the lower frequency components. Thus, it is quite clear that the listeners did not use optimal weights as defined by the *acoustical* properties of the stimuli.

In terms of *auditory processing* of the acoustical information, and spread of excitation in particular, optimal weights were expected to be elevated for the lowest and highest frequency components of the tone complexes. This results because spread of excitation causes a greater number of auditory channels to encode the frequency-component level for the lowest and highest frequency components than for frequency components in the middle of the complexes. For the lowest and highest frequency components, this effectively reduces internal noise. The effect is expected to increase with increasing level. The weights obtained in this study agree only partially with such an excitation-pattern argument. Consistent with this argument, the highest frequency component generally shows the highest weight. For example, the weights for the 7-tone complexes with $k=1$ show increased weights for the highest two frequency components as level increases from 30 to 75 dB SPL (see Fig. 3). Somewhat similar trends are apparent for the 3-tone complexes (see Fig. 2). Thus, for the 3- and 7-tone complexes, the weights may be close to optimal when optimality is defined in terms of auditory processing.

On the other hand, the weights obtained for most listeners and stimuli fail to show an increase for the lowest frequency component, which is inconsistent with the excitation-pattern argument. Furthermore, the weights for several frequency components of the 15- and 24-tone complexes are essentially zero although they ought to contribute significant level-discrimination information in at least one auditory channel. Finally, the strongest argument against the weights being optimal in terms of spread of excitation comes from the general lack of an effect of the flanking noise bands in experiment II. These maskers ought to mask information contributed by spread of excitation, and consequently, weights ought to be more or less uniform across frequency components. Except for the 15-tone complexes with $k=1$, the weights were virtually identical for the masked and unmasked conditions.

It should be noted, however, that the precise ratios of optimal weights based on auditory processing are not straightforward to predict. At the level of the auditory nerve, for instance, the coding of the individual frequency components is the result of a number of nonlinear processes. Spread of excitation is nonlinear and causes the excitation level to increase more in critical-band channels tuned to frequencies above those contained in the stimulus than in critical-band channels tuned at and below the range of frequencies encompassed by the stimulus. Further complications arise because the variance in excitation due to the external noise—i.e., the random level perturbation of a single frequency component—will be correlated across on- and off-frequency auditory channels. Even though the nonlinear increase of excitation should reduce the correlation, it generally will be high. On the other hand, internal noise sources such as physiological noise are usually considered independent across auditory channels. Therefore, the importance of individual frequency components and the corresponding optimal weights depends on the ratio of the external and internal noise. Moreover, the precise way in which excitation by multiple frequency components adds within individual auditory channels will affect the shape of the optimal weight patterns. For example, if the total excitation is determined by the frequency-component excitation having the greatest power (''winner takes all''), it may be nearly impossible to determine the amount of information in off-frequency channels for individual frequency components. Despite these uncertainties about the coding of level and addition of excitation, however, it seems reasonable to assume that the edge frequency components, in particular the highest frequency component, have the highest probability of dominating upward spread of excitation. These frequency components therefore are expected to provide the largest amount of information for level discrimination at moderate and high levels.

The current findings of clearly unequal frequency-component weights that are more or less invariant across increment and masking conditions nevertheless are difficult to explain. Doherty and Lutfi (1996) found bowl-shaped weight patterns for most of their normal-hearing listeners, whereby the greatest weight in most cases was found for the lowest frequency component. One explanation for the difference between their findings and the present results derives from the fact that the lowest component frequency in Doherty and Lutfi's (1996) stimuli was 250 Hz. This frequency is lower than the lowest component frequency of the complexes used in the present study, except for the 24-tone complexes. Because Doherty and Lutfi's (1996) average frequency component level of 65 dB SPL was well within the compressive range of the basilar-membrane I/O function, the response to the level increment would be strongly compres-

sive for most of the frequency components. However, compression is reduced at low frequencies (Cooper and Yates, 1994). Therefore, the increase in excitation produced by some fixed ΔL would be larger at low than at middle and high frequencies, which could increase the importance of the 250-Hz frequency component's contribution to the listeners' decision. In the present study, the 24-tone complexes indeed yielded the highest weights on the lowest frequency components at 0.5 and 1.5 Barks (50 and 150 Hz) for listeners L3 and L4. Willihnganz *et al.* (1997), however, used 3-tone complexes at 250, 1000, and 4000 Hz with an average frequency-component level of 62 dB SPL. Inconsistent with the compression argument, the weights obtained for three out of six adult, normal-hearing listeners were similar to those for the present 3-tone complexes. The weights obtained for the remaining listeners varied widely and were inconsistent across sets of trials.

Although reduced compression at low frequencies might explain the tendency for weights to increase at low frequencies, it is unlikely to account for the increased weights observed for the highest frequency components in the present study as well as in Doherty and Lutfi's (1996) and Willihnganz *et al.*'s (1997) studies. To our knowledge no evidence exists to support reduced compression for moderately high frequencies. In addition, the increased weight on the upper frequency components is apparent for the 3-tone complexes whose highest frequency component was 1.85 kHz, but also for the 15-tone complexes whose highest frequency component was 4 kHz. Thus, it is difficult to explain the high weights on the highest frequency components in terms of frequency-dependent compression.

A more likely explanation for the high weights obtained for the upper frequency components is that the excitation produced by individual frequency components is affected when simultaneously presenting three or more frequency components due to suppression on the basilar membrane. In the case of two-tone suppression for instance, the auditory-nerve activity evoked by a probe tone at the characteristic frequency of a fiber is more readily suppressed by a tone above the probe than by a tone below it (Javel, 1981). This asymmetry in suppression might explain why the highest frequency component generally showed the greatest weight for the tone complexes used in the present study.

Finally, it is quite clear that the weights deviate from optimal, but it appears that most components made some contribution to the listeners' decisions. The finding that the weights typically were significantly greater than zero for only a handful of components does not necessarily mean that only a small number of components contribute to the listeners' decision. It may simply reflect that 1000 trials were too few to obtain a significant correlation coefficient when the weight was small. For example, one may estimate the number of truly positive weights by subtracting the number of negative correlation coefficients from the number of positive correlation coefficients, because equal numbers of positive and negative correlation coefficients ought to result if the true value were zero. Estimated in this manner, we find that the average number of components that contribute to the listeners' decisions is 3.0 for the three-tone complexes, 6.1 for the seven-tone complexes, 11.0 for the 15-tone complexes, and 13.5 for the 24-tone complexes. These findings clearly indicate that the decision variable in level discrimination is derived by combining excitation-level information across a number of critical bands. This result is inconsistent with the single-band decision rule used in Zwicker's (1956; see also Zwicker and Feldtkeller, 1967) original excitation-pattern model, which derived the decision from the channel showing the largest increase in excitation level when the stimulus level is increased by ΔL. One might argue that significant weights on several channels could be obtained if the listeners' decision were based on the excitation in a single, but different auditory channel on every trial. However, this explanation is not tenable. Given the ratios between ΔL (see Table I) and the 2-dB standard deviation of the perturbation, a single-band decision rule would yield d''s much lower than those obtained.

B. Weighting or selection

The weights obtained by Doherty and Lutfi (1996) and Willihnganz *et al.* (1997) provided information about the importance of individual frequency components for level discrimination, but did not distinguish if listeners are able to apply arbitrary weights to each channel or whether they are limited to merely use a more or less optimal selection of unweighted channels. *Weighting* implies that listeners are able to attend to all auditory channels. In addition, they are able to grade their attention to individual channels to optimize their decision. *Selection* implies that auditory channels are either turned on or off as sources of information for the listeners' decision. Thus, the importance of individual channels would not be determined by listener-controlled weighting of information, but rather is determined by stimulus transformations in the auditory system, such as frequency-dependent compression, and on external and internal noise.

The most revealing clue to deciding between optimal—or, perhaps, somewhat suboptimal—selection and optimal weighting in the present study is that the weights for $k=1$ and $k=1.1$ hardly differed. That is, progressively increasing the $\Delta L(z)$ with frequency did not change the listeners' weighting strategy appreciably. This finding indicates that listeners were not able to change the weight on a channel arbitrarily. Rather, it appears that they were limited to either including or excluding any given channel in forming the decision variable. The apparent inability of the listeners to set the weights to any arbitrary value—together with the nonuniform weights obtained in most conditions—indicates that some frequency components in the complexes had the ability to change the decision variable more than others and that listeners rather consistently selected channels tuned to those frequency components.

C. Independence of level-information processing

The trial-by-trial correlational method is based on the assumption that the level information of the individual frequency components is processed independently. Given the 1-Bark spacing of the frequency components for our stimuli, we additionally assumed independent processing in separate

TABLE III. Test conditions and outcome for the test of independent processing of level information. The first column specifies whether the analysis was conditional on the lower or higher adjacent component. The second column shows the figure to which the analysis pertains. The third, fourth, and fifth columns specify the stimuli. The sixth column specifies the frequency component that the analysis pertains to. The remaining columns show Fisher *z*-transformed point bi-serial correlation coefficients for each of the listeners. Here, "r+" and "r−" refer to the selection of trials for the analysis. For "r+," only those trials were used for which the level perturbation of the target component was *greater* than the perturbation of the adjacent frequency component in both presentation intervals. Conversely, "r−" refers to the case where only those trials were used for which the level perturbation of the target component was *smaller*. Those cases for which the difference between "r+" and "r−" is statistically significant ($p<0.05$; see text) are underlined.

Conditional frequency component	Figure	Component level (dB SPL)	k	N	Component CB rate (Bark)	L1		L2		L3		L4	
						r+	r−	r+	r−	r+	r−	r+	r−
lower	2	80	1	3	12.5	0.462	0.418	0.344	0.522	0.443	0.512	0.333	0.370
	3	75	1	7	11.5	0.083	−0.054	0.009	0.111	−0.000	−0.080	0.198	0.179
	4	60	1	15	18.5	0.230	0.290	0.186	0.204	0.134	0.103	0.272	0.197
	5	60	1	24	2.5	0.030	−0.048	−0.029	0.028	0.180	0.085	0.300	0.010
	5	60	1	24	23.5	0.099	0.204	0.050	0.072	0.008	0.007	−0.045	0.096
higher	2	80	1	3	11.5	0.312	0.353	0.391	0.350	0.421	0.402	0.408	0.345
	3	75	1	7	13.5	0.398	0.210	0.268	0.291	0.438	0.265	0.319	0.167

auditory channels. The assumption of independent processing is critical to the validity of the estimated weights. Should this assumption be invalid, however, we would expect this to be due to spread of excitation or some other (nonlinear) process in the auditory coding of the level of simultaneous frequency components. Irrespective of the particular process, we would expect the level coding for a particular frequency component for the current stimuli to be most affected by the presence of its nearest-neighbor frequency components, rather than by the presence of more remote frequency components. Moreover, we would expect the coding to be least affected at the lowest frequency-component level of 30 dB SPL.

To test the assumption of independent processing, the following modification was made to the trial-by-trial correlational method. First, rather than calculating complete weight patterns, correlation coefficients for single frequency components were determined. Second, instead of using all trials administered for a certain condition, conditional correlation coefficients were calculated: those trials were selected for which the level perturbation of a particular frequency component under analysis was *greater* than the perturbation for a (single) nearest neighbor, both in the first and second presentation interval. The remaining trials were discarded. The nearest neighbor could be either lower or higher in frequency. Coefficients determined in this way will be labeled "r+." Conversely, "r−" refers to the selection of trials for which the level perturbation of the frequency component under analysis was *smaller* than the perturbation of its nearest neighbor, again for both presentation intervals. If the processing of level information depends on the level of (the nearest) neighboring frequency components, then we would expect the correlation coefficients to differ between the "r+" and "r−" conditions. For instance, the effect of spread of excitation may appear if the correlation coefficient is conditional on the nearest neighbor lower in frequency. Alternatively, the effect of suppression may appear conditional on the nearest neighbor higher in frequency. Using the "r+" and "r−" selection criteria, the (absolute) difference in level perturbation between the analysis- and neighboring frequency component was 2 dB on average.

Table III lists Fisher *z*-transformed correlation coefficients calculated for the "r+" and "r−" conditions. The data shown in Table III were thought to represent points of interest in the weights observed in this study. Only conditions with k equal to 1 were selected to avoid an effect of the progressive increase of $\Delta L(z)$ across frequency components. On average, each of these coefficients is based on 250 trials. Given this number of trials, differences between (Fisher *z*-transformed) correlation coefficients are statistically significant at the $p<0.05$ level whenever they exceed ± 0.176. As shown in Table III, the "r+" and "r−" correlation coefficients differ significantly from one another in only 3 out of 28 pairs, or about 11% of the pairs. This percentage is slightly larger than the 5% expected, but no systematic trends are apparent in these data. Altogether these results lend support to the assumption that level information of individual frequency components is processed independently, as would be expected from the attenuation of about 14 dB provided by an auditory filter for tones that are one critical band away from its center frequency.

D. Alternative decision strategies

Rather than comparing the information in particular auditory channels across intervals consistently, listeners might have chosen the interval that had the highest partial loudness for any single frequency component. This strategy employs several auditory channels because it requires a comparison of partial loudnesses across frequency components, and because spread of excitation makes a number of channels contribute to the loudness. This means that the edge frequency components, and the highest frequency component in particular, will be most important for such a strategy. The fact that the weights in the absence and presence of masking differed in a few cases only, however, does not support such an explanation of the results.

Finally, it is worthwhile considering whether the listeners compared the two intervals in each trial as postulated by most models of level discrimination. The present study calculated weights based on the difference in perturbation levels between the second and first interval (Lutfi, 1995; Doherty

and Lutfi, 1996). This presumes that the listeners compare the stimuli across intervals. However, it is conceivable that listeners ignored one of the intervals. For example, they might make their decision by comparing the level of the first interval to a template stored in long-term memory. Such behavior, if it exists, can be revealed by additional analyses of the raw trial data. For example, if the listeners attended only to the first stimulus in every trial, the correlation coefficients between the frequency component perturbations in the second interval and the listeners' responses should be randomly distributed around zero. To examine if listeners used any such single-interval strategies, weights for a subset of conditions were calculated using the level perturbations in only one of the two intervals in each trial. The weights obtained using perturbations in only the first interval, only the second interval, only the target interval, and only the pedestal interval differed only slightly from those obtained by using the perturbation-level difference between the two intervals in each trial. This finding indicates that listeners attended to both the first and the second intervals.

Altogether, the most parsimonious explanation of the present results appears to be that listeners compare excitation levels in many auditory channels across intervals. However, it appears that the listeners cannot weight the channels arbitrarily as needed to obtain a truly optimal decision rule, but are limited to selecting whether the decision variable should include or exclude any given channel. Such a selection scheme is similar to the optimal-selection decision rule proposed for detection by Buus *et al.* (1986), but limitations may exist on the total number of channels that can be included in the listeners' decision.

V. CONCLUSIONS

The present study used a correlational method (Richards and Zhu, 1994; Lutfi, 1995) to examine how listeners use excitation-level information in different auditory channels to discriminate between stimuli that differ in level. The results show the following.

(1) Listeners use information from many auditory channels for level discrimination, as postulated by the multiband excitation-pattern model for level discrimination (Florentine and Buus, 1981).
(2) The weights generally are not optimal. The highest frequency components usually make the largest contributions to the listeners' decisions.
(3) In most cases, the high weights on the upper frequency components are not changed by flanking maskers designed to eliminate information from spread of excitation. Thus, spread of excitation does not account for the high weights of the high-frequency components.
(4) Listeners were able to exclude bands excited by the flanking maskers from their decisions.
(5) No consistent change in weights was obtained by increasing the level increment progressively with frequency. This finding indicates that listeners may be unable to change the weights on different auditory channels arbitrarily as required by an optimum decision rule.
(6) No appreciable difference was found between correlation coefficients calculated only across trials in which the level perturbation of a neighboring frequency component was either higher (for "r+") or lower (for "r−") than that of the target component in both observation intervals. This finding lends support to the assumption that processing of level information is independent across frequency components.
(7) Altogether the results indicate that listeners are able to select which channels to include in the decision for level discrimination, but are limited to either including or excluding any particular channel. The channel selection may be slightly suboptimal when many channels contribute information, because a few frequency components appear to make little or no contribution to the level-discrimination decision for 15- and 24-tone complexes.

ACKNOWLEDGMENTS

The authors would like to thank listeners L1, L2, and L3 for their many hours spent in the listening booth. Katie Keating assisted in processing data. The authors also thank two anonymous reviewers for their many valuable comments on an earlier version of this manuscript. This study was supported by NIH/NIDCD Grant No. R01DC00187.

[1]Auditory filter characteristics (e.g., Glasberg and Moore, 1990) indicate that components one critical band away from the center frequency are attenuated at least 14 dB. Thus, the effects of level perturbations of any one component are largely confined to the critical band on which the component is centered.

[2]ΔL is already a logarithmic quantity. Calculating the averages as geometric means of ΔL_{DL}'s (i.e., averaging on a logarithmic scale) may be considered as taking the logarithm of the logarithm. However, d' is nearly proportional to ΔL (Buus and Florentine, 1991). Therefore, logarithmic plots of ΔL_{DL}'s show equal ratios of sensitivity as equal visual distances, and lead to conclusions consistent with those obtained from logarithmic plots of d' for a fixed ΔL. In addition, the standard deviation of ΔL_{DL}'s tends to be proportional to the ΔL_{DL}'s (e.g., Florentine *et al.*, 1987). Accordingly, level-discrimination performance is reasonably represented by ΔL_{DL} on a logarithmic scale. (For further discussion, see Buus and Florentine, 1991).

[3]Note that this normalization differs from that used by Doherty and Lutfi (1996), who normalized the sum of absolute values. The present study used the signed correlation coefficients, because truly negative weights ought not occur and using signed numbers for normalization ought to cancel out the small, randomly positive and negative correlation coefficients resulting from perceptual weights with a true value of zero.

Ahumada, A., and Lovell, J. (**1971**). "Stimulus features in signal detection," J. Acoust. Soc. Am. **49**, 1751–1756.
ANSI (**1989**). ANSI S3.6-1989, "Specifications for audiometers" (American National Standards Institute, New York).
Berg, B. G. (**1989**). "Analysis of weights in multiple observation tasks," J. Acoust. Soc. Am. **86**, 1743–1746.
Berg, B. G., and Green, D. M. (**1990**). "Spectral weights in profile listening," J. Acoust. Soc. Am. **88**, 758–766.
Buus, S., and Florentine, M. (**1991**). "Psychometric functions for level discrimination," J. Acoust. Soc. Am. **90**, 1371–1380.
Buus, S., and Florentine, M. (**1995**). "Sensitivity to excitation-level increments as a function of level and frequency," in *Advances in Hearing Research*, edited by G. A. Manley, G. M. Klump, C. Köppl, H. Fastl, and H. Oeckinghaus (World Scientific, Singapore), pp. 401–414.
Buus, S., Florentine, M., and Poulsen, T. (**1997**). "Temporal integration of loudness, loudness discrimination, and the form of the loudness function," J. Acoust. Soc. Am. **101**, 669–680.

Buus, S., Florentine, M., and Zwicker, T. (**1995**). ''Psychometric functions for level discrimination in cochlearly impaired and normal listeners with equivalent-threshold masking,'' J. Acoust. Soc. Am. **98**, 853–861.
Buus, S., Zhang, L., and Florentine, M. (**1996**). ''Stimulus-driven, time-varying weights for comodulation masking release,'' J. Acoust. Soc. Am. **99**, 2288–2297.
Buus, S., Schorer, E., Florentine, M., and Zwicker, E. (**1986**). ''Decision rules in detection of simple and complex tones,'' J. Acoust. Soc. Am. **80**, 1646–1657.
Cooper, N. P., and Yates, G. K. (**1994**). ''Nonlinear input-output functions derived from the responses of guinea-pig cochlear nerve fibers: Variations with characteristic frequency,'' Hear. Res. **78**, 221–234.
Doherty, K. A., and Lutfi, R. A. (**1996**). ''Spectral weights for overall level discrimination in listeners with sensorineural hearing loss,'' J. Acoust. Soc. Am. **99**, 1053–1058.
Doherty, K. A., and Lutfi, R. A. (**1999**). ''Level discrimination of single tones in a multitone complex by normal-hearing and hearing-impaired listeners,'' J. Acoust. Soc. Am. **105**, 1831–1840.
Florentine, M. (**1983**). ''Intensity discrimination as a function of level and frequency and its relation to high-frequency hearing,'' J. Acoust. Soc. Am. **74**, 1375–1379.
Florentine, M., and Buus, S. (**1981**). ''An excitation-pattern model for intensity discrimination,'' J. Acoust. Soc. Am. **70**, 1646–1654.
Florentine, M., and Buus, S. (**1995**). ''Masked level discrimination: Detering profile listening,'' J. Acoust. Soc. Am. **97**, 2460–2467.
Florentine, M., Buus, S., and Mason, C. R. (**1987**). ''Level discrimination as a function of level for tones from 0.25 to 16 kHz,'' J. Acoust. Soc. Am. **81**, 1528–1541.
Glasberg, B. R., and Moore, B. C. J. (**1990**). ''Derivation of auditory filter shapes from notched-noise data,'' Hear. Res. **47**, 103–138.
Javel, E. (**1981**). ''Suppression of auditory nerve responses: I. Temporal analysis, intensity effects and suppression contours,'' J. Acoust. Soc. Am. **69**, 1735–1745.
Jesteadt, W., Wier, C. C., and Green, D. M. (**1977**). ''Intensity discrimination as a function of frequency and sensation level,'' J. Acoust. Soc. Am. **61**, 169–177.
Levitt, H. (**1971**). ''Transformed up-down methods in psychoacoustics,'' J. Acoust. Soc. Am. **49**, 467–477.
Lutfi, R. D. (**1995**). ''Correlation coefficients and correlation ratios as estimates of observer weights in multiple-observation tasks,'' J. Acoust. Soc. Am. **97**, 1333–1334.
McGill, W. J., and Goldberg, J. P. (**1968**). ''A study of the near-miss involving Weber's law and pure-tone intensity discrimination,'' Percept. Psychophys. **4**, 105–109.
Moore, B. C. J., and Raab, D. H. (**1974**). ''Pure-tone intensity discrimination: some experiments relating to the ''near-miss'' to Weber's law,'' J. Acoust. Soc. Am. **55**, 1049–1054.
Moore, B. C. J., and Raab, D. H. (**1975**). ''Intensity discrimination for noise bursts in the presence of a continuous, bandstop background: effects of level, width of the bandstop, and duration,'' J. Acoust. Soc. Am. **57**, 400–405.
Plack, C. J., and Carlyon, R. P. (**1995**). ''Loudness perception and intensity coding,'' in *Handbook of Perception and Cognition, Volume 6. Hearing*, edited by B. C. J. Moore (Academic, Orlando, FL), pp. 123–160.
Richards, V. M., and Zhu, S. (**1994**). ''Relative estimates of combination weights, decision criteria, and internal noise based on correlation coefficients,'' J. Acoust. Soc. Am. **95**, 423–434.
Scharf, B. (**1970**). ''Critical bands,'' in *Foundations of Modern Auditory Theory, Vol. I*, edited by J. V. Tobias (Academic, New York), pp. 157–202.
Scharf, B., and Buus, S. (**1986**). ''Audition I: Stimuli, physiology, thresholds,'' in *Handbook of Perception and Human Performance, Vol. 1*, edited by K. Boff, L. Kaufman, and J. Thomas (Wiley, New York), pp. 14-1–14-61.
Viemeister, N. F. (**1972**). ''Intensity discrimination of pulsed sinusoids: the effects of filtered noise,'' J. Acoust. Soc. Am. **51**, 1265–1269.
Viemeister, N. F. (**1974**). ''Intensity discrimination of noise in the presence of band-reject noise,'' J. Acoust. Soc. Am. **56**, 1594–1600.
Willihnganz, M. S., Stellmack, M. A., Lutfi, R. A., and Wightman, F. L. (**1997**). ''Spectral weights in level discrimination by preschool children: Synthetic listening conditions,'' J. Acoust. Soc. Am. **101**, 2803–2810.
Zwicker, E. (**1956**). ''Die elementaren Grundlagen zur Bestimmung der Informationskapazität des Gehörs (The elementary foundations of determining the information capacity of the auditory system),'' Acustica **6**, 356–381.
Zwicker, E. (**1958**). ''Über psychologische und methodische Grundlagen der Lautheit,'' Acustica **8**, 237–258.
Zwicker, E. (**1961**). ''Subdivision of the audible frequency range into critical bands (Frequenzgruppen),'' J. Acoust. Soc. Am. **33**, 248.
Zwicker, E., and Feldtkeller, R. (**1967**). *Das Ohr als Nachrichtenempfänger* (Hirzel-Verlag, Stuttgart, Germany). Available in English translation by H. Müsch, S. Buus, and M. Florentine as *The Ear as a Communication Receiver* (Acoustical Society of America, Woodbury, NY, 1999).

Pitch discrimination of diotic and dichotic tone complexes: Harmonic resolvability or harmonic number?

Joshua G. Bernstein[a] and Andrew J. Oxenham[b]
Research Laboratory of Electronics, Massachusetts Institute of Technology, Cambridge, Massachusetts 02139 and Harvard—MIT Division of Health Sciences and Technology, Speech and Hearing Bioscience and Technology Program, Cambridge, Massachusetts 02139

(Received 31 October 2002; revised 16 March 2003; accepted 17 March 2003)

Three experiments investigated the relationship between harmonic number, harmonic resolvability, and the perception of harmonic complexes. Complexes with successive equal-amplitude sine- or random-phase harmonic components of a 100- or 200-Hz fundamental frequency (f_0) were presented dichotically, with even and odd components to opposite ears, or diotically, with all harmonics presented to both ears. Experiment 1 measured performance in discriminating a 3.5%–5% frequency difference between a component of a harmonic complex and a pure tone in isolation. Listeners achieved at least 75% correct for approximately the first 10 and 20 individual harmonics in the diotic and dichotic conditions, respectively, verifying that only processes before the binaural combination of information limit frequency selectivity. Experiment 2 measured fundamental frequency difference limens (f_0 DLs) as a function of the average lowest harmonic number. Similar results at both f_0's provide further evidence that harmonic number, not absolute frequency, underlies the order-of-magnitude increase observed in f_0 DLs when only harmonics above about the 10th are presented. Similar results under diotic and dichotic conditions indicate that the auditory system, in performing f_0 discrimination, is unable to utilize the additional peripherally resolved harmonics in the dichotic case. In experiment 3, dichotic complexes containing harmonics below the 12th, or only above the 15th, elicited pitches of the f_0 and twice the f_0, respectively. Together, experiments 2 and 3 suggest that harmonic number, regardless of peripheral resolvability, governs the transition between two different pitch percepts, one based on the frequencies of individual resolved harmonics and the other based on the periodicity of the temporal envelope. [DOI: 10.1121/1.1572146]

PACS numbers: 43.66.Hg, 43.66.Fe, 43.66.Ba [NFV]

I. INTRODUCTION

The mechanisms underlying pitch perception have been a matter of intense debate ever since Ohm (1843) disputed Seebeck's (1841) description of the phenomenon of the missing fundamental frequency (f_0). More recently, one aspect of this debate has been concerned with the mechanisms underlying the different contributions that low- and high-frequency harmonics make to the overall perceived pitch of a harmonic complex. Early work showed a dominant frequency region for pitch that was determined by both relative and absolute frequency relations. Ritsma (1967) demonstrated that the third through fifth harmonics dominated the perceived pitch for various f_0's, such that the dominant frequency region for pitch was relative to the complex's f_0. Investigating a wider range of f_0's, Plomp (1967) found that the harmonics that dominated the perceived pitch also depended on the f_0 of the complex, suggesting that absolute frequency also influenced the dominance region.

Most models of pitch perception can account qualitatively for the dominance of low harmonics in determining the overall pitch and for the greatly reduced pitch salience observed when only high harmonics are presented. However, the mechanisms by which they do so differ considerably. For instance, models that rely on the spatial separation of frequency components along the cochlear partition (e.g., Goldstein, 1973; Wightman, 1973; Terhardt, 1974, 1979) predict that pitch salience will deteriorate as the spacing between the individual components within a complex becomes so small that the individual peaks in the cochlear representation are no longer resolved. Because the components of a harmonic complex are equally spaced on a linear frequency scale, but the absolute bandwidths of auditory filters increase with increasing center frequency (CF), the density of harmonics per auditory filter increases with increasing harmonic number. As a result, low-order harmonics are resolved from one another, but higher-order harmonics begin to interact within single auditory filters and eventually become unresolved. In contrast, models based on the autocorrelation of auditory-nerve fiber activity, pooled across the total population of fibers (e.g., Meddis and Hewitt, 1991a,b; Cariani and Delgutte, 1996; Meddis and O'Mard, 1997), predict poorer resolution within the model (and hence reduced performance in f_0 discrimination) as the *absolute* frequency of components increases (Cariani and Delgutte, 1996; Carlyon, 1998), due primarily to the roll-off in the phase-locking properties of auditory-nerve fibers above about 1.5 kHz (Weiss and Rose, 1988). These two categories of models are often referred to as ''place'' and ''temporal'' models, respectively.

[a]Corresponding author electronic mail: jgbern@mit.edu
[b]Electronic mail: oxenham@mit.edu

However, it should be noted that the term ''place model'' does not necessarily imply that the frequencies of individual harmonics are encoded via a place mechanism. Instead it is possible that the frequency information at each place is encoded via a temporal mechanism (Srulovicz and Goldstein, 1983; Shamma and Klein, 2000). Nevertheless, it is important for these place models that the components are sufficiently well resolved for the frequency of each to be estimated individually.

The defining role of absolute frequency and phase locking, implied by temporal models based on the pooled autocorrelation function, has been called into question by various psychophysical experiments indicating that relative frequency relationships play an important role in the deterioration of pitch salience for high-order harmonics. Houtsma and Smurzynski (1990) estimated pitch salience, in terms of melodic interval recognition and fundamental frequency difference limens (f_0 DLs), for complex tones comprising 11 successive harmonics as a function of the lowest harmonic present. They found that for both measures, performance was much poorer when only harmonics above the 10th were presented than when at least some harmonics below the 10th were present. Although they carried out their experiment at only one f_0 (200 Hz), meaning that the respective influences of absolute and relative frequencies could not be distinguished, earlier research with two harmonics (Houtsma and Goldstein, 1972), and later research with many harmonics (Carlyon and Shackleton, 1994; Shackleton and Carlyon, 1994; Kaernbach and Bering, 2001), strongly support the idea that performance in such tasks is limited primarily by the lowest harmonic number present, and not by the lowest absolute frequency present.

While it has been generally assumed that pitch discrimination deteriorates when only high harmonics are present because the harmonics are peripherally unresolved (Houtsma and Smurzynski, 1990; Carlyon and Shackleton, 1994; Shackleton and Carlyon, 1994), certain results in the literature cast some doubt on this interpretation. Houtsma and Goldstein (1972) estimated the pitch strength of harmonic complexes consisting of two successive components by measuring performance in musical interval identification. Harmonics that are unresolved when both are presented to the same ear (monotic) become resolved when presented to opposite ears (dichotic). If strong pitch salience required the presence of resolved harmonics, we might expect stronger pitch salience when two normally unresolved harmonics (i.e., unresolved under monotic presentation) are presented dichotically. However, the decrease in performance with increasing harmonic number was the same under monotic and dichotic presentations, suggesting that the decrease in pitch salience with increasing harmonic number may not be due to the harmonics becoming unresolved *per se*. Arehart and Burns (1999) reported similar results using three musically trained hearing-impaired listeners.

This paper further investigates the transition in f_0 DLs found in the data of Houtsma and Smurzynski (1990), to determine whether the frequency at which it occurs is defined by harmonic resolvability, harmonic number regardless of resolvability, or absolute frequency. An f_0 DL paradigm (Houtsma and Smurzynski, 1990) was used to test whether presenting normally unresolved components to opposite ears improves performance. Under diotic presentation, all components were presented to both ears, such that the peripheral spacing between components was the f_0. Under dichotic presentation, even and odd components were presented to opposite ears, such that peripheral spacing between components was twice the $f_0(2\,f_0)$. The approach differs from those of two earlier studies addressing this issue (Houtsma and Goldstein, 1972; Arehart and Burns, 1999) in two principal ways. First, the f_0 discrimination task does not require the musical training that is necessary for a musical interval identification task. Second, 12-component complexes yield a much stronger pitch salience than the relatively weak pitch elicited by two-tone complexes, even with low-order harmonics.

Underlying this study was the important assumption that approximately twice as many harmonics should be resolved in the dichotic conditions, where the peripheral frequency spacing between components is twice that of the diotic conditions. The first experiment was designed to test the validity of this assumption. In addition, experiment 1 addressed the discrepancy in the literature between direct and indirect estimates of harmonic resolvability, as described below.

II. EXPERIMENT 1: RESOLVABILITY OF INDIVIDUAL HARMONICS

A. Rationale

The existing studies on pitch perception show very good consistency in terms of the locus of the transition region between good and poor f_0 discrimination (Cullen and Long, 1986; Houtsma and Smurzynski, 1990). However, as pointed out by Shackleton and Carlyon (1994), while these data sets show a transition that occurs between harmonic numbers 10 and 13, direct measures of individual component resolvability have shown that listeners are generally only able to hear out the first five to eight harmonics of a harmonic complex (Plomp, 1964; Plomp and Mimpen, 1968). Similarly, Shackleton and Carlyon (1994) concluded that the limits of the resolvability of individual components within an inharmonic tone complex, as measured by Moore and Ohgushi (1993), were also lower than those estimated indirectly using f_0 DLS for harmonic tone complexes.

One reason for this discrepancy might be the nature of the respective tasks. Musicians have been shown to have better performance than nonmusicians in ''hearing out'' harmonics (Soderquist, 1970; Fine and Moore, 1993), while their auditory filter bandwidths are not significantly different (Fine and Moore, 1993). The difference between direct and indirect estimates of peripheral resolvability may be attributable to attentional limitations, whereby, in hearing out individual partials, subjects may have difficulty overcoming their perceptual fusion of the complex into a single auditory object. The difference could also be due to other nonperipheral limitations. In contrast to the Plomp (1964) and Moore and Ohgushi (1993) studies, which required subjects to hear out an individual partial presented simultaneously with a complex, this study gated the target harmonic on and off repeatedly within the presentation interval. This strategy was de-

signed to help overcome any nonperipheral limitations and to encourage perceptual segregation, while not affecting peripheral resolvability.[1] If good f_0 discrimination depends on the presence of peripherally resolved harmonics, we expect that listeners should be able to hear out approximately ten harmonics—more than the five to eight measured by Plomp (1964).

B. Methods

In this and subsequent experiments, all subjects had some degree of musical training. The least musically trained subject had 4 years of instruction in middle school, while the most musically trained were two professional musicians with more than 18 years formal training. All subjects had normal hearing (15 dB HL or less *re* ANSI-1969 at octave frequencies between 250 Hz and 8 kHz). Four subjects (ages 18–26, two female) participated in this experiment.

All stimuli were presented in a background noise, uncorrelated between the two ears which we will call modified uniform masking noise (UMN_m). This noise is similar to uniform masking noise (UMN) (Schmidt and Zwicker, 1991), in that it is intended to yield pure-tone masked thresholds at a constant sound pressure level (SPL) across frequency, but the spectrum is somewhat different; UMN_m has a long-term spectrum level that is flat (15 dB/Hz SPL in our study) for frequencies below 600 Hz, and rolls off at 2 dB/oct above 600 Hz. The noise was low-pass filtered with a cutoff at 10 kHz. Thresholds for pure tones at 200, 500, 1500, and 4000 Hz in UMN_m in the left ear were estimated via a three-alternative forced-choice, two-down, one-up adaptive algorithm (Levitt, 1971). For each subject, pure tone thresholds in UMN_m fell within a 5-dB range at all four frequencies tested, such that harmonic components presented at equal SPL had nearly equal sensation level (SL). As an approximation, we defined 0 dB SL for each subject as the highest of the thresholds across the four frequencies tested, which ranged from 29.7 to 33 dB SPL across all subjects in this and subsequent experiments.

The stimuli were generated digitally and played out via a soundcard (LynxStudio LynxOne) with 24-bit resolution and a sampling frequency of 32 kHz. The stimuli were then passed through a programmable attenuator (TDT PA4) and headphone buffer (TDT HB6) before being presented to the subject via Sennheiser HD 580 headphones. Subjects were seated in a double-walled sound-attenuating chamber.

Each trial in the experiment consisted of two intervals, each with a 1-s duration, separated by 375 ms. The first interval contained three bursts of a 300-ms sinusoid (referred to as the comparison tone), including 20-ms Hanning window onset and offset ramps, separated by 50-ms silent gaps. The second interval consisted of a harmonic complex with the first 40 successive harmonics of the f_0 with duration 1000 ms, including 20-ms Hanning window onset and offset ramps. Components were presented in random phase to ensure that the frequency of the target component was detectable only if the component was spectrally resolved.[2] The target component was gated on and off in the same manner as in the first interval, while all the other components were on continuously throughout the interval. Each component was presented at a nominal 15 dB SL (adjusted for each subject), such that the stimuli in this experiment were similar in level to those used in experiment 2. The task was a two-alternative forced-choice task, where the listener was required to discriminate which of the comparison tone (interval 1) or target tone (interval 2) was higher in frequency. A schematic of the stimuli is shown in Fig. 1.

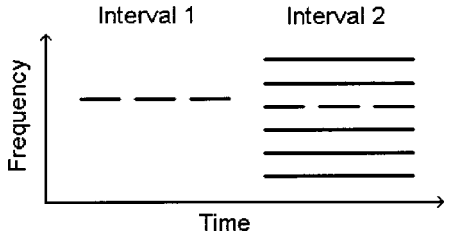

FIG. 1. Schematic of the stimuli used in experiment 1. Interval 2 contains a 40-component harmonic complex, with the target harmonic gated on and off to perceptually segregate it from the complex. Interval 1 contains a pure-tone probe, higher or lower in frequency than the target harmonic in interval 2, gated in the same way as the target harmonic.

Four conditions were presented, for all combinations of the harmonic complex in interval 2 presented diotically or dichotically, with a 100- or 200-Hz average f_0 ($\overline{f_0}$). Fifty trials for each of ten target harmonic numbers in each condition were presented (diotic: 5 through 14, inclusive; dichotic: 11, 12, 13, 14, 16, 18, 20, 22, 25, and 28), for a total of 500 trials per condition. The trials were presented in runs, each consisting of five trials for each of the ten harmonics for one condition, presented in random order. In the dichotic conditions, the comparison and target harmonics were always presented to the same ear throughout a run, and the distribution of the even and odd harmonics of the complex in interval 2 to the left and right ears was varied accordingly. For example, for a trial where the target 14th harmonic and comparison tone were presented to the right ear, the even harmonics in interval 2 were also presented to the right ear. In the dichotic conditions, five runs were presented with the target in the left ear, and five runs were presented with the target in the right ear.

The difference (Δf) between the frequency of the comparison tone (f_{comp}) and that of the target tone (f_{targ}) was set as a proportion of f_{targ}. This is different from Plomp's (1964) experiment, where he required listeners to identify which of two pure tones was in fact a component of the complex. One comparison tone was at the frequency of one of the components, and the other was halfway between the frequencies two successive components, such that it always fell at the same place relative to the target tone on a *linear* scale. In our experiment, the comparison tone was adjusted relative to the target tone on a *logarithmic* scale, ensuring that any decrease in performance with increasing harmonic number reflects a reduction in resolvability, and not the increase in linear pure tone DLs with increasing frequency (Moore, 1973).

In each trial, f_{comp} was either higher or lower than f_{targ}, each with probability 0.5, with $\Delta f = |f_{targ} - f_{comp}|$ chosen from a uniform distribution of 3.5 to 5.0% of the f_{targ}. The value of Δf was always at least 3.5% of the f_{targ}, which is well above the frequency discrimination threshold for tones in quiet (Moore, 1973). The f_0 of the complex was randomly chosen from a uniform distribution between $0.935\,\overline{f_0}$ and

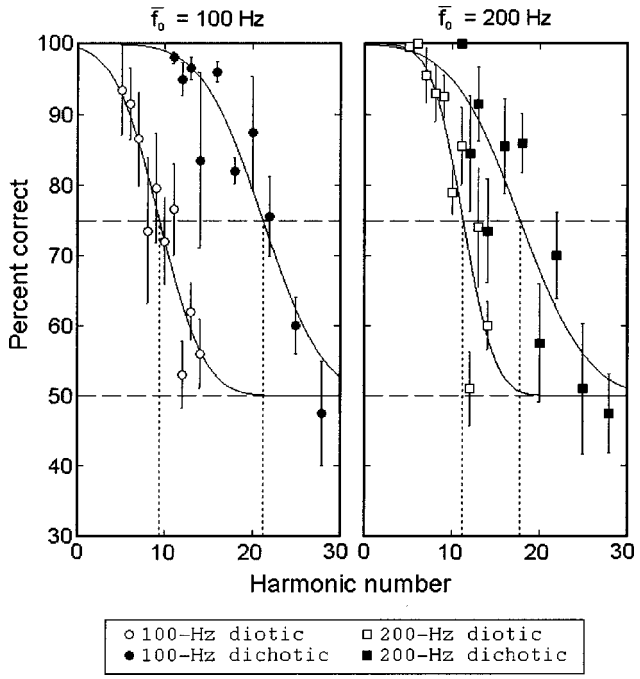

FIG. 2. Mean results of experiment 1, showing percent correct in identifying the probe tone as higher or lower than the target tone as a function of harmonic number. Error bars represent plus and minus one standard error across the individual scores for the four subjects. Open symbols indicate diotic conditions, with all harmonics presented to both ears; filled symbols indicate dichotic conditions, with odd and even harmonics presented to opposite ears. The left and right panels show results with f_0's of 100 and 200 Hz, respectively. Solid lines represent the best fits of the erfc function [Eq. (1), footnote 4] to the pooled data. The limit of harmonic resolvability, defined as the harmonic that yields 75% correct performance, is depicted by a vertical dotted line. The upper and lower horizontal dashed lines indicate 75% correct (limit of harmonic resolvability) and 50% correct (chance), respectively.

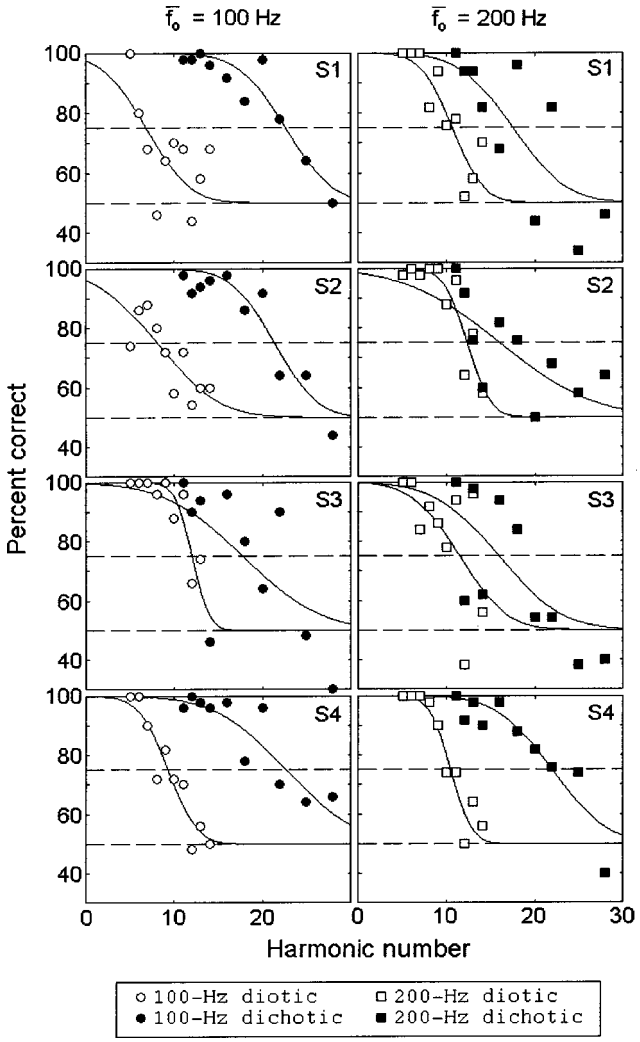

FIG. 3. Results from the individual subjects in experiment 1, showing percent correct in identifying the probe tone as higher or lower than the target tone as a function of harmonic number. Each data point represents performance over 50 stimulus trials. Each row represents results from one subject. The left column (circles) and right column (squares) show results with f_0's of 100 and 200 Hz, respectively. The solid curves respresent best fits of the erfc function [Eq. (1)] to the individual data. The upper and lower dashed lines in each plot represent 75% and 50% correct, respectively.

$1.065\,\bar{f}_0$. Randomizing Δf was intended to prevent the listener from correctly identifying the frequency relationship without actually hearing out the target tone by memorizing the frequency relationship between the comparison tone and the complex's f_0. Testing a large number of target harmonics (ten per condition) and randomizing f_0 further prevented this type of alternative cue.[3]

Each subject began with a training phase, where runs rotated through the four conditions, during which feedback was provided. Training continued until a subject was reliably obtaining nearly 100% correct for the lowest harmonic tested in each condition. The training period varied across subjects from 15 min to 2 h. During the data collection phase, feedback was not provided.

C. Results

Figure 2 shows the mean data. The error bars denote ± 1 standard error of the mean performance across all listeners. Although there was significant variability in performance across subjects, a systematic trend is clear in the data. Percent correct generally decreases with increasing harmonic number, with the 75% correct point corresponding roughly to the 10th harmonic in the diotic conditions, and to the 20th harmonic in the dichotic conditions. For each condition, the pooled data from all subjects were fit (solid lines in Fig. 2) to a complementary error function (erfc) bound to 50% and 100% correct at the extremes.[4] The nonlinear least squares Gauss–Newton method was used to fit the data to Eq. (1) with two free parameters (n_0 and w). The estimated n_0 was taken to be the estimated limit of harmonic resolvability, in accordance with the methods of Plomp (1964). Judgments of the goodness of fit were based on a 95% confidence interval ($\pm 2\sigma$) measure of uncertainty in the n_0 estimate. The values obtained for the estimated limits of resolvability and 95% confidence interval, $n_0 \pm 2\sigma$, for the pooled data were: 9.34 ± 1.03 (diotic 100 Hz), 21.18 ± 1.65 (dichotic 100 Hz), 11.20 ± 0.74 (diotic 200 Hz), and 17.73 ± 1.91 (dichotic 200 Hz).

Figure 3 shows the individual data. The left column shows data from the 100-Hz $\bar{f}_0$ and the right column shows data from the 200-Hz $\bar{f}_0$. There was considerable intersubject variability in performance, as well as certain nonmonotonic trends within individual subjects. One subject (S2) had

difficulty hearing out even the lowest harmonics in the 100-Hz diotic condition. Two subjects (S1 and S3) showed nonmonotonicities in the diotic conditions near the 12th harmonic. In the dichotic conditions, large nonmonotonicities were exhibited by one subject (S3) at the 100- and 200-Hz $\overline{f_0}$'s, and by two others (S1 and S2) at the 200-Hz $\overline{f_0}$. For these subjects, performance decreased below 75% in the vicinity of the 12th to 16th harmonics, and then increased before once again dropping below 75% for higher harmonics. The nonmonotonicities in the diotic and dichotic conditions in the vicinity of the 12th and 14th harmonics are also present in the mean data (Fig. 2).

Individual subject data in each condition were fit to the erfc function [Eq. (1)]. Fits ranged from good for subjects and conditions where the psychometric function exhibited few nonmonotonicities (e.g., subject S4, diotic 200 Hz, $2\sigma = 0.71$ harmonics), to extremely poor for subjects and conditions where the psychometric function exhibited many nonmonotonicities (e.g., subject S3, dichotic 100 Hz, $2\sigma = 6.67$ harmonics).

D. Discussion

Five aspects of the results merit attention. First, roughly twice as many harmonics can be heard out in the dichotic conditions as in the diotic conditions. This is the most important result of the experiment, as it verifies the central assumption for experiment 2, that only processes before the combination of binaural information limit harmonic resolvability.

Second, our estimates of the limits of harmonic resolvability in the diotic conditions are greater than those reported by Plomp (1964). Our results indicate that the first 9 to 11 harmonics of a complex for $\overline{f_0}$'s of 100 and 200 Hz are peripherally resolved. This estimate closely matches the indirect estimate of the limits of harmonic resolvability (Houtsma and Smurzynski, 1990; Shackleton and Carlyon, 1994), where the lowest harmonic present must be the 10th or below in order to yield small f_0 DLs. This indicates that enough harmonics are peripherally resolved to account for the limits of good f_0 discrimination, thereby resolving the apparent discrepancy between direct and indirect measures of resolvability (Shackleton and Carlyon, 1994). A caveat to this conclusion is that the ''enhancement'' effect (see footnote 1) may have helped to overcome some nonperipheral limitation to harmonic resolvability that occurs before the detection of pitch. Therefore, in the absence of ''enhancement,'' all of these peripherally resolved harmonics might not be available to the pitch detector. Also, this is an operational definition of resolvability, which depends on the 3.5%–5.0% Δf used in this experiment. A smaller Δf may have yielded a lower estimate of the number of resolved harmonics.

Third, there was some indication of more resolved harmonics for the 200-Hz than the 100-Hz f_0, consistent with results of Shera *et al.* (2002) indicating that the cochlear filter bandwidths relative to CF decrease with increasing absolute frequency at low signal levels. Nevertheless, this difference was small, indicating that harmonic number largely determines resolvability. The limited range of f_0's used in this study prevents a comparison with the effects of f_0 reported by Plomp (1964), where for f_0's greater than 200 Hz, the number of resolved harmonics decreased with increasing f_0.

Fourth, some subjects experienced difficulties with even low-frequency harmonics, or displayed nonmonotonic psychometric functions. For example, for subject S2 at the 200-Hz f_0 and subject S3 at both f_0's, the initial drop below 75% correct performance in the dichotic conditions occurred at a similar harmonic number as in the diotic conditions. This suggests that there may be some central limitation on resolution for these subjects and conditions that operates on both diotic and dichotic complexes. However, for all subjects, harmonics above the 14th are well resolved under dichotic presentation, and any central limitation of harmonic resolvability seems to appear only near the 14th harmonic.

Fifth, the estimate of n_0 in the dichotic 200-Hz condition had a large 95% confidence interval ($\pm 10.8\%$), consistent with the poor fit apparent in a visual inspection of the data. Given the high range of pure tone frequencies presented in this condition, this large uncertainty may reflect absolute frequency effects. However, even at the highest frequencies tested (5.6 kHz), the minimum Δf we used (3.5%) is still greater than the 0.5% obtained for similar frequency long-duration tones in quiet (Moore, 1973). Although the 60 dB SPL tones used in the Moore (1973) study are not comparable to the 15 dB SL tones used in this study, Hoekstra (1979) showed that a reduction from moderate (40 dB) to low (15 dB) SLs increased DLs for a 2-kHz pure tone by less than a factor of 2. This suggests that the variable results found at these very high frequencies cannot be ascribed solely to the coding limitations of individual components.

III. EXPERIMENT 2: FUNDAMENTAL FREQUENCY DIFFERENCE LIMENS

A. Rationale

In experiment 2 we measured f_0 DLs as a function of the lowest harmonic number present for diotic and dichotic harmonic complexes. If good discrimination ability were dependent on the presence of resolved harmonics *per se*, the auditory system should be able to utilize the information provided by the additional resolved harmonics available under dichotic presentation, such that the order of magnitude increase in f_0 DLs (Houtsma and Smurzynski, 1990) would occur at twice the harmonic number as compared to diotic presentation. Alternatively, if good discrimination ability were dependent only on the presence of low-numbered harmonics, regardless of resolvability, the additional resolved harmonics should provide no benefit, such that the increase in f_0 DLs would occur at the same lowest harmonic number in both dichotic and diotic conditions.

In order to determine if the increase in f_0 DLs is due to absolute or relative frequency effects, we performed the measurements at two different f_0's (100 and 200 Hz). Based on the results of Shackleton and Carlyon (1994), suggesting that the DL shift is due to relative frequency effects (i.e., the presence or absence of resolved harmonics), we expect that

the DL shift should occur at approximately the same harmonic number for both f_0's. Alternatively, if the DL shift were mainly due to absolute frequency effects as implied by many temporal pitch models, then the DL shift should occur at about the same absolute frequency, or twice the harmonic number for the 100-Hz f_0 as compared to the 200-Hz f_0 conditions. While we measured f_0 DLs with harmonics in random phase in order to allow a direct comparison with the harmonic resolvability data of experiment 1, we also performed the measurements with harmonics in sine phase to allow a more direct comparison with earlier data.

B. Methods

Stimuli were 500-ms (including 30-ms Hanning window rise and fall) harmonic complexes with 12 successive components. Each component was presented at 10 dB SL in UMN_m background noise (see experiment 1). This low level was used to prevent the detection of combination tones. Stimuli were presented diotically and dichotically with f_0's of 100 and 200 Hz, in sine phase and random phase, for a total of eight conditions. Discrimination thresholds were estimated for eight normal-hearing subjects. Four subjects (ages 18–24, two female), including the first author, participated in the sine-phase conditions. Two had also participated in experiment 1. Four new subjects (ages 18–24, one female) participated in the random-phase conditions. The setup for stimulus delivery was the same as in experiment 1.

Fundamental frequency DLs as a function of the complex's average lowest harmonic number ($\overline{N}$) were estimated via a three-alternative forced-choice, two-down, one-up adaptive algorithm tracking the 70.7% correct point (Levitt, 1971). The f_0 difference (Δf_0) was initially set to 10% of the f_0. The starting step size was 2% of the f_0, decreasing to 0.5% after the first two reversals, and then to 0.2% after the next two reversals. The f_0 DL was estimated as the average of the Δf_0's at the remaining six reversal points.

Two of the intervals contained harmonic complexes with a base $f_0(f_{0,\mathrm{base}})$, while one interval contained a complex with a higher $f_0(f_{0,\mathrm{base}}+\Delta f_0)$. The task was to identify the interval with the higher f_0. Subjects were informed that two of the intervals had the same pitch, and one had a higher pitch, and were asked to identify the interval with the higher pitch. In order to prevent subjects from basing their judgments on the frequency of the lowest harmonic, the lowest harmonic number (N) was roved from interval to interval, such that in the three intervals it was $\overline{N}-1$, $\overline{N}$, and $\overline{N}+1$, in random order. The highest harmonic number was also roved, such that 12 components were presented in each stimulus interval. For the dichotic conditions, odd and even components were presented randomly to the left or right ear on a trial-by-trial basis. Feedback was provided after each trial. Subjects were informed that there were different sound qualities that varied from interval to interval. They were told to ignore the timbre (''treble/bass quality'') of the sounds, as responses based on timbre would result in incorrect answers, and to respond based solely on the pitch. Fundamental frequency discrimination was tested for $\overline{N}=3$, 6, 9, 12, 15, 18 and 24 in all eight conditions.

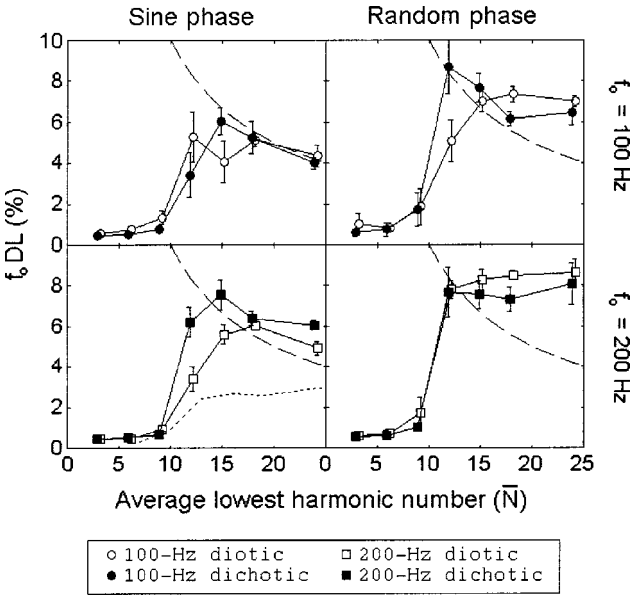

FIG. 4. Mean results from experiment 2. Each data point represents the mean f_0 DL (%) across four subjects; error bars denote plus and minus one standard error of the mean. The long-dashed curves show the limit of performance based only on the lower spectral edge of the complexes (see text for details). The short-dashed curve in the lower left panel shows data from Houtmsa and Smurzynski (1990) for a monotic complex with a 200-Hz f_0.

Each subject went through a training phase of at least 1 h, which continued until performance was no longer showing consistent improvement. During the measurement phase, four adaptive runs were made per subject, for each value of $\overline{N}$ in each condition, and the estimated f_0 DL for a subject was taken as the mean of these four estimates. If the standard deviation across the last six reversals points in any one run was greater than 0.8%, the data for that run was excluded and the run was repeated at the end of the experiment.

C. Results

Figure 4 shows the estimated f_0 DLs (expressed as a percentage of the f_0) as a function of $\overline{N}$. Each data point represents the arithmetic mean and the error bars represent $\pm$ the standard error across the mean f_0 DLs measured for four subjects. The central finding of this study is that the dramatic increase in f_0 DLs occurs at the same $\overline{N}$ under diotic and dichotic presentation. Furthermore, this increase occurs at the same $\overline{N}$ at both f_0's.

To investigate other trends in the data, an analysis of variance (ANOVA) with three within-subject factors [f_0, $\overline{N}$ and mode of presentation (diotic or dichotic)] and one between-subject factor (phase) was conducted. While the f_0 DL measurement used f_0 steps on a linear frequency scale in accordance with the methods of Houtsma and Smurzynski (1990), the statistical analysis was performed with logarithmically (log) transformed data, in an attempt to satisfy the uniform variance assumption. Only the following main effects and interactions were found to be significant ($p<0.05$). There was a main effect of $\overline{N}$ [$F(1,6)=179.5$, $p<0.0001$], two-way interactions between f_0 and $\overline{N}$ [$F(1,6)=5.60$, $p<0.0005$] and between f_0 and mode of presenta-

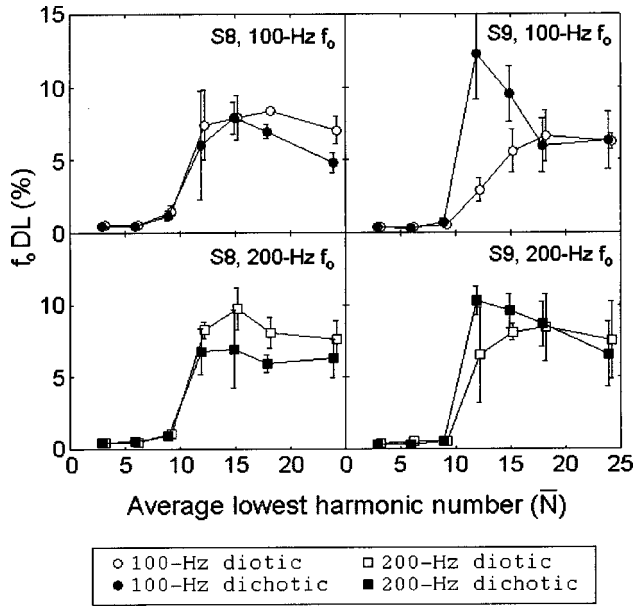

FIG. 5. Individual results from experiment 2 for two sample subjects. Error bars show plus and minus one standard deviation across four stimulus trials. Subject S9 (right column) shows larger f_0 DLs under dichotic presentation for $\overline{N}=12$ and 15. Subject S8 (left column) shows smaller f_0 DLs under dichotic presentation for $\overline{N}=18$ and 24.

tion [$F(1,6)=6.8$, $p<0.05$], a three-way interaction between mode of presentation, phase and f_0 [$F(1,6)=8.32$, $p<0.05$] and a four-way interaction between all factors [$F(6,36)=5.84$, $p<0.0005$].

The significant four-way interaction suggests caution in interpreting main effects and low-order interactions. Nevertheless, the ANOVA supports two trends in the data concerning $\overline{N}$ and f_0. First, the main effect of $\overline{N}$ clearly reflects the result that good performance in f_0 discrimination requires $\overline{N}\leqslant 9$. Second, the two-way interaction between f_0 and $\overline{N}$ does not reflect an absolute frequency effect on the frequency of the increase in f_0 DLs, since this transition occurs at the same $\overline{N}$ for both f_0's. Rather, this interaction probably reflects an absolute frequency effect for complexes with $\overline{N}>9$, where larger f_0 DLs are seen for the 200-Hz f_0 as compared to the 100-Hz f_0. Interpreting the effects of mode of presentation and phase requires a closer examination of the data.

The significant higher-order interactions probably reflect the result that dichotic f_0 DLs were somewhat higher or lower than diotic f_0 DLs depending on f_0, phase and $\overline{N}$. Two trends in the difference between f_0 DLs measured under dichotic versus diotic presentation were apparent in the data. The first trend was that dichotic f_0 DLs were larger than diotic f_0 DLs presentation at $\overline{N}=12$ or $\overline{N}=15$ for all combinations of f_0 and phase except for the 200-Hz random phase case. This trend will be addressed further in conjunction with results of experiment 3. The second, less apparent, trend was that dichotic f_0 DLs were slightly smaller for $\overline{N}=18$ and $\overline{N}=24$ at both f_0's. Differences between diotic and dichotic f_0 DLs were seen in some subjects, but not in others. Figure 5 shows mean DLs for two sample subjects who participated in the random-phase conditions. At one extreme, subject S9 (right column) shows larger DLs under dichotic presentation near $\overline{N}=12$ for both f_0's. Of the 16 combinations of subject and f_0, seven showed larger dichotic DLs near $\overline{N}=12$ (four of eight in sine-phase, three of eight in random-phase). At the other extreme, subject S8 (left column) shows larger DLs under diotic presentation at $\overline{N}=18$ and 24. While no subjects showed larger diotic DLs near $\overline{N}=18$ for sine-phase stimuli, two did for random-phase stimuli.

The results of Houtsma and Smurzynski (1990) suggested that the phase relationship between harmonics affected the f_0 DLs for high-order, but not low-order harmonics. While this trend also appears in our data, the ANOVA indicated no significant main effect of phase or two-way interactions between phase and any other factor ($p>0.05$). Although the f_0 DLs appear larger in the random phase conditions for $\overline{N}>9$, this difference is not statistically significant for the logarithmically transformed data. The lack of a significant phase effect in our data may be due to the fact that phase was a between-subjects factor, giving the test less statistical power than if random and sine phase complexes had been tested in the same subjects.

Another possibility is that even though the lowest harmonic number was roved from interval to interval, for large Δf_0's it is possible for listeners to achieve above chance performance without extracting f_0 information. Phase effects may not be present in any condition where f_0 information was not used to perform the task. Both in our 3IFC study and in the Houtsma and Smurzynski (1990) study, if the listener were to base their answer on the frequency of the lowest harmonic present in each interval (or the low-frequency edge of the excitation pattern for unresolved complexes), they would achieve 66.7% correct (near the 70.7% correct point approximated by the two-up, one-down adaptive procedure) if $\Delta f_0/f_0>1/\overline{N}$. Any data point falling above the DL $=(100/\overline{N})\%$ dashed line in Fig. 4 could reflect responses based on the "lowest harmonic" cue, rather than f_0 extraction. Performance is slightly worse than the "lowest harmonic" prediction for $\overline{N}=18$ and 24 in the sine-phase conditions, and much worse for $\overline{N}>12$ in all random-phase conditions. Thus in this study, listeners may be using lowest harmonic cues, rather than f_0 pitch cues, to perform f_0 discrimination for complexes with high $\overline{N}$, especially when the components are in random phase. In the Houtsma and Smurzynski (1990) study, f_0 DLs are much smaller than the lowest harmonic cue prediction, and therefore most likely reflect actual f_0 discrimination performance.

To look for possible phase effects, Scheffe *post-hoc* tests compared sine- and random-phase data for the four combinations of f_0 and mode of presentation for $\overline{N}=12$, which is above the resolved harmonic region, but below the region where the "lowest harmonic" cue may have influenced the results. Results indicate that f_0 DLs were significantly different ($p<0.05$) in the 100-Hz dichotic and 200-Hz diotic conditions, providing some weak evidence for the presence of phase effects in these conditions.

D. Discussion

The fact that the transition from small to large f_0 DLs occurs at the same $\overline{N}$ under diotic and dichotic presentation indicates that the auditory system is unable to utilize the information provided by the additional resolved harmonics in the dichotic case for f_0 discrimination. While two subjects did show slightly smaller f_0 DLs for dichotic complexes than for diotic complexes when $\overline{N} \geqslant 18$, the f_0 DLs (around 6%) are still much larger than those found for lower numbered harmonics. This supports the hypothesis that good f_0 discrimination is not limited by harmonic resolvability, but by harmonic number, regardless of resolvability. This result also indicates that subjects cannot ignore the input from one ear in performing the f_0 discrimination task. Remember that the ear with the even harmonics contains consecutive harmonics of $2f_0$, with a lowest harmonic around $\overline{N}/2$. If subjects were able to ignore the ear with odd harmonics, we would expect the transition between good and poor f_0 discrimination to occur at twice the average lowest harmonic number, i.e., around $\overline{N}=20$. Thus, this result is consistent with the idea that pitch is derived from a combined ''central spectrum'' (Zurek, 1979) that prevents an independent pitch percept derived from the input to one ear. Note, however, that the odd and even harmonics were presented to left and right ears at random in each trial, making it impossible for the listener to know which ear to ignore. It is possible that if odd and even harmonics were presented consistently to the same ears, subjects may have been able to learn to ignore the input from the ear with odd harmonics.

The transition from small to large f_0 DLs occurs at the same $\overline{N}$ at both f_0's, consistent with the results of Kaernbach and Bering (2001). This confirms our expectation (Shackleton and Carlyon, 1994) that the dramatic increase in f_0 DLs is due to a relative frequency effect that depends more on harmonic number than on an absolute frequency effect, such as the roll-off of phase-locking with increasing absolute frequency. Nevertheless, effects of absolute frequency are also present, in that the f_0 DLs for $\overline{N}>9$ are greater for the 200-Hz f_0 than for the 100-Hz f_0. These absolute frequency effects may be related to phase locking, where the additional information available from phase locking to the fine structure at a lower absolute frequency region in the 100-Hz condition aided f_0 discrimination. Also, because we tested only f_0's of 100 and 200 Hz, we did not observe the absolute frequency effects reported in other studies where the f_0 DL transition occurs at a lower $\overline{N}$ for f_0's below 100 Hz and above 200 Hz (Ritsma, 1962; Krumbholz *et al.*, 2000; Pressnitzer *et al.*, 2001).

For the diotic 200-Hz sine-phase condition, f_0 DLs for complexes with $\overline{N}>10$ are approximately twice as large as those of the monotic 200-Hz sine-phase results of Houtsma and Smurzynski (1990), depicted as a dashed line in the lower left panel of Fig. 4, although the transition from small to large f_0 DLs occurs at the same $\overline{N}$ in both studies. The difference in DL between this and the earlier study can be probably explained in terms of differences in sensation level. Hoekstra (1979) showed that an increase in sensation level from the 10 dB used in our study to the 20 dB used in the Houtsma and Smurzynski (1990) study decreased f_0 DLs for harmonic complexes by a factor of 2 to 4, depending on f_0 and subject.

IV. EXPERIMENT 3: PERCEIVED PITCH OF DICHOTIC STIMULI

A. Rationale

Flanagan and Guttman (1960) investigated the pitch of same- and alternating-polarity click trains. A same-polarity click train has a click rate equal to the f_0, and a spectrum consisting of all the harmonics of f_0, whereas an alternating-polarity click train has a click rate that is $2f_0$, and a spectrum consisting of only the odd harmonics of the f_0. According to Flanagan and Guttman (1960), stimuli with $f_0<150$ Hz elicit a pitch corresponding to the click rate, regardless of polarity, while stimuli with $f_0>150$ Hz elicit a pitch corresponding to the f_0. This result is consistent with a two-mechanism model of pitch perception. Click trains with a high f_0 that contain resolved components in the absolute frequency dominance region for pitch (Plomp, 1967) yield a pitch at the f_0, consistent with a mechanism that extracts pitch from spectral cues. Click trains with a low f_0 that contain only unresolved components in the dominance region yield a pitch consistent with a mechanism that extracts pitch from peaks in the temporal envelope of the waveform. The temporal envelope of the alternating polarity click train repeats at the difference frequency between components of $2f_0$, whereas the waveform of the same polarity click train repeats at the f_0.

Experiment 3 estimated the perceived pitch of the dichotic stimuli used in experiment 2. If, as suggested by the results of experiment 2, the individual resolved components above the 10th harmonic are not used in f_0 discrimination, then the pitch of dichotic complexes with $\overline{N}>10$ may be derived from the repetition rate of the temporal envelope. If so, these complexes should yield a perceived pitch at $2f_0$, consistent with the peripheral difference frequency between adjacent components. Alternatively, the central pitch mechanism may be able to make some, but poor, use of the higher-order resolved harmonics. If so, these dichotic stimuli should yield a pitch at the f_0 derived from the combined central spectrum, but with the poor f_0 discrimination performance seen in experiment 2.

B. Methods

Assuming that listeners would only perceive a pitch at the f_0 or at $2f_0$ for their alternating-phase stimuli, Shackleton and Carlyon (1994) asked listeners to identify which of two sine-phase stimuli, with fundamental frequencies equal to the f_0 or to $2f_0$ of the alternating-phase stimulus, most closely matched each alternating-phase stimulus. Similarly, we assumed that our dichotic stimuli would yield perceived pitches corresponding to either the f_0, consistent with spectral cues, or to $2f_0$, consistent with monaural temporal envelope cues. However, we used a different experimental paradigm. Subjects compared the pitch of a dichotic stimulus with that of a diotic stimulus, where the f_0 of the diotic

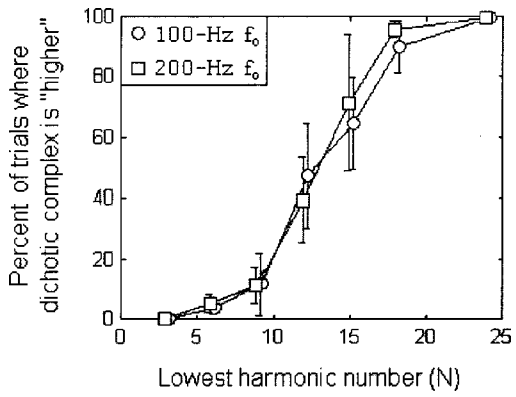

FIG. 6. Mean results from experiment 3, showing the percentage of trials where subjects reported a dichotic complex to have a higher pitch than a diotic complex with f_0 a factor of $\sqrt{2}$ higher. Error bars indicate plus or minus one standard error of the mean across the individual subjects. For lowest harmonic number $N<12$, subjects nearly always identified the diotic complex as "higher;" for $N>15$ subjects nearly always identified the dichotic complex as "higher." The transition from 0% to 100% occurs at approximately the same harmonic number for both f_0's tested.

stimulus was a half-octave (a factor of $\sqrt{2}$) higher than that of the dichotic stimulus. We assumed that the diotic sine-phase stimulus yielded a perceived pitch near its f_0. Thus, if the dichotic stimulus was judged as "higher" we assumed that the subject perceived its pitch to be $2\,f_0$. Similarly, if the dichotic stimulus was judged "lower," we assumed the subject perceived its pitch to be the f_0.

The dichotic stimuli were sine-phase complexes identical to those described in experiment 2. The diotic stimuli were sine-phase harmonic complexes with f_0 half an octave above the f_0 of the dichotic stimulus in the same trial, with harmonics chosen such that the bandwidth was limited to that of the dichotic stimulus. The diotic and dichotic stimuli were presented randomly in the first and second intervals and the subject was asked to identify the "higher" interval. Lowest harmonic number was not roved from interval to interval. Each run consisted of seven trials for each of the seven average lowest harmonic numbers tested in experiment 2, for a total of 49 trials. Twelve runs were performed at both the 100- and 200-Hz f_0's, such that each dichotic complex was presented a total 84 times per subject. To acquaint subjects with the task, they underwent a short (15 min) training session during which they were required to identify the higher of two pure tones separated by $\frac{1}{2}$ octave. Four subjects (ages 18–24, one female) took part in this experiment. Three had already participated in experiment 1 or 2. The setup for stimulus delivery was identical to that described in experiment 1.

C. Results

The results shown in Fig. 6 clearly indicate that subjects perceived a pitch lower than $\sqrt{2}$ times the f_0 for dichotic stimuli with a low lowest harmonic number and a pitch higher than $\sqrt{2}$ times the f_0 for dichotic stimuli with a high lowest harmonic number. The transition between the two pitch percepts occurred between lowest harmonic numbers 9 and 18, roughly the same region as was seen for the f_0 DL shift in experiment 2. If our assumption that listeners always perceive a pitch corresponding to either the f_0 or $2\,f_0$ holds, then listeners are perceiving a pitch corresponding to the f_0 for complexes containing harmonics lower than the 10th, consistent with spectral cues, and a pitch corresponding to $2\,f_0$ for complexes containing only harmonics above the 15th, consistent with temporal envelope cues. In between, the pitch appears to be ambiguous. Further testing would be necessary to determine if this ambiguity reflects two simultaneous pitches (at the f_0 and at $2\,f_0$) deriving from different mechanisms.

D. Discussion

The values of N that yielded an ambiguous pitch in this experiment correspond well to the values of $\overline{N}$ that yielded elevated f_0 DLs under dichotic presentation in experiment 2. This suggests that neither a mechanism that operates on resolved harmonics nor a mechanism that extracts the pitch from the temporal envelope responds well to dichotic stimuli in this region. Since approximately 20 harmonics are resolved under dichotic presentation (experiment 1), listeners had difficulty extracting the f_0 from these high-order, but resolved harmonics. Since dichotic complexes have fewer components falling within an auditory filter, the resulting temporal envelopes will be less modulated than the envelopes associated with the diotic stimuli, reducing the effectiveness of the envelope as a pitch cue.

The data show that listeners nearly always perceived a pitch near the f_0 for $N<12$. This result is in conflict with the results of Hall and Soderquist (1975), where subjects reported two pitches, one at each f_0, when three successive components each of a 200- and a 400-Hz f_0 were presented to opposite ears. The larger number of harmonics presented in the current study (six to each ear) may have encouraged the fusion of binaural information in processing pitch.

V. GENERAL DISCUSSION

A. Absolute or relative frequency?

The transitions from strong to weak pitch salience in experiment 2, and from a perceived pitch of the f_0 to $2\,f_0$ in experiment 3, occur at approximately the same lowest harmonic number for both the 100- and 200-Hz f_0's. These results are consistent with the idea that relative frequency relationships, such as those that govern harmonic resolvability, underlie the different pitch percepts associated with complexes containing low- and high-order harmonics (Houtsma and Smurzynski, 1990; Carlyon and Shackleton, 1994; Shackleton and Carlyon, 1994; Kaernbach and Bering, 2001). If the change in pitch salience were due to absolute frequency effects, as suggested by autocorrelation models (Cariani and Delgutte, 1996; Carlyon, 1998), the transition should have occurred at the same absolute frequency, and not the same harmonic number, for the two f_0's.

B. Resolvability or harmonic number?

Taken together, the results from the experiments demonstrate an interrelationship between harmonic number, resolvability, and pitch. Specifically, the region around the 10th harmonic appears to be important in defining transitions in

harmonic resolvability, f_0 discrimination, and pitch height, at least for the f_0 range between 100 and 200 Hz. First, experiment 1 showed that for diotic stimuli approximately the first ten harmonics are resolved, while higher harmonics are unresolved. Second, consistent with Houtsma and Smurzynski (1990), experiment 2 showed that small f_0 DLs require the presence of harmonics below the 10th. Third, experiment 3 showed that a perceived pitch associated with the f_0 of the combined binaural spectrum requires the presence of harmonics below the 10th. Taken together, these three observations are consistent with the idea that complexes containing resolved harmonics below the 10th yield fundamentally different pitch percepts from those containing only harmonics above the 10th.

Consistent with earlier data from two-tone complexes (Houtsma and Goldstein, 1972; Arehart and Burns, 1999), the interpretation that harmonic resolution *per se* is responsible for the changes in pitch perception is not supported by the comparison of the diotic and dichotic results in experiments 2 and 3. The additional resolved harmonics in the dichotic case yield neither small f_0 DLs in experiment 2, nor a pitch match consistent with extraction of cues from a centrally combined spectrum in experiment 3, both of which would be expected if the shift from a salient spectral pitch to a weak temporal pitch were due to harmonics becoming unresolved. For example, although a dichotic stimulus with $N=15$ contains resolved components, it yields poor f_0 discrimination performance and an ambiguous pitch percept. Thus, harmonic number, regardless of resolvability, seems to underlie the changes in pitch perception.

C. Implications for pitch theories

''Harmonic template'' pitch theories propose that a pitch detection mechanism codes the individual frequencies of the peripherally resolved partials and compares them to an internally stored template to derive a pitch at the f_0 (e.g., Goldstein, 1973; Terhardt, 1974, 1979). The failure of these models to explain how periodicity information is extracted from complexes containing only high-order harmonics has driven an opposing view that f_0 extraction is performed by a single autocorrelation or similar mechanism that operates on all harmonics, regardless of resolvability (Licklider, 1951, 1959; Meddis and Hewitt, 1991a, b; Meddis and O'Mard, 1997; de Cheveigné, 1998). Meddis and O'Mard (1997) have claimed that their model accounts for the different pitch percepts associated with resolved and unresolved harmonic complexes, due to the inherent differences in the result of the autocorrelation calculation for resolved versus unresolved harmonics, although the validity of this claim has been put into doubt by further analysis of their model (Carlyon, 1998). Alternatively, several studies have suggested that pitch may be processed via two different mechanisms, a harmonic template mechanism operating on resolved harmonics, and a separate mechanism operating on the temporal envelope resulting from unresolved harmonics (Houtsma and Smurzynski, 1990; Carlyon and Shackleton, 1994; Shackleton and Carlyon, 1994; Steinschneider *et al.*, 1998; Grimault *et al.*, 2002).

The results of experiment 2 argue against a pitch processing mechanism that responds inherently differently to unresolved versus resolved harmonics. With such a mechanism, we would expect f_0 discrimination performance to improve when normally unresolved harmonics are artificially resolved under dichotic presentation, whereas experiment 2 showed that f_0 discrimination performance was the same or worse in the dichotic conditions. Therefore, any theory of pitch perception must account for relative frequency effects without relying on harmonic resolvability.

''Temporal'' theories could account for this relative frequency effect if the autocorrelation in each channel were constrained to be sensitive to a limited range of periodicities relative to the inverse of the channel's CF, thereby limiting the range of harmonic numbers contributing to the pitch percept (Moore, 1982). This modification would also need to somehow account for a pitch derived from the temporal envelope for complexes containing only high-order components. If this requirement could be met, the modified theory would be consistent with the ambiguous pitch and elevated f_0 DLs seen for dichotic complexes with $N=12$ and $N=15$, which have relatively ineffective envelope cues (see Sec. IV D).

''Place'' theories could account for this relative frequency effect if the templates that derive the pitch from low-order harmonics were constrained to consist of only those harmonics that are *normally* resolved. This is consistent both with the idea of harmonic templates learned from exposure to harmonic sounds (Terhardt, 1974) and the more recent proposal that templates for low-order harmonics may emerge from any form of wideband stimulation (Shamma and Klein, 2000). With this constraint, even though artificially resolved harmonics (above the 10th and up to the 20th partial) are available under dichotic presentation, the pitch processing mechanism will be unable to utilize these additional resolved harmonics since no template will have developed to match them.

Even with this constraint, ''harmonic template'' theories do not fully explain the results for dichotic complexes containing artificially resolved harmonics. For these stimuli, we would expect that the even harmonics in one ear would match a template corresponding to $2f_0$, yielding f_0 DLs on the order of those measured for complexes containing low-order harmonics. While ambiguous pitch matches suggest that listeners may sometimes perceive a pitch corresponding to $2f_0$ for these dichotic complexes, f_0 DLs are *larger* than those for diotic complexes with the same N. Apparently, the presence of the odd harmonics in the opposite ear has a substantial detrimental effect on f_0 discrimination.

One possible explanation for these results postulates the existence of inhibitory inputs to harmonic templates, tuned to partials of subharmonics of the f_0. Under normal circumstances, where all harmonics of a complex are present, such inhibition might be useful in preventing erroneous pitch percepts at multiples of the f_0. According to this scheme, while the resolved (mn)th partials of a complex (where m and n are integers) would facilitate a template for a pitch corresponding to n times the $f_0(nf_0)$ of the complex, the remaining resolved partials of the complex would inhibit this tem-

plate. Thus, only the template for a pitch at the f_0 would respond to the stimulus, yielding a pitch percept corresponding to the f_0 and good f_0 discrimination. For dichotic complexes with $N>10$, templates for pitches corresponding to nf_0 would still be inhibited, but in this case the template for a pitch corresponding to the f_0, with a limited number of harmonics represented, would not respond to the high-order harmonics. With no template available, the pitch could only be derived from temporal cues.

Another interpretation of the results is that the pitch is extracted from a combined ''central spectrum'' representation (Zurek, 1979) that prevents an independent pitch percept derived from the input to one ear. The additional *peripherally* resolved components might not be available in the central spectrum representation used to derive pitch. Listeners may have been able to overcome this central fusion in hearing out individual harmonics in experiment 1, but not when deriving a pitch from the sum of components in experiments 2 and 3. The nonmonotonic psychometric functions seen in some subjects in experiment 1 may reflect an inability to overcome the binaural fusion even in the ''hearing out'' task.

VI. SUMMARY AND CONCLUSIONS

In experiment 1 approximately twice as many harmonics are resolved under dichotic as compared to diotic presentation, verifying that harmonic resolvability is not limited by binaural interactions. A direct estimate of the limits of harmonic resolvability indicated that approximately 9 and 11 harmonics are resolved for 100- and 200-Hz f_0's, respectively. The results from our direct measure, which minimizes nonperipheral limitations by gating the target component on and off, resolve the discrepancy between previous direct estimates that only five to eight harmonics are resolved (Plomp, 1964), and indirect estimates suggesting that approximately ten harmonics are resolved (Houtsma and Smurzynski, 1990; Shackleton and Carlyon, 1994).

In experiment 2, listeners were unable to utilize the additional resolved harmonics available under dichotic presentation for f_0 discrimination. This implies that the deterioration in f_0 DLs with increasing lower cutoff frequency is due not to harmonics becoming unresolved *per se*, but instead to the increasing lowest harmonic number, regardless of resolvability. This result suggests constraints to both ''place'' and ''temporal'' models of pitch perception. For a ''harmonic template'' theory to account for the data, only those harmonics that are *normally* resolved should be represented in the templates. For an ''autocorrelation'' theory to do so, the range of periodicities to which the autocorrelation in each channel is sensitive should be CF-dependent (Moore, 1982).

The results of experiments 2 and 3 are consistent with a two-mechanism model of pitch perception (e.g., Carlyon and Shackleton, 1994). When harmonics below the 10th are present, a harmonic template mechanism is able to extract pitch from the resolved components, yielding small f_0 DLs and a pitch consistent with spectral cues. When only harmonics above the 10th are present, the auditory system relies on temporal envelope cues for pitch extraction, regardless of resolvability, yielding some ambiguous pitch percepts for dichotic complexes, and poor f_0 discrimination performance in all cases. A temporal model, constrained as described above, may nevertheless be able to account for these results within the framework of a single autocorrelation mechanism.

ACKNOWLEDGMENTS

This work was supported by NIH Grant No. R01 DC 05216 and by NIH Training Grant No. 5T32 DC 00038. We thank Christophe Micheyl, Peninah Rosengard, Chris Plack, Neal Viemeister, and two anonymous reviewers for their helpful comments on previous versions of this manuscript. We also thank Chris Plack for suggesting the existence of inhibitory inputs to a 2 f_0 template, tuned to the frequencies of the odd harmonics of a complex with fundamental frequency f_0.

[1]Viemeister and Bacon (1982) found that a component whose onset is delayed relative to the remaining component produced more forward masking than when the entire complex is gated synchronously. Even if this ''enhancement'' effect can be thought of as ''amplifying'' the representation in a subset of auditory nerve fibers, this should not have any effect on peripheral resolvability, as the signal-to-noise ratio within that population would be unaffected. In fact, physiological enhancement of the response to a component of a harmonic complex with delayed onset time has been found in the cochlear nucleus (Scutt *et al.*, 1997) but not in the auditory nerve (Palmer *et al.*, 1995) of the guinea pig.

[2]The temporal waveform for several harmonics of a sine-phase complex that fall in one auditory filter is click-like, with brief peaks occurring at intervals of the f_0, separated by low-level epochs. Eliminating a spectrally unresolved harmonic component (i.e., adding it out of phase) will result in that component appearing during the low-level epochs, thereby allowing the detection of the subtracted component's frequency by ''listening in the valleys,'' or ''dip listening'' (Duifhuis, 1970). Since random-phase complexes generally have much flatter temporal envelopes and are not conducive to listening in the valleys (Alcántara and Moore, 1995), this greatly reduced the possibility of dip listening.

[3]In fact, the combined randomizations ensured that, for a given f_{comp}, the probability that the frequency of the target harmonic was higher than f_{comp} was approximately equal to the probability of it being lower (except when $f_{\text{comp}}<f_{\text{targ}}$ when the lowest target component was tested or $f_{\text{comp}}>f_{\text{targ}}$ when the highest target component was tested), so that subjects were prevented from answering correctly based only on the frequency of the comparison tone.

[4]$$\text{Percent correct } (n)=100\left[\frac{1}{2}+\frac{1}{2\sqrt{\pi}}\int_n^{\infty} e^{-[w(n'-n_0)]^2}\,dn'\right], \quad (1)$$

where n is harmonic number, n' is the harmonic number integration variable, w is a factor describing the slope of the psychometric function, and n_0 is the harmonic number that yields 75% correct.

Alcántara, J. I., and Moore, B. C. J. (**1995**). ''The identification of vowel-like harmonic complexes: Effects of component phase, level, and fundamental frequency,'' J. Acoust. Soc. Am. **97**, 3813–3824.

Arehart, K. H., and Burns, E. M. (**1999**). ''A comparison of monotic and dichotic complex-tone pitch perception in listeners with hearing loss,'' J. Acoust. Soc. Am. **106**, 993–997.

Cariani, P. A., and Delgutte, B. (**1996**). ''Neural correlates of the pitch of complex tones. I. Pitch and pitch salience,'' J. Neurophysiol. **76**, 1698–1716.

Carlyon, R. P. (**1998**). ''Comments on 'A unitary model of pitch perception [J. Acoust. Soc. Am. **102**, 1811–1820 (1997)],' '' J. Acoust. Soc. Am. **104**, 1118–1121.

Carlyon, R. P., and Shackleton, T. M. (**1994**). ''Comparing the fundamental frequencies of resolved and unresolved harmonics: Evidence for two pitch mechanisms?'' J. Acoust. Soc. Am. **95**, 3541–3554.

Cullen, J. K., and Long, G. R. (**1986**). ''Rate discrimination of high-pass-filtered pulse trains,'' J. Acoust. Soc. Am. **79**, 114–119.

de Cheveigné, A. (**1998**). ''Cancellation model of pitch perception,'' J. Acoust. Soc. Am. **103**, 1261–1271.

Duifhuis, H. (**1970**). ''Audibility of high harmonics in a periodic pulse,'' J. Acoust. Soc. Am. **48**, 888–893.
Fine, P. A., and Moore, B. C. J. (**1993**). ''Frequency analysis and musical ability,'' Music Percept. **11**, 39–53.
Flanagan, J. L., and Guttman, N. (**1960**). ''On the pitch of periodic pulses,'' J. Acoust. Soc. Am. **32**, 1308.
Goldstein, J. L. (**1973**). ''An optimum processor theory for the central formation of the pitch of complex tones,'' J. Acoust. Soc. Am. **54**, 1496–1516.
Grimault, N., Micheyl, C., Carlyon, R. P., and Collet, L. (**2002**). ''Evidence for two pitch encoding mechanisms using a selective auditory training paradigm,'' Percept. Psychophys. **64**, 189–197.
Hall, J. W., and Soderquist, D. R. (**1975**). ''Encoding and pitch strength of complex tones,'' J. Acoust. Soc. Am. **58**, 1257–1261.
Hoekstra, A. (**1979**). ''Frequency discrimination and frequency analysis in hearing,'' Ph.D. Thesis, Institute of Audiology, University Hospital, Groningen, Netherlands.
Houtsma, A. J. M., and Goldstein, J. L. (**1972**). ''The central origin of the pitch of pure tones: Evidence from musical interval recognition,'' J. Acoust. Soc. Am. **51**, 520–529.
Houtsma, A. J. M., and Smurzynski, J. (**1990**). ''Pitch identification and discrimination for complex tones with many harmonics,'' J. Acoust. Soc. Am. **87**, 304–310.
Kaernbach, C., and Bering, C. (**2001**). ''Exploring the temporal mechanism involved in the pitch of unresolved harmonics,'' J. Acoust. Soc. Am. **110**, 1039–1048.
Krumbholz, K., Patterson, R. D., and Pressnitzer, D. (**2000**). ''The lower limit of pitch as determined by rate discrimination,'' J. Acoust. Soc. Am. **108**, 1170–1180.
Levitt, H. (**1971**). ''Transformed up-down methods in psychoacoustics,'' J. Acoust. Soc. Am. **49**, 467–477.
Licklider, J. C. R. (**1951**). ''A duplex theory of pitch perception,'' Experientia **7**, 128–133.
Licklider, J. C. R. (**1959**). ''Three auditory theories,'' in *Psychology, a Study of Science*, edited by S. Koch (McGraw–Hill, New York).
Meddis, R., and Hewitt, M. (**1991a**). ''Virtual pitch and phase sensitivity studied of a computer model of the auditory periphery. I: Pitch identification,'' J. Acoust. Soc. Am. **89**, 2866–2882.
Meddis, R., and Hewitt, M. (**1991b**). ''Virtual pitch and phase sensitivity studied of a computer model of the auditory periphery. II: Phase sensitivity,'' J. Acoust. Soc. Am. **89**, 2883–2894.
Meddis, R., and O'Mard, L. (**1997**). ''A unitary model of pitch perception,'' J. Acoust. Soc. Am. **102**, 1811–1820.
Moore, B. C. J. (**1973**). ''Frequency difference limens for short-duration tones,'' J. Acoust. Soc. Am. **54**, 610–619.
Moore, B. C. J. (**1982**). *An Introduction to the Psychology of Hearing*, 2nd ed. (Academic, London), pp. 140–144.
Moore, B. C. J., and Ohgushi, K. (**1993**). ''Audibility of partials in inharmonic complex tones,'' J. Acoust. Soc. Am. **93**, 452–461.
Ohm, G. S. (**1843**). ''Über die Definition des Tones, nebst daran geknüpfter Theorie der Sirene und ähnlicher tonbildender Vorrichtungen [On the definition of the tone and the related theory of the siren and similar tone-producing devices],'' Ann. Phys. Chem. **59**, 513–565.
Palmer, A. R., Summerfield, Q., and Fantini, D. A. (**1995**). ''Responses of auditory-nerve fibers to stimuli producing psychophysical enhancement,'' J. Acoust. Soc. Am. **97**, 1786–1799.
Plomp, R. (**1964**). ''The ear as a frequency analyzer,'' J. Acoust. Soc. Am. **36**, 1628–1636.
Plomp, R. (**1967**). ''Pitch of complex tones,'' J. Acoust. Soc. Am. **41**, 1526–1533.
Plomp, R., and Mimpen, A. M. (**1968**). ''The ear as a frequency analyzer II,'' J. Acoust. Soc. Am. **43**, 764–767.
Pressnitzer, D., Patterson, R. D., and Krumbholz, K. (**2001**). ''The lower limit of melodic pitch,'' J. Acoust. Soc. Am. **109**, 2074–2084.
Ritsma, R. J. (**1962**). ''Existence region of the tonal residue. I.,'' J. Acoust. Soc. Am. **34**, 1224–1229.
Ritsma, R. J. (**1967**). ''Frequencies dominant in the perception of the pitch of complex sounds,'' J. Acoust. Soc. Am. **42**, 191–198.
Schmidt, S., and Zwicker, E. (**1991**). ''The effect of masker spectral asymmetry on overshoot in simultaneous masking,'' J. Acoust. Soc. Am. **89**, 1324–1330.
Scutt, M. J., Palmer, A. R., and Summerfield, A. Q. (**1997**). ''Psychophysical and physiological responses to signals which are enhanced by temporal context,'' Abstr., Assoc. Res. Otolaryngol. MidWinter Meeting.
Seebeck, A. (**1841**). ''Beobachtungen über einige Bedingungen der Entstehung von Tönen [Observations on some conditions for the creation of tones],'' Ann. Phys. Chem. **53**, 417–436.
Shackleton, T. M., and Carlyon, R. P. (**1994**). ''The role of resolved and unresolved harmonics in pitch perception and frequency modulation discrimination,'' J. Acoust. Soc. Am. **95**, 3529–3540.
Shamma, S., and Klein, D. (**2000**). ''The case of the missing pitch templates: How harmonic templates emerge in the early auditory system,'' J. Acoust. Soc. Am. **107**, 2631–2644.
Shera, C. A., Guinan, J. J., and Oxenham, A. J. (**2002**). ''Revised estimates of human cochlear tuning from otoacoustic and behavioral measurements,'' Proc. Natl. Acad. Sci. U.S.A. **99**, 3318–3323.
Soderquist, D. R. (**1970**). ''Frequency analysis and the critical band,'' Psychonomic Sci. **21**, 117–119.
Srulovicz, P., and Goldstein, J. L. (**1983**). ''A central spectrum model: A synthesis of auditory-nerve timing and place cues in monaural communication of frequency spectrum,'' J. Acoust. Soc. Am. **73**, 1266–1276.
Steinschneider, M., Reser, D. H., Fishman, Y. I., Schroeder, C. E., and Arezo, J. C. (**1998**). ''Click train encoding in primary auditory cortex of the awake monkey: Evidence for two mechanisms subserving pitch perception,'' J. Acoust. Soc. Am. **104**, 2935–2955.
Terhardt, E. (**1974**). ''Pitch, consonance, and harmony,'' J. Acoust. Soc. Am. **55**, 1061–1069.
Terhardt, E. (**1979**). ''Calculating virtual pitch,'' Hear. Res. **1**, 155–182.
Viemeister, N. F., and Bacon, S. P. (**1982**). ''Forward masking by enhanced components in harmonic complexes,'' J. Acoust. Soc. Am. **71**, 1502–1507.
Weiss, T. F., and Rose, C. (**1988**). ''Stages of degradation of timing information in the cochlea—a comparison of hair-cell and nerve fiber responses in the alligator lizard,'' Hear. Res. **33**, 167–174.
Wightman, F. L. (**1973**). ''The pattern-transformation model of pitch,'' J. Acoust. Soc. Am. **54**, 407–416.
Zurek, P. M. (**1979**). ''Measurements of binaural echo suppression,'' J. Acoust. Soc. Am. **66**, 1750–1757.

Enhancing interaural-delay-based extents of laterality at high frequencies by using "transposed stimuli"

Leslie R. Bernstein[a)]
Department of Neuroscience, University of Connecticut Health Center, Farmington, Connecticut 06030

Constantine Trahiotis
Department of Neuroscience and Department of Surgery (Otolaryngology), University of Connecticut Health Center, Farmington, Connecticut 06030

(Received 18 September 2002; revised 12 February 2003; accepted 10 March 2003)

An acoustic pointing task was used to determine whether interaural temporal disparities (ITDs) conveyed by high-frequency ''transposed'' stimuli would produce larger *extents of laterality* than ITDs conveyed by bands of high-frequency Gaussian noise. The envelopes of transposed stimuli are designed to provide high-frequency channels with information similar to that conveyed by the waveforms of low-frequency stimuli. Lateralization was measured for low-frequency Gaussian noises, the same noises transposed to 4 kHz, and high-frequency Gaussian bands of noise centered at 4 kHz. Extents of laterality obtained with the transposed stimuli were greater than those obtained with bands of Gaussian noise centered at 4 kHz and, in some cases, were equivalent to those obtained with low-frequency stimuli. In a second experiment, the general effects on lateral position produced by imposed combinations of bandwidth, ITD, and interaural phase disparities (IPDs) on low-frequency stimuli remained when those stimuli were transposed to 4 kHz. Overall, the data were fairly well accounted for by a model that computes the cross-correlation subsequent to known stages of peripheral auditory processing augmented by low-pass filtering of the envelopes within the high-frequency channels of each ear.
[DOI: 10.1121/1.1570431]

PACS numbers: 43.66.Pn, 43.66.Ba [MRL]

I. INTRODUCTION

We have recently reported (Bernstein and Trahiotis, 2002) that the relatively poor sensitivity to changes in ongoing interaural temporal disparities (ITDs) often measured with high-frequency signals (e.g., Klumpp and Eady, 1956; Zwislocki and Feldman, 1956; McFadden and Pasanen, 1976; Neutzel and Hafter, 1976; Henning, 1980; Bernstein and Trahiotis, 1982, 1994; Blauert, 1983) can be mitigated by the use of specially constructed high-frequency ''transposed'' stimuli. As described by van de Par and Kohlrausch (1997), transposed stimuli are designed with the goal of providing the high-frequency channels of the binaural auditory system with *envelope-based* inputs that, other things being equal, essentially mimic *waveform-based* inputs normally available in low-frequency channels.

The principal conclusion from our previous study was that the relatively poor resolution of ITDs typically observed with conventional high-frequency stimuli was not attributable to a general insensitivity to ITD of the high-frequency channels of the binaural processor. Rather, in accord with a hypothesis first advanced by Colburn and Esquissaud (1976), it appeared that frequency-related differences in sensitivity to ongoing ITDs resulted primarily from properties of the temporal signatures of the ''internal'' stimuli that are produced by peripheral rectification and low-pass filtering.

It is also the case that previous studies with conventional high-frequency stimuli have shown that the functions relating extent of laterality (displacement of the intracranial image from midline) to ITD are typically much more shallow than those measured with low-frequency stimuli (e.g., Blauert, 1982; Bernstein and Trahiotis, 1985b). Said differently, for a given ITD, intracranial images produced by conventional high-frequency stimuli are perceived to be much closer to the midline than are intracranial images produced by low-frequency stimuli.

The purpose of this study was to determine whether ITDs conveyed by high-frequency transposed stimuli would also result in larger *extents of laterality* than those obtained with conventional high-frequency stimuli. At the outset, it was not clear whether the greater *sensitivity* to ITD measured with transposed stimuli would translate to there being greater ITD-based extents of laterality for transposed stimuli. Consequently, we conducted a limited series of pilot studies to determine whether high-frequency, transposed stimuli would, indeed, produce large extents of ITD-based laterality. The results of the pilot studies were positive in that they indicated that high-frequency transposed stimuli (1) can yield larger extents of laterality than do conventional high-frequency stimuli and (2) can yield extents of laterality of comparable magnitude to those produced by conventional low-frequency stimuli.

Consequently, a formal investigation was undertaken in which an acoustic pointing task was used to measure extents of laterality produced by (1) low-frequency narrow-band, Gaussian noise; (2) low-frequency narrow-band Gaussian noise transposed to 4 kHz; and (3) high-frequency narrow bands of Gaussian noise centered at 4 kHz. The larger set of

a)Electronic mail: les@neuron.uchc.edu

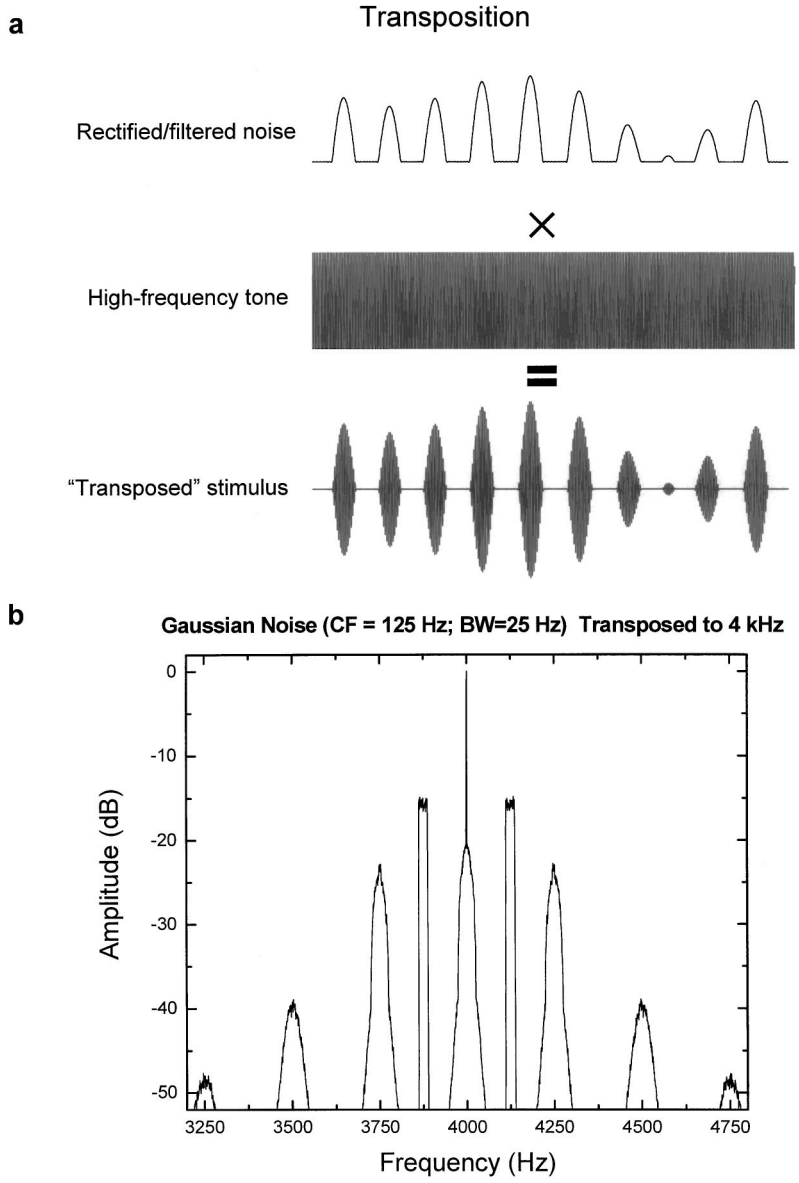

FIG. 1. (a) Schematic representation of the method used to generate transposed stimuli. (b) Power spectrum of a Gaussian noise (CF=125 Hz;BW=25 Hz) transposed to 4 kHz (see text).

data, reported here, confirmed that high-frequency transposed stimuli do, indeed, yield extents of laterality that are greater than those produced by conventional high-frequency stimuli and, depending on the particular stimulus condition, are equivalent to those produced by conventional low-frequency stimuli. In addition, a second experiment revealed that the general effects on lateral position produced by imposed combinations of bandwidth, ITD, and interaural phase disparities (IPDs) on low-frequency stimuli remained when those stimuli were transposed to 4 kHz.

II. EXPERIMENT 1

A. Stimuli and procedures

High-frequency transposed bands of noise were generated by employing a technique similar to that described by van de Par and Kohlrausch (1997). The general technique, which was also used by Bernstein and Trahiotis (2002), is illustrated in Fig. 1(a). First, the time-domain representation of a low-frequency band of Gaussian noise was (linearly) half-wave rectified by setting all negative values to zero. The rectified waveform was then transformed to the frequency-domain and the magnitudes of components above 2 kHz were filtered out by setting them to zero. Then, the signal that resulted was transformed back to the time-domain (top row) and multiplied by a 4-kHz sinusoidal ''carrier'' (middle row). The product (bottom row) was a high-frequency transposed stimulus having an envelope whose time signature mimicked that of the rectified and filtered low-frequency band of noise. It is important to understand that had the rectified waveform not been low-pass filtered, then its spectrum, as well as the spectrum of the transposed stimulus, would have been essentially unbounded and might have been able to provide low-frequency channels with useful binaural information.

As discussed by Bernstein and Trahiotis (2002), if one assumes (1) that whatever form of ''rectification'' that occurs in the peripheral auditory system removes all, or essentially all, of the negative portions of the external waveform and (2) that the cutoff of internal low-pass filtering is substantially

below 2 kHz, then one would expect, all other things being equal, that the internal, neural pattern of activity would be the same for our low-frequency stimuli and their high-frequency, transposed counterparts. Both assumptions are supported by numerous physiological data and analyses (e.g., Rose *et al.*, 1967; Brugge *et al.*, 1969; Johnson, 1980; Palmer and Russell, 1986).

As discussed by Bernstein and Trahiotis (2002), there are two other lines of evidence that attest to the suitability of the overall procedure used to yield the desired stimuli. First, we previously verified via computer simulations that employing a low-pass cutoff of 2 kHz had, at most, negligible effects on the envelopes of the transposed stimuli. These negligible effects are manifest as the almost imperceptible ripples in the ''flat'' portions of the waveform depicted in the top trace of Fig. 1(a). Second, van de Par and Kohlrausch (1997) have shown that restricting the spectra of transposed stimuli in a similar manner such that only three or five central components remained did not adversely affect improvements in binaural detection thresholds. Thus, it appears that the transposition technique yields physical stimuli, *per se*, that fulfill our requirements.

Figure 1(b) displays a portion of the power spectrum of one of the transposed stimuli used in the experiment. In this case, a 25-Hz-wide band of Gaussian noise centered at 125 Hz was transposed to 4 kHz. For this example, the technique results in the presence of sidebands centered at 4000 ± 125, ± 250, ± 500, ± 750, ± 1000, ± 1250, ± 1500, ± 1750, ± 2000 Hz. Only the sidebands having amplitudes within 50 dB of the amplitude at the center frequency are shown. Note that the vast majority of the power in this stimulus is contained within the region between 3750 and 4250 Hz. Thus, the energy in the transposed stimulus occurs over a broader spectral region than does the energy in either its 25-Hz-wide low-frequency counterpart or the energy in a conventional 25-Hz-wide conventional band of Gaussian noise centered at 4 kHz. As will be seen when the data are presented and discussed, the differential effects among the stimuli in terms of the extent of laterality produced by the ITDs conveyed by them *cannot* be accounted for by their differences in spectral extent, *per se*.

All three types of stimuli (low- and high-frequency bands of Gaussian noise and high-frequency transposed stimuli) were generated digitally with a sampling rate of 20 kHz (TDT AP2), were low-pass filtered at 8.5 kHz (TDT FLT2), and were presented via Etymotic ER-2 insert earphones at a level matching 72 dB SPL as produced by TDH-39 earphones in a 6-cc coupler.[1] The center frequency of the conventional bands of noise was 125, 250, or 4000 Hz. Bandwidth was 25, 50, 100, 200, or 400 Hz, depending on center frequency. For the center frequencies of 125, 250, and 4000 Hz, the largest of the bandwidths employed was 200, 400, and 400 Hz, respectively. The transposition method (i.e., rectification, filtering, and multiplication) was applied to each of the bands of noise centered at 125 and 250 Hz in order to construct the set of transposed stimuli centered at 4000 Hz. For all three types of stimuli, ongoing ITDs (0, 200, 400, 600, 800, and 1000 μs, left ear leading) were imposed by applying linear phase shifts to the representation of the signals in the frequency domain and then gating the signals destined for the left and right ears coincidentally, after transformation to the time-domain.

Extents of laterality were measured for four normal-hearing young adult listeners (one male and three female) via an acoustic pointing task in which the listeners varied the interaural intensitive difference (IID) of a 200-Hz-wide band of noise centered at 500 Hz (the pointer) so that it matched the intracranial position of a second, experimenter-controlled, stimulus (the target). This procedure has been used previously in several studies (e.g., Trahiotis and Stern, 1989; Buell *et al.*, 1991; Heller and Trahiotis, 1996) and is described fully in Bernstein and Trahiotis (1985a). The pointer was generated in a manner similar to that described above and its overall level, when presented diotically (IID $=0$), was 65 dB SPL. Listeners adjusted the intracranial position of the pointer by rotating a knob. Rotation of the knob produced symmetric changes of the IID (in dB) of the pointer (i.e., increases in level at one ear and decreases in level at the other ear). The IID adjusted by the listener served as a metric of the intracranial position of the target. An arbitrary and randomly chosen value of the IID was inserted in the pointer prior to each match. This served to randomize the initial position of the pointer with respect to the absolute position of the knob. Each sequence of stimuli consisted of three presentations of the target (each separated by 200 ms), a pause of 300 ms, three presentations of the pointer (each separated by 200 ms), and a pause of 600 ms. The duration of target and pointer stimuli was 100 ms including 20-ms $\cos^2$ rise/decay ramps.

Targets and pointers were repeated until the listeners indicated that they had matched the intracranial positions of the target and pointer. Prior to completing a match, listeners had the option of halting, and then restarting, the sequence in order to ''check'' their adjustments after a period of silence.

All of the aforementioned stimulus conditions were visited in random order. Having chosen a particular stimulus condition as the target, a random process was used to select a value of ITD from the set to be tested until the listeners had completed three independent matches for each value of ITD. Within each series of matches to a particular target, three matches were also made when the target was presented diotically. The mean IID inserted by the listener to match these diotic targets was typically about 1 dB or so and served as a ''correction factor.'' That is, it was subtracted from the IIDs resulting from all the matches in the run. Finally, all of the stimulus conditions (targets) were revisited in reverse order and the data reported in the figures represent the mean ''corrected'' value of IID of the pointer across the six matches made by each listener for a particular combination of target and ITD.

Additional, ''control'' data were obtained to evaluate the possibility that listeners' matches for high-frequency transposed stimuli were influenced or depended upon distortion products present in low-frequency regions. For that purpose, three of the listeners remade matches using the procedure described above and, separately, in the presence of a continuous diotic noise low-pass filtered at 1300 Hz (N0 equivalent to 30 dB SPL; see, for example, Nuetzel and Hafter, 1976,

1981; Bernstein and Trahiotis, 2002). In the latter case, the pointer was a 200-Hz-wide band of noise centered at 4 kHz. In short, the data obtained with and without the continuous low-pass noise were, for practical purposes, identical. Therefore, the advantage of being able to compare directly the data obtained in this experiment to our previous studies by employing the same acoustic pointing procedure as before appears to carry no cost.

B. Results and discussion

Each panel in Fig. 2 displays the mean IID of the pointer (taken across the four listeners) as a function of the ITD imposed on the target. The positive values along the ordinate indicate IIDs favoring the left (leading) ear. For purposes of comparison, data obtained using three stimulus conditions are displayed within each panel. The closed squares (left column) represent data obtained with bands of *low-frequency Gaussian* noise centered at 125 Hz and the open squares (right column) represent data obtained with bands of *low-frequency Gaussian* noise centered at 250 Hz. The bandwidth of each low-frequency noise is indicated at the top left of each panel.

The triangles within each panel represent data obtained when the respective low-frequency Gaussian noises were transposed to 4 kHz. The circles represent lateralization data obtained with high-frequency conventional bands of Gaussian noise centered at 4 kHz. The bandwidths of those high-frequency Gaussian noises are indicated at the upper left of each panel. For purposes of comparison, the data obtained with high-frequency, conventional bands of Gaussian noise are plotted twice, once in each column.

For example, in the top-left panel, the closed squares represent the data obtained with a 25-Hz-wide band of Gaussian noise centered at 125 Hz, the closed triangles represent the data obtained with a 25-Hz-wide band of Gaussian noise centered at 125 Hz that was transposed to 4 kHz, and the circles represent data obtained with a 25-Hz-wide band of Gaussian noise centered at 4 kHz. In the top-right panel, the closed squares represent the data obtained with a 25-Hz-wide band of Gaussian noise centered at 250 Hz, and the closed triangles represent the data obtained with a 25-Hz-wide band of Gaussian noise centered at 250 Hz that was transposed to 4 kHz. The circles are replotted from the top-left panel and represent data obtained with a 25-Hz-wide band of Gaussian noise centered at 4 kHz.

In order to present most clearly the important trends among the data, no error bars are shown. Rather, the relative precision of the measurements will be discussed below in terms of the amounts of variance accounted for by the independent variables. Suffice it to say that the trends in the averaged data are truly representative of the data obtained both within and across listeners.

Three major outcomes are readily apparent. First, the extents of laterality obtained with both the ''125-Hz'' and ''250-Hz'' transposed stimuli centered at 4 kHz (left and right columns, respectively) are much greater than those obtained with bands of Gaussian noise centered at 4 kHz. Second, when the low-frequency Gaussian noise was centered at 125 Hz, it and its transposed counterpart produced extents of laterality that were highly similar and, in many cases, essentially equivalent. Third, when the low-frequency Gaussian noise was centered at 250 Hz, its transposed counterpart produced somewhat smaller extends of laterality than did the low-frequency Gaussian noise itself. In fact, those extents of laterality were also smaller than those obtained with the ''125-Hz'' transposed stimuli. The somewhat smaller extents of laterality obtained with the 250-Hz transposed stimuli appear to be consistent with and, perhaps related to, our recent finding that threshold-ITDs obtained with 256-Hz tones transposed to 4 kHz are larger than those obtained with 128-Hz tones transposed to 4 kHz (Bernstein and Trahiotis, 2002).

It should be emphasized, however, that quite substantial extents of laterality were produced by the ''250-Hz'' transposed stimuli when the larger ITDs were imposed. For example, looking across the different bandwidths, the intracranial images produced by an ITD of 600 μs, a value which approaches the maximum ITD encountered by human listeners in a natural environment, were matched by acoustic pointer IIDs of 12 ± 1 dB. IIDs of this magnitude are well known to produce intracranial images far toward or at the ear (e.g., Watson and Mittler, 1965; Yost, 1981). It is also the case that IIDs larger than about 12 dB have been reported to produce only small, albeit reliable, increases in extent of laterality (Trahiotis and Bernstein, 1986). As IID is increased from 0 to 12 dB, the position of the intracranial image changes essentially linearly from midline to very near the more intense ear. Taken together, these findings support the position that differences in pointer IID measured with the 250-Hz-centered low-frequency stimuli and their transposed counterparts with large ITDs are not indicative of large changes in extent of laterality.

In order to compare the relative potency of transposed stimuli centered at 4 kHz and bands of Gaussian noise centered at 4 kHz, the most conservative approach is to use as a standard of comparison the extends of laterality produced by the 400-Hz-wide band of Gaussian noise. This is so because it has been shown that ITD-based extents of laterality produced by bands of Gaussian noise centered at 4 kHz are relatively constant for bandwidths of 400 Hz and greater (Trahiotis and Bernstein, 1986). Therefore, this strategy has the advantage of precluding what may be ''unfair'' comparisons between the (smaller) extents of laterality produced by narrower bands of noise centered at 4 kHz. Comparisons among the data in Fig. 2 clearly indicate that transposed stimuli centered at 4 kHz produce extents of laterality that (1) are greater than those produced by even the 400-Hz-wide band of Gaussian noise centered at 4 kHz and (2) can be as great as those produced by Gaussian bands of noise centered at 125 Hz. Both of these outcomes appear to indicate that when high-frequency transposed stimuli convey an ITD, its potency is enhanced relative to when that ITD is conveyed by conventional high-frequency stimuli.

The data in Fig. 2 obtained with the low-frequency Gaussian noises and their transposed counterparts were subjected to a four-factor (type of stimulus [low-frequency noise, transposed counterpart] $\times$ center frequency [125, 250 Hz] $\times$ bandwidth [25, 50, 100, 200 Hz] $\times$ ITD

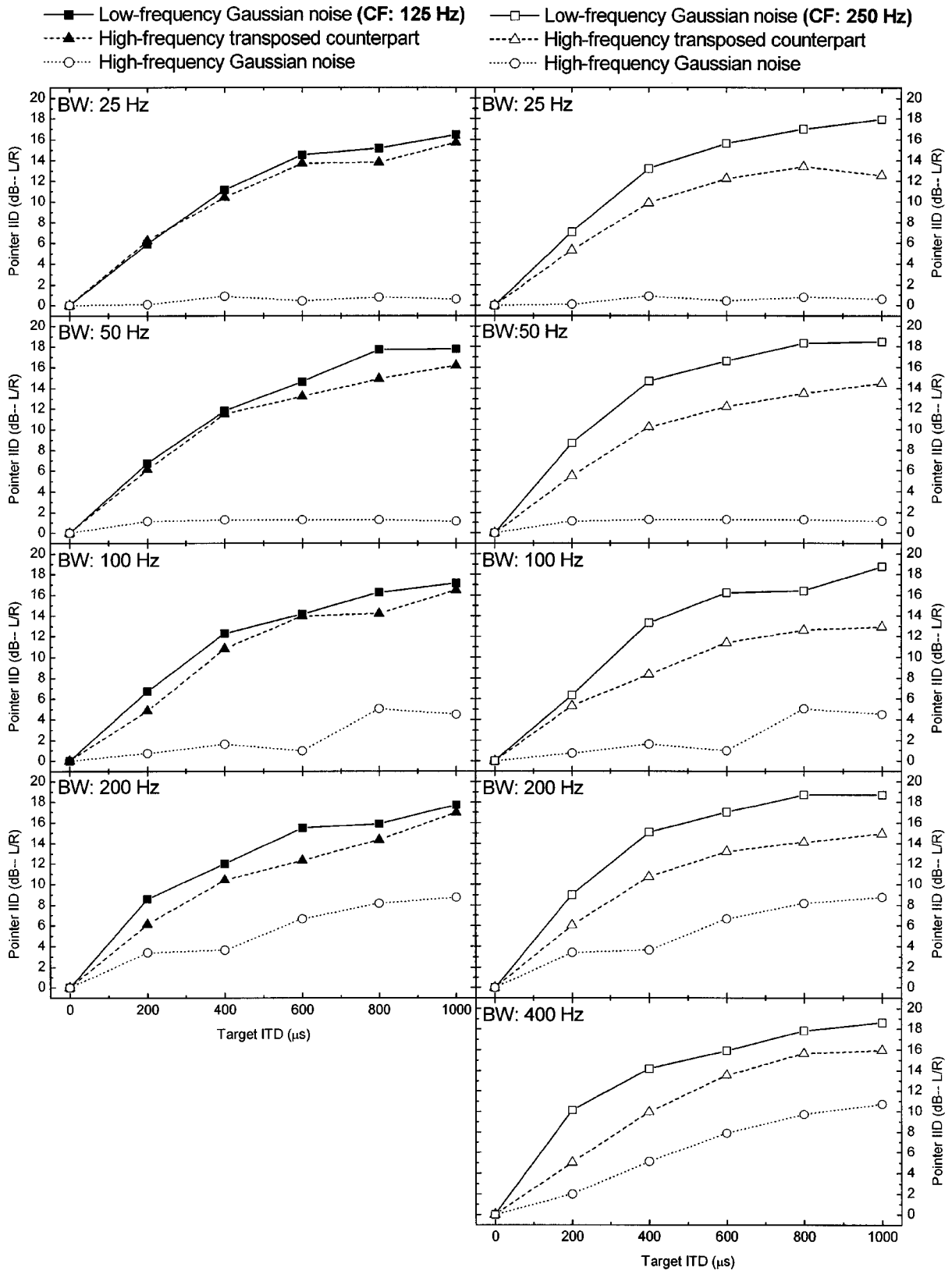

FIG. 2. IID of the pointer (in dB) required to match the intracranial position of the target as a function of the ITD (left ear leading) of the target. The data points represent the mean values computed across the four listeners. The positive values along the ordinate indicate IIDs favoring the left (leading) ear. The parameter within each plot is the type of stimulus employed. Squares represent data obtained with the indicated bandwidth of low-frequency Gaussian noise; triangles represent data obtained when that low-frequency noise was transposed to 4 kHz; circles represent data obtained with Gaussian noises of the indicated bandwidth centered at 4 kHz. Panels on the left contain data for low-frequency noises centered at 125 Hz; panels on the right contain data for low-frequency noises centered at 250 Hz.

[0, 200, 400, 600, 800, 1000 μs]) within-subjects, analysis of variance. In addition, the proportion of variance accounted for (ω^2) was determined for each significant main effect and interaction (Hays, 1973). Both the data obtained with a bandwidth of 400 Hz and the data obtained with the Gaussian bands of noise centered at 4 kHz were not included in the analysis. The former were omitted in order to make the statistical analysis completely factorial. The latter were omitted because the goal was to conduct a statistical analysis that compared extents of laterality produced by high-frequency transposed stimuli with extents of laterality produced by their low-frequency counterparts.

The error terms for the main effects and for the interactions were the interaction of the particular main effect (or the particular interaction) with the subject ''factor'' (Keppel, 1973). In order to remove interlistener differences (i.e., ''biases'') in the overall use of the acoustic pointer, we normalized the data. This was done, listener-by-listener, by dividing the IID of the pointer obtained for each stimulus condition by the value of IID required to match the 200-Hz-wide band of Gaussian centered at 250 Hz having an ITD of 1000 μs. While any of the stimuli could be used as the reference for normalization, that particular stimulus was chosen because it consistently produced, both within and across listeners, very large extents of laterality. The reasoning was that a stimulus that produces large extents of laterality would be one that could most clearly reveal differences among the listeners in their use of the acoustic pointer.

Consistent with visual evaluation of the data, the main effect of ITD was highly significant [$F(5,15)=69.13$, $p<0.0005$, $\omega^2=0.75$] and accounted for 75% of the variability of the data. The main effect of stimulus type (Gaussian noise or transposed noise) only approached significance [$F(1,3)=8.4$, $p=0.0629$, $\omega^2=0.04$], but did account for 3.5% of the variability in the data. Although the main effect of stimulus type was not significant, the interaction of center frequency by stimulus type was significant [$F(1,3)=35.91$, $p=0.009$, $\omega^2=0.006$] but only accounted for 0.6% of the variability in the data. This outcome provides statistical validation to the conclusion reached by visual inspection of the data that differences in extent of laterality produced by the bands of Gaussian noise and their high-frequency transposed counterparts are smaller at 125 Hz than at 250 Hz. The interaction of stimulus type by ITD was also significant [$F(5,15)=4.15, p=0.015, \omega^2=0.009$] but accounted for only 0.9% of the variability in the data. This outcome confirms statistically the observation that the differences found between the effects produced by low-frequency bands of Gaussian noise and their high-frequency transposed counterparts depend upon the magnitude of the ITD. These two interactions must be interpreted in light of the fact that the triple interaction of center frequency by stimulus type by ITD was also significant [$F(5,15)=4.11$, $p=0.015$, $\omega^2=0.002$] but only accounted for 0.2% of the variability in the data. The significance of the triple interaction means that the differences found between the effects produced by the low-frequency bands of Gaussian noise and their high-frequency transposed counterparts at the different ITDs depend upon center frequency. None of the other main effects or interactions reached statistical significance. The total proportion of variability in the data accounted for by the independent variables was 82% with 75% of the variance accounted for by ITD. Based on all of these numerical outcomes and visual inspection of the data, we conclude that high-frequency transposed stimuli produce extents of laterality that are substantial and comparable to those produced by low-frequency Gaussian noises.

III. EXPERIMENT 2

Measures of ITD-based extents of laterality obtained with *low-frequency stimuli* have revealed that across-frequency consistency of interaural timing information can influence greatly the intracranial position of acoustic images (e.g., Jeffress, 1972; Stern *et al.*, 1988; Trahiotis and Stern, 1989; Shackleton *et al.*, 1992; Buell *et al.*, 1994; Stern and Trahiotis, 1998; Trahiotis *et al.*, 2001). Stern and his colleagues (e.g., Stern *et al.*, 1988; Stern and Trahiotis, 1992, 1998) have discussed how across-frequency effects on lateralization can be accounted for within interaural cross-correlation models of binaural processing. Their explanation rests upon two aspects of a putative internal representation of the binaural stimuli. One aspect is termed ''straightness.'' It refers to the extent to which maxima of the internal interaural cross-correlation of the stimuli are consistent in that they occur at the same internal delay over a range of frequencies. The second aspect, termed ''centrality,'' refers to the extent to which maxima of the cross-correlation function are located at internal delays of small magnitude (i.e., near midline).

Within this conceptual framework, straightness and centrality are cast as two, sometimes conflicting, weighting functions that determine the relative salience of individual peaks of the cross-correlation function. The relative influences of straightness and centrality can be understood by considering the intracranial position of acoustic images produced by stimuli that have a constant value of ITD but differ in bandwidth.

To illustrate such effects, Fig. 3 represents trajectories of the peaks of the internal interaural cross-correlation function for bands of Gaussian noise centered at 250 Hz for values of internal delay between ± 4.0 ms. In what follows, combinations of ITD and interaural phase disparity (IPD) refer to the single value of ITD and the single value of IPD that were applied to all spectral components of any given bandwidth of noise. The top panel represents the condition when the bandwidth of the noise is 25 Hz and the stimulus has an ongoing ITD of 3.0 ms favoring the right ear. That ITD is equal to three-quarters of the period of the 250-Hz center frequency and produces peaks of activity in the cross-correlation function at an internal delay of 3.0 ms, -1.0 ms, and other ''slipped cycles'' of the spectral components of the 25-Hz-wide band of noise that would occur at internal delays with magnitudes greater than those depicted.

This 25-Hz-wide band of noise produces an intracranial image that is heard far toward the *left* (lagging) side of the head in accord with the activity at -1.0 ms. This stimulus condition represents a case in which centrality carries the greatest weight in determining lateral position because the

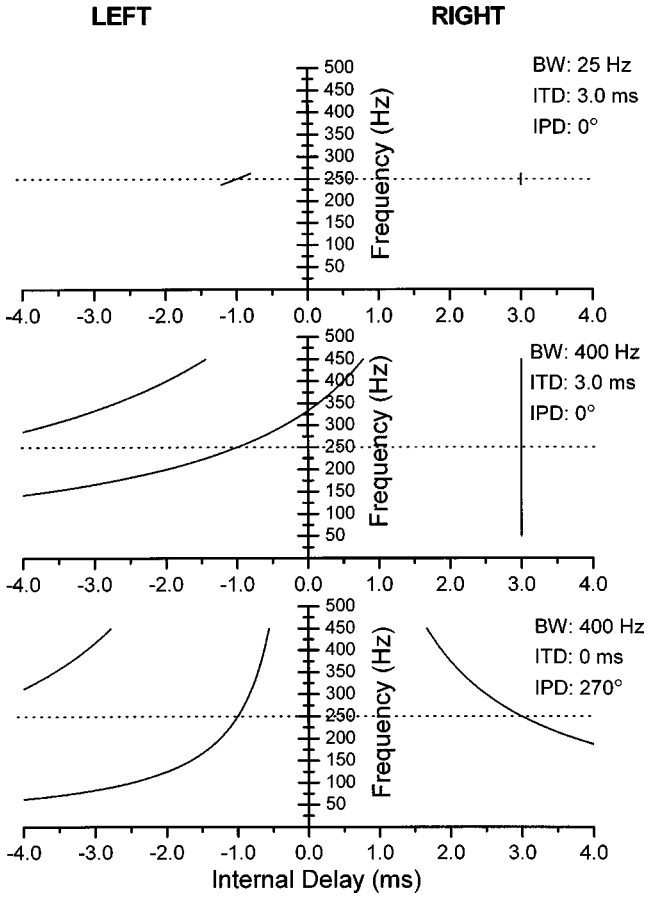

FIG. 3. Trajectories of the peaks of the internal interaural cross-correlation function for bands of Gaussian noise centered at 250 Hz. The three panels depict the trajectories for three combinations of bandwidth, ITD, and IPD.

activity at −1.0 ms (which is closer to the midline) outweighs the activity at the ''true'' delay of 3.0 ms.

The middle panel of Fig. 3 depicts the case when the bandwidth of the noise is increased to 400 Hz. In this case, across-frequency consistency is evident within the cross-correlation function as an extended straight vertical line at the true delay of 3.0 ms. Concomitantly, the trajectory passing through −1.0 ms exhibits ''curvature'' in that it spans a very large range of internal delay in a frequency-dependent manner. Also note the appearance of a third trajectory at the upper-left portion of the panel. This slipped-cycle trajectory also exhibits curvature over a large range of internal delay. This stimulus is lateralized far toward the *right* (leading) side of the head, consistent with the notion that the straight activity at an internal delay of 3.0 ms dominates perception.

The bottom panel of Fig. 3 depicts the cross-correlation function when the bandwidth of the noise remains 400 Hz and an IPD of 270° is imposed on the noise, rather than an ITD of 3.0 ms. At the 250-Hz center frequency of the noise, an IPD of 270° is equivalent to an ITD of 3.0 ms. Because this is so, the values of internal delay at 250 Hz, the center frequency of the noise, are the same in all three panels of the figure. That is, the trajectories for an IPD of 270° are ''anchored'' at the same positions as are the trajectories in the upper two panels for an ITD of 3.0 ms.

This 400-Hz-wide band of noise is lateralized toward the left side of the head. As can be seen from the figure, the only region within the cross-correlation function that is more or less straight occurs along the trajectory anchored at −1.0 ms and between about 250 and 450 Hz. Within our theoretical framework, this region would be expected to dominate perceived laterality because it is both the straightest and most central portion of the cross-correlation function.

It seemed natural and important to determine whether manipulations of ITD and IPD conveyed by the envelopes of high-frequency transposed stimuli would produce effects on perceived laterality that are similar to those observed with low-frequency stimuli. Beyond their empirical value, such data could provide valuable theoretical insights concerning the mechanisms underlying how *high-frequency envelope-based* binaural information is processed *vis a vis low-frequency, waveform-based* information. In order to obtain the necessary data, we used the same acoustic pointing task that was used in experiment 1 with the same four listeners.

It will be seen that manipulations of ITD and IPD within the envelopes of high-frequency transposed stimuli can, indeed, produce changes in lateralization that are very much like those observed with conventional low-frequency bands of noise. It will also be seen that, despite that similarity, a satisfactory theoretical account of the data appears to require different sorts of central processing of the pattern of activity within low versus high spectral regions.

A. Stimuli

The stimuli that served as targets in the acoustic pointing task were either (1) low-frequency bands of Gaussian noise centered at 250 Hz and having bandwidths of 25, 50, 100, 200, or 400 Hz or (2) such noises transposed to 4 kHz. In one low-frequency stimulus condition, the noise carried an ITD of 3.0 ms favoring the left ear and an IPD of 0°. In a second low-frequency stimulus condition, the noise carried an ITD of 0 ms and an IPD of 270° that favored the left ear. The high-frequency stimuli were centered at 4 kHz and were the transposed counterparts of the low-frequency stimuli. All other details of the generation of the stimuli and their presentation were the same as those described under experiment 1.

B. Results and discussion

Figure 4 is a plot of the mean IID of the pointer (taken across the four listeners) as a function of the bandwidth of the targets. The standard errors of the measures were typically less than 2.5 dB and never exceeded 5.5 dB. The parameter of the plot is the stimulus condition. Data obtained with low-frequency Gaussian noises are represented by open symbols and data obtained with their transposed counterparts are represented by closed symbols.

We begin with the data obtained with low-frequency bands of Gaussian noise having an ITD of 3.0 ms and an IPD of 0° (open squares). When the bandwidth was either 25 or 50 Hz, the mean IID of the pointer was about −16 dB, indicating an intracranial image far toward the right (lagging) ear. As bandwidth was increased, pointer IIDs became progressively and dramatically less negative. The data clearly indicate that, as bandwidth was increased, the intracranial position of the acoustic image moved away from the lagging

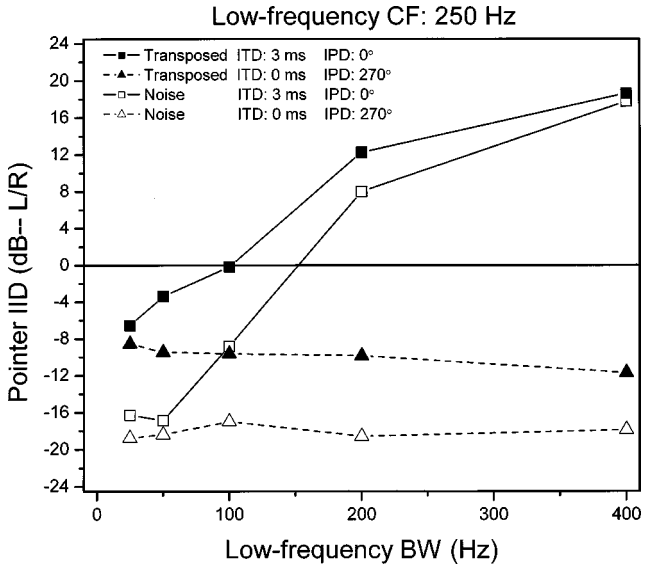

FIG. 4. IID of the pointer (in dB) required to match the intracranial position of the target as a function of the bandwidth of the target. The data points represent the mean values computed across the four listeners. Positive values along the ordinate indicate IIDs favoring the left (leading) ear; negative values indicate IIDs favoring the right (lagging) ear. The parameter of the plot is the type of stimulus employed. Open symbols represent data obtained with Gaussian noises centered at 250 Hz; closed symbols represent data obtained with their transposed counterparts centered at 4 kHz. Squares represent ITD/IPD combinations of 3000 μs/0°; triangles represent ITD/IPD combinations of 0 μs/270°.

ear, crossed the midline and, once the bandwidth reached 400 Hz, was essentially fully lateralized toward the leading (left) ear. In contrast, when the same bandwidths of Gaussian noise had an ITD of 0 ms and an IPD of 270° (open triangles), the mean pointer IID was about −18 dB or so for all bandwidths, indicating intracranial images very far toward the right ear. The pattern of these low-frequency data, obtained at a center frequency of 250 Hz, replicate the ''straightness/centrality'' effects reported by Trahiotis and Stern (1989) for bands of noise centered at 500 Hz.

The patterning of the data obtained with the transposed stimuli shows the same trends as the patterning of their low-frequency counterparts. One difference between the two sets of data is that the transposed versions of the noises having an ITD of 0 ms and an IPD of 270° (closed triangles) are not lateralized quite as far toward the lagging (right) ear as are the low-frequency bands of Gaussian noise.

The principal finding is, however, that the effects on lateral position brought about by imposing combinations of bandwidth, ITD, and IPD on low-frequency stimuli were also exhibited when such stimuli were transposed to 4 kHz. One might conclude from this that straightness and centrality along the internal cross-correlation surface influence lateral position in much the same manner for high-frequency transposed stimuli and low-frequency bands of noise. This is not necessarily true, as will become clear when the data are discussed further in Sec. IV A.

IV. ACCOUNTING FOR THE DATA

The primary objective of the theoretical analysis was to determine whether the observed extents of laterality could be accounted for by a correlation-based model that incorporates physiologically valid stages of peripheral processing. That type of model has been used to provide quantitative predictions for binaural detection, discrimination, and lateralization data (e.g., Bernstein and Trahiotis, 1996; Bernstein *et al.*, 1999; Trahiotis *et al.*, 2001; Bernstein and Trahiotis, 2002). The first stage of peripheral processing was bandpass filtering implemented via a bank of Gammatone filters (see Patterson *et al.*, 1995). For purposes of computational efficiency, the center frequencies of the filters ranged from 25 to 2000 Hz for stimuli centered at 125 and 250 Hz and ranged from 2000 to 8000 Hz for stimuli centered at 4000 Hz. The center frequencies of the filters were spaced in terms of their respective equivalent-rectangular bandwidths [according to Glasberg and Moore's (1990) ''ERB'' function] with the density of the filterbank being four filters per ERB. The output of each filter was subjected to ''envelope compression'' (exponent=0.23), square-law rectification, and low-pass filtering at 425 Hz to capture the loss of neural synchrony to the fine-structure of the stimuli that occurs as the center frequency is increased (for details, see Bernstein *et al.*, 1996). A stage of additional low-pass filtering at 150 Hz was imposed on the outputs of the high-frequency filters in order to capture a ''rate limitation'' that serves to ''smooth'' the fluctuations of their envelopes. Bernstein and Trahiotis (2002) have recently discussed several instances in which this rate limitation appears to operate and, further, they demonstrated how incorporating such a stage of low-pass filtering within the model was necessary in order to predict threshold-ITDs for high-frequency conventional and transposed stimuli.

The central binaural processor was implemented by generating cross-correlograms (i.e., cross-correlation surfaces) with one dimension representing frequency in steps defined by the density of the aforementioned filterbanks and a second dimension representing values of delay (τ) spanning the range −3500 to 3500 μs in 12.2-μs steps. The third dimension (height) was the value of the cross-products integrated over the 100-ms duration of the stimuli.

Predicted laterality was determined by computing the across-frequency average of the cross-correlogram and locating the value of τ associated with the most central peak of activity, i.e., the peak that was closest to the midline ($\tau=0$). This choice was based on the knowledge that, all other things being equal, peaks of the cross-correlation function that are closest to midline dominate perceived lateral position (e.g., Stern *et al.*, 1988). Examination of the cross-correlation functions revealed that the most central peak was, with very few exceptions, also the peak of the average correlogram that had the greatest magnitude. Consequently, the evaluation of the ability of the model to predict the data does not depend critically upon the choice of the most central peak as the decision variable.

A. Predictions of extents of laterality

Ten independent tokens of each combination of type of stimulus, bandwidth, and ITD used in experiment 1 served as inputs to the model. The output of the model for each token was an estimate of the position of the most central peak of activity in the across-frequency averaged correlogram. The

ten independent estimates obtained for each combination of type of stimulus, bandwidth, and ITD were averaged to yield a single prediction of the model for that stimulus. The predictions were in units of τ (*internal* delay).

In order to compare the predictions of the model to the empirical data, it was necessary to relate the "raw" predictions from the model, which were in units of τ, to units of IID of the acoustic pointer. In order to derive the required relation, we used the 25 and 200-Hz-wide bands of Gaussian centered at 125 and 250 Hz. For each combination of center frequency (125 or 250 Hz), bandwidth (25 or 200 Hz), and ITD (0 to 1000 μs in steps of 200 μs), the model's predicted value of τ was paired with the mean IID (in dB) of the pointer required by the listeners to match the intracranial position of that particular stimulus. That is, we assembled corresponding pairs of predicted τ and IID of the pointer for the 24 stimulus conditions of interest (2 CFs$\times$2 bandwidths $\times$6 values of ITD). Next, we found the exponential of the form $\mathrm{IID(dB)} = a(1-e^{-b\tau})$ that best fit (in the least-squares sense) the 24 pairs of τ and IID. This single function was used to obtain predicted values of IID for all of the stimuli.

Only the low-frequency stimuli were used to "calibrate" the model because (1) they, as a group, yielded the largest values of IID of the pointer for a given value of ITD and (2) their functions relating lateral position to ITD were quite similar over the range of ITDs used in the experiment. Therefore, each of the low-frequency stimulus conditions used in the analysis served to provide an independent estimate of the function relating pointer IID to predicted τ, the model's metric of lateral position.

Figure 5 displays both the obtained data (symbols) and the predictions of the model (lines). The format of the figure is similar to that of Fig. 2. A primary outcome is that the model correctly predicts that ITDs conveyed by low-frequency Gaussian noises and their transposed counterparts yield large and comparable extents of laterality. Quantitatively, the model accounts for 91% of the variance[2] in those data. That said, the model does not capture the finding that extents of laterality measured with low-frequency bands of noise centered at 250 Hz are slightly greater than those measured with their transposed counterparts. As discussed when the data were presented, the differences observed in terms of IID of the pointer must be interpreted while recognizing that IIDs greater than about 12 dB yield only very small, albeit reliable, changes in extent of laterality. Thus, overall, the model provides a fairly good account of the data obtained with low-frequency bands of noise and their transposed counterparts.

We now consider the predictions of the model for the data obtained with bands of conventional, Gaussian noise centered at 4 kHz (dotted lines). The model does appear to, at least qualitatively, account for two important aspects of these data. First, the model is generally correct in predicting that extents of laterality measured with the transposed stimuli centered at 4 kHz should be much greater than those measured with bands of Gaussian noise centered at that frequency. Second, the model is also generally correct in predicting that extent of laterality should, for a given value of ITD, increase with the bandwidth of the Gaussian noise. At the same time, the model consistently overpredicts the extents of laterality measured empirically.

We did attempt to improve the accuracy of the predictions by increasing the complexity of the model in several ways. This included applying several different functions that have been used by other investigators to emphasize activity within the cross-correlogram occurring at relatively small delays [i.e., the "centrality" functions specified by Colburn (1977), Stern and Shear (1996), and Shackleton *et al.* (1992)] and *ad hoc* modifications of them. We also investigated the utility of employing the centroid of activity of the cross-correlogram as the indicator of lateral position instead of its most central peak. These modifications of the model always diminished, sometimes dramatically, its overall ability to predict the major trends in the data. Based on the examination of many (more than 20) sets of predictions, it appears that at least some of the difficulty stems from not being able to specify and apply valid centrality weighting for frequency regions from as low as 125 Hz to as high as 4 kHz, or so. Said differently, it appears that at least some of the difficulty surrounds the fact that functional analogs of Stern and Colburn's centrality weighting function $[p(\tau)]$ have not been specified for frequencies below 250 Hz and above 1200 Hz (see Stern and Shear, 1996). This lack of knowledge concerning how to weight differentially portions of the patterns of activity that occur within different spectral regions of the cross-correlogram will also be seen to limit the model's ability to account for the data obtained in experiment 2.

We believe the qualitative successes of the model are potentially quite important and should not be discounted. In order to understand this conclusion, consider the data and predictions obtained when the bandwidth of the Gaussian noise centered at 4 kHz was 25 Hz (top panel in each column) and the ITD was 1000 μs. Note that the model correctly predicts that the Gaussian noise will be heard near midline while, simultaneously, predicting that the transposed stimulus centered at 4 kHz will be heard far toward the left (leading) ear. This means that, despite their common ITDs, the most central peaks of the cross-correlograms produced by these two stimuli, respectively, are in very different locations: one near the midline and the other one far toward the leading ear.

This outcome was, at least to us, highly nonintuitive. Specifically, it was not apparent how, according to the model, a large ITD conveyed by a 25-Hz-wide band of Gaussian noise centered at 4 kHz would produce a peak of activity near midline while the same ITD conveyed by a transposed noise centered at 4 kHz would produce a peak of activity far toward the leading ear. Our investigations revealed that envelope compression was a major factor. When compression was omitted, the peak of activity for the 25-Hz-wide band of high-frequency Gaussian noise (and indeed, for wider bandwidths) indicated a lateral position far toward the leading ear.

Figure 6 displays predictions of the data obtained in experiment 2.[3] The reader is reminded that the purpose of that experiment was to determine whether the patterns of laterality produced by low-frequency stimuli characterized by differential degrees of straightness and centrality (as depicted in

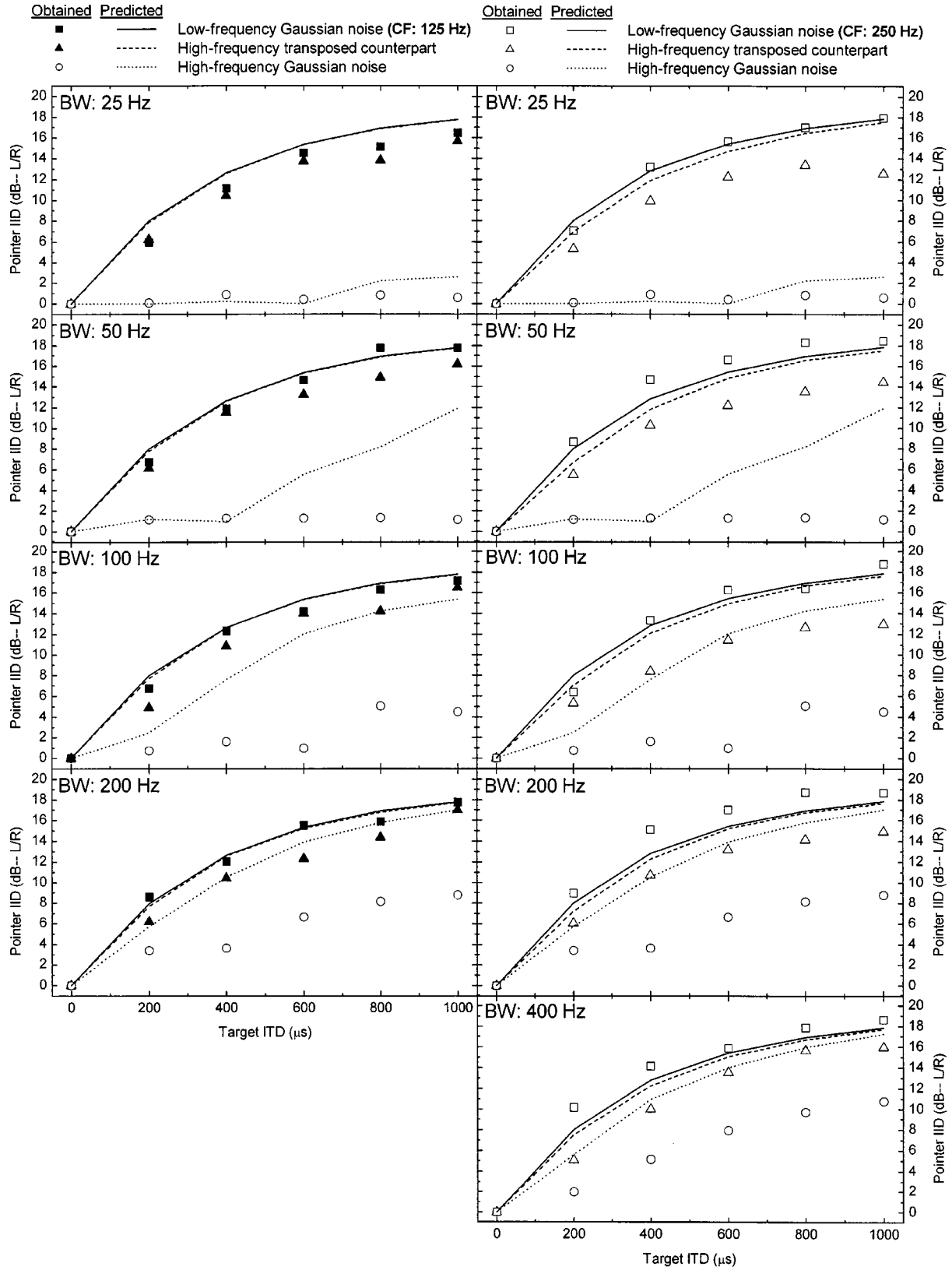

FIG. 5. Data and predictions for the stimuli utilized in experiment 1. The format of the figure is similar to that of Fig. 2. The symbols represent the obtained values of IID of the pointer and are replotted from Fig. 2. The lines represent predictions from the cross-correlation-based model described in the text.

Fig. 3) would also occur when those stimuli were transposed to 4 kHz.

The behavioral data from experiment 2 (Fig. 4) are replotted as an inset. The predictions of the model capture the important qualitative aspects of the data. The model correctly predicts that low-frequency Gaussian noises and their high-frequency transposed counterparts are lateralized toward the lagging ear for the ITD/IPD combination of 0 ms/270°. The

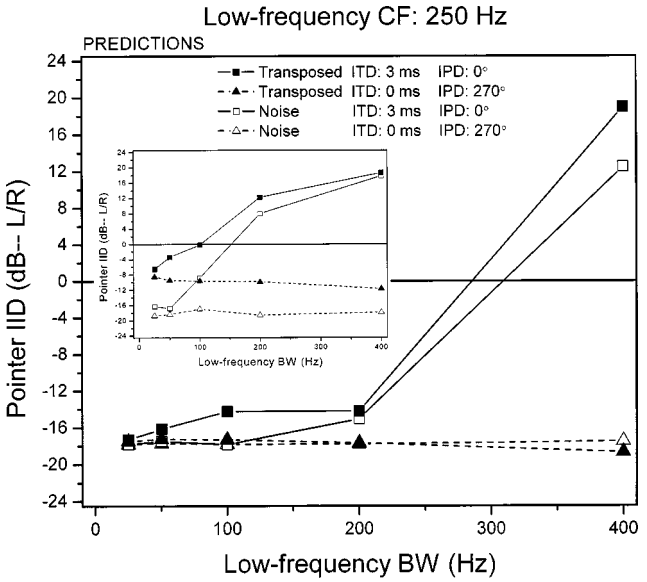

FIG. 6. Predictions for the stimuli utilized in experiment 2. The format of the figure is similar to that of Fig. 3. The behavioral data are replotted as an inset for comparison.

model, however, fails to capture the differences in laterality between the low-frequency Gaussian noises having an ITD/IPD combination of 0 ms/270° and their high-frequency transposed counterparts. A similar type of shortcoming was also evident for the predictions of the data in experiment 1 (see Fig. 4) for low-frequency Gaussian noises centered at 250 Hz and their transposed counterparts. There too, the transposed stimuli were incorrectly predicted to have essentially the same extent of laterality as their low-frequency counterparts.

For the 3.0 ms/0° case, the model correctly predicts that the narrowest bands of Gaussian noise and their high-frequency transposed counterparts are lateralized toward the lagging ear and that the 400-Hz-wide band of noise and its high-frequency transposed counterpart are lateralized far toward the leading ear. The predictions of the model, however, do not capture the gradual nature of the changes in the locus of the intracranial image evident in the empirical data as bandwidth is increased from 50 to 200 Hz. As shown by Stern and his colleagues (e.g., Stern *et al.*, 1988; Stern and Trahiotis, 1992, 1998), a successful account of such data, at least for stimuli centered at 500 Hz, stems from the incorporation of functions that weight differentially portions of the patterns of activity that occur within different spectral regions of the cross-correlogram. As discussed above, the specific weighting function required as a function of the center frequency of the stimuli are unknown. Our initial attempts to augment the model with several versions of such functions actually led to poorer predictions for the lateralization of our high-frequency stimuli centered at 4 kHz.

Another issue deserves comment. The similarities in the psychophysical data that did occur with low-frequency noises and their high-frequency transposed counterparts as a function of combinations of bandwidth and ITD/IPD need not have resulted from the operation of similar or identical pattern processing of their respective cross-correlograms. Consider that, at low center frequencies, the combining of binaural timing information *must occur* across narrow-band elements or filters in order for straightness to emerge. This is so because the bandwidths of the external stimuli that exhibit the effects of straightness often greatly exceed the relatively narrow bandwidths of the low-frequency auditory filters through which they are processed. For example, the 400-Hz-wide bands of noise centered at 250 Hz exceed by a factor of about 8 the equivalent rectangular bandwidth of the auditory filter at that center frequency (see Fig. 1 of Moore, 1997). Therefore, it seems inescapable that the observed effects of straightness on lateralization at low center frequencies must involve some type of, most likely central, across-auditory-filter integration.

In contrast, it appears that effects like those attributed to straightness can occur for *high-frequency transposed stimuli*, even *without* across-auditory-filter integration. In order to understand why this is so, consider that the vast majority of the energy of transposed stimuli centered at 4 kHz is contained within the approximately 500-Hz-wide auditory filter centered at that frequency. In fact, predictions of the model obtained using *only one* pair of left/right auditory filters centered at 4 kHz proved to be, for all intents and purposes, *identical* to those obtained when predictions were made using the entire bank of Gammatone filters.

Examination of cross-correlograms revealed that the envelope-based effects of consistency of internal delay for transposed stimuli centered at 4 kHz come about via changes in the damping of the cross-correlation function. Figure 7 illustrates these effects. The two panels display the cross-correlograms that result when an ITD of 3.0 ms is applied to either a 25-Hz-wide (upper panel) or a 400-Hz-wide (bottom panel) band of Gaussian noise centered at 250 Hz that is transposed to 4 kHz. As indicated by the arrows, the most central peak occurs at −0.9 ms for the 25-Hz-wide case and at 2.9 ms (essentially, at the ITD) for the 400-Hz-wide case. In fact, for the 400-Hz-wide case, the damping has changed the shape of the cross-correlogram such that *no peak* closer to the midline than 2.9 ms occurs. Therefore, it appears that, at least for high-frequency transposed stimuli, *within-filter effects* are sufficient to produce changes in laterality as large as those (almost certainly) produced by *across-filter* integration for low-frequency bands of noise.

V. SUMMARY AND CONCLUSIONS

The primary purpose of this investigation was to determine whether ITDs conveyed by high-frequency transposed stimuli would produce larger extents of laterality than ITDs conveyed by bands of high-frequency Gaussian noise. To that end, we employed an acoustic pointing task in order to measure extents of laterality for low-frequency Gaussian noises, the same noises transposed to 4 kHz, and high-frequency Gaussian bands of noise centered at 4 kHz.

The three major findings were the following: (1) Extents of laterality obtained with the transposed stimuli were much greater than those obtained with the bands of high-frequency Gaussian noise; (2) The low-frequency Gaussian noises centered at 125 Hz and their high-frequency transposed counterparts produced extents of laterality that were highly similar and, in many cases, essentially equivalent; (3) The low-

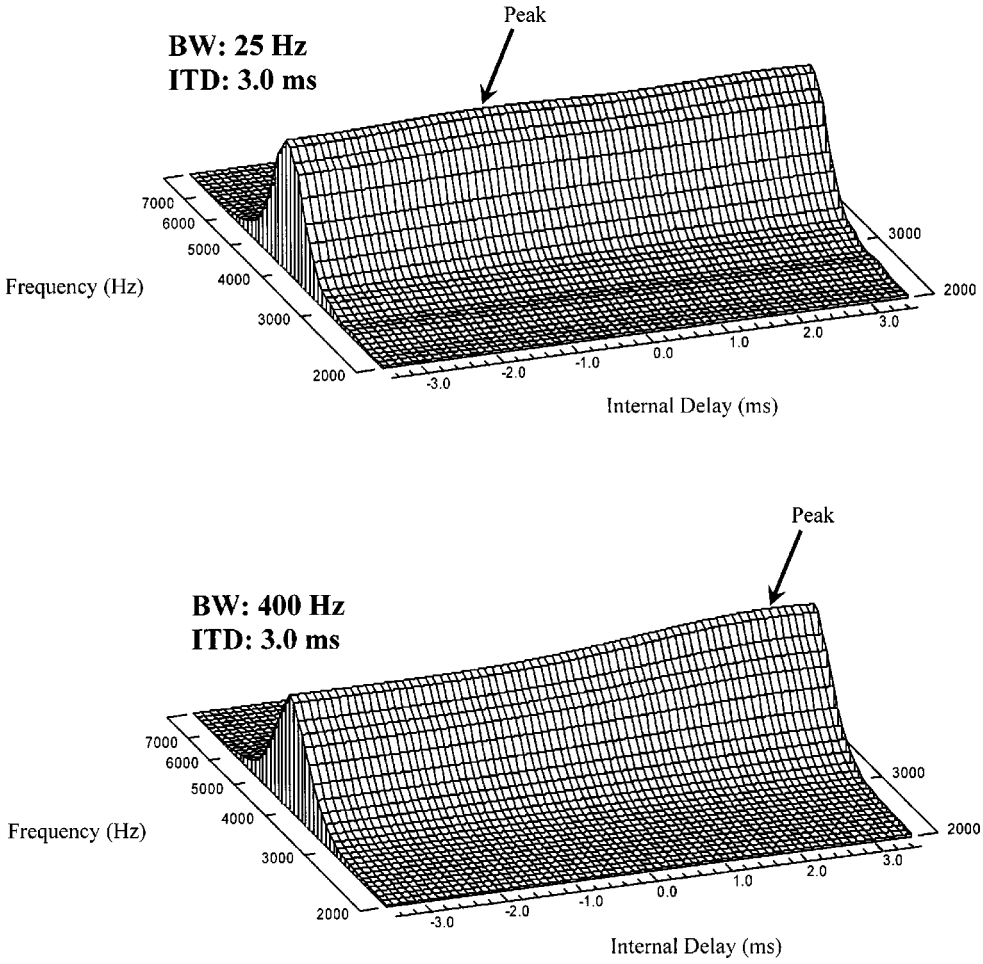

FIG. 7. Cross-correlograms for transposed stimuli generated by transposing 250-Hz-centered, 25-Hz-wide (upper panel) and 400-Hz-wide (lower panel) Gaussian noises to 4 kHz. The ITD is 3.0 ms. The arrows indicate the positions of the peaks of the respective cross-correlograms.

frequency Gaussian noises centered at 250 Hz produced somewhat greater extents of laterality than did their high-frequency transposed counterparts. The overall patterning of the data was fairly well accounted for by a cross-correlation-based model similar to the one used recently by Bernstein and Trahiotis (2002) to account for threshold ITDs obtained with similar conventional and transposed stimuli.

A second experiment was conducted to determine whether patterns of laterality produced by low-frequency stimuli characterized by differential degrees of straightness/centrality would also be produced when those stimuli were transposed to 4 kHz. It was found that the data obtained with the transposed stimuli exhibited much the same trends as did their low-frequency counterparts. That is, the general effects on the lateral positions of the intracranial images brought about by imposed combinations of bandwidth, ITD, and IPD on low-frequency stimuli remained when those stimuli were transposed to 4 kHz. The general features of the data were accounted for by the same cross-correlation-based model used to account for the data obtained in the first experiment.

The behavioral data obtained in this study, the masking-level difference (MLD) data obtained by van de Par and Kohlrausch (1997), and the ITD discrimination data obtained by Bernstein and Trahiotis (2002) all point to the same conclusion. That is, differences in the salience of and sensitivity to ITDs found between low and high spectral regions stem mostly from differences in the nature of the inputs to the central binaural processor, as opposed to inherent differences in the ability to process ITDs.

ACKNOWLEDGMENTS

This research was supported by Research Grant Nos. NIH DC-04147, DC-04073 and DC-00234 from the National Institute on Deafness and Other Communication Disorders, National Institutes of Health. The authors wish to acknowledge the extraordinary efforts of Dr. Michael Akeroyd who authored the software ''toolbox'' that facilitated greatly our ability to derive quantitative predictions of the data using a variety of versions of our cross-correlation-based model. We especially appreciate the diligence and care with which he documented his work, making the software easily accessible and useful to the scientific community at large. In addition, the authors thank Dr. D. Wesley Grantham and one anonymous reviewer for their insightful comments.

[1]We chose to ''calibrate'' the outputs of the Etymotic earphones to the nominal levels produced by the TDH-39s so that listeners in this study would receive levels of stimulation directly comparable to those utilized by us and others in prior psychophysical experiments employing TDH-39s. As discussed in detail by Bernstein and Trahiotis (2002), in order to do so, it was

necessary to impose a 10-dB larger voltage on the Etymotic ER-2 than would be expected on the basis of its calibration.

[2]The formula used to compute the percentage of the variance for which our predicted values of threshold accounted was $100\times(1-[\Sigma(O_i-P_i)^2]/[\Sigma(O_i-\overline{O})^2])$, where O_i and P_i represent individual observed and predicted values of threshold, respectively, and $\overline{O}$ represents the mean of the observed values of threshold.

[3]For these data, 100 independent estimates were obtained for each combination of type of stimulus, bandwidth, and ITD/IPD combination. The estimates were averaged to yield a single prediction of the model for each of these combinations.

Bernstein, L. R., and Trahiotis, C. (**1982**). ''Detection of interaural delay in high-frequency noise,'' J. Acoust. Soc. Am. **71**, 147–152.

Bernstein, L. R., and Trahiotis, C. (**1985a**). ''Lateralization of low-frequency, complex waveforms: The use of envelope-based temporal disparities,'' J. Acoust. Soc. Am. **77**, 1868–1880.

Bernstein, L. R., and Trahiotis, C. (**1985b**). ''Lateralization of sinusoidally-amplitude-modulated tones: Effects of spectral locus and temporal variation,'' J. Acoust. Soc. Am. **78**, 514–523.

Bernstein, L. R., and Trahiotis, C. (**1994**). ''Detection of interaural delay in high-frequency SAM tones, two-tone complexes, and bands of noise,'' J. Acoust. Soc. Am. **95**, 3561–3567.

Bernstein, L. R., and Trahiotis, C. (**1996**). ''The normalized correlation: Accounting for binaural detection across center frequency,'' J. Acoust. Soc. Am. **100**, 3774–3784.

Bernstein, L. R., and Trahiotis, C. (**2002**). ''Enhancing sensitivity to interaural delays at high frequencies by using 'transposed stimuli,'" J. Acoust. Soc. Am. **112**, 1026–1036.

Bernstein, L. R., van de Par, Steven, and Trahiotis, C. (**1999**). ''The normalized correlation: Accounting for $NoS\pi$ thresholds obtained with Gaussian and 'low-noise' masking noise,'' J. Acoust. Soc. Am. **106**, 870–876.

Blauert, J. (**1982**). ''Binaural localization: Multiple images and applications in room- and electroacoustics,'' in *Localization of Sound: Theory and Application*, edited by R. W. Gatehouse (Amphora, Groton).

Blauert, J. (**1983**). *Spatial Hearing* (MIT, Cambridge).

Brugge, J. F., Anderson, D. J., Hind, J. E., and Rose, J. E. (**1969**). ''Time structure of discharges in single auditory nerve fibers in the squirrel monkey in response to complex periodic sounds,'' J. Neurophysiol. **32**, 386–401.

Buell, T. N., Trahiotis, C., and Bernstein, L. R. (**1991**). ''Lateralization of low-frequency tones: Relative potency of gating and ongoing interaural delay,'' J. Acoust. Soc. Am. **90**, 3077–3085.

Buell, T. N., Trahiotis, C., and Bernstein, L. R. (**1994**). ''Lateralization of bands of noise as a function of combinations of interaural intensitive differences, interaural temporal differences and bandwidth,'' J. Acoust. Soc. Am. **95**, 1482–1489.

Colburn, H. S., and Esquissaud, P. (**1976**). ''An auditory-nerve model for interaural time discrimination of high-frequency complex stimuli,'' J. Acoust. Soc. Am. Suppl. 1 **59**, S23.

Colburn, H. S. (**1977**). ''Theory of binaural interaction based on auditory-nerve data II. Detection of tones in noise,'' J. Acoust. Soc. Am. **61**, 525–533.

Glasberg, B. R., and Moore, B. C. J. (**1990**). ''Derivation of auditory filter shapes from notched-noise data,'' Hear. Res. **47**, 103–138.

Hays, W. L. (**1973**). *Statistics for the Social Sciences* (Holt, Rinehart, and Winston, New York).

Heller, L. M., and Trahiotis, C. (**1996**). ''Extents of laterality and binaural interference effects,'' J. Acoust. Soc. Am. **99**, 3632–3637.

Henning, G. B. (**1980**). ''Some observations on the lateralization of complex waveforms,'' J. Acoust. Soc. Am. **68**, 446–453.

Jeffress, L. A. (**1972**). ''Binaural signal detection: Vector theory,'' in *Foundations of Modern Auditory Theory (Vol. 2)*, edited by J. V. Tobias (Academic, New York), pp. 349–368.

Johnson, D. (**1980**). ''The relationship between spike rate and synchrony in responses of auditory-nerve fibers to single tones,'' J. Acoust. Soc. Am. **68**, 1115–1122.

Keppel, G. (**1973**). *Design and Analysis: A Researchers Handbook* (Prentice-Hall, Englewood Cliffs, NJ).

Klumpp, R. G., and Eady, H. R. (**1956**). ''Some measurements of interaural time difference thresholds,'' J. Acoust. Soc. Am. **28**, 859–860.

McFadden, D., and Pasanen, E. G. (**1976**). ''Lateralization at high frequencies based on interaural time differences,'' J. Acoust. Soc. Am. **59**, 634–639.

Moore, B. C. J. (**1997**). ''Frequency analysis and pitch perception,'' in *Handbook of Acoustics*, edited by M. Crocker (Wiley, New York), Vol. III, pp. 1447–1460.

Nuetzel, J. M., and Hafter, E. R. (**1976**). ''Lateralization of complex waveforms: Effects of fine-structure, amplitude, and duration,'' J. Acoust. Soc. Am. **60**, 1339–1346.

Nuetzel, J. M., and Hafter, E. R. (**1981**). ''Discrimination of interaural delays in complex waveforms: Spectral effects,'' J. Acoust. Soc. Am. **69**, 1112–1118.

Palmer, A. M., and Russell, I. J. (**1986**). ''Phase-locking in the cochlear nerve of the guinea-pig and its relation to the receptor potential of inner hair-cells,'' Hear. Res. **24**, 1–15.

Par, S. van de, and Kohlrausch, A. (**1997**). ''A new approach to comparing binaural masking level differences at low and high frequencies,'' J. Acoust. Soc. Am. **101**, 1671–1680.

Patterson, R. D., Allerhand, M. H., and Giguere, C. (**1995**). ''Time-domain modeling of peripheral auditory processing: A modular architecture and a software platform,'' J. Acoust. Soc. Am. **98**, 1890–1894.

Rose, J. E., Brugge, J. F., Anderson, D. J., and Hind, J. E. (**1967**). ''Phase locked response to low-frequency tones in single auditory nerve fibers of the squirrel monkey,'' J. Neurophysiol. **30**, 769–793.

Shackleton, T. M., Meddis, R., and Hewitt, M. J. (**1992**). ''Across frequency integration in a model of lateralization,'' J. Acoust. Soc. Am. **91**, 2276–2279.

Stern, R. M., and Shear, G. D. (**1996**). ''Lateralization and detection of low-frequency binaural stimuli: Effects of distribution of interaural delay,'' J. Acoust. Soc. Am. **100**, 2278–2288.

Stern, R. M., and Trahiotis, C. (**1992**). ''The role of consistency of interaural timing over frequency in binaural lateralization,'' in *Auditory Physiology and Perception*, edited by Y. Cazals, L. Demany, and K. Horner (Pergamon, New York), pp. 547–554.

Stern, R. M., and Trahiotis, C. (**1998**). ''Binaural mechanism that emphasize consistent interaural timing information over frequency,'' in *Psychophysical and Physiological Advances in Hearing*, edited by A. R. Palmer, A. Rees, A. Q. Summerfield, and R. Meddis (Whurr, London), pp. 384–395.

Stern, R. M., Zeiberg, A. S., and Trahiotis, C. (**1988**). ''Lateralization of complex binaural stimuli: A weighted image model,'' J. Acoust. Soc. Am. **84**, 156–165.

Trahiotis, C., and Bernstein, L. R. (**1986**). ''Lateralization of bands of noise and sinusoidally amplitude-modulated tones: Effects of spectral locus and bandwidth,'' J. Acoust. Soc. Am. **79**, 1950–1957.

Trahiotis, C., and Stern, R. M. (**1989**). ''Lateralization of bands of noise: Effects of bandwidth and differences of interaural time and phase,'' J. Acoust. Soc. Am. **86**, 1285–1293.

Trahiotis, C., Bernstein, L. R., and Akeroyd, M. A. (**2001**). ''Manipulating the 'straightness' and 'curvature' of patterns of interaural cross-correlation affects listeners' sensitivity to changes in interaural delay,'' J. Acoust. Soc. Am. **109**, 321–330.

Watson, C. S., and Mittler, B. (**1965**). ''Time-intensity equivalence in auditory lateralization: A graphical method,'' Psychonomic Sci. **2**, 219–220.

Yost, W. A. (**1981**). ''Lateral position of sinusoids presented with interaural intensive and temporal differences,'' J. Acoust. Soc. Am. **70**, 397–409.

Zwislocki, J., and Feldman, R. S. (**1956**). ''Just noticeable differences in dichotic phase,'' J. Acoust. Soc. Am. **28**, 860–864.

A comparison of psychophysical procedures for level-discrimination thresholds[a)]

Peter Marvit[b)] and Mary Florentine[c)]
Institute for Hearing, Speech, & Language and Department of Speech-Language Pathology & Audiology (106-A FR), Northeastern University, 360 Huntington Avenue, Boston, Massachusetts 02115

Søren Buus[d)]
Institute for Hearing, Speech, & Language and Communications & Digital Signal Processing Center, Department of Electrical & Computer Engineering (440 DA), Northeastern University, 360 Huntington Avenue, Boston, Massachusetts 02115

(Received 18 December 2001; revised 22 February 2003; accepted 5 March 2003)

Five different psychophysical procedures were used to measure level-discrimination (also called intensity discrimination) thresholds for 1-kHz tones at two levels (30 and 90 dB SPL) and two durations (10 and 500 ms). The procedures were the classic transformed up–down staircase method with a two-alternative forced-choice (2AFC) paradigm (UPD), 15- and 50-trial implementations of the method of maximum likelihood (MML) with a cued yes–no paradigm, and 18-trial implementations of ZEST using both cued yes–no and 2AFC paradigms. Results obtained from nine normal listeners show that estimates of level-discrimination thresholds for the four conditions are similar across all five procedures when different points of convergence are accounted for. The variance of threshold estimates within listener and condition was smallest for UPD, largest for the MML with 15 trials, and statistically indistinguishable among the others. The sweat factors ranged from 5.5 for MML with 50 trials to about 1.4 for UPD and ZEST. Simulations show that ideal performance of procedures may be far from real-life experience and that these deviations are likely to depend on complex interactions between listener behavior and parameter choices used for implementing the procedures. Therefore, empirical verification is important for judging the effectiveness of psychophysical procedures.
[DOI: 10.1121/1.1570445]

PACS numbers: 43.66.Yw, 43.66.Fe [MRL]

I. INTRODUCTION

Psychophysical procedures must satisfy three conditions: accuracy, speed, and reliability. Despite a great deal of literature on individual adaptive psychophysical procedures and their variations (see Macmillan and Creelman, 1991), relatively few studies have performed empirical comparisons across several procedures (e.g., Creelman and Macmillan, 1979; Kollmeier *et al.*, 1988; Plattsmier and McFadden, 1988). This paper compares some psychophysical procedures that may be useful for rapid assessment of an individual's auditory processing. It examines several procedures not included in the existing studies and extends the prior work by using a supra-threshold level-discrimination task.

The investigation and comparison of psychophysical procedures has historically been fraught with ambiguities in their descriptions. Here, we propose a taxonomy that attempts to provide a common set of terms and a structure within which to understand both the current study and other results from the literature (see also Buus, 2002). Most psychophysical procedures comprise two aspects that, at least in principle, are quite separate although in practice are intertwined. The first aspect of *procedure* we call *paradigm*. The *paradigm* is further decomposed to the *mode of stimulus presentation* (i.e., the way stimuli are presented) and the *listener's task*. The *mode of stimulus presentation* also has two parts—the number of intervals in a trial and the content of those intervals. The *listener's task* (or just *task*) describes exactly what the listener must do when presented with the stimuli during a trial. Two typical examples of paradigms are the one-interval yes–no paradigm and the symmetrical 2I-2AFC (two-interval, two-alternative forced choice) paradigm. The first paradigm presents a single stimulus and the listener's task is to decide whether *that* stimulus fulfills some criterion or not. The second paradigm presents two sequential stimuli and the task requires the listener to choose *which one* satisfies some criterion. The second aspect of *procedure* we call *method* (after Fechner and in deference to the common usage in naming methods such as the method of limits, method of adjustment, etc.). The *method* describes the rules used to select the series of stimuli in the course of a measurement and a definition of the result of the measurement. Whereas the word ''method'' is also used as a major heading for describing the entire experimental design (including stimuli, apparatus, etc.), we believe that the chance of confusion over this double usage is small. We expect that the context of discussing an aspect of a psychophysical procedure will make clear this narrower, more technical usage of

[a)]Portions of this work were presented at the 25th Annual Midwinter Research Meeting of the Association for Research in Otolaryngology in January 2002 [Marvit *et al.*, Abs. 25th Ann. Mid-Winter Mtng. Assoc. Res. Otolaryngol., 178 (2002)].
[b)]Electronic mail: peter@marvit.org. Current affiliation: University of Maryland Medical School, Dept. of Anatomy & Neurobiology, 685 West Baltimore St., HSF 222, Baltimore, MD 21201.
[c)]Electronic mail: florentin@neu.edu
[d)]Electronic mail: buus@neu.edu

''method'' to describe what is often a named method. In our terminology, the method also has two parts. First, the *measurement strategy* (or just *strategy*) describes the set of three rules that govern the progress of a procedure: (1) the *starting rule* determines the stimulus for the first trial, (2) the *progression rule* determines the stimulus for the next trial given the stimuli presented and responses received, and (3) the *stopping rule* determines when to end the set of trials. Second, the *datum definition* specifies how to derive the result of the measurement given the stimuli that were presented and the listener's response to them [e.g., the mean of a presented even number of reversals at the end of the staircase, the mean of the final probability density function (p.d.f.) for ZEST, the midpoint of the most probable psychometric function for MML, etc.]. Ideally, comparisons of different procedures account for this taxonomy.

The current study investigated various combinations of two paradigms and three methods. The two paradigms we chose were cued yes–no and two-alternative forced-choice (2AFC). In many situations (e.g., clinical testing), it may be preferable to use a yes–no paradigm. There are at least three distinct advantages. First, listeners often like it and find it easy to perform. Second, it is conceptually easy to understand. Third, psychometric functions are steep because they encompass a large range of response rates (i.e., it maximizes the slope of the psychometric function being measured). However, a significant disadvantage of the yes–no paradigm is that it is highly sensitive to both the position and stability of listeners' response criterion (Florentine *et al.*, 2001). The 2AFC paradigm, on the other hand, is relatively insensitive to the listener's response criterion; however, the psychometric function is relatively shallow—typically the slope is about half that for the yes–no paradigm. Other paradigms may be better for precision, stability, and psychometric-function range (e.g., 3AFC, Schlauch and Rose, 1990), but tend to require more time for a single trial, which is counter to our goal of rapid and sufficiently precise difference-limen measurements. Moreover, the difference in performance between 2AFC and 3AFC is negligible when used with up–down methods that target around 80% correct (Schlauch and Rose, 1990). Thus, in the interest of obtaining short testing times we chose the 2AFC paradigm for the present investigation.

The first of the three methods tested in the present study is the method of maximum likelihood (MML, see Green, 1993), which is a promising method that offers a relatively reliable measurement using far fewer trials than many traditional up–down methods (e.g., Florentine *et al.*, 2000; see, however, Buss *et al.*, 2001). Recent work has shown that MML can produce reliable threshold estimates for detection (Green, 1993; Leek *et al.*, 2000), frequency and level discrimination (He *et al.*, 1998), and gap detection (He *et al.*, 1998; Florentine *et al.*, 2000, 2001). Further, it has been shown that as few as 12–15 trials per block are sufficient to produce accurate threshold estimates (Green, 1993; Florentine *et al.*, 2001), though some experiments have used as many as 50 (e.g., He *et al.*, 1998).

The MML employs a set of candidate psychometric functions that can be described by a small number of parameters such as their midpoints and false-alarm rates. The most probable psychometric function is used to determine the next stimulus presentation value or the final threshold estimate, based on the cumulative set of listener responses to prior stimulus values. In general, MML has been used with yes–no paradigms, although there has been at least one successful application of MML using a standard 2AFC paradigm using a 93% correct progression rule and datum definition (Dai and Green, 1992). We are unaware of any systematic investigations of the effect of a 2AFC paradigm on the MML method. So, to keep with the preponderance of the MML implemented with yes–no paradigms in the literature, we have chosen to follow suit.

The present study employs two variations of the MML. They differ only in the number of trials, 15 or 50, used to obtain one estimate of the difference limen. Using our terminology, these two procedures employ the same paradigm and their methods differ only in the number of trials (i.e., the stopping rule). Varying this parameter allows us to examine further Florentine *et al.*'s (2001) finding that the reliability of the MML did not necessarily improve when the number of trials increased by investigating whether it generalizes to a different task—i.e., level discrimination instead of gap detection.

The second method to be tested in the present study is the transformed up–down method (UPD, see Levitt, 1971). The transformed up–down method has several advantages. It is widely accepted in the literature, providing a ''reference procedure'' with which to compare other procedures. Its accuracy and reliability are very high, even in the face of listener inattention and guessing (Levitt, 1971). A variety of progression rules allow the threshold estimate to converge on almost any desired percentage of correct responses (Levitt, 1971; Kaernbach, 1991). The current study uses a three-down, one-up progression rule, converging on 79.4% correct, because it tends to be more stable and less variable than the popular two-down one-up (for discussion, see Kollmeier *et al.*, 1988) and because it is used extensively in our laboratory (e.g., Hicks and Buus, 2000; Oxenham and Buus, 2000). Finally, the transformed up–down progression rule requires few assumptions about the underlying psychometric function. One disadvantage, at least in common practice, is that robustness comes at the price of a relatively large number of trials per threshold estimate (see, however, Hicks and Buus, 2000; Buss *et al.*, 2001). The transformed up–down method is often employed with a 2AFC paradigm, so we employ this pairing as another of the tested procedures for the current study.

The last method to be tested is ZEST (King-Smith *et al.*, 1994). Like its immediate predecessor QUEST (Watson and Pelli, 1983), ZEST is used in the field of visual psychophysics, but is nearly unknown in auditory research. It offers much of the same promise of fast, accurate, and reliable estimates as MML, but with possibly more general applicability. Only simple changes of parameters are needed to use ZEST in a 2AFC rather than a yes–no paradigm. Its major features are the use of an *a priori* estimate of an initial probability distribution for each parameter used to describe the psychometric functions, and the subsequent use of a Baye-

sian framework to calculate new p.d.f.'s based on likelihood functions of the listener's response to the stimulus value presented. Recent simulations and empirical work (King-Smith *et al.*, 1994) suggest that ZEST is robust to variations in a number of the different method parameters (e.g., shape and placement of the initial p.d.f., the response probability estimated by the datum definition, and slope of the psychometric function). Like MML, ZEST can produce a threshold estimate in relatively few trials and so was implemented in this study to use the same number of trials per block as the shorter version of MML. Additionally, the ZEST method was paired with the 2AFC and cued yes–no paradigms to create the last two procedures to be tested. These procedures round out the set investigated in the present study and provide a bridge between the transformed up–down and MML procedures by comparing the 2AFC and yes–no paradigms while keeping the method constant.

A recent study investigating MML with a level-discrimination task (He *et al.*, 1998) concentrated on a limited range of difference limens. It is an open question whether the method they used and other rapid methods maintain their reliability and accuracy over a wider range of stimuli and difference limens. To allow comparison with the existing literature and provide relatively extreme stimulus values in a level-discrimination task, we chose relatively extreme values of two parameters of the stimuli. Keeping the frequency of stimulus tones constant at 1000 Hz, we chose parameter values that produce relatively large difference limens (10 ms duration and 30 dB SPL pedestal level), relatively small difference limens (500 ms duration and 90 dB SPL pedestal level), and difference limens between the extremes (10 ms duration at 90 dB SPL and 500 ms duration at 30 dB SPL). Thus, while holding procedure constant, we can compare the performance in conditions that yield a wide range of difference limens.

Keeping within the taxonomy of psychophysical procedures, we tested five different procedures in the same listeners so that we could directly compare the implemented methods (including block lengths) and paradigms using stimuli that would cover a wide range of underlying psychometric functions. Ideally, one would want to keep all related parameters constant across procedures—or, better yet, vary them systematically to optimize the performance of each procedure. Practical limitations constrained the present study to a small selection of the myriad possible permutations and thus restricted the range of detailed comparisons. However, despite the many differences between the procedures implemented in this study, many of the essential properties can be realistically compared. Thus, at least, the results of this investigation will provide an empirical assessment of successes and limitations of the specific implementations of the procedures for one task; at most, they will provide sufficient information to make tentative generalizations about different aspects of the procedures and point to areas for further study and systematic comparison.

II. METHODS

A. Stimuli

Tones at 1000 Hz were presented at two pedestal levels (30 and 90 dB SPL) and with two durations (10 and 500 ms). All signals were shaped with 5-ms raised-cosine ramps. Durations were determined between the half-amplitude points of the envelope. The ''signal'' was an increase in overall level (ΔL) that was produced by digitally scaling the amplitude of the stimulus. The initial ΔL presented for each procedure was 10 dB for 10-ms tones at 30 dB SPL, 5 dB for 10-ms tones at 90 dB SPL and 500-ms tones at 30 dB SPL, and 3 dB for 500-ms tones at 90 dB SPL.

B. Apparatus

Each listener was individually tested in a double-walled sound-attenuating booth. Stimuli were generated on a PC-compatible computer with a digital signal processor (TDT AP2). The computer also recorded the listeners' responses and executed the psychophysical procedures. The digitally synthesized stimuli were output from a D/A converter (TDT DD1, sample rate$=41.67$ kHz) and led to a low-pass filter (TDT FT5, $f_c=20$ kHz, 135 dB/octave). The analog signals were then fed to a programmable attenuator (TDT PA4) and a headphone amplifier (TDT HB6), which then played the stimuli through one earpiece of a Sony MDF-V6 headphone. The programmable attenuator was used to set the pedestal level.

C. Listeners

Nine listeners with normal hearing participated: three men and six women, with ages spanning 18–40 years. Their pure-tone audiometric thresholds between 0.25 and 8 kHz were less than or equal to 15 dB HL (ANSI, 1989). Three had previous experience with psychophysical tasks, but none had experience with level discrimination.

D. Procedures

Five different psychometric procedures were used, repeated over six testing sessions. Procedure order was counter-balanced over listeners and sessions. One testing session generally took 1.5–2 h. Listeners could take a break at any time and were required to take a break halfway through a session. Before difference-limen (ΔL_{DL}) estimates were taken, all listeners practiced level discrimination using the transformed up–down procedure (UPD, detailed below) for 2–3 sessions. A brief description of each procedure follows.

UPD—This procedure uses a two-interval, two-alternative forced-choice paradigm with feedback. Difference limens were estimated using an adaptive staircase method with a three-down, one-up progression rule converging on 79.4% correct (Levitt, 1971). When the progression rule of the UPD procedure increased ΔL, the ΔL was multiplied by a step factor; when ΔL decreased, it was divided by a step factor. The initial step factor was $10^{0.25}$ ($\sim$1.78) and then decreased to $10^{0.1}$ ($\sim$1.26) after two reversals. Listeners were presented with two tone bursts separated by a 500-ms ISI (interstimulus interval). Lights on the response

box were illuminated to indicate whether the sound was the first or second of the pair. The listener's task was to decide which of the pair of tones was louder, and then press the appropriate response button. The more intense (i.e., putatively louder) signal could be in either interval with equal probability. After choosing, listeners received visual feedback as to which interval actually had the higher-level tone. As with prior studies from this laboratory (e.g., Florentine *et al.*, 1996; Hicks and Buus, 2000), a single difference limen measurement was computed from three concurrent interleaved tracks within a single condition. The stopping rule specified that each track stopped after five reversals and the datum definition used the geometric mean of the level differences at the last two reversals as that track's ΔL_{DL}. A single ΔL_{DL} estimate was computed as the geometric mean of the three tracks' thresholds. On average, 85 trials were required to obtain one ΔL_{DL} estimate.[1]

The use of three interleaved tracks is unusual in the literature; much more frequent is a single track with around 50 trials (Shelton *et al.*, 1982). Functionally, the interleaved tracks provide three separate threshold estimates. Prior work in this laboratory (Hicks and Buus, 2000) has shown that this implementation is extremely stable, provides a reliable metric that can be used to eliminate outliers, and produces threshold estimates similar to those obtained from psychometric functions measured by the method of constant stimuli. Buss *et al.* (2001) similarly demonstrated that short track lengths produced reliable threshold estimates. Finally, simulations conducted in the present study indicate that our three-track procedure is as efficient as single 50-trial tracks.

MML-50—This procedure uses a cued yes–no paradigm [also called a ''reminder same–different'' paradigm by Macmillan and Creelman (1991)] without feedback, and estimates ΔL_{DL} by the method of maximum likelihood (MML, Green, 1993; Florentine *et al.*, 2000). The parameters used for the MML procedure are similar, though not identical, to those used by He *et al.* (1998). Each threshold estimate consisted of 50 trials, plus three supra-threshold ''warm-up'' trials at the beginning of a block. Each trial had two tone bursts separated by a 500-ms ISI, with lights on the response box illuminated to indicate the first or second sound. The first interval (the ''cue'') was always at the pedestal level and the second (target) interval was always more intense. ''Catch trials'' with an inaudible 0.05-dB level difference were included to provide an estimate of the false-alarm rate; 20% or 10 trials of the 50 in a block were randomly selected to be catch trials to improve the false-alarm estimate.[2] Listeners pressed ''Different'' on a response box if they decided that the second interval sounded louder and ''Same'' if it did not. No feedback was provided because the correct answer depended on the listener's perception and could not be defined objectively.

The MML procedure has been detailed in a previous paper from this laboratory (Florentine *et al.*, 2000) and is similar to the one described by Green (1993). Briefly, for a given block, a set of candidate psychometric functions is represented by a logistic function of the form

$$P_{\mathrm{yes}} = a + \frac{1-a}{1+\exp(-k[\log\langle \Delta L\rangle - \log\langle M\rangle])}, \tag{1}$$

where a is the false-alarm rate, ΔL is the level difference in dB, M is the midpoint of the psychometric function, and k is a free parameter that determines the slope. The log transforms in the equation were used to produce psychometric functions that maintain their shape on a logarithmic scale of ΔL; Buus and Florentine (1991) have shown that d' is proportional to ΔL, so a log scale of ΔL is the most appropriate scale. The value of k ($k=6$ in this study) was chosen to produce a logistic function whose slope closely matched that of the cumulative Gaussian function obtained when d' is proportional to ΔL and the false-alarm rate is fixed at 10%. The set of candidate psychometric functions was uniformly spaced on a log scale of ΔL (i.e., equal ratios across 81 midpoints from 0.01 to 20 dB) and the set of false alarm rates ranged from 0% to 40% in steps of 10%. The progression rule specifies that, after each trial, the method chooses the psychometric function that yields the highest probability for obtaining the responses provided by the listener given the stimuli presented. The ΔL for the next trial is set to yield 60% ''yes'' responses according to the most probable psychometric function.

At the end of the experiment, the datum definition specifies that the midpoint, M, of the most probable psychometric function be used to estimate ΔL_{DL}. In our implementation, at the end of a block, the most probable psychometric function was recomputed based on the set of responses for that block using a finer granularity of possible functions. That is, a new set of candidate psychometric functions was examined using a midpoint step size of 0.1 times and a false-alarm rate step size of 0.5 times the original, centered around the previously estimated most likely function. This was done in case the original granularity introduced quantization error in the estimates. In practice, there was no difference between the original estimates and the recomputed estimates using a finer-grained set of potential functions.

MML-15—This procedure is identical to MML-50, except a threshold estimate used only 15 trials (plus three supra-threshold ''warm-up'' trials) with 20% (i.e., three) of the trials being catch trials. For both MML procedures, threshold estimates were excluded from analysis and were rerun when the estimated false-alarm rate (i.e., the false-alarm rate of the most probable psychometric function) was 25% or more.

ZEST—Like the MML procedures, this procedure uses the cued yes–no paradigm without feedback. The method has been detailed elsewhere (King-Smith *et al.*, 1994) and is a variation of QUEST (Watson and Pelli, 1983). It begins with a p.d.f. that represents the experimenter's ''guess'' of the probable distribution of the listener's threshold. This guess is represented by a p.d.f., because the exact value of the threshold is not known and is therefore best represented by a range of values with associated probabilities. The initial p.d.f. was a modified hyperbolic secant of the form

$$q_0(T) = A/[Be^{-C(T-t)} + Ce^{B(T-t)}], \tag{2}$$

where T is $\log(\Delta L_{\mathrm{DL}})$, A is a scale factor, which determines the maximum value of the function and can be set to ensure that the area under the p.d.f. is equal to unity, B and C determine the slopes at high and low thresholds respectively, and t is the log of the difference limen at which the p.d.f. reaches its maximum. In the present study, we used $B=C=2.5$ (i.e., symmetric slopes) and the initial t was the logarithm of the first ΔL used for each condition (see Sec. II A).[3] After each trial, Bayes' theorem is then applied to calculate a new p.d.f. based on the listener's response; essentially, the value of the prior p.d.f. at any given T is multiplied by the probability for the response to the stimulus presented assuming that the actual threshold equals T. The psychometric function used in ZEST has a Weibull distribution and is given by

$$P_{\mathrm{yes}}=1-\delta-(1-\gamma-\delta)\exp[-10^{\beta(x-T+\varepsilon)}], \tag{3}$$

where γ is the false-alarm rate, δ is the false-negative (miss) rate, β determines the slope of the psychometric function, x is the stimulus value being presented, and ε determines the threshold criterion (King-Smith *et al.*, 1994). The values of the parameters used in the present study are $\gamma=0.10$, $\delta=0.02$, $\beta=6$, and $\varepsilon=0$ (corresponding to a probability of 0.6566 for responding "yes" to a stimulus at threshold). After completion of the experiment, we noted that the value of β caused the central part of the Weibull function to have a slope about four times steeper than that of the psychometric functions for human listeners. As will be evident from the results, ZEST performed well despite this error. Note also that our implementation of the ZEST procedure keeps the false-alarm rate fixed. Given this form of the psychometric function, the new p.d.f. after trial i is given by

$$q_i(T)=p(r_i,T,x_i)q_{i-1}(T), \tag{4}$$

where $p(r_i,T,x_i)$ is the probability of response r_i (0=no [difference] or wrong, 1=yes [there was a difference] or correct), given that the stimulus was $x_i=\log(\Delta L)$ and assuming that the listener's true difference limen is equal to T (i.e., P_{yes} for $r_i=1$ and $1-P_{\mathrm{yes}}$ for $r_i=0$). For each T, $p(r_i,T,x_i)$ is pointwise multiplied by $q_{i-1}(T)$, which is the p.d.f. from the previous trial. The progression rule and datum definition are similar; the mean of the new p.d.f. is used to determine the next stimulus value, or the final estimate of ΔL_{DL} at the end of a block. Figure 1 uses experimental parameters and initial values for the 90-dB, 500-ms condition to illustrate the initial state of the ZEST method and subsequent calculations for the first trial. This ZEST procedure used 18 trials in a block to duplicate the total number of trials employed by the MML-15 procedure.

ZEST2—This procedure is essentially the same as ZEST, but uses the same 2AFC with feedback paradigm as the UPD procedure. The parameters in ZEST2 were therefore the same as ZEST except that the false-alarm rate, γ, was set at 0.50 (i.e., random guessing) and the miss-rate, δ, was set to 0.01 to reflect an inattention rate of 0.02 similar to that implied by the miss-rate of 0.02 used in ZEST. These parameters made the threshold probability of a correct response equal to 0.810 for a stimulus at threshold.

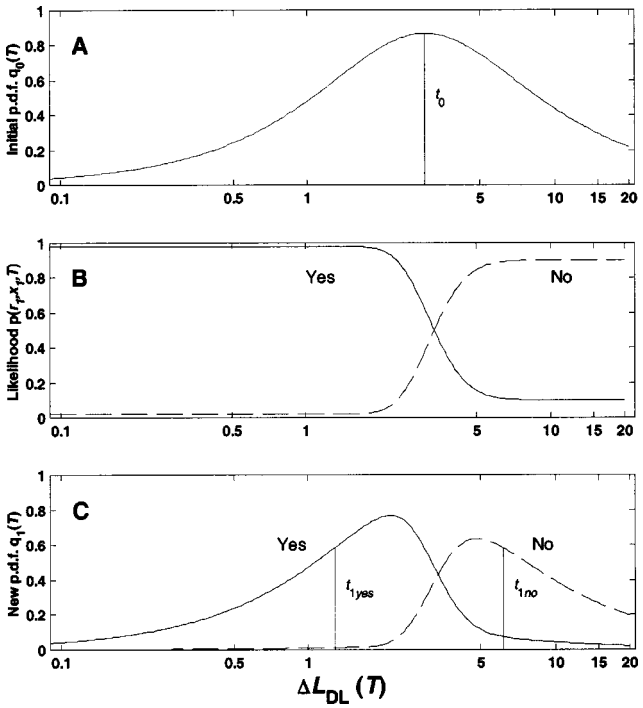

FIG. 1. Illustration of calculations associated with the initial state and first trial for the ZEST method for the stimulus condition of 90 dB SPL and 500 ms using the yes–no paradigm. All the illustrated functions use the ZEST parameter values described in the text. (a) The initial probability density function (p.d.f.), $q_0(T)$. The range of ΔL_{DL}'s is limited for visual clarity. The vertical line indicates the initial ΔL ($t_0=3$ dB). (b) Likelihood functions for "yes" and "no" responses to the first trial. The "yes" likelihood function is the probability that the listener responds "yes" to the 3-dB level difference if the ΔL_{DL} were T (on the abscissa). (c) The initial p.d.f. in (a) is pointwise multiplied by the appropriate likelihood function in (b) to produce the new p.d.f., $q_1(T)$. The next trial is presented with ΔL set to the mean of $q_1(T)$, which is also an estimate of ΔL_{DL}.

In summary, parameters of the procedures were chosen to create areas of commonality and comparison. All procedures used the same starting rule (initial ΔL for a condition) and the same number of stimulus intervals per trial. MML-15, ZEST, and ZEST2 all had the same number of trials per block. The number of trials was varied while keeping everything else the same with MML-15 and MML-50. A 2AFC paradigm was used with UPD and ZEST2, while a cued yes–no paradigm was used with ZEST, MML-15, and MML-50; the common ZEST method allows a direct comparison of the effect of paradigm.

E. Simulations

To examine factors that might help explain the results obtained in the present study, simulations of the five procedures (plus some variants) were performed using a model listener whose d' is proportional to ΔL in accord with the psychometric functions measured by Buus and Florentine (1991). For each procedure and variant, 10 000 simulated ΔL_{DL} were obtained for each of the four stimulus conditions. Hence simulation results are based on 40 000 total runs per procedure. For each condition, the ΔL necessary to produce $d'=1$ was chosen to yield a ΔL_{DL} for UPD simulations equal to the average ΔL_{DL} obtained in the actual experiment. For the yes–no paradigms, the model listener's response cri-

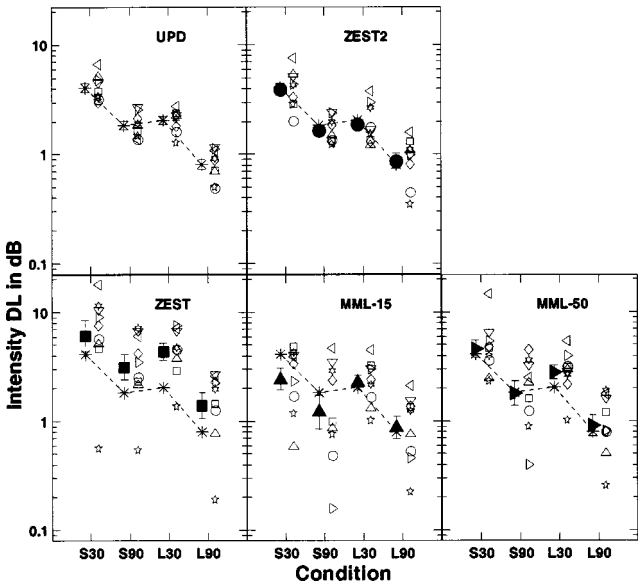

FIG. 2. The ΔL_{DL}'s for five procedures (UPD, ZEST2, ZEST, MML-15, and MML-50) are plotted in five panels. The procedures' geometric mean thresholds for each condition are plotted with filled markers and displaced to the left. Error bars show plus and minus one standard error of the mean log threshold. The geometric means across six repetitions for the individual listeners are plotted displaced to the right for each condition, using a different open symbol for each listener. Each listener is represented by the same symbol in all five panels. For comparison, the mean thresholds from the UPD procedure are plotted with an asterisk displaced to the left and connected by dotted lines in each panel.

terion was similarly chosen to yield average simulated ΔL_{DL}'s equal to the average ΔL_{DL}'s of the experiment (given that the ΔL yielding d' of unity was set according to the UPD simulations). All simulations exactly replicated the procedures used in the experiment, except as indicated when variations of a procedure were investigated to examine factors that might have affected its performance.

III. RESULTS

Since ΔL_{DL} is proportional to the criterion d' used to indicate that the level difference can just be noticed (Florentine and Buus, 1981), all analyses were performed on the log of the ΔL_{DL}'s (for further discussion, see Buus and Florentine, 1991). The ΔL_{DL}'s obtained with the UPD procedure in the different conditions are in general agreement with prior studies (Florentine, 1986; Florentine *et al.*, 1987; Buus and Florentine, 1991). For example, the magnitudes of the mean ΔL_{DL}'s at 500 ms are roughly the same as those obtained for similar stimuli by Florentine *et al.* (1987). In the present study, changing the duration from 500 to 10 ms increased the ΔL_{DL}'s by a factor of 2 at 30 dB SPL and 2.28 at 90 dB SPL; these ratios are slightly smaller than, but comparable to, those found by Florentine (1986) and Oxenham and Buus (2000). As the "reference procedure," individual and group means for UPD are depicted in the top left panel of Fig. 2 and group means are listed in Table I. Individual and group thresholds for the four other procedures are depicted in the other four panels of Fig. 2, with the mean thresholds for the UPD procedure added to each plot for comparison. For all four procedures, the pattern of thresholds for different conditions is generally consistent with that for the UPD procedure, though the mean thresholds sometimes appear to differ from those of the UPD procedure.

TABLE I. Geometric mean ΔL_{DL} for each stimulus condition in each of the five procedures, plus the grand geometric mean for each procedure. Values are in dB.

Stimulus	Initial ΔL (dB)	UPD	ZEST2	ZEST	MML-15	MML-50
30 dB, 10 ms	10	4.09	3.93	6.09	2.44	4.62
90 dB, 10 ms	5	1.85	1.65	3.14	1.21	1.81
30 dB, 500 ms	5	2.05	1.88	4.33	2.67	2.79
90 dB, 500 ms	3	0.81	0.88	1.39	0.87	0.91
Grand mean		1.88	1.81	3.28	1.56	2.15

A three-way ANOVA (using the three fixed factors of condition—four levels, procedure—five levels, and repetition—six levels; listener—nine levels—was a random factor, which produces a repeated-measures ANOVA) showed no main effect of repetition [i.e., no learning effect over the tested sessions; $F(5,40)=1.42$, $p=0.24$]. There was also no significant interaction of repetition with either condition [$F(15,120)=0.865$, $p=0.60$] or procedure [$F(20,160)=1.12$, $p=0.39$]. Note that the variance of the data differs across procedures, as discussed further below. Thus, the basic assumption of equal variance within all cells of an ANOVA is probably violated. However, this experiment used a balanced design, so nonuniform variance should have little effect on the correctness of the F inferences (Hildebrand, 1986). Nevertheless to verify the effects (or lack thereof) shown by the ANOVA, the analysis of the main effect of repetition was repeated using the Kruskal–Wallis nonparametric test of multiple observations with all nine listeners. The results confirmed no significant effect of repetition ($X^2=4.38$, $p=0.50$). Accordingly, subsequent analyses pooled data across repetitions.

To examine further how well each procedure estimated the difference limen, the correlation was computed between the mean logarithms of ΔL_{DL}'s for individual listeners and conditions obtained with UPD and those obtained for each of the other four procedures. Figure 3 depicts a log-log plot of these correlations, with ΔL_{DL} for UPD on the ordinate and ΔL_{DL} for each of the other labeled procedures on the abscissa. A dashed diagonal line indicates equal ΔL_{DL}'s for the two procedures. The Pearson correlation coefficient was greatest for UPD vs ZEST2, the two 2AFC procedures, and lowest for UPD vs MML-15.

A two-way ANOVA was subsequently performed (using the fixed factors of procedure and condition; listener was a random factor to produce a repeated-measures ANOVA). There were main effects of procedure [$F(4,32)=6.71$, $p<0.001$] and condition [$F(3,24)=63.29$, $p<0.001$], but no interaction between procedure and condition [$F(12,96)=1.79$, $p=0.06$]. The main effect of condition on ΔL_{DL} is expected (Florentine, 1986; Florentine *et al.*, 1987; Buus and Florentine, 1991). The effect of procedure could be considered undesirable because the ΔL_{DL}'s should ideally be the same across all procedures. However, it probably stems pri-

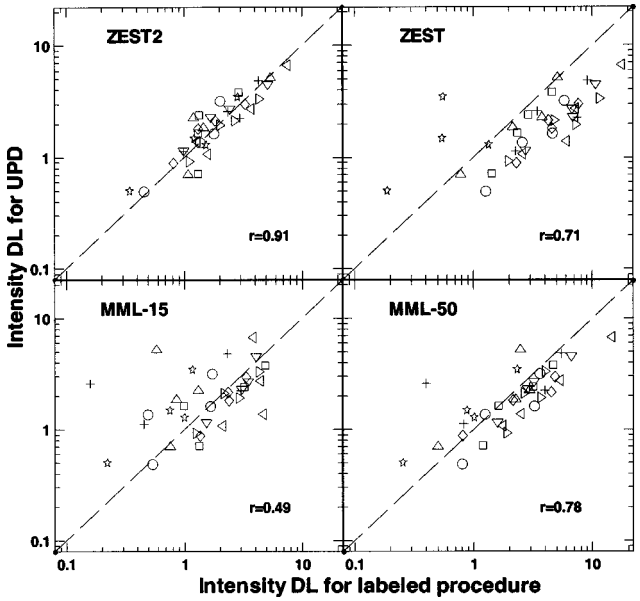

FIG. 3. The ΔL_{DL}'s for UPD (per listener and condition) are plotted as a function of the corresponding ΔL_{DL} for four procedures (ZEST2, ZEST, MML-15, and MML-50) in four panels. The symbols for different listeners are the same as in Fig. 2. A dashed diagonal line indicates equal ΔL_{DL}'s for the two procedures. Pearson's correlation coefficient (r) is shown in the lower right of each panel.

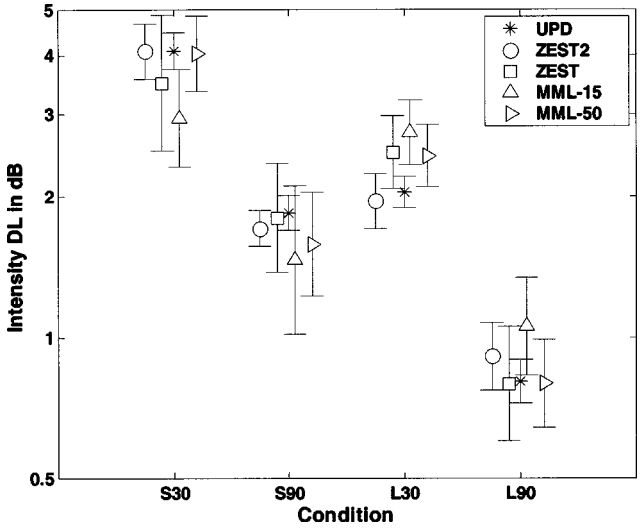

FIG. 4. Mean ΔL_{norm} for all five procedures are shown for each of the four conditions. (See text for details.) The symbols are slightly displaced horizontally within a condition for visual clarity. The error bars represent the standard error across listeners.

marily from the fact that the different procedures converge on different values of d' (i.e., the difference limens estimated by the different procedures correspond to different criteria for ''just audible'' even if they measure the same underlying psychometric function). Thus, normalizing all thresholds within a procedure to a common d' across procedures should leave only a main effect of condition, plus an interaction of condition and procedure if one exists.

Because UPD converges on a known percentage correct response rate (and, assuming negligible bias, a known d') and is by far the most commonly used procedure, ΔL_{DL}'s for all procedures were normalized to the mean threshold for UPD across conditions according to the following formula:

$$\Delta L_{\mathrm{norm}}(P=i,C=j) = \Delta L_{DL}(P=i,C=j)\,\frac{\sqrt[4]{\Pi_{k=1}^{4}\Delta L_{DL}(P=\mathrm{UPD},C=k)}}{\sqrt[4]{\Pi_{k=1}^{4}\Delta L_{DL}(P=i,C=k)}}, \tag{5}$$

where ΔL_{norm} is the normalized threshold for procedure i and condition j. Subsequent analyses were performed on logarithms of these normalized thresholds. A plot of the mean normalized thresholds can be found in Fig. 4 and the values are listed in Table II. As a check, any main effect of procedure should disappear with these transformed thresholds in the two-way ANOVA—as it does [$F(4,32)=0$, $p=1.0$]. There is the expected main effect of condition [$F(3,24)=5.76$, $p<0.01$], but also an interaction between condition and procedure [$F(12,96)=2.33$, $p<0.025$]. However, Scheffé *posthoc* tests for contrast reveal no significant effect of procedure within a condition. That is, for any given stimulus condition, the normalized jnd's do not differ significantly across procedures. Hence, we conclude that the significant interaction of condition and procedure reflects only unsystematic variations that are unlikely to be important.

Given that all the procedures, on average, appear to yield similar results except for differences resulting from converging on different d' values, the main issue is the reliability with which they determine a listener's difference limen for a given stimulus. Thus, the variance associated with the different procedures, as depicted in Fig. 5, is of particular interest. For each listener, the variance was computed for each procedure-condition pair [i.e., variance of $\log(\Delta L_{\mathrm{DL}})$ across repetitions]. Subsequent analyses were then performed on these variances across listeners.

The average variances ranged from 0.017 for UPD to 0.22 for MML-15, corresponding to error factors of 1.35 for UPD and 2.94 for MML-15 (cf. Florentine *et al.*, 1987). This means that the ΔL_{DL}'s obtained in individual repetitions with UPD generally (i.e., 70% of the time) were between three-fourths and four-thirds times the mean ΔL_{DL}, whereas for MML-15 they were between one-third and three times the mean ΔL_{DL}.

In a two-way ANOVA (four levels of conditions, five levels of procedures; again, listener was a random factor), there was no significant effect of condition on variance [$F(3,24)=1.60$, $p=0.22$] nor any interaction of condition and procedure [$F(12,96)=0.76$, $p=0.69$]. However, there

TABLE II. Geometric mean ΔL_{DL} for each stimulus condition in each of the five procedures after ΔL_{DL}'s were normalized to the mean value across conditions in UPD (see text). Values are in dB.

Stimulus	UPD	ZEST2	ZEST	MML-15	MML-50
30 dB, 10 ms	4.09	4.08	3.49	2.94	4.04
90 dB, 10 ms	1.85	1.71	1.80	1.46	1.58
30 dB, 500 ms	2.05	1.96	2.49	2.74	2.44
90 dB, 500 ms	0.81	0.91	0.80	1.06	0.80
Grand mean	1.88	1.88	1.88	1.88	1.88

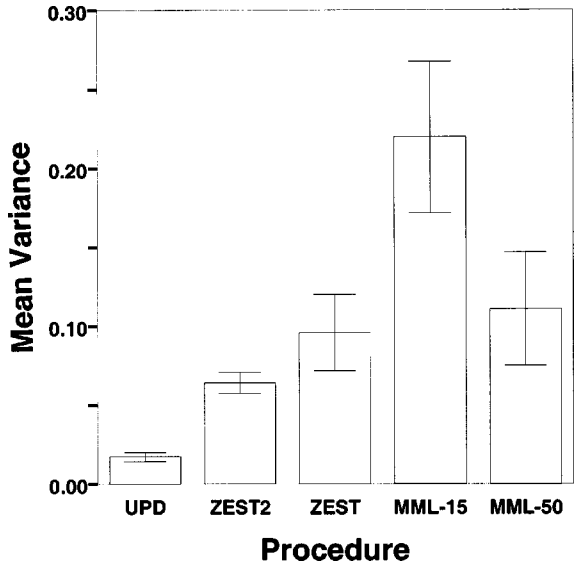

FIG. 5. The mean variance of the log ΔL_{DL}'s are calculated as the average of the variance of each listener's log ΔL_{DL}'s in each condition. The error bars represent the standard errors of those means.

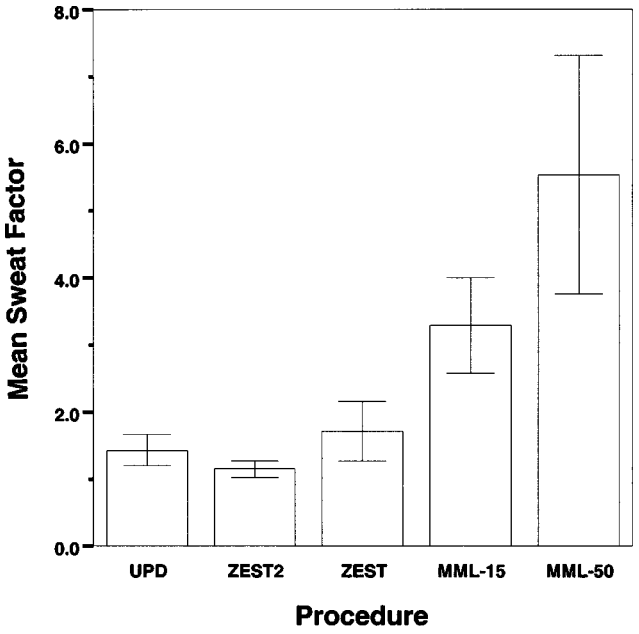

FIG. 6. Sweat factor, defined as a procedure's variance multiplied by the number of trials, is derived from the variances plotted in Fig. 5. The larger the sweat factor is, the less efficient the procedure. Error bars are standard errors of the means.

was a significant main effect of procedure [$F(4,96)=5.98$, $p<0.01$]. Because of possible nonuniform variance, analyses were rerun using the nonparametric Friedman test of *k*-related samples, confirming no significant effect of condition ($X^2=2.496$, df$=3$, $p=0.49$) and a significant effect of procedure ($X^2=55.022$, df$=4$, $p<0.001$). *Posthoc* analysis of pairwise comparisons (using the nonparametric Wilcoxon signed ranks test of related samples comparing procedure within listener–condition combinations) showed that the variance of UPD (mean$=0.017$) is significantly smaller than that of ZEST2 (mean$=0.064$; $Z=-5.021$, $p<0.001$). There was no significant difference between the variance of ZEST2 and that of ZEST (mean$=0.095$; $Z=-0.141$, $p=0.89$), nor between the variance of ZEST and that of MML-50 (mean $=0.11$; $Z=-0.707$, $p=0.48$). Finally, the variance of MML-15 (mean$=0.22$) is significantly greater than that of MML-50 ($Z=-2.796$, $p<0.01$). Thus, these analyses confirmed that the variance of UPD was the least, the variance of MML-15 was the greatest, and the variances of the other three procedures are statistically indistinguishable from one another but are different from the extremes. The 13-fold increase in mean variance from UPD to MML-15 can in part be ascribed to the use of different numbers of trials (around 85 versus 15), but other factors must play a role because the ratio of variances is considerably larger than the ratio of trials.

A related measure of performance of psychophysical procedures is the sweat factor (SF)—defined as the product of the variance and the number of trials (see Taylor *et al.*, 1983) and commonly used as a measure of efficiency. The SFs were computed by multiplying the variance for each listener in each condition and procedure by the number of trials for that procedure.[4] The mean sweat factor for each procedure was subsequently computed for each listener and condition-procedure pair. The average sweat factor across listeners and conditions for each procedure is graphed in Fig. 6. Clearly, the sweat factors are much higher for the MML procedures than for the others. This is confirmed by the nonparametric Friedman test of *k*-related samples, which shows a significant effect of procedure on sweat factor ($X^2=25.067$, df$=4$, $p<0.001$). The best procedure (ZEST2) is nearly five times as efficient as the worst (MML-50). Pairwise comparisons of the procedures with the Wilcoxon signed rank test of two related samples show no statistical difference between the three best performers (ZEST2, UPD, and ZEST). The sweat factors for ZEST2 and ZEST are significantly less than that of MML-15 ($Z=-4.289$, $p<0.001$, and $Z=-2.624$, $p<0.01$, respectively), and the MML-15 sweat factor is significantly less than the MML-50 sweat factor ($Z=-2.168$, $p<0.030$).

Simulations of the UPD procedure provide great confidence in our basic listener model because they replicate all aspects of the listeners' within-session performance. The average number of simulated trials across conditions was 85.6 (with the 500-ms, 90-dB SPL condition taking the longest at 90.2 trials and the 10-ms, 30-dB condition taking the shortest at 83.5 trials—mirroring the pattern obtained in the experiment). The simulated standard error across the three interleaved tracks [i.e., variability *within* a block, about log(1.24)] was similarly consistent with that obtained from the experiment [about log(1.21)]. As expected, the squared standard error across three tracks in the simulations was close to the *across*-block variance calculated from the simulations. This variance (0.0078) is less than half that obtained from real listeners (0.017), which indicates that one or more sources of across-block variance are not accounted for by the simulations, because the within-block performance appears to be modeled quite accurately, as noted above. Similarly, simulations of ZEST2 produced ΔL_{DL}'s closely matching those obtained in the real experiment, but the across-block variance (0.044) was only 70% of that obtained from real

listeners. For the yes–no paradigms (i.e., the MML and ZEST procedures), simulations with a listener model that employed a fixed response criterion (chosen to reproduce the ΔL_{DL}'s obtained with each procedure) yielded across-block variances much smaller than those from real listeners. Specifically, the simulations yielded variances of 0.061 for MML-15, 0.0042 for MML-50, and 0.0053 for ZEST. For the latter two procedures, the simulated variances are only 4% and 6% of the measured variance!

IV. DISCUSSION

Five different psychophysical procedures were tested with a level-discrimination task. The results showed significant differences in variance and sweat factors among the procedures. In particular, the procedures using yes–no paradigms performed less well than those using 2AFC, and the MML procedures (as implemented in the present study) proved relatively inefficient. These findings will be addressed first. Then follows a discussion of simulations, including considerations of what can and cannot be learned from them. Finally, strengths and weaknesses of the tested procedures will be evaluated. This section includes some qualitative issues that might influence the choice of psychophysical procedure.

A. Yes–no versus 2AFC paradigms

This section concerns the stability of the yes–no paradigm for level discrimination, which is a relatively subtle task. The data indicate that the yes–no paradigm does not fare well. The procedures using the yes–no paradigm yield larger variances and larger sweat factors than those using the 2AFC paradigm. The variance of the MML procedures (using a yes–no paradigm) was greater than that of UPD and ZEST2 (both 2AFC). One explanation for the relatively poor performance of some of the procedures that use the yes–no paradigm is that they may be sensitive to shifts in listener's response criterion (Florentine *et al.*, 2001). Moreover, our listeners claimed to prefer the 2AFC paradigm with feedback (UPD and ZEST2) to the cued yes–no paradigm (e.g., the MML procedures and ZEST). They claimed to be much less certain and more tentative about their responses in the yes–no procedures, which might also increase variance. In part, this may be due to the lack of feedback. However, the yes–no paradigm can yield reasonably good performance, as indicated by the results for ZEST. The yes–no paradigm yielded only 1.5 times the variance of the 2AFC when both were combined with the ZEST method. On the other hand, the ZEST and MML-15 procedures had the same number of trials and used the same cued yes–no paradigm, yet the latter had a significantly higher variance than the former. So, the large variance obtained with the MML procedures cannot be accounted for by paradigm alone.

Theoretical arguments and some simulations (e.g., Macmillan and Creelman, 1991; King-Smith *et al.*, 1994) suggest that yes–no should be more efficient and less variable than 2AFC. Indeed, this result is supported by our simulations of listeners with a fixed response criterion. However, empirical studies have shown that 2AFC can outperform yes–no in discrimination tasks (Jesteadt and Bilger, 1974; Creelman and Macmillan, 1979). Strictly, however, the present cued yes–no paradigm might be classified under ''same–different'' or ''reminder'' paradigm for purposes of theoretic analysis. Macmillan and Creelman (1991, pp. 156–157) summarize a number of studies that show that cued yes–no reminder paradigms actually perform better than classic yes–no, but worse than 2AFC. Thus, it is perhaps not surprising that the present study also found 2AFC to outperform yes–no, even if simulations based on the assumption of a stable psychometric function and a fixed response criterion might suggest otherwise.

B. Performance of the MML procedures

The performance obtained by the MML procedures in the present study differs from previous work with a gap-detection task, which showed that the MML procedure could perform quite well (Florentine *et al.*, 2000) and that there was no significant difference in accuracy *or* reliability between 15 and 50 trials using an otherwise identical MML procedure (Florentine *et al.*, 2001). The present study shows a palpable and significant effect of the number of trials used for the MML procedures. Why is there a difference between the gap-detection and level-difference tasks? One reason may relate to the slopes of the psychometric functions. The psychometric functions for level discrimination ($k=6$) are much shallower than those for gap detection ($k=11$ at 1 kHz and $k=16$ at 4 kHz). Indeed, Florentine *et al.*'s (2001) data showed a noticeable effect of the number of trials for gap detection at 1000 Hz, but hardly any effect at 4000 Hz where the slope is steeper. The increased within-block listener variance that occurs for tasks that have relatively shallow psychometric functions is likely to require an increased number of trials to converge on a stable threshold estimate. The slope of the psychometric function is not an issue with UPD, which changes the stimulus in fixed step sizes that can (and should) be scaled according the slope. On the other hand, ZEST and MML do not vary the stimulus in fixed steps and some of their parameters are chosen on the basis of the range of thresholds that may be expected across listeners and stimulus conditions. Thus, these parameters generally do not scale with the slope of the psychometric function. Accordingly, the speed of convergence for ZEST and MML is likely to depend on the slope of the psychometric function.

A somewhat related reason concerns the nature of the task. Intuitively, and from listeners' anecdotal responses, level discrimination is a subtler task (some listeners said ''much harder'') than gap detection, which would tend to increase any variance of a listener's performance. Although Florentine *et al.*'s (2001) task used a cued yes–no paradigm, with the aim of creating an across-interval comparison, the task might also be accomplished as a within-interval comparison—detecting the presence or absence of a gap in the second stimulus without necessarily referring to the first stimulus. Level discrimination depends on a comparison between one stimulus and the memory of the other. Such quantitative across-interval comparisons can be subtle, which may make it difficult for listeners to maintain a stable criterion for the discrimination decisions. This might lead to in-

consistent decisions that—together with the shallow slope of the psychometric functions—may contribute to slow convergence toward the threshold, which in turn causes the procedure to benefit from an increased number of trials.

Apart from the shallow slope of the psychometric function for level discrimination, one aspect of the implementation used in the present study may contribute to the poor performance of the MML procedures. There is a difference in range of midpoints used by this implementation of MML and the other procedures. That is, the MML started with a set of candidate psychometric functions that spanned 3.3 log units. In comparison, the candidate functions in the gap detection study (Florentine *et al.*, 2001) spanned about 2.6 log units. Green's (1993) listeners demonstrated approximately a 1.4-fold increase in standard deviation for pure-tone thresholds when the range increased 1.5-fold (from 40 to 60 dB). In the current study, the effective range used by the MML method (as measured by the standard deviation, 0.953 log units) was about 1.5 times that of the ZEST methods' initial p.d.f. (about 0.638 log units). Thus, the search space for the ZEST method was considerably smaller than that for MML. Similarly, the UPD method stays within a relatively constrained range, based on the starting and progression rules. It is likely that judicious reductions of the initial range of the MML procedure, so that its standard deviation was comparable to ZEST, could reduce the variance. Indeed, simulations of MML (using a listener model with stable response criterion) comparing ranges of 3.3 and 2.18 log units (chosen to have the same width as the initial p.d.f. used for the ZEST procedures, as measured by the standard deviation of 0.638 log units) show a reduction of across-block variance by nearly half for MML-15. However, the range made virtually no difference for MML-50. Thus, range alone does not account for the poor performance of the MML procedures. This conclusion is further supported by the finding that the variances obtained in the simulations with a range of 3.3 log units were only a small fraction of those obtained experimentally as described in Sec. III.

If variations in range are combined with other factors, however, the effects of range can be considerable. Simulations using a listener model with a variable response criterion indicate that the effect of midpoint range is much larger than that for a fixed criterion. In particular, the variability of the response criterion for the simulated listener was chosen to reproduce the variance of ΔL_{DL}'s, the proportion of runs with false-alarm rates exceeding 20%, and the mean estimated false-alarm rates obtained with real listeners. With this listener model, a range of 2.18 log units produced a simulated variance that was only 40% of that obtained with a range of 3.3 log units for both MML-15 and MML-50. Thus, the wide range of midpoints used in the real experiments is likely to have contributed to the poor performance of the MML procedures. Indeed, if such a 2.5-fold improvement were to materialize with real listeners, the sweat factors for MML (especially MML-15) would be competitive with those for the other procedures.

Part of the excess variance obtained with real listeners may also reflect occasional inattention, which is not modeled in the simulations. Inattention may affect MML more strongly than the other methods. Because MML initially searches the midpoint range in a manner closely resembling repeated bisections, MML can be quite sensitive to the initial few listener responses (Green, 1995); a ''mistake'' early in a block can produce an unreasonably high or low threshold estimate. On the other hand, the initial p.d.f. and Bayesian estimation method employed by ZEST limit the excursions. Thus, it can ''recover'' from ''mistakes'' more rapidly and completely, providing ultimately more stable threshold estimates even with the same number of trials. An associated effect is that the initial trials in a MML procedure present stimuli that are probably far above and below threshold—especially when the range of midpoints is wide—which effectively wastes the first few trials.

C. Simulations and their limitations

Whereas simulations may produce useful information about some properties of psychophysical methods, they do not necessarily duplicate the outcome of real experiments. In particular, the standard model of a listener, which presumes a static psychometric function, is likely to be much too simple and may lead to erroneous conclusions. For example, simulations with such a listener model indicated that ZEST and MML-50 should have produced the best sweat factors. In fact, the simulations suggested that these procedures should be three to eight times as efficient as the 2AFC procedures. In contrast, the experimental results show that the 2AFC procedures outperformed the yes–no procedures.

Even within a paradigm, the simulations can produce incorrect predictions. The simulations indicated that UPD should have a sweat factor about 16% less than that of ZEST2, but the data indicate the reverse. For the yes–no procedures, the simulations using static psychometric functions correctly predict ZEST as having the best sweat factor, but they also predict that MML-50 should be more than four times as efficient as MML-15, whereas the data show that MML-50 was only about $\frac{2}{3}$ as efficient as MML-15. Thus, even though the basic listener model includes psychometric functions that are in accord with measured psychometric functions and that produce the ΔL_{DL} obtained in the experiment, it clearly fails to capture some crucial elements of real-life performance. This is especially true in the simulations of the yes–no procedures, but discrepancies are also apparent in the simulations of the 2AFC procedures.

Two conclusions suggest themselves. First, even with a ''criterion-free'' paradigm, it is likely that there are factors in level discrimination that cause day-to-day variability. This follows from the finding that simulations of UPD yield results that are exceedingly close to the within-block data obtained experimentally, but yield less variance than that obtained in real listeners across multiple sessions. Second, if real listeners vary their response criterion across blocks, the results will diverge considerably from simulations that use fixed response criteria. The actual data are closely matched by simulations of MML with a listener model using normally distributed response criteria chosen to conform to the experimentally obtained ΔL_{DL}'s and false-alarm rate estimates. For MML-50, a mean criterion of 1.75 (corresponding to a false-alarm rate of 4%) and a standard deviation equal to 1.2

was found to provide a good match for the data. For MML-15, simulation results closely matching the actual data were obtained when the mean criterion was 1.4 and the standard deviation 0.9. Likewise, the ΔL_{DL}'s, the across-block variance, and the mean width of the final p.d.f. for ZEST were reproduced by simulations with a mean criterion of 2.15 and a standard deviation of 0.9.

Prior work indicates the importance of variable response criteria to across-block variance (Florentine *et al.*, 2001). The present data indicate that the distributions of such variable response criteria probably differ across procedures. Because the procedures present different sequences of the stimuli, this effect may reflect that the response criterion depends on the stimuli. This conjecture is further supported by the finding that the simulated false-alarm rates (needed to obtain ΔL_{DL}'s equal to those from the experimental results) varied considerably across the methods for both fixed- and variable-criterion listener models, which indicates that intrinsic properties of the procedures are likely to affect the position as well as the stability of the listeners' response criteria.

Although variable response criteria offer compelling simulations of the real data, it is possible that factors not examined in the present study may account for the sometimes large discrepancies between real data and those obtained from simulations with the standard fixed-criterion listener model. In addition, the factors that govern a listener's response criterion are not well understood, and are likely to vary across procedures and tasks. Until all these factors have been clarified and included in the listener model, predictions derived from simulations must be regarded with considerable caution. Whereas simulations certainly can be helpful in examining some aspects of the performance that can be expected from a given procedure, it is clear that reliable assessment of actual performance in experimental settings still requires empirical measurements.

D. Strengths and weaknesses of the procedures

We can now turn to an overall assessment of the advantages and disadvantages of the procedures tested in the present study. An obvious caveat is that the answer is highly dependent on the tested implementations of the different procedures and the resulting data. While applicable to level discrimination, and likely generalizable to other subtle tasks, the conclusions may change with other tasks. Further, greater optimization is possible with all the tested procedures (especially the MML), so the results may not represent the best case. Indeed, fully optimizing each of the procedures in this study would certainly lessen the commonalities, which could make comparisons less meaningful. Moreover, in practice it is difficult and time consuming to fully optimize psychometric procedures empirically and optimizations would otherwise be limited by the accuracy of the listener model used for simulations (which can be rather far away from reality, as discussed above), so the findings of the present study are likely to be reasonably representative of real-world experience.

Accuracy is the first concern for evaluating and comparing different psychometric procedures. The results generally show that, when the thresholds from the procedures are normalized to compensate for different d' convergence points, all five are equally accurate. That is, all the procedures provide reasonably unbiased estimates of the relations among the ΔL_{DL}'s in the different stimulus conditions. Thus, all the procedures perform well in characterizing how a change of stimulus parameters affects the ΔL_{DL}'s. Whereas this issue often is the primary focus of an experiment, the precision with which the procedures converge on the theoretically targeted point on the listener's psychometric function—i.e., the extent to which they provide an unbiased estimate of the absolute magnitude of the ΔL_{DL}—is also of some interest. This question is most easily answered by examining the results of simulations where the model-listener's true ΔL_{DL} is known. Simulations of the 2AFC procedures (UPD and ZEST2) show that they both converge on a d' of 1.29, which is just slightly above the theoretical values of 1.16 (corresponding to 79.4% correct) for UPD and 1.24 (corresponding to 81% correct) for ZEST2. In other words, small biases in these procedures cause the estimated ΔL_{DL}'s to be above the true ΔL_{DL}'s by about 11% for UPD and 4% for ZEST2. This outcome of the simulations is supported by the data for real listeners, which show almost identical ΔL_{DL}'s for UPD and ZEST2 (see Table I). The bias in the estimates produced by the yes–no procedures is more difficult to evaluate because the targeted d' depends on the listener's response criterion, which is not well estimated by the procedures used in the present study. The simulations indicate that the obtained ΔL_{DL} may be up to 20% above or below the ΔL_{DL} corresponding to the theoretical point of convergence and the model listener's response criterion. The magnitude and direction of this bias depends on the false-alarm rate assumed for the model listener and whether it is fixed or variable. However, for a given listener model, the bias varies little across the four stimulus conditions. In other words, whatever d' may be targeted by a yes–no procedure, this target does not appear to depend on the stimulus condition. Thus, the simulations and the data agree that all five procedures provide unbiased estimates of how stimulus variables affect a listener's ΔL_{DL}.

Reliability of psychometric procedures is the next interest. For both research and clinical applications, the variance of ΔL_{DL} within listener and across blocks is a useful measure of reliability. The variance was significantly smaller for UPD than for the other four procedures. This finding is expected on simple statistical grounds. Procedures using more trials ought to produce more stable threshold estimates and thus lower variance (i.e., variance is generally inversely proportional to the number of trials). However, when comparisons are made across the procedures tested here, that expectation is not always fulfilled. The variance obtained with the ZEST procedure is similar to that offered by MML-50, which has around three times the number of trials. Further, MML-15 has much greater variance than the two ZEST procedures, although they used about the same number of trials per block. Nevertheless, the present UPD implementation uses the most trials and produces the least variance, in part due to its use of three interleaved tracks that produce three independent estimates per block. Although the tracks were short, they provide quite reliable data, in agreement with recent

observations (Hicks and Buus, 2000; Buss *et al.*, 2001). In fact, simulations in the present study indicate that the present short tracks are as efficient as the 50-trial single-track version of UPD that is used in many studies. Moreover, the variability across the three tracks in the present version of UPD provides a metric that allows aberrant results to be identified (Hicks and Buus, 2000). Thus, the UPD with three short tracks is a strong contender if high reliability is of paramount importance.

If it is not feasible to use the relatively large number of trials required by the three interleaved tracks, it seems straightforward to reduce the number of trials by using only a single track. A simple-minded calculation of multiplying the UPD variance by 3 yields an estimated per-track variance of 0.051. This suggests that an up–down procedure employing just one short track would be at least as reliable as the ZEST2 procedure, which yielded a variance of 0.064. However, such a shortened up–down procedure would still use more trials than ZEST2. The approximately 28 trials used for the present five-reversal tracks probably is at or near the lower limit of practical track lengths. Simulations of an up–down method using just 20 trials per track showed such tracks to be considerably less efficient than the five-reversal tracks. Thus, it is unlikely that an up–down procedure can provide efficient threshold estimates as quickly as a ZEST procedure. Of course, threshold estimates obtained rapidly with a ZEST procedure may be too variable to satisfy the requirements of an experiment, but this potential problem is easily solved. Repeated measurements with a brief ZEST procedure can readily reduce the variance to whatever level may be required for a particular experiment and may well do so with equal or better efficiency than longer up–down procedures, as discussed below.

Within the limits of granularity imposed by the fact that any procedure needs a certain number of trials to converge on a threshold estimate, tradeoffs between accuracy and speed can often be made with ease. The sweat factor considers the variance obtained within a fixed time (i.e., one trial). Thus, sweat factor is probably a more relevant metric than variance itself. The sweat factors show that UPD, ZEST, and ZEST2 procedures all do approximately equal work per trial and we could claim that they are approximately equally efficient, whereas the two MML procedures trail behind. However, if the MML procedures had been implemented more optimally than they were, the results of the simulations indicate that MML-15 might have performed about as well as UPD, ZEST2, and ZEST. It should also be noted that using an incorrect slope for the Weibull function in the ZEST procedures made them suboptimal, but simulations indicate that the gain from using a correct slope is quite modest (10%–20%). So, despite the range of number of trials necessary for different procedures (i.e., 18 for ZEST and ZEST2 to around 28 for each of three tracks—or about 85 in total—for UPD), there is no significant performance advantage to using more trials within a single block using these procedures.

Given approximately equal efficiencies in terms of sweat factors, one can then look to the number of trials required to produce a threshold. In general, fewer trials are better. Attention can be a problematic issue for special listener populations (e.g., infants, developmentally delayed, elderly) as well as young, adult listeners. Long blocks and long times in the testing apparatus can evoke boredom, promote inattention, and diminish listeners' compliance. In addition, the highly accurate threshold with low variance that, in theory, should be obtained with long blocks may not materialize. Comparisons between simulations and experimental results indicate that across-block variance diminishes the reliability of the ΔL_{DL}'s measured by any of the procedures. To the extent that this across-block variance cannot be controlled, spending a large number of trials on a highly accurate measurement in a single session probably has limited utility. Listeners' performance is characterized more reliably by obtaining less accurate measurements across a larger number of blocks. So, the ''fewer trials are better'' mantra is further reinforced by the combined advantages to the listeners' comfort and the possibility of averaging multiple thresholds taken in the same clock time as a single long block.

Although efficiency and number of trials are important considerations for choosing among psychometric procedures, more qualitative criteria might also affect the choice. Two examples here are the number and types of assumptions required for a procedure, and the flexibility of the algorithm embodied in the method. For example, an often-heard claim is that up–down methods require few assumptions about the shape of the underlying psychometric function apart from monotonicity. They can readily be used for stimuli and tasks for which no prior information is available. However, an up–down method must still have starting rules and progression rules, each of which embodies certain assumptions about the probable values of threshold and the slope of the psychometric function because the reliability of the measurement depends on relations among the values of the first stimulus, the step size, the slope of the psychometric function, and the threshold. Nevertheless, the datum definition can be simple and straightforward, without explicit reference to the underlying psychometric function. The MML and ZEST procedures, on the other hand, require more assumptions about the shape and placement of the underlying psychometric functions. The MML method requires the two dimensions of the initial search space to be specified (i.e., false-alarm rates and midpoints) plus an estimate of the slope of the psychometric function. The ZEST method requires a number of fixed parameters to be set with reasonable precision (e.g., false-alarm, miss rate, and slope of the psychometric function), as well as an initial guess as to the probable value of threshold. So, if one has little or no information about the task under study, UPD may be preferable. However, in practice, it is rare to be confronted by a problem without *any* prior information (e.g., from the literature). Even if that information were suboptimum, it would seem wasteful not to use it. Theoretical studies of both MML (Green, 1993, 1995) and ZEST (King-Smith *et al.*, 1994) show that errors in slope estimation and other parameters can have relatively little effect on the results. The latter result is supported by the favorable performance of ZEST and by simulations in the present study. While a little bit of knowledge might be dangerous in some situations, it is a good thing with psychophysical procedures. Crude information

and even ''best guesses'' of parameter values may suffice, which should make a reasonable implementation of ZEST possible in many situations. Thus, ZEST may help experimenters take maximum advantage of existing knowledge.

Flexibility (and, in concert, understandability) rounds out the criteria for comparing procedures. UPD can be applied to a variety of paradigms (e.g., yes–no, 2AFC, 3AFC), is conceptually simple to understand and implement, and has a clear algorithm for converging on different percentages of correct responses (or different values of d'). In fact, Kaernbach's (1991) weighted up–down procedure allows targeting any point on the psychometric function. The MML procedures were originally designed for, and so far have primarily been implemented with, ''yes–no'' paradigms. Although there has been at least one study successfully combining a 2AFC paradigm with MML (Dai and Green, 1992), the generality of the method to different paradigms remains uncertain until further theoretic or empiric studies are done. If short MML implementations are feasible only with yes–no paradigms, MML may not be well suited for subtle tasks that are subject to variations in the listeners' response criteria. In addition, the algorithm is computationally intensive and more difficult to understand than UPD. The ZEST method apparently has enough parameters to be applicable to a wide variety of paradigms and arbitrary d' convergence points. For example, simple adjustments to the false-alarm and miss-rate parameters allowed the ZEST method to produce reasonably efficient measurements with both a yes–no paradigm and a 2AFC procedure paradigm. Both the ZEST (yes–no) and ZEST2 (2AFC) procedures performed well with the level discrimination task. However, the ZEST method is also computationally more intense and complicated than UPD.

On balance, it seems that both ZEST and UPD are excellent choices. Both are flexible, robust, and efficient, but they offer slightly different trade-offs between simplicity of implementation and measurement speed. UPD is easy to implement, but it apparently requires more trials than ZEST to obtain reliable convergence. ZEST, on the other hand, is somewhat more complex to implement but appears to converge reliably in a small number of trials.

V. CONCLUSIONS

The present experiment investigated five different psychophysical procedures for measurement of difference limens for level. The procedures encompassed two paradigms (cued yes–no and 2AFC) and three methods (UPD, MML, and ZEST). The results show the following.

(1) For subtle tasks like level discrimination, the 2AFC paradigm holds many advantages over yes–no. In particular, the performance of yes–no procedures may be severely diminished by variability in the listeners' response criterion.
(2) UPD combined with 2AFC holds its place as the ''reference procedure'' of psychometric procedures. Its performance is very good and its relatively large number of trials could be reduced with little or no loss in efficiency.
(3) MML did not perform well in the present study, in part because we used an excessively large range of midpoints for the candidate psychometric functions. To the extent that MML works best with a yes–no paradigm, it may not be a good choice for subtle tasks.
(4) ZEST combined with 2AFC seems to provide an excellent combination of reliability, performance, and flexibility and should be considered as a prime candidate for the procedure of choice.
(5) Simulations are not reality. Simulations using a static psychometric function to model listeners failed to reproduce major features of the present results. The performance of all procedures is affected by across-block variance. This is especially true for yes–no procedures, whose performance is likely to be diminished considerably by variability of the listeners' response criterion.

ACKNOWLEDGMENTS

This study was supported by NIH/NIDCD Grant No. R01DC0187. We thank Dr. Marjorie Leek, Dr. Christian Kaernbach, and an anonymous reviewer for their helpful comments.

[1]A computer error prevented computation of the precise average number of trials used for UPD in this study. However, the data files for six of the nine listeners were recovered; an analysis of these files yielded averages of 82.3 trials for 10-ms tones at 30 dB SPL, 82.6 trials for 10-ms tones at 90 dB SPL, 82.9 trials for 500-ms tones at 30 dB SPL, and 91.0 trials for 500-ms tones at 90 dB SPL.

[2]Note that the catch trials were not used to compute false-alarm rates directly, but rather were used to provide data that let the MML procedure converge on an estimate for the false-alarm rate with some certainty. This number of catch trials is in accordance with prior studies from this laboratory (e.g., Florentine *et al.*, 2001) and follows the procedures used by Green (1993).

[3]Note that the initial t does not really represent our best guess of the true distribution of difference limens. The original description of the ZEST method suggested that t should be the experimenter's ''best guess'' of threshold. In this study, t was actually chosen to be easily detectable rather than the most likely difference limen. In particular, the initial t for each condition was set equal to the initial ΔL used for all the other procedures to ensure that all procedures had a common starting point.

[4]Because the MML method was inactive during the ''warm-up'' trials, they were not counted when calculating sweat factors.

ANSI (**1989**). ''Specifications for Audiometers'' (American National Standards Institute, New York).

Buss, E., Hall, J. W., Grose, J. H., and Dev, M. B. (**2001**). ''A comparison of threshold estimation methods in children 6–11 years of age,'' J. Acoust. Soc. Am. **109**, 727–731.

Buus, S. (**2002**). ''Psychophysical methods and other factors that affect the outcome of psychoacoustic measurements,'' in *Genetics and the Function of the Auditory System*, edited by L. Tranebjærg, J. Christensen-Dalsgaard, T. Andersen, and T. Poulsen (GN ReSound, Tåstrup, Denmark), pp. 183–225.

Buus, S., and Florentine, M. (**1991**). ''Psychometric functions for level discrimination,'' J. Acoust. Soc. Am. **90**, 1371–1380.

Creelman, D., and Macmillan, N. A. (**1979**). ''Auditory phase and frequency discrimination: A comparison of nine procedures,'' J. Exp. Psychol. Hum. Percept. Perform. **5**, 146–156.

Dai, H., and Green, D. M. (**1992**). ''Auditory intensity perception: Successive versus simultaneous, across-channel discrimination,'' J. Acoust. Soc. Am. **91**, 2845–2854.

Florentine, M. (**1986**). ''Level discrimination of tones as a function of duration,'' J. Acoust. Soc. Am. **79**, 792–798.

Florentine, M., and Buus, S. (**1981**). ''An excitation-pattern model for intensity discrimination,'' J. Acoust. Soc. Am. **70**, 1646–1654.
Florentine, M., Buus, S., and Geng, W. (**2000**). ''Toward a clinical procedure for narrowband gap detection I: A psychophysical procedure,'' Audiology **39**, 161–167.
Florentine, M., Buus, S., and Mason, C. R. (**1987**). ''Level discrimination as a function of level for tones from 0.25 to 16 kHz,'' J. Acoust. Soc. Am. **81**, 1528–1541.
Florentine, M., Buus, S., and Poulsen, T. (**1996**). ''Temporal integration of loudness as a function of level,'' J. Acoust. Soc. Am. **99**, 1633–1644.
Florentine, M., Marvit, P., and Buus, S. (**2001**). ''Maximum-likelihood Yes-No procedure for gap detection: Effect of track length,'' J. Am. Acad. Audiol **12**, 113–120.
Green, D. M. (**1993**). ''A maximum-likelihood procedure for estimating thresholds in a yes-no task,'' J. Acoust. Soc. Am. **93**, 2096–2105.
Green, D. M. (**1995**). ''Maximum-likelihood procedures and the inattentive observer,'' J. Acoust. Soc. Am. **97**, 3749–3760.
He, N., Dubno, J. R., and Mills, J. H. (**1998**). ''Frequency and intensity discrimination measured in a maximum-likelihood procedure from young and aged normal-hearing subjects,'' J. Acoust. Soc. Am. **103**, 553–565.
Hicks, M. L., and Buus, S. (**2000**). ''Efficient across-frequency integration: Evidence from psychophysical functions,'' J. Acoust. Soc. Am. **107**, 3333–3342.
Hildebrand, D. K. (**1986**). *Statistical Thinking for Behavorial Scientists* (Duxbury, Boston).
Jesteadt, W., and Bilger, R. C. (**1974**). ''Intensity and frequency discrimination in one- and two-interval paradigms,'' J. Acoust. Soc. Am. **55**, 1266–1276.
Kaernbach, C. (**1991**). ''Simple adaptive testing with the weighted up-down method,'' Percept. Psychophys. **49**, 227–229.
King-Smith, P. E., Grigsby, S. S., Vingrys, A. J., Benes, S. C., and Supowit, A. (**1994**). ''Efficient and unbiased modifications of the QUEST threshold method: Theory, simulations, experimental evaluation and practical implementation,'' Vision Res. **34**, 885–912.
Kollmeier, B., Gilkey, R. H., and Sieben, U. K. (**1988**). ''Adaptive staircase techniques in psychoacoustics: A comparison of human data and a mathematical model,'' J. Acoust. Soc. Am. **83**, 1852–1862.
Leek, M. R., Dubno, J., He, N.-J., and Ahlstrom, J. B. (**2000**). ''Experience with a yes–no single interval maximum-likelihood procedure,'' J. Acoust. Soc. Am. **107**, 2674–2684.
Levitt, H. (**1971**). ''Transformed up-down methods in psychoacoustics,'' J. Acoust. Soc. Am. **49**, 467–477.
Macmillan, N. A., and Creelman, C. D. (**1991**). *Detection Theory: A User's Guide* (Cambridge U.P., Cambridge, England).
Oxenham, A. J., and Buus, S. (**2000**). ''Level discrimination of sinusoids as a function of duration and level for fixed-level, roving-level, and across-frequency conditions,'' J. Acoust. Soc. Am. **107**, 1605–1614.
Plattsmier, H. S., and McFadden, D. (**1988**). ''Temporary threshold shift measured with two psychophysical procedures,'' Audiology **27**, 334–343.
Schlauch, R. S., and Rose, R. M. (**1990**). ''Two-, three-, and four-interval forced-choice staircase procedures: Estimator bias and efficiency,'' J. Acoust. Soc. Am. **88**, 732–740.
Shelton, B. R., Picardi, M. C., and Green, D. M. (**1982**). ''Comparison of three adaptive psychometric procedures,'' J. Acoust. Soc. Am. **71**, 1527–1533.
Taylor, M. M., Forbes, S. M., and Creelman, C. D. (**1983**). ''PEST reduces bias in forced-choice psychophysics,'' J. Acoust. Soc. Am. **74**, 1367–1374.
Watson, A. B., and Pelli, D. G. (**1983**). ''QUEST: A Bayesian adaptive psychometric method,'' Percept. Psychophys. **33**, 113–120.

Effects of speaking rate on second formant trajectories of selected vocalic nuclei[a)]

Gary Weismer[b)] and Jeff Berry
Department of Communicative Disorders and Waisman Center, University of Wisconsin—Madison, Madison, Wisconsin 53705

(Received 6 September 2002; accepted for publication 17 March 2003)

The effect of speaking rate variations on second formant (F2) trajectories was investigated for a continuum of rates. F2 trajectories for the schwa preceding a voiced bilabial stop, and one of three target vocalic nuclei following the stop, were generated for utterances of the form ''Put *a bV* here, where V was /i/, /æ/ or /oɪ/. Discrete spectral measures at the vowel-consonant and consonant-vowel interfaces, as well as vowel target values, were examined as potential parameters of rate variation; several different whole-trajectory analyses were also explored. Results suggested that a discrete measure at the vowel consonant (schwa-consonant) interface, the F2off value, was in many cases a good index of rate variation, provided the rates were not unusually slow (vowel durations less than 200 ms). The relationship of the spectral measure at the consonant-vowel interface, F2 onset, as well as that of the ''target'' for this vowel, was less clearly related to rate variation. Whole-trajectory analyses indicated that the rate effect cannot be captured by linear compressions and expansions of some prototype trajectory. Moreover, the effect of rate manipulation on formant trajectories interacts with speaker and vocalic nucleus type, making it difficult to specify general rules for these effects. However, there is evidence that a small number of speaker strategies may emerge from a careful qualitative and quantitative analysis of whole formant trajectories. Results are discussed in terms of models of speech production and a group of speech disorders that is usually associated with anomalies of speaking rate, and hence of formant frequency trajectories. [DOI: 10.1121/1.1572142]

PACS numbers: 43.70.Fq, 43.70.Bk [AL]

I. INTRODUCTION

Formant frequency data have an important history and role in speech production research. Most frequently, target values extracted from a single point in time within a vocalic nucleus have been used as acoustic representations of vowel categories (Fant, 1960; Sussman *et al.*, 1998). Whereas there may be some debate about which point in time should be used to represent these targets, or even if the concept of a target is useful at all (Strange, 1989; Hillenbrand *et al.*, 2001), formant frequencies measured in this way have served the field well. They have been related systematically to articulatory variables (e.g., Ladefoged *et al.*, 1978; Perkell and Nelson, 1985), are known to be relevant to the perception of vowel categories (see review in Nearey, 1989), and may predict speech intelligibility in both neurologically normal speakers and speakers with certain speech disorders (Bradlow *et al.*, 1996; Turner *et al.*, 1995; Weismer *et al.*, 2000). Formant frequencies also contribute in an important way to the definition of speaking clearly (Picheny *et al.*, 1986) and the influence of phonological systems on certain aspects of speech production (e.g., Manuel, 1990).

There appear to be reasons, however, to supplement these target values with more complete representations of formant trajectories throughout a vocalic nucleus (for the purposes of this report, we define a formant trajectory as the time history of a particular formant frequency, extending from the first to last glottal pulse of a vocalic nucleus). For example, statistical and human categorization of vowels may be improved with some representation of trajectory information, as compared to the single-point measures described above (Hillenbrand and Gayvert, 1993; Hillenbrand *et al.*, 2001; Watson and Harrington, 1999), and trajectory information has been shown to be useful and perhaps critical in speech perception (Strange, 1989). In terms of speech production, formant trajectories may be used to infer time-varying changes in vocal tract configuration (Stevens, 1998), and are sensitive indicators of the speech production deficit in motor speech disorders (Weismer *et al.*, 1988, 1992, 1995). One particular parametrization of formant trajectories, locus equations (Sussman *et al.*, 1998), has been claimed to have great relevance to both speech production and perception, and the influence of experimental variables such as speaking rate and stress on formant trajectories has direct relevance to gesture theories of speech production (Browman and Goldstein, 1992a; and see Tjaden and Weismer, 1998).

Surprisingly, there are few data on the characteristics of formant trajectories, their stability across speakers, vocalic nucleus types, and contexts, as well as across the various manipulations often used in speech production experiments (such as rate and stress). An early attempt to model formant trajectories was reported by Stevens *et al.* (1966) who ex-

[a)]Portions of this work were presented previously in ''An acoustic model of gesture overlap: further studies,'' 134th meeting of the Acoustical Society of America, San Diego, CA, Fall 1997, and ''Effects of speaking rate on vowel formant trajectories,'' 140th meeting of the Acoustical Society of America, Newport Beach, CA, Fall 2000.

[b)]Electronic mail: weismer@waisman.wisc.edu

 0001-4966/2003/113(6)/3362/17/$19.00

plored the effects of consonantal environments on vowel target undershoot and transition characteristics in CVC syllables. Stevens *et al.* (1966) fit parabolas to vocalic trajectories extracted from CVC frames spoken by three speakers and reported several interesting and by-now well-known vowel and consonant effects; these investigators also alluded to some fairly substantial speaker effects even when identical CVC sequences were produced. Broad and Fertig (1970) performed an extensive analysis of the C/I/C productions of a single speaker and demonstrated that the formant trajectories are at any single point throughout their course the sum of effects from the preceding and following consonants, with the magnitude of the effects of the respective consonants increasing or decreasing with time elapsed (or remaining) from (to) the consonant boundary.

The systematic nature of the formant trajectories studied by Stevens *et al.* (1966) and by Broad and Fertig (1970) suggested the possibility of a general set of rules for generating many different kinds of trajectories from the study of just a few, but Broad and Clermont (1987) found such rules elusive, even in the best case of VC transitions [see Broad and Clermont 2002, for rules that relate vowel formant frequencies *across a vowel set* at any point in time throughout a vowel nucleus in a given context; the effect of speaking rate variation on such rules remains unknown]. Pitermann's (2000) review of acoustic and perceptual investigations of formant transitions also describes the failure of a number of studies to find general transition rules for human production, perception, machine classification, and/or recognition.

To the extent that formant transitions are good representations of the time-varying vocal tract geometry, their careful study may bear on important theoretical issues in speech production, despite the difficulties mentioned above. Moreover, it could be useful to identify and possibly understand the variables responsible for the difficulty of specifying simple rules for the transformation and/or scaling of formant trajectories. There are several candidate variables that are relatively easy to identify, based on previous work. First, it is clear that the same phonetic sequence may reveal different trajectory characteristics across speakers (Tjaden and Weismer, 1998). Moreover, the speaker variation for a given trajectory may be amplified when experimental manipulations (e.g., stress, rate, clear speech) are used to investigate interesting theoretical issues. For example, rate variations have been shown in certain cases to result in vowel reduction (Lindblom, 1963), to produce varying patterns of coarticulation (Gay, 1978; Tjaden and Weismer, 1998), and to differentially affect the onglide, offglide, and transition components of diphthongs (Gay, 1968, but see Dolan and Mimori, 1986). The generality of these findings is unknown, however, and has not been based on either multiple speakers or a sufficiently dense time sampling of the formant trajectories (but see Clermont, 1993) or of the speaking rate continuum. The second variable is vocalic nucleus type, investigated by Broad and Clermont (1987) in a limited way. Here there are two relevant questions: (1) are trajectories transformable across different vocalic nucleus types, and (2) do the trajectories associated with these different types react to experimental manipulations in the same way?

For example, variations in the overlap of adjacent consonant and vowel gestures (Saltzman and Munhall, 1989; Browman and Goldstein, 1992a), induced by stress and/or rate manipulations, should be reflected in the extent to which pieces of formant trajectories in the region of the consonant-vowel interface are either revealed or obscured. This reasoning has been used to infer the ''breaking apart'' of successive vocal tract gestures in motor speech disorders via analysis of formant trajectory onset and offset frequencies, time delays from consonant release to the major transitional component of the vocalic nucleus, and slopes of major transitions (e.g., Liss and Weismer, 1992; Weismer *et al.*, 1995). Because many motor speech disorders are characterized by speaking rate anomalies, however, the natural influence on formant trajectories of rate variation may be confounded with the effects on speech production of neurological disease.

The current investigation explores the effect of speaking rate variation on formant trajectories for three different vocalic nuclei in constant phonetic context. Whereas Tjaden and Weismer (1998) reported preliminary evidence of nucleus-specific effects, their speech sample was not sufficiently well controlled (that is, vowel nucleus type was confounded with word-initial consonant) and therefore prevented straightforward interpretation of specific effects. A second purpose of the present investigation was to explore different approaches to the analysis of formant trajectories. As described above, several different parametrizations of formant trajectories have been described (Stevens *et al.*, 1966; Broad and Clermont, 1987; Pitermann, 2000), but there is little work on the representation of formant trajectory variation with changes in speaking rate.

II. METHODS

A. Participants

Six speakers, three females and three males, were recruited for the experiment. All six speakers were either students or staff at the University of Wisconsin—Madison. The speakers ranged in age from 21 to 40 years, and had dialects typical of the Upper Midwestern part of the United States (Wisconsin, Minnesota, Iowa). None of the speakers had a history of speech, language, or hearing pathology, and all speakers demonstrated the ability to grade their speaking rate before data were collected (see Tjaden and Weismer, 1998).

B. Graded rate task

Each speaker completed a graded speaking rate task in which the rate of production of a target phrase was increased (or decreased) gradually within blocks of four repetitions. The task was described and modeled for each subject by the experimenter prior to data collection. Subjects were told to produce the first repetition of each block at a self-determined habitual speaking rate and then to increase (or decrease) their rate with each of the remaining repetitions in the block so that they reached their self-determined fastest (or slowest) speaking rate with the fourth repetition. A simple schematic providing a graphical illustration of the task was placed in each subject's view throughout data collection. The task required subjects to alternate between blocks of increasing rate

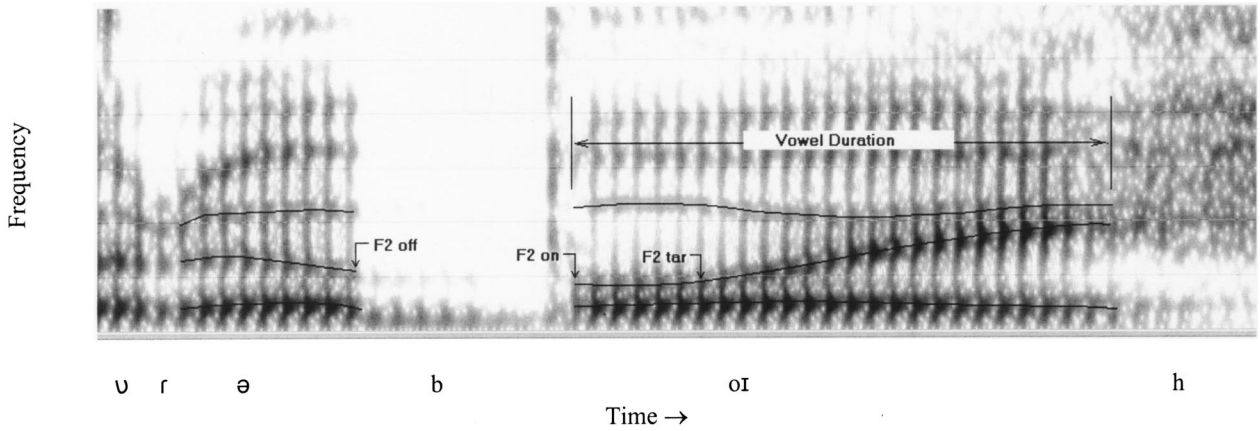

FIG. 1. Spectrogram of 'Put a boy here,' showing formant tracks and measured parameters.

(''up'' blocks) and blocks of decreasing rate (''down'' blocks). For the blocks of progressively decreasing rate, the experimenter cautioned subjects not to increase the pause time between words to achieve slower speaking rate. This technique for eliciting rate variation has been used successfully in previous experiments (Byrd and Tan, 1996; Tjaden and Weismer, 1998).

Subjects rehearsed the graded rate task before data collection began. Since the objective was to collect a series of repetitions that would generate a fairly wide and more or less continuously populated range of speaking rates, consistency among rate extremes (fastest and slowest rates) or among ''habitual rate'' tokens across repetition blocks was not important. The experimenter required only that the repetitions within a block varied by rate. Accordingly, when a subject demonstrated in the rehearsal blocks perceptible rate variation across repetitions, proficiency with the task was confirmed and data collection was initiated. All subjects were able to demonstrate task proficiency with no more than 10 min of rehearsal.

After data collection had been initiated, repetition blocks in which perceptible rate variation did not occur, or in which speaking rate was altered by pause time, were noted by the experimenter and later withdrawn from further data processing. Immediately following unsatisfactory repetition blocks, subjects were reminded to increase (or decrease) speaking rate with each repetition or to refrain from altering speaking rate by modifying pause time. Each subject continued to repeat a target phrase until 40 satisfactory blocks (20 ''up'' and 20 ''down'') had been produced. Consequently, 160 acceptable repetitions of each target phrase were produced by each subject. All subjects were able to produce the necessary repetitions of the three target phrases analyzed for this study in a single session of data collection lasting no more than 45 min. Subjects were given frequent breaks from the task and drinks of water to minimize fatigue.

The data were recorded in a sound-attenuated booth using a Shure SM-58 dynamic microphone and a Tascam Digital Audio Tape recorder with a 44.1-kHz sampling rate and 16-bit quantization level. The subjects were seated at a table on which the microphone rested in a short stand. Mouth-to-microphone distance was maintained within a range of approximately 6 to 12 in. throughout data collection.

C. Target phrases and acoustic analysis

The target phrases produced for this investigation were comprised of monosyllabic target words embedded in the carrier phrase ''put a__here'' (/pʊɾə__hir/). The three target words consisted of an initial voiced bilabial stop /b/ followed by the high front vowel /i/, the low front vowel /æ/, or the diphthong /oɪ/. The monophthongs were followed by word final voiced stops, creating comparable real word tokens; the diphthong was left open to do the same. The resulting target phrases, ''put a bead here,'' ''put a bag here,'' and ''put a boy here,'' were written on note cards and laid in view of the subjects during data collection. No specific directions were given with respect to stress placement. However, all experimenter models were produced with primary stress on the target word. All subjects followed these examples when producing the experimental utterances, placing primary stress on the target word. The three vocalic nucleus types were chosen to sample a range of vocalic articulations, and especially to include one nucleus (/ae/) that typically has a relatively complex acoustic pattern in the Upper Midwest dialect, and one diphthong (/oi/) typically having extensive change in F2. For the present analysis, the initial consonant of the target word was limited to /b/ to allow maximum freedom between the consonant and vowel gestures in responding to rate changes.

After the utterances had been collected on DAT, they were redigitized on a laboratory computer at 22.05 kHz (16 bit) using the program Cspeech (Milenkovic, 1994) in conjunction with a Sound Blaster 16 audio card. The waveforms were truncated to include the segments of interest, extending from the onset of the neutral vowel /ə/ to the offset of the target vowel (/i/, /æ/, or /oɪ/). Figure 1 shows a spectrogram of one of the utterances, with the formant tracks and measures that were the basis of the analysis described below. An LPC-based formant tracking algorithm in Cspeech was used to mark the first three formants at 5-ms intervals over the vocalic segments of interest. These formant tracks were subsequently hand corrected and smoothed using linear interpolation to eliminate unrealistic variation in the calculated formant frequencies between adjacent LPC estimates.

Using the resulting formant tracks, F2 values were obtained at the offset of the schwa (F2off) and the onset (F2on) of the target vowel. The beginning and end of each vowel was identified by the first and last complete vertical striations along the spectrogram that extended through F2; the F2off and F2on values were extracted from the tracks at these boundary points. Additionally, for each vocalic nucleus, a ''target'' F2 value (F2tar) was measured. For the vowels /i/ and /æ/, the target was defined as the maximum F2 value along the track. For the diphthong /ɔɪ/, the target was defined as the F2 value at the first point along the track where frequency increased by at least 20 Hz over the preceding 20 ms [i.e., the target was taken as the onset of the major, rising F2 transition, usually coincident with the lowest F2 value along the trajectory; see Watson and Harrington (1999) for similar measurement conventions].

For the present study, observations were confined to F2 for several reasons. First, previous work (Tjaden and Weismer, 1998) suggests that F2 trajectories are very sensitive to rate variation, and that the observed effects may not gain in interpretability from inclusion of F1 and F3 data. Second, F2 is known to be more sensitive to context effects than F1 and F3 (Stevens and House, 1963). Finally, the large volume of data for a single formant trajectory produced many times by six speakers precludes presentation and discussion of additional tracks. F1 and F3 may indeed turn out to provide insight to rate effects on formant trajectories, but this question will have to await a future study.

The measures described above are shown in Fig. 1 for a production of ''boy.'' The duration of each target vocalic event (hereafter referred to as ''vowel duration'' for simplicity) was recorded as an index of speaking rate. Also, the duration of the transition from vowel onset to vowel ''target'' was calculated for each target vowel. Finally, the complete formant track from each target vowel was saved for the analysis of changes in formant trajectory shape as a function of rate.

III. RESULTS

A. Reliability

Intrarater reliability estimates for the discrete spectral measures of interest were made by comparison of replicate measurements from 1 of the 160 token data sets (that is, from a single female speaker). The mean absolute differences between matched replicate tokens for F2off, F2on, and F2tar were 69, 41, and 44 Hz, respectively. These values are consistent with those reported in prior investigations (e.g., Tjaden and Weismer, 1998). Mean absolute difference values estimating interrater reliability were of similar magnitude. The values obtained from a comparison of 40 matched replicate tokens were 63, 42, and 55 Hz for F2off, F2on, and F2tar, respectively. These measurement errors are not very different from empirically derived estimates reported for ''ideal'' recording and measurement conditions (e.g., Lindblom, 1962; Monsen and Engebretson, 1983).

TABLE I. Descriptive statistics for vowel duration (ms) by context and speaker. Speaker identification subscript (m or f) indicates speaker gender.

Context	Speaker	Mean	Standard Deviation	Minimum	Maximum	Range	*N*
''bead''	C_m	275	192	70	745	675	160
	J_m	150	66	40	420	380	160
	K_f	324	143	135	775	640	160
	M_f	226	153	85	710	625	160
	R_m	352	337	75	1160	1085	160
	T_f	272	72	150	510	360	160
''bag''	C_m	346	237	135	1020	885	160
	J_m	233	108	90	530	440	160
	K_f	368	141	155	760	605	160
	M_f	288	180	105	890	785	160
	R_m	381	327	95	1275	1180	160
	T_f	339	96	205	595	390	160
''boy''	C_m	324	205	100	830	730	160
	J_m	313	182	95	765	670	160
	K_f	432	234	195	1090	895	160
	M_f	274	147	95	685	590	160
	R_m	452	383	95	1375	1280	160
	T_f	427	131	220	705	485	160

B. Vowel duration

The graded rate task was designed to elicit a wide and nearly continuous range of speaking rates. Table I provides summary statistics on vowel duration by speaker and word. Speaker gender is indicated by subscript. Interspeaker differences were most apparent at the extremes of the speaking rate continua (see minimum and maximum values in Table I), and perhaps especially for the very slow rates. The most extreme speaking rate tendencies were demonstrated by speakers R and T.

The distribution of vowel duration data for a single speaker/context is described by the leftmost bar (black fill) of the histogram in Fig. 2, where the bins increase in duration from left to right on the abscissa; each bin is 59 ms wide. The positive skew of this distribution is typical of the data from all speakers and contexts. The skewed distributions reflect the fact that the range of vowel durations between habitual and extreme fast rates of speech was smaller than the range of vowel durations between habitual and extreme slow rates.

C. Spectral distributions

Compared to the positively skewed distributions for vowel duration, histograms of the discrete spectral measures typically revealed more symmetrical distributions, with some speakers/contexts demonstrating a tendency toward negatively skewed distributions for F2tar (see Fig. 2, rightmost [cross-hatched] bar in each bin). To evaluate more directly the covarying distribution characteristics of the temporal and spectral measures, quantile-quantile plots were constructed. These plots, such as the one shown in Fig. 3 for a single speaker (speaker R), allowed a direct comparison of the relative distributions of vowel duration and the spectral measures (Chambers *et al.*, 1983). The reference line in each plot indicates the path along which the distributions would have

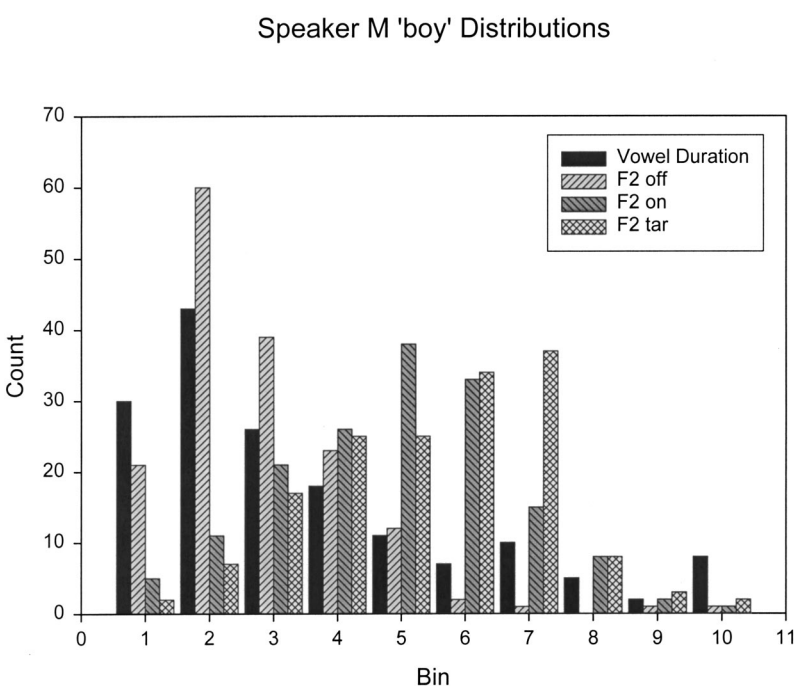

FIG. 2. Distributions of temporal and spectral parameters. Bins are arranged along the abscissa from lowest values (bin 1) to highest values (bin 10). Bin widths for vowel duration, F2off, F2on, and F2tar are 59 ms, 122, 34, and 38 Hz, respectively.

the same shape. The data shown in Fig. 3 are representative of all speakers and contexts in the current investigation, for whom quantiles fell below the reference line for the shortest vowel durations, indicating a heavy positive skew for vowel duration relative to the distribution of each of the spectral measures. As vowel duration increased, representing the more ''habitual'' speaking rates, quantile-quantile relationships reveal an inflection associated with ''heaviest'' portion of the spectral distributions. Finally, in regions associated with the longest vowel durations, the relative distributions tend to be identical, or differ by an additive factor, running parallel to the reference line. Taken together, these observations suggest that the quality of the relationships between vowel duration and the spectral measures may vary across different ranges of vowel duration.

D. Effects of speaking rate on discrete spectral measures

Regression analyses revealed that the relationships between speaking rate and the discrete spectral measures varied widely with respect to speaker, context, and measure. Table II documents the variation in spectral measures that was explained by vowel duration as well as the variation in F2on that was explained by F2tar. Linear fits were used initially for all comparisons. Linear fits were replaced by quadratic fits if this resulted in at least a 5% increase in the explained variation. In Table II linear fits are marked with a single asterisk, and quadratic fits are marked with double asterisks. For the vowel duration-spectral measures relationships, we arbitrarily designated an r^2 of 0.15 as worthy of attention, and note here that an $r = 0.40$ or greater was taken as statistically significant with a conservative alpha level of $p < 0.001$ ($t[120] = 4.65$, $p < 0.001$, is the critical value for each t-test). Figure 4 contains scatterplots and best-fit lines derived from the regression analysis, which are representative of the full range of results reported in Table II. In some of these scatterplots, there appear to be two distributions of points, those for vowel durations below 200 ms, and those for vowel durations above this value; this observation is taken up in the discussion. The plots provide evidence that discrete spectral measures can index rate effects for some speakers and contexts. However, the overall results suggest that no discrete spectral measure can sufficiently index rate effects for all speakers and all contexts.

The most promising parameter appeared to be F2off, for which statistical significance was obtained in 12 of the 18 speaker/context subsets (five of these had significantly improved fits when quadratic regression formulas were employed to fit the data). Most of the nonsignificant effects were associated with ''boy;'' five of six speakers had significant effects for ''bead'' and ''bag.''[1]

The relationship between vowel duration and F2tar was also inconsistent across speakers and contexts. Although the magnitudes of explained variation tended to be somewhat larger than those for F2on, no speaker or context provided convincing evidence that F2tar measures can be used as a sufficient index of rate effects.

Previous work (Tjaden and Weismer, 1998) suggested that F2tar may affect F2on, thereby complicating its relation to vowel duration. Analysis of F2tar–F2on relationships was further motivated by the theoretical significance that has been afforded these measures through work on locus equations (Sussman *et al.*, 1998). The relationship between these two spectral parameters was most robust in the diphthong context, revealing considerable effects for all speakers (Table II). In the ''bead'' context only one speaker demonstrated a significant relationship, while the ''bag'' context revealed no noteworthy effects.

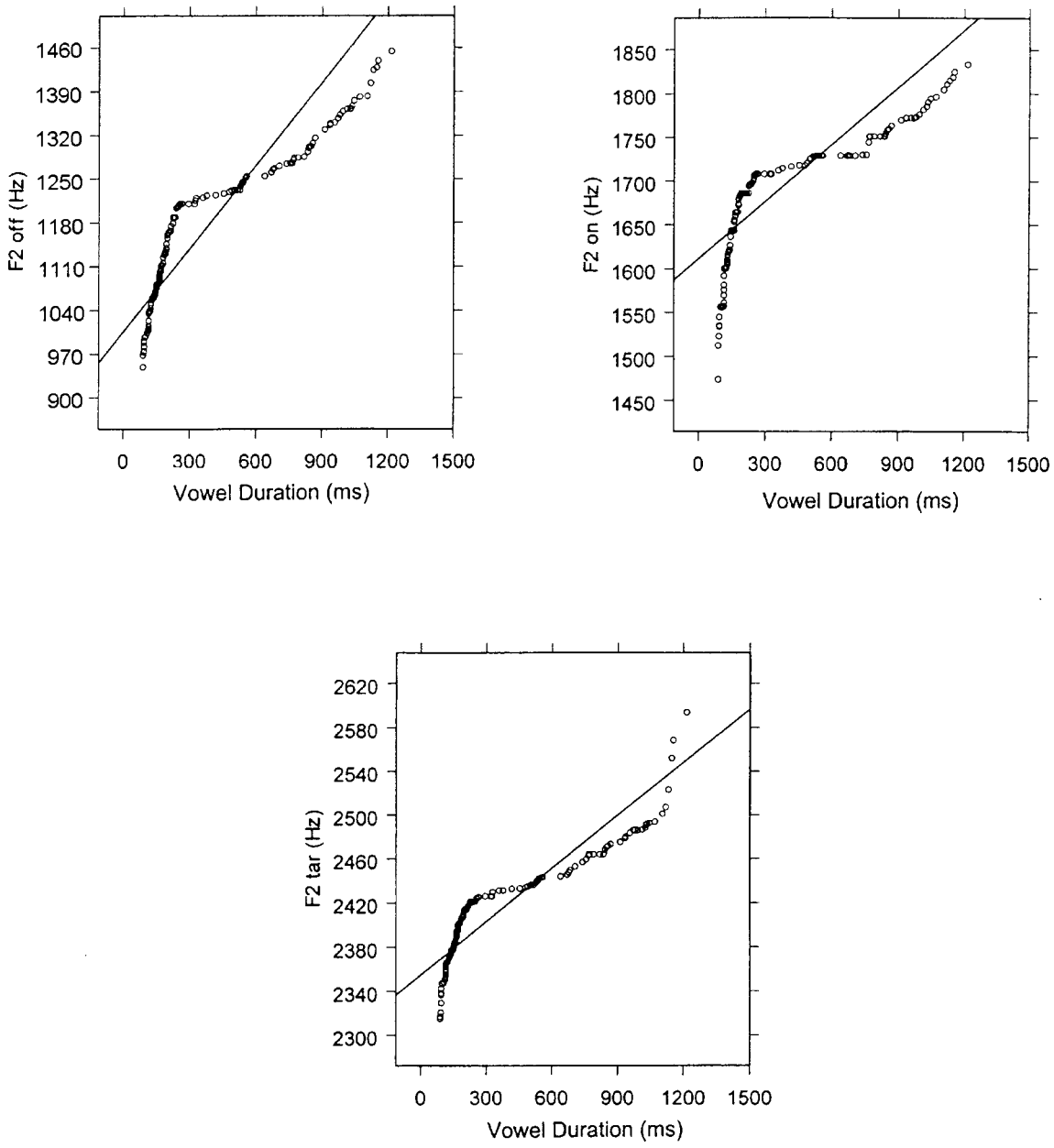

FIG. 3. Quantile-quantile plots for vowel duration and the three discrete spectral measures, for speaker R. The diagonal line shows the distribution of points associated with equal shapes of the distributions for the two plotted parameters in each graph.

E. Complete formant tracks

The entire formant time histories of all 160 tokens were plotted for each speaker/context. The objective of this analysis was to search for qualitative variations in formant movement as a function of speaking rate that could be further analyzed for measurable effects. Figure 5 shows the complete formant tracks for all examples of each speaker saying ''boy.'' A striking feature of these plots is the tendency of speakers to differentially alter three distinct portions of the formant movement. Speakers T, M, and R appear to primarily extend the duration of the plateau associated with F2on as rate decreased. Speaker C appears to primarily extend the duration of the plateau associated with the maximum F2 value as speaking rate changes. Speakers J and K appear to utilize ''hybrid'' strategies, extending the F2on plateau and altering the slope of the major diphthong transition. Quantification of these observations suggests a more complex picture.

One index of the slope of the major diphthong transition is the maximum rate of change in F2. This is an instantaneous measure derived from the peak in the first derivative of the F2 history. Unlike average rate of F2 change, it does not require calculations involving transition duration, which may be heavily coupled with vowel duration and, as a result, vulnerable to the problem of part–whole correlation. The variation in F2 maximum rate of change explained by vowel duration is presented in Table III. All speakers demonstrate robust relationships between vowel duration and F2 maximum rate of change. The magnitude of the variation explained by vowel duration appears to follow a pattern across

TABLE II. Variance accounted for (r^2) by regression functions for pairs of variables listed in first column. Significant comparisons are indicated by single asterisk for a linear regression fit, and double asterisks for a quadratic regression fit. Empty cells indicate nonsignificant effects.

		Speaker					
Parameters	Context	C_m	J_m	K_f	M_f	R_m	T_f
Vowel duration	''bead''	**70%	*29%	*30%	*22%	**64%	*54%
versus	''bag''	**67%	*52%	*33%		**44%	**62%
F2off	''boy''						*53%
Vowel duration	''bead''				*15%	*39%	
versus	''bag''						
F2on	''boy''						
Vowel duration	''bead''			*28%		**53%	
versus	''bag''	*22%	*42%			*19%	
F2tar	''boy''		**22%		*20%	**25%	
F2tar	''bead''					*38%	
versus	''bag''						
F2on	''boy''	*77%	**65%	*56%	*75%	**36%	*32%

speakers that is generally consistent with the qualitative observations made above. However, all speakers do appear to change the slope of the major transition, albeit to varying degrees, as they change speaking rate.

The variation in the duration of the first F2 plateau of the diphthong explained by vowel duration is also presented in Table III. Again, the relationships appear to be robust for all speakers. From a quantitative perspective, all speakers appear to use ''hybrid'' strategies. What may distinguish speakers is the relative effect of speaking rate on transition slope versus ''steady-state'' duration. This conclusion implies that some speakers may differentially alter the overall shape of the formant movement as a function of speaking rate. The behavior of these speakers cannot be accurately modeled as a linear compression or expansion of some ''idealized'' formant movement. It is still unclear, however, whether or not speaking rate strategies are generalized across contexts. Unfortunately, the ''bead'' and ''bag'' contexts were not amenable to the parametric analyses used for ''boy.'' F2 maximum rate of change was less systematically related to vowel duration in these contexts and the definition of ''steady-state'' components seemed far more arbitrary, given the lack of reliable ''elbows'' in the formant trajectory. In response to these limitations, an alternative approach to this analysis was explored using time normalization.

F. Time normalized formant movements

An alternative approach to evaluating trajectory shape variability for /æ/ and /i/ is to analyze formant movements that have been normalized with respect to time, using a conventional normalization scheme. The formant histories for each speaker/context were sampled at 20 points (number of points chosen arbitrarily), with the sampling rate of each token reflecting a first-order linear relationship with vowel duration [see Broad and Fertig (1970), Broad and Clermont (2002), and Van Son and Pols (1992) for similar normalization schemes]. For each speaker/context an ''idealized'' formant movement was calculated from a subset of the data associated with the speaker's self-determined habitual speaking rate. The graded rate task required speakers to begin each ''up'' and ''down'' block of repetitions at a self-determined habitual rate. Each speaker produced 40 replicates for each context at or near this habitual rate. In order to avoid outliers among these 40 replicates, formant histories were selected that had vowel durations falling within $\frac{1}{2}$ the standard deviation above and below the mean vowel duration for all 40 replicates. An average of 11 replicates contributed to each idealized trajectory. For each speaker/context the contributing (time-normalized) formants tracks were averaged at each of the 20 sample points, resulting in an estimated average-habitual formant movement. Figure 6 shows time-normalized formant tracks in black with the average-habitual (idealized) formant movement superimposed as thin white trajectories. For each speaker/context, the correlation between the idealized formant movement and each of the 160 time-normalized formant tracks was calculated. These correlations were plotted as a function of vowel duration and interpreted as an index of formant shape change as a function of speaking rate. For example, correlations remaining near unity across the range of vowel durations would suggest that a particular trajectory retained its shape across speaking rate. Significant vowel duration-trajectory correlation functions, on the other hand, would indicate shape change as a function of speaking rate.

Table IV lists the variation in F2 correlation explained by vowel duration for each speaker/context. Noteworthy relationships are presented as scatterplots in Fig. 7. In this figure, points associated with formant tracks that contributed to the definition of the average-habitual formant movement are marked with white crosses. Overall, the method of analysis appears to be consistent with the parametric analyses of the ''boy'' context, suggesting that three speakers show a greater tendency to change the shape of F2 as a function of speaking rate. These same three speakers demonstrate the most robust relationships in the ''bag'' context. There appears to be little evidence of a relationship between formant shape and speaking rate for any of the speakers in the ''bead'' context. This conclusion is based on the observations

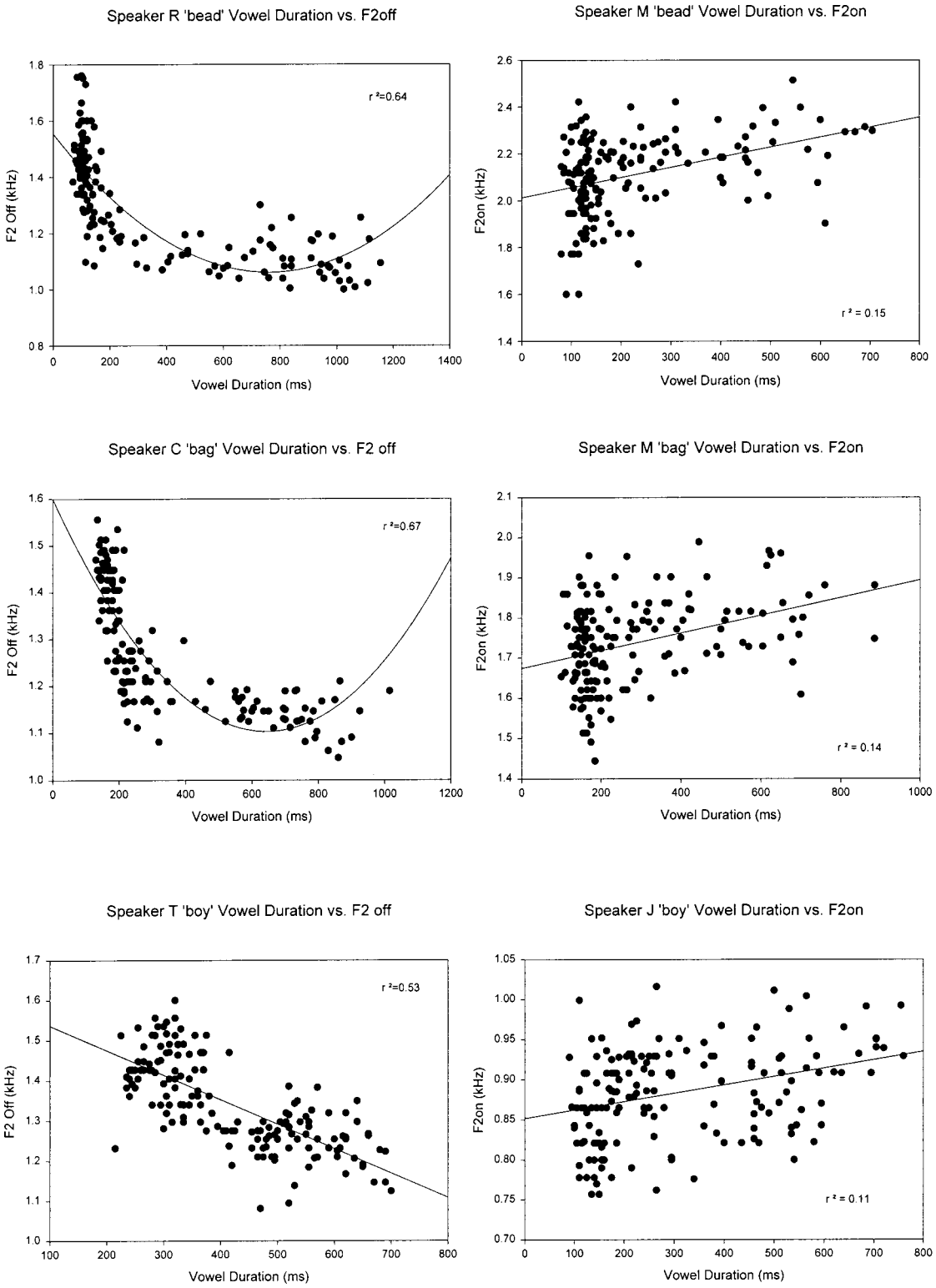

FIG. 4. Scatterplots showing selected relationships of vowel duration and spectral measures, and of F2tar and and F2on.

that the correlations between the prototype and the tokens did not appear to change as a function of vowel duration.

IV. DISCUSSION

The present study used a graded rate task to generate a continuum of speaking rates and to observe the resulting effects on selected spectral measures as well as on qualitative characteristics of formant time histories. Graded rate tasks have been used previously (Tjaden and Weismer, 1998; Byrd and Tan, 1996) and result in a substantially more complete sampling of the rate continuum as compared to experiments in which two or three categories [e.g., habitual versus fast; habitual versus slow; see for example Adams *et al.* (1993) and Shaiman (2001)] are used to study rate effects. An interesting feature of the continua elicited in the present experiment is that several of the dependent spectral measures are

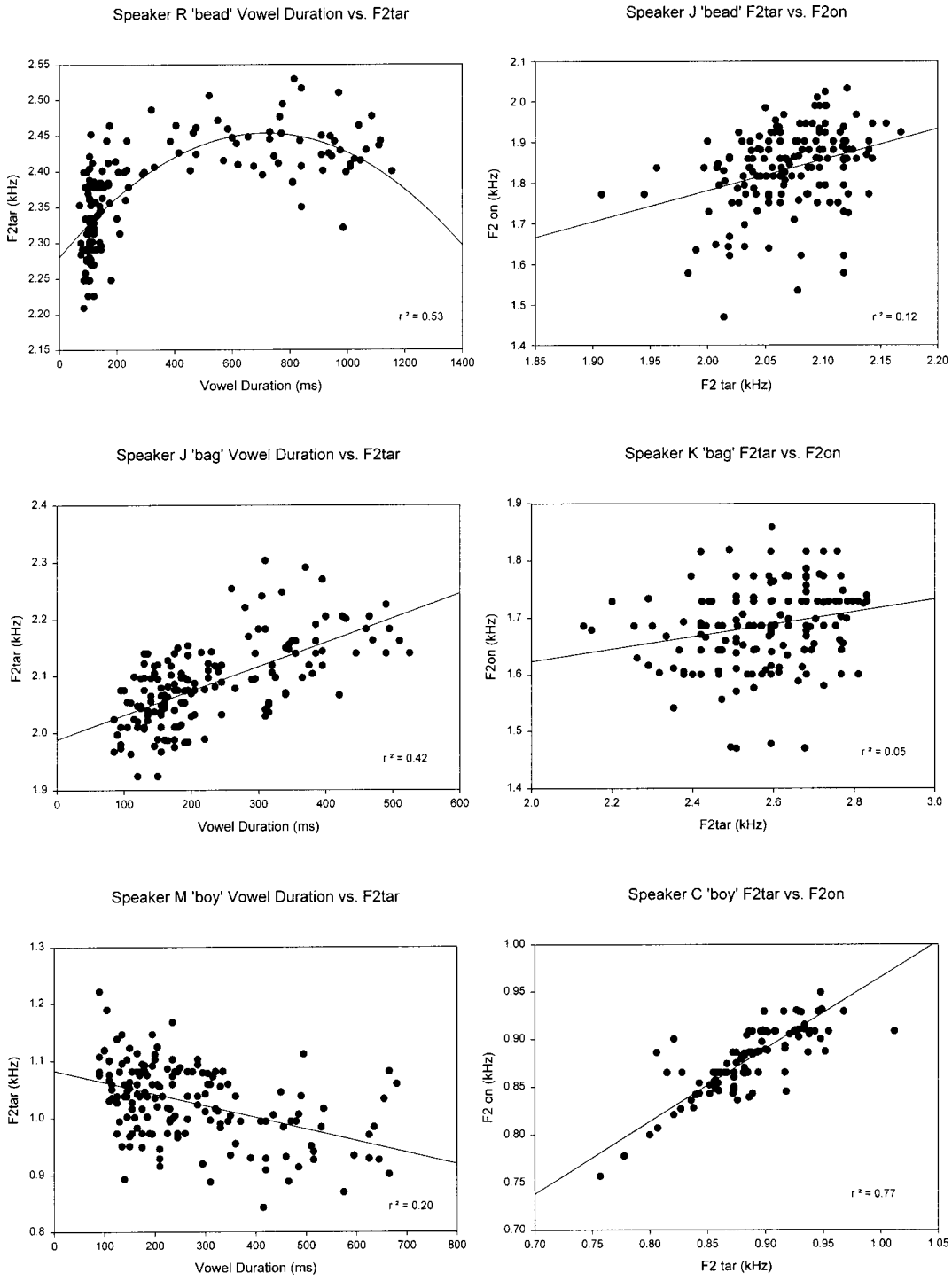

FIG. 4. (*Continued.*)

clearly not distributed across rate in a continuous fashion, as shown by quantile-quantile plots (Fig. 3) and scatterplots (Fig. 4). The breaks in the functions, such as the one relating speaking rate to F2off (Fig. 4), have implications for theories of speech production as well as the use of rate as an experimental variable in speech production experiments.

A. F2off and speaking rate

The most systematic effects were found for the relations between vowel duration and F2off. The F2off value varied significantly with speaking rate for ''bead'' and ''bag,'' as indicated by the significant regression functions. These best-fit functions were often quadratic (Fig. 4), but the plots can also be described as having two distinct populations of points. One population, associated with vowel durations in the 0–200-ms range, shows a steeply sloped column of points along the F2off axis, with longer vowels associated with lower F2off values (e.g., subject ''R'' ''bead,'' and ''C'' ''bag''). The spread of F2off values within this duration range is quite large, typically on the order of 500 Hz (see Fig. 4). This spectral variation is roughly comparable to coar-

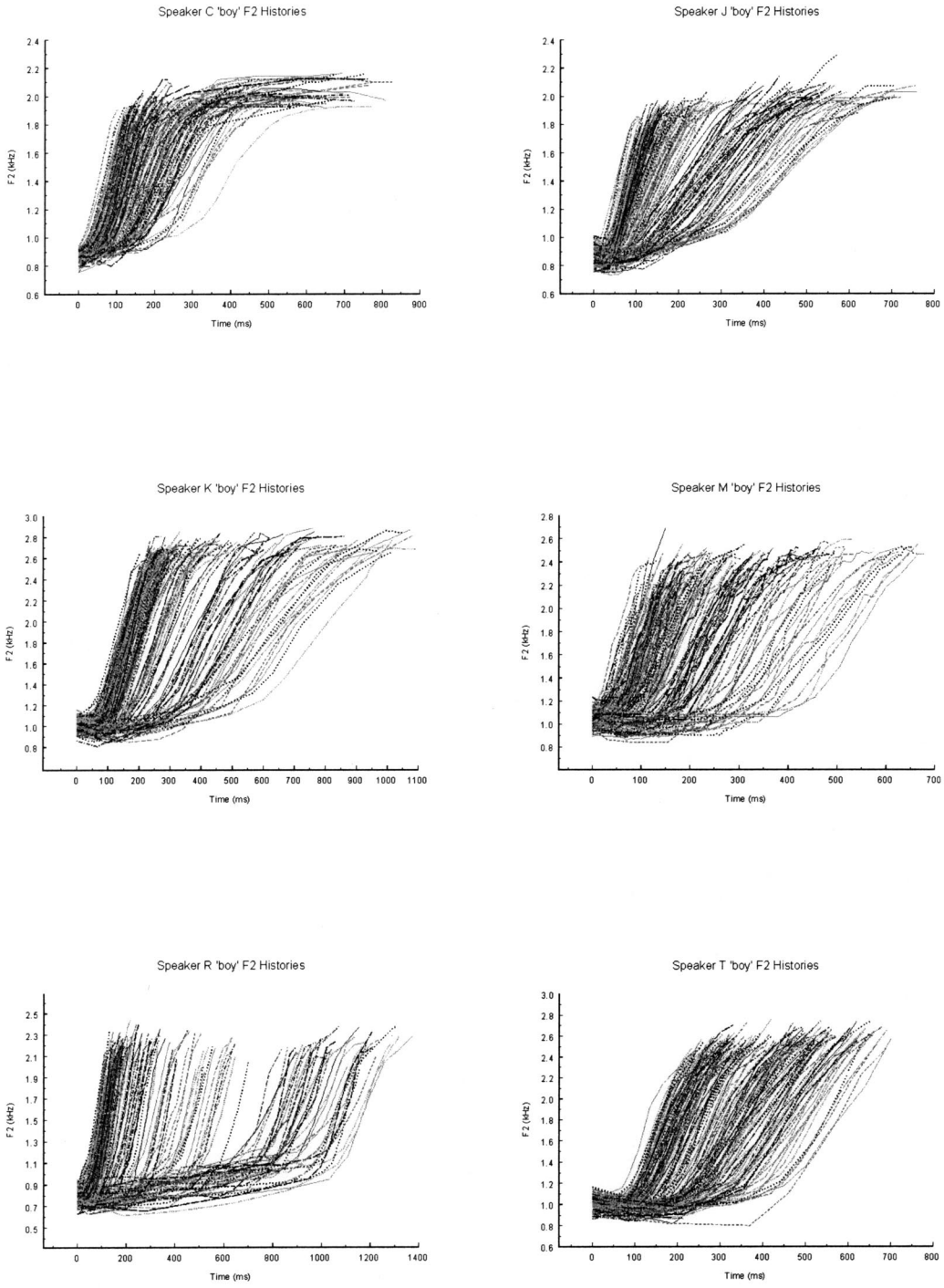

FIG. 5. Complete formant tracks for ''boy,'' as a function of vowel duration; moving from left to right on the *x*-axis represents increasingly slower speaking rate.

ticulatory effects of varying vowel environments on consonant onset measures (i.e., F2on) reported by Recasens (1985) [see a similar comment regarding the influence of rate on F2on measures in Tjaden and Weismer (1998)]. The rate effect therefore appears to be a real coarticulatory effect, reflecting varying and apparently systematic degrees of phasing between the V and C gestures.

At vowel durations greater than 200 ms, the F2off values are spread out across the duration continuum in a nearly flat fashion, more or less at values found at the bottom of the steep function for the 0–200-ms range. Whatever phasing is realized at the longest vowel durations in the 0–200-ms range, therefore, does not appear to be subject to further modification by additional slowing of speaking rate. Thus the quadratic functions shown in Fig. 4 are apparently the result of a floor effect on the pulling apart of the vowel and consonant gestures, perhaps like the boundary of a ''phase window'' (Byrd, 1996). The flattened distribution of the F2off values beyond vowel durations of 200 ms is an acoustic manifestation of this boundary.[2] When the present acoustic

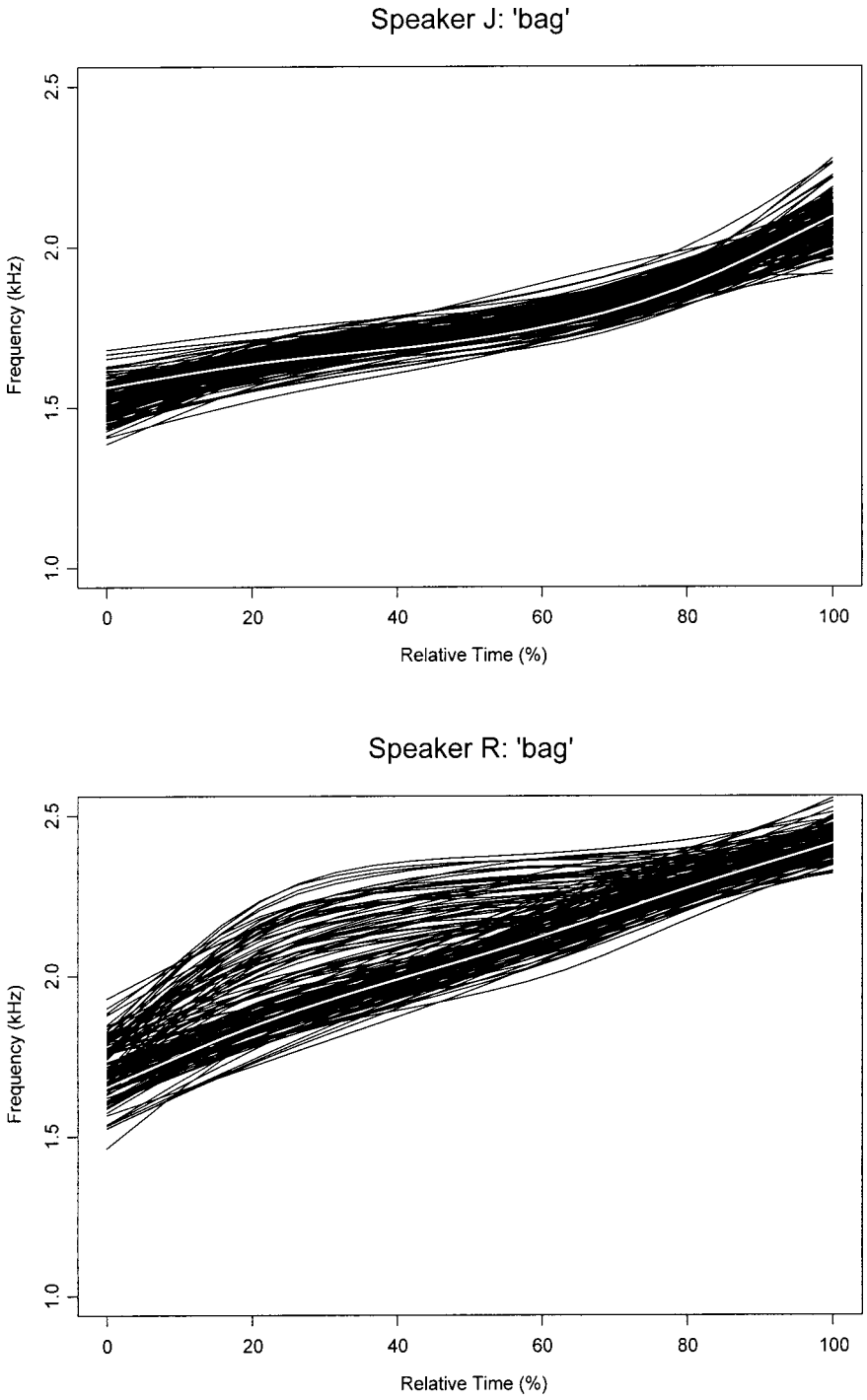

FIG. 6. Time normalized formant tracks with average-habitual formant tracks, the latter shown as thin white lines within the multiple black trajectories.

data are interpreted within the framework of coproduction variations associated with different degrees of gesture phasing, the potential for continuous phasing (Byrd, 1996; Saltzman and Byrd, 2000) may have validity when vowel durations are less than 200 ms, but not at durations above this value. Very slow speaking rates, therefore, may produce articulatory behavior qualitatively different from the behaviors observed in the habitual-fast rate range (Adams *et al.*, 1993; Shaiman *et al.*, 1997). More specifically, rate variations that cover a range of very slow rates may induce behaviors that are not representative of rate variations within a more ''normal'' range. The straightforward acoustic effects predicted by coproduction models are not reflected in the present data at

TABLE III. Variance accounted for (r^2) by vowel duration for measure of F2 maximum rate of change and duration of the first plateau for ''boy.''

	Speaker					
Measure	C_m	J_m	K_f	M_f	R_m	T_f
F2 maximum rate of change	84%	91%	84%	60%	80%	65%
Duration of the first plateau	58%	77%	77%	62%	72%	78%

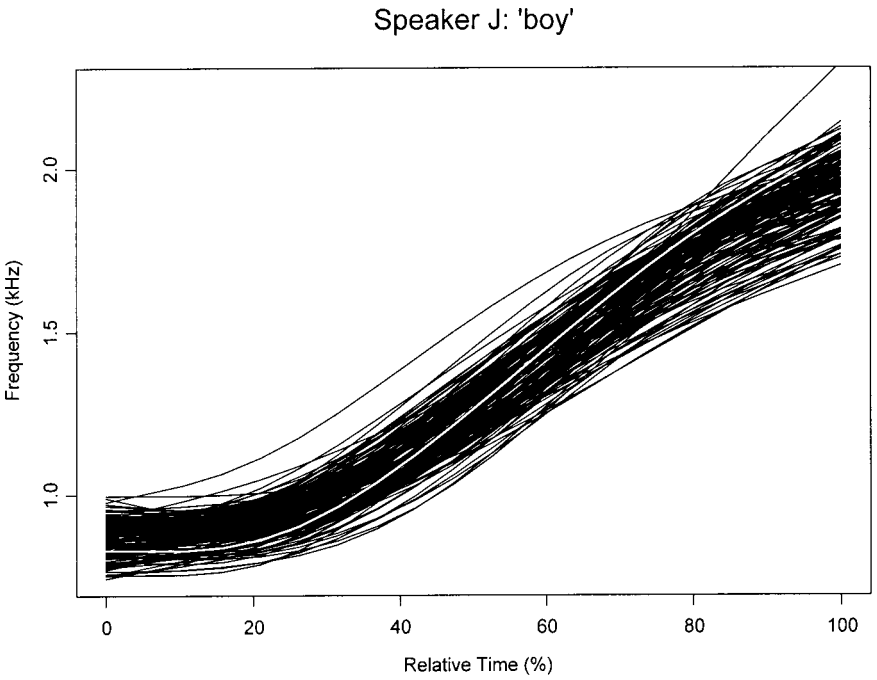

FIG. 6. (*Continued.*)

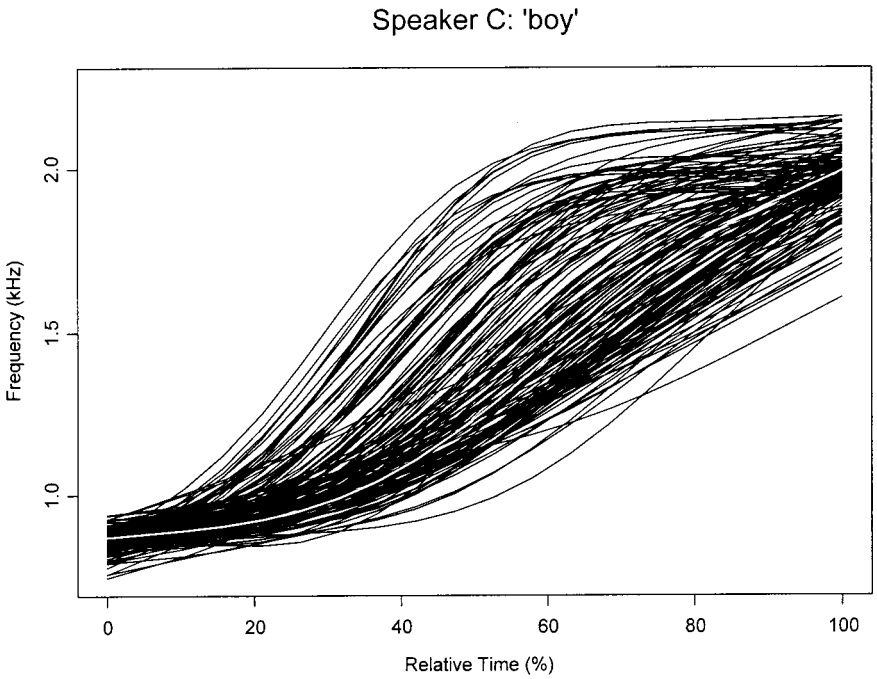

very slow speaking rates. This observation may be important for experiments in which extremely slow rates, where vowel durations clearly exceed 200 ms, are used to make theoretical points concerning the linear sliding of gestures and their blending and superposition (e.g., see Munhall and Löfqvist, 1992).

The ''bottomed out'' F2off values can be thought of as nearly ''pure'' bilabial loci. Within the 0–200-ms range there is a continuous variation of coarticulatory effects, down to the (slow-rate) limit of gesture phasing where the vocal tract configuration for the schwa is minimally affected by the vowel on the other side of the stop. Tongue movements in relation to and during the /b/ closure interval should show

TABLE IV. Variation in F2 shape correlation explained by vowel duration. Large values indicate those cases in which the trajectory shape was dependent on vowel duration, indicating shape change with rate; values close to zero indicate shape preservation across rate.

	Word		
Speaker	''bead''	''bag''	''boy''
C_m	2%	**22%**	**63%**
J_m	2%	5%	2%
K_f	0%	4%	8%
M_f	14%	11%	**34%**
R_m	9%	**77%**	**55%**
T_f	3%	8%	1%

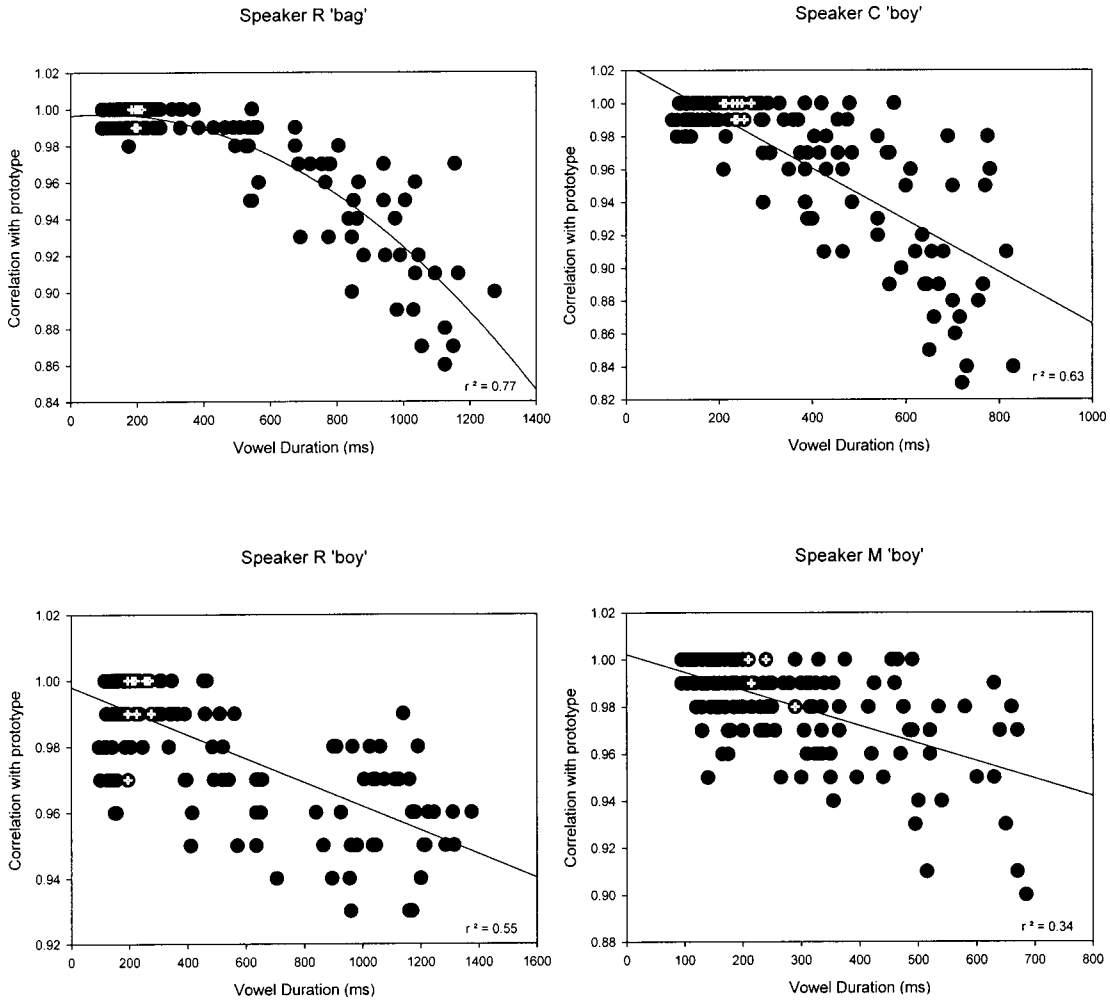

FIG. 7. Scatterplots demonstrating the relationship between vowel duration and trajectory prototype correlations. White crosses in the plots (confined to the upper left quadrant of each plot) indicate formant tracks that contributed to the definition of the average-habitual formant movement.

corresponding changes with rate. Löfqvist and Gracco (1999) describe some data (see also Engstrand, 1988) relevant to this issue, in the form of lingual motions during the closure intervals of bilabial stops in VCV sequences. In the majority of VCV sequences they studied, such as /abi/, /ibu/, and /iba/, Löfqvist and Gracco (1999) found that over half the tongue motion from the first to second vowel took place during the bilabial stop closure interval. These tongue motion paths did not appear to be perturbed by the onset or offset of the closure, but rather gave the appearance of continuous trajectories occurring ''under cover'' of the labial closure.

For the present data, the tongue motion paths shown in Fig. 8 for the target VCV sequence in /pʊtəbidhɪr/, modeled after the plots of Löfqvist and Gracco (1999, e.g., their Fig. 2, pp. 1868–1869), illustrate how rate might affect the relative phasing of the vowel and consonant gestures and hence the F2off value at the VC boundary. Three tongue trajectories are shown, one for a very fast production (right-most arrowhead), the second for a slow-habitual (vowel duration close to 200 ms) production (middle arrowhead), and the third for a very slow (vowel duration >200 ms) production (left-most arrowhead). The three trajectories should be considered as derived from the same front pellet (or receiver) motion; they are arrayed horizontally for illustration purposes only. The beginning of each trajectory corresponds in time to the first glottal pulse of /ə/, the end (the tip of the arrowhead) to the glottal pulse at which the highest F2 value for /i/ is first reached. The tongue shape for /ə/ and the palate shape have

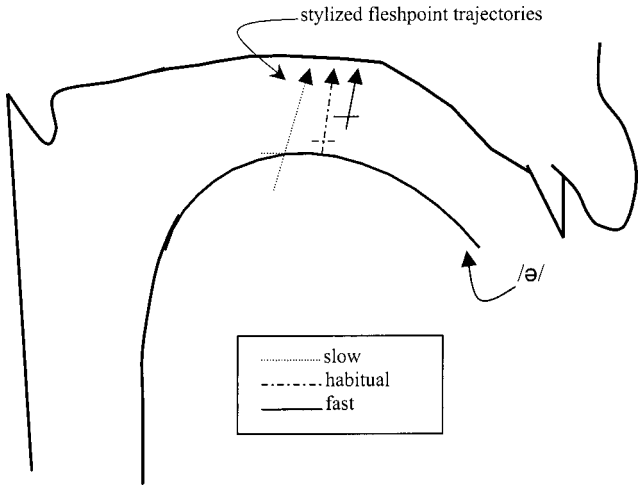

FIG. 8. Schematic tongue trajectories for three speaking rates; see text for additional details.

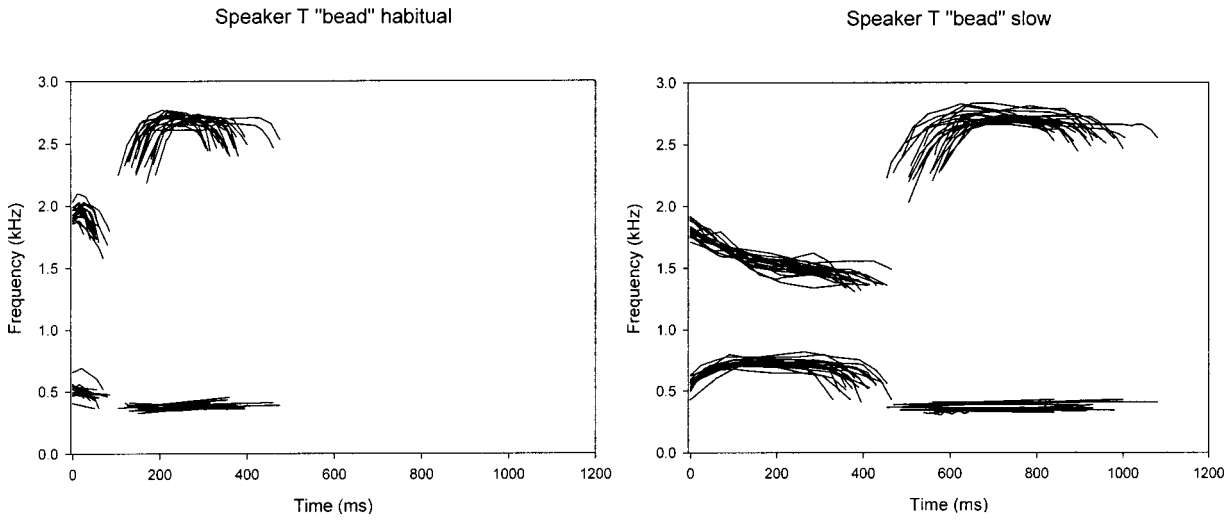

FIG. 9. Formant tracks for schwa plus target vowel in two rate categories—habitual (left panel) and slow (right panel).

been estimated from a single speaker in the x-ray microbeam database (Westbury, 1994). The rightmost path, which schematizes a very fast production, shows the pellet trajectory starting somewhat above the /ə/ shape and finishing close to the hard palate, with the onset of the closure interval, indicated by the horizontal line crossing the trajectory, approximately $\frac{1}{3}$ of the way up the path. The F2off value will, in this situation, be raised in the direction of the F2 ''target'' value for /i/, reflecting substantial coarticulation with the transconsonantal vowel. The middle or slow-habitual trajectory is somewhat longer than the fast trajectory but has roughly the same proportional phasing of the onset of the closure interval relative to the overall pathway length. The lengthening is primarily a result of a lower jaw/tongue position at the start of the tongue path, a little above the schwa configuration. For this production at the slow end (~200 ms) of the habitual rate range the F2off will be close to the ''pure'' bilabial locus mentioned above (see van Bergem, 1994, p. 159). As rate is changed between these first two examples the phasing of the lingual and labial gestures will change more or less continuously but their proportional timing will be roughly maintained. This is because the scale of the movement is modified, suggesting that rate-induced changes in gesture overlap must account for changes in movement scale as well as timing. Roughly the same thing will happen for tongue paths at very slow rates (leftmost arrow), where the trajectory distance will be greater still but the proportional phasing of the closure onset will result in an F2off much like that observed for the 200-ms rate. For even slower rates the F2off will remain roughly at this value, of course, only if the phonetic characteristic of the schwa is acceptable as schwa (or perhaps /ʌ/). The current speakers typically produced the vowel preceding the /b/ as an unambiguous /ə/ at the fast and habitual rates, and in some cases as a slightly lowered /ʌ/ at the very slow rates, but they did not produce the vowel as, for example, /ɑ/.

The acoustic manifestations of such articulatory behavior are exemplified in Fig. 9, where sets of formant trajectories for habitual-rate (left panel) productions of /əbi/ (from ''Put *a bead* here'') can be compared to sets for very slow rate (right panel) productions. These data are from one of the speakers who showed significant regression functions for vowel duration and F2off (Table II, speaker T). Clearly the slow-rate productions pull the schwa F2 trajectory to an endpoint that is very much like that expected from the classical, ''neutral'' F-pattern, whereas the habitual-rate schwa F2 endpoints are much higher, reflecting the influence of the transconsonantal /i/. Note the similarity across rates of the F2 trajectories for /i/, and especially the virtual identity of the ''target'' values corresponding to the equivalent tongue-path endpoints across rate, shown in Fig. 8. This acoustic example highlights the changing scale across rates of the underlying vocal tract adjustments, and by inference the movements affecting those adjustments, and demonstrates the importance of scale in a theory of coarticulation/coproduction. Whereas it has been shown previously that schwa is sensitive to the coarticulatory effects of phonetic context and stress (e.g., Browman and Goldstein, 1992b; van Bergem, 1994; Magen, 1997), the specific effects of rate variation on schwa have not been well studied. Interestingly, the rate-induced acoustic effects on schwa shown in Fig. 9 are only slightly less in magnitude than the phonetic context effects on F2 of schwa reported by van Bergem (1994). Presumably both rate and context effects such as these can ultimately be jointly explained, perhaps by an elaboration of the simple articulatory model shown in Fig. 8.

It is not clear why the F2off-vowel duration functions are typically so weak for /boɪ/. The one subject with a significant function (Table II, speaker T) produces it in the direction of the bilabial locus, but the scatterplot does not show the two data ranges discussed above, possibly because there are essentially no vowel durations less than 200 ms. This speaker produced the longest minimum vowel and diphthong durations in the experiment, and so perhaps the significant effect is tied to her particular operating range for vocalic durations. This does not explain, however, why her /boɪ/ F2off-vowel duration function is not characterized by bottomed-out F2off values around 200 ms. Rather, the function shows a fairly linear decrease in F2off values from about 1.6 to 1.1 kHz over a diphthong duration range of 200–700

ms. Interestingly, the bottomed-out values of about 1.1 kHz are quite similar to the lowest F2off values in the *bead* and *bag* functions shown in Fig. 4.

B. F2on and speaking rate

Significant F2on-vowel duration functions were much less frequent than significant F2off-vowel duration functions and, when they occurred, generally accounted for relatively small amounts of shared variance. Like the F2off-vowel duration data, several of the F2on-vowel duration plots revealed a split between the behavior of the data below and above vowel durations of 200 ms (see also Tjaden and Weismer, 1998). It is unclear why F2on is not as effective as F2off in reflecting the phasing of successive articulatory gestures, but one possibility is that the kinds of pellet trajectories shown in Fig. 8 are not, when displayed as a function of time, linearly scalable across speaking rate variations (i.e., at slow rates tongue motions during the stop closure interval may not be a smoothly changing function of time). This would complicate the relationship between F2on and speaking rate, as would rate-related changes in the closure duration. Articulatory observations of these kinds of tongue motions, together with closure duration measurements, are needed to resolve this issue.

C. Formant trajectory shapes

The redundancy inherent in the speech-acoustic signal allows speakers great individual latitude in their use of articulatory strategies. A tendency that has been observed in a subset of the current data, toward changing the basic topology of the formant movement, appears to be a function of both speaker and context. Changes in the shape of the acoustic realization of a segment may create difficulties for acoustic-domain models that assume a fixed gestural form. Highly parametric (and parsimonious) models may be concerned only with changes in F2on and F2tar values as a function of speaking rate. However, some of the speakers analyzed in this study have demonstrated that, in certain contexts, the shape of the acoustic movement between F2on and F2tar may be the primary aspect of the signal that is affected by rate change, with little or no explainable variation in conventional parametric measures. Clearly, the experimental manipulation of speaking rate may produce effects on formant trajectories that depend on both speaker and type of vocalic nucleus.

Qualitative changes in behavior, as a function of rate, were also observed by Adams *et al.* (1993) in their kinematic data. Movement velocity histories of the lower lip and tongue were analyzed for five speakers producing approximately five speaking rates. Adams *et al.* (1993) reported a tendency for speakers to produce movements at faster rates, for a particular phonetic gesture, characterized by a single, predominant velocity peak. Slower rate productions for the same gesture appeared to involve submovements, characterized by multiple, lower magnitude velocity peaks (see also Shaiman *et al.*, 1997). The data presented in Tables III and IV, and the full trajectory analyses of Figs. 5 and 6 suggest the conclusion that linear time compression and expansion schemes are generally not appropriate for the representation of rate influences on formant trajectory shapes. This extends the conclusion of Broad and Clermont (1987), who could not find general rules for specifying a variety of formant trajectory shapes from a few model exemplars. Rate influences on formant trajectories can be added to this problem, as well as the influences from the apparent interactions between rate and vowel nucleus type.

D. Models of slow speaking rate: Implications

The speech behaviors of unimpaired speakers at extremely slow rates have features in common with speech produced by individuals with motor speech disorders. Atypical topologies of formant trajectories were reported by Weismer *et al.* (1992) in their study of complete F2 trajectories produced by speakers with amyotrophic lateral sclerosis (ALS). In fact, their speakers demonstrated covariation between shape deviations and vowel duration. Speakers with ALS who exhibited the slowest rates also produced formant trajectories with the most deviant shapes. This parallels the fact that speakers who demonstrated shape-shifting tendencies in the current data set also presented the most extreme speaking rates.

One use of the current observations is to consider how much of the shape changes in formant trajectories produced by individuals with dysarthria and slow speaking rates is due to the rate factor alone, as compared to the other disruptions of speech motor control that may occur. Slow speaking rate has been observed with virtually all types of dysarthria (Nishio and Niimi, 2000), with the exception of some patients with Parkinson disease or other Parkinsonian disorders. Although we have not yet attempted a formal quantitative evaluation of this question, it is clear from the present data that at least some aspect of formant trajectory shape in the speech of persons with dysarthria is probably explained by the rate anomaly. The reason why this is an important consideration is that a very popular rehabilitation strategy, even for patients who present with very slow speaking rate as a symptom of their disorder, is to slow rate even further to allow patients sufficient time to ''hit the targets'' and therefore increase speech intelligibility (e.g., Yorkston *et al.*, 1995). The present data suggest that increased slowing of rate will lead to greater topological change of the formant trajectories, and presumably of the underlying articulatory behavior, perhaps with added physiological cost in producing such relatively complicated motions. Moreover, there is very little evidence that slowing rate actually increases speech intelligibility in persons with dysarthria, and in fact some evidence against the theoretical basis of slow-rate therapies (see Weismer *et al.*, 2000).

Because slow speaking rates have not been studied very carefully, little is known about the acoustic implications of the accompanying changes in articulatory control. This information would not only be useful for gaining a more complete understanding of rate and speech production, but is also likely to shed light on perceptual characteristics of slow-rate speech, which are important in dysarthria. For example, it is likely that the kinds of formant trajectory shape-shifting described above have an effect on speech intelligibility and/or

speech naturalness, but these effects are essentially unknown. Formant trajectory shape changes may be perceptually tolerable, and yet non-negligible since they may convey aspects of vowel quality that relate to the more global issue of speaker intelligibility. Currently, there is much to be revealed about the interrelationships among intelligibility, perception, acoustics, and articulation.

E. Conclusion

In summary, the current work demonstrates that conventional discrete-time parameters of the acoustic signal (i.e., F2off, F2on, and F2tar) can be significantly affected by speaking rate changes made by some speakers in certain contexts. Of these parameters, F2off appears to be the best single index of rate across speakers for the two monophthong contexts studied. The variation of this acoustic index is consistent with the idea of rate-induced, linear sliding of adjacent articulatory gestures, but only for a range of vowel durations typical of the habitual-to-fast end of the rate continuum. The F2off index tends to be fairly constant for a wide range of slow rates (i.e., vowel durations$>$200 ms), perhaps reflecting a limit to the separation of adjacent articulatory gestures. None of these parameters is systematically influenced by rate across speakers in the diphthong context. For the production of /bɔɪ/, speakers tend to alter the duration of the initial F2 plateau (associated with the onglide) and the maximum rate of change in F2 (associated with the major diphthong transition). Speakers can be distinguished with regard to the proportion of variation between these parameters that is accounted for by speaking rate. Three of the six speakers demonstrate tendencies toward changing the basic shape of the F2 trajectory for /bɔɪ/ as they change rate. Two of these three speakers also do this for /bæg/. One conclusion from these observations is that interactions of rate variation with speaker and vocalic nucleus type are probably the rule, rather than the exception. Taken together the findings of this study have implications regarding the importance of accounting for changes in movement scale and gestural form in models of gestural overlap. Also, the similarities between the extreme slow speech of speakers in this study and some speakers with dysarthria suggest that some anomalous patterns of dysarthric speech may be explained by extreme slow speaking rate, independent of the specific neurological effects on speech production.

ACKNOWLEDGMENTS

The work reported here was supported by NIH Award No. NIDCD P60 DC01409. We thank Yana Yunusova and Jordan Green for comments on an earlier draft of the manuscript.

[1]The F2on parameter appeared to be the weakest of the three discrete spectral measures in documenting rate effects. It was hypothesized that the somewhat surprising weakness in the relationship between vowel duration and F2on could have been the result of a masking effect of the stop burst on F2on. To evaluate this proposition, the second resonance frequency of the stop burst was measured for a subset of data (speaker R ''bag''). The F2on data were ''corrected'' using linear regression coefficients that described the relationship between F2on and the second resonance frequency of the stop burst. However, the variation in these ''corrected'' F2on values explained by vowel duration reveal no increase in magnitude.

[2]The notion of overlapping gestures and their degree of variation due to factors such as stress, rate, context, and so forth, carries with it at least the implicit, and sometimes explicit, expectation of systematic acoustic variations reflecting the articulatory variation: ''An utterance is described not only by the parameter values of the component gestures but by how the gestures are coordinated or phased with one another. This approach captures coproduction by allowing gestures to overlap in time, with the acoustic consequences of the coproduced units reflecting their combined influence on the vocal tract'' (Saltzman and Byrd, 2000, p. 501).

Adams, S. G., Weismer, G., and Kent, R. D. (**1993**). ''Speaking rate and speech movement velocity profiles,'' J. Speech Hear. Res. **36**, 41–54.

Bradlow, A. R., Torretta, G. M., and Pisoni, D. B. (**1996**). ''Intelligibility of normal speech I: Global and fine-grained acoustic-phonetic talker characteristics,'' Speech Commun. **20**, 255–272.

Broad, D. J., and Clermont, F. (**1987**). ''A methodology for modeling vowel formant contours in CVC context,'' J. Acoust. Soc. Am. **81**, 155–165.

Broad, D. J., and Clermont, F. (**2002**). ''Linear scaling of vowel-formant ensembles (VFEs) in consonantal contexts,'' Speech Commun. **37**, 175–195.

Broad, D. J., and Fertig, R. H. (**1970**). ''Formant frequency trajectories in selected CVC-syllable nuclei,'' J. Acoust. Soc. Am. **47**, 1572–1582.

Browman, C. P., and Goldstein, L. (**1992a**). ''Articulatory phonology: An overview,'' Phonetica **49**, 155–180.

Browman, C. P., and Goldstein, L. (**1992b**). '' 'Targetless' '' schwa: an articulatory analysis,'' in *Papers in Laboratory Phonology II. Gesture, Segment, Prosody*, edited by G. J. Docherty and D. R. Ladd (Cambridge U.P., New York), pp. 26–56.

Byrd, D. (**1996**). ''A phase window framework for articulatory timing,'' Phonology **13**, 139–169.

Byrd, D., and Tan, C. C. (**1996**). ''Saying consonant clusters quickly,'' J. Phonetics **24**, 263–282.

Chambers, J. M., Cleveland, W. S., Kleiner, B., and Tukey, P. A. (**1983**). *Graphical Methods for Data Analysis* (Wadsworth, Belmont).

Clermont, F. (**1993**). ''Spectro-temporal description of diphthongs in F_1-F_2-F_3 space,'' Speech Commun. **13**, 377–390.

Dolan, W. B., and Mimori, Y. (**1986**). ''Rate-dependent variability in English and Japanese complex vowel F2 transitions,'' UCLA Working Papers in Phonetics, Vol. 63, pp. 125–153.

Engstrand, O. (**1988**). ''Articulatory correlates of stress and speaking rate in Swedish VCV utterances,'' J. Acoust. Soc. Am. **83**, 1863–1875.

Fant, G. (**1960**). *Acoustic Theory of Speech Production* (Mouton, The Hague).

Gay, T. (**1968**). ''Effect of speaking rate on diphthong formant movement,'' J. Acoust. Soc. Am. **44**, 1570–1573.

Gay, T. (**1978**). ''Effect of speaking rate on vowel formant movements,'' J. Acoust. Soc. Am. **63**, 223–230.

Hillenbrand, J. H., and Gayvert, R. T. (**1993**). ''Vowel classification based on fundamental frequency and formant frequencies,'' J. Speech Hear. Res. **36**, 694–700.

Hillenbrand, J. H., Clark, M. J., and Nearey, T. M. (**2001**). ''Effects of consonant environment on vowel formant patterns,'' J. Acoust. Soc. Am. **109**, 748–763.

Ladefoged, P., Harshman, R., Goldstein, L., and Rice, L. (**1978**). ''Generating vocal tract shapes from formant frequencies,'' J. Acoust. Soc. Am. **64**, 1027–1035.

Lindblom, B. (**1962**). ''Accuracy and limitations of sona-graphic measurements,'' in Proceedings of the 4th International Congress of Phonetic Sciences, Helsinki 1961 (Mouton, The Hague).

Lindblom, B. (**1963**). ''Spectrographic study of vowel reduction,'' J. Acoust. Soc. Am. **35**, 1773–1781.

Liss, J. M., and Weismer, G. (**1992**). ''Qualitative acoustic analysis in motor speech disorders,'' J. Acoust. Soc. Am. **92**, 2984–2987.

Löfqvist, A., and Gracco, V. L. (**1999**). ''Interarticulator programming in VCV sequences: Lip and tongue movements,'' J. Acoust. Soc. Am. **105**, 1864–1876.

Magen, H. S. (**1997**). ''The extent of vowel-to-vowel coarticulation in English,'' J. Phonetics **25**, 187–205.

Manuel, S. (**1990**). ''The role of contrast in limiting vowel-to-vowel coarticulation in different languages,'' J. Acoust. Soc. Am. **88**, 1286–1298.

Milenkovic, P. (**1994**). *Cspeech Version 4.0* (Computer Program), University of Wisconsin—Madison.

Monsen, R., and Engebretson, A. (**1983**). ''The accuracy of formant frequency measurements: A comparison of spectrographic analysis and linear prediction,'' J. Speech Hear. Res. **26**, 89–97.
Munhall, K., and Löfqvist, A. (**1992**). ''Gestural aggregation in speech: laryngeal gestures,'' J. Phonetics **20**, 111–126.
Nearey, T. (**1989**). ''Static, dynamic, and relational properties in vowel perception,'' J. Acoust. Soc. Am. **85**, 2088–2113.
Nishio, M., and Niimi, S. (**2000**). ''Speaking rate and its components in dysarthric speakers,'' Clin. Ling. Phon. **15**, 309–317.
Perkell, J. S., and Nelson, W. L. (**1985**). ''Variability in the production of the vowels /i/ and /a/,'' J. Acoust. Soc. Am. **77**, 1889–1895.
Picheny, M. A., Durlach, N. I., and Braida, L. D. (**1986**). ''Speaking clearly for the hard of hearing II: Acoustic characteristics of clear and conversational speech,'' J. Speech Hear. Res. **29**, 434–446.
Pitermann, M. (**2000**). ''Effect of speaking rate and contractive stress on formant dynamics an vowel perception,'' J. Acoust. Soc. Am. **107**, 3425–3437.
Recasens, D. (**1985**). ''Coarticulatory patterns and degrees of coarticulatory resistance in Catalan CV sequences,'' Lang Speech **28**, 97–114.
Saltzman, E., and Byrd, D. (**2000**). ''Task-dynamics of gestural timing: Phase windows and multifrequency rhythms.,'' Hum. Mov. Sci. **19**, 499–526.
Saltzman, E., and Munhall, K. G. (**1989**). ''A dynamical approach to gestural patterning in speech production,'' Ecological Psychol. **1**, 333–382.
Shaiman, S. (**2001**). ''Kinematics of compensatory vowel shortening: the effect of speaking rate and coda composition on intra- and inter-articulatory timing.,'' J. Phonetics **29**, 89–107.
Shaiman, S., Adams, S. G., and Kimelman, M. D. Z. (**1997**). ''Velocity profiles of lip protrusion across changes in speaking rate,'' J. Speech Hear. Res. **40**, 144–158.
Stevens, K. N. (**1998**). *Acoustic Phonetics* (MIT, Cambridge, MA).
Stevens, K. N., and House, A. S. (**1963**). ''Perturbation of vowel articulations by consonantal context: An acoustical study,'' J. Speech Hear. Res. **6**, 111–128.
Stevens, K. N., House, A. S., and Paul, A. P. (**1966**). ''Acoustical description of syllabic nuclei: An interpretation in terms of a dynamic model of articulation,'' J. Acoust. Soc. Am. **40**, 123–132.
Strange, W. (**1989**). ''Dynamic specification of coarticulated vowels spoken in sentence context,'' J. Acoust. Soc. Am. **85**, 2135–2153.
Sussman, H. M., Fruchter, D., Hilbert, J., and Sirosh, J. (**1998**). ''Linear correlates in the speech signal: The orderly output constraint,'' Behav. Brain Sci. **21**, 241–299.
Tjaden, K., and Weismer, G. (**1998**). ''Speaking-rate-induced variability in F2 trajectories,'' J. Speech Hear. Res. **41**, 976–989.
Turner, G. S., Tjaden, K., and Weismer, G. (**1995**). ''The influence of speaking rate on vowel space and speech intelligibility for individuals with amyotrophic lateral sclerosis,'' J. Speech Hear. Res. **38**, 1001–1013.
van Bergem, D. R. (**1994**). ''A model of coarticulatory effects on the schwa,'' Speech Commun. **14**, 143–162.
van Son, R. J. J. H., and Pols, L. C. W. (**1992**). ''Formant movements of Dutch vowels in text, read at normal and fast rate,'' J. Acoust. Soc. Am. **92**, 121–127.
Watson, C. I., and Harrington, J. (**1999**). ''Acoustic evidence for dynamic formant trajectories in Australian English vowels,'' J. Acoust. Soc. Am. **106**, 458–468.
Weismer, G., Kent, R. D., Hodge, M., and Martin, R. (**1988**). ''The acoustic signature for intelligibility test words,'' J. Acoust. Soc. Am. **84**, 1281–1291.
Weismer, G., Laures, J. S., Jeng, J-Y., Kent, R. D., and Kent, J. F. (**2000**). ''Effect of speaking rate manipulations on acoustic and perceptual aspects of the dysarthria in amyotrophic lateral sclerosis,'' Folia Phoniatr Logop **52**, 201–219.
Weismer, G., Martin, R., Kent, R. D., and Kent, J. F. (**1992**). ''Formant trajectory characteristics of males with ALS,'' J. Acoust. Soc. Am. **91**, 1085–1098.
Weismer, G., Tjaden, K., and Kent, R. D. (**1995**). ''Articulatory characteristics in motor speech disorders: relationships to models and theories of normal speech production,'' J. Phonetics **23**, 149–164.
Westbury, J. R. (**1994**). *X-ray Microbeam Speech Production Database User's Handbook* (Waisman Center on Mental Retardation, UW—Madison, Madison, WI).
Yorkston, K. M., Miller, R. M., and Strand, E. A. (**1995**). *Management of Speech and Swallowing in Degenerative Diseases* (Communication Skill Builders, Tucson, AZ).

Functional differences between vowel onsets and offsets in temporal perception of speech: Local-change detection and speaking-rate discrimination[a)]

Hiroaki Kato[b)]
ATR Human Information Science Laboratories, Hikaridai, Seika-cho, Kyoto 619-0288, Japan

Minoru Tsuzaki
ATR Spoken Language Translation Research Laboratories, Hikaridai, Seika-cho, Kyoto 619-0288, Japan

Yoshinori Sagisaka
Graduate School of Global Information and Telecommunication Studies, Waseda University Nishi-Waseda, Shinjuku-ku, Tokyo 169-0051, Japan and ATR Spoken Language Translation Research Laboratories, Hikaridai, Seika-cho, Kyoto 619-0288, Japan

(Received 8 January 2002; accepted for publication 5 February 2003)

To provide a perceptual framework for the objective evaluation of durational rules in speech synthesis, two experiments were conducted to investigate the differences between vowel (V) onsets and V-offsets in their functions of marking the perceived temporal structure of speech. The first experiment measured the detectability of temporal modifications given in four-mora (CVCVCVCV) Japanese words. In the V-onset condition, the inter-onset intervals of vowels were uniformly changed (either expanded or reduced) while their inter-offset intervals were preserved. In the V-offset condition, this was reversed. These manipulations did not change the duration of the entire word. Each of the modified words was paired with its unmodified counterpart, and the pair was given to listeners, who were asked to rate the difference between the paired words. The results show that there were no significant differences in the listeners' abilities to detect the temporal modification between the V-onset and V-offset conditions. In the second experiment, the listeners were asked to estimate the differences they perceived in speaking rates for the same stimulus set as that of the first experiment. Interestingly, the results show a clear difference in the listeners' performance between the V-onset and V-offset conditions. Specifically, changing the V-onset intervals changed the perceived speaking rates, which showed a linear relation ($r=-0.9$) despite the fact that the duration of the entire word remained unchanged. In contrast, modifying the V-offset intervals produced no clear relation with the perceived speaking rates. The second experiment also showed that the listeners performed well in speaking rate discrimination (3.5%–5% in the change ratio). These results are discussed in relation to the differences in the listeners' temporal processing range (local or global) between the two experiments.
[DOI: 10.1121/1.1568760]

PACS numbers: 43.72.Lc, 43.66.Mk, 43.71.Gv, 43.70.Fq [DOS]

I. INTRODUCTION

Since temporal structures such as rhythm and tempo can be perceived in ordinary speech, there should be cues that give us reference points for such structures in speech. The overall goal of our series of temporal perception studies has been to systematically identify which cues humans use in perceiving temporal structures of speech and describe how they use them. By way of breaking down the problem, we have studied how accurately humans perceive the temporal structures of speech and how phonetic and phonological factors affect this ability by measuring sensitivities to modifications made in segments of speech, i.e., the vowels and consonants. This approach was originally motivated by the requirement of evaluating rules for assigning segmental durations in speech synthesis.

Many of the duration rules used for speech synthesis have been developed to replicate temporal structures in natural speech (Carlson and Granström, 1986; Iwahashi and Sagisaka, 2000; Kaiki and Sagisaka, 1992; Klatt, 1979; van Santen, 1994). To estimate the requisite temporal precision for these rules, studies have investigated perceptual sensitivity to temporal modifications in a single speech segment or two (Bochner *et al.*, 1988; Carlson and Granström, 1975; Klatt, 1975). Along these lines, we have also investigated the factors affecting the temporal perception of speech: (1) the sensitivity to a single vowel (V) duration (Kato *et al.*, 1998), (2) that of a single consonantal (C) duration (Kato *et al.*, 2002), and (3) the perceptual interaction, e.g., the compensation relation between modifications in two consecutive segments (CV or VC) (Kato *et al.*, 1997). However, three or

[a)]Part of this work was done while the first and second authors were with ATR Human Information Processing Research Laboratories and the third author was with ATR Interpreting Telecommunications Research Laboratories. Some of the material in this manuscript was presented at the 132nd meeting of the Acoustical Society of America [J. Acoust. Soc. Am. **100**, 2829(A) (1996)].

[b)]Electronic mail: kato@atr.co.jp

more segmental errors should be simultaneously dealt with to make such an estimation more practical. Even a single segmental error below the sensing threshold may become obvious when it accumulates over a number of segments.

As a way to extend the previous attempts to multiple (more than two) segments, the current study focuses on multiple segmental boundaries and investigates their perceptual functions to mark the temporal structure of speech. This approach is taken because the control of segmental duration is interchangeable with the temporal alignment of segmental boundaries (including those between pauses and utterances). That is, any change in a segmental duration can be described by the change in the distance of the segmental boundaries. Such a generalized representation is beneficial to a wide range of application fields that involve perceptual modeling of temporal changes in speech. In addition to an objective assessment of synthesis rules, it can be applied, for instance, to an automatic speech recognition system or to computer-assisted training methods in second-language prosody acquisition (Tajima *et al.*, 2002).

Among various types of segmental boundaries, the current study deals with the boundaries between vowels and either consonants or pauses, i.e., vowel onsets (V-onsets) and vowel offsets (V-offsets), because they generally coincide with large and rapid acoustical changes, suggesting that they are perceptually salient. An argument for the perceptual saliency of V-onsets and V-offsets was made in a previous study (Kato *et al.*, 1997). In that study, they measured the human sensitivity to temporal displacements of a single V-onset or V-offset in a four-mora word (i.e., CVCVCVCV) introduced by a compensatory durational change in a pair of a vowel and either its preceding or following consonant. Each durational modification was achieved by a resynthesis technique that did not require splicing. The results showed no significant differences between C-to-V boundaries, or V-onsets, and V-to-C boundaries, or V-offsets, in the listeners' ability to detect the temporal displacements. This finding implies that the functions of V-onsets and V-offsets are comparable in a certain aspect of temporal perception.

On the other hand, quite a few other studies have reported evidence suggesting functional differences between V-onsets and V-offsets or the dominance of V-onsets. Typical examples can be found in the many studies on perceptual centers (P-centers) (Marcus, 1981; Scott, 1993), which have tried to determine the acoustical correlates to the temporal location of perceived beats in speech. Although the central focus of these studies has been the accurate calculation of beat locations in relation to acoustical features of speech, they have commonly regarded the contribution of V-onsets as greater than that of V-offsets. In particular, the studies of Ventsov (1981) and Pompino-Marschall *et al.* (1982) compared the contributions of V-onsets and V-offsets to tempo perception. Both studies used the alternation of synthesized segment /m/ and segment /a/ and controlled the tempi of V-onsets and V-offsets separately. The results of tempo matching tests showed that their listeners preferred the tempi of the V-onsets to those of the V-offsets. In addition, several empirical studies using reproducing tasks have suggested the locations of perceptual beats to be near V-onsets. Allen (1972) and Sato (1977) both found that the locations of syllable beats were at V-onsets or the release points of stop consonants toward vowels. They determined this by using methods such as the synchronization of finger tapping with cyclic speech and the matching of an auditory click to a perceptual beat. All of these findings imply that the functions of V-onsets eclipse those of V-offsets in some aspects of temporal perception. These studies relating P-centers or beat locations are referred to as the ''P-center studies'' in the remainder of this paper.

The discrepancies between Kato *et al.*'s (1997) study and the P-center studies can be attributed to differences in the range of stimulus manipulation and the listeners' task. Kato *et al.* (1997) manipulated only two segments (CV or VC) out of eight (CVCVCVCV), and the listeners could achieve their task by detecting just a local, i.e., within a two-segment range, temporal distortion in an isolated word. On the other hand, the P-center studies generally used long stimulus sequences such as a sentence or a repetition of a single syllable, and the tasks required the listeners to process the target sequence as a whole. This contrast in the processing range, i.e., local in Kato *et al.* (1997) versus global in the P-center studies, possibly caused the apparent discrepancies in the functions of the vowel onsets and offsets.

The goal of the current study is to explore the functional differences between V-onsets and V-offsets in the temporal perception of speech by addressing the possible significance of the local-global contrast outlined above. Two steps were introduced in the experimental setup to help the listeners process a wider range of information than in Kato *et al.*'s (1997) study. First, in experiment 1, the stimulus manipulations covered an entire word, i.e., all V-onsets or V-offsets in the word were subjected to temporal modification, while Kato *et al.* (1997) only changed one of the V-onsets or V-offsets in a word. The listeners' task was to detect these manipulations. Accordingly, the stimulus conditions fundamentally differed from those of Kato *et al.*'s (1997) experiment: the current study involves a global manipulation while the previous work involved a local one. As the second step, in experiment 2, the listeners were asked to estimate changes in the perceived speaking rate for the same stimuli as in experiment 1. Accordingly, the listeners' task in experiment 2 fundamentally differed from that in experiment 1: the speaking-rate task required the listeners to use global information, while the detection task could be achieved by observing only local differences for the stimuli.

Experiment 2 is also useful in answering two key questions: (1) What is the major cue in the speech signal to perceive the speaking rate? There seems to be no doubt that we can judge the rate of natural speech. However, it is unclear which cue allows us to perceive the speaking rate. This study focuses on V-onsets and V-offsets and estimates their contributions to the perceived speaking rate. (2) To what extent is the rate perception accurate? Little is known about the human ability to discriminate changes in the rate or tempo of speech sounds, despite the fact that speaking rate is one of the most basic control factors in speech synthesis.[1]

TABLE I. Temporal profiles of the ten speech tokens used in experiments 1 and 2. (1) word duration and mean syllable (CV) duration, (2) total and mean inter-V-onset intervals, and (3) total and mean inter-V-offset intervals. All tokens are four-mora (and four-syllable) Japanese words (CVCVCVCV, i.e., each possesses four V-onsets and four V-offsets) spoken naturally by a native-Japanese male speaker at a normal speed.

Token	*bakugeki*	*hachigatsu*	*hanahada*	*minogasu*	*monosashi*
Word duration (ms)	720	695	675	730	710
(Mean syllable duration (ms))	(180.0)	(173.8)	(168.8)	(182.5)	(177.5)
Total inter-V-onset interval (ms)	520	515	445	530	550
(Mean inter-V-onset interval (ms))	(173.3)	(171.7)	(148.3)	(176.7)	(183.3)
Total inter-V-offset interval (ms)	535	550	545	605	595
(Mean inter-V-offset interval (ms))	(178.3)	(183.3)	(181.7)	(201.7)	(198.3)
Token	*nagedasu*	*nakanaka*	*sakasama*	*samazama*	*sashidasu*
Word duration (ms)	740	670	735	722.5	735
(Mean syllable duration (ms))	(185.0)	(167.5)	(183.8)	(180.6)	(183.8)
Total inter-V-onset interval (ms)	550	470	495	480	535
(Mean inter-V-onset interval (ms))	(183.3)	(156.7)	(165.0)	(160.0)	(178.3)
Total inter-V-offset interval (ms)	575	530	565	535	565
(Mean inter-V-offset interval (ms))	(191.7)	(176.7)	(188.3)	(178.3)	(188.3)

II. EXPERIMENT 1: DETECTION

The purpose of experiment 1 was to test whether there are differences in listeners' performances in detecting temporal displacements in multiple segmental boundaries, i.e., global modifications, between the V-onset and V-offset conditions.

A. Method

1. Subjects

Eight adults with normal hearing participated in experiment 1. All of them were native speakers of Japanese.

2. Stimuli

Ten words were selected from the ATR speech database (Kurematsu *et al.*, 1990) as the original material (Table I). All of them were common four-mora Japanese words, and each comprised four CV syllables. The selected words were spoken naturally by one native-Japanese male speaker at a normal speed and were digitized at a 12-kHz sampling frequency with 16-bit precision.

Each of the original tokens was temporally modified in three ways: (1) entire word modification, (2) inter-V-onset interval modification, and (3) inter-V-offset interval modification, as schematically shown in Fig. 1. In the entire-word condition, the entire word duration was either expanded or reduced by 20, 40, 60, or 80 ms by changing each segmental duration proportionally. The proportions of these modification sizes to the average word duration (713.25 ms) were 2.8%, 5.6%, 8.4%, and 11.2%, respectively. This condition was included as the reference condition and also to confirm whether the subjects judged the speaking rates consistently with the physical tempi (in experiment 2).

In the V-onset or V-offset condition, each of the three inter-V-onset intervals or inter-V-offset intervals in a word was either expanded or reduced by 5, 10, or 15 ms, i.e., the change in the total inter-V-onset interval or inter-V-offset intervals was 15, 30, or 45 ms. To preserve the entire word durations and the intervals among the segmental boundaries of no interest, each of the duration modifications of the vow-

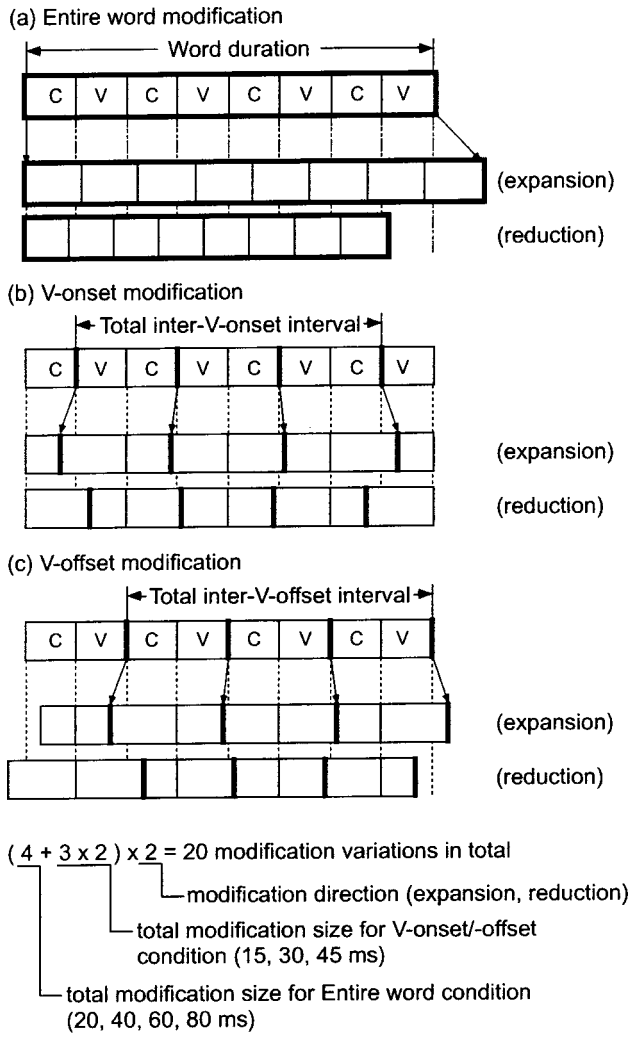

FIG. 1. Schematic diagrams showing the three types of modification applied to speech materials in experiments 1 and 2: (a) entire modification of total word duration, (b) inter-V-onset interval modification, and (c) inter-V-offset interval modification. Each "C" or "V" marks a consonant segment or a vowel segment, respectively, composing a four-mora word. The solid vertical lines represent segmental boundaries, with thick ones being the targets of temporal displacement. Note that the modifications yield no change in the (b) intervals between V-offsets, (c) intervals between V-onsets, and (b and c) word duration.

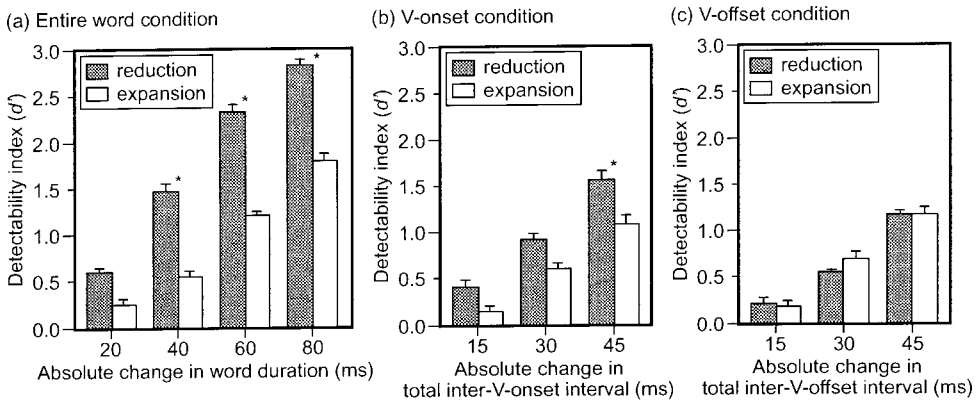

FIG. 2. Mean detectability index d' for each of the three modification conditions as a function of the change in (a) entire word duration, (b) total inter-V-onset interval, and (c) total inter-V-offset interval. The filled and open bars represent the indices for reduction and expansion modifications, respectively. The error bars show the standard errors. The asterisks show pairs of bars whose differences are statistically significant (HSD, $p<0.05$). A larger d' implies easier detection.

els was compensated with the corresponding modification of either the preceding consonant duration (V-onset condition) or the following consonant duration (V-offset condition). To expand every inter-V-onset interval by 15 ms, for instance, the first to fourth vowels in a word were modified as +22.5, +7.5, −7.5, and −22.5 ms, while the first to fourth consonants were modified as −22.5, −7.5, +7.5, and +22.5 ms [positive and negative values indicate expansion and reduction, respectively; see Fig. 1(b)].

The ranges of all temporal modifications were chosen, on the basis of preliminary experiments, as ranges within which phonetic identity would not change. In addition to the above modified stimuli, unmodified stimuli were prepared for reference. In total, 210 word stimuli were prepared (10 tokens×(2 modification directions×(4 modification sizes in the entire-word condition+3 modification sizes×2 modified boundary types in the V-onset and V-offset conditions)+1 unmodified)).

The modifications were made by a cepstral analysis and resynthesis technique with the log magnitude approximation (LMA) filter (Imai and Kitamura, 1978) and were carried out with 2.5-ms frame intervals. The duration change in a segment was achieved by deleting or doubling every nth frame in the synthesis parameters where $(n-1)$ is the quotient of the total number of frames in the entire to-be-modified part divided by the number of frames to be deleted/doubled. The parts subject to the modification were carefully trimmed out so as to exclude transient parts at both ends of the vowels, and the on-and-after burst parts of plosives or affricates were trimmed out as much as possible to prevent the modification of dynamic aspects around the segmental boundaries, which could have conceivably degraded the perceptual naturalness.

3. Stimulus presentation

Each of the prepared stimuli was paired with its counter unmodified stimulus (in the order of unmodified first), and the pairs were presented to the subjects diotically through a D/A converter (MD-8000 mkII, PAVEC), an anti-aliasing low-pass filter (FV-665, NF Electronic Instruments, f_c = 5700 Hz, −96 dB/oct), and headphones (SR-Λ Professional, driven by SRM-1 MkII, STAX). The experiment was conducted in a sound-treated room whose average background noise level was 16 dB SPL (A-weighted), which was measured at the location of the subject with a sound level meter (Type 2231, Brüel & Kjær) and a condenser microphone (Type 4155, Brüel & Kjær). The average presentation level was 73 dB SPL (A-weighted) measured with a sound level meter (Type 2231, Brüel & Kjær) through a condenser microphone (Type 4134, Brüel & Kjær) mounted on an artificial ear (Type 4153, Brüel & Kjær). All three stimulus conditions [Figs. 1(a)–(c)] were tested in the same experimental session. Fifteen percent of the trials were control trials in which the two presented stimuli were identical.

4. Task

In each trial, the subjects were asked to rate the difference between the paired word stimuli by using eight numerical categories: "0" to "7," with a larger number corresponding to a larger subjective difference. Twelve judgments were collected from each subject for each stimulus. The obtained responses were pooled over all subjects for each of the eight response categories, and then the detectability index d' was estimated in accordance with the rating procedure[2] of the theory of signal detection (Green and Swets, 1966; Macmillan and Creelman, 1991) for each comparison stimulus, i.e., each combination of token, modified boundary type, modification size, and modification direction.

B. Results

Figure 2 shows d' for each of the modified boundary types, modification sizes, and modification directions. An ANOVA was carried out on the d' data of both V-onset and V-offset conditions [Figs. 2(b) and (c)] with the boundary type (V-onset or V-offset), the absolute modification size (15, 30, or 45 ms), and the modification direction (expansion or reduction) as main factors (tokens as repetition). This showed no significant effect of the boundary type [$F(1,9)=4.44$, $p=0.064$] but a significant effect of the absolute modification size [$F(2,18)=134.53$, $p<0.0001$]: d' increased with increasing modification size. The interaction between the factors of boundary type and absolute modification size was not significant [$F(2,18)=0.036$, $p=0.76$]. The main effect of modification direction and the interaction between the factors of boundary type and modification direction were significant [$F(1,9)=7.75$, $p<0.05$, and $F(1,9)=12.48$, $p<0.01$, respectively]. No other main effect or interaction was significant.

As shown in Fig. 2(b), the effect of the modification direction seemed to be obvious in the V-onset condition: V-onset modifications tended to be more easily detected when the direction was reduction than when it was expansion. Multiple comparisons using Tukey-Kramer's HSDs

(honestly significant differences)[3] indicated that a significant difference due to the modification direction exists in a 45-ms modification of the V-onset condition, while no difference due to the modification direction was significant in the V-offset condition [$p<0.05$, $q(0.05,12,108)=4.72$, HSD $=0.42$]. A similar tendency of the modification direction was observed in the entire-word, i.e., reference, condition as shown in Fig. 2(a). Multiple comparisons using Tukey-Kramer's HSDs indicated that significant differences exist when the modification size was 40 ms or larger [$p<0.05$, $q(0.05,8,72)=4.42$, HSD$=0.36$]. Psychophysical implications of this directional effect are discussed in Sec. IV.

C. Discussion

Experiment 1 showed that detectability in general does not differ between the V-onset and V-offset modifications, even though they are globally manipulated modifications. The listeners could achieve almost the same overall performance in the detection of changes in both V-onset and V-offsets. These results suggest that the temporal markability of the V-offsets was comparable with that of the V-onsets in terms of the superficial performance level.

However, this does not necessarily mean that the listeners used the same strategy in both conditions. One should keep in mind that a detection task can be achieved by focusing on any local change and that listeners in general tend to rely on the most prominent cue. A detailed examination of the results revealed a significant difference in detectability due to the modification direction in the V-onset condition. A similar difference in d' was also observed in the entire-word condition but not in the V-offset condition. This discrepancy suggests that the listeners' strategy used in the V-onset condition was similar to that in the entire-word condition but differed from that in the V-offset condition. A uniform expansion or reduction of the entire word duration should reflect the physical change in the speaking rate. The listeners, therefore, could make reliable responses by using the perceived speaking rate. If the speaking-rate criterion was truly used in the entire-word condition, this criterion was probably used in the V-onset condition too but not in the V-offset condition. To test this assumption, experiment 2 restricted the listeners' task to speaking-rate estimation.

III. EXPERIMENT 2: SPEAKING-RATE ESTIMATION

Although experiment 1 used globally modified stimuli, the listeners' task was still one that could be achieved by simply using a local-range observation, i.e., a simple change detection. Consequently, this potential lack of global processing in the listeners' task might have prevented elucidation of overall differences between the V-onset and V-offset conditions. Experiment 2, therefore, employed a task explicitly involving a global processing, i.e., speaking-rate estimation. This task requires listeners to consider global relationships among temporal cues distributed over the entire length of a stimulus. Therefore, experiment 2 may be a viable way to compare the listeners' performance between the V-onset and V-offset conditions in a global-range processing.

As mentioned in the Introduction, the contribution of V-onsets to tempo perception has been reported to be larger than that of V-offsets (Ventsov, 1981; Pompino-Marschall *et al.*, 1982). However, the stimuli of these previous studies were mostly laboratorylike and more unnatural in character than natural speech. In short, they used a concatenation of acoustically steady-state segments /m/ and /a/ with a fixed fundamental frequency and repeated it in a temporally equidistant manner; they only varied the duty ratio of the consonant and vowel segments. Obviously, the listeners could establish a strong impression of the tempo for such isochronous stimuli. This perceived tempo did not appear analogous with that yielded from natural speech. Therefore, we need another experimental setting that uses sufficiently natural stimuli before answering the current question. The stimuli of the current study were precisely synthesized by analysis results of natural speech and, therefore, the power spectrum envelope, fundamental frequency, short-term power, and their dynamic patterns were identical to those of the original speech material.

A. Method

1. Subjects

Eight adults with normal hearing participated in experiment 2. All of the subjects participated in experiment 1, so we maintained a period of at least three months between the two experiments to minimize the carry-over of judgment strategies.

2. Stimuli and stimulus presentation

The stimuli and their presentation procedures were the same as in experiment 1, except that there was no additional control trial in which the two presented stimuli were identical.

3. Tasks

The subjects were asked to estimate the speaking rate of the second word of each of the paired stimuli compared to that of the first word by using 11 numerical categories from -5 to $+5$, with a higher number corresponding to a faster rate. Each subject estimated each stimulus pair ten times in total. The obtained responses were pooled over all of the subjects for each category, and then each stimulus was mapped on a uni-dimensional linear psychometric scale in accordance with Torgerson's law of categorical judgment (Torgerson, 1958).[4]

B. Results

1. Speaking-rate estimation

The scaled estimation scores for the speaking rate of each stimulus of the entire-word condition, i.e., the reference condition, are plotted as a function of the change in total word duration in Fig. 3. The estimated speaking rate was highly correlated with the change in total duration [Student's t-test $t(90)=-32.6$, $p<0.0001$; the Pearson product-moment correlation coefficient $r=-0.96$], where the speaking rate decreased with increasing total duration. This rela-

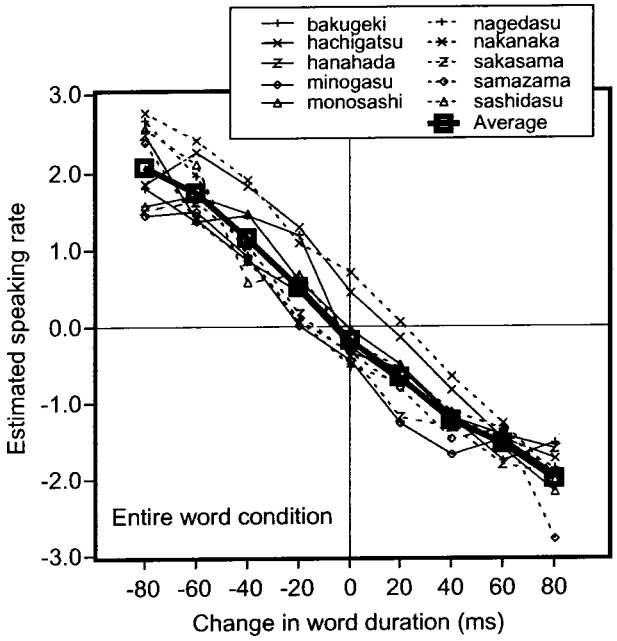

FIG. 3. Estimated changes in speaking rate for each token as a function of the change in word duration.

tion demonstrates that the subjects judged the speaking rates of the presented stimuli based on the physical rate or total duration.

The scaled estimation scores for the speaking rate of each stimulus in the V-onset condition are plotted as a function of the change in total inter-V-onset interval in Fig. 4. Although the word durations remained unchanged, the estimated speaking rate decreased with increasing inter-V-onset interval. This correlation was, indeed, significant [$t(70) = -16.8$, $p < 0.0001$; $r = -0.90$], and the tendency was in good agreement with that observed in the reference condition.

In the V-offset condition, on the other hand, the correlation between the estimated speaking rate and the change in total inter-V-offset interval was also significant but rather low [$t(70) = 2.4$, $p < 0.05$; $r = 0.28$] (Fig. 5). The tendency of this shallow inclination was, furthermore, opposite to that of the reference condition. Consequently, we cannot state with certitude that the estimated speaking rate shows a consistent relation with the inter-V-offset interval.

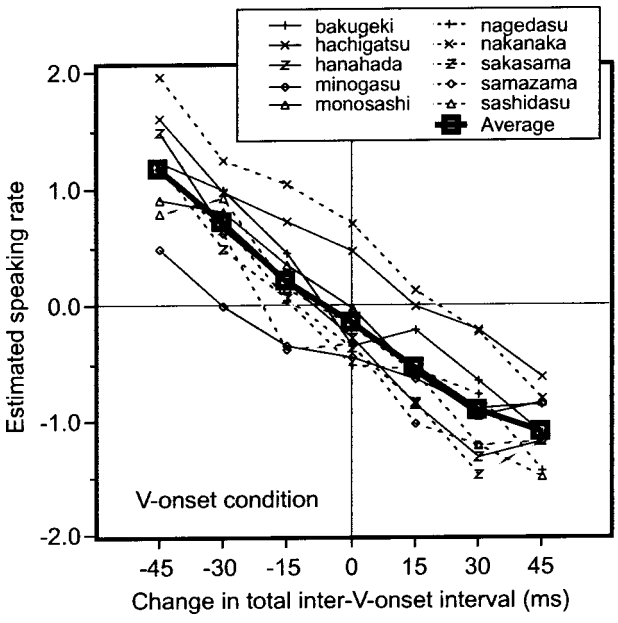

FIG. 4. Estimated changes in speaking rate for each token as a function of the change in total inter-V-onset interval.

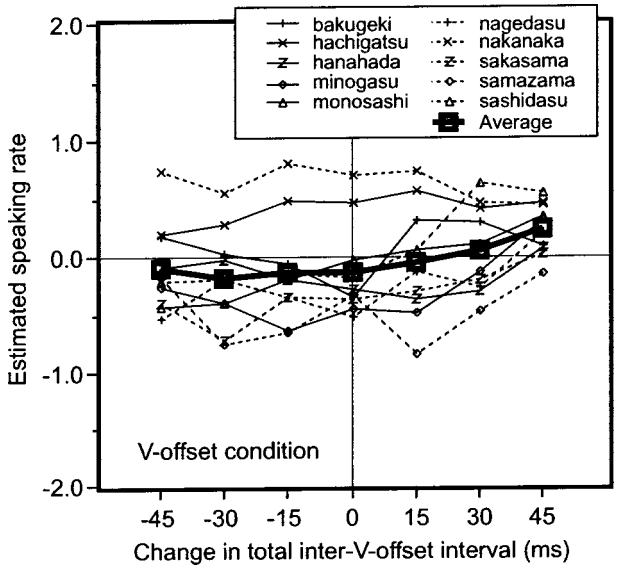

FIG. 5. Estimated changes in speaking rate for each token as a function of the change in total inter-V-offset interval.

2. Discriminability of speaking rates

The listeners' responses in the current experiment could be useful in estimating the discriminability of different speaking rates on the basis of the percentage of correct responses. The "faster" responses ("+1" to "+5") were regarded as correct and the "slower" responses ("−1" to "−5") were regarded as incorrect when the subject intervals were reduced, and vice versa. Half of the "same" responses ("0") were counted as "faster" and the other half were counted as "slower."[5]

Each just noticeable difference (JND) was estimated as the point of 75% correctness on the regression line, with Müler-Urban weighting, for the obtained probability of a correct response plotted on normal coordinates. Figure 6 shows the obtained JNDs for each token and for each modification condition; JNDs for the V-offset condition are omitted due to the unreliability of the statistical model fitting. The presented values are those pooled over the subjects along with the upper and lower thresholds and divided by the corresponding base durations to show Weber's ratio; the base durations were the entire word duration in the entire-word condition and the interval between the onset of the first vowel and that of the fourth, i.e., final, vowel in the V-onset condition.

The average Weber fractions (3.5% for the entire word duration, 5.1% for the V-onset interval) were rather smaller than those reported for the discrimination of single segmental durations, which are on the order of 10%–50% (Huggins, 1972; Klatt and Cooper, 1975; Bochner *et al.*, 1988; Kato *et al.*, 1992). This difference is further discussed in Sec. IV

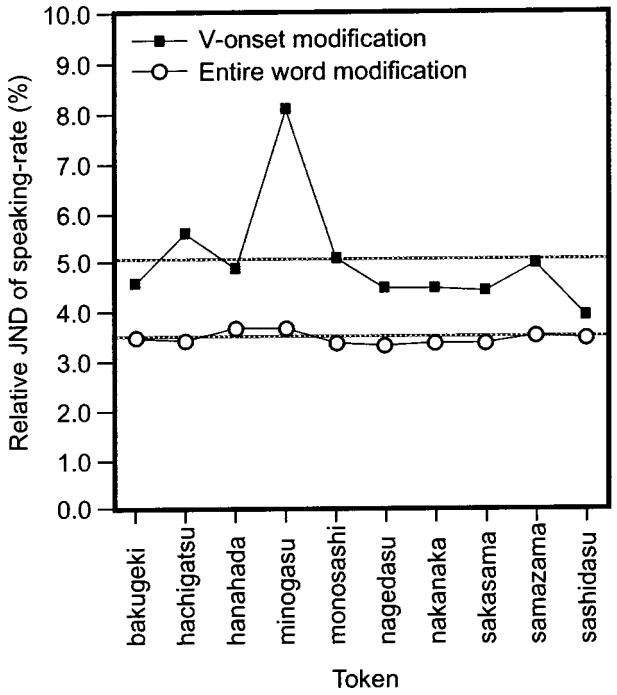

FIG. 6. Relative just noticeable differences (JNDs) of speaking rates as a function of token and modified boundary type. The corresponding base duration of each JND is either the total duration (entire word modification) or the total inter-V-onset interval (V-onset modification) (see Table I). The gray horizontal lines show the average JNDs for each modified boundary type, i.e., 3.5% for the entire word modification and 5.1% for the V-onset modification.

in relation to the literature on nonspeech temporal perception.

C. Discussion

In the speaking-rate estimation, a clear difference could be observed between the V-onset and V-offset conditions. The perceived speaking rates slowed as the inter-V-onset intervals increased, while only a marginal linear relation was observed between the perceived speaking rates and inter-V-offset intervals. These contrasting tendencies of V-onset and V-offset in their contribution to tempo perception is in agreement with the results reported for artificial syllable sequences (Ventsov, 1981; Pompino-Marschall *et al.*, 1982).

As mentioned earlier, the tasks in the current two experiments differed in the extent of time. That is, the change detection was a locally processed task, which could be achieved if any local difference were found between the standard and comparison stimuli, while the speaking-rate estimation was a global task, which required the listeners to compare the global relationships of the temporal cues distributed over the entire length of each of the stimuli.

Accordingly, the results of experiment 2 along with those of experiment 1 imply that V-onsets and V-offsets contribute almost equally to locally processed tasks, while the importance of V-onsets increases when global processing is required. This interpretation can explain the apparent discrepancies between Kato *et al.*'s (1997) study and the P-center studies. That is, Kato *et al.* (1997) did not observe any functional difference between V-onsets and V-offsets because they required listeners to detect just a local displacement. On the other hand, the P-center studies found the dominance of V-onsets over V-offsets because their experimental condition commonly required listeners to perform relatively global examinations.

The following section discusses the mechanisms mediating the perceptual difference between the contributions of V-onsets and V-offsets and then attempts to clarify the detailed differences between the local and global temporal processings mentioned above as well as the ranges determined as either local or global processing.

IV. GENERAL DISCUSSION

A. Psychoacoustical nature of the difference between V-onsets and V-offsets in perceiving the temporal structure of speech

The current study estimated human sensitivity to the temporal modification of either V-onsets or V-offsets by using two perceptual tasks. There was no significant difference in the listeners' overall performance between the V-onset condition (which selectively changed the intervals between the V-onsets while those between the V-offsets remained unchanged) and the V-offset condition (vice versa) in the simple detection task; however, there was a clear difference in the speaking-rate estimation task: the contribution of the V-onsets was much larger than that of the V-offsets. This subsection interprets these results from the psychophysical point of view. Such an interpretation is likely to be valuable because quite a few of the latest psychoacoustical studies have demonstrated that variations in the acoustical characteristics of temporal markers, e.g., differences between ramped contours (=onsets) and damped contours (=offsets), affect the human internal measurement of time [see, e.g., the review by Grondin (2001)]. We believe this psychophysical discussion is useful for understanding the mechanism underlying the effects found in speech experiments and for estimating the extent to which the current results can be generalized.

As a first-order approximation, we assumed that any influence of the temporal markers other than that of the V-onsets and V-offsets was marginal or random in the current study. Under this assumption, the listeners had to respond according to the results from the perceptual measurements of the intervals between combinations of two kinds of markers, i.e., V-onsets and V-offsets. Therefore, the current experimental results could be interpreted solely in terms of the information on the accuracy and implications of the perceptual measurements between all combinations of V-onsets and V-offsets, i.e., V-onset to V-onset, V-onset to V-offset, V-offset to V-onset, and V-offset to V-offset.

The perceptual precision of the temporal measurements among the V-onsets and V-offsets could be roughly estimated from existing psychoacoustical data. Kato and Tsuzaki (1998) investigated the perceptual measurement of time intervals marked by rising amplitude changes (onsets) and/or falling amplitude changes (offsets). This study measured temporal discriminability by using 1-kHz tone stimuli whose amplitude contours are described in Fig. 7 and obtained JND

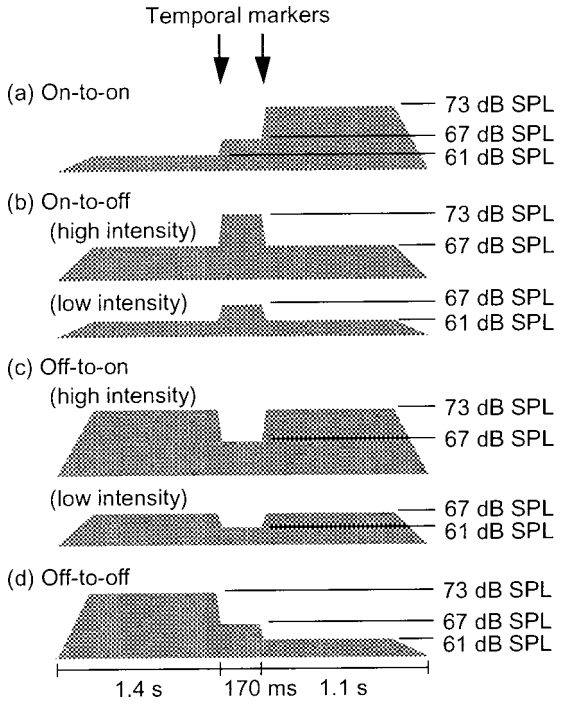

FIG. 7. Schematic examples showing the amplitude envelopes of nonspeech stimuli used in the temporal discrimination test in Kato and Tsuzaki (1998). The horizontal and vertical axes refer to time and level, respectively. All stimuli were 1-kHz tones. The targets tested were intervals between the successive amplitude changes (temporal markers) in the middle, as indicated by two arrows. Four combinations of either ''on'' or ''off'' markers were adopted, i.e., (a) on-to-on, (b) on-to-off, (c) off-to-on, and (d) off-to-off. [Reproduced from Kato and Tsuzaki (1998).]

data as summarized in Table II. To summarize the results, the listeners were very accurate in the measurements of both on-to-on and on-to-off intervals, much less accurate in the measurements of the off-to-on intervals, and extremely inaccurate in the measurements of the off-to-off intervals (or it was nearly impossible to measure these intervals). These results suggest that offsets function as temporal markers only in combination with onsets as their counterparts.

By implying that the role of V-onsets and V-offsets as temporal markers is analogous to the role of nonspeech onset and offset markers, the psychoacoustical data above account for the perceptual phenomena observed here. Experiment 1 did not show significant differences in the detectability performance between the two conditions because the task could be achieved for either condition by detecting the change in at least one vowel duration that requires the on-to-off measurement. According to Kato *et al.*'s (1998) data, this is done with as high an accuracy as for change involving the on-to-on measurement. On the other hand, experiment 2 showed no clear contribution of the V-offsets to the speaking-rate estimation in contrast to the large contribution of the V-onsets. This is because the on-to-on intervals could be accurately measured, while the listeners could not make use of the inter-V-offset intervals due to the difficulty of the off-to-off measurement.

TABLE II. Dependency of temporal discriminability on the slope direction (on or off) of markers that define the target interval. Changes in on-to-on and on-to-off intervals are easily detected, i.e., these intervals can be accurately measured. Off-to-on intervals are poorly measured, and the measurement of off-to-off intervals is extremely poor. [Reproduced from Kato and Tsuzaki (1998).]

Marker combination	JND (in Weber fraction)
On-to-on	0.26
On-to-off	0.26
Off-to-on	0.63
Off-to-off	1.34

To clarify the basic ideas of this implication, the relationship between acoustically informative and perceptually reliable, i.e., accurately measurable, intervals are illustrated for each task in each stimulus condition in Table III. The third column of the table lists the acoustically informative intervals, namely intervals with changes that are effective to achieve each task. In the simple detection task of experiment 1, any single interval can be used except for those preserved unchanged, i.e., off-to-off intervals in the V-onset condition and on-to-on intervals in the V-offset condition. In the speaking-rate task of experiment 2, no consistent response can be expected other than the cases of using intervals whose rates are uniformly changed, i.e., on-to-on intervals in the V-onset condition and off-to-off intervals in the V-offset condition. The fourth column lists the intervals that appear to be reliably measured from those listed in the third column. The reliability of the perceptual measurement for each interval is estimated in accordance with the psychoacoustical data by Kato and Tsuzaki (1998) shown as above (Table II). In the simple detection task, at least one type of the informative intervals is perceptually reliable in both V-onset and V-offset conditions. In the speaking-rate task, on the other hand, the informative interval type is also perceptually reliable in the V-onset condition (i.e., on-to-on) but not reliable in the V-offset condition (i.e., off-to-off).

Although one should be prudent in simply applying a pure tone case to a speech case, in the current study of speech the V-onsets and V-offsets certainly corresponded to the steep rise and fall of acoustic power. That is, the V-onsets and V-offsets were also acoustic onsets and offsets, respectively, and this is also the case generally observed in natural speech. Furthermore, although perceptual findings using synthesized speech stimuli cannot necessarily be generalized to cases involving natural speech, the perceptual phenomena found in the current study, i.e., the functional differences between vowel onsets and offsets, appear to be of fairly broad generality thanks to the psychoacoustical, namely nonspeech-specific, interpretation mentioned in this section. We expect similar perceptual functions in both synthetic and natural speech regardless of the difference in languages, as far as the speech sound in question preserves signal-level characteristics similar to those of the stimuli used in the current study, i.e., the power of vowel segments exceeds that of the surrounding segments so that the V-onsets and V-offsets correspond to acoustic onsets and offsets, respectively.

In estimating to what extent the ''local'' and ''global'' processes in the current experiments were involved according to the interpretation above, we suggest that the former process ranged about one segment while the latter process was equal to or extended over the range between two adja-

TABLE III. Summary of the acoustically informative and perceptually reliable intervals for each task in each stimulus condition. The third column lists the acoustically informative intervals, i.e., the intervals with changes that are effective for achieving each task. In the simple detection task (experiment 1), any single interval can be effectively used except for those preserved unchanged, i.e., either off-to-off or on-to-on intervals in V-onset or V-offset conditions, respectively. In the speaking-rate task (experiment 2), no consistent response can be expected unless the intervals whose rates are linearly changed (either on-to-on or off-to-off intervals in V-onset or V-offset conditions, respectively) are used. The fourth column lists the intervals that appear to be reliably measured from those listed in the third column. The reliability of the perceptual measurement for each interval is estimated in accordance with the data reproduced in Table II from a psychophysical investigation by Kato and Tsuzaki (1998).

Modification condition	Task	Interval with an effective change for each task	Interval with an effective change for each task and with reliability in perceptual measurement
V-onset	Experiment 1: Detection of any difference	on-to-on, on-to-off, off-to-on	on-to-on, on-to-off, (off-to-on)
	Experiment 2: Estimation of speaking rate difference	on-to-on	on-to-on
V-offset	Experiment 1: Detection of any difference	off-to-off, on-to-off, off-to-on	on-to-off, (off-to-on)
	Experiment 2: Estimation of speaking rate difference	off-to-off	—

cent vowel onsets, i.e., a range involving three or more segments.

B. Discriminability of speaking rates and its implications

Despite the importance of speaking rate as one of the most basic factors in the control of synthetic speech, the ability of listeners to discriminate changes in the rate or tempo of speech signals has seldom been examined. It is acknowledged that the human accuracy to discriminate the tempi of nonspeech sound sequences is, in general, higher than that of durations of single sounds. It would be interesting to investigate whether analogous relations can also be observed in speech cases because ordinary speech, in general, has no explicit regular temporal markers, as do the stimuli of nonspeech studies.

As mentioned above, the listeners in the current study showed a high accuracy in the discrimination of speaking rates; the Weber fractions were 3.5%–5.1%. Although there are large variations among previous studies, due to differences in psychophysical methodology and to the influence of variables such as segment type and/or utterance context, they all tend to show that the accuracy to discriminate changes in a single segmental duration is relatively low; the Weber fraction is 10%–50% (Huggins, 1972; Klatt and Cooper, 1975; Bochner *et al.*, 1988; Kato *et al.*, 1992).

The literature on temporal discriminability for nonspeech sounds of segmentlike durations (50–200 ms) has shown a similar tendency. In these papers, the Weber fraction ranges between 10% and 20% for single filled durations (Abel, 1972b; Lehiste, 1979; Bochner *et al.*, 1988) and 20% and 40% for single empty intervals (Abel, 1972a; Bochner *et al.*, 1988). In contrast, much smaller fractions have been reported for tempi in regular tone/click sequences, e.g., 0.6%–4% for monotonic and isochronous sequences with 200-ms intervals (Drake and Botte, 1993; Michon, 1964). The discriminability of speaking rates obtained here is, therefore, as high as that of nonspeech tempi. This fact supports the view that the listeners could perceive temporal markers during the test utterances in addition to the start and end points, all of which could entail speaking rate judgment, and argues against the view that the listeners judged stimulus differences only on the basis of local durational differences even in the task of speaking-rate estimation.

These results suggest that any single temporal deviation that cannot be detected may become as perceptually salient as the deviation of the speaking rate when it occurs over multiple segments in a cumulative manner. This implies, in speech synthesis applications, that the synthetic rules of duration control occasionally require a higher precision (based on the JND of the speaking rate) than the margin generally allowed to each single segment (based on the JND of a single segmental duration); the reference error in this high precision control should be, for instance, only 25 ms per 700-ms base duration.

Regarding the difference in discriminability between the modification conditions, the listeners consistently showed a higher accuracy in the entire-word condition than in the V-onset condition. This inclination can be partly accounted for by the contribution of the entire word duration, which was fixed in the V-onset condition. Another possibility is the difference in the uniformity setting of stimulus modifications. The entire-word condition employed uniform modifications, and all of the temporal cues, including on-to-on, on-to-off, off-to-on, and off-to-off intervals, indicated the same direction of modification (expansion or reduction), while the temporal cues in the nonuniform modifications of the V-onset condition did not; only the on-to-on intervals indicated a single modification direction in the latter case. Such conflicts among temporal cues in the V-onset condition perhaps lowered the listeners' ability to discriminate the speaking rate, even though the dominant cues were on-to-on intervals.

C. Possible sources of the detectability difference between expansion and reduction modifications

This final subsection discusses the source of the effect of modification direction observed in experiment 1 from a psychophysical point of view. The listeners more easily detected the reduction modification than the expansion one in the

entire-word and V-onset conditions. Two possibilities might account for this effect. The first one is based on the difference in the proportion between modified and unmodified stimuli. The listener's task was paired comparison, and the absolute size of modification was the same in both modification directions. As a result, the proportion of the longer duration to its shorter counterpart was larger in the reduction condition than in the expansion condition as shown in Eq. (1):

Proportion in the reduction condition:

$$F_{-} = T/(T - \Delta T),$$

Proportion in the expansion condition:

$$F_{+} = (T + \Delta T)/T,$$

therefore,

$$F_{-} > F_{+} \tag{1}$$

where T and ΔT denote the original duration and the absolute size of modification, respectively.

The second possibility involves an asymmetry in detectability between increasing and decreasing changes in tempo. The change in tempo within an auditory sequence with a slow-to-fast pattern can be perceptually more salient than that with a fast-to-slow pattern. Using short-tone trains whose cycle is shorter than about 500 ms, a slow-to-fast change has been reported as more easily detected than a fast-to-slow change by both McAuley and Kidd (1998) and Vos *et al.* (1997). They argued that the latter pattern is not salient because it approaches the indifference interval [500–700 ms (Woodrow, 1951; Allan, 1979)] or preferred tempo, while the former pattern goes away from it. Ventsov (1981) also observed a similar tendency by using a sequence of synthesized syllables; his listeners were more sensitive to an abrupt increase in tempo than to a decrease in tempo. In the current study, the presentation order of the standard and comparison stimuli was fixed as the first order, namely, standard first. Thus, the listeners always heard a long-to-short pattern with an interstimulus interval in-between, in each trial of the reduction condition. Assuming the V-onset sequence of the current stimulus was utilized to perceive the tempo, the long-to-short pattern would correspond to a slow-to-fast pattern whose cycle is shorter than 500 ms (the average inter-V-onset interval was about 170 ms). Therefore, the sequence pattern in the reduction condition (slow-to-fast) could be more perceptually salient than that in the expansion condition (fast-to-slow).

As the two possibilities mentioned above are not mutually exclusive, they could simultaneously explain the observed effect of modification direction.

V. CONCLUSIONS

The primary purpose of this study was to examine the functions of vowel onsets and offsets and to determine the differences between them in the temporal perception of speech. Experiment 1 examined the detectability of multiple displacements of either V-onsets or V-offsets and found no obvious difference between the V-onset and V-offset conditions; the average accuracy of listeners did not differ between these conditions. This finding agrees with the detection test of Kato *et al.* (1997), in which either a single V-onset or V-offset was displaced and no significant difference was observed between V-onsets and V-offsets, and also extends this previous finding.

Experiment 2, on the other hand, examined the change in the perceived speaking-rate while using the same stimulus set as experiment 1. It showed a clear predominance of V-onsets over V-offsets. The intervals between V-onsets inversely correlated with the perceived speaking rate ($r = -0.90$), while no such linear and consistent relation was observed for the V-offset intervals.

These two observations can be explained by the interpretation that the time span of perceptual processing depends on the task, and, accordingly, that the role of V-onsets becomes more important than that of V-offsets in processing that uses relatively global information. This is because experiments 1 and 2 differed only in their tasks: the task of experiment 1 could be achieved by merely making a local observation of a single boundary between vowel and consonant segments, while that of experiment 2 required a broader observation involving multiple segmental boundaries. This view of a local-global contrast in the temporal perception of V-onsets and V-offsets is psychophysically supported by findings that demonstrate a difference between onsets and offsets in their contributions to human accuracy in nonspeech duration measurements.

All of the notions mentioned in this paper suggest, in terms of the duration control of synthesis rules, that the temporal alignment of V-onsets generally requires wider control windows than that of V-offsets. However, one should be careful in generalizing this suggestion because speaking-rate perception is only a single aspect of the temporal processing of speech involving such global information. Further perceptual studies, such as naturalness or acceptability tests, are needed to confirm the plausibility of the above suggestion and to incorporate it in the evaluation of durational rules.

The listeners' responses in experiment 2 could also be helpful in calculating acuity in speaking-rate perception. The results showed that listeners' ability to discriminate speaking rates is extremely high (on the order of 3.5%) and comparable with those of nonspeech sound sequences. This suggests that a rate deviation of this order may influence the human evaluation of synthesized speech. In a typical case (four-mora words in the current study), such a deviation would amount to just 25 ms for a 700-ms word, or a 3-ms error per 87.5-ms segment.

ACKNOWLEDGMENTS

This work was supported in part by the Telecommunicatios Advancement Organization of Japan. We thank Nick Campbell, Hideki Kawahara and Eric Vatikiotis-Bateson for their helpful comments on early versions of this paper. We would also like to thank Yoh'ichi Tohkura for the initial impetus to the current study.

[1]Although some of these questions have been addressed by Ventsov (1981) and Pompino-Marschall *et al.* (1982), both studies used artificial temporal structures that did not reflect precise temporal structures of natural speech, as the current study does. They used regularly aligned sequences of a single artificial syllable that achieved a precise isochronous structure, although no naturally produced speech shows such isochronism.

[2]This is a variation of the theory of signal detection procedures that provides multiple hit and false-alarm pairs from a single-session experiment to yield an ROC (receiver operating characteristics) curve. While the ordinary yes–no procedure conducts separate sessions by using different *a priori* probabilities and/or applying different payoffs and penalties to set multiple response biases, the rating procedure assumes that the observer maintained several response biases simultaneously in a single session. Observers are asked to provide a graded rather than a binary response, rating their experience on an ordered scale (e.g., 0,1,...,7). Then, different boundaries between two successive categories of the scale (e.g., 0 and 1, 1 and 2,...,6 and 7) are regarded as different response criteria. For instance, in a change detection task, a 0-1 boundary corresponds to the criterion with the highest bias to ''yes'' responses and a 6-7 boundary corresponds to the criterion with the highest bias to ''no'' responses. Accordingly, a pair of hit and false-alarm rates is calculated from the cumulative rates of signal and no-signal intervals with a criterion corresponding to each boundary. Thus, multiple pairs of hit and false-alarm rates can be obtained up to the number of the category boundaries (or the number of the ordered categories minus 1).

[3]This is a variation of statistical criteria to test the difference between all pairs of observed means. It is formulated as

$$\mathrm{HSD}=q(\alpha,n,df)\sqrt{(}\mathrm{MSE/ND}),$$

where q is the Studentized range with α as the significance level, n as the total number of to-be-compared means, and df as the degree of freedom. MSE is the mean of squared errors that is calculated in the ANOVA procedure and ND is the number of observed data per mean.

[4]This is a method of psychological scaling that uses the outputs of a rating scale method. Each of the categorical boundaries and stimuli used in the rating is mapped on a uni-dimensional interval scale.

[5]The theory of signal detection can be applied to calculate the just noticeable differences (JNDs) in the current experimental design. However, we refrained from publishing the results according to this method because of the low frequency of control trials in which the standard and comparison stimuli were identical. The JND values by this method were actually almost the same as those published herein.

Abel, S. M. (**1972a**). ''Discrimination of temporal gaps,'' J. Acoust. Soc. Am. **52**, 519–524.

Abel, S. M. (**1972b**). ''Duration discrimination of noise and tone bursts,'' J. Acoust. Soc. Am. **51**, 1219–1223.

Allan, L. G. (**1979**). ''The perception of time,'' Percept. Psychophys. **26**, 340–354.

Allen, G. D. (**1972**). ''The location of rhythmic stress beats in English: An experimental study I and II,'' Lang. Speech **15**, 72–100, 179–195.

Bochner, J. H., Snell, K. B., and MacKenzie, D. J. (**1988**). ''Duration discrimination of speech and tonal complex stimuli by normally hearing and hearing-impaired listeners,'' J. Acoust. Soc. Am. **84**, 493–500.

Carlson, R., and Granström, B. (**1975**). ''Perception of segmental duration,'' in *Structure and Process in Speech Perception*, edited by A. Cohen and S. Nooteboom (Springer-Verlag, Berlin), pp. 90–106.

Carlson, R., and Granström, B. (**1986**). ''A search for durational rules in a real-speech database,'' Phonetica **43**, 140–154.

Drake, C., and Botte, M.-C. (**1993**). ''Tempo sensitivity in auditory sequences: Evidence for a multiple-look model,'' Percept. Psychophys. **54**, 227–286.

Green, D. M., and Swets, J. A. (**1966**). *Signal Detection Theory and Psychophysics* (Wiley, New York), pp. 40–42, 99–107.

Grondin, S. (**2001**). ''From physical time to the first and second moments of psychological time,'' Psychol. Bull. **127**, 22–44.

Huggins, A. W. F. (**1972**). ''Just noticeable differences for segment duration in natural speech,'' J. Acoust. Soc. Am. **51**, 1270–1278.

Imai, S., and Kitamura, T. (**1978**). ''Speech analysis synthesis system using the log magnitude approximation filter,'' Trans. Inst. Electron. Commun. Eng. Jpn., Part A **J61-A**, 527–534 (in Japanese with English figure captions).

Iwahashi, N., and Sagisaka, Y. (**2000**). ''Statistical modelling of speech segment duration by constrained tree regression,'' Trans. Inst. Electron. Commun. Eng. Jpn., Part D **E83-D**, 1550–1559.

Kaiki, N., and Sagisaka, Y. (**1992**). ''The control of segmental duration in speech synthesis using statistical methods,'' in *Speech Perception, Production and Linguistic Structure*, edited by Y. Tohkura, E. Vatikiotis-Bateson, and Y. Sagisaka (IOS, Amsterdam), pp. 391–402.

Kato, H., and Tsuzaki, M. (**1998**). ''Evidence for functional differences between rise and fall markers in discrimination of auditory filled durations,'' J. Acoust. Soc. Jpn. (E) **19**, 73–76.

Kato, H., Tsuzaki, M., and Sagisaka, Y. (**1992**). ''Acceptability and discrimination threshold for distortion of segmental duration in Japanese words,'' in *Proceedings of the 2nd International Conference on Spoken Language Processing* (Univ. of Alberta, Edmonton, AB), pp. 507–510.

Kato, H., Tsuzaki, M., and Sagisaka, Y. (**1997**). ''Acceptability for temporal modification of consecutive segments in isolated words,'' J. Acoust. Soc. Am. **101**, 2311–2322.

Kato, H., Tsuzaki, M., and Sagisaka, Y. (**1998**). ''Acceptability for temporal modification of single vowel segments in isolated words,'' J. Acoust. Soc. Am. **104**, 540–549.

Kato, H., Tsuzaki, M., and Sagisaka, Y. (**2002**). ''Effects of phoneme class and duration on the acceptability of modifications in speech,'' J. Acoust. Soc. Am. **111**, 387–400.

Klatt, D. H. (**1975**). ''Vowel lengthening is syntactically determined in a connected discourse,'' J. Phonetics **3**, 129–140.

Klatt, D. H. (**1979**). ''Synthesis by rule of segmental durations in English sentences,'' in *Frontiers of Speech Communication Research*, edited by B. Lindblom and S. Öhman (Academic, London), pp. 287–299.

Klatt, D. H., and Cooper, W. E. (**1975**). ''Perception of segment duration in sentence contexts,'' in *Structure and Process in Speech Perception*, edited by A. Cohen and S. G. Nooteboom (Springer-Verlag, Berlin), pp. 69–89.

Kurematsu, A., Takeda, K., Sagisaka, Y., Katagiri, S., Kuwabara, H., and Shikano, K. (**1990**). ''ATR Japanese speech database as a tool of speech recognition and synthesis,'' Speech Commun. **9**, 357–363.

Lehiste, I. (**1979**). ''The perception of duration within sequences of four intervals,'' J. Phonetics **7**, 313–316.

Macmillan, N. A., and Creelman, C. D. (**1991**). ''The rating experiment and empirical ROCs,'' in *Detection Theory: A User's Guide* (Cambridge U. P., Cambridge, UK), pp. 58–87.

Marcus, S. M. (**1981**). ''Acoustic determinants of perceptual center (P-center) location,'' Percept. Psychophys. **30**, 247–256.

McAuley, J. D., and Kidd, G. R. (**1998**). ''Effect of deviations from temporal expectations on tempo discrimination of isochronous tone sequences,'' J. Exp. Psychol.: Hum. Percept. Perform. **24**, 1–15.

Michon, J. A. (**1964**). ''Studies on subjective duration. I. Differential sensitivity in the perception of repeated temporal intervals,'' Acta Psychol. **22**, 441–450.

Pompino-Marschall, B., Piroth, H. G., Hoole, P., Tilk, K., and Tillmann, H. G. (**1982**). ''Does the closed syllable determine the perception of 'momentary tempo,'" Phonetica **39**, 358–367.

Sato, H. (**1977**). ''Segmental duration and timing location in speech,'' Acoustical Society of Japan, Trans. Tech. Comm. Speech S77-31, 1-8 (in Japanese with English abstract and English figure captions).

Scott, S. K. (**1993**). ''P-centres in speech—An acoustic analysis,'' doctoral dissertation, University College London, London, UK.

Tajima, K., Akahane-Yamada, R., and Yamada, T. (**2002**). ''Perceptual learning of second-language syllable rhythm by elderly listeners,'' in *Proceedings of the 7th International Conference on Spoken Language Processing* (Univ. of Colorado, Boulder, CO), pp. 249–252.

Torgerson, W. S. (**1958**). ''The law of categorical judgment,'' in *Theory and Methods of Scaling* (Wiley, New York), pp. 205–246.

van Santen, J. P. H. (**1994**). ''Assignment of segmental duration in text-to-speech synthesis,'' Comput. Speech Lang. **8**, 95–128.

Ventsov, A. V. (**1981**). ''Temporal information processing in speech perception,'' Phonetica **38**, 193–203.

Vos, P. G., van Assen, M., and Fraňek, M. (**1997**). ''Perceived tempo change is dependent on base tempo and direction of change: Evidence for a generalized version of Schulze's (1978) internal beat model,'' Psychol. Res. **59**, 240–247.

Woodrow, H. (**1951**). ''Time perception,'' in *Handbook of Experimental Psychology*, edited by S. S. Stevens (Wiley, New York), pp. 1224–1236.

Acoustic correlates of caller identity and affect intensity in the vowel-like grunt vocalizations of baboons

Drew Rendall[a)]
Department of Psychology and Neuroscience, University of Lethbridge, Lethbridge, Alberta T1K 3M4, Canada

(Received 3 August 2002; revised 21 February 2003; accepted 3 March 2003)

Comparative, production-based research on animal vocalizations can allow assessments of continuity in vocal communication processes across species, including humans, and may aid in the development of general frameworks relating specific constitutional attributes of callers to acoustic-structural details of their vocal output. Analyses were undertaken on vowel-like baboon grunts to examine variation attributable to caller identity and the intensity of the affective state underlying call production. Six hundred six grunts from eight adult females were analyzed. Grunts derived from 128 bouts of calling in two behavioral contexts: concerted group movements and social interactions involving mothers and their young infants. Each context was subdivided into a high- and low-arousal condition. Thirteen acoustic features variously predicted to reflect variation in either caller identity or arousal intensity were measured for each grunt bout, including tempo-, source- and filter-related features. Grunt bouts were highly individually distinctive, differing in a variety of acoustic dimensions but with some indication that filter-related features contributed disproportionately to individual distinctiveness. In contrast, variation according to arousal condition was associated primarily with tempo- and source-related features, many matching those identified as vehicles of affect expression in other nonhuman primate species and in human speech and other nonverbal vocal signals. [DOI: 10.1121/1.1568942]

PACS numbers: 43.80.Ka [WA]

I. INTRODUCTION

Over the last half century, there has been growing research interest in the natural vocal communication systems of nonhuman primates, in part because their phylogenetic affinity to humans recommends them as models for studying potential precursors to human vocal communication, including language. Such comparatively based research has revealed a number of differences between human and nonhuman primates, for example, in detailed features of vocal anatomy that are likely to influence the range and quality of possible sounds that can be produced (Negus, 1949; Lieberman *et al.*, 1969; Schön Ybarra, 1995; Mergill *et al.*, 1999; reviewed in Fitch and Hauser, 1995; Fitch, 2000; Hewitt *et al.*, 2000), and seemingly also in the relative contribution of experiential influences to vocal development (reviewed in Owren *et al.*, 1993; Seyfarth and Cheney, 1997). It has also revealed a number of important parallels. These include similarities between the two groups in some of the functional properties of vocal signals (e.g., Seyfarth *et al.*, 1980; Gouzoules *et al.*, 1984); in the basic structure, layout, and modes of operation of the principle sound production components of the vocal tract (i.e., larynx and supralaryngeal airways: reviewed in Fitch and Hauser, 1995; Owren and Linker, 1995; Fitch, 2000); and thus also in the resulting acoustic-structural features of the signals produced including certain speech sounds (e.g., Owren *et al.*, 1997). Given the latter vocal-anatomical and acoustic-structural similarities, acoustic research on primates has also begun to make productive use of speech-related conceptual and analytical tools (e.g., Owren and Bernacki, 1988; Seyfarth *et al.*, 1994; Fitch, 1997; Rendall *et al.*, 1998; reviewed in Fitch and Hauser, 1995; Owren and Linker, 1995; Owren and Bernacki, 1998).

This kind of mix of similarities and differences between human and nonhuman primate communication is, of course, exactly what would be expected from the evolutionary process. Because both outcomes are ultimately equally informative in efforts to trace the trajectory of human communication, the results of such comparatively based research are promising. This paper extends these research efforts through acoustic analyses of the grunt vocalizations of baboons, focusing specifically on potential acoustic correlates of caller identity and affect intensity. These are important talker-dimensions in human communication, including language, supporting a variety of basic social activities. They are also likely to have significance in baboons and many other similarly social species. Hence, comparative analyses of these dimensions may contribute to developing frameworks that can relate a variety of constitutional attributes of signalers to the acoustic-structural details of the signals they produce.

A. Baboon vocal communication

Baboons are well-suited to such comparatively based acoustic research. They are the most thoroughly studied nonhuman primate species. As a result, a great deal is known about their social behavior and the general contexts of communication. There is also a recent and expanding literature on the acoustic structure and specific social-behavioral functions of different calls in their vocal repertoire (e.g., Andrew, 1976; Richman, 1976; Cheney *et al.*, 1995, 1996; Owren

a)Electronic mail: d.rendall@uleth.ca

et al., 1997; Rendall *et al.*, 1999, 2000; Fischer *et al.*, 2002; Semple *et al.*, 2002). Recent work by Owren *et al.* (1997) is especially pertinent to the present study. These authors undertook a detailed analysis of the acoustic structure of grunts produced by adult female baboons (*Papio cynocephalus ursinus*) to examine the salient dimensions of variation in these calls, and to investigate the underlying vocal tract mechanisms responsible for their production. Their results strongly suggest that grunts reflect the independent action of stable vocal-fold vibration and subsequent spectral shaping by the supralaryngeal airways, the latter imparting a clear resonant, or formant, structure to the calls. In fact, they found that grunts are remarkably vowel-like in their spectral structure with the mean fundamental frequency (F_0) and the means of the first three formant frequencies of female grunts matching very closely the mean F_0 and formant frequencies of vowels produced by English-speaking males (see Fig. 5, Owren *et al.*, 1997). This acoustic convergence between the two species was attributed to a likely similarity in vocal-fold and vocal-tract lengths, the latter probably resulting from baboons' relatively long muzzle.

In addition to documenting the vowel-like characteristics of grunts, Owren *et al.* found consistent differences in call structure between individual females. Differences were noted in a variety of acoustic features. However, Owren *et al.* suggested that the most salient were probably due to the filtering effects of the vocal tract imparting individually distinctive resonance patterns to the calls, echoing an earlier proposal based on analyses of rhesus monkey vocalizations (Rendall, 1996; Rendall *et al.*, 1998).

There was also some indication that the acoustic structure of grunts might differ consistently according to the behavioral context in which they were produced. Specifically, grunts produced in two very distinct behavioral contexts appeared to differ in the frequency of the second formant ($F2$F) and in the slope of the formant-frequency spectrum derived from linear predictive coding (LPC). Grunts produced by animals who were about to embark on a move across open terrain (the move context), where they might become separated from one another or be more vulnerable to predators, were found to have a comparatively flat LPC-slope and a higher $F2$F compared to grunts produced in the context of social interactions involving the inspection and handling of the young infants of other females in the group (the infant context), which had a steeper LPC-slope and lower $F2$F. Follow-up experimental work in the field confirmed the salience to the animals of both the individual differences in grunt structure and the differences associated with these two different contexts of production (Rendall *et al.*, 1999).

The present study builds on this foundation, undertaking additional analyses of the potential identity cues available in grunts and extending them to consider potential correlates of arousal, or affect, in grunts produced in these two previously studied behavioral contexts. Although not always formally quantified, cues to arousal are held to be common in animal vocalizations, just as they are manifest also in human speech, where they likely serve an important social-communicative role, regulating the details of social interactions. Field observations suggest that caller arousal might be an additional important dimension of variation in baboon grunts in particular as the circumstances associated both with group movements and with interactions involving mothers and their young infants vary in ways that suggest connections to variable underlying motivation and arousal (described further in Sec. II).

It is, however, extremely difficult to assess with any degree of specificity the type of emotion, or state of arousal, associated with particular behavioral contexts. Therefore, no attempt is made in this study to label the type of emotion underlying grunt production, nor even to assume that it is necessarily of the same general character in the two behavioral contexts. Inferences of this sort are notoriously difficult to make even in research on human subjects where studies are designed to induce specific emotions or to have experienced actors simulate them (reviewed in Goldbeck *et al.*, 1988). Nevertheless, it is often possible to make reliable inferences about the relative intensity of generalized (i.e., nonspecific) psychophysiological arousal, or affect—the so-called ''activity dimension'' of emotion—in different circumstances, and this approach has been used to good effect to evaluate concomitant acoustic variation in human speech and other nonverbal vocal signals (e.g., Lieberman and Michaels, 1962; Williams and Stevens, 1972; Porter *et al.*, 1986; Bachorowski and Owren, 1995a; Protopapas and Eimas, 1997; Protopapas and Lieberman, 1997). In fact, recent reviews of human emotional expression argue that such ''nonspecific affective intensity'' may be the most reliable characterization of emotional variation in the voice from both an empirical and a theoretical standpoint (Bachorowski, 1999; Russell *et al.*, 2003). Hence, a similar strategy is adopted here using the obvious qualitative variation that exists in the circumstantial details of infant interactions and group movements, and in the accompanying behavior of callers, both of which imply at least crude distinctions in the relative intensity of the associated affective states (see Sec. II). These distinctions then form the basis for comparisons of the structure of grunts for evidence of correlated variation in specific acoustic features of the calls.

B. Vocal affect expression

While the specific acoustic features associated with variation in affect intensity are far from fully documented for either human or nonhuman primates, there is a reasonable empirical literature and even some relevant processual theories (Scherer, 1986) to guide acoustic analyses. Thus, arousal-based physiological changes are hypothesized to influence vocal production in numerous ways. For example, basic changes in respiration might affect the amplitude, tempo, and absolute F_0 of calling, while changes in vocal-fold tension and coordination (resulting from changes in overall muscle tonus and control) might also affect F_0 and aspects of voice quality traceable to disruptions in F_0 control. Spectral resonance properties might also be influenced, for example, by accompanying facial movements, or by changes in mucosal production that affect the reflective or absorptive properties of the vocal tract walls (Tartter, 1980; Scherer, 1986).

Research to date has described some of these phenomena in nonhuman primate vocalizations. For example, vervet monkeys produce several discrete types of alarm call, each of which is given to a different class of predator. However, the amplitude, amount, and rate of calling appear to vary with the level of arousal associated with the degree of predator threat (Seyfarth *et al.*, 1980). These same acoustic features vary with the intensity of hunger-related arousal in rhesus monkeys producing food calls, or ''coos'' (Hauser and Marler, 1993), as do the F_0 and relative tonality (or harshness) of the calls (Hauser, 2000). Similarly, the amplitude, F_0, and relative tonality of calling for several different calls in the repertoire of squirrel monkeys appear to reflect variation in the intensity of the affective state experienced (Jürgens, 1979; Hammerschmidt and Fichtel, 2001), while the amplitude and F_0 of alarm calls given by redfronted lemurs to terrestrial predators likewise vary with the degree of threat involved (Fichtel and Hammerschmidt, 2001; see also Fichtel *et al.*, 2001).

Many of these same features have been identified as correlates of affect intensity in humans. Thus, variation in amplitude, tempo, F_0, F_0 range, and F_0 contours are among the most commonly cited features associated with arousal variation (reviewed in Murray and Arnot, 1993; Scherer, 1995; Bachorowski, 1999). Although their connection to different discrete emotions (e.g., joy, sadness, anger, surprise) is more equivocal, increases in each feature are typically associated with an increase in generalized psychophysiological arousal. Several additional features related to voice quality are also commonly examined as indices of affect intensity in humans. These include short term variation in the frequency and amplitude of vocal-fold vibration (''jitter'' and ''shimmer,'' respectively), and the relative emphasis of F_0 compared to its harmonics. These various measures of voice quality are often connected to perceptions of roughness, hoarseness, or breathiness in the voice and have been studied as potential indices of age and vocal pathology, but also of arousal variation (e.g., Williams and Stevens, 1972; van Bezooyen, 1984; Bachorowski and Owren, 1995a; Protopapas and Eimas, 1997; Protopapas and Lieberman, 1997).

Using such relationships as a guide, this paper reports acoustic analyses of a large sample of grunts recorded from wild baboons under circumstances associated with varying affect intensity. It begins with a general review of the acoustic features of grunts, including further analysis of the potential correlates of individual identity and their possible primary connection to features associated with vocal tract resonance. It then examines variation in the acoustic structure of grunts associated with variation in the circumstances of call production during concerted group movements and interactions with mothers and their infants as these relate to basic distinctions in the intensity of the underlying affective states.

II. METHODS

A. Study site and subjects

Research was conducted between February 1996 and March 1997 on free-ranging baboons (*Papio hamadrayas ursinus*, formerly *P. cynocephalus ursinus*) in the Okavango Delta of northern Botswana. The habitat is a vast wetlands created by seasonal flooding of the Okavango River that yields a mixture of open, grassy floodplains and wooded islands that rise a few meters above the floodplains. The subjects of this study were the sexually and physically mature adult females (>7 years) of a single group that had been under continuous observation since 1977. As a result, the animals were fully habituated to human observers, and the social and genealogical history of all natal animals was known.

B. Data collection and vocalization recording

Data were collected in one-hour observational samples of ''focal'' females conducted throughout the day but concentrated between 6:00 and 14:00 as the baboons left their sleeping site in the morning and then moved, foraged, and socialized for the first few hours each day. Data collection included a continuous record of the focal female's general activity state (e.g., resting, moving, foraging) and social behavior, and additional information related to spatial and ecological factors (e.g., group dispersion, location within the home range, habitat visibility). For additional details regarding the collection of behavioral data, see Rendall *et al.* (2000).

Vocalizations were recorded during the course of observational sampling. Special emphasis was placed on recording bouts of grunting, particularly those produced in the context of concerted group movements across open terrain (the move context) and those produced when adult females made attempts to inspect or handle the young infants of other females in the group (the infant context). A detailed commentary of the contextual details associated with each bout of grunting was made at the same time, including information on the identity of the caller and its behavior immediately before and after calling, and, in the case of infant grunts, the identity of the recipient and the quality of the interaction between caller and recipient. It also included a record of the time that could be used later to reconstruct the temporal details of events. All recordings were made on Sony Type IV metal tapes using a Sony WM-D6C Professional Walkman cassette recorder and a Sennheiser ME 80 directional microphone with K3U power module. Because the animals were fully habituated to researchers and their equipment, high-quality recordings could be made at relatively close range (0.5–2.0 m).

C. Delimiting categories of arousal variation

To examine the potential effects of caller arousal on the acoustic structure of grunts, additional criteria were used to delimit two discrete arousal conditions (high versus low) within both the move and infant contexts. The criteria were based on natural variation in the contextual details associated with infant interactions and episodes of group movement and their predicted connection to underlying arousal variation.

For example, in the infant context, a female would often approach a new mother and her young infant from some distance (5–20 m), striding—even trotting—purposefully to-

wards them, sometimes showing moderately exaggerated gaits and postures, such as head bouncing and shoulder swaying, grunting as she approached. The approaching female would then reach for the infant, sometimes quite forcefully tugging on it despite clear resistance from the infant or its mother, or she would crouch very low to the ground and peer intently at the infant, sometimes bobbing from side-to-side to get a better look. At other times, interactions with mothers and their infants were far more subdued and were accompanied by little overt behavior. Thus, a female who had been sitting with or near a mother and her infant for some time would simply glance toward them, or reach out casually to touch the infant briefly, grunting as she did so.

Using this natural contextual variability, interactions involving mothers and their infants were classified into two subcategories according to whether they occurred in the context of a deliberate social approach by the caller toward a mother and her infant from a distance of more than 5 m after a period of at least 30 min during which there had been no interaction between the two parties, or they occurred after a period of at least 5 min during which the caller and the mother and her infant had been sitting together calmly either resting or engaged in reciprocal grooming. The former was designated the ''high arousal'' condition and the latter the ''low arousal'' condition on the logic that females who had not recently interacted with a mother or her new infant were likely then to be more motivated to do so and more intensely affected by that motivation than females who had been in recent prolonged contact with a mother and her infant.

There was similar natural variability in the circumstances surrounding group movement. Concerted group movements typically occurred either first thing in the morning as the group descended from its sleeping site to begin daily foraging, or after a long midday rest period when afternoon feeding resumed, or late in the afternoon after a protracted feeding bout in anticipation of returning to a sleeping site. In each case, the impetus to move developed gradually. Thus, early in a developing move sequence, one or a few animals distributed about in space and either sitting, resting or foraging in place began to grunt but otherwise showed little overt behavior apart from an occasional glance in the direction of probable movement. As a move became imminent, however, the initially diffuse calling of a few dispersed animals spread, building to a chorus of grunting involving most animals, accompanied at first by far more frequent glances and prolonged visual scanning in the direction of a move and finally by actual movement.

Using this natural variability, episodes of moving were contextually classified into two subcategories on the basis of their temporal connection to actual movement, a period immediately prior to (less than 5 min before) the group's movement across open terrain, and a period much earlier in the developing move episode (more than 15 min before actual movement by the group) as the impetus to move was just beginning. The former condition was designated the ''high arousal'' condition and the latter the ''low arousal'' condition on the logic that the motivation to move and the relative intensity of arousal associated with that motivation increases closer to the time of actual movement.

TABLE I. Means, standard deviations, and coefficients of variation for acoustic features of grunts.

Acoustic features	Mean	SD	CV
I. Tempo-related			
Calls per bout (no.)	4.4	3.4	0.78
Intercall interval (ms)	550.9	319.3	0.58
Call duration (ms)	137.9	38.9	0.28
II. Source-related			
Amplitude (dB)	79.7	3.0	0.04
F_0 (Hz)	118.4	22.4	0.19
F_0 Contour-begin (Hz)	5.7	6.2	1.08
F_0 Contour-end (Hz)	2.8	6.8	2.34
Jitter (%)	4.6	6.8	1.47
H1A−H2A (dB)	0.8	5.3	3.47
III. Filter-related			
*F*1F (Hz)	458	54.9	0.12
*F*2F (Hz)	1383	127.0	0.09
*F*3F (Hz)	2680	198.7	0.07
LPC slope (dB)	−15.2	9.4	0.62

D. Grunt sample

Using these contextual criteria, an equal number of grunt bouts for each arousal condition within both contexts was selected for as many females as possible from the database of all available recordings. Because there was considerable variability in the number of grunt bouts recorded from each of the group's females in the different contexts, the fully balanced sample ultimately available for analysis was comprised of eight bouts of both move and infant grunts—four bouts each from the high- and low-arousal conditions in each context—for each of eight females (i.e., 16 bouts per female). This sample yielded a total of 606 grunts from 128 different bouts of calling.

E. Acoustic analysis

Analog field recordings of grunts were digitized for analysis with 16-bit accuracy using a sampling rate of 22 050 Hz, after low-pass filtering at 10 kHz. Acoustic analyses were performed using Version 5.3 of the Entropic Signal Processing System Waves+ software package (ESPS/Waves+©) implemented on the Linux operating system (Red Hat 6.0©). Guided by the relationships identified in previous research, 13 acoustic features variously predicted to reflect either caller identity or relative arousal level were measured for each grunt bout. The features are listed in Table I and illustrated in Fig. 1.

Three features predicted to reflect variation in caller arousal were related to the tempo of call production, namely the number of calls produced in each bout (calls per bout), the time interval between successive calls within each bout (intercall interval), and the duration of each call (call duration). The latter two features were measured from time-domain (waveform) representations of grunt bouts.

Six features also predicted to reflect variation in caller arousal were attributable to the source of sound production. The first of these was simply the maximum amplitude of each call (amplitude), calculated as the peak signal intensity (dB) attained within each call. Five additional features were

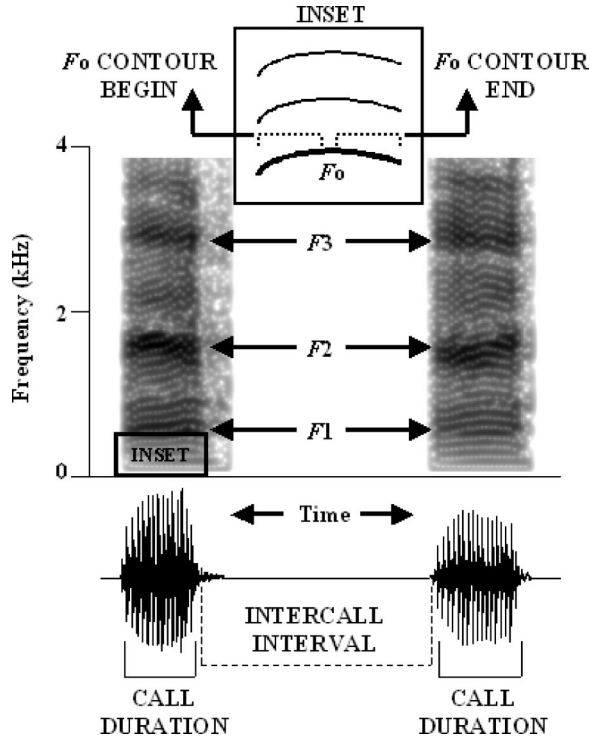

FIG. 1. Waveform and spectrogram (1024-point FFT) displays of a short bout of two move grunts recorded from an adult female baboon illustrating several of the acoustic features of the calls evaluated in acoustic analyses.

used to characterize the pattern of vocal-fold vibration and voice quality. The most basic of these was the average fundamental frequency (F_0) of each grunt. Because most grunts included at least a modest frequency inflection (i.e., showed a slight chevron-shaped F_0 contour), two measures of the F_0 contour were also included. These were simply the beginning and ending slope of the F_0 contour (F_0 contour-begin and F_0 contour-end). Two additional measures of voice quality attributable to source effects were measured. The first of these was a measure of vocal-fold jitter. In this analysis, jitter was calculated as the mean difference in the period (or frequency) of successive cycles of vocal-fold opening and closing (correcting for variation due to the longer-term trend of the F_0 contour) expressed as a percentage of the mean F_0 for that call. The second measure of voice quality concerned the amplitude difference between F_0 and its second harmonic (i.e., H1A−H2A). In humans, this feature of voicing reflects the extent to which the vocal-folds close completely (i.e., are fully adducted) during phonation. Incomplete closure, or adduction, results in a stronger F_0 relative to the second harmonic (i.e., high values of H1A−H2A) and translates perceptually as hoarseness, or breathiness, in the voice (Holmberg *et al.*, 1995).

All source-related characteristics, except H1A−H2A, were calculated from six cycles of vocal-fold vibration from the middle of each grunt. Most grunts contained 8–12 such cycles in total, so that the middle six cycles encompassed 50%–75% of each grunt around its midpoint. The H1A−H2A parameter was measured from a 2048-point (approximately 90 ms) fast Fourier transform (or FFT) bracketing the middle $\frac{2}{3}$ of each grunt. From this FFT, the difference in amplitude between H1 and H2 was calculated.

Finally, four features related to the filtering effects of the supralaryngeal vocal tract cavities were measured. The first three of these were simply the frequency of the first three resonances of the vocal tract ($F1$F,$F2$F,$F3$F). The resonant, or formant, frequencies of each grunt were identified via autocorrelation-based linear predictive coding (LPC). In this analysis, a LPC spectrum was generated from a 1024-point (approximately 50 ms) segment from the midpoint of each grunt, using a Hanning window, 18 coefficients, and no preemphasis. This LPC spectrum was then overlaid on an independently derived FFT for the same segment of the grunt to ensure the goodness of fit of the LPC-derived frequency spectrum. The frequencies of the first three poles of the LPC spectrum were then extracted and retained [see Fig. 1 in Rendall *et al.* (1999) for LPC spectra of move and infant grunts and Owren and Bernacki (1998) for additional details of LPC analysis of nonhuman primate vocalizations]. Preliminary screening and previous analyses (Owren *et al.*, 1997) showed that the formant frequencies of grunts do not vary much within single calls, suggesting that dynamic modification of vocal tract cavities during call production is uncommon. As a result, the formant structure of each grunt could be accurately characterized using a single, broad spectral slice around its midpoint. Based on previous empirical work and theorizing (Rendall, 1996; Rendall *et al.*, 1998; Owren *et al.*, 1997), these features of grunts were included as potential correlates of caller identity.

The fourth filter-related feature measured for each grunt was the slope of the LPC spectrum (LPC slope) and was calculated as the amplitude difference between the first and third formants (i.e., $F3$A-$F1$A). This feature of grunts was labeled ''LPC tilt'' in an earlier analysis of grunts (Owren *et al.*, 1997) where it was identified as the most reliable feature distinguishing grunts produced in the move and infant contexts. It was included in this analysis because there is some evidence from human speech that the amplitude difference between $F1$ and $F3$ is one manifestation of variable voicing effort or intensity (Holmberg *et al.*, 1995; see also van Bezooyen, 1984). By extension, any analogous effort-related effects in baboon grunts might be expected to reflect variation in the intensity of arousal underlying call production.

F. Statistical tests

All statistical tests were conducted using the Number Cruncher Statistical System software package (NCSS 2000: Hintze, 1999). Screening of variables prior to statistical testing revealed strongly right-skewed distributions for both jitter and intercall interval. These two variables were log-transformed prior to statistical analysis.

III. RESULTS

Summary statistics of the acoustic features of all grunts combined appear in Table I. The relative variability of the different features is indicated by their coefficients of variation, which ranged from a low of 0.07 to a high of 3.47. In

TABLE II. Confusion matrix for split-sample, discriminant function classification of calls based on caller identity.

	Predicted ID								
Actual ID	LX	BT	CT	SH	SS	WR	AL	BL	% Correct
LX	**31**	0	3	0	2	0	0	3	79.5
BT	0	**26**	0	5	3	1	7	2	59.1
CT	8	1	**15**	2	6	0	0	3	42.9
SH	0	8	0	**26**	1	1	8	3	55.3
SS	0	6	5	2	**29**	0	1	2	64.4
WR	0	0	0	0	0	**23**	0	0	100.0
AL	1	4	0	2	0	1	**23**	0	74.2
BL	4	1	6	3	1	0	1	**23**	59.0
									196/303(64.7)

general, formant frequencies showed relatively low variability, whereas many (but not all) of the tempo- and source-related features showed comparatively high variability.

A. Acoustic correlates of caller identity

To evaluate the distinctiveness of grunts by caller identity and the relative contribution of specific acoustic features, a stepwise discriminant function analysis was conducted. Variables were entered in this analysis according to the magnitude of their contribution to individual differentiation of calls as determined by the criterion of largest F-value, or greatest percentage change in the test statistic (Wilk's lambda) used to evaluate overall distinctiveness. The results of discriminant function classification of calls are given in Table II, and the order of entry of each acoustic feature in the stepwise process, its F-value and associated probability level, and its percentage contribution to Wilk's lambda are given in Table III.

With all acoustic features making significant contributions to differentiation between individuals entered in the analysis, the overall Wilk's lambda was 0.07. The value of this test statistic ranges from 0 to 1, where "1" indicates no differentiation among groups (in this case, individuals) and "0" indicates perfect or complete differentiation. A value of 0.07 thus indicates a high degree of individual differentiation. It is possible to evaluate the statistical significance of Wilk's lambda using an approximation to the chi-square distribution with $p(g\text{-}1)$ degrees of freedom, where "p" refers to the number of predictor variables used in the analysis and "g" refers to the number of groups to be discriminated (Klecka, 1980). Using this approach, the Wilk's lambda value of 0.07 represents a highly statistically significant degree of differentiation among individuals ($\chi^2=1578.5$, $df=91$, $P<0.001$).

TABLE III. Relative influence of specific acoustic features in discriminant function analysis based on caller identity.

Order of entry of acoustic features	F value	% change in Wilk's lambda
1. $F1$F	*61.04*[a]	41.68
2. F_0	*37.50*[a]	30.54
3. $F2$F	*36.40*[a]	29.95
4. LPC slope	*27.68*[a]	24.56
5. Call duration	*20.90*[a]	*19.76*
6. $F3$F	*20.59*[a]	19.58
7. H1A−H2A	*20.49*[a]	19.48
8. F_0 Contour-end	*10.65*[a]	11.20
9. Jitter	*10.14*[a]	10.74
10. Intercall interval	*7.27*[a]	7.95
11. Amplitude	*5.90*[a]	6.56
12. F_0 Contour-begin	*3.63*[a]	4.15
13. Calls per bout	*2.86*[b]	3.30

[a]$P<0.001$.
[b]$P<0.01$.

This conclusion is borne out in more practical terms in Table II which presents the "confusion matrix" resulting from discriminant analysis classification of the calls by caller identity. In this analysis, the entire sample of 606 grunts was split in half, using calls from one half of the sample to generate discriminant functions that were then used to classify calls from the other half of the sample. Of the 303 grunts to be classified in this way, 196 (or 64.7%) were correctly assigned to the individual that produced them. This level of correct classification represents a 58.3% reduction in the error that would accompany random classification of the calls. There was considerable variability across females in the proportion of calls correctly classified, ranging from a low of 43% to a high of 100%, suggesting that some females were more distinctive sounding than others in the context of this sample.

Table III shows that all acoustic features made statistically significant contributions to the differentiation of grunts by individual identity. However, some variables contributed more to this differentiation than others as evidenced by their higher associated F-values and their greater percentage contributions to the Wilk's lambda test statistic. Both statistics show a discontinuity between steps 7 and 8 of the stepwise discriminant analysis process, indicating that the first seven features contributed disproportionately to the individual differentiation of grunts. There was some patterning within this set of seven features, which included all four of the filter-related features ($F1$F, $F2$F, $F3$F, LPC slope), two of the six source-related features (F_0, H1A−H2A) and one of the three tempo-related features (call duration). Thus, although the grunts of different individuals varied along a number of acoustic dimensions, a large portion of the distinctiveness in

TABLE IV. Acoustic features showing significant variation between high- and low-arousal conditions of the infant and move contexts.

	Infant context Wilk's lambda=0.653 df 13, 421 $F=17.21$, $P<0.001$	Move context Wilk's lambda=0.660 df 13, 157 $F=6.23$, $P<0.001$
Tempo-related	Calls per bout[a] Intercall interval[a] Call duration[b]	Calls per bout[a] Intercall interval[a] Call duration[a]
Source-related	F_0[a] F_0 Contour-begin[a] F_0 Contour-end[a] H1A−H2A[b]	F_0[a] F_0 Contour-begin[b] F_0 Contour-end[b] H1A−H2A[b] Jitter[b]
Filter-related	$F2$F[a]	$F2$F[a]

[a]$P<0.01$.
[b]$P<0.05$.

individuals' calls was accounted for by acoustic features related to the effects of vocal tract filtering.

B. Acoustic correlates of affect intensity

Potential acoustic variation in grunts attributable to differences in caller arousal, or affect, was evaluated using multivariate analysis of variance (MANOVA) with arousal condition (high versus low) as the factor. Separate MANOVA tests were conducted on arousal condition in each context (infant and move) as a test of the consistency of any possible effects. To remove variation in grunt acoustics attributable to the effects of different callers, the data for all acoustic features were first standardized within individuals.

Results of MANOVA tests on arousal condition for grunts produced in each context are given in Table IV. Both tests produced a statistically significant overall effect for arousal condition (infant context: Wilk's lambda=0.653, $F=17.21$, $P<0.001$; move context: Wilk's lambda=0.660, $F=6.23$, $P<0.001$). In each context, this was attributable to statistically significant variation in several acoustic features between high- and low-arousal conditions. The specific features showing significant variation according to arousal condition were extremely consistent between the infant and move contexts (listed in Table IV). In fact, with one exception, the acoustic features varying significantly between high- and low-arousal conditions of the infant context were identical to those that varied significantly between the high- and low-arousal conditions of the move context. The one exception was jitter, which varied significantly in the move but not the infant context.

As in the case of individuals, there was clear patterning in the set of acoustic features that varied according to arousal condition in both contexts, this time involving all three of the tempo-related features (calls per bout, intercall interval, call duration), four of the six source-related features (F_0, F_0 contour-begin, F_0 contour-end, H1A−H2A), and only one of the four filter-related features ($F2$F). Thus, while much of the variation between individuals was attributable to filter-related features, that associated with arousal differences stemmed largely from tempo- and source-related features.

Not only was there a high degree of consistency in the specific acoustic features varying between high- and low-arousal conditions of the infant and move contexts, but the direction of variation between arousal conditions for each acoustic feature was also consistent in both contexts (Fig. 2). Thus, by comparison to bouts of grunts produced in the low-arousal condition of both the infant and move contexts, those produced in the high-arousal condition of both contexts were characterized by a greater number of calls, of longer individual duration, strung together in more rapid succession (i.e., shorter intervals between calls), with a higher F_0, steeper F_0 contours, higher values of H1A−H2A (i.e., increased ''breathiness'' or ''hoarseness'') and a lower second formant frequency.

C. Interrelationships among acoustic correlates of affect

To further evaluate relationships among the acoustic features identified as varying significantly by arousal condition, a principal components analysis (PCA) was conducted. The goal of this analysis was to construct a small set of orthogonal factors (principle components) that would summarize the major dimensions of independent acoustic variation in the grunts when the effects attributable to individuals had been controlled. To this end, a standard PCA with no factor rotation was conducted using the data standardized within individuals. The resulting scree plot and eigenvalues were then examined for obvious discontinuities in order to select the minimum number of factors needed to best account for the greatest share of variance in the data. This process highlighted four factors—all with eigenvalues greater than 1—which accounted for 55% of the variation. The PCA was then run again, this time specifying retention of only four factors and using a varimax rotation to improve the interpretability of the resulting factors (i.e., to maximize variance in the loadings of different acoustic features on each factor). The resulting factors, proportion of variance accounted for by each, and the sign of the loading of specific acoustic features on each factor are given in Table V.

The first factor, accounting for nearly double the variation accounted for by any of the remaining three, was associated with all three acoustic features related to the tempo of call production (i.e., intercall interval, calls per bout, call duration) as well as F_0. The signs associated with each feature indicate that as the number of calls per bout increased, so too did the duration and F_0 of each call, while the interval between successive calls decreased. The second factor was associated with the two F_0 contour features (F_0 contour-begin, F_0 contour-end) and H1A−H2A. In this case, when the F_0 contour was steeper the amplitude difference between H1 and H2 was greater (i.e., relatively more energy in H1). The third factor was associated with the three formant frequencies, which varied directly with one another. Finally, the fourth factor was associated with amplitude and LPC slope. When the amplitude of calls was high, LPC slope was flatter (i.e., less negative).

As an internal check on the results of MANOVA and PCA, one final analysis was conducted, a MANOVA on

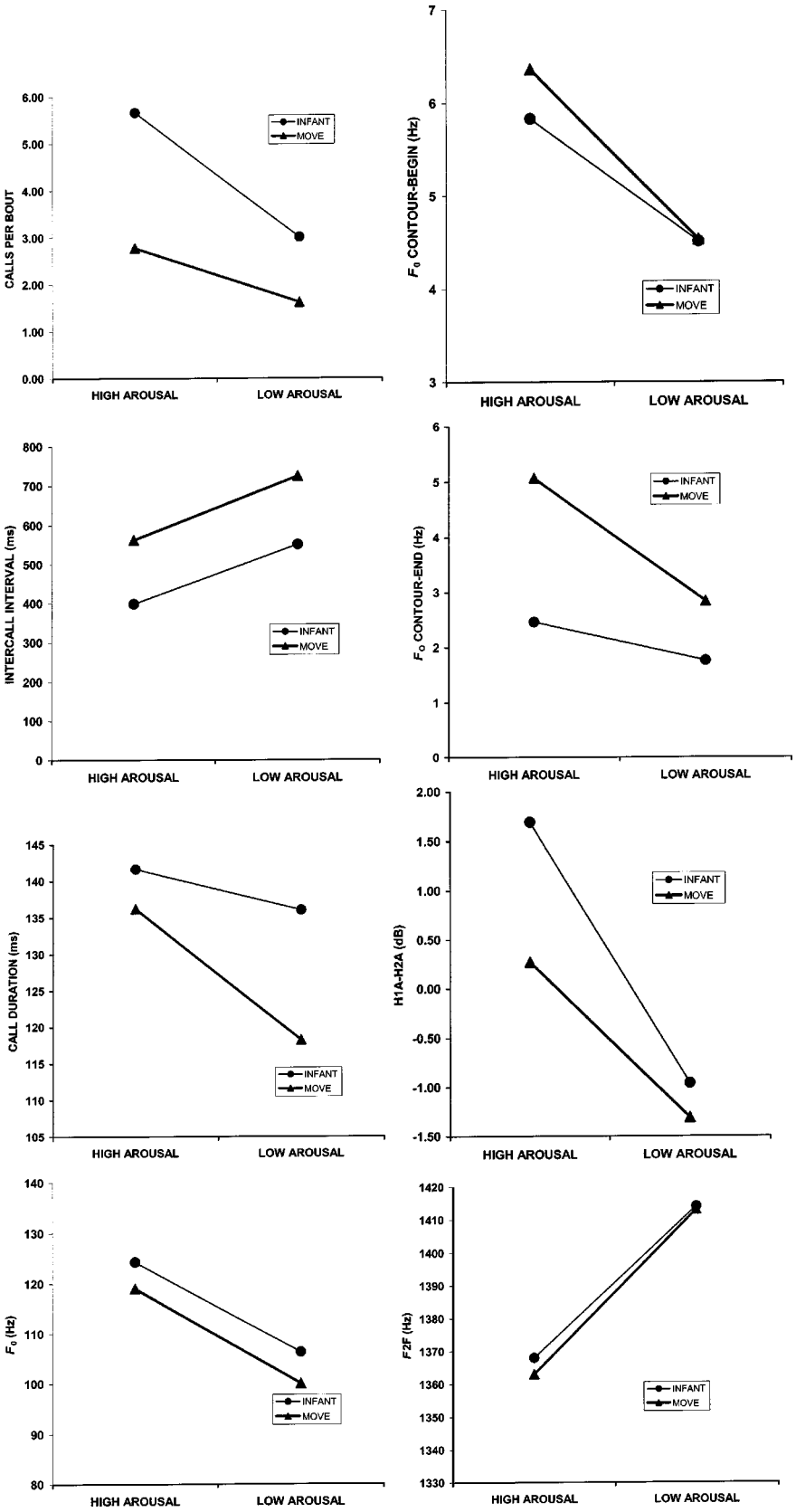

FIG. 2. Acoustic features of grunt bouts that varied significantly between high- and low-arousal conditions of both the move and infant contexts. Values plotted are the overall means after removing variation attributable to individuals.

arousal condition using each grunts' score on each of the first four principal components. For this analysis, the data were collapsed across the infant and move contexts to produce a single grouping of calls according to arousal level (high versus low). This MANOVA on PCA scores revealed significant variation by arousal condition in only the first two factors (Table V). This outcome corroborated the results of the original MANOVA tests, as the seven acoustic features associated with the first two principal components were exactly those identified from the original MANOVA as varying signifi-

TABLE V. Acoustic features associated with specific factors from principal components analysis, and the percentage of variation explained by each factor.

Factor 1[a]	Factor 2[a]	Factor 3	Factor 4
F_0 (+)	F_0 Contour-begin (+)	$F1$F (+)	Amplitude (+)
Intercall interval (−)	F_0 Contour-end (+)	$F2$F (+)	LPC slope (−)
Calls per bout (+)	H1A−H2A (+)	$F3$F (+)	
Call duration (+)			
19.11%	12.62%	12.57%	11.11%

[a]PCA factors showing significant variation according to arousal condition in MANOVA test on data collapsed across the infant and move contexts (see text for additional details).

cantly between high- and low-arousal conditions of both the infant and move contexts.

IV. DISCUSSION

A. General acoustic features of baboon grunts

Results of acoustic analyses performed here accord well with those of the only previous detailed study of the structure of baboon grunts by Owren *et al.* (1997), which also focused on the calls of adult females. Thus, the mean number of calls contained in bouts of grunting (4.4) was identical in the two studies, while mean values for the F_0 (118.4 Hz versus 114.5 Hz) and frequency of each of the first three formants (458, 1383, 2680 Hz versus 438, 1442, 2706 Hz) differed by only 1%–4%. The only feature whose mean value varied appreciably between the two studies was call duration which was approximately 25% longer in this study (137.9 ms) than in that by Owren *et al.* (109.4 ms). This difference might have been due simply to variation in the average signal-to-noise ratio (SNR) of recordings used in the two studies which could have affected the delineation of signal onsets and offsets used to measure call duration. The mean SNR of calls in the present study was 33.2 dB, while that in the earlier study was 15.8 dB. Given that the conditions of fieldwork inevitably introduce some spurious variation into the recording process, such a high degree of concordance in the basic acoustic features of grunts argues strongly for the reliability of the values obtained.

B. Acoustic cues to identity

Paralleling another result of the earlier study, the acoustic structure of adult female grunts was found to be highly individually distinctive. Where successful classification based on chance for the sample of eight females studied here would have been 12.5%, discriminant analysis using 13 acoustic features of grunts successfully classified 65% of the calls.

Individual differences in grunts could be traced to a variety of acoustic features including tempo-, source- and filter-related features, suggesting that various dimensions of vocal production might differ between individuals. However, a stepwise discriminant analysis of individual distinctiveness tended to favor entry of filter-related features—specifically the frequencies of the first three formants and the slope of the LPC spectrum—suggesting that, as a group, these features contributed more to the individual differentiation of grunts than did either tempo- or source-related features. Filter-related features also contributed to individual differentiation of grunts in the analysis by Owren *et al.*, but their importance relative to other acoustic features was difficult to evaluate in that study because only 2 of the 15 features measured were not filter related.

The relative predominance of filter-related features in the present study does, however, replicate the results of earlier research on rhesus monkey ''coo'' vocalizations, which are structurally and functionally analogous to baboon grunts. Like baboon grunts, rhesus monkey coos have a stable F_0 and a rich harmonic structure revealing prominent vocal tract resonances, and they are produced in a variety of behavioral contexts including both face-to-face social interactions and concerted group movements. Earlier systematic analyses of the acoustic structure of coos, analogous to those conducted here on grunts, revealed strong differentiation by individual caller (Rendall, 1996; Rendall *et al.*, 1996, 1998; see also Hauser, 1991). In that work, a large and equal number of filter-related and tempo- and source-related features of coos were measured. As was true of baboon grunts, many acoustic features contributed to individual distinctiveness in coos, but those related to formant patterning appeared to play the largest role.

This outcome led to the general proposal that distinctive resonance patterns attributable to minor differences in vocal tract morphology (e.g., length, shape, and tissue properties) might be a widespread and reliable source of identity cues in nonhuman primate calls, at least in those calls whose source properties permit a clear ''imprint'' of vocal tract resonances (Rendall, 1996; Rendall *et al.*, 1998). This proposal was driven in part by two additional, complementary observations. The first of these was the fact that, although clearly capable of modifying various vocal-tract articulators (e.g., tongue, jaw, lips; Hauser *et al.*, 1993; Hauser and Schön Ybarra, 1994), dynamic vocal-tract modifications during sound production do not appear to be a routine part of call production in nonhuman primates nor do they produce obvious resonance shifts of the sort seen in human speech (Lieberman, 1984; Seyfarth *et al.*, 1994; Rendall, 1996). The second and complementary observation was that, by contrast, tempo- and source-related features of calls tend to vary far more widely within individuals according to the detailed circumstances of call production. Taken together, filter-related features appear to be comparatively stable within individuals and thus potentially functional as reliable cues to identity, while the greater variability of tempo- and source-related features is naturally suited to indexing other, more transient characteristics of callers, such as arousal level.

Although there are few specific empirical comparisons that can be used to judge the validity of both components of this proposal, the results for both baboon grunts and rhesus monkey coos vis a vis identity-cueing are encouraging as are the present results for baboon grunts vis a vis caller arousal (discussed below). There is also some evidence from humans

in support of the identity-cueing component. Here, dynamic modifications of the vocal tract that generate the variable formant patterns of different speech sounds would seem to obscure any potentially individualistic formant patterns, and individually distinctive voice patterns then have often been sought in a variety of tempo- and source-related features of speech. Nevertheless, filter-related features, such as the higher formants (above F2) that are not so centrally involved in variable linguistic encoding, and nasal resonances, have sometimes been implicated (reviewed in Bricker and Pruzansky, 1976; Nolan, 1983; Remez *et al.*, 1997). Furthermore, recent work in speech perception indicating that vowel identification is significantly better when listeners are familiar with the speaker suggests that, despite their obvious linguistic variability, formant patterns might be quite individualistic (Palmeri *et al.*, 1993; Nygaard *et al.*, 1995). In fact, very recent detailed MRI studies suggest that, despite significant linguistically driven vocal tract variability, the average configuration of a speaker's vocal tract (what would approximate a neutral configuration like that associated with the schwa vowel) may be unique to the individual (Titze and Story, 2002; see also Story and Titze, 2001, 2002). The latter MRI work has fully characterized only four individuals to date, however. So it remains to be seen whether this result is robust.

An important extension of the latter findings, though, is that some of the individual differences in formants, both in baboon grunts and the vocal signals of other species, might be traceable ultimately to differences in body size. Formants manifest the resonating properties of the vocal tract, which are determined in large part by its length. Vocal tract length, in turn, has been proposed to scale predictably with overall body size (Fitch, 1997, 2000). There are data from several species that support these various connections, either indirectly in the form of consistent differences in the formant frequencies of vocal signals produced by individuals of different age or sex classes that also vary consistently in body size (e.g., humans: Hollien *et al.*, 1994; rhesus monkeys: Fitch, 1997; baboons: Fischer *et al.*, 2002; Rendall *et al.*, 2003), or more directly in the form of correlations between biometric measures of vocal tract length and body size (humans: Fitch and Giedd, 1999; dogs: Riede and Fitch, 1999). There are also some data that contradict the proposal. For example, Fitch (1999) has shown that the trachea in several bird species has been drastically elongated, thereby lengthening the vocal tract out of all proportion to body size, and Fitch and Reby (2001) have shown that the larynx in some species of deer can be dramatically retracted in the vocal tract, thereby quite flexibly altering overall vocal tract length and its associated resonant frequencies. Such ambiguities notwithstanding, it seems very likely that at least some portion of the formant differences between individuals reflects differences in the length of the vocal tract that arise ultimately from differences in overall body size.

C. Acoustic cues to arousal

Bouts of grunts produced by baboons in the context of group movements and during social interactions with mothers and their young infants also differed consistently as a function of caller arousal. This analysis identified a set of eight acoustic features that varied significantly between the high- and low-arousal conditions of these two contexts, with the direction of variation for each feature consistent across both contexts. In contrast to the pattern observed with respect to individual identity, most of the variation in grunt structure associated with arousal condition pertained to tempo- and source-related acoustic features: all three tempo-related features and four of the six source-related features varied between the high- and low-arousal conditions, but only one filter-related feature did so.

These results are consistent with the bulk of previous work on acoustic correlates of affect which likewise emphasizes tempo- and source-related features. In fact, many of the specific features identified in this study are ones commonly connected to arousal intensity. Thus, the amount and rate of calling as well as the absolute F_0 and relative tonality (or harshness) of calls and the peakedness of their F_0 contours are frequently cited indices of arousal intensity in human speech (reviewed in Murray and Arnot, 1993; Scherer, 1995; Bachorowski, 1999) and other nonverbal vocal signals (e.g., crying: Porter *et al.*, 1986) as well as in the calls of other animal species where known (see the Introduction). Moreover, the direction of arousal-related variation in these features of grunts matches that observed in other studies, with increases in arousal producing increases in each feature. For example, just as bouts of baboon grunts produced in the high- as compared to low-arousal condition consisted of more calls, delivered at a faster rate, with higher average F_0, greater F_0 excursions, and increased harshness or breathiness, bouts of food-associated vocalizations (coos) in rhesus monkeys produced under conditions of increased hunger consisted of more calls, produced at a more rapid rate, with higher average F_0, and increased harshness (Hauser, 2000). The same pattern is reported for humans: increased arousal is typically associated with increases in overall speaking rate, F_0, and modulations of the F_0 contour. Similarly, in human infants, bouts of crying induced by increasingly invasive, and thus painful, surgical procedures include more cries, produced at a faster rate, with higher average F_0, greater F_0 excursions, and more irregularities in the F_0 contour (Porter *et al.*, 1986).

Although most of the features varying with arousal intensity in baboon grunts are consistent with those identified as vehicles of affect expression in other studies, two features of grunts that varied with arousal level are not so readily corroborated, namely the duration of individual calls (call duration) and the frequency of the second formant ($F2$F). The results for call duration are consistent with the overall pattern. Like the other tempo- and source-related features varying with arousal intensity, the duration of individual grunts increased in the high-arousal compared to the low-arousal condition. Longer calls under conditions of higher arousal could plausibly reflect attempts to signal more emphatically or conspicuously in this condition, just as producing more calls at a faster rate under high-arousal conditions would seem to be parallel components of such an effort.

Although plausible, the relationship for call duration is more difficult than the others to confirm because call dura-

tion seems not to be routinely measured in studies of vocal affect. Research on human speech has shown that vowel durations vary between different simulated emotions (Leinonen *et al.*, 1997). It has also consistently shown that vowel duration increases with increased vocal effort. For example, vowels are longer in shouted, as opposed to comfortably spoken or whispered speech (e.g., Fónagy and Fónagy, 1966; Traunmüller and Eriksson, 2000). In as much as the latter effort-related increases in vowel duration parallel effects associated with increased arousal, they may help to corroborate the results for call duration in baboon grunts. However, research into the effects of arousal variation on the acoustics of human infant crying is more equivocal. For example, Zeskind *et al.* (1985) describe a ''classic pattern'' for cries produced in response to the application of a brief painful stimulus (a rubber-band snap to the foot) involving a single long cry as the stimulus is applied followed by a series of cries of shorter individual duration as the pain subsides, while Porter *et al.* (1986) report the opposite pattern: increased (pain-induced) arousal is associated with cries of shorter, not longer, individual duration.

Results for $F2$F are also difficult to corroborate because, as with call duration, formant features have not always been a standard component of vocal affect research. However, some researchers have proposed plausible arousal-related formant changes mediated through effects either on accompanying facial gestures, exaggerated effortful articulations, or on general tensing or relaxation of supralaryngeal airways (Scherer, 1986). Although many of the relationships remain to be tested formally, there are already some supporting data. For example, Hauser *et al.* (1993) reported variation in the facial gestures that accompany several different rhesus monkey vocalizations and also variation specifically in mandibular position during the production of ''coo'' vocalizations that affected the ''dominant frequency'' of these calls. Although neither result was related specifically to arousal-variation or to formants *per se*, the variable facial gestures described do probably manifest variable underlying arousal and would plausibly affect any resonance structure in the associated calls. Among humans, Tartter (1980) reported that smiling while speaking resulted in predictable increases in the formants (as well as F_0) of vowel sounds. Bachorowski and Owren (1995a, b) also reported variation in vowel formants that was associated with variation in the intensity of both positive and negative emotions. Variable vowel formants have also been linked to variable vocal effort and associated voice loudness, probably as a result of effort-related differences in mouth opening or flaring (Traunmüller and Eriksson, 2000).

Finally, while a number of acoustic features of grunts varied with arousal intensity, some of those specifically predicted to do so, in fact, did not. One of these was amplitude, which is widely held to reflect varying arousal intensity. The other was LPC slope. Although not commonly associated with arousal variation (cf. Van Bezooyan, 1984), LPC slope was nevertheless included here because of a proposed connection to voicing effort or intensity in human vowels. For example, Holmberg *et al.* (1995) report a positive correlation between the slope of the LPC spectrum (measured as the amplitude difference between $F1$ and $F3$) and sound pressure level, higher frequencies increasingly emphasized in vowels as voice ''loudness'' increases (see also Holmberg *et al.*, 1988; Traunmüller and Eriksson, 2000). Extrapolating from this work, any similar effort- or intensity-related effects on the spectral slope of baboon grunts were predicted to reflect variation in the intensity of arousal underlying call production. And, in fact, amplitude and LPC slope were correlated in the baboon grunts as evidenced by their grouping together in the same factor of the principal components analysis. However, neither feature varied significantly by arousal condition. This is surprising for two reasons. First, as noted, call amplitude is probably the feature of vocal production most widely assumed to index arousal intensity. Second, the voice quality feature, H1A−H2A, did vary significantly by arousal condition, and one reliable correlate of this feature—at least in humans—is variable emphasis of higher frequencies and thus variable LPC slope (Holmberg *et al.*, 1995).

One possible explanation for the association between arousal condition and H1A−H2A but not either amplitude or LPC slope is that the latter two acoustic features may be more adversely affected by variation in subject–microphone (i.e., recording) distances. Although all recordings used in this analysis were made under ideal field conditions at relatively close range, there was nevertheless some inevitable variation in the recording distance (from 0.5 to 2 m). Such variation is a routine obstacle to the use of amplitude in analyses of field-based recordings, and so amplitude results must always be interpreted cautiously. In this case, variable recording distances might have obscured some of the natural amplitude difference between arousal conditions with similar effects on spectral slope (given the association between the two), but have had comparatively little impact on the low frequency end of the spectrum from which the H1A−H2A measure derives.

Another possibility for LPC slope is that this acoustic feature of grunts also varies with behavioral context. Owren *et al.* (1997) found that LPC slope was the acoustic feature that best distinguished grunts produced in the move and infant contexts, a finding later confirmed by field playback experiments (Rendall *et al.*, 1999). Hence, this feature of baboon grunts may reflect an interaction of the effects of context and vocal intensity that precluded it from sorting cleanly according to the two arousal conditions studied here.

One additional acoustic variable that did not vary consistently by arousal condition was the voice quality feature, jitter. Although a second voice quality feature, H1A−H2A, did vary consistently between high- and low-arousal conditions of both contexts, jitter did so only in the move context. Although equivocal, this variable pattern of results is actually consistent with the history of work on features of voice quality in humans, in which jitter, and other measures of vocal perturbation, sometimes show up as related to arousal or anxiety and other times do not (reviewed in Protopapas and Lieberman, 1997). The failure to find consistent effects for jitter across both contexts of grunting, then, might indicate that it is not a reliable marker of affect intensity, or that it interacts with other production processes in complex ways

that produce this sort of variable outcome. Another possibility is that the inconsistent effect reflects variable association with different emotional states (Scherer, 1986). This study focused only on variation in the intensity of nonspecific arousal in two contexts of grunt production. While this operationalization seems to have captured some of the arousal-related variation in these calls, the tone or quality of emotional state associated with grunt production might well vary between the two contexts (in addition to varying in its intensity within each), and jitter might not be associated with variation in the intensity of the emotion accompanying grunting in the infant context.

In sum, the results of this study tend to support theoretical predictions and a small set of empirical findings on the relative importance of formants in identity cueing in nonhuman primate vocalizations. They also reveal a variety of potential acoustic correlates of affect intensity in baboon grunts, many of which show signs of continuity with vehicles of vocal affect expression in other species, including humans. Both results are promising vis a vis the development of general, production-based schemes that can relate enduring constitutional attributes of callers (e.g., sex, age, individual identity, general health and vigor), as well as their more transient physiological and psychological states (e.g., arousal, motivational, and cognitive states; acute pathologies), to specific dimensions of variation in their vocal output.

ACKNOWLEDGMENTS

Thanks are extended to the Office of the President and the Department of Wildlife and National Parks of the Republic of Botswana for permission to conduct research in the Moremi Game Reserve, and to Robert Seyfarth and Dorothy Cheney for the opportunity to conduct this research at their field site. Thanks also to Robert, Dorothy, Sergio Pellis, and two anonymous reviewers for many helpful comments on an earlier version of this manuscript. Research support was provided by the Natural Sciences and Engineering Research Council of Canada, the L.S.B. Leakey Foundation, and the University of Lethbridge.

Andrew, R. J. (**1976**). ''Use of formants in the grunts of baboons and other nonhuman primates,'' Ann. N.Y. Acad. Sci. **280**, 673–693.

Bachorowski, J-A. (**1999**). ''Vocal expression and perception of emotion,'' Curr. Dir. Psychol. Sci. **8**, 53–57.

Bachorowski, J.-A., and Owren, M. J. (**1995a**). ''Vocal expression of emotion: Acoustic properties of speech are associated with emotional intensity and context,'' Psychol. Sci. **6**, 219–224.

Bachorowski, J.-A., and Owren, M. J. (**1995b**). ''Vocal expression of emotion is associated with formant characteristics,'' J. Acoust. Soc. Am. **98**, 2936–2937.

Bricker, P. D., and Pruzansky, S. (**1976**). ''Speaker recognition,'' in *Contemporary Issues in Experimental Phonetics*, edited by N. J. Lass (Academic, New York), pp. 295–326.

Cheney, D. L., Seyfarth, R. M., and Silk, J. B. (**1995**). ''The role of grunts in reconciling opponents and facilitating interactions among adult female baboons,'' Anim. Behav. **50**, 249–257.

Cheney, D. L., Seyfarth, R. M., and Palombit, R. A. (**1996**). ''The function and mechanisms underlying baboon 'contact' barks,'' Anim. Behav. **52**, 507–518.

Fichtel, C., and Hammerschmidt, K. (**2001**). ''Information content of red-fronted lemur (*Eulemur fulvus*) alarm calls,'' Adv. Ethol. **36**, 16–17.

Fichtel, C., Hammerschmidt, K., and Jürgens, U. (**2001**). ''On the vocal expression of emotion: A multi-parametric analysis of different states of aversion in the squirrel monkey,'' Behaviour **138**, 97–116.

Fischer, J., Hammerschmidt, K., Cheney, D. L., and Seyfarth, R. M. (**2002**). ''Acoustic features of male baboon loud calls: Influences of context, age, and individual identity,'' J. Acoust. Soc. Am. **111**, 1465–1474.

Fitch, W. T. (**1997**). ''Vocal tract length and formant frequency dispersion correlate with body size in rhesus macaques,'' J. Acoust. Soc. Am. **102**, 1213–1222.

Fitch, W. T. (**1999**). ''Acoustic exaggeration of size in birds by tracheal elongation: comparative and theoretical analyses,'' J. Zool. **248**, 31–49.

Fitch, W. T. (**2000**). ''The evolution of speech: A comparative review,'' Trends Cog. Sci. **4**, 258–267.

Fitch, W. T., and Hauser, M. D. (**1995**). ''Vocal production in nonhuman primates: Acoustics, physiology, and functional constraints on ''honest'' advertisement,'' Am. J. Primatol **37**, 179–190.

Fitch, W. T., and Giedd, J. (**1999**). ''Morphology and development of the human vocal tract. A study using magnetic resonance imaging,'' J. Acoust. Soc. Am. **106**, 1511–1522.

Fitch, W. T., and Reby, D. (**2001**). ''The descended larynx is not uniquely human,'' Proc. R. Soc. London, Ser. B **268**, 1669–1675.

Fónagy, I., and Fónagy, J. (**1966**). ''Sound pressure level and duration,'' Phonetica **15**, 14–21.

Goldbeck, T., Tolkmitt, F., and Scherer, K. R. (**1988**). ''Experimental studies of vocal affect communication,'' in *Facets of Emotion*, edited by K. R. Scherer (Erlbaum, Hillsdale, NJ), pp. 119–137.

Gouzoules, S., Gouzoules, H., and Marler, P. (**1984**). ''Rhesus monkey (*Macaca mulatta*) screams: representational signaling in the recruitment of agonistic aid,'' Anim. Behav. **32**, 182–193.

Hammerschmidt, K., and Fichtel, C. (**2001**). ''Call pitch' as an indicator of the intensity of affective states,'' Adv. Ethol. **36**, 16.

Hauser, M. D. (**1991**). ''Sources of acoustic variation in rhesus macaque (*Macaca mulatta*) vocalizations,'' Ethology **8**, 29–46.

Hauser, M. D. (**2000**). ''The sound and the fury: Primate vocalizations as reflections of emotion and thought,'' in *The Origins of Music*, edited by N. Wallin, B. Merker, and S. Brown (MIT, Cambridge, MA), pp. 77–102.

Hauser, M. D., and Marler, P. (**1993**). ''Food-associated calls in rhesus macaques (Macaca mulatta): I. Socioecological factors,'' Behav. Ecol. **4**, 194–205.

Hauser, M. D., and Schön Ybarra, M. A. (**1994**). ''The role of lip configuration in monkey vocalizations: Experiments using xylocaine as a nerve block,'' Brain Lang **46**, 232–244.

Hauser, M. D., Evans, C. S., and Marler, P. (**1993**). ''The role of articulation in the production of rhesus monkey, *Macaca mulatta*, vocalizations,'' Anim. Behav. **45**, 423–433.

Hewitt, G., MacLarnon, A., and Jones, K. E. (**2000**). ''The functions of laryngeal air sacs in Primates: A new hypothesis,'' Folia Primatol (Basel) **73**, 70–94.

Hintze, J. L. (**1999**). *Number Cruncher Statistical System, 2000* (Kaysville, Utah).

Hollien, H., Green, R., and Massey, K. (**1994**). ''Longitudinal research on adolescent voice change in males,'' J. Acoust. Soc. Am. **96**, 2646–2654.

Holmberg, E. B., Hillman, R. E., and Perkell, J. S. (**1988**). ''Glottal airflow and transglottal air pressure measurements for male and female speakers in soft, normal, and loud voice,'' J. Acoust. Soc. Am. **84**, 511–529.

Holmberg, E. B., Hillman, R. E., Perkell, J. S., Guiod, P. C., and Goldman, S. L. (**1995**). ''Comparisons among aerodynamic, electroglottographic, and acoustic spectral measures of female voice,'' J. Speech Hear. Res. **38**, 1212–1223.

Jürgens, U. (**1979**). ''Vocalization as an emotional indicator: A neuroethological study in the squirrel monkey,'' Behaviour **69**, 88–117.

Klecka, W. R. (**1980**). *Discriminant Analysis. Series: Quantitative Applications in the Social Sciences* (Sage, London).

Leinonen, L., Hiltunen, T., Linnankoski, I., and Laakso, M. (**1997**). ''Expression of emotional-motivational connotations with a one-word utterance,'' J. Acoust. Soc. Am. **102**, 1853–1863.

Lieberman, P. (**1984**). *The Biology and Evolution of Language* (Harvard U. P., Cambridge, MA).

Lieberman, P., and Michaels, S. B. (**1962**). ''Some aspects of fundamental frequency and envelope amplitude as related to the emotional content of speech,'' J. Acoust. Soc. Am. **34**, 922–927.

Lieberman, P. H., Klatt, D. H., and Wilson, W. H. (**1969**). ''Vocal tract limitations on the vowel repertoires of rhesus monkey and other nonhuman primates,'' Science **164**, 1185–1187.

Mergill, P., Fitch, T., and Herzel, H. (**1999**). ''Modeling of the role of nonhuman vocal membranes in phonation,'' J. Acoust. Soc. Am. **105**, 2020–2028.
Murray, I. R., and Arnot, J. L. (**1993**). ''Toward the simulation of emotion in synthetic speech: A review of the literature on human vocal emotion,'' J. Acoust. Soc. Am. **93**, 1097–1108.
Negus, V. E. (**1949**). *The Comparative Anatomy and Physiology of the Larynx* (Hafner, New York).
Nolan, F. (**1983**). *The Phonetic Bases of Speaker Recognition* (Cambridge U. P., Cambridge, MA).
Nygaard, L. C., Sommers, M. S., and Pisoni, D. B. (**1995**). ''Speech perception is a talker-contingent process,'' Psychol. Sci. **5**, 42–46.
Owren, M. J., and Bernacki, R. H. (**1988**). ''The acoustic features of vervet monkey alarm calls,'' J. Acoust. Soc. Am. **83**, 1927–1935.
Owren, M. J., and Bernacki, R. H. (**1998**). ''Applying linear predictive coding (LPC) to frequency-spectrum analysis of animal acoustic signals,'' in *Animal Acoustic Communication: Sound Analysis and Research Methods*, edited by S. L. Hopp, M. J. Owren, and C. S. Evans (Springer-Verlag, Heidelberg), pp. 129–162.
Owren, M. J., and Linker, C. D. (**1995**). ''Some analysis methods that may be useful to acoustic primatologists,'' in *Current Topics in Primate Vocal Communication*, edited by E. Zimmerman, J. D. Newman, and U. Jürgens (Plenum, New York), pp. 1–27.
Owren, M. J., Seyfarth, R. M., and Cheney, D. L. (**1997**). ''The acoustic features of vowel-like grunt calls in chacma baboons (*Papio cynocephalus ursinus*): implications for production processes and functions,'' J. Acoust. Soc. Am. **101**, 2951–2963.
Owren, M. J., Dieter, J. A., Seyfarth, R. M., and Cheney, D. L. (**1993**). ''Vocalizations of rhesus (Macaca mulatta) and Japanese (M. fuscata) macaques cross-fostered between species show evidence of only limited modification,'' Dev. Psychobiol. **26**, 389–406.
Palmeri, T. J., Goldinger, S. D., and Pisoni, D. B. (**1993**). ''Episodic encoding of voice attributes and recognition memory for spoken words,'' J. Exp. Psychol. Learn. Mem. Cogn. **19**, 309–328.
Porter, F. L., Miller, R. H., and Marshall, R. E. (**1986**). ''Neonatal pain cries: Effect of circumcision on acoustic features and perceived urgency,'' Child Dev. **57**, 790–802.
Protopapas, A., and Eimas, P. D. (**1997**). ''Perceptual differences in infant cries revealed by modifications of acoustic features,'' J. Acoust. Soc. Am. **102**, 3723–3734.
Protopapas, A., and Lieberman, P. (**1997**). ''Fundamental frequency of phonation and perceived emotional stress,'' J. Acoust. Soc. Am. **101**, 2267–2277.
Remez, R. E., Fellowes, J. M., and Rubin, P. E. (**1997**). ''Talker identification based on phonemic information,'' J. Exp. Psychol. Hum. Percept. Perform. **23**, 651–666.
Rendall, D. (**1996**). ''Social communication and vocal recognition in free-ranging rhesus monkeys (Macaca mulatta),'' Ph.D. dissertation, University of California—Davis.
Rendall, D., Owren, M. J., and Rodman, P. S. (**1998**). ''The role of vocal tract filtering in identity cueing in rhesus monkey (*Macaca mulatta*) vocalizations,'' J. Acoust. Soc. Am. **103**, 602–614.
Rendall, D., Rodman, P. S., and Emond, R. E. (**1996**). ''Vocal recognition of individuals and kin in free-ranging rhesus monkeys,'' Anim. Behav. **51**, 1007–1015.
Rendall, D., Cheney, D. L., and Seyfarth, R. M. (**2000**). ''Proximate factors mediating 'contact' calls in adult female baboons and their infants,'' J. Comp. Psychol. **114**, 36–46.
Rendall, D., Owren, M. J., Weerts, E., and Hienz, R. J. (**in press**). ''Sex differences in the acoustic structure of vowel-like baboon grunts and their perceptual salience to listeners,'' J. Acoust. Soc. Am.
Rendall, D., Seyfarth, R. M., Cheney, D. L., and Owren, M. J. (**1999**). ''The meaning and function of grunt variants in baboons,'' Anim. Behav. **57**, 583–592.
Richman, B. (**1976**). ''Some vocal distinctive features used by gelada monkeys,'' J. Acoust. Soc. Am. **60**, 718–724.
Riede, T., and Fitch, W. T. (**1999**). ''Vocal tract length and acoustics of vocalizations in the domestic dog (*Canis familiaris*),'' J. Exp. Biol. **202**, 2859–2867.
Russell, J. A., Bachorowski, J-A., and Fernández-Dols, J-M. (**2003**). ''Facial and Vocal Expressions of,'' Ann. Rev. Psychol. **54**, 329–349.
Scherer, K. (**1986**). ''Vocal affect expression: A review and a model for future research,'' Psychol. Bull. **99**, 143–165.
Scherer, K. (**1995**). ''Expression of emotion in voice and music,'' J. Voice **9**, 235–248.
Schön Ybarra, M. (**1995**). ''A comparative approach to the nonhuman primate vocal tract: Implications for sound production,'' in *Current Topics in Primate Vocal Communication*, edited by E. Zimmerman, J. D. Newman, and U. Jürgens (Plenum, New York), pp. 185–198.
Semple, S., McComb, K., Alberts, S., and Altmann, J. (**2002**). ''Information content of female copulation calls in yellow baboons,'' Am. J. Primatol **56**, 43–56.
Seyfarth, R. M., and Cheney, D. L. (**1997**). ''Some general features of vocal development in nonhuman primates,'' in *Social Influences on Vocal Development*, edited by C. T. Snowdon and M. Hausberger (Cambridge U. P., Cambridge), pp. 249–274.
Seyfarth, R. M., Cheney, D. L., and Marler, P. (**1980**). ''Monkey responses to three different alarm calls: evidence for predator classification and semantic communication,'' Science **210**, 801–803.
Seyfarth, R. M., Cheney, D. L., Harcourt, A. H., and Stewart, K. J. (**1994**). ''The acoustic features of gorilla double grunts and their relation to behavior,'' Am. J. Primatol **33**, 31–50.
Story, B. H., and Titze, I. R. (**2001**). ''The relationship of vocal tract shape to three voice qualities,'' J. Acoust. Soc. Am. **109**, 1651–1667.
Story, B. H., and Titze, I. R. (**2002**). ''A preliminary study of voice quality transformation based on modifications to the neutral vocal tract area function,'' J. Phonetics **30**, 485–509.
Tartter, V. C. (**1980**). ''Happy talk: Perceptual and acoustic effects of smiling on speech,'' Percept. Psychophys. **27**, 24–27.
Titze, I. R., and Story, B. H. (**2002**). ''Voice quality: What is most characteristic about 'you' in speech,'' Acoust. Soc. Am. Newsletter, Echoes **12**, 1–4.
Traunmüller, H., and Eriksson, A. (**2000**). ''Acoustic effects of variation in vocal effort by men, women, and children,'' J. Acoust. Soc. Am. **107**, 3438–3451.
van Bezooyan, R. (**1984**). *Characteristics and Recognizability of Vocal Expressions of Emotion* (Foris, Dordrecht).
Williams, C. E., and Stevens, K. N. (**1972**). ''Emotions and speech: Some acoustical correlates,'' J. Acoust. Soc. Am. **52**, 1238–1250.
Zeskind, P. S., Sale, J., Maio, M. L., Huntington, L., and Weisman, J. R. (**1985**). ''Adult perceptions of pain and hunger cries: A synchrony of arousal,'' Child Develop. **56**, 549–554.

Patterns in the vocalizations of male harbor seals

Sofie M. Van Parijs[a)]
Norwegian Polar Institute, Tromsø N-9296, Norway and Norwegian College of Fisheries Science, University of Tromsø, Tromsø N-9037, Norway

Peter J. Corkeron
Norwegian Institute of Fisheries and Aquaculture, N-9291 Tromsø, Norway

James Harvey
Moss Landing Marine Laboratories, 8272 Moss Landing Road, California 95039

Sean A. Hayes
Biology Department, Earth/Marine Sciences, University of California, Santa Cruz, California 95064

David K. Mellinger
Monterey Bay Aquarium Research Institute, 7700 Sandholdt Road, Moss Landing, California 95039 and Oregon State University, Cooperate Institute for Marine Resource Studies, 2030 South Marine Science Drive, Newport, Oregon 97365

Philippe A. Rouget
Bamfield Marine Station, Bamfield, British Columbia V0R 1B0, Canada and Department of Biology, University of Victoria, Victoria, British Columbia, Canada

Paul M. Thompson
Lighthouse Field Station, University of Aberdeen, Cromarty, Ross-Shire IV11 8YJ, United Kingdom

Magnus Wahlberg
National Board of Fisheries, Institute of Coastal Research, Nya Varvet 31, 426 71 Va Frölunda, Sweden and Center for Sound Communication, Department of Zoophysiology, Århus University, Building 131, CF Møllers Alle, DK-8000 Århus C, Denmark

Kit M. Kovacs
Norwegian Polar Institute, Tromsø N-9296, Norway

(Received 19 July 2002; revised 10 February 2003; accepted 26 February 2003)

Comparative analyses of the roar vocalization of male harbor seals from ten sites throughout their distribution showed that vocal variation occurs at the oceanic, regional, population, and subpopulation level. Genetic barriers based on the physical distance between harbor seal populations present a likely explanation for some of the observed vocal variation. However, site-specific vocal variations were present between genetically mixed subpopulations in California. A tree-based classification analysis grouped Scottish populations together with eastern Pacific sites, rather than amongst Atlantic sites as would be expected if variation was based purely on genetics. Lastly, within the classification tree no individual vocal parameter was consistently responsible for consecutive splits between geographic sites. Combined, these factors suggest that site-specific variation influences the development of vocal structure in harbor seals and these factors may provide evidence for the occurrence of vocal dialects.
[DOI: 10.1121/1.1568943]

PACS numbers: 43.80.Ka [WA]

I. INTRODUCTION

Geographic variation in vocal patterns may occur for a variety of reasons, such as genetic variation, founder effects, and adaptations to the environment through contextual learning. Variations in vocalizations have been shown to be genetically based in several bird species (Kroodsma and Canady, 1985; Baker and Bailey, 1987; Medvin *et al.*, 1992; McCracken and Sheldon, 1997) and a few mammals (Lieblich *et al.*, 1980; Nevo *et al.*, 1987). Founder effects appear to be relatively rare, but have been suggested to be the probable cause of vocal variation in the northern elephant seal, *Mirounga angustriostris* (Le Boeuf and Petrinovich, 1974). Environmental factors affecting transmission properties can influence animals to adapt their call types to increase the likelihood of transmission, even among species that are capable only of contextual learning (e.g., Janik and Slater, 1997). Although several studies have shown geographic variation in the usage of call types or site-specific calls, few studies conclusively demonstrate which mechanisms are responsible for these differences (Nevo *et al.*, 1987; McCracken and Sheldon, 1997).

Vocal communication involves two types of learning, contextual and production learning. Contextual learning is

a)Electronic mail: sofievp@nfh.uit.no

defined as ''associating an existing signal with a new context as a result of experience with the usage of signals by other individuals,'' and production learning is defined as ''signals that are modified as a result of experience with other individuals'' (Janik and Slater, 2000). Vocal learning can be defined as production learning in the vocal domain. Vocal learning has primarily been studied in birds (e.g., Todt, 1975; Pepperberg, 1981; Kroodsma and Baylis, 1982; Baptista and Schuchmann, 1990; Gaunt *et al.*, 1994). Evidence for vocal learning in nonhuman mammals is still scarce, but vocal learning has been demonstrated in bats, phocid seals and cetaceans (see review in Janik and Slater, 1997). Clear evidence for vocal learning in nonhuman mammals is often difficult to obtain. To date, the most convincing evidence comes from experimental studies performed with captive animals (e.g., Caldwell and Caldwell, 1972; Reiss and McCowan, 1993).

Demonstrating vocal learning from observational data is much more difficult. In the case of marine mammals, the difficulties associated with keeping captive animals often means that observational data is the only possible source of information. Unfortunately, observational data can almost never exclude the occurrence of usage learning based on a pre-existing repertoire (Janik and Slater, 2000). Nonetheless, vocal learning has been demonstrated from observational data in humpback whales, *Megaptera novaeangliae*, in the wild (e.g., Payne and McVay, 1971; Payne *et al.*, 1983; Guinee *et al.*, 1983; Payne and Payne, 1985; Noad *et al.*, 2000).

In phocid seals, vocal learning has been clearly demonstrated in two captive harbor seals. *Phoca vitulina*, that were shown to be capable of imitating speech sounds (Ralls *et al.*, 1985). Some observational data also exist suggesting that vocal dialects between adjacent colonies in Weddel seals, *Leptonychotes weddellii*, may provide evidence for vocal learning (Green and Burton, 1988; Morrice *et al.*, 1994). However, to date, studies of geographical vocal variation in phocids have concentrated on sites that are several hundreds or thousands of kilometers apart (e.g., Cleator *et al.*, 1989; Terhune, 1994; Thomas and Golladay, 1995).

Harbor seals are the most widely distributed pinniped species, ranging from the eastern Baltic, westward across the Atlantic and Pacific Oceans to southern Japan. The distribution of harbor seals is such that they are exposed to a wide range of varying environmental constraints and they are composed of several subspecies (Bigg, 1981; Lamont *et al.*, 1996; Stanley *et al.*, 1996; Kappe *et al.*, 1997; Goodman, 1998; Burg *et al.*, 1999). Although harbor seals are capable of long-distance movements (e.g., Thompson *et al.*, 1989; Thompson, 1993; Ries *et al.*, 1998), populations tend to be philopatric over distances of around 100 km (Härkönen and Harding, 2001). Harbor seals are vocally versatile. They are capable of vocal learning (Ralls *et al.*, 1985) and evidence from two sites show that they exhibit geographic variation in vocalizations (Van Parijs *et al.*, 2000a). Therefore, they offer an interesting opportunity to explore vocal variation between ''distant'' and ''neighboring'' mammalian populations on a wide-ranging geographic scale. Comparisons of vocal variation at this scale have not been made previously in marine mammals, as few species are distributed over such a wide area.

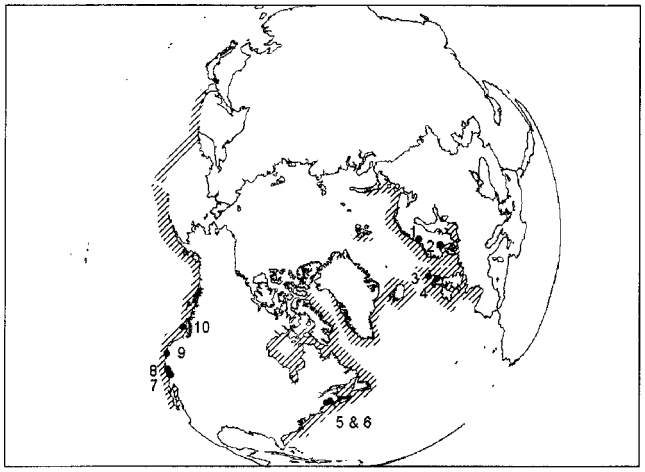

FIG. 1. Map of the Northern Hemisphere denoting the ten sites where recordings of male harbor seal vocalizations were made. The recording sites were located within (a) Eastern Atlantic Ocean—(1) Froan (FR), Norway, (2) Ursholmen (UR), Sweden, (3), the Orkneys (OR), and (4) the Moray Firth (MF), Scotland. (b) Western Atlantic Ocean—(5) Long Island (LI) and (6) St. Croix Island (SC), Eastern Canada, (c) Eastern Pacific Ocean—(7) Hopkins Marine Station, Monterey Bay (MB), (8) Elkhorn Slough (ES), and (9) Point Reyes (PR), CA and (10) Barkley Sound (BS), Western Canada. The striped lines show the distribution of the harbor seal, *Phoca vitulina*.

Male harbor seals, *Phoca vitulina*, produce simple stereotyped underwater roar vocalizations for the purpose of attracting females and competing with other males (Hanggi and Schusterman, 1994; Van Parijs *et al.*, 1997; Nicholsen, 2000). This study examined the vocal variation in male harbor seals from ten sites throughout the northern hemisphere, spanning most of its distribution. We hypothesized that if genetic factors control vocal variation, variation would be consistent with genetically differentiated populations and that vocal variation would increase as genetic differentiation increases with increased distances between populations. We show that genetic variation may not provide a complete explanation for geographic variation in male harbor seal vocalizations and demonstrate a possible influence of vocal dialects.

II. MATERIALS AND METHODS

Acoustic recordings were made of underwater vocalizations produced by male harbor seals from ten sites in three distinct geographic regions: the eastern and western Atlantic Ocean and the eastern Pacific Ocean (Fig. 1, Table I). Within the eastern Atlantic Ocean, two sites were located in Scotland, the Moray Firth (57° 30′ N, 4° 14′ W) and the Orkneys (59° 08′ N, 3° 05′ W), one site was in Froan Nature Reserve, Norway (64° N, 9° E) and another in Ursholmen, Sweden (58° 50′ N, 10° 59′ E). In the western Atlantic Ocean, two sites were located in Canada off the coast of New Brunswick, at Long Island in Passamoquoddy Bay (45° 05′ N, 67° 00′ W) and St. Croix Island in the St Croix River (45° 07′ N, 67° 01′ W). In the eastern Pacific Ocean, three of the four sites were in California, outside Hopkins Marine Station in Monterey Bay (36° 37′5 N, 121° 52′5 W), at Point Reyes (38° 02′15 N, 122° 56′41 W) and Elkhorn Slough (36°

TABLE I. The shortest distance in kilometers between the ten harbor seal recording sites.

Kilometers	Moray Firth	Orkney	Froan	Ursholmen	Long Island	St. Croix	Barkley Sound	Point Reyes	Monterey Bay	Elkhorn Slough
Moray Firth (MF)	0									
Orkney (OR)	193	0								
Froan (FR)	767	624	0							
Ursholmen (UR)	422	453	584	0						
Long Island (LI)	4890	4779	4962	5223	0					
St. Croix (SC)	4888	4777	4960	5221	4	0				
Barkley Sound (BS)	7306	7118	6843	7389	4321	4318	0			
Point Reyes (PR)	8300	8119	7910	8429	4622	4620	1215	0		
Monterey Bay (MB)	8399	8220	8022	8537	4616	4614	1385	183	0	
Elkhorn Slough (ES)	8376	8197	7998	8513	4598	4596	1365	169	23	0

48′77 N, 121° 46′47 W) and the fourth site was in Western Canada, at Wizard Island, Barkley Sound, British Columbia (48° 51′ N, 125° 09′ W).

All sites from which harbor seals were recorded, except those in California and Eastern Canada, form genetically discrete populations (Lamont *et al.*, 1996; Stanley *et al.*, 1996; Kappe *et al.*, 1997; Goodman, 1998; Burg *et al.*, 1999). Sites were arranged into groups and populations according to Stanley *et al.* (1996) to allow direct comparison between vocal and genetic variation (Table II). All recordings were made between 1990 and 2000, during the mating season (eastern Atlantic sites during July and August; western Atlantic and eastern Pacific sites during May and June) except for those in Western Canada, which were recorded in November. A wide range of hydrophones was used with both digital and analog recorders, which covered the entire range of vocalizations for this species (Table III). All recordings were made with no or minimal disturbance to the seals either remotely from land or a boat from 20 m up to several hundreds of meters from the vocalizing individuals.

Throughout their geographical range, male harbor seals emit a typical roar vocalization underwater (see Hanggi and Schusterman, 1994; Van Parijs *et al.*, 1997; Bjørge *et al.*, 1995; Van Parijs *et al.*, 1999, 2000b). This roar vocalization was used for comparative analyses in this study. Recordings were analyzed as spectrograms using the BatSound analysis program (Pettersson, 1996). Only good signals, where all spectral contours were distinctly measurable, were used for these analyses (fast Fourier transforms, dt: 10 ms, df: 102 Hz, FFT size: 512, sampling frequency: 52 kHz). Four standard vocal parameters were measured (see Van Parijs *et al.*, 1999, 2000a, 2000b), the average of the lowest measurable frequency measured at both sides of the pulse, kHz (Min), the frequency with the greatest energy, kHz (Peak frequency), the total duration, seconds (Total), and the pulse duration, seconds (Pulse) (Fig. 2). These parameters were selected based on experience from previous studies, which determined the most useful variables for exploring variability in male harbor seal vocalizations [see van Parijs *et al.* (2000a, 2000b) for spectrograms with details of the measured parameters]. The number of vocalizations available for analyses varied between sites from 33 to 215 (Table II). In order to undertake balanced comparative analyses, random samples of 33 vocalizations were extracted for each site (except for Point Reyes, where only 33 samples were available). Recordings were made either at several locations (separated by more than several 100 m) within a site or at a single location where it was certain that more than one male was vocalizing. Male harbor seals have been shown to vocalize on average once every minute (see Van Parijs *et al.*, 1997), therefore a crude measure of the mean number of vocal males was calculated for all recordings using this estimate.

Call parameters were log 10 transformed. Variation in vocal parameters across sites was investigated using classification trees. Tree-based methods offer a useful approach to exploring complex data. For mathematical details, see Chap. 10 in Venables and Ripley (1999); De'ath and Fabricius (2000) discuss their use with ecological data and provide a conceptually accessible approach for biologists. Classification trees are generated by repeated binary splitting of a data

TABLE II. Classification of the genetic differentiation of harbor seal populations from the ten sites used in this study according to regional and population divisions (derived from 30–34) and the number of male vocalizations recorded at each site.

Site	No. of vocalization	Estimated No. of vocal males	Subspecies	Regional		Population
Moray Firth (MF)	215	67	*P.v. vitulina*	Eastern Atlantic	Ireland-Scotland	Scotland
Orkney (OR)	197	43	*P.v. vitulina*	Eastern Atlantic	Ireland-Scotland	Scotland
Froan (FR)	62	29	*P.v. vitulina*	Eastern Atlantic	W. Scandinavia	Norway
Ursholmen (UR)	42	13	*P.v. vitulina*	Eastern Atlantic	W. Scandinavia	Skagerrak
Long Island (LI)	74	16	*P.v. concolor*	Western Atlantic	E. Canada	Miquelon/Sable
St. Croix (SC)	70	19	*P.v. concolor*	Western Atlantic	E. Canada	Miquelon/Sable
Barkley Sound (BS)	51	11	*P.v. richardsi*	Eastern Pacific	British Columbia/Washington	Washington
Point Reyes (PR)	33	4	*P.v. richardsi*	Eastern Pacific	Oregon/California	San Francisco
Monterey Bay (MB)	52	18	*P.v. richardsi*	Eastern Pacific	Oregon/California	San Francisco
Elkhorn Slough (ES)	51	11	*P.v. richardsi*	Eastern Pacific	Oregon/California	San Francisco

TABLE III. Details of the recording equipment used to record male harbor seal vocalization at each recording site.

Site	Period	Hydrophone	Recorder
Moray Firth (MF)	07–08/1995, 1996, 1997	SSQ906 (−170 dB, 5 Hz to 15 kHz)	Tascam Porta II (40 Hz to 12.5 kHz±3 dB)
Orkney (OR)	07–08/1998	As above	As above
Froan (FR)	07–07/1990, 1991	Vemco VHLFS (−147 dB, 30 Hz to 20 kHz)	UHER 4400 (25 Hz to 13 kHz, −12 dB)
Ursholmen (UR)	07/08/1999	BANDK 8101 (−184 dB *re* 1 V/μPa)	Sony TCD-D7 (20 Hz to 20 kHz)
Long Island (LI)	05–6/1989	Vemco VHFS (−147 dB, 30 Hz to 20 kHz)	UHER 4200 (25 Hz to 13 kHz, −12 dB)
St. Croix (SC)	05–06/1989	As above	As above
Barkley Sound (BS)	11/1999	Offshore Acoustics (149 dB V *re* 1 μPa ±3 dB, 10 Hz to 25 kHz)	Marantz PMD201 (40 Hz to 12.5 KHz ±3 dB)
Point Reyes (PR)	05–06/2000	HTI-ssq-41b (10 Hz to 30 kHz (−170 dB, 5 Hz to 30 kHz)	SONY TCF-8 DAT (10 Hz to 32 Hz)
Monterey Bay (MB)	05/06/1998, 1999	Int. Transducers Inc. ISOSENS™ (±1 dB, 7 Hz to 10 kHz)	SignaLogic Sig32-C data acquisition board see Baggeroer *et al.* (1994)
Elkhorn Slough (ES)	05/06/1998–2000	As above	Tascam DA-38 (20 Hz to 48 kHz)

set, so that each split minimizes the probability of misclassification of the classifying variable (in this instance, site). Splits sequentially generate the most homogeneous possible groups; equations for these are presented in Venables and Ripley (1999, Chap. 10). With noisy data, trees can become overlarge, and pruning is used to achieve an optimal tree. Here, this was achieved using V-fold cross validation, i.e., the data were divided into ten subsets, which were tested

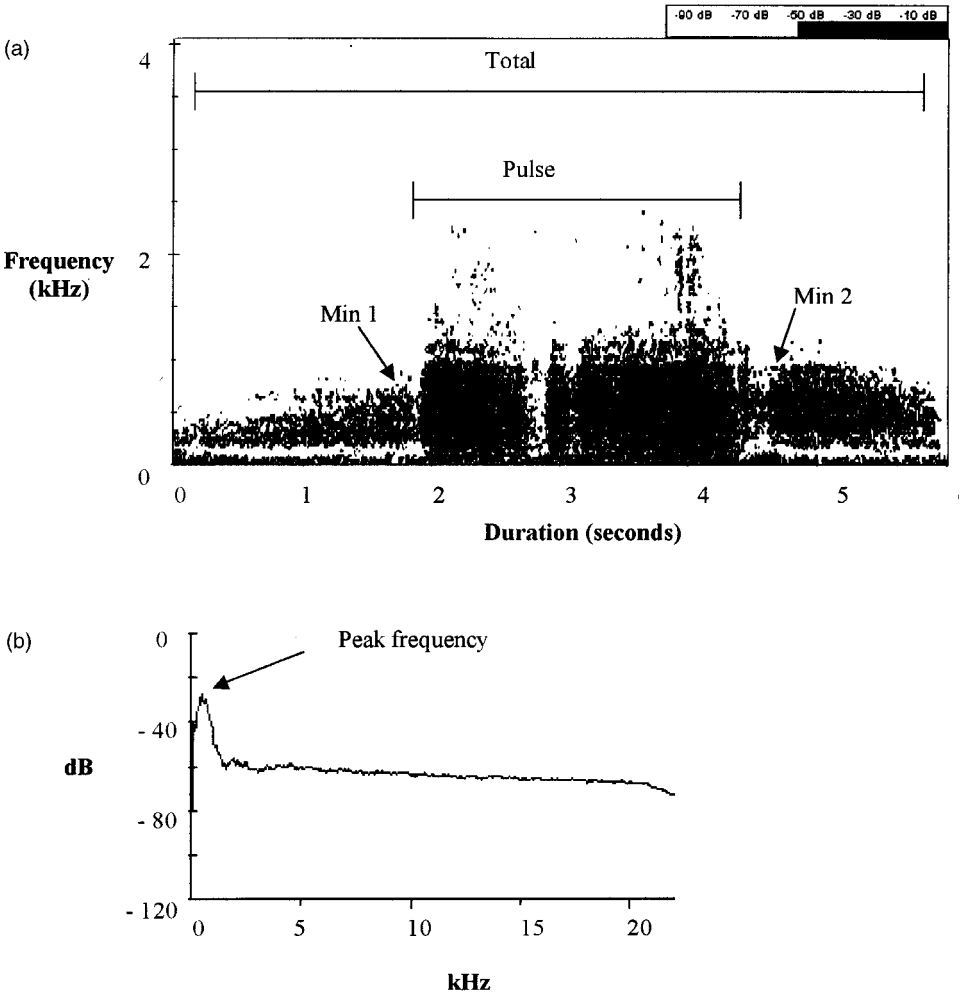

FIG. 2. A spectrogram and power spectrum of an example of a male harbor seal underwater vocalization. Four standard vocal parameters were measured, the average of the lowest measurable frequency measured at both sides of the pulse, kHz (Min); the frequency with the greatest energy, kHz (Peak frequency); the total duration, seconds (Total), and the pulse duration, seconds (Pulse).

TABLE IV. Classification of male harbor seal vocal parameters according to linear discriminant analyses.

Kilometers	Moray Firth	Orkney	Froan	Ursholmen	Long Island	St. Croix	Barkley Sound	Point Reyes	Monterey Bay	Elkhorn Slough
Moray Firth	25	8	0	0	0	0	0	0	0	0
Orkney	0	33	0	0	0	0	0	0	0	0
Froan	0	0	33	0	0	0	0	0	0	0
Ursholmen	0	0	0	33	0	0	0	0	0	0
Long Island	0	0	0	0	19	14	0	0	0	0
St. Croix	0	0	0	0	14	19	0	0	0	0
Barkley Sound	0	0	0	0	0	0	33	0	0	0
Point Reyes	0	0	0	0	0	0	0	33	0	0
Monterey	0	0	0	0	0	0	0	1	31	1
Elkhorn Slough	0	0	0	0	0	0	0	0	0	33

against each other (see Venables and Ripley, 1999, Chap. 10, for details). Analyses were carried out in R version 1.4.0 (Ihaka and Gentleman, 1996), using the RPART library version 3.1-5 for classification trees, and the MASS library version 6.3-2 for other analyses.

III. RESULTS

The mean number of vocal males estimated at each recording site ranged from 4 to 67, with only one site having less than 10 individuals present (Table II). Linear discriminant analysis was carried out using sites as the predictor variable. The first two discriminant axes explained 96.6% of the variance in call parameters. Predictions from the discriminant analysis resulted in 38 misclassifications (11.5% of all classifications). Of these, 28 were between St. Croix and Long Island (14 misclassifications for each site), eight were of calls from the Moray Firth classified to Orkney, and two Monterey Bay calls were misclassified, one each to Point Reyes and Elkhorn Slough (Table IV).

An initial 12-node classification tree was pruned using cross-validation. Using the 1-SE rule [i.e., the smallest tree for which the cross validated relative error rate is within one standard error of the minimum (De'ath and Fabricius, 2000)] suggested that the appropriate descriptive tree was one with ten nodes (Fig. 3). This tree is shown in Fig. 4. In the figure, the vertical depth of each split indicates the proportion of total variation in the data explained by that split. Splits early in the tree (i.e., nearer the top of the page) explain more of the variability in the data than those later in the tree (i.e., towards the bottom of the page). In this tree, most Atlantic sites (Froan, Ursholman, St. Croix, and Long Island) split early from the Pacific sites. However, the two Scottish sites, Moray Firth and Orkney, split from Californian sites after the other Pacific site, Barkley Sound. No individual call parameter was consistently responsible for consecutive splits (Fig. 4).

In this tree there was 37 (11.2%) misclassifications of calls most (24) due to Long Island calls being classified as St. Croix calls. However, this division explained a relatively small proportion of the remaining deviance, as indicated by the short vertical lines to the LI and SC nodes in Fig. 3. Six calls from the Moray Firth were misclassified as Orkney calls, and one Orkney call was reciprocally misclassified. Three Point Reyes calls were misclassified as Monterey Bay calls, and three Monterey Bay calls were misclassified as Elkhorn Slough calls.

IV. DISCUSSION

This study shows male harbor seals show clear geographic variation in vocalizations at the oceanic, regional, and population level. The misclassification of calls classified to neighboring nongenetically distinct populations provides further evidence for regionally distinctive vocalizations. These results are in general agreement with the findings of genetic structure of harbor seal populations at oceanic and regional levels (Lamont *et al.*, 1996; Stanley *et al.*, 1996; Kappe *et al.*, 1997; Goodman, 1998; Burg *et al.*, 1999). Since harbor seals are regionally philopatric on the scale of several hundred kilometers, mixing between populations is likely to be limited and genetic barriers between harbor seal populations appear to present a likely explanation for most of the observed vocal variation displayed in this species.

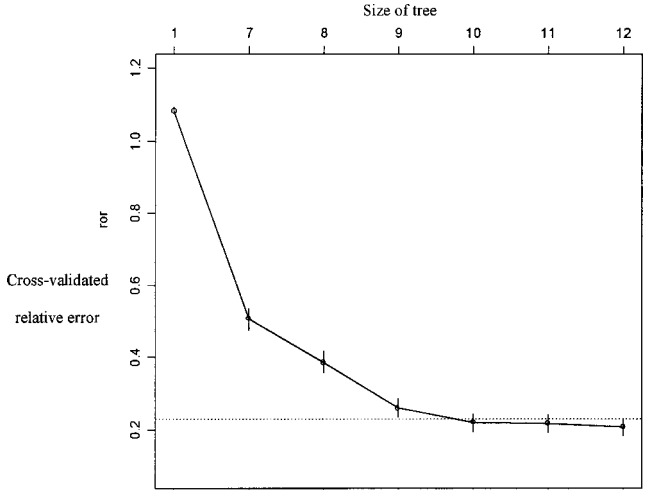

FIG. 3. Cross-validation results of an initial 12-node classification tree of male harbor seal vocalizations from ten sites. Points show the cross-validation relative errors and their standard errors from a ten-fold cross-validation for the classification tree of harbor seal vocalizations by site. Using the 1-SE rule [i.e., the smallest tree for which the cross-validated relative error rate is within one standard error of the minimum (De'ath and Fabricius, 2000)] suggests that the appropriate descriptive tree was one with ten nodes. The horizontal dashed line shows the cutoff point when using the 1-SE rule. Values along the *x* axis were chosen automatically to provide the most informative graph.

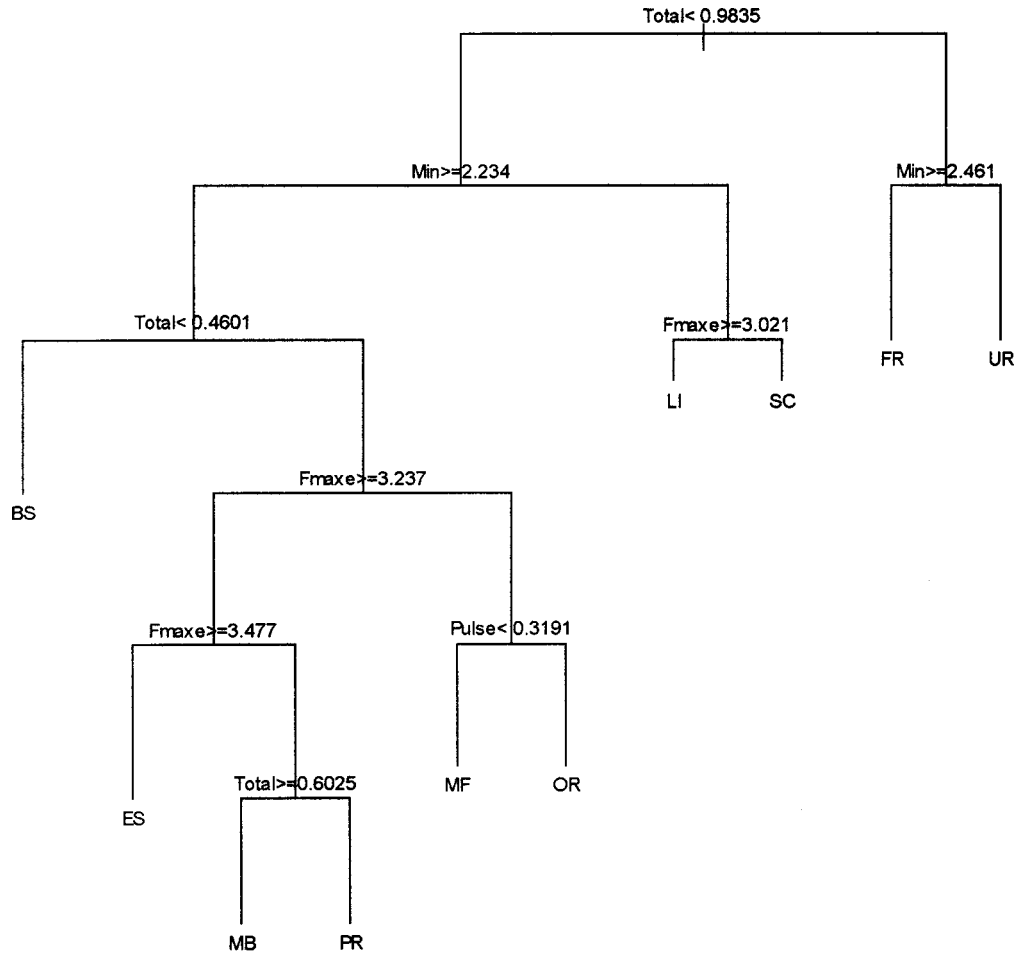

FIG. 4. A ten-node classification tree showing how male harbor seal vocalizations from ten sites throughout their distribution split, based on log 10 transformed data of the four measured vocal parameters [total duration, s (Total), pulse duration, s (Pulse), frequency with the greatest energy, kHz (Peak frequency), and lower frequency, kHz (Min)]. The vertical depth of each split indicates the proportion of total variation in the data explained by that split. Splits early in the tree (i.e., nearer the top of the page) account for more of the variability in the data than those later in the tree (i.e., towards the bottom of the page). The recording sites labels are as in Fig. 1.

However, genetics alone is unable to explain all the observed vocal variation for three main reasons. First, vocal variation between sites in California did not reflect known genetic structure. Population genetic structure (based on mtDNA) demonstrated little genetic variance between Californian populations, suggesting that regional groups mix in the geographic area (Stanley *et al.*, 1996). In addition, individuals have been shown to move between Monterey Bay and Elkhorn Slough sites for haul out purposes (Eguchi, 1998). In contrast, there was clear vocal variation between Californian sites. Furthermore, Monterey Bay and Point Reyes split from Elkhorn Slough, even though Monterey Bay is much closer in physical distance to Elkhorn Slough. We suggest that these results provide evidence for the existence of site-specific vocal dialects in Californian harbor seals.

Second, Scottish (Moray Firth/Orkney) sites split from other Atlantic sites and were classified alongside the western Pacific sites. If genetic barriers were responsible for vocal variation, we would expect these sites to be classified within the Atlantic region. A small-scale comparative analysis of the two Scottish sites showed evidence for geographic variation (Van Parijs *et al.*, 1999). However, this between site variation was considerably reduced when sites were compared within the analyses of this study. It is important to note that small-scale comparative studies, comparing only a few sites, may overly simplify the factors influencing vocal development.

Finally, no one specific vocal parameter was responsible for classifying the sites. All parameters were responsible for the creation of nodes at different stages throughout the classification tree analysis. This suggests that variation in vocalizations may be driven by site-specific selection for changes in certain vocal parameters, providing further support towards the possible existence of vocal dialects in this species.

There may be other possible explanations for the observed variation. Geographic variation in vocalizations could have arisen as a result of ecological influences. Harbor seals occur over a wide region, spanning a range of environments (Bigg, 1981). Studies have shown that male harbor seals exhibit plasticity in the timing of their vocal behavior in response to environmentally driven variation in female distribution (Van Parijs *et al.*, 1997, 1999). Aquatic harbor seal mating habitats differ between riverine, estuarine, and open ocean areas. For example, narrow, shallow, and muddy habitats are likely to affect vocal transmission very differently from deep open ocean habitats. Similarly, habitats with high

ambient noise will affect vocal transmission substantially compared with environments that contain less ambient noise. It is reasonable to assume that differing habitats could influence sound propagation and encourage vocal variation.

Another possible explanation for some of the observed vocal variation in this study could be individual variation in male vocalizations (Van Parijs *et al.*, 2000a). However, as recordings came from multiple individuals at all sites, it is therefore unlikely that individual variation will have influenced the clear divisions that are observed in this study.

Over a wide geographic area the factors influencing vocal variation are not clear-cut. Instead a combination of factors appears to be responsible for the observed variance. While genetic barriers provided a partial explanation for the observed patterns in harbor seal vocalizations, site-specific variations also appear to be a significant factor influencing vocal patterns. Male harbor seals appear to exhibit vocal dialects, with both vocal learning and selective pressures for the evolution of vocal structure influencing the vocalizations of this species.

ACKNOWLEDGMENTS

We thank Dave Thompson for providing recordings of male harbor seals from Froan, Norway, and Sarah Allen for facilitating our ability to record male vocalizations from Point Reyes, CA. SVP was funded by a European Union Marie Curie postdoctoral fellowship. DKM was funded by the David and Lucile Packard Foundation and by the Office of Naval Research Order No. N00014-00-F-0395. We are grateful to the R Core Development Team for producing their powerful Open Source program. Thanks to Brad Page for constructive comments on manuscript.

Baggeroer, A. B., Sperry, B., Lashkari, K., Chiu, C. S., Miller, J. H., Mikhalevsky, P. N., and Vonderheydt, K. (**1994**). ''Vertical array receptions of the Heard Island transmissions,'' J. Acoust. Soc. Am. **96**, 2395–2413.

Baker, J. A., and Bailey, E. D. (**1987**). ''Sources of phenotypic variation in the separation call of northern bobwhite (*Clinus virginianus*),'' Can. J. Zool. **65**, 101–105.

Baptista, L. F., and Schuchmann, K. (**1990**). ''Song learning in the Anna humming bird (*Calypte anna*),'' Ethology **84**, 15–26.

Bigg, M. A. (**1981**). ''Harbor seal, *Phoca vitulina* and *phoca largha*,'' in *Handbook of Marine Mammals 2. Seals*, edited by S. H. Ridgway and R. J. Harrison (Academic, New York), pp. 1–28.

Bjørge, A., Thompson, D., Hammond, P., Fedak, M., Bryant, E., Aarefjord, H., Roen, R., and Olsen, M. (**1995**). ''Habitat use and diving behavior of harbor seals in a coastal archipelago in Norway,'' in *Whales, Seals, Fish, and Man*, edited by A. S. Blix, L. Walløe, and Ø. Ulltang (Elsevier, Amsterdam), pp. 211–223.

Burg, T. M., Trite, T. W., and Smith, M. J. (**1999**). ''Mitrochondrial and microsatellite DNA analyses of harbor seal population structure in the northeast Pacific Ocean,'' Can. J. Zool. **77**, 930–943.

Caldwell, M. C., and Caldwell, D. K. (**1972**). ''Vocal mimicry in the whistle mode by an Atlantic bottlenosed dolphin,'' Cetology **9**, 1–8.

Cleator, H. J., Stirling, I., and Smith, T. G. (**1989**). ''Underwater vocalizations of the bearded seal (*Erignathus barbatus)*,'' Can. J. Zool. **67**, 1900–1910.

De'ath, G., and Fabricius, K. E. (**2000**). ''Multivariate regression trees: a new technique for modeling species–environment relationships,'' Ecology **81**, 3178–3192.

Eguchi, T. (**1998**). ''Morphology of the Pacific harbor seal (*Phoca vitulina richardsi*) using Elkhorn Slough, California, and their movements and diving behavior in the Monterey Bay area,'' M.Sc. thesis, California State University at Fresno.

Gaunt, S. L. L., Saptista, L. F., Sanchez, J. E., and Hernandez, D. (**1994**). ''Song learning as evidence from song sharing in two hummingbird species (*Colibri coruscans* and *C. Thalassinus*),'' Auk **111**, 87–103.

Goodman, S. J. (**1998**). ''Patterns of extensive genetic differentiation and variation among European harbor seals (*Phoca vitulina vitulina*) revealed using microsatellite DNA polymorphisms,'' Mol. Biol. Evol. **15**, 104–118.

Green, K., and Burton, H. R. (**1988**). ''Do Weddell seals sing?'' Polar Biol. **8**, 165–166.25.

Guinee, L. N., Chu, K., and Dorsey, E. M. (**1983**). ''Changes over time in the song of known individual whales (*Megaptera novaeangliae*),'' in *Communication and Behavior of Whales*, edited by R. Payne (Westview, Colorado), pp. 9–57

Hanggi, E. B., and Schusterman, R. (**1994**). ''Underwater acoustic displays and individual variation in male harbor seals, *Phoca vitulina*,'' Anim. Behav. **48**, 1275–1283.

Härkönen, T., and Harding, K. C. (**2001**). ''Spatial structure of harbor seal populations and the implications thereof,'' Can. J. Zool. **79**, 2115–2127.

Ihaka, R., and Gentleman, R. (**1996**). ''R: A language for data analysis and graphics,'' J. Comput. Graph. Stat. **5**, 299–314.

Janik, V. M., and Slater, J. B. (**1997**). ''Vocal learning in mammals,'' Adv. Study Anim. Behav. **26**, 59–99.

Janik, V. M., and Slater, P. J. B. (**2000**). ''The different roles of social learning in vocal communication,'' Anim. Behav. **60**, 1–11.

Kappe, A. L., Bijlsma, R., Osterhaus, A. D. M. E., Vandelden, W., and VandeZande, L. (**1997**). ''Structure and amount of genetic variation at minisatellite loci within the subspecies complex of *Phoca vitulina* (the harbor seal),'' Heredity **78**, 457–463.

Kroodsma, D. E., and Baylis, J. R. (**1982**). ''A world survey of evidence for vocal learning in birds,'' in *Acoustic Communication in Birds*, edited by D. E. Kroodsma and E. H. Miller (Academic, New York), pp. 311–337.

Kroodsma, D. E., and Canady, R. A. (**1985**). ''Differences in repertoire size, singing behavior and associated neuroanatomy among marsh wren populations have a genetic basis,'' Auk **102**, 439–446.

Lamont, M. M., Vida, J. T., Jeffries, S., Brown, R., Huber, H. H., DeLong, R., and Thomas, W. K. (**1996**). ''Genetic substructure of the Pacific harbor seal (*Phoca vitulina richardis*) off Washington, Oregon, and California,'' Marine Mammal Sci. **12**, 402–413 .

LeBoeuf, B. J., and Petrinovich, L. F. (**1974**). ''Dialects of northern elephant seals, *Mirounga angustirostris:* Origin and reliability,'' Anim. Behav. **22**, 565–663.

Lieblich, A. K., Symmes, D., Newman, J. D., and Shapiro, M. (**1980**). ''Development of the isolation peep in laboratory-bred squirrel monkeys,'' Anim. Behav. **28**, 1–9.

McCracken, K. J., and Sheldon, F. H. (**1997**). ''Avian vocalizations and phylogenetic signal,'' Proc. Natl. Acad. Sci. U.S.A. **94**, 3833–3836.

Medvin, M. B., Stoddard, P. K., and Beecher, M. D. (**1992**). ''Signal for parent-offspring recognition: strong sib-sib call similarity in cliff swallows but not barn swallows,'' Ethology **90**, 17–28.

Morrice, M. G., Burton, H. R., and Green, K. (**1994**). ''Microgeographic variation and songs in the underwater vocalization repertoire of the Weddell seal (*Leptonychotes weddellii*) from the Vestford Hills, Antarctica,'' Polar Biol. **14**, 441–446.

Nevo, E., Heth, G., Beiles, A., and Frankenberg, E. (**1987**). ''Geographic dialects in blind mole rates: Role of vocal communication in active speciation,'' Proc. Natl. Acad. Sci. U.S.A. **84**, 3312–3315.

Nicholsen, T. E. (**2000**). ''Social structure and underwater behavior of harbor seals in southern Monterey Bay, California,'' M.S. thesis, San Francisco State Univ., CA.

Noad, M. J., Cato, D. H., Bryden, M. M., Jenner, M. N., and Jenner, K. C. S. (**2000**). ''Cultural revolution in whale songs,'' Nature (London) **408**, 537.

Payne, R. S., and McVay, S. (**1971**). ''Songs of humpback whales,'' Science **173**, 585–597.

Payne, K., Tyack, P., and Payne, R. (**1983**). ''Progressive changes in the songs of humpback whales (*Megaptera novaengliae)*: A detailed analysis of two seasons in Hawaii,'' in *Communication and Behavior of Whales*, edited by R. Payne (Westview, Colorado), pp. 9–57.

Payne, K., and Payne, R. (**1985**). ''Large scale changes over 19 years in songs of humpback whales in Bermuda,'' Z. Tierpsychol. **68**, 89–114.

Pepperberg, I. M. (**1981**). ''Functional vocalizations by an African grey parrot,'' Z. Tierpsychol. **55**, 139–160.

Pettersson Elektronik AB. (**1996**). ''Batsound,'' Tallbacksvagen 51, S-75645 Uppsala, Sweden.

Ralls, K., Fiorelli, P., and Gish, S. (**1985**). ''Vocalizations and vocal mimicry

in captive harbor seals, *Phoca vitulina*,'' Can. J. Zool. **63**, 1050–1056.
Reiss, D., and McCowan, B. (**1993**). ''Spontaneous vocal mimicry and production by bottlenose dolphins (*Tursiops truncatus*): Evidence for vocal learning,'' J. Comp. Psychol. **107**, 301–312.
Ries, E. H., Hilby, L. R., and Reijnders, P. J. H. (**1998**). ''Maximum likelihood population size estimation of harbor seals in the Dutch Wadden Sea based on a mark-recapture experiment,'' J. Appl. Ecol. **35**, 332–339.
Stanley, H. F., Casey, S., Carnahan, J. M., Goodman, S., Harwood, J., and Wayne, R. K. (**1996**). ''Worldwide patterns of mitochondrial DNA differentiation in the harbor seal (*Phoca vitulina*),'' Mol. Biol. Evol. **76**, 1178–1185.
Terhune, J. M. (**1994**). ''Geographical variation of harp seal underwater vocalizations,'' Can. J. Zool. **72**, 892–897.
Thomas, J. A., and Golladay, C. L. (**1995**). ''Geographic variation in leopard seal (*Hydrurga leptonyx*) underwater vocalizations,'' in *Sensory Systems of Aquatic Mammals*, edited by R. A. Kastelein, J. A. Thomas, and P. E. Nachtigall (De Spil, Woerden), pp. 201–221.
Thompson, P. M. (**1993**). ''Harbor seal movement patterns,'' Symp. Zool. Soc. Lond. **66**, 225–239.
Thompson, P. M., Fedak, M. A., McConnell, B. J., and Nicholas, K. S. (**1989**). ''Seasonal and sex-related variation in the activity patterns of common seals, *Phoca vitulina*,'' J. Appl. Ecol. **26**, 521–535.
Todt, D. (**1975**). ''Social learning of vocal patterns and modes of their application in grey parrots (*Psitacus erithacus*),'' Z. Tierpsychol. **39**, 178–188.
Van Parijs, S. M., Hastie, G. D., and Thompson, P. M. (**1999**). ''Geographic variation in temporal and spatial patterns of aquatic mating male harbor seals,'' Anim. Behav. **58**, 1231–1239.
Van Parijs, S. M., Hastie, G. D., and Thompson, P. M. (**2000a**). ''Individual and geographic variation in the vocal behavior of the harbor seal,'' Anim. Behav. **59**, 559–568.
Van Parijs, S. M., Hastie, G. D., and Thompson, P. M. (**2000b**). ''Display area size, tenure and site fidelity in the aquatic mating male harbor seal,'' Can. J. Zool. **78**, 2209–2217.
Van Parijs, S. M., Thompson, P. M., Tollit, D. J., and Mackay, A. (**1997**). ''Distribution and activity of male harbor seals during the mating season,'' Anim. Behav. **54**, 35–43.
Venables, W. N., and Ripley, B. D. (**1999**). *Modern Applied Statistics in S-PLUS* (Springer-Verlag, New York).

Variation in humpback whale (*Megaptera novaeangliae*) song length in relation to low-frequency sound broadcasts

Kurt M. Fristrup[a)]
Bioacoustics Research Program, Cornell Laboratory of Ornithology, Ithaca, New York 14853

Leila T. Hatch
Department of Ecology and Evolutionary Biology, Cornell University, Ithaca, New York 14853

Christopher W. Clark
Bioacoustics Research Program, Cornell Laboratory of Ornithology, Ithaca, New York 14853

(Received 27 December 2000; revised 19 February 2003; accepted 17 March 2003)

Humpback whale song lengths were measured from recordings made off the west coast of the island of Hawai'i in March 1998 in relation to acoustic broadcasts (''pings'') from the U.S. Navy SURTASS Low Frequency Active sonar system. Generalized additive models were used to investigate the relationships between song length and time of year, time of day, and broadcast factors. There were significant seasonal and diurnal effects. The seasonal factor was associated with changes in the density of whales sighted near shore. The diurnal factor was associated with changes in surface social activity. Songs that ended within a few minutes of the most recent ping tended to be longer than songs sung during control periods. Many songs that were overlapped by pings, and songs that ended several minutes after the most recent ping, did not differ from songs sung in control periods. The longest songs were sung between 1 and 2 h after the last ping. Humpbacks responded to louder broadcasts with longer songs. The fraction of variation in song length that could be attributed to broadcast factors was low. Much of the variation in humpback song length remains unexplained. [DOI: 10.1121/1.1573637]

PACS numbers: 43.80.Nd, 43.80.Ka, 43.30.Vh [WA]

I. INTRODUCTION

In 1997–1998, a series of experiments was undertaken to quantify the responses of selected baleen whale species to powerful, low-frequency acoustic broadcasts, including the proposed operational use of the U.S. Navy SURTASS LFA sonar system. One phase of this research focused on endangered humpback whales in Hawai'i (Clark and Tyack, 1998; Miller *et al.*, 2000). Several factors suggested that Hawaiian humpbacks were appropriate subjects for this work. The near-shore distribution of humpback whales in Hawai'i has fostered extensive research, providing an excellent record of behavior prior to the experiments. The waters around the Hawaiian Islands host high densities of breeding humpbacks and their calves, so there would be significant impact on reproductive activities if they were displaced or their behavior was seriously disrupted. Lastly, the long, elaborate songs produced by males have substantial signal energy in the range of frequencies produced by the SURTASS LFA sonar system, so humpbacks are assumed to hear and potentially be responsive to LFA signals.

Several studies have used detailed visual observation methods to investigate the responses of humpback whales to acoustic stimuli. Dramatic behavioral responses have been observed to playbacks of conspecific sounds (Tyack, 1983; Baker and Herman, 1984; Mobley *et al.*, 1988). Behavioral responses were documented in reaction to active sonar (3.1–3.6 kHz) (Maybaum, 1990, 1993). During the Acoustic Thermometry of the Ocean Climate (ATOC) Marine Mammal Research Program, subtle, short-term effects on the surface behaviors of Hawaiian humpback whales were observed in response to low-frequency (75 Hz) sound broadcasts (Frankel and Clark, 1998, 2000). Although there was no decrease in humpback whale abundance in relation to broadcast activity, ATOC did reveal changes in the distribution of animals relative to the transmitter (Frankel and Clark, 2002). These results document the potential complexity of responses to a sound source. On average, the distance of pods from the transmitter increased, but the number of animals sighted near the source also increased. Miller *et al.* (2000) made focal animal behavioral observations in parallel with the data reported here. They compared the lengths of songs sung by six individuals before, during, and after exposure to low-frequency broadcasts, and found that songs were significantly longer during broadcasts.

Additional studies have documented behavioral reactions of humpback whales to vessels (reviewed in Richardson *et al.*, 1995; see also Corkeron, 1995; Frankel and Clark, 1998, 2000; Au and Green, 2000). These reactions include changes in direction and swimming speed, and changes in the pattern of surfacing. Humpback whales also modify some elements of their acoustic behavior when approached by boats: the duration of song units (notes) decreased, increasing the ''tempo'' of songs (Norris, 1994).

Humpback whale song is an extraordinarily long and complex acoustic display. It consists of sequences of broadband units of sound, exhibiting repetition within sequences of units and on the longer time scales of themes and songs.

a)Electronic mail: kmf6@cornell.edu

The diversity of units is considerable, spanning a range of frequencies from approximately 30 to 5000 Hz. The general structure of songs sung by the majority of males at any one time and place is similar (Payne and McVay, 1971; Cerchio *et al.*, 2001). However, the detailed structure of successive songs sung by an individual varies (Payne *et al.*, 1983; Payne and Payne, 1985; Helweg *et al.*, 1992). Variation in the structure of an individual's song may relate to interactions within a humpback chorus.

Studies have shown that singers are male, and that singing is mainly associated with low-latitude, coastal areas where calves are born and mating is presumed to occur. The function of humpback whale song is disputed, but hypotheses have focused on its probable reproductive context (Payne and McVay, 1971; Clapham, 1996), and have sought analogs in the mating systems of birds, frogs, and insects. As has been well documented in many terrestrial systems, humpback song may mediate interactions among males (Tyack, 1981; Darling, 1983; Frankel *et al.*, 1995), and advertise species, gender, location, and condition to females (Payne and McVay, 1971; Winn and Winn, 1978; Tyack, 1981).

Any analysis of response to potentially aversive stimuli must incorporate provisions for differences among individuals, and for the variation in each individual's behavior. With respect to humpback song in particular, differences among individuals are expected if song plays a role in female mate choice or mutual assessment of competitive ability among males. Aspects of acoustic displays that reveal differences among individuals have been shown to evoke predictable female responses in insect, frog, and bird species (*e.g.*, Catchpole, 1980; Klump and Gerhardt, 1987; Eiriksson, 1994; Brown *et al.*, 1996; Welch *et al.*, 1998; Gentner and Hulse, 2000).

Humpback song length is a simple summary of a complex behavior that is likely to provide an informative measure of response to LF broadcasts for several reasons. As an indicator of the regularity and rhythm of display behavior, song length provides a relatively easily extracted measure of response to potential disturbance. Also, it has been argued that the consistent production of longer humpback songs is a reliable indication of superior condition, due to the constraints that longer songs place on respiration (Chu and Harcourt, 1986; Chu, 1988). It also seems plausible that longer songs imply greater energetic investment in a ''unit'' of display. Although a complete humpback song may not be analogous to a single frog call, Taigen and Wells (1985) demonstrated that female frogs were more attracted to longer calls, which were more energetically expensive. However, Helweg *et al.* (1992) theorized that humpback song comprises a negligible fraction of their energy budget, which suggests that physiological constraints on song length and loudness are not likely to be related to energetics.

Data are presented on the lengths of 378 humpback songs recorded before, during, and after low-frequency acoustic broadcasts. Statistical models of song length in relation to a variety of natural and experimental factors were developed. Song length was analyzed in relation to date and time of the song, the identity of the singer, and several factors related to the acoustic broadcast. Song length variability during control periods was documented to provide a context for assessing the biological significance of changes related to low-frequency broadcasts.

II. METHODS

These data were collected from 26 February to 29 March 1998 off the western coast of the island of Hawai'i, between Mahaiula and Kawaihae. The study area was chosen to utilize extensive baseline data on the abundance, densities, movements, and associations of humpback whales (Gabriele, 1992; Craig and Herman, 1997; Frankel *et al.*, 1995; Mobley *et al.*, 1994, 1995, 1999). Several of these studies showed that the majority of whales were found within the 100-fathom contour, though the fraction of singers farther offshore has been as high as 30% (Herman and Antinoja, 1977; Frankel *et al.*, 1995). Photo identification studies showed that most whales remained in the area for 4 to 7 days (Gabriele, 1992). This short residency time suited the objectives of this study by limiting the number of times any one animal would be exposed to the experimental sounds. The study was conducted after the peak in seasonal abundance, because previously the research team was conducting related research during the peak of gray whale migration off Central California.

This research used U.S. Navy SURTASS LFA sound projectors to broadcast low-frequency (''LF'') sounds in the 150–320-Hz frequency band. An LF signal (or ''ping,'' a bit of sonar jargon borrowed for brevity) consisted of nine sound units lasting a total of 36 s and spanning a total of 42 s. Two types of pings were alternated, a ''high'' ping (260–320 Hz) and a ''low'' ping (150–230 Hz). Each day an initial series of reduced amplitude pings were transmitted to test the equipment and to allow animals to become aware of the sound source before full experimental amplitude was reached. The first ping of each day was transmitted at a source level (SL) of 155 dB *re* 1 μPa at 1 m (in the remainder of the paper, dB used). SL increased progressively until the predicted received level reached the desired value. During an experiment, pings were broadcast in a series of ten, on intervals of 6 min (see Fig. 1), for a total of 54 min in a ping series. SL was monitored via a calibrated hydrophone array system, and did not exceed 205 dB. Source levels were adjusted to realize maximum received levels of between 120 and 155 dB *re* 1 μPa at the nearest whale, while ensuring that exposure to animals within 3 miles of shore and to human divers did not exceed 140 dB *re* 1 μPa. These broadcasts achieved the same range of received levels that over 95% of the animals are predicted to experience during the operational training exercises for this equipment (Navy, 2001, appendix D). These received levels were accomplished, in spite of lower source levels, by closely approaching the experimental subjects. This procedure minimized exposure levels to animals not under observation. Ping series were separated by at least 2 to 3 hours. Up to three ping series were produced each day.

Data were collected regarding the short-term responses of individual whales, and longer-term changes in the distribution and sighting rates of animals in the area. Two methods

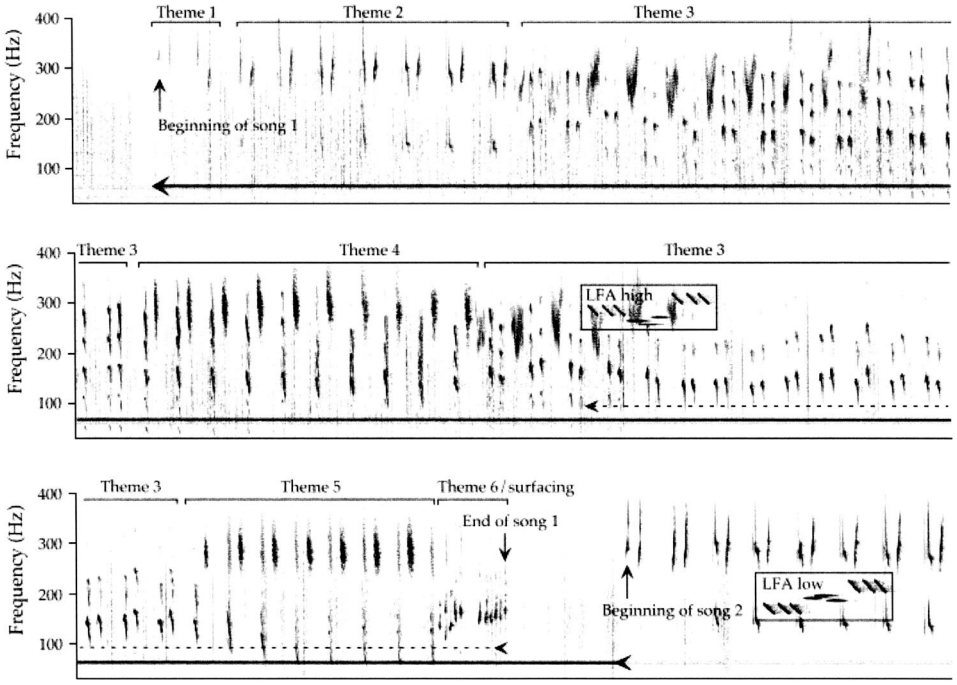

FIG. 1. Spectrogram of humpback song and two pings, with themes and song length measurements marked. Each panel represents five minutes of sound. The solid line marks the measurement of song length. The dotted line marks the measurement of minutes from the start of the last ping to the end of the song.

were used to follow the short-term behavior of individual singers. Visual and acoustic methods were used to locate and follow humpback singers from a small inflatable boat (Miller *et al.*, 2000). If the visual observers selected a focal animal, its behaviors were recorded for at least two dive cycles before the SURTASS LFA vessel moved toward the singer and broadcast sounds. In parallel, acoustic observers on the SURTASS LFA vessel collected the data reported here. Beamforming software was used to locate humpback singers who were candidates for broadcast experiments. If the acoustic observers selected a focal animal, baseline acoustic behavior was recorded for at least three complete songs before a ping series began.

Long-term changes in distribution and abundance were monitored using visual surveys from a shore station and from the SURTASS vessel. Shore station observations followed standardized protocols (Frankel *et al.*, 1995; Frankel and Clark, 1998, 2000). SURTASS vessel observations followed a protocol adapted from established visual survey techniques (Barlow, 1995). Five observers rotated through four stations (three observing, one data recording) on half-hour intervals throughout the day. A senior National Marine Fisheries Service (NMFS) observer continuously oversaw this effort. A portion of these data is used here to indicate possible social contexts for the acoustical patterns exposed by the analysis.

The acoustic behaviors of whales in the vicinity (<4 km) of the playback vessel were monitored and recorded using a long, low-frequency, horizontal hydrophone array towed behind the playback vessel. Fifteen elements in the array were used to collect time series data. The acoustic data collection system operated from 0400 h until approximately 1800 h local time each day, although data collection effort often continued throughout the night. The data were recorded digitally on a Windows 98 computer at a sampling rate of 1002 Hz per hydrophone.

These array data were intensively analyzed to identify singers and follow their acoustic behavior, focusing on the song duration. The songs of individual singers were followed for as long as possible. The ability to keep track of individual singers relied on the stereotyped structure of the humpback whale song (Fig. 1), and spatial cues provided by the array recordings (relative intensities, time delays). For the purpose of these analyses, two themes of humpback song were relevant. A series of trills, also called the ''ratchet,'' was designated theme 6. It was typically followed by a short period with no acoustic activity between 0 and 500 Hz. This hiatus in low-frequency activity was followed by a series of frequency-modulated (FM) upsweeps, which was designated theme 1. Theme 6 has been observed across many seasons and populations, and has typically preceded a respiratory surfacing. Although singing whales do not surface exclusively at this point in the song, the end of this theme has previously been referred to as the end of a song (Winn and Winn, 1978; Cerchio *et al.*, 2001).

A data visualization program written in MATLAB (The Mathworks, Inc., 1999) enabled discrimination among different humpback singers and facilitated measurement of humpback song duration. An operator used the program to transcribe acoustic data into information about the beginning and ending song units, including the identity of the singer and the temporal and frequency bounds of the units. Four spectrogram windows, representing 2.5 min of sound from the selected channel, displayed a total of 10 min of contiguous sound per screen. The temporal extent of this display permitted viewing most of a song while providing sufficient resolution to see structure in song units. A point in the song could be selected with a cursor, and two other windows displayed an expanded view of 20 s of data from two channels of the array.

Although each broadcast experiment sought to isolate single singers within a kilometer of the vessel, several singers were usually detectable within the array's acoustic range.

Difficulties in following the thematic structure of low-amplitude songs, or songs in dense choruses, limited the conditions under which a sequence of humpback sounds could be unambiguously attributed to one animal. The songs of an isolated, loud, slow moving singer could be followed for many songs, but most singers were followed for a few songs.

A continuous sequence of sounds could be attributed to one singer using a combination of cues: continuity of song units and themes, the pattern of received levels across the array, and the pattern of arrival time delays across the array. Song length was measured as the interval between successive starts of theme 1 or successive endings of theme 6, which ever was clearer (Fig. 1). Note that this measurement is unambiguous, even in this example, which Frumhoff (1983) would term an ''aberrant'' song. The continuity of a singer's acoustic behavior became ambiguous when (1) there was a break of over 2.5 min (one browser panel) in the middle of a song (due to changes in detection and/or singing behavior), and (2) when multiple singers were at similar distances and similar bearings and were singing the same theme. Both cases produced uncertainty regarding singer identity, and subsequent songs were attributed to a new singer. Note that some individuals were sampled more than once, so the number of singers in these analyses overstates the number of individuals.

These measurements of song duration were analyzed in relation to several factors that could systematically affect singing behavior. These factors were day of year ($1 = 1$ January 1998), time of day (00:00:00–23:59:59), singer identification number, minutes since last ping, minutes since the beginning of a ping series, minutes of pings during a song, and LF source level. The distinction between the number of minutes since the last ping and the number of minutes since the beginning of a ping series was used to investigate a potential cumulative effect. Figure 1 provides an example of the measurements taken on song duration and the timing relationship measured between songs and pings.

Two statistical procedures were used. The simplest assessment of playback effects was to examine differences in song length in relation to discrete temporal categories. Miller *et al.* (2000) defined temporal categories based on *a priori* assumptions regarding behavioral response: before ping series, during ping series, after ping series. The analysis presented here identified temporal categories that produced maximal contrasts in song length. These categories were identified using a tree-based regression (Chambers and Hastie, 1991) of song length on the minutes elapsed since the last ping. The six-category tree provides a detailed picture of potential responses while retaining reasonable sample sizes within categories. The significance of differences among these categories was measured by pairwise *t*-tests; no correction was made for multiple inferences. Differences in song length were also examined in relation to the amount of overlap by pings.

These simple analyses ignored the potential confounding effects of other factors. Three accessible factors seemed important to incorporate into a model of response: date (seasonal effects), time of day (diurnal effects), and ping source level. Source level was incorporated for two reasons. It seemed plausible that whales have evolved the capacity to gauge the source levels of nearby sounds, especially if song source level provides important clues to the singers' status. Second, source level served as a proxy for received level, with the caution that extensive variation in transmission loss could cause source and received levels to be weakly correlated.

It would be preferable to analyze and compare models using both source and received levels, but significant obstacles remain. Receiver depth is the critical factor affecting received levels, especially when the source to receiver distance exceeds 1 km (as it did in virtually all of these experiments). Matched-field processing has been used to infer the depths of singing blue whales (Thode *et al.*, 2000), and ongoing research may yield fruitful methods for these data. However, the subsequent analysis of response would be much more complex than the material presented here. Unlike source level, received level varies significantly during and among pings, as the animal moves and changes depth. Alternative methods of summarizing each subject's received level history would need to be developed and tested to identify summary values that provide the best predictors in a response model.

Multivariate general linear models do not allow for the nonlinear pattern revealed by the categorical analysis, so generalized additive models (GAMs) were used (Hastie and Tibshirani, 1998). Generalized additive models are analogs of linear statistical models, in which the effects of factors are represented by nonparametric smooth curves. These smooth curves provide estimates of the local average of the data, extending the notion of categorical averages to a continuous representation. The models used here employed smoothing splines to estimate the nonlinear effects of all the factors that, when added together, provided the best fit to the observed data. These splines were fitted using an iterative backfitting routine, whose convergence properties are specified by analyses of the Gauss–Seidel algorithm (Hastie and Tibshirani, 1998).

The divergence of these splines from linear models was constrained by specifying the equivalent degrees of freedom used in their computation. Hastie and Tibshirani (1998) discuss the theoretical bases for calculating degrees of freedom for smoothing functions. The extent of the data used to estimate the local averages is inversely proportional to the degrees of freedom used in fitting the spline. As more degrees of freedom are used, the bias of local estimates decreases at the cost of increasing the variance of the estimates (and the confidence intervals for prediction). This bias-variance tradeoff is unavoidable. Three degrees of freedom were used for all smoothing splines in these models, with the exceptions that the factor representing the minutes elapsed since the last ping used 6 degrees of freedom, and the factor representing the minutes of ping overlap with each song used 2 degrees of freedom. The goal in all cases was to achieve a relatively uniform distribution of residual errors while consuming the fewest degrees of freedom.

The significance of a fit between the smooth trends and the data was assessed by relating the amount of variation explained to the degrees of freedom in the model. *F*-ratio

tests were used to test for the significance of contributions from the different factors. All analyses were performed in S-Plus (Statistical Sciences, Inc., 2000).

In addition to the minutes elapsed since the last ping (''single ping'' models), two other factors were used to investigate potential temporal patterns in the responses to LF broadcasts. The minutes elapsed since the beginning of a ping series was included to see if the effects of exposure to a series of pings were cumulative (''ping series'' models). The total number of minutes of pings that overlapped each song was included to see if males reacted to the amount of potential interference during each song (''overlap'' models).

The categorical analyses and generalized additive models pooled data across song series and across days and times of day to utilize as many measurements as possible to estimate response. Contrasts could have been formed between the preexposure, experimental, and postexposure behaviors within each song series. However, it was difficult to obtain a full matched sample of data in a song series. This ''matched sample'' approach would have been limited to a maximum of 15 song series in this data set; these limited data would not support models testing the effects of diurnal and seasonal effects.

By pooling the data, song length measurements for 113 singers were available for analysis in the models incorporating date and time of day. As noted earlier, songs from a single individual may have been labeled with a succession of singer numbers, and there is no way to determine exactly how many individuals were studied. The maximum number of simultaneous singers gives a lower bound for the number of individuals present on each day. The sum of these maxima for all days was 60. Some of these animals represent repeat sightings across days. During this project, Biassoni (2000) found that 3 of 23 animals selected for focal behavioral studies had been selected as the focal animal previously. The upper 95% confidence interval for this proportion is about 0.25. Thus, a conservative lower bound on the number of individuals sampled for this study is 45.

The magnitude of individual variation in song length was investigated by examining the residuals of the multivariate GAM that fitted time of day, day of year, minutes since last ping, and source level to the song length measurements. After removing the variation in song length that can plausibly be attributed to generic factors, this analysis should provide a reliable indication of the extent of variation among individuals. Song series consisting of five or more songs were used, resulting in a sample of 25 song series comprising 189 songs. A tree-based regression was utilized to identify homogeneous groupings of song series, and a Kruskal–Wallis test was used to assess the significance of differences among these groupings.

Although the song series measurements were not long enough to enable simultaneous estimation of singer idiosyncrasies with time of day and day of year effect in a GAM, a second group of GAM analyses were computed replacing the generic diurnal and seasonal factors with a factor that allowed each song series to have a different average value. For brevity, these models will be called ''singer ID'' models. Comparison of these singer ID models with the generic models was used to assess how consistent the estimated effects of the LF broadcasts were. Song series containing at least three song measurements were used for the singer ID models, which restricted the data set to the behavior of 52 song series comprising 290 songs.

The contributions of each smoothing factor are plotted as smooth curves against a background that depicts the range of variation in song length. These smooth curves illustrate the song lengths predicted by each factor, assuming all other factors make an average contribution. A series of curves are presented for each factor, illustrating the results obtained from different generalized additive models. With the exception of Fig. 10, the null hypothesis of no effect corresponds to a horizontal line in these figures.

For Fig. 10, the null hypothesis must reflect the fact that if whales were oblivious to the pings, then minutes of overlap should be proportional to song length. In particular, a song of any length could be overlapped by a single ping, but songs overlapped by two pings would have to be more than 6 min long, and songs overlapped by three pings would have to be more than 12 min long. The appropriate null hypothesis—no reaction to the pings—thus corresponds to a linear relationship between song length and overlap with a slope equal to the inverse of the ping duty cycle $(6*60\ \text{s}/42\ \text{s})$.

The plots of smoothing factors (Figs. 8, 9, and 11) contain three indications of the extent of variation in humpback song length. A background scatter plot shows the humpback song length measurements against the values of the factor. A background histogram shows the distribution of lengths for songs sung before the first ping of each day. More than 12 h elapsed between the last ping on the previous day and any of these songs, and analyses presented below indicate that responses to LFA signals disappear 2 h after the last ping. However, these songs do not represent a balanced sample with respect to diurnal factors. The early morning is disproportionately represented, so average differences between these control song lengths and other samples may include diurnal effects. The third measure of variation is represented by a dark bar near the vertical axes whose length depicts 2.5 min, which is the average difference between the lengths of successive songs sung by an individual. These graphic displays of variation provide a natural scale for interpreting the magnitude of fitted effects.

Three exceptional songs exceeded 30 min in length; the next longest song was 22.9 min long. Two of these songs were sung consecutively by one individual, starting at 1500 h, 13 min after the end of a ping series, 24 days after the LF broadcast experiments began (4 days before they concluded). The third song was sung the following day, at 1639 h, 45 min after the end of a ping series. These songs were excluded from all statistical models to avoid disproportionate influence on the results.

III. RESULTS

Array recordings were collected in conjunction with LF broadcast experiments from 2 to 29 March 1998. Song length measurements were obtained by browsing 121 h of data distributed across 23 days. No experiments were per-

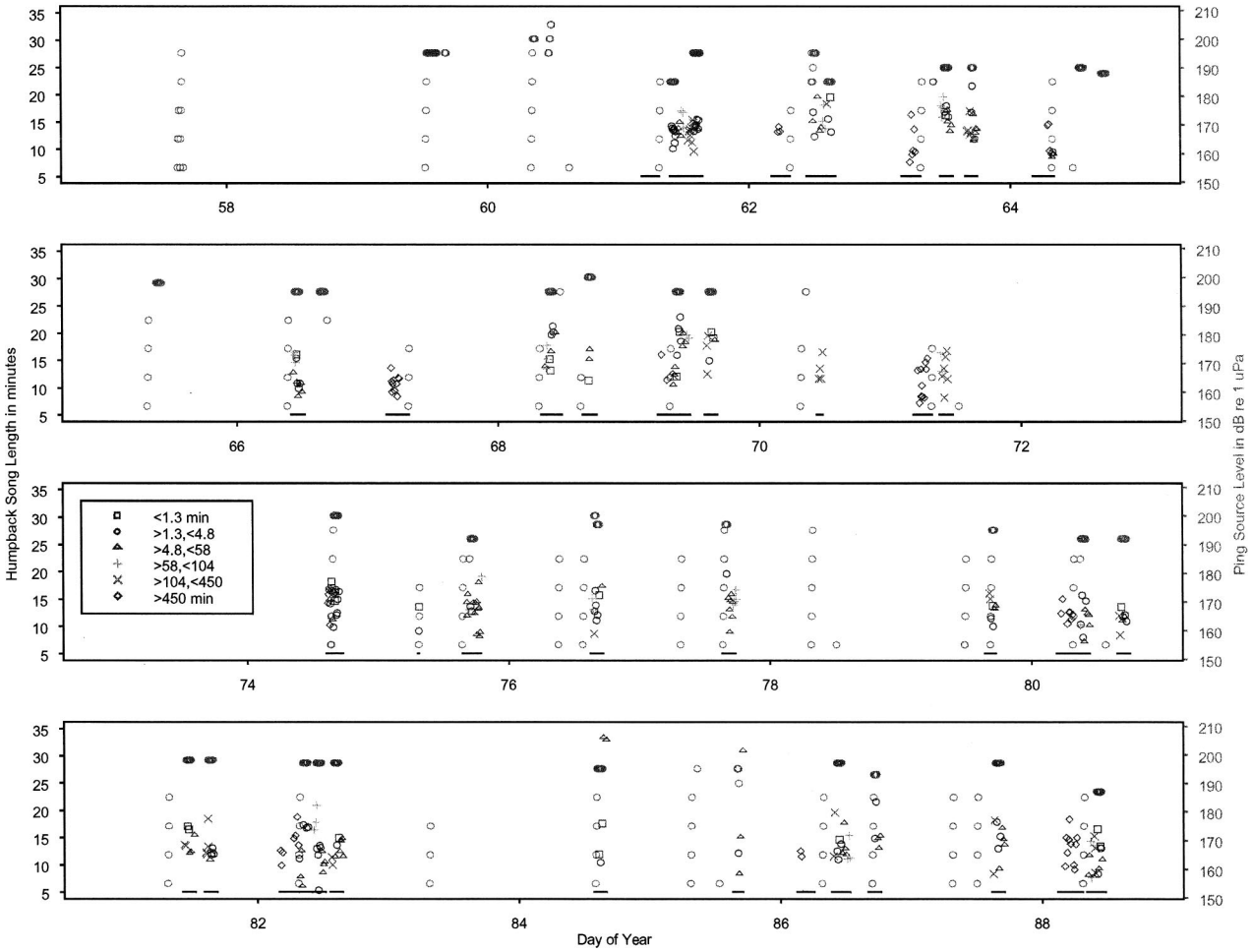

FIG. 2. History of humpback song length in relation to ping source level. Song length measurements are represented by one of six symbols, which show the categories from the analysis presented in Fig. 3. The gray circles show the time and source level of each ping. The solid lines near the bottom of each panel show the extent of acoustic sampling effort.

formed on 7 days due to high winds and other impediments to operations. Humpback song length was highly variable. Mean song length was 13.8 min (s.d.=3.1, minimum =5.4, 1st quartile=11.7, median=13.5, 3rd quartile=15.5, maximum=33.3 min, $N=378$). The difference between the shortest and longest songs measured on all days exceeded 10 min. The average difference in the lengths of successive songs sung by a singer was about 2.5 min. The average standard deviation for a series of songs sung by an individual was 2.76 min ($N=341$). These measures of intrinsic variation provide an important basis for assessing the scale of response. These measures consistently indicate that the variation among songs sung by an individual constitutes most of the pooled variation in song length.

Figure 2 graphically displays the time course of the project at a glance. The durations of 378 songs are displayed against the source levels of the pings and the temporal extent of the acoustic data analysis. Each song length measurement is coded by a symbol indicating its assignment into one of six categories, based on the tree-based regression of song length on minutes since the last ping. ''Minutes since the last ping'' were measured as illustrated in Fig. 1. These categories were: less than 1.3, 1.3 to 4.8, 4.8 to 58.5, 58.5 to 104, 104 to 450, and more than 450 min since the last ping. The relatively even distribution of these symbols across all ping series supports the conclusion that the differences found among these categories are not potentially influenced by correlation with diurnal or seasonal factors, or the idiosyncrasies of a few trials.

Humpback whale songs that were overlapped by pings were longer than songs that were not overlapped. A Student's t test indicates that this difference is on the border of the conventional test for significance ($t=1.961$, df=373, p-value=0.0506), while a Wilcoxon rank sum test does not yield as strong a result ($Z=1.6368$, p-value=0.1017). Although it is conceivable that songs of less than 6 min in length could fall between pings, and thus bias this result by their inclusion in the zero ping overlap category, no such songs were observed. However, these data cannot distinguish between the effects of overlap and immediacy of the last ping, because these factors are highly correlated. The sample with zero overlap contains only two songs that ended within 12 min of the last ping, and only two songs that were overlapped ended more than 12 min after the last ping.

To illustrate the differences in song length predicted by the minutes since the last ping, Fig. 3 illustrates boxplots of the song length data for the divergent subsets identified by the tree-based regression. These boxplots illustrate the loca-

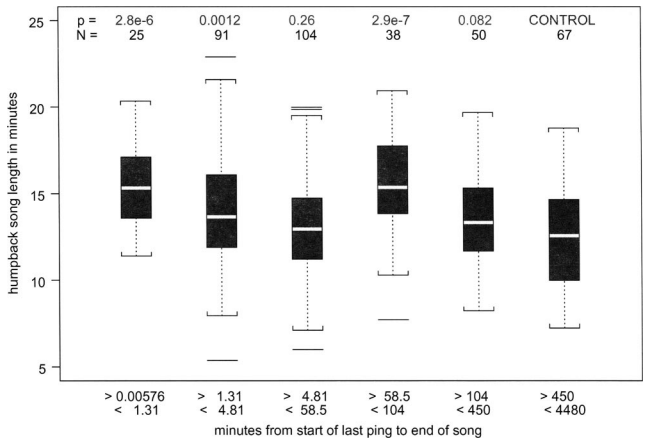

FIG. 3. Boxplots of humpback song lengths in relation to LF broadcasts. These boxplots depict distributions of song lengths in the six most distinct subsets of data, grouped by the minutes elapsed since the last ping. The solid bars indicate the range of song length values between the 25% and 75% percentile order statistics (the quartiles). The white line within the solid bars indicates the median value. The square brackets indicate the range of song length values or the range limit. The range limit was defined as one and a half times the interquartile range beyond the quartile. The horizontal bars mark measurements that fell beyond the range limit (outliers). The divisions in the data were selected by a tree-based regression of song length on the minutes from the start of the last ping, to maximize contrasts. The probability (*t*-test) that the subsample is drawn from the same distribution as the rightmost subsample is shown at the top, along with the sample size.

tion, scale, and asymmetry of each set of data; boxplots also mark clear outliers in the data. Songs in the last category, to the far right in Fig. 3, can be interpreted as behavior during control periods. These were recorded between 11 and 73 h after the last ping. As noted previously, these data do not provide an ideal control because they are not evenly distributed throughout the day.

Two subsets of data in Fig. 3 were not significantly different from the ''control'' subset. Songs that ended 104–450 min after a ping were slightly longer than those in the control subset, but overlapped sufficiently to fall short of the 5% criterion for statistical significance. Although it is possible that some of this difference is due to a lingering effect of LF broadcasts, the songs in this subset were recorded significantly later in the day than the songs in the control subset (Wilcoxon rank-sum test $Z=-7.9753$, p-value$=0$). A significant diurnal trend for song length is documented in the multivariate analyses below.

The third subset, songs that ended 4.8–58.5 min after the last ping, provides a counterintuitive result. This result shows that songs overlapped by a ping more than 5 min from their endings had the same distribution of lengths as all of the songs that ended within an hour of the last broadcast. About 40% of the songs in this sample ($N=42$ of 104) were overlapped. The mean length of these overlapped songs was not different from the controls ($t=0.7102$, df$=107$, p-value$=0.4791$) or the nonoverlapped songs in this subset ($t=-0.3116$, df$=102$, p-value$=0.756$).

Immediate and delayed responses were revealed by the remaining categories. Humpback songs were significantly longer when a ping occurred close the end of the song (leftmost category in Fig. 3). The magnitude of the song length increase diminished as the time since last ping increased. This pattern may indicate that humpback whales only changed the song they were singing when a ping occurred late in a long song. Alternatively, this pattern could indicate that humpbacks increased their song length in proportion to the number of pings that overlapped their song. Pings were 6 min apart during the ping series. A song that had a ping near its end might have had one or even two ping overlaps earlier in the song.

The delayed response is represented by the fourth boxplot in Fig. 3. Songs that ended between 58.5 and 104 min after a series of pings (median length: 15.4 min) had the largest increase in mean song length relative to the control subset (median length 12.6 min). Given the documented lack of response for songs that ended between 4.8 and 58.5 min after the last LF broadcast, this delayed response is surprising. It is unlikely that this result is an artifact of an idiosyncratic distribution of these samples in relation to other factors. This sample of 38 songs is drawn from a wide range of days and times of day (Fig. 2). Additional support for this observation arises from detailed examination of the 13-song series containing at least three song length measurements ($N=3,4,4,4,5,7,7,8,8,9,10,11,13$), with at least one of these measurements between 58.5 and 104 min after the last ping. Six of these series had their maximum song length between 58.5 and 104 min after the last ping, and five others had long songs in this interval that were nearly equal to the maximum for each series.

A simple test for the effect of overlap is to compare the average lengths of songs that were overlapped versus songs that were not overlapped by pings. The mean length of the overlapped songs was slightly greater (14 vs 13.3 min), and a *t*-test indicates that this difference is statistically significant ($t=-1.961$, df$=373$, p-value$=0.0506$). However, chance alone would cause longer songs to be more often (and extensively) overlapped by pings, if whales were oblivious to these LF signals. The ''oblivious hypothesis'' predicts that an increase in song length of 6 min would result in one additional overlapping ping (42 s) for songs sung entirely within the bounds of a ping series. For songs that do not fall entirely within the span of a ping series, the expected amount of overlap would still rise with increasing song length.

Figure 4 exhibits the relationship between song length and the minutes of ping overlap per song, showing that song length increases with increasing amounts of ping overlap. The three solid gray lines have a slope equal to the inverse of the duty cycle (''oblivious hypothesis'') and are drawn to pass through the mean song lengths for songs overlapped by one, two, and three pings. The oblivious hypothesis predicts much steeper increases in song length, as a function of overlap, than was observed. These deviations from the prediction are statistically significant (*t*-test results presented in Fig. 4). The three dotted gray lines in Fig. 4 pass through the same mean values, and have a slope equal to one. They correspond to a simple form of compensation in which whales increase the length of their songs by the amount of ping overlap. This form of compensation is also inconsistent with the observations.

Both of these univariate analyses neglected differences among singers, and the data in one or more categories may

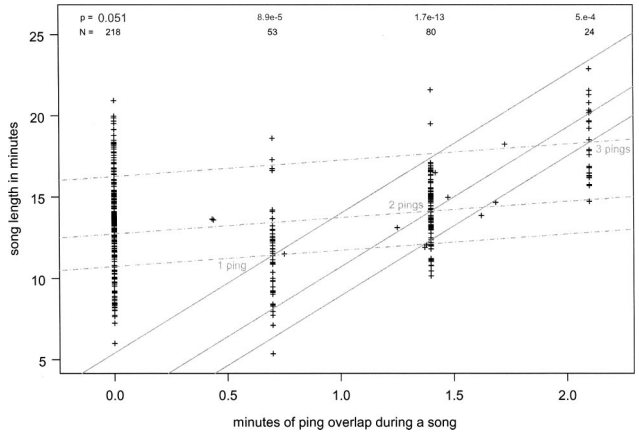

FIG. 4. Song length in relation to ping overlap. This scatterplot depicts the lengths of humpback songs in relation to the minutes of ping overlap. The sample sizes for each grouping of points are given above the clusters representing exactly zero, one, two, and three pings overlapping the songs (no fractions of a ping). The *p*-value in the upper left corner (0.051) is derived from a *t*-test comparing the songs with zero overlap with the songs that were overlapped by pings. The second *p*-value (8.9e-5) is derived from a *t*-test comparing the zero- and one-ping categories. The three solid lines are drawn through the median values for three categories of overlap (one, two, three pings), with a slope equal to the inverse of the duty cycle (the oblivious hypothesis). The third and fourth *p*-values compare the respective categories of song length measurements against the previous category, after adjusting for the slope of the solid lines. The dotted lines are drawn through the same median values, but have a slope of one (assumes songs are lengthened by the amount of time that they are overlapped).

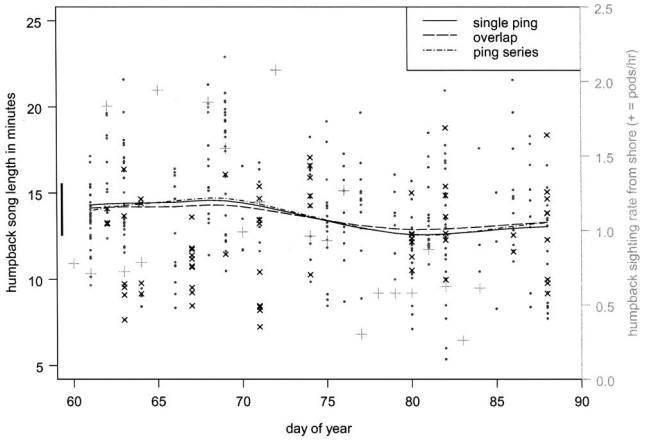

FIG. 5. Seasonal trend in song length and pod sighting rates from 1–28 March 1998. The plus symbols are normalized pod sighting rates from a shore station several miles from the site of the experiments. The small gray dot symbols indicate the song length measurements. The length of the solid bar near the left-hand axis represents the average change in the lengths of successive songs sung by a singer. The solid and dashed curves represent the smoothing splines for day of year in three generalized additive models (GAMs). These GAMs differ by the substitution of minutes from the start of last ping series or ping overlap for minutes from the start of the last ping (response to ping series or overlap vs. single pings).

represent skewed distributions for other factors such as date and time of day. To account for the effects of these factors simultaneously, generalized additive models were fitted. A total of 369 song length measurements from 113 song sessions were used in these analyses. Song length was fitted to day of year, hour of day, source level of the last ping, and a factor involving the timing of the broadcasts. Three broadcast timing factors were used: minutes since the start of the last ping (log 10 transformed, in the ''single-ping model''), minutes since the last ping series began (log 10 transformed, in the ''ping-series model''), and minutes of pings overlapping each song (in the ''overlap model'').

The statistical results of these multivariate models are summarized in Table I. The results on the left pertain to the generic models using time of day and day of year; the results on the right pertain to the singer ID models. Each row in Table I presents the statistical significance attributed to each factor by the different models. Although there are no corrections for multiple inferences in these calculations (e.g., Bonferroni), consistently significant results provide broader support for attributing behavioral meaning to a factor.

All three models produced estimates of seasonal and diurnal factors that were remarkably consistent (Figs. 5 and 6). These figures present the fitted effects as lines, with a scatter plot of the raw data in the background. Day of year (Fig. 5) shows a modest effect, which roughly corresponded to the density of animals seen from a nearby shore station. Time of

TABLE I. Statistical results of the generalized additive models. The results on the left pertain to the generic models using time of day and day of years; the results on the right pertain to the singer ID models. Each row presents the statistical significance attributed to each factor by the different models. There are no corrections for multiple inferences in these calculations.

	Date and hour of day models			Singer models		
	Min. since last ping	Min. since last series	Min. of overlap	Min. since last ping	Min. since last series	Min. of overlap
s(day of years)	$F=3.638\,278$	$F=5.067\,14$	$F=2.3724$			
nonparametric df=3	$p=0.013\,088\,27$	$p=0.001\,909\,5$	$p=0.070\,135\,57$			
s(hour of day)	$F=2.381\,553$	$F=3.895\,104$	$F=3.565\,49$			
nonparametric df=4	$p=0.051\,337\,87$	$p=0.004\,168\,2$	$p=0.007\,238\,68$			
s(source level)	$F=7.212\,696$	$F=1.745\,241$	$F=6.309\,77$	$F=0.856\,559$	$F=2.818\,95$	$F=0.843\,97$
nonparametric df=1	$p=0.007\,608\,76$	$p=0.187\,369\,8$	$p=0.012\,483\,63$	$p=0.355\,808\,8$	$p=0.094\,571\,9$	$p=0.359\,339\,2$
s(log 10(min since last ping))	$F=4.187\,802$			$F=3.343\,22$		
nonparametric df=7	$p=0.000\,190\,69$			$p=0.002\,096\,1$		
s(log 10(min since last series))		$F=1.484\,326$			$F=1.347\,82$	
nonparametric df=5		$p=0.171\,76$			$p=0.229\,102\,3$	
s(pings per song)			$F=4.03\text{E}+01$			$F=18.867\,39$
nonparametric df=2			$p=2.22\text{E}-16$			$p=2.68\text{E}-08$
null deviance/d.f.	3495/362	3458/358	3494/362	2636/280	2597/276	2636/280
residual deviance/d.f.	2687/343	2756/339	2308/348	1303/219	1351/217	1176/224

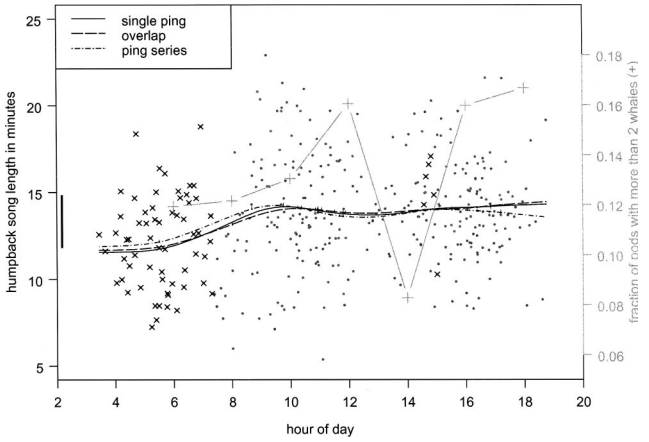

FIG. 6. Diurnal trend in song length and index of social activity. The small gray dots indicate the song length measurements. The "x" symbols indicate the lengths of songs sung before the first ping of the day. The length of the solid bar near the left-hand axis represents the average change in the lengths of successive songs sung by a singer. The plus symbols represent an index of social activity: the fraction of pods with more than two animals as seen from the source vessel. The solid and dashed curves represent the smoothing splines for the time of day factor in the same GAMs as Fig. 4.

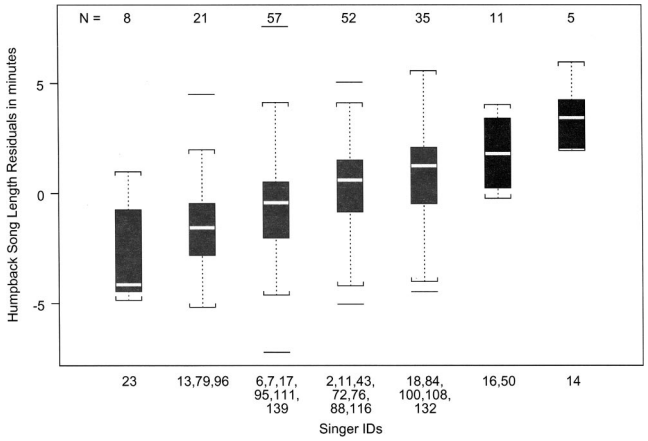

FIG. 7. Boxplots of song length residuals for groups of singers. The residual errors from model 1 in Table I were fitted using a tree-based regression on singer ID (categorical variables). The number of songs in each group are at the top of the plot. The horizontal axis labels list the singer IDs in each group. Singer IDs were assigned chronologically in this study.

day (Fig. 6) shows a stronger effect: songs were much shorter in the early morning. The diurnal trend in song length roughly parallels an index of social activity. These seasonal and diurnal factors made significant contributions as measured by F-ratio comparisons of the models without and with each factor (Table I, first three models). However, the ranges of these factors' effects were approximately equal to the average difference in the lengths of successive songs sung by an individual (dark vertical bar on the left in Figs. 5 and 6).

It may appear reasonable to assert that the diurnal pattern reflects a cumulative response to LF broadcasts, because the earliest broadcasts started at 0730. The data suggest, however, that this diurnal pattern was unchanged on days when no broadcasts took place in the morning (Fig. 6). For songs sung more than 450 min after the last LF transmission, songs sung before 0730 were significantly shorter than those sung after 1400($t=-2.3683$, df$=65$, p-value$=0.0209$). A second caution concerns the apparent slump in song length and singing activity in the early afternoon. The apparent decrease in the number of songs (and possibly song length) in the early afternoon is largely due to sparse acoustic data analysis effort for those hours. However, the index of social activity is supported by consistent sampling effort.

Before presenting the fitted effects of the broadcast factors, a modest digression is warranted to investigate the differences in singer song length tendencies. The models discussed above neglected idiosyncratic differences among singers in order to use as many song length measurements as possible. Many song series were relatively short: 1 song length measurement was obtained from 38 song series, 2 measurements from 24 song series, 3 from 10, 4 from 16, 5 from 5, 6 from 5, 7 from 2, 8 from 5, 9 from 4, 10 from 2, 11 from 1, and 13 from one song series. A univariate analysis of song series measurements may tend to overestimate individual variation. The contributions of diurnal and seasonal factors should be factored out in order to ensure that they do not inflate the apparent differences among singers. Thus, the residuals of the single ping model (Table I, first model) were analyzed for all song series containing more than four songs ($N=25$ series). There are significant differences in song length among singers. A tree-based regression of song length residuals on singer ID produced seven distinct clusters (Fig. 7). Differences among all clusters are highly significant (Kruskal-Wallis chi-square$=42.775$, df$=6$, p-value$=1.29\times10^{-7}$). The two most extreme clusters represent single singers. Singer IDs were numbered consecutively during the study. The random distribution of the singer IDs on the horizontal axis indicates that singer idiosyncrasies did not exhibit a generic seasonal pattern.

In order to control for differences among singers in the multivariate analyses, additional GAMs were fitted by substituting a song series factor for the time of day and day of year factors. These models were compared with the previous generic time/date models to assess the stability of the fitted shapes of the broadcast factors with respect to changes in other fitted factors. Song series were too brief to investigate diurnal and seasonal trends for each singer, so in these models the singer ID term captured both temporal and individual sources of variation. These singer ID models used measurements from song series with three or more songs (52 series, 290 measurements). The results in Table I (models 4–6) indicate that the single-ping and overlap factors remained significant in the singer ID models, but the ping-series factor did not.

Figure 8 reinforces the conclusion that the ping series factor does not consistently predict song length in these models. In Table I the F-ratio tests for the second and fifth models indicate that the ping series factor does not explain a significant amount of variation in song length in either the generic or singer ID models. Figure 8 shows that the shape of the fitted curve changes dramatically when a singer ID factor is substituted for the date and time factors. In tandem, these indicate that ping series is not as good a predictor as single-ping and overlap factors. Again, the data on the extreme right provide an estimate of baseline behavior, though

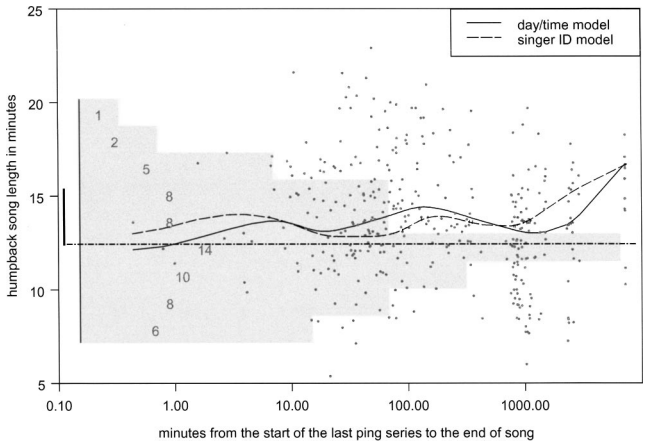

FIG. 8. The effect of time since the last ping series. The solid and dashed curves represent the smoothing spline for the ping-series factor. The solid curve is from the GAM using day of year and time of day; the dashed curve is from the GAM using individual ID. The light gray dots provide a scatterplot of the data. The underlying histogram indicates the distribution of song lengths during morning periods before the first transmission of the day. The length of the solid bar near the left-hand axis represents the average change in the lengths of successive songs sung by a singer.

songs sung in the early morning are disproportionately represented.

The multivariate single-ping model (Fig. 9) confirms the univariate results presented in Fig. 3. Baseline behavior is represented on the extreme right. Both the immediate and delayed increases in song length are evident in the multivariate models. Furthermore, the generic and singer ID models match quite closely for songs sung up to 100 min after the last ping. This indicates that the shape of this fitted factor reflects a salient relationship between the time since the last ping and song length, and not artifacts of interactions with other factors in the model. The subsequent divergence of the curves, for the data to the right of 100 min, is a consequence of the narrow horizontal span of any singer's data in this

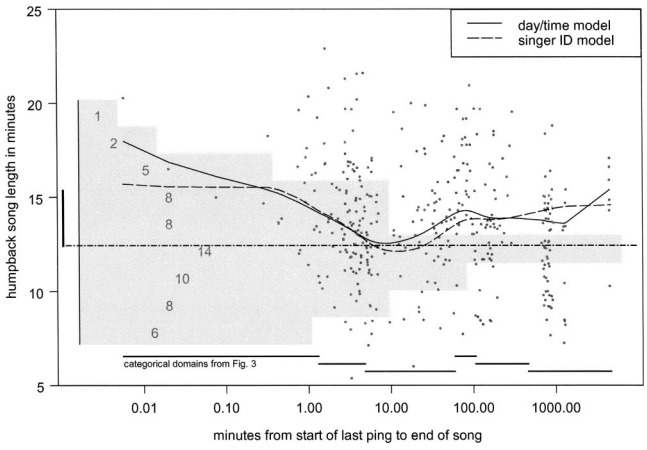

FIG. 9. The effect of time since the last ping. The solid and dashed curves represent the smoothing splines for the single-ping factor. The solid curve is from the GAM using day of year and time of day; the dashed curve is from the GAM using individual ID. The underlying histogram indicates the distribution of song lengths during morning periods before the first transmission of the day. The length of the solid bar near the left-hand axis represents the average change in the lengths of successive songs sung by a singer. The horizontal bars schematically represent the categorical groupings used in Fig. 3.

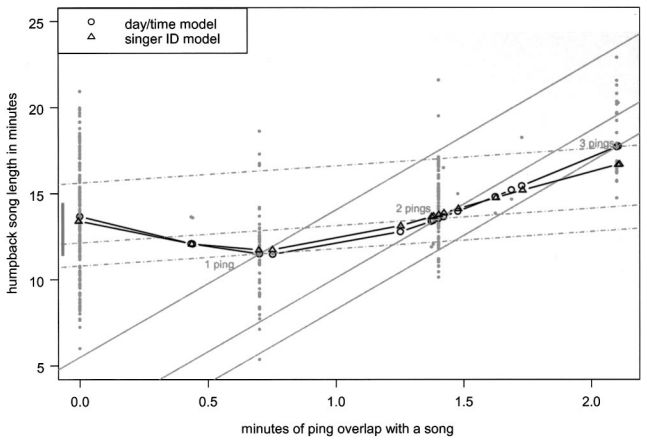

FIG. 10. The effect of ping overlap. The curves represent the smoothing splines for the minutes of ping overlap during a song. The curve marked with circles is from the GAM using day of year and time of day; the curve marked with triangles is from the GAM using individual ID. The three solid gray lines are drawn through the circles corresponding to zero, one, two, and three full pings of overlap, with a slope equal to the inverse of the duty cycle for the broadcasts (6*60/42 s). This slope corresponds to the null hypothesis (singers were oblivious to the broadcasts). The three dotted lines have slopes equal to 1.0. The length of the solid bar near the left-hand axis represents the average change in the lengths of successive songs sung by a singer.

region. The singer ID factors can be arbitrarily assigned in this region, so the fitting process does not strongly constrain the shape of the time since last ping factor.

The scatterplot of song length versus the time since the last ping suggests that in addition to changes in average song length, variability of song length may increase in response to LF broadcasts. Using the categories from Fig. 3, songs ending 1.3 to 4.8 min after the last ping exhibited the largest variance in length when compared to those in the control group, songs ending more than 450 min after the last ping. Significance, however, falls short of the conventional criterion ($F_{90,66}=1.4795$, $p=0.0949$).

Figure 10 confirms the univariate analysis of Fig. 4: song length increases rapidly with increased ping overlap, but not quite as steeply as predicted by the oblivious hypothesis. Song length increases more rapidly than would be predicted if whales simply lengthened their songs by an amount equal to the duration of overlap. There is substantial agreement between the fitted curves from generic and singer ID models, once again indicating that this pattern is not an artifact of interactions among the modeled factors.

These data will not support models that include both the single-ping and overlap factors in a single model, because these factors covary: only two songs that ended within 12 min of the last ping were not overlapped, and only two songs that were overlapped ended more than 12 min after the last ping. However, the conclusion that ping overlap is intrinsic to the mechanism of response is contradicted by the tree-based regression of song length on time since the last ping (Fig. 3). This regression pooled songs by their mean lengths, and the 4.8-to-59-min category included songs that were and were not overlapped by pings. A *t*-test within this category confirmed that there was no significant difference in song length related to overlap. Thus, the single-ping model seems more broadly supported.

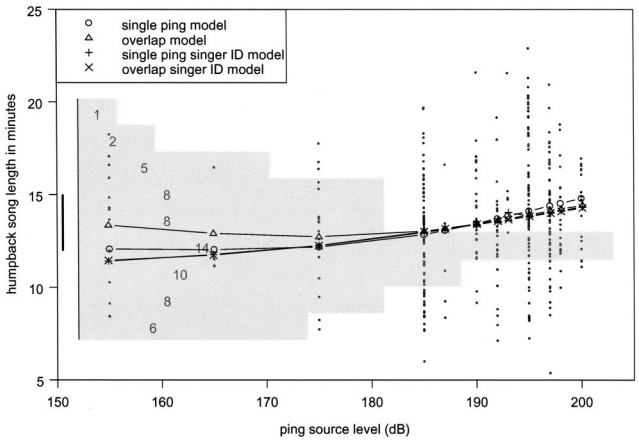

FIG. 11. The effect of ping source level. The four curves represent the smoothing splines for the source level factor from the different models. The underlying histogram indicates the distribution of song lengths during morning periods before the first transmission of the day. The length of the solid bar near the left-hand axis represents the average change in the lengths of successive songs sung by a singer.

The curves in Figs. 8 and 9 reveal the bias due to limiting the degrees of freedom of the smoothing splines used to represent the response factors. A few song length measurements were made more than a day after the last ping. This corresponds to values on the horizontal axis in excess of 2200 min. These six songs, which were recorded between 1400 and 1500 in the afternoon, had an average duration of 14.8 min. All of the songs sung 450 to 1000 min after the last ping were sung in the early morning (before 0730 h), and were characteristically shorter. Thus, the fitting algorithm used by the generalized additive model skewed the LF broadcast response factor to fit this diurnal shift in song length. This skew has two consequences: the curves do not pass through the mean of the control data, and the positive slopes of curves at the extreme right of Figs. 8 and 9 are artifacts.

The broadcast factors made stronger contributions in the single-ping and overlap models than in the ping-series model. Note, however, that the extremely strong contribution of the overlap factor (Table I, third model) must be interpreted with caution. As noted previously, the null hypothesis (no reaction to broadcasts) would predict a positive correlation between song length and minutes of overlap.

Figure 11 shows the smoothed fits of source level to song length, from four of the GAM analyses. These models yielded remarkably consistent increases in song length as source levels increased from 175 to 200 dB, the range in which most of the data were distributed. Humpback whales sang longer songs in the intervals following louder broadcasts. These models fitted the source level of the last ping to all of the data, including songs that occurred hours after the last ping. However, a regression of source level on song length for songs overlapped by a ping yielded a very similar result (slope$=0.0864$, $F_{1,144}=2.073$, $p=0.152$).

IV. DISCUSSION

The methodological approach of this study differs in three respects from the affiliated research reported in Miller *et al.* (2000). No *a priori* assumptions were made regarding the timing of responses to broadcasts. Natural factors affecting song length were explicitly modeled instead of relying on a matched sample approach to minimize their effects. Natural variation in song length was quantified, to provide a scale for assessing the magnitude of observed responses. The goal was a more comprehensive understanding of variation in song length, to provide the broadest biological context for evaluating the observed response to the LF broadcasts.

The most daunting challenge in any study of the impacts of human activities on free-ranging animals is incorporating natural variability in behavior. In the absence of adequate predictive models, this uncontrolled variation diminishes the opportunities to measure behavioral response. Thus, the statistical power of such studies depends on both the sample size and the ability to control for other factors influencing behavioral patterns. When natural factors are not taken into account, detectable responses can be obscured, and false impressions of human impact can be developed.

The matched sample approach adopted by Miller *et al.* (2000) categorized response in relation to hour-long intervals: prebroadcast, broadcast, postbroadcast. If these three intervals are identical in all other respects, then other factors affecting song length can be ignored. However, as the ''matched sample'' spans 3 h the assumption that all other factors remain constant is problematic. Also, it was difficult to follow free-ranging whales for 3 h, which curtailed the sample size. Sample size issues aside, the strength of the matched sample approach is also its most serious weakness: the focus on a single factor degrades the capacity of the data to provide more general insights into the natural patterns and biological significance of the behaviors under study.

The multivariate models accounted for additional factors and used songs from a much larger number of animals. However, the multivariate models lose the intrinsic control inherent in the matched sample, and are vulnerable to biases due to unmeasured factors. Factors that remain constant for 3 h but vary within the field season are no longer controlled. This concern was addressed by comparing results across several models that utilized different combinations of factors. When the fitted curves for one factor retain the same shape across models, the results are less likely to represent bias due to unmeasured factors or artifacts of the model structure.

In spite of methodological differences, the results presented here generally agree with the findings of Miller *et al.* (2000). Both studies indicate that humpback whales increase their song length in response to LF broadcasts. In this study, statistically significant differences were documented that lasted up to 2 h after the last broadcast. Source level was a significant factor in humpback responses, and higher source levels were associated with longer songs.

Additionally, this study documents that the magnitude of the response was well within the range of variation in song lengths in the absence of LF broadcasts. The responses were of the same magnitude as the average difference in the lengths of successive songs sung by an individual. The modeled responses to broadcasts also fell within the range of variation in song length observed during periods when many hours had elapsed since the last ping.

These results differ from Miller *et al.* (2000) by documenting that increases in song length were contingent on the timing of pings in relation to songs. Songs that were overlapped in the latter portion of the song showed the greatest increase in song length. Songs that were overlapped by one ping, near the start of the song, showed no increase in song length. The dependency of response to stimuli on the phase of an animal's behavior has been observed in frog playback experiments: ''stimuli occurring too soon after the end of a call (inhibitory phase) are postulated to increase the delay until the next call onset, while those occurring later (in the excitatory phase) decrease the delay by stimulating a call'' (Brush and Narins, 1989).

A delayed response to the LF broadcasts was also documented. The largest increases in song length were observed in songs that were sung between 1 and 2 h after the last ping. This result was based on 38 songs that were evenly distributed throughout the entire experimental period, which decreases the likelihood that it could be attributed to some other factor. It should be further noted that the three exceptionally long songs, which were excluded from the analyses, provide additional evidence for this delayed response. Two were sung 1 to 2 h after the last ping, while the third ended 37 min after the last ping. It was not possible to determine whether the delayed response scaled with the number of pings, because most ping series were of the same length.

Aside from this delayed response, other measures failed to indicate cumulative effects from the LF broadcasts. The duration of the ping series preceding songs was tested as an experimental factor. It did not provide as strong or consistent a predictor as the minutes since the last ping. This suggests that the song length response depends solely on the most recent ping, and not the immediate history leading up to that ping. The modeled seasonal and diurnal factors do not show trends that can plausibly be explained by cumulative exposure to pings. The increase in song length from early morning to afternoon was the same on days with and without pings. The seasonal trend was not unidirectional, and it appears to be correlated with local humpback population density. Finally, idiosyncratic differences among singers did not correlate with duration of potential prior exposure.

These data provide clues regarding the biological significance of song length. Humpback song length increased on days with higher local population density, and also during hours of day with higher social activity (afternoon). Similar correlations between call length and chorus density have been observed in other species, such as gray treefrogs (Welch *et al.*, 1998). This pattern could indicate a compensatory response to increased ambient noise, a competitive response to other singers' displays, or mutual correlations of chorus density and song length with a third factor, such as the availability of potential mates. Humpback responses to LF broadcasts can be viewed as consistent with these mechanisms, as if singers reacted to the pings as they would to another singer. However, better understanding of the observed responses will require more detailed studies of singing behavior and the social function of this display. The modest scale of the measured responses to LF broadcasts may reflect high fitness costs to changes in singing behavior. Male singing behavior may appear relatively unchanged under noisome conditions because more dramatic alterations would diminish mating success.

It has been suggested previously that song length provides an index of condition because of the constraints that song structure imposes on opportunities for respiration (Chu *et al.*, 1986; Chu, 1988). However, these data show that song length is highly variable, and may play a dynamic role in social signaling. Although these analyses did reveal differences among singers in average song length, all singers exhibited substantial variation. Song length does not seem to be a rigidly stereotyped advertisement or tightly constrained by physiological condition.

The evidence of a response that scaled with source level poses questions. In the GAM models presented here, source level was assumed to have a lasting effect on song length, regardless of the time elapsed since the most recent ping. These GAM models also indicated that there was a delayed response to LF broadcasts, and these effects subsided 2 h after the last broadcast. Future research might clarify the effects of source level on the magnitude and duration of the delayed response. A more complex model would estimate the decay of source level effects as a function of the time since the last ping.

The literature on marine mammal responses to noise has not adequately addressed the interrelated effects of source level, proximity, and received level. Estimation of received level requires precise knowledge of the depths of singing whales. Position and depth of singers can be measured using acoustic localization methods. The accuracy of such methods is contingent upon developing high-resolution models for the positions of hydrophone elements in towed arrays. For these data, the hydrophones were embedded in a long cable and towed by a ship executing complex maneuvers in order to approach whales. Ongoing research effort is focused on array shape estimation, automatic detection, and localization.

Future studies should incorporate provisions to study delayed responses by varying the duration of exposure and providing for longer-term monitoring of behavioral responses. The ability of humpbacks to orient and navigate may be compromised by exposure to explosions (Todd *et al.*, 1996), even when visual observations did not detect altered residency or movement patterns in feeding areas while the whales were being exposed to the sounds (Malme *et al.*, 1985). ''This suggests that caution is needed in interpreting the lack of visible reactions to sounds as an indication that whales are not affected, or harmed by an acoustic stimulus'' (Todd *et al.*, 1996), and underscores the importance of examining both short-term and long-term behavioral evidence.

Rational environmental policy requires reliable measures of potential impact, combined with a plausible interpretation of their demographic significance. These results offer a detailed picture of short-term response in the context of behavioral variation observed in the absence of the stimulus. These responses were relatively brief in duration, with all observed effects occurring within 2 h of the last ping. Some changes in behavior can be expected for any perceptible stimulus, especially one associated with a large ship maneuvering nearby. The effects documented here were revealed by

careful statistical analysis, but they were not salient to the acoustic observers on the scene. Dramatic changes in humpback singing behavior would have demographic consequences, but the effects documented here do not seem to pose this risk.

ACKNOWLEDGMENTS

The successful completion of this multi-faceted research project was the result of close cooperation by a large team. The project included personnel from Cornell University, Marine Acoustics, Inc., Woods Hole Oceanographic Institution, Harvard University, the University of Hawaii, the University of Washington, the Naval Facilities Engineering Service Center, Raytheon Corp., and the US Navy.

The following research personnel represented Cornell University in the collection of the field data: Carol Carson, Christine Gabriele, David Larom, and Scott Sinclair. Lars Bejder, Nicoletta Biassoni, Frank Cipriano, Bete Jones, Patrick Miller, Amy Samuels, and Peter Tyack, represented Woods Hole Oceanographic Institution in the collection of the shore station visual data and vessel-based focal follow data. William Ellison and Stan Laback from Marine Acoustics Inc. assisted in the collection of the acoustic and environmental field data. Kathy Dunsmore, Tom Calupca, and Harold Mills developed software for acoustic data collection and analysis. We owe special thanks to Joseph Johnson, the program manager who directed and motivated the entire project. We are indebted to the Navy for access to the LFA system and use of the R/V CORY CHOUEST. We gratefully acknowledge the important contributions of Chief Warrant Officer Mike Lamczyk and the Navy crew in the successful collection of visual sighting, environmental, and acoustic data. We thank the captain and crew of the R/V CORY CHOUEST, including Jeff Mentzer, Mark Test, Tom Oliphant, Trish Mackay, John Demler, Bill Cermak, Mark Fuller, Howard Hanway, Roger Buckmann, Larry Lewis, Rene Osias, Charles Bain, Jim Bennet, Dave Bentley, Rick Mroch, Terry Miranda, and Keith Nicholaus. We thank personnel from the State of Hawaii's Division of Land and Natural Resources, the Hawaiian Islands Humpback Whale National Marine Sanctuaries, and the National Marine Fisheries Service for advice and constructive criticism. Funding for the Cornell research was provided by the Strategic Environmental Research and Development Program (SERDP) through the Office of Naval Research Grant No. N00014-97-1-1027.

Au, W. W. L., and Green, M. (**2000**). ''Acoustic interaction of humpback whales and whale-watching boats,'' Mar. Environ. Res. **49**, 469–481.

Baker, C. S., and Herman, L. M. (**1984**). ''Aggressive behavior between humpback whales (*Megaptera novaeangliae*) wintering in Hawaiian waters,'' Can. J. Zool. **62**, 1922–1937.

Barlow, J. (**1995**). ''The abundance of cetaceans in California waters: Part I. Ship surveys in summer and fall of 1991,'' U.S. National Marine Fisheries Service Fish. Bull. **93**, 1–14.

Biassoni, N. (**2000**). ''Preliminary results of the effects of SURTASS-LFA sonar on singing humpback whales,'' W. H. O. I. Tech. Report 2000-06, Woods Hole, MA.

Brown, W. D., Wideman, J., Andrade, M. C. B., Mason, A. C., and Gwynne, D. T. (**1996**). ''Female choice for an indicator of male size in the song of the black-horned tree cricket, *Oecanthus nigricornis* (Orthoptera: Gryllidae: Oecanthinae),'' Evolution (Lawrence, Kans.) **50**, 2400–2411.

Brush, J. S., and Narins, P. M. (**1989**). ''Chorus dynamics of a neotropical amphibian assemblage: comparison of computer simulation and natural behavior,'' Anim. Behav. **37**, 33–44.

Catchpole, C. K. (**1980**). ''Sexual selection and the evolution of complex songs among European warblers of the genus *Acrocephalus*,'' Behaviour **74**, 149–166.

Cerchio, S., Jacobsen, J., and Norris, T. (**2001**). ''Geographic and temporal variation in songs of humpback whales (Megaptera novaeangliae): synchronous change in Hawaiian and Mexican breeding assemblages,'' Anim. Behav. **62**, 313–329.

Chambers, J. M., and Hastie, T. J. (editors) (**1991**). *Statistical Models in S* (Wadsworth and Brooks, Pacific Grove, CA).

Chu, K. C. (**1988**). ''Dive times and ventilation patterns of singing humpback whales,'' Can. J. Zool. **66**, 1322–1327.

Chu, K., and Harcourt, P. (**1986**). ''Behavioral correlations with aberrant patterns in humpback whale *Megaptera novaeangliae songs*,'' Behav. Ecol. Sociobiol. **19**, 309–312.

Clapham, P. J. (**1996**). ''The social and reproductive biology of humpback whales: an ecological perspective,'' Mammal. Rev. **26**, 27–49.

Clark, C. W., and Tyack, P. L. (**1998**). ''Low-frequency sound scientific research program. Phase III: responses of humpback whales to SURTASS LFA off the Kona coast, Big Island Hawai'I 26 February–31 March 1998,'' Quick Look Report. Marine Acoustics, Inc., 809 Aquidneck Ave., Middletown, RI.

Corkeron, P. J. (**1995**). ''Humpback whales (*Megaptera novaeangliae*) in Hervey Bay, Queensland-behavior and responses to whale-watching vessels,'' Can. J. Zool. **73**, 1290–1299.

Craig, A. S., and Herman, L. M. (**1997**). ''Sex differences in site fidelity and migration of humpback whales (*Megaptera novaeangliae*) to the Hawaiian Islands,'' Can. J. Zool. **75**, 1923–1933.

Darling, J. D. (**1983**). ''Migrations, abundance and behavior of Hawaiian humpback whales, *Megaptera novaeangliae* (Borowski),'' Ph.D. Thesis, University of California, Santa Cruz.

Eiriksson, T. (**1994**). ''Song duration and female response behavior in the grasshopper *Omocestus viridulus*,'' Anim. Behav. **47**, 707–712.

Frankel, A. S., and Clark, C. W. (**1998**). ''Results of low-frequency playback of M-sequence noise to humpback whales, *Megaptera novaeangliae*, in Hawai'i,'' Can. J. Zool. **76**, 521–535.

Frankel, A. S., and Clark, C. W. (**2000**). ''Behavioral responses of humpback whales (*Megaptera novaeangliae*) to full-scale ATOC signals,'' J. Acoust. Soc. Am. **108**, 1930–1937.

Frankel, A. S., and Clark, C. W. (**2002**). ''ATOC and other factors affecting the distribution and abundance of humpback whales (*Megaptera novaeangliae*) off the north short of Kauai,'' Marine Mammal Sci. **18**, 644–662.

Frankel, A. S., Clark, C. W., Herman, L. M., and Gabriele, C. M. (**1995**). ''Spatial distribution, habitat utilization, and social interactions of humpback whales, *Megaptera novaeangliae*, off Hawaii, determined using acoustic and visual techniques,'' Can. J. Zool. **73**, 1134–1146.

Frumhoff, P. (**1983**). ''Aberrant songs of humpback whales (*Megaptera novaeangliae*): clues to the structure of humpback songs,'' in *Communication and Behavior of Whales*, edited by R. Payne (Westview, Boulder, CO), pp. 81–127.

Gabriele, C. M. (**1992**). ''The behavior and residence characteristics of reproductive classes of humpback whales (*Megaptera novaeangliae*) in the Hawaiian Islands,'' M.A. thesis, University of Hawaii, Honolulu.

Gentner, T. Q., and Hulse, S. H. (**2000**). ''Female European starling preference and choice for variation in conspecific male song,'' Anim. Behav. **59**, 443–458.

Hastie, T. J., and Tibshirani, R. J. (**1998**). *Generalized Additive Models* (Chapman and Hall/CRC, Boca Raton, FL).

Helweg, D. A., Frankel, A. S., Mobley, J. R., Jr., and Herman, L. M. (**1992**). ''Humpback whale song: our current understanding,'' in *Sensory Systems of Marine Mammals*, edited by J. Thomas, R. Kastelein, and A. Supin (Plenum, New York), pp. 459–483.

Herman, L. M., and Antinoja, R. C. (**1977**). ''Humpback whales in the Hawaiian breeding waters: population and pod characteristics,'' Sci. Rep. Whales Res. Inst. Tokyo. **29**, 59–85.

Klump, G. M., and Gerhardt, H. C. (**1987**). ''Use of non-arbitrary acoustic criteria in mate choice in female gray tree frogs,'' Nature (London) **326**, 286–288.

Malme, C. I., Miles, P. R., Tyack, P. L., Clark, C. W., and Bird, J. E. (**1985**). ''Investigation of the potential effects of underwater noise from petroleum industry activities on feeding humpback whale behavior,'' Report to U.S.

Department of the Interior, Minerals Management Service, Anchorage, Alaska (NTIS PB86-218385).
The Mathworks, Inc. (**1999**). Matlab 5.3., Natick, MA.
Maybaum, H. L. (**1990**). ''Effects of a 3.3 kHz sonar system on humpback whales, *Megaptera novaeangliae*, in Hawaiian waters,'' EOS **71**, 92.
Maybaum, H. L. (**1993**). ''Responses of humpback whales to sonar sounds,'' J. Acoust. Soc. Am. **94**, 1848–1849.
Miller, P. J. O., Biassoni, N., Samuels, A., and Tyack, P. L. (**2000**). ''Humpback whales sing longer songs when exposed to LFA sonar,'' Nature (London) **405**, 903.
Mobley, Jr., J. R., Bauer, G. B., and Herman, L. M. (**1999**). ''Changes over a ten-year interval in the distribution and relative abundance of humpback whales (*Megaptera novaeangliae*) wintering in Hawaiian waters,'' Aquat. Mammals **25**, 63–72.
Mobley, J. R., Jr., Forestall, P. H., and Grotefendt, R. A. (**1994**). ''Results of 1993 aerial surveys in Hawaiian waters,'' University of Hawaii at West Oahu.
Mobley, J. R., Jr., Forestall, P. H., and Grotefendt, R. A. (**1995**). ''Preliminary results of 1993 and 1995 aerial surveys of Hawaiian waters,'' report to the ATOC-MMRP.
Mobley, Jr., J. R., Herman, L. M., and Frankel, A. S. (**1988**). ''Responses of wintering humpback whales *Megaptera novaeangliae* to playback of recordings of winter and summer vocalizations and of synthetic sound,'' Behav. Ecol. Sociobiol. **23**, 211–224.
Navy, Dept. of the (**2001**). ''Final overseas environmental impact statement and environmental impact statement for surveillance towed array sensor system low frequency active (SURTASS LFA) sonar,'' SURTASS LFA Sonar Program Manager, Chief of Naval Operations.
Norris, T. F. (**1994**). ''The effects of boat noise on the acoustic behavior of humpback whales (*Megaptera novaeangliae*),'' J. Acoust. Soc. Am. **96**, 3251.
Payne, R. S., and McVay, S. (**1971**). ''Songs of humpback whales,'' Science **173**, 585–597.
Payne, K., and Payne, R. (**1985**). ''Large scale changes over 19 years in songs of humpback whales in Bermuda,'' Z. Tierpsychol **68**, 89–114.
Payne, K., Tyack, P. L., and Payne, R. (**1983**). ''Progressive changes in the songs of humpback whales (*Megaptera novaeangliae*): a detailed analysis of two seasons in Hawaii,'' in *Communication and Behavior of Whales*, edited by R. Payne (Westview, Boulder, CO), pp. 9–57.
Richardson, W. J., Greene, C. R., Malme, C. I., and Thompson, D. H. (**1995**). *Marine Mammals and Noise* (Academic, San Diego, CA).
Statistical Sciences, Inc. (**2000**). ''S-Plus 2000 Professional Release 1.''
Taigen, T. L., and Wells, K. D. (**1985**). ''Energetics of vocalizations by an anuran amphibian (*Hyla versicolor*),'' J. Comp. Physiol. **155**, 163–170.
Thode, A. M., D'Spain, G. L., and Kuperman, W. A. (**2000**). ''Matched-field processing, geoacoustic inversion, and source signature recovery of blue whale vocalizations,'' J. Acoust. Soc. Am. **107**, 1286–1300.
Todd, S., Stevick, P., Lien, J., Marques, F., and Ketten, D. (**1996**). ''Behavioural effects of exposure to underwater explosions in humpback whales (*Megaptera novaeangliae*),'' Can. J. Zool. **74**, 1661–1672.
Tyack, P. L. (**1981**). ''Interactions between singing Hawaiian humpback whales and conspecifics nearby,'' Behav. Ecol. Sociobiol. **8**, 105–116.
Tyack, P. L. (**1983**). ''Differential response of humpback whales, *Megaptera novaeangliae*, to playback of song or social sounds,'' Behav. Ecol. Sociobiol. **13**, 49–55.
Welch, A. M., Semlitsch, R. D., and Gerhardt, H. C. (**1998**). ''Call duration as an indicator of genetic quality in male gray tree frogs,'' Science **280**, 1928–1930.
Winn, H. E., and Winn, L. K. (**1978**). ''The song of the humpback whale (*Megaptera novaeangliae*) in the West Indies,'' Mar. Biol. (Berlin) **47**, 97–114.

Temporary threshold shifts and recovery following noise exposure in the Atlantic bottlenosed dolphin (*Tursiops truncatus*)

Paul E. Nachtigall,[a] Jeffrey L. Pawloski, and Whitlow W. L. Au
Marine Mammal Research Program, Hawaii Institute of Marine Biology, University of Hawaii, P.O. Box 1106, Kailua, Hawaii 96734

(Received 20 September 2002; revised 28 February 2003; accepted 10 March 2003)

Behaviorally determined hearing thresholds for a 7.5-kHz tone for an Atlantic bottlenosed dolphin (*Tursiops truncatus*) were obtained following exposure to fatiguing low-frequency octave band noise. The fatiguing stimulus ranged from 4 to 11 kHz and was gradually increased in intensity to 179 dB *re* 1 μPa and in duration to 55 min. Exposures occurred no more frequently than once per week. Measured temporary threshold shifts averaged 11 dB. Threshold determination took at least 20 min. Recovery was examined 360, 180, 90, and 45 min following exposure and was essentially complete within 45 min. © *2003 Acoustical Society of America.* [DOI: 10.1121/1.1570438]

PACS numbers: 43.80.Nd, 43.80.Lb [FD]

I. INTRODUCTION

Some odontocete cetaceans, particularly the bottlenosed dolphin, produce very intense echolocation signals (source levels up to 225 dB *re* 1 μPa) that are very brief (about 70 μs) but are emitted in trains that can last well over a second. The frequencies of the clicks are very broadband (Q between 2 and 3) with peak frequencies that may extend from 40 to 130 kHz (Au *et al.*, 1974; Nachtigall and Moore, 1988; Au, 1993). At the same time the echoes coming back from high-intensity broadband clicks may be relatively low. Social sounds produced by dolphins by slapping flukes on the water, jaw clapping, and breaching have lower peak-to-peak amplitude but are much longer than ecolocation clicks and therefore have more energy (Finneran *et al.*, 2000; Nachtigall *et al.*, 2000b). Odontocete cetaceans have very sensitive hearing systems (Nachtigall *et al.*, 2000a) yet they must deal with high sound intensity from sound produced by conspecifics and sound they produce themselves.

Human hearing is affected by exposure to noise. If a very high level of noise is heard for an extended period of time, hearing can be permanently damaged. Exposure to intense noise for a limited period of time can result in a temporary reduction in hearing ability termed the temporary threshold shift. The amplitude of the noise, the frequency of the noise, and the length of exposure can all influence the amount of hearing reduction and whether it is permanent or temporary (Melnick, 1991). There is a growing concern about the effects of anthropogenic acoustic energy on the hearing and behavior of marine mammals exposed to noise in the oceans (Richardson *et al.*, 1995). This concern interestingly parallels the concern about noise exposure in human workers. Government regulations are in place to protect the hearing of workers exposed to noise in order to avoid loss of hearing. Most all of the experimental work on human hearing loss does not lead to people losing their hearing, but rather relies on the examination of temporary threshold shifts (TTS) because . . . ''Studies of TTS still represent the only ethical method with sufficient control for developing information regarding the effects of noise on human hearing'' (Melnick, 1991, p. 152). Unfortunately, it is difficult to fully generalize the results on noise research on the auditory systems of air-adapted humans to marine echolocating dolphins (Richardson *et al.*, 1995; Wartzok and Ketten, 1999; Nachtigall *et al.*, 2000a). But, if one is concerned about the effects of noise on the hearing of odontocete cetaceans, the first logical question to ask is ''Does a temporary threshold shift occur in these animals?'' Results of Ridgway *et al.* (1997), Finneran *et al.* (2002) and Schlundt *et al.* (2000) indicate that bottlenosed dolphins (*Tursiops truncatus*) and belugas (*Delphinaperus leucas*) show temporary threshold shifts after a single very high intensity (near 200 dB *re* 1 μPa) one second (or shorter) exposure per day. Most studies of temporary threshold shifts in animals (Clark, 1991; Kastak *et al.*, 1999) and humans (Yost, 1994) are conducted with sound exposures longer than one second with typical exposures at lower levels on the order of hours or days (e.g., Mills *et al.*, 1979). Generally, there is a tradeoff between time and amplitude with lower amplitude sound exposures producing TTS after longer periods of exposure time.

The transitory nature of temporary threshold shift means that hearing completely recovers following the shift. The course and time of recovery generally depend on the amount of exposure to noise and the amount of shift incurred. Human college students exposed to octave band noise of various amplitudes took from 24 to 72 h to totally recover. Generally speaking, the greater the threshold shift, the longer the recovery period (Mills *et al.*, 1979). Students exposed to the highest noise level of 88 dB SPL in air reached an asymptote of shift within 1 h, were only exposed for 4 h, and yet took 72 h to fully recover. Carder and Miller (1972) found that chinchillas, which have audiograms similar to humans, demonstrated TTS after 60 min of exposure to intense noise but also took relatively longer to recover. Cetaceans have not previously been exposed to controlled noise for long time periods. Kastak *et al.* (1999) exposed sea lions, a harbor seal, and an elephant seal to 20–22 min of controlled noise, demonstrated a TTS, and showed complete recovery in 24 h. An earlier opportunistic study (Kastak and Schusterman, 1996) indicated that a harbor seal inadvertently exposed to broad-

[a]Electronic mail: nachtiga@hawaii.edu

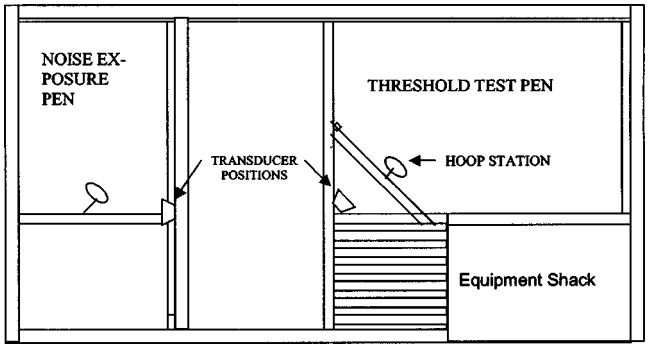

FIG. 1. Threshold testing and fatiguing noise pens.

band construction noise averaging 6 to 7 h per day for 6 days showed a temporary threshold shift.

The purpose of this study was to (1) examine the hearing thresholds of an Atlantic bottlenosed dolphin exposed to lower amplitudes but longer duration of noise than those previously presented by Finneran *et al.* (2002) and Schlundt *et al.* (2000) in order to estimate the exposure level and time required to induce TTS, and (2) to measure recovery time following a temporary threshold shift.

II. METHODS AND MATERIALS

A. Subject

The subject used in this experiment was Boris, a 12-year-old male Atlantic bottlenosed dolphin (*Tursiops truncatus*) born in the breeding colony at the marine mammal research facility in Kaneohe Bay off the island of Oahu. Threshold testing was conducted in the bay pens of the Hawaii Institute of Marine Biology moored off of Coconut Island in Kaneohe Bay. The pen complex, in which the animal was housed, measured 64×12.2 m^2 and floated in waters about 12 m deep.

B. Equipment and procedure

1. Behavioral hearing thresholds

Behavioral thresholds were obtained using a staircase procedure based on the animal's behavior in response to presented pure tone stimuli. The animal was trained to station in a padded circular metal hoop 1 m under water attached via an extension to a 4×4-in. piece of wood extended across the pen floating structure (Fig. 1). The hoop was placed so that the animal was at a fixed position 2 m in front of the projecting Massa TR-61A transducer. The hoop was positioned so as to align the center of the subject's lower jaw with the center of the sound source of the projecting transducer. Both the transducer and the hoop were positioned underwater at a depth of approximately 1 m. An acoustic baffle was located midway between the transducer and the hoop. The baffle, constructed of aluminum, measured $61\times46\times1.6$ cm with a layer of cork on the side facing the projecting hydrophone. The baffle reduced sound variability by blocking the surface reflected path between the transmitter and the receiver. The animal's thresholds for a 7.5-kHz outgoing sinusoidal signal were repeatedly tested. The transducer was calibrated using a receiving Naval Research laboratory H-52 hydrophone mounted in the hoop in a position corresponding to the animals lower jaw. The pure tone outgoing signal was produced using a QuaTech WSB-10 board installed in a Compaq Portable 33 personal computer. The signal was then fed into a signal shaping box that included a 1-dB step attenuator and a remote controller that was used to initiate the trial sequence and the trial condition. The 3-s-long tone-burst signal was turned on and off gradually with a linear rise and fall time of 160 ms and fed directly into the projecting transducer. The outgoing amplitude was initially set using the computer-driven signal-generating system in which the amplifier input voltage was regulated to precise levels. Generally, voltages were set so as to achieve an initial SPL at the hoop that was 20–30 dB above the hearing threshold. This level was determined by performing a quick preliminary staircase procedure to bracket the SPL of interest.

The animal's initial position for each trial was at the side of the pen with its snout touching a sponge styrofoam pad. Upon receiving a 7-kHz 1-s signal the animal left the stationing pad and swam into the hoop. The animal was trained on a go/no-go procedure to leave the hoop and press a small styrofoam response ball attached to a wand in the air above the hoop when a sound was detected and to remain in the hoop if no sound was presented. Equal numbers of sound present and sound absent trials were presented in a random series with Gellermann (1933) constraints. All correct responses were reinforced with a fish and a conditioned whistle reinforcer. The whistle was blown immediately after the animal pressed the response ball on sound present trials and 5 s after holding in the hoop on sound absent trials. Each threshold determination session began with the sound amplitude at a predetermined comfortable, easily heard, level. Using the staircase procedure the sound level was reduced by 2 dB following each correct sound-present response until an error (miss) was made. Following the error, the amplitude of the sound on next sound-present trial was increased by 2 dB until the animal correctly reported its presence. Thresholds were calculated based on the sound amplitude levels during five of these reversals. A preliminary test showed that the thresholds obtained with five reversals were not significantly different from those obtained with ten reversals. The animal's threshold was determined each test day.

2. Fatiguing noise

The fatiguing noise was generated with a Micronetics NZG-5-500K solid state noise generator integrated circuit chip that produced white noise out to a frequency of 500 kHz. The noise IC chip was housed in a chassis that also contained a rotary attenuator to control the output level. The output of the noise chassis was connected to an Ithaco 4210 filter-amplifier having a 24 dB per octave roll-off. The output of the Ithaco filter-amplifier was connected to a Khron Hite 3500 bandpass filter also having a roll-off of 24 dB per octave. A Hafler P3000 Transnova power amplifier was then used to drive a Massa TR-61A transducer to project the fatiguing noise. The noise spectral density of the fatiguing signal measured with a hydrophone located at the center of the hoop for a 0-dB noise attenuator position is shown in Fig. 2. The spectrum of the fatiguing noise was relatively flat be-

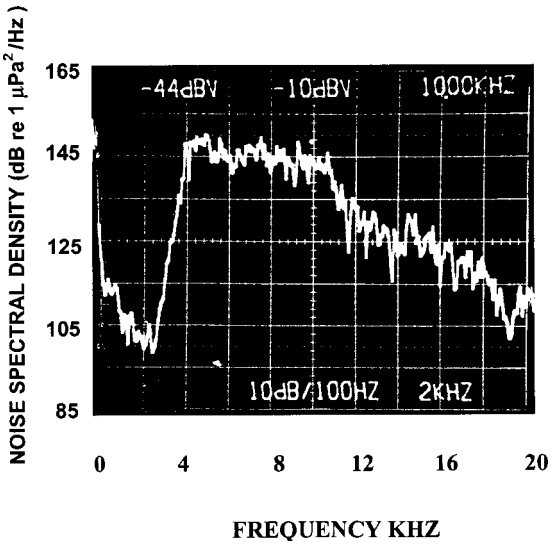

FIG. 2. Noise spectral density of fatiguing noise.

tween 4 and 11 kHz and fell off at a rate of 60 dB per octave for frequencies below 4 kHz and about 40 dB per octave for frequencies above 11 kHz.

3. Noise presentation

When starting this experiment little was known about the amount of energy required to produce temporary threshold shifts in bottlenosed dolphins. In order to provide safety for the dolphin, the fatiguing noise was only presented each time after 7 days of no noise presentation. Behavioral thresholds for the 7.5-kHz pure tone were obtained each day. On those days that the noise was to be presented the sessions began with a behavioral threshold test in the threshold test pen (see Fig. 1) followed by noise exposure in the noise exposure pen. The animal voluntarily swam to the noise exposure pen and positioned within the noise exposure hoop. That hoop positioned the animal 1 m under water and 2 m in front of the fatiguing noise transducer. Exposure times exceeded breath-holding times and the animal repeatedly swam back down into the hoop following each breath. The time that the animal was actually stationed within the hoop was limited to 30 min, but overall exposure time sometimes exceeded 55 min. After the animal surfaced it was given a fish reward and then directed to reenter the hoop. The animal would often delay reentering the hoop and stay either at the surface or at the side of the hoop as depicted in Fig. 3. The times at these two nonhoop positions were recorded for each trial. Each noise exposure session was followed by a return to the threshold test pen and a second behavioral threshold test to examine for TTS using the same behavioral procedure used to determine the baseline level prior to exposure. The fatiguing noise level and length of presentation were both gradually increased until a temporary threshold shift was obtained. Upon obtaining the first demonstrated shift, the fatiguing noise level was not increased but was presented at the same level once per week for an additional six times (6 weeks) with repeated baseline threshold determinations between exposure sessions.

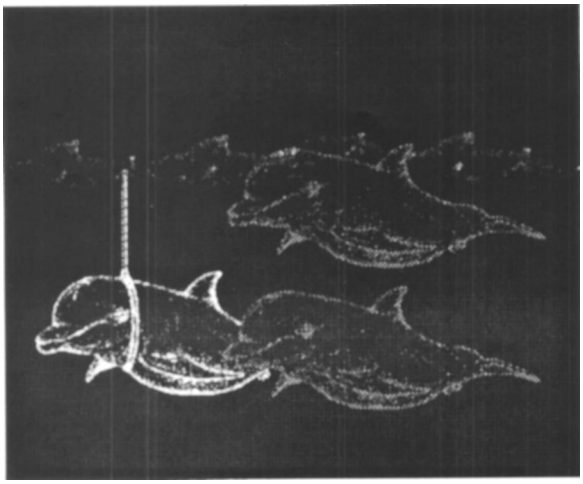

FIG. 3. Three positions taken by the dolphin during noise presentation. Calculation of overall noise spectral densities taken at these three positions.

4. Noise level determination

The fatiguing noise remained on until the animal spent 30 min within the hoop. The total acoustic energy that the animal was exposed to for each noise session was estimated by summing the acoustic energy at the three locations in Fig. 3. The noise spectral density was measured at the place of the animal's head in those three positions: (1) at the hoop, (2) at the side of the hoop, and (3) at the surface. We measured 30 min in the hoop and an average of 10 min at each of the other two positions per noise session. Measured noise spectral density at each of the two nonhoop positions is presented

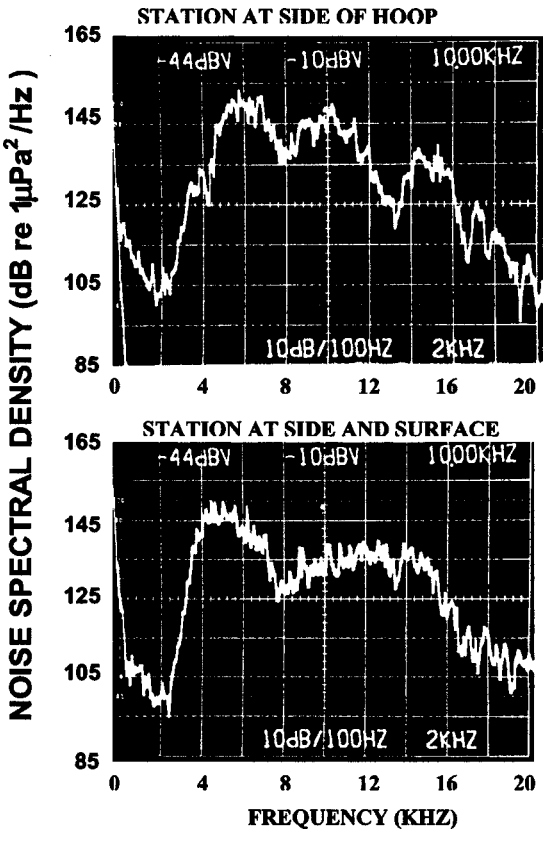

FIG. 4. Measured noise spectral density at the three positions.

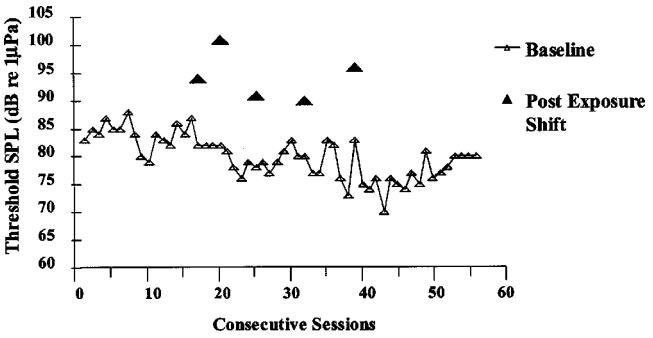

FIG. 5. Baseline threshold measures and postexposure temporary threshold shifts.

in Fig. 4. The spectra of the noise at the side of the hoop and at the surface were not flat because of surface reflected interference. The noise was also recorded on a Sony TD7 DAT recorder and then digitized at a sample rate of 44 kHz using a PC sound card in order to calculate the energy flux density at the three typical dolphin locations. Total energy received by the animal was summed as shown by the equation:

$$e_{\text{total}} = \int_0^{T_{hp}} p_{NH}^2(t)\, dt + \int_0^{T_{sd}} p_{NS}^2(t)\, dt + \int_0^{T_{ss}} P_{NSS}^2(t)\, dt,$$

$$E_{\text{total}} = 10 \text{ Log } (e_{\text{total}}) = 213 \text{ dB } re \text{ } 1 \text{ } \mu\text{Pa}^2\text{s},$$

where p_{NH} is the acoustic pressure of the noise measured at the hoop, p_{NS} is the acoustic pressure of the noise measured at the side of the hoop, and p_{NSS} is the acoustic pressure of the noise measured at the surface position of the dolphin. The noise level was measured at different times during the experiment and the results were essentially the same. Thus the fatiguing noise stimulus at the energy flux density of 213 dB *re* 1 μPa^2 s was received by the animal. This is essentially equivalent to a noise pressure level of 179 dB *re* 1 μPa for 50 min.

III. RESULTS

Immediately following the noise exposure the animal was returned to the threshold test pen to determine his threshold for the 7.5-kHz pure tone stimulus. The amplitude of the fatiguing noise was gradually increased during the once per week noise exposure sessions until a temporary threshold shift was measured. No shifts were obtained at 165 dB or 171 dB *re* 1 μPa, but when the fatiguing noise at 179 dB *re* 1 μPa was presented the animal showed the first temporary threshold shift of 10.4 dB above baseline. After each measured temporary threshold shift, a second behavioral threshold was measured after some period of time to examine recovery from the shift. Following full recovery without noise exposure, additional individual fatiguing sessions, separated by at least 4 days, were presented. Additional temporary threshold shifts of 18.8, 12.0, 2.0, 10.4, and 12.4 dB above baselines gathered just prior to the fatiguing noise were measured. Baseline threshold levels and the actual measured threshold shifts are provided in Fig. 5. Details of noise exposure times and shifts are provided in Table I.

Recovery apparently occurred rapidly. Second behavioral measures following 6 h, 3 h, 1.5 h and 45 min after the fatiguing noise showed no remnant of the shift. Full recovery therefore apparently occurred within the 45 min following noise exposure. Each threshold determination required at least 20 min.

IV. DISCUSSION

While it has long been known that dolphins produce high-intensity echolocation signals over 225 dB *re* 1 μPa (Au, 1980), and therefore must have some sort of ability to handle high peak intensity, brief sounds, the fact that no threshold shifts were observed until the animal had been exposed to 179 dB for nearly 50 min is not surprising. The sounds a dolphin receives, and their effect on its auditory system, need to be considered from an energy flux density perspective. The energy flux density in a single echolocation click having a peak-to-peak amplitude of 220 dB will only be about 167 dB *re* 1 μPa^2 s compared to the energy flux density of 213 dB in the fatiguing noise stimulus over a 50-min time period. Approximately 40 000 echolocation clicks would be needed in order to equal the energy flux density the dolphin received over a 50-min time period.

Schlundt *et al.* (2000) previously showed small temporary threshold shifts in belugas and bottlenosed dolphins when they were exposed to short 1-s fatiguing stimuli between 192 and 201 dB. Since their stimulus was over a 1-s

TABLE I. Exposure levels, thresholds, times, and recovery from shifts following delays.

Exposure level (dB)	165	171	179	179	179	179	179	179
Pre-exposure threshold (dB)	83	84	83	82	79	81	80	77
Post-exposure threshold (dB)	82	87	93	100	91	83	90	89
Shift (dB)	−1	3	10	18	12	2	10	12
Time in Hoop (min)	30	31	30	30	30	29	30	30
Minutes of exposure	41	44	54	49	47	52	48	50
Delay—minutes after exposure	NA	NA	NA	360	180	NA	90	45
Threshold following delay	NA	NA	NA	82	78	NA	80	78
Shift after delay				0	−1	NA	0	1

duration, the energy flux density is equal to the intensity (192–201 dB *re* 1 μPa^2 s). The upper limit of energy flux density of 201 dB is only 12 dB lower than the 213 dB and can be considered relatively consistent with our data if their small TTS of 6 dB is compared to a maximum of 18 dB TTS for our animal. Finneran *et al.* (2002) found that a beluga exhibited a 6-dB TTS when subjected to a short impulse from a water-gun having an energy flux density of only 186 but did not observe any TTS for a bottlenose dolphin exposed to same fatiguing stimulus at an energy flux density level of 188 dB. Perhaps the auditory system of the beluga is more sensitive to impulse sounds than bottlenose dolphins.

We also did not anticipate that recovery from an 11-dB shift would occur so rapidly. Given that it took roughly 20 min to obtain a behavioral threshold demonstrating that a shift had in fact occurred, by the time we had obtained the second threshold, at 45 min following the cessation of the fatiguing stimulus, the threshold had returned to the preexposure baseline levels. Finneran *et al.* (2002) found an even faster recovery time of 4 min after exposure to the brief impulse sound from the seismic watergun for the beluga. The auditory systems of the beluga and the bottlenose dolphin apparently have the capability to recover relatively rapidly from TTS.

Both Schlundt *et al.* (2000) and Finneran *et al.* (2002) working with whales and dolphins and Kastak *et al.* (1999) working with pinnipeds report that the animal's trained responses were disrupted by the fatiguing noise during temporary threshold shift experiments. Our animal also showed disruption of trained behaviors as the fatiguing noise was presented. This disruption may well indicate that the animals did not respond favorably to the fatiguing noise. Mills *et al.* (1981) reported that human subjects participating in TTS experiments show a manifestation of similar behavior . . . ''Invariably, the number of the subjects who fail to keep appointments increases as the experiment progresses'' (p. 393). While the reluctance of the animal to participate was overcome with additional training and patience, a subjective evaluation of the procedure would indicate that the animal did not appreciate the fatiguing noise.

In a summary paper on temporary threshold shifts, Ward (1997) cautioned that individual differences in the magnitude of temporary threshold shifts are substantial. Many experiments on the sensory systems of highly protected and valuable marine mammals are based on data from a single animal. These data are also from a single bottlenosed dolphin. Without additional measures it is impossible to know whether large individual differences among bottlenosed dolphins would be found. A conservative extrapolation based on data from other species would predict that bottlenosed dolphins will also show considerable individual differences in their susceptibility to fatiguing noise.

ACKNOWLEDGMENTS

This research was supported by a grant from the Office of Naval Research to Paul E. Nachtigall and Whitlow W. L. Au from Robert Gisiner, Award No. N00014-98-1-0687. Specific gratitude must be extended to the well-trained dolphin Boris, who, despite the ability to leave the noise situation, persevered and provided the data. This is Contribution No. 1138 from the Hawaii Institute of Marine Biology.

Au, W. W. L. (**1980**). ''Echolocation signals of the Atlantic bottlenose dolphin (*Tursiops truncatus*) in open waters,'' in *Animal Sonar Systems*, edited by J. F. Fish and R. G. Busnel (Plenum, New York).

Au, W. W. L. (**1993**). *The Sonar of Dolphins* (Springer-Verlag, New York).

Au, W. W. L., Floyd, R. W., Penner, R. H., and Murchison, A. E. (**1974**). ''Measurement of echolocation signals of the Atlantic bottlenose dolphin, *Tursiops truncatus Montagu*, in open waters,'' J. Acoust. Soc. Am. **56**, 1280–1290.

Carder, H. M., and Miller, J. D. (**1972**). ''Temporary threshold shifts from prolonged exposure to noise,'' J. Speech Hear. Res. **15**, 603–623.

Clark, W. W. (**1991**). ''Recent studies of temporary threshold shifts (TTS) and permanent threshold shifts (PTS) in animals,'' J. Acoust. Soc. Am. **90**, 155–163.

Finneran, J. J., Carder, D. A., Ridgway, S. H., and Schlundt, C. W. (**1999**). ''Technique for the generation and frequency compensation of bandlimited white noise and its application in studies of masked hearing thresholds.'' J. Acoust. Soc. Am. **106**, 2130(A).

Finneran, J. J., Oliver, C. W., Schaefer, K. M., and Ridgway, S. H. (**2000**). ''Source levels and estimated yellowfin tuna (*Thunnus albacares*) detection ranges for dolphin jaw pops, breaches, and tail slaps,'' J. Acoust. Soc. Am. **107**, 649–656.

Finneran, J. J., Schlundt, C. E., Dear, R., Carder, D. A., and Ridgway, S. H. (**2002**). ''Emporary shift in masked hearing thresholds in odontocetes after exposure to single under-water impulses from a seismic watergun,'' J. Acoust. Soc. Am. **111**, 2929–2940.

Gellermann, L. W. (**1933**). ''Chance orders of alternating stimuli in visual discrimination tasks,'' J. Genet. Psychol. **42**, 206–208.

Kastak, D., and Schusterman, R. J. (**1996**). ''Temporary threshold shift in a harbor seal (*Phoca vitulina*).'' J. Acoust. Soc. Am. **100**, 1905–1908.

Kastak, D., Schusterman, R. J., Southall, B. L., and Reichmuth, C. J. (**1999**). ''Underwater temporary threshold shift induced by octave-band noise in three species of pinniped,'' J. Acoust. Soc. Am. **106**, 1142–1148.

Melnick, W. (**1991**). ''Human temporary threshold shifts (TTS) and damage risk,'' J. Acoust. Soc. Am. **90**, 147–154.

Mills, J. H., Adkins, W. Y., and Gilbert, R. M. (**1981**). ''Temporary threshold shifts produced by wideband noise,'' J. Acoust. Soc. Am. **70**, 390–396.

Mills, J. H., Gilbert, R. M., and Adkins, W. Y. (**1979**). ''Temporary threshold shift in humans exposed to octave bands of noise for 16 to 24 hours,'' J. Acoust. Soc. Am. **65**, 1238–1248.

Nachtigall, P. E., and Moore, P. W. B. (**1988**). *Animal Sonar: Processes and Performance* (Plenum, New York).

Nachtigall, P. E., Lemonds, D. W., and Roitblat, H. L. (**2000a**). ''Psychoacoustic Studies of Dolphin and Whale Hearing,'' in *Hearing by Whales and Dolphins*, edited by W. W. L. Au, A. N. Popper, and R. R. Fay (Springer-Verlag, New York), pp. 330–363.

Nachtigall, P. E., Au, W. W. L., Pawloski, J. L., Andrews, K., and Oliver, C. W. (**2000b**). ''Measurements of the low frequency components of active and passive sounds produced by dolphins,'' Aquat. Mammals **26**(3), 167–175.

Richardson, W. J., Green, Jr., C. R., Malme, C. I., and Thomson, D. H. (**1995**). *Marine Mammals and Noise* (Academic, San Diego).

Ridgway, S. H., Carder, D. A., Smith, R. R., Kamolnick, T., Schlundt, C. E., and Elsberry, W. R. (**1997**). ''Behavioral responses and temporary shift in masked hearing threshold of bottlenosed dolphins *Tursiops truncatus*, to 1 second tones of 141 to 201 dB *re* 1 μPa,'' Technical Report No. 1751, Naval Command, Control and Ocean Surveillance Center, RDT&E Division, San Diego, CA.

Schlundt, C. E., Finneran, J. J., Carder, D. A., and Ridgway, S. H. (**2000**). ''Temporary shift in masked hearing thresholds of bottlenose dolphins, *Tursiops truncatus*, and white whales, *Delphinapterus leucas*, after exposure to intense tones,'' J. Acoust. Soc. Am. **107**, 3496–3508.

Ward, W. D. (**1997**). ''Effects of high-intensity sound,'' in *Encyclopedia of Acoustics V. III*, edited by Malcolm Crocker (Wiley, New York), pp. 1497–1508.

Wartzok, D., and Ketten, D. R. (**1999**). ''Marine Mammal Sensory Systems,'' in *Biology of Marine Mammals*, edited by J. E. Reynolds III and S. A. Rommel (Smithsonian Institution Press, Herndon, VA), pp. 117–175.

Yost, W. A. (**1994**). *Fundamentals of Hearing: An Introduction* (Academic, New York).

Statistics of ultrasonic scatterer size estimation with a reference phantom[a)]

Anthony Gerig,[b)] James Zagzebski, and Tomy Varghese
Department of Medical Physics, University of Wisconsin—Madison, 1300 University Avenue, Room 1530, Madison, Wisconsin 53706

(Received 12 September 2002; revised 23 February 2003; accepted 24 February 2003)

A theoretical expression for the variance of scatterer size estimates is derived for a modified least squares size estimator used in conjunction with a reference phantom method for backscatter coefficient measurement. A Gaussian spatial autocorrelation function is assumed. Simulations and phantom experiments were performed to verify the results for backscatter and size variances. The dependence of size estimate errors upon free experimental parameters is explored. Implications of the findings for the optimization of scatterer size estimation are discussed. The utility of scatterer size parametric imaging is examined through the signal to noise ratio comparison with standard ultrasonic B-mode imaging. © *2003 Acoustical Society of America.* [DOI: 10.1121/1.1568945]

PACS numbers: 43.80.Vj, 43.80.Qf [FD]

I. INTRODUCTION

The feasibility of estimating and imaging scatterer size using backscattered ultrasound signals and spectral analysis techniques has been thoroughly demonstrated over the past two decades.[1–6,16] Much of the early work in the field involved the use of single element transducers, although in subsequent years the work progressed to accommodate clinical transducers and systems through the development of novel techniques to account for echo signal system dependencies.[4,7,8] In many cases, size estimation, although computationally intensive, has proven to be useful for the monitoring, diagnosis, and study of disease.[3,4]

The following paper has two objectives. The first is to define the theoretical error associated with ultrasonic scatterer size estimation, and its dependence upon parameters that characterize both the measurement system and the insonified tissue. The results make the optimization of estimate error possible through the informed adjustment of free parameters. Others have investigated size estimation error in previous work.[9,10] Chaturvedi and Insana, in particular, have derived an expression for the variance of scatterer size estimates. However, the results assumed knowledge of both the instrumentation transfer function and the scattering strength of the insonified object. The following work extends their inquiry to a particularly simple and flexible method of scatterer size estimation.[4] A reference phantom is used to account for clinical system dependencies in backscatter estimation, and a modified least squares fit, which eliminates the need for knowledge of scattering strength, is used in size estimation. The second objective is to evaluate scatterer size imaging as a diagnostic tool through signal-to-noise ratio (SNR) comparison with standard B-mode imaging.

The following background section gives a brief introduction to scatterer size estimation using a reference phantom. The subsequent theory and verification sections derive and validate expressions for the error inherent in both backscatter coefficient measurement and size estimation. Finally, the discussion and conclusion sections explore the dependence of errors in size estimates upon experimental parameters, discuss the adjustment of free parameters to achieve error optimization, and outline implications for the diagnostic utility of scatterer size imaging.

II. BACKGROUND—SIZE ESTIMATION METHOD

Size estimation, for the purposes of this paper, is accomplished by performing a modified least squares fit between a measured backscatter coefficient for a tissue segment, and a theoretical backscatter coefficient, which is dependent upon tissue/scatterer properties including size. The scatterer size estimate, $\hat{a}$, is given by

$$\hat{a} = \arg\min \frac{1}{n} \sum_{\omega_{\min}}^{\omega_{\max}} [\psi(\omega,\hat{a}) - \overline{\psi}(\hat{a})]^2 \tag{1a}$$

where

$$\psi(\omega,\hat{a}) = 10\ln[\mathrm{BSC}_s(\omega)] - 10\ln[\mathrm{BSC}_t(\omega)] \tag{1b}$$

and

$$\overline{\psi}(\hat{a}) = \frac{1}{n} \sum_{\omega_{\min}}^{\omega_{\max}} \psi(\omega,\hat{a}). \tag{1c}$$

The summation is over the usable bandwidth of the backscatter coefficient measurement [BSC(ω)], ω represents angular frequency, and the subscripts s and t refer to measured sample and theoretical model values, respectively. Unlike the standard least squares fitting technique, this method is insensitive to differences between measured and theoretical values by a multiplicative constant, and therefore requires no knowledge of tissue scattering strength for accurate size estimation.[6]

A reference phantom method is used for backscatter estimation.[4,8,18] Backscatter coefficients are calculated according to

[a)]Presented as "Statistics of scatterer size estimation," *Symposium on Ultrasonic Imaging and Tissue Characterization*, Arlington, VA, June 2002.
[b)]Author to whom correspondence should be addressed. Electronic mail: algerig@wisc.edu

 0001-4966/2003/113(6)/3430/8/$19.00

$$\hat{\mathrm{BSC}}_s(\omega)=\frac{\overline{|S_s(\omega)|^2}}{\overline{|S_r(\omega)|^2}}\mathrm{BSC}_r(\omega)\exp\{4z[\alpha_s(\omega)-\alpha_r(\omega)]\}, \quad (2)$$

where $|S(\omega)|^2$ is the power spectrum for a gated rf signal from a segment of the scattering medium, z is the depth of that segment, and the α 's are attenuation coefficients. The bars represent spatial averages, and the subscripts s and r represent the sample and reference media, respectively. Reference media can be of any type, given that the backscatter coefficient is known and that scattering is incoherent. This method yields accurate results given that the distance from the transducer to the interrogated medium segment is larger than both the size of the active transducer face, and the effective width of the medium spatial autocorrelation function (SAF).[8] System settings must also remain unchanged between reference and sample data acquisition.

The theoretical backscatter coefficient values required for Eq. (1) can be obtained as a function of scatterer size using

$$\mathrm{BSC}(k)=Ck^4\int_{-\infty}^{\infty}b_\gamma(\Delta\mathbf{r})e^{-i2\mathbf{k}\cdot\Delta\mathbf{r}}d\Delta\mathbf{r}, \quad (3)$$

which is valid for sparse media when scattering is weak, and shear wave effects are negligible.[6,11] C is a function of tissue properties and is constant with frequency. $\mathbf{k}$ is the scattering vector, which has magnitude $k=$ wave number and points in the direction of insonification. $b_\gamma(\Delta\mathbf{r})$ is the correlation coefficient of the medium SAF, which is assumed to be statistically stationary and is defined according to $E\{\gamma(\mathbf{r}+\Delta\mathbf{r}),\gamma(\mathbf{r})\}=E\{\gamma^2(\mathbf{r})\}b_\gamma(\Delta\mathbf{r})$. $\gamma(\mathbf{r})$ is the reflectivity of the medium at $\mathbf{r}$, and is a function of the fluctuation in material acoustic properties at that location, $\gamma(\mathbf{r})=(\kappa(\mathbf{r})-\kappa_0)/\kappa_0-(\rho(\mathbf{r})-\rho_0)/\rho(\mathbf{r})$. κ and ρ are compressibility and density, respectively, and κ_0 and ρ_0 are their corresponding mean values for the medium.

For random media with a single dominant scatterer type, the integral of the correlation coefficient can be properly associated with scatterer volume. As a result, an effective scatterer size can be related to the characteristic dimension of the medium correlation coefficient by equating the volume of a sphere to the coefficient integral.[6,11] Throughout the remainder of this paper, only sample media whose correlation coefficients are adequately described by an isotropic Gaussian function will be addressed.[5,6] Thus,

$$b_\gamma(\Delta r)=e^{-\Delta r^2/2d^2}, \quad (4)$$

where the following describes the relationship between effective scatterer radius and the characteristic dimension of the correlation coefficient, d:

$$2a=(12\sqrt{2\pi})^{1/3}d\approx 3.1d=d_1d. \quad (5)$$

The backscatter coefficient for such a medium is given by

$$\mathrm{BSC}(k)=C'k^4e^{-2k^2d^2}, \quad (6)$$

where the frequency dependence is determined solely by effective scatterer size. It is this property, which, in conjunction with the use of the modified least squares fitting technique outlined in Eq. (1), permits size estimation without knowledge of other descriptive parameters for the insonified medium.

III. THEORY

Before calculating the expected error in size estimates for the procedure outlined above, it is necessary to derive an expression for the variance of BSC estimates obtained using the reference phantom method. Neglecting windowing effects and assuming that both sample and reference spectra are estimated using a periodogram, spectra variances are given by[9]

$$\mathrm{var}(\hat{S}(k))\approx S(k)^2. \quad (7)$$

$S(k)$ is an arbitrary power spectrum, and k is the wave number. Given this result and Eq. (2), the variance of the backscatter estimates can be evaluated using[12]

$$\mathrm{var}(\hat{\mathrm{BSC}}_s(k))\approx\left(\frac{\partial(\hat{\mathrm{BSC}}_s(k))}{\partial(\overline{S_s(k)})}\right)^2\mathrm{var}(\overline{S_s(k)})+\left(\frac{\partial(\hat{\mathrm{BSC}}_s(k))}{\partial(\overline{S_r(k)})}\right)^2\mathrm{var}(\overline{S_r(k)}), \quad (8)$$

where $\overline{S_s(k)}$ and $\overline{S_r(k)}$ are independent. Calculating the partial derivatives at expected values, and assuming that the individual power spectra used to obtain the sample and reference averages are independent, yields

$$\mathrm{var}(\hat{\mathrm{BSC}}_s(k))\approx\left[\frac{1}{S_r(k)}\mathrm{BSC}_r(k)e^{4(\alpha_s-\alpha_r)z}\right]^2\frac{1}{N_s}S_s^2(k)+\left[\frac{S_s(k)}{S_r^2(k)}\mathrm{BSC}_r(k)e^{4(\alpha_s-\alpha_r)z}\right]^2\frac{1}{N_r}S_r^2(k), \quad (9)$$

where N_s and N_r represent the number of sample and reference waveforms used to calculate the spectral averages, respectively. Finally, substituting

$$S(k)=|G(k)|^2\mathrm{BSC}(k)e^{-4\alpha z}, \quad (10)$$

where $|G(k)|^2$ is the system transfer function, gives

$$\mathrm{var}(\hat{\mathrm{BSC}}_s(k))\approx\left(\frac{N_s+N_r}{N_sN_r}\right)\mathrm{BSC}_s^2(k). \quad (11)$$

According to this result, the standard deviation of backscatter estimates should be both proportional to the backscatter coefficient itself, and inversely proportional to the square root of the number of data segments used to generate those estimates. Note that Eq. (11) is nearly identical to the result derived by Chaturvedi *et al.*,[9] but contains the additional leading factor, which accounts for both imperfect knowledge of the reference power spectrum, and the possibility of the availability and utilization of multiple sample power spectra.

Solving Eq. (1) for estimated scatterer size, assuming a Gaussian correlation coefficient and using a standard calculus minimax approach,[17] yields

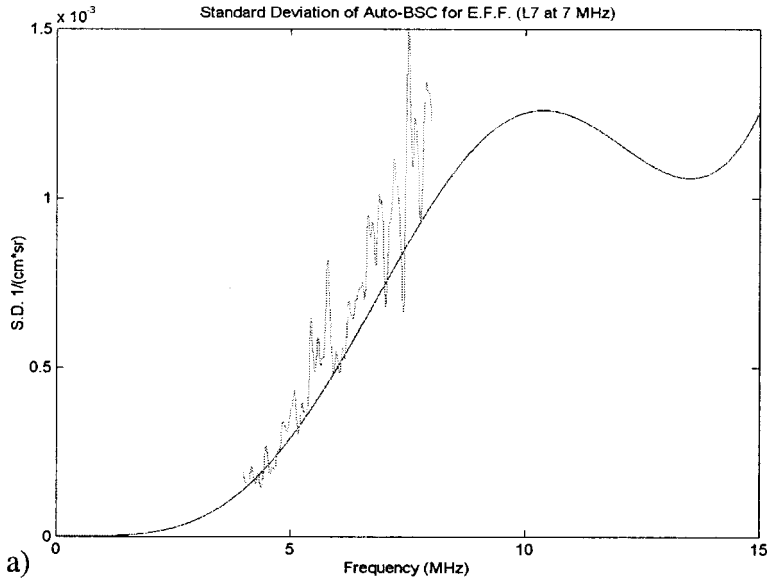

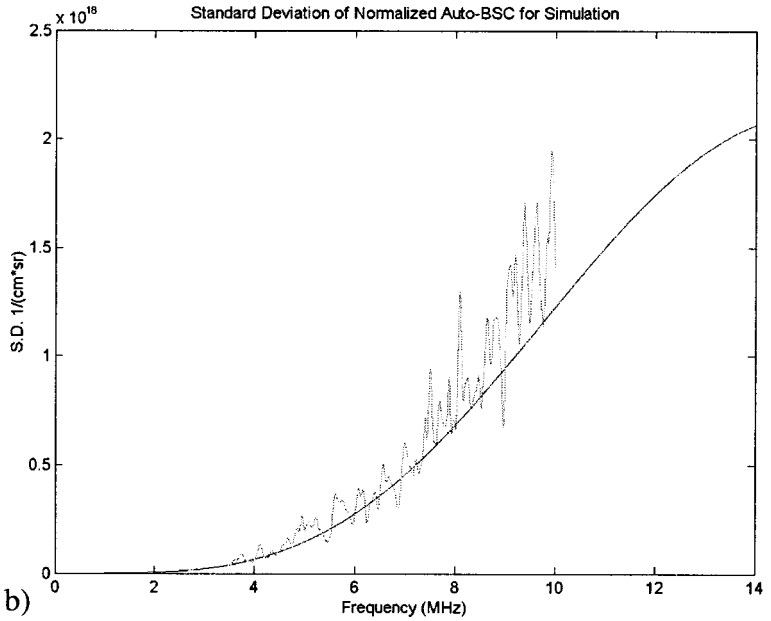

FIG. 1. Theoretical and experimental standard deviations of backscatter coefficient estimates for a tissue-mimicking phantom containing glass beads (a) and a simulated phantom containing scatterers with a Gaussian spatial autocorrelation function (b). The term Auto-BSC indicates that backscatter estimates were generated using reference and sample waveforms from the same phantom.

$$\hat{a}^2 = \frac{-d_1^2 c^2}{80} \frac{\Sigma_{\omega_{\min}}^{\omega_{\max}} (y(\omega)\omega^2 - \overline{y}\,\overline{\omega^2})}{\Sigma_{\omega_{\min}}^{\omega_{\max}} (\omega^2 - \overline{\omega^2})^2}, \tag{12}$$

where $y(\omega) = 10 \ln(\mathrm{BSC}(\omega)/\omega^4)$, c is the speed of sound, and d_1 remains from Eq. (5). For real values of scatterer size, using[12]

$$\mathrm{var}(\hat{a}) \approx \sum_{\omega_{\min}}^{\omega_{\max}} \left(\frac{\partial \hat{a}}{\partial\, \mathrm{BSC}(\omega)} \right)^2_{\mathrm{BSC}(\omega,\hat{a})} \mathrm{var}(\mathrm{BSC}(\omega)), \tag{13}$$

in conjunction with Eqs. (12) and (11) yields

$$\mathrm{var}(\hat{a}) \approx \frac{c^4 d_1^4}{16^2 \hat{a}^2} \left(\frac{N_s + N_r}{N_s N_r} \right) \sum_{\omega_{\min}}^{\omega_{\max}} \left[\frac{\omega^2 - \overline{\omega^2}}{\Sigma_{\omega_{\min}}^{\omega_{\max}} (\omega^2 - \overline{\omega^2})^2} \right]^2, \tag{14}$$

where the summation is limited to frequencies for which the associated backscatter estimates are uncorrelated. When the reference phantom method, in particular, is used to estimate backscatter over a frequency band, the interval between uncorrelated estimates is a function of data window type, and is inversely proportional to window length. Note that this approximation is valid for any particular experimental case, given that the probability for obtaining imaginary size estimates is low, and that size estimates are unbiased.

IV. EXPERIMENTAL VERIFICATION

A. Frequency dependence of backscatter variance

The frequency dependence of Eq. (11) was verified using both simulated rf waveforms, and experimentally derived signals obtained from an agar phantom. The phantom con-

tained spherical glass scatterers of mean diameter 48 μm and standard deviation 6.8 μm, distributed randomly with a density of 1.36 g/L (approximately 10 000 scatterers/cm^3). The speed of sound and attenuation for the phantom, both measured using a narrow-band substitution technique, were 1490 m/s and 0.5 dB/cm/MHz, respectively. The agar density was calculated to be 1.04 g/cm^3. Thirty independent planes of phantom data were acquired using an Acuson 128 XP and L7 linear array transducer operating at 7 MHz. System settings remained unchanged throughout the data collection procedure. The rf echo signals were digitized with a Gage Applied Science (Canada) A/D converter and PC. Data were collected with 12-bit resolution and at a sampling rate of 50 MHz.

Eleven independent planes of simulated rf data were generated for a random distribution of Gaussian SAF scatterers (4000/cm^3) with effective diameters of 50 μm. To accomplish this, the scattered pressure amplitudes at each frequency for simulated pointlike scatterers were modified by multiplication with the square root of the form factor for a Gaussian SAF, $e^{-k^2d^2}$, where d is related to the scatterer size through Eq. (5). The phantom speed of sound was set to 1490 m/s and the attenuation to zero.[15] The simulated transducer was a 300-line linear array operating at 7 MHz with a 50 mm focal length and 100% bandwidth, which could be artificially reduced during processing. The data acquisition rate was 38 MHz (a value determined by the simulation code).

Backscatter estimates for both the agar and simulated phantoms were generated according to the reference phantom method outlined in Sec. II. In both cases, the reference and sample phantoms were identical, eliminating the need for an attenuation correction term in Eq. (2). Power spectral estimates for each waveform were calculated using a 1 cm Hanning windowed segment centered about the transducer transmit focus (3.5 cm for the L7, 5 cm for the simulation). Spectral averaging for each transducer line was done over independent planes. Fifteen reference and sample planes were used for the agar phantom estimates, and one sample and ten reference planes for the simulation estimates. Standard deviation estimates at each frequency were made using the backscatter estimates obtained for each of the transducer lines (220 for the L7, 300 for the simulated transducer).

Results are plotted in Fig. 1. Theoretical values were calculated using Eq. (11), where the known backscatter coefficient originates from Faran's theory[13] for the agar/glass phantom, and the SAF input for the simulation. Agreement between theoretical and experimental values for both cases appears to be good over the bandwidth of the transducer used. The slight bias at higher frequencies is a result of backscatter estimate bias, which, in turn, is due to the inherent noise in the reference spectral estimates. Including additional reference spectral estimates in the spatial averaging of Eq. (2) reduces this effect.

B. Dependence of backscatter variance upon the number of spectral estimates

Log transformation of both the standard deviation for backscatter estimates and the number of spectra used to generate those estimates in Eq. (11), assuming equal numbers of reference and sample waveforms, yields

$$\log\{\mathrm{std}[\hat{\mathrm{BSC}}(k,N)]\} = -\tfrac{1}{2}\log(N) + C(k).$$

According to this equation, the relationship between the two transformed values is a linear one defined by a slope of negative one-half. This was verified experimentally using the same phantom data and signal processing method described above. Standard deviation estimates, however, were generated using variable numbers of sample and reference waveforms ($N_s = N_r = N = 5-15$). The slope of the linear least squares fit to the log of standard deviation estimates versus the log of the number of spectra used in generating those estimates was calculated for each frequency resulting from

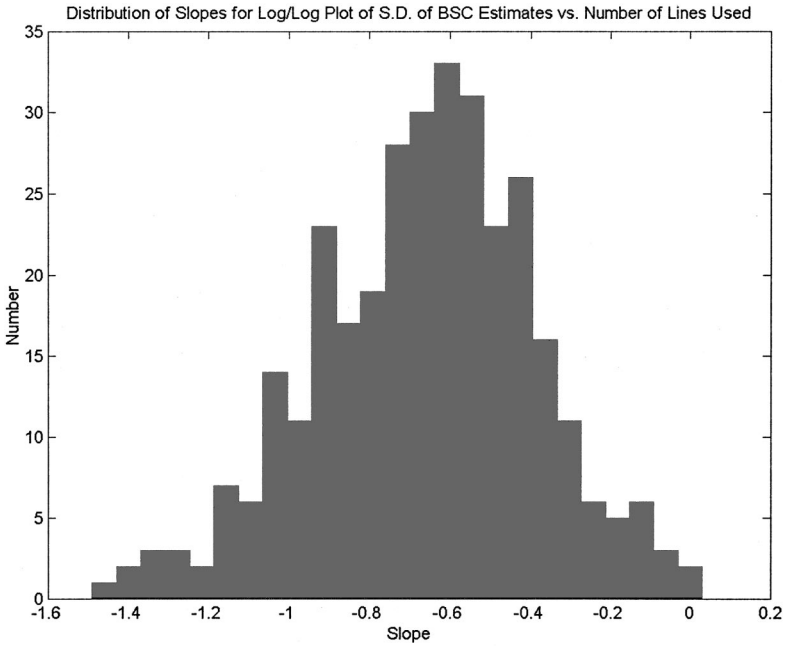

FIG. 2. Histogram of linear regression slopes (each obtained at a different frequency) for the log of the standard deviation of backscatter coefficient estimates as a function of the log of the number of A lines used to generate those estimates.

the discrete Fourier transform of the rf data over the bandwidth of the L7 transducer. A histogram of those slopes is plotted in Fig. 2. Note that the approximate center of the distribution is negative one-half, as theory predicts.

C. Size variance

The validity and accuracy of Eq. (14) were tested using the simulated waveforms described in Sec. IV A, with the inclusion of waveforms from several additional independent planes. Windowed data segments used in backscatter estimation were again centered about the transmit focus of the transducer (5 cm for simulated data). Size estimates were obtained using the method outlined in Eq. (1), with the modified sum of squares value being calculated for a restricted range of possible scatterer sizes (diameter=1–300 μm in intervals of one micron). As a result, imaginary size estimates were excluded. Standard deviation estimates were generated using 300 partially correlated size estimates corresponding to the number of lines produced by the simulated linear transducer. Note that all estimated backscatter values, including correlated ones, were used in size estimation.

Figure 3(a) displays both theoretical and experimental results for the standard deviation of size estimates as a function of the bandwidth used to produce those size estimates. Ten reference and one sample waveform segments (eleven independent planes of data total), each one cm in length, were used to generate the necessary backscatter estimates. The theoretical result was calculated using Eq. (14). The frequency interval for which uncorrelated backscatter estimates could be obtained was determined experimentally by estimating the correlation of those estimates, and found to be approximately 2.4/T for complete decorrelation, where *T* corresponds to the length of the Hanning window used in units of time. The resulting number of uncorrelated frequencies included in the summation of Eq. (14) as a function of bandwidth was noticeably steplike, leading to the discontinuities evident in the theoretical curve. With the exception of the estimate at 3 MHz, the experimental and theoretical results agree well. The most likely explanation for the poor agreement at low bandwidths is that imaginary estimates would typically play a dominant role in this region for scatterers of this size. As a result, the conditions for the validity of Eq. (14) are not met, and the experimental standard deviation is artificially limited by the exclusion of imaginary estimates.

Figure 3(b) shows similar results for a fixed bandwidth of 6 MHz, but a variable number of sample waveforms. Ten reference waveforms were used throughout. Again, theoretical and experimental results agree fairly well.

Finally, Fig. 3(c) contains results for a fixed bandwidth of 6 MHz, a fixed number of waveforms (10 reference and 1 sample), and a variable data window length. The theoretical and experimental results agree well for larger window sizes. For lengths shorter than 4 cm, the results diverge for what is likely the same reason they do so in Fig. 3(a) for shorter bandwidths, namely that imaginary estimates typically become more prevalent as the standard deviation for estimation approaches the scatterer diameter value. Equation (14) therefore ceases to be valid, and the experimental standard deviation is limited.

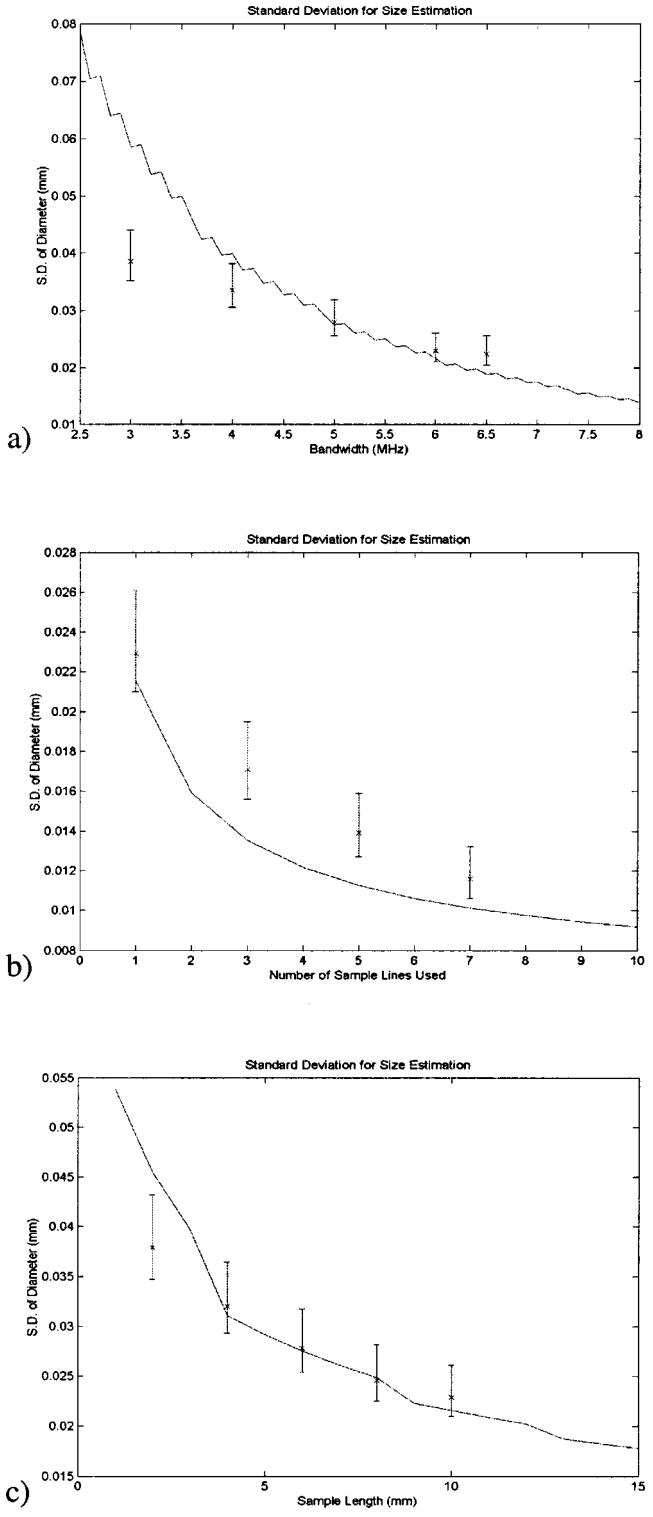

FIG. 3. Theoretical predictions and experimental results for the standard deviation of scatterer size estimates as a function of transducer bandwidth (a), the number of sample A lines used (b), and A-line length (c). Error bars are located approximately at alpha=0.5.

V. DISCUSSION

A. Optimization

Given the demonstrated accuracy and applicability of Eq. (14), it becomes possible to use the equation to optimize

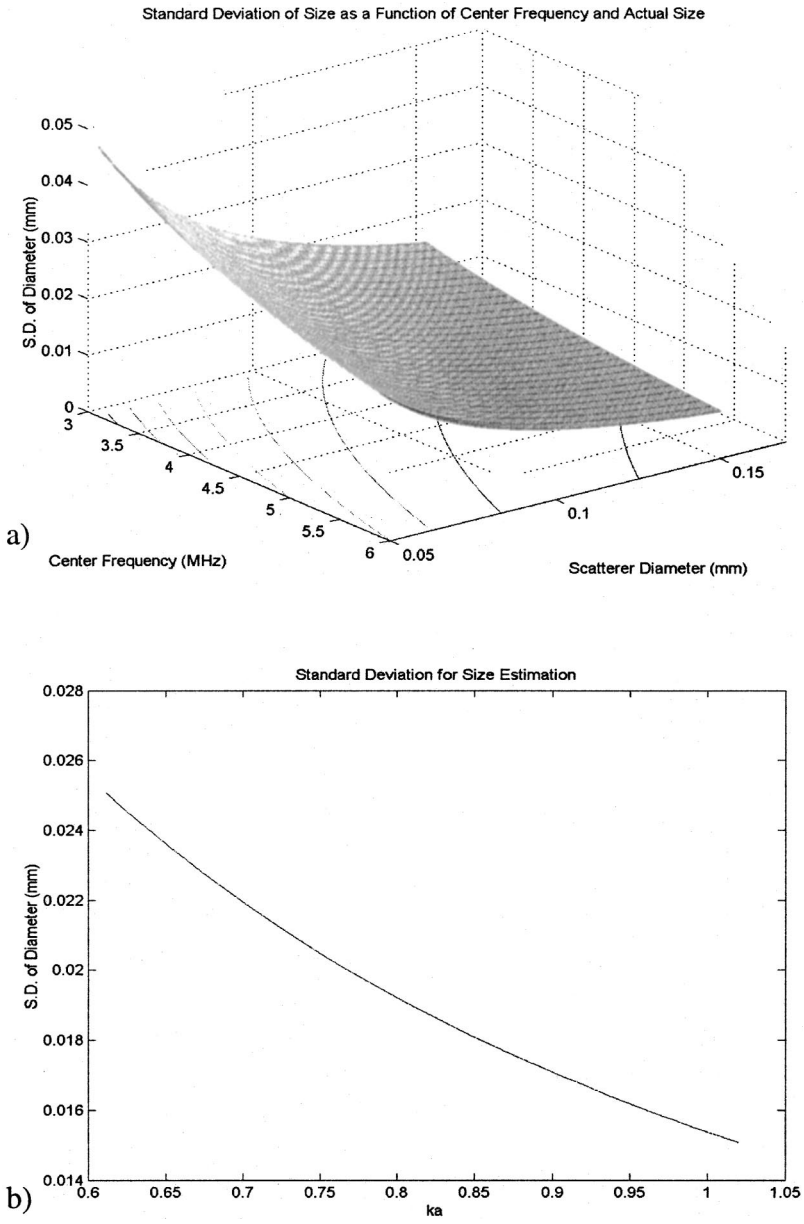

FIG. 4. Mesh and contour plots of the theoretical standard deviation of scatterer size estimates as a function of transducer center frequency and actual scatterer size (a). (b) displays standard deviation as a function of the product of the two parameters.

experimental parameters for the minimization of uncertainty in size estimates. As is obvious from Fig. 3, monotonic decreases in standard deviation are associated with increases in transducer bandwidth, the number of independent sample (and reference) waveforms used to generate backscatter estimates, and window length. Increases in the first of these are limited by the capabilities of the imaging system. Changes in the second are generally restricted both by the inherent resolution of the system, and the desired resolution of the scatterer size image. Finally, the window length is constrained by the desired axial resolution of the resultant image.

Two parameters remain in Eq. (14). The first of these is transducer center frequency, and the second is actual scatterer size. Figure 4(a) displays estimate standard deviation as a function of both parameters for a bandwidth of 6 MHz, a window length of 1 cm, a single sample waveform, and ten reference waveforms. Below the mesh plot of standard deviation is a contour plot of the same, the isobars of which correspond approximately to constant values of the product of the two independent variables. As a result of this correspondence, the dependence of Eq. (14) upon the two separate parameters appears to reduce to a dependence upon one, namely *ka*, where *k* is the wave number corresponding to the center frequency value, and *a* the actual scatterer radius. Figure 4(b) illustrates the dependence of the standard deviation upon *ka* for a 6 MHz bandwidth, a 1 cm window, one sample waveform, and ten reference waveforms. Because the standard deviation is inversely proportional to *ka*, optimization would entail size estimation at high frequencies. However, failure of the Gaussian SAF to appropriately model scatterer behavior at high frequencies places an upper limit upon *ka* of approximately 1.2. At frequencies above this limit, shear wave and resonance effects, which are not included in the scattering model, become appreciable.[2,6,11]

B. Evaluation

To evaluate size estimation, and the method outlined in this paper in particular, as a diagnostic aid, the SNR for a

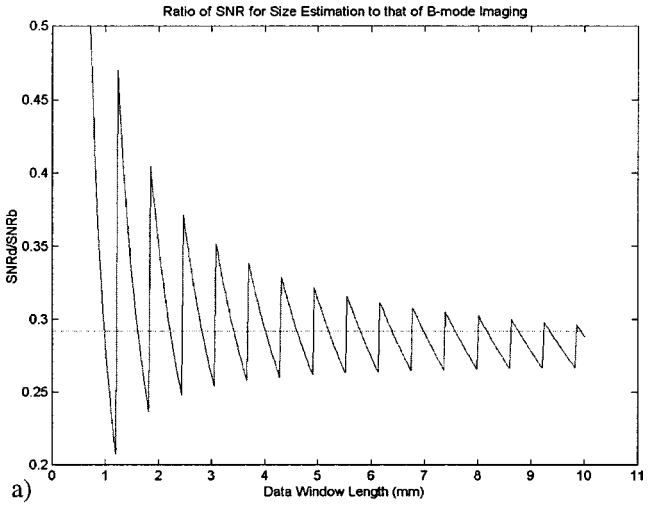

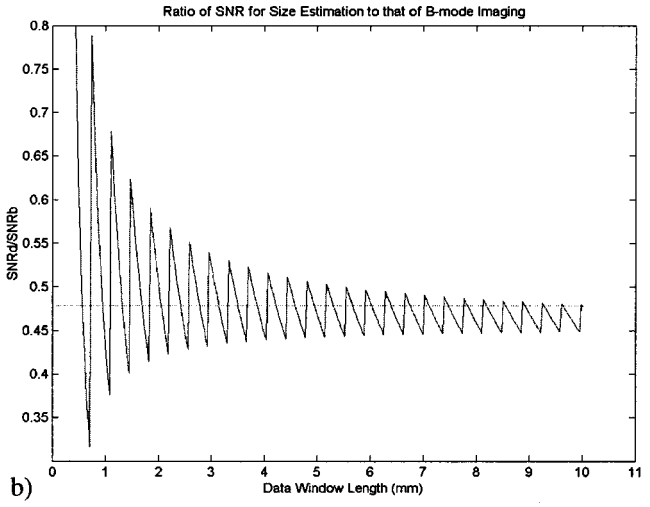

FIG. 5. Ratios of the theoretical signal-to-noise for size estimation to that of B-mode imaging for bandwidths of 3 MHz (a) and 5 MHz (b). A horizontal line is located at the mean value of the ratio over the plotted function domain in each case.

parametric image of size was compared to that for a standard B-mode image of identical resolution. The SNR for the scatterer size image was defined as

$$\mathrm{SNR}_d = \frac{E(\hat{D})}{\mathrm{std}(\hat{D})}, \tag{15}$$

where $E(\hat{D})$ and $\mathrm{std}(\hat{D})$ are the expected value and standard deviation of the size estimator, respectively. The SNR for a B-mode image with fully developed speckle is

$$\mathrm{SNR}_b = 1.91\sqrt{\frac{T}{C_z}}, \tag{16a}$$

where 1.91 is the SNR for a single resolution cell, and the square root factor corrects for differences in axial resolution between the two image types. T is the window length used in size estimation, C_z is the axial length of a resolution cell, and their quotient is the number of uncorrelated cells contained within a single window. C_z is related to the bandwidth of the insonifying transducer and is approximated by[14]

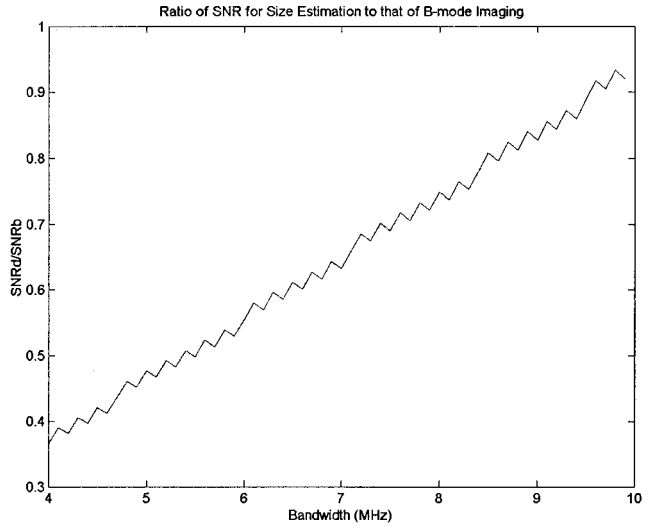

FIG. 6. Ratio of the theoretical signal to noise for size estimation to that of B-mode imaging as a function of transducer bandwidth.

$$C_z = \frac{0.9}{\mathrm{FWHM}_{\mathrm{txdcr}}}. \tag{16b}$$

Figure 5 displays the ratio of the SNRs as a function of window length for two different bandwidths. Free parameters were set to typical values, including a scatterer diameter of 100 μm, a center frequency of 5 MHz ($ka \approx 1$), and a reference waveform number effectively approaching infinity. Sample waveform number was restricted to one by the identical resolution condition. As before, the discontinuity evident in both graphs is a result of the discrete nature of the summations in Eq. (14). Although the ratio appears to be independent of window size, increasing the bandwidth from 3 to 5 MHz, improves the value. Figure 6 is a plot of the SNR ratio versus bandwidth for conditions identical to those above (fixed window length = 10 mm). Notice that the ratio increases substantially with increasing bandwidth, however, the bandwidths necessary to produce values approaching one are well above current technical limits.

VI. CONCLUSION

Expressions for the theoretical variance of backscatter coefficient and scatterer size estimates were derived. Both agreed well with experimental results. The variance of backscatter estimates was found to scale directly with the square of the backscatter coefficient being measured, and inversely with the number of power spectra used to generate estimates. The variance of size estimates decreased with increasing values of bandwidth, number of sample and reference power spectra, data segment length, and *ka*.

Although the feasibility of generating size estimates and images using a reference phantom method to estimate backscatter has been established, improvements in transducer bandwidth are necessary for performance to approach that of B-mode imaging. As a result, size imaging is most beneficial when knowledge of physical structure is necessary, or B-mode contrast is low, which occurs when scattering strength contrast and size contrast offset one another.

ACKNOWLEDGMENTS

The authors would like to extend thanks to Quan Chen, Yadong Li, Fang Dong, and Thaddeus Wilson for their technical assistance. This work was supported in part by NIH grants No. R01CA39224 and No. T32CA09206.

[1] M. Insana, Int. Rev. Exp. Pathol. **36**, 73 (1996).
[2] M. Insana and T. Hall, Ultrason. Imaging **12**, 245 (1990).
[3] M. Insana, T. Hall, J. Wood *et al.*, Invest. Radiol. **28**, 720 (1993).
[4] T. Hall, M. Insana, L. Harrison *et al.*, Ultrasound Med. Biol. **22**, 987 (1996).
[5] M. Insana and T. Hall, Phys. Med. Biol. **35**, 1373 (1990).
[6] M. Insana, R. Wagner, D. Brown *et al.*, J. Acoust. Soc. Am. **87**, 179 (1990).
[7] M. Insana, T. Hall, and L. Cook, IEEE Trans. Ultrason. Ferroelectr. Freq. Control **41**, 714 (1994).
[8] J.-F. Chen, J. Zagzebski, F. Dong *et al.*, Med. Phys. **25**, 648 (1998).
[9] P. Chaturvedi and M. Insana, J. Acoust. Soc. Am. **100**, 392 (1996).
[10] F. Lizzi, E. Feleppa, M. Astor *et al.*, IEEE Trans. Ultrason. Ferroelectr. Freq. Control **44**, 935 (1997).
[11] M. Insana and D. Brown, in *Ultrasonic Scattering in Biological Tissues*, edited by Kirk Shung (CRC Press, Boca Raton, 1993), p. 75.
[12] P. Bevington and K. Robinson, *Data Reduction and Error Analysis for the Physical Sciences*, 2nd ed. (McGraw-Hill, New York, 1992).
[13] J. Faran, J. Acoust. Soc. Am. **23**, 405 (1951).
[14] R. Wagner, M. Insana, and S. Smith, IEEE Trans. Ultrason. Ferroelectr. Freq. Control **35**, 34 (1988).
[15] When using sample and reference waveforms from the same medium, the value chosen for attenuation in the simulation code is actually irrelevant when estimating backscatter because the code does not include an additive noise term due to the measurement system.
[16] E. Feleppa, F. Lizzi, D. Coleman *et al.*, Ultrasound Med. Biol. **12**, 623 (1986).
[17] M. Oelze and W. O'Brien, Jr., J. Acoust. Soc. Am. **112**(6), 3053 (2002).
[18] L. X. Yao, J. Zagzebski, and E. Madsen, Ultrason. Imaging **12**, 58 (1990).